ECCM21

02-05 July 2024 | **Nantes - France**

Proceedings of the 21st European Conference on Composite Materials

Vol 2

Material science

WWW.ECCM21.ORG

UNDER THE PATRONAGE OF:

ESCM European Society For Composite Materials

Association pour les Matériaux Composites AMAC

EuCIA The European Voice of Composites

WITH THE SUPPORT OF:

RÉGION PAYS DE LA LOIRE

ORGANIZED BY:

CENTRALE NANTES

Nantes Université

SUPPORTING PARTNER:

JEC CONNECTING THE WORLD WITH COMPOSITES

Edited by:

Prof. Christophe BINETRUY
ECCM21 Conference Chair
Institute of Civil Engineering and Mechanics (GeM)
Centrale Nantes
Nantes Université

Prof. Frédéric JACQUEMIN
ECCM21 Conference Co-Chair
Institute of Civil Engineering and Mechanics (GeM)
Nantes Université

Published by:

The European Society for Composite Materials (ESCM) and the Ecole Centrale de Nantes.

©2024 ECCM21/The publishers
The Proceedings are published under the CC BY-NC 4.0 license in electronic format only, by the Publisher. The CC BY-NC 4.0 license permits non-commercial reuse, transformation, distribution, and reproduction in any medium, provided the original work is properly cited. For commercial reuse, please contact the authors. For further details please read the full legal code at:
http://creativecommons.org/licenses/by-nc/4.0/legalcode

These Proceedings have an ISBN (owned by the Publisher) and a DOI (owned by the Ecole Centrale de Nantes).

ISBN: 978-2-912985-01-9
DOI: 10.60691/yj56-np80

The Authors retain every other right, including the right to publish or republish the article, in all forms and media, to reuse all or part of the article in future works of their own, such as lectures, press releases, reviews, and books for both commercial and non-commercial purposes.*

Disclaimer:

The ECCM21 organizing committee and the Editors of these proceedings assume no responsibility or liability for the content, statements and opinions expressed by the authors in their corresponding publication.

Editorial

This collection contains the proceedings of the 21st European Conference on Composite Materials (ECCM21), held in Nantes, France, July 2-5, 2024. ECCM21 is the 21st in a series of conferences organized every two years by the members of the European Society of Composite Materials (ESCM). As some of the papers in this collection show, this conference reaches far beyond the borders of Europe.

The ECCM21 conference was organized by the Nantes Université and the Ecole Centrale de Nantes, with the support of the Research Institute in Civil and Mechanical Engineering (GeM).

Each volume gathers contributions on specific topics:

Vol 1. Industrial applications
Vol 2. Material science
Vol 3. Material and Structural Behavior – Simulation & Testing
Vol 4. Experimental techniques
Vol 5. Manufacturing
Vol 6. Multifunctional and smart composites
Vol 7. Life cycle performance
Vol 8. Special Sessions

Nantes, the birthplace of the novelist Jules Verne, is at the heart of this edition, as are the imagination and vision that accompany the development of composite materials. They are embodied in the work of numerous participants from the academic world, but also of the many industrialists who are making a major contribution to the development of composite materials. Industry is well represented, reflecting the strong presence of composites in many application areas.

With a total of 1,064 oral and poster presentations and over 1,300 participants, the 4-day event enabled fruitful exchanges on all aspects of composites. The topics that traditionally attracted the most contributions were fracture and damage, multiscale modeling, durability, aging, process modeling and simulation and additive manufacturing.

However, the issues of energy and environmental transition, and more generally the sustainability of composite solutions, logically appear in this issue as important contextual elements guiding the work being carried out. This includes bio-sourced composites, material recycling and reuse of parts, the environmental impact of solutions, etc.

We appreciated the high level of research presented at the conference and the quality of the submissions, some of which are included in this collection. We hope that all those interested in the progress of European composites research in 2024 will find in this publication sources of inspiration and answers to their questions.

Prof. Christophe BINETRUY
ECCM21 Conference Chair
Institute of Civil Engineering and Mechanics (GeM)
Centrale Nantes
Nantes Université

Prof. Frédéric JACQUEMIN
ECCM21 Conference Co-Chair
Institute of Civil Engineering and Mechanics (GeM)
Nantes Université

Under the Patronage of:

ESCM
European Society For Composite Materials

Association pour les Matériaux Composites

EuCIA
The European Voice of Composites

Organized by:

CENTRALE NANTES

Nantes Université

With the support of:

RÉGION PAYS DE LA LOIRE

Supported by:

EMC2

JEC
CONNECTING THE WORLD WITH COMPOSITES

Sponsored by:

Bronze Partner:

BRUKER

INSTRON

MatchID
Metrology beyond colors

Other partners:

CAPACITÉS
De la recherche à l'innovation

CARBON AXIS

CETIM

Depestele

EikoSim

ELSEVIER

FAIRMAT

metravib
material testing

NOVITOM

Quantiflex
simulations

Surface Measurement Systems
World Leader in Sorption Science

Hosting Organizations

Conference chairs

Prof. Christophe BINETRUY
ECCM21 Conference Chair
Institute of Civil Engineering and Mechanics (GeM)
Centrale Nantes
Nantes Université

Prof. Frédéric JACQUEMIN
ECCM21 Conference Co-Chair
Institute of Civil Engineering and Mechanics (GeM)
Nantes Université

International Scientific Committee

Malin Akermo (Sweden)
Remko Akkerman (Netherlands)
Andrey Aniskevich (Latvia)
Leif Asp (Sweden)
Emmanuel Baranger (France)
Janice Barton (UK)
Johnny Beaugrand (France)
Andrea Bernasconi (Italy)
Christophe Binetruy (France)
Thomas Bohlke (Germany)
Alain Bourmaud (France)
Nicolas Boyard (France)
Joël Breard (France)
Richard Butler (UK)
Baris Caglar (Netherlands)
Pedro Camanho (Portugal)
Pierpaolo Carlone (Italy)
Paolo Andrea Carraro (Italy)
Valter Carvelli (Italy)
Nuno Correia (Portugal)
Gergely Czél (Hungary)
Clemens Dransfeld (Netherlands)
Sylvain Drapier (France)
Klaus DRECHSLER (Germany)
Andreas ECHTERMEYER (Norway)
Paolo Ermanni (Switzerland)
Martin Fagerström (Sweden)
Ewald Fauster (Austria)
Julien Ferec (France)
Antonio Ferreira (Portugal)
Bodo Fiedler (Germany)
Stefanos Giannis (UK)
Nathalie Godin (France)
Carlos Gonzalez (Spain)
Sotirios Grammatikos (Norway)
Christoph Greb (Germany)
Emile Greenhalgh (UK)
Gianmarco Griffini (Italy)
Stephen Hallett (UK)
Nahiene Hamila (France)
Roland Hinterhoelzl (Austria)
Martin Hirsekorn (France)
Darko Ivančević (Hungary)
Frédéric Jacquemin (France)
Mikko Kanerva (Finland)
Luise Karger (Germany)
Vassilis Kostopoulos (Greece)
Theodosia Kourkoutsaki (Germany)
Thomas Kruse (Germany)
Ugo Lafont (France)
Jacques Lamon (France)
Frédéric Laurin (France)
Antoine Le Duigou (France)
Stepan Lomov (Belgium)
Theodoros Loutas (Greece)
Staffan Lundstrom (Sweden)
António Marques (Portugal)
David May (Germany)
Véronique Michaud (Switzerland)
Jörg Mussig (Germany)
Thomas Neumeyer (Germany)
Philippe Olivier (France)
Alkiviadis Paipetis (Greece)
Federico Paris (Spain)
Chung Hae Park (France)
John-Alan Pascoe (Netherlands)
Alessandro Pegoretti (Italy)
Ton Peijs (UK)
Rob Pierce (Denmark)
Soraia Pimenta (UK)
Silvestre Pinho (UK)
Gerald Pinter (Austria)
Connie Qian (UK)
Marino Quaresimin (Italy)
Andrew Rhead (UK)
Paul Robinson (UK)
Essi Sarlin (Finland)
Yentl Swolfs (Belgium)
Sofia Teixeira du Freitas (Netherlands)
Julie Teuwen (Netherlands)
Ole Thomsen (UK)
Stavros Tsantzalis (Greece)
Konstantinos Tserpes (Greece)
Albert Turon (Spain)
Julien van Campen (Netherlands)
Wim Van Paepegem (Belgium)
Anastasios Vassilopoulos (Switzerland)
Ignaas Verpoest (Belgium)
Michael Wisnom (UK)
Dimitrios Zarouchas (Netherlands)
Daiva Zeleniakiene (Lithuania)
Dan Zenkert (Sweden)

Local Organizing Committee

Suresh Advani
Romain Agogué
Sylvain Chataigner
Sébastien Comas-Cardona
Sofiane Guessasma
Suzanne Laïk
Philippe Le Bot
Mael Peron
Luisa Silva
Vincent Sobodka
Alexandre Ripoche
Elena Syerko

Table of Contents

Click on **CONTENTS** on the right side to return to the table of contents

AUTHORS'S INDEX | *COUNTRY*	TOPIC	ARTICLE TITLE	PAGE
ALIOTTA Laura | *ITALY*	Bio-composites	Investigation of novel poly(lactic acid) (PLA)/ Hazelnut Shell Powder biocomposites for 3D printing applications	454
AL-MAQDASI Zainab | *SWEDEN*	Bio-composites	Characterization and Performance Evaluation of Lignin-Modified Epoxy Resin for potential use in Natural Fiber Reinforced Composites	784
ANIŚKO Joanna | *POLAND*	Poster	The use of black tea waste as a thermo-oxidation stabilizer for polyethylene composites in rotational molding technology	35
ASANO Kazunori | *JAPAN*	Poster	Fabrication and Damping Capacity of Short Alumina Fiber and VGCF Hybrid Reinforced Aluminum Alloy Composites	203
ASSENHEIMER Sabrina | *SWEDEN*	Bio-composites	Improved curing and reduced moisture sensitivity of structural composites based on active cellulose nanofibril fibres and epoxy resin	396
BABA Haruya | *JAPAN*	Nanocomposites	Study on dispersion mixing of cellulose nanofiber reinforced polyvinyl chloride composite materials using a single screw extruder	239
BADE Raja | *GERMANY*	Bio-composites	Toward adhesives-free bio-based composites via uv-assisted interfacial cross-linking	492
BARCZEWSKI Mateusz | *POLAND*	Bio-composites	Process aspects of forming polyethylene-based composites filled with functional waste-plant fillers by rotational molding technology	133
BAUMANN Jonas-Rumi | *GERMANY*	Poster	Resources from sustainable land use for natural fibre composite injection moulding	498
BAVASSO Irene | *ITALY*	Bio-composites	Trade-off between performance and processability of PLA/ PBAT/PHBV-Flax composites: effect of flax fibers surface modification	42
BEHRENS Alexander | *GERMANY*	Poster	Towards improving the fibre-matrix adhesion in oleaginous flax fibre polylactide (PLA) composites	503
BLAL Abdelhadi | *CANADA*	Fibers & textiles	Increasing the tensile properties of a unidirectional/mat dry reinforcement for composite applications via the addition of nanocellulose combined with click chemistry modifications.	141
BORIUS Zoé | *FRANCE*	Matrix materials: polymers, metals, ceramics, concrete, geopolymer	Microstructural analysis and mechanical behaviour of oxide/oxide CMCs prepared by continuous tow impregnation	510
BOTTA Luigi | *ITALY*	Poster	Polymeric biocomposites from cactus pear by-products: utilizing glochids and peel for sustainable materials	247
BUGAUT Mathieu | *FRANCE*	Nanocomposites	Cellulose nanocrystals as reinforcements in thermoplastic composites: processing routes as key	518

Table of Contents

AUTHORS'S INDEX | *COUNTRY*	TOPIC	ARTICLE TITLE	PAGE
CAFARO Fabrizio | *ITALY*	Poster	Reduction of environmental impact of epoxy resins used in composite materials	524
CALABRESE Luigi | *ITALY*	Energy storage and harvesting	Mechanical and adsorption characterization of a calcium lactate/S-PEEK composite coating for thermochemical energy storage	253
CARVALHO TEIXEIRA Maria Helena | *PORTUGAL*	Bio-composites	Bio-based sandwich panels for sustainable building construction and rehabilitation	540
ÇELIK Murat | *UNITED KINGDOM*	Poster	Tailored Hybrid Composite Preforms by Automated Fibre Placement of Powder Epoxy-Based Towpregs	459
CHIANG Chin-Lung | *TAIWAN*	Poster	Preparation of a bio-inspired halogen-free flame retardant containing sugarcane bagasse, phosphorus and nitrogen through a hydrothermal method and its application in epoxy resin	1
CHIANG Yu-Chun | *TAIWAN*	Poster	Carbon nanofiber composites doped with different ZIF-8 nanoparticles for carbon dioxide capture	22
CORVO ALGUACIL Marina | *SWEDEN*	Fibers & textiles	Scaling up a Two-Step Pyrolysis of CFRP: Study of Validation and Robustness	260
DIETRICH Sarah | *GERMANY*	Foams, cellular and lattice materials	Investigation of the thermoviscoelastic behaviour of a closed-cell polymer structural foam under pressure for processing in hybrid LCM processes	548
DRANSFELD Clemens | *NETHERLANDS*	Matrix materials: polymers, metals, ceramics, concrete, geopolymer	Controlling Dual scale Morphologies of Epoxy and Poly(ether imide) towards improved Interlayer toughening of composites.	555
GACON Damien | *FRANCE*	Matrix materials: polymers, metals, ceramics, concrete, geopolymer	Experimental and computational study of the polymerization kinetics of a reactive acrylic thermoplastic resin	49
GARCIA-MAYO Susana | *BELGIUM*	Fibers & textiles	Do basalt fibers corrode in highly alkaline environments?	561
GARING Clare | *BELGIUM*	Bio-composites	Effect of Moisture Cycling Duration and Temperature on the Strengthening and Stiffening of Cycled Flax Fibres	345
GIGANTE Vito | *ITALY*	Bio-composites	Performance Evaluation of Novel Biobased Thermoplastic Composites Reinforced with different plies of Hemp Fabrics	233
GOH Xue Yang | *SINGAPORE*	Poster	Advanced Polyethylene Terephthelate (PET) Aerogels and their Composites from Plastic Waste for Load Bearing Thermal Insulation and Radiative Cooling Applications	568
GRAUPNER Nina | *GERMANY*	Bio-composites	Fibrillationmproving the fibre/matrix adhesion of Lyocell fibres for use in short fibre-reinforced and 3D-printed composites	404
HAOHUI Hao | *FRANCE*	Matrix materials: polymers, metals, ceramics, concrete, geopolymer	Micro-zone and macro mechanical behavior of SiCf/Si3N4 composite modified by intra-bundle matrix	57

Table of Contents

AUTHORS'S INDEX | *COUNTRY*	TOPIC	ARTICLE TITLE	PAGE
HAO P. | *BELGIUM*	Matrix materials: polymers, metals, ceramics, concrete, geopolymer	Advanced Characterization and Thermomechanical Modeling of PP/PE Blends for Innovations in Recycled Composites	576
HARRELL Timothy | *UNITED KINGDOM*	Fibers & textiles	Investigating Lightning-Induced Damage: A Comparative Analysis of CFRP Specimens Subjected to Varied Strikes, Inductance, and Charge	268
HEIDARIAN Pejman | *FRANCE*	Bio-composites	b-phase Induced Poly(3-hydroxybutyrate-co-3-hydroxyvalerate) Nanofibers Synergized by Vapor Solvent Interfiber Welding for Self-reinforcing Effect	466
HIGUMA Daisuke | *JAPAN*	Manufacturing of short & long fiber composites	Study on dispersion mixing of nanosilica by extensional flow using a twin-screw extruder	274
HU Jian | *FRANCE*	Poster	Characterization and optimization of the forming behavior of the textile preforms by trimming	282
IVANOV Dmitry S. | *UNITED KINGDOM*	Hybrid composites	Metal-epoxy-matrix carbon-fibre hybrids for functional and structural applications	583
IVARS Jean | *FRANCE*	Fibers & textiles	Influence of carding parameters on the mechanical properties of carded recycled carbon fibers with a Weibull statistical approach	209
KAGYUNG Bibhuti Bikash | *INDIA*	Poster	Effect of Carbon Black as a Conductive Filler on The Electrical, Thermal and Mechanical Property of Epoxy	590
KAITHERI Amruth | *ITALY*	Nanocomposites	Silver phosphate–bacterial cellulose nanocomposites as visible light photocatalyst for wastewater purification	598
KIM Kyeongmin | *SOUTH KOREA*	Poster	Modification of Thermoplastic Starch with Chain Extenders to its thermal, barrier and mechanical properties	65
KOMYO Takeru | *JAPAN*	Poster	First-principles study on the mechanical properties of citric acid-modified cellulose composite polymeric materials	289
LABASTIE Karine | *FRANCE*	Poster	Influence of the prepreg morphology on the properties of OOA consolidated composites	605
LALLE Ginevra | *ITALY*	Nanocomposites	Plasma-enhanced growth of carbon nanotubes with in-situ catalyst generation for multifunctional basalt fabrics	474
LEACH David | *UNITED STATES OF AMERICA*	Matrix materials: polymers, metals, ceramics, concrete, geopolymer	The Transition from Thermoset to Thermoplastic Composites	352
LI Carina Xiaochen | *UNITED STATES OF AMERICA*	Karl Schulte Session	Electrical and Thermal Properties of High Volume Fraction Aligned Carbon-Nanotube/Bismaleimide Nanocomposite Laminates	360
LINDERBÄCK Paula | *FINLAND*	Poster	Common reed as novel Biosource composite production	217
LIU Jinrong | *JAPAN*	Matrix materials: polymers, metals, ceramics, concrete, geopolymer	Turning machinability of cast aluminum alloy matrix composites	294
LUCIJA Pustahija | *AUSTRIA*	Poster	Surface functionalized pyrolytic carbon composites for wastewater treatment	613

Table of Contents

AUTHORS'S INDEX | *COUNTRY*	TOPIC	ARTICLE TITLE	PAGE
LU Zhehong | *UNITED KINGDOM*	Graphene, graphene-based composites	Functionalized graphene oxide/ EPDM composites with enhanced barrier properties	149
MACCAFERRI Emanuele | *ITALY*	Nanocomposites	Rubbery nanofibers via blend and emulsion electrospinning for structural modification of composite laminates	412
MADI Salaheddine | *BELGIUM*	Fracture and damage	Digital volume correlation analysis of thermoplastic carbon fibre sheet moulding compound composites	419
MCBEAN Melany | *UNITED KINGDOM*	Matrix materials: polymers, metals, ceramics, concrete, geopolymer	Comparison of high-performance matrix materials as candidates for additive processes	619
MITTELHAUS Janina | *GERMANY*	Matrix materials: polymers, metals, ceramics, concrete, geopolymer	Understanding the scale dependent ductility of epoxies	300
MOGHIMIARDEKANI Ali | *BELGIUM*	Bio-composites	The effect of fibre alignment on the fatigue behaviour of unidirectional flax fibre composites	627
NAYAK Jasomati | *INDIA*	Poster	Advancements in MWCNT-Enhanced Porous Thermoplastic Elastomeric Composite Foam for Electromagnetic Radiation Suppression	308
NGUYEN Nguyen Le Thao | *AUSTRALIA*	Fibers & textiles	The effect of polymer composition on the fibre production process and final mechanical properties	8
NOBRE Luís | *PORTUGAL*	Poster	Multiscale Natural Fiber-Reinforced Thermoplastic Composites Towards Enhanced Mechanical Performance	479
NOUR EL DEIN Ali Al Hadi | *FRANCE*	Bio-composites	Investigating the influence of flax shives fractionation on tensile properties of thermoplastic biocomposites using 3D microstructural analysis	632
NOVOTNÁ Jana | *CZECH REPUBLIC*	Poster	Applications of plasma treatment of recycled carbon fibres	425
NUKUI Yosuke | *JAPAN*	Poster	Approach to reduce environmental impact of fiber reinforced plastic by using Flat glass fiber	640
NURSEL Nursel | *NETHERLANDS*	Hybrid-Molding Technologies for Thermoplastic Composites	Hybrid composite structures of thermoset composites and thermoplastics produced through overmolding	155
NUSS Dominik | *GERMANY*	Fibers & textiles	Integral woven near-net-shape fabrics for shell-shaped FRP components	71
OH Yoon Min | *SOUTH KOREA*	Poster	The manufacturing of auxetic and conductive foam composites utilizing a novel kinetic model	163
OMICHI Hironobu | *JAPAN*	Matrix materials: polymers, metals, ceramics, concrete, geopolymer	Simulating the crystal growth of PPS using molecular dynamic	645
PECHOČIAKOVÁ Miroslava | *CZECH REPUBLIC*	Poster	Change in dynamic-mechanical properties of PLA film due to UV radiation	776
PEIGNON Axel | *FRANCE*	Poster	Influence of the number of plies on the Stiffness of Laminated Veneer Lumber	316

Table of Contents

AUTHORS'S INDEX | *COUNTRY*	TOPIC	ARTICLE TITLE	PAGE
PERERA Yasith Sanura | *UNITED KINGDOM*	Graphene, graphene-based composites	Mechanical properties of 3D-printed PLA composites reinforced with carbon-based fillers	652
PERRIN Théo | *FRANCE*	Fibers & textiles	Bending behavior of fabrics made of flax/PA12 comingled yarns	660
PRAPAVESIS Alexandros | *BELGIUM*	Hybrid composites	Designing Stiff and Tough Biocomposites by Hybridization of Flax and Silk Fibres: Scrutinizing the Effects of Fibre Ratio and Laminate Lay-up Configuration	322
PRUNIER Clément | *FRANCE*	Hybrid composites	Enhancing the mechanical performance of locally sourced wood-based plywood through hybridization with natural fibre composites	668
REDONNET Juliette | *FRANCE*	Fibers & textiles	Relation between Process, Microstructure and Mechanical Properties of a continuous ceramic fiber under development	330
RESTIF Noé | *FRANCE*	Interfaces	From the PEEK microstructure at welded interfaces to the mechanical properties of thermoplastic composites manufactured by a Laser-Assisted Tape Placement process	674
RODRÍGUEZ Paula | *SPAIN*	Poster	Advanced lightweight of battery tray for electric vehicles (ALBATROSS Project)	682
RONCONI Giulia | *ITALY*	Bio-composites	Effectiveness of enzymatic treatment on a continuous flax fibre reinforced composites	170
SAITO Seita | *JAPAN*	Karl Schulte Session	The effects of processing/curing temperature and viscosity of epoxy resins on the flexural/tensile properties of GNP-epoxy resin nanocomposites	79
SAMKOVÁ Alžbeta | *CZECH REPUBLIC*	Poster	Change in the physical properties of plaster composites reinforced with carbon fibers.	87
SCHNELL Carla Natali | *LUXEMBOURG*	Bio-composites	Optimizing Interfacial Shear Strength in Bamboo Fiber Composites Through Polydopamine Surface Modification	690
SHAFFER Milo S. P. | *UNITED KINGDOM*	Graphene, graphene-based composites	Multiscale and multidimensional characterisation of graphene-related nanomaterials and nanocomposites	698
SIEGMUND Frederik | *GERMANY*	Hybrid composites	Additive manufacturing and mechanical testing of interpenetrating metal composites	433
SONG Xinyi | *CHINA*	Fibers & textiles	Multiscale modeling of 3D braided CMCs with void defects using unsupervised machine learning	225
SORZE Alessandro | *ITALY*	Bio-composites	Development of Xanthan-Based Bio-Composites for the Production of Topsoil Covers	14
SZCZEPANIAK Robert | *POLAND*	Poster	Influence of the use of additive phase change materials in the matrix of fibre composites on the ablative properties	337
TANAKA Mototsugu | *JAPAN*	Bio-composites	Optimization of Microstructural Factors of HAp/collagen Composite Fiber Bundles as Artificial Bone Unit	706
TANIGUCHI Hiroya | *JAPAN*	Poster	Evaluation on ablation behavior of ZrO2 nanoparticle-dispersed porous carbon composites	441
TAO Yunyun | *AUSTRALIA*	Fibers & textiles	Eco-friendly Surface Modification of Carbon Fibres for Application in Cement-based Composites	95

Table of Contents

AUTHORS'S INDEX | *COUNTRY*	TOPIC	ARTICLE TITLE	PAGE
TARIN Hamza | *FRANCE*	Matrix materials: polymers, metals, ceramics, concrete, geopolymer	Dynamics of Moisture Diffusion in Epoxy Resin: Empirical and Simulated Insights into Absorption-Desorption Behavior	714
TERRASI Giovanni Pietro | *SWISS*	Multiscale modeling	Characterization and modelling of tensile damage in unidirectional all-carbon hybrid laminates	176
TERZOPOULOU Zoi | *GREECE*	Poster	Composite hydrogels based on modified chitosan with haemostatic and antimicrobial activity	367
THOMASON James | *UNITED KINGDOM*	Interfaces	A new method to prepare more representative coated glass fibres for screening and development of sizings at the laboratory scale	103
TOMKOVA Blanka | *CZECH REPUBLIC*	Poster	Determination of reinforcing fiber fineness – comparison of measurement methods, their accuracy, advantages and limitations	764
TRAUTH Anna | *GERMANY*	Poster	Sustainability of hybrid materials: Approaches to manufacture and characterize fiber-metal laminates with activatable interfaces	722
TZATZADAKIS Vasileios | *GREECE*	Poster	MXenes Embedded PLA Nanocomposites for Challenging Versatile Applications	730
VALETTE Julien | *FRANCE*	Poster	Experimental investigation on dry or impregnated tow mechanical behaviour under multiaxial loads	770
VARLEY Russell J. | *AUSTRALIA*	Matrix materials: polymers, metals, ceramics, concrete, geopolymer	Partially bio-derived phosphazene-tannic acid microspheres as fire retardant additives for an epoxy tannic acid resin system.	737
VATS Shameek | *LUXEMBOURG*	Fibers & textiles	Electrospun CNC-reinforced Composite Fibers for Advanced 3D Printing Composite Applications	744
WANG Junhao | *JAPAN*	Karl Schulte Session	Large-area high thermal conductivity graphite film easily produced by mechanical exfoliation of natural graphite using a three-roll mill	183
WANG Xinlei | *CHINA*	Nanocomposites	Structure and electromagnetic properties of Ti3C2Tx MXene derived from Ti3AlC2 with different microstructures	111
WANG Zijian | *CANADA*	Fibers & textiles	Mechanical characterization of thermoplastic polymers used in fused filament fabrication reinforced by recycled glass fiber epoxy composite	752
WEI Ziyue | *UNITED KINGDOM*	Fibers & textiles	Miss	119
WOLLERT Lars | *GERMANY*	Poster	Saxophone and clarinet reeds, made from bio-based materials in a thermoplastic pultrusion process	190
XINDI Hu | *JAPAN*	Nanocomposites	Preparation and Characterization of Carbon Nanotubes Reinforced Polyamide 66 Nanocomposites	127
YAMAMOTO Go | *JAPAN*	Karl Schulte Session	In-situ X-ray Nanoimaging of Fracture Mechanisms in CNT Yarn Reinforced Plastic Composites	373
ZAMBOULIS Alexandra | *GREECE*	Poster	Tannic acid: An interesting natural filler for HDPE	449

Table of Contents

AUTHORS'S INDEX | *COUNTRY*	TOPIC	ARTICLE TITLE	PAGE
ZANELLI Marco | *ITALY*	Hybrid composites	Characterization of mechanical properties of a 3d-printed continuos basalt fiber-reinforced composite	**198**
ZECCHI Silvia | *ITALY*	Fibers & textiles	Optimizing of stabilization and carbonization processes for sustainable lignin-derived carbon fiber production	**378**
ZELENIAKIENE Daiva | *LITHUANIA*	Nanocomposites	Novel layered double hydroxide/epoxy nanocomposites for corrosion protective coatings	**30**
ZHANG Zhenghao | *UNITED KINGDOM*	Nanocomposites	Investigation of the piezoresistivity of CNT/PLA nanocomposite with an improved solvent-casting process	**487**
ZUBAIR Junaid | *FINLAND*	Poster	Finite element analysis of micro peel test for evaluating pulp fibre interfacial adhesion	**386**
ZUKIENE Kristina | *LITHUANIA*	Interfaces	Wettability and interfacial properties of basalt fibres/ biobased epoxy composites with star-like poly(butyl methacrylate)-poly(glycidyl methacrylate) block copolymer additives	**760**

PREPARATION OF A BIO-INSPIRED HALOGEN-FREE FLAME RETARDANT CONTAINING SUGARCANE BAGASSE, PHOSPHORUS AND NITROGEN THROUGH A HYDROTHERMAL METHOD AND ITS APPLICATION IN EPOXY RESIN

Cing-Yu Ke[1], Ming-Yuan Shen[2] and Chin-Lung Chiang[3*]

[1] Department of Safety, Health and Environmental Engineering, Hung-Kuang University, No. 1018, Sec. 6, Taiwan Boulevard, Shalu Dist., Taichung City 433304, Taiwan, R.O.C.
Email: n74731@gmail.com
[2] Department of Mechanical Engineering, National Chin-Yi University of Technology, No.57, Sec. 2, Zhongshan Rd., Taiping Dist., Taichung 411030, Taiwan, R.O.C.
Email: myshen@ncut.edu.tw
[3] Green Flame Retardant Material Research Laboratory, Department of Chemical and Materials Engineering, National Chin-Yi University of Technology, No.57, Sec. 2, Zhongshan Rd., Taiping Dist., Taichung 411030, Taiwan, ROC
Email: dragon@ncut.edu.tw

Keywords: hydrothermal method, sugarcane bagasse, epoxy, halogen-free flame retardant, ammonium dihydrogen phosphate (ADP)

Abstract
Bagasse- ammonium dihydrogen phosphate (ADP) flame retardant was added to an epoxy resin to prepare epoxy/bagasse-ADP composites, an effective flame-retarding composite material. Adding bagasse-ADP increased the thermal stability and flame retardancy of the composite materials compared with that of pure epoxy. For the material with 30 wt% added bagasse-ADP, the char yield was 32.3 wt%, which was 18.2 wt% higher than that of pure epoxy (14.1 wt %). In addition, the LOI increased from 21 to 30 %, and the UL-94 classification improved from “Fail” to “V-0.” This performance was attributed to the nitrogen, phosphorus, and silicon content of the flame retardant.

1. Introduction

Epoxy is a common thermosetting resin that has superb properties, such as excellent chemical corrosion resistance, low shrinkage rate after curing, and outstanding electrical performance [1-2]. Consequently, epoxy is often applied in fiber-reinforced composite materials, adhesives, matrix, and encapsulation materials. However, epoxy is very flammable and it emits large amounts of toxic gases and smoke during combustion, which greatly limits its usage in certain applications, such as electrical and electronic equipment [3-4].

Recently, increasing attention has been paid to environment protection and human health. The toxicity and environmental problems of conventional halogen flame retardants have resulted in a demand to replace them with halogen-free flame retardants [5-6]. Bio-based, green, flame-retardant composite materials have thus been promoted worldwide and include agricultural waste, such as straw, rice hulk, and sugarcane bagasse. Sugarcane bagasse is an easily accessible agricultural waste that can strengthen the mechanical properties and physical properties of materials while reducing their combustibility and avoiding the use of chemical flame retardants. Therefore, bio-based composite materials merit further

academic research and could be applied in fields such as optics, electronics, energy, smart coatings, fuels, flame retardants, and composite materials [7].
Intumescent flame retardant (IFR) is a composite flame retardant, which has attracted more and more attention due to its good compatibility, excellent fire resistance, low smoke, low toxicity, and environmental protection [8]. The intumescent flame retardant is mainly composed of three elements, which are acid source, gas source (foaming agent), and carbon source. When it was decomposed by heat, the acid source which contained phosphorus will decompose firstly, and then react with the carbon source to form a stable viscous cross-linked carbonaceous material. The foaming agent which contained nitrogen releases inert or non-combustible gases through decomposition. These gases will be trapped in the carbon, thereby forming an expanded char layer of foamed structure formed by carbon. The expansion volume change may reach tens to hundreds of times, thereby protecting the expanded carbonized layer of the underlying polymer. These expanded carbonized layers can effectively reduce heat transfer and isolate oxygen from the matrix and prevent gas generated by pyrolysis from escaping to protect the polymer matrix to achieve flame retardant effect [9]. In this study, we use sugarcane bagasse as the carbon source of IFR. Sugarcane bagasse is mainly composed of cellulose. It can be used as a candidate of char-forming agent in IFR, which can replace the traditional, expensive and petroleum-based char source (pentaerythritol, PER) to relieve the crisis of shortage for petrochemical resources.
In this study, we use the hydrothermal method to prepare novel flame retardant containing bagasse, phosphorus and nitrogen, which the method is facile and effective. To the best of our knowledge, there is few relevant research on the preparation of halogen-free flame retardants using hydrothermal method. This study recycled and reused agricultural waste to prepare a intumescent flame retardant. This flame retardant was mixed with epoxy resin to prepare a composite material containing polymer matrix with improved thermal properties and flame retardancy, achieving a novel application of such macromolecules. This study is in line with the concept of circular economy and sustainability

2. Experimental

2.1. Materials

DGEBA type epoxy resin was supplied by Nan-Ya Plastics Corporation, Taipei, Taiwan. 4, 4'-Diaminodiphenylmethane (DDM) as curing agent for epoxy resin was purchased from Sigma-Aldrich Co. Ltd, Irvine, UK. Bagasse was obtained from local markets in Taiwan. The size of the crushed bagasse was 0.053 mm. 85 wt% phosphoric acid was purchased from Taiwan Lianhua Factory Co., Ltd. 30 wt% ammonia solution was purchased from Aike Chemical Co., Ltd., Miaoli, Taiwan. Anhydrous stabilized tetrahydrofuran (THF) was purchased from Lancaster Co., Morecambe, Lancashire, UK.

2.2. Preparation of epoxy/bagasse-ADP composites

Sugarcane bagasse was crushed, washed in 100 ºC deionized (DI) water three times, filtered three times, and then placed in a 100 ºC oven for dehydration as shown in scheme 1. Next, 1.82 g sugarcane bagasse was placed in a 100 mL serum bottle, and 20 mL of DI water was added to the serum bottle to form solution A. Afterward, 3.3 mL of phosphoric acid was dripped in solution A and mixed for 10 minutes before 3.73 ml of ammonia water was dripped into solution A. The solution reacted for 1 hour at 60 ºC. Solution A was then poured into a polytetrafluoroethylene container and placed into an autoclave, which was heated in an oven at 100 ºC for 2 hours. The solution was removed from the oven and cooled at room temperature for 2 hours, poured in an evaporating dish, and then heated in the oven again at 100 ºC for 4 hours for drying, finally obtaining the bagasse–ammonium dihydrogen phosphate (bagasse-ADP) flame retardant, as depicted in scheme 2. An appropriate amount of bagasse-ADP powder was poured into 10 g of epoxy, heated to 60 ºC, and mixed for 2 hours. Next, 2.75 g of 4, 4'-bis-(diaminodiphenyl) methane was poured into the mold as a hardener, and the mold was placed at room temperature for 24 hours. Subsequently, the mold was placed in a 60 ºC oven, and the temperature was increased by 20 ºC every 2 hours until it reached 160 ºC to form the composite material, as depicted in scheme 3. The produced samples were denoted epoxy/bagasse-ADP x%, where *x* denotes the weight percent of bagasse-ADP in the composite.

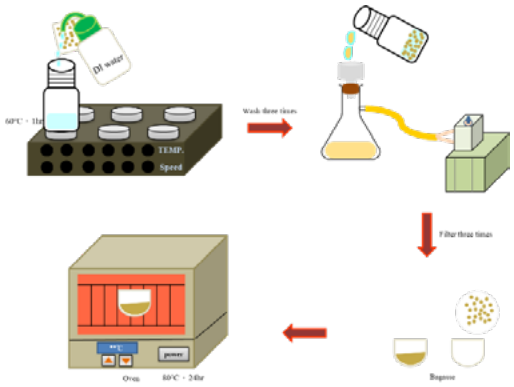

Scheme 1 Washing sugarcane bagasse

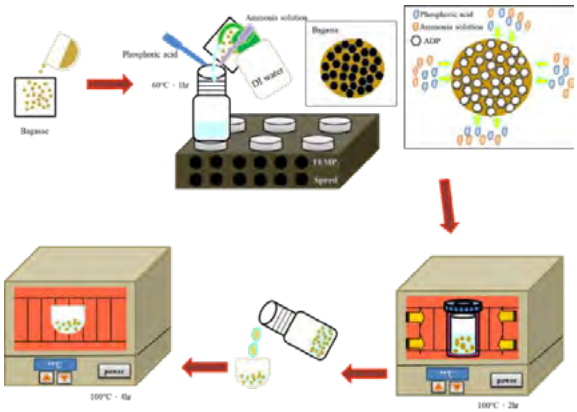

Scheme 2 Hydrothermal process

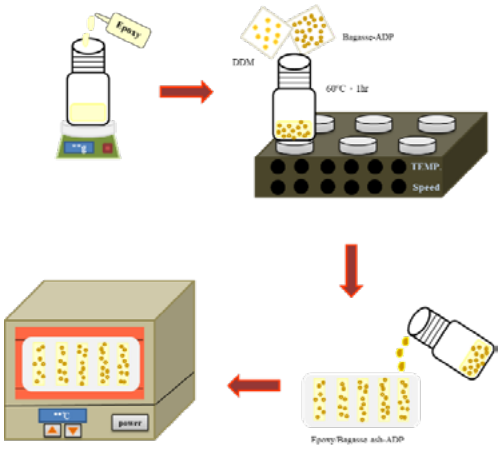

Scheme 3 The preparation of Epoxy/Bagasse-ADP composites

2.3 Measurements

The thermal degradation of samples were detected by a Perkin Elmer TGA 7 at a heating rate of 10 °C/min ranged from 30 to 800 °C, and a dynamic flow was 30 mL/min under N_2. 6-10mg samples were measured to plot weight loss/temperature curves.

An oxygen index meter (ATLAS Fire Science Product, U.S.A) was used to study LOI following the ASTM D 2836 standard. Each sample was prepared into 150 × 6.5 × 3 mm^3.

UL-94 ratings of samples were tested using a vertical flame tester (ATLAS Fire Science Product, U.S.A) based on the ASTM D 3801 standard. Each sample was tailored into 127 × 12.7 × 3 mm^3, vertically ignited for 10 s to get t_1, and ignited again for 10 s to get t_2.

3. Results and discussion

3.1 Interaction between polymer matrix and flame retardant

To further investigate the interaction between epoxy matrix and bagasse-ADP flame retardant during pyrolysis, this study calculated the mass of the epoxy/bagasse-ADP composite material, W_c, as follows:

$$W_c=\chi_1*W_1+\chi_2*W_2\text{……..(1)}$$

where χ_1 and χ_2 represent the mass fractions of epoxy and bagasse-ADP in the composite material, respectively. W_1 and W_2 represent the epoxy and bagasse-ADP remaining mass during pyrolysis [10]. The theoretical and experimental thermogravimetric analysis (TGA) curves were presented in Fig. 1. At the low temperature stage below 400 ℃, the phosphorus component will start to degrade to produce phosphoric acid, which acts as a catalyst and quickly forms char to protect the polymer matrix [11]. As the amount of bagasse-ADP in the composite was increased from 5 wt% to 30 wt%, the char yield in the experimental TGA curve was higher than in the theoretical TGA curve at temperatures above 400 ºC, particularly for epoxy/bagasse-ADP 30% (the char yield of the experimental TGA curve was 15.4% higher than that of the theoretical TGA curve). Hence, the flame retardant interacted with the polymer matrix, and this interaction facilitated the formation of char, which improved the thermal stability.

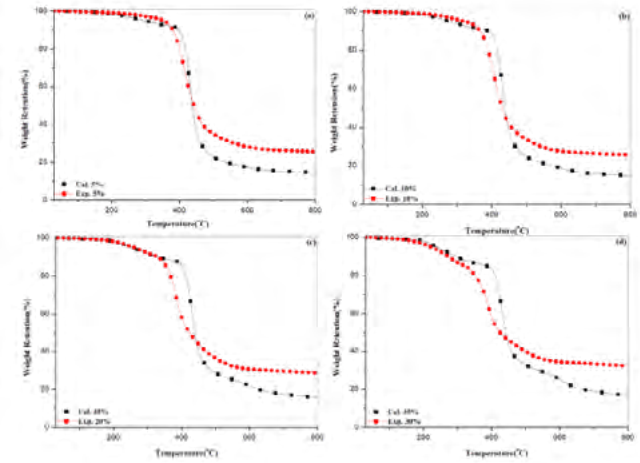

Fig. 1 Comparison of the experimental and calculated TGA curves for epoxy/bagasse-ADP (a) 5%, (b) 10%, (c) 20%, and (d) 30% composites.

3.2 Thermal stability of the composites

TGA was performed under a nitrogen atmosphere at 30–800 ºC for both pure epoxy and epoxy/bagasse-ADP composites to reveal their thermal stability. The TGA curves demonstrates the thermal stability, and the derivative TGA curves reveal the pyrolysis rate; these are presented in Fig. 2 and Fig. 3, respectively. Pyrolysis metrics, namely initial degradation temperature (IDT) at which the weight loss of the sample reaches 10% (Td10), the temperature at which the maximum thermal degradation rate occurs (Tmax), the maximum thermal degradation rate (Rmax), and char yield, are listed in Table 3.

Fig. 2, Fig. 3, and Table 1 reveal that the Td10 of all epoxy/bagasse-ADP composites were lower than that of epoxy. The O=P–O bond of epoxy/bagasse-ADP was degraded more easily than the C–C bond of pure epoxy [16-17]. Pyrolysis at more than 100 ºC caused ADP to slowly release ammonia, and when the phosphoric acid in ADP was heated, it dehydrated and formed pyrophosphoric acid [12]. Therefore, the Td10 of pure epoxy was 400 ºC, whereas the Td10 of epoxy/bagasse-ADP 30% was much lower at 264 ºC. The epoxy/bagasse-ADP composite also had a much lower Rmax (−11.3 wt%/min) compared with pure epoxy (−33.4 wt%/min). Its maximum char yield (32.3 wt%) was also much greater than that of epoxy (14.1 wt%) because the phosphorus in bagasse-ADP captured free radicals in the gas phase during pyrolysis. In addition, in the condensed phase, the phosphorus element catalyzed the formation of phosphine oxide, and the nitrogen elements within the bagasse-ADP released nonflammable gases during pyrolysis, such as NH3, thereby facilitating the expansion of the charred layer, preventing the

flame from burning further [13]. The cyclic structured rings of cellulose in the bagasse enabled the formation of char, and the resistance to oxidation of the charred layer blocked high-temperature combustion. The curves of pure epoxy and the composite materials were substantially different, indicating that adding bagasse-ADP improves the thermal stability of epoxy.

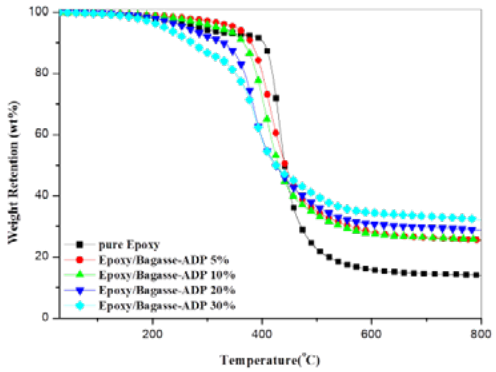

Fig. 2 TGA curves for pure epoxy and epoxy/bagasse-ADP composites under nitrogen.

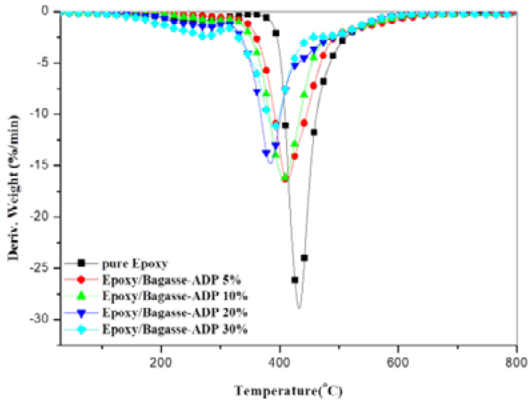

Fig. 3 Derivative curves of pure Epoxy and Epoxy/Bagasse-ADP composites in pyrolyzed under nitrogen.

Table 1 Thermal properties of epoxy and epoxy/bagasse-ADP composites.

Sample NO.	T_{d10} (ºC)	T_{max} (ºC)	R_{max} (wt%/min)	IPDT (ºC)	C.Y. (wt%)
pure Epoxy	400	430	-33.4	619	14.1
Epoxy/Bagasse -ADP 5%	377	412	-16.4	863	25.5
Epoxy/Bagasse -ADP 10%	362	406	-16.2	861	25.7
Epoxy/Bagasse -ADP 20%	318	384	-14.8	931	28.8
Epoxy/Bagasse -ADP 30%	264	389	-11.3	980	32.3

[a]T_{d10} is the temperature at which the weight loss of the sample reaches 10%.
[b]T_{max} is the temperature at which the maximum thermal degradation rate occurs.
[c]R_{max} is the maximum thermal degradation rate.

3.3 Flame retardancy of the composites

Table 2 presents the limiting oxygen index (LOI) and UL-94 vertical and horizontal test results for the epoxy/bagasse-ADP composites. The LOI of epoxy was 21%, indicating that epoxy is a flammable material. At the highest concentration of bagasse-ADP (30%), the LOI of the composite increased by 9%. Epoxy did not pass any UL-94 test and was therefore classified as "Fail." In addition, the epoxy had intense combustion during the test. Increasing the concentration of bagasse-ADP to 20 wt% achieved the "V-1" classification; the flame stopped after 8.8 and 3.8 seconds in the vertical and horizontal tests, respectively. Epoxy/bagasse-ADP 30% was classified as "V-0;" the flames stopped after 1.5 seconds for both tests, indicating that bagasse-ADP has excellent flame retardant performance. During pyrolysis, the phosphorus components in ADP captures free radicals generated by combustion in the gas phase, catalyzing the formation of char in the condensed phase. In addition, the nitrogen components in the composites released nonflammable gases during pyrolysis, expanding the charred layer and preventing further burning [14]. The benzene ring enabled the formation of char, producing a charred layer that blocked high-temperature combustion.
Table 2 reveals that the flame retardant effectivity (EFF) initially increased but then decreased as the amount of bagasse-ADP added was increased. Although epoxy/bagasse-ADP 30% was classified as flame retardant on the basis of its LOI, the EFF of epoxy/bagasse-ADP 5% was the highest, demonstrating superior flame retardant performance [15].

Table 2 Flame retardancy of epoxy/bagasse-ADP composites in terms of LOI and UL-94 results

Sample	UL-94				LOI	ΔLOI	P-content (wt %)	[b]EFF
	t_1(s)	t_2(s)	Ranking	Dripping				
pure Epoxy	[a]BC	-	Fail	No	21	0	0	0
Epoxy/Bagasse-ADP 5%	BC	-	Fail	No	24	3	0.8	3.8
Epoxy/Bagasse-ADP 10%	BC	-	Fail	No	25	4	1.8	2.2
Epoxy/Bagasse-ADP 20%	8.8	3.8	V1	No	28	7	3.6	1.9
Epoxy/Bagasse-ADP 30%	1.5	1.5	V0	No	30	9	5.4	1.7

4. Conclusions

Bagasse-ADP flame retardant was added to an epoxy resin to prepare epoxy/bagasse-ADP composites, an effective flame-retarding composite material. Adding bagasse-ADP increased the thermal stability and flame retardancy of the composite materials compared with that of pure epoxy. For the material with 30 wt% added bagasse-ATP, the char yield was 32.3 wt%, which was 18.2 wt% higher than that of pure epoxy (14.1 wt %). In addition, the LOI increased from 21 to 30 %, and the UL-94 classification improved from "Fail" to "V-0." This performance was attributed to the nitrogen, phosphorus, and silicon content of the flame retardant. During combustion, phosphorus groups released nonflammable gases in the gas phase, diluting oxygen in the atmosphere, and pyrolyzed early in the condensed phase, catalyzing carbon formation, which served as a barrier to protect the polymer matrix, block heat transfer, and inhibit fuel supply. During pyrolysis, nitrogen groups also release nonflammable gases, facilitating the expansion of the charred layer and thereby preventing further burning. During combustion, the surface migration of silicon facilitated the formation of silicon dioxide, protecting the substrate. The flame retardant demonstrated excellent flame retardancy after its addition to the matrix, and this epoxy resin

could be applied in transportation or in coating, composite, or construction materials to effectively reduce fire hazards.

Acknowledgments
The authors would like to express their appreciation to the National Science and Technology Council for financial support of this study under Grant MOST 109-2221-E-2441-003-MY3

References

[1] W. He, P. Song, B. Yu, Z. Fang, H.Wang. Flame retardant polymeric nanocomposites through the combination of nanomaterials and conventional flame retardants. *Prog. Mater Sci.*, 114:100687, 2020.
[2] Y. T. Pan, Z. Zhang, R. Yang. The rise of MOFs and their derivatives for flame retardant polymeric materials: A critical review. *Compos. B Eng.*,199: 108265, 2020.
[3] H. Vahabi, H. Wu, M. R. Saeb, J. H. Koo. Ramakrishna S., Electrospinning for developing flame retardant polymer materials: Current status and future perspectives. *Polymer*, 217: 123466, 2021.
[4] C. Zhang, H. Wu, R. M. Kessler. High bio-content polyurethane composites with urethane modified lignin as filler. *Polymer*, 69: 52-57, 2015.
[5] V. S. Bonab, I.M. Zloczower. Chemorheology of thermoplastic polyurethane and thermoplastic polyurethane/carbon nanotube composite systems. *Polymer*, 99: 513-520, 2016.
[6] R. Kumar, R. Yadav, A. M. Kolhe, S. R. Bhosale, R. Narayan. 8-Hydroxypyrene-1,3,6-trisulfonic acid trisodium salt (HPTS) based high fluorescent, pH stimuli waterborne polyurethane coatings. *Polymer*, 136: 157-165, 2018.
[7] B. Hui, L. Ye. Highly heat-resistant silicon-containing polyurethane-imide copolymers: Synthesis and thermal mechanical stability. *Eur. Polym. J.*,91: 337-353, 2017.
[8] Z. Liu, B. Wu, Y. Jiang, J. Lei, C. Zhou, J. Zhang, J. Wang. Solvent-free and self-catalysis synthesis and properties of waterborne polyurethane. *Polymer*, 143: 129-136, 2018.
[9] M. Baqar, T. Agag, H. Ishida, S. Qutubuddin. Poly(benzoxazine-co-urethane)s: A new concept for phenolic/urethane copolymers via one-pot method. *Polymer*, 52: 307-317, 2011.
[10] M. Zajac, H. Kahl, B. Schade, T. R€odel, M. Dionisio, M. Beiner. Relaxation behavior of polyurethane networks with different composition and crosslinking density. *Polymer*, 111: 83-90, 2017.
[11] M. Tryznowski, T. Gołofit, A. Świderska. Poly(hydroxyurethane)s with diethyl tartrate-based amide backbone by an isocyanate-free route: Use as adhesives. *Polymer*, 144: 1-6, 2018.
[12] L. I. Ronco, A. Basterretxea, D. Mantione, H. R. Aguirresarobe, R. J. Minari, L. M.Gugliotta, D. Mecerreyes, H. Sardon. Temperature responsive PEG-based polyurethanes " à la carte ". *Polymer*, 122: 117-124, 2017.
[13] J. Pagacz, E. Hebda, B. Janowskic, D. Sternikd, M. Jancia, K. Pielichowski. Thermal decomposition studies on polyurethane elastomers reinforced with polyhedral silsesquioxanes by evolved gas analysis. *Polym. Degrad. Stab.*, 149: 129-142, 2018.
[14] Y. Huang, S. Jiang, R. Liang, Z. Liao, G. You. A green highly-effective surface flame-retardant strategy for rigid polyurethane foam: Transforming UV-cured coating into intumescent selfextinguishing layer. *Compos. A Appl. Sci. Manuf.*, 125: 105534, 2019.
[15] Y. Wang, F. Wang, Q. Dong, M. Xie, P. Liu, Y. Ding, S. Zhang, M. Yang, G. Zheng. Core-shell expandable graphite @ aluminum hydroxide as a flame-retardant for rigid polyurethane foams. *Polym. Degrad. Stab.*, 146: 267-276, 2017.

THE EFFECT OF POLYMER COMPOSITION ON THE FIBRE PRODUCTION PROCESS AND FINAL MECHANICAL PROPERTIES

N.L.T. Nguyen[1*], C. Creighton[1], M. Maghe[1], S. Nunna[1], R. Varley[1]
[1] Carbon Nexus, the Institute for Frontier Materials, Deakin University, Geelong, Victoria, 3216, Australia
* Corresponding author (lethaon@deakin.edu.au)

Keywords: *Carbon fibre, carbon fibre production, itaconic acid.*

Abstract

This study investigates the effect of polymer composition containing methyl acrylate (MA) and itaconic acid (IA) comonomers concentration on the conversion of PAN co-polymers into carbon fiber. Itaconic acid concentration varies from 0.3 to 3 wt% and with higher IA content reduces energy consumption during thermal oxidative stabilization (TOS) and enhances reactivity, leading to improved mechanical properties in carbon fibers. Specifically, fibers with higher IA content exhibit a 20% increase in tensile strength. Overall, these findings suggest that precursor design plays a crucial role in optimizing fiber properties and reducing energy consumption in carbon fiber production, and to ultimately strategy high-performance, lightweight, and sustainable materials.

1. Introduction

Carbon fibre (CF), an ideal reinforcing material for advanced composite materials, has been gained tremendous attention in a wider range of industry such as aircraft, automobile manufacturing, and spacecraft parts, chemical engineering, prosthetics, superconductors, sport equipment and high-energy-density fuel, etc. where lightweight and higher strength can convert directly into energy [1-3] (**Error! Reference source not found.**). The super properties of carbon fibre include high stiffness, high-temperature tolerance, high tensile strength, high chemical resistance, and low thermal expansion. There are many different precursors using to manufacture CFs, however, PAN precursor is hardly used to commercialize due to poor processibility and time-consuming pre-oxidation step [4, 5]. Therefore, utilising the small content of copolymer precursor fibres instead of homopolymer PAN chains have been improved the drawability, hydrophilicity, spinnability and solubility effectively and in thermal oxidation in the presence of an ionic cyclization mechanism [2,3]. In this present work, the effect of different IA concentrations (0.3 to 3 wt%) while methyl acrylate (MA) concentration remained constant for all polymers at 3wt% in PAN precursor, were produced as both wet spinning line and carbonization procedures were carried on continuous pilot scale analogous to industrial processes, are investigated.

2. Method

The preparation of precursors plays its important role in the manufacture carbon fibres. Materials includes the different comonomers were successfully manufactured by solution polymerization in dimethyl sulfoxide via wet spinning. From the manufacture, the comonomers with a high purity were used as received without further purification. For this study, the stabilization and carbonization of the precursor materials were conducted at the Carbon Nexus Research Centre (Deakin University, Australia), as shown in Figure 1.

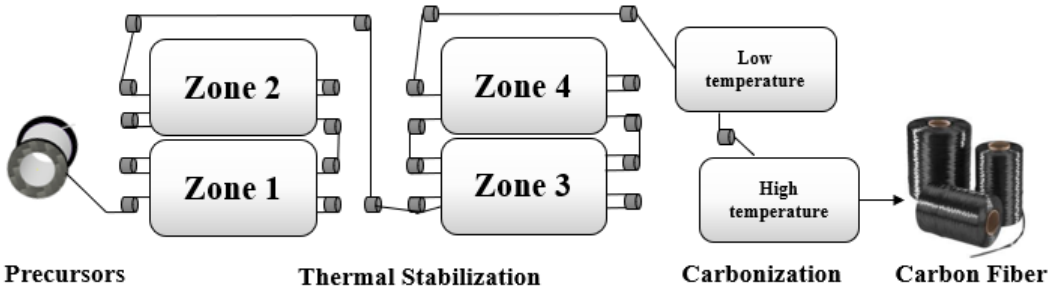

Figure 1: Schematic representation of the carbon fibre manufacturing process

3. Results

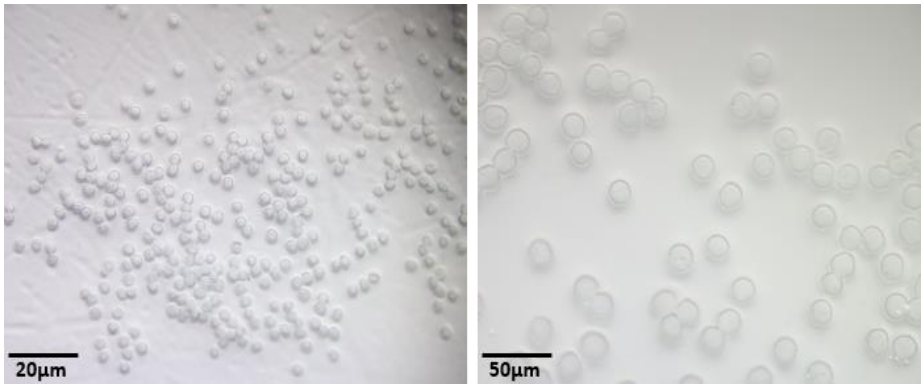

Figure 2: Optical microscopy images of PAN precursor fibres along the cross section.

The copolymers carbon fibre precursor including 0.3 to 3-PAN were polymerized under the similar conditions. **Error! Reference source not found.** presents the cross-section of precursor fibre observed using optical microscopy. It can be found that all the cross-section shapes were circular and spun by wet spinning.

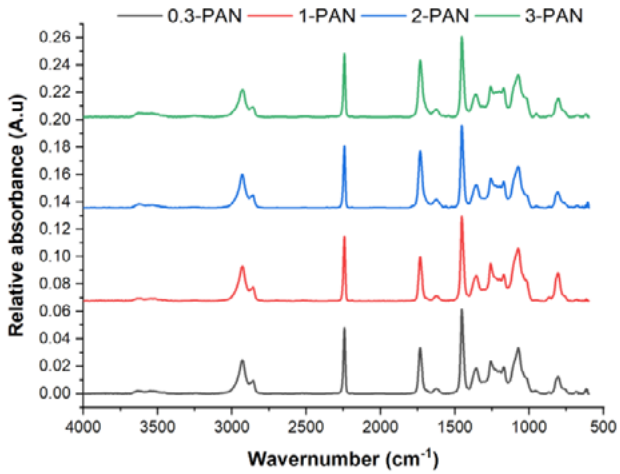

Figure 3: Fourier Transform Infrared Spectroscopy (FTIR) analysis of PAN copolymer fibres

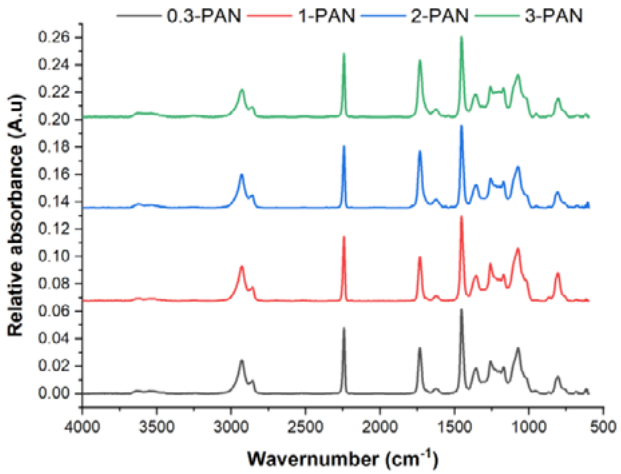

Figure displays the FTIR spectra of PAN copolymer from 0.3 to 3-PAN. In both cases, the major absorption band is ascribed to the –C≡N stretching vibration at 2243cm^{-1}. The peaks at around 2945cm^{-1} and 1450 cm^{-1} are attributed to stretching and bending vibrations of –CH_2 groups, respectively. The weak peak (at approximately 1602 cm^{-1}) is assigned to the hydrolysis of AN units throughout the process of polymerization. PAN copolymer exhibited a peak at 1725 cm^{-1}, which suggested the stretching vibration of -COOH group stemmed from IA monomers, and it became sturdier with higher IA content. Several C=N bonds are converted into C-N stretching vibrations, and this is verified by the existence of absorption band at 1255 cm^{-1}.

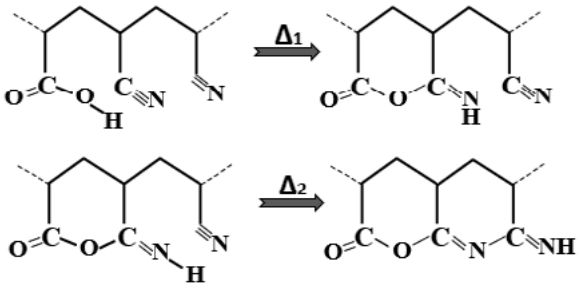

Figure 4: Suggested cyclization reaction through a free radical

The oxygen uptake reaction generates these correspondent groups which are of paramount important factors in stabilizing PAN precursors. Firstly, it functions as a dehydrogenative representators in the transition process from C–C to C=C bonds to join with cyclization forming a conjugated naphthyridine ring structure. Secondly, it creates oxygen-bearing groups to encourages inter-molecular crosslinking between the polymer chains (Figure 4). The FT-IR spectra confirm that the surface chemical modification was successful.

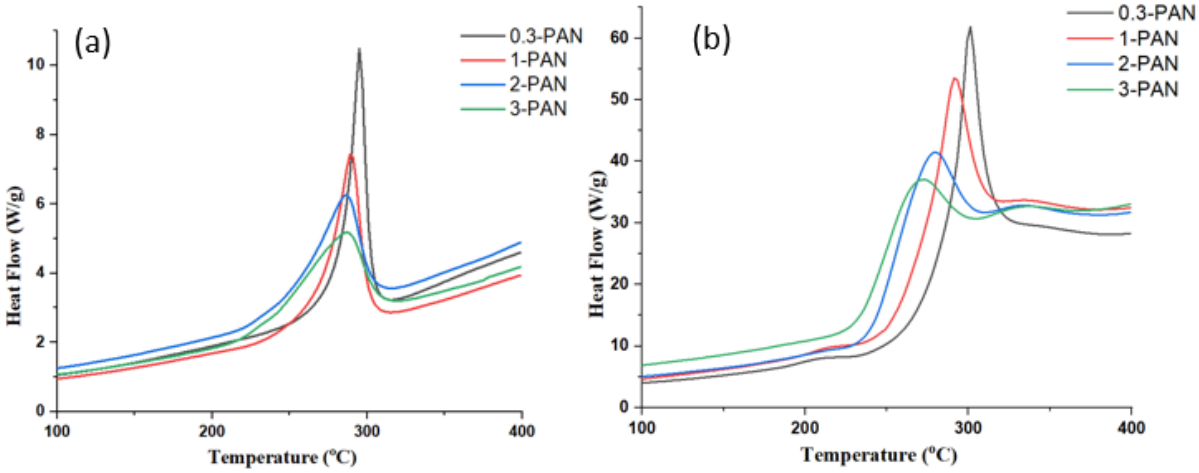

Figure 5: Differential Scanning Calorimetric (DSC) curves of PAN copolymers in nitrogen (a) and in air (b) atmosphere

The DSC thermograms of PAN copolymers heated at 10°C/min to 400°C under N_2 and air atmosphere, respectively, as illustrated in

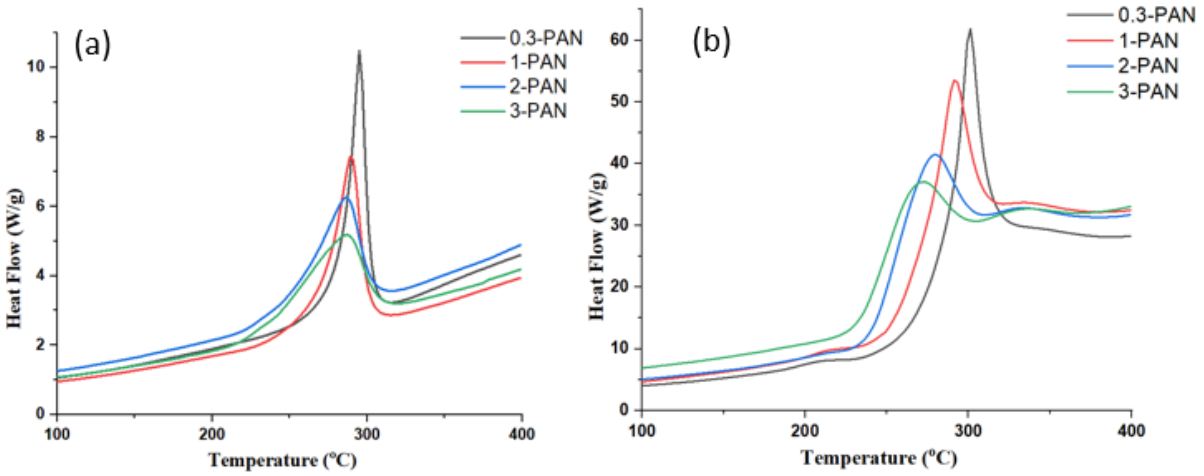

Figure . It was also revealed that the exothermal peaks of 3-PAN were significantly narrower than those of 0.3 to 2-PAN and the peak intensity of 0.3-PAN was larger than that of 1 to 3-PAN. The results indicate the exothermal behaviour of 0.3-PAN is more intensive than that of 1-PAN, 2-PAN through the process of cyclization. Compared to air atmosphere, the exothermic peaks in nitrogen are narrower and single which occurred because of the absence of oxidation reactions. With increasing comonomer content, the sharp of melting peaks becomes broader while the area of the melting peaks become smaller as illustrated in Figure 5. More specifically, the sequence length of the comonomer decreases when the contents of the comonomer are increased.

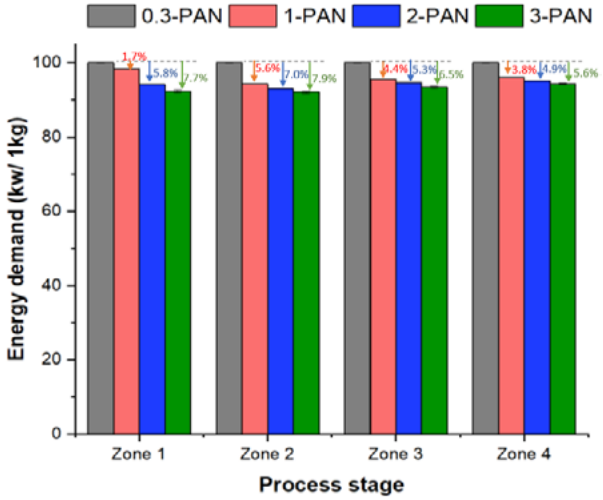

Figure 6: An evaluation of energy consumption during stabilization in the different process stages

In order to evaluate the energy-saving potential of precursors with higher itaconic acid (IA) content and increased reactivity, energy consumption during the stabilization process was measured. Adjusting processing conditions according to precursor reactivity, energy analysis focused on this thermal stablization stage. Results showed that higher IA content led to lower overall processing temperatures, initiating cyclization and subsequent reactions at lower temperatures. This trend, illustrated in Figure 6, resulted in the reduced energy demand during stabilization. Particularly, the precursor with 3% IA content consumed the least energy, approximately 7% less than that of the 0.3% IA precursor. These findings underscore the importance of considering both desired material properties and processing efficiency when designing precursor compositions and comonomer contents.

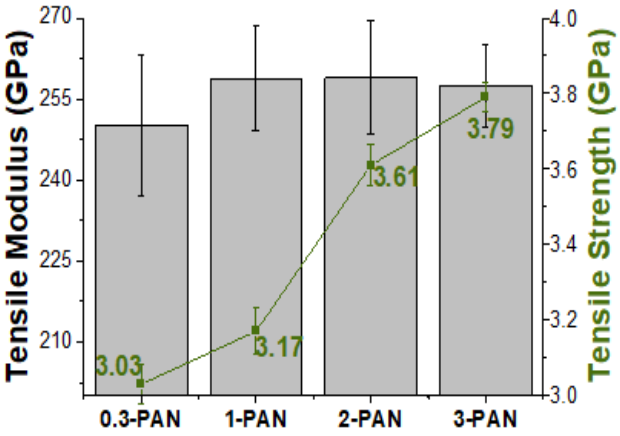

Figure 7: The property of carbon fibres

The development of the mechanical characteristics during the production process was illustrated in Figure 7 which reported the fibre's average tensile strength and modulus improved from 0.3 to 3-PAN. The improvement could be thankful to the improved thermal properties of 3-PAN, despite exhibiting the lowest energy consumption. This maybe because PAN underwent a chemical transition that resulted in a large cyclic ladder structure in the oxidised material. Higher IA content leads to a carbon fibre with good mechanical properties. Promising benefits of carbon fibres are for energy and high-tech applications.

3. Conclusions

This study systematically investigated the impact of varying concentrations of itaconic acid (IA) in PAN precursors on the conversion into carbon fibers using pilot-scale wet spinning and carbonization facilities. Results demonstrated that higher IA concentrations led to a precursor material with lower exothermicity and enhanced reactivity, promoting a higher degree of chemical conversion and improved thermal stability during thermal oxidative stabilization. Additionally, fibers derived from higher IA concentrations exhibited increased mechanical properties, particularly tensile strength, indicating enhanced structural transformation. Overall, these findings contribute to a comprehensive understanding of the relationship between IA concentration, material properties, and processing efficiency, offering insights for more energy-efficient and high-quality carbon fiber production

Acknowledgments

The authors would like to acknowledge the support from Deakin University advanced characterization facility and Carbon Nexus operation team for their kind support and guidance.
Notes: The authors declare no competing financial interest.

References

[1] D. Edie and R. Diefendorf, "Carbon fiber manufacturing," Carbon-carbon materials and composites, pp. 19-37, 1993.
[2] P. Bajaj and A. Roopanwal, "Thermal stabilization of acrylic precursors for the production of carbon fibers: an overview," Journal of Macromolecular Science, Part C: Polymer Reviews, vol. 37, no. 1, pp. 97-147, 1997.
[3] J. Kaur, K. Millington, and S. Smith, "Producing high-quality precursor polymer and fibers to achieve theoretical strength in carbon fibers: A review," Journal of Applied Polymer Science, vol. 133, no. 38, 2016.
[4] D. Jang, M. E. Lee, J. Choi, S. Y. Cho, and S. Lee, "Strategies for the production of PAN-Based carbon fibers with high tensile strength," Carbon, vol. 186, pp. 644-677, 2022.
[5] E. Frank, F. Hermanutz, and M. R. Buchmeiser, "Carbon fibers: precursors, manufacturing, and properties," Macromolecular materials and engineering, vol. 297, no. 6, pp. 493-501, 2012.

DEVELOPMENT OF XANTHAN-BASED BIO-COMPOSITES FOR THE PRODUCTION OF TOPSOIL COVERS

A. Sorze[1,2], F. Valentini[1,2], A. Dorigato[1,2] and A. Pegoretti[1,2]

[1]Department of Industrial Engineering, University of Trento, via Sommarive 9, 38123 Trento, Italy
[2]National Interuniversity Consortium of Materials Science and Technology (INSTM), via G. Giusti 9, 50121 Florence, Italy
Email: alessandro.sorze@unitn.it, francesco.valentini@unitn.it, andrea.dorigato@unitn.it, alessandro.pegoretti@unitn.it

Keywords: Xanthan gum, wood fibres, hydrogels, topsoil covers, composites

Abstract
In this work, different hydrogels based on Xanthan gum (XG) and reinforced with wood fibers were investigated in order to develop novel bio-based multifunctional topsoil covers (TSCs) that could be used in forestry and agricultural applications. Different compositions were produced and characterized by varying the type and the content of cross-linking agents. Initially, three different thermal treatment were tested on samples in order to find the most suitable cross-linking degree for the intended application. From infrared spectroscopy and water absorption tests, it was shown that the optimal cross-linking was achieved with a thermal treatment in oven at 165 °C for 3 minutes and 30 seconds. Climate chamber conditioning demonstrated the high dimensional stability of the produced hydrogels after multiple temperature and humidity cycles. From tensile tests it was found that the films showed poor tensile strength (less than 1 MPa) due to the presence of high porosity in the structure. However, for some specific compositions, the elongation at break was about 12 %, which is comparable to that of bio-mulching films in literature.

1. Introduction

Topsoil covers (TSCs) are mulching films aimed to support reforestation and agriculture in arid conditions, by the inhibition of weed growth and the reduction of soil moisture losses after transplantation [1,2]. Commonly, mulching films are based on plastic films like polyethylene and polypropylene due to their low cost of production [3,4]. However, different environmental drawbacks are related with this kind of plastic products. Specifically, prolonged outdoor exposure of these films could lead to the release of macro- and micro-plastics into the soil [5,6]. The use of a bio-based and biodegradable polysaccharide such as Xanthan gum (XG), which derived from the aerobic fermentation of a bacterium (*Xanthomonas campestris*), seems very promising [7,8]. Xanthan gum is soluble in both cold and hot water and therefore, in order to have stable hydrogel structures, it can be to be cross-linked through both chemical or physical methods [9]. Chemical methods are based on the use of cross-linking agents, such as citric acid (CA) or sodium trimetaposhate (STMP), which can react with XG through an esterification reaction. The use of tannins or derivatives, such as tannic acid (TA), characterized by phenolic groups and high molecular weight could be an innovative strategy to cross-link XG chains.

As demonstrated by the autors, the incorporation of natural fillers based on cellulose in the Xanthan-based hydrogels is demonstrated to enhance their water retention capability and mechanical properties [10]. The present study intends to further improve the properties of Xanthan-based hydrogels by reinforcing them with short wood fibres and cross-linking them with different types of agents at different concentrations. Moreover, different thermal treatments are investigated in order to obtain the optimal

degree of cross-linking. On the basis of these considerations, the aim of this work is to find the best formulation of Xanthan-based hydrogel to be used as multifunctional bio-based topsoil covers as a viable solution compared to the plastic-based products.

2. Materials and Methods

2.1. Materials

Xanthan Gum (XG) was provided by Galeno srl (Prato, Italy) in form of fine powder. Wood fibers STEICO® Flex-036 was provided by STEICO SE (Feldkirchen, Germany) with an aspect ratio in the range 22.5-75 mm/mm. Vegetable glycerol (or glycerine) produced by Farmalabor srl (Assago, Italy) was used as a plasticizing agent. Citric acid monohydrate (CA) supplied by Riedel-de Haën GmbH (Seelze, Germany), sodium trimetaphosphate (STMP) produced by Thermo Fisher Scientific Inc. (Massachusetts, USA) and tannic acid (TA) supplied by Galeno srl (Prato, Italy) were used as a cross-linking agents.

2.2. Sample preparation

Hydrogels were produced starting from mixing Xanthan gum and glycerol in a 1.2:1 weight ratio. Wood fibres (1:1 weight ratio to XG) and water (T ~ 60 °C) were then added to the mixture until a lump-free solution was reached. The three different cross-linking agents (CA, STMP and TA) were previously dissolved in 50 ml water solution and added to the mixture at different concentrations, as reported in Table 1. A reference sample (XG_WF) was also produced without adding any cross-linking solution. The compositions were manually spread on a plate into discs of 16 cm in diameter and approximately 3 mm thick. The samples were left to dry at room temperature and, once dried, were subjected to three different thermal treatments: 80 °C in oven for 15 minutes (T1), 165 °C in oven for 3.5 minutes (T2) and 25 °C overnight (RT). These parameters and the selected cross-linking agent concentrations were identified after preliminary trials and on the basis of literature studies on Xanthan hydrogels.

Table 1. Sample coding for the produce Xanthan-based hydrogels.

Sample Code	*XG* (phr)	*WF* (phr)	*CA* (phr)	*STMP* (phr)	*TA* (phr)
XG_WF	100	100	-	-	-
CA10	100	100	10	-	-
CA50	100	100	50	-	-
CA60	100	100	60	-	-
CA100	100	100	100	-	-
STMP50	100	100	-	50	-
STMP60	100	100	-	60	-
STMP150	100	100	-	150	-
TA5	100	100	-	-	5
TA20	100	100	-	-	20
TA50	100	100	-	-	50

2.3. Experimental techniques

2.3.1 Fourier-Transformed Infrared Spectroscopy (FTIR)

Fourier-transformed infrared spectroscopy (FTIR) was performed through the use of a Spectrum One spectrometer (PerkinElmer, Waltham, MA, USA) operating in the wavenumber range of 650-4000 cm^{-1} in attenuated total reflection (ATR) mode. Each spectrum was obtained from the superposition of four scans. The test was conducted to investigate the effect of the different thermal tratements on the chemical composition of the produced samples.

2.3.2 Water Uptake

Water uptake test was carried out in order to determine the behavior of produced samples under extreme flood conditions and to get further information on the necessity of a thermal treatment for the cross-linking of XG. For each sample, three specimens, approximately 3×5 cm^2 in size, were placed in a container filled with water and left immersed. The mass of the samples was recorded at specific time intervals, until the samples broke completely or reached the plateau of the absorption curve. Water uptake (WU%) capability of the samples was obtained according to Eq. (1).

$$WU\% = \frac{M_i - M_0}{M_0} \cdot 100 \quad (1)$$

where M_0 is the initial mass of the sample and M_i is the sample's mass at time "i".

2.3.3 Conditioning in climatic chamber

Specimen of NEAT and of compositions with maximum, minimum, and intermediate concentrations of cross-linking agent were subjected to cyclic conditioning in a Discovery My climatic chamber (ACS, Massa Martana, Italy). Specimens were dried for 5 h at 40 °C and 10 % RH and then subjected for seven days to a temperature and humidity cycle corresponding to the temperature and humidity detected by an ARPAV weather station located in Molini (pre-alpine forest, municipality of Laghi, Italy). Coordinates of the weather station are here reported: altitude 623 m asl., long. 11.256013 E, lat. 45.833332 N. Figure 1 shows the temperature and relative humidity cycles to which the samples were subjected in the climatic chamber. Mass before and after the test were recorded.

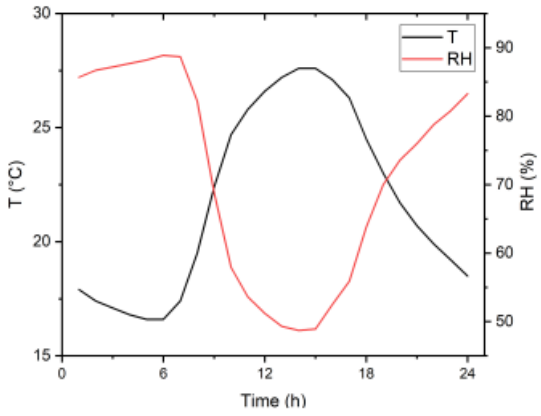

Figure 1. Temperature and relative humidity cycles performed on the produced hydrogels in the climatic chamber.

2.3.4 Quasi-static tensile tests

Tensile tests were performed with an INSTRON 5969 (Instron, USA) testing machine equipped with a load cell of 100 N and operating at cross-head speed of 2 mm/min for the determination of the maximum tensile stress and the elongation at break. At least 5 rectangular specimens of dimensions 100×10 mm^2 were prepared and tested according to ASTM 3039 standard. Specimens were clamped so that to avoid sliding.

3. Results and Discussion

3.1 Fourier-Transformed Infrared Spectroscopy (FTIR)

The analysis was conducted to evaluate the effect of the thermal treatment on the samples and ensure that the cross-linking reaction of the XG occurred. However, there is no difference in peak transmittance when comparing the spectra of each sample treated under the three different thermal conditions. Therefore, only one representative FTIR spectrum of each sample is shown in Figure 2.

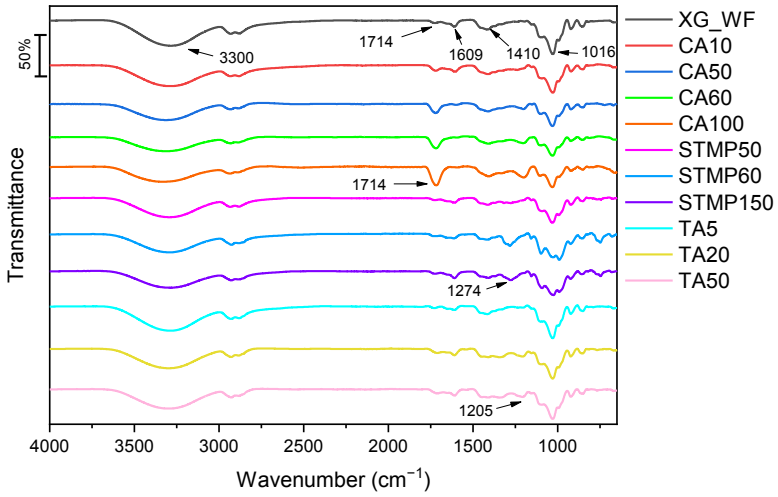

Figure 2. FTIR spectra of produced Xanthan-based samples.

The broad peak visible at 3300 cm^{-1} is ascribed to the O-H stretching vibration of hydroxyl groups, while the peak at 1016 cm^{-1} is associated to the C-O stretching vibration of the primary alcohol in XG and wood fibers. Peaks at 1410 and 1609 cm^{-1} are ascribed to the symmetrical and asymmetrical C=O vibration of the carboxylate anion (-COO−), respectively, while peak at 1714 cm^{-1} is due to the presence of carbonyl groups of the carboxylic acid (-COOH) in XG and wood fibers. It can be observed that the intensity of the peak at 1609 cm^{-1} gradually decreases with the concentration of cross-linking agent, while the intensity of the peak at 1714 cm^{-1} increases. This could suggest an increase in the cross-linking degree, since more ester groups are present in the chemical structure after the esterification reaction between citric acid and Xanthan gum [11,12]. However, due to the fact that described behavior can only be observed in samples cross-linked with acids, and since peak at 1714 cm^{-1} was observed at all treatment temperatures, said peak is could be ascribed to the deprotonation of COOH group which could have happened even at RT [11]. Samples with STMP show a peak between 1250-1300 cm^{-1} whose intensity increases with the cross-linking agent content, this peak corresponds to the P=O stretching vibrations occurring from the reaction between STMP and XG. For samples with TA, rising the content of the tannic acid, it is possible to notice an increase in the intensity of the peak at 1205 cm^{-1}, which can be associated to the C-O stretching vibration of the carbonyl groups of the aromatic esters of the tannic acid.

3.2 Water Uptake

In Figure 3a-c, the results of the water absorption test on the produced Xanthan-based hydrogels, treated under different thermal conditions, are reported.

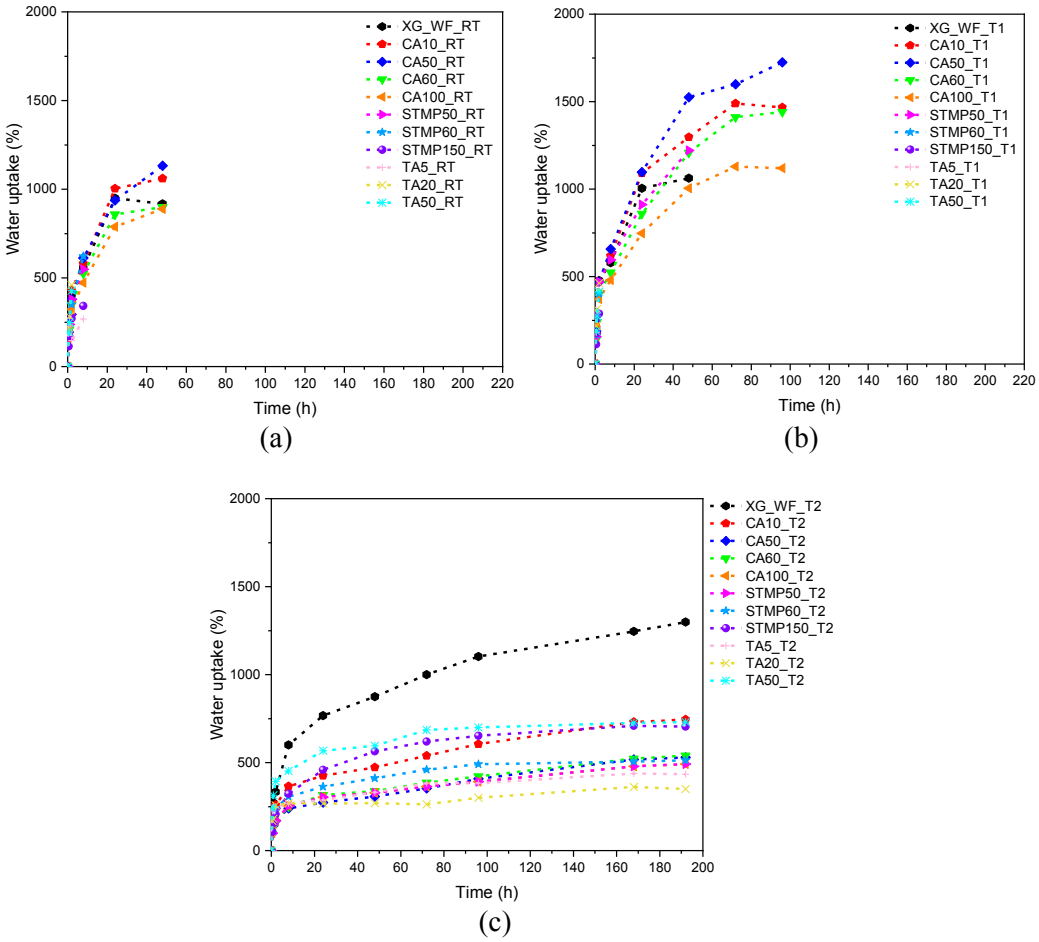

Figure 3. Results of water absorption test performed on Xanthan-based hydrogels treated at: (a) RT (b) T1 and (c) T2.

Figure 3a shows that, for all the samples, the measurement ends after 48 hours, before any sample reach a curve plateau. This is because the samples undergo high swelling and dissolve completely in water. Therefore, the RT treatment is not sufficient to proper carry out the cross-linking reaction between Xanthan gum and the cross-linking agents. However, it is interesting to notice that samples with STMP and TA dissolve even just after 10 hours of immersion and prior the CA samples and the reference XG_WF_RT. A slight improvement in the WU behavior of the samples can be observed in Figure 3b. All of the samples with TA fully dissolve in the first 8 h of the test and so most of the samples made with STMP, with the sole exception of STMP50_T1 which dissolve after 48 h of immersion. On the other hand, all samples cross-linked with CA are able to resist 4 full days (96 h) of immersion, showing instability and leaking only after the 72 h mark, thus showing better stability than the reference sample which is able to resist for only 48 h. Maximum absorption for samples with CA ranges from 1120 % (CA100_T1) to 1470 % (CA10_T1), while the maximum WU of the reference is found to be 1063 % at this treatment temperature. Despite these results, which confirm the necessity for a thermal treatment of the material at high temperatures, none of the specimen is able to reach the absorption plateau, implying that thermal treatment at T1 is still not acceptable for the desired application. From Figure 3c, it is clearly visible that all the tested specimen are now able to reach WU plateau and resist in immersion for 9 days. This confirms that thermal treatment must be carried out at T2 conditions. In all cases, the plateau reached by the various compositions is found to be smaller than that of XG_WF_T2 (1300 %).because the addition of cross-linking agents leads to an increase of the cross-linking density and thus to a lower swelling capacity. Indeed, WU of samples made with CA ranges from 490 to 740 % and it decreases with increase of cross-linking agent content. The WU of samples made with STMP and TA, tends to increase by increasing the cross-linking agent content. This can be attributed to the fact that, in addition

to the cross-links, both the reactions with STMP and TA introduce more anionic charges and hydrophilic groups, thus increasing swelling capacity.

3.3 Conditioning in climatic chamber

The conditioning in climatic chamber was perfomed only samples that underwent the thermal treatment T2, since previous tests showed that only this thermal treatment could give materials with suitable properties for the desired application. The results of the conditioning test in climatic chamber are reported in Table 2.

Table 2. Results of the cyclic conditioning test in climatic chamber for the produced Xanthan-based hydrogels.

Sample	*Weight Increase* (%)
XG_WF_T2	40.5 ± 1.2
CA10_T2	39.9 ± 1.5
CA50_T2	37.3 ± 0.9
CA60_T2	34.6 ± 0.3
CA100_T2	33.5 ± 0.5
STMP50_T2	38.1 ± 1.2
STMP60_T2	38.8 ± 1.3
STMP150_T2	30.6 ± 2.1
TA5_T2	38.4 ± 1.1
TA20_T2	38.3 ± 0.9
TA50_T2	32.2 ± 2.0

Due to the humid test environment, all tested samples absorb moisture and an increase in weight has been recorded at the end of the test. Specifically, the weight increase correspondent to moisture absorption ranges from 32.2 % of TA50_T2 to 40.5 % of XG_WF_T2. In all compositions a decrease of moisture absorption ability is observed with the increase of cross-linking agent content. These results are in line with what was found during the water absorption tests. For CA cross-linked samples this decrease goes from 39.9 to 33.5 %, for STMP cross-linked samples it ranges from 38.1 % to 30.6 % and, for TA cross-linked samples the decrease goes from 38.4 % to 32.2 %. Overall, at the end of the test, all the samples are geometrically unchanged. This means that the produced hydrogels are characterized by high dimensional stability and they are able to retain their shape and properties after multiple cycles of temperature and humidity.

3.4 Quasi-static tensile tests

Mechanical properties tests were also performed only on samples treated at T2 and they were investigated as a function of cross-linking agent content. Figure 4a-b show the results of the tensile tests on the produced Xanthan-based hydrogels.

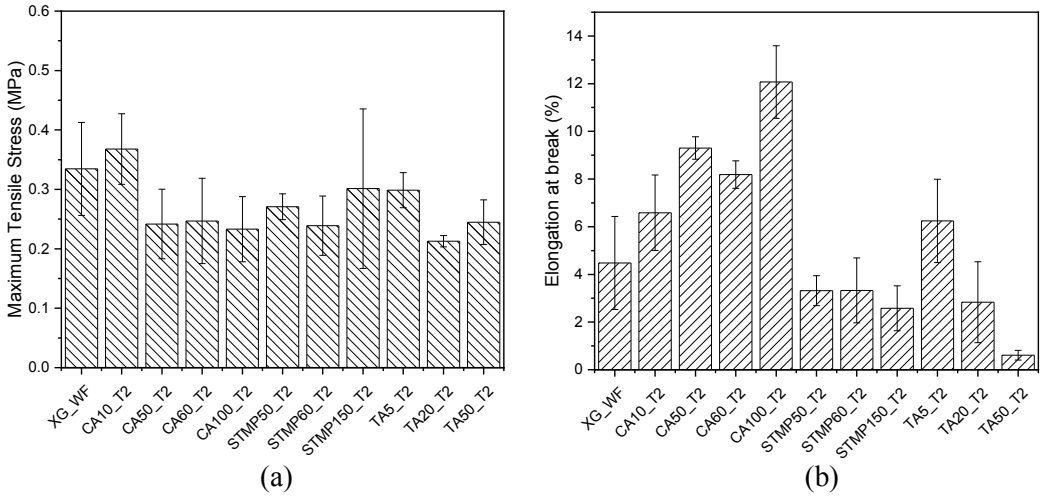

Figure 4. Tensile test properties of the produced Xanthan-based hydrogels: (a) maximum tensile stress and (b) elongation at break.

From Figure 4a, it can be seen that all the produced Xanthan-based samples show similar maximum tensile stress with values lower than 0.5 MPa. These results can be explained by the high porosity within the samples, which is formed during the production process when, due to the mixing operations, air is trapped in the Xanthan solution and between the network of wood fibres. In general, the type and concentration of the crosslinking agent have no influence for the tensile strength. From Figure 4b, it is possible to observe an improvement of the elongation at break for sample cross-linked with CA compared to both the reference (XG_WF) and the samples with the other cross-linking agents. The addition of an increasing content of CA appears to confer more flexibility to the XG chain structure, thus increasing the elongation at break of the samples. In particular, sample CA60_T2 exhibits the highest elongation at break, reaching values of up to 12%. These results are very interesting when comparing the elongation at break of other bio-based mulching films in literature [13].

4. Conclusions

This study was aimed to investigate the effect of different types and contents of cross-linking agents in order to develop hydrogels based of Xanthan gum and reinforced with wood fibers. These materials are meant to be use as multifunctional topsoil cover in both forestry and agricultural applications, to support the plant growth under drought conditions. Different thermal treatment were conducted on the produced hydrogels to obtain the optimal cross-linking degree. Combining FTIR spectroscopy and water uptake measurements it was noticed that the complete cross-linking reaction of the XG chains was obtained upon a thermal treatment in oven at 165 °C for 3 minutes and 30 seconds. For thermal treatments at lower temperatures the produced hydrogels completely dissolve in water after few days. The materials showed good dimensional stability after being subjected to multiple temperature and humidity cycling conditions in a climatic chamber, with final weight increase ranging from 30% to 40%. The quasi-static tests highlighted a poor mechanical tensile strength due to the presence of porosity in the structure. However,some specific composition of hydrogels cross-linked with citric acid showed good elongation at break (12%). The present study demonstrated the potential of the produced Xanthan-based hydrogels to be used as topsoil covers due to their bio-based nature, interesting water absorption capability and good dimensional stability.

Acknowledgments

This project has received funding from the European Union's Horizon 2020 research and innovation programme under grant agreement No 101000406 – ONEforest: A Multi-Criteria Decision Support System For A Common Forest Management to Strengthen Forest Resilience, Harmonise Stakeholder Interests and Ensure Sustainable Wood Flows.

References

[1] S. M. Benigno, K. W. Dixon, and J. C. Stevens, "Increasing Soil Water Retention with Native-Sourced Mulch Improves Seedling Establishment in Postmine Mediterranean Sandy Soils," *Restoration Ecology,* 21(5): 617-626, 2013

[2] N. Yang, Z.-X. Sun, L.-S. Feng, M.-Z. Zheng, D.-C. Chi, W.-Z. Meng, Z.-Y. Hou, W. Bai, and K.-Y. Li, "Plastic film mulching for water-efficient agricultural applications and degradable films materials development research," *Materials and Manufacturing Processes,* 30(2): 143-154, 2015

[3] E. Liu, W. He, and C. Yan, "'White revolution'to 'white pollution'—agricultural plastic film mulch in China," *Environmental Research Letters,* 9(9): 091001, 2014

[4] Z. Steinmetz, C. Wollmann, M. Schaefer, C. Buchmann, J. David, J. Tröger, K. Muñoz, O. Frör, and G. E. Schaumann, "Plastic mulching in agriculture. Trading short-term agronomic benefits for long-term soil degradation?," *Science of the total environment,* 550: 690-705, 2016

[5] Y. Qi, X. Yang, A. M. Pelaez, E. Huerta Lwanga, N. Beriot, H. Gertsen, P. Garbeva, and V. Geissen, "Macro- and micro- plastics in soil-plant system: Effects of plastic mulch film residues on wheat (Triticum aestivum) growth," *Science of the Total Environment,* 645: 1048-1056, 2018

[6] J. Wang, S. Lv, M. Zhang, G. Chen, T. Zhu, S. Zhang, Y. Teng, P. Christie, and Y. Luo, "Effects of plastic film residues on occurrence of phthalates and microbial activity in soils," *Chemosphere,* 151: 171-177, 2016

[7] M. H. Abu Elella, E. S. Goda, M. A. Gab-Allah, S. E. Hong, B. Pandit, S. Lee, H. Gamal, A. Rehman, and K. R. Yoon, "Xanthan gum-derived materials for applications in environment and eco-friendly materials: A review," *Journal of Environmental Chemical Engineering,* 9(1): 104702, 2021

[8] A. Becker, F. Katzen, A. Pühler, and L. Ielpi, "Xanthan gum biosynthesis and application: a biochemical/genetic perspective," *Applied microbiology and biotechnology,* 50(2): 145-152, 1998

[9] J. Patel, B. Maji, N. Moorthy, and S. Maiti, "Xanthan gum derivatives: review of synthesis, properties and diverse applications," *RSC Advances,* 10(45): 27103-27136, 2020

[10] A. Sorze, F. Valentini, A. Dorigato, and A. Pegoretti, "Development of a Xanthan Gum Based Superabsorbent and Water Retaining Composites for Agricultural and Forestry Applications," *Molecules,* 28(4): 1952, 2023

[11] Y. Li, D. Zhang, J. Ash, X. Jia, A. Leone, and A. Templeton, "Mechanism and Impact of Excipient Incompatibility: Cross-Linking of Xanthan Gum in Pediatric Powder-for-Suspension Formulations," *Journal of Pharmaceutical Sciences,* 108(11): 3609-3615, 2019

[12] V. B. Bueno, R. Bentini, L. H. Catalani, and D. F. Petri, "Synthesis and swelling behavior of xanthan-based hydrogels," *Carbohydrate Polymers,* 92(2): 1091-1099, 2013

[13] M. Menossi, M. Cisneros, V. A. Alvarez, and C. Casalongué, "Current and emerging biodegradable mulch films based on polysaccharide bio-composites. A review," *Agronomy for Sustainable Development,* 41(4): 1-27, 2021

Carbon nanofiber composites doped with different ZIF-8 nanoparticles for carbon dioxide capture

Yu-Chun Chiang and Wei-Ting Chin

Department of Mechanical Engineering, Yuan Ze University, Chung-Li, Taoyuan 320, Taiwan
Email: ycchiang@saturn.yzu.edu.tw, s1105004@mail.yzu.edu.tw

Keywords: carbon nanofibers, zeolitic imidazolate framework, characterization, carbon dioxide, adsorption

Abstract
In order to develop appropriate adsorbents for CO_2 capture, zeolitic imidazolate framework-8 (ZIF-8) nanoparticles were prepared using a rapid colloidal chemistry route and the ZIF-8 doped polyacrylonitrile (PAN) nanofibers were fabricated using the electrospinning technique, followed by the processes including stabilization, carbonization, and activation. The properties of the products were investigated and their adsorption capacities of CO_2 were discussed. The ZIF-8 nanoparticles prepared using different processes exhibited a rhombic dodecahedron structure mixed with cube structure, in which the crystal sizes had a significant difference while the elemental compositions were similar. The surface of ZIF-8 doped PAN fibers was not smooth as the pure PAN fibers; moreover, the nodes usually appeared in the doped nanofibers. All ZIF-8/PAN nanocomposites were characterized as microporous materials. The CO_2 uptakes followed the order: ZIF-8 (4MZ)/PAN > ZIF-8 (8MZ)/PAN > ZIF-8 (16MZ)/PAN > ZIF-8 (4ZM)/PAN > PAN. The optimal adsorption capacities of CO_2 at 25 ^oC were 3.45 (1 atm) and 1.13 (0.15 atm) mmol/g on ZIF-8 (4MZ)/PAN. This could be attributed to the specific surface area, pore volume, bulk nitrogen content and the Zn content.

1. Introduction

Net zero emissions have been one of the most important issues in recent years. During the transition towards net zero, the development of effective adsorbents for CO_2 capture is a top priority. It is known that good CO_2 adsorbents are dependent on pore volumes of sizes less than 0.7 nm and the presence of surface functional groups [1]. Several porous materials have been intensively studied, such as zeolitic imidazolate frameworks (ZIFs), carbon nanofibers, metal organic frameworks, etc.

ZIFs are a new class of porous crystals with extended three-dimensional structures constructed from tetrahedral metal ions (e.g., Zn, Co) bridged by imidazolate. Among the ZIFs, ZIF-8 comprises tetrahedral Zn^{2+} nodes bridged by 2-MeIM– linkers to form a sodalite-like topology, and is currently the most widely investigated ZIF material for a range of applications. By controlling the reaction conditions, various crystal morphologies of ZIF-8, such as sphere, nanosheet, rhombic dodecahedron, truncated rhombic dodecahedron, cube, and other polyhedrons, can be synthesized. Reaction time, the concentration of surfactant are crucial parameters [2] The rhombic dodecahedron shape is reported to be the stable equilibrium morphology of ZIF-8 [3]. The sizes of nanocrystals were highly related to the molar ratio of 2-MeIM to zinc salt [4]. In addition, the precursor of Zn^{2+} and the mixing procedures also controlled the particle sizes and appearance of the ZIF-8 [5].

An in-situ growth method [6], composed of electrospinning and hydrothermal treatment, was used to prepare a ZIF-8/PAN fibrous filter. It reported that U(VI) chelated with the N atoms of 2-MeIM was the major adsorption mechanism, and in situ ZIF-8/PAN fibers exhibited a high adsorption capacity for applications to nuclear wastewater. Another in situ growth method was used to prepare ZIF-8/cellulose

nanofiber composites [7]. Due to the electrostatic forces between Zn metal in ZIF-8 and –COO- groups on nanofibers, ZIF-8 crystals could be homogenously deposited on nanofibers. The composites showed good CO_2/N_2 selectivity. A novel structure of PAN nanofibers was fabricated using an electrospinning technique, decorated with ZIF-8 using a phase conversion growth method, and investigated for CO_2 capture [8]. The result indicated that electrostatic interaction and hydrogen bonds existed between the PAN matrix and the ZIF-8 nanocrystals confined to the PAN nanofiber surface. However, the CO_2 uptakes were only 7.0 cm^3/g at 25 °C, 1 bar.

In order to develop appropriate adsorbents for CO_2 capture, zeolitic imidazolate framework-8 (ZIF-8) nanoparticles were prepared using a rapid colloidal chemistry route and the ZIF-8 doped polyacrylonitrile (PAN) nanofibers were fabricated using the electrospinning technique, followed by the processes including stabilization, carbonization, and activation. The properties of the products were investigated and their adsorption capacities of CO_2 were discussed.

2. Experimental Methods

2.1. Preparation of ZIF-8

ZIF-8 nanoparticles were prepared using a rapid colloidal chemistry route at room temperature [9-10]. In a typical process, 0.74 g of zinc nitrate hexahydrate and 23 mg CTAB were dissolved in 25 mL methanol, and 0.82 g of 2-MeIM was dissolved in 25 mL methanol, respectively. CTAB was used as a surfactant. The mole ratio of Zn^{2+} to 2-MeIM was controlled as 1:4. Then the solution was mixed by pouring 2-MeIM solution into Zn^{2+} solution under thoroughly stirring. After rigorous and continuous stirring for 30 min, the resulting mixture was aged for 24 h at room temperature [11]. Finally, the white precipitate was collected by centrifugation, thoroughly washed with methanol to remove the excess 2-MeIM, and dried at 80 °C for 24 h. The product was denoted as ZIF-8 (4MZ). In order to investigate the effect of particle size, two approaches were applied. One was to change the synthesis route where only one change considered that the solution was mixed by pouring Zn^{2+} solution into 2-MeIM solution under thoroughly stirring and the product was denoted as ZIF-8 (4ZM). The other was to change the ratio of the precursors. Another two ratios of Zn^{2+} to 2-MeIM, 1:8 and 1:16, were selected, and the products were denoted as ZIF-8 (8MZ), and ZIF-8 (16MZ), respectively [12].

2.2. Fabrication of ZIF-8 Doped Carbon Nanofiber Composites

Nanofiber composites were prepared using an electrospinning process. Initially, PAN was dissolved in DMAc to form a polymer solution with 10 wt.% PAN. The resulting solutions were subjected to continuous magnetic stirring at 60 °C for 24 h in order to obtain a homogeneous polymer solution. Next, 10 wt. % different ZIF-8 products were added into the polymer solution and continuously stirred for another 24 h at room temperature. The electrospinning was carried out by an electrospinning equipment (FES-COE, Falco Tech Enterprise Co., Ltd.) under an applied electrical voltage of 15 kV onto a metal drum collector (∅ 15 cm). The mixture solution was injected at a flow rate of 1.0 mL/h, and a tip-to-collector distance of 15 cm was used. The electrospun fibers were stabilized at 280 °C for 2 h in air, carbonized at 800 °C for 1 h in a nitrogen atmosphere, and then activated at electro spun 850 °C for 1 h in a CO_2 atmosphere. The composite product obtained by doping ZIF-8 (4MZ) was denoted as ZIF-8 (4MZ)/PAN, and so on. For comparison, the pure PAN carbon nanofibers were prepared and labeled as PAN.

2.3. Characterizations

The resulting products were characterized by field emission scanning electron microscopy (FESEM) to probe the morphology of the samples. X-ray diffraction (XRD) was performed to examine to the degree of crystallinity for the ZIF-8 samples. Elemental analysis (EA) was used to analyze the weight percent of the carbon, nitrogen and hydrogen elements in the samples. The surface properties of the samples were determined from N_2 adsorption–desorption isotherms measured at −196 °C. The specific surface areas (SSAs) of the samples were measured in P/P_o = 0.05~0.3 using the Brunauer–Emmett–Teller (BET) method. The micropore (< 2.0 nm) surface area (S_{mi}) was determined using the t-plot method. The single point total pore volume (V_t) was obtained at $P/P_o \approx 0.99$. The mesopore volume (V_{me}), micropore volume

(V_{mi}), and ultra-micropore (< 0.7 nm) volume ($V_{<0.7nm}$) were obtained by applying a non-local density functional theory (NLDFT) model. Pore size distribution curves were also acquired with an NLDFT model. The chemical states on the surface of the samples were determined by X-ray photoelectron spectroscopy (XPS).

2.4. CO_2 Adsorption

The CO_2 adsorption isotherms on the samples were measured using the Micromeritics ASAP 2020 system. The samples were degassed at 350 °C for 24 h for removal of adsorbed contaminants prior to the measurement. The equilibration time for each pressure point was 45 s. An ISO Controller (Micromeritics), a thermoelectric cooled Dewar, was utilized for temperature control during the CO_2 adsorption process. Based on our previous studies [13], the Freundlich equation [14] was used for adsorption data fitting. The Freundlich adsorption isotherm (Equation (1)), an empirical model, assumes heterogeneous adsorption, due to the diversity of adsorption active sites, where q_e (mmol/g) is the equilibrium adsorption capacity, K_F [(mmol/g) $(1/kPa)^{1/n}$] is the Freundlich adsorption coefficient, P (kPa) is the gas pressure, and n is a constant indicating the isotherm curvature.

$$q_e = K_F P^{1/n} \tag{1}$$

3. Results and Discussion

3.1. Characteristics of the Samples

The FESEM images of ZIF-8 nanoparticles prepared under different conditions are shown in Figure 1. The rhombic dodecahedron and partly cube shapes were observed. Pouring Zn^{2+} solution into 2-MeIM solution produced a smaller crystal size, where ZIF-8 (4mz) had a uniform size with an average of approximately 200 nm, while that of ZIF-8 (4zm) was only approximately 130 nm. However, ZIF-8 (4ZM) was easy to happen the truncated rhombic dodecahedron and or cube shapes under the same preparation process, thus pouring 2-MeIM solution in to Zn^{2+} solution was used in the successive investigation. Increase in the ratio of 2-MeIM to Zn^{2+} would decrease the crystal size of ZIF-8, where ZIF-8 (8mz) had a size of about 100 nm, and that of ZIF-8 (16mz) was around 80 nm. Figure 2a-d shows the FESEM images of ZIF-8/PAN composites, and the images of PAN nanofibers is shown in Figure 2e for comparison. It could be observed that the average diameter of PAN nanofibers was approximately 350 nm. When introducing ZIF-8 into PAN precursor solution, the resulting nanofibers had a rough surface and even some nodes appeared in the fibers.

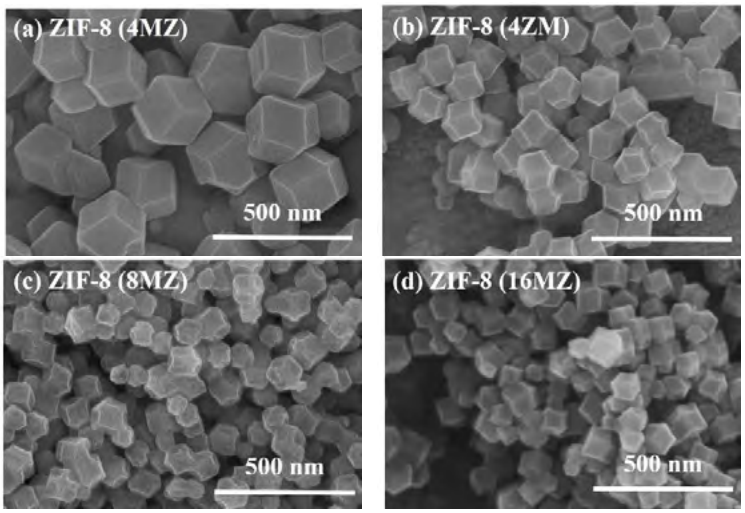

Figure 1. FESEM images of the ZIF-8 samples.

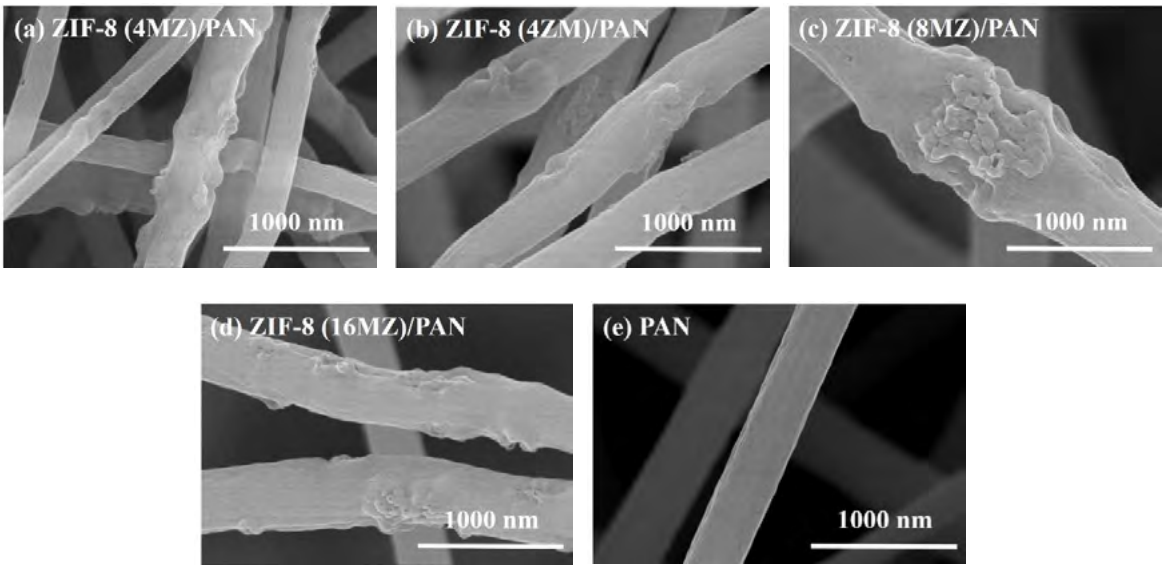

Figure 2. FESEM images of the ZIF-8/PAN composite samples.

The XRD patterns of four ZIF-8 samples are shown in Figure 3. The typical characteristic peaks at 2θ of 7.3, 10.4, 12.7, 14.6, 16.4, 18.0, 19.5, 22.1, 24.5, 25.6, 26.6 and 29.6◦ are ascribed to the (011), (002), (112), (022), (013), (222), (123), (114), (233), (224), (134) and (044) planes of ZIF-8 (CCDC 602542, [41]), respectively. It should be noted that the relative intensities of peaks (011), (112) and (222) were different depending on the mixing sequence or the ratio of 2-MeIM to Zn^{2+}. Nevertheless, the elemental compositions of C, N, and H for all ZIF-8 samples were quite similar, shown in Table 1. However, the N contents exhibited a significant difference in the ZIF-8/PAN nanocomposites. When ZIF-8 was incorporated into the PAN nanofibers, ZIF-8 (4ZM)/PAN had almost 2-fold N contents compared with that of PAN fibers.

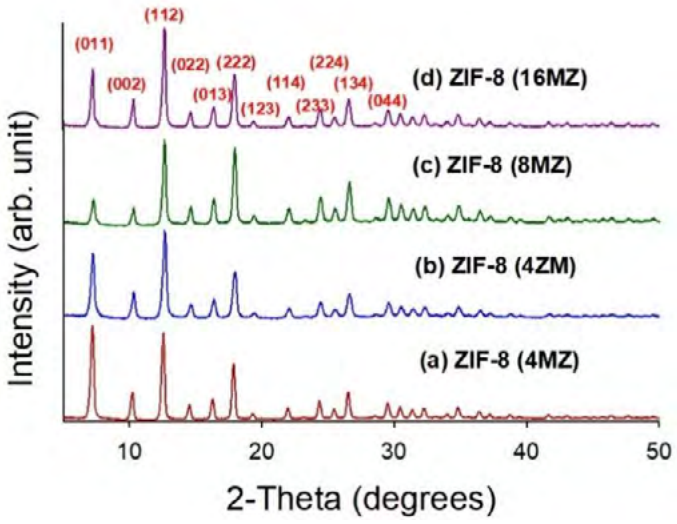

Figure 3. The XRD patterns of ZIF-8 samples.

Table 1. The EA results of the ZIF-8/PAN composite samples.

Specimen Type	Elemental composition (wt. %)			
	C	H	N	Others
ZIF-8 (4MZ)	41.715	4.364	24.555	29.367
ZIF-8 (4ZM)	41.570	4.361	24.490	29.580
ZIF-8 (8MZ)	41.540	4.359	24.525	29.576
ZIF-8 (16MZ)	41.635	4.357	24.555	29.453
ZIF-8 (4MZ)/PAN	56.67	2.63	7.42	33.28
ZIF-8 (4ZM)/PAN	60.00	2.55	11.10	26.35
ZIF-8 (8MZ)/PAN	60.52	2.46	9.47	27.56
ZIF-8 (16MZ)/PAN	62.65	2.41	9.39	25.55
PAN	67.66	3.13	6.41	22.80

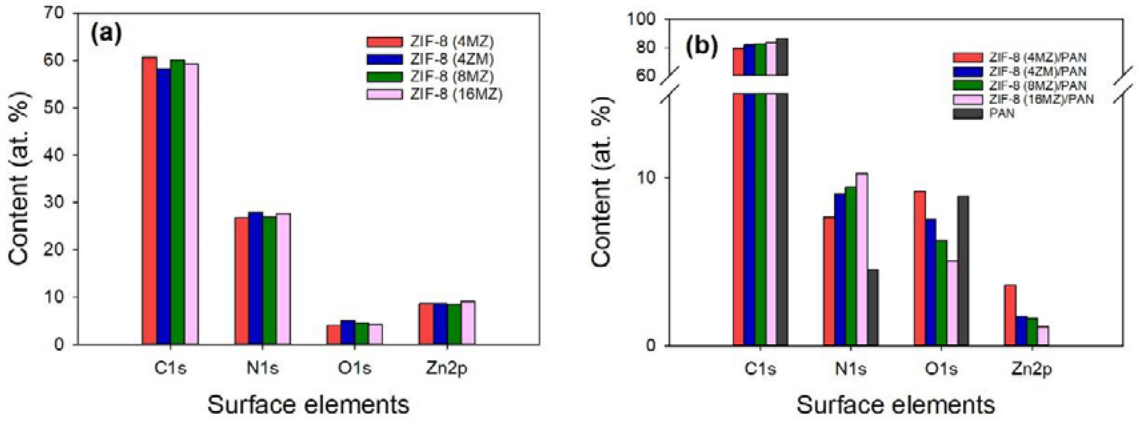

Figure 4. The compositions of surface atoms derived from X-ray photoelectron spectroscopy (XPS) profiles of the samples.

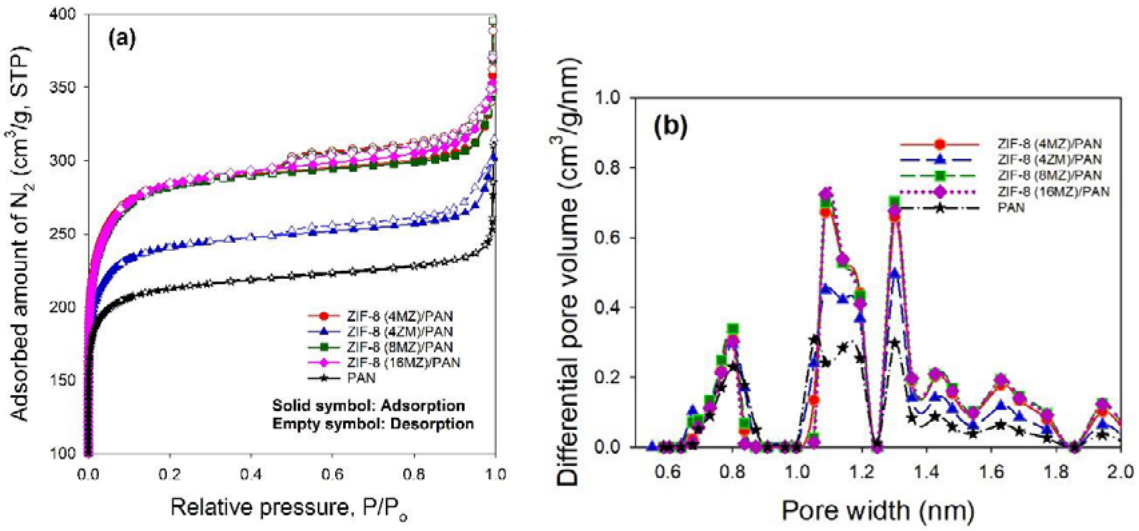

Figure 5. Adsorption–desorption measurements of N_2 for the samples at -196 °C: **(a)** isotherms; **(b)** pore size distributions of the samples.

The atomic ratios of the surface elements on all ZIF-8 samples obtained from XPS were similar to that of EA analysis (Figure 4a). On the other hand, the surface N atoms on ZIF-8/PAN composites had the reverse trend with the crystal size of incorporated ZIF-8 (Figure 4b). However, the Zn and O contents were higher as the crystal size of ZIF-8 was larger. Figure 5a shows the N_2 adsorption–desorption isotherms of the composite samples at –196 °C, with hysteresis loops and belong to type IV according to the Brunauer–Emmett–Teller (BET) classification. There is a significant difference on N_2 isotherms between MZ and ZM samples, while almost no distinguishable difference among the MZ samples. The pore size distributions in the range of 0.4–2 nm can be seen in Figure 5b, and the pores in all composites appeared almost in similar sizes, which could be attributed to the characteristics of ZIF-8.

3.2. CO_2 Adsorption

Figure 6a-e shows the CO_2 adsorption isotherms for all nanofibers under a pressure less than 123 kPa at 25, 40 or 55 °C. The CO_2 adsorption capacities increased with increasing CO_2 pressure, while decreased with increasing adsorption temperature, manifesting the characters of the exothermic reactions. Figure 7f depicts the CO2 adsorption isotherms of all samples at 25 °C. The CO_2 uptakes at 25 °C and 1 atm followed the order: ZIF-8 (4MZ)/PAN (3.45 mmol/g) > ZIF-8 (8MZ)/PAN (3.31 mmol/g) > ZIF-8 (16MZ)/PAN (3.16 mmol/g) > ZIF-8 (4ZM)/PAN (3.00 mmol/g) > PAN (2.91 mmol/g). At 25 °C and 0.15 atm (a typical untreated flue gas composition), the CO_2 adsorption capacities had a similar order—i.e., ZIF-8 (4MZ)/PAN (1.13 mmol/g) > ZIF-8 (8MZ)/PAN (1.08 mmol/g) > ZIF-8 (16MZ)/PAN (1.01 mmol/g) ~ ZIF-8 (4ZM)/PAN (1.01 mmol/g) > PAN (0.94 mmol/g), which means that there are no local effects. The consequences for the curve-fitting of the CO_2 measurement data using the Freundlich equation are summarized in Table 2. As seen from the data, the values of K_F varied inversely proportional to the adsorption temperature. The values of n ranged from 1.32 to 1.74 and were indicative of feasible adsorption.

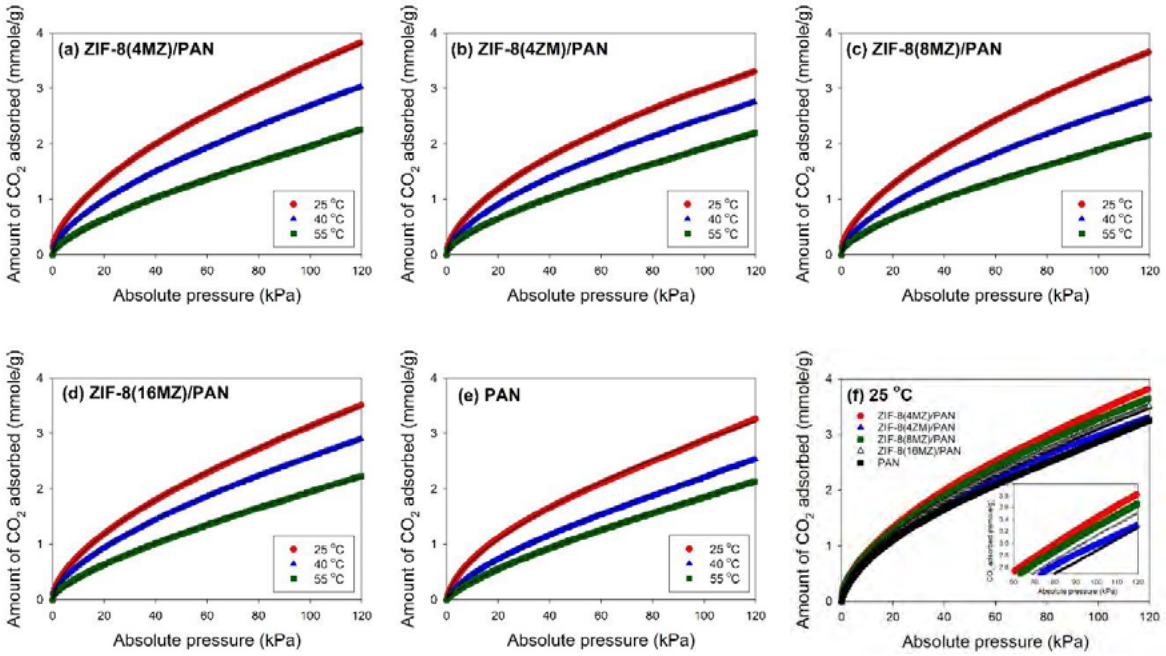

Figure 6. Adsorption isotherms of CO_2 of the samples.

Table 2. Fitted results of Freundlich equation for the CO_2 adsorption data collected on the samples at different temperatures.

Adsorbent	Temp. (°C)	K_F	n	R^2
ZIF-8 (4MZ)/PAN	25	0.2290	1.70	0.9998
	40	0.1488	1.59	0.9996
	55	0.0766	1.42	0.9995
ZIF-8 (4ZM)//PAN	25	0.2115	1.74	0.9999
	40	0.1411	1.61	0.9999
	55	0.0837	1.47	0.9994
ZIF-8 (8MZ)/PAN	25	0.2179	1.70	0.9999
	40	0.1445	1.61	0.9997
	55	0.0867	1.49	0.9991
ZIF-8 (16MZ)/PAN	25	0.1943	1.66	0.9999
	40	0.1425	1.59	0.9998
	55	0.0756	1.42	0.9996
PAN	25	0.1781	1.65	0.9995
	40	0.0885	1.43	0.9996
	55	0.0566	1.32	0.9999

4. Conclusions

Results show that the ZIF-8 prepared by different processes with rhombic dodecahedron structure mixed with cube structure were observed, where the particle sizes ranged from 40 to 200 nm. The nodes occurred in the doped carbon nanofibers which were microporous materials. ZIF-8 doped samples exhibited a more curled morphology. The specific surface areas, pore volumes, and CO_2 adsorption performance were improved for ZIF-8 doped PAN nanofibers, compared with those of pure PAN fibers. The optimal adsorption capacities of CO_2 at 25 °C and 1 atm were 3.45 mmol/g on ZIF-8 (4MZ)/PAN. This could be attributed to the specific surface area, pore volume, bulk nitrogen content and the Zn content. Freundlich equation could be used to fit the adsorption data of CO_2 isotherms. The adsorption mechanisms of CO_2 on the doped PAN nanofibers were believed to the comprehensive interactions of hierarchical porous structures, surface functional groups, and the zinc active sites.

References

[1] N. P. Wickramaratne and M. Jaroniec. Importance of small micropores in CO_2 capture by phenolic resin-based activated carbon spheres. *J. Mater. Chem. A*, 1: 112-116, 2013.

[2] Y. Wu, S. Cao, S. Xuan, M. Sang, L. Bai, S. Wang, J. Zhang, Y. Wang, W. Jiang and X. Gong. High performance zeolitic imidazolate framework-8 (ZIF-8) based suspension: Improving the shear thickening effect by controlling the morphological particle-particle interaction. *Advanced Powder Technology*, 31: 70-77, 2020.

[3] L. He, L. Li, L. Zhang, S. Xing, T. Wang, G. Li, X. Wu, Z. Sua and C. Wang. ZIF-8 templated fabrication of rhombic dodecahedron-shaped ZnO@SiO_2, ZIF-8@SiO_2 yolk–shell and SiO_2 hollow nanoparticles. *CrystEngComm*, 16: 6534–6537, 2014.

[4] W. Zheng, R. Ding, K. Yang, Y. Dai, X. Yan and G. He. ZIF-8 nanoparticles with tunable size for enhanced CO_2 capture of Pebax based MMMs. *Sep. Purif. Technol.,* 214: 111–119, 2019.

[5] N. L. Torad, M. Hu, Y. Kamachi, K. Takai, M. Imura, M. Naito and Y. Yamauchi. Facile synthesis of nanoporous carbons with controlled particle sizes by direct carbonization of monodispersed ZIF-8 crystals. *Chem. Commun.*, 49: 2521–2523, 2013.

[6] C. Wang, T. Zheng, R. Luo, C. Liu, M. Zhang, J. Li, X. Sun, J. Shen, W. Han and L. Wang. In situ growth of ZIF-8 on PAN fibrous filters for highly efficient U(VI) removal. *ACS Appl. Mater. Interfaces,* 10: 24164−24171, 2018.

[7] M. Jia, X. F. Zhang, Y. Feng, Y. Zhou and J. Yao. In-situ growing ZIF-8 on cellulose nanofibers to form gas separation membrane for CO_2 separation. *J. Membr. Sci.,* 595: 117579, 2020.

[8] Z. Li, Z. Cao, C. Grande, W. Zhang, Y. Dou, X. Li, J. Fu, N. Shezad, F. Akhtar and A. Kaiser. A phase conversion method to anchor ZIF-8 onto a PAN nanofiber surface for CO_2 capture. *RSC Adv.,* 12: 664-670, 2022.
[9] J. Cravillon, S. Munzer, S. J. Lohmeier, A. Feldhoff, K. Huber and M. Wiebcke. Rapid room-temperature synthesis and characterization of nanocrystals of a prototypical zeolitic imidazolate framework. *Chem. Mater.,* 21: 1410–1412, 2009.
[10] X. L. Sui, L. M. Zhang, L. Zhao, D. M. Gu, G. S. Huang and Z. B. Wang. Nitrogen-doped graphene aerogel with an open structure assisted by in-situ hydrothermal restructuring of ZIF-8 as excellent Pt catalyst support for methanol electro-oxidation. *Int. J. Hydrogen Energy,* 43: 21899-21907, 2018.
[11] S. R. Venna, J. B. Jasinski and M. A. Carreon. Structural evolution of zeolitic imidazolate framework-8. *J. Am. Chem. Soc.,* 132: 18030−18033, 2010.
[12] W. Guan, Y. Dai, C. Dong, X. Yang and Y. Xi. Zeolite imidazolate framework (ZIF)-based mixed matrix membranes for CO_2 separation: A review. *Journal of Applied Polymer Science*, 48968, 2020.
[13] Y. C. Chiang, C. Y. Wu and Y. J. Chen. Effects of activation on the properties of electrospun carbon nanofibers and their adsorption performance for carbon dioxide. *Sep. Purif. Technol.,* 233: 116040, 2020.
[14] M. Suzuki. *Adsorption Engineering*. Elsevier Science: Amsterdam, Netherlands, 1990.

NOVEL LAYERED DOUBLE HYDROXIDE/EPOXY NANOCOMPOSITES FOR CORROSION PROTECTIVE COATINGS

Daiva Zeleniakiene[1], Rochele Pinto[1], Claudia M. Rocha[2], Stanislav Stankevich[3], Marie Novakova[4], Katerina Zetkova[4], Andrey Aniskevich[3], Frederico Maia[2], and Joao Tedim[5]

[1]Department of Mechanical Engineering, Kaunas University of Technology, Studentu st. 56, 51424 Kaunas, Lithuania
Email: daiva.zeleniakiene@ktu.lt, rochele.pinto@ktu.edu, Web Page: http://www.ktu.edu/
[2]Smallmatek - Small Materials and Technologies, Lda, Rua dos Canhas, 3810-075 Aveiro, Portugal
Email: claudia.rocha@smallmatek.pt, frederico.maia@smallmatek.pt, Web Page: https://www.smallmatek.pt/
[3]Institute for Mechanics of Materials, University of Latvia, Jelgavas st. 3, LV-1004 Riga, Latvia
Email: stanislavs.stankevics2@lu.lv, andrejs.aniskevics@lu.lv, Web Page: https://www.lu.lv/en/
[4]SYNPO a.s., S. K. Neumanna 1316, Pardubice 532 07, the Czech Republic
Email: marie.novakova@synpo.cz, katerina.zetkova@synpo.cz, Web Page: https://www.synpo.cz/en
[5]DEMaC-Aveiro Institute of Materials, University of Aveiro, Campus Universitário de Santiago 3810-193 Aveiro, Portugal
Email: joao.tedim@ua.pt, Web Page: https://www.ua.pt/

Keywords: polymer nanocomposite, double layered hydroxides, mechanical properties

Abstract
This study was aimed to develop a novel Mg-Al/NO_3 layered double hydroxides (LDH) and epoxy resin nanocomposite for anti-corrosive steel protection and to comprehensively evaluate the mechanical properties of this nanocomposite. Two methods were trialled to incorporate LDH particles into epoxy resin. In the first approach, a Mg-Al/NO_3 LDH slurry in water was utilised. A nine-step particle washing procedure was employed, gradually replacing water with ethanol, acetone, and finally xylene. LDH particles in xylene were added to bisphenol A epoxy in specific volume fractions and mixed with a high shear stirrer. Subsequently, an isophorone diamine hardener was added and epoxy/LDH nanocomposites were obtained. Dog-bone shaped specimens were prepared for characterisation and mechanical testing. As an alternative method for particle incorporation into epoxy resin, the insertion of dried LDH powder into the resin was used. Epoxy/LDH samples prepared in this way were also thoroughly examined. Comparative analysis of all sample groups revealed that the mechanical properties of the new nanocomposites, if reduced, were only slightly so, and in some cases, even improved.

1. Introduction

Eco-friendly Mg-Al/NO_3 layered double hydroxides (LDH) represent a unique class of nanomaterials. These compounds are characterised by their layered structure, composed of magnesium and aluminium hydroxide layers, with nitrate anions intercalated between them. Owing to this, LDH have versatile applications in various fields. One of the promising applications is utilising these materials as nanofillers in polymer matrix coatings to protect metals against corrosion [1, 2]. When incorporated into coatings, LDH enhance the barrier properties of the layer, significantly reducing the penetration of corrosive elements. Furthermore, the addition of Mg-Al/NO_3 LDH to coatings can improve the adhesion and mechanical strength of the layer, maintaining the integrity of the coating under diverse environmental conditions.

2. Materials and Methods

2.1. Preparation of Epoxy/LDH nanocomposites

Epoxy/LDH nanocomposites were prepared by two different methods. In the first approach, the MgAl-NO_3 LDH slurry in water (solids 15-20 wt%) provided by Smallmatek LDA (Aveiro, Portugal) was used. A nine-step LDH particle washing procedure was employed to gradually replace water with ethanol, acetone, and finally xylene. The MgAl-NO_3 LDH slurry in water was mixed with ethanol (slurry to ethanol ratio 1:4) by mechanical stirring at 2100 for 15 min and centrifuged at 6000 rpm for 15 mins. After the centrifugation the supernatant was removed and another dose of ethanol was added keeping the same ratio. This procedure of mixing with ethanol and centrifugation was repeated 2 more times, 3 times in total. Then this washing procedure under the same conditions was repeated only washing agents were changed. Acetone was used for washings 4^{th} to 6^{th} and xylene was used for washings 7^{th} to 9^{th}. During the 7^{th} washing, the change from acetone to xylene produced a change in appearance in the suspension from matte to gel consistency. LDH particles washing procedure is shown in Figure 1. The Tyndall effect was clearly seen in the obtained material, which indicated that the suspension contained relatively fine particles. After the last centrifugation, the LDH particles in the gel-type xylene solution were collected from the centrifuge tubes. The concentration of LDH in the xylene solution ranged between 23-26 wt% depending on the batch.

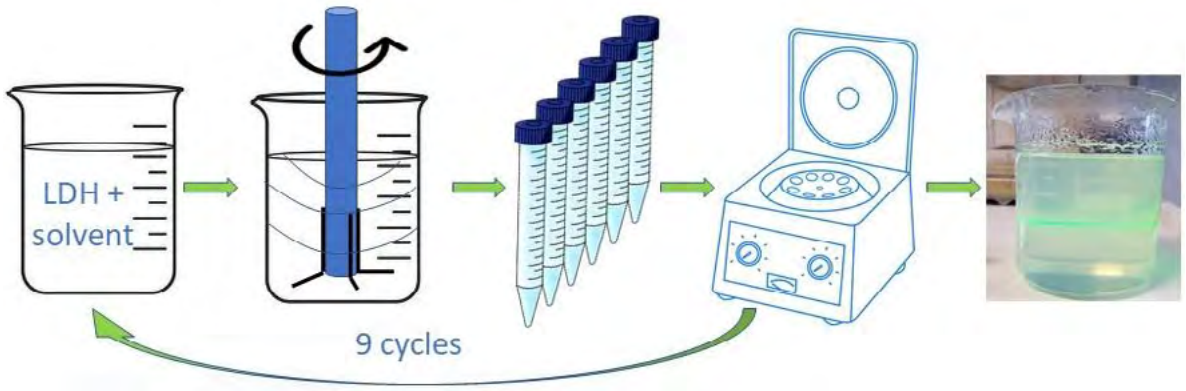

Figure 1. LDH washing procedure and gel-type xylene solution with clearly expressed Tyndall effect.

LDH particles in xylene were added to bisphenol A epoxy CHS 582 (supplied by Synpo a.s., Pardubice, the Czech Republic) in specific volume fractions (1, 2 and 5 wt% of LDH) and mixed using a high shear stirrer ULTRA TURRAX® T18 for 5 min at 15 000 rpm. Additionally, mixing was performed using an ultrasonic probe Vibra Cell Sonicator VCX 500 for 5 min with a one-minute pause after each minute in the ice bath to prevent overheating. Subsequently, an isophorone diamine hardener Telalit 0420 (Synpo a.s., Pardubice, the Czech Republic) was added in an epoxy:hardener 4:1 weight ratio, the mixture was manually stirred for 10 min and degassed using vacuum.

An alternative method for particle incorporation into epoxy resin was based on the use of MgAl-NO_3 LDH particles in powder (Smallmatek, Aveiro, Portugal). A wetting additive Disperbyk 180 (supplied by BYK Additives & Instruments, Wesel, Germany) was used to achieve a higher-quality dispersion of LDH particles within the hardener. The LDH powder was placed in a mortar and grounded for 15 min to achieve a finer texture. Disperbyk 180 was then added to the mortar (ratio 2.3:1) and mixed for an additional 10 min. The subsequent step involved blending (15 min under 15 000 rpm) this paste with required amount of Telalit 0903 to prepare a well-dispersed thick mixture. The mixture was vacuumed for 30 min, after which epoxy was added and the mixture was stirred for another 10 min, followed by a further 10 min of vacuuming.

2.2. Characterisation and Testing

The morphology of epoxy/LDH nanocomposite was checked using optical microscopy. The unhardened liquid state epoxy/LDH samples were placed onto microscope glass slides. Images intended for morphological analysis were captured utilising magnifications of 20× and 100×.

A total of six groups of epoxy/LDH specimens were prepared, with an additional group consisting of pure epoxy samples serving as a reference. Each group of specimens comprised six samples. Three groups of epoxy/LDH specimens were prepared using LDH particles in xylene gel with concentrations of 1, 2, and 5% by weight. The remaining three groups were prepared using the same concentrations, but the LDH particles were in powder form. Dog-bone shaped specimens with a gauge section cross area of 3×1 mm following ISO 527 standard were prepared. All samples were maintained at room temperature for 24 h, followed by post-curing in the oven for 2 h at 60 °C, 1 h at 80 °C and 1 h at 120 °C.

The tensile tests of developed nanocomposites were performed using H10 KT universal column testing machine (Tinius Olsen, UK), with a crosshead strain rate of 2 mm/min.

3. Results

3.1. Characterisation of LDH nanoparticles

Optical microscopy images of epoxy/LDH nanocomposite (2 wt% of LDH) are presented in Figure 2. A smooth distribution without agglomeration of LDH particles in the epoxy matrix can be seen. There are particles around 50-100 µm in length surrounded by smaller10 µm particles.

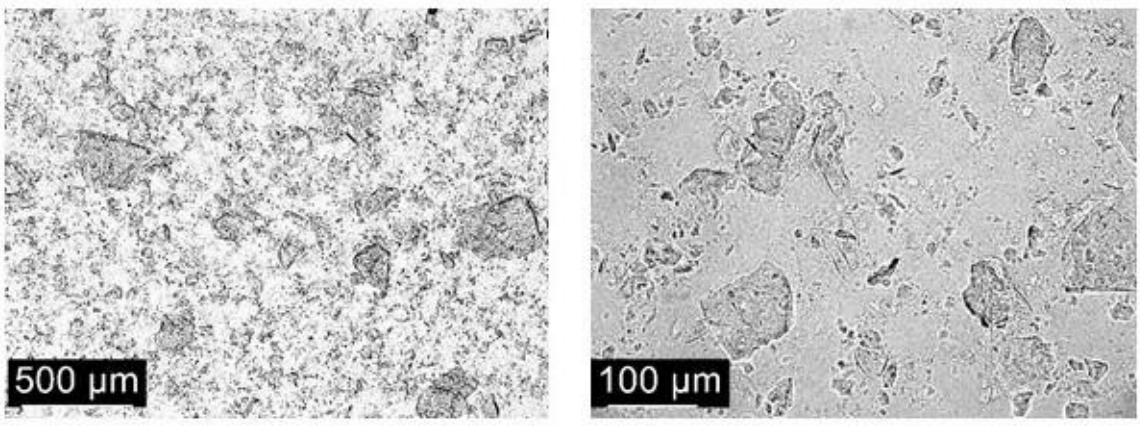

Figure 2. Optical microscopy of epoxy/LDH nanocomposite (2 wt% of LDH).

The tensile testing curves are presented in Figure 3. It is evident that mechanical behaviour of the epoxy/LDH nanocomposites prepared using both LDH particles in xylene gel (Fig. 3a) and LDH particles in a powder form (Fig. 3b) is influenced by the presence of LDH particles in the epoxy matrix. However, this influence is not the same for all investigated cases. Therefore, for a deeper analysis, the dependency of Young's modulus, tensile strength, and elongation at break on LDH weight percentage is presented in Figure 4. It can be observed that incorporating LDH, both in the xylene gel and in the powder form, increases the Young's modulus in all examined concentration cases (Fig. 4a). When 1 wt% of LDH is added into the epoxy resin by both methods, the Young's modulus increases by approximately 1.3 times, and by adding 2 wt% of LDH, it increases by as much as 1.7 times. However, when 5 wt% of LDH are incorporated, the modulus no longer increases, and even decreases, although it remains 1.5 times higher compared to pure epoxy. Analysing the strength of the nanocomposites (Fig. 4b), the most promising concentration is therefore 2 wt% of LDH. Using LDH particles in the powder form, the strength increases by 9% in comparison with pure epoxy, while it only slightly decreases for samples with LDH particles in the xylene gel. However, at a concentration of 5 wt% of LDH, the strength starts

to significantly decrease. As for elongation at break (Fig. 4c), LDH has a more negative impact, although 2 wt% of LDH in powder demonstrated similar elongation as pure epoxy.

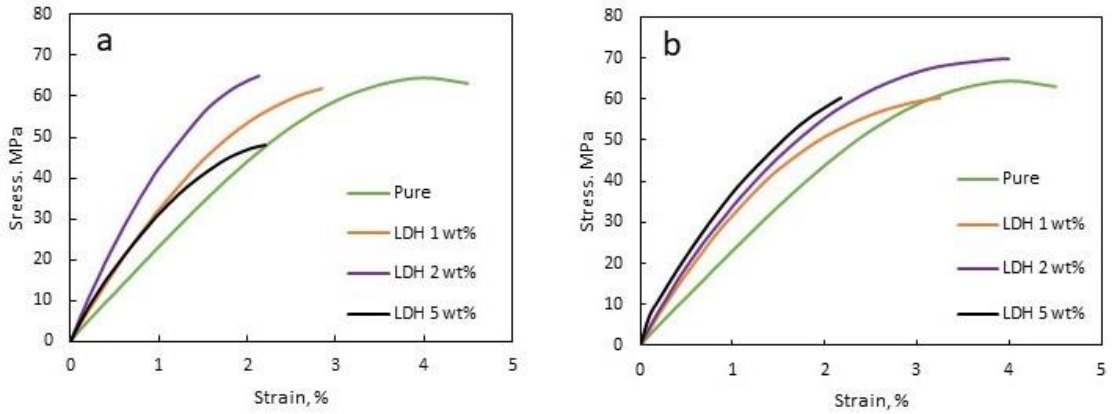

Figure 3. Tensile curves of epoxy/LDH nanocomposites prepared using LDH particles in xylene gel (a), and LDH particles in powder form (b) in comparison with pure epoxy.

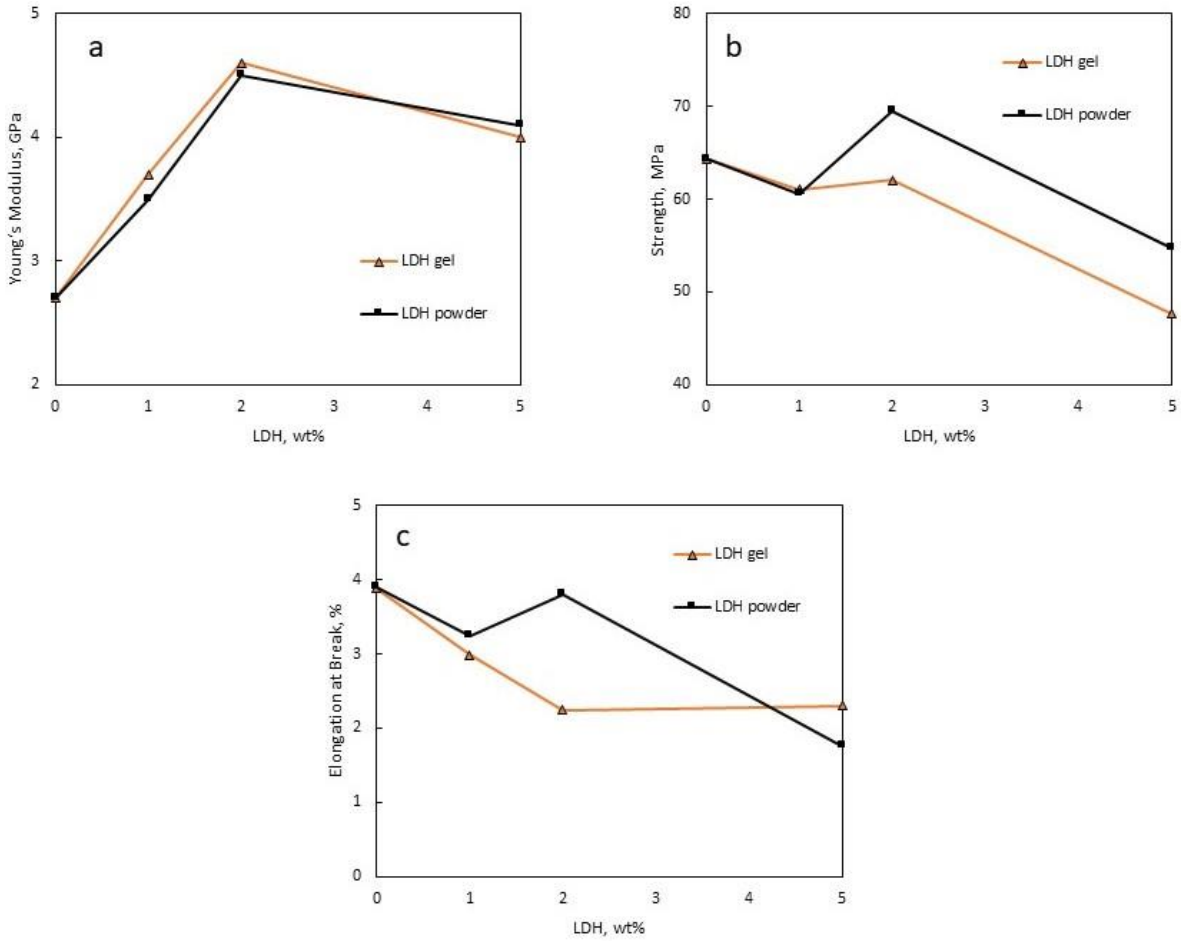

Figure 4. Effect of LDH weight percentage on the mechanical properties of epoxy/LDH nanocomposite: Young's modulus (a), tensile strength (b), and elongation at break (c).

3. Conclusions

A novel Mg-Al/NO_3 LDH and epoxy resin nanocomposite was developed and its mechanical properties were evaluated. The presence of LDH particles in the epoxy resin alters the mechanical properties of the nanocomposite, but this change is not a simple enhancement or deterioration of properties. LDH particles, regardless of their method of incorporation into the matrix, increase the Young's modulus by up to 1.7 times (at a 2wt% LDH loading). Incorporating 1-2 wt% LDH particles in the nanocomposite does not significantly affect the material's strength, although higher particle loadings may decrease this parameter. Elongation at break decreases with the insertion of LDH particles. Nevertheless, the most promising nanocomposite could potentially be the epoxy/2wt% LDH, produced from powder-type LDH.

Acknowledgments

The project has received funding from the European Union's Horizon 2020 research and innovation programme under the Marie Skłodowska-Curie grant agreement No 101007430.

References

[1] J. Tedim, S.K. Poznyak, A. Kuznetsova, D. Raps, T. Hack, M.L. Zheludkevich, et al. "Enhancement of active corrosion protection via combination of inhibitor- loaded nanocontainers". *ACS Applied Materials and Interfaces*, Vol. 2, pp 1528–35, 2010.

[2] M. Wilhelm, M. Quevedo, A. Sushkova, T. Galvão, A.C. Bastos, M. Ferreira, J. Tedim "Hexacyanoferrate-intercalated layered double hydroxides as a nanoadditive for detection of early-stage corrosion of steel: the revival of Prussian Blue". *European Journal of Inorganic Chemistry*, Vol. 2, No. 2, pp 2063–2073, 2020.

THE USE OF BLACK TEA WASTE AS A THERMO-OXIDATION STABILIZER FOR POLYETHYLENE COMPOSITES IN ROTATIONAL MOLDING TECHNOLOGY

Joanna Aniśko[1], Paulina Kosmela[2] and Mateusz Barczewski[1]

[1]Institute of Materials Technology, Faculty of Mechanical Engineering, Poznan University of Technology, Piotrowo 3, 61-138 Poznan, Poland
Email: joanna.anisko@put.poznan.pl; mateusz.barczewski@put.poznan.pl
[2]Department of Polymer Technology, Faculty of Chemistry, Gdansk University of Technology, G. Narutowicza 11/12, 80-233 Gdansk, Poland
Email: paulina.kosmela@pg.edu.pl

Keywords: black tea waste, polyethylene, thermo-oxidation, stabilization

Abstract
In this study, the antioxidant properties of black tea wastes as a filler of polyethylene composites were investigated. An extensive analysis was carried out to evaluate the possibility of stabilization the polyethylene composite. The used matrix was biobased low-density polyethylene (LDPE SEB 853 I'm Green®). The filler was introduced in 1, 2, 5, and 10 wt% in the extrusion process. First, the antioxidant properties of the natural filler were investigated using UV-Vis assays. To obtain thermal properties as the temperature of the beginning of degradation, we conducted a thermogravimetric analysis of composites in an inert and oxidative atmosphere. The composites were also evaluated in terms of their thermal properties in the presence of oxygen by OIT (oxygen induction time) determination to confirm stabilization effects. Adding 10 wt% of black tea waste increases OIT nearly 36 times compared to the unmodified polymer. Prepared composites have also been tested after accelerated aging under thermo-oxidative conditions to determine the carbonyl index in the FTIR test. Then, a thoroughly investigated material was cryogenically milled to a fine powder for rotational molding purpose. The rotomolded samples were subjected to the Fourier transform infrared spectroscopy; it appears that the addition of 10 wt% black tea waste prevents the formation of carbonyl compounds in polyethylene.

1. Introduction

Polyethylene is highly susceptible to thermal oxidation. The presence of oxygen at elevated temperatures causes chain scission, leading to the degradation of the material. This process starts with forming free radicals in the initiation mechanism, and then in the next step, the peroxy radicals are formed due to the propagation mechanism [1].

Rotational molding is the most dynamically developing technology for forming thin-walled, large-size products. It enables the manufacturing of tanks and containers from thermoplastic polymers, especially polyethylene, in one operation. It involves heating the polymer powder in a mold rotating in two axes, covering the entire internal surface of the mold in the polymer sintering process, followed by densification, cooling of the material, and demolding of the ready-to-use product [2]. Due to the polymer's low thermal conductivity and the process's nature in which no technological procedures are used in its initial phase to accelerate the first sintering phase, the polymer is subjected to long-term exposure to high temperatures in oxidizing conditions. This makes rotational molding one of the most material-demanding technologies for processing thermoplastics, generating the need to stabilize the molded polymer [3].

Antioxidants are added to prevent this degradation. The commercially available materials have artificial stabilizers, with the most commonly used pentaerythritol tetrakis(3,5-di-tert-butyl-4-hydroxyhydrocinnamate) known commercially as Irganox 1010. The use of stabilizers allows not only the manufacturing of a product free of defects and good quality but also extends the life of the molded parts by limiting the amount of free radicals in their structure. As an effect, polymeric products are less vulnerable to deterioration of mechanical properties due to degradation of their macromolecular structure during processing and long-term exposure to environmental conditions [4,5]. Furthermore, the growing ecological awareness of society leads not only to the development of new sustainable technologies and materials but also allows to determine humans' long-term ecological negative impact on the environment. Currently considered a threat, "microplastics" are one of the actuall research topics on the effects of synthetic materials on the environment [6,7]. However, the latest studies indicates that the presence of migrating modifiers from polymers to the environment is an increasingly severe problem. Several studies have proved the migration of stabilizers directly to foods and the environment [8–10].

The possible way to reduce potential environmental hazards related to synthetic antioxidants is to utilize compounds naturally occurring in fruits, herbs, and vegetables [11]. Phenolic compounds like quercetin [12,13], gallic acid [14], curcumin [15], and α-Tocopherol [13] are commonly used to stabilize polyethylene. The next group of compounds are extracts from plants like rosemary [16,17], oregano, green tea, and grapefruit seeds [18] for food packaging. The newest trend is to incorporate ground plant parts as fillers, especially waste like spent coffee grounds, cocoa husk [19], black tea waste [20], and agro wastes [21].

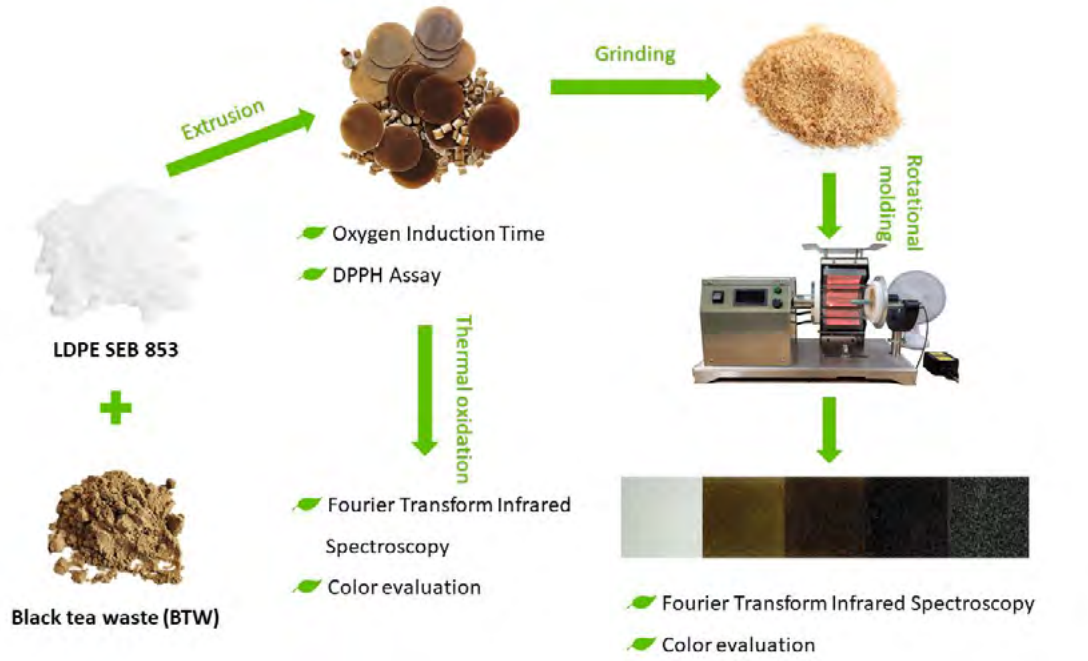

Figure 1. Schematic diagram of the production process and assessment of the properties of polyethylene composites filled with black tea waste.

Research shows that the addition of extracted active compounds alone and the addition of fragmented plant parts used as active fillers can produce beneficial stabilization effects. The low-molecular-weight compounds rich in flavonoids and polyphenols contained in them migrate to the polymer matrix, increasing the oxidation resistance of polymers [22–24]. Due to biomass diversification, this is an uncontrolled process and, therefore, requires further detailed research. It should be emphasized that while individual plants have been described as potential active fillers, the impact of pre-processing and final melt-mixing processes on their effectiveness is still undescribed.
This study aims to provide a comprehensive summary of preliminary research on using black tea waste (BTW) as a functional filler with antioxidant properties in polyethylene composites formed in the rotational molding process. As part of the experimental work, composites were produced in the extrusion process and characterized for changes in oxidation stability in the molten state by determination of oxygen induction time (OIT) and those caused by thermal aging (90 °C for 15 days). Then, these materials were processed in a laboratory and up-scalable [25] uniaxial rotational molding process to assess the effectiveness of the BTW impact on changes in the chemical structure and mechanical properties of biobased polyethylene. A flowchart showing a comprehensive approach to problem description is shown in Figure 1.

2. Experimental

2.1. Materials and sample preparation

The matrix for manufacturing the composites is biobased low-density polyethylene SEB 853 I'm Green® Braskem. The used waste filler is black tea dust collected by a tea packaging and distribution company (Poland). The filler was introduced into the polyethylene matrix in 1, 2, 5, and 10 wt%.
Composite materials were mixed in melt state using a twin-screw extruder, a ZAMAK EH16.2D. Parameters in this process are 100 rpm of the rotational speed of screws and 120 °C set as the highest temperature. To better homogenize the material second extrusion was performed at the same temperature set but higher rotational speed of screws (250 rpm). LDPE matrix as well as black tea waste (BTW), were dried before extrusion for 12 h at 60 °C. Samples prepared for evaluation properties after the thermo-oxidation aging were compression molded with a Remiplast hydraulic press; the temperature was set at 130 °C, and the highest pressure during forming was 18 MPa. The heating step lasted 2 min, followed by cooling in forced airflow for 4 min. Thermo-oxidation was established to investigate the free radical scavenging ability of the rich-in-active-compounds filler. This process was held in an air-circulating oven for 15 days at 100°C.
Materials used for rotational molding must be in a powder form; therefore, pelleted material was ground using a centrifugal mill Retsch ZM 200 with a 500 µm sieve, operating at 6,000 rpm. To prevent material from overheating, dry ice was added during grinding. The rotational molding was performed using a uniaxial rotomolding machine Rotorocket by 493K (Fig.1). Heating process continued until the temperature inside the mold reached 200 °C. After that, the mold was cooled in a forced airflow. The rotational speed of the mold was 10 rpm.

2.2. Methods

To analyze the possible stabilization effect of the fillers rich in antioxidants, the oxygen induction time (OIT) method was established. This method is based on differential scanning calorimetry (DSC) in the presence of oxygen. For each extruded and compression-molded material, 5 mg samples were taken and placed in aluminum crucibles with pierced lids. In the first method section, the temperature increases at a rate of 20 °C/min to finally reach 190 °C, then the isothermal phase for 5 min, it takes place in an atmosphere of nitrogen. This is followed by switching the atmosphere to oxygen and recording the time after which oxidation of the material occurs. This test was performed using the Netzsch 204 F1 Phoenix instrument in a triplicate.
The antioxidant activity of composites can be evaluated using the procedure proposed by Rojas-Lema et al. [26]. To do this, the 63 µM solution of DPPH (2,2-diphenyl-1-picrylhydrazyl) in methanol was prepared. The 100 mg samples were cut off from each composite material and immersed with 5 ml of prepared solution, which was contained in dark glass flasks for 2, 24, 48, and 96 h. Subsequently, the solution after each of that time was subjected to UV-vis spectroscopy at UV wavelength of 517 nm. The

control vials contain only the DPPH solution in dark glass to protect it from UV light. This analysis aims to calculate inhibition (IC), determining the percentage of radical scavenging ability as follows:

$$IC = \frac{A_{control} - A_{sample}}{A_{control}} \cdot 100\% \quad (1)$$

Where $A_{control}$ – absorbance of DPPH solution at 517 nm, A_{sample} – absorbance of the sample at 517 nm. All measurements were performed using Spectrophotometer UV-VIS UviLine 9400.

Samples submitted to thermal oxidation and the one formed in rotational molding were evaluated using Fourier transform infrared spectroscopy (FTIR). Measurements were performed using the Jasco FT/IR-4600 apparatus with a resolution 4 cm^{-1} and 64 scans in a wavenumber range of 4000 - 400 cm^{-1}. Recorded spectra and their absorbance in the range 1800 - 1650 cm^{-1} indicating carbonyl group ($A_{C=O}$) and absorbance of a methylene group (A_0 - 1500 to 1420 cm^{-1}) helped to calculate carbonyl index - CI (2). This is a commonly used indicator to evaluate oxidation levels.

$$CI = \frac{A_{C=O}}{A_0} \quad (2)$$

Thermo-oxidation and rotational molding caused changes in the color of initially obtained composites. To determine the influence of high-temperature and processing conditions on color, the total color change (ΔE) was calculated (3). Color measurements were performed in CIELab color space to carry out this analysis. The apparatus used in this evaluation is NR145 Precision Colorimetry 3nh supplied with the light source D65, the measuring aperture is Φ8mm, and the viewing geometry 45°/0°.

$$\Delta E = \sqrt{\Delta L^2 + \Delta a^2 + \Delta b^2} \quad 3)$$

3. Results and discussion

Increasing filler content has a positive impact on the stabilization of LDPE composites. Adding black tea waste gradually increases OIT with the rising filler concentration in the composite structure. The same phenomenon was observed in the reduction of absorbance of the DPPH solution after soaking in it the LDPE composites. Increasing immersion time results in increased inhibition. This proved the migration of low molecular polyphenolic compounds from fillers dispersed in a composite structure with the highest effectiveness for samples with 5 and 10 wt% BTW.

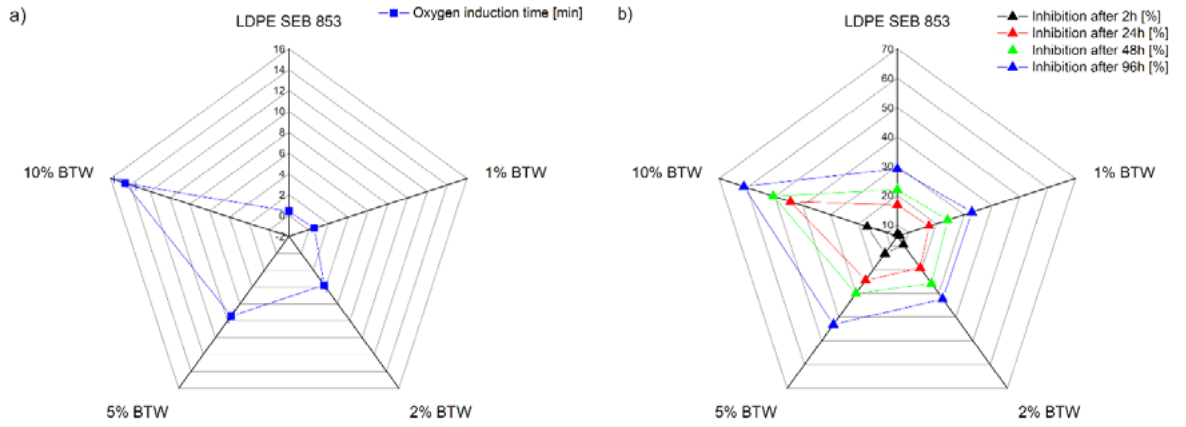

Figure 2. Antioxidant properties of the samples expressed as oxygen induction time (a) and DPPH inhibition (b).

As proven in the previously mentioned study, the phenomenal antioxidant properties of black tea waste have been tested in processing conditions and during accelerated aging. Rotational molding is a process where the material is exposed to elevated temperatures for a long time. The oxidation level measured as carbonyl index (CI) is much higher in rotomolded samples than for aged samples for 15 days at 90 °C. Rotational molding conditions caused extensive oxidation of the polyethylene; however, the addition of 10 wt% of black tea waste prevents complete chain scission reactions, leading to oxidation and material degradation. Increasing the amount of filler slightly decreased the carbonyl index compared to neat

LDPE. On the other hand, keeping the material for 15 days at 90 °C did not cause extensive oxidation; only neat LDPE exhibits oxidation. Composite samples were "self-stabilized" from the effects of elevated temperatures in an oxidizing atmosphere by indirectly introducing a filler with antioxidant properties. Thermal oxidation and rotational molding resulted in the discoloration of used materials compared to untreated compression molded samples. Higher total color change was noted for rotomolded samples. Specimens with a lower filler content exhibit higher discoloration due to the higher oxidation level. Thermally oxidized materials have the highest discoloration for 2% BTW; the same effect was confirmed for rotomolded samples, but the color change coefficient for rotomolded material is almost five times higher.

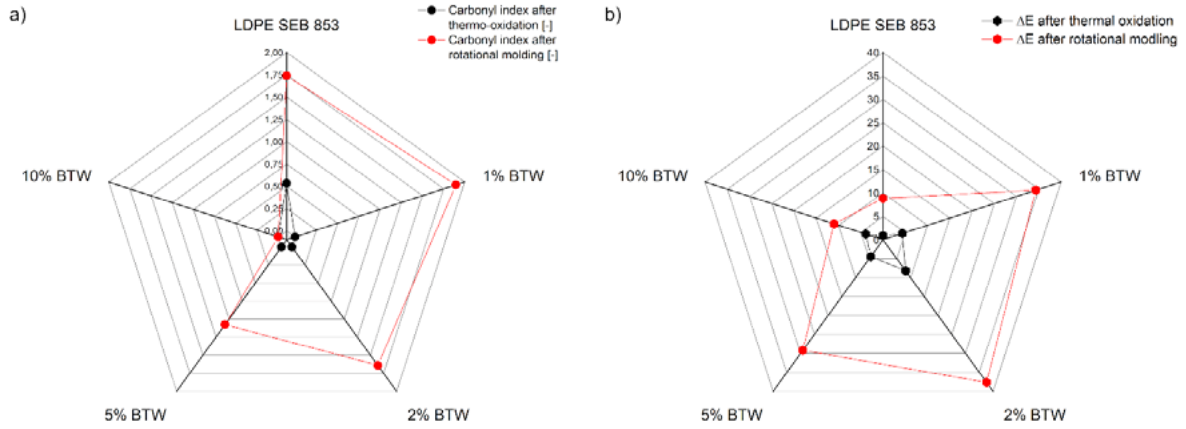

Figure 3. Properties after thermal oxidation and uniaxial rotational molding.

4. Conclusions

An analysis of carbonyl index values confirmed the demanding processing conditions of rotational molding technology. A comparison of this index between rotomolded and thermally oxidized samples shows a considerable difference. This phenomenon confirms the importance of carefully selecting stabilizers for polyethylene in the case of rotational molding technology. Using 10 wt% of BTW avoided oxidation of the material; it is also a sample with the highest oxidation induction time. It can be concluded that the filler selected for this study can serve as a sustainable stabilizer of polyethylene in thermal aging conditions in all its concentrations. Only the previously mentioned material with 10% BTW reveals sufficient antioxidant efficiency in the rotational molding conditions.

Data availability statement

The data is deposited in an open repository database and will be provided after contacting the corresponding author.

Acknowledgments

This work was funded under the project "Research on the influence of the polymer composites processing conditions on the stabilizing effect of functional plant-derived fillers" SONATA-17 2021/43/D/ST8/01491, funded by the National Science Center.

References

[1] Y. Bolbukh, P. Kuzema, V. Tertykh, I. Laguta, Thermal degradation of polyethylene containing antioxidant and hydrophilic/hydrophobic silica, J Therm Anal Calorim 94 (2008) 727–736.
[2] R.J. Crawford, J.L. Throne, Rotational molding technology, 2002.
[3] I. Emaldi, C.M. Liauw, H. Potgieter, Stabilization of Polypropylene for Rotational Molding Applications, 2015.
[4] A. Plota, A. Masek, Analysis of the aging and stabilization processes in cyclic polyolefins containing various natural or synthetic stabilizers, Polymer (Guildf) 273 (2023).
[5] A. Plota-Pietrzak, A. Masek, Functionalized metal oxide particles with antioxidant as new carriers providing higher stability of polyolefin products, Sustainable Materials and Technologies 40 (2024).
[6] R.C. Hale, M.E. Seeley, M.J. La Guardia, L. Mai, E.Y. Zeng, A Global Perspective on Microplastics, J Geophys Res Oceans 125 (2020).
[7] A. Tirkey, L.S.B. Upadhyay, Microplastics: An overview on separation, identification and characterization of microplastics, Mar Pollut Bull 170 (2021).
[8] N. Haider, S. Karlsson, Kinetics of migration of antioxidants from polyolefins in natural environments as a basis for bioconversion studies, Biomacromolecules 1 (2000) 481–487.
[9] M.S. Dopico-García, J.M. López-Vilariño, M. V. González-Rodríguez, Antioxidant content of and migration from commercial polyethylene, polypropylene, and polyvinyl chloride packages, J Agric Food Chem 55 (2007) 3225–3231.
[10] J.N. Hahladakis, C.A. Velis, R. Weber, E. Iacovidou, P. Purnell, An overview of chemical additives present in plastics: Migration, release, fate and environmental impact during their use, disposal and recycling, J Hazard Mater 344 (2018) 179–199. https://doi.org/10.1016/j.jhazmat.2017.10.014.
[11] O. Pınar, F.E. Koc, M.B. Alanalp, N. Sivri, A. Ezdesir, A. Durmus, Utilization of Silybum marianum extract as a high-performance natural antioxidant for polyethylene, J Mater Sci 59 (2024) 3725–3741.
[12] D. Tátraaljai, E. Földes, B. Pukánszky, Efficient melt stabilization of polyethylene with quercetin, a flavonoid type natural antioxidant, Polym Degrad Stab 102 (2014) 41–48.
[13] J.L. Koontz, J.E. Marcy, S.F. O'Keefe, S.E. Duncan, T.E. Long, R.D. Moffitt, Polymer processing and characterization of LLDPE films loaded with α-tocopherol, quercetin, and their cyclodextrin inclusion complexes, J Appl Polym Sci 117 (2010) 2299–2309.
[14] [14] L. Quiles-Carrillo, S. Montava-Jordà, T. Boronat, C. Sammon, R. Balart, S. Torres-Giner, On the Use of Gallic Acid as a Potential Natural Antioxidant and Ultraviolet Light Stabilizer in Cast-Extruded Bio-Based High-Density Polyethylene Films, Polymers (Basel) 12 (2019) 31. https://doi.org/10.3390/polym12010031.
[15] J. Zia, U.C. Paul, J.A. Heredia-Guerrero, A. Athanassiou, D. Fragouli, Low-density polyethylene/curcumin melt extruded composites with enhanced water vapor barrier and antioxidant properties for active food packaging, Polymer (Guildf) 175 (2019) 137–145.
[16] T. Zaharescu, S. Jipa, D.A. Mariş, M. Mariş, W. Kappel, Effect of rosemary extract on the radiation stability of UHMWPE, E-Polymers (2009).
[17] K. Doudin, S. Al-Malaika, H.H. Sheena, V. Tverezovskiy, P. Fowler, New genre of antioxidants from renewable natural resources: Synthesis and characterisation of rosemary plant-derived antioxidants and their performance in polyolefins, Polym Degrad Stab 130 (2016) 126–134.
[18] A. Sanches-Silva, D. Costa, T.G. Albuquerque, G.G. Buonocore, F. Ramos, M.C. Castilho, A.V. Machado, H.S. Costa, Trends in the use of natural antioxidants in active food packaging: a review, Food Additives & Contaminants: Part A 31 (2014) 374–395.
[19] A. Hejna, M. Barczewski, P. Kosmela, O. Mysiukiewicz, Comparative Analysis of the Coffee and Cocoa Industry By - Products on the Performance of Polyethylene - Based Composites, Waste Biomass Valorization i (2023).
[20] M. Barczewski, Z. Ortega, P. Piaskowski, J. Aniśko, P. Kosmela, J. Szulc, A case study on the rotomolding behavior of black tea waste and bio-based high-density polyethylene composites: Do active compounds in the filler degrade during processing?, Composites Part C: Open Access 13 (2024).

[21] K.A. Iyer, L. Zhang, J.M. Torkelson, Direct Use of Natural Antioxidant-rich Agro-wastes as Thermal Stabilizer for Polymer: Processing and Recycling, ACS Sustain Chem Eng 4 (2016) 881–889.
[22] M. Barczewski, J. Aniśko, A. Hejna, O. Mysiukiewicz, P. Kosmela, Ground lemon and stevia leaves as renewable functional fillers with antioxidant activity for high - density polyethylene composites, Clean Technol Environ Policy (2023).
[23] H.T.N. Kuan, M.Y. Tan, M.Z. Hassan, M.Y.M. Zuhri, Evaluation of Physico-Mechanical Properties on Oil Extracted Ground Coffee Waste Reinforced Polyethylene Composite, Polymers (Basel) 14 (2022).
[24] O.O. Awolu, R.O. Osemeke, B.O.T. Ifesan, Antioxidant, functional and rheological properties of optimized composite flour, consisting wheat and amaranth seed, brewers' spent grain and apple pomace, J Food Sci Technol 53 (2016) 1151–1163.
[25] A. Vignali, S. Iannace, G. Falcone, R. Utzeri, P. Stagnaro, F. Bertini, Lightweight Poly(ε-Caprolactone) Composites with Surface Modified Hollow Glass Microspheres for Use in Rotational Molding: Thermal, Rheological and Mechanical Properties, Polymers (Basel) 11 (2019) 624.

TRADE-OFF BETWEEN PERFORMANCE AND PROCESSABILITY OF PLA/PBAT/PHBV-FLAX COMPOSITES: EFFECT OF FLAX FIBERS SURFACE MODIFICATION

I. Bavasso[1], A. Pantaleoni[1], C. Sergi[1], M.P. Bracciale[1], J. Tirillò[1] and F. Sarasini[1]

[1] Department of Chemical Engineering Materials Environment, Sapienza-Università di Roma, Via Eudossiana 18, 00184, Roma, Italy

irene.bavasso@uniroma1.it
alessia.pantaleoni@uniroma1.it
claudia.sergi@uniroma1.it
mariapaola.bracciale@uniroma1.it
jacopo.tirillo@uniroma1.it
fabrizio.sarasini@uniroma1.it

Keywords: polymer blend, biodegradable polymer, flax fibers, green composites, fiber modification

Abstract
In this study, the research focused on exploring the reinforcing effect of varying amounts of short flax fibers (from 10 wt.% to 20 wt.%) in a ternary blend consisting of PLA/PBAT/PHBV (12 wt.%/ 48 wt.%/ 40 wt.%). The composite materials were manufactured via melt extrusion and injection molding techniques. A thorough material analysis was conducted, encompassing mechanical assessments via tensile and 3-point bending tests, as well as thermal evaluations through thermogravimetric and differential scanning calorimetry analyses. The results revealed enhancements in both tensile and bending strengths (20 % and 73 %, respectively) and moduli (99 % and over 100 %) upon the incorporation of 20 wt.% flax fibers, as opposed to the pristine polymer blend. However, there was a marginal decline in thermal stability. It was observed that the inclusion of flax fibers had an effect on the macromolecular chain mobility, evident from a significant decrease of about 66 % in the melt mass flow rate (MFR). This reduction in MFR raised concerns about the material's suitability for 3D printing filament production. To address this limitation, surface modifications of flax fibers were explored as a potential strategy to alter the flow properties of the biocomposites, maintaining or improving their mechanical and thermal properties.

1. Introduction

Biopolymers and biodegradable materials are attracting increasing interest as substitutes for petroleum-derived polymers, while their widespread adoption faces challenges due to their constrained thermo-mechanical properties and cost competitiveness compared to traditional petroleum-based alternatives [1]. Among the biodegradable polymers, polylactic acid (PLA), poly(butylene adipate-co-terephthalate) (PBAT), and poly(hydroxybutyrate-co-valerate) (PHBV) are noteworthy but they have pros and cons: PLA holds a prominent position due to its widespread use, driven by its high biodegradability and cost-effectiveness. However, its use is hampered by some drawbacks, including a high glass transition temperature and brittleness, which pose challenges in processing [2]. PBAT emerges as a promising alternative with its biodegradable copolymer structure offering high flexibility, making it suitable for specific applications where elasticity is a prerequisite. However, PBAT applicability is somewhat restricted due to its softer nature [3]. PHBV has similar properties to polypropylene but it is rigid and brittle [4]. Combining polymers with opposite properties in blend formulations offers a straightforward and cost-effective strategy to address the limitations of individual materials [5]. For example, by blending the rigid PLA with the flexible PBAT, the ductility and processability of PLA can be

augmented and incorporating PHBV it is possible to enhance the mechanical strength of PBAT. While numerous studies have delved on binary blend formulations, revealing limitations in enhancing mechanical properties [6], research on ternary blends combining PLA, PBAT, and PHBV remains relatively poor: Yang et al. investigated PLA-rich mixtures tailored for 3D printing filament production [7], while Quiles Carrillo et al. examined equal mass fraction blends intended for packaging applications as films [8]. These studies focused on the potential of ternary blends to offer unique material characteristics suitable for specific uses, highlighting a promising direction for further exploration in polymer blend research. While blending polymers helps to achieve a balance of properties rather than creating synergistic effects, incorporating a reinforcing agent can potentially promote the properties of resulting composites to a superior level. Such reinforcing materials must maintain biodegradability and, in this context, natural fibers represent a viable and eco-friendly option [9]. Flax fibers represent one of the most used as reinforcing agent in polymer composites thanks to the good specific stiffness and the cost-effectiveness [10]. One significant challenge in natural fiber/polymer composites is the lack of compatibility between hydrophilic fibers and hydrophobic matrices. This mismatch can result in poor adhesion between the fiber and matrix, primarily due to the presence of hydroxyl and polar groups in the fibers. Consequently, the composite may exhibit high moisture absorption, leading to a degradation of mechanical properties over time [11]. Hence, a crucial focus in researching polymer/natural fiber composites involves enhancing the interaction between the fiber and matrix. This can be achieved by either modifying the surface of the fiber [12] or by modifying the matrix using additives known as coupling agents [13].

In this work, a ternary blend PLA/PBAT/PHBV was used as matrix for the manufacture of green polymer composites with short flax fibers as reinforcing agents. The study involved the i) optimization of the blend formulation, ii) the evaluation of flax fiber reinforcing effect by the adoption of different fiber dosages (10 wt.%, 15 wt.% and 20 wt.%) and iii) the study of flax fiber modification using Acrylated Epoxidized Soybean Oil (AESO) jointly with specific pretreatments (alkaline and O_3) to promote the chemical bond between fiber and oil. The performances of the blends and the composites were evaluated by measuring the mechanical properties (tensile, flexural) and the thermal properties (thermogravimetry, differential scanning). The effectiveness of fiber modification was preliminary proved by Fourier Transform InfraRed (FT-IR) spectroscopy and morphological (scanning electron microscopy) analysis.

2. Materials and Methods

The ternary blend was obtained by mixing a PLA/PBAT (20 wt.%/80 wt.%) blend with different amount of PHBV (from 20 wt.% to 80 wt.%). A two-stage process was adopted for the manufacture of blends involving extrusion (co-rotating twin-screw extruder, Thermo Scientific Process 11, ThermoFisher Scientific) and injection molding (Haake MiniJet IIPro, Thermo Fisher Scientific). The temperature profile used during the extrusion from feeder to die was 145 °C—155 °C—155 °C—160 °C—170 °C—170 °C—165 °C—165 °C. The mold was heated at 85 °C while the loading cylinder was kept at 190 °C.

A specific blend composition (PLA/PBAT/PHBV 12 wt.%/48 wt.%/40 wt.%) was adopted for the manufacture of composites by adding different amount of flax fibers (FF) as 10 wt.%, 15 wt.% and 20 wt.%. For the fiber modification, alkalization, using NaOH (5 wt.%) [14] for 4 h, and/or ozonation according to the procedure reported elsewhere [15] were considered. The further modification with Acrylated Epoxidized Soybean Oil (AESO) was conducted according to the procedure proposed by Boukerrou et al. [16].

The tensile and flexural properties of specimens were measured on a Zwick/Roell Z010 universal testing machine according to ISO 527–2 (type 1 BA, $l_0 = 30$ mm) and ISO 178, respectively. Thermogravimetric (TGA) analysis was carried out by heating the samples from room temperature to 800 °C under nitrogen atmosphere and with a heating rate of 10 °C/min (TG 209 F1 Libra thermogravimetric analyzer (NETZSCH, Selb, Germany). Differential scanning calorimetry (DSC) analysis of the samples was performed with a nitrogen flow of 60 mL/min (DSC 214 Polyma by Netzsch) and thermal program as heating −150 °C to 200 °C (5 min hold), cooling to −150 °C (5 min hold) and a second heating to 200 °C, all steps performed with a rate of 10 °C/min. Molecular characterization was performed by Fourier Transform InfraRed (FT-IR) spectroscopy. IR spectra were acquired on a Bruker VERTEX 70

spectrometer, equipped with a diamond attenuated total reflectance (ATR) cell, in the mid-infrared region (400 - 4000 cm^{-1}) and collecting 128 scans with a resolution of 4 cm^{-1}. Flax fibers and the fracture surface of composite morphologies were studied by means of a scanning electron microscope (FE-SEM Mira3 by Tescan). The specimens were sputter coated with gold before the analysis.

3. Results

The mechanical properties evaluated through quasi-static tests revealed that as the PHBV content increased in the ternary blend, both the strength and modulus were improved. Specifically, when comparing results from PLA/PBAT alone (with a tensile strength of 10.42 MPa ± 1.86 MPa and Young's modulus of 0.30 GPa ± 0.06 GPa), blending with 40 wt.% PHBV led to a remarkable increase of approximately 95.4 % in strength and over 100 % in modulus. Similarly, in bending properties, there was a substantial increase of about 152 % and 357 % in strength and modulus, respectively, compared to those of the neat PLA/PBAT (with a strength of 8.51 MPa ± 0.16 MPa and modulus of 0.19 GPa ± 0.09 GPa). However, there was a decrease in maximum elongation by up to 109.2 % ± 0.4 %.

The introduction of flax fibers (FF) into the polymer blend resulted in notable improvements in both tensile and flexural strength, with increases of approximately 11.3 % and 52 % (with 10 wt.% of FF), 13.7 % and 66.8 % (with 15 wt.% of FF), and 20.1 % and 73.4 % (with 20 wt.% of FF), respectively. Such results proved the effectiveness of flax fibers as reinforcing agents and in reducing polymer consumption. In addition, the presence of fibers did not lead to significant alterations in thermal stability, noticeable only at temperatures exceeding 300 °C, nor in the overall crystallinity of the polymers in the blend. A notable change was observed in the appearance of a bimodal melting peak of PHBV in the presence of FF, highlighting the influence of fibers on the mobility of polymer macromolecules, as also evidenced by the decrease in melt mass flow rate (MFR), with increasing FF content (10 wt.%), by about 48.2% compared to that of the polymer blend (28.2 ± 0.5 g/10min). This reduction in MFR raised concerns about the material's suitability for 3D printing filament production. To address this limitation, surface modifications of fibers were explored as a strategy to modify the flow properties of the biocomposites and to promote fiber/matrix adhesion. Before the treatment with an AESO solution [16], the fibers underwent pretreatment involving alkalinization alone, ozonation alone, and a combination of both, to assess the effectiveness of the two-step modification approach.

FT-IR analysis revealed a reduction in signals in the range of 2990-2754 cm^{-1} (CH stretching) in alkali-treated fibers, along with decreased absorptions at 1734 cm^{-1} (C=O stretching) and 1157 cm^{-1} (C-O-C stretching). These changes are indicative of the partial removal of the hemicellulosic component of the fiber, confirming the efficacy of the treatment [17]. In the O_3-treated fibers spectrum, a new signal at 1735 cm^{-1}, assigned to the carboxyl group (C=O), was detected, confirming the ozone effect in oxidizing cellulose hydroxyl groups to carboxyl groups [18]. In the spectrum of AESO treated fibers, shifts in the signals associated with CH, C-O-C, and C=O stretching of cellulose, were observed [19]. Fibers subjected to the combined alkaline-O_3 pretreatment exhibited more pronounced shifts compared to those treated with only one of the pretreatments. This indicates a higher loading of AESO on the surface, likely due to the increased reactivity of fibers toward oil bond formation.

The SEM micrographs included in Figure 1 reveal a coating on the FF resulting in a smoother and more uniform surface (Figure 1b) with respect to the neat FF (Figure 1a), where waxy substances and grooves are visible [20].

Regarding the thermal stability of FF (Figure 2), the alkalinization and ozonation preceding the AESO treatment resulted in a shift of the maximum degradation peak by approximately 13.7 °C (NaOH/AESO_FF) and 16.4 °C (O_3/AESO_FF), possibly due to partial degradation of FF in alkaline and oxidizing environments [21]. Moreover, when both pretreatments were applied, even to a slight extent, a shift to a higher temperature of the degradation peak (351.1 °C) was observed, likely attributed to the presence of a higher amount of AESO on FF (whose dTG is reported as inset in Figure 2b).

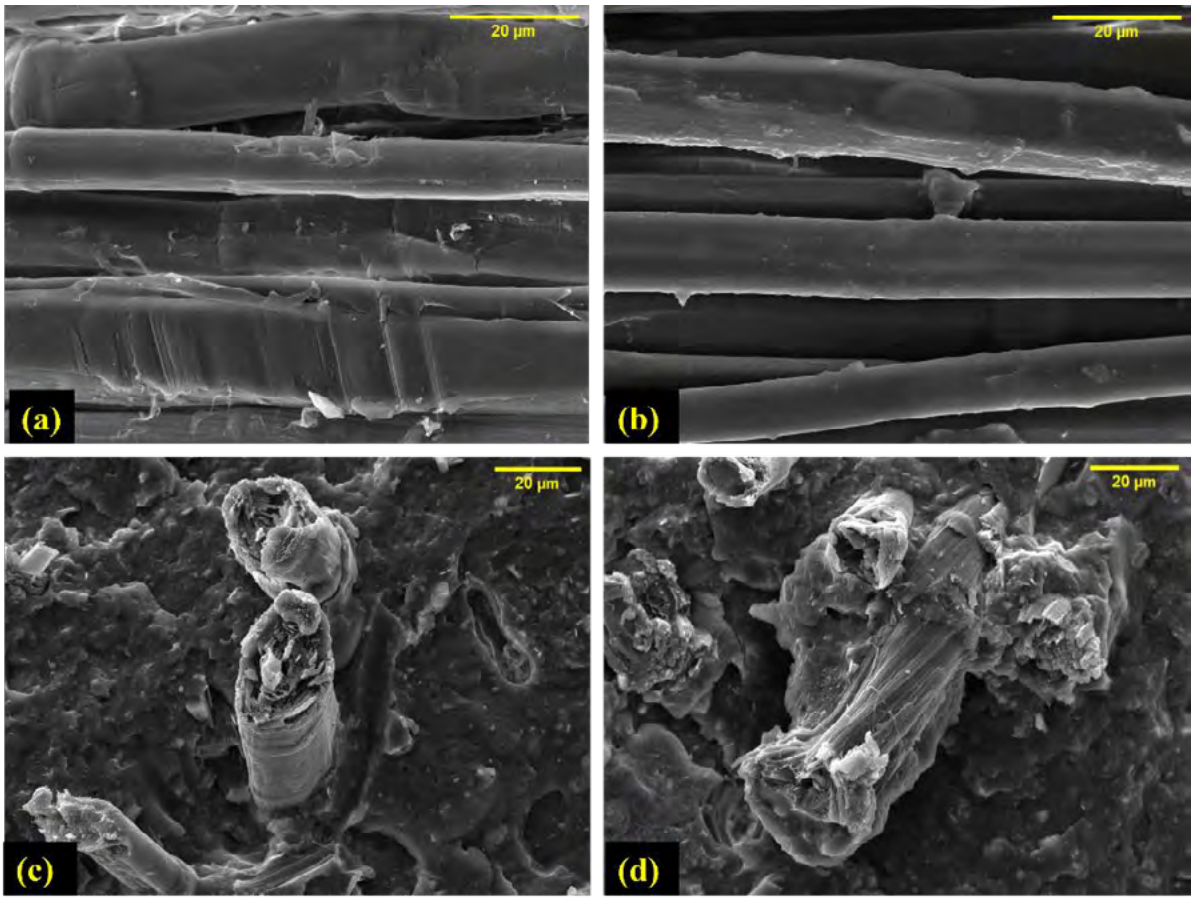

Figure 1. SEM micrographs of (a) neat FF, (b) NaOH/O_3/AESO_FF, (c) PLA/PBAT/PHBV_neat FF and (d) PLA/PBAT/PHBV_ NaOH/O_3/AESO_FF.

The modified FF were used in the fabrication of polymer composites using the ternary blend PLA/PBAT/PHBV (12 wt.%/48 wt.%/40 wt.%). To assess the compatibility between the polymer and the FF, specimens were fractured under cryogenic conditions, and the fracture surface images are depicted in Figure 1, specifically for the composites with neat FF (Figure 1c) and NaOH/O_3/AESO_FF (Figure 1d). The FF surface modification promoted fiber/matrix adhesion, while in the absence of modification, a cleaner fiber surface and debonding marks from the matrix are evident. Additionally, from this preliminary study, the MFR of composites with 10 wt.% of NaOH/O_3/AESO_FF was higher (36.9 %) than that of the composite with neat FF (14.6 g/10min ± 0.7 g/10min), demonstrating the feasibility of this strategy as promoter of composite processability.

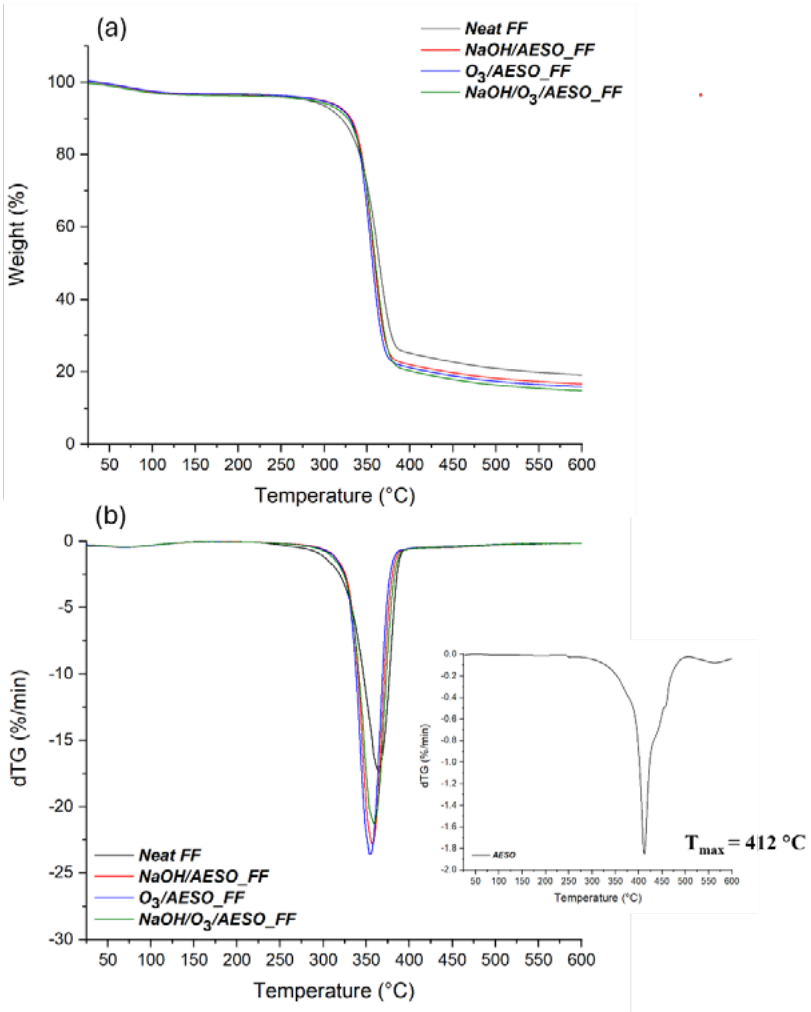

Figure 2. Thermogravimetric results of neat and modified FF.

4. Conclusions

In this work, the properties of a ternary polymer blend based on PLA/PBAT/PHBV and its composites with flax fibers as reinforcing agents were studied. The addition of PHBV to the PLA/PBAT blend was found to enhance both the strength and modulus of the final polymer formulation under quasi-static condition. Furthermore, the incorporation of 20 wt.% of flax fibers led to notable enhancements in tensile and bending strengths (20.1 % and 73.4 %, respectively) and moduli (over 100 %) compared to the neat PLA/PBAT/PHBV blend. The inclusion of flax fibers affected the mobility of polymer molecules, leading to a notable decrease of 48.2 % in the melt mass flow rate (MFR) with an amount of fibers equal to 10 wt.%. To overcome this limitation, surface modifications of the fibers were investigated to promote the flow properties of the biocomposites and enhance adhesion between the polymer matrix and the filler. Employing a combined alkalinization and ozonation pretreatment before AESO dipping facilitated the chemical bonding of a superior amount of oil onto the surface of FF compared to using a single pretreatment. This enhancement in adhesion was supported by micrographs of the fracture surface of the composites, and the flowability of the composite formulation was improved, as indicated by preliminary measurements of the MFR. Future tests will be conducted to assess how fiber surface modifications influence the mechanical/thermal properties of the composites.

Acknowledgments
Financed by the European Union - NextGenerationEU (National Sustainable Mobility Center CN00000023, Italian Ministry of University and Research Decree n. 1033 - 17/06/2022, Spoke 11 - Innovative Materials & Lightweighting).

References

[1] J.D. Badia, O. Gil-Castell, A. Ribes-Greus. Long-term properties and end-of-life of polymers from renewable resources. *Polymer Degradation and Stability,* 137: 35-57, 2017.
[2] H.R. Dana and F. Ebrahimi. Synthesis, properties, and applications of polylactic acid-based polymers. *Polymer Engineering and Science*, 22-43, 2022.
[3] N. Perumal, S. Sreekantan, Z. A. A. Hamid, A. Rusli, K. Bhubalan, J. N. Appaturi. Effect of Plasticizer and Compatibilizer on Properties of Polybutylene Adipate-Co-Terephthalate (PBAT) with Acetylated Starch. *Journal of Polymers and the Environment*, 32: 289-302, 2024.
[4] R. Muthuraj, M. Misra, A. K. Mohanty. Biodegradable compatibilized polymer blends for packaging applications: A literature review. *Journal of Applied Polymer Science,* 135(24): n/a-n/a, 2018.
[5] A. K. Pal, M. Misra, A. K. Mohanty. Silane treated starch dispersed PBAT/PHBV-based composites: Improved barrier performance for single-use plastic alternatives. *International Journal of Biological Macromolecules*, 229: 1009-1022, 2023.
[6] H. Qiao, A. Maazouz, K. Lamnawar. Study of Morphology, Rheology, and Dynamic Properties toward Unveiling the Partial Miscibility in Poly(lactic acid)—Poly(hydroxybutyrate-co-hydroxyvalerate) Blends. *Polymers*, 14(24):5359, 2022.
[7] M. Yang, J. Hu, N. Xiong, B. Xu, Y. Weng, Y. Liu. Preparation and properties of PLA/PHBV/PBAT blends 3D printing filament. *Materials Research Express*, 6(9), 2019.
[8] L. Quiles-Carrillo, N. Montanes, J.M. Lagaron, R. Balart, S. Torres-Giner. In situ compatibilization of biopolymer ternary blends by reactive extrusion with low-functionality epoxy-based Styrene–Acrylic oligomer. *Journal of Polymers and the Environment*, 27(1): 84-96, 2019.
[9] M. Akter, M.H. Uddin, H.R. Anik. Plant fiber-reinforced polymer composites: a review on modification, fabrication, properties, and applications. *Polymer Bulletin*, 81:1–85, 2024.
[10] A.P. More. Flax fiber–based polymer composites: a review. *Advanced Composites and Hybrid Materials*, 5: 1-20, 2022.
[11] Y. Feng, H. Hao, H. Lu, C. L. Chow, D. Lau. Exploring the development and applications of sustainable natural fiber composites: A review from a nanoscale perspective. *Composites Part B: Engineering*, 276: 111369, 2024.
[12] X. Xia, W. Liu, L. Zhou, Z. Hua, H. Liu, S. He. Modification of flax fiber surface and its compatibilization in polylactic acid/flax composites. *Iranian Polymer Journal*, 25: 25–35, 2016.
[13] P. Georgiopoulos, A. Christopoulos, S. Koutsoumpis, E. Kontou. The effect of surface treatment on the performance of flax/biodegradable composites. *Composites Part B: Engineering*, 106: 88-98, 2016.
[14] A. Arbelaiz, G. Cantero, B. Fernández, I. Mondragon, P. Gañán, J.M. Kenny. Flax fiber surface modifications: Effects on fiber physico mechanical and flax/polypropylene interface properties. *Polymer Composites*, 26(3): 324-332, 2005.
[15] A. Pantaleoni, F. Sarasini, P. Russo, J. Passaro, L. Giorgini, I. Bavasso, M.L. Santarelli, E. Petrucci, F. Valentini, M.P. Bracciale, A. Marrocchi. Facile and Bioinspired Approach from Gallic Acid for the Synthesis of Biobased Flame Retardant Coatings of Basalt Fibers. *ACS Omega*, 9(17): 19099–19107, 2024.
[16] A. Boukerrou, M. Beztout, H. Djidjelli, S. Krim, D. Hammiche. The Effect of Chemical Treatment of Cellulose with Epoxidized Soybean Oil (ESO) on the Properties PVC/Cellulose Composites. *Molecular Crystals and Liquid Crystals*, 556: 223-232, 2012.
[17] R. Bahrami, R. Bagheri, C. Dai. Influence of Fine Structure on the Variations of Thermal and Mechanical Properties in Flax Fibers Modified with Different Alkaline Treatment Conditions. *Journal of Natural Fibers*, 19(13): 5239–5257, 2022.

[18] B. Fathi, M. Harirforoush, M. Foruzanmehr, S. Elkoun, R. Mathieu. Effect of TEMPO oxidation of flax fibers on the grafting efficiency of silane coupling agents. *Journal of Material Science*, 52: 10624–10636, 2017.
[19] S. Kasetaite, S. De la Flor, A. Serra, J. Ostrauskaite. Effect of Selected Thiols on Cross-Linking of Acrylated Epoxidized Soybean Oil and Properties of Resulting Polymers. *Polymers*, 10(4):439, 2018.
[20] A. Rana, R. W. Evitts. Development and characterization of flax fiber reinforced biocomposite using flaxseed oil-based bio-resin. *Journal of Applied Polymer Science*, 132(15): n/a-n/a, 2014.
[21] B. Fathi, M. J. Harirforoush, M. R. Foruzanmehr, S. Elkoun, M. Robert. Effect of TEMPO oxidation of flax fibers on the grafting efficiency of silane coupling agents. *Journal of Material Science*, 52: 10624–10636, 2017.

EXPERIMENTAL AND COMPUTATIONAL STUDY OF THE POLYMERIZATION KINETICS OF A REACTIVE ACRYLIC THERMOPLASTIC RESIN

D. Gacon[1*], O. De Almeida[2*], R. D'Elia[3*], F. Schmidt[4*]

[*]Institut Clément Ader, Université de Toulouse, CNRS UMR 5312, IMT Mines Albi, UPS, INSA, ISAE-SUPAERO, Campus Jarlard, F-81013 Albi, France
[1]Email: damien.gacon@mines-albi.fr
[2]Email: olivier.dealmeida@mines-albi.fr
[3]Email: raffaele.delia@mines-albi.fr
[4]Email: fabrice.schmidt@mines-albi.fr

Keywords: Polymerization kinetics, Elium® resin, Trommsdorff effect, Exothermic reaction, Reactive thermoplastic

Abstract
A good comprehension of the reaction kinetics during thermoplastic composite manufacturing by liquid-reactive processes is crucial to limit the formation of porosities by monomer evaporation. This study focuses on the free-radical polymerization kinetics of Elium® C195E acrylic resin initiated by a mixture of 3 different organic peroxides over a wide range of synthesis temperature. As the polymerization of methyl methacrylate is chemically and diffusionally controlled, a variety of curve shapes were obtained from DSC experiments. To account for the different polymerization regimes, a new hybrid kinetic modelling approach based on mechanistic models has been introduced. Experimental observations have shown that an overall factor including initiator efficiency and termination rate constant can be expressed in terms of conversion and temperature as the contribution of two peaks related to the intensities of the Trommsdorff effect and vitrification. Promising simulation results of this overall factor using Richards-type equations were obtained over a broad range of isothermal synthesis temperature.

1. Introduction

Recyclability is currently driving the transition from thermoset to thermoplastic matrices for the manufacture of long-fiber composites. The high viscosity of thermoplastics, which implies significant liquid processing temperatures and pressures, has long held back market growth for these composites. However, they are now gaining in popularity thanks to the development of liquid-reactive processes suitable for thermoplastic composites [1-3]. Polymerization of reactive mixtures of low-viscosity monomers takes place in-situ, enabling reinforcements to be impregnated at lower temperatures and pressures. Among these reactive mixtures, acrylic resins composed of poly(methyl methacrylate) (PMMA) and methyl methacrylate (MMA) have been extensively studied recently [1-6].

Bulk free-radical polymerization of MMA into PMMA has been widely employed in a broad range of applications [3], [4], [7], [8]. This reaction follows the typical steps of initiation (formation of free radicals by decomposition of initiators), propagation (chain growth by monomer addition), termination (deactivation of active macroradicals) and possible transfer [9]. Diffusional hindrances of the molecules resulting from the increase in viscosity lead to phenomena which complicate the kinetic control of the reaction. Among them, a sudden auto-acceleration phenomenon, known as 'gel effect' or 'Trommsdorff effect', is observed [10]. Its occurrence and intensity depend strongly on the curing parameters, but also on the viscosity and the composition of the reactive mixture and the amount of resin in composites.

Due to the low evaporation temperature of the monomers, the highly exothermic nature of the reaction and self-accelerating nature of gel effect, voids induced by monomer boiling can form during processing of thick composite parts, leading to a sharp decrease of their mechanical properties [3-5]. The nucleation and growth of voids by monomer evaporation is a complex multiphysical phenomenon, requiring a good understanding of the polymerization kinetics of these reactive mixtures and therefore the development of a robust kinetic model.

In the present work, the reaction kinetics of an Elium® acrylic resin grade (C195E) initiated by organic peroxides is analyzed by differential scanning calorimetry (DSC) under dynamic and isothermal conditions. The measured data are fitted to a temperature, conversion and composition dependent kinetic model. Combined with heat transfer models adapted to the processing techniques, this model will provide better control of composite processing and limit the formation of porosities within the matrix [3-5]. The literature reports two main approaches to model the free-radical polymerization of MMA: mechanistic [2-4], [11-13] and semi-empirical models [1], [5], [6]. Taking into account the various phenomena which occur during the reaction requires the use of several assumptions and the development of complex models. Hence, this work proposes a hybrid modelling approach to describe the various reaction stages observed during the polymerization of this reactive mixture.

2. Material and methods

2.1. Materials

Elium® C195E (Arkema, France), a pultrusion-grade acrylic resin which contains around 20 to 25 % of acrylic pre-polymers diluted in reactive MMA monomers according to TGA measurements, was kindly supplied by Arkema, France. Due to its low viscosity at room temperature and high reactivity, this mixture is well suited to the manufacture of thick composite parts by reactive pultrusion. The combined action of three organic peroxides is considered for the initiation of the polymerization reaction. 1 phr of each peroxide is added to the mixture and their dissociation leads to the formation of two free radicals. They intervene at various stages of the reaction owing to their different thermal stability.

2.2. DSC Analysis

Reaction kinetics and physico-chemical phenomena were analyzed using a power-compensation Perkin-Elmer 8500 DSC under nitrogen. Reactive mixtures of approximately 10 g were prepared by gently stirring Elium® resin with the various peroxides until homogenisation. Samples containing 4 to 5 mg of this reactive mixture were hermetically sealed in 30 µl aluminium pans. A low sample mass was chosen to minimize the impact of the heat generated by the reaction on the medium temperature and to prevent the capsule from collapsing due to monomer evaporation.
Reaction kinetics were investigated under isothermal conditions at various temperatures ranging from 50 to 120 °C in order to develop a polymerization kinetics model. Samples initially at 0 °C were first heated at 300 °C.min^{-1} to rapidly reach the isothermal temperature T_{iso}. This temperature was maintained until the end of the polymerization reaction and the heat of polymerization ΔH_p^{iso} was measured by integrating the exothermic peak heat flux as a function of time. Since the experimental isothermal conditions can lead to an incomplete cure (due for instance to vitrification effect), dynamic DSC scans were also performed to the reactive mixture at 10 °C.min^{-1} from 0 °C to 200 °C. These non-isothermal conditions allowed fully polymerizing the mixture and gave access to the total heat of reaction $\Delta H_p^{100\%}$. Conversion α and conversion rate $d\alpha/dt$ can be calculated based on Eq.1 and Eq.2.

$$\alpha = \frac{\Delta H_p^{iso}}{\Delta H_p^{100\%}} \qquad [-] \tag{1}$$

$$\frac{d\alpha}{dt} = \frac{d\Delta H_p^{iso}}{dt}\frac{1}{\Delta H_p^{100\%}} \qquad [s^{-1}] \tag{2}$$

3. Experimental study

3.1. Non-isothermal syntheses

Heat flow as a function of temperature captured from dynamic scans of Elium® C195E polymerization with 3 phr peroxide at 10 °C.min^{-1} is shown in Figure 1. A total enthalpy of polymerization $\Delta H_p^{100\%} = 453 \pm 6\ J.g^{-1}$ was calculated with good repeatability over 4 trials. Considering the initial presence of pre-polymer in the Elium® resin, this heat of polymerization is in good agreement with values of around $550\ J.g^{-1}$ reported in the literature for pure MMA [8]. At this heating rate, 3 different polymerization regimes can be identified after induction. Polymerization begins at 80 °C and the reaction kinetics accelerate with increasing temperature. This acceleration becomes significant over 40 % conversion due to the Trommsdorff effect, with a polymerization peak $T_{peak} = 112.4 \pm 1.6$ °C. Finally, a shoulder is observed at the end of curing due to diffusional limitations related as vitrification effect.

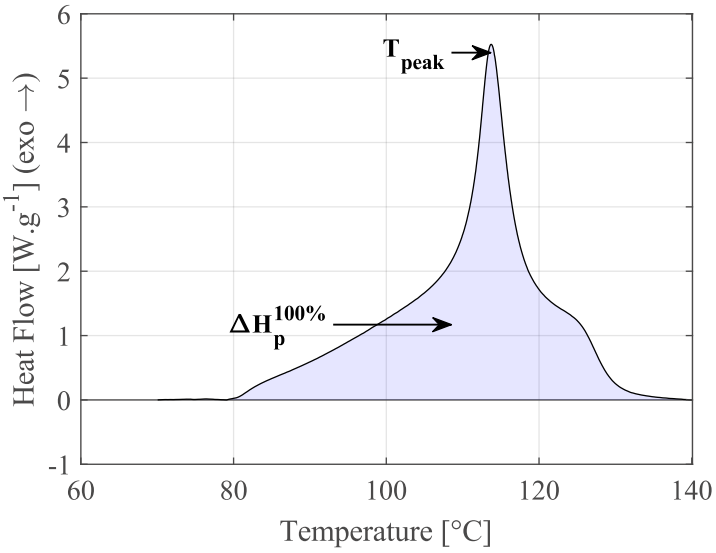

Figure 1. DSC thermogram of non-isothermal synthesis of Elium® C195E resin initated by 3 phr of organic peroxides at 10 °C.min^{-1}.

3.2. Isothermal syntheses

A wide range of synthesis temperatures was examined throughout the isothermal test campaign. An overview of the various thermograms obtained from the polymerization of this reactive mixture is shown in Figure 2. One of the striking features of these DSC scans is the diversity of heat flow curve shapes observed in this temperature range. From the 75 °C isothermal thermogram presented in Figure 3.a, 5 polymerization regimes can be identified. The presence and intensity of each of these regimes depends on various criteria, such as sample mass, synthesis temperature and composition of the reactive mixture.

All DSC tests showed that the reaction takes place after an induction time t_{ind}, related to the dissociation of organic peroxides to start the reaction. This induction time thus depends on the nature and quantity of initiator and exhibits an Arrhenius-type dependence with activation energy $E_{a,ind} = 126.6\ kJ.mol^{-1}$ and pre-exponential factor $A_{ind} = 8.931 \times 10^{-18}\ s$ yielding a coefficient of determination $R^2 = 0.973$ (Eq.3).

$$t_{ind} = A_{ind} \times \exp\left(\frac{E_{a,ind}}{\mathcal{R}T_{iso}}\right) \qquad [s] \tag{3}$$

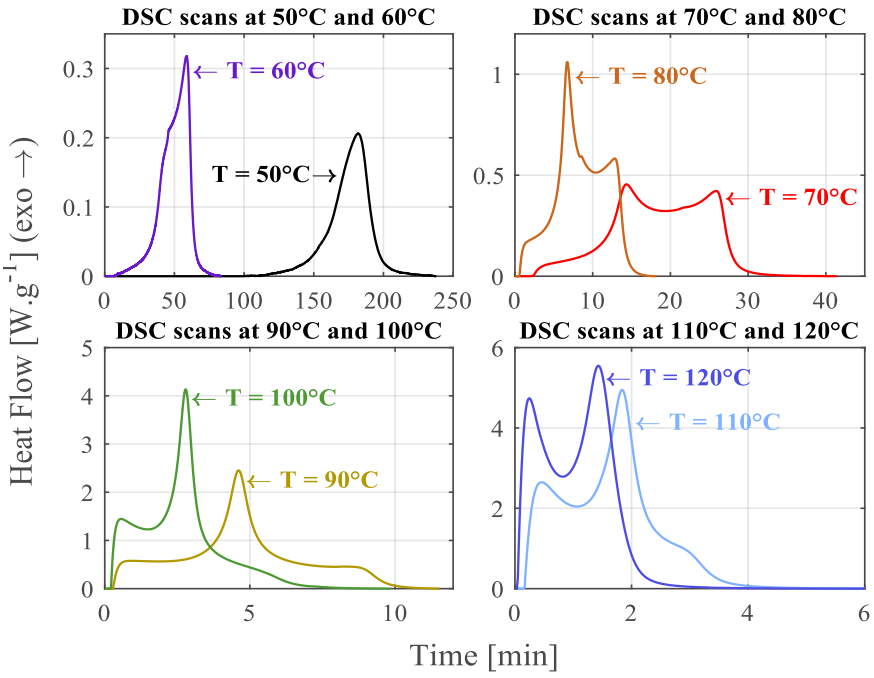

Figure 2. DSC thermograms of isothermal syntheses of Elium® C195E resin initated by 3 phr of organic peroxides at curing temperatures ranging from 50 to 120 °C.

While the first peroxides dissociate, propagation of the first chains begins, leading to an increase in heat flow in phase 2. The higher the temperature of the isotherm, the faster this rise until a peak is reached, followed by a decrease in flux. This decrease in flux is in line with the classical free-radical polymerization theory [5], [11], [14]. However, syntheses at lower temperatures differ from this theory as the flux increases until it reaches a plateau. This phase is therefore strongly correlated with the dissociation kinetics of peroxides and consequently with the number of chains activated by free radicals.

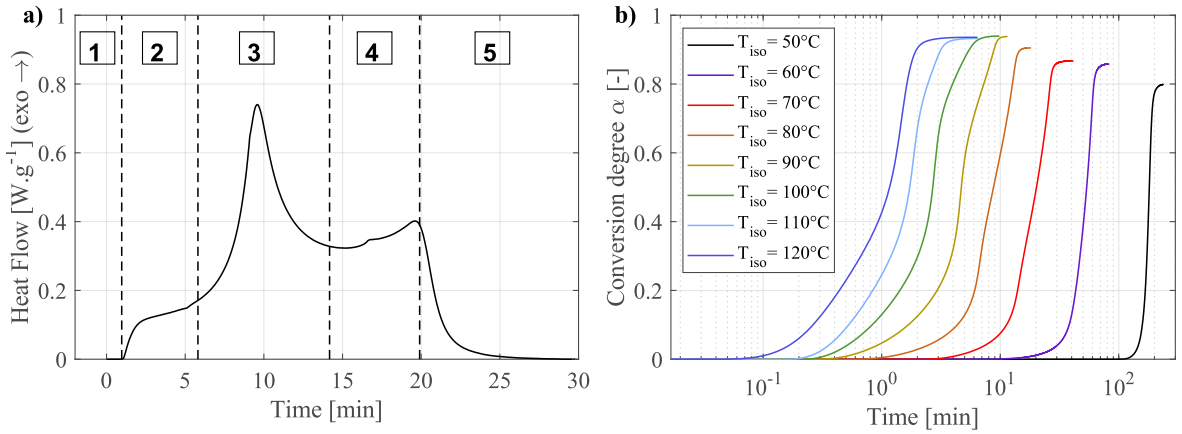

Figure 3. (a) Polymerization regimes during isothermal synthesis of Elium® C195E at 75 °C. (b) Conversion versus reaction time measured by DSC of Elium® C195E resin polymerization initated by 3 phr of organic peroxides at curing temperatures ranging from 50 to 120 °C.

The sudden rise in reaction rate observed in phase 3 corresponds to Trommsdorff effect. This effect is attributed to the entanglement of macroradicals, which are less able to diffuse due to the increased viscosity of the medium. Termination rate drops as reaction becomes diffusion-controlled, resulting in a disruption of the equilibrium between the number of chains activated by initiation and deactivated by termination. Less impacted than macroradicals, monomers are still highly mobile and propagation is

therefore not greatly affected by viscosity. As a consequence, the overall reaction rate and the medium temperature increases significantly [10], [11]. It is particularly important to note that the use of power-compensated DSC together with a low sample mass limits the increase in temperature of the medium and therefore the intensity of the Trommsdorff effect.

As the Trommsdorff effect is less important or even non-existent at lower temperatures and the dissociation of peroxides continues, another polymerization regime (phase 4) can be observed following this phenomenon.

The last phase (phase 5), characterised by a sharp drop in polymerization kinetics, is related to vitrification. As the reaction proceeds, the glass transition temperature of the material rises and may exceed the synthesis temperature. The medium then becomes glassy and the monomers can no longer diffuse, leading to an incomplete reaction. The conversion versus time curves of the isothermal DSC tests are displayed in Figure 3.b. It clearly shows that the final conversion increases with isothermal temperature but never reaches 100 %. Although the T_g of PMMA is about 114 °C, the eventual monomer evaporation may hinder the reaction at high synthesis temperature [3].

4. Numerical study

Several models were proposed in the literature to model the polymerization kinetics of Elium® resins. Among these models, Han et al. [5] and Palmieri et al. [1] applied an easy-to-implement semi-empirical approach using an autocatalytic Kamal-Sourour model to estimate conversion rate (Eq. 4).

$$\frac{d\alpha}{dt} = \left(A_1 \exp\left(-\frac{E_{a,1}}{\mathcal{R}T}\right) + A_2 \exp\left(-\frac{E_{a,2}}{\mathcal{R}T}\right)\alpha^m\right)(1-\alpha)^n \qquad [s^{-1}] \tag{4}$$

In Eq. 4, A_i and $E_{a,i}$ are the pre-exponential factors and activation energies of the rate constants and m and n are the reaction orders. The heat flux curves as a function of time, simulated after parametric identification on MATLAB®, are compared to the experimental curves at 100, 110 and 120 °C in Figure 4. Although this model correctly accounts for the Trommsdorff effect at high polymerization temperatures, it presents significant limitations to describe the occurring phenomena. It is quite important to note that it suggests a high heat flow at the start of the isothermal cycle. Thus, global semi-empirical models do not transcribe the induction and heat flux increase phases at the start of the reaction, nor the post-Trommsdorff polymerization phase observed at lower temperatures.

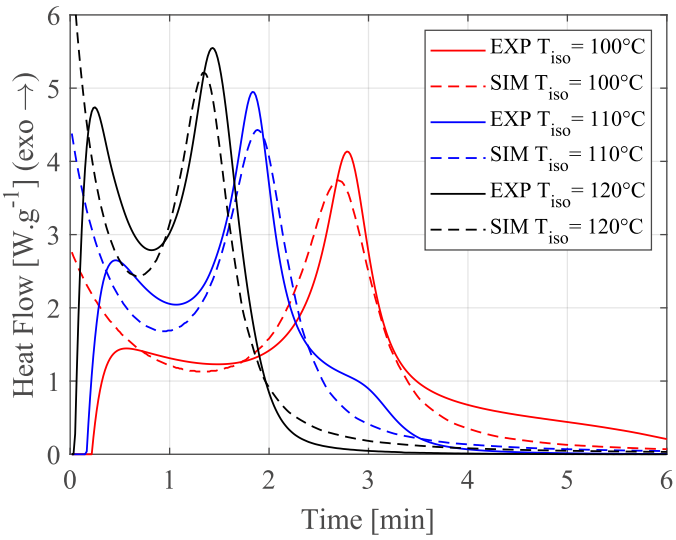

Figure 4. Comparison of the experimental (solid lines) and simulated (dashed lines) heat flow over time during Elium® C195E polymerization at high isothermal temperature [100-120]°C.

Another approach consists in modelling the evolution of the monomer concentration on the basis of the MMA free-radical polymerization reaction scheme. Based on various assumptions, such as quasi-steady state approximation (QSSA) for live radicals throughout the reaction or long-chain hypothesis (LCH), the rate of change of monomer concentration *d[M]/dt* can be expressed using Eq. 5.

$$\frac{d[M]}{dt} = -k_p \sqrt{\frac{2f \sum_i k_{d,i}[I]_i}{k_t}} M \qquad [mol.m^3.s^{-1}] \tag{5}$$

In Eq. 5, *[M]* is the monomer concentration, $[I]_i$ is the i-th initiator concentration, k_p, $k_{d,i}$ and k_t are the rate coefficients of the propagation, dissociation of the i-th initiator and termination steps respectively and f is the initiator efficiency factor [9], [12]. This expression can be rewritten in terms of α as in Eq. 6.

$$\frac{d\alpha}{dt} = k_p \sqrt{\frac{2f \sum_i k_{d,i}[I]_i}{k_t}} (1-\alpha) \qquad [s^{-1}] \tag{6}$$

Numerous studies have investigated the evolution of these kinetic parameters over the course of the reaction, using notably the free volume theory. However, the influence of the reactive mixture composition, the operating temperature, the viscosity of the medium and the various physical phenomena described earlier make this determination more than challenging. Among these factors, f and k_t are extremely sensitive to the curing conditions and molecular entanglement, which requires the use of empirical models [2], [3], [6], [15].

In this study, the dissociation of each peroxide is supposed to follow a first-order reaction kinetics according to the values of $k_{d,i}$ given by the supplier. For defining k_p, Gayot et al. [3] proposed an expression and parameters based on free volume theory. This parameter is indeed commonly considered to be almost constant up to high conversion levels owing to the high mobility of monomers. In their expression, k_p therefore takes into account the evolution of diffusion coefficient of the monomers upon conversion and temperature. Instead, we propose to define the parameter f/k_t following the methodology suggested by Biondi et al. [6] and to analyze its evolution as a function of conversion and synthesis temperature. The evolution of the f/k_t factor for each isothermal condition can be determined from the DSC experimental data of conversion and conversion rate by rearranging Eq. 6.

The curves showing polymerization rate $d\alpha/dt$ (Figure 5.a) and f/k_t factor (Figure 5.b) as a function of conversion degree α presented in Figure 5 highlight the presence of two peaks. Their occurrence and intensity are correlated with the synthesis temperature of the isothermal DSC tests. Based on the analysis of these two graphs, we assume that the first peak that occurs is linked to the Trommsdorff Effect (drop of the termination rate constant k_t), while the second peak is linked to polymerization-induced vitrification. Comparison of these curves also underlines the thermodependence of the peak conversion of both phenomena. By representing each of these two peaks by a Richards-type sigmoidal growth equation, the f/k_t factor can be expressed with Eq. 7 where n_p corresponds to the number of peaks and $K_{a,i}$, $K_{b,i}$, B_i and $\alpha_{p,i}$ are the normalization factor, intensity factor, shape factor and peak conversion of the i-th peak respectively [16].

$$\frac{f}{k_t} = \sum_{i=1}^{n_p} K_{a,i} \frac{K_{b,i}\, exp\left(-K_{b,i}(\alpha - \alpha_{p,i})\right)}{\left(1 + B_i\, exp\left(-K_{b,i}(\alpha - \alpha_{p,i})\right)\right)^{\frac{1+B_i}{B_i}}} \qquad [mol.s.m^{-3}] \tag{7}$$

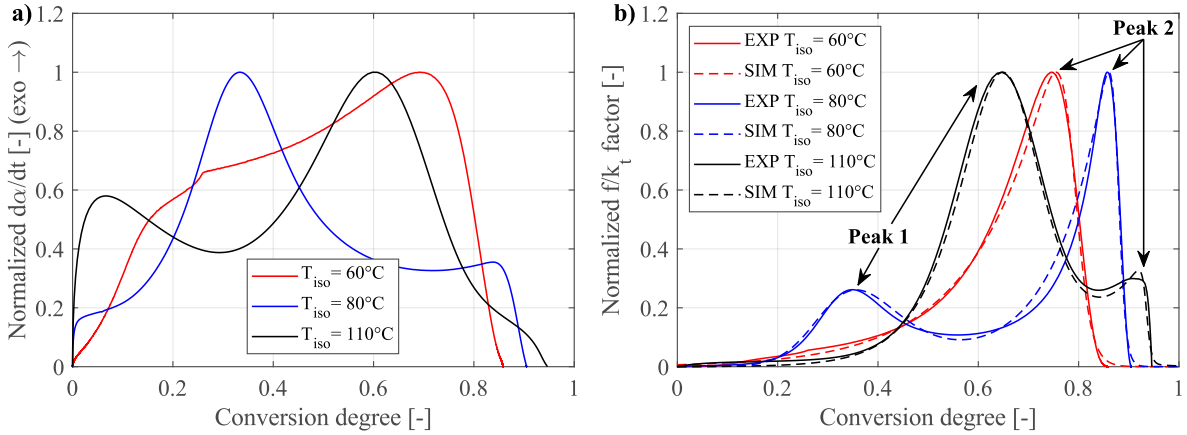

Figure 5. (a) Normalized reaction rate curves versus conversion obtained from isothermal DSC tests and (b) experimentally (solid lines) and numerically (dashed lines) determined normalized f/k_t factor as a function of conversion for Elium® C195E polymerization at 60, 80 and 110 °C.

After identifying the 8 fitting parameters on MATLAB®, first results from simulations at 60, 80 and 110 °C are compared with experimental measurements in Figure 5.b. Comparison of these curves shows that modelling the f/k_t factor using this expression seems effective over a wide range of isothermal synthesis temperatures and from the start to the end of the reaction. In fact, this new modelling approach provides a good representation of the influence of the Trommsdorff effect and vitrification on polymerization, and provides encouraging leads to simulate the various curve shapes observed throughout the isothermal DSC experiments.

5. Conclusions

As the free-radical polymerization of MMA is controlled not only kinetically but also by diffusion, several phenomena such as Trommsdorff effect and vitrification occur during the reaction. Although the Elium® C195E reaction is highly exothermic ($\Delta H_p^{100\%} = 453 \pm 6\ J.g^{-1}$), the use of a power-compensated DSC and low-mass samples allows reducing the effects of heat transfer on the polymerization kinetics.

Initial simulations of the reaction kinetics using the semi-empirical Kamal-Sourour equation show that this type of model is limited in describing this complex reaction system, particularly at low synthesis temperatures. In this research work, a hybrid model based on the mechanistic approach employed in the literature has been introduced. From the isothermal DSC results, we were able to highlight that the evolution of the kinetic factor f/k_t with conversion could be represented as the contribution of two distinct peaks. Thus, this new approach offers simply implementable Richards-type equations to model the f/k_t factor while preserving the physical meaning of the model.

Preliminary modelling results of this factor are quite promising across the entire conversion range. Analyses of the thermodependence of the fitting parameters and of the evolution of the heat flux as a function of time by reinjecting this expression of f/k_t into the polymerization equation, as well as an application of this model to anisothermal conditions, will be explored in future work. Coupled with thermal and evaporation kinetics models, this reaction kinetics model will enable us to predict the formation of porosities during the manufacture of thick composite parts.

References

[1] B. Palmieri, A. Petriccione, G. De Tommaso, M. Giordano, and A. Martone, 'An Efficient Thermal Cure Profile for Thick Parts Made by Reactive Processing of Acrylic Thermoplastic Composites', *J. Compos. Sci.*, vol. 5, no. 9, p. 229, Aug. 2021, doi: 10.3390/jcs5090229.

[2] A. Zoller, P. Escalé, and P. Gérard, 'Pultrusion of Bendable Continuous Fibers Reinforced Composites With Reactive Acrylic Thermoplastic ELIUM® Resin', *Front. Mater.*, vol. 6, p. 290, Dec. 2019, doi: 10.3389/fmats.2019.00290.
[3] S. F. Gayot, C. Bailly, T. Pardoen, P. Gérard, and F. Van Loock, 'Processing maps based on polymerization modelling of thick methacrylic laminates', *Mater. Des.*, vol. 196, p. 109170, Nov. 2020, doi: 10.1016/j.matdes.2020.109170.
[4] Y. Suzuki, D. Cousins, J. Wassgren, B. B. Kappes, J. Dorgan, and A. P. Stebner, 'Kinetics and temperature evolution during the bulk polymerization of methyl methacrylate for vacuum-assisted resin transfer molding', *Compos. Part Appl. Sci. Manuf.*, vol. 104, pp. 60–67, Jan. 2018, doi: 10.1016/j.compositesa.2017.10.022.
[5] N. Han, I. Baran, J. S. M. Zanjani, O. Yuksel, L. An, and R. Akkerman, 'Experimental and computational analysis of the polymerization overheating in thick glass/Elium® acrylic thermoplastic resin composites', *Compos. Part B Eng.*, vol. 202, p. 108430, Dec. 2020, doi: 10.1016/j.compositesb.2020.108430.
[6] M. Biondi, A. Borzacchiello, and P. A. Netti, 'Isothermal and non-isothermal polymerization of methyl methacrylate in presence of multiple initiators', *Chem. Eng. J.*, vol. 162, no. 2, pp. 776–786, Aug. 2010, doi: 10.1016/j.cej.2010.06.004.
[7] D. S. Achilias and I. Sideridou, 'Study of the effect of two BPO/Amine initiation systems on the free-radical polymerization of mma used in dental resins and bone cements', *J. Macromol. Sci. Part A*, vol. 39, no. 12, pp. 1435–1450, Jan. 2002, doi: 10.1081/MA-120016045.
[8] A. Maffezzoli, D. Ronca, G. Guida, I. Pochini, and L. Nicolais, 'In-situ polymerization behaviour of bone cements', *J. Mater. Sci. Mater. Med.*, vol. 8, pp. 75–83, 1997.
[9] G. Odian, *Principles of polymerization*, 4th ed. Hoboken, N.J: Wiley-Interscience, 2004.
[10] S. K. Soh and D. C. Sundberg, 'Diffusion-controlled vinyl polymerization. I. The gel effect', *J. Polym. Sci. Polym. Chem. Ed.*, vol. 20, no. 5, pp. 1299–1313, 1982, doi: 10.1002/pol.1982.170200513.
[11] D. S. Achilias, 'A Review of Modeling of Diffusion Controlled Polymerization Reactions', *Macromol. Theory Simul.*, vol. 16, no. 4, pp. 319–347, May 2007, doi: 10.1002/mats.200700003.
[12] D. S. Achilias and C. Kiparissides, 'Modeling of diffusion-controlled free-radical polymerization reactions', *J. Appl. Polym. Sci.*, vol. 35, no. 5, pp. 1303–1323, 1988.
[13] S. Beuermann *et al.*, 'Critically evaluated rate coefficients for free-radical polymerization, 2.. Propagation rate coefficients for methyl methacrylate', *Macromol. Chem. Phys.*, vol. 198, no. 5, pp. 1545–1560, 1997, doi: 10.1002/macp.1997.021980518.
[14] V. Jašo, D. Stoiljković, R. Radičević, and O. Bera, 'Kinetic modeling of bulk free-radical polymerization of methyl methacrylate', *Polym. J.*, vol. 45, no. 6, pp. 631–636, Jun. 2013, doi: 10.1038/pj.2013.6.
[15] N. Tefera, G. Weickert, and K. R. Westerterp, 'Modeling of free radical polymerization up to high conversion. II. Development of a mathematical model', *J. Appl. Polym. Sci.*, vol. 63, no. 12, pp. 1663–1680, 1997, doi: 10.1002/(SICI)1097-4628(19970321)63:12<1663::AID-APP17>3.0.CO;2-0.
[16] A. Greco and A. Maffezzoli, 'Statistical and kinetic approaches for linear low-density polyethylene melting modeling', *J. Appl. Polym. Sci.*, vol. 89, no. 2, pp. 289–295, 2003, doi: 10.1002/app.12079.

MICRO-ZONE AND MACRO MECHANICAL BEHAVIOR OF SIC_F/SI_3N_4 COMPOSITE MODIFIED BY INTRA-BUNDLE MATRIX

Haohui Hao[1], Xiaomeng Fan[2], Xinlei Wang[3]

[1] Science and Technology on Thermostructural Composite Materials Laboratory, Northwestern Polytechnical University, Xi'an, Shaanxi, PR China
Email: haohaohui@mail.nwpu.edu.cn
[2] Science and Technology on Thermostructural Composite Materials Laboratory, Northwestern Polytechnical University, Xi'an, Shaanxi, PR China
Email: fanxiaomeng@nwpu.edu.cn
[3] Science and Technology on Thermostructural Composite Materials Laboratory, Northwestern Polytechnical University, Xi'an, Shaanxi, PR China
Email: wangxinlei@mail.nwpu.edu.cn

Keywords: ceramic matrix composites, fiber push-in test, mechanical properties, interphase

Abstract
In this work, the microstructure of the interfacial zone is optimized to improve the mechanical properties of SiC_f/Si_3N_4 composite, and the relationship between micro-zone and macro mechanical behavior was revealed. For SiC_f/Si_3N_4, the interphase destruction occurred during the Si_3N_4 deposition process, leading to the existence of discontinuous interphase in the outside of intra-bundle area. After incorporating SiBCN and SiC matrices into the fiber bundle, the BN interphase can be well protected, and the uniformity of the matrix microstructure within the fiber bundle is further enhanced, which increases the Weibull modulus of the interfacial shear strength (IFSS), resulting in the higher load sharing efficiency in fiber bundle and the enhanced macro-mechanical properties. Especially after incorporating SiC matrix into intra-bundle area, the higher IFSS also can be obtained, corresponding to the higher load transferring efficiency, and the strength and toughness of the composites are improved significantly.

1. Introduction

Ceramic matrix composites (CMCs) have the advantages of low density, thermal shock resistance, excellent high temperature mechanical properties, so they can be used as high temperature structural materials in the field of aero-engine and hyper-sonic vehicle thermal protection system [1-3]. In CMCs, the introduction of continuous fibers can significantly improve the toughness and avoid the brittle fracture [4]. By introducing the interphase into the micro-zone between fiber and matrix, the matrix crack can effectively deflect at the interfacial zone, ensuring the load-bearing capacity of the fiber [5]. Thus, the microstructure of interfacial zone has an important influence on the macro-mechanical properties [6].

The interphase in the composite mainly plays the role of transferring the matrix load, deflecting the crack and relieving the thermal residual stress (TRS) [7]. In previous studies, the interface model assumed that the interfacial state of all fibers in the composites was the same, and the variation of stress distribution in different zones within the fiber bundle was ignored [8]. However, even under ideal preparation conditions, the matrix distribution is not uniform, which would result in the uneven stress distribution, and the effect of stress distribution on the interfacial zone should be considered. The interfacial micro-zone mechanical behavior of the CMCs can be studied through push-in and push-out test. The push-in test can be conducted directly on the polished specimen surface, with little

requirements for specimen thickness, while the thickness of the push-out test specimens should to be 20-40 μm [9].

SiC fiber reinforced Si_3N_4 composite (SiC_f/Si_3N_4) prepared by chemical vapor infiltration (CVI) process is a new type of CMC that shows interesting characters [10, 11]. However, the flexural strength of SiC_f/Si_3N_4 was 380 MPa, which was obviously lower than that of the SiC fiber reinforced SiC composite (SiC_f/SiC) prepared by CVI process (~534 MPa) [10, 12]. The thermal expansion mismatch between SiC fiber and Si_3N_4 matrix is more severe, which results in interphase destruction during the deposition process of Si_3N_4. According to the previous analysis, the interphase destruction due to the non-uniform matrix distribution in the intra-bundle areas might be the main factor that caused the decrease of mechanical properties. It is essential to carry out the related study to optimize the interfacial zone microstructure to improve the mechanical properties of SiC_f/Si_3N_4.

2. Experimental

2.1. Materials preparation

In this work, plain woven SiC fiber cloth (Fujian Leadasia new material, Co., Ltd, Quanzhou, China) was employed as reinforcement. The preforms were obtained by stacking the SiC fiber cloth and fixed with a graphite mold. A BN interphase with a thickness of 400-500 nm was deposited on the surface of the fiber through CVI process at 650 °C for 40 h. Then the three composites were prepared by the different matrix densification process, as shown in Fig. 1. Si_3N_4 matrix was prepared by CVI process. After infiltration Si_3N_4 matrix for 640 h, SiC_f/Si_3N_4 can be obtained. SiBCN matrix was introduced into the fiber preform by precursor infiltration and pyrolysis process (PIP). The PIP process was repeated for 5 cycles. Finally, Si_3N_4 matrix was introduced by CVI process for 400 h to complete the matrix densification and SiC_f/SiBCN-Si_3N_4 was obtained. SiC matrix was firstly deposited on the BN-coated preform by CVI process at 1000 °C for 40 h [13]. After deposition of Si_3N_4 matrix for 540 h through CVI process, SiC_f/SiC-Si_3N_4 was fabricated.

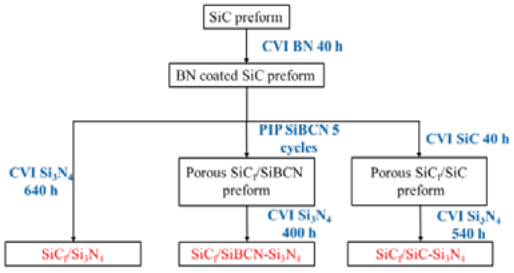

Fig. 1. Preparation process of all the three composites.

2.2. Micro-zone mechanical and macro-mechanical properties

The push-in test was conducted on a nano-indenter (Hysitron TI 950 TriboIndenter, Hysitron, USA). In this work, the diameter of SiC fiber is 14 μm, and the diameter of the flat indenter in the push-in test is 10 μm. The diameter ratio of indenter to fiber is 0.71, and the influence of the indenter on the push-in test can be neglected [14]. When the indenter contacted the fiber, it was loaded at a rate of 30 nm/s, and immediately unloaded at a rate of 30 nm/s when the displacement of the indenter reached 1000 nm. In order to ensure that the test results can fully reflect the fiber debonding state in the composite, at least 20 push-in tests were performed on each sample. In order to study the difference between the mechanical properties of the three composites, the flexural strength (σ_f) and fracture toughness of all the three composites were tested respectively. To ensure the accuracy of the test, five samples were measured in each test. For flexural strength test, the dimensions of the samples were 40 mm × 5 mm × 3 mm, and the loading rate during the test was 0.5mm/min with a span of 30 mm [15]. Fracture toughness of the composites was tested by single-edge notched beam (SENB) method [16]. The dimensions of the

specimens were 30 mm × 6 mm × 3 mm, and the test was carried out under a loading speed of 0.05 mm/min with a span of 24 mm. The above mechanical tests were all carried out on the universal test machine (Sans Materials Testing Co. Ltd., Shenzhen, China).

2.3. Characterization

The bulk density and open porosity of all the three composites were tested by the Archimedes' method. The microstructure, element distribution, fracture morphology of all the three composites were characterized by scanning electron microscope (SEM, Sigma 300, ZEISS, Germany). The surface morphology of the composite after fiber push-in test was also characterized by atomic force microscopy (AFM, Dimension Icon, Bruker, Germany).

3. Results and discussion

3.1. Phase composition and microstructure

As listed in Table 1, the densities of SiC_f/Si_3N_4, $SiC_f/SiBCN\text{-}Si_3N_4$ and $SiC_f/SiC\text{-}Si_3N_4$ composites are 2.5, 2.2 and 2.6 g/cm^3, respectively. All the three composites were densified by the same CVI process of Si_3N_4 matrix, and their open porosity is close and in the range of 6-8 vol.%. The SiC fiber volume content of all the three composites is 36 vol.%. For SiC_f/Si_3N_4, the volume content of Si_3N_4 matrix is 49 vol.%. For $SiC_f/SiBCN\text{-}Si_3N_4$, the volume content of Si_3N_4 and SiBCN matrices are 30 and 11 vol.%, respectively. For $SiC_f/SiC\text{-}Si_3N_4$, the volume content of Si_3N_4 and SiC matrices are 41 and 8 vol.%, respectively. As listed in Table 2, the densities of Si_3N_4, SiBCN and SiC matrices are 2.9, 2.0 and 3.2 g/cm^3, respectively. The closed porosities of the composites were calculated through the open porosity and density of all the three composites. It was shown that the closed porosities of the composites were 9, 11 and 7 vol.%, respectively.

Table 1. Density, porosity and phase composition of all the three samples.

Composite	Density (g/cm^3)	Open porosity (vol.%)	Closed porosity (vol.%)	Volume content (vol %)			
				SiC fiber	Si_3N_4 matrix	SiC matrix	SiBCN matrix
SiC_f/Si_3N_4	2.5	6	9	36	49	-	-
$SiC_f/SiBCN\text{-}Si_3N_4$	2.2	7	11	36	30	-	11
$SiC_f/SiC\text{-}Si_3N_4$	2.6	8	7	36	41	8	-

Table 2. Properties of all phase in the samples.

	SiC fiber	SiC matrix	Si_3N_4 matrix	SiBCN matrix	BN interphase
Young's modulus (GPa)	339	441	272	150	62
CTE ($10^{-6}\cdot K^{-1}$)	5.1	4.6	2.8	3.0	3.2
Density (g/cm^3)	3.0	3.2	2.9	1.8	1.4

Fig. 2 shows the BSE images of cross-sectional morphology of three composites. In Fig. 2a, both the inter-bundle and intra-bundle pores exist in SiC_f/Si_3N_4, which were caused by the bottleneck effect of CVI process. As shown in Fig. 2b, for some fibers, BN interphase is continuous and wrapped on the outside of the fiber tightly, while for another part of fibers located in the outside of fiber bundle, the interphase is discontinuous, and Si_3N_4 matrix embeds between the fiber and the interphase. During the CVI process, Si_3N_4 matrix was deposited layer by layer. When cooling from preparation temperature, the interphase would peel off for part of fiber due to the thermal expansion mismatch between SiC fiber and Si_3N_4 matrix, and the gap would be formed between SiC fiber and BN interphase. During the subsequent matrix deposition process, the reaction gas reached to the gap and generates Si_3N_4 matrix.

Thus, Si_3N_4 matrix was embed into the interfacial damage zone, resulting in the discontinuous BN interphase (as shown in Fig. 2b). As can be seen from Fig. 2c, the intra-bundle matrix of SiC_f/SiBCN-Si_3N_4 is mainly composed of SiBCN matrix. The inter-bundle pores are caused by the bottleneck effect during CVI, while the intra-bundle pores are mainly caused by the gas release and matrix volume contraction during PIP. As shown in Fig. 2d, all the BN interphase is continuous. In addition, the cracks in the SiBCN matrix are filled by the Si_3N_4 matrix, resulting in a two-phase hybrid structure in the intra-bundle area. For SiC_f/SiC-Si_3N_4, as can be seen from Fig. 2e, the intra-bundle and inter-bundle pores also exist, which is similar to that of SiC_f/Si_3N_4. As shown in Fig. 2f, different from SiC_f/Si_3N_4, all the interphase is continuous.

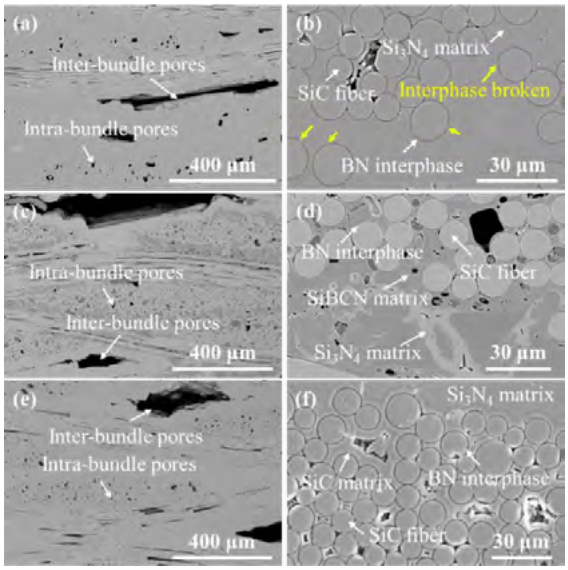

Fig. 2. The low-magnification images showing cross-sectional morphology and the high-magnification images showing intra-bundle microstructure for (a, b) SiC_f/Si_3N_4, (c, d) SiC_f/SiBCN-Si_3N_4 and (e, f) SiC_f/SiC-Si_3N_4.

3.2. Micro-zone mechanical behavior

Fig. 3 shows the load-displacement curves of all the three composites in the fiber push-in test. In consideration of loading characteristics of push-in curves, the curves of SiC_f/Si_3N_4 are divided into two types, noted as SiC_f/Si_3N_4-I (Fig. 3a) and SiC_f/Si_3N_4-II (Fig. 3b), corresponding to the continuous and discontinuous interphase (As shown in Fig. 2b). As shown in Fig. 3a, the inflection point can be clearly found at the end of the linear segment, exhibiting the same characteristics as reported for BN interphase [17], which is caused by the interphase fracture. The same phenomenon also can be found for SiC_f/SiBCN-Si_3N_4 (Fig. 3c) and SiC_f/SiC-Si_3N_4 (Fig. 3d). While for curves of SiC_f/Si_3N_4-II, the slope of the curve gradually decreases when the linear segment changes to the nonlinear segment, and no obvious inflection point can be found, which is similar to the reported mechanical response in the push-in curves of PyC interphase. In the push-in curves, the end of the linear section means that cracks appear in the interfacial micro-zone and fiber debonding begins, the indenter load at this point is called as the critical load P_c [18]. The maximum load of different composite was recorded, and the maximum load distributes in a large range that from 240 to 840 mN for SiC_f/Si_3N_4-I, while that in the range of 230-370 mN, 280-460 mN and 440-700 mN for SiC_f/Si_3N_4-II, SiC_f/SiBCN-Si_3N_4 and SiC_f/SiC-Si_3N_4 composites. After the introduction of SiC and SiBCN matrices, the maximum load distribution is more concentrated.

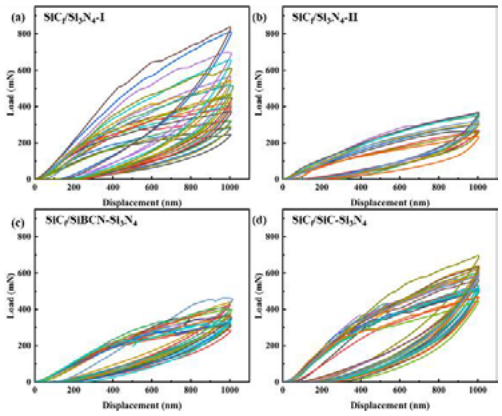

Fig. 3. Fiber push-in curves of the samples. (a) SiC_f/Si_3N_4-I, (b) SiC_f/Si_3N_4-II, (c) SiC_f/SiBCN-Si_3N_4 and SiC_f/SiC-Si_3N_4.

Fig. 4a shows the typical load-displacement curves extracted from the Fig. 3. In the load-displacement curve, the initial stiffness S_0 (the slope of the linear segment in the curve) reflects the elastic response of the composite [19]. It can be seen from the figure that the initial stiffness S_0 are different. In view of the fact that elastic deformation occurs at this stage, the initial stiffness S_0 is related to the elastic modulus of the fiber, interphase and the matrix around the tested fiber.

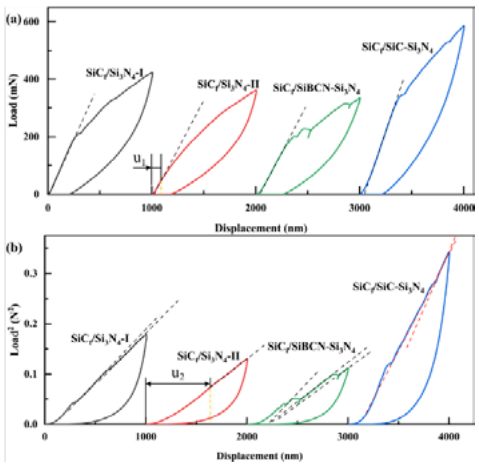

Fig. 4. Typical fiber push-in curves of the samples. (a) Load-displacement curves of the samples; (b) Square of load-displacement curves of the samples.

Table 3. Fiber push-in test results of the composites.

Samples	Initial stiffness S_0 (N/mm)	Critical debond load P_c (μN)	IFSS (MPa)	Webull modulus of IFSS m
SiC_f/Si_3N_4-I	830	269810	77.4	2.31
SiC_f/Si_3N_4-II	586	98605	28. 5	2.32
SiC_f/Si_3N_4[#]	746	210959	60.6	1.68
SiC_f/SiBCN-Si_3N_4	655	198532	59.4	4.77
SiC_f/SiC-Si_3N_4	1009	294721	128.0	8.08

[#] This means the summarized results which ignoring the difference between SiC_f/Si_3N_4-I and SiC_f/Si_3N_4-II.

As listed in Table 3, the initial stiffness S_0 of SiC_f/Si_3N_4-I, SiC_f/Si_3N_4-II, SiC_f/SiBCN-Si_3N_4 and SiC_f/SiC-Si_3N_4 are 830±218, 586±136, 655±97 and 1010±113 N/mm, respectively. Since the three

composites have the same SiC fiber and BN interphase, the effect of radius on the initial stiffness is negligible, and S_0 is mainly determined by the modulus of intra-bundle matrix. The intra-bundle matrices of all the three composites are Si_3N_4, SiBCN and SiC, with Young's modulus of 187, 150 and 326 GPa (as shown in Table 2), respectively, leading to the variation of initial stiffness. When the Young's modulus of the intra-bundle matrix is higher, the initial stiffness S_0 would be lager.

When the indenter load reaches the critical load P_c, the interfacial zone is destroyed and the interface debonding begins. The interfacial shear strength (IFSS) of the measured fiber can be calculated by the following formula [20]:

$$\tau_c = \frac{S_0 P_c}{2\pi^2 r^3 E_f} \tag{1}$$

Where S_0 is the initial stiffness mentioned above and E_f is the Young's modulus of the fiber. It can be found that the IFSS values of SiC_f/Si_3N_4-I, SiC_f/Si_3N_4-II, and $SiC_f/SiBCN$-Si_3N_4 are 77.4±36.3, 28.5±13.7, and 59.4±15.1 MPa, respectively. While the IFSS of SiC_f/SiC-Si_3N_4 is 128.0±16.3 MPa, which is significantly higher than the other composites. The Weibull modulus m of IFSS is calculated, and the m of SiC_f/Si_3N_4-I, SiC_f/Si_3N_4-II, $SiC_f/SiBCN$-Si_3N_4 and SiC_f/SiC-Si_3N_4 are 2.31, 2.32, 4.77 and 8.08, respectively. The smaller m means a larger dispersion degree of the data. Among the three composites, the Weibull modulus of SiC_f/Si_3N_4 is much lower than that of the other two composites, indicating that its interfacial mechanical properties are more discrete. As listed in Table 3, when the difference of SiC_f/Si_3N_4-I, and SiC_f/Si_3N_4-II composites was neglected, the summarized IFSS and the Weibull modulus are 60.6 MPa and 1.68. It can be found that the Weibull modulus become smaller, corresponding to the non-uniformity of interfacial zone microstructure. When the load of the indenter is higher than the critical load P_c, the fiber debonding begins. In this case, the fiber sliding resistance needs to be overcome is the friction force of the debonding surface and the crack tip propagation resistance. The relationship between fiber surface displacement and indenter load can be expressed by [21, 22]:

$$u = u_0 + \frac{F^2}{8\pi^2 r^3 E_f \tau_{friction}} \tag{2}$$

Where u is the fiber end displacement, u_0 is the residual fiber end displacement after unloading, F is the applied load and $\tau_{friction}$ is frictional sliding stress. It can be seen from the formula (2) that the square of the indenter load (F^2) increases linearly with the increase of the indenter displacement (u) during the fiber slipping process. While the curve is parabolic, the sample is in the elastic deformation stage. Fig. 4b shows the F^2-u curves of all the three composites. As can be seen from the image that for SiC_f/Si_3N_4-I, $SiC_f/SiBCN$-Si_3N_4 and SiC_f/SiC-Si_3N_4 composites, F^2 increases linearly with the increase of u when the indenter load is higher than P_c, and it suggests that, for these composites, fiber slipping occurs in the form of frictional slippage after interfacial debonding. By comparison, for SiC_f/Si_3N_4-II, the fiber surface displacement u_2 at the starting point of the linear segment in the F^2-u curve is much larger than the displacement u_1 in the F-u curve where the critical load P_c located. This indicates that the fiber slipping occurs only after the indenter is pressed down for a large distance after the interface failure in SiC_f/Si_3N_4-II. As can be seen from the F^2-u curves of SiC_f/Si_3N_4-I, SiC_f/SiC-Si_3N_4 and $SiC_f/SiBCN$-Si_3N_4 composites, when the fibers are in the elastic deformation stage, the curves exhibit a parabolic shape. For SiC_f/Si_3N_4-II, when the displacement is smaller than u_2, although the curve is not steep as other curves, it is still close to a parabolic shape. This suggests the fiber and matrix have not completely debond and elastic deformation still exist, when the fiber displacement is less than u_2.

3.3. The relationship between micro-zone and macro mechanical behavior

For CMCs, the fiber bundles are the basic units. Within a fiber bundle, all fibers form a stress transferring network and share load through this network. The different micro-zone mechanical behavior of each fiber affects the failure probability of the stress transferring chain in the network, and then affects the load sharing behavior of the entire stress transferring network. Under the ideal load condition, when a fiber is broken, the load originally borne by the fiber will be uniformly dispersed to other fibers in the

composite. With the increase of load, after the broken fibers reaching to a certain degree, the rest of the fibers would fracture as a whole, and the composite material would fail [23].

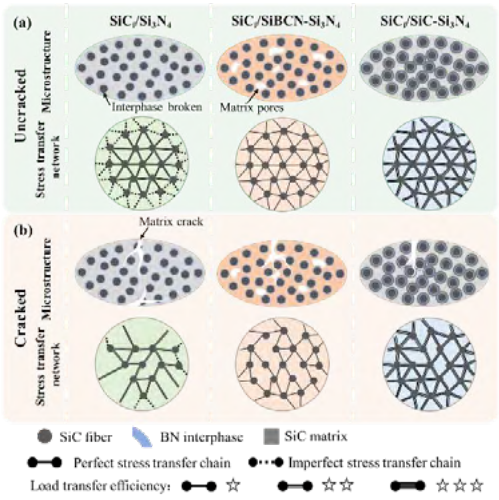

Fig .5. The stress transferring network model of all the three composites (a) before and (b) after matrix cracking.

Fig. 5a shows the stress transferring network model of all the three composites before cracking. For SiC_f/Si_3N_4, due to the existence of two types of interphases in the fiber bundle, stress transferring chain can be divided into two types, perfect stress transferring chain for SiC_f/Si_3N_4-I and imperfect stress transferring chain for SiC_f/Si_3N_4-II. After incorporating SiBCN and SiC matrix into the fiber bundle, all the interphases in the composite are undamaged, and their stress transferring chains are all perfect. Furthermore, the higher IFSS means the higher load transferring efficiency.

Fig. 5b shows the influence of the intra-bundle matrix cracks on the stress transferring network. When the matrix cracks penetrate into the fiber bundle, the fiber fracture and crack deflection would influence the load carrying ability of the stress transferring network. For SiC_f/Si_3N_4, the fibers with destructed interphase are prone to fracture. The decrease of the nodes makes the load in the remaining stress transferring network increase rapidly, and the destroy possibility of the remaining nodes and chains increases, resulting in that the failure of the entire network would occur earlier. After the introduction of SiBCN matrix into the fiber bundle, the well protected interphase avoids the shear fracture of the fiber. After incorporating SiC matrix in to the intra-bundle area, both the IFSS and the corresponding Weibull modulus are the highest in all the three composites.

3. Conclusions

In this work, SiC and SiBCN matrices were introduced into the fiber bundle of SiC_f/Si_3N_4 composite to optimize the microstructure uniformity of the interfacial zone. By optimizing the intra-bundle microstructure, the uniformity of interfacial micro zone mechanical behavior is improved. The results showed that the Weibull modulus of the interfacial shear stress were 1.68, 4.77, and 8.08, respectively. The enhancement of interfacial zone microstructure uniformity improved the load bearing capacity of the stress transferring network and the mechanical properties of the composites can be improved.

Acknowledgments

This work was supported by the National Key R&D Program of China (No. 2022YFC2204500), the National Natural Science Foundation of China (Nos. 52231007, 52072303 and 52372095), and the National Science and Technology Major Project (Grant No. J2019-VI-0014-0129).

References

[1] Yilmaz S, Theodore M, Ozcan S. Silicon carbide fiber manufacturing: Cost and technology. Compos Part B-Eng. 269:13, 2024.
[2] Yin XW, Cheng LF, Zhang LT, Travitzky N, Greil P. Fibre-reinforced multifunctional SiC matrix composite materials. Int Mater Rev. 62(3):117-72, 2017.
[3] Song CK, Ye F, Cheng LF, Liu YS, Zhang Q. Long-term ceramic matrix composite for aeroengine. J Adv Ceram. 11(9):1343-74, 2022.
[4] Zhao CW, Tu ZC, Mao JK. The dynamic thermophysical properties evolution and multi-scale heat transport mechanisms of 2.5D C/SiC composite under high-temperature air oxidation environment. Compos Part B B-Eng. 263:16, 2023.
[5] Appiah KA, Wang ZL, Lackey WJ. Characterization of interfaces in C fiber-reinforced laminated C–SiC matrix composites. Carbon. 38(6):831-8, 2000.
[6] Evans AG, Zok FW, Davis J. The role of interface in fiber-reinforced brittle matrix composites. Compos Sci Technol. 42(1-3):3-24, 1991.
[7] Kerans RJ, Hay RS, Pagano NJ, Parthasarathy TA. The role of the fiber matrix interface in ceramic composites. Am Ceram Soc Bull. 68(2):429-42, 1989.
[8] Kerans RJ, Parthasarathy TA. Crack deflection in ceramic composites and fiber coating design criteria. Compos Part A-Appl S. 30(4):521-4, 1999.
[9] Cao XY, Yin XW, Fan XM, Cheng LF, Zhang LT. Effect of PyC interphase thickness on mechanical behaviors of SiBC matrix modified C/SiC composites fabricated by reactive melt infiltration. Carbon. 77:886-95, 2014.
[10] Pompidou S, Lamon J. Analysis of crack deviation in ceramic matrix composites and multilayers based on the Cook and Gordon mechanism. Compos Sci Technol. 67(10):2052-60, 2007.
[11] De Meyere RMG, Gale L, Harris S, Edmonds IM, Marrow TJ, Armstrong DEJ. Optimizing the fiber push-out method to evaluate interfacial failure in SiC/BN/SiC ceramic matrix composites. J Am Ceram Soc. 104(6):2741-52, 2021.
[12] Mo R, Yin XW, Ye F, Liu XF, Ma XK, Li Q, et al. Electromagnetic wave absorption and mechanical properties of silicon carbide fibers reinforced silicon nitride matrix composites. J Eur Ceram Soc. 39(4):743-54, 2019.
[13] Hao HH, Fan XM, Wang XL, Dang XL, Ye F, Xue JM. Oxidation behavior of microwave absorbing SiC_f/Si_3N_4 composites by incorporating self-healing phase. Corros Sci. 219:11, 2023.
[14] Rodríguez M, Molina-Aldareguía JM, González C, Llorca J. A methodology to measure the interface shear strength by means of the fiber push-in test. Compos Sci Technol. 72(15):1924-32, 2012.
[15] Ma XK, Yin XW, Fan XM, Sun XN, Yang LW, Ye F, et al. Microstructure and properties of dense Tyranno-ZMI SiC/SiC containing $Ti_3Si(Al)C_2$ with plastic deformation toughening mechanism. J Eur Ceram Soc. 38(4):1069-78, 2018.
[16] Ding JX, Ma XK, Fan XM, Xue JM, Ye F, Cheng LF. Failure behavior of interfacial domain in SiC-matrix based composites. J Mater Sci Technol. 88:1-10, 2021.
[17] Marshall DB, Oliver WC. Measurement of interfacial mechanical properties in fiber-reinforced ceramic composites. J Am Ceram Soc. 70(8):542-8, 1987.
[18] Kharrat M, Chateauminois A, Carpentier L, Kapsa P. On the interfacial behaviour of a glass/epoxy composite during a micro-indentation test: assessment of interfacial shear strength using reduced indentation curves. Compos Part A-Appl S. 28(1):39-46, 1997.
[19] Wang J, Feng YJ, Zhao G, Yang LW, Xu J. Effect of elastic and thermal mismatch on push-in mechanism and shear strength measurement of fiber/matrix interface. Compos Interface. 27(10):921-35, 2020.
[20] Cox HL. The elasticity and strength of paper and other fibrous materials. Br J Appl Phys. 3(3):72-9, 1952.
[21] Marshall DB, Oliver WC. Measurrment of interfacial mechanical-properties in fiber-reinforced ceramic composites. J Am Ceram Soc. 70(8):542-8, 1987.
[22] Bansal NP. Mechanical properties of Hi-Nicalon fiber-reinforced celsian composites after high-temperature exposures in air. J Eur Ceram Soc. 29(3):525-35, 2009.
[24] Calard V, Lamon J. Failure of fiber bundles. Compos Sci Technol. 4(5):701-106, 2004.

MODIFICATION OF THERMOPLASTIC STARCH WITH ADDITIVES TO ITS HYDROPHOBICITY

Kyeongmin Kim[1,2], Joseph Jang[2], Sera Im[2,3], Hyuk Jun Kwon[2], Jun-young Lee[2], Kiseob Hwang[2*]

[1]Sungkyunkwan University/2066, Seobu-ro, Jangan-gu, Suwon-si, Gyeonggi-do, Republic of Korea
[2]Korea Institute of Industrial Technology/87 Yangdaegiro-gil, Ipjang-myeon, Cheonan-si 31056, Republic of Korea
[3]Seoul Women's University/01797 Hwarangro, Nowon-gu, Seoul 621, Republic Korea

Email: ks_hwang@kitech.re.kr, Web Page: http://www.kitech.re.kr

Keywords: Theromplastic starch, Hydrophobicity, Citric acid, Water resistance

Abstract

Thermoplastic starch (TPS) is a sustainable and biodegradable alternative to conventional petroleum-based plastics. However, its high hydrophilicity limits its applications in various industries. In this study, we aim to enhance the hydrophobicity of TPS by modifying it with citric acid (CA) and epoxidized soybean oil (ESO). The modification was achieved through twin-screw extrusion, which allowed for efficient blending and reaction of TPS with the hydrophobic agents. The characterization of these samples revealed a significant decrease in water uptake from 250% to 60%, indicating a substantial increase in hydrophobicity. This improvement in TPS properties expands the range of its potential applications in packaging, agriculture and other fields requiring biodegradable materials. Our study provides valuable insights into the modification of TPS, highlighting the role of CA and ESO in developing environmentally friendly plastics with enhanced hydrophobicity.

1. Introduction

The increasing environmental impact of petroleum-based plastics has prompted significant interest in the development of biodegradable alternatives. Thermoplastic starch (TPS) is a promising candidate due to its renewable nature, biodegradability, and abundance. Starch, a natural polymer primarily sourced from agricultural crops such as corn, potatoes, and cassava, can be converted into thermoplastic form by plasticizing with agents such as glycerol of sorbitol. The resulting TPS offers considerable potential for sustainable packaging and disposable applications, aligning with the principles of the circular economy. But the properties of TPS, especially the poor mechanical properties and water resistance limit the application of TPS in many areas. It can be improved by blending with synthetic polymers, such as poly(lactic acid), poly(caprolactone), poly(hydroxyalkanoate) and polyethylene[1]. Additionally, TPS generally exhibits relatively low tensile strength and impact resistance compared to conventional plastics, limiting its applicability. Thermal degradation at elevated temperatures hampers processing and restricts application temperatures. Furthermore, over time, TPS tends to crystallize due to starch retrogradation, resulting in brittleness and loss of flexibility.

Given these challenges, enhancing TPS's hydrophobicity has emerged as a critical area of research. Imprving TPS's hydrophobic properties not only reduces its water absorption but also improves its mechanical properties and dimensional stability, expanding its potential applications. Enhancing TPS's hydrophobicity through chemical modification offers several key benefits, including reduced water absorption, improved mechanical strength and impact resistance, and broader applicability in packaging

and related fields. Additionally, sustainable TPS formulations can contribute to the reduction of plastic pollution by replacing conventional plastics.

In this study, we focus on chemically modifying TPS using various additives to improve its hydrophobicity. The modifiers selected include citric acid, a multifunctional carboxylic acid that can form ester linkages with starch hydroxyl groups to enhance hydrophobicity. In previous works citric acid (CA) has been proved to increase the plasticization and melt processing properties of TPs effectively[2]. Epoxidized soybean oil (ESO), a renewable plasticizer that can reacy with hydroxyl groups to form hydrophobic networks. Currently, ESO is a low epoxy compound derived from a renewable resource, and one of the most utilized epoxidized oil mainly used as a polyvinyl chloride additive but also as a starting material to produce polyol and polyurethane foam[3]. ESO, containing multiple epoxy groups per molecule, can react with the hydroxyl groups present in TPS. These reactions lead to crosslinking, enhancing the hydrophobicity of TPS.

The primary objectives of this study are to evaluate the effectiveness of CA and ESO as hydrophobizing agents for TPS, to fabricate modified TPS samples via twin-screw extrusion, and to characterize their water uptake properties. This research aims to investigate the potential of hydrophobized TPS as a biodegradable alternative to conventional plastics. By improving TPS's hydrophobicity, this work seeks to address one of the most significant barriers to its broader commercial use, contributing to global effects to reduce plastic pollution. The finding of this study offer promising insghts into the development of biodegradable TPS-based materials for packaging and other related applications.

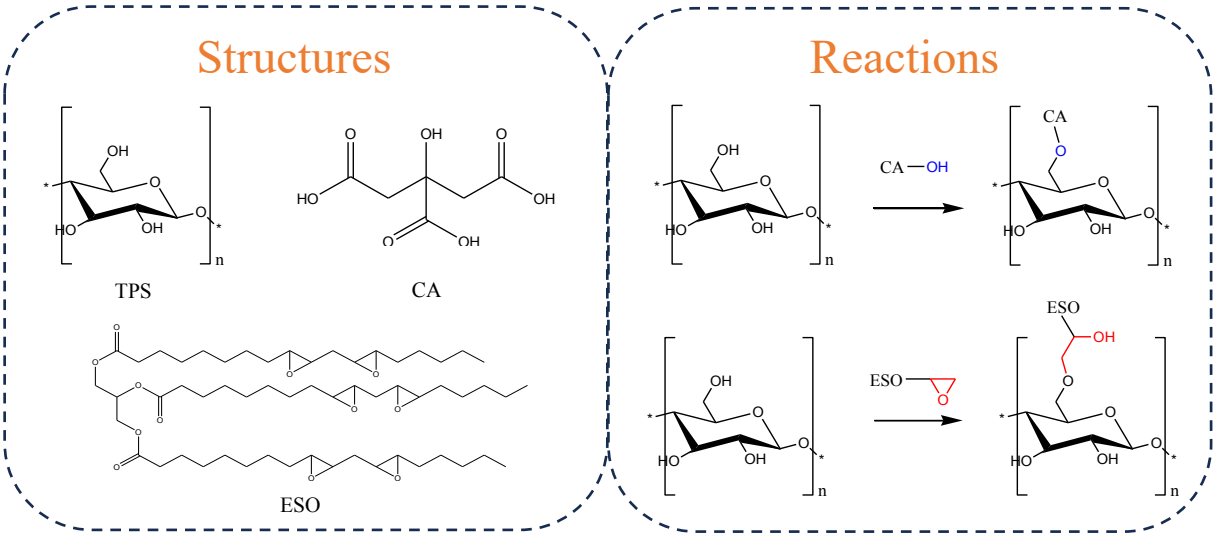

Figure 1. Possible mechanism of the reaction between TPS and modifiers.

2. Experimental

2.1. Materials

Thermoplastic starch (ROSECO™ T1002), purchased from TWPC. Citric acid (CA) was purchased from Sigma Aldrich. Epoxidized soybean oil (ESO) was purchased from Sigma Aldrich.

2.2. Fabrication of samples

The TPS composites were prepared and charactertized. Table 1 shows the material composition of the samples. CA and ESO were utilized as hydrophobic modifiers at weight percentages of 1 and 3%, respectively. TPS and additives were premixed to ensure uniform distribution. The premixed materials were processed using a twin-screw extruder, with a temperature profile ranging from 145℃ to 165℃ and a screw speed of 220 rpm. The extrudate was cooled and stored in a sealed container before further characterization.

Table 1. Composition of modified TPS.

Sample	*TPS (wt%)*	*CA (wt%)*	*ESO (wt%)*
Neat TPS	100		
TPS-CA	99	1	
TPS-ESO	97		3

2.3. FT-IR

FT-IR analysis was performed using a FTIR spectrometer (Thermo Fisher Nicolet IS50) in attenuated total reflection (ATR) mode to analyze chemical structure of the composites with a wave number range of 3800-700cm^{-1}.

2.4. XRD

XRD analysis was performed using an X-ray diffractometer (Rigaku Smartlab SE) with Cu-Kα radiation (λ = 0.154178 nm). The diffraction patterns were recorded in the range of 10-30˚ (2θ) at a scanning rate of 0.5 ˚/s under operating conditions of 40 KV and 15mA.

2.5. Water resistance properties

To evaluate the water resistance of the modified TPS composite, water absorption tests were conducted. Samples were cut 1cm*1cm*1mm sizes and dried at 60℃ for 24h. The dried samples were then immersed in distilled water at two temperatures, 25℃, for 24h. The initial weight of each sample was recorded before immersion, and the final weight was measured after immersion. Water uptake was calculated based on the weight gain after immersion using the formula:

$$Water\ Uptake\ (\%) = \frac{W_t - W_0}{W_0} \times 100 \quad (1)$$

where: W_t is the sample weight after immersion, and W_0 is the sample weight before immersion.

3. Result and discussion

3.1. FT-IR

The FTIR specta of neat TPS and TPS modified with CA and ESO are shown in Figure 1. The specta reveal notable changes that indicate successful modification and crosslinking of TPS. The broad band observed at 3290cm^{-1}, attributed to the stretching vibrations of hydroxyl groups (O-H) in starch, decrease in intensity in the modified TPS samples compared to the control TPS. This reduction is due to the reaction between the hydroxyl groups in starch and the epoxy groups in ESO or the carboxyl groups in

CA, leading to crosslinking. The peak at 1745cm^{-1}, corresponding to the stretching vibrations of carbonyl groups (C=O), is present in TPS-CA and TPS-ESO samples but absent in control TPS, confirming the incorporation of CA. The peak is also present on TPS-ESO, likely due to the presence of carbonyl groups in ESO. Furthermore, the characteristic peaks for epoxy groups (C-O-C) in ESO are observed between 1250cm^{-1} and 950cm^{-1}. In the TPS-ESO, indicating that the epoxy groups have reacted with the hydroxyl groups in starch, resulting in crosslinking. This analysis confirms the successful modification of TPs with CA and ESO, where crosslinking enhances hydrophobicity by reducing hydroxyl group content.

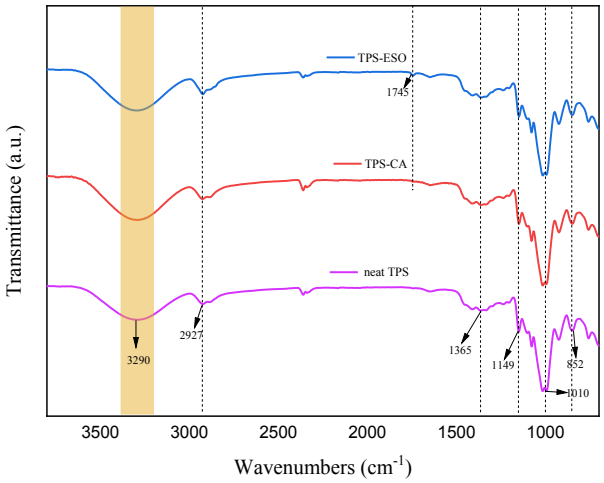

Figure 1. FT-IR specta of neat TPS and TPS modified with CA and ESO.

3.2. XRD

XRD patterns of TPS and TPS modified with CA and ESO are shown in Figure 2. The pattern of the control TPS shows a broad peak near a diffraction angle (2θ) of approximately 20˚, indicating an amorphous structure with limited crystallinity. In the TPS-CA sample, a slighy increase in the intensity of the peak near 20 degrees suggests an increase in the degree of crystallinity due to the crosslinking effect of CA, which induces more ordered structures. Conversely, the TPS-ESO sample shows a decrease in peak intensity near 20 degrees, indicating reduced crystallinity, likely due to the crosslinking reaction between the epoxy groups in ESO and the hydroxyl groups in starch, leading to a mor amorphous structure.

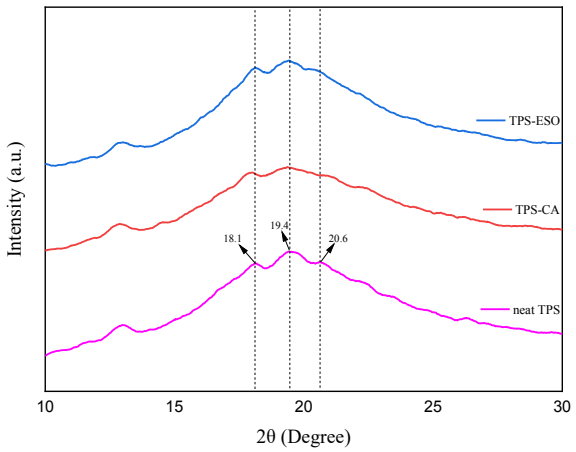

Figure 2. XRD patterns of neat TPS and TPS modified with CA and ESO.

3.3. Water resistance properties

Water resistance of TPS and TPS modified with CA and ESO was evaluated by measuring water uptake and migration, as shown in Figure 3. Neat TPS shows the highest W.U. at approximately 250% due to its high hydrophilicity, stemming from the abundant hydroxyl groups in starch. When CA is incorporated, W.U. decreases to about 60% as CA acts as a crosslinking agent, reducing the availability of hydroxyl groups. In the ESO-modified sample, W.U. is reduced to about 200%, as ESO provides hydrophobicity and also crosslinks with hydroxyl groups, decreasing water absorption. Neat TPS exhibits a high migration value of around 93%, indicating significant leaching of water-soluble components. In TPS-CA, the incorporation of CA reduces migration to approximately 80% due to its crosslinking effect. In TPS-ESO, migration is reduced to about 35%, as ESO forms a hydrophobic barrier that limits the dissolution of TPS components.

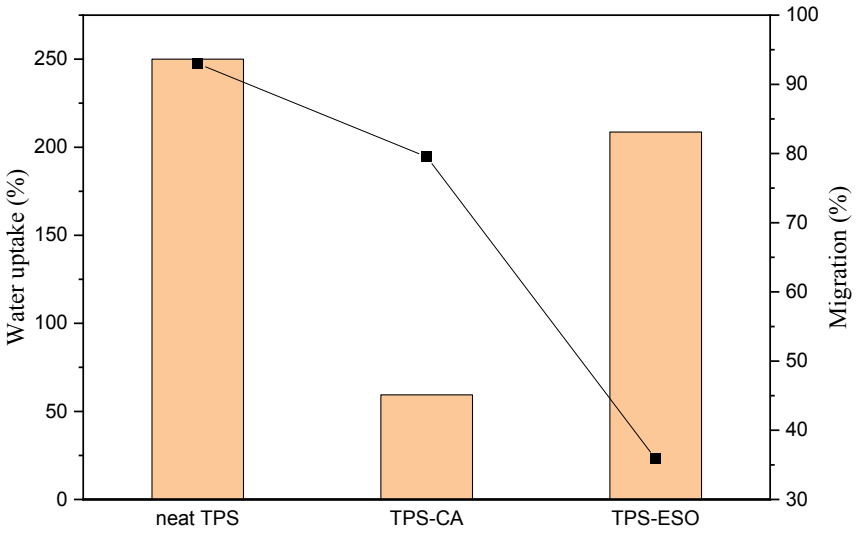

Figure 3. Water resistance properties of neat TPS and TPS modified with CA and ESO.

4. Conclusions

The modification of TPS with CA and ESO significantly improves its hydrophobicity. FTIR confirmed successful modification through crosslinking reactions between the hydroxyl groups in TPS and the epoxy groups in ESO, as well as the carbonyl groups in CA. XRD analysis revealed that incorporating CA and ESO leads to reduced crystallinity and a more amorphous structure. Water resistance analysis showed that CA-modified TPS reduces water uptake to around 60%, while ESO-modified TPS decreases migration to approximately 30%, enhancing hydrophobicity and reducing leaching. These modifications expand the potential applications of TPS in biodegradable packaging and other fields requiring water resistant materials.

References

The accuracy of the references in the paper is under the full responsibility of the Author/Authors of the paper. All publications cited in the text should be referred to by a number in square brackets, [1,2,3]. The full reference should be given in a list at the end of the paper according in the following format:

[1] Wang, N., Yu, J. G., Chang, P. R., &MA, X. F. (2008). Influence of formamide and water on the properties of thermoplastic starch/poly(lactic acid) blends. *Carbohydrate Polymers, 71*, 109-118.

[2] Wang, N., Yu, J. G., & Han, C. M. (2007). Influence of citric acid on the properties of glycerol-plasticised Cornsatrch extrustion blends. *Polymers & Polymer Composites, 15*, 545-552.

[3] Lin, B., Yang, L. T., Dai, H.H., Yi, A.H., (2008). *Kinetic studies on oxirane cleavage of epoxidized soybean oil by methanol and characterization of polyols. J. Am. Oil Chem. Soc. 85*, 113-117

INTEGRAL WOVEN NEAR-NET-SHAPE FABRICS FOR SHELL-SHAPED FRP COMPONENTS

Dominik Nuss[1], Thị Anh Mỹ Huỳnh[1], Cornelia Sennewald[1] and Chokri Cherif[1]

[1] TU Dresden, Institute of Textile Machinery and High Performance Material Technology, Dresden, Germany
Web Page: https://tu-dresden.de/ing/maschinenwesen/itm
Email: dominik.nuss@tu-dresden.de
Email: thi_anh_my.huynh@tu-dresden.de
Email: cornelia.sennewald@tu-dresden.de
Email: chokri.cherif@tu-dresden.de

Keywords: Technical fabrics, fibre-reinforced plastic components, wide weaving machines, novel reed design, simulation process development, curved woven fabrics, woven fabrics, load adapted woven structre

Abstract
Technical fabrics play a crucial role as reinforcements in plastic components across various applications. Woven fabrics crafted from high-performance fibers are utilized to bolster composite components in numerous scenarios. Traditionally, these fabrics are manufactured using wide weaving machines that produce a constant fabric width. Subsequently, the fabric is cut to achieve the desired component geometry, resulting in significant waste generation and disruption of the load path of the utilized fibers. An effective strategy to enhance lightweight potential, minimize waste, and conserve resources involves employing fabrics with outer contours that align with the desired component geometry from the outset, along with load-adapted thread orientation within the fabric. However, until now, the production of width-variable fabrics with adapted warp thread courses during the weaving process has not been achievable using wide weaving machines. Addressing this limitation, this paper introduces a novel reed design specifically developed for wide weaving machines, along with associated calculations to simulate the optimum load paths within a component, which are then transferred to the fabric structure.
The paper outlines the developed simulation process, the design concept of the new weaving reed, and the fabric development process aimed at reinforcing an exemplary fan blade component for air engines.

1. Introduction

Fiber-plastic composites present a promising avenue for lightweight construction, owing to their distinctive structural composition. These composites amalgamate high-performance fibers such as carbon, glass, or aramid, facilitating load transfer along the fiber's length, while a plastic matrix manages compressive and shear loads [1–3]. Consequently, these composites demonstrate remarkable anisotropic material characteristics, boasting high specific tensile strength and stiffness aligned with the reinforcement direction [4]. The manufacturing process encompasses various stages, including textile semi-finished product fabrication, preforming, infiltration, and consolidation [5].
Convential preforming involves segmenting textile reinforcement structures with uniform surface characteristics into sizable segments. These segments are then arranged, layered, shaped, and partially affixed to fashion the desired component [6]. However, this method primarily relies on geometric design and alignment of cut parts to address specific load scenarios, resulting in cutting wastage and necessitating over-sizing due to unfavorable reinforcement thread paths. To overcome these limitations, advancements in textile manufacturing processes have been actively pursued. These advancements aim to integrate required component geometries directly into the manufacturing process through the textile structure [7–9]. Nonetheless, accommodating component-specific textile structures poses a challenge, particularly with large-format shell-shaped components.
Currently, no existing solutions cater to adjusting the component width to match the fabric width, especially in textile production. Woven fabrics are commonly employed to reinforce fiber-reinforced

plastic composite components. Traditional weaving processes yield fabrics with constant yarn orientation and width. Several developments have endeavored to modify this proc
ess. For example, open reed weaving permits a limited lateral offset of additional threads (≤ 300 mm) along existing lines of force, thereby enhancing reinforcement [10, 11]. However, it fails to achieve localized changes in warp yarn density or adapt fabric width to produce near-net-shape fabric structures. Directly translating applied load paths within a component into a transferable textile architecture remains a challenge, hindering the full exploitation of lightweight construction potential. Alongside design limitations, a dearth of tools for calculating load paths and transferring them into a fabric structure further compounds the issue.

To address the challenge of adjusting fabric width and warp yarn density during weaving, an adjustable reed concept has been proposed. V-shaped reeds offer a solution but are confined to narrow weaving machines, with only shuttle weaving by Mageba International GmbH accommodating their use, albeit limited to a maximum nominal fabric width of 1000 mm.

Several innovations for wide weaving machines, particularly rapier weaving machines, have been introduced, yet none address fabric width adjustments during the weaving process. Only experimental designs, such as grooved roller mechanisms, concertina mechanisms, or segmented rail mechanisms, have been explored. However, these have not gained industrial traction due to limited flexibility, complex construction, or high moving mass.

Given the inadequacies of existing methods, a novel reed concept has been devised to rectify these shortcomings and provide a viable solution for adjusting warp density and fabric width during fabric production on rapier weaving machines, especially those with a working width exceeding 1000 mm.

Furthermore, none of the existing developments outline a process chain for transferring mappable forces within a component to the textile structure, ensuring continuous reinforcement threads.

In order to address this challenge, the authors developed a method that enables the forces occurring within a component to be calculated and transferred into continuous load paths. To implement the textile structure, a new type of weaving reed was developed for broadlooms, which enables the fabric to be finished close to the final contour. The entire developments were demonstrated and validated using a fan blade for potential use in aircraft turbines.

2. Material and Method

2.1 Developed Simulation process:

The objective of the devised method is to calculate component stresses and subsequently integrate them into load paths within the component, culminating in their incorporation into a fabric (Figure 1). To achieve this goal, both a simulation process and corresponding weaving technology were developed in this study, facilitating the production of such a fabric.

The developed simulation framework allows for the calculation of warp thread courses, simulating the load paths present in the 3D component to be manufactured. Initially, the stresses required for the component are computed, from which the load paths are derived. The orientation of threads on the 3D component follows these load paths as closely as possible to optimize mechanical properties within the component. In the stress calculation, the 3D component, comprising a combination of textile structure and epoxy resin,

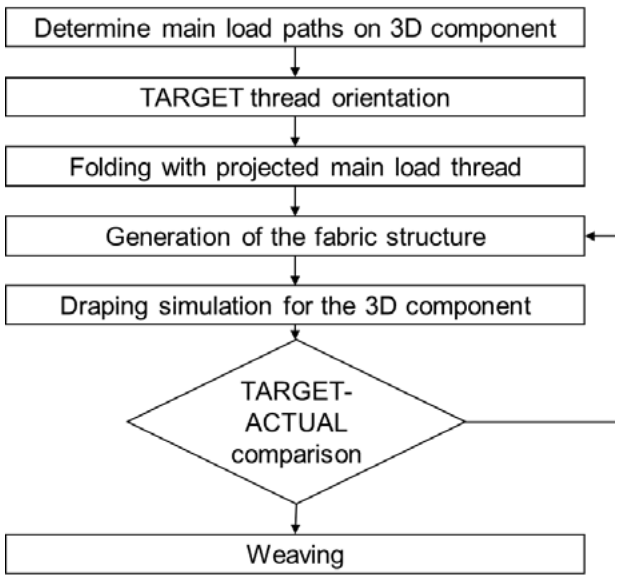

Figure 1: Simulation process chain

is initially modeled using shell elements at a macroscale level, incorporating boundary conditions that accurately represent real-world scenarios. The output of this load analysis simulation results in the generation of the 3D component, which includes considerations for load paths and yarn orientation.
The next step involves transforming the main load paths into a 3D geometry by projecting them onto a plane. To delineate the path of the warp threads, the contour of the resulting 2D component is drawn. Subsequently, other threads within these contours are sketched using the middle curve method. In developing the fabric, various warp thread densities are simulated using a mesoscale model. This involves simulating the mechanical behavior of both warp and weft threads, representing them as solid elements with elliptical cross-sections, and comparing them with predetermined material parameters. Given the intended use of carbon filament yarn 24k in subsequent processes, the model was calibrated to accommodate this material, as depicted in Figure 2.

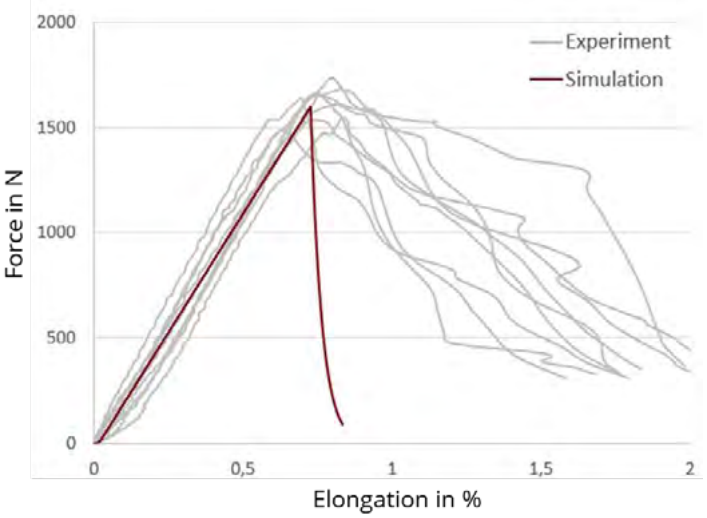

Figure 2: Simulation of the mechanical thread behaviour

Following this, a draping simulation of the unfolded fabric is conducted to facilitate a comparison between the developed fabric structure and the initially calculated "target thread orientation," aligning with the component tensions. This step allows for necessary adjustments to be made in the event of any deviations encountered.

2.2 Developed weaving technology

To ensure a continuous presence of load-bearing warp threads within fabric, a novel variable-width reed has been developed, capable of adjusting warp density and, consequently, fabric width during production. This reed design permits the adjustment of distances between reed bars through external force, achieved by compressing segments positioned between these bars. This dynamic adjustment facilitates changes in fabric width throughout the weaving process.
In this innovative design, force is applied to the segments via a linear spindle unit, powered by laterally mounted stepper motors on the weaving machine. These motors drive the spindles using flexible shafts, ensuring smooth operation. To prevent breakage, the reed bars and segments are threaded onto a guide shaft.
The reed's design allows for asymmetrical adjustments in warp yarn density and fabric width. This is achieved through independent control of two laterally mounted stepper motors, while the central reed bar remains securely clamped throughout the process. These stepper motors are positioned outside the fabric production zone, on the left and right sides of the reed.The capability for asymmetrical adjustment offers a notable advantage, enabling precise replication of component geometries during weaving. The entire design configuration is illustrated in Figure 2.Moreover, the reed is configured to facilitate the transmission of rotary motion from the stepper motors to the spindles via flexible shafts. These shafts regulate carriage positions, compressing the springs between the reed rods and consequently altering fabric width as desired.
In order to enable continuous load-bearing warp threads in a fabric, a new type of variable-width reed was developed to change the warp density and consequently the fabric width during the fabric production. This reed is designed to allow the distances between the reed bars to be adjusted by an external force, achieved by compressing segments located between the reed bars. This adjustment enables changes in fabric width during the weaving process. For the developed constructive solution the force is applied to the segments through a linear spindle unit powered by laterally mounted stepper motors on the weaving machine that drive the spindles using a flexible shaft. The reed bars and segments are threaded onto a guide shaft to prevent any breakage. The design of the reed allows for asymmetrical

adjustments in warp yarn density and fabric width. This is made possible by the independent control of two laterally mounted stepper motors, while the middle reed bar remains firmly clamped during the process. The stepper motors are installed on the left and right side of the reed outside the fabric production zone. This asymmetrical adjustment capability offers a significant advantage as it allows for the accurate replication of component geometries during the weaving process. The entire design is shown in Figure 2. The reed is configured to facilitate the transmission of rotary motion from the stepper motors to the spindles through flexible shafts. These shafts in turn regulate the carriage positions, compressing the springs between the reed rods and thereby altering the fabric width.
The authors presented the complete process parameters for weaving using the newly developed flexible reed in [12]. Additionally, the transfer of fabric geometry to the adjustment control system is outlined herein. This involves importing the geometry into a program via an STL file, where fabric edges and their positions are computed, corresponding to the movement of the stepper motors. Furthermore, the fabric weave is determined, with the weft thread density calculated for each warp thread density based on the fabric width, ensuring a consistent relative fabric density.
These methods are linked to the simulation process chain detailed in section 2.1, facilitating the conversion of results into a textile structure.

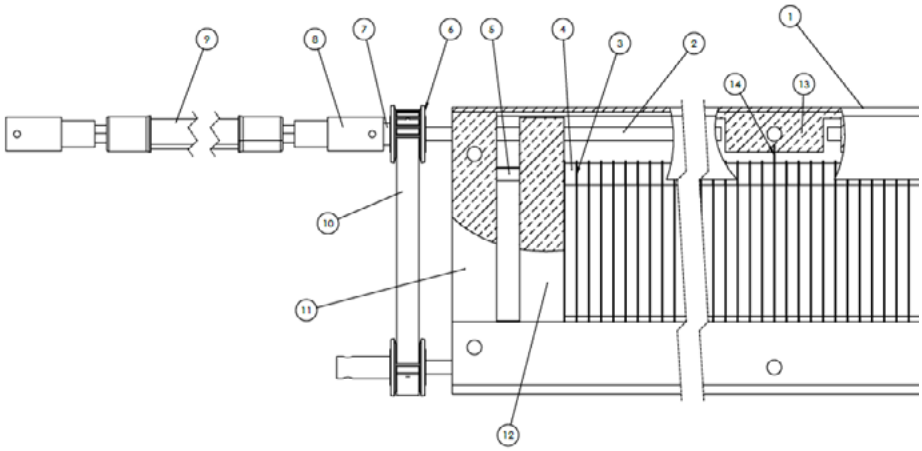

1 reed frame, 2 spindle, 3 bar, 4 elastomer, guide shaft, pinion, 7&8 adapters, 9 flexible shaft, 10 belt, 11 reed bracket, 12 slider, 13, middle bracket, 14 fixed bar

Figure 3: Contruction design of the flexible reed

3. Results

To validate the methods and technologies developed, a fan blade was implemented for potential use in aircraft turbines. The geometry has an asymmetrical contour (Figure 3). The fan blade is designed and manufactured using 24K carbon filament yarn.

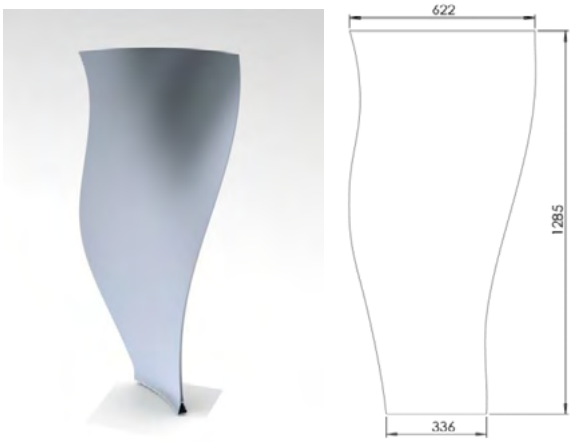

Figure 4: CAD-Design of the fanblade and dimsenions in mm

To investigate the load paths within the 3D component, the entire structure was initially simulated within the machine component. Initially, the 3D geometry was converted from the CAD software to LS DYNA using the finite element method (FEM), resulting in a ventilator comprising 12 fan blades. The physical properties of the composite were derived. The chosen E-Modul of the compound is 2,0 x10 ^{7}, the mass density 2,0 g/cm³. These parameters served solely as inputs for the load analysis simulation and will subsequently undergo validation during the experimental phase.
The load calculation involved simulating the rotor's movement to generate a radial velocity of 100 rad/s within an ideal air box. The results of the stress analysis are depicted in Figure 5 (left). Subsequently, the primary load paths were visualized based on the stress distribution on the 3D component in LS DYNA (Figure 5, right). This calculation is in accordance with the concept of "target thread orientation," facilitating visualization of the highest attainable stresses.

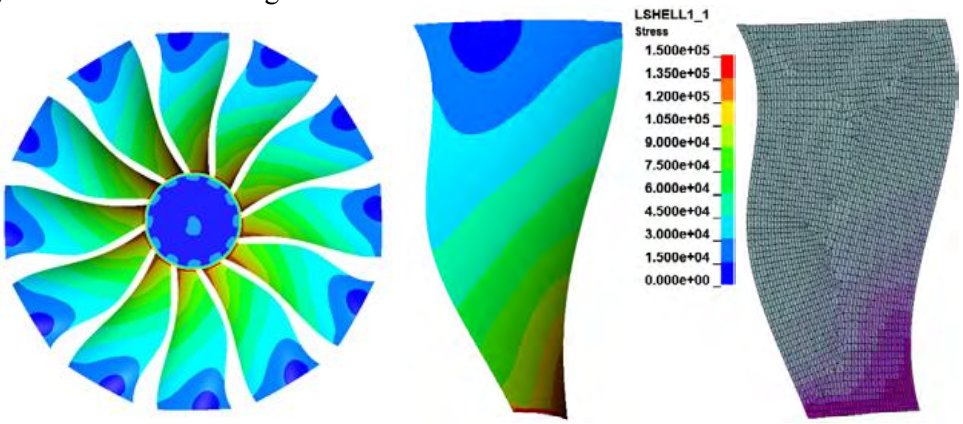

Figure 5: Mapping the CAD-geometry and Generation of the simulation of the occurring forces

The fabric structure is devised based on meticulous calculations, wherein the unfolded geometry of the component is integrated into the program routine. To unfold the geometry and calculating the warp thread courses the developed simulation routine has been used (Figure 6). Utilizing these calculations, a total of 150 warp threads are employed. The fabric is woven as plain weave. To maintain a consistent relative fabric density, the weft density is adjusted accordingly, as delineated in Table 1. The specific wefts required based on the geometry are depicted in Figure 6. Concurrently with the weave development, the control values for the stepper motors are computed to correspondingly adjust the weave operation. Notably, the left and right motors execute independent movements.

Weft insertion number	*Weft density* (thread/cm)
1-145	2,0
146-200	1,5
201-220	1,0

Table 1: Weft inerstion area

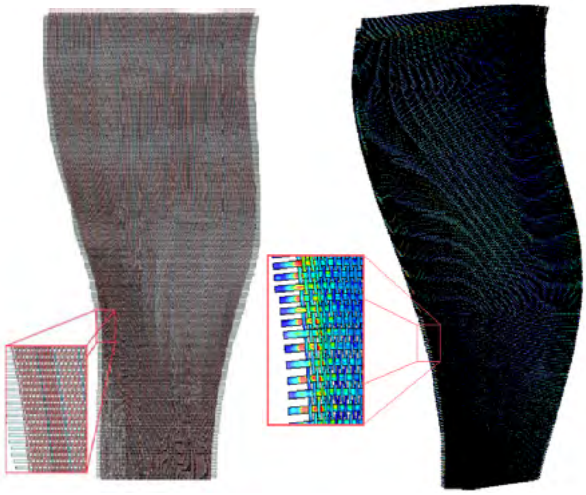

Figure 6: Calculation of the unfolding with corresponding warp thread course

As alterations in fabric width lead to varying angles of warp threads between the weaving reed and fabric take-off, process-related transverse thread forces emerge, influencing the adjustment of the weaving reed. These relationships are elaborated upon in [12]. To minimize any resultant deviation between the initial geometry and the woven end geometry, the control values for the stepper motors are finely tuned accordingly (refer to Figure 7 left, indicated by the red marked line).
After the fabric has been developed, the preforms are produced on a Dornier P1 rapier weaving machine (see Figure 7, right).

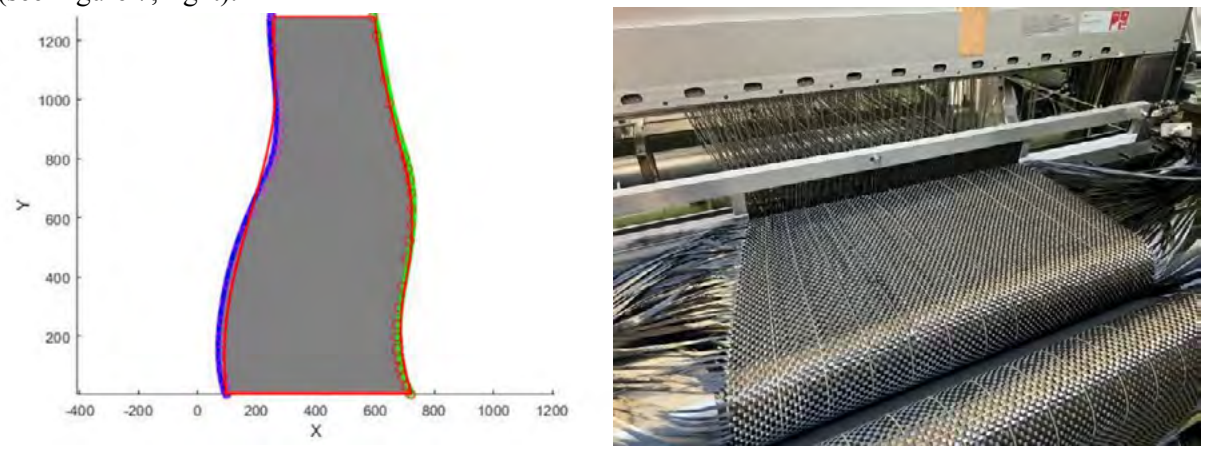

Figure 7: Calculation of the reed motion and weave pattern development and weaving the preform

Prior to consolidation, the preform underwent thorough analysis and evaluation, which included recording the outer contour of the fabric (Figure 8). This assessment revealed a maximum deviation of 9 mm on the left side of the fabric, with a fabric length of 978 mm. In relation to the total width at this point, this represents a deviation of 1.56%. Notably, the deviation observed on the left half of the fabric indicates a hysteresis effect when the fabric width is altered, despite accounting for transverse forces generated by warp thread tension. This effect is partially attributed to frictional forces within the reed mechanism and fabric relaxation.

To mitigate frictional forces, employing spring elements with higher stiffness proves advantageous, aiding in overcoming the forces acting on the reed rods. Additionally, a leno thread is utilized to secure the fabric edge; however, minimal slippage of the outer warp threads occurs due to the smooth material properties of carbon fiber and polyester thread, consequently altering the fabric edge.
Additionally, a comparison was conducted between the "actual thread orientation" of the preform and the calculated "target thread orientation." To accomplish this, the path of 10 warp threads was chosen across the fabric width and subsequently dyed (yellow) for validation purposes. The calculated unwinding, along with the corresponding warp thread path, was then juxtaposed with the manufactured preform, and the trajectory of the warp threads was measured using a digital protractor. The comparison, depicted in Figure 9

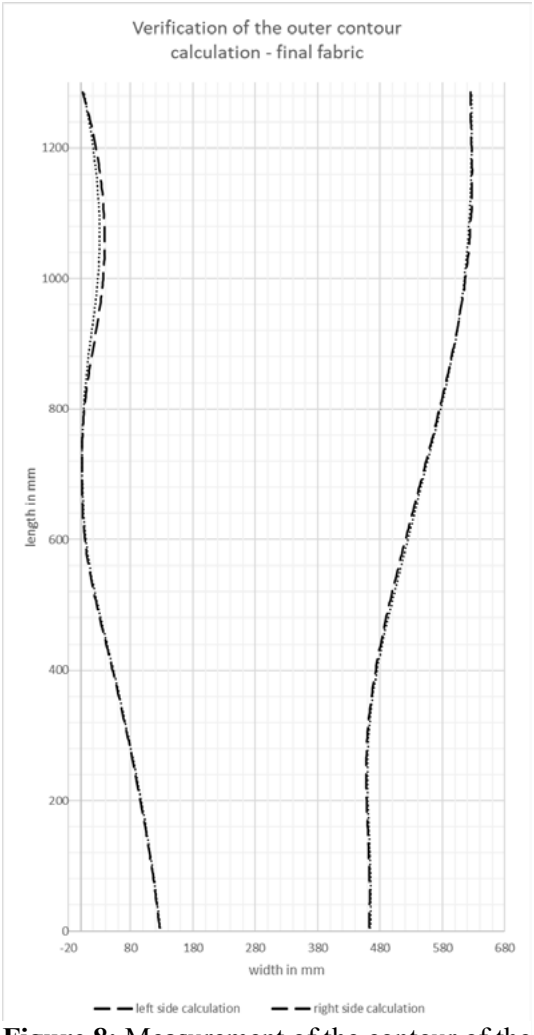

Figure 8: Measurement of the contour of the woven preform

on the right, illustrates a deviation of 2° to 3° in the area of highest stress.
Finally, the exemplary consolidation of the fan blade was carried out using the vacuum infusion method. A total of 6 layers were chosen with an average square mass of 800 g/m² (Figure 10).

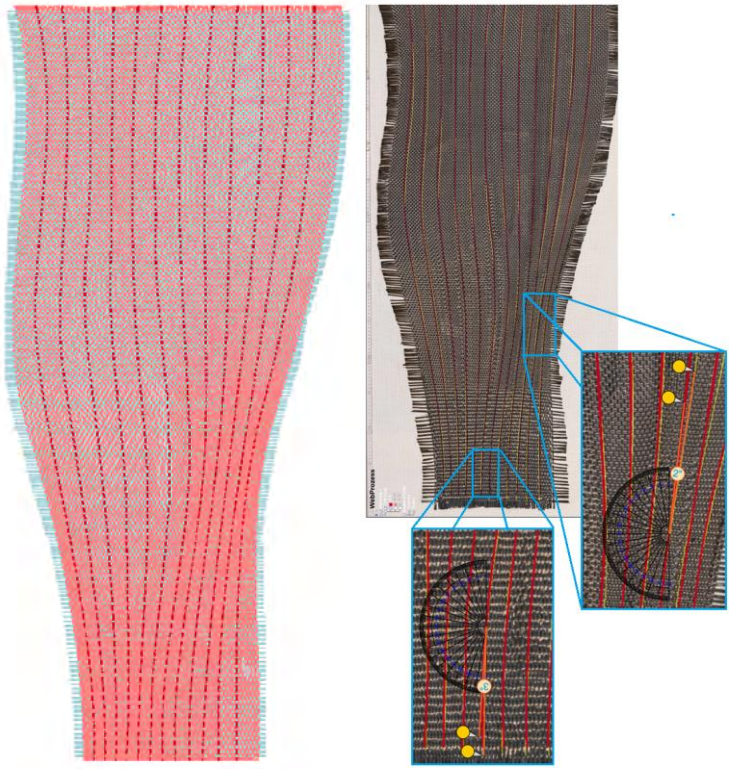

Figure 9: Comparsion of the Simulation and woven fabric

Figure 10: Final Fanblade

3. Conclusions

In conclusion, the development of fiber-plastic composites for lightweight construction represents a significant advancement in material science. This study has addressed several key challenges associated with traditional preforming methods and textile manufacturing processes. By integrating load paths directly into the fabric structure and adjusting warp density and fabric width during weaving, we have successfully demonstrated a novel approach to optimize component reinforcement while minimizing waste.

The devised simulation process, coupled with the innovative weaving technology using a variable-width reed, has enabled the production of fabric structures closely aligned with component geometries. This not only enhances the mechanical properties of the final components but also streamlines the manufacturing process by reducing material wastage and manual adjustments.

The validation of our methods and technologies through the fabrication of an exemplary fan blade for aircraft turbines showcases the practical applicability of our approach. The close correlation between calculated load paths and actual fabric structures confirms the efficacy of our methodology.

Moving forward, further refinements in weaving technology and simulation techniques could lead to even greater advancements in lightweight construction. By continuing to integrate computational modeling with manufacturing processes, we can unlock new possibilities for the design and production of high-performance composite components across various industries.

Acknowledgments

The authors express their gratitude to the “Arbeitsgemeinschaft industrieller Forschungsvereinigungen” for the financial support of the project IGF 21984 BR.

References

[1] Thielemann K. Adaptive Strukturoptimierung von Faserkunststoffverbunden unter berücksichtigung bionischer aspekte. Kaiserslautern, Germany: Kaiserslautern, Techn. Univ, 2006. Als Ms. gedr. Kaiserslautern : inst. für Verbundwerkstoffe, 2006 (IVW-Schriftenreihe 65).

[2] Ehrenstein GW. Faserverbund-kunststoffe : werkstoffe - verarbeitung - eigenschaften. München, Germany. Carl Hanser Verlag GmbH & Co. KG, 2006.

[3] Paul R. High performance technical textiles. Hoboken, NJ: JohnWiley&Sons, 2019. 2. Völlig überarbeitete Auflage.

[4] Friedrich HE and Hrsg. Leichtbau in der Fahrzeugtechnik. 2. Auflage. Wiesbaden.Wiesbaden, Germany: Springer Vieweg, 2017. (ATZ/MTZ-Fachbuch).

[5] Boisse P. Advances in composites manufacturing and process design. Amsterdam, Netherlands: Elsevier Science, 2015.

[6] Henning F and Moeller E. Handbuch leichtbau : methoden, werkstoffe, fertigung. München, Germany: Hanser, 2011. (Hanser eLibrary).

[7] Trümper W, Lin H, Callin T, et al. Recent developments in multi-layer flat knitting technology for waste free production of complex shaped 3D-reinforcing structures for composites. IOP Conf Ser Mater Sci Eng 2016; 141: 12015.

[8] Hahn L, Zierold K, Golla A, et al. 3D textiles based on warp knitted fabrics: a review. In: Materials 16. Basel, Switzerland, 2023, Nr. 10, S. 3680. URL https://www.mdpi.com/1996-1944/16/10/3680

[9] Chen X. Advances in 3D textiles. 1st edition. Cambridge, UK: Woodhead Publishing Limited in associationWith The Textile Institute, 2015. (Woodhead publishing series in textiles number 167).

[10] Sugun BS and Shimpi P. Orthogonal weaving. In: Practical approach to 3D weaving. Cham: Springer, 2021, pp. 1–28.

[11] Wahhoud A and Dornier P. Neuartige Herstellung textiler flächen dank prozessintegration im webvorgang. In: 4th aachen-Dresden international textile conference, Dresden, Germany, 25–26 November 2010.

[12] Nuss, D.; Cornelia, S.; Chokri, C.: Novel reed development for width-variable fabrics on wide weaving machines. Journal of Industrial Textiles 54(2024), S. 1-25

The effect of processing/curing temperature and viscosity of epoxy resins on the flexural/tensile properties of GNP-epoxy resin nanocomposites

Seita Saito[1], Shunki Sato[1] and Yoshihiko Arao[12]

[1]Department of Applied Mechanics and Aerospace Engineering, Waseda University, Bldg. 59-317A, 3-4-1, Okubo, Shinjuku-ku, Tokyo 169-8555, Japan
[2]Kagami Memorial Research Institute for Materials Science and Technology, Waseda University, 2-8-26 Nishiwaseda, Shinjuku-ku, Tokyo, 169-0051, Japan
Email: seitasaito130130@akane.waseda.jp(Seita Saito),
over4670whelming@akane.waseda.jp (Shunki Sato),
arao@waseda.jp (Yoshihiko Arao)

Keywords: Graphene nanoplatelet, Graphene dispersion, Graphene re-aggregation, Graphene-epoxy systems, Epoxy nanocomposite

Abstract
Despite the problem of graphene aggregation in cured epoxy resin, no studies have clarified the tendency of graphene aggregation in a wide variety of material processes. Investigating several studies, it was found that curing epoxy resins at high temperatures tends to degrade the mechanical properties of graphene-epoxy resin nanocomposites. We hypothesized that the use of epoxy resins at high temperatures leads to an extreme decrease in resin surface tension and viscosity of epoxy, which would cause re-aggregation of graphene once dispersed. So, we examined process/material with/without high temperature treatment. Properties of nanocomposites were evaluated by flexural/tensile test. Experiments revealed that treatments not including treatment at high temperatures suppressed graphene re-aggregation and maintained the high mechanical properties of nanocomposites. In particular, when epoxy was treated and cured at 20 ˚C at all times to keep the surface tension of epoxy desirable, recorded the increased tensile modulus by 18.44% and strength decrease only by 5.64% (@ 1 wt.% graphene loading), which were quite high for non-functionalized graphene. However, to achieve a fundamental improvement in mechanical properties, the interfacial adhesion with epoxy resin must be improved.

1. Introduction

Epoxy resins are thermosetting resins with many excellent properties such as high mechanical properties, adhesive strength, thermal stability, and electrical insulation, leading them to be used in various fields including aerospace, automotive, coating, construction structural materials [1]. Today, research has been conducted to add nanofillers with excellent properties in order to further enhance the functionality of epoxy resins. Graphene is particularly noteworthy as a nanofiller due to its excellent properties. One of the major issues to be addressed in graphene-epoxy system is that despite the problem of graphene aggregation limiting its unique properties [1,2,3,4], it has not been investigated how graphene aggregates during the diverse processes involved in the fabrication of epoxy resin nanocomposites.

Inferring from some studies, we hypothesized that the treatment of epoxy resins at high temperatures leads to a decrease in the viscosity and surface tension of the resin [5], causing graphene to re-aggregate. Taking the mechanical properties of epoxy resin nanocomposites as an example, Zaman et al. [6] used two different epoxy resin curing agents with different temperatures and found that the reinforcing effect of graphene was more pronounced in the Young's modulus and strength of the epoxy resin nanocomposite when the lower temperature one was used. Parente et al. [7] pre-cured graphene nanoplatelets(GNP)-epoxy resin nanocomposites at 7, 25, 30, and 40 °C and reported that both the flexural strength and modulus of the nanocomposites increased as the temperature decreased from 40 °C to 7 °C. As expected, the low temperature of the epoxy resin seems to enhance the mechanical

properties of nanocomposites, but neither Zaman et al. [6] nor Parente et al. [7] could determine the cause of this. On the other hand, it is well known that the optimal surface tension of the dispersant (40~50 mJ・m^{-2}) contributes to the productivity and dispersibility of graphene in the liquid [8,9] and that a high viscous matrix limits the mobility of the nanoparticles and affects their dispersibility [10]. However, as far as we have been able to determine, there are no studies that have investigated the relationship between resin temperature/viscosity and graphene re-aggregation in epoxy resin systems.

In this study, we examined processes with/without high temperature treatment. Specifically, we compared the dispersion of GNPs by solution mixing using acetone (in this case, please note that the epoxy resin must be heated at a high temperature to remove residual acetone in the epoxy resin), and the direct dispersion of GNPs into epoxy resin by three-roll mill (in this case, please note that the direct mixing is done by shearing and therefore no high temperature treatment is required). We also compared four different curing agents with different curing temperatures. The properties of the final GNP/epoxy resin nanocomposites were evaluated by flexural and tensile testing of the resins.

2. Experimental

2.1 Materials

XG Science xGNP M-25 (25 μm particle size, 6-8 nm thickness) was adopted for the graphene nanoplatelets. There are no significant functional groups on the GNP surface as a result of FT-IR. The epoxy resins used was jER™ 828 purchased from Mitsubishi Chemical Corporation. The amine type epoxy resin curing agents used were JEFFAMINE® D230 Polyeheramine from HUNTSMAN Corporation, m-Phenylenediamine (m-PDA) from Sigma-Aldrich Co. LLC, and 4,4'-Diaminodiphenyl Sulfone (DDS) from Fujifilm Wako Chemicals. Curing temperature for each hardener is shown in Table 1.

Table 1 Curing temperature for each epoxy hardener.

Hardener	Curing condition
D230 (Cured at 20 ˚C)	20 ˚C・48 h. ➡ 60 ˚C・6 h. ➡ 110 ˚C・10 h. ➡ 140 ˚C・4h.
D230 (Cured at 60 ˚C)	60 ˚C・6 h. ➡ 110 ˚C・10 h. ➡ 140 ˚C・4h.
m-PDA	80 ˚C・2h. ➡ 160 ˚C・1h.
DDS	190 ˚C・6 h.

2.2 Fabrication of GNP-epoxy resin nanocomposites by solution mixing method

Solution mixing is widely used method in the fabrication of nanocomposites. Detailed method is shown in Fig. 1 and as followed. GNPs were added to 150 mL of acetone and sonicated at 20 kHz, 260 W for 30 min. using an ultrasonic disperser (UH-600S, SMT, Japan). Next, 90 g of epoxy resin was added, and the same sonication was performed for another 30 min. to disperse GNPs in the epoxy resin. The acetone was then evaporated in an evaporator (ARE-V1200, AS ONE CORPORATION, Japan) at 70 ˚C for 2 h., followed by full evaporation in vacuum oven (FVO-30, Tokyo Garasu Kikai Co., Ltd, Japan) at 70 ˚C for 2h.. After cooling to room temperature, an equivalent ratio of hardener was added, and the mixture was stirred at 2000 rpm for 4 min. and then stirred at 2200 rpm for 4 min. using a mixing/defoaming machine (ARE-310, Thinky Corporation, Japan). The mixture was defoamed in vacuum oven for 45 min.~1 h. 30 min. (depending on the viscosity of mixture). Finally, this mixture was poured into stainless molds and heated in oven. For all samples, the amount of GNP added was 1 wt. % in the cured epoxy.

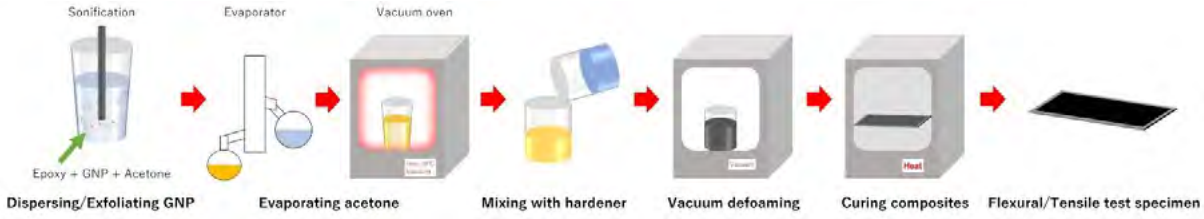

Fig. 1 Diagram illustrating Fabrication of nanocomposites by solution mixing method.

2.3 Fabrication of GNP-epoxy resin nanocomposites by calendaring method.

Detailed method is shown in Fig. 2 and as followed. The GNPs were pre-stirred in a homogenizer (S/N J22-15844, Mitsui electric Co., Ltd, Japan) at 3000 rpm for 25 min.. The three-roll mill (BR-150 VIII, IIMEX, Japan) was then used to disperse GNPs in epoxy resin. Three rolls rotating at different speeds and narrow gaps between the rolls allow high shear stresses to be applied to the fluid as it passes through the mill. The distance between the Center roll and the Apron roll was set at 30 μm, the rotation speed of the Apron roll was set at 350 rpm, and the slurry was run 10 times repeatedly. The exfoliation/dispersion temperature were set at 35 ˚C. The procedure after the hardener was added was the same as that for the solution mixing method.

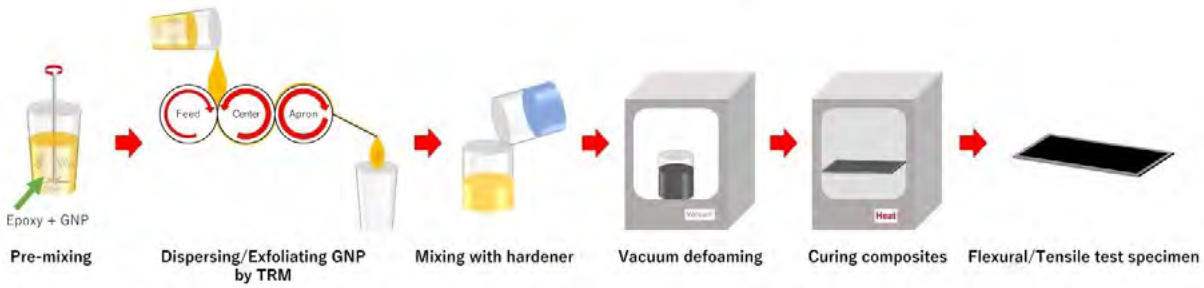

Fig. 2 Diagram illustrating Fabrication of nanocomposites by calendering method.

2.4 Characterization

The mechanical properties of each GNP-epoxy resin nanocomposites were evaluated by tensile test based on JIS K7161. GNPs immediately after dispersion were extracted from the uncured epoxy resin, and the morphology of GNPs was observed using a transmission electron microscope (TEM) (JEM-1400Flash, JEM-2100F, JEOL, Japan). For GNP thickness, the number of layers was measured by observing the edges of GNP particles protruding from the plane of copper grid, and multiplied by the thickness of one graphene layer, 0.335 nm. The morphology of the GNPs before treatment was observed using a scanning electron microscope (SEM) (JSM-6510, JEOL, Japan). In addition, the out-of-plane crystallite thickness of GNPs as received was estimated by Scherrer's equation using X-ray diffraction (XRD) (RINT-UltimaIII, RIGAKU, Japan).

Re-aggregation of GNPs in epoxy resin was observed using an optical microscope (BX51, OLYMPUS, Japan) in addition to SEM observation of fracture surfaces of tensile/flexural test specimen. For observation using an optical microscope, samples containing 0.2 wt.% GNP were prepared, and a resin droplet was placed on a glass slide. A cover glass was placed over the droplet for observation.

3. Results and Discussion

3.1 Morphology of GNPs

Fig. 3 shows the analysis of GNPs as received; the thickness of GNPs calculated from Scherrer's equation is 32.53 nm, and the SEM observation also shows that GNPs exist in an aggregated state. On the other hand, Table 2 shows that the thickness has decreased to about the catalog value of xGNP M-

25 (6-8 nm thickness), suggesting that both solution mixing and calendering methods can disperse GNPs into epoxy resin. The aspect ratio (Particle diameter/thickness) of GNPs from TEM measurement is also shown in Table 2. Please note that in general, it has been proposed that larger aspect ratio of nanofillers contribute to improved mechanical properties of nanocomposites. But in our study, although higher aspect was obtained when solution mixing method was applied, higher mechanical properties were obtained when calendaring method was applied (please see section 3.3).

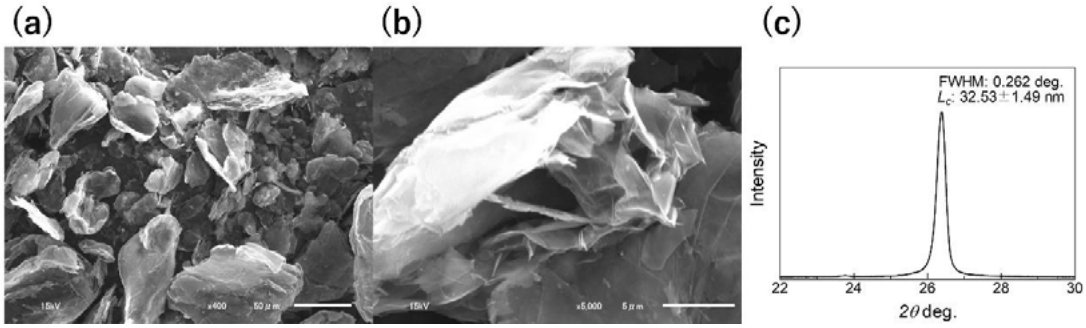

Fig. 3 (a), (b): SEM observation and (c): Crystallite thickness of GNPs as received.

Table 2 Aspect ratio of GNP exfoliated/dispersed by each method.

Disoersing/exfoliating method	Average size *L* (Measured by TEM) µm	Average thickness *t* (Measured by TEM) nm	Aspect ratio *L/t*
Solution mixing	11.63	6.14	1895
Calandering	5.91	7.71	767

3.2 Re-aggregation of GNPs

To evaluate the re-aggregation of GNPs in epoxy resin, observations were made over time using an optical microscope, and the results are shown in Fig. 4. From Fig. 4, the re-aggregation of GNPs became pronounced as the resin became hotter, which would be attributed to the decrease in viscosity or surface tension of the epoxy. This tendency is consistent with the SEM observations of the nanocomposite fracture surfaces. As shown in Fig. 5, larger GNP aggregates were observed when curing agents requiring high temperature were used (please see Table 1 for the curing agent temperature).

Additionally, compared to the solution mixing method, GNP aggregates appeared to be slightly smaller when the calendering method was used (Fig. 5(b), (d)). This result can also be explained by optical microscopic observation and can be attributed to the fact that GNPs are re-aggregated even at slightly higher temperatures (60~80 ˚C), as shown in Fig. 6. Not only that, acetone used as a dispersant also has a low surface tension of 23.7 mN・m^{-1} [11], which may accelerate the re-aggregation. In particular, D230 + Calendering (Cured at 20 °C) sample showed the least aggregation, this is because the surface tension of JEFFAMINE® D230 and jER™ 828 at 20°C is 32.7 mN・m^{-1} and 46.0 mN・m^{-1} respectively [12], which is relatively close to the a suitable surface tension (40~50 mN・m^{-1}) for graphene dispersion [8,9].

However, while the re-aggregation of GNPs was suppressed, the observed fracture surfaces of the specimens cured at 20 ˚C (Fig. 5(c)) are still far from the smooth fracture surface of neat epoxy shown in Fig. 7(a), and some GNPs appear to have protruded or been pulled out as indicated by blue arrows. This is due to the fact that the xGNP M-25 used has almost no functional groups and there is fundamentally no interfacial interaction between matrix. This interfacial interaction has a significant influence on the mechanical properties of the nanocomposites (please see Section 3.4)

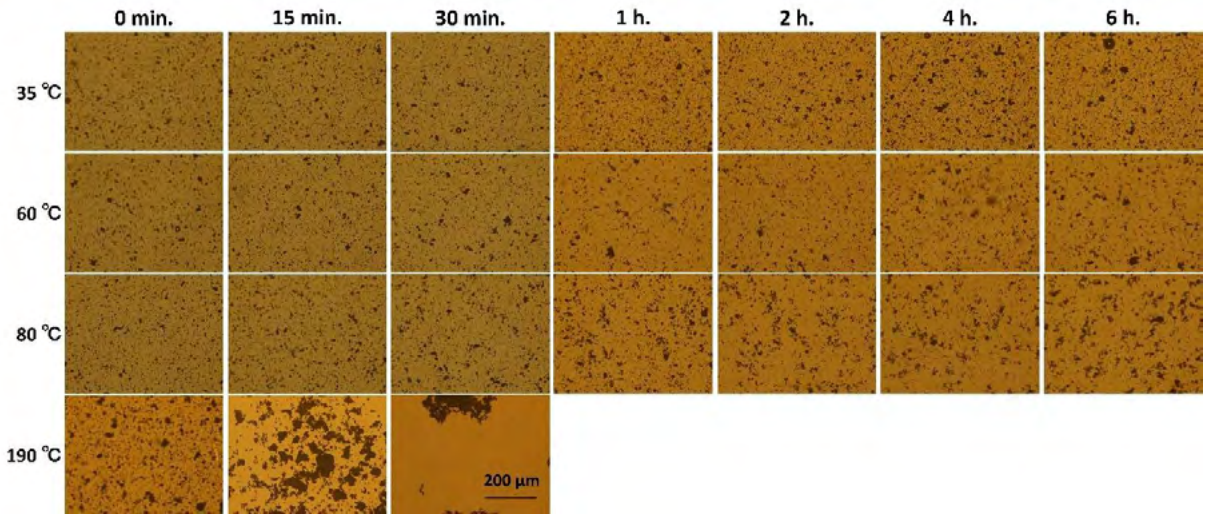

Fig. 4 Relation between GNP re-aggregation formation and epoxy temperature.

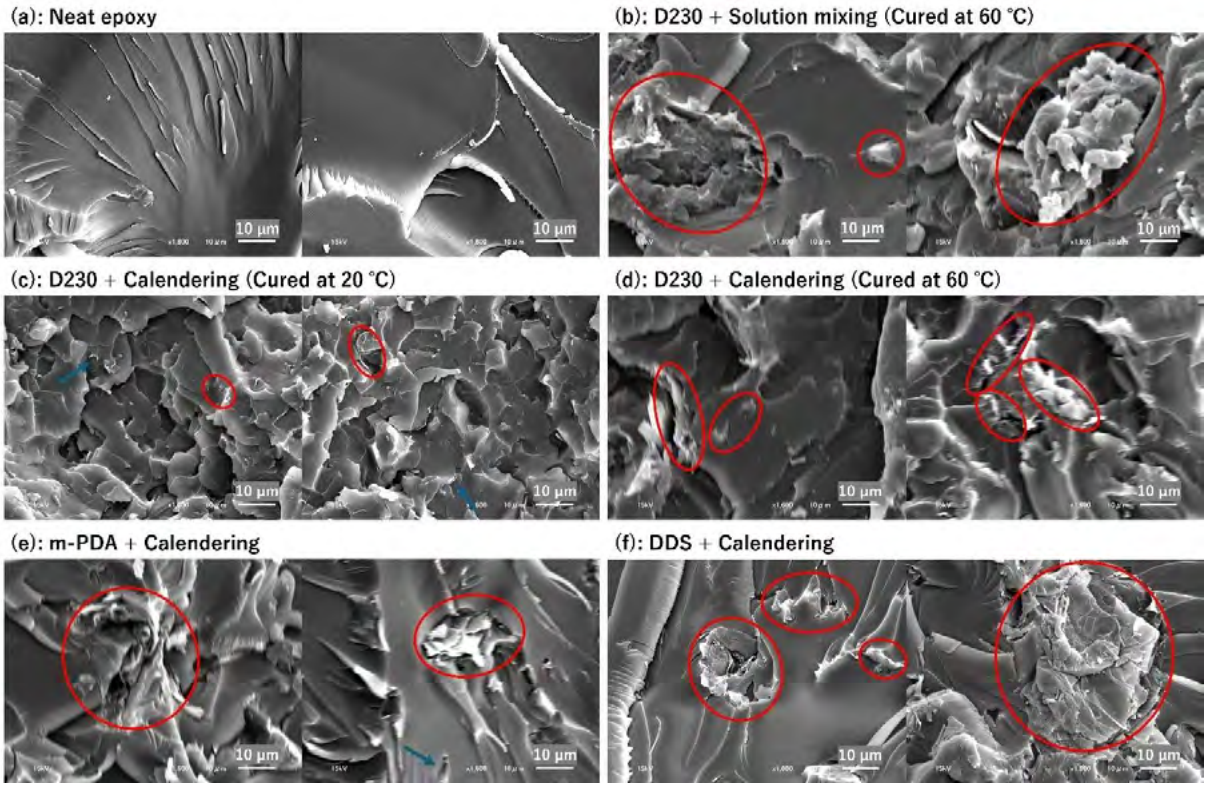

Fig. 5 Fracture surface of GNP/epoxy resin nanocomposites
fabricated by each method and cured at different temperature.

3.3 Mechanical properties of GNP-epoxy resin nanocomposites

Table 3, 4 show the results of tensile tests of the nanocomposites fabricated by each process and cured under various temperature.

Table 3 shows the differences in mechanical properties of GNPs depending on the exfoliation/dispersion method. Both the rate of increase in elastic modulus and the rate of decrease in strength are better with the calendering method than with the solution mixing method. The aspect ratio of GNPs is 1895 for the solution mixing method and 767 for the calendering method and the solution mixing method also produces thinner layers, so the results are not due to GNP quality. In the case of

the solution mixing method, the re-aggregation of GNPs may have been more pronounced because the process involves evaporation of acetone at 70 ˚C (please see Section 3.2).

Table 4 shows differences in mechanical properties depending on the curing temperature. Section 3.2 shows that the use of m-PDA, which requires a very high curing temperature of 80 ˚C, causes significant re-aggregation of GNPs due to a decrease in the viscosity or surface tension of the epoxy, resulting in only 3.94% increase in tensile modulus and 18.75% decrease in tensile strength. In contrast, when D230 (Cured at 20 ˚C), which possess desirable surface tension for GNP dispersion in liquid epoxy, is used, the re-aggregation of GNPs is reduced. Finally, the modulus and strength increase by 18.44% and 5.64%, respectively. Additionally, stress-strain curves of typical samples (Cured by D230) are in Fig. 6. Even with the same material, mechanical properties vary significantly depending on dispersion methods and temperature conditions.

Table 3 Tensile properties of GNP/epoxy resin nanocomposites by exfoliation/dispersion method.

Sample	Tensile modulus GPa	Tensile strength MPa	Modulus increase %	Strength increase %
Neat epoxy (Cured by D230)	3.05±0.12	66.91±0.80	-	-
D230 + Solution mixing (Cured at 60 ˚C)	3.12±0.11	55.74±2.65	+2.25%	-16.71%
D230 + Calendering (Cured at 60 ˚C)	3.39±0.05	60.78±0.94	+11.11%	-9.16%

Table 4 Tensile properties of GNP/epoxy resin nanocomposites under different curing temperature.

Sample	Tensile modulus GPa	Tensile strength MPa	Modulus increase %	Strength increase %
Neat epoxy (Cured by D230)	3.05±0.12	66.91±0.80	-	-
Neat epoxy (Cured by m-PDA)	3.17±0.12	72.46±7.04	-	-
D230 + Calendering (Cured at 20 ˚C)	3.61±0.13	63.14±1.39	+18.44%	-5.64%
D230 + Calendering (Cured at 60 ˚C)	3.39±0.05	60.78±0.94	+11.11%	-9.16%
m-PDA + Calendering	3.30±0.05	58.87±3.36	+3.94%	-18.75%

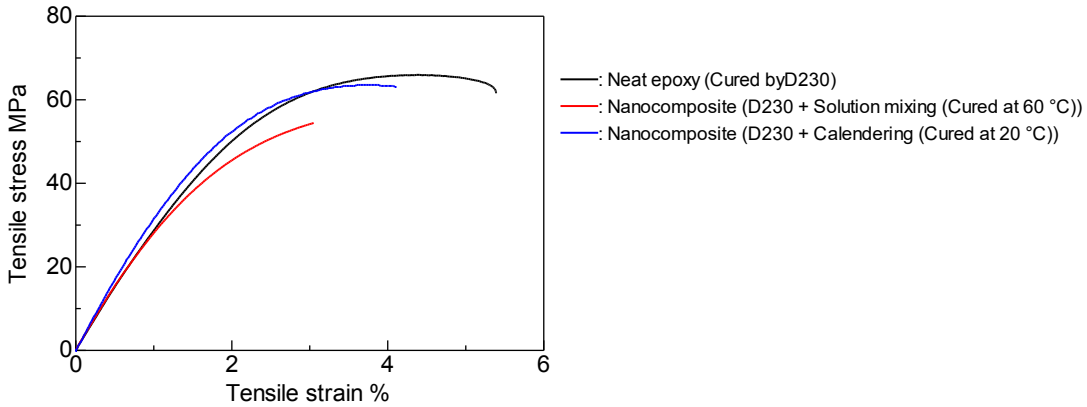

Fig. 6 Tensile stress-strain curve of nanocomposites fabricated by different method and cured at different temperature.

3.4 Comparison with other studies and theories of elastic modulus.

The theoretical elastic modulus was predicted by the Halpin-Tsai semi-empirical model with the shape factor modified to fit the Mori-Tanaka theory [13]. The model follows the equation.

$$E_{composites} = E_{epoxy}\left(0.51\frac{1+2\eta_{\perp}\varphi_{GNP}}{1-\eta_{\perp}\varphi_{GNP}} + 0.49\frac{1+\zeta\eta_{\parallel}\varphi_{GNP}}{1-\eta_{\parallel}\varphi_{GNP}}\right) \quad (1)$$

$$\eta_{\perp} = \frac{\frac{E_{GNP}}{E_{epoxy}} - 1}{\frac{E_{GNP}}{E_{epoxy}} + 2}, \quad \eta_{\parallel} = \frac{\frac{E_{GNP}}{E_{epoxy}} - 1}{\frac{E_{GNP}}{E_{epoxy}} + \zeta}, \quad \zeta = \frac{2}{3} \times Aspect\ ratio \tag{2}$$

$E_{composites}$, E_{epoxy}, and E_{GNP} are the elastic moduli of composites, epoxy resin, and GNP, respectively, and φ_{GNP} is the volume content of GNP in the composite material. In line with the results of this study, E_{epoxy}=3 GPa, E_{GNP}=250 GPa, the density of epoxy resin was calculated as 1.2 g/cm^3 , and $Aspect\ ratio$ =550, 1900. The elastic moduli obtained in this study were compared to those predicted by this model and to other studies using graphene-based epoxy nanocomposites [14-26], as shown in Fig. 7. For each plot, we have classified them according to the type of GNP used. ● plots are GNPs which are considered to have few functional groups on its surface based on the results of EDS, FTIR, XRD, and so on. ▲ plots are GNPs that would contains functional groups that unintentionally allow for good GNP dispersion and stress transfer between the matrix and GNPs. ▼ plots are GNPs that has been functionalized by intentionally adsorbing and binding molecules to them in order to improve GNP dispersion and stress transfer with the matrix. Except for a few plots recorded extremely high modulus, most plots above the theoretical lines are ▲ or ▼ shaped. In this study, our data has reached the straight line simply by improving the dispersion of GNP particles in epoxy. However, like other ▲ or ▼ shaped studies, Further improvement in Young's modulus requires improvement of the adhesion between the matrix and GNPs by functionalizing GNPs.

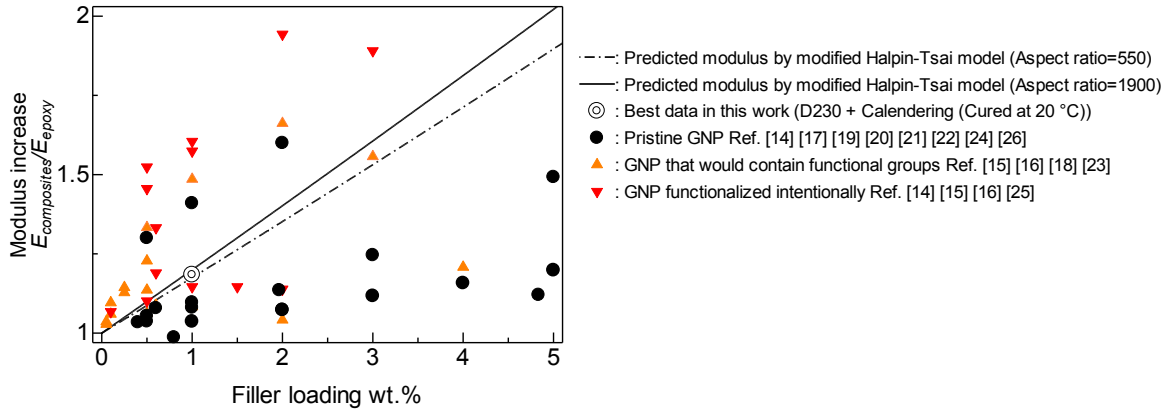

Fig. 7 Modulus comparison with that of other researches [14-26]
or that predicted by modified Halpin-Tsai model as a function of GNP loading [13].

4. Conclusion

In this study, we investigated changes in the mechanical properties of GNP/epoxy resin nanocomposites using different processes with/without high-temperature treatment. This is the first study, above all, to find that the re-aggregation of GNPs varies greatly depending on the process and epoxy resin used. Specifically, processes involving high-temperature processing, such as solution mixing and high-temperature curing agents, resulted in large re-aggregation of GNPs, which reduced the mechanical properties of nanocomposites.

The Young's modulus of epoxy resins can be improved by combining materials and processes that are optimized to suppress re-aggregation. The tensile modulus of D230 + Calendering (Cured at 20 ˚C) sample improved by 18.44% and by 2.81% respectively, compared to the pure epoxy resin. These values are quite high for GNPs without surface functional groups, especially Young's modulus, which reached the values predicted by the modified Halpin-Tsai model (: model assuming no aggregation). However, since pure GNPs with smooth surfaces were used, stress transfer between GNPs and epoxy resin was poor, resulted in inferior strength and modulus improvement compared to the top data. To achieve fundamental improvement in mechanical properties, improvement of interfacial adhesion with epoxy resin is required.

References

[1] J. S. George, P. Vijayan P, J. K. Paduvilan, N. Salim, J. Sunarso, N. Kalarikkal, N. Hameed, S. Thomas, Advances and future outlook in epoxy/graphene composites for anticorrosive applications. Prog Org Coat, 162:Article106571, 2022.
[2] R. Wazalwar, M. Sahu, A. M. Raichur, Mechanical properties of aerospace epoxy composites reinforced with 2D nano-fillers: current status and road to industrialization. Nanoscale Adv, 3(10):2741-2776, 2021.
[3] M. Y. Khalid, A. Kamal, A. Otabil, O. Mamoun, K. Liao, Graphene/epoxy nanocomposites for improved fracture toughness: A focused review on toughening mechanism. Chem Eng J Adv, 16:Article100537, 2023.
[4] Q. Liu, Y. Zhao, S. Gao, X. Yang, R. Fan, M. Zhi, M. Fu, Recent advances in the flame retardancy role of graphene and its derivatives in epoxy resin materials. Compos Part A, 149:Article106539, 2021.
[5] Y. Li, H. Zhang, M. Crespo, H. Porwal, O. Picot, G. Santagiuliana, Z. Huang, E. Barbieri, N. M. Pugno, T. Peijs, E. Bilotti, In Situ Exfoliation of Graphene in Epoxy Resins: A Facile Strategy to Efficient and Large Scale Graphene Nanocomposites. ACS Appl Mater Interfaces, 8(36):24112-24122, 2016.
[6] I. Zaman, H.-C. Kuan, J. Dai, N. Kawashima, A. Michelmore, A. Sovi, S. Dong, L. Luong, J. Ma, From carbon nanotubes and silicate layers to graphene platelets for polymer nanocomposites. Nanoscale, 4(15):4578-4586, 2022..
[7] J. M. Parente, R. Simões, P. N. B. Reis, Effect of graphene nanoparticles on suspension viscosity and mechanical propertiews of epoxy-based nanocomposites. Procedia Struct Integrity, 37:820-825, 2022.
[8] Y. Hernandez, V. Nicolosi, M. Lotya, F. M. Blighe, Z. Sun, S. De, I. T. McGovern, B. Holland, M. Byrne, Y. K. Gun'Ko, J. J. Boland, P. Niraj, G. Duesberg, S. Krishnamurthy, R. Goodhue, J. Hutchison, V. Scardaci, A. C. Ferrari, J. N. Coleman, High-yield production of graphene by liquid-phase exfoliation of graphite. Nat Nanotechnol, 3(9):563-568, 2008.
[9] A. O'Neill, U. Khan, P. N. Nirmalraj, J. Boland, J. N. Coleman, Graphene Dispersion and Exfoliation in Low Boiling Point Solvents. J Phys Chem C, 115(13):5422-5428, 2011.
[10] A. Alipour, T. Giffney, R. Lin, K. Jayaraman, Effects of matrix viscosity on morphological and rheological properties and the electrical percolation threshold in graphene/epoxy nanocomposites. eXPRESS Polym Lett, 15(6):541-553, 2021.
[11] C. Weng, W. Li, J. Wu, L. Shen, W. Yang, C. Deng, N. Bao, Thermal shock exfoliated and siloxane cross-linked graphene framework for high performance epoxy-based thermally conductive composites. J Mater Sci, 56(31):17601-17614, 2021.
[12] R.D. van de Grampel, W. Ming, W.J.H. van Gennip, F. van der Velden, J. Laven, J.W. Niemantsverdriet, R. van der Linde, Thermally cured low surface-tension epoxy films. Polymer, 46(23):10531-10537, 2005.
[13] M. A. van Es, Polymer-Clay Nanocomposites: The importance of particle dimensions. TU Delft, Delft University of Technology:13-44, 2001.
[14] J. Ma, Q. Meng, A. Michelmore, N. Kawashima, Z. Izzuddin, C. Bengtsson, H.-C. Kuan, Covalently bonded interfaces for polymer/graphene composites. J Mater Chem A, 1(13):4255-4264, 2013.
[15] J. Kim, J. Cha, G. H. Jun, S. C. Yoo, S. Ryu, S. H. Hong, Fabrication of Graphene Nanoplatelet/Epoxy Nanocomposites for Lightweight and High-Strength Structural Applications. Part Part Syst Char, 35(6):Article1700412, 2018.
[16] J. Kim, J. Kim, S. Song, S. Zhang, J. Cha, K. Kim, H. Yoon, Y. Jung, K.-W. Paik, S. Jeon, Strength dependence of epoxy composites on the average filler size of non-oxidized graphene flake. Carbon, 113:379-386, 2017.
[17] N. Tiwari, A. A. Shaikh, Effect of the amine and carboxyl functionalized graphene on the thermomechanical and properties of the shape memory polymer nanocomposites. Polym Bull, 80(11):11797-11815, 2023.
[18] M. M. Shokrieh, M. Esmkhani, H. R. Shahverdi, F. Vahedi, Effect of Graphene Nanosheets (GNS) and Graphite Nanoplatelets (GNP) on the Mechanical Properties of Epoxy Nanocomposites. Sci Adv Mater, 5(3):260-266, 2013.
[19] Y. Li, H. Zhang, H. Porwal, Z. Huang, E. Bilotti, T. Peijs et al, Mechanical, electrical and thermal properties of *in-situ* exfoliated graphene/epoxy nanocomposites. Compos Part A, 95:229-236, 2017.
[20] J. A. King, D. R. Klimek, I. Miskioglu, G. M. Odegard, Mechanical properties of graphene nanoplatelet/epoxy composites. J Appl Polym Sci, 128(6):4217-4223, 2013.
[21] Y. Bie, T. Miyase, Y. Arao, Production of high-aspect-ratio boron nitride nanosheets via oxygen doping and exfoliation by micro fluidization. J Mater Sci, 58(46):17512-17526, 2023.
[22] F. Wang, L. T. Drzal, Y. Qin, Z. Huang, Mechanical properties and thermal conductivity of graphene nanoplatelet/epoxy composites. J Mater Sci,50(3):1082-1093, 2015.
[23] B. Debelak, K. Lafdi, Use of exfoliated graphite filler to enhance polymer physical properties. Carbon, 45(9):1727-1734, 2007.
[24] S. Chatterjee, F. Nafezarefi, N.H. Tai, L. Schlagenhauf, F.A. Nüesch, B.T.T. Chu, Size and synergy effects of nanofiller hybrids including graphene nanoplatelets and carbon nanotubes in mechanical properties of epoxy composites. Carbon、50(15):5380-5386, 2012.
[25] S. Chatterjee, J.W. Wang, W.S. Kuo, C. Salzmann, W.L. Li, R. Hollertz, F.A. Nüesch, B.T.T. Chu, Mechanical reinforcement and thermal conductivity in expanded graphene nanoplatelets reinforced epoxy composites. Chem Phys Lett, 531:6-10, 2012.
[26] A. Manta, M. Gresil, C. Soutis, Tensile and flexural behaviour of a graphene/epoxy composite: experiments and simulation. JPhys Mater, 3(1):Article014006, 2020.

CHANGE IN THE PHYSICAL PROPERTIES OF PLASTER COMPOSITES REINFORCED WITH CARBON FIBERS

Samková A.[1], Pechočiaková M.[2] and Tunáková V.[3]

[1]Department of Material Engineering, Technical university of Liberec, Studentská 1402/2 461 17, Czech Republic
Email: alzbeta.samkova@tul.cz
[2]Department of Material Engineering, Technical university of Liberec, Studentská 1402/2 461 17, Czech Republic
Email: miroslava.pechociakova@tul.cz
[3]Department of Material Engineering, Technical university of Liberec, Studentská 1402/2 461 17, Czech Republic
Email: veronika.tunakova@tul.cz

Keywords: plaster composites, carbon fiber, mechanical properties, humidity, electromagnetic shielding

Abstract

Given the constantly growing demand for materials with high specific stiffness, strength, and the ability to selectively influence their key properties, composite materials are currently experiencing significant expansion across all industrial sectors. The properties of composite materials can be tailored to the requirements of modern construction applications, thus enabling effective technical solutions in demanding and changing operational conditions. Composite materials have now become part of construction, commonly used in the construction of bridges, facades, roof structures, tunnels, and other buildings. Fiber reinforcement is increasingly used in such composites to enhance the strength, flexibility, and durability of structures against static and dynamic loads.

The aim of this article is to assess whether the desired improvement in physical properties also occurs in fiber-reinforced structural materials. This study initially focuses on evaluating changes in the mechanical properties of cementitious and gypsum composites. Selected plaster mixes are commonly used in building constructions. Carbon fiber dispersions with a fiber length of 8 mm were added to the matrices used. The fiber content in the selected matrices was 1, 2, and 3% by weight.

Indoor humidity significantly affects the health and comfort of occupants. Relative humidity (RH) influences the perception of indoor air quality and thermal comfort. If the RH value is too low or too high, there is an increased risk of allergies and other illnesses. Therefore, efforts are made to maintain the optimal RH value indoors (in the range of 40-60%). In the case of higher RH values (above 80%), not only biological growth can occur, but in some cases, it may lead to a shorter expected lifespan of a specific building material. For these reasons, it was appropriate to test the effect of the amount of fibrous reinforcement on water transport in gypsum composites.

Modern developments in electronics, particularly in wireless and communication systems, bring many advantages to everyday life. However, it is also important to realize that these advancements lead to increased presence of electromagnetic waves in our environment. Excessive exposure to these waves can have a negative impact on human health. Therefore, for a material to have the ability to shield

electromagnetic fields, it must be electrically conductive. Carbon fibers meet this requirement, and thus the ability of the composite to shield electromagnetic fields was tested.

1. Introduction

Current science primarily focuses on studying the fundamental factors influencing the mechanical strength of composites. One of the main issues is the bond between the fiber and the matrix. Fiber reinforcement prolongs the initiation of cracks and prevents their propagation. Stress from the matrix is transferred to the fibers crossing the crack plane, thereby preventing composite failure. Subsequently, the stress is transferred back to the surrounding matrix through the fiber/matrix interface. [1][2] Another factor influencing the strength of the composite is fiber distribution. This is a crucial factor in achieving the desired mechanical performance. However, achieving uniform fiber distribution is challenging in practice, making this problem the subject of many studies. [3]

Moisture is one of the main factors contributing to the degradation of building materials. Water can penetrate into the material structure through processes such as capillary rise or condensation of airborne moisture, which can result in physical and chemical changes. [4][5] Composites typically have a tendency to absorb a larger amount of water than pure matrices. Some studies have shown that the most significant increase in moisture content occurs in composites with a higher fiber volume fraction. [6][7] In recent times, many scientists have been researching moisture-absorbing/desorbing materials capable of regulating moisture through their porous structure. Moisture exchange allows for autonomous moisture regulation, making these composites promising for achieving permanent control of indoor humidity and reducing energy costs. [8][9]

Commonly used metallic shielding suffers from a number of drawbacks such as high weight, susceptibility to corrosion, or difficult processing. [10][11] In studies focusing on electromagnetic shielding (SE), additives with high electrical conductivity or carbon-based materials are often used, which can lead to increased SE and, at the same time, an increase in construction costs. [12][13] Among carbon-based fillers, carbon fibers appear to be the most advantageous due to their lower production costs (compared to, for example, carbon nanotubes) and their high strength, high modulus of elasticity, and good electrical conductivity.[14][15]

The aim of this study is to explore whether adding short fibers to cement and gypsum matrices will have a positive impact on mechanical properties. Furthermore, it is assumed that adding electrically conductive fibers to the matrix will lead to the material's ability to shield electromagnetic fields. Additionally, whether a greater amount of fibers in the material will affect its water absorption capability will be investigated.

2. Material and method

2.1. Materials

Commonly available plaster mixes were used for the production of composite materials: cement plaster (MC 660, Weber SAINT-GOBAIN) and gypsum plaster (Rimat 100 DLP, Rigips SAINT GOBAIN). Additionally, 8 mm long carbon fibers with a diameter of 7,2 μm (Havel composites) were used.

2.2. Preparation of samples

The fiber content in concrete matrices is typically around 6% by weight. However, mixing such a large amount of fibers with plaster leads to poor fiber-matrix dispersion. For this reason, the fiber reinforcement content for this experiment was set at 1, 2, and 3 wt.%. The calculation of the mixing ratio (1) is based on the percentage composition of the components in the composite and their densities:

$$w_i = (V_i \rho_i) / \sum(V_i \rho_i). \quad (1)$$

Where: w_i [%] is the mass fraction of the i-th component, V_i [%] the volume fraction of the i-th component and ρ_i [kg/m^3] is the density of the i-th component.

The dry mixture made of plaster and fibers was first homogenized for 10 minutes. Subsequently, water was added to the resulting mixture. Since commercial plasters were used for the experiment, the amount of water recommended by the manufacturer was maintained. The water-cement ratio was 0.1 and the water-gypsum ratio was 0.6, with mixing continuing for another 10 minutes. Five test specimens were produced for each type of sample (combination of matrix and amount of reinforcement).

3. Experiment part

3.1. Mechanical properties

Great emphasis is placed on the mechanical properties of building materials. Plaster should always effectively collaborate with other materials within the entire system, protecting the wall from mechanical damage while simultaneously enhancing the technical properties of the structure, such as thermal and acoustic insulation properties and the building's resistance to moisture. Plaster damage occurs due to the effects of physical and chemical processes.

Flexural strength was tested using a three-point bending setup with a Tiratest T2400 dynamometer. The measurements were conducted (after 28 days) on test specimens (5 pieces) with dimensions of 40 x 40 x 160 mm according to the standard ČSN EN 1015-11. The result of this test is the maximum force reached at the failure of the test specimen. Subsequently, the flexural strength (Rf) was determined from this value using equation (2):

$$R_f = (3Fl_p) / (2bh)^2. \quad (2)$$

Where: b is width of the sample [mm], h is the height of the sample [mm], l_p is the distance of the cylindrical supports [mm] and F is the breaking load [N]. The resulting values are given with an accuracy of 0.1 MPa.

3.2. Transport of liquid water

The effects of physical and chemical processes play a significant role in the durability of building materials. Due to the nature of construction materials (hydrophilicity, porosity), water can quickly penetrate the material structure, influencing various technological processes such as material degradation. The transport of liquid water was determined based on the change in sample weight according to the standard ČSN EN ISO 15148. For this sorption experiment (Fig. 1), it is necessary for the samples to be isolated around the perimeter using epoxy resin, ensuring unidirectional water transport. A sample (50 x 50 x 50 mm) with the front side not isolated is submerged 2 - 3 mm below the water surface while being suspended on an automatic digital scale, which records the increase in sample weight at regular intervals (every 60 minutes). Measurements were conducted in a laboratory under constant climatic conditions (RH 30 ± 5 %, temperature 23 ± 2 °C). The change in weight M [%] was determined using equation (3):

$$M = [(M_t - M_0) / M_0] \, 100. \quad (3)$$

Where M_t [g] is the measured weight value at time t and M_0 [g] is the initial weight.

Gypsum composites were tested for a period of 70 hours. For cement composites, the liquid water transport was slower, so the testing period lasted for 120 hours.

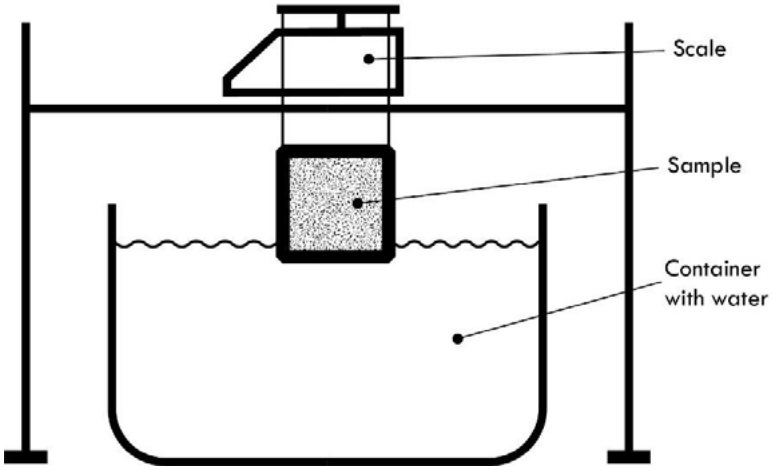

Figure 1. Measuring device for liquid water transport.

3.3. Electromagnetic shielding

Shielding is a tool that allows preventing the spread of disruptive electromagnetic fields from a defined area or into this area. Shielding covers and shields, which shield the entire device or its part acting as a source of interference, are very often used. This is a highly effective way of electromagnetic protection against interference of both continuous and impulse nature.

For common use, the effectiveness of electromagnetic shielding SE [dB] is determined, which expresses the attenuation of the interfering field by shielding (4):

$$SE = 20 \log (1 / K_S). \quad (4)$$

Where K_S is shielding coefficient [-].

The effectiveness of electromagnetic shielding was measured using a test setup consisting of the Rhode & Schwarz ZN3 vector network analyzer and the Electrometric model EM-2107A interrupted coaxial transmission line (sample holder). The measurements were conducted according to the ASTM D 4935-18 standard in the range of 30 - 3000 MHz. For the experiment, samples with dimensions of 100 x 100 x 10 mm were manufactured and tested after 28 days. Figure 2 depicts the test setup for electromagnetic shielding.

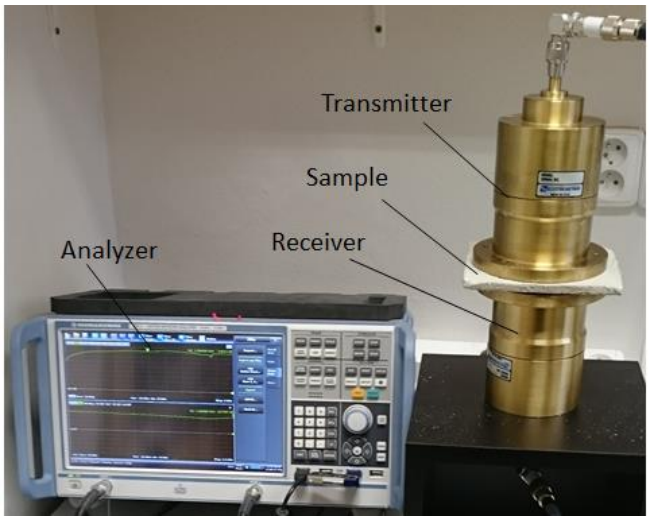

Figure 2. The testing setup for SE.

4. Result and discussion

4.1. Mechanical properties

On Figure 3, average values from 5 measurements along with 95% confidence intervals are provided for all used wt.% of carbon reinforcement for each type of plaster. The results indicate that with higher fiber content in the samples, the bending stress decreases. This is due to the fact that with a higher amount of fibers, there is a reduction in the matrix content, leading to poorer bonding between the fibers and the matrix and resulting in poor stress transfer between individual fibers.

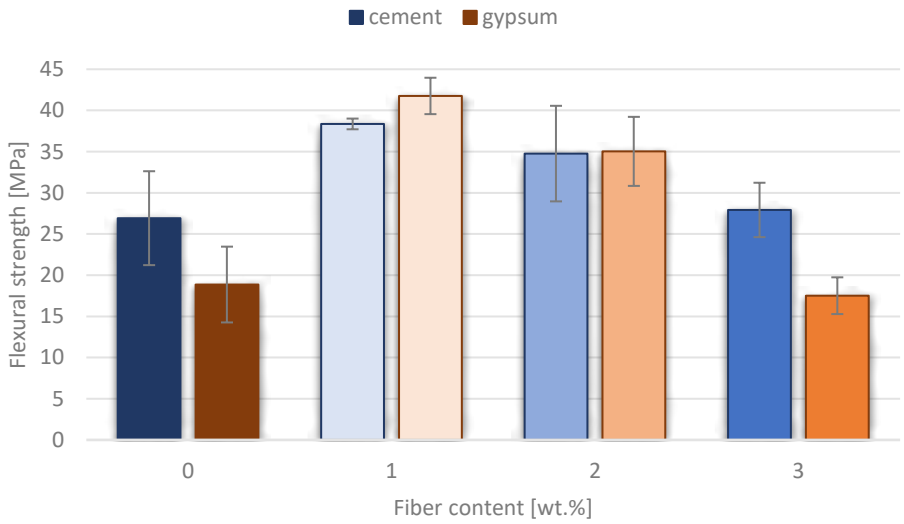

Figure 3. The flexural strength of cement and gypsum composites.

Cement matrix contains larger aggregates, which hinder the distribution of fibers in the sample. In the case of gypsum matrix, optimal fiber distribution in the sample and a good bond between fiber and matrix were achieved (fig. 4).

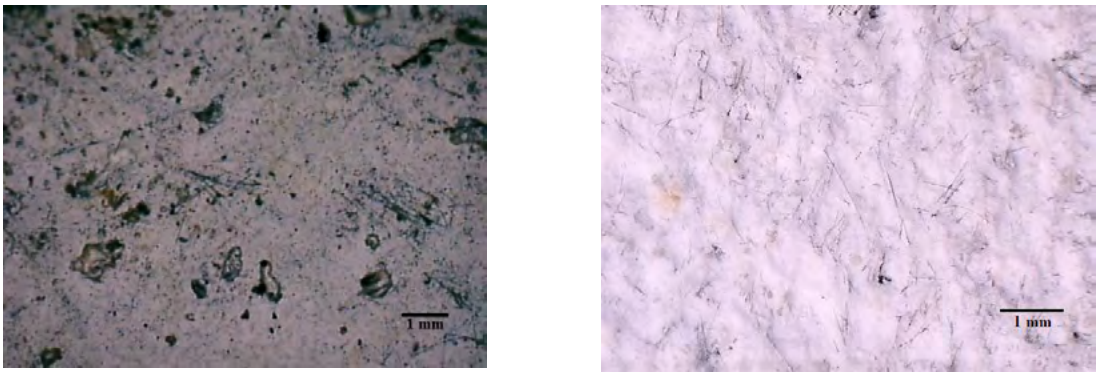

Figure 4. Cat of the samples, a) cement with 1 wt.% fibers, b) gypsum with 1 wt.% fibers

4.2. Transport of liquid water

In Figure 5a, the dependence of the average value of mass change *M* on the time of plaster composites is depicted. The cement plaster itself absorbs 20% of water since it has a firmer and tighter structure, thus water doesn't easily penetrate its structure. It has been shown that adding short-fiber reinforcement in combination with the pebbles contained in cement plaster leads to the formation of pores, resulting in increased water transport into the plaster structure.

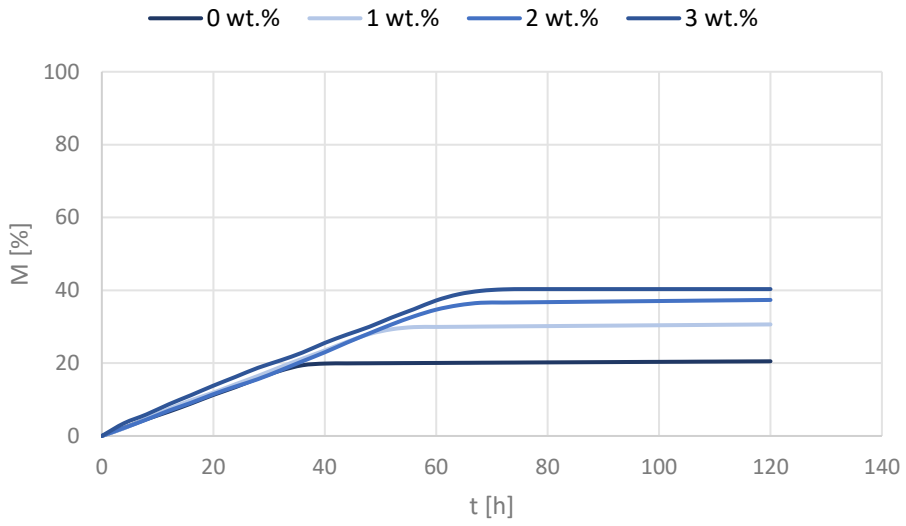

a)

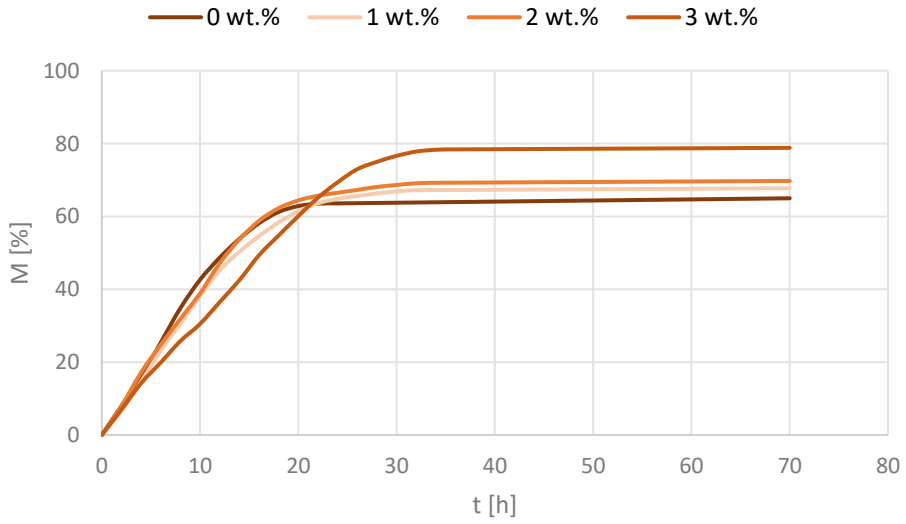

b)

Figure 5. Change in mass *M* over time: a) cement composites, b) gypsum composites.

In Figure 5b, the results of gypsum composites are presented. The influence of reinforcement on the mass increase of samples is evident from the results. Furthermore, we can observe that with an increasing fiber content in the sample, the soaking times are prolonged. By adding 1 and 2 wt.% there was an increase in mass by 3 and 5%, which compared to the increase in M of cement samples appears acceptable.

4.3. Electromagnetic shielding

From the results, it is evident that with the increasing proportion of carbon fibers in the matrix, the ability of plaster composites to shield electromagnetic fields significantly increases, confirming the theoretical analysis. Figure 6 illustrates the average values of SE (from 5 measurements) for individual types of plasters and for the given amount of reinforcement. Gypsum samples achieve higher SE values. This fact could be influenced by the distribution of fibers in the matrix. Cement plaster contains pebbles that hinder achieving the most uniform fiber distribution and prevent the interconnection of fiber contacts to create a conductive network.

©2024 | 2_SAMKOVÁ_Alžbeta_VAXQW.pdf:6

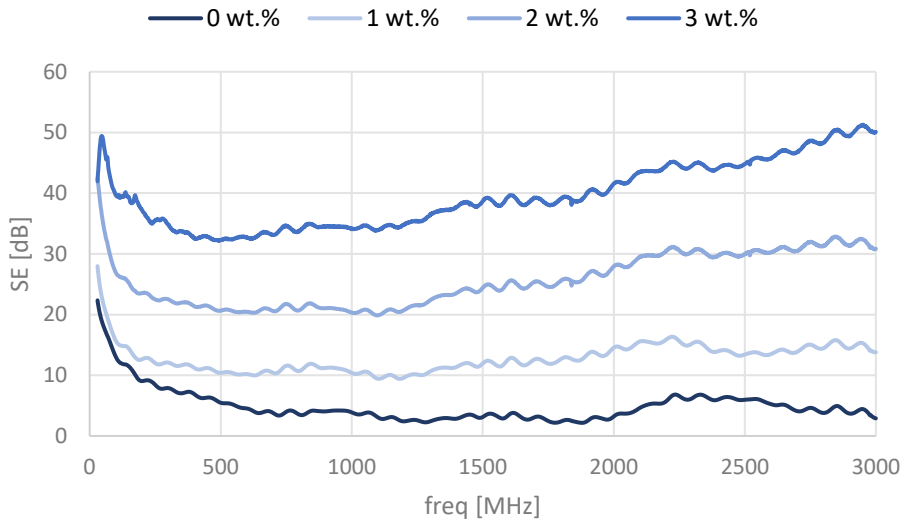

a)

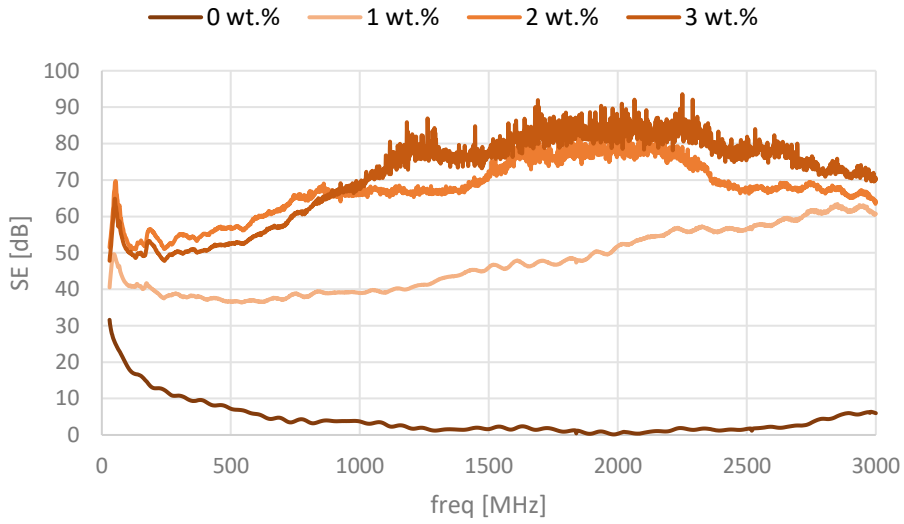

b)

Figure 6. The influence of fiber content on the SE of composite samples: a) cement composites, b) gypsum composites.

5. Conclusion

To create test samples, two commonly used plaster matrices were used, to which short carbon fibers were added in three weight ratios. The results showed that the use of 1 wt.% of carbon fibers was optimal. It was found that with higher fiber content in the samples, the flexural stress decreased. When testing composites with short-fiber reinforcement, fiber bridging after sample failure was observed, which was very positive.

During the testing of liquid water transport, it was observed that as the amount of fibers in the matrix increased, the weight gain of the samples also increased. This indicates that the amount of reinforcement affects the increased water transport by these samples.

From the SE results, it is evident that with an increasing proportion of carbon fibers in the matrix, the ability of plaster composites to shield electromagnetic fields significantly increases. The majority of

©2024 | 2_SAMKOVÁ_Alžbeta_VAXQW.pdf:7

authors use cement matrix in their experiments. However, it has been shown that using a gypsum matrix can achieve higher SE values than with a cement matrix.

References

[1] C. Ding, L. P. Guo, and B. Chen, "Theoretical analysis on optimal fiber-matrix interfacial bonding and corresponding fiber rupture effect for high ductility cementitious composites," *Constr. Build. Mater.*, vol. 223, pp. 841–851, Oct. 2019.

[2] C. Lu and C. K. Y. Leung, "Effect of fiber content variation on the strength of the weakest section in Strain Hardening Cementitious Composites (SHCC)," *Constr. Build. Mater.*, vol. 141, pp. 253–258, Jun. 2017.

[3] M. Cao, Y. Mao, M. Khan, W. Si, and S. Shen, "Different testing methods for assessing the synthetic fiber distribution in cement-based composites," *Constr. Build. Mater.*, vol. 184, pp. 128–142, Sep. 2018.

[4] N. Karagiannis, M. Karoglou, A. Bakolas, M. Krokida, and A. Moropoulou, "Drying kinetics of building materials capillary moisture," *Constr. Build. Mater.*, vol. 137, pp. 441–449, Apr. 2017.

[5] B. Seng, C. Magniont, and S. Lorente, "Characterization of a precast hemp concrete. Part I: Physical and thermal properties," *J. Build. Eng.*, vol. 24, p. 100540, Jul. 2019.

[6] L. Randazzo, G. Montana, A. Hein, A. Castiglia, G. Rodonò, and D. I. Donato, "Moisture absorption, thermal conductivity and noise mitigation of clay based plasters: The influence of mineralogical and textural characteristics," 2016.

[7] N. Benmansour, B. Agoudjil, A. Gherabli, A. Kareche, and A. Boudenne, "Thermal and mechanical performance of natural mortar reinforced with date palm fibers for use as insulating materials in building," *Energy Build.*, vol. 81, pp. 98–104, Oct. 2014.

[8] Y. Cui, Y. Zhang, and H. Janssen, "EMPD-based moisture buffering quantification with moisture-dependent properties (I): Modelling and simulations," *Build. Environ.*, vol. 205, p. 108266, Nov. 2021.

[9] H. Wan, G. Huang, S. Liu, S. Fan, X. Xu, and J. Yu, "Optimal moisture buffering thickness of the hygroscopic material layer: Modeling and derivation," *Build. Environ.*, vol. 205, p. 108257, Nov. 2021.

[10] X. Li, X. Yin, S. Liang, M. Li, L. Cheng, and L. Zhang, "2D carbide MXene Ti 2 CT X as a novel high-performance electromagnetic interference shielding material," 2019.

[11] W. wu Jin, W. kai Wang, S. Mazumdar, G. zhong Xu, and Q. Q. Zhang, "Carbon foams with Fe-organic network-derived Fe3O4 for efficient electromagnetic shielding," *Mater. Chem. Phys.*, vol. 304, p. 127797, Aug. 2023.

[12] Y. Li, Y. Liu, C. Jin, J. Mu, and J. Liu, "Research on mechanical and electromagnetic shielding properties of cement paste with different contents of fly ash and slag," *NDT E Int.*, vol. 133, p. 102736, Jan. 2023.

[13] X. Zhang and W. Sun, "Microwave absorbing properties of double-layer cementitious composites containing Mn-Zn ferrite," 2010.

[14] G. Logesh *et al.*, "Carbon fiber reinforced composites from industrial waste for microwave absorption and electromagnetic interference shielding applications," *Ceram. Int.*, vol. 49, no. 2, pp. 1922–1931, Jan. 2023.

[15] H. N. Yoon, D. Jang, H. K. Lee, and I. W. Nam, "Influence of carbon fiber additions on the electromagnetic wave shielding characteristics of CNT-cement composites," *Constr. Build. Mater.*, vol. 269, p. 121238, Feb. 2021.

©2024 | 2_SAMKOVÁ_Alžbeta_VAXQW.pdf:8

ECO-FRIENDLY SURFACE MODIFICATION OF CARBON FIBRE FOR APPLICATION IN CEMENT-BASED COMPOSITES

Y. Tao[1*], S.A. Hadigheh[1], David J. Hayne[2], B. Newman[2] and L.C. Henderson[2]

[1]School of Civil Engineering, Faculty of Engineering, The University of Sydney, Sydney, New South Wales 2006, Australia
[2]Institute for Frontier Materials, Deakin University, Waurn Ponds, Victoria 3216, Australia
*Corresponding Author: Yunyun Tao (yunyun.tao@sydney.edu.au)

Keywords: tannic acid, citric acid, carbon fibre, surface modification, bond strength.

Abstract
Interfacial bonding properties between carbon fibre (CF) and cement-based matrix are subjects of great research interest given their critical role in the load transfer mechanism within the fibre-reinforced cementitious composite (FRCC). In this study, two bio-based solutions were utilised to modify CFs separately, offering innovative strategies with minimum environmental impact and enhanced safety benefits. The surface morphology and chemistry of CF were characterised and comprehensively analysed using SEM, XPS and Raman after each treatment to confirm the effective modification of fibres using bio-based solutions. Single-fibre tensile and fibre bundle pullout tests were performed to examine the influence of the treatment on the fibre tensile strength as well as bond strength between CF and cementitious matrix. The experimental results showed that the tannic acid (TA) and citric acid (CA) can effectively modify CF surface through polymerisation and the interfacial bond strength between CF and cementitious matrix was increased compared to the virgin CF. The functional groups on the surface of the bio-acid-treated CF were expected to chemisorb ions within the matrix, forming chemical or ionic bonds at the interface between CF and the matrix, which in turn facilitated the development and precipitation of hydration products around CF.

1. Introduction

The growing demand for concrete characterised by high strength and ductility has expanded the application of FRCC. In the construction industry, there is a rising interest in cementitious composites reinforced with short CF, which exhibits superior mechanical performance, increased durability, and excellent electrical conductivity [1, 2]. Nevertheless, some limitations, such as non-polarity, incompatibility with the cementitious matrix, and challenges in achieving uniform dispersion hinder the widespread utilization of this construction material [3, 4]. Hence, implementing certain approaches such as surface modifications become essential to enhance the bonding adhesion between CF and cementitious matrix, consequently improving FRCC performance.

Acid-mediated oxidative modification is one of the most commonly used chemical treatments. In this process, CF surface undergoes oxidisation by employing strong acids such as nitric and sulfuric acid, which enhances the nano-scale roughness and introduces functional groups like carboxyl (COOH), hydroxyl (OH) and carbonyl (C=O). For example, Lavagnaet al. [5] reported that the optimal condition for acidic oxidation of CF involves using a piranha solution ($3H_2SO_4$:$1H_2O_2$) for 30 minutes at 30°C. Improved electrical and mechanical properties of CF-reinforced cement composite were observed after the treatment, which were owing to the strong effect on the interaction and adhesion of fibre with the cement. Gallyamovaet al. [6] modified CF surface by immersing CF in the nitrosulphuric acid. The efficacy of the acid treatment was confirmed, and it was noted that an increase in temperature, concentration, and duration of treatment could have an impact on the CF surface by increasing carboxyl and ketone reactive groups. However, the development of acid oxidative modification has encountered limitations due to its complex operational procedures, high operational risks, toxicity concerns, and environmental pollution implications. Eco-friendly alternatives to traditional inorganic acids offer a sustainable solution for addressing these challenges mentioned above. Research has been carried out on

the potential use of greener alternatives for modifying carbon-based materials. Tannic acid (TA), a natural plant polyphenol, was utilised to functionalise substrates, such as graphene oxides (GO) [7], carbon nanofibre/tubes (CNF/T) [8-10], CF [11-13] and carbon black (CB) [14], to enhance surface wettability and interfacial properties between the substrate and the matrix. It was reported that TA could modify the substrate surface through either covalent or non-covalent routes [7]. Additionally, it could undergo polymerisation with amino-terminated substances to create a thin layer coating on the surface. The integration of citric acid (CA) treatment, as a weak organic acid from natural sources or other eco-friendly options, has been gradually recognised in various studies focusing on the surface modification of CNTs [15-18] and natural fibres [19-21] through functionalisation and polymerisation. Additional functional groups such as carboxyl and hydroxide were reported to be present on the sample surface following CA treatment.

As highlighted above, enhancing the bonding adhesion between CF and the cementitious matrix is crucial for improving the performance of FRCC. However, the use of transitional acid oxidative modifications for CF has limitations such as environmental concerns and relatively high costs. Therefore, there is a need to explore more eco-friendly alternatives to traditional inorganic acids for modifying the CF surface. This research aims to develop environmentally friendly and effective modification methods to treat CF surface, enhancing microfibre dispersions and fibre-matrix interactions in cementitious composites through the application of organic acids.

2. Materials and methods

2.1. Raw materials

12K T700SC (T700SC-12000-50C) carbon fibre (CF) was manufactured and produced by Toray Industries, Inc. (France). TA and ethanolamine (EA) were purchased from Sigma-Aldrich Pty Ltd. CA monohydrate AJAX Finechem was purchased from Thermo Fisher Scientific Inc. Acetone and ethanol used were analytical grade. All the chemicals in this study were used as received. The cement used in this study was general-purpose cement (type GP) as specified in Australian Standard AS3972 [22] and the minimum 7-day mortar compressive strength was reported 35 MPa. The cement paste (cementitious matrix) was prepared at a water/cement ratio of 0.55 in accordance with previous research on CF-reinforced cementitious composite [1] .

2.2. Surface modification methods

Acetone was chosen as the solvent for desizing due to its lower energy, minimizing the likelihood of damaging the CF surface compared to high-temperature heating [23]. The desizing procedure involved immersing CF in acetone and using a reflux system at 60°C for a duration of 12 hrs (Figure 1). This initial size-removing process enables the subsequent gas oxidation of CF surface at a lower temperature (instead of high-temperature desizing), reducing energy consumption. The thermal weight loss curve of T700 CF without sizing, as investigated by Jiang [24], revealed a 1% weight loss rate at 300°C, which doubled between 300-700°C. Low-temperature oxidations result in the formation of strong acidic groups, whereas high temperatures may lead to the creation of weak acid groups while decomposing some surface functional groups [24, 25]. Desized CFs were placed in an oven and heated at a low temperature of 275°C for 30 mins for air oxidation.

In the next phase, two different bio-based acids (namely TA and CA) were utilised for the CF surface modification and their performances were compared. During the first modification method, TA and ethanolamine (EA) were mixed in an alkaline aqueous (pH = 8.5, 1L) with a mass ratio of 2:5 as suggested by Bashiri Rezaieet et al. [26], followed by using a magnetic stirrer until the chemicals dissolved completely in the aqueous solution. CFs were then added to the solution and a sonicator was employed to facilitate enhanced interactions between the chemicals and the surface of the CFs. Subsequently, the reaction was allowed to proceed at room temperature for the next 12 hrs. In parallel, for the second bio-based modification method, a mixture was prepared by dissolving 10g CA monohydrate in 200 mL distilled water followed by magnetic stirring until complete dissolution of CA. CF was then added and mixed with the assistance of ultrasonic vibration. The mixture was subjected to

heating in a reflux system at 90°C for 1 hour. After the acid modification, functionalised CFs were thoroughly rinsed with ethanol and distilled water to ensure the removal of any unreacted coatings from the surface, followed by drying. The corresponding surface-modified CFs with/without the air oxidation process were named as TA-CF-A/B and CA-CF-A/B respectively, as shown in Figure 1.

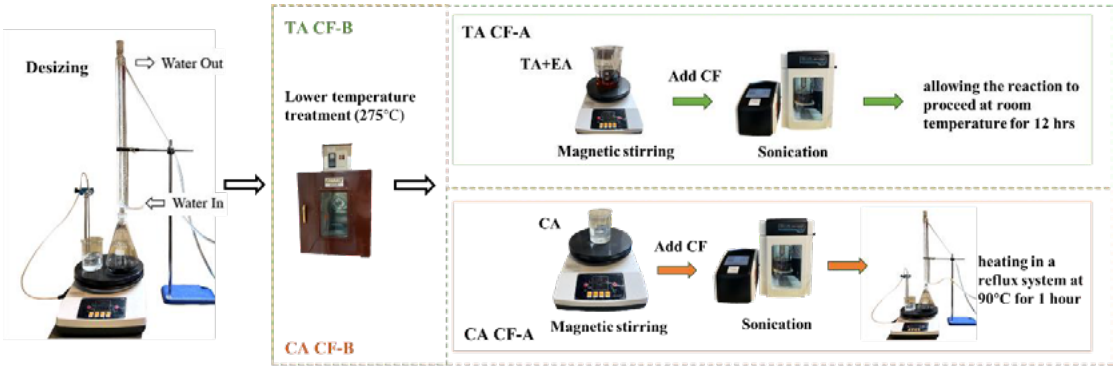

Figure 1. Process flow of surface modification methods.

2.3. Characterisation

The surface morphology of virgin CF, desized CF, TA-CF-A/B and CA-CF-A/B was observed by scanning electron microscopy (SEM) (Zeiss ULTRA Plus). The operating voltage was 20kV. The element types and contents on the CF surface were examined by energy dispersive spectrometer (EDS) and recorded by Thermo Fisher Scientific K-Alpha+ X-ray Photoelectron Spectroscopy (XPS). Raman spectra of the CF surface were recorded on a Renishaw Raman InVia Qontor Microscope employing a Renishaw RL532C CW diode laser emitting at 532nm.

2.4. Single-fibre tensile and fibre bundle pullout test

Single fibre tensile tests were performed according to ASTM C1557-20 [27] using Dynamic Mechanical Analyzer (DMA) 850 with an 18N load cell. Single CFs were randomly sampled from virgin and treated CF bundles for testing. For the preparation of the test specimens, typical mounting tabs (24mm×7mm) were used with a 12mm gauge length [28]. The axis of a single CF was oriented perpendicular to the crosshead of the machine. An initial load of 0.01N was introduced before the commencement of the loading phase. The crosshead was then set to operate at a speed of 0.2 mm/min. To study the interfacial properties of the fibre in the FRCC, the bond strength between the CF bundle (approximately 0.5mm in diameter) and cementitious matrix was tested by a fibre bundle pullout test. The fresh mortar was poured into a specially designed steel mould following the setup described by Katz and Li [29], which was designed for micro-fibres with fine diameters in a cementitious matrix. The specimen was demoulded after 1 day and cured in a standard moist environment at a temperature of 23°C and relative humidity of 95% until testing. To capture the entire displacement-force curve during pull-out, a smaller embedded fibre length (5mm) was used. An initial load of 0.01N was introduced before the commencement of the loading phase. The crosshead was then set to operate at a speed of 0.5 mm/min.

3. Results and discussions

3.1. Characteristics of functionalised CF surface

The surface morphologies of virgin CF and CFs subjected to various treatments were examined using SEM. The untreated virgin CF exhibits a smooth surface (Figure 2 (a)). Following desizing with acetone, no significant surface defects were observed, but there was an increase in roughness, as seen in (Figure 2 (b)). For TA CF-A and TA CF-B (Figure 2 (c) and (d)), raised points and a deposition layer were visible on the surface. An EDS mapping example (Figure 2 (g)) highlighted the intense presence of oxygen in specific locations, corresponding to the coating particles on the surface following TA treatment. This observation also confirmed the alteration in the surface chemical composition. CA treatment without oxidation did not result in significant visible change ((Figure 2 (e))). However,

subsequent to oxidation, as depicted in (Figure 2 (f)), CA could be seen covering the fibre surface and led to an increase in surface roughness.

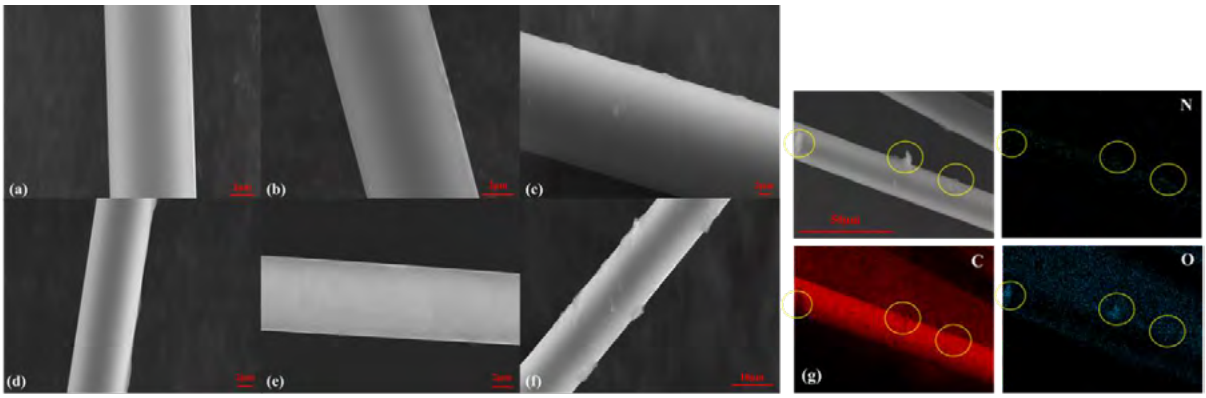

Figure 2. SEM images on the surface morphologies of (a) virgin CF; (b) desized CF; (c) TA CF-A; (d) TA CF-B; (e) CA CF-A; (f) CA CF-B; and (g) EDS mapping images of CF after TA treatment.

XPS was used to characterise the chemical composition changes on the CF surface before and after treatments. The untreated virgin CF initially contained chemical elements comprising carbon (72.2%), oxygen (21.32%), nitrogen (2.16%) and silica (4.33%). After sizing removal, as indicated in Figure 3 (a), the relative percentage of carbon increased to 78.42%, accompanied by a notable decrease in the O/C ratio from 0.296 to 0.177. Concurrently, the relative percentage of C-C/C=C peak increased, while the C-O/C=O peak decreased (Figure 4). These changes suggest a reduction in surface activity and indicate the effective removal of the sizing from the virgin CF [23, 30]. Following air oxidation at a low temperature, the ratio of O/C increased to 0.235. Both the relative percentage of C-O/C=O (35.90%) and O-C=O/COOH (17.96%) peaks increased remarkably, confirming a significant augmentation in the presence of active oxygen-containing functional groups on the surface of CF [30]. Following the bio-acid chemical treatment, the ratio of O/C ranges from 0.20 to 0.24, indicating an increasing trend compared to the desized CF. This confirms the effective chemical modification on the CF surface. After co-deposited with TA and EA, the ratio of N/C increased, and a new peak of C-N was assigned to approximately 285.7 eV (Figure 3(a) and Figure 4), due to the amino groups of EA became covalently bonded to the CF surface [31]. Moreover, in contrast to virgin CF, where nitrogen functional groups were not easily identifiable, the presence of NH_2, N-H and -N= functional groups were observed in the N1s spectrum (Figure 4), further confirming the involvement of EA and TA in the Michael addition or Schiff base reaction [11-13]. Upon the reaction of CA and CF to form CA CF-A/B, the hydroxyl groups (OH) of CA mainly reacted with the carboxyl groups (COOH) presented on the oxidized CF surface. During this esterification reaction, carboxyl groups were consumed, resulting in an increase in the appearance of ester groups (O-C=O). The enhanced formation of carbonyl, carboxyl and ester groups has the potential to improve wettability and facilitate the creation of chemical and ionic bonds at the interface between CF and matrix. C-O/C=O bonds on the surface of CA CF-B showed higher than that on the surface of CA CF-A, which can be also attributed to the oxidation process, while they may decrease during the reaction and be transformed into ester groups.

To evaluate the surface defects of CFs subjected to different treatments, the ID to IG ratio from Raman spectra (calculated as the ratio between the areas under the D and G bands) was calculated. D band presents the disorder structures within graphite cells; thus ID/IG ratio is used for measuring any degradation resulting from treatments. Figure 3 (b) shows the Raman spectrum and ratio of ID/IG obtained by averaging data from two measurements. The ID/IG was 0.99 for untreated virgin CF, and it rose to 1.01 and 1.20 for desized and oxidised CF respectively, which indicates a higher degree of surface defects resulting from acetone desizing and especially the air oxidisation process. Compared to the virgin CF, the ID/IG of CF treated with TA and EA showed a moderate decrease to 0.96 and 0.98 for non-oxidized and oxidized samples respectively, indicating fewer detected defects in Raman analysis. CF modified with CA exhibited a slightly higher ratio of 1.04 and 1.07, which led to an increase in the

presence of active functional groups consistent with expectations, while the ratio was lower than the ratio observed for oxidized CFs of 1.20.

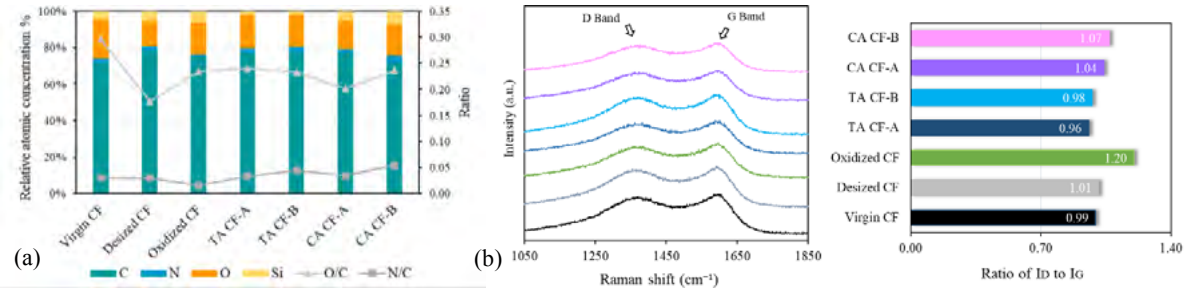

Figure 3. (a) XPS surface composition analysis; (b) Raman spectrum and ID/IG ratio of virgin CF and CF with different treatments.

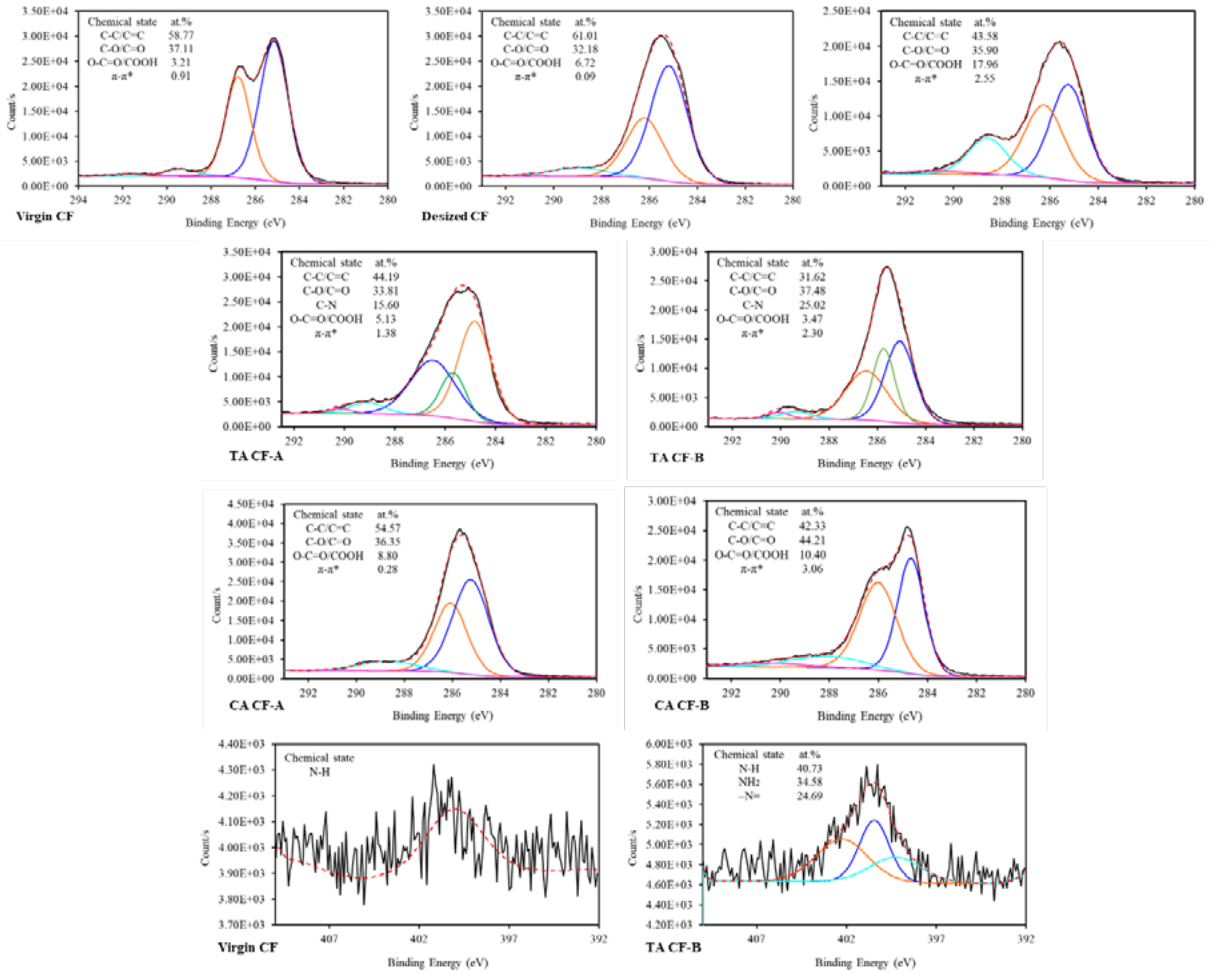

Figure 4. XPS C1 and N1s peak fitting analysis of CFs.

3.2. Mechanical performance of functionalised CF

Figure 5 summarises the tensile performance of virgin CF and CF with different treatments. Results demonstrated that the bio-acid-treated CFs have a high tensile capacity even after TA and CA reaction on their surface. A two-parameter Weibull statistical analysis was employed to evaluate the adequacy of the data points (comprising 27 measurements in this study) in determining the variability of single fibre tensile strength. The correlation coefficients (R^2) of all plots from tensile testing were greater than 0.9, which indicated these measurements followed a statistical distribution and were acceptable for evaluating the tensile performance with negligible variability [32, 33]. The average and median single

fibre tensile strength was 3.78 and 3.61 GPa, respectively. The tensile strength of desized caron fibre slightly varied. By comparing the functionalised CF and virgin CF, the bio-acid-treated CFs after oxidation possessed a higher average tensile strength of 3.85 GPa with an approximately 1.9% increase. This can be explained by the surface morphology that nano layer coverage resulting from the treatment with TA and EA covered the existing defects and irregularities on fibre surface [12]. The reaction between CA and CF surface functional groups may have a smoothing effect on fibre flaws as indicated by Raman and SEM images when compared to the desized and oxidized CF. Both of the modification methods contributed to a reduction in stress concentration points during tensile testing.

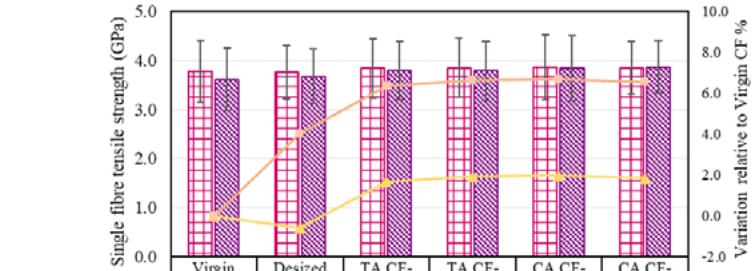

	Virgin CF	Desized CF	TA CF-A	TA CF-B	CA CF-A	CA CF-B
Average	3.78	3.76	3.84	3.85	3.85	3.85
Median	3.61	3.68	3.79	3.79	3.85	3.87
Average variation	0.00	-0.57	1.67	1.94	1.97	1.86
Medium variation	0.00	4.01	6.35	6.63	6.66	6.55

Figure 5. Tensile strength of single CF with/without surface modification.

The analysis of interfacial bond performance involved assessing the maximum bond strength (τ) and the interface friction bond strength (τ_f) based on the pullout tests (Figure 6). τ represents the peak pull load that the embedded CF bundle can withstand before being pulled out. Once reaching the maximum load, the pullout force would suddenly decrease to a smaller load, marking the onset of slippage, which is used to determine τ_f. The maximum bond strength between fibre bundle and matrix was 3.10 MPa for virgin CF, while it increased to 3.67 and 3.50 MPa for CF modified with CA and TA, which were about 18.3% and 12.8% higher than that of virgin CF. Although the operational constraints during the modification process may have impacted the behaviour of surface-modified CF, the maximum bond strength was improved, which can be attributed to both interfacial bond strength and chemical adhesion between the fibre and matrix. The surface-modified CF exhibited higher frictional bond strength (τf) and chemical bonding energy (Gd) compared to virgin CF. This improvement in bond strength can be ascribed to the increased surface roughness, frictional forces and chemical adhesion achieved by functional groups present on the CF surface. CA-modified CF showed higher frictional bond strength improvement (τf =2.67MPa), while the bond strength enhancement observed for TA-modified CF was primarily attributed to the reinforcement of chemical adhesion between the fibre and the matrix (Gd =3.58J/m²). SEM images of CF surface after the pullout test in Figure 6 depicted the formation of hydration products surrounding the modified CF surface, which revealed the chemical bonding between the fibre and the cementitious matrix.

Conclusions

In this paper, eco-friendly methods for CF surface modification were explored to enhance the bonding properties between CF and cement-based matrices. Through material characterization, it was found that TA and EA could be co-deposited onto the CF surface via Michael addition or Schiff base reactions to improve the interfacial properties. Pre-treatment processes, including sizing removal and air oxidation, were shown to increase the presence of active oxygen-containing functional groups on the CF surface. Subsequently, CA could react with these carboxyl groups, further facilitating the formation of chemical and ionic bonds at the interface between CF and the cementitious matrix. As a result, the surface-modified CF demonstrated higher tensile strength and improved interfacial bond performance with the cementitious matrix compared to untreated CF. The use of bio-acids for surface modification is environmentally friendly and cost-effective, implying promising application prospects in fibre surface treatment and potential for further development in the field.

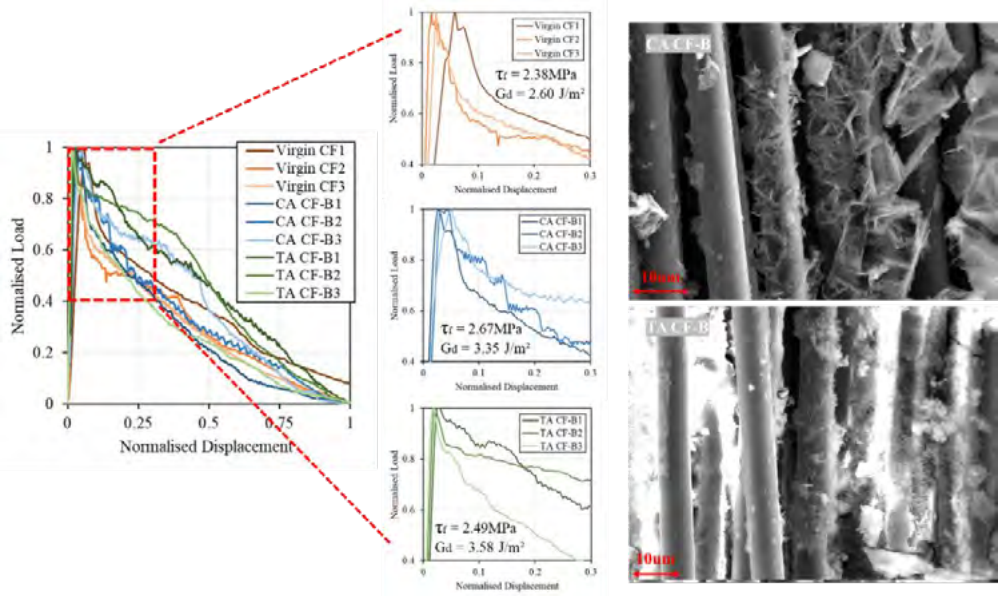

Figure 6. Normalised pullout curves of CF in cementitious matrix; and SEM images of CF after tests.

Acknowledgments
This research was supported by the Australian Government through the Australian Research Council's Discovery Early Career Researcher Award (DECRA) fellowship scheme (project DE200100406). The authors would acknowledge the facilities and technical assistance of Sydney Microscopy and Microanalysis and Sydney Analytical at the University of Sydney.

References

[1] Y. Tao, S.A. Hadigheh, and Z. Wang. Void geometry analysis and multifaceted characterisation of cementitious mortar reinforced with short carbon and glass fibres – A comparative study. J. Build. Eng., 89: 109283, 2024.
[2] H. Fatemi, S.A. Hadigheh, Y. Tao, et al. Development of a novel and specialised cementitious matrix overlay for anode embedment in impressed current cathodic protection (ICCP) systems for reinforced concrete bridges. Case Stud. Constr. Mater., 20: e02908, 2024.
[3] H. Li, M. Liebscher, D. Zhao, et al. A review of carbon fiber surface modification methods for tailor-made bond behavior with cementitious matrices. Progress in Materials Science, 132: 101040, 2023.
[4] M.S. Ansari, S. Zafar, and H. Pathak. A comprehensive review of surface modification techniques for carbon fibers for enhanced performance of resulting composites. Results in Surfaces and Interfaces, 12: 100141, 2023.
[5] L. Lavagna, S. Musso, G. Ferro, et al. Cement-based composites containing functionalized carbon fibers. Cem. Concr. Compos., 88: 165-171, 2018.
[6] R. Gallyamova, V. Dokichev, and F. Musin. Acid treatment of carbon fiber surface. in MATEC Web of Conferences. EDP Sciences, 2023.
[7] C. Sainz-Urruela, S. Vera-López, M. Paz San Andrés, et al. Surface functionalization of graphene oxide with tannic acid: Covalent vs non-covalent approaches. J. Mol. Liq., 357: 119104, 2022.
[8] X. Zhang, m. liu, X. Zhang, et al. Interaction of Tannic Acid with Carbon Nanotubes: Enhancement of Dispersibility and Biocompatibility. Toxicol. Res., 4: 160-168, 2014.
[9] X. Qian, H. Yang, J. Wang, et al. Eco-friendly treatment of carbon nanofibers in cementitious materials for better performance. Case Stud. Constr. Mater., 16: e01126, 2022.
[10] C. Wang, P.-X. Hou, Y. Zhao, et al. Tannic acid coated single-wall carbon nanotube membranes for the recovery of Au from trace-level solutions. Nano Res., 16(8): 11350-11357, 2023.
[11] M. Zhang, C. Cheng, C. Guo, et al. Co-depositing bio-inspired tannic acid-aminopropyltriethoxysilane coating onto carbon fiber for excellent interfacial adhesion of epoxy composites. Compos. Sci. Technol., 204: 108639, 2021.

[12] D. Wu, X. Liu, Y. Sheng, et al. Polyhedral Oligomeric Silsesquioxane Encountering Tannic Acid: A Mild and Efficient Strategy for Interface Modification on Carbon Fiber Composites. Langmuir, 38(27): 8334-8341, 2022.
[13] X. Cui, J. Liu, L. Ma, et al. Grafting of the hierarchical natural tannic acid and polyethyleneimine onto carbon fiber for significantly improved surface/interface properties. Polym. Adv. Technol., 31(12): 3126-3133, 2020.
[14] J. Li, X. Shao, B. Zhang, et al. Hydrophilic surface modification of carbon black through a mussel-inspired reaction of tannic acid and diethlyenetriamine. Colloid. Polym. Sci., 300, 2022.
[15] S.H. Lim, J. Wei, and J. Lin. Electrochemical genosensing properties of gold nanoparticle–carbon nanotube hybrid. Chem. Phys. Lett., 400(4): 578-582, 2004.
[16] R.L. Garnica-Gutiérrez, L.A. Lara-Martínez, E. Palacios, et al. Effect of functionalized carbon nanotubes and their citric acid polymerization on mesenchymal stem cells in vitro. J. Nanomater., 2018: 5206093, 2018.
[17] M.N.Z. Abidin, P.S. Goh, A.F. Ismail, et al. Antifouling polyethersulfone hemodialysis membranes incorporated with poly (citric acid) polymerized multi-walled carbon nanotubes. Mater. Sci. Eng., C, 68: 540-550, 2016.
[18] P. de Leon Martinez, A. Galindo, C. Ávila-Orta, et al. Ultrasound-Assisted Surface Modification of MWCNT Using Organic Acids. Materials, 14: 72, 2020.
[19] S. Sujito, E. Hidayah, A. Sjaifullah, et al. Influence of Citric Acid Addition and Fiber Treatment on Tensile Properties of Ramie Fiber Reinforced Poly-lactic Acid (PLA) Green Composite. Journal of Advanced Research in Dynamical and Control Systems, 12: 809-814, 2020.
[20] J. De and R. Baxi. Experimental Investigation and Analysis of Mercerized and Citric Acid Surface Treated Bamboo Fiber Reinforced Composite. IOP Conference Series: Mater. Sci. Eng., 225: 012154, 2017.
[21] S. Chafei, L.F. Dutra, and A. Jamali. Enhancing Mechanical Behavior of Cement Composites through Citric Acid Treatment of Flax Fibers. J. Mater. Civ. Eng. 36(1): 04023486, 2024.
[22] AS 3972 General purpose and blended cements. Standards Australia: Australia, 2021.
[23] K. Kim, M. Kim, G. Kim, et al. The Effect of Chemical and Thermal Treatment for Desizing on the Properties and Chemical Functional Groups of Carbon Fiber. Materials (Basel), 16(20), 2023.
[24] L. Jiang, The Preparation of a Carbon Fibre Hybrid with Improved Thermal Stability. 2019.
[25] M.S. Shafeeyan, W.M.A.W. Daud, A. Houshmand, et al. A review on surface modification of activated carbon for carbon dioxide adsorption. J Anal Appl Pyrolysis, 89(2): 143-151, 2010.
[26] A. Bashiri Rezaie, M. Liebscher, A. Drechsler, et al. Tannic acid/ethanolamine modification of PE fiber surfaces for improved interactions with cementitious matrices. Cem. Concr. Compos., 131: 104573, 2022.
[27] ASTM C1557 Standard Test Method for Tensile Strength and Young's Modulus of Fibers. ASTM International: West Conshohocken, United States, 2020.
[28] Y. Wei and S.A. Hadigheh. Enhancing carbon fibre recovery through optimised thermal recycling: Kinetic analysis and operational parameter investigation. Materials Today Sustainability, 25: 100661, 2024.
[29] A. Katz and V.C. Li. A special technique for determining the bond strength of micro-fibres in cement matrix by pullout test. J. Mater. Sci. Lett., 15(20): 1821-1823, 1996.
[30] Z.Q. Yao, C.G. Wang, and Y.X. Wang. In situ growth of CNTs on carbon fiber by chemical vapor deposition. IOP Conference Series: Environ. Earth Sci., 354(1): 012075, 2019.
[31] X. Cui, J. Liu, m. Lichun, et al. Grafting of the hierarchical natural tannic acid and polyethyleneimine onto carbon fiber for significantly improved surface/interface properties. Polym. Adv. Technol., 31, 2020.
[32] K.M. Beggs, L. Servinis, T.R. Gengenbach, et al. A systematic study of carbon fibre surface grafting via in situ diazonium generation for improved interfacial shear strength in epoxy matrix composites. Compos. Sci. Technol., 118: 31-38, 2015.
[33] D. He, V.K. Soo, F. Stojcevski, et al. The effect of sizing and surface oxidation on the surface properties and tensile behaviour of recycled carbon fibre: An end-of-life perspective. Compos. Part A Appl. Sci. Manuf., 138: 106072, 2020.

A NEW METHOD TO PREPARE MORE REPRESENTATIVE COATED GLASS FIBRES FOR SCREENING AND DEVELOPMENT OF SIZINGS AT THE LABORATORY SCALE

Prof James Thomason[1], Roya Akrami[1], Dr Liu Yang[1]

[1]Department of Mechanical and Aerospace Engineering, University of Strathclyde, 75 Montrose Street, Glasgow G1 1XJ, UK
Email: james.thomason@strath.ac.uk

Keywords: Glass fibre, size, sizing, adhesion, characterisation

Abstract
Conventional laboratory scale glass fibre sizing analysis commonly involves sample preparation by dip coating, resulting in a thick size layer with a higher Loss of Ignition (LoI) than industrial sized fibres. This makes it difficult to make useful comparisons between industrial and lab-scale prepared samples when evaluating size performance. This paper presents a novel, but simple, fibre coating technique that produces a size layer similar to industrial sized samples with an average layer thickness one tenth that obtained by dip-coating. Thermogravimetric analysis and electron microscopy results show how the size layer on lab-coated fibres had a morphology much more comparable to that on industrial samples. Average size LoI could be easily controlled in a range from 1 to 5 %, compared to the 11 % obtained on samples dip coated with the same size formulation. Microbond tests results of interfacial shear strength in two different polypropylenes indicate that the lab-sized fibres exhibited comparable values to the industrial-sized fibres and enhanced values compared to the dip coated fibres. These findings highlight the considerable potential of this novel lab-scale coating technique as a viable alternative to dip coating in laboratory research, as it provides a more realistic representation of industrial-scale sizings.

1. Introduction

Glass fibre reinforcements form the backbone of the composites industry. Today glass fibre products account for more than 95% of fibre reinforcements used in the composites industry, primarily due to their highly attractive performance to price ratio. Despite their relatively low-tech image as a composite reinforcement, the production of glass fibres has evolved into a very complex technology with requirements that challenge the state of the art in materials science research and development [1,2]. Possibly the most critical component involved in the manufacture of glass fibres and their composites is the fibre size. Size is a thin surface coating of mainly organic materials applied, most often as a dilute aqueous solution or emulsion, to nearly all types of man-made fibres during their manufacture. In the case of glass fibres, sizing is probably the key component influencing the commercial success (or failure) of most reinforcement products and their composites. This is due to the major role played by the sizing in the profitability, processability, and performance of that product. Continuous reinforcement grade glass fibre could not be manufactured in a high volume, cost-effective, manner without the correct sizing formulations. Similarly, most composite production processes could not be operated in a cost-effective manner without appropriately sized glass fibres. Finally, both short-term and long-term composite performances are critically influenced by the optimization of the fibre sizing and the closely associated fibre-matrix interphase in the composite [2-7]. However, due to the lack of reliable and verifiable information on the physical and chemical nature of sizings, the generally available understanding of these complex chemical mixtures does not reflect the level of importance that they have in determining the success of any glass reinforced composite material in a specific application [7].

Despite the critical need of the composite industry to fully understand all aspects of the materials it uses, size and sizing remains a "black box" technology in composites since glass fibre producers are very reticent to reveal much information about the complex formulations they use. Consequently openly available descriptions of sizes tend to be highly generic in nature. Commercial glass fibres are often supplied with only two sizing related details. The first is the chemical “compatibility” of the sizing with a general class of matrix polymer. The second is a value for the Loss on Ignition (LoI), a measurement of the amount of size present on the fibres. This paucity of information on the physical and chemical nature of the sizing on a glass fibre product is an issue for many users of glass fibres, be they interested in quality control for manufacturing through to the fundamentals of the fibre-matrix interphase. Typically the user will be told that sizes are dilute water based emulsions or dispersions containing a complex mixture of components. These will often be described more by their generic function rather than by their chemical formulae. The primary components are the film former and the coupling agent [2-5]. The film former is designed to protect and lubricate the fibres and hold them together prior to composite processing, yet also to promote their separation and wetout when in contact with resin. The coupling agent is often said to serve primarily to bond the fibre to the matrix resin. Beyond these two major components, sizes also may include lubricating agents, antistatic agents and surfactants. A complex size formulation may contain five or more components. The interaction of these components with each other, with the fibre surface, with the matrix polymer, within a particular processing environment is extremely complex and quite inadequately researched. A number of recent reviews have highlighted some serious issues for the composites industry related to the state of play in glass fibre sizing technology [5-7]. It has been suggested that the nature of all the complex interactions involved in size formulations, size application, fibre drying, fibre wetting impregnation and composite performance are not at all fully understood, even by those with inside knowledge of size formulations. It has also been highlighted that there is virtually no information available in the open literature on what methods the manufacturers of glass fibres use to characterise their sizings and control the quality and consistency of their sized products. This problem extends to their customers who consequently have little, or no, real guidance on tools to employ for quality control of sized glass fibres, other than monitoring issues during full production processing. Even then, quality issues with sizings may only become apparent after many years in the long term performance of the final composite parts.

Notwithstanding the critical importance of size formulations to the composites industry, the enormous diversity of the applications which make use of sized glass fibre as reinforcements, coupled with the veil of industrial secrecy which covers sizing formulations have combined to hinder the development of a sound foundation to the “science” of sizing. Unlike in many other fields of materials science of a similar age the available literature on sizes, size formulations and the role of individual and combinations of size components is highly fragmented and does not form a continuous and comprehensive foundation for those outside of the glass fibre industry to build meaningful research and development programs in order to progress the knowledge base in this area. Even where research groups have been able to cooperate with glass fibre manufacturers, the knowledge generated is nearly always unsatisfactorily incomplete due to the non-disclosed information on the precise details of size formulations. Furthermore, published results are very rarely reproduced and checked by other researchers due to the non-availability of replicate glass fibre samples which have been identically manufactured and sized. This results in even this meagre amount of published information on sizings being of little help in its application to a slightly different size formulation or to assist in the reinforcement of a different polymer system. One consequence of this situation is that, while rapid and expanding progress is made in developing areas of materials science where background information is more openly available, new size development continues to be carried by an extremely small number (in proportion to the size of the composites industry) of researchers in glass fibre manufacturers’ laboratories. To make matters even more challenging, these small research groups (or individuals) cannot even discuss the subject with their peers in other companies. Hence size development actually takes place in an extraordinarily isolated environment in comparison to many other fields of materials science. Having to operate in such restricted silos is highly detrimental to innovation, indeed studies on the effect of silos in large corporations have concluded that “a silo is where collaboration goes to die. The reality is that the number

©2024 | 2_THOMASON_James_9E2EJ.pdf:2

one thing slowing innovation is a lack of effective cross-silo communication" [8]. Small wonder then that trial and error is still a predominant method of new size development, although nowadays the trial and error method is frequently dressed up to look more scientific by using design of experiment methods combined with statistical analysis.

From a wider perspective this situation has potentially enormous consequences for the slowing and limiting of innovation in the composites environment. Because of the lack of any comprehensive or reliable database on the science and technology of glass fibre sizings and the lack of accepted analysis and characterisation techniques and standards for sizings the number of knowledgeable researchers outside of the glass fibre producers is extremely small. This is compounded by the secrecy surrounding size formulations and the unique conditions of size application during fibre manufacture [4] and the very small concentration of the complex size mixtures in a final composite part. This situation makes it challenging for those without insider knowledge to draw any significant conclusions about whether any real progress is being made in this important area of composites science. However, there is little evidence of any real innovation in commercial glass fibre sizing development and it seems likely that the area is in near stagnation as many glass fibre products and their sizes are high up on the development S-curve, resulting in rapidly diminishing returns on effort. Indeed the glass fibre industry is on record as saying that product (i.e. sizing) development across the industry is moving at a slower pace than in the past [9].

It is well established that the pace of technology development in any scientific field is directly proportional to the level of information sharing and to the number of well-informed researchers active in the field [10-12]. While rapid and expanding progress is made in developing areas of materials science where background information is more openly available, new size development continues to be carried out by an exceedingly small number of researchers. These very limited numbers of researchers operate in an isolated and restricted environment with little or no open exchange of information. This situation seriously reduces the probability of an innovation in the field leading to a jump to a new S-curve which could bring rapid acceleration in the performance of resultant new composite products. Consequently, it seems that it is highly likely that the current overall state of size development is a serious barrier to the innovation of improved glass fibre reinforced composite materials and is something that urgently needs to be addressed on an industry-wide level. Researchers in the composite industry urgently need to acquire a better understanding of glass fibre sizings and how they can be tailored to improve composite performance. One possible way to assist this would be to develop some size screening tools which could be used in any laboratory and do not require the resource-intensive facilities of a glass fibre manufacturing plant. One of the principal roles of a glass fibre size, of importance to the end-user, is the ensuring the quality and endurance of the fibre-polymer interphase in a composite. Conventional lab-scale sizing research and development, outside of the glass fibre manufacturing companies, commonly involves sample preparation by dip coating of fibre samples in a test size formulation. Although this enables investigation of chemicals that might be used in sizing formulations, this process lacks any connection with the high speed and high shear of real-world sizing application during glass fibre manufacture. Moreover, when used with sizes containing a normal concentration of components this method usually results in an unrealistically thick size layer on the fibres with a significantly higher LoI than industrial sized fibres. This makes useful evaluation of size performance and the related composite interface performance from lab-scale prepared samples highly uncertain. Consequently, there is a pressing need for the development of a lab-scale sizing process that more closely mirrors the results of the industrial process. This paper presents a novel, but simple, fibre coating method that gives a size layer similar to industrial sized samples with an layer thickness one tenth that obtained by dip-coating.

2. Materials and Methods

2.1. Materials

Aminopropyltriethoxysilane (APS) was purchased from Sigma-Aldrich. The film former aqueous emulsion was supplied by Şişecam. A commercial E-glass fibre product (GFref) sized with a proprietary polypropylene compatible sizing was also supplied by Şişecam for comparison purposes. The fibre coating experiments were conducted using bare (water-sized) E-glass fibres taken from a large roving

©2024 | 2_THOMASON_James_9E2EJ.pdf:3

supplied by Şişecam. To create 100 g of sizing S1A, 1.6 g of APS were mixed with 50 g deionized water and agitated for 10 min. Subsequently, 24.2 g of film former emulsion were added to the mixture along with deionized water, resulting in a total of 100 g of sizing with a solids concentration of 10 wt% which is also common for industrial sized fibres. Furthermore, for the dip-coated S1A a sizing dispersion with a concentration of ~2.6 wt% was prepared. This was accomplished by diluting the sizing concentration and solid content by a factor of 10. The purpose of this step was to evaluate the impact of the dip coating solution concentration on the LoI of sized fibres. The homopolymer polypropylene (HPP) used for the microbond testing was PETOPLEN EH102 and the maleic anhydride modified polypropylene (MPP) used was Polybond® 3200.

2.2. Methods

Thermal gravimetric analysis (TGA) was used to determine the Loss on Ignition of the sizing coated on to glass fibres. TGA temperature scans with a heating rate of 10 °C/min were performed using a TA Instruments Q50 TGA. The weight loss of the sized glass fibres was recorded as a function of the temperature under the air atmosphere. The LoI value was taken as the sample weight loss recorded at 500 °C. A platinum TGA pan was used for the dedicated TGA analysis. The fibre samples of around 5-15 mg were carefully positioned in the pan with fibres covering the entire surface area, ensuring good contact between fibres and pan. The structure and morphology of sized glass fibre bundles were examined using Scanning Electron Microscopy (SEM). The analysis was conducted using a Hitachi TM3000 scanning electron microscope with an accelerating voltage of 15.0 kV. All SEM samples were sputter gold coated under Argon atmosphere with an operating pressure of 0.08 mbar, 30 mA current, and a 40 s coating time. Glass fibre to polymer apparent interfacial shear strength (IFSS) was determined using the microbond test [13,14]. Sample preparation for the microbond testing was carried out following the procedure described by Nagel et al. [14]. The samples were processed at 220 °C for HPP and 200 °C for MPP for 2 h in a vacuum oven under nitrogen flow and then cooled to ambient temperature still under nitrogen flow for about 4-5 h. The droplets were examined under a Leitz Ergolux microscope (200x) and only axisymmetric droplets were chosen for the test. The fibre diameter, length of the droplet (embedded length) and droplet diameter were measured using the image processing software package ImageJ. A total of thirty samples were prepared for each batch and were subjected to microbond test using an Instron 3342 universal tensile testing machine at a rate of 0.1 mm/min using a 10 N load cell. The apparent interfacial shear strength was calculated using the standard equation.

3. Results and Discussion

Figure 1 compares typical TGA curves obtained from fibres dip coated at 10% and 1% solids compared to the industrially manufactured reference sample. Average LoI values for these three samples were 11.2%, 2.3% and 0.8% respectively. These values emphasise the comments in the Introduction that dip coating glass fibre bundles with sizings containing a normal (for commercial glass fibre production) solids content produced unacceptably high LoI values. Moreover, even by diluting the sizing solids concentration by a factor of 10 it was still not possible to reach the lower LoI levels which are typical of industrial sized fibres. Of course further reduction of the sizing solids content could eventually bring the dip coated samples LoI into an acceptable (<1%) LoI range. However, it is extremely questionable as to whether the use of such dilute sizing solutions would in any way result in a sample which is representative of an industrially manufactured sample using the same sizing ingredients. In other words, dip coating does not appear to be a useful technique to screen sizing formulations or to carry our more fundamental studies of the influence of sizing formulation on fibre-polymer adhesion.

Table 1 summarises the TGA obtained LoI values for the glass fibre sample laboratory coated with a 10% solids sizing at different process intensities along with values for the dip coated fibres and the industrially sized fibres. The laboratory coated fibres exhibit a much lower LoI compared with the dip coated fibres, and the LoI approaches that of the industry-sized fibres when the process intensity is increased. A value for the average sizing layer thickness was calculated using the LoI values, an average fibre diameter of 17 µm, and assuming a uniform sizing (density = 1 g/cc) layer distribution around the fibres. It can be seen that the developed laboratory coating technique is quite capable of producing glass fibre samples with an LoI in the same range as industrially coated fibres.

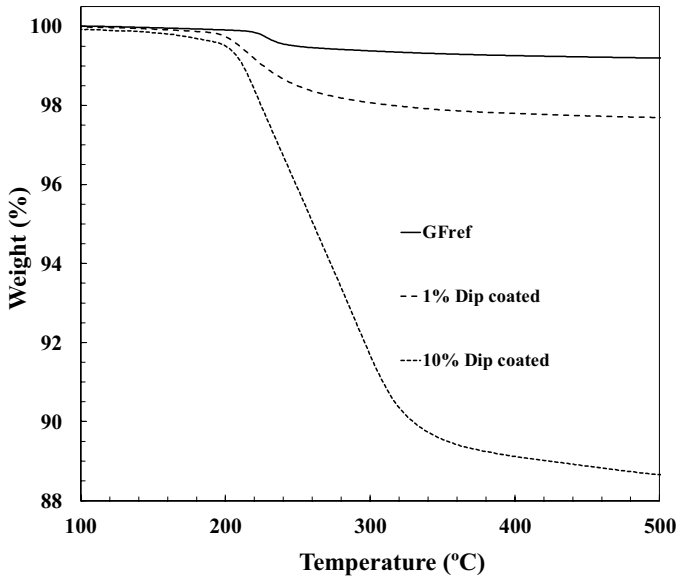

Figure 1. TGA results for dip-coated and reference glass fibres.

Table 1. Sized glass fibre LoI and calculated average size layer thickness.

Specimen type	Process intensity	LoI (%)				Size layer average thickness (nm)
		1	2	3	Average	
Dip coated	-	11.3	12	10.5	11.2	1280
S1A coated	0	6.5	6.2	5.8	6.1	685
S1A coated	0.5	4.9	4.9	6.8	5.5	618
S1A coated	1	3.8	3.5	2.9	3.4	376
S1A coated	2	2.2	3.4	2.6	2.7	302
S1A coated	5	1.5	1.4	1.4	1.4	156
S1A coated	8	1.1	1.1	1.2	1.15	125
S1A coated	10	1	1.2	1	1.0	116
GFref	-	0.9	0.8	0.7	0.8	86

Figure 2 presents typical results for weight loss (TGA) and differential weight loss (DTG) of these fibre samples. It is clear that there are major differences in the TGA results depending on the sizing technique and the laboratory coating process intensity. Given that E-glass is thermally stable in this temperature region, it is reasonable to assume that the weight changes are caused primarily by the degradation of the organic materials in the fibre sizing layer. Upon examining the TGA and DTG graphs, a distinct change in the curves becomes evident beyond a process intensity value of 0.5. It can be seen in Figure 2a that the main weight loss is observed in the temperature range of 200–350 °C. However, for process intensities higher than 0.5 the width of the degradation temperature range appears to be smaller. This can be seen more clearly in the DTG curves (Figure 2b) which appear to exhibit two overlapping thermal degradation events, a “low temperature” event peaking around 220-230 °C and a “high temperature” event peaking around 280-300 °C. It appears that once the coating process intensity exceeds 0.5 the sizing component responsible for the high temperature degradation event is reduced and eventually removed. Unfortunately, the lack of available information regarding the exact formulation of the commercial film former emulsions precludes any detailed discussion of what component may be preferentially lost during the higher speed spin coating.

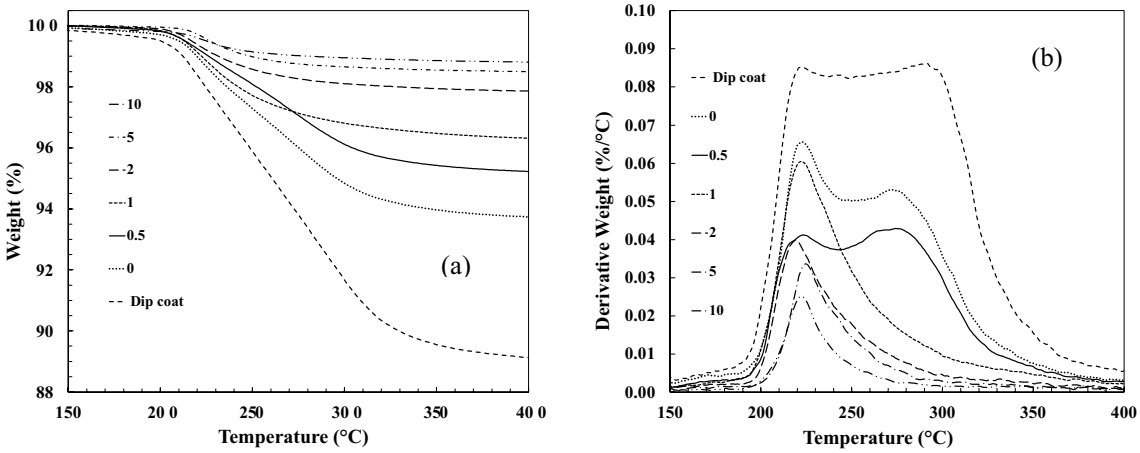

Figure 2. TGA and DTG results for S1A glass fibres coated at different process intensities.

Figure 3 compares TGA and DTG results for both the reference fibre GFref and S1A-10, bare fibre coated with size S1A using a process intensity value of 10. Both these fibre samples exhibit a single major weight loss event in the temperature range 200–300 °C, and the graphs follow a very similar pattern. The peak in the differential mass change data occurs at 225 °C, signifying the maximum rate of weight change. Thomason et al investigated the thermal degradation in air of the sizings on a range of industrial coated PP compatible glass fibre products. They reported that the majority of the weight loss between 200-300 °C which appeared to be due to degradation of the MPP film former and the aminosilane coupling agent [15]. Given that the exact formulation of the sizing on GFref is unknown and that the exact composition of the film former emulsions used in this work are also unknown due to industrial confidentiality, then the similarity in these results is notable. Thomason published a review of industrial sizing formulation patents and also noted that the same two main constituents of PP compatible sizings from different fibre manufacturers does consistently appear to be MPP and APS [4].

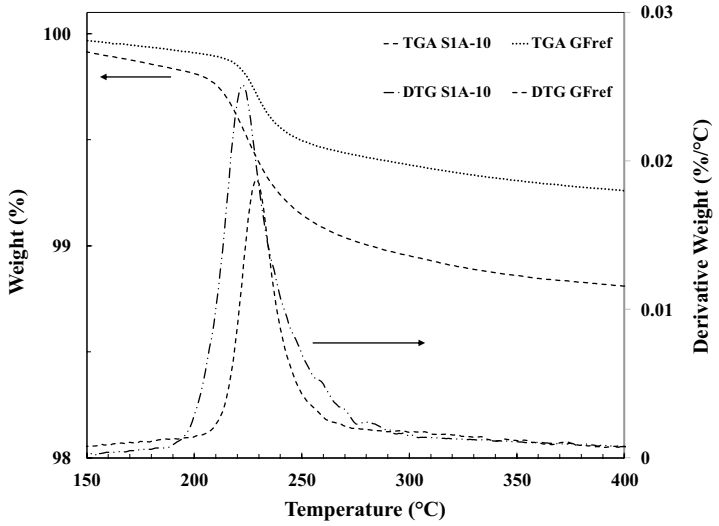

Figure 3. TGA and DTG results for GFref and S1A-10 glass fibres.

Figure 4 presents SEM images of the sized glass fibre bundles where the effects on the sizing structure on the fibre surface of the different coating methods are compared. In Figure 4a, the 10% dip-coated fibre bundle is heavily covered with sizing, rendering the fibres poorly visible as they are fully coated with a high thickness of size. More fibres are visible in the 1% dip-coated bundle in Figure 4b, which is

clearly related to the lower thickness of the size deposit. However, there is still a thick sizing coverage visible on some parts of the bundle. The micrographs in Figures 4c and 4d show that the S1A-10 lab-coated and GFref fibre bundles exhibit a similar sizing distribution pattern, with less sizing coverage in the bundle and little sign of any thick areas of sizing connecting the individual fibres.

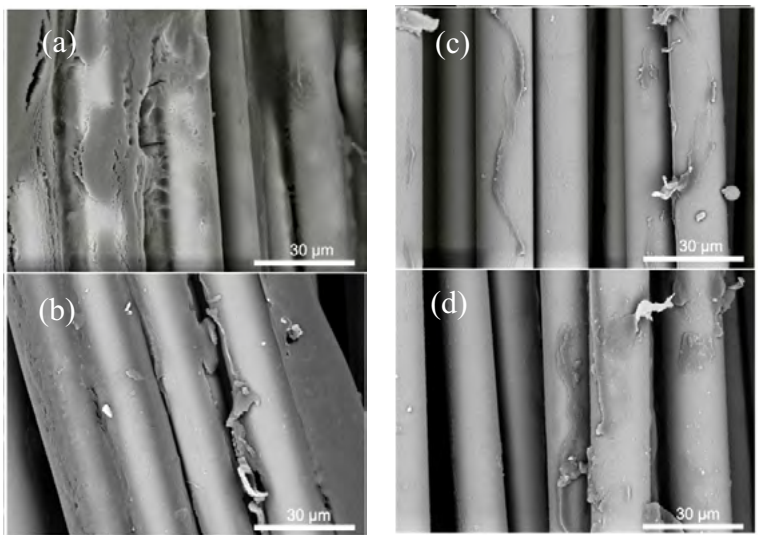

Figure 4. SEM micrographs of glass fibre bundles.

Figure 5 compares the microbond determined IFSS vales for three glass fibre samples (GFref, 10% and 1% dip-coated, and S1A-10 lab-coated at process intensity 10) embedded in either HPP or MPP. It can be observed that generally the dip coated average IFSS values are lower than those of the commercial reference sample whereas the lab coated samples have higher average IFSS. However, when analysing the IFSS results of the PP matrix systems statistically, it was noted that lab-coated S1A-10 displayed a significantly (at 95% confidence level) higher IFSS compared to dip-coated fibres. No significant differences were observed between the other fibre-polymer systems.

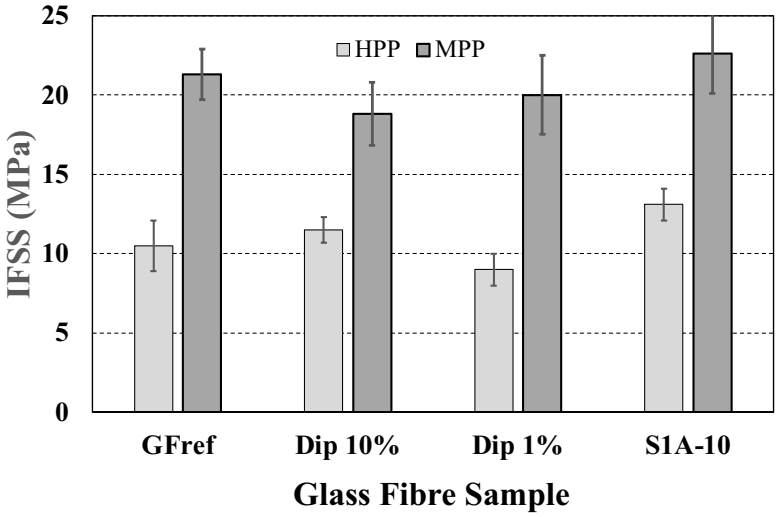

Figure 5. Microbond test results for glass fibres in two polypropylene matrices.

3. Conclusions

This study has demonstrated the feasibility of preparing small samples, suitable for micro-mechanical adhesion measurements, of sized glass fibre using a novel laboratory-based coating method. The resulting sized fibres exhibited a similar LoI and size layer thickness compared to industrially produced fibres. Moreover, this method offered the advantage of simple control of the glass fibre sample LoI in order to enable exploration of the effects of different sizing variations and thicknesses. Compared to the commonly employed dip-coating method this new laboratory scale method shows promise as it eliminates the need to alter the concentration of the sizing formulations to unreasonable levels to obtain normal LoI values. In contrast to dip-coated fibres the TGA fingerprint of the thermal degradation profile of the lab-coated sizing layer was very comparable with that of industrially produced fibres.

Acknowledgments

The authors would like to extend thanks to Şişecam company and the University of Strathclyde (ISP fund) as the sponsors of this project.

References

[1] Q. Zu, M. Solvang, H. Li. Commercial glass fibers. *Fiberglass Science and Technology: Chemistry, Characterization, Processing, Modeling, Application, and Sustainability*. 1-87. Springer Nature, Cham, Switzerland, 2021.
[2] K. L. Loewenstein. *Glass science and technology 6, The manufacturing technology of continuous glass fibres*. Amsterdam: Elsevier, 1993.
[3] J. L. Thomason. *Glass fibre sizing: A review of the literature*. Blurb Incorporated 2015. URL: http://www.blurb.co.uk/b/6244677-glass-fibre-sizing
[4] J. L. Thomason. *Glass fibre sizing: A review of size formulation patents*. Blurb Incorporated 2015. URL: http://www.blurb.co.uk/b/6244662-glass-fibre-sizing
[5] J. L. Thomason, Glass fibre sizing: a review, *Compos Part A Appl Sci Manuf*. 127:105619, 2019.
[6] J. L. Thomason, A review of the analysis and characterisation of polymeric glass fibre sizings. *Polymer Testing*, 85:106421, 2020.
[7] J. L. Thomason, Glass fibre sizings and the composites industry: The current state of play. In *Aachen Reinforced: Glass & Carbon Fibres* 2021.
[8] S. Hassett, This one problem stifles innovation at big companies. *Forbes.com* 24 March 2020. https://www.forbes.com/sites/forbestechcouncil/2020/03/24/this-one-problem-stifles-innovation-at-big-companies/
[9] P. Mapleston. Reinforcing options for compounders. *Compounding World*, 80-84: Oct. 2018.
[10] W. B. Shockley. p29 *Secrecy and Science*, US Government Printing Office, Washington, 1959.
[11] T. Takalo, V. Kanniainen, Do patents slow down technological progress?: Real options in research, patenting, and market introduction. *Int J Ind Organ*, 18:1105-1127, 2000.
[12] J. A. Evans. Industry collaboration, scientific sharing, and the dissemination of knowledge. *Soc Stud Sci,* 40:757–791, 2010.
[13] J. L. Thomason, An overview of some scaling issues in the sample preparation and data interpretation of the microbond test for fibre-matrix interface characterisation. *Polymer Testing*. 111:107591,2022.
[14] U. Nagel, L. Yang, C. Kao, J.L. Thomason. Effects of thermal recycling temperatures on the reinforcement potential of glass fibers. Polymer Composites. 39:1032-40,2018.
[15] J. L. Thomason, U. Nagel, L. Yang, D. Bryce. Thermal degradation of glass fibre sizings at composite processing temperatures. *Compos Part A Appl Sci Manuf*. 121:56-63, 2019.

STRUCTURE AND ELECTROMAGNETIC PROPERTIES OF TI_3C_2TX MXENE DERIVED FROM TI_3ALC_2 WITH DIFFERENT MICROSTRUCTURES

Xinlei Wang[1], Xiaomeng Fan[2] and Minghang Li[3]

[1]School of Materials Science and Engineering, Science and Technology on Thermostructural Composite Materials Laboratory, Northwestern Polytechnical University, Xi'an 710072, China
Email: wangxinlei@mail.nwpu.edu.cn
[2]School of Materials Science and Engineering, Science and Technology on Thermostructural Composite Materials Laboratory, Northwestern Polytechnical University, Xi'an 710072, China
Email: fanxiaomeng@mail.nwpu.edu.cn
[3]School of Materials Science and Engineering, Science and Technology on Thermostructural Composite Materials Laboratory, Northwestern Polytechnical University, Xi'an 710072, China
Email: lmh@mail.nwpu.edu.cn

Keywords: MAX, MXene, Microstructure, Dielectric properties, Electromagnetic absorption

Abstract
As the precursor of MXene, the microstructure of MAX phases would directly influence the structures and electromagnetic(EM) absorbing properties of MXenes. To reveal this effect, five kinds of Ti_3AlC_2 with different microstructures and compositions were chosen, and then were etched by HF solution to prepare $Ti_3C_2T_x$ MXene. The results showed that the larger flake area and less impurity content in Ti_3AlC_2 powder can lead to better EM absorption ability of as derived $Ti_3C_2T_x$ MXene. This study provides a new way to regulate the EM absorbing performance of MXene by changing the structures of MAX phases.

1. Introduction

Transition metal carbides/carbonitrides (MXenes) are a new family of two-dimensional materials discovered in 2011 [1]. MXenes have a general formula of $M_{n+1}X_nT_x$, where M is an early transition metal (such as Sc, Ti, Cr, V, Zr, Nb, Mo, Hf, etc.), X is C and/or N, n = 1, 2, or 3, and T_x represents surface functional groups, such as –F, –OH, or –O [1,2]. MXenes are fabricated by selective etching the MAX phases ($M_{n+1}AX_n$), where A represents the elements from groups 13 and 14 of the periodic table [3].

The electromagnetic (EM) wave absorbing materials attract great attention in recent years [4,5]. With the advantages of high specific surface areas, many active sites [6], excellent hydrophilicity [7] and metal conductivity [8], MXenes have great application potential in the field of EM absorption [6,9]. As a typical MXene, the EM absorption properties of $Ti_3C_2T_x$ has been studied. As reported, the dielectric and EM absorption properties would change with the microstructure evolution of $Ti_3C_2T_x$ [10, 11]. Up to now, the research focused on the optimization of EM absorption properties by tailoring etching conditions [12]. Tong et al. reported that with the growing etching time in HF etching condition, the structure and EM absorption properties of $Ti_3C_2T_x$ changed [11]. Xu et al. studied the effect of intercalation of organic molecules (dimethylformamide, ethanol and dimethyl sulfoxide) on the EM absorption properties of $Ti_3C_2T_x$ [13].

As the precursor of $Ti_3C_2T_x$, Ti_3AlC_2 has a typical laminated structure and attracts great attention [14]. Several raw materials and synthesis methods have been developed to produce Ti_3AlC_2. The raw

materials include Ti/Al/C [15], Ti/Al/TiC [16], Ti/Al_4C_3/TiC [17] and TiH_2/Al/TiC [18] etc., and the synthesis methods include hot isostatic pressing [19], spark-plasma sintering [16-18] and self-propagating high-temperature synthesis [20,21] etc. Different raw materials and synthesis methods would lead to different structures and compositions of Ti_3AlC_2 [18,22]. For example, the grain sizes of Ti_3AlC_2 strongly depend on the sintering temperature and time [18]. Therefore, as the precursor of $Ti_3C_2T_x$, Ti_3AlC_2 will inevitably influence the microstructures and properties of $Ti_3C_2T_x$ due to the diversity of its structures and compositions. But until now, the effect of Ti_3AlC_2 microstructure on as-derived $Ti_3C_2T_x$ is rarely reported. It's essential to carry out the related study.

The purpose of this work is to study the effect of the structures and compositions of Ti_3AlC_2 on the EM absorption performance of $Ti_3C_2T_x$. Five kinds of Ti_3AlC_2 were etched by HF solution to prepare $Ti_3C_2T_x$, and then the microstructure and composition of Ti_3AlC_2 and as-derived $Ti_3C_2T_x$ were studied to reveal the influence mechanism.

2. Experimental section

2.1. Materials

Five kinds of Ti_3AlC_2 powder were respectively purchased from 11 Technology Co., Ltd. (Jilin, China), Lianlixin Materials Co., Ltd. (Beijing, China), Ningbo Institute of Materials Technology and Engineering, Kai Xi Ceramic Materials Co., Ltd. (Laizhou, China) and Youran Yisen Technology Co., Ltd. (Beijing, China). All the powders have the same particle size of 38 μm. Hydrofluoric acid solution (40 wt%) was bought by Fuyu Chemical Co., Ltd. (Tianjin, China). Paraffin wax was provided from Sinopharm Chemical Reagent Co., Ltd.

2.2. Preparation of $Ti_3C_2T_x$

15g of Ti_3AlC_2 powder was added gradually (in the course of 5 min) into 300 ml of 40 wt% hydrofluoric acid solutions. The reaction was proceeded at 35 ◦C for 120 h. After that, the obtained solution was washed with deionized water by centrifugation at 3500 rpm for 5 min in each cycle. And then $Ti_3C_2T_x$ would be separated from the solution and precipitated at the bottom of the centrifuge tube. During each cycle, the supernatant was decanted into waste and the $Ti_3C_2T_x$ sediment was collected as well as dispersed with deionized water again. This washing process would end when the pH value of the supernatant reached about 6 [23]. Finally, the sediment product $Ti_3C_2T_x$ was collected after freeze-drying. According to the different manufacturer of Ti_3AlC_2 powder, five kinds of Ti_3AlC_2 powder was respectively labeled as TAC1 (11 Technology Co., Ltd.), TAC2 (Lianlixin Materials Co., Ltd.), TAC3 (Ningbo Institute of Materials Technology and Engineering), TAC4 (Kai Xi Ceramic Materials Co., Ltd.) and TAC5 (Youran Yisen Technology Co., Ltd.). Five kinds of $Ti_3C_2T_x$ obtained from them were labeled as TC1, TC2, TC3, TC4 and TC5 one by one.

2.3. Characterization

Scanning electron microscopy (SEM) images of the samples were captured on S-4700 equipment (Hitachi Co., Japan). Energy-dispersive spectroscopy (EDS) mappings of the samples were recorded on a Verios G4 (FEI, USA). X-ray diffraction (XRD) patterns were performed on an X' Pert Pro Type X-ray diffraction (λ = 0.154 nm, Panalytical B. V). $Ti_3C_2T_x$ was mixed with paraffin by 1:1 mass fraction to test the electric properties. Electrical conductivities of Ti3C2Tx-paraffin composites were measured by RTS-8 (Guangzhou Four Probes Technology Corp., China). Dielectric performances of $Ti_3C_2T_x$-paraffin composites were analyzed by an MTAC4644A Vector Network Analyzer instrument (Anritsu Corp., Japan), which used the wave-guide method in the X-band frequency range according to ASTM D5568-08, and the dimensions of the corresponding sample were 22.86 mm × 10.16 mm × 2 mm.

3. Results and discussion

XRD patterns of Ti_3AlC_2 powders were shown in Figure 1. Three strongest peaks at 39.037°, 41.815° and 9.517° corresponded to (1 0 4), (1 0 5) and (0 0 2) crystal planes of Ti_3AlC_2, respectively. While, the peaks at 35.906° and 41.710° corresponded to (1 1 1) and (2 0 0) crystal planes of TiC, which proved the existence of TiC impurities in samples TAC1, TAC3 and TAC5. The TiC contents can be calculated by the k-value method according to the (0 0 2) peak strength of Ti_3AlC_2 and (1 1 1) peak strength of TiC. The calculation results were shown in Table 1. The TiC content in sample TAC5 was 12.48 wt.%, which was significantly higher than that in samples TAC1 and TAC3. The crystal growth mechanism of Ti_3AlC_2 was preferential in-plane growth [21]. The (0 0 2) peak represented the growth direction parallel to the lamella, while the (1 0 4) peak represented the growth direction perpendicular to the lamella. According to XRD patterns, the strengths of (0 0 2) peak of samples TAC1, TAC4 and TAC5 were significantly higher than those of samples TAC2 and TAC3. It showed that samples TAC1, TAC4 and TAC5 had better preferential growth on the (0 0 2) plane, which meant that the flake areas of them might be larger than samples TAC2 and TAC3.

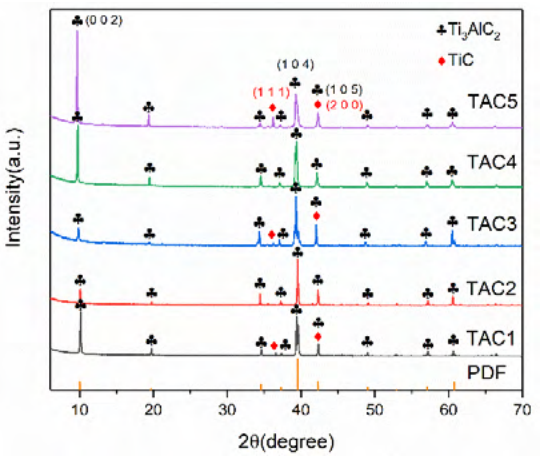

Figure 1. XRD patterns of Ti_3AlC_2 powders.

Table 1. TiC impurity content in Ti_3AlC_2.

Samples	TAC1	TAC2	TAC3	TAC4	TAC5
Ti_3AlC_2 content(wt.%)	99.03	100	98.04	100	87.52
TiC content(wt.%)	0.97	0	1.96	0	12.48

Figure 2(a)-(e) showed the SEM images of all Ti_3AlC_2 powders. The morphologies of the five kinds of Ti_3AlC_2 were different. Samples TAC1, TAC4 and TAC5 showed typical layered structure, while samples TAC2 and TAC3 showed serious particle aggregation, and it was difficult to calculate the lamellar area of samples TAC2 and TAC3. The flake areas of samples TAC1, TAC4 and TAC5 were 23.43, 26.34 and 26.13 μm^2, respectively. The results were obtained by calculating the average lamellar area based on 50 pieces of particles for each sample. It can be found that the flake areas of samples TAC1, TAC4 and TAC5 were larger than samples TAC2 and TAC3, which was consistent with the XRD results.

It was noticed that there were particles on the surface of samples TAC1 and TAC5. In order to identify the composition of these particles, EDS was used to analyze the element content in those particles. The spectrums of the red rectangle areas in Figure 2(a) and Figure 2(e) were shown in Figure 2(f)-(i). The spectrums 1 to 4 contained Ti, Al and C elements, but the value of Ti/Al atomic ratio of spectrums 1 and 3 were 9.6 and 6.6 (Table 2), which were much bigger than that of spectrums 2 and 4. This means that the particles in rectangles 1 and 3 contained a small amount of Al element. Combined with XRD results,

it can be deduced that the particles on the surface of samples TAC1 and TAC5 were TiC impurities. Due to small size of the particles, the presence of Al in spectrums 1 and 3 may be attributed to the Ti_3AlC_2 under the particles. Sample TAC3 also contained TiC particles, but it was not observed in Figure 2(c) due to serious aggregation.

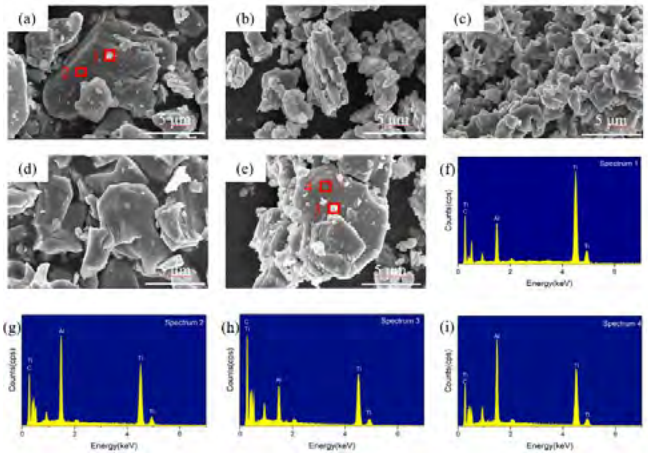

Figure 2. SEM images of samples: (a) TAC1, (b) TAC2, (c) TAC3, (d) TAC4 and (e) TAC5; EDS results of the red rectangle areas: (f) rectangle 1, (g) rectangle 2, (h) rectangle 3 and (i) rectangle 4.

Table 2. The energy dispersive spectroscopy (EDS) results from Figure 2.

Spectrum	Al(atom%)	Ti(atom%)	Ti/Al
1	7.94	76.60	9.6
2	18.56	59.37	3.2
3	8.49	56.28	6.6
4	18.75	61.61	3.3

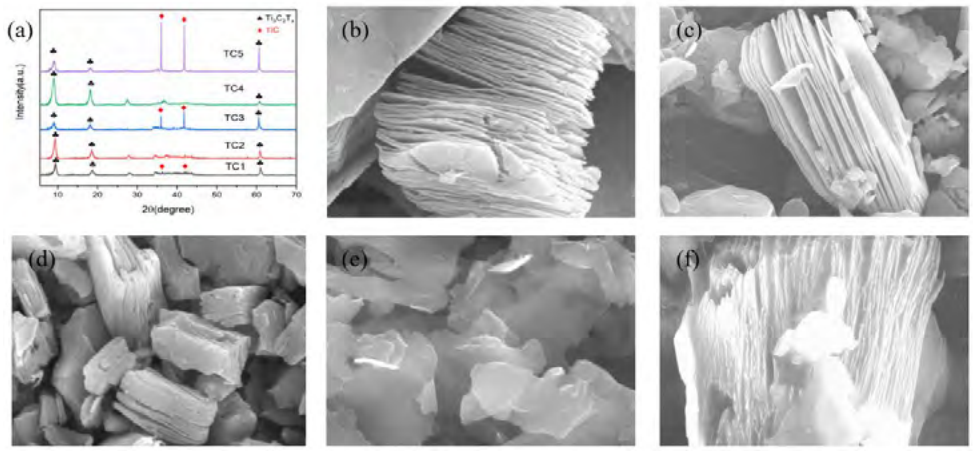

Figure 3. (a) XRD patterns of all the $Ti_3C_2T_X$-based samples; SEM images of sample: (b) TC1, (c) TC2, (d) TC3, (e) TC4 and (f) TC5.

After etching with HF for 120 h, the etching products were collected by centrifugation. In the XRD patterns of etching products (Figure 3(a)), the peak (1 0 4) at 39° disappeared, and the sharp diffraction peak at 9° and weak diffraction peak at 19° corresponded to the (0 0 2) and (0 0 4) crystal planes of $Ti_3C_2T_x$ [24]. It indicated that the Al layers were completely etched out and the layered structure of $Ti_3C_2T_x$ was formed. Because the TiC impurity would not be affected by the etchant, TiC peaks also can

be detected in the XRD patterns of samples TC1, TC3 and TC5. During the etching process, only the transformation from Ti_3AlC_2 to $Ti_3C_2T_x$ took place. The TiC impurity kept stable and the impurity content can be obtained by the mass loss from the transformation from Ti_3AlC_2 to $Ti_3C_2T_x$. It can be calculated that the impurity contents of samples TC1, TC3 and TC5 were 1.12, 2.27 and 14.20 wt.%, respectively. Figure 3 (b)-(f) presented the SEM images of as-derived $Ti_3C_2T_x$. All of them showed layered structure and there were obvious gaps between the layers. It is noted that the flake areas of samples TC1, TC2, TC3, TC4 and TC5 were different, which were 25.62, 14.83, 11.33, 25.07 and 24.13 μm^2, respectively. The flake areas of samples TC1, TC3 and TC5 were larger than that of samples TC2 and TC3, which was consistent with the result of Ti_3AlC_2. It indicated that the etchant only removed the Al layers and didn't affect the flake area.

Electromagnetic (EM) wave absorption properties of $Ti_3C_2T_x$-based samples are related to their complex permittivity, where the real part (ε′) represents the storage ability of electric energy, and the imaginary part (ε″) represents the loss ability of electric energy. The tangent dielectric loss, tan δ (tan δ=ε″/ε′), are used to evaluate the attenuation ability. Figure 4(a)-(c) depicted the complex permittivity and tangent dielectric loss of all the $Ti_3C_2T_x$-based samples. The average values of real parts from sample TC1 to TC5 were 18.51, 9.14, 8.35, 29.66 and 10.62, and the corresponding imaginary parts were 2.31, 0.66, 0.26,7.91 and 0.69, and the values of their tangent loss were 0.13, 0.07, 0.03, 0.27 and 0.07. It can be found that the dielectric properties of $Ti_3C_2T_x$-based samples showed great difference due to their different microstructures.

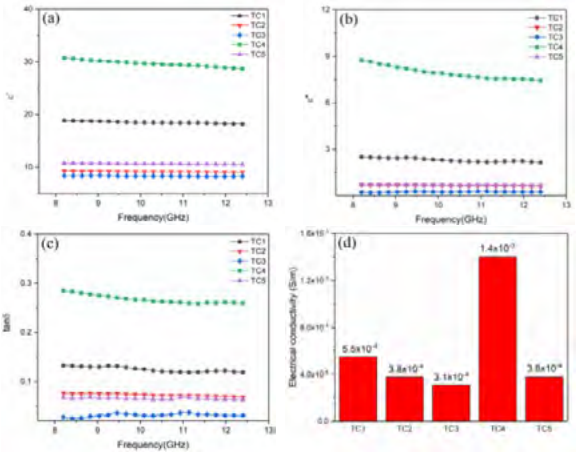

Figure 4. The (a)real part, (b)imaginary part of permittivity, (c)tangent dielectric loss and (d)conductivity for different $Ti_3C_2T_x$-based samples.

The EM wave absorption abilities of $Ti_3C_2T_x$ were evaluated by reflection coefficient (RC). The RC values could be simulated based on the relative complex permittivity (ε_r) and permeability (μ_r), with a given frequency (f) and absorber thickness (d), by means of the following equations:

$$RC = 20\log_{10}\left|\frac{Z-1}{Z+1}\right| \quad (1)$$

$$Z = \sqrt{\frac{\mu_r}{\varepsilon_r}}\tanh\left[j\left(\frac{2\pi fd}{c}\right)\sqrt{\mu_r\varepsilon_r}\right] \quad (2)$$

Where Z is the normalized impedance, c is the velocity of light, f is the given frequency and d is the absorber thickness. Figure 5 showed the two-dimensional plots of RC of samples TC1, TC2, TC3, TC4 and TC5. It can be seen that the RC values of samples TC2, TC3 and TC5 were higher than -10 dB.

Compared with samples TC2, TC3 and TC5, sample TC1 had better EM wave absorption abilities. The RC_{min} value reached -46 dB at 10.6 GHz with a thickness of 4.9 mm, but the effective absorption bandwidth (EAB) of sample TC1 was only 0.9 GHz. The RC_{min} of sample TC4 (Figure 5(d)) was -40 dB with an EAB of 2.3 GHz at a thickness of 1.3 mm. Although the RC_{min} of sample TC4 was similar to sample TC1, sample TC4 had bigger EAB and much thinner thickness, which means the sample TC4 was the best EM wave absorber among five $Ti_3C_2T_x$-based samples.

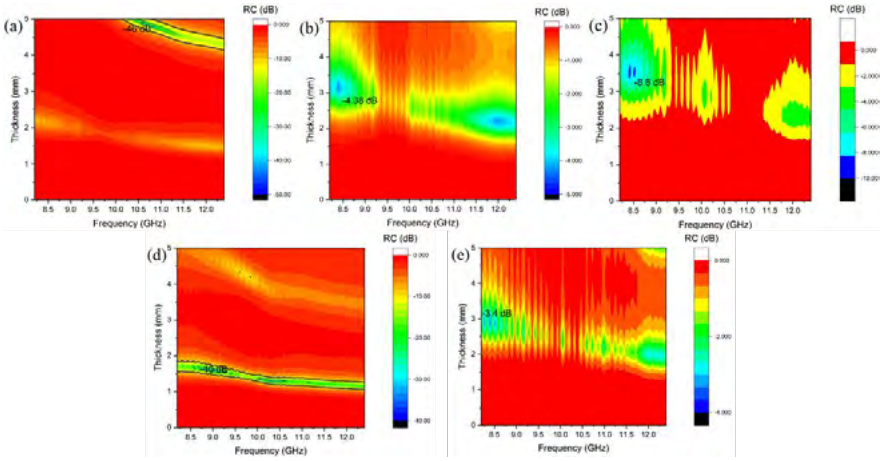

Figure 5. Two-dimensional plots of RC of samples: (a) TC1, (b) TC2, (c) TC3, (d) TC4 and (e) TC5.

The flake area, impurity content and surface functional groups were the main factors of affecting the dielectric properties. Since the surface functional groups of five $Ti_3C_2T_x$ were the same type, this factor can be ignored. The dielectric properties and microstructures of $Ti_3C_2T_x$ are listed in Table 3. Sample TC3 with the smallest flake area and moderate impurity content had the lowest dielectric loss. The larger flake area and less impurities made the dielectric loss of sample TC1 higher than that of samples TC2, TC3 and TC5. Although the flake area of sample TC4 was similar to sample TC1, less impurity content made its dielectric loss much higher. It showed that the flake area and impurity content could influence the dielectric properties of $Ti_3C_2T_x$-based samples, leading to different EM wave absorption abilities.

Table 3. The dielectric properties and microstructures of $Ti_3C_2T_x$-based samples.

Sample	ε'	ε″	tanδ	Flake area(μm^2)	TiC content(wt.%)
TC4	29.66	7.91	0.27	25.07	0
TC1	18.51	2.31	0.13	25.62	1.12
TC5	10.62	0.69	0.07	24.13	14.20
TC2	9.14	0.66	0.07	14.83	0
TC3	8.35	0.26	0.03	11.33	2.27

Dielectric loss includes conductive loss and polarization loss. Free electron theory states that if conductive loss plays a dominant role in affecting ε″, the value of ε″ will show a decreasing trend with increasing frequency (2-18 GHz) [25], which is obvious in all $Ti_3C_2T_x$-based samples. Therefore, the electrical conductivity of $Ti_3C_2T_x$-paraffin composites was measured to explore the influence mechanism of flake area and impurity content on dielectric properties, as shown in Figure 4(d). The electrical conductivities of samples TC1 to TC5 were 5.5×10^{-4}, 3.8×10^{-4}, 3.1×10^{-4}, 1.4×10^{-3} and 3.8×10^{-4} S/m, which was consistent with their complex permittivity.

The relationship between $Ti_3C_2T_x$ microstructures and conductivity were analyzed and presented in Figure 6(a, b). The increase of the flake area would reduce the internal resistance and accelerate the carrier movement in the layer. It also improved the directionality of sheet stacking and prevented the

sheets from deflecting. So, the electrical conductivity of $Ti_3C_2T_x$-based samples raised with the increase of flake area. When a large amount of TiC impurities existed, the contacts between the $Ti_3C_2T_x$ sheets were reduced. It was not conducive to the formation of a conductive network, and thus the TiC impurities will lead to low electrical conductivity. The EM absorption mechanism of $Ti_3C_2T_X$-based samples is shown in Figure 6(c). The layered structure of $Ti_3C_2T_X$ will reflect and scatter the incident EM wave and attenuate its energy. The high electrical conductivity can make $Ti_3C_2T_X$ excite more hopping charge carriers. These carriers will move through the conductive network and attenuate the EM wave, which improves the conductivity loss. The surface functional groups and localized defects of $Ti_3C_2T_X$ act as polarized centers and provide the dipole polarization loss [26].

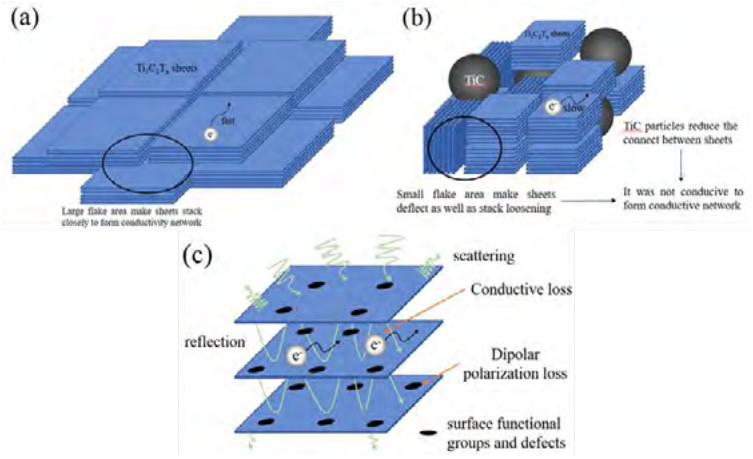

Figure 6. Schematic illustrating (a, b) the influence mechanism of $Ti_3C_2T_x$ microstructure to conductivity and (c) the EM absorption mechanism of $Ti_3C_2T_x$.

4. Conclusions

The effect of Ti_3AlC_2 microstructure on the dielectric properties and microwave absorption ability of as-derived $Ti_3C_2T_x$ was studied. The flake area and impurity content of $Ti_3C_2T_x$ affect the carrier movement speed and the construction of the conductive network, which eventually influence the EM absorption ability. As the precursor of $Ti_3C_2T_x$, Ti_3AlC_2 will influence these two factors through different microstructure and composition. Preferential growth of Ti_3AlC_2 crystal will lead to the large flake area of $Ti_3C_2T_x$ and then improve the EM absorption ability of $Ti_3C_2T_x$. The residual TiC particles would destroy the conductive network, leading to poor EM absorption ability. In the future work, researchers can control the structure and EM absorption performance of MXenes by regulating the crystal growth orientation and impurity content of MAX phases.

References

[1] Naguib M, Kurtoglu M, Presser V, et al. Two-dimensional nanocrystals produced by exfoliation of Ti3AlC2. Adv. Mater. 2011, 23, 4248-53.

[2] Naguib M, Gogotsi Y. Synthesis of two-dimensional materials by selective extraction. Acc. Chem. Res. 2015, 48, 128-35.

[3] Barsoum M. W. Properties of machinable ternary carbides and nitrides, Libgen Librarian (Eds.), MAX Phases, Wiley-VCH, Weinheim, 2013, p. 436.

[4] Zhou W, Li Y, Long L, et al. High-temperature electromagnetic wave absorption properties of Cf/SiCNFs/Si3N4 composites. J. Am. Ceram. Soc. 2020, 103(12): 6822-6832.

[5] Cheng Z, Ye F, Liu Y, et al. Mechanical and dielectric properties of porous and wave-transparent Si3N4-Si3N4 composite ceramics fabricated by 3D printing combined with chemical vapor infiltration. J. Adv. Ceram. 2019, 8(3):399-407.

[6] Qing Y, Zhou W, Luo F, et al. Titanium carbide (MXene) nanosheets as promising microwave absorbers. Ceram. Int. 2016,42, 16412-16416.

[7] Anasori B, Luhatskaya M R, Gogotsi Y. 2D metal carbides and nitrides (MXenes) for energy storage. Nat. Rev. Mater. 2017, 2, 16098.

[8] Fafarman A T, Ghidiu M J, Gogotsi Y, et al. L, et al. Highly conductive optical quality solution-processed films of 2D titanium carbide. Adv. Funct. Mater. 2016, 26, 4162-4168.

[9] Han M, Yin X, Wu H, et al. Ti3C2 MXenes with modified surface for high-performance electromagnetic absorption and shielding in the X-band. ACS Appl. Mater. Inter. 2016, 8(32): 21011-21019.

[10] Dai B, Zhao B, Xie X, et al. Novel two-dimensional Ti3C2TX MXenes/nano-carbon sphere hybrids for high-performance microwave absorption. J. Mater. Chem. C. 2018;6(21):5690-5697.

[11] Tong Y, He M, Zhou Y, et al. Electromagnetic wave absorption properties in the centimetre-band of Ti3C2Tx MXenes with diverse etching time. J. Mater. Sci- Mater. El. 2018, 29(10): 8078-8088.

[12] Maleski K, Ren C E, Zhao M Q, et al. Size-dependent physical and electrochemical properties of two-dimensional MXene flakes. ACS Appl. Mater. Inter. 2018, 10, 24491-24498.

[13] Xu G, Wang X, Gong S, et al. Solvent-regulated preparation of well-intercalated Ti3C2Tx MXene nanosheets and application for highly effective electromagnetic wave absorption. Nanotechnology, 2018, 29(35): 355201.

[14] Dang X, Fang X, Yin X, et al. Research progresses on multi-functional integration MAX phases modified continuous fiber-reinforced ceramic matrix composites. J. Inorg. Mater. 2019:400.

[15] Chen K X, Guo J M, Ge Z B, et al. A novel route for preparing Ti3AlC2 ceramics. Rare Metal Mat. Eng. 2002, 31: 20-23.

[16] Zhou W B, Mei B C, Zhu J Q, et al. Rapid synthesis of Ti2AlC by spark plasma sintering technique. Mater. Lett. 2005, 59(1): 131-134.

[17] Zou Y, Sun Z M, Tada S, et al. Synthesis reactions for Ti3AlC2 through pulse discharge sintering Ti/Al4C3/TiC powder mixture. Scripta Mater. 2006, 55(9): 767-770.

[18] Zou Y, Sun Z M, Tada S, et al. Rapid synthesis of single-phase Ti3AlC2 through pulse discharge sintering a TiH2/Al/TiC powder mixture. Scripta Mater. 2007, 56(9): 725-728.

[19] Tzenov N V, Barsoum M W. Synthesis and characterization of Ti3AlC2. J. Am. Ceram. Soc. 2000, 83(4): 825-832.

[20] Łopaciński M, Puszynski J, Lis J. Synthesis of ternary titanium aluminum carbides using self-propagating high-temperature synthesis technique. J. Am. Ceram. Soc. 2001, 84(12): 3051-3053.

[21] Liu G, Chen K, Zhou H, et al. Layered growth of Ti2AlC and Ti3AlC2 in combustion synthesis. Mater. Lett. 2007, 61(3): 779-784.

[22] Manmen L, Jialin C, Hao C, et al. Temperature-driven deintercalation and structure evolution of Ag/Ti3AlC2 composites. Ceram. Int. 2018, 44:18129-18134.

[23] Alhabeb M, Maleski K, Anasori B, et al. Guidelines for synthesis and processing of two-dimensional titanium carbide (Ti3C2Tx MXene). Chem. Mater. 2017, 29(18):7633-7644.

[24] Ghidiu M, Lukatskaya M, Zhao M, et al. Conductive two-dimensional titanium carbide 'clay' with high volumetric capacitance. Nature, 2014;516(7529):78-81.

[25] Liang H, Xing H, Qin M, et al. Bamboo-like short carbon fibers@Fe3O4@phenolic resin and honeycomb-like short carbon fibers@Fe3O4@FeO composites as high-performance electromagnetic wave absorbing materials. Compos. Part A-Appl. S. 2020, 135:105959.

[26] Xu H, Yin X, Zhu M, et al. Carbon hollow microspheres with a designable mesoporous shell for high-performance electromagnetic wave absorption. ACS Appl. Mater. Inter. Feb 22 2017;9(7):6332-6341.

EXPERIMENTAL ANALYSIS OF CROSSING WARP EFFECT ON IN-PLANE AND OUT-OF-PLANE TENSILE BEHAVIOUR OF 3D WOVEN COMPOSITE T-JOINTS

Ziyue Wei[1], Xiaogang Chen[1]

[1]Department of Materials, Faculty of Science and Engineering, University of Manchester, Oxford Road, Manchester, M13 9PL
Email: ziyue.wei@manchester.ac.uk / Email: xiaogang.chen@manchester.ac.uk

Keywords: 3D woven composite T-joints, internal crossing warps, external crossing warps, in-plane failure mode, out-of-plane failure mode

Abstract
This paper presents the development and evaluation of ten crossing warp architectures designed to enhance the mechanical behaviour of 3D woven composite T-joints. These architectures utilize 3D woven orthogonal structures at the junctions. The study focused on the impact of these architectures on the tensile performance of both 3D woven T-shaped preforms and composite T-joints under quasi-static tensile loads. The crossing warp structures effectively improved the in-plane tensile performance of both T-shaped preforms and composite T-joints. Resistance to the in-plane tensile failure of the composite T-joints witnessed an increase as more warp yarns from the web were arranged to cross into the flanges. However, incorporating crossing warps resulted in a reduction in the out-of-plane tensile behaviour of composite T-joints. To further understand the influence of 3D weave architectures on the mechanical performance of T-shaped preforms and composite T-joints, this study characterized and compared the effects of internal and external crossing warps. Regardless of the crossing warp proportions, the external crossing warp led to a higher in-plane performance for T-shaped preforms and composite T-joints than the internal crossing warp. By contrast, the internal crossing configurations resulted in better out-of-plane behaviour for the composite T-joint than its external crossing counterpart.

1. Introduction

Composite T-joints are one of the often preferred joints in engineering applications such as wind turbine blades and aircraft wings as the skin-spar stiffener for preventing bulking and ship hulls for connecting two orthogonally plate panels [1, 2].
A persistent challenge for composite T-joints is that the junction is susceptible to delamination failure. Various methods, including 3D weaving, are gaining popularity in the fabrication of composite T-joints as they allow the production of integral through-the-thickness fibres to preforms to improve the delamination resistance [3]. There has been considerable effort to develop innovative woven architectures by modifying the arrangement and order of yarns at the junction to enhance the junction of composite T-joints [4-7], to demonstrate the influence of weave variations at the web and flanges on the in-plane and out-of-plane tensile mechanical performance of 3D woven composite T-joints which was studied by Umair et al [8] and Hajdaei [3].
In these research, weave variations were confirmed to play a paramour role in affecting the mechanical properties of the composite T-joints. However, the relationship between weave variations and the delamination behaviour of composite T-joints remains inadequately understood due to the many design parameters involved in 3D woven architectures used for composite T-joints. Accordingly, this paper aims to investigate the role of innovative woven architectures at the junction in improving the mechanical performance of 3D woven T-shaped preforms. To further demonstrate the effect of yarn arrangements on delamination resistance, composite T-joints were manufactured, evaluated and

analysed. A comparative study was performed on the specimens using internal and external crossing yarn architectures for exploring optimal weave architecture. The mechanical performance of the specimens was evaluated under quasi-static tensile loading in the in-plane direction to determine the delamination and failure mechanisms.

2. Structural Designs

To understand how weave variations would affect the delamination resistance in composite T-joints, crossing warp architectures with different crossing proportions and arrangements were designed and studied. In these structures, the warp yarns in the web were divided into two halves and were arranged to cross with the proportions of 0%, 20%, 40%, 60%, 80% and 100% into the flanges. Warp yarns crossing with different proportions were also incorporated either externally (represented by 'Ext') or internally (denoted by 'Int') arrangement. An illustration of Int crossing warp architectures is shown in Figure 1(a) which 6 layers of warp yarns (say, number 3, 4, 5, 3', 4' and 5') exchanged their positions. Figure 1(b) displays an example of Ext crossing warp structures with warp yarns in layers 1, 2, 3, 1', 2' and 3' swapping their positions after crossing at the junction. Table 1 gives the codes of the composite T-joints reinforced by 3D woven orthogonal structures with different proportions of warp yarns crossed either internally or externally.

Table 1. Design list of 10 3D woven crossing warp architectures

Proportion of crossing warp		0%	20%	40%	60%	80%	100%
Preform code	Internal crossing warp	0CW	20CWInt	40CWInt	60CWInt	80CWInt	100CW
	External crossing warp		20CWExt	40CWExt	60CWExt	80CWExt	

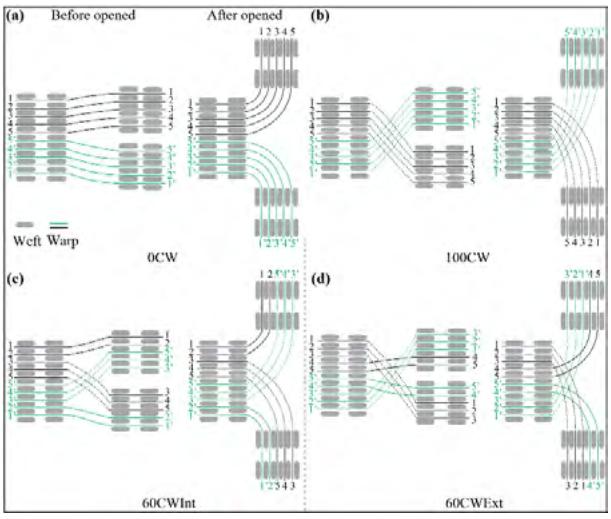

Figure 1. Illustration of Int and Ext architectures with 60% crossing warps [9]

3. Materials and Manufacture

The research on influence of different crossing warps on the in-plane mechanical performance of 3D woven T-shaped preforms used Diolen® Polyester staple yarn with a linear density of 98tex. In the investigation of weave variations effect on the in-plane and out-of-plane tensile behaviour of composite T-joints, preforms were manufactured using a 110 tex Twaron® yarn. T-shaped were produced in a flat form with bifurcations and then opened into the desired T-shape afterwards. The ARM AG CH-3507

BIGLEN semiautomatic hand loom was used for preform manufacture. Figure 2 display 3D woven T-shaped preforms made using Diolen® and Twaron® yarn. Composite T-joints were made using vacuum assisted resin transfer moulding (VARTM) method, as shown in Figure 3.

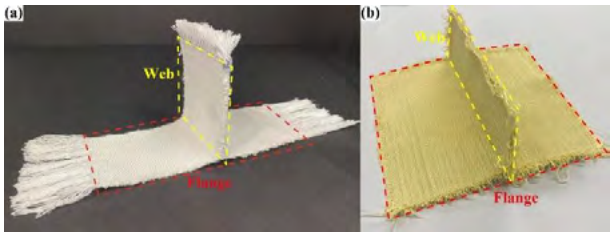

Figure 2. 3D woven T-shaped preforms made using (a) Diolen® yarn; (b)Twaron® yarn

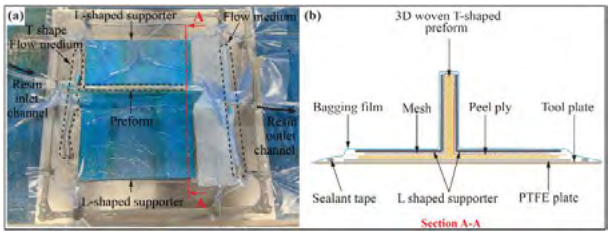

Figure 3. Vacuum assisted resin infusion mould of a composite T-joints. (a) Vacuum bagging; (b) Illustration of materials layout at section A-A

4. Mechanical Evaluation

The in-plane tensile load was applied to the two flanges with the web remained unloaded as shown in Figure 4. In terms of out-of-plane performance evaluation, the tensile loading was applied on the web, while two flanges were clamped at two ends by the top clamp of the fixture, as illustrated in Figure 5.

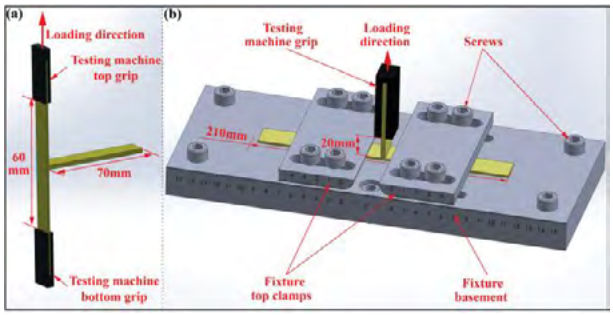

Figure 4. (a) In-plane tensile test set-up; (b) Out-of-plane tensile test layout

5. Testing Results and Discussions

5.1. Tensile behaviour comparison between Int and Ext preforms

In order to investigate the effect of different crossing yarn arrangements on the in-plane tensile behaviour, the preforms which have the same crossing yarn proportion but use either Int or Ext crossing yarn arrangements were studied. Through the result comparison between Int and Ext crossing warp, the optimisation of crossing warp arrangements for the T-shaped preforms was demonstrated.

The analysis was carried out by employing Int and Ext crossing warp yarns with varying proportions from 20% to 100%, and the comparative curves representing different crossing arrangements are shown in Figure 5. The Ext crossing leads to an increase in the mechanical performance than the Int crossing for the preforms with 20% crossing warps. This can be indicated in Figure 5(a), where the preforms with the Ext crossing show a higher linear slope and force at the highest peak and less failure strain than that of the Int crossing. This also is demonstrated in Figure 6 with the results of the stiffness, tensile strength and breaking strain of each preform, and also with the difference indicators (DI) to imply the discrepancy

between the Int crossing warp and the Ext crossing warp regarding the above mechanical performance. Figure 6(a) shows that the stiffness of 20CWExt specimens is 174.04 N/mm, while 20CWInt specimens only show a 110.34 N/mm. Although Figure 6(b) indicates a slight increase in tensile strength with the 20% Ext crossing warp, a significant DI of 158.03% in breaking strain is found when comparing 20CWExt with 20CWInt as shown in Figure 6(c). The increase in the tensile behaviour was also found in Figure 5(b) for specimens with 40% crossing warps between the Int and Ext crossing warps. With 40% of the Ext crossing warp, the stiffness and tensile strain were considerably increased by 27.63% and 100.26% respectively in comparison with the Int counterparts, as indicated in Figure 6(a) and 6(c). However, the application of the Ext crossing warp results in similar tensile strength for the specimens than that of the Int crossing warp, demonstrating by a 1.68% increase in maximum force as shown in Figure 6(b). The distinction between the Int and Ext crossing warp architectures shows a reduction with an increase of crossing warp proportion. This is demonstrated in Figure 5(c) that the gap of the two curves for 60CWInt and 60CWExt was decreased with increasing the crossing warp proportions, and in Figure 5(d) that the curve of 80CWInt is found identical to that of 80CWExt. In addition, this is supported by a decrease in the DI of stiffness and failure strain with a higher crossing warp proportion as shown in Figure 6. However, the 60CWExt preforms show an outstanding peak in the F-S curve, and considerable DI of 23.86% in the tensile strength compared to the 60CWInt preforms. This can be attributed to the similar proportion of crossing warp to straight warp and the tension applied to the binding warps was believed to be equal to the tension on the straight and crossing warp, leading to a weave architecture with good structural tightness and integrity.

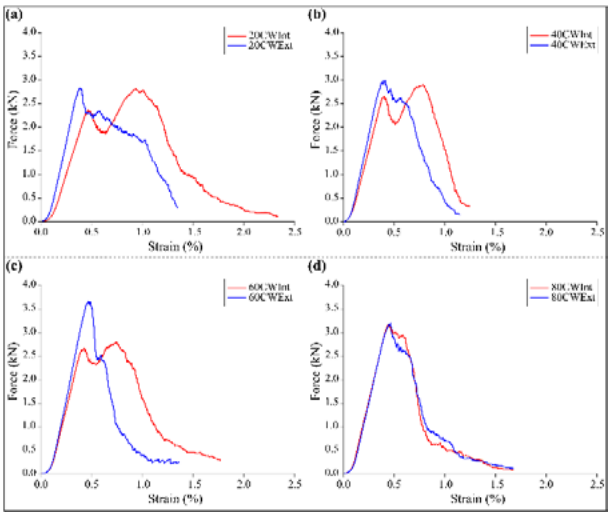

Figure 5. In-plane tensile results comparison between Int and Ext T-shaped preforms. (a) 20CWInt vs 20CWExt; (b)40CWInt vs 40CWExt; (c) 60CWInt vs 60CWExt; (d) 80CWInt vs 80CWExt

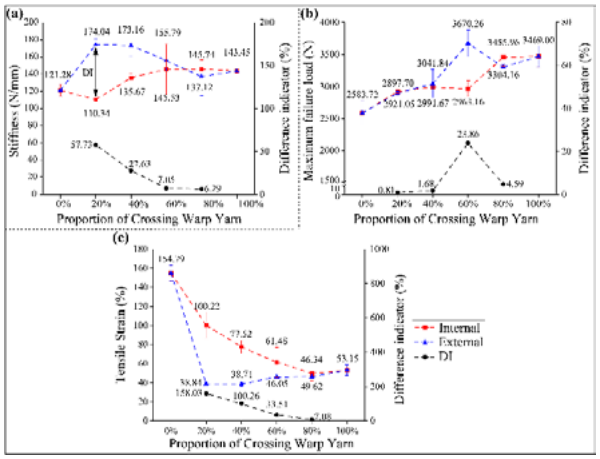

Figure 6. Mechanical testing results and difference indicators: (a) Stiffness; (b) Maximum failure load; (c) Tensile strain

5.2. Optimum crossing warp arrangements for improving in-plane tensile behaviour of 3D woven Composite T-joints

To optimize the arrangements of crossing warps for composite T-joints, the stress-strain response of Int specimens were compared to Ext specimens, while maintaining identical crossing warp proportions as illustrated in Figure 7. The average values and standard deviations of tensile strength, strain and Young's modulus at the strain of 0.5% for all composite T-joints are plotted in Figure 8, with the Difference Indicator (DI) to quantify the distinction between specimens of Int and of Ext composite T-joints regarding the tensile results.

Figure 7 indicates that although varying proportion of crossing warps from 20% to 80%, the Ext composite T-joints performed higher in-plane tensile performance than Int counterparts. which aligns with previous findings [21]. As shown in Figure 7(a), it is demonstrated that specimens reinforced by 20% Ext crossing warps behaved much higher tensile performance than those by 20% Int crossing warps, as supported by a higher linear slope and peak and less failure strain in the stress-strain curve. Both specimens of 20CWInt and 20CWExt displayed a similar linear stress-strain response at the start of tensile loading. A slight increase in the tensile strain to 0.5% induced a greater degradation in tensile strength for the specimen of 20CWInt, while the 20CWExt specimen maintained a consistent linear tensile behaviour until the catastrophic failure occurred. As a result of the considerable reduction in tensile strength, the Young's modulus of 20CWInt specimens is 7.16% lower than that of 20CWExt. Furthermore, the advantage of the Ext arrangement over the Int method in reinforcing composite T-joints is also highlighted in Figure 7(b) and 7(c), which shows a 68.75% and 116.81% increase in tensile strength and failure strain of the composite T-joints reinforced by 20% Ext crossing warps compared to that by 20% Int crossing warps respectively. The notable difference in failure strain can be further understood by analysing the damage situation after the catastrophic failure of Int and Ext specimens. For composite T-joints with 40% crossing warps, Figure 7(b) shows obvious difference in the stress-strain curve between the Int and Ext specimens. This observation is also supported by the significant DI of 30.04%, 25.63% and 39.23% in tensile strength, modulus, and failure strain respectively as shown in Figure 8. However, the distinction in tensile results between Ext and Int specimens was greatly reduced if 60% and 80% crossing warps were integrated into composite T-joints, as evident by the similar stress-strain response as indicated in Figure 7(c) and 7(d) respectively. Additionally, the modulus and tensile strength of Ext and Int specimens differ by less than 10% and 5% after incorporating 60% and 80% crossing warps as observed in Figure 8(a) and 8(c) respectively. This is attributed to the improvements in modulus, tensile strength and failure strain for the composite T-joints with a higher proportion of Ext crossing warps were not as significant as that of Int crossing warps. Although the difference between Int and Ext specimens was reduced with a high proportion of crossing warps, the composite T-joints reinforced by external crossing warps have higher tensile performance and delamination resistance than that those by internal crossing warps.

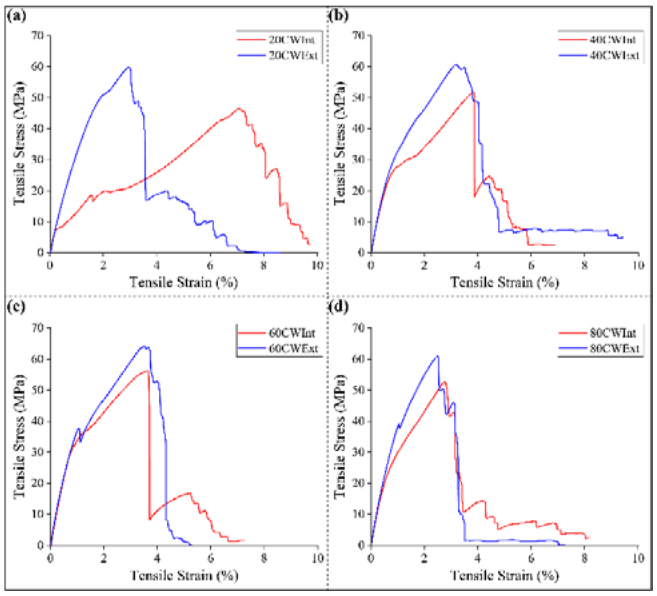

Figure 7. The comparison study on the in-plane tensile performance between Int and Ext composite T-joints in proportion of (a) 20%; (b) 40%; (c) 60%; (d) 80%

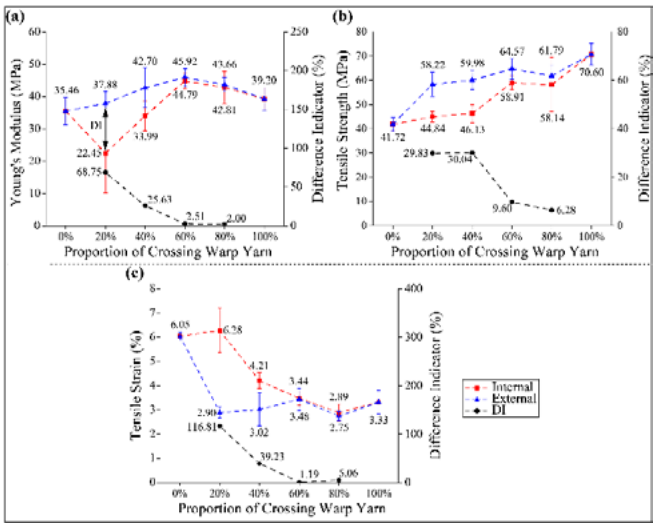

Figure 8. In-plane tensile performance comparison between composite T-joints with Int and Ext crossing warp architecture (a) Young's Modulus; (b) Tensile strength; (c) Tensile strain

5.3. Optimum crossing warp arrangements for improving out-of-plane tensile behaviour of 3D woven Composite T-joints

Figure 9 indicates that Int composite T-joints outperformed their Ext counterparts in resisting the out-of-plane tensile failure regardless of crossing warp proportions. Notably, the stress-strain of 20CWInt shows significantly higher slope and peak values than that of 20CWExt as displayed in Figure 9(a). The DI as shown in Figure 10, representing the comparison between Int and Ext crossing warp architectures in out-of-plane tensile performance, further demonstrates this findings. An increase of 105.22% in Young's modulus and 67.70% in tensile strength was observed in Int configurations, as shown in Figures 10(a) and 10(b), respectively. Conversely, the incorporation of Int crossing warps was associated with a reduced tensile strain for the composite T-joints. Figure 10(c) presents a decrease of 12.15% in tensile strain for 20CWInt compared to 20CWExt. Increasing the crossing warp proportions to 40% led to similar results for the composite T-joints. The slope and curve peak of 40CWInt indicates a higher value than that of 40CWExt as demonstrated in Figure 9(a) and the Young's Modulus and tensile strength of

was increased by 29.08% and 19.03% respectively with using Int crossing warps to reinforce composite T-joints. Additionally, a 10.06% decrease in tensile strain was also demonstrated as a result of the application of 40% Int architectures during manufacturing composite T-joints. Despite increasing the crossing warp proportions to 60% and 80%, the Int composite T-joints exhibited higher Young's Modulus and tensile strength than those of Ext counterparts. Similarly, the application of Int crossing warp architectures reduced the tensile strain of composite T-joints although using 60% or 80% crossing warps.

Integrating higher crossing warp proportions reduced the difference between Int and Ext specimens. As shown Figure 10(a) and 10(b), the DI of Young's Modulus and tensile strength was decreased with increasing the proportions of crossing warps, whereas that of tensile strain was reduced and then increase with more crossing warps introduced into composite T-joints. Accordingly, using 20% Int crossing warps led to the maximum increase in out-of-plane tensile behaviour for the composite T-joints.

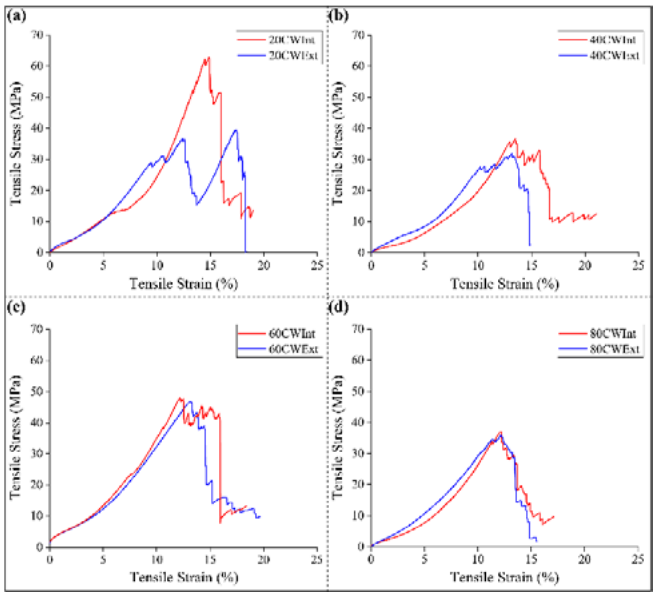

Figure 9. Comparison of out-of-plane tensile performance between Int and Ext composite T-joints in proportion of (a) 20%; (b) 40%; (c) 60%; (d) 80%

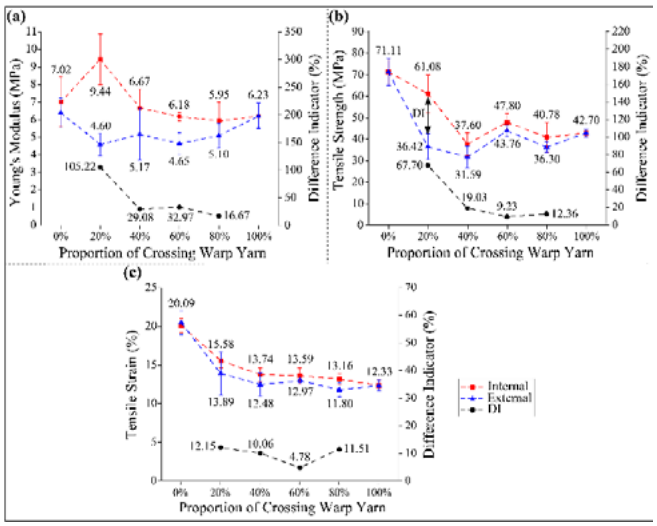

Figure 10. Comparative analysis of out-of-plane tensile performance in composite T-Joints with Int and Ext crossing warp architectures

6. Conclusions

Woven architecture with crossing warps was designed and evaluated for influence on the mechanical performance under in-plane tensile tear-off load on the two flanges of 3D woven T-shaped preforms. The effect of these architectures on the in-plane and out-of-plane tensile behaviour of 3D woven composite T-joints was also investigated. The tensile behaviour between Int and Ext crossing warp architectures was compared to optimise the weave structures for developing the tensile performance of specimens. The following conclusions were summarized:

(1) Compared with the internal crossing warp architectures, the external crossing warp architectures were shown to be more effective to improve the in-plane mechanical performance of 3D woven T-shaped preforms. The tensile test results demonstrated that the maximum increase in stiffness, tensile strength and failure strain of the Ext crossing preforms were 57.73%, 23.86% and 158.03% higher respectively than the corresponding Int crossing preforms.

(2) Results confirms that the in-plane tensile performance of composite T-joints was effectively improved by incorporating the Ext crossing warp architecture, regardless of the proportion of crossing warps. The maximum difference at 29.83%, 68.75% and 116.81% in tensile strength, Young's modulus and tensile strain respectively were identified in the comparison study of Int and Ext composite T-joints.

(3). On the contrary, the out-of-plane tensile behaviour of Int composite T-joints performed higher than that of Ext composite T-joints, independent of the crossing warp proportions. Comparative studies highlighted considerable improvements in the Int composite T-joints, with increases in tensile strength, Young's modulus, and tensile strain by 67.70%, 105.22% and 12.15% respectively, compared to Ext composite T-joints.

Acknowledgments

The authors gratefully acknowledge the support provided by Ms. Elizabeth Carlton for her technical understanding and assistance during preforms preparation. Thanks are also extended to Mr. Stuart Morse and Mr. Ryan Delve throughout the mechanical performance evaluation of work.

References

[1] Trask R, Hallett S, Helenon F, and Wisnom M. *Influence of process induced defects on the failure of composite T-joint specimens.* Composites Part A: Applied Science and Manufacturing, 2012. 43(4): p. 748-757.

[2] Rispler A R, Steven G P, and Tong L. *Failure analysis of composite T-joints including inserts.* Journal of reinforced plastics and composites, 1997. 16(18): p. 1642-1658.

[3] Hajdaei A. *Extending the fatigue life of a T-joint in a composite wind turbine blade*, PhD Thesis. The University of Manchester (United Kingdom), 2013

[4] Zhu H and Chen X. *Design of T-shaped fabrics with interweaving structure.* Journal of Textile Research, 2008. 29(10): p. 47-51.

[5] Ali M, Kausar F, Shahid S, Zeeshan M, Nawab Y, Riaz R, Memon A A, Mengal N, and Anjum A S. *Novel derivatives of 3D woven T-shaped composites with improved performance.* The Journal of The Textile Institute, 2019. 110(2): p. 267-273.

[6] Soden J and Hill B. *Conventional weaving of shaped preforms for engineering composites.* Composites Part A: Applied Science and Manufacturing, 1998. 29(7): p. 757-762.

[7] Yan S, Zeng X, and Long A. *Experimental assessment of the mechanical behaviour of 3D woven composite T-joints.* Composites Part B: Engineering, 2018. 154: p. 108-113.

[8] Umair M, Shaker K, Javaid M U, Hussain M, Kashif M, and Nawab Y. *Effect of weaving patterns on damage resistance of 3D woven jointless T and H shaped reinforcements.* Mechanics of Advanced Materials and Structures, 2022. 29(1): p. 104-117.

[9] Wei Z and Chen X. *Effect of crossing warp architecture on tear strength of 3D orthogonal woven T-shaped reinforcements.* Textile Research Journal, 2024: p. 00405175231226103.

PREPARATION AND CHARACTERIZATION OF CARBON NANOTUBES REINFORCED POLYAMIDE 66 NANOCOMPOSITES

Xindi Hu[1], Seira Morimune-Moriya[2], Daisuke Ogawa[2], Keiji Nakamura[2]

[1]Graduate School of Engineering, Chubu University, Matsumoto, Kasugai, Aichi 487-8501, Japan
[2]College of Engineering, Chubu University, Matsumoto, Kasugai, Aichi 487-8501, Japan
Email: seiram@isc.chubu.ac.jp

Keywords: Nanocomposite, Polyamide66, Carbon-nanotube, In-situ polymerization, Urea bonds

Abstract
In general, carbon nanotubes (CNTs) tend to form agglomerates in polymer matrices because of their van der Waals forces and inert surface. Therefore, it is difficult to exploit the excellent properties of CNTs to polymer nanocomposites. In this study, polyamide 66 (PA66) nanocomposites with carbon nanotubes (CNTs) were developed. Surface modification of CNTs via plasma treatment was conducted and isocyanate groups were introduced on CNTs surface to improve the dispersibility of CNTs in PA66 and to obtain the strong interfacial interaction between PA66 and CNTs. The nanocomposites were synthesized via *in-situ* polymerization, where the polymerization was proceeded under the presence of CNTs. The structure anc properties of PA66 nanocomposites with non-treated CNTs (nCNTs) or plasma-treated CNTs (pCNTs) were investigated. Structural studies revealed that the dispersibility of pCNTs was higher than that of nCNTs in the PA66 nanocomposites. In addition, new bonds of urea bonds were formed at the interface between PA66 and pCNTs. The PA66/CNTs nanocomposites exhibited significant increase in the mechanical and thermal properties compared to those of PA66.

1. Introduction

In recent decades, the demand for advanced materials in high-performance applications such as aerospace and automotive industries has significantly increased. Polymer nanocomposites, known for their lightweight and superior mechanical properties, have emerged as a pivotal solution in these fields. Carbon nanotubes (CNTs) including single-walled, double-walled and multi-walled CNTs have intensively been used as nanofillers for polymer nanocomposites since the discovery by Iijima at 1991. [1,2] The high aspect ratio of 300-1000, excellent mechanical properties (~1 TPa Young modulus), high thermal conductivity (3000 – 6000 W m^{-1} K^{-1}) and remarkable electrical conductivity (10^4 – 10^6 S cm^{-1}) of CNTs have attracted a great deal of attention and it has been regarded as an ideal nanofiller to develop high performance polymer nanocomposites for aerospace, automotive and electronics industry as sensors, actuators, capacitors and so on. Despite their potential, however, the integration of CNTs into polymer matrices have often faced critical challenges. Primarily, the strong van der Waals forces between CNTs lead to agglomeration in polymer matrices. The agglomerates reduce the interfacial area and diminish the reinforcing effects of CNTs, for example, the scattering of electrons or phonons and hampered load transfer which degrade the performance of the composites. Therefore, polymer nanocomposites with CNTs often failed to exploit the excellent properties of CNTs and to achieve the expected propeties.

Polyamide 66 (PA66), renowned for its robust mechanical properties and chemical stability, serves as an excellent matrix for polymer nanocomposites. So far, various reports on PA/nanocarbons nanocomposites have been published and the enhanced properties have been revealed. [3,4] However, the dispersibility of nanocarbons in PA as well as the interfacial interactions between PA and nanocarbons has still been a challenge to exploit the strong reinforcement effect of nanocarbons to PA nanocomposites. Above all, to employ CNTs as effective reinforcement in polymer nanocomposites,

proper dispersion and appropriate interfacial adhesion between the CNTs and polymer matrix have to be guaranteed. [5]

This study introduces a novel method to enhance the dispersion and interfacial bonding of CNTs within a PA66 matrix through plasma treatment. In order to achieve the high dispersibility, we prepared the nanocomposites by in-situ polymerization. The effect of plasma treatment of CNTs on the structure and the properties of the PA6 nanocomposites were investigated.

2. Experimental

2.1. Materials

MWNTs was acquired from Beijing Deke Daojin Co., Ltd. with lengths from 0.5 to 2 μm, diameters of <8 nm, and a purity of greater than 95 wt%, and 3.86% of the surface carbon atoms were carboxylic. Hexamethylenediamine, carbon tetrachloride, adipoyl chloride, sodium hydroxide, methanol, and phenol were purchased from Wako Pure Chemical Industries Ltd. (Osaka, Japan). All reagents were used as received.

2.2. Plasma treatment of CNTs

CNTs was added to pure water and ultrasonicated, followed by drying to remove moisture for the plasma treatment. CNTs was subjected to plasma for 20 minutes under N_2 and CO_2 atmosphere. The sample was dispersed in pure water, ultrasonicated and centrifuged. The supernatant was collected, and its transmittance was measured to determine the concentration of CNTs in the suspension. Nontreated CNTs and plasma treated CNTs are termed as nCNTs and pCNTs, respectively.

2.3. Synthesis of PA66/CNTs Nanocomposites

PA66/CNTs nanocomposites were prepared by in-situ polymerization. PA66 was synthesized by condensation polymerization by using hexamethylenediamine/sodium hydroxide aqueous solution and adipoyl chloride/carbon tetrachloride solution. Prior to the polymerization, CNTs aqueous suspension was subjected to ultrasonication, and added to hexamethylenediamine/sodium hydroxide aqueous solution. The obtained PA66/CNTs was washed and then purified by reprecipitation using phenol and methanol. After washing with ultra pure water and drying under vacuum for 24h at 50 °C and then72 h at 40 °C. PA66/CNTs nanocomposites were prepared by hot pressing at 270 °C. The thickness of the nanocomposite was 0.2 mm. The filler content was controlled as 0, 0.01, 0.03,and 0.05 wt%

3. Results and discussion

3.1. Structure

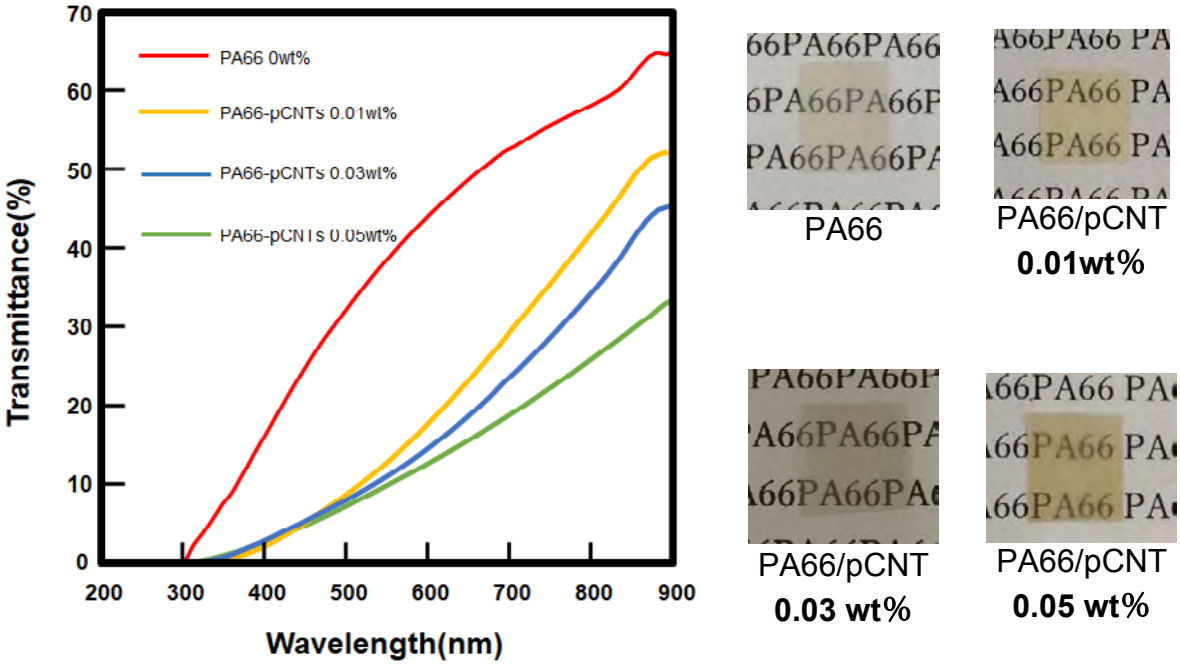

Figure 1. UV–vis spectra and photographs of PA66 and PA66/pCNTs nanocomposites.

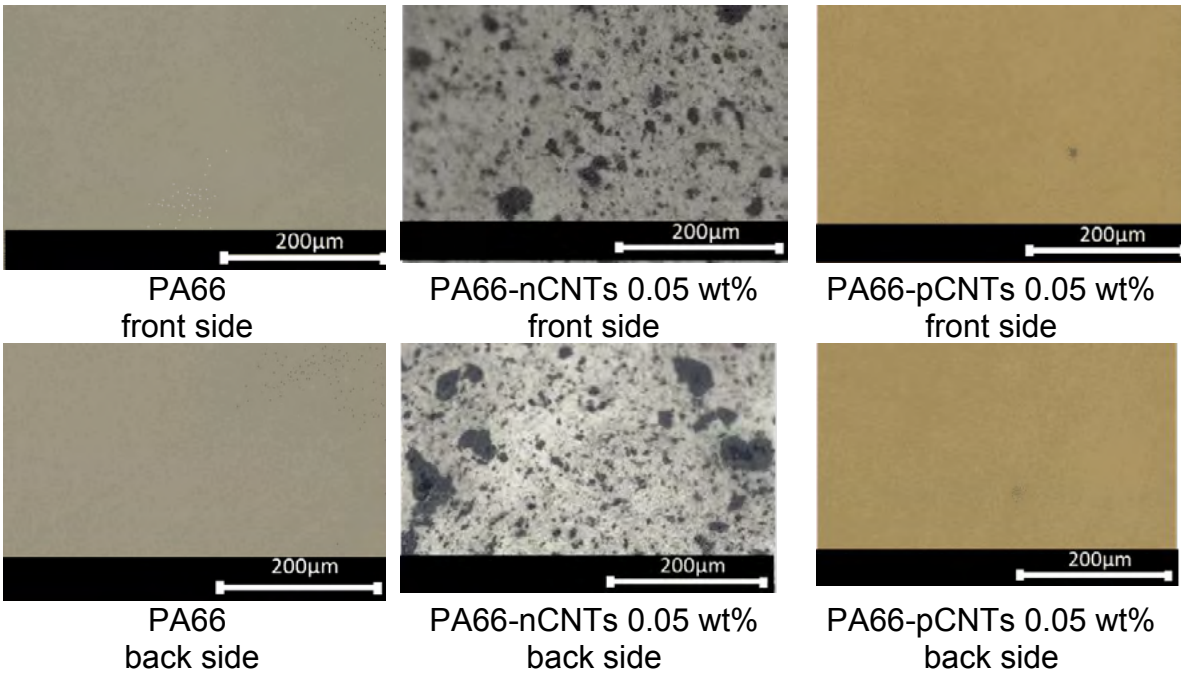

Figure 2. Digital microscope photographs of PA66 and PA66/CNTs nanocomposites.

Figure 1 shows the optical images and the UV-Vis spectra of PA66 and PA66/pCNTs nanocomposites. From the UV-vis spectra, the transmittance of the samples decreased with increasing carbon nanotube

(CNT) content.While the transparency slightly decreased by the incorporation of pCNTs, it was homogeneously dispersed in the nanocompostes. Compared to the nanocomposites with nCNTs, the nanocomposites with pCNTs showed high transparency.It also shows the typical result on CNT dispersion in polyamide matrix by employing ultrasonication method to disperse CNT in water.

Figure 2 shows the optical image taken by digital microscope of PA66, PA66/nCNTs nanocomposites and PA66/pCNTs nanocomposites. It was obvious that nCNTs formed large agglomerates with the size up to 100 μm in the nanocomposites. On the otherhand, pCNTs was homogeneously dispersed in the nanocomposites so that the agglomerate was not observed, indicating that the compatibility of CNTs with PA66 was significantly improved by the plasma treatment of CNTs.

3.2. Properties

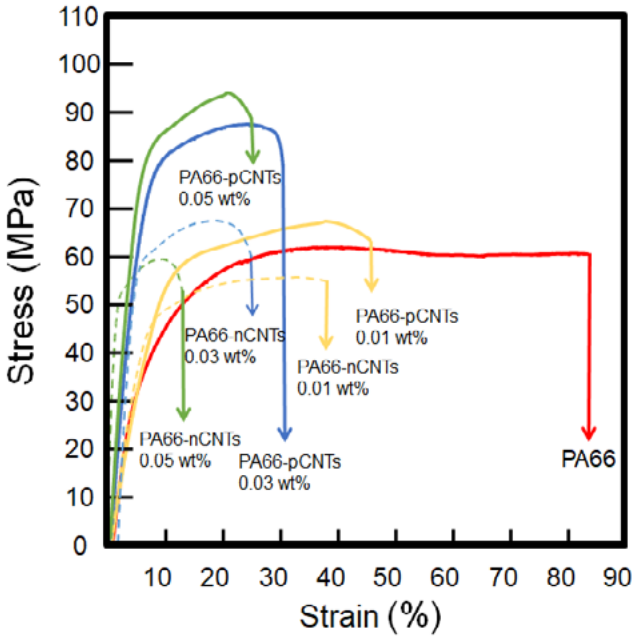

Figure 3. Stress–strain curves of PA66, PA66/nCNTs nanocomposites and PA66/pCNTs nanocomposites.

Figure 3 shows the stress-strain curves of PA66, PA66/nCNTs nanocomposites and PA66/pCNTs nanocomposites. Tables 1 summarizes the Young's modulus, tensile strength, elingation at break and toughness of PA66, PA66/nCNTs nanocomposites and PA66/pCNTs nanocomposites. Compared to the nanocomposites with nCNTs, the remarkable improvements in the mecchanical properties for the nanocompsites with pCNTs were revealed. For instance, the tensile strength of the PA66/pCNTs nanocomposites with the filler content of 5wt% increased by 1.5 times than PA66.

The Young's modulus and the tensile strength of PA66/nCNTs nanocomposites tend to decrease at 0.05 wt%, indicating the formation of excessive agglomerates. These agglomerates can be the initial point for the crack propergation, resulting in the distruction of the whole material. They disrupt the uniform distribution of energy under tension, producing the stress concentration point. On the other hand, the Young's modulus and the tensile strength significantly increased by the incorporation of pCNTs even at 0.05 wt%. These improvements are attributed to the high dispersion of pCNT within the PA66

matrix through in-situ polymerization and the strong interfacial interactions of covalent bonds between the PA66 and pCNTs. [6-8]

Table 1. Mechanical properties of PA66, PA66/nCNTs nanocomposites and PA66/pCNTs nanocomposites.

	Young's modulus (GPa)	Tensile strength (MPa)	Elongation at break (%)	Toughness (J/g)
PA66	1.5	62	83	5.1
PA66/nCNT 0.01 wt%	1.6	54	38	2.9
PA66/nCNT 0.03 wt%	1.8	69	26	1.8
PA66/nCNT 0.05 wt%	1.4	59	13	0.8
PA66/pCNT 0.01 wt%	1.7	69	46	3.1
PA66/pCNT 0.03 wt%	2.3	89	32	2.8
PA66/pCNT 0.05 wt%	2.4	93	25	2.3

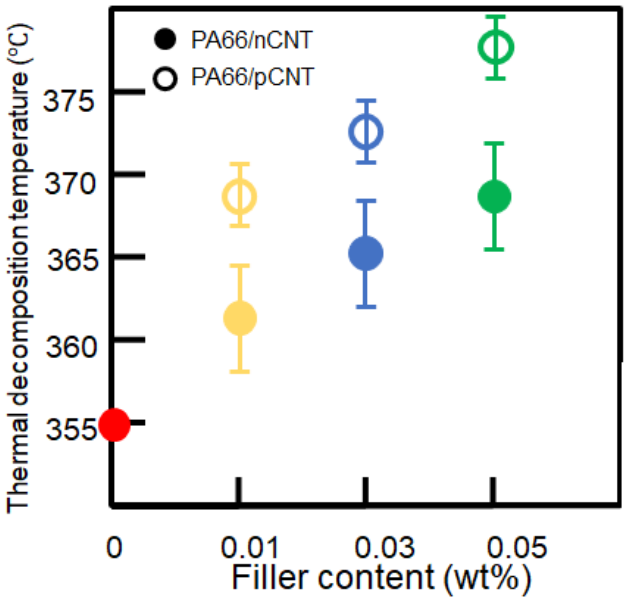

Figure 4. Thermal decomposition temperatures of PA66, PA66/nCNTs nanocomposites and PA66/pCNTs nanocomposites.

Figure 4 shows the thermal decomposition temperature of PA66, PA66/nCNTs nanocomposites and PA66/pCNTs nanocomposites. The thermal decomposition temperature was determined as the temperature at 5% weight loss in the thrmogravimetric traces. The thermaldecomposition temperature increased by the incorporation of CNTs, and it increased with increasing of CNTs content. The nanocomposites with pCNTs exhibited the higher thermal decomposition temperature than that of the nanocomposites with nCNTs. The thermal decomposition temperature was incerased by 7 °C to 13 °C by the addition of nCNTs, while it was increased by 13 °C to 20 °C by the addition of pCNTs. As for the standard deviation, the PA66/nCNTs nanocomposites showed larger deviation than that of PA66/pCNTs nanocomposites, indicating that the formation of agglomerates which caused the heterogeneous destribution in the sample. On the other hand, pCNTs effectively restricted the molecular motion of PA66 by the high dispersibility and the strong interfacial interactions. It was revealed that the high thermal resistance can be achieved by the incorporation of CNTs with optimum chemical structure on the surface.

4. Conclusions

In this study, the PA66/CNTs nanocomposites were prepared by in-situ polymerization. In order to achieve the high dispersibility and the strong interfacial interactions, plasma treatment of CNTs under N_2 and CO_2 atmosphere was conducted and isocyanate groups were introduced on the surface of CNTs. From the structural studies, the improvement in the dispersibility by the plasma treatment was revealed. In addition, it was shown that the covalent bond of urea bond was formed at the interface between PA66 and pCNTs. The nanocomposites with pCNTs showed significant enhancement in the mechanical properties and thermal resistance. These enhancements indicate the high potential of PA66/pCNTs composites in demanding applications such as automotive and aerospace.

References

[1] S. Iijima, Synthesis of Carbon Nanotubes. Nature, 354, 56–58, 1991.
[2] S. Iijima, T. Ichihashi, Single-Shell Carbon Nanotubes of 1 nm Diameter. Nature, 363, 603–605, 1993.
[3] R. Haggenmueller, F. Du, J. E. Fischer, K. I. Winey, Polymer 47, 2381–2388, 2006.
[4] R. Sengupta, A. Ganguly, S. Sabharwal, T. K. Chaki, A. K. Bhowmick, J. Mater. Sci., 42, 923–934, 2007.
[5] Ma, Peng-Cheng, Siddiqui, Naveed A., Marom, Gad, Kim, Jang-Kyo., Dispersion and functionalization of carbon nanotubes for polymer-based nanocomposites: A review., Composites Part A: Applied Science and Manufacturing, Volume 41, Issue 10, 2010.
[6] Park, M., Jang, J., Park, J. H., Yu, J., Kim, S. Y. Enhanced Tensile Properties of Multi-Walled Carbon Nanotubes Filled Polyamide Composites Based on Interface Modification and Reactive Extrusion. In Proceedings of the Polymer Processing and Engineering Section, vol. 12, pp. 997, 2020.
[7] T. Liu, Y. Zhang, and L. Wang, Influence of Carbon Nanotube Surface Modifications on the Mechanical Properties of Polyamide 66/CNT Composites, Journal of Composite Materials, vol. 56, pp. 123-131, 2022.
[8] J. K. Lee and S. Y. Choi, Mechanical Enhancement of Polyamide 66 by Multi-Walled Carbon Nanotubes via Melt Mixing Method, Composites Science and Technology, vol. 77, pp. 60-68, 2021.

PROCESS ASPECTS OF FORMING POLYETHYLENE-BASED COMPOSITES FILLED WITH FUNCTIONAL WASTE-PLANT FILLERS BY ROTATIONAL MOLDING TECHNOLOGY

Mateusz Barczewski[1], Joanna Aniśko[1], Paulina Kosmela[2], Mariusz Marć[3], Joanna Szulc[4], Wiktoria Kanciak[1], Patryk Mietliński[5] and Aleksander Hejna[1]

[1]Institute of Materials Technology, Faculty of Mechanical Engineering, Poznan University of Technology, Piotrowo 3, 61-138 Poznan, Poland
Email: mateusz.barczewski@put.poznan.pl; joanna.anisko@put.poznan.pl; aleksander.hejna@put.poznan.pl; wiktoria.kanciak@doctorate.put.poznan.pl
[2]Department of Polymer Technology, Faculty of Chemistry, Gdansk University of Technology, G. Narutowicza 11/12, 80-233 Gdansk, Poland
Email: paulina.kosmela@pg.edu.pl
[3]Department of Analytical Chemistry, Faculty of Chemistry, Gdansk University of Technology, G. Narutowicza 11/12, 80-233 Gdansk, Poland
Email: mariusz.marc@pg.edu.pl
[4]Faculty of Chemical Technology and Engineering, Bydgoszcz University of Science and Technology, Seminaryjna 3, 85-326 Bydgoszcz, Poland
Email: joanna.szulc@pbs.edu.pl
[5]Institute of Mechanical Technology, Faculty of Mechanical Engineering, Poznan University of Technology, Piotrowo 3, 61-138 Poznan, Poland
Email: patryk.mietlinski@put.poznan.pl

Keywords: polyethylene, rotational molding, nut shells, composite, waste-based fillers.

Abstract
This study compares the impact of a one- or two-stage manufacturing processing procedure of high-density polyethylene-based (HDPE) composites filled with ground pistachio (PS), pecan (PES) shells (2-15 wt%) on the rheological, mechanical properties, and the structure of rotomolded products. The investigations were supplemented with an analysis of changes in the resistance of polyethylene composites to oxidation induced by the migration of low molecular weight compounds with antioxidant activity from plant-based fillers to HDPE matrix.

1. Introduction

Rotational molding (RM) technology is currently the most dynamically developing technology for manufacturing thin-walled and large-sized products made of thermoplastic polymers. It involves (i) introducing into a mold, reflecting the external shape of the product, a thermoplastic polymer in the form of powder with defined granulometric characteristics [1]; (ii) putting it in motion in two axes while simultaneously supplying the heat necessary to sinter the polymer and next melting it, guaranteeing the coverage of all walls of the mold; (iii) the subsequent slow cooling and demolding [2–4]. One of the major problems of RM is the long forming time and the resulting energy consumption. Therefore, new solutions for improving its sustainability are sought.

As in the case of other technologies, many attempts have been made to produce polymer composites in RM. The main goal is to change its thermal properties [5] or improve its mechanical properties by introducing fibers [6,7]. Due to the non-pressure nature of the process and the lack of the impact of shear forces during melting, the use of fillers is often associated with their inhomogeneous distribution in product, agglomeration, or porosity of the final rotomolded composite parts [8,9].

During the forming of polymer composites in the rotational molding process, technological problems are encountered as limitations related to passive participation in the initial stage of the molding process,

i.e., the sintering process, as well as difficult degassing of the product caused by increased viscosity from bulk and residual moisture in the filler resulting in additional porosity.
Several methods have been reported in the literature to improve the quality and properties of products, including the use of additional melt processing to obtain a composite micro powder containing filler particles saturated by the polymeric matrix [10], performing the process in multiple stages to get a layered structure of the composite, including with an increased share filler in the internal layers [11,12] or the use of an additional pressurization step, which increases the degree of suction of the filler by the polymer, increases the efficiency and shortens the time of the densification process [13,14].
The development of new sustainable material solutions in the processing of thermoplastic polymers concerns both the application of biopolymers and the use of valorized plant derivatives as fillers and modifiers of petrochemical polymers [15]. The dominant global share of polyethylene in RM is making plant-originated fillers a more frequently used solution. At the same time, after many years of research, they are not only considered materials that make the product cheaper by reducing the amount of polymer but also consciously use new functional features resulting from their complex chemical composition. Considering the fragile nature and low thermal stability of organic compounds having functional features, including antioxidant effects, it is advisable to undertake research not only to determine the final properties of the composites containing them but also to describe the degradation accompanying the processing qualitatively. At the same time, due to the harsh processing environment in rotomolding technology resulting in the need for polymer stabilization, using functional fillers enabling the production of self-stabilizing wood-polymer composites requires combining the analysis of the structure-property relationship with a simultaneous comprehensive analysis of processing and active compounds passivation effects [16].
Taking into account the beneficial role of the slip agent during RM described in [17] and the possibility of the active impact of phytochemicals contained in fillers of plant origin [18,19], attempts were made in this study to verify the possibility of using nut shells as fillers. These fillers were used to achieve a simultaneous effect, plasticization, and stabilization of polyethylene due to the migration of oils rich in antioxidants from nut shells to the polyethylene matrix. The work also refers to the influence of the filler introduction procedure, i.e., using one- or two-step processing.

2.1. Experimental

2.1.1. Materials

The polymer used as a matrix to produce rotomolded composites was the high-density polyethylene (HDPE) KT 10000 UE (Dow, USA), with a melt flow index (MFI) of 8.0 g/10 min (190°C; 2.16 kg), 0.964 g/cm^3 density. Pistachio nut shells (PS) were obtained mechanically by manually cracking the nuts from the NATURAL EXPERT PPH Kamil Chojnowski (Poland). Pecan nut shells (PES) were obtained mechanically in the manual cracking of nuts obtained from the Just-And Andrzej Błachowicz company (Poland). The country of origin of both nuts is the USA. Both nut grades were ground using a centrifugal Retsch ZM 200 knife mill in cryogenic conditions and then fractionated using 800 µm sieve.

2.1.2. Sample preparation

The rotomolding processing was performed by two routes, depending on the pre-processing steps. In the first case (named physical mixing and assigned as x1), the polymer pellets were ground in a high-speed mill Retsch ZM 200 at 8,000 rpm. The fillers were introduced at 2, 5, 10 and 15 wt% and mixed with the polymer powder; the blends were then dried at 70 °C for 24 h before rotational molding. 100 g of such premixes were introduced into the mold (180×60×60 mm), made of 2 mm-thick steel. The rotational molding was performed in a lab-scale single-arm shuttle rotational molding machine REMO GRAF (Poznan, Poland) [20], with rotation speeds of 10 and 8 rpm (horizontal and vertical axes, respectively). The heating chamber was settled to 230 °C, measuring a maximum of 200 °C in the spindle axis with a K-type thermocouple. The process inside the heating chamber lasted for 25 min, after which the mold was cooled with forced air flow for 15 min. The second method, i.e. melt mixing (x2), consisted of the preliminary blend preparation by an extrusion process. The compounding process was realized by a twin-screw co-rotating extruder Zamak 16/40 EHD, at 180 °C as maximum temperature, with a rotational speed of the screws of 100 rpm. The extrudates were cooled down with forced air before pelletizing. Pellets were ground in the high-speed mill Retsch ZM 200 in cryogenic

conditions at a knife rotational speed of 8,000 rpm. The prepared composite powders were processed by RM, using the same conditions as the material prepared by physical mixing (x1).

2.1.3. Methods

The chemical composition of nut shells, i.e., holocellulose, cellulose, lignin, mineral substances, and extractives, was analyzed using extraction methods following the procedures described in [21].
For both fillers, the standard Soxhlet procedure was used to determine the amount of oil. The oil content in organic waste fillers was assessed using the Büchi Universal Extraction System B-811, operating with petroleum ether as a solvent and a total extraction time of 150 min.
The DPPH free radical scavenging assay assessed the antioxidant properties of the used fillers. Samples of 1 g of each filer type were extracted in 100 ml of methanol for 30 min using a magnetic stirrer operating at 300 rpm at room temperature to obtain the required extracts for testing. Then, the filtered extracts were diluted to the concentration of 1 g/l. The antioxidant activity can be specified because of a stable organic nitrogen radical in 2,2-diphenyl-1-picrylhydrazyl (DPPH); its solution in alcohol has a violet color, which fades in the presence of the antioxidant. The UV-VIS spectrophotometer UviLine 9400 was used for analysis according to the procedure described in [10].
The particle size distribution of fillers was characterized using a laser particle sizer Fritsch ANALYSETTE 22 apparatus operating in the range of 0.08–2000 μm.
Rheological investigations were carried out using an Anton Paar MCR 301 rotational rheometer, with 25 mm diameter parallel plates and a 1.5 mm gap under the oscillatory mode. The experiments were conducted at 200°C. The angular frequency used during the studies was 0.05-500 rad/s with a strain of 1% (in the LVE range).
The oxidation induction time (OIT) of analyzed materials was determined by differential scanning calorimetry (DSC). The 5±0.2 mg samples were placed in aluminum crucibles with pierced lids. They were heated from 20 to 190 °C with a heating rate of 20 °C/min in nitrogen, then kept at 190 °C for 5 min in nitrogen, and then the gas was switched to oxygen, and the time required for sample oxidation was measured. The measurements were conducted using a Netzsch 204 F1 Phoenix apparatus.
Tensile testing was used to study the elastic modulus, elongation at break, and tensile strength. The tensile tests were performed per ISO 527 standard with the Zwick/Roell Z020 model 5101 universal testing machine. The crosshead speed was set at 10 mm/min.
The impact strength was evaluated using the Dynstat method as in DIN 53435 standard on unnotched samples with dimensions of 4x10x15mm. A Dys-e 8421 apparatus with a 0.98 J hammer was used.
The composite samples were examined using measuring X-ray tomography, model v|tome|x s240 (Waygate Technologies / GE Sensing & Inspection Technologies GmbH). Micro-computed tomography (μCT) was used to evaluate the porosity in the rotomolded samples. Following scanning, parameters were used during the measurements - microfocus x-ray tube (voltage 150 kV/current 200 μA); the exposure time for one picture was 150 ms, and the voxel size was 123 μm.

3. Results and discussion

The results of the analysis of the chemical composition of plant-based fillers, along with their antioxidant activity, are summarized in Table 1 (all results of chemical compositions are given on a dry mass basis). PS is characterized by a lower lignin content compared to PES. The results are consistent with the literature data for this biomass group [22,23]. As shown in the literature [23,24], lignin, a compound rich in phenolic groups, has significant antioxidant activity. The results show a significantly higher PES antioxidant activity than PS. Analyzes showed four times greater inhibition ability and over 5 times greater value of Trolox equivalent antioxidant capacity (TEAC), which measures the antioxidant capacity of a given substance compared to the standard Trolox. This effect may probably be due to the increased content of oil, which contains low-molecular-weight active compounds.
Analysis of the particle size of the materials used showed different characteristics for fillers and polymer powder (Fig. 1). In the case of fillers, a bimodal particle size distribution was observed, with a dominant share of the fraction below 100 μm for PES and a more uniform distribution for PS. In both cases, the maximum particle size did not exceed 800 μm, which results from the cutting system used in the mill. In the case of polyethylene, the particle size distribution is much narrower and ranges from 20 to 1200 μm, with the dominant share of fractions in the range of 300-800 μm. The differences in particle size

may be related to a different chemical structure, including an increased cellulose content in the case of PS, resulting in more significant higher filler fractions [25].

Table 1. Chemical composition and results of antioxidant activity of PS and PES fillers.

Parameter	Unit	*PS*	*PES*
Chemical composition			
Holocellulose	[%]	88.26	75.88
Cellulose	[%]	32.69	27.92
Lignin	[%]	29.27	44.57
Mineral substances	[%]	0.2	1.67
Extractives	[%]	1.07	0.87
Oil	[%]	1.44	3.26
Antioxidant activity			
Inhibition	[%]	20.9 ± 2.1	88.4 ± 0.5
TAEC	[mg/g dry mass]	26.2 ± 3.8	148.3 ± 0.9

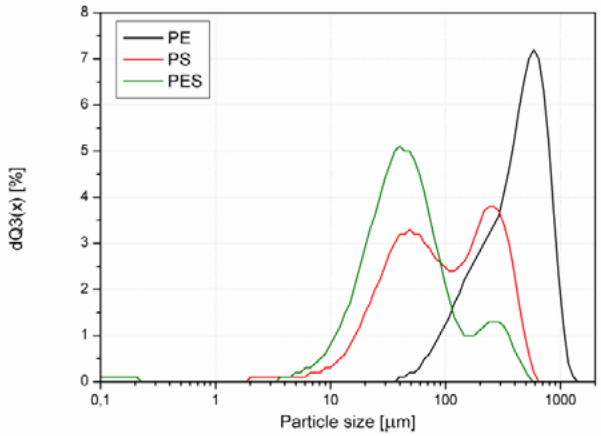

Figure 1. Particle size distribution of ground plant-based fillers and polymeric powder.

Complex viscosity curves made for samples taken from RM-products formed by one- and two-step processing procedures and made of HDPE and HDPE-PS/PES composites are presented in Fig. 2. The expected effect of introducing lignocellulosic fillers into the polymeric matrix is an increase in the viscosity [26]. In a considered case, using two varieties of fillers resulted in the opposite effect. Taking into account the results of our previous research related to the use of waste of plant origin with a high oil content (linseed cake) [27,28], the plasticizing effect resulting from the migration of oil from the filler during the technological process at elevated temperature, a gradual reduction in the viscosity of composites in the molten state is justified. At the same time, opposing effects of increasing viscosity caused by the presence of the HDPE-dispersed fraction and the plasticizing effect of reducing viscosity are observed. When using relatively low concentrations of fillers with a small fraction, the dominant phenomenon turned out to be the influence of oil. The presence of the polymeric bulk filler is evidenced by the gradual inflection of the curves in the range of small values of angular frequencies, observed in the case of concentrations of 10 and 15 wt%, which is related to hindering aggregated structures of rigid filler particles dispersed in polymeric bulk. Different rheological behaviors of composites with varying nutshells as fillers can be observed. In the case of composites containing PS, the lowest concentration of filler did not cause practically any changes in the relative viscosity curve of the reference material. However, a noticeably lower viscosity can be noted for the composite containing 2 wt% of PES. This effect is lower for melt processed series. It may be related to the better dispersed, smaller filler in HDPE. The significant reduction in viscosity in the case of PES-filled composites may result from, on the one hand, the higher oil content in the filler and its lower viscosity compared to pistachio oil [29,30].

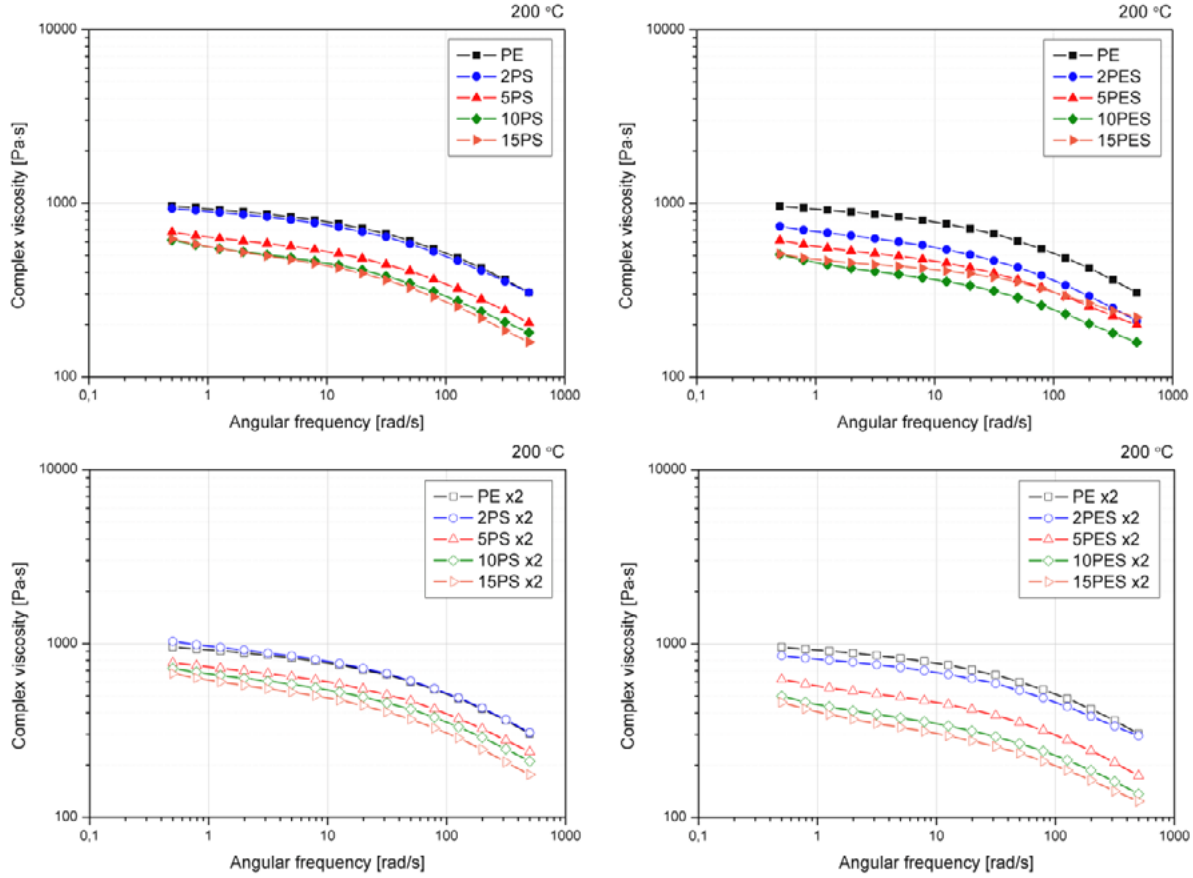

Figure 2. Complex viscosity curves of HDPE and HDPE-PS/PES composites.

Table 2 lists the mechanical properties determined in the static tensile test (elastic modulus - E, tensile strength - Rm), impact strength (a_K), and porosity determined by μCT. Introducing fillers into the polyethylene structure resulted in a gradual decrease in the elastic modulus and an increasing share of fillers. Reinforcing the effect of the presence of rigid filler structures in the PE matrix has been suppressed by two phenomena. The first is the plasticizing effect resulting in the oil migration from the filler, as described in [27]; the reduction in stiffness can also be associated with the increasing porosity of the composite. While nut shells were already introduced into the PE [31], causing an increase in stiffness, in the case of the RM, the much longer exposure time to elevated temperature during the technological cycle probably resulted in an intensification of the oil migration process into the polymer. In the case of all series produced with the two-step method (x2), the values of both elastic modulus and tensile strength are higher than for one-step processing (x1). This is related to the much lower porosity due to the use of regulated polymer filler particles dispersed in composite powder, as well as to the better dispersion of the filler in the matrix. Composites containing PES were characterized by increased porosity compared to the PS-filled series, resulting in worse mechanical properties. An agglomerated finely dispersed filler (PES) structure cannot be ruled out, as it accumulates stresses during loads. Powder fillers with regular shapes and limited relative adhesion of the polymer form micro notches, causing stress accumulation [32], mainly observed in dynamic loads. The impact strength values were significantly reduced due to the addition of both fillers. A more significant decrease in a_K was observed for PES composites. While a favorable melt-processing effect was observed in the case of PS-filled composites, the a_K values for the PES series were lower for most concentrations than for the composites formed using the physical mixing procedure.

Table 2. Mechanical properties of rotomolded HDPE and its' composites.

Material	*E [MPa]*	*Rm [MPa]*	*a_K [kJ/m^2]*	*Porosity [%]*
PE x1	1140 (45)	22.8 (0.7)	16.5 (1.8)	0.01
PE x2	1160 (57)	25.8 (0.9)	16.0 (2.9)	0.04
2PS x1	1040 (60)	20.7 (1.8)	7.13 (1.5)	2.83
2PS x2	1200 (24)	24.7 (0.9)	22.1 (5.8)	0.05
5PS x1	1090 (40)	19.5 (1.1)	4.6 (0.9)	3.99
5PS x2	1150 (46)	21.9 (1.5)	7.7 (1.4)	0.49
10PS x1	1020 (44)	14.8 (0.9)	3.5 (0.7)	6.39
10PS x2	1200 (27)	20 (0.8)	5.8 (2.1)	1.98
15PS x1	948 (36)	11.8 (0.8)	3.5 (0.8)	10.04
15PS x2	1150 (20)	15.1 (0.4)	3.3 (1.1)	7.97
2PES x1	1040 (29)	20.7 (0.4)	9.2 (1.8)	3.24
2PES x2	1100 (72)	23 (1.46)	9.4 (2.2)	0.39
5PES x1	897 (27)	15.7 (0.8)	6.4 (1.1)	7.05
5PES x2	1010 (21)	21.9 (0.9)	6.0 (1.0)	1.35
10PES x1	816 (15)	11.9 (0.6)	4.6 (0.7)	11.79
10PES x2	949 (50)	16.9 (0.9)	3.7 (0.8)	8.59
15PES x1	662 (53)	8.4 (0.8)	3.4 (0.7)	15.36
15PES x2	915 (72)	15.1 (0.7)	3.6 (0.4)	9.4

Table 3 presents the OIT values for polyethylene and composites formed in one- and two-step processing. Based on the change in the OIT value recorded for pure PE, it can be concluded that the process and the associated exposure to oxidizing conditions resulted in a decrease in the thermo-oxidative resistance of the polymer. This can be attributed to the formation of free radicals due to the extrusion process in the presence of high shear forces. The introduction of both fillers increased OIT compared to unfilled HDPE. More favorable results were measured for PES-filled composites. Taking into account the determined TAEC values, this effect was expected. The reduction in the OIT value in the case of composites subjected to two-stage preparation is related to the consumption of antioxidant compounds during extrusion. It should be emphasized that the resistance to melt oxidation was increased in the case of both nut varieties used.

Table 2. Oxygen induction time.

Filler amount wt%	Oxygen Induction Tim (OIT) [min]			
	PS x1	*PES x1*	*PS x2*	*PES x2*
0	69.2		16.4	
2	81.2	100.4	54.7	57.3
5	85.8	100.8	60.0	65.8
10	94.4	105.7	71.2	77.2
15	96.8	110.9	85.4	88.9

4. Conclusions

The completed tests allowed to successfully obtain composites in the RM process using two varieties of nut shells. It has been shown that it is possible to get a simultaneous interaction of the oil contained in the plant-originated filler as a plasticizer and stabilizer, increasing the resistance of the composite to thermooxidation. The use of a two-stage composite processing method, including initial homogenization of the composition using twin-screw co-rotating extrusion before pulverization, allowed for improvement in processability (limited porosity) and mechanical properties (higher tensile and impact strength) of rotomolded products compared to those made with the one-step procedure (physically mixed powdered polymer and fillers). Simultaneously, the oxidation resistance assessed by oxygen induction time (OIT-DSC) has been significantly improved after adding plant-based fillers; however, it reduced

in the case of melt-mixed composites. The PES-containing composites showed significantly higher oxidation resistance than the PS-filled series. It was found that a certain amount of antioxidants was consumed during melt-processing and rotomolding in the oxidative atmosphere, suppressing polyethylene process degradation, as a result of which the polymer was stabilized, but the number of active compounds in the final product was limited.

Acknowledgments
This work was funded under the project "Research on the influence of the polymer composites processing conditions on the stabilizing effect of functional plant-derived fillers" SONATA-17 2021/43/D/ST8/01491, funded by the National Science Center.

References

[1] J. L. Throne and M. -S. Sohn, Characterization of rotational molding grade polyethylene powders, Advances in Polymer Technology, 9:181–192,1989.
[2] K. O. Ogila, M. Shao, W. Yang and J. Tan, Rotational molding: A review of the models and materials, Express Polymer Letters, 11:778–798, 2017.
[3] M. A. Rao and J. L. Throne, Principles of rotational molding, Polymer Engineering and Science, 12(4):237–264, 1972.
[4] K. Głogowska, F. Longwic and K. Ludziak, Effect of mould speed on selected properties of moulded parts and energy consumption in rotational moulding, Bulletin of the Polish Academy of Sciences Technical Sciences, 70(5):143106–143106, 2022.
[5] A. Vignali, R. Utzeri, M. Canetti and F. Bertini, Crystallization Behavior of Poly(ε-Caprolactone)-Hollow Glass Microspheres Composites for Rotational Molding Technology, Polymers, 14(20):4326, 2022.
[6] Z. Ortega, M. D. Monzón, A. N. Benítez, M. Kearns, M. McCourt and P. R. Hornsby, Banana and Abaca Fiber-Reinforced Plastic Composites Obtained by Rotational Molding Process, Materials and Manufacturing Processes, 28(8):879-883, 2013.
[7] R. H. López-Bañuelos, F. J. Moscoso, P. Ortega-Gudiño, E. Mendizabal, D. Rodrigue and R. González-Núñez, Rotational molding of polyethylene composites based on agave fibers, Polymer Engineering and Science, 52(12):2489–2497, 2012.
[8] J. Aniśko, D. Bartczak and M. Barczewski, Limitations of Short Basalt Fibers Use as an Effective Reinforcement of Polyethylene Composites in Rotational Molding Technology, Advances in Science and Technology Research Journal, 17(3):110–123, 2023.
[9] A. Arribasplata-Seguin, R. Quispe-Dominguez, W. Tupia-Anticona and J. Acosta-Sullcahuamán, Rotational molding parameters of wood-plastic composite materials made of recycled high density polyethylene and wood particles, Composites Part B: Engineering, 217:108876, 2021.
[10] J. Aniśko, M. Barczewski, A. Piasecki, K. Skórczewska, J. Szulc and M. Szostak, The Relationship between a Rotational Molding Processing Procedure and the Structure and Properties of Biobased Polyethylene Composites Filled with Expanded Vermiculite, Materials, 15(17):5903, 2022.
[11] S. Díaz, Z. Ortega, M. McCourt, M.P. Kearns and A.N. Benítez, Recycling of polymeric fraction of cable waste by rotational moulding, Waste Management, 76:199–206, 2018.
[12] Z. Ortega, L. Suárez, J. Kelly-Walley and M. McCourt, Mechanical properties of rotomolded parts with abaca fiber: effect of manufacturing with 1, 2 or 3 layers, Composites Theory and Practice, 23(3):158–166, 2023.
[13] Z. Ortega, P. Douglas, P. R. Hanna, J. Kelly-Walley and M. McCourt, Influence of mold pressurization on cycle time in rotational molding composites with welded ignimbrite as loading, Composites Communications, 45:101797, 2024.
[14] Z. Ortega, L. Suárez, J. Kelly-Walley, P. R. Hanna, M. McCourt and B. Millar, Use of Pressure in Rotational Molding to Reduce Cycle Times: Comparison of the Thermomechanical Behavior of Rotomolded Reed/Polyethylene Composites, Journal of Composites Science, 8(1):17, 2024.
[15] A. S. M. Bashir and Y. Manusamy, Recent Developments in Biocomposites Reinforced with Natural Biofillers from Food Waste, Polymer-Plastics Technology and Engineering 54(1):87–99, 2015.

[16] J. Aniśko and M. Barczewski, Uniaxial Rotational Molding of Bio-Based Low-Density Polyethylene Filled with Black Tea Waste, Materials, 16(10):3641, 2023.
[17] M. I. Baumer, J. L. Leite and D. Becker, Influence of calcium carbonate and slip agent addition on linear medium density polyethylene processed by rotational molding, Materials Research, 17(1):130–137, 2013.
[18] O. Pınar, F. E. Koc, M. B. Alanalp, N. Sivri, A. Ezdesir and A. Durmus, Utilization of Silybum marianum extract as a high-performance natural antioxidant for polyethylene, Journal of Materials Science, 59:3725–3741, 2024.
[19] M. Barczewski, Z. Ortega, P. Piaskowski, J. Aniśko, P. Kosmela and J. Szulc, A case study on the rotomolding behavior of black tea waste and bio-based high-density polyethylene composites: Do active compounds in the filler degrade during processing?, Composites Part C: Open Access, 13:100437, 2024.
[20] M. Barczewski, M. Szostak, D. Nowak and A. Piasecki, Effect of wood flour addition and modification of its surface on the properties of rotationally molded polypropylene composites, Polimery, 63(11-12):772–784, 2018.
[21] M. Herkowiak, A. Osuch, E. Osuch, B. Waliszewska and G. Zając, Analysis of the Possibility of Management of Curly-Leaf Pondweed for Energetic Purposes, Energies, 14(17):5477, 2021.
[22] J. B. Engel, M. Mac Ginity, C. L. Luchese, I. C. Tessaro and J. C. Spada, Reuse of Different Agroindustrial Wastes: Pinhão and Pecan Nutshells Incorporated into Biocomposites Using Thermocompression, Journal of Polymers and the Environment, 28:1431–1440, 2020.
[23] M. Čolnik, M. Irgolič, A. Perva and M. Škerget, The Conversion of Pistachio and Walnut Shell Waste into Valuable Components with Subcritical Water, Processes, 12(1):195, 2024.
[24] C. E. Okonkwo, S. Z. Hussain, H. Onyeaka, A. A. Adeyanju, C. O. Nwonuma, A. A. Bashir, A. Farooq, C. Zhou and T. D. Shittu, Lignin polyphenol: From biomass to innovative food applications, and influence on gut microflora, Industrial Crops and Products, 206:117696, 2023.
[25] F. S. P. P. Neto, E. A. de Lucca and F. Masarin, Particle Size Influence on the Chemical Composition from Waste Eucalyptus in the Processing for Industrial Production of Cellulose Pulp, Chemical Engineering Transactions, 50:337–342, 2016.
[26] V. Mazzanti and F. Mollica, A Review of Wood Polymer Composites Rheology and Its Implications for Processing, Polymers, 12(10):2304, 2020.
[27] M. Barczewski, O. Mysiukiewicz and A. Kloziński, Complex modification effect of linseed cake as an agricultural waste filler used in high density polyethylene composites, Iranian Polymer Journal, 27:677–688, 2018.
[28] M. Barczewski, O. Mysiukiewicz, J. Szulc and A. Kloziński, Poly(lactic acid) green composites filled with linseed cake as an agricultural waste filler. Influence of oil content within the filler on the rheological behavior, Journal of Applied Polymer Science, 136(24):47651, 2019.
[29] A. Rabadán, J. E. Pardo, R. Gómez, A. Alvarruiz and M. Álvarez-Ortí, Usefulness of physical parameters for pistachio cultivar differentiation, Scientia Horticulturae, 222:7–11, 2017.
[30] K. Okafor, M. Danjaji and M. Figura, Viscosity Modeling and Flow Properties of Non-Edible Oils as Feed- Stocks in Biodiesel Production, International Journal of Earth & Environmental Sciences, 4:162, 2019.
[31] K. Salasinska and J. Ryszkowska, The effect of filler chemical constitution and morphological properties on the mechanical properties of natural fiber composites, Composite Interfaces, 22(1):39–50, 2015.
[32] V. Švehlová and E. Polouček, About the influence of filler particle size on toughness of filled polypropylene, Die Angewandte Makromolekulare Chemie, 153(1):197–200, 1987.

INCREASING THE TENSILE PROPERTIES OF A UNIDIRECTIONAL/MAT DRY REINFORCEMENT FOR COMPOSITE APPLICATIONS VIA THE ADDITION OF NANOCELLULOSE COMBINED WITH CLICK CHEMISTRY MODIFICATIONS

A.Blal[1], G.Lebrun[1,2], E.Loranger[1,2] and F.brouillette[1,3]

[1]Innovations Institute in Ecomaterials, Ecoproducts and Econergies biomass based (I2E3)
[2]Department of Mechanical Engineering
[3]Department of Chemistry, Biochemistry, and Physics
Université du Québec à Trois-Rivières (UQTR), 3351 boul. des Forges, C.P. 500, (QC) G9A 5H7
Trois-Rivières, Canada
abdelhadi.blal@uqtr.ca, Gilbert.Lebrun@uqtr.ca, Eric.Loranger1@uqtr.ca,
Francois.Brouillette@uqtr.ca

Keywords: Nanocellulose, Flax fiber, Surface treatment, Click-chemistry, Mechanical properties

Abstract
The mechanical characteristics of natural fiber composites (NFCs) are closely linked to the properties of fiber-matrix and fiber-fiber interfaces [1]. These properties can be enhanced through physical or chemical modifications of the resin or fibers [2]. One effective strategy consists in creating covalent bonds between the fibers using the Huisgen cycloaddition also known as click chemistry [3]. This study focuses on the click chemistry modification of flax fibers used in unidirectional-mat (UDM) flax reinforcements. The objective is to create enhanced reinforcements for composite applications. The fibers undergo a three-step process for functionalization: the surface fibrillation of short flax fibers, a chemical pretreatment to clean and remove different surface chemicals, and finally the fiber functionalization using click chemistry. In addition, fiber compaction and the integration of nanocellulose was considered to further strengthen the dry reinforcement for its use in composites. The developed reinforcements undergo testing to evaluate their performance in tension and elongation. The results demonstrate significant enhancements in the force per unit width , elongation at break, and tensile stiffness.

1. Introduction

In recent years, the quest for sustainable and eco-friendly materials has led to a significant shift towards the use natural fiber-reinforced composites in various industries, including construction, automotive, and aerospace. Unlike synthetic fibers, natural fibers such as flax, hemp, and jute offer environmental benefits, including biodegradability and a lower carbon footprint, while also providing cost-effective alternatives to traditional reinforcement materials [4]. Despite their advantages, the full potential of natural fibers in composite applications has yet to be realized, primarily due to limitations related to the fiber-matrix interface and the mechanical properties of the fibers themselves. The performance of natural fiber composites is fundamentally governed by the interactions at the fiber-matrix interface. These interactions are crucial for stress transfer and the overall mechanical integrity of the composites [5]. Traditional methods to enhance these interactions have focused on mechanical and chemical treatments aimed at improving the surface properties of the fibers [6]. Among the forefront of innovative solutions is the application of click chemistry, particularly the Huisgen 1,3-dipolar cycloaddition. This chemical strategy offers a mechanism to create strong covalent bonds, enhancing the fiber-fiber and fiber-matrix adhesion significantly more effectively than traditional treatments [7]. Furthermore, the integration of

nanocellulose into the fiber reinforcement presents an opportunity to further reinforce the composite materials. Nanocellulose, due to its high strength and stiffness, can significantly impact the mechanical properties of the fiber reinforcements when appropriately integrated [8].
This study aims at addressing the aforementioned challenges by exploring a novel approach to enhance the mechanical properties of unidirectional-mat (UDM) flax fiber reinforcements through a combination of click chemistry reactions and nanocellulose integration. By systematically investigating the effects of surface fibrillation, chemical cleaning, and chemical treatments, we seek to develop an optimized reinforcement material. FTIR and EDX analyses of the fibers obtained at each intermediate stages (alkaline pretreated, propargylated, tosylated, azidated, and crosslinked) will be performed to confirme the presence of expected chemical functions on the surface of the modified fibers and their degrees of substitution. Tensile tests are finally performed on the dry reinforcements to validate the influence of the treatments on the dry properties.

2. Experimental methods

2.1. Materials.

Flax fibers were sourced from Safilin Inc. (Szczytno, Poland), provided as a Tex 5000 ribbon, which was cut into short fibers (approximately 6 ± 1 mm in length) to be used in the mat layer of the reinforcement, and a Tex 400 yarn for the unidirectional (UD) layer. Chemicals including propargyl bromide (80% in toluene), p-toluenesulfonyl chloride, and sodium azide were obtained from Alfa Aesar (Haverhill, Massachusetts, USA). Sodium hydroxide and copper sulfate pentahydrate ($CuSO_4 \cdot 5H_2O$) were obtained from Acros Organics (Geel, Belgium). Dimethylformamide (DMF), sodium ascorbate, and triethylamine were supplied by Sigma-Aldrich (Saint Louis, Missouri, USA). A commercial bleached softwood kraft pulp was provided by Fraser Paper (Thurso, Canada), the catalyst 4-acetamido-TEMPO is purchased from Sigma-Aldrich (Canada) and the sodium bromide from Fisher Scientific (Canada). The sodium hypochlorite used is 6 % concentrated as found in supermarkets.

2.2. Alkaline pretreatment and fibrillation of flax fibers.

For this procedure, 25 g of dry short flax fibers (cut from the Tex 5000 ribbon), were initially immersed in 2 liters of deionized water, for no less than four hours, ensuring complete saturation. The fiber suspension was then processed in a pulp disintegrator at 1000 rpm for ten minutes to achieve a uniformly dispersed fiber slurry. Both short and UD fibers were immersed in a 5 w/w NaOH solution for 24 hours at room temperature to enhance the accessibility of reactive cellulose hydroxyl (OH) groups by removing a fraction of other surface components such as pectin, lignin, and hemicelluloses. Then, fibers underwent a thorough rinsing process with water and acidified water (pH around 4) to neutralize any residual NaOH, followed by another rinsing with water to ensure complete removal of alkaline residues. To further increase the specific surface area, the alkaline pretreated short fibers were subjected to mechanical fibrillation, according to the method of Amir et al. [9], using a PFI laboratory refiner. Finally, the pretreated fibers were dispersed in a 2.5% w/v alkaline solution and stirred for 30 minutes to homogenize.

2.3. Preparation of nanocellulose.

A nanocellulose gel was prepared from oxidized kraft pulp fibers using a shear processing approach facilitated by an IKA defibrillation system (figure 1), according to the procedure described by Lassoued et al. [10]. First, 30 g of dry kraft pulp fibers were dispersed in deionized water. Concurrently, 2.2 g of TEMPO and 5 g of sodium bromide were dissolved in a minimal volume of deionized water. This solution was then introduced into the reactor. Additional deionized water was added to adjust the total volume to 3 L at a 1% consistency. The temperature of the mixture was maintained at 25°C, and the pH was regulated between 10 and 11. The oxidation reaction was initiated by adding 250 ml of sodium hypochlorite and allowed to proceed for two hours. The reaction was terminated by adding 75 ml of 3% hydrogen peroxide to neutralize any remaining sodium hypochlorite. The oxidized pulp was then filtered

and weighted. This oxidized pulp was transferred to a Plexiglas tank connected to a defibrillation system, which included a pump, a defibrillator, and a bubble cooler to control the heat generated during defibrillation. The defibrillation process lasted two hours and progressively increased the viscosity of the mixture, resulting in the formation of a nanocellulose gel. This method successfully yielded a 2.5% nanocellulose gel with a carboxylate content of 1559,7 mmol/kg.

Figure 1. System for mechanical treatment of oxidized cellulose fibers using an IKA homogenizer.

2.4. Click chemistry reactions.

Chemical modifications of flax fibers followed a series of treatments described in previous works by Blal et al. [3]. Initially, pretreated flax fibers were immersed in in a basic solution (2.5% w/v) with 114 ml of propargyl bromide and stirred at room temperature for 10 days to obtain the propargylated fibers (Pr). The next step was tosylation, where the fibers, after a 24-hour NaOH pretreatment and fibrillation to further activate their surface, were introduced into a mixture of 166 ml triethylamine and 221 g of tosyl chloride, yielding tosylated fibers (Ts). For the azidated fibers (Az), 55 g of sodium azide was added to Ts fibers suspended in 2 L of DMF, heated at 75°C, and stirred for 10 days, followed by a cooling phase and thorough cleaning. The final stage of this process was the cross-linking, where Pr and Az fibers were combined in equal proportions (50% propargylated and 50% azidated fibers) and reacted under ambient conditions for a period of 10 days to obtain triazole formation through the click chemistry reaction. For this final click chemistry reaction, short flax fibers were azidated while the unidirectional fibers underwent propargylation, a strategic choice to leverage different chemical functionalities for optimal reinforcement.

2.5. Characterization of treated fibers.

Treated fibers were analyzed using a Thermo Scientific Nicolet iS10 FT-IR spectrophotometer for infrared spectroscopy, capturing 32 scans at room temperature with a resolution of ± 4 cm^{-1} to identify the chemical modifications. Morphological changes were examined via a Hitachi SU1510 scanning electron microscope (SEM) in secondary electron mode, using a 100 mA beam current and 15 kV accelerating voltage. Complementary chemical characterization was provided by energy-dispersive X-ray spectroscopy (EDX, Oxford X-Max 20 mm^2 instrument) on metallized, ground samples, offering insights into the elemental composition at the nanometer scale..

2.6. Fabrication of reinforcement and mechanical characterization.

The fabrication of UDM flax reinforcements was realized using a dynamic former (from ALIMAND Inc., France), following a procedure well detailed in previous works [9, 11]. The process yielded various reinforcements with a basis weight of 300 g/m^2 (composed of around 250 g/m^2 for the UD layer and 50 g/m^2 for the mat binder) designed to assess the impact of different fiber treatments on mechanical performance. The assortment of reinforcements included the untreated UDM (serving as reference) and those subjected to treatments such as fibrillation (UDM-FIB), compaction (UDM-COMP), a combination of fibrillation and compaction (UDM-FIB-COMP), and fibrillation followed by click chemistry treatment (UDM-FIB-CLICK). Additionally, to evaluate the effect of nanocellulose integration, reinforcements were produced with varying nanocellulose contents (1.5%, 3%, 6%, and 9% by weight), labeled as UDM-1.5, UDM-3, UDM-6, and UDM-9, respectively. Further variations included treatments combining fibrillation, compaction, and 3% nanocellulose (UDM-FIB-COMP-3), as well as fibrillation, click chemistry modification, and 3% nanocellulose (UDM-FIB-CLICK-3). Mechanical characterization was conducted through tensile tests on samples measuring 25 mm by 150 mm to evaluate the tensile stiffness, elongation at break, and strength per unit width of the reinforcement. These tests were performed using an Instron-U150 LM equipped with a 10 kN load cell, with a constant speed of 2 mm/min (following ASTM D3039 standard).

3. Results and Discussion

3.1. FTIR Analysis

Figure 2 shows FTIR curves of Pr, Az, and unmodified flax fibers, confirming the successful grafting Pr and Az functional groups onto the fiber surface. The untreated fibers, designated as Flax-RAW, displayed characteristic absorption peaks for C-H stretching vibrations within the 2900-3000 cm^{-1} range and C-O vibrations at 1050-1100 cm^{-1}, serving as our control for subsequent comparisons. In treated fibers, the propargylation was confirmed by the appearance of a new peak around 2100-2200 cm^{-1}, attributed to the triple bond of the propargyl group. Azidation introduced a new band at 2112 cm^{-1}, corresponding to the -N=N-N- group vibration, indicating the successful addition of the azide group. In addition, the bands associated with hydroxyl groups change in intensity and position, due to their reaction with propargyl bromide and azide sodium. These changes in the FTIR spectrum confirm that the flax fibers have been modified by the propargylation and azidation reaction.

3.2. SEM-EDX Analysis

Surface and compositional changes of flax fibers due to various treatments were thoroughly investigated via Scanning Electron Microscopy (SEM) and corroborated by Energy-Dispersive X-ray (EDX) analysis. Table 1 shows the EDX results, highlighting the elemental compositions by percentage and the degree of substitution (DS) across various stages of chemical treatments of flax fibers. Flax-Raw fibers show an O/C ratio of 0.53, indicating the natural state of the fibers with prevalent hydroxyl groups. After the NaOH treatment, fibers display a decrease in carbon to 58.6% and an increase in oxygen to 40.0%, increasing the O/C ratio to 0.68. This change suggests the exposure and increase of hydroxyl groups due to the removal of non-cellulosic substances. Following the propargylation, fibers exhibit a significant modification with a carbon increase and an oxygen reduction, leading to a lower O/C ratio of 0.46 and a DS of 2.52. These changes imply a successful substitution of hydroxyl groups with more carbon-rich propargyl groups. The intermediate reaction of tosylation shows a further increase in carbon content to 75.8%, a drop in oxygen to 20.5%, and the appearance of sulfur at 2.8%, with the lowest O/C ratio observed at 0.27 and the highest DS of 2.68. This indicates a dense incorporation of tosyl groups, to facilitate the azidation reaction. After azidation, the carbon further decreased to 60.2%, and oxygen increased at 33.7%, The presence of nitrogen at 4.5%, and a low sulfur presence at 0.7% were also observed. The DS is 2.09, and the O/C ratio adjusts to 0.56. The introduction of nitrogen indicates successful azidation, preparing the fibers for subsequent click chemistry reactions.

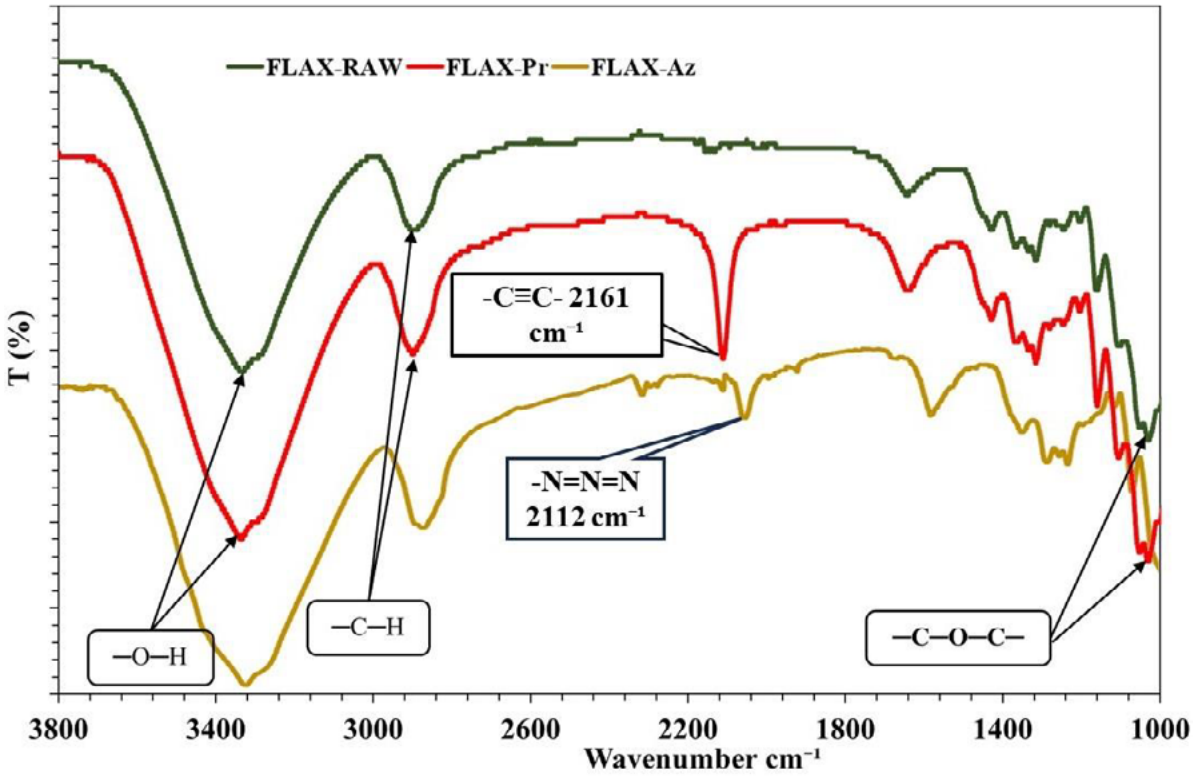

Figure 2. FTIR spectra of unmodified flax (RAW) and modified fibers (propargylated (Pr), and azidated (Az)).

Table 1. Chemical composition and degree of substitution for chemically treated flax fibers.

Sample	Element (EDX atomic %)				O/C	Surface DS
	C	O	S	N		
Flax-Raw	65,4	34,4	-	-	0,53	-
Flax-NaOH	58,6	40,0	-	-	0,68	-
Flax-Pr	68,3	31,5	-	-	0,46	2,52
Flax-Ts	75,8	20,5	2,8	-	0,27	2,68
Flax-Az	60,2	33,7	0,7	4,5	0,56	2,09

3.3. Mechanical testing of flax unidirectional-mat

The tensile characterization (Figures 3 to 5) of the flax UD-Mat reinforcements clearly demonstrate the efficiency of the individual and combined treatments. Using the the untreated UDM as reference, after adding nanocellulose a notable enhancement in the mechanical properties is observed. The 3% nanocellulose content of UDM-3 yielded a 109% increase in strain at break, enhancing flexibility. Meanwhile, UDM-6 achieved a 141% improvement in force per unit width at break to 27.7 kN/m, indicating a highly improved load-bearing capacity. However, a further increase in nanocellulose to 9% resulted in a performance decline, demonstrating the possible negative effect of nanocellulose aggregation, This hypothesis aligns with known challenges in achieving uniform dispersion at higher concentrations. Fibrillation treatment (UDM-FIB) alone also had a positive impact, with a 101% increase in the mean force per unit width, demonstrating the importance of interfacial bonding within the fiber network. When combined with 3% nanocellulose (UDM-FIB-3), an additional increase in the

CONTENTS

tensile stiffness of 64% is observed, underscoring the benefit of integrating this physical treatments. The addition of compaction with fibrillation and nanocellulose (UDM-FIB-COMP-3) didn't significantly

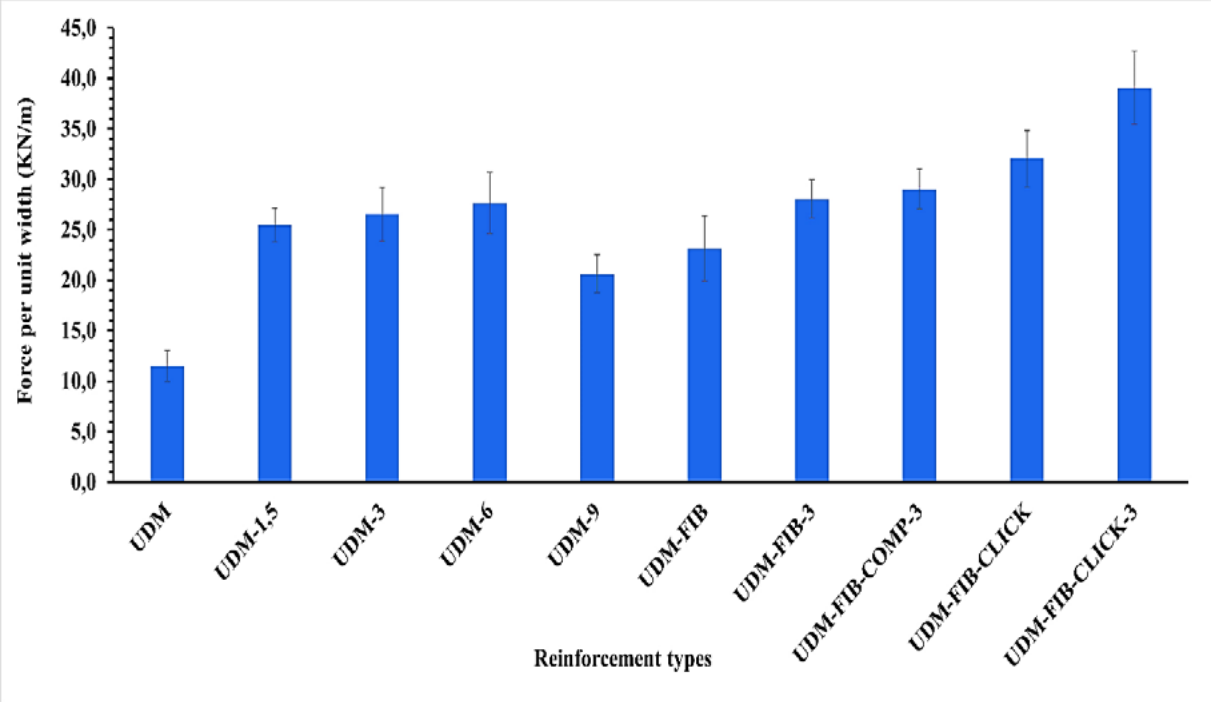

Figure 3. Force per unit width across different treatments of flax UD-Mat reinforcements.

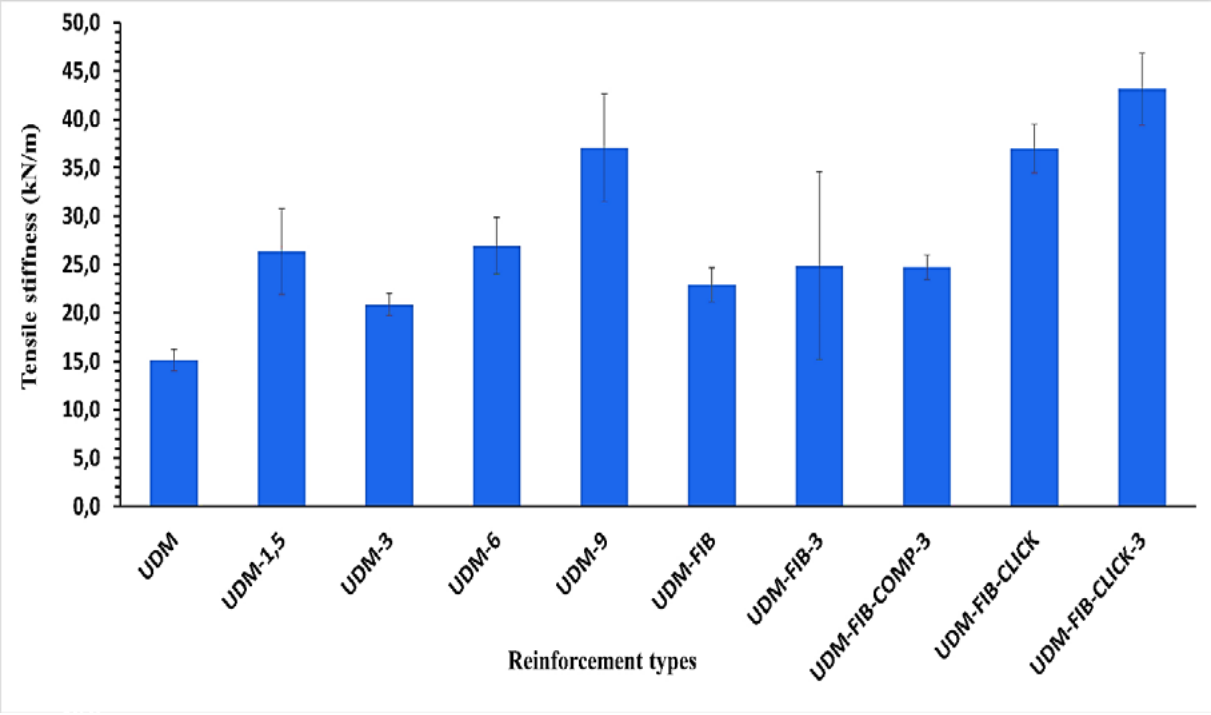

Figure 4. Tensile stiffness enhancement in flax UD-Mat reinforcements post various surface treatments

alter the tensile stiffness, which remained at around 24.7 kN/m, suggesting a saturation point (at least for the dry reinforcement) in the benefits derived from physical treatments. The introduction of click chemistry (UDM-FIB-CLICK) marked the most substantial improvements, with a 179% enhancement in force per unit width and a 145% increase in tensile stiffness. This trend peaked with the UDM-FIB-CLICK-3 variant, which combined fibrillation, click chemistry, and a 3% nanocellulose concentration, resulting in the highest enhancements across all measured properties. A 239% increase in force per unit width to 39.1 kN/m, and a remarkable 185% improvement in tensile stiffness to 43.1 kN/m and a significant increase in ductility, as shown by a 140% rise in elongation at break, are observed. The intrinsic mechanical strength of nanocellulose, along with the functionality of surface carboxyl groups, contributed to this improved performances by facilitating increased bonding through hydrogen.

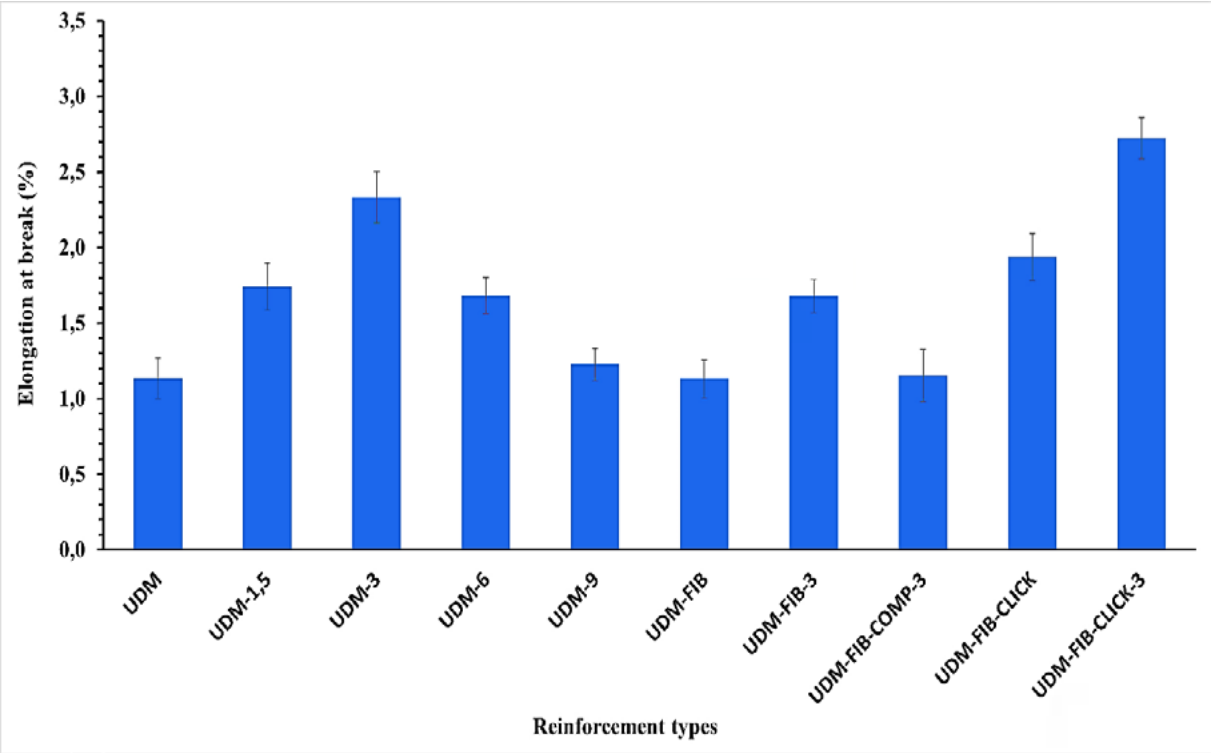

Figure 5. Comparative elongation at break of flax UD-Mat reinforcements with varied treatments

3. Conclusions

This study presents a comprehensive examination of the mechanical enhancements achieved through various treatments on flax fiber reinforcements. The integration of nanocellulose, fibrillation, and click chemistry have shown significant improvements in the mechanical properties of the dry flax UDM reinforcement, underscoring the potential for these treatments for composite applications. The addition of nanocellulose, particularly at 3% by weight, significantly increased the tensile properties. The largest tensile improvements were realized when the click chemistry treatment was applied, which facilitated strong covalent bonding within the fiber network. The UDM-FIB-CLICK-3 samples, combining fibrillation, 3% nanocellulose, and click chemistry, exhibited the highest tensile stiffness and force per unit width among all variants tested. Globally, the tensile tests performed on dry and treated UD-mat reinforcements showed maximum increases in the force per unit width, elongation at break, and tensile stiffness of up to 239%, 140% and 185% compare to the base untreated UDM respectively. This finding highlights the effectiveness of a multifaceted treatment approach, suggesting that the interplay between physical and chemical modifications can be tailored to meet specific mechanical requirements.

Acknowledgments

The authors gratefully acknowledge the financial support of the Natural Sciences and Engineering Research Council of Canada (NSERC).

References

[1] K. L. Pickering, M. G. A. Efendy, and T. M. Le, "A review of recent developments in natural fibre composites and their mechanical performance," *Composites Part A: Applied Science and Manufacturing*, vol. 83, pp. 98–112, Apr. 2016
[2] S. B. Hosseini, M. Gaff, H. Li, and D. Hui, "Effect of fiber treatment on physical and mechanical properties of natural fiber-reinforced composites: A review," *Reviews on advanced materials science,* vol. 62, no. 1, Jan. 2023
[3] A. Blal, F. Brouillette, É. Loranger, and G. Lebrun, "Click chemistry modifications for the selective crosslinking of wood pulp fibers – effect on the physical and mechanical properties of paper," *RSC Advances*, vol. 14, no. 14, pp. 9656–9667, 2024
[4] M. Y. Khalid, A. Al Rashid, Z. U. Arif, W. Ahmed, H. Arshad, and A. A. Zaidi, "Natural fiber reinforced composites: Sustainable materials for emerging applications," *Results in Engineering,* vol. 11, p. 100263, Sep. 2021
[5] M. Mohammed et al., "Interfacial bonding mechanisms of natural fiber-matrix composites: An overview," *BioResources*, vol. 17, no. 4, Aug. 2022
[6] A. Ramachandran, S. Mavinkere Rangappa, V. Kushvaha, A. Khan, S. Seingchin, and H. N. Dhakal, "Modification of Fibers and Matrices in Natural Fiber Reinforced Polymer Composites: A Comprehensive Review," *Macromolecular Rapid Communications*, vol. 43, no. 17, Jun. 2022,
[7] M. Wang et al., "Chemical grafting of nano-SiO2 onto graphene oxide via thiol-ene click chemistry and its effect on the interfacial and mechanical properties of GO/epoxy composites," *Composites Science and Technology*, vol. 182, p. 107751, Sep. 2019
[8] F. Ferreira, I. Pinheiro, S. de Souza, L. Mei, and L. Lona, "Polymer Composites Reinforced with Natural Fibers and Nanocellulose in the Automotive Industry: A Short Review," *Journal of Composites Science*, vol. 3, no. 2, p. 51, May 2019
[9] A. Bernaoui, G. Lebrun, and E. Ruiz, "High-performance natural fiber composites from mat and UD flax reinforcements backed with a mat Binder: A study of mat fiber surface fibrillation," *Composites Part A: Applied Science and Manufacturing*, vol. 160, p. 107064, Sep. 2022
[10] M. Lassoued, F. Crispino, and E. Loranger, "Design and synthesis of transparent and flexible nanofibrillated cellulose films to replace petroleum-based polymers," *Carbohydrate Polymers*, vol. 254, p. 117411, Feb. 2021.
[11] R. S. Mbakop, G. Lebrun, and F. Brouillette, "Effect of compaction parameters on preform permeability and mechanical properties of unidirectional flax fiber composites," *Composites Part B: Engineering*, vol. 176, p. 107083, Nov. 2019.

FUNCTIONALIZED GRAPHENE OXIDE/ EPDM COMPOSITES WITH ENHANCED BARRIER PROPERTIES

Zhehong Lu[1,2], Yuan Zhang[1], Ziqiang Zhu[1], Yubing Hu[1], Wei Jiang[1,*]

[1]National Special Superfine Powder Engineering Research Center of China, School of Chemistry and Chemical Engineering, Nanjing University of Science and Technology, Nanjing, 210094, China
[2]School of Mechanical and Aerospace Engineering, Queen's University Belfast, Belfast, BT9 5AH, UK

Abstract
Ethylene Propylene Diene Terpolymer Rubber (EPDM) is an excellent sealing material for spacecraft, attributed to its commendable chemical resistance, weather resistance, and low density. In this work, sulfur-graphene oxide (S-GO) hybrids were prepared by in-situ growth of sulfur on the surface of GO sheets through the reaction between thiosulfate and hydrochloric acid. The incorporation of S-GO hybrids into EPDM, facilitated by the emulsion compounding method, serves to further fortify its barrier performance against plasticizer migration. As the contact area between GO and sulfur particles increases, the degree of reaction between GO and sulfur increases, thereby constructing a chemical covalent cross-linked interface of GO-S-EPDM. These strong interfaces and complex filler network contribute to a notable reduction of 24.9% and 14.1% in plasticizer migration for S-GO/EPDM in comparison to pure EPDM and GO/EPDM, respectively. This research not only advances the understanding of high-barrier EPDM composites but also provides valuable insights for their industrial applications.

Keywords: EPDM, Graphene oxide, Barrier properties, Rubber composites

1. Introduction

Rubber composites find extensive applications across diverse sectors, including aerospace, chemical protective equipment, and sealing rings due to their high elasticity, great barrier performance and excellent compressibility recovery[1-3]. In particular, Ethylene Propylene Diene Terpolymer Rubber (EPDM), with its remarkable chemical resistance, weather resistance, and low density, has become an ideal sealing material for spacecraft[4-6]. However, since the use temperature of EPDM composites is above its glass transition temperature, resulting a significant amount of free volume within the composites. This makes small molecule penetrants can easily pass through, consequently reducing the barrier properties of EPDM composites.

To effectively improve the barrier properties of EPDM composites, adding nano-fillers to the EPDM matrix is undoubtedly a simple and efficient approach. These nanoparticles include graphene, montmorillonite, titanium dioxide, carbon nanotubes, and so on[7-10].Graphene oxide (GO) is an ideal filler to enhance the barrier properties of EPDM composites. As a derivative sharing a structural similarity to graphene, GO can get a better overall performance of composites while only using a tiny filling amount compared with traditional nanofillers. In recent years, GO has been widely used to enhance the barrier properties of polymers due to its excellent polymer compatibility, wide specific surface area and easy modification[11]. GO nanosheets have a larger specific surface area, which enables them to form better barrier effects when dispersed in polymers[12]. Meanwhile, GO has excellent strength and hardness, which enables it to increase strength in composites and provide excellent mechanical stability[13]. Furthermore, GO exhibits favorable compatibility with numerous polymers, enabling its effective dispersion within the polymer matrix to create composites with outstanding overall properties [14]. However, due to the presence of oxygen-containing groups of GO, there is a problem of poor interfacial compatibility between GO and EPDM. Therefore, surface modification of GO is required to improve the interfacial interaction between GO and rubber molecular chains to further improve the barrier properties.

In this work, sulfur-graphene oxide (S-GO) hybrids were prepared by in-situ growth of sulfur on the surface of GO sheets through the reaction between thiosulfate and hydrochloric acid. The incorporation of S-GO hybrids into EPDM, facilitated by the emulsion compounding method, serves to further fortify its barrier performance against plasticizer migration. As the contact area between GO and sulfur particles increases, the degree of reaction between GO and sulfur increases, thereby constructing a chemical covalent cross-linked interface of GO-S-EPDM. These strong interfaces and complex filler networks contribute to a notable reduction of 24.9% and 14.1% in plasticizer migration for S-GO/EPDM in comparison to pure EPDM and GO/EPDM, respectively. This research not only advances the understanding of high-barrier EPDM composites but also provides valuable insights for their industrial applications.

2. Experimental

2.1. Materials

Natural graphite powder was sourced from The Sixth Element (Changzhou) Materials Technology Co., Ltd., China. Analytical-grade chemicals including potassium permanganate (KMnO4), concentrated sulfuric acid (H_2SO_4, 95–98%), ethanol, tetrahydrofuran (THF), hydrochloric acid (37%), and sodium nitrate were obtained from Aladdin Reagent Shanghai Co., Ltd., China. EPDM was procured from Lanxess Co., Ltd., Germany. Triallylisocyanurate (TAIC), zinc oxide, and stearic acid, $NH_3 \cdot H_2O$, sulfur powder (S), and antioxidant 1010 were provided by Sinopharm Chemical Reagent Co., Ltd., China.

2.2 Preparation of S-GO hybrids, GO/EPDM and S-GO/EPDM composites

GO was synthesized via a modified Hummers' method [15], while S-GO hybrid nanoparticles were prepared through the in situ growth of sulfur on GO sheets [16]. The sulfur content in S-GO hybrids was quantified at 39.92% using a vario EL cube elemental analysis instrument (Elementar Analysensysteme GmbH). EPDM and GO/S-GO were compounded using a two-roll mixing mill (LRM-S-150, Labtech) at a roll temperature of 40°C. The resulting composites underwent multiple extrusions within the roll gaps until reaching a thickness of less than 1 mm to ensure optimal filler dispersion. Subsequently, the composites were allowed to stand for 24 hours before being vulcanized in molds at 160°C and 15 MPa for 30 minutes. Formulation details for all composites are provided in Table 1.

Table 1. Formulations of the EPDM composites

Samples	EPDM	GO	SGO	ZnO	SA	4010NA	CZ	S
EPDM	100	-	-	5	1	2	2	2
GO/EPDM	100	3	-	5	1	2	2	2
S-GO/EPDM	100	-	5	5	1	2	2	-

2.3 Characterization

X-ray diffraction (XRD) analysis was performed using a D8 Advance instrument (Bruker, Germany). Surface morphology was examined via transmission electron microscopy (TEM, JEOL-2010). Oxygen permeability was determined using a gas transmissivity tester (VAC-V3) following GB/T 1038-2022 standards. Migration experiments were conducted using the immersion absorption method [17]. Cure characteristics were investigated according to ISO 6502 utilizing a rotorless vulcanizer (HD-R811-1).

3. Results and discussion

3.1 Characterization of S-GO Hybrids

Figure 1(a) displays the XRD patterns of sulfur, GO, and S-GO hybrids. In the sulfur pattern, two distinct peaks are evident at 23.1° and 27.7°, corresponding to the (222) and (040) reflections of orthorhombic α-sulfur S8 (JCPSD no. 08-0247). A sharp diffraction peak is observed at 10.88° for GO. In the case of S-GO hybrids, all characteristic sulfur peaks are present, while the GO peak vanishes, indicating the exfoliation of GO layers due to the in situ growth of sulfur particles between them. TEM image of S-GO hybrids is shown in Figure 1(b).

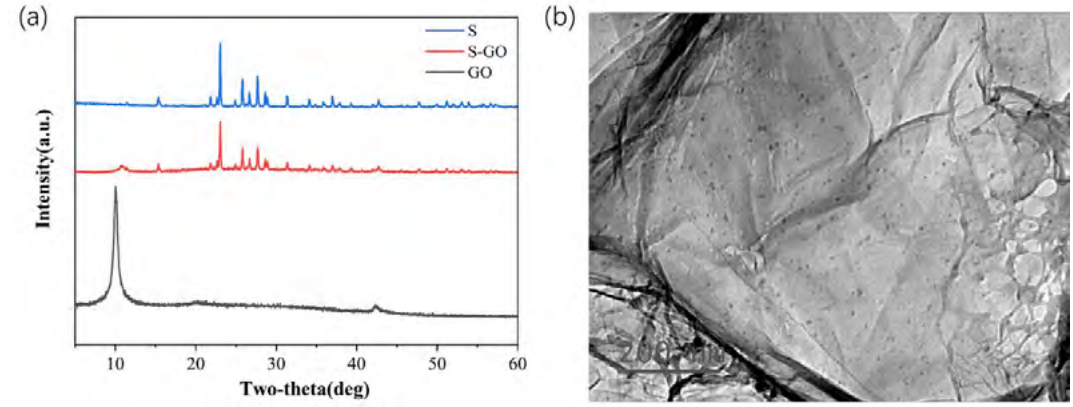

Figure 1. (a) XRD patterns of sulfur, GO and S-GO hybrids, (b) TEM image of S-GO hybrids.

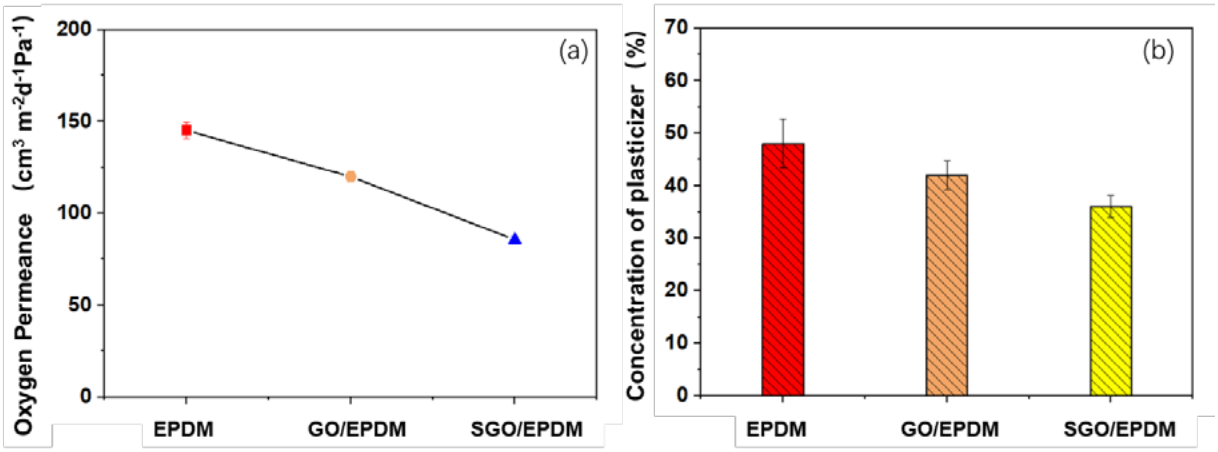

Figure 2. The oxygen permeability(a) and concentration of plasticizer(b) of the different EPDM composites.

3.2 Barrier Performance

The gas barrier performance of the EPDM composites were tested by differential pressure method [14], and the oxygen permeability is shown in Figure 6(a). The oxygen permeability of GO/EPDM composites decreased after the addition of GO, which indicated that the presence of GO layers obstruct the passage of oxygen molecules. Nevertheless, there are still certain imperfections, such as voids, between the GO layers and EPDM molecular chains, facilitating easy passage for oxygen molecules. Following the incorporation of S-GO hybrids into EPDM composites, the oxygen permeability decreased by 50.7% and 23.3% compared to pure EPDM and GO/EPDM composites, respectively. As shown in Figure 6(b), the introduction of S-GO hybrids is also beneficial to inhibit plasticizer migration.The introduction of S-GO hybrids contribute to a notable reduction of 24.9% and 14.1% in plasticizer migration for S-GO/EPDM in comparison to pure EPDM and GO/EPDM, respectively.The significant reduction in free volumes is mainly due to the robust interfacial interactions between S-GO and EPDM molecules. In S-GO/EPDM composites, GO and sulfur readily undergo chemical reactions, forming strong interfaces facilitated by their ample contact. These intricate filler networks and robust interfacial interactions effectively diminish the free volumes between EPDM molecules. Consequently, they extend the

pathways and diffusion times of molecules within EPDM matrices, leading to enhanced barrier properties.

3.3 Vulcanization properties

To assess the impact of nano-fillers on EPDM vulcanization properties, EPDM vulcanization at 160℃ was examined using a rotorless vulcanizer (Figure 3). Key parameters such as maximum torque (M_H), minimum torque (M_L), scorch time (t_{10}), and optimum cure time (t_{90}) were recorded (Table 2). M_L predominantly reflects filler-filler interactions within the rubber. Addition of GO and S-GO resulted in increased M_L values for EPDM composites, indicating gradual reinforcement of filler networks. M_H, on the other hand, is influenced by filler-filler, filler-rubber, and rubber-rubber interactions.The addition of GO and S-GO resulted in an increase in the M_H value, primarily attributed to enhanced chemical crosslinking and a more robust filler-rubber interaction. Among the composites, S-GO/EPDM exhibited the highest M_H and M_L values, indicative of a strong interfacial interaction between S-GO and EPDM. ΔM signifies the rubber's crosslinking degree, with higher values indicating greater crosslinking. S-GO/EPDM also demonstrated the largest ΔM, reflecting its highest crosslinking degree. The heightened crosslinking density in the S-GO/EPDM composite is advantageous for reducing free volume between EPDM molecules and enhancing barrier performance.

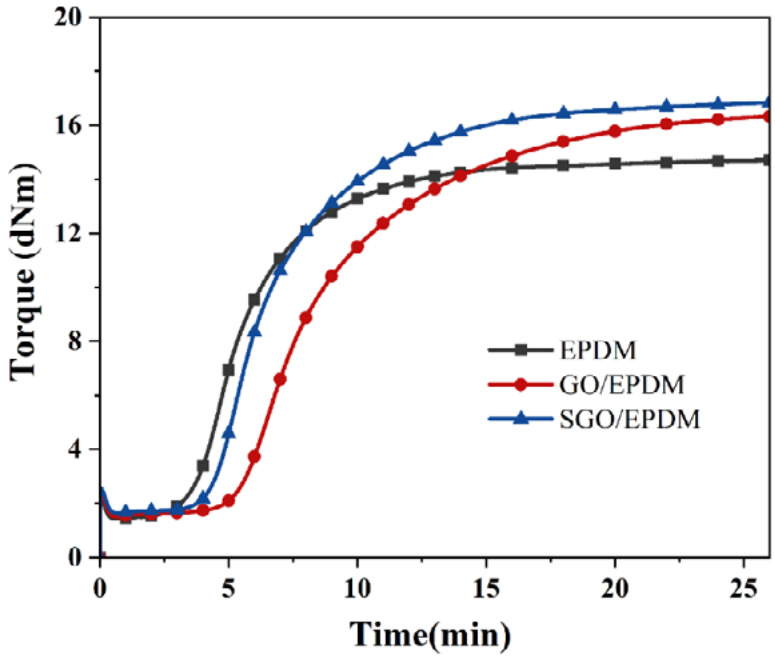

Figure 3 Vulcanization curves of EPDM composites.

Table 2. Vulcanization properties of EPDM composites.

Samples	M_H (dN · m)	M_L (dN · m)	ΔM (dN · m)	t_{10} (min)	t_{90} (min)
EPDM	14.56	1.09	13.47	3:37	9:58
GO/EPDM	16.26	1.14	15.12	5:37	16:35
S-GO/EPDM	16.85	1.27	15.58	4:31	13:28

4. Conclusions

In this study, S-GO hybrids was synthesized and incorporated into EPDM matrix to improve the barrier properties. During the high-temperature crosslinking process, sulfur on the surface of GO served dual roles: crosslinking rubber chains and inhibiting GO sheet agglomeration through sulfur melting and spreading. Additionally, sulfur reacted with GO, forming bridges between GO and EPDM molecules, establishing robust interfaces and filler networks within EPDM matrices. Consequently, S-GO/EPDM composites exhibited superior crosslinking compared to GO/EPDM composites. Compared with the introduction of GO, S-GO hybrids contribute to decreasing by 14.1% in plasticizer migration and 23.3% in gas permeability. In summary, this study presents an efficient approach for designing a versatile rubber crosslinking agent and fabricating high-performance rubber composites.

Acknowledgments
This work was financially supported by the National Natural Science Foundation of China (No. 22005145).

References

[1]Guo Y, Qiu H, Ruan K, et al. Flexible and insulating silicone rubber composites with sandwich structure for thermal management and electromagnetic interference shielding[J]. Composites Science and Technology, 2022, 219: 109253.
[2] Wei Z, Cai Y, Zhan Y, et al. Ultra-low loading of ultra-small Fe3O4 nanoparticles on nonmodified CNTs to improve green EMI shielding capability of rubber composites[J]. Small, 2024, 20(9): 2307148.
[3] Yang H, Yuan L, Yao X F, et al. Monotonic strain sensing behavior of self-assembled carbon nanotubes/graphene silicone rubber composites under cyclic loading[J]. Composites Science and Technology, 2020, 200: 108474.
[4] Chen J, He J, Liu L, et al. Effect of hybrid cross-linked polyphosphazene microspheres on ablative and mechanical properties of ethylene propylene diene monomer[J]. Journal of Applied Polymer Science, 2021, 138(45): 51348.
[5] Rezaei-Vahidian H, Farajpour T, Abdollahi M. Using an inhibitor to prevent plasticizer migration from polyurethane matrix to EPDM based substrate[J]. Chinese Journal of Polymer Science, 2019, 37: 681-686.
[6] Ji Y, Han S, Xia L, et al. Synergetic effect of aramid fiber and carbon fiber to enhance ablative resistance of EPDM-based insulators via constructing high-strength char layer[J]. Composites Science and Technology, 2021, 201: 108494.
[7] Huang Z, Nie H, Zhang Y, et al. Migration kinetics and mechanisms of plasticizers, stabilizers at interfaces of NEPE propellant/HTPB liner/EDPM insulation[J]. Journal of hazardous materials, 2012, 229: 251-257.
[8] Wu W, Yang Y, Chen J, et al. Nitroglycerine migration to polyurethane used for inhibition of double-base propellants through thermal analysis techniques[J]. Journal of Thermal Analysis and Calorimetry, 2016, 125: 881-886.
[9] Lu Z, Zhou Q, Zhang Y, et al. Enhanced gas and plasticizer barrier HTPB composite liner implanted with parallel orientation Fe_3O_4/RGO nanosheets by an ultrasound/magnet-coassisted method[J]. Ultrasonics Sonochemistry, 2024: 106827.
[10] Zhang P, Sun L, Yuan J, et al. Synthesis of multifunctional additives for solid propellants: Structure, properties and mechanism[J]. Defence Technology, 2024, 33: 308-316.
[11] Zheng L, Jerrams S, Su T, et al. Enhanced covalent interface, crosslinked network and gas barrier property of functionalized graphene oxide/styrene-butadiene rubber composites triggered by thiol-ene click reaction[J]. Composites Part B: Engineering, 2020, 197: 108186.
[12] Lu Z, Hu Y, Zhang B, et al. EPDM/GO composite insulation for anti-migration of plasticizers[J]. Journal of Polymer Research, 2022, 29(9): 385.

[13]Lu Z, Hu Y, Zhang B, et al. Anti-migration performance of EPDM composite improved by octadecylamine-functionalized graphene oxide[J]. Journal of Applied Polymer Science, 2022, 139(31): e52713.
[14] Lu Z, Zhu Z, Zhang Y, et al. Enhancing the Anti-Migration Performance and Mechanical Properties of EPDM Insulation through Functionalized GO[J]. Polymers, 2023, 15(7): 1731.
[15] S. Stankovich, D. Dikin, G. Dommett, K. Kohlhaas, E. Zimney, E. Stach, R. Piner, S. Nguyen, R. Ruoff, Graphene-Based Composite Materials, Nature, 442 (2006) 282-286.
[16]Zheng L, Jerrams S, Xu Z, et al. Enhanced gas barrier properties of graphene oxide/rubber composites with strong interfaces constructed by graphene oxide and sulfur[J]. Chemical Engineering Journal, 2020, 383: 123100.
[17] Lu Z, Hu Y, Zhang T, et al. Preparation and anti-migration performance of ethylene propylene diene terpolymer composites modified with GO-SiO_2 hybrid nanomaterials[J]. Journal of Applied Polymer Science, 2023, 140(3): e53341.

HYBRID COMPOSITE STRUCTURES OF THERMOSET COMPOSITES AND THERMOPLASTICS PRODUCED THROUGH OVERMOLDING

N. Karakaya[1], M. Papila[2] and G. Ozkoc[1,3]

[1]Xplore Instruments B.V., R&D Department, Arendstraat 5, 6135KT, Sittard, The Netherlands
Email: nursel.karakaya@xplore-together.com, Web Page: https://www.xplore-together.com
[2]Mechanical Engineering Department, California State University, Northridge, 18111 Nordhoff Street Northridge CA 91330, USA
Email: melih.papila@csun.edu, Web Page: https://w2.csun.edu
[3]Istinye University, Department of Chemistry, Istanbul, Turkey
Email: guralp.ozkoc@xplore-together.com, Web Page: https://www.xplore-together.com

Keywords: Interface, Injection molding, Overmolding, Hybrid, Thermosetting resin

Abstract
This research mainly focused on exploring an alternative method for joining thermoplastics with thermoset composites through overmolding, to facilitate the production of hybrid thermoset composites. Specifically, the study investigated the factors influencing the adhesion between overmolded polyamide-6 (PA6) and continuous glass or epoxy fiber-reinforced composites. Three key factors were examined: the type of reinforcing fiber (glass and carbon), the molding temperature during overmolding (30°C and 80°C), and the use of peel-ply on the composite surface. The results indicated that applying peel ply, using a higher molding temperature (80°C), and having a composite surface with carbon fiber reinforcement led to better adhesion. Various tests such as three-point bending, dynamic mechanical analysis (DMA), roughness measurements, and contact angle assessments demonstrated strong adhesion. Scanning electron microscopy (SEM), micro-computed tomography (micro-CT) images, and energy-dispersive X-ray spectroscopy (EDS) results supported the positive impact of peel-ply application. Thermal analysis findings confirmed the influence of the type of reinforcement material on the crystallinity of the overmolded polymer, emphasizing the crucial role of contact surface chemistry.

1. Introduction

Fuel economy and environmental impact are top concerns in the automotive and transportation industry. Using lightweight materials is key to reducing vehicle weight, which directly impacts fuel consumption and CO2 emissions. Composite materials are effective in creating lightweight, long-lasting, chemically resistant, and corrosion-resistant parts [1,2]. In automotive applications, thermoplastics (TP) and their composites, especially organo-sheet composites, are widely studied. This process involves heating and shaping impregnated technical textiles in an injection mold to make TP composites, with TP design details overmolded onto them. Despite their advantages, thermoplastic composites have drawbacks like high cost and limited thermal resistance [3].

Structural composites with a thermoset (TS) matrix, which are relatively more established, outperform in applications requiring thermal resistance and strength. Thermosets offer advantages such as no melting behavior, high thermal resistance, minimal changes in modulus or strength with temperature variations compared to TPs, and superior creep properties. However, challenges arise when designing components with intricate assembly and connector details, especially with technical textile composites. Welding options are limited and shaping complex structures can be problematic.

To address the difficulties in assembling TS composites, researchers are exploring the production of hybrid structures combining TS and TP materials. Overmolding is an effective method for assembling

different polymeric materials without using adhesives or mechanical bonding [4, 5]. In this process, a plastic material is molded onto a previously produced plastic or composite, acting as the substrate.

This study investigates the potential of implementing overmolding between thermoplastic (TP) and thermoset (TS) composites. To our knowledge, this approach has not been previously explored in research. The proposed method aims to facilitate the production of hybrid thermoset composites with joints and intricate details using thermoplastics.

2. Experimental

2.1. Materials and Preparation of Composites and Hybrid (Overmolded) Samples

Eurotec provided PA6 in the form of injection grade NB40NLE, which is unfilled natural PA6 with a density of 1.14 g/cm^3. Kordsa, Turkey, supplied prepregs as grade OM10-KG with 43% epoxy content, specifically phenol novolac based epoxy. Each prepreg layer had a thickness of 0.36 mm and consisted of two fabric layers - woven carbon fiber and glass fiber, as shown in Fig.1(a).

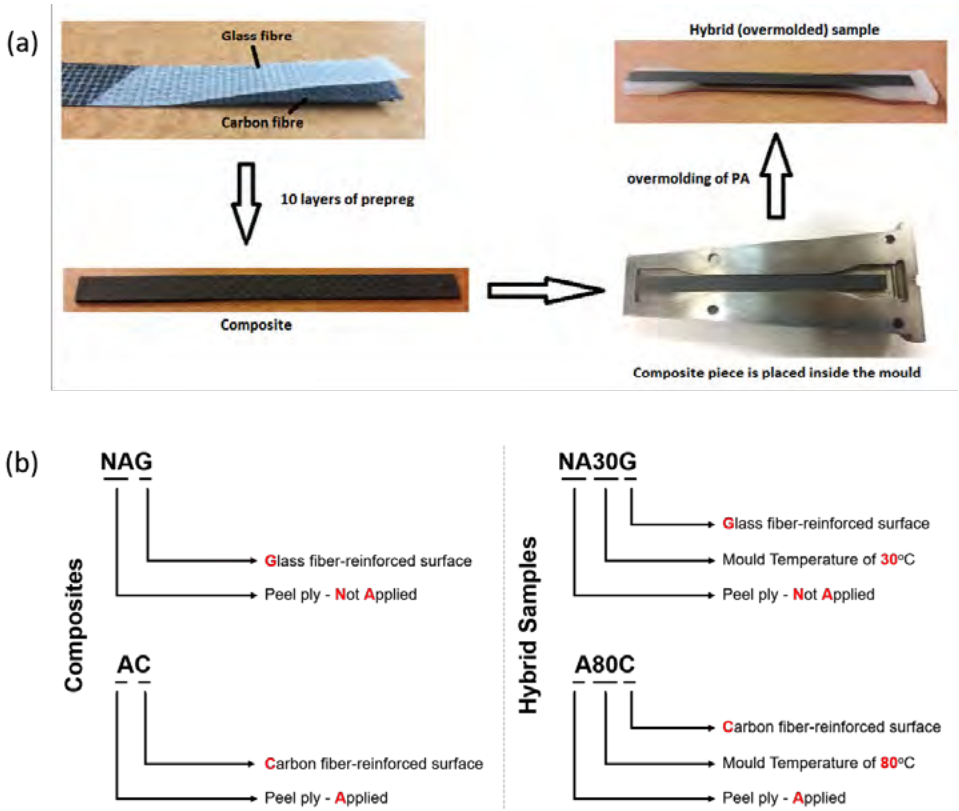

Fig.1. (a) Process steps for preparation of hybrid (overmolded) samples. (b) Nomenclature examples for composite and hybrid samples.

The laminated composites were produced by stacking 10 layers of prepregs using vacuum bagging. A polyamide-based plain peel ply was used for surface treatment to improve roughness. The effect of applying peel ply was studied; therefore, certain samples were prepared without peel ply. The final structure was cured in a hot press to produce composite sheets with thickness of 2.6+/-0.1 mm, featuring glass fiber on one side and carbon fiber on the other side. Afterwards, the composites were accurately cut into pieces measuring 146*10.7 mm using a waterjet to ensure proper fitting into the mold.

Polyamide (PA) (pre-dried at 80°C for 24 hours) was processed through melt mixing in a lab-scale twin-screw extruder (DSM Xplore MC15) at 230°C and 100 rpm for one minute under an argon atmosphere.

For the overmolding process, a microinjection-molder injection machine (DSM Xplore IM12) was utilized with a barrel temperature of 250°C and an injection pressure of 15 bar.

The composite piece was positioned as a substrate (insert) in the injection mold (ISO-527-2 Type 1B), with PA overmolded as a second layer (Fig. 1(a)). The final thickness of the overmolded hybrid samples ranged from 4.18 +/- 0.01 mm.

The first parameter examined was the type of composite reinforcement, either glass fiber or carbon fiber, applied to the composite surface before overmolding. As the overmolding process parameters, two different mold temperatures, 30°C and 80°C, were tested to evaluate their effect on the interface adhesion between PA and the composite as the second parameter. Surface roughness, affecting adhesion due to increased contact surface areas, was also considered. Peel ply has been used in various studies to assess its impact on the roughness effect in adhesive bonding of composite structures, thus investigating its effect was the third parameter. The parameters investigated in the overmolded hybrid composite formulations are outlined in Table 1. Subsequently, the nomenclature provided in Table 1 and Fig. 1(b) will be used to refer to the hybrid composites.

Table 1. Parameters investigated in sample preparation

Hybrid Sample Code	Peel Ply (Applied (A) / Not Applied (NA))	Mould Temperature (°C)	Composite reinforcement on the overmolded surface	Composite Code
A30C	A	30	Carbon	AC
A30G	A	30	Glass	AG
NA30C	NA	30	Carbon	NAC
NA30G	NA	30	Glass	NAG
A80C	A	80	Carbon	AC
A80G	A	80	Glass	AG
NA80C	NA	80	Carbon	NAC
NA80G	NA	80	Glass	NAG

2.2. Characterization

The Zwick Z10 universal testing machine was utilized to conduct a three-point bending test following the ASTM D790 standard configuration, at a speed of 2 mm/min with a span length of 57 mm. During the tests, the PA layer consistently remained in the upper position.

The contact angle of the composites was measured using an optical contact angle meter (KSV Attension Theta Lite) with distilled water at room temperature. Surface roughness was evaluated by two methods: profilometry and a 3D surface measurement system. The Mahr MarSurf M300C profilometer employed a stylus method with a 2 µm radius stylus, 8 nm resolution, and a 5.6 mm scanning length to measure roughness on composite surfaces. Additionally, roughness analysis was conducted using the Nanofocus µsurf 3D surface measurement system with a 10x lens per ISO 25178 standards. The Sa parameter, indicative of rough and anisotropic surfaces, was derived from surface profiles.

The hybrid samples underwent analysis of their surface and cross-section compositions using a LEO Supra VP35 field emission scanning electron microscope at a 3 kV voltage after applying conductive carbon coating. The chemical composition of the surfaces was studied using EDS (Oxford X-MaxN). The middle section of the hybrid specimens was subjected to a micro-CT scan with a SkyScan 1172 at 1K resolution (1000x668 pixels). The X-ray source operated at 62 kV voltage and 161 µA current.

The thermal properties of the samples were evaluated using a TA Q2000 DSC instrument. The tests were conducted at a heating rate of 10°C/min from 0 to 300°C, with N_2 as the purge gas. The sample

surfaces were scratched using a snap blade from both the composite and mold sides of the PA layer. Dynamic properties were determined using a Metravib DMA50 dynamic mechanical analyzer at a constant frequency of 3 Hz, over a temperature range of 30-200°C, with a ramp rate of 10°C/min in three-point bending mode.

3. Results and Discussion

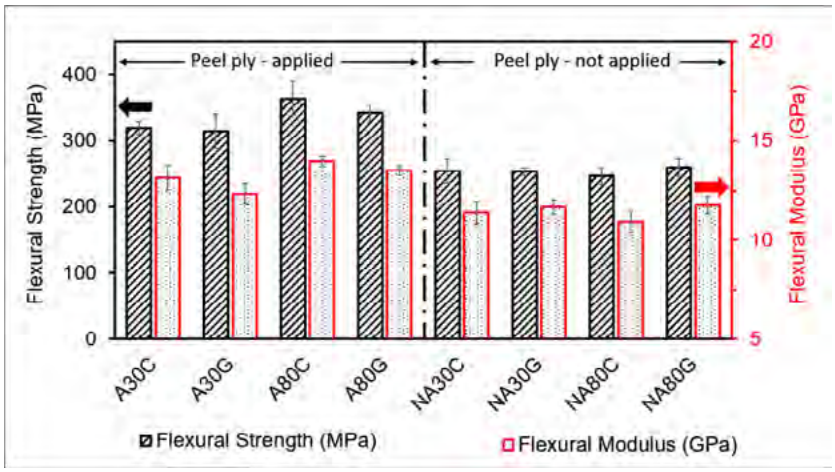

Fig. 2. Flexural strength and modulus of hybrid samples.

Figure 2 illustrates the variations in the flexural strength and modulus of hybrid samples in relation to the use of peel-ply, the type of bonding side (carbon or glass), and the temperature of the mold. Results from three-point bending tests indicate that the presence of peel ply has the most significant impact on both flexural strength and modulus (Figure 2). It is expected that increased roughness enhances adhesion by providing a larger contact surface area. In cases where peel ply is not utilized, the mold temperature and the choice of fiber type on the composite surface do not have a substantial effect. However, for hybrid specimens with peel ply on the bonding surface, a mold temperature of 80°C leads to slightly improved flexural properties. Comparing carbon fiber to glass fiber on the bonding surface with peel ply application, there is a minor increase of approximately 6% in average flexural strength values when overmolding is done at 80°C mold temperature. This difference diminishes to around 1.5% at a mold temperature of 30°C.

Table 2. Contact angle, roughness and flexural strength measurements (typical errors in paranthesis).

Composite and Hybrid Sample Code	Contact Angle (°)	Roughness (µm)			Flexural Strength (MPa)	
		R_a	R_z	S_a	*Ultimate Failure*	*Initial Onset of Failure*
AC	58.2 (±12.6)	10.6 (±0.7)	52.1 (±5.6)	21.0	-	-
A30C	-	-	-	-	320 (±9.5)	270 (±29.7)
A80C	-	-	-	-	364 (±26.2)	300 (±16.2)
AG	70.8 (±9.7)	9.7 (±0.6)	51.8 (±3.6)	19.0	-	-
A30G	-	-	-	-	315 (±25.5)	266 (±37.4)
A80G	-	-	-	-	342 (±12.5)	313 (±4.3)
NAC	89.8 (±5.5)	0.7 (±0.1)	3.1 (±0.7)	10,3	-	-
NA30C	-	-	-	-	255 (±19.0)	174 (±10.4)
NA80C	-	-	-	-	247 (±13.2)	168 (±12.6)
NAG	87.1 (±5.1)	1.5 (±0.2)	5.9 (±1.2)	10,5	-	-
NA30G	-	-	-	-	254 (±5.9)	187 (±16.1)
NA80G	-	-	-	-	260 (±13.8)	190 (±10.2)

Table 2 presents measurements of contact angle, roughness, and flexural strength. The contact angle measurements show that the composite surfaces become more hydrophilic when peel ply is used, indicating an enhanced bonding quality. These findings align with previous studies suggesting that polyamide peel plies increase the polarity of the composite surface, thereby raising the surface free energy for better bonding (references [6, 7-9]. Our research demonstrates that enhancing the polarity of the surface improves adhesion between the polar over-injected PA and the composite with an epoxy-based matrix having an inherently non-polar characteristic.

The application of peel ply on carbon fiber/epoxy surfaces led to notably lower contact angle values in comparison to surfaces with glass fiber/epoxy. For hybrid samples lacking peel ply application, the type of surface ply reinforcement and mold temperature did not significantly affect the contact angle and flexural strength. These findings suggest that the interaction between the epoxy matrix composite and PA layers plays a crucial role in ensuring effective bonding between them.

The roughness measurements are detailed in Table 2. The outcomes reveal an inverse relationship between roughness and contact angle for composite surfaces. Without peel ply application, the roughness of glass fiber surfaces exceeded that of carbon fiber surfaces. However, with peel ply application, carbon fiber/epoxy composites exhibited greater benefits with increased roughness compared to glass fiber composites. In essence, the roughness and contact angle measurements differed between glass and carbon fiber/epoxy composite surfaces despite using the same polyamide peel ply. This disparity stems from variations in the surface chemistry of the composites, which also significantly impacts interface adhesion [8, 9].

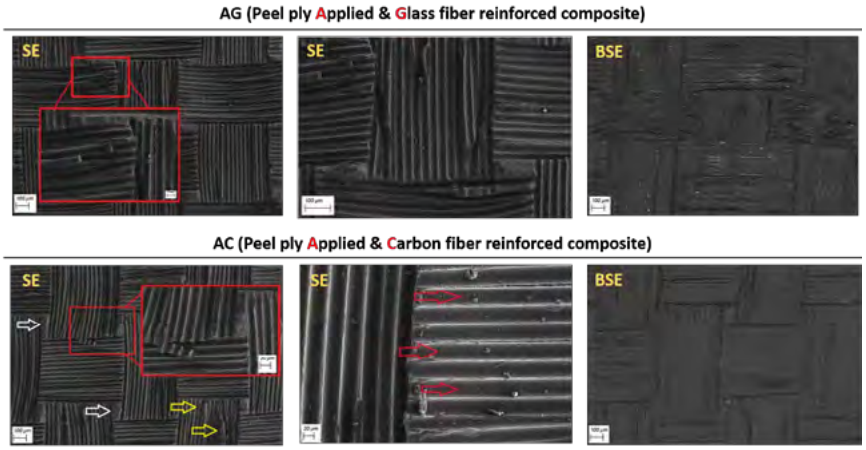

Fig. 3. SEM images for AG (glass fiber side of peel ply applied composites) and AC (carbon fiber side of peel ply applied composites).

Analyzing the SEM images of the composites prior to overmolding (Figure 3), it is evident that composites treated with peel ply exhibit a distinct morphology attributed to the texture of the peel ply fabric. Due to the different compositions of glass fibers and the epoxy matrix, protrusions of glass fibers are visible in peel ply treated composites, as shown in SEM images with backscattered electron (BSE) mode. In contrast, upon removing the peel ply from carbon fiber/epoxy surfaces, no exposed reinforcing fibers are visible. The SEM images show fresh and fractured epoxy surfaces indicated by white arrows, and deep cavities on the composite surface marked by yellow arrows [9]. These cavities can act as sites for mechanical interlocking, enhancing the interfacial adhesion area between the thermoset composite and the overmolded polyamide (PA). The carbon fibers are covered with epoxy as observed by red arrows. Since both epoxy and carbon fibers consist mainly of carbon, the SEM analysis in BSE mode does not reveal any elemental differences.

After detachment using 3-point bending, the composite surfaces of the hybrid structures were further examined using SEM (Figure 4). The presence of a thin layer of PA film aligned with the injection flow direction on the epoxy matrix surface of peel ply treated composites (highlighted by yellow arrows) indicates successful wetting and penetration of PA, enhancing interface formation. Conversely, no residual PA was observed on non-peel ply treated composite surfaces, suggesting poor adhesion of overmolded PA in these cases. The poor adhesion observed is attributed to thermal shrinkage of the PA layer post-injection process, which effectively locks the PA and composite layers together [10].

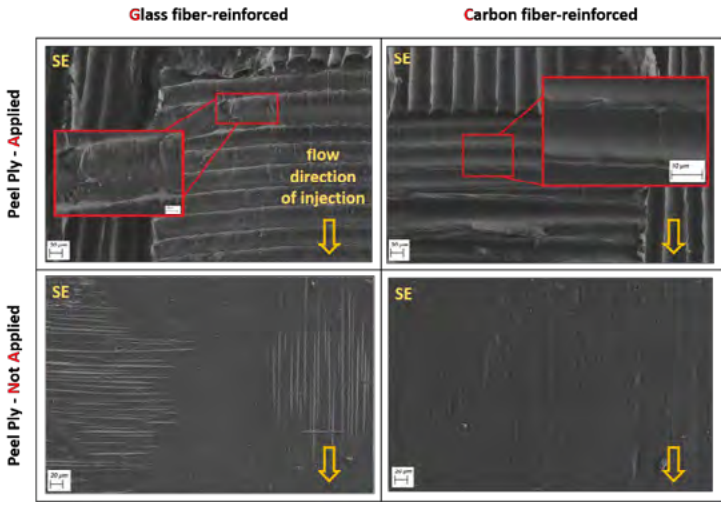

Fig. 4. SEM images for composite surfaces after detaching with 3-point bending.

The results of Energy Dispersive X-ray Spectroscopy (EDS) analysis (% atomic) conducted on composite surfaces are detailed in Table 3. These outcomes indicate that removal of polyamide peel ply led to surface cleaning by eliminating fluorine and introducing nitrogen onto the surface [7, 11]. The presence of chemical contaminant fluorine is believed to be from PTFE self-adhesive release tape used on molds during thermoset composite production. The findings for NAC and AC prior to peel ply removal provide additional supporting evidence for this theory.

Table 3. EDS analysis of composite surfaces.

Composite Code	C	O	N	F	S
AC – After peel ply removal	80.7	16.1	3.2	-	-
NAC	86.4	12.4	-	0.9	0.3
AC – Before peel ply removal	86.0	12.7	-	0.7	0.6

It is important to note that the transparency of the overmolded PA side of the samples with a peel ply treated bonding surface differs significantly from the samples prepared without peel ply. This visual difference in appearance can be associated with the performance of interface adhesion. The reason behind could be that voids larger than wavelength of visible light (380-700 nm) result in light scattering, making the structure appear opaque. To address this issue, micro-CT analysis, which allows non-destructive imaging of samples, was conducted. The resulting images (volume rendered, transverse, and sagittal) are displayed in Fig. 6. In the sample without peel ply surface treatment (NA80C), an interfacial gap measuring between 50 – 70 µm, indicated by a white arrow, is clearly visible. This finding provides evidence supporting the benefit of using peel ply for enhancing interface adhesion during overmolding.

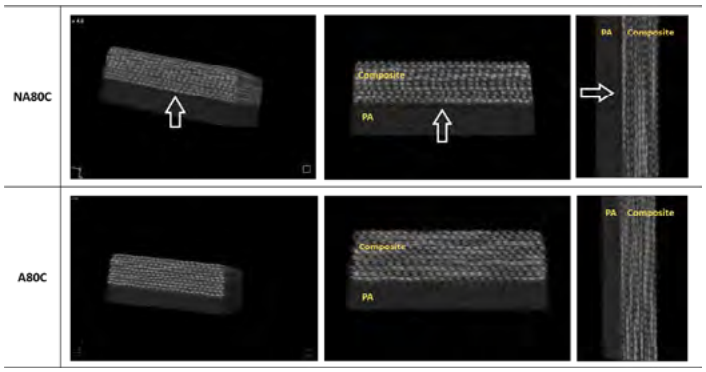

Fig. 6. Micro-CT images of NA80C and A80C hybrid samples. GF is seen as white colour.

Another possible factor could be differences in the crystallinity of the PA layer between composites with and without peel ply application. Thermal analysis studies were carried out on samples obtained by scratching the surface with a snap blade from both the composite side and mold side of the overmolded PA. The T_{onset} of PA at the composite side was calculated using the onset method from 4 points. The degree of crystallinity (%X_c) was determined using the following equation.

$$Xc(\%) = \Delta Hm * 100 / \Delta Hm^{o} \quad (1)$$

Fig. 7 (a) displays the Xc and T_{onset} findings of the overmolded PA layer specimens. It is recognized that during crystallization, polymers mimic the characteristics of the contact surface. The lower crystallization observed on the glass fiber side, which is amorphous, compared to the carbon fiber side, inherently crystalline, is evident in Fig. 7(a). Carbon fibers exhibit crystallized graphitic basal planes on their surface with a non-polar nature. Fig. 7.(a) shows that the composite side has higher crystallinity than the mold side for all setups when carbon fiber reinforces the overmolded composite. Likewise, samples with carbon fiber surfaces showed lower T_{onset} values than those with glass fiber surfaces, implying that carbon fiber acts as a nucleation site with reactive properties, enhancing crystal growth at the interphase.

a)
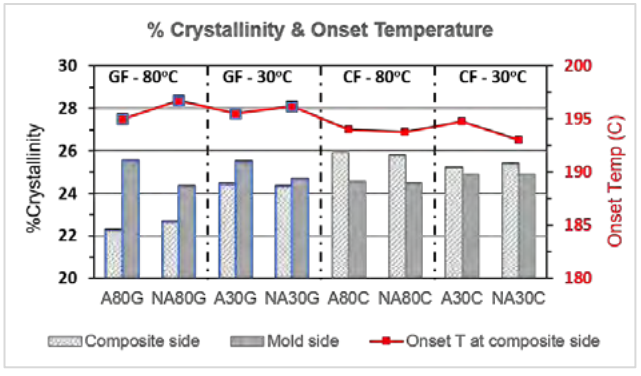

b)
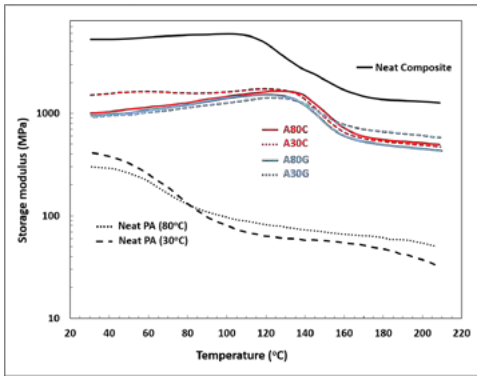

Fig. 7. a) Crystallinity and onset temperature of overmolded PA (from the composite and mould side of the PA layer) b) Storage modulus of hybrid samples.

An intriguing discovery was that the contact angle or roughnes/s of the composite surface did not affect the crystallinity of the overmolded polymer, as similar crystallinity results were obtained with and without peel ply treatment (e.g., A80G and NA80G). These thermal analysis results emphasize the crucial role of contact surface chemistry influenced by carbon or glass fiber protrusions in the crystallinity behavior of the overmolded polymer. DSC results indicate that the reinforcement type affects the polymer's crystallinity, highlighting the importance of surface chemistry.

According to DMA analysis in 3-point bending mode, depicted in Fig. 7(b), the storage modulus (E') of hybrid samples falls between values of neat composite and neat PA, as expected. Carbon fiber reinforced surfaces, indicated in red, exhibited higher E', implying better adhesion performance compared to glass fiber reinforced surfaces.

4. Conclusions

This study focused on investigating and applying overmolding technology to combine thermoset composites and thermoplastics, aiming to create hybrid thermoset composites. To address adhesion issues caused by layer incompatibility between epoxy matrix composite and PA, the research explored the impact of reinforcing fiber material, overmolding process parameters, and surface roughness resulting from peel ply application on interface adhesion.

The comprehensive analysis of results from 3-point bending, SEM, micro-CT, and DMA tests reveals that treating the overmolding interface/bonding surface with peel ply significantly enhances adhesion performance. Another key discovery is that a mold temperature of 80°C offers better bonding results than 30°C. Considering the effect of reinforcement material - carbon or glass fibers - the study suggests that the surface chemistry of composites plays a crucial role in controlling interface adhesion. The enhanced adhesion at the interface is linked to the increased hydrophilicity of composite surfaces when peel ply is used, leading to improved roughness and wetting. Consequently, the flexural strength rises with composite roughness. Comparing carbon and glass fiber sides, the carbon fiber side exhibits higher roughness in peel ply-treated composites and demonstrates superior adhesion due to its surface chemistry. This research could lay the groundwork for future studies on overmolding, focusing on alternative methods for interface adhesion or composite surface treatments.

Acknowledgments

Funding: This work was supported by Kocaeli University BAP, Turkey [grant number 2017/120].

References

[1] M. Y. Lyu and T. G. Choi. Research trends in polymer materials for use in lightweight vehicles. *Int J Precis Eng Manuf*, 16:213–20, 2015.

[2] M. Biron. *Thermosets and Composites*. *Second Edi.* Elsevier Ltd, 2014.

[3] U. K. Vaidya and K. K. Chawla. Processing of fibre reinforced thermoplastic composites. *Int Mater Rev,* 53:185-218, 2008.

[4] B. B. Sauer, W. G. Kampert, M. D. Wakeman and S. Yuan. Screening method for the onset of bonding of molten polyamide resin layers to continuous fiber reinforced laminate sheets. *Compos Sci Technol,* 129:166-72, 2016.

[5] R. Giusti and G. Lucchetta. Modeling the adhesion bonding mechanism in overmolding hybrid structural parts for lightweight applications. *Key Eng Mater*, 611-612:915-21, 2014.

[6] Q. Bénard, M. Fois and M. Grisel. Peel ply surface treatment for composite assemblies: Chemistry and morphology effects. *Compos Part A Appl Sci Manuf,* 36:1562-8, 2005.

[7] Q. Bénard, M. Fois, M. Grisel, P. Laurens and F. Joubert. Influence of the polymer surface layer on the Adhesion of polymer matrix composites. *J Thermoplast Compos Mater*, 22:51-61, 2009.

[8] Q. Bénard, M. Fois and M. Grisel. Influence of fibre reinforcement and peel ply surface treatment towards adhesion of composite surfaces. *Int J Adhes Adhes*, 25:404-9, 2005.

[9] M. Kanerva and O. Saarela. The peel ply surface treatment for adhesive bonding of composites: A review. *Int J Adhes Adhes,* 43:60-9, 2013.

[10] C. Huang, M. Chen, W. Yang, K. Chang and S. Tseng. Investigation on warpage and its behavior in sequential overmolding, *Journal of Engineering and Science Research,* 1-6, 2011.

[11] M. Kanerva, E. Sarlin, M. Hoikkanen, K. Rämö, O. Saarela and J. Vuorinen. Interface modification of glass fibre-polyester composite-composite joints using peel plies. *Int J Adhes Adhes*, 59:40-52, 2015.

THE MANUFACTURING OF AUXETIC AND CONDUCTIVE FOAM COMPOSITES UTILIZING A NOVEL KINETIC MODEL

Yoon Min Oh[1], Kyeong Mo Kang[1], Jin Soo. Choi[1], In Eui JEE[2] and Woong-Ryeol Yu[1*]

[1] Department of Materials Science and Engineering, Seoul National University, 1 Gwanak-ro, Gwanak-gu, Seoul 151-742, Republic of Korea
[2] Surface treatment Materials Development Team, Hyundai Motor Group, 150 Hyundaiyeonguso-ro, Hwasung, Gyeonggido, 18280, Republic of Korea
*woongryu@snu.ac.kr

Keywords: Kinetic modeling, Real-time pressure monitoring, Curing reaction, Auxetic and conductive composites

Abstract
Polymer foam, renowned for its exceptional attributes such as lightweight, compressibility, and shock absorption, has garnered substantial attention across automotive and aerospace sectors. Recent studies have focused on enhancing foam properties through the integration of nano-fillers like carbon black or graphene into composite materials. Achieving reliable formation of such composite foam necessitates precise synchronization of polymer curing and foaming agent expansion. Excessive foaming speed risks premature deformation, while overly rapid curing may stiffen the polymer, hindering expansion. Establishing a dynamic model for curing and foaming reactions is pivotal in designing foam materials. However, conventional dynamic modeling faces challenges in distinguishing simultaneous curing and foaming reactions within comparable temperature ranges, as observed in foam production processes. In this study, we proposed a novel methodology to define the degree of curing using materials without foaming agents and to evaluate material expansion by monitoring real-time pressure fluctuations of materials containing foaming agents. By amalgamating these datasets, our dynamic modeling accurately forecasts foam behavior in relation to time and temperature. We aim to ultimately extend this modeling methodology to composite materials and produce an auxetic and conductive foam composite.

1. Introduction

Polymer foam has gained attention in aerospace, electronics, automotive, and healthcare industries due to its lightweight, compressibility, and superior shock absorption compared to traditional metals, reflecting evolving material needs. Polyurethane, PVC, and epoxy commonly serve as the matrix material, while recent research strives to enhance foam properties by incorporating nano-fillers like carbon black or graphene into composite materials. [1] The blowing agents used in manufacturing polymer foam can be broadly categorized into two types: physical blowing agents injecting strong gases and chemical blowing agents generating foaming gas through reaction Chemical blowing agents generating foaming gas through heat- or light-triggered reactions are particularly popular in research due to their simple processes, uniform foam production, and quantifiable reaction analysis. On the other hand, recent research emphasizes the use of thermally and chemically stable thermosetting polymers in foam production. Here, synchronizing the timing of polymer curing and foaming agent expansion is crucial. If the foaming reaction is too rapid, the foam might lose its shape before curing, while excessively fast curing could hinder expansion by solidifying the polymer skeleton. Establishing kinetic models for curing and foaming reactions forms the foundation for designing foam materials based on these reactions.

However, using conventional kinetic modeling approaches, distinguishing between curing and foaming reactions becomes challenging when they occur simultaneously in a similar temperature range, as

observed in the foam production process. To address this, firstly this study defines the degree of curing using base materials without blowing agents. Second, the extent of expansion of the material is characterized by observes real-time pressure changes within a sealed pressure cylinder during the reaction. Using these two data, kinematic modelling combining curing and expansion as functions of time and temperature was performed, enabling to predict the foaming behaviour of material precisely. Recent attention has been directed towards developing composite structures of auxetic foam, known for their negative Poisson's ratio, but there has been scarce research dedicated to kinetic modeling in this context. Therefore, a new molding process has been explored to manufacture auxetic and conductive foams in a mold at a once using graphene and developed kinematic modelling.

2. Kinetic modeling of polymer foam

2.1. Curing kinetic modeling

Thermoset polymers such as epoxy and polyurethane undergo cross-linking between molecular chains due to external energy sources like heat or light, a process known as curing. The degree of curing (DOC) quantifies this process from its initiation to completion on a scale from 0 to 1. This DOC can be defined over time and temperature through phenomenological kinetic models, necessitating measurement of material curing over varying time and temperature conditions. Measurement methods for DOC include differential scanning calorimetry (DSC), Fourier transform infrared (FTIR), and rheometer, depending on material characteristics. In this study, DSC was employed for measurement, where exothermic or endothermic reactions produce peaks by detecting differences between reference and sample heat capacities. The onset of curing corresponds to the beginning of the peak, while its completion marks the peak's end . The DOC is defined, as illustrated in Figure 1, by appropriately drawing a baseline and calculating the area under the curve up to the current time($\alpha(t)$), relative to the total area under the peak(Q_{total}). DSC measurements were conducted under isothermal and non-isothermal conditions, each with three variations. Isothermal conditions were set at 170, 185, and 200℃, while non-isothermal conditions involved heating rates of 2, 5, and 10℃/min .

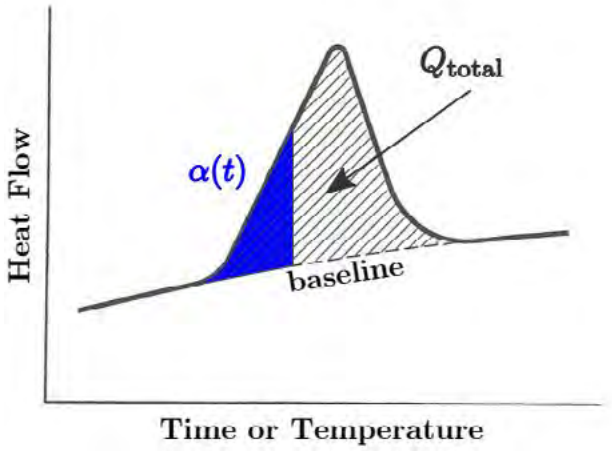

Figure 1. Determining the DOC using the DSC curve [2]

2.2. Foaming kinetic modeling

In the manufacturing process of polymer foam, typically, the curing and foaming are adjusted to occur at similar rates in terms of time and reaction rate. If curing happens too quickly, it becomes challenging to create pores, whereas if it occurs too slowly, the foam formed may not maintain its shape. The foaming is induced by the decomposition of chemical blowing agents, which are exothermic reactions. Therefore, various thermal kinetic studies have been conducted on foaming reactions. [3] However, if only the

foaming reaction exists, kinetic modeling using DSC is feasible, but distinguishing between curing and foaming becomes difficult when both reactions occur simultaneously. Hence, in some limited studies, the degree of foaming (DOF) has been defined separately from curing by measuring pressure using a capillary rheometer. [4] When the foaming reaction occurs, gas is generated, and the pressure generated at this time can serve as a reference point for the reaction. Therefore, DOF is defined as the difference between the maximum and minimum pressures measured compared to the difference between the current pressure and the minimum pressure, as shown in Eq. (1).

$$\alpha_d = \frac{P_t - P_i}{P_f - P_i} \tag{1}$$

P_f represents the final pressure, P_i represents the initial pressure, and P_t represents the pressure at time t. However, the pressure measured in the rheometer suggested in the literature appears too high to be solely generated by the foaming reaction. Therefore, in this study, a new pressure measurement device was designed as shown in Fig.2. It allows real-time measurement of changes in internal temperature and pressure by placing the material in a sealed pressure vessel and heating it externally. Using this equipment, pressure was measured at different temperature profiles up to a maximum temperature of 170, 165, and 160 ℃, and then converted into DOF.

Figure 2. Fabricated foaming pressure measurement device

2.3. Empirical model equation

Phenomenological models are useful tools for studying the kinetics of reactions. A representative form is given by Eq. (2), where these models consist of equations relating reaction rate to temperature and a degree of reaction formula. In this equation, A represents the pre-exponential factor or Arrhenius frequency factor (s^{-1}), E_a denotes the activation energy (J mol^{-1}), R is the gas constant (8.314 J mol^{-1} K^{-1}), and T represents the absolute temperature (K). Additionally, α in this study refers to either the Degree of Curing (DOC) or the Degree of Foaming (DOF), '$d\alpha/dt$' stands for the reaction rate, and $f(\alpha)$ represents the conversion function.

$$\frac{d\alpha}{dt} = Aexp\left(-\frac{E_a}{RT}\right) f(\alpha) \tag{2}$$

Phenomenological models concerning reaction rate typically fall into two main categories: the first being the n-th order model (Eq. 3), where the reaction rate is initially fastest and gradually slows down, and the second being the autocatalytic model (Eq. 4), where the presence of products catalyzes the reaction, causing the reaction rate to peak midway. Furthermore, the Kamal-Sourour model (Eq. 5) has been proposed to address situations where both of these reaction mechanisms occur simultaneously. In this case, K_1 and K_2 correspond to distinct Arrhenius equations. Depending on the model, the function f(α) varies. [5]

$$\frac{d\alpha}{dt} = Aexp\left(-\frac{E_a}{RT}\right)(1-\alpha)^n \tag{3}$$

$$\frac{d\alpha}{dt} = Aexp\left(-\frac{E_a}{RT}\right)(1-\alpha)^n\alpha^m \tag{4}$$

$$\frac{d\alpha}{dt} = K_1(1-\alpha)^n + K_2(1-\alpha)^n\alpha^m \tag{5}$$

The models were modified considering previous studies, which indicated increased errors when modeling isothermal and non-isothermal conditions together using a single kinetic model, especially at high heating rates. [6] Therefore, a modified model including a term for heating rate was utilized. For the curing reaction, the modified Kamal-Sourour model (Eq. (6)) was employed, while for the foaming reaction, the modified autocatalytic model (Eq. (7)) was used.

$$\frac{d\alpha}{dt} = K_1[(1-\alpha)^p + c_1(1-\alpha)^{c_2}(\frac{dT}{dt})^{c_3}] + K_2[(1-\alpha)^q\alpha^r + c_4(1-\alpha)^{c_5}(\frac{dT}{dt})^{c_6}] \tag{6}$$

$$\frac{d\alpha}{dt} = K[(1-\alpha)^p\alpha^q + c_1(1-\alpha)^{c_2}(\frac{dT}{dt})^{c_3}] \tag{7}$$

The modeling approach involved developing MATLAB code based on the ODE45 subroutine and nonlinear least squares method. This code was used to optimize model parameters to best fit the experimental data for each reaction.

3. Results and Discussion

The results of the curing degree modeling are depicted in Fig. 3. The curing behavior was modeled using materials without foaming agents. It is observed that at higher temperatures, curing progresses more rapidly under isothermal conditions, while under non-isothermal conditions, the temperature at which curing is completed increases with higher heating rates. Six experiments were modeled simultaneously, and the model generally fits the experimental results well. However, it was noted that errors occur as the heating rate increases. The parameter values are presented in Table 1

The DOF modeling utilized materials containing foaming agents, and the foaming pressure apparatus described in Section 2.2 was employed. Unlike the curing degree modeling, the temperature and heating rate were not fixed during modeling. First, Fig. 4 illustrates an example of foaming pressure measurements, where the pressure variation can be divided into three regions. Region 1 involves the heating of air inside, causing pressure to increase; Region 2 depicts pressure rise due to foaming reaction;

and Region 3 shows pressure increase due to material degradation within the polymer composite. It is crucial to extract only the foaming pressure to define foaming degree. In Region 3, pressure increase was observed at around 175℃ when conducting pressure measurements with materials without foaming agents, indicating that this temperature range is irrelevant to foaming reaction. Therefore, experiments were conducted only below this temperature range. In Region 1, the proportional increase of pressure with temperature led to the assumption of a linear relationship between temperature and pressure, after eliminating the influence of air. The processed experimental results were then modeled using the model described in Section 2.3, and the results are presented in Fig. 5, with the parameter values listed in Table 2. It was confirmed that the model reasonably fits three temperature profiles, and the accuracy was validated using other experiments not used in the modeling process (Fig. 6). When only temperature variation was inputted into the model, it accurately predicted the experimental results.

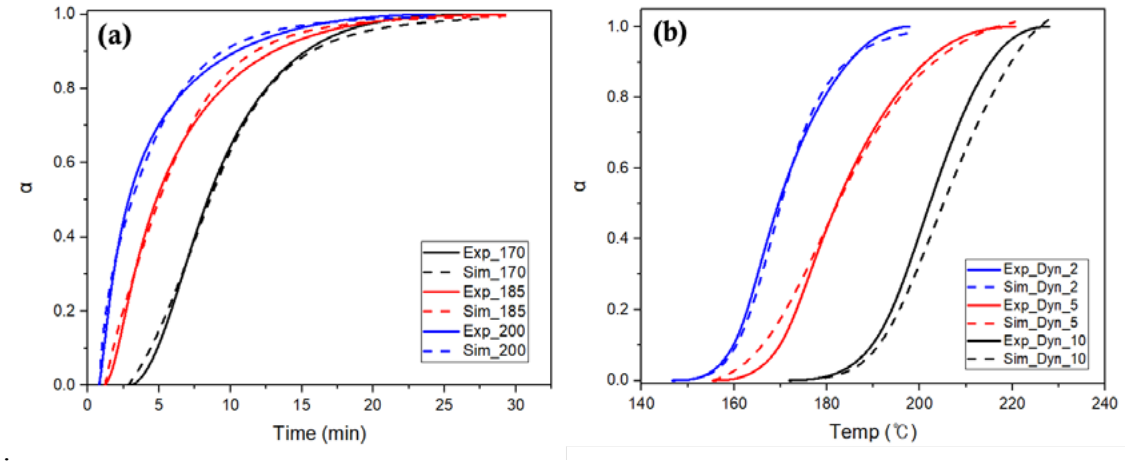

Figure 3. Results of the curing modeling (a) as a isothermal condition and (b) as a non-isothermal condition

Parameter	Value	Parameter	Value
$\ln A_1$	40.02	C_1	-1.44
E_1 (kJ mol^{-1})	158.58	C_2	6.33
$\ln A_2$	0.76	C_3	0.57
E_2 (kJ mol^{-1})	5.94	C_4	0.0029
p	6.22	C_5	0.15
q	1.25	C_6	2.32
r	0.87		

Table 1. Parameter values of curing modeling

4. Conclusions

In this study, kinetic modeling of polymer foam, where both curing and foaming occur simultaneously, was conducted. For this purpose, the Degree of Curing (DOC) modeling was carried out using materials without blowing agents, while a novel foaming degree (DOF) model was proposed using materials containing foaming agents. DOF was defined by measuring pressure in a sealed vessel, as it represents the amount of gas generated by foaming reaction, hence reflecting pressure changes. Both DOC and DOF were successfully defined, and further investigation into the relationship between these two reactions is intended. Particularly, since foaming reaction can be influenced by curing degree, additional modeling considering this interaction is necessary. Moreover, it is crucial to verify if the modeling established with materials lacking fillers can be applied to composite materials. Through these steps, the ultimate goal is to fabricate an auxetic and conductive foam.

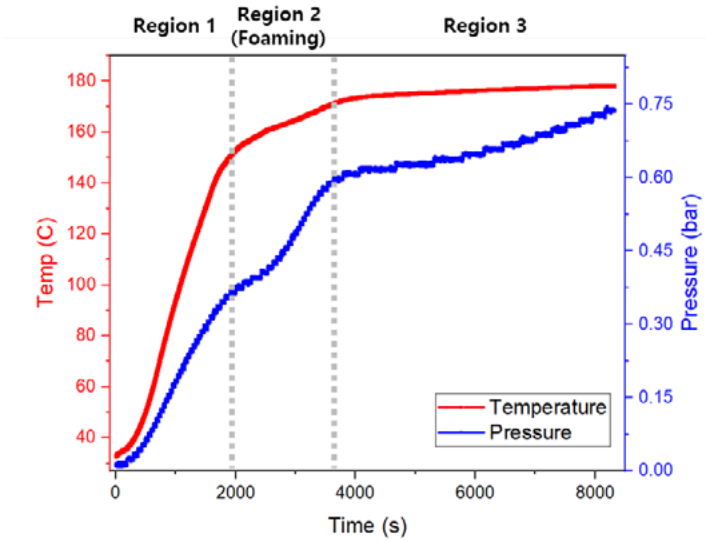

Figure 4. Three regions of foaming pressure variation

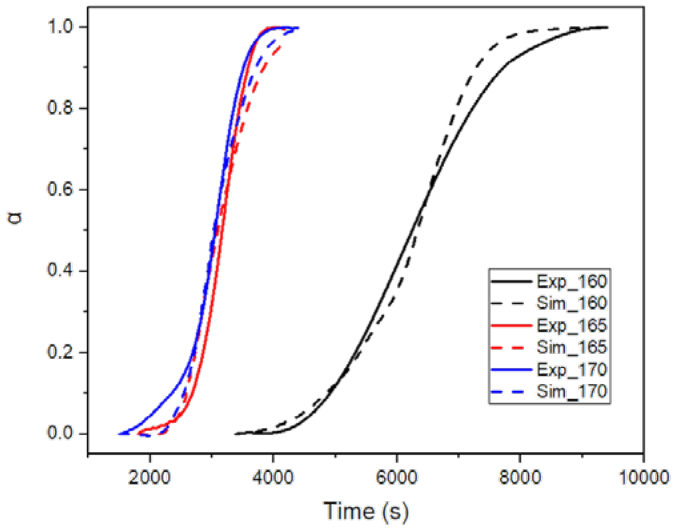

Figure 5. Result of foaming modeling

Parameter	Value	Parameter	Value
lnA	27.41	C_1	-1.34
E (kJ mol^{-1})	122.47	C_2	1.90
p	0.92	C_3	0.15
q	0.03		

Table 2. Parameter values of foaming modeling

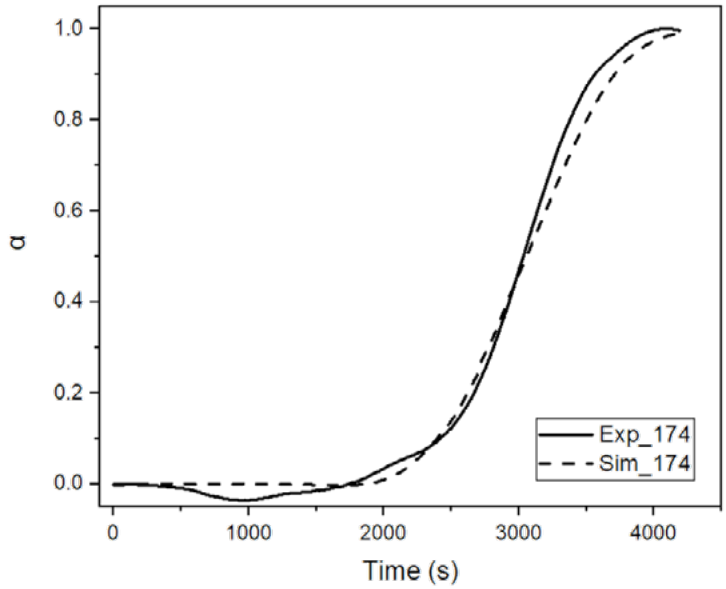

Figure 6. Prediction results of experimentsn not used in modeling

Acknowledgments

This work was supported by Hyundai Motor Group (0417-20230106) in Republic of Korea.

References

[1] Antunes, Marcelo, and José Ignacio Velasco. "Multifunctional polymer foams with carbon nanoparticles". *Progress in Polymer Science,* 39.3: 486-509, 2014.
[2] Heinze, Søren, and Andreas T. Echtermeyer. "A Practical Approach for Data Gathering for Polymer Cure Simulations". *Appl. Sci*, 8(11): 2227, 2018.
[3] Guo, Rui-Lei, Shang-Hao Liu, and Yi-Ming Lu. "Investigation of how pressure influences the thermal decomposition behavior of azodicarbonamide". *Journal of Loss Prevention in the Process Industries,* 83(105062), 2023.
[4] Robledo-Ortiz, J. R., et al. "Non-isothermal decomposition kinetics of azodicarbonamide in high density polyethylene using a capillary rheometer". *Polymer Testing,* 27.6:730-735,2008.
[5] Zhang, Chao, et al. "Kinetic study of the novolac resin curing process using model fitting and model-free methods". *Thermochimica acta,* 523.1-2: 63-69, 2011.
[6] Choi, J. H., Shim, W., Rhie, C. H and Yu, W. R. (2021). "A new cure kinetics model to simulate thermomechanical behavior of polymeric sealants for automotive applications". *Functional Composites and Structures*, 3(4): 045008, 2021

EFFECTIVENESS OF ENZYMATIC TREATMENT ON A CONTINUOUS FLAX FIBRE REINFORCED COMPOSITE

G. Ronconi[1], A. Behrens[2], R. Hirschberg[2], M. Zanelli[1], P. Russo[3], N. Graupner[2], J. Müssig[2], F. Mollica[1], V. Mazzanti[1]

[1] Department of Engineering, University of Ferrara, Via Saragat 1, 44122 Ferrara, Italy
e-mail: giulia.ronconi@unife.it
[2]HSB – University of Applied Sciences Bremen, Faculty 5 - Biomimetics/Biological Materials, Bremen, Germany
[3]Institute for Polymers, Composites and Biomaterials — National Research Council, 80078 Pozzuoli, Naples, Italy

Keywords: Biocomposite, Flax fibers, Mechanical properties, Enzymatic treatment, Poly-(lactid acid)

Abstract
Replacing conventional petroleum-based composites with natural fiber reinforced biodegradable plastics is an important milestone to increase environmental sustainability, but research still needs to solve some important issues before fully achieving this goal. Many drawbacks in the use of vegetable fibers can be overcome by introducing dew-retting treatments, but typically these are performed using substances that are not eco-sustainable or difficult to dispose. In this paper the application of an enzymatic treatment, i.e. pectinase, is considered an alternative to traditional dew retting. The effect of this treatment is investigated directly on flax fibers and on a flax/poly-(lactid acid) composite by tensile tests and Scanning Electron Microscopy. A significant reduction in fiber diameter induced by the removal of pectin and an increase in fiber stiffness are the major results obtained on the treated fibers. A similar trend can be observed on the composite reinforced with treated fibers: the mechanical properties are increased, both in terms of strength and stiffness, and a better fiber impregnation by the matrix is achieved.

1. Introduction

Over the past decade, natural fibers such as hemp, kenaf, wood gained more and more attention as an alternative to synthetic fibers, e.g. glass and carbon fibers. Their low density, high specific mechanical properties, limited abrasiveness, and high availability makes them interesting to be used as reinforcement for thermoplastic composites [1]. However, some critical issues such as a limited compatibility between fiber and matrix, a strong tendency to adsorb water and a high difficulty in dispersing the fiber in the thermoplastic matrix still limit their widespread diffusion [2].

Some of these disadvantages are due to the chemical nature of vegetable fibers. In fact, the main constituents are cellulose, hemicellulose, lignin and pectin, but the major contribute to achieve good mechanical properties is due to the presence of cellulose, while other constituents tend to aggravate these well-known disadvantages. For this reason, many studies in the scientific literature were oriented to perform chemical treatment on the fibers to reduce the amount of non-cellulosic constituents [3]. For example, traditional treatments are based on soaking the fibers in water, where microorganisms degrade hemicellulose and pectin [3], while other treatments, such as the alkaline treatment, can remove lignin [4]. All these treatments are effective, but the long treatment times or the possible use of non-ecosustainable substances made them less and less attractive.

A sustainable substitute of classical dew retting makes use of enzymes [5]. Enzymatic treatments are

specific in removing different constituents. De Prez et al. [6] evaluated this group of treatments deeply concluding that a very promising one was pectinase. This enzyme degrades the pectin layers that are present on the surface of the fibers. Since pectin acts as a binder, this treatment is effective in refining fibers by opening the bundles and reducing absorbable moisture content [7]. Some authors evaluated the use of enzyme-treated continuous fibers as reinforcement in composites, in particular on an epoxy matrix [6,8,9], but to the best of the authors' knowledge there are no studies where a thermoplastic matrix was used.

In this paper, a pectinase treatment was performed on a ribbon of continuous flax fibers and the same fibers were used to prepare flax/poly-(lactid acid) composites. The fiber morphology, the reduction in fiber diameter and the mechanical properties of the single fibers were evaluated before and after treatment. Treated and untreated composites were characterized in tension and by microscopy analysis to evaluate the mechanical properties and the fiber dispersion within the matrix, respectively.

2. Materials and methods

2.1. Raw materials

Poly-(lactid acid) (PLA), named Luminy LX175, was provided by Total Corbion, Netherlands. Its melting temperature is 155°C, the melt flow index is 3 g/10 min (190 °C/2.16 kg) and the density is 1.24 g cm^{-3}. Raw flax fibers were purchased from Depestele, France. The fibers were obtained in the form of untwisted single end ribbon (1000 Tex) with a density of 1.41 g cm^{-3}. The pectinase enzyme Texazym BFE was supplied by Inotex Ltd., (DvűrKrálovi, Czech Republic).

2.2. Enzymatic treatment

A part of the natural fibers was treated with the pectinase enzyme Texazym BFE. The conditions utilized were those recommended by the supplier. Briefly, the enzymatic treatment solution was obtained by mixing 15 ml of enzyme in 3000 ml of distilled water, which is ideal for 150 g of fibers. The flax fibers were soaked in the solution for 1 h at 50°C and the pH of the solution was in 8 – 9 range. After treatment, the fibers were washed twice with distilled water at 60°C and dried overnight in oven at 60 °C. In this paper we will refer to enzymatic treated fibers with TF and to untreated flax fibers with UF.

2.3. Composites preparation

PLA was obtained in the form of films (about 0.25 mm in thickness) by compression molding using a LaboPress P200S (Vogt Maschinenbau GmbH, Germany). The procedure consisted in heating the dried pellets at a processing temperature of 185°C and apply a pressure of 15 bar for 5 minutes. The composite was prepared following a two-step procedure: a winding phase and a compaction phase. Thus, natural fibers were first wound on an aluminum frame, then two layers of PLA film were placed on top of the fiber winding, and this was repeated until the final thickness was obtained, in this case using 8 fiber layers. Finally, the flax fiber/PLA laminate was dried overnight at 60°C and then compression molded. The compression molding procedure consisted of a pre-heating step of 5 minutes at 185°C, followed by two compression phases, the first one at 10 bar and the second one at 30 bar, for 5 minutes each. UF and TF laminae contained a fiber volume fraction of about 35%.

2.4. Tensile test

UF and TF single fibers were characterized in simple tension using a Fafegraph M testing device (Textechno, Germany) with a 100 cN load cell. The tests were performed with a gauge length of 20 mm and a crosshead speed of 10 mm/min. A total of 75 specimens were tested for each group. The dimensions of the fibers were acquired using a Canoscan scanner CS 4000 (Canon, USA) and the pictures were analyzed with the image processing program.

Mechanical characterization in simple tension of UF/PLA and TF/PLA composites was performed with the universal testing machine INSTRON 4467 (INSTRON, USA), equipped with a 30 kN load cell. The tests were carried out following the standard ASTM D3039. Five rectangular samples (120 x 15 x 4 mm) were tested parallel to the fiber direction at a 2 mm/min crosshead speed. The strain was acquired

using a Digital Imaging Correlation apparatus (Dantec Dynamics, Denmark).

2.2. Scanning electron microscopy (SEM)

Morphological observations of UF, TF and all the composites were performed using a Scanning Electron Microscopy (SEM) JSM6510, Jeol, Germany. All the samples were sputtered with gold, high voltages of 5 kV and 10 kV were used to acquire the fibers and composite micrographs, respectively.

3. Results and discussion

Representative SEM micrographs with the surface appearance of UF and TF are shown in Fig. 1. The main modifications that can be appreciated are a reduction of the surface roughening and a clear separation of the fibers. In fact, the pectinase effect is to hydrolyze the pectin that is present in the cell walls of plants and allows to isolate the elementary fibers from the fiber bundles. De Prez et al. describe in detail the pectin removal mechanism in [6] and a similar change in fiber morphology is observed also by Liu et al. in a hemp/epoxy system [8].

In Fig. 2, the UF and TF diameter distributions are shown. The individualization of the thinner fibers obtained by the enzymatic treatment is clearly evident. The UF fibers distribution shows that the most frequent diameter is in the 25-35 μm range, while TF fibers are in the 20-30 μm range. An average diameter and the standard deviation of the UF and TF fibers can be found in Tab.1
The mechanical properties in tension of UF and TF single fibers are also displayed in Tab. 1. Although a high standard deviation is evident, the enzymatic treatment increases the Young's modulus, and the difference is statistically significant (through Student's T-test), while the strength and the strain at break do not change significantly. A change in crystallinity could justify this difference.

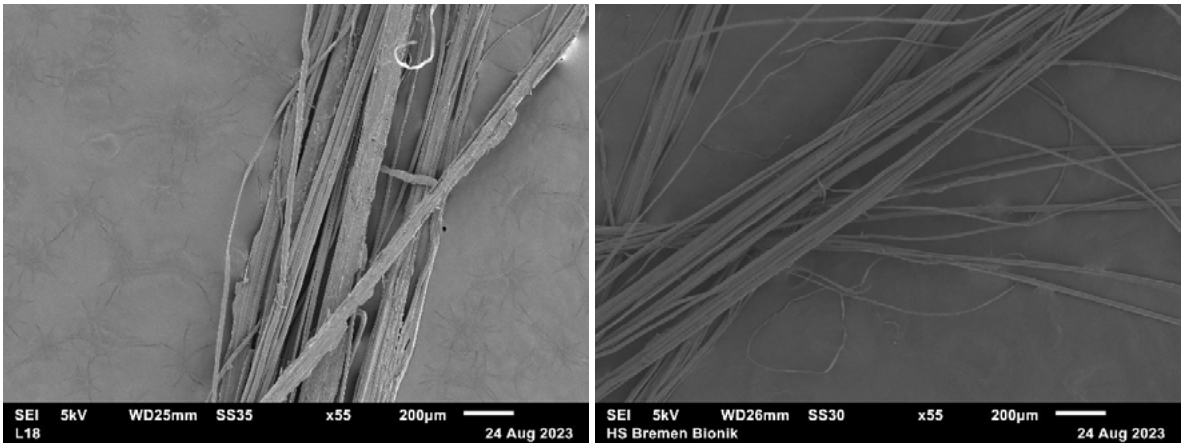

Figure 1. SEM micrographs. (a) UF 55X, (b) TF at 55X.

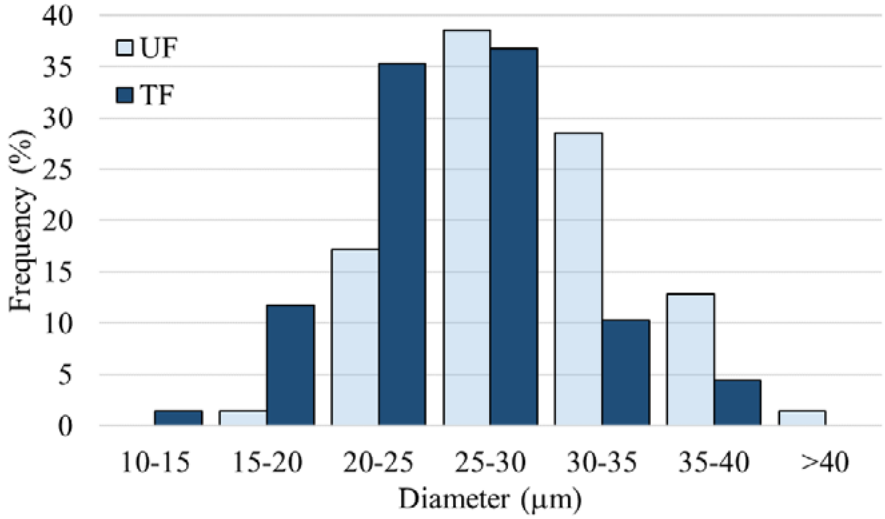

Figure 2. UF and TF fiber diameter distributions.

Table 1. Mechanical properties of the UF and TF single fibers.

Specimen Type	Diameter (µm)	Strength (MPa)	Strain at break (%)	Young's modulus (GPa)
UF	29.2 ± 4.9	382.2 ± 162.9	1.37 ± 0.41	30.6 ± 9.50
TF	24.6 ± 4.8	434.6 ± 206.1	1.33 ± 0.41	35.6 ± 11.8

SEM micrographs of UF/PLA and TF/PLA are shown in Fig. 3. Overall, the main difference between the two samples is the presence of a net stratification of the PLA matrix and the flax fiber layers in the UF sample. Furthermore, the UF/PLA sample shows a greater presence of fiber bundles compared to the TF/PLA composite. From this it can be deduced that the elimination of pectin in the TF sample is effective during the preparation of the composite, as the separation of the elementary fibers makes the impregnation of the matrix easier. In fact, the fiber bundles and the layers are significantly less evident in the TF sample.

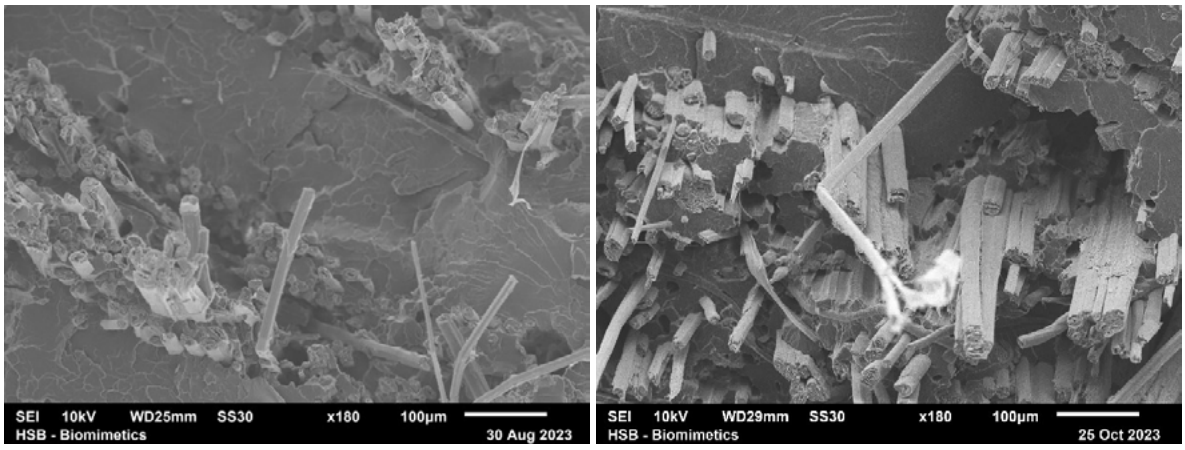

Figure 3. Fracture surface of the (a) PLA/UF and the (b) PLA/TF composites at 180X.

Concerning the mechanical properties of neat PLA, UF/PLA and TF/PLA composites, Young's modulus, strength, and strain at break are summarized in Tab.2. For both composites, the presence of the fibers increases stiffness and also strength, albeit to a lesser extent, while the strain at break decreases. A similar trend to that observed on the single fiber tests can be appreciated also by comparing the properties of the UF/PLA and TF/PLA composites. The enzymatic treatment increases the mechanical properties of the single fibers slightly, and this effect is detected also in the TF/PLA composite. Moreover, the treatment improves a better distribution of the fibers and the fiber bundles opening, thus increasing the impregnation quality.

Table 2. Mechanical properties of the neat PLA and UF/PLA and TF/PLA composites

Specimen Type	Strength (MPa)	Strain at break (%)	Young's modulus (GPa)
PLA	60.81 ± 5.06	3.40 ± 0.10	2.62 ± 0.09
UF/PLA	171.15 ± 3.06	1.98 ± 0.04	14.59 ± 0.15
TF/PLA	184.65 ± 6.65	1.71 ± 0.02	15.22 ± 1.05

4. Conclusions

The efficacy of the enzymatic treatment in a flax/PLA composite system was investigated. Tensile properties of the flax fibers after enzymatic treatment were higher compared to the same fibers before treatment, and a similar trend was visible also on the composites. The morphological analysis showed that pectinase individualized the elementary fibers and reduced the presence of fiber bundles. These effects promoted fiber impregnation by the matrix and allowed to achieve a better dispersion. Further analyses will be carried out to evaluate whether the enzymatic treatment induces also changes in fiber crystallinity and in the overall cellulose architecture within the fibers, but will appear elsewhere.

References

[1] O. Adekomaya, T. Jamiru, R. Sadiku and Z. Huan. A review on the sustainability of natural fiber in matrix reinforcement - A practical perspective. Journal of Reinforced Plastics and Composite, 35: 3-7, 2016.

[2] V. Mazzanti, L. Malagutti, A. Santoni, F. Sbardella, A. Calzolari, F. Fabrizio and F. Mollica. Correlation between mechanical properties and processing conditions in rubber-toughened wood polymer composites. *Polymers*, 12: 1170, 2020.

[3] M.R. Sanjay, S. Siengchin, J. Parameswaranpillai, M. Jawaid, C.I. Pruncu and A. Khan. A comprehensive review of techniques for natural fibers as reinforcement in composites: Preparation, processing and characterization. *Carbohydrate Polymers*. 207: 108-121, 2019.

[4] V. Mazzanti, R. Pariante, A. Bonanno, O. Ruiz de Ballesteros, F. Mollica and G. Filippone. Reinforcing mechanisms of natural fibers in green composites: Role of fibers morphology in a PLA/hemp model system. *Composites Science and Technology*. 180: 51-59, 2019.

[5] J. De Prez, A. W. Willem Van Vuure, J. Ivens, G. Aerts and I. Van de Voorde. Enzymatic treatment of flax for use in composites. *Biotechnology Reports*, 20: e00294, 2018.

[6] J. De Prez, A. W. Willem Van Vuure, J. Ivens, G. Aerts and I. Van de Voorde. Effect of enzymatic treatment of flax on fineness of fibers and mechanical performance of composites. *Composites Part A*. 123: 190-199, 2019.

[7] M. George, P. G. Mussone, K. Alemaskin, M. Chae, J. Wolodko and D. C. Bressler. Enzymatically treated natural fibres as reinforcing agents for biocomposite material: mechanical, thermal, and moisture absorption characterization. *Journal of Materials Science*. 51: 2677-2686, 2016.

[8] M. Liu, A. S. Meyer, D. Fernando, D. A. S. Silva and G. Daniel, A. Thygesen. Effect of pectin and hemicellulose removal from hemp fibres on the mechanical properties of unidirectional hemp/epoxy composites. *Composite part A*, 90: 724-735, 2016.

[9] Y. Yao, H. Dou, T. Liu, S. Wang b, Y. Gao, J. Kang, X. Ga, C. X, Y. Lu and W. Fan. Micro- and nano-scale mechanisms of enzymatic treatment on the interfacial behaviors of sisal fiber reinforced bio-based epoxy resin. *Industrial Crops and Products*, 194: 116319, 2023.

©2024 | 2_RONCONI_Giulia_6HV0B.pdf:6

CHARACTERIZATION AND MODELLING OF TENSILE DAMAGE IN UNIDIRECTIONAL ALL-CARBON HYBRID LAMINATES

Thomas Martinoni[1,2], Valentin Ott[2], Valter Carvelli[1], Giovanni Pietro Terrasi[2]

[1] Department A.B.C., Politecnico di Milano, Milan, Italy
Email: thomas.martinoni@mail.polimi.it, valter.carvelli@polimi.it
[2] Swiss Federal Laboratories for Materials Science and Technology, Ueberlandstrasse 129, 8600 Dübendorf, Switzerland
Email: valentin.ott@empa.ch, giovanni.terrasi@empa.ch

Keywords: all-carbon hybrid laminates; pseudo-ductility; damage characterization, numerical model

Abstract
Hybridization of fiber reinforced polymers is a strategy to overcome the abrupt and brittle failure mechanism when reaching the ultimate strength of the typically brittle carbon, glass or aramid fibres. By combining fibres with different breaking strain, complex failure mechanisms are exploited, leading to pseudo-ductile behavior of the composite. The tensile pseudo-ductile behavior and the damage evolution of an all-carbon unidirectional hybrid laminate was studied in detail using an available analytical model, a developed 2D finite element model and various measurement and observation techniques including integrated fiber optic sensors, digital image correlation and X-ray micro computer tomography. A good correlation between the analytical as well as finite element models and the various experimental techniques was found.

1. Introduction

The lack of ductility of unidirectional long fibre reinforced polymers under tensile loading can be overcome by interlayer hybridization where low elongation (LE) material is sandwiched between high elongation (HE) material. This results in complex failure mechanisms, including multiple interacting damage modes, such as ply fragmentation and delamination [1], leading to pseudo-ductile tensile behavior of the laminate.
In this study, thick ply unidirectional all-carbon hybrid laminates with different layup sequences were manufactured to investigate their pseudo-ductile behaviour and damage evolution. High elongation Toho® Tenax® IMS60 (I) [2] and low elongation DIALEAD® K13916 (K) carbon fibres [3] were used. An available analytical model was exploited to design the laminates and predict the damage scenario by damage mode maps [4]. Quasi-static tensile tests were carried out using different measurement and observation techniques including digital image correlation (DIC), embedded distributed fibre optic sensors (DFOS) and micro X-ray computed tomography (microCT). A two-dimensional finite element model, inspired by [5], was also developed to predict the damage mechanisms. The model simulates the main damage modes observed experimentally, namely fragmentation and delamination. Fragmentation in the LE layer was predicted using translaminar embedded cohesive elements governed by a unimodal Weibull strength distribution. Delamination at the LE and HE layers interface was simulated using interlaminar cohesive elements. Validated by experimental results, the numerical model was found to accurately predict the quasi-static tensile damage modes and their evolution in the considered thick ply unidirectional all-carbon hybrid laminates and to accurately predict the pseudo-ductile tensile stress - strain behaviour.

2. Materials and numerical model features

Thick ply prepregs with a thickness of 0.2mm were used. One prepreg layer of fibre K was sandwiched between two 0.2mm thick prepregs of type I. This resulted in laminates with a total thickness of 0.6mm

and a width of 25mm (see Figure 1a). The material properties of the fibers and prepregs used are listed in Table 1. The fibre volume content was determined based on the weight of the prepreg and the density of the fibres. The theoretical Young's modulus E_1 was determined based on the rule of mixture.
GFRP tabs, 2mm thick and 70mm long, were glued to the specimen to clamp it in the universal testing machine using a hydraulic system. Two optical fibres Fibercore SM1250BI-(9.8/125) [6] with a coating diameter of 155µm were integrated during manufacturing of the specimens. One fibre was placed at the outer surface of the I layer, while the other was placed at the interface between I and K (see Figure 1a). According to the analytical model proposed in [4], the damage mode map predicts a failure of the considered laminate I/K/I driven by delamination after the first fragmentation, as illustrated in Figure 1b.

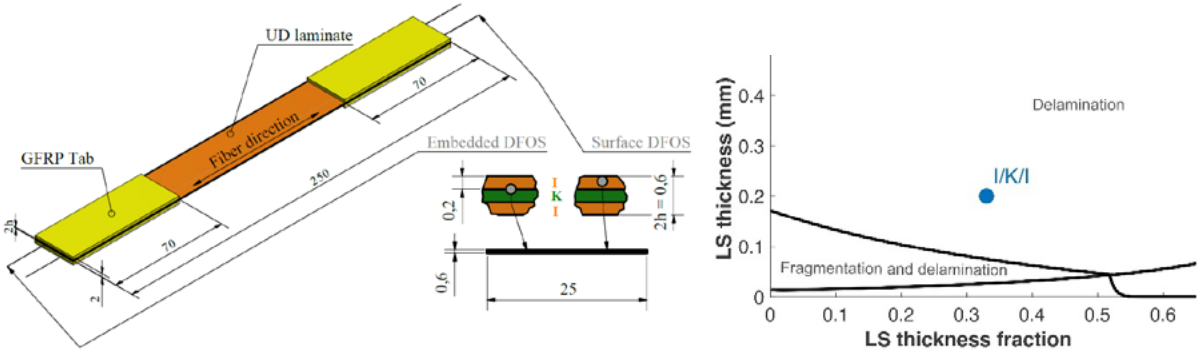

(a) (b)

Figure 1. (a) Geometry of tested specimens with integrated fibre optical sensors (gray), (b) Damage mode map according to the analytical model in [4].

Table 1. Properties of fiber K and I, and prepregs.

ID	*K*	*I*
Role	Low elongation material (LE)	High elongation material (HE)
Fiber	DIALEAD® K13916	Tenax® IMS60
Young's modulus E_{fl} (GPa)	760 [3]	290 [2]
Stress at failure σ_{fULT} (MPa)	3000 [3]	5600 [2]
Strain at failure ε_{fULT} (%)	0.4 [3]	1.9 [2]
Prepreg layer		
Thickness t (mm)	0.2	0.2
Measured fibre volume fraction (%)	61	61
Theoretical Young's modulus E_1 (GPa)	463	177

For the finite element analysis, a 2D model was developed, inspired by [5]. A total length of l = 50mm was modelled (see Figure 2). Plane strain 4-node elements were used, as provided by the commercial finite element software Abaqus® 2021. One layer of LE and two layers of HE with thickness $h_{HE} = h_{LE}$ = 0.2mm were considered. The material properties of the I and K layers used in the model are summarized in Table 3.
Cohesive elements were implemented to simulate the main damage modes, fragmentation and delamination. The cohesive elements at the LS/HS interface were used to simulate delamination, while the translaminar cohesive elements in the LS layer were used for fragmentation (see Figure 2). The thickness of the cohesive elements were selected as h_0 = 0.3µm, which is less than 1% of the thickness of the whole laminate as suggested by [7]. For all cohesive elements, a constitutive damage evolution law (linear softening at damage onset) was assumed. A large penalty stiffness K was used for the cohesive elements to avoid unrealistic material softening behavior (see Table 4 and Table 5). Moreover, ill-conditioning of the stiffness matrix was prevented by adding a low viscosity behavior to the cohesive

elements (μ=10^{-7} Pa·s). The interlaminar shear strength and the fracture energy of the cohesive elements were selected according to [4] (see Table 4 and Table 5). The random strength variability of carbon fibers was represented by a unimodal Weibull distribution in the LE carbon layer [8]. The characteristic strength was estimated as 2072 MPa to have the first failure at the nominal failure stress of the LS carbon layer, calculated using Hooke's law.

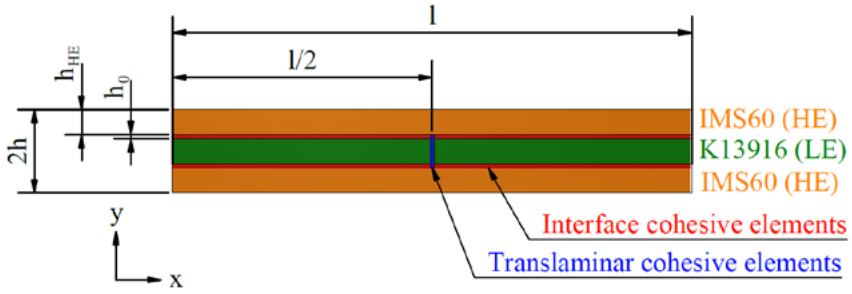

Figure 2. Sketch of the 2D *I/K*/I laminate model.

Table 2. Geometry dimensions of the I/K/I laminate 2D model.

Geometry parameters (see Figure 2*)*			
l (mm)	$2h$ (mm)	h_0(μm)	$h_{HE} = h_{LE}$ (mm)
50	0.6	0.3	0.2

Table 3. Mechanical properties and fiber volume fraction of the UD layers.

Role	E_x	E_y	G_{xy}	v_{xy}	V_f
LE	463 GPa	5 GPa	3.7 GPa	0.25	61 %
HE	177 GPa	7.7 GPa	4.14 GPa	0.3	61 %

Table 4. Properties of cohesive elements at the LE/HE interface.

K (N/mm^3)	$\sigma_n^0 = \tau_{tn}^0 = \tau_{sn}^0$ (MPa)	G_{Ic} (N/mm)	$G_{IIc} = G_{IIIc}$ (N/mm)
10^6	80	0.62	0.62

Table 5. Properties of translaminar cohesive elements in the LE layer.

K (N/mm^3)	Nominal failure stress (MPa)	G_{Ic} (N/mm)	$G_{IIc} = G_{IIIc}$ (N/mm)
10^9	1856	1.0	1.0

3. Results and discussion

The results for the thick ply laminate I/K/I are presented below. Additional information, including another layup I/K_3/I with 3 layers of LE material instead of 1 layer, are given in [8].

3.1. Stress-strain curves

The pseudo-ductile tensile response of the hybrid laminate can be described by three regions in the stress-strain diagram (Figure 3). In the first region, the initial stiffness (E_0) is well predicted by the analytical and FE model. The LE failure stress and the corresponding strain (ε_p) predicted by the FE model are closer to the measured than the analytical solution. This is due to hybrid effects [8], which are not considered in the analytical model. All three experimental measurement techniques show similar results. The gap in the DIC curve is due to the lower data acquisition rate of the system after the LE first

failure. The second region represents the pseudo-ductile plateau. Its strain range is also well predicted by the FE model, with good agreement with the experimental value of the maximum strain level in the plateau (ε_{pd}). In the third region, the experimental slope (E_1) of the second branch of the stress-strain curve is also well predicted by both models. The corresponding values and deviations of the models from the experimental results are summarized in Table 6.

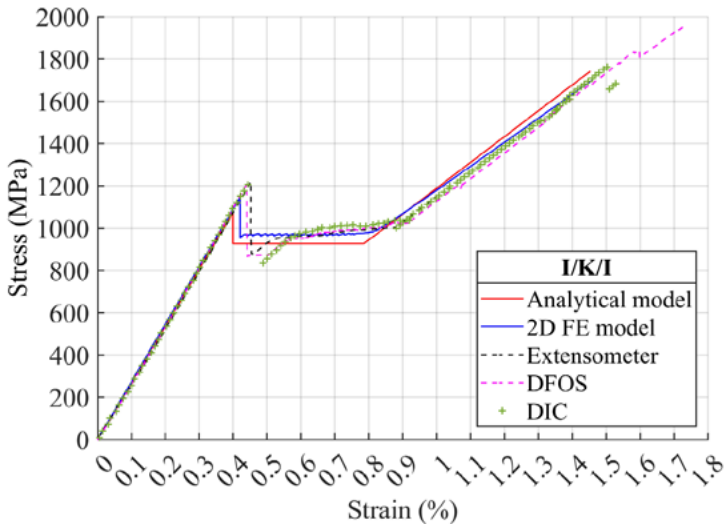

Figure 3. Comparison of stress vs. strain curves obtained by the analytical model, FE model and experimental tests measured by extensometer, DFOS and DIC.

Table 6. Experimental vs. predicted mechanical properties.

Property	*Experimental* *Mean ± Std dev.*	*Analytical model* *(Deviation from exp.)*	*FE 2D-model* *(Deviation from exp.)*
E_0 (GPa)	272 ± 4.8	272.3 (+0.1%)	272 (0%)
E_1 (GPa)	116.6 ± 10.9	119.8 (+2.7%)	114.1 (-2.1%)
ε_p (%)	0.436 ± 0.021	0.4 (-8.3%)	0.429 (-1.6%)
ε_{pd} (%)	0.836 ± 0.085	0.786 (-6.0%)	0.815 (-2.5%)

3.2. DIC

The full-field strain estimated by the DIC technique is obtained by measuring the relative movement of a speckle pattern on the surface. The test set-up used here is shown in Figure 4a. Discrete points along the stress-strain curve are shown in Figure 4b, their corresponding strain field is shown in Figure 4c. Apparently, the first damage of this specimen was initiated at a strain of 0.43% in the free length. The damage evolution can be clearly followed. A stable propagation of the delamination is detected by the DIC maps. The strain map at the end of the pseudo-ductile plateau (0.81%) showed an almost full delamination before following the second branch of the stress-strain curve. At a strain of 1%, a rather homogeneous strain map is shown, as predicted by the theory.

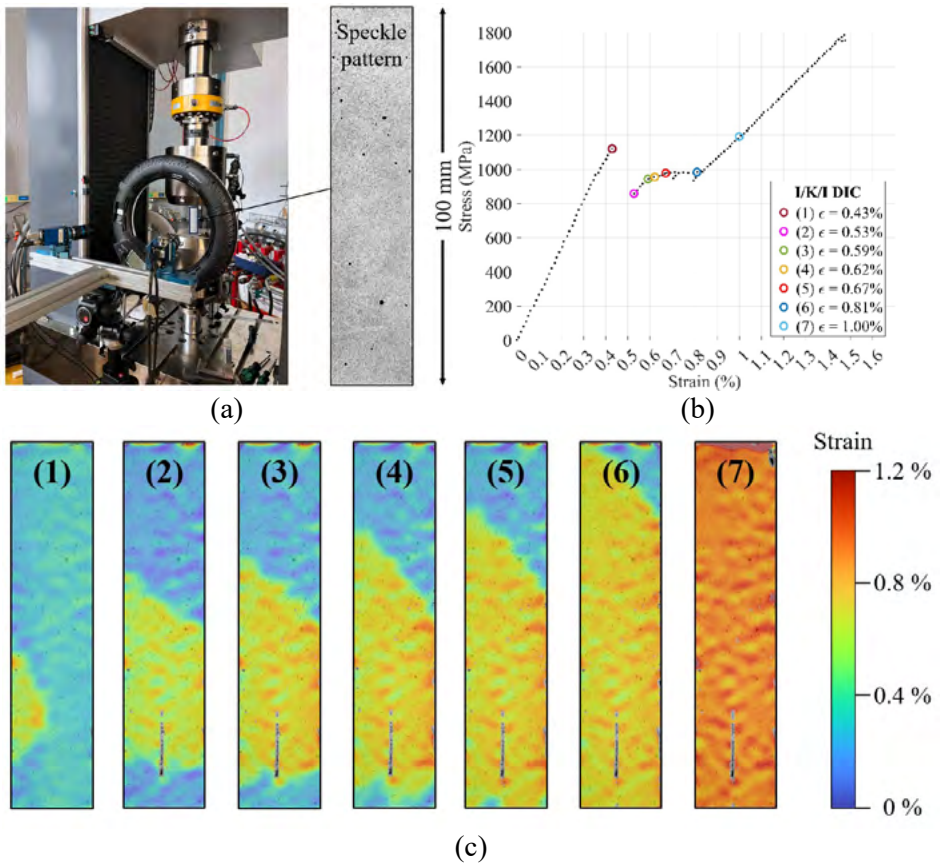

Figure 4. (a) DIC set-up, (b) stress-strain diagram obtained with DIC, (c) strain maps for different macro-strain levels.

3.3. Fiber Optic Sensing

Failure of CFRP specimens may be affected by the clamping system. Neither extensometer measurements, nor DIC can provide this information. In contrast, an integrated optical fibre, passing also through the clamping zone, can be used to detect it. Figure 5a shows the stress-strain curves of two specimens measured by the extensometer in a central section of 50mm. Figure 5b shows the strain distributions by the two optical fibers along the whole laminate, including the anchorage zone. A new zero measurement of the optical fibre was done after application of the hydraulic pressure on the clamps of the universal testing machine. Therefore, the stress concentration due to the lateral pressure of the clamps cannot be seen in this plots. Nonetheless, specimen 1 failed in the front region of the tab, while specimen 2 failed in the free length. Not surprisingly, specimen 2 reached also the higher first ply failure. The strain distribution of the surface DFOS in the HE material differs from the one at the HE/LE interface, where delamination takes place. The strain levels before and after the first ply failure in the region not delaminated are consistent.

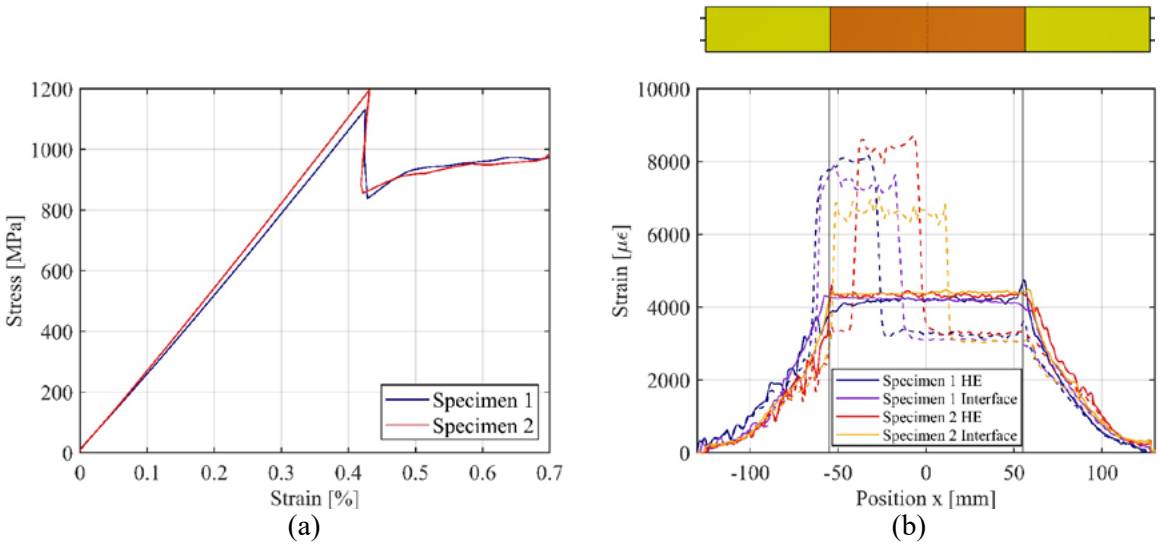

Figure 5. (a) Stress-strain curves of two specimens measured by extensometer; (b) strain distribution just before first failure of the K-layer (continuous) and after first failure (dashed).

3.4. X-Ray micro-CT

X-Ray micro-CT of different cross sections for a specimen loaded up to a strain of 0.54% is shown in Figure 6. Apparently, the mechanism of delamination is confirmed. Especially at the position between 66mm and 70mm, significant separation is present. At positions located closer than 52mm from the tab, delamination is not detected. This means that the 52mm portion near the tab has not been delaminated. Moreover it can be clearly observed that the ply thickness is not uniform. This variation is not taken into account in the model. In addition, a considerable porosity in the LE ply can be observed.

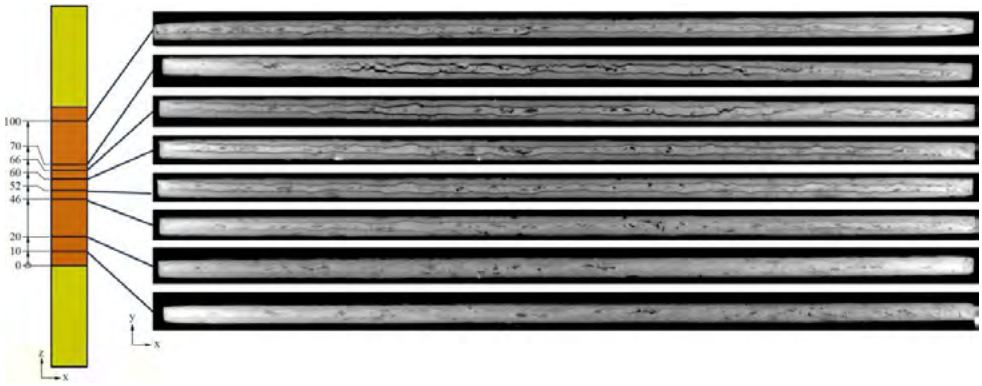

Figure 6. X-Ray micro-CT cross-sections of the I/K/I specimen loaded up to 0.54% strain (failure of LE ply at 0.44%).

4. Conclusions

An experimental and numerical study of the tensile pseudo-ductile behavior of thick ply all-carbon unidirectional laminates has been presented. The experimental characterization was supported by three strain measurement techniques: extensometer, distributed fiber optic sensing (DFOS) for strain distribution along a line inside the laminate, and digital image correlation for full-field strain on the surface. Moreover, X-ray microCT allowed to observe the delamination pattern at selected strain levels. The proposed numerical finite element 2D model shows a good accuracy in predicting the overall tensile behavior of the hybrid laminate compared to the experimental measurements. In addition, it allows the prediction of the evolution of the main damage modes, namely fragmentation of the LE ply and

delamination. This numerical model provided an in-depth understanding of the tensile damage behaviour and it is a useful tool for the design of such pseudo-ductile hybrid laminates.

Acknowledgments
The experimental support of Dr. Michele Griffa, Iurii Burda and Christian Rohrer is greatly acknowledged.

References
[1] Y. Swolfs, L. Gorbatikh, I. Verpoest, Fibre hybridisation in polymer composites: A review, Compos. Part Appl. Sci. Manuf. 67 (2014) 181–200. https://doi.org/10.1016/j.compositesa.2014.08.027.
[2] Toho Tenax, IMS60, (n.d.). https://www.ezentrumbilder.de/rg/pdf/td_en_IMS60_en.pdf.
[3] Mitsubishi Chemical Carbon Fiber and Composites, DIALEAD K13916, (2024). https://www.m-chemical.co.jp/carbon-fiber/pdf/tow/Carbon%20Fiber%20Tow%20(Continuous%20Fiber)%2020220630.pdf.
[4] M. Jalalvand, G. Czél, M.R. Wisnom, Damage analysis of pseudo-ductile thin-ply UD hybrid composites – A new analytical method, Compos. Part Appl. Sci. Manuf. 69 (2015) 83–93. https://doi.org/10.1016/j.compositesa.2014.11.006.
[5] M. Jalalvand, G. Czél, M.R. Wisnom, Numerical modelling of the damage modes in UD thin carbon/glass hybrid laminates, Compos. Sci. Technol. 94 (2014) 39–47. https://doi.org/10.1016/j.compscitech.2014.01.013.
[6] Dual Band Bend Insensitive Fiber, (n.d.). https://fibercore.humaneticsgroup.com/products/single-mode-sm-fiber/dual-band-bend-insensitive-fiber/sm1250b398125 (accessed December 7, 2022).
[7] W. Wagner, F. Gruttmann, W. Sprenger, A finite element formulation for the simulation of propagating delaminations in layered composite structures, Int. J. Numer. Methods Eng. 51 (2001) 1337–1359. https://doi.org/10.1002/nme.210.
[8] T. Martinoni, V. Ott, V. Carvelli, G.P. Terrasi, Tensile behavior of unidirectional thick-ply all-carbon hybrid laminates: a systematic experimental and numerical study, Compos. Part C(2024) 100462. https://doi.org/10.1016/j.jcomc.2024.100462.

LARGE-AREA HIGH THERMAL CONDUCTIVITY GRAPHITE FILM EASILY PRODUCED BY MECHANICAL EXFOLIATION OF NATURAL GRAPHITE USING A THREE-ROLL MILL

WANG Junhao[1], LIN Hongsheng[2] and ARAO Yoshihiko[3]

[1] Department of Applied Mechanics and Aerospace Engineering, Graduate School of Fundamental Science and Engineering, Shinjuku, Tokyo, JAPAN, Waseda University, Japan
Email: wangjunhao29@ruri.waseda.jp
[2] Department of Applied Mechanics and Aerospace Engineering, Graduate School of Fundamental Science and Engineering, Shinjuku, Tokyo, JAPAN, Waseda University, Japan
Email: hiromori@akane.waseda.jp
[3] Department of Applied Mechanics and Aerospace Engineering, Shinjuku, Tokyo, JAPAN, Waseda University, Japan
Email: arao@waseda.jp

Keywords: Thermal conductivity, Natural graphite, Roll-mill, Composites

Abstract
This paper concerns the thermal properties of exfoliated graphite films. Films made from mechanically exfoliated graphite by three-roll milling and blade coating, without relying on the environmentally hazardous GO, EG, strong acid processes, or using high temperature annealing that requires high energy and cost, which are commonly used in other produces graphene films with high thermal conductivity. The roll-milling process resulted in a dispersion of large, thick graphite coexisting with small, thin graphene nanoplatelet, with a thermal conductivity of 298.5 $W(mK)^{-1}$ for the film, which is as 3.16 times as that of the film produced by graphene nano platelet. The presence of large-grain graphite, which is small in number but large in mass ratio, led to a significant reduction in interfacial thermal resistance and an increase in thermal conductivity.

1. Introduction

With the rapid development of device performance in recent years, the amount of heat generated by devices have risen proportionally. In addition, as devices become smaller, they tend to heat up more easily, increasing the demand for better heat dissipation materials with higher thermal conductivity and lower density [1,2].

Graphene is a sheet-like material with a hexagonal lattice structure made up of carbon atoms and their bonds. Due to its high thermal conductivity (up to 5300 $W(mK)^{-1}$ for monolayer graphene [3,4]) and low density (2.2 $g(cm)^{-3}$), graphene has been actively investigated as a heat dissipating material.

As a general perception, the thermal conductivity of graphene increases as the number of layers decreases [5], reaching its maximum in a single layer. However, this holds true only under conditions where graphene is suspended. Where graphene is dispersed in the matrix, the thermal conductivity of graphene decreases as the number of layers decreases due to interface leakage of phonons [6], recovers to thermal conductivity close to that of bulk graphite over 30 layers [7]. Additionally, it has been reported that the thermal conductivity of graphite flakes increases with larger particle sizes [8].

There are two main methods for the preparation of existing graphene films: chemical/thermal reduction of graphene oxide (GO) and mechanical exfoliation of expanded graphite (EG) in the liquid phase, and there are quite few previous attempts to prepare graphene films from natural graphite. Graphene sheets

prepared by GO reduction have a relatively high thermal conductivity, The production of GO requires the use of strong acids, and the wastewater containing large amounts of them is a major environmental burden. The chemical reduction of GO also involves the use of hydroiodic acid, a strong acid that is toxic and extremely dangerous. Thermal treatment for defect healing requires extremely high temperatures (2600-3000°C), consumes large amounts of energy and costs and is not cost-effective. EG, like GO, is also environmentally hazardous because of the use of acids during its preparation. In addition, mechanical exfoliation in the liquid phase has a relatively low thermal conductivity compared to the reduction of GO, which is around 300 $W(mK)^{-1}$ at best without annealing at high temperatures [9, 10]. As for film formation methods, most existing graphene films are produced by vacuum filtration, which is time-consuming and difficult to form large-area films.

In this study, only natural graphite and carboxymethylcellulose (CMC) are used as raw materials, without the environmentally harmful GO, EG and strong acids as described above. The process also does not use annealing at extremely high temperatures, which consumes a huge amount of energy and costs, as described above, but uses a quite simple process of dispersion by roll milling, film production by blade coating. The reason for adopting roll mill is that large graphite flakes alone, which logically have high thermal conductivity, have poor dispersibility, so roll milling can create a state where large graphite flakes and small graphene coexist, aiming to improve dispersibility. Films made with a graphite:CMC mass ratio of 85:15 had a thermal conductivity of 213.2 $W(mK)^{-1}$ at low density (1.37 $g(cm)^{-3}$) without pressing, and films with a maximum density of 1.90 $g(cm)^{-3}$ and a thermal conductivity of 298.5 $W(mK)^{-1}$ were successfully produced by pressing.

2. Materials and Methods

2.1. Materials

The materials used in this study are ALDRICH graphite flakes (808113, +50 mesh) and Nippon Paper Industries' Sunrose CMC-Na (F04HC). The GNP for comparison is xGNP (M25) from XG Sciences.

2.2. Graphite film production method

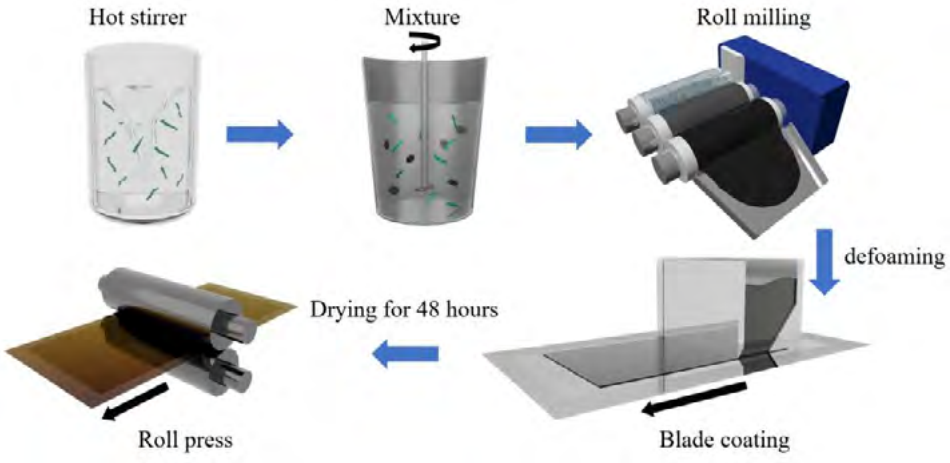

Figure 1. Schematic diagram of the graphene film fabrication procedure

Add CMC to pure water to a mass concentration of 3% and stirred in a hot stirrer (100°C, 1400 rpm) for 40 minutes to produce CMC aqueous solution. The mixture of graphite and CMC aqueous solution is prepared so that the graphite content in the solid is 35%, 45%, 55%, 65%, 70%, 75%, 80%, 85% and 90% (fixed at 85% for comparison of pass count) and stirred in a homogenizer at 5000 rpm for 10 minutes. The mixture is then dispersed in an AIMEX three-roll mill (BR-150HCV III). The mixture is passed through 1, 3, 5, 10, 20 and 30 (fixed at 10 passes for content comparison) passes at a finishing

roll speed of 350 rpm, a gap of 20 µm on the preparation side and 10 µm on the finishing side. The resulting slurry is defoamed in an oil-rotary vacuum pump (Azwan, AVRD-60A) for about 15 min and then the film is produced by blade coating. The blade height is set so that the film thickness after drying is 100 µm and the film is fed at a speed of about 0.8 m/min. The resulting film is dried at room temperature for at least 48 h. Finally, the graphite film is sandwiched between Kapton films with a total thickness of 50 µm and roll-pressed with a gap width of 65 µm. An overview of these operations is shown in Fig. 1.

2.3. GNP film production method

Add CMC to pure water to a mass concentration of 3% and stirred in a hot stirrer (100°C, 1400 rpm) for 40 minutes to produce CMC aqueous solution. The mixture of GNP and CMC aqueous solution is prepared so that the graphite content in the solid is 55%, 70% and 85%, and stirred in a homogenizer at 5000 rpm for 10 minutes. The resulting slurry is defoamed with an oil rotary vacuum pump (Azwan, AVRD-60A) for about 15 min and then the film is produced by blade coating. The resulting film is dried at room temperature for at least 48 hours and finally pressed at 200 MPa.

2.4. GNP film production method

The particle size of the prepared graphite was measured using a SHIMADZU nanoparticle size analyzer (SALD-7500nano). The dispersion was prepared so that the absorbance fell within the range of 0.1-0.15. The number of particles measured was 128.

To observe the morphology and orientation of graphite and porosity in the prepared films, measurements were made using a JEOL scanning electron microscope (JEM-6510LA) and a KEYENCE digital 3D microscope (VHX-5000). The CP surface was treated with a JEOL cross section polisher (IB-09020 CP) with an argon ion beam and treated for 5 hours to produce a cross-section.

Thermal conductivity was measured using a steady-state thermal conductivity measuring device. The sample size for the measurement was 2 cm wide and 15 cm long and the thermal conductivity was calculated from the heat transfer calculated from the temperature drop of the heater under steady state conditions and the temperature difference between the heater and each measured temperature point at a fixed distance from the heater.

3. Results

3.1. Effect of pass count

Fig.2.a shows a photograph taken from above in a dark room with a smartphone displaying a white image under the film. The white areas are voids where neither graphite nor CMC exist, indicating that dispersion is extremely poor without roll milling process and a film full of voids would be produced. These voids, which are visible to the naked eye, almost disappear after three or more passes of roll milling. Changes in dispersibility can also be observed from SEM, which shows that the film thickness becomes more uniform as the number of passes increases (Fig.2.c). Cross-sectional observation with an optical microscope differs from SEM in that the graphite reflects light and appears white, allowing the dispersion status of graphite and CMC to be determined. At low pass counts, the graphite is present as an agglomerate, but as the pass count increases, the graphite shows good dispersion as thin graphite between thick graphite, indicating that both thin and thick graphite are nicely orientated in the in-plane direction (Fig.2.d). In terms of density, the effect of roll milling is also significant, especially after pressing, where the density increases more than twice even after one pass (Fig.2.e). Due to this dispersion, thickness uniformity and density increase, the rate of increase in thermal conductivity is extremely high, especially in areas where the pass count is low (Fig.2.f). The particle size hardly changes up to 10 passes, and from 15 passes, the particle size decreases as the number of passes increases (Fig.2.b). This is thought to be due to an increase in pass count, which evaporates the water and increases the viscosity, which in turn increases the compressive and shear forces that the slurry is subjected to when it passes between the rolls. The saturating trend in thermal conductivity after 10 passes can be

attributed to the fact that the increase in thermal conductivity due to improved dispersion and film thickness uniformity is offset by the decrease in thermal conductivity due to reduced particle size.

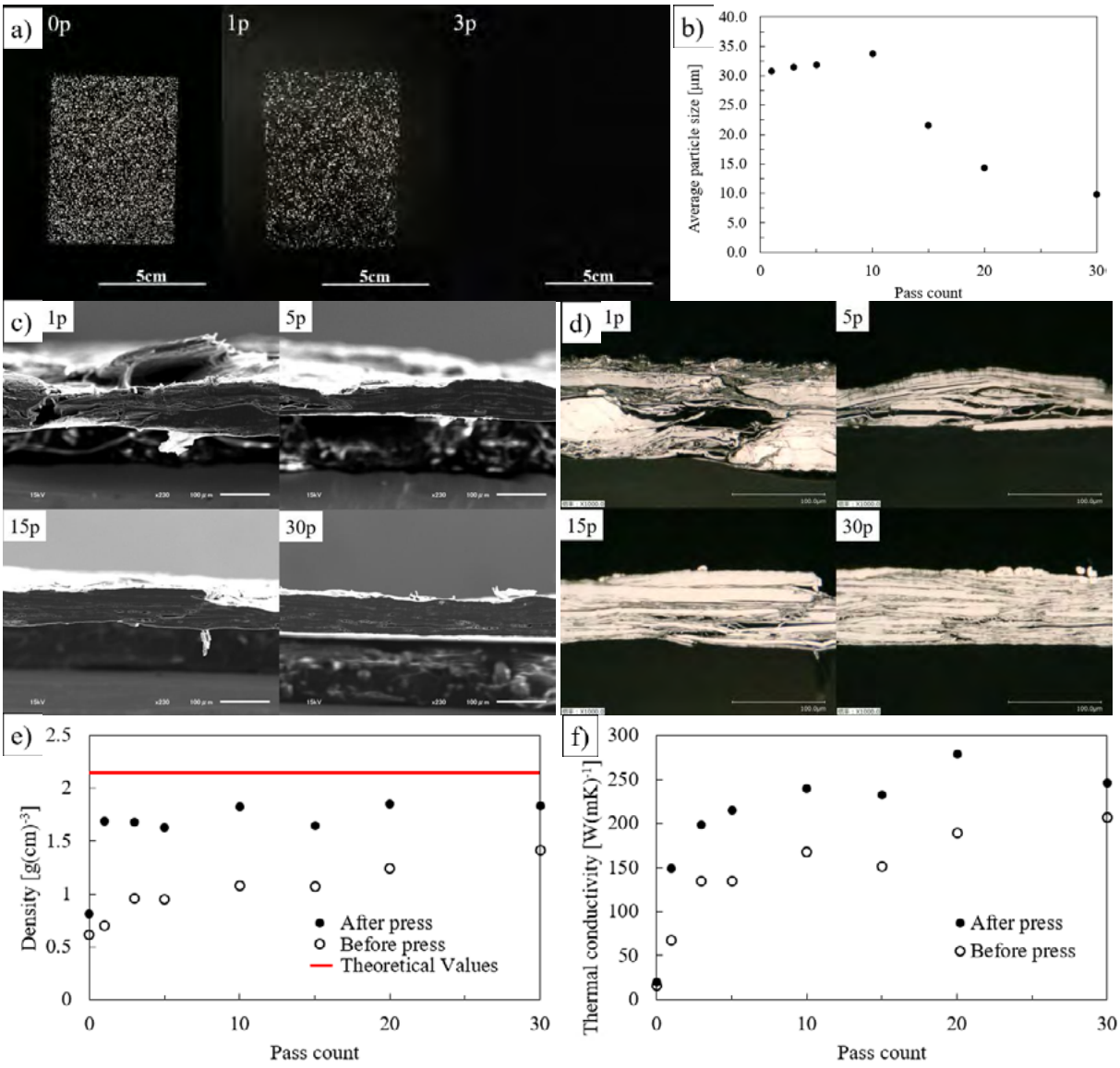

Figure 2. Comparison under different pass count. a) Film voids (before press), b) Average particle size, c) SEM images of cross-sections(before press), d) Optical microscope images of cross-sections(before press), e) Density, f) Thermal conductivity.

3.2. Effect of Graphite content

In comparison with graphite content, the thermal conductivity roughly increased with the increase graphite content, regardless of pressing, and a maximum thermal conductivity of 298.5 $W(mK)^{-1}$ and density of 1.90 gcm^{-3} could be measured at 85% graphite content (Figs 3.a and 3.b). 90% product have low strength and will fracture if pressed excessively, so the pressing pressure was reduced. The density and thermal conductivity of the film made from GNP were quite low before pressing, and after pressing the density reached a value similar to or slightly lower than that of the film made from natural graphite, while the thermal conductivity was less than half of the film made from natural graphite at all content ratios. Optical microscopy of the films made from natural graphite showed that large and thick graphite could be observed in large numbers, indicating that graphite was superior to GNP in terms of thermal conductivity of the composite. The presence of large graphite is considered to have significantly reduced

the interfacial thermal resistance, leading to an increase in thermal conductivity.

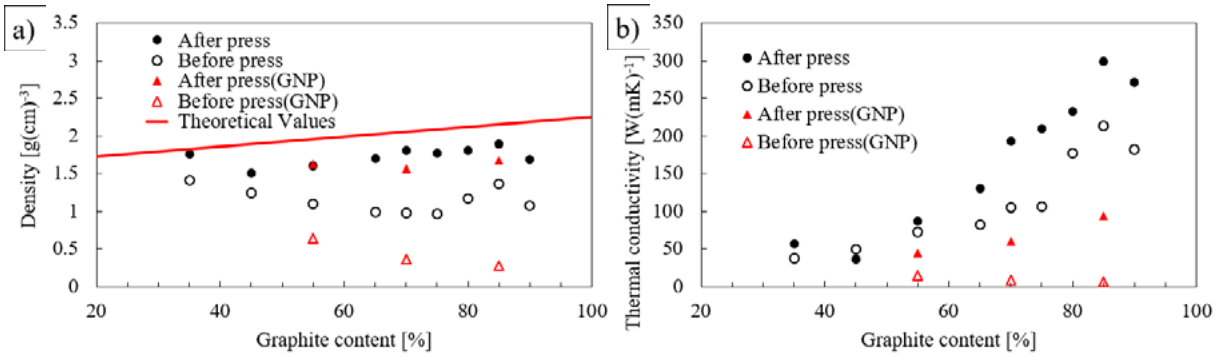

Figure 3. Comparison under different graphite content. a) Density, b) Thermal conductivity.

3.3. Comparison with theoretical values

The in-plane thermal conductivity of the films in this study is calculated using the Lin et al. model [14], which considers the interfacial thermal resistance.

$$K_{e11} = K_{e22} = K_m \frac{2 + f[\beta_{11}(1 - L_{11})(1+< cos^2\theta >) + \beta_{33}(1 - L_{33})(1-< cos^2\theta >)]}{2 - f[\beta_{11}L_{11}(1+< cos^2\theta >) + \beta_{33}L_{33}(1-< cos^2\theta >)]} \quad (1)$$

$$K_{e33} = K_m \frac{1 + f[\beta_{11}(1 - L_{11})(1-< cos^2\theta >) + \beta_{33}(1 - L_{33}) < cos^2\theta >]}{1 - f[\beta_{11}L_{11}(1-< cos^2\theta >) + \beta_{33}L_{33} < cos^2\theta >]} \quad (2)$$

$$\beta_{ii} = \frac{K_{fii} - K_m}{K_m + L_{ii}(K_{fii} - K_m)} \quad (3)$$

$$L_{11} = L_{22} = \frac{p^2}{2(p^2 - 1)} + \frac{p}{2(1 - p^2)^{3/2}} cos^{-1} p \quad (4)$$

$$L_{33} = 1 - 2L_{11} \quad (5)$$

$$K_{f11} = K_{f22} = \frac{B}{2R_k + B/K'_{f11}} \quad (6)$$

Where K_{e11} $(=K_{e22})$ is the effective thermal conductivity in the in-plane direction of the composite, K_{e33} is the effective thermal conductivity in the out-of-plane direction of the composite, f is the volume fraction of the filler, K_m is the thermal conductivity of the matrix, K_{f11} $(= K_{f22})$ is the theoretical thermal conductivity of the filler in the in-plane direction, p is the reciprocal of the filler aspect ratio (thickness/particle size), $<\cos^2\theta>$ is the statistical orientation of the filler.

The material constants are set as follows. Theoretical thermal conductivity of graphite in in-plane direction K_{f11}= 1600 W(mK)$^{-1}$, thermal conductivity of CMC K_m = 0.4 W(mK)$^{-1}$, orientation constant $<\cos^2\theta>$= 1, Aspect ratio = 400, film density is 0.9 times the theoretical density, graphite grain size B = 20 µm.

The calculation results are shown in Fig. 4. As the interface thermal resistance between graphene and CMC is unknown, the calculations were performed to fit the experimental values, which showed good agreement with the experimental values for natural graphite at 1.5 × 10^{-8}m^{2}KW^{-1} and for GNP at 7 × 10^{-8} m^{2}KW^{-1}.

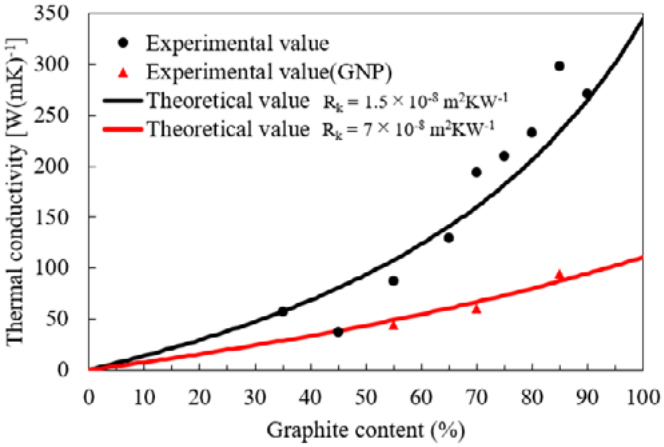

Figure 4. Comparison of theoretical and experimental values of thermal conductivity under different graphite content.

4. Conclusions

This study succeeded in producing a graphite composite film with almost the highest thermal conductivity in similar studies, using only roll-milling and blade-coating methods, which are suitable for industrial production. The roll-milling process significantly reduced the voids in the film and increased dispersion and orientation, leading to a significant increase in thermal conductivity, proving the usefulness of roll-milling. The highest thermal conductivity of 298.5 $W(mK)^{-1}$ was recorded after pressing 85% product, and relatively high thermal conductivities were recorded even for films of low density and low graphite content. Graphite was found to be better than GNP in terms of thermal conductivity of composites, and that making films with graphite flakes of large particle size, which can form a proper heat path, can lead to higher thermal conductivity.

Acknowledgments

This work was the result of using research equipment (G1016, G1023, G1039) shared in MEXT Project for promoting public utilization of advanced research infrastructure (Program for supporting construction of core facilities) Grant Number JPMXS0440500024.

References

[1] Balandin, Alexander A. "Thermal properties of graphene and nanostructured carbon materials." Nature materials 10.8 (2011): 569-581.

[2] Feng, Wei, Mengmeng Qin, and Yiyu Feng. "Toward highly thermally conductive all-carbon composites: Structure control." Carbon 109 (2016): 575-597.

[3] Balandin, Alexander A., et al. "Superior thermal conductivity of single-layer graphene." Nano letters 8.3 (2008): 902-907.

[4] Ghosh, D. S., et al. "Extremely high thermal conductivity of graphene: Prospects for thermal management applications in nanoelectronic circuits." Applied Physics Letters 92.15 (2008): 151911.

[5] Ghosh, Suchismita, et al. "Dimensional crossover of thermal transport in few-layer graphene." Nature materials 9.7 (2010): 555-558.

[6] Jang, Wanyoung, et al. "Thickness-dependent thermal conductivity of encased graphene and ultrathin graphite." Nano letters 10.10 (2010): 3909-3913.

[7] Sadeghi, Mir Mohammad, Insun Jo, and Li Shi. "Phonon-interface scattering in multilayer graphene on an amorphous support." Proceedings of the National Academy of Sciences 110.41 (2013): 16321-16326.

[8] Nika, Denis L., Artur S. Askerov, and Alexander A. Balandin. "Anomalous size dependence of the thermal conductivity of graphene ribbons." Nano letters 12.6 (2012): 3238-3244.

[9] Yang, Weixing, et al. "Completely green approach for the preparation of strong and highly conductive graphene composite film by using nanocellulose as dispersing agent and mechanical compression." ACS Sustainable Chemistry & Engineering 5.10 (2017): 9102-9113.

[10] Yang, Weixing, et al. "Strong and highly conductive graphene composite film based on the nanocellulose-assisted dispersion of expanded graphite and incorporation of poly (ethylene oxide)." ACS Sustainable Chemistry & Engineering 7.5 (2019): 5045-5056.

Saxophone and Clarinet Reeds made from Thermoplastic Composite Materials

Lars Wollert[1], Jan Kallweit[1], Julia Lenz[1], and Thomas Gries[1]

[1]Institut für Textiltechnik , RWTH Aachen University, Otto-Blumenthal-Str. 1, 52074 Aachen, Germany
Email: lars.wollert@ita.rwth-aachen.de, Web Page: https://www.ita.rwth-aachen.de/

Keywords: natural fibre composite, flax fibre, saxophone reeds, thermoplastic composites

Abstract
As part of the research work, the production of saxophone reeds from synthetic materials is being investigated in more detail. For this purpose, sheets are produced using the thermopress process on the basis of hybrid yarn semi-finished products. Semi-finished products based on woven glass-PP and glass-LPET are used as materials. In addition, the use of the material pairing flax and PP made from woven fabrics and unidirectional fabrics is being investigated. To analyse the mechanical properties, the samples are subjected to three point bending tests and the flexural modulus and flexural strength are determined.

1. Introduction

Traditionally, instrument reeds, which are necessary for sound production, are made from the wood of the pile cane (Arundo Donax). The material properties of Arundo Donax are influenced by different cultivation and harvesting conditions. These irregularities occur even when material from the same trunk is considered. As a result, depending on the musician and reed manufacturer, only a fraction of the natural reeds are judged to be playable and tonally usable. In addition, the Arundo Donax is susceptible to unavoidable influences such as moisture and saliva bacteria, which limits its lifespan. Due to the fluctuations in quality of the reeds resulting from the variability of the material and their limited lifespan, synthetic replacement materials have been used for many years. These enable increased durability and reproducible quality.
The use of raw materials from renewable sources such as natural fibre reinforcements or bio-based matrix materials offers great potential for sustainable fibre composite components. The use of thermoplastics in particular is ecologically and economically promising. In contrast to thermosets, it is already possible to produce thermoplastics completely biobased. In addition, cycle times can be reduced to a minimum.
As part of the research work, a sustainable composite material is being developed that is similar to the acoustomechanical properties of Arundo Donax. For this purpose, different material combinations of various natural fibres and thermoplastic matrix materials are combined to specifically adjust the stiffness, density and damping.

1.1. saxophone reeds

The sound of a saxophone is produced by periodic movements of the thin tip of the reed, which is caused to vibrate by a stream of air. Fig. 2.1 shows the structure of a classic saxophone reed.

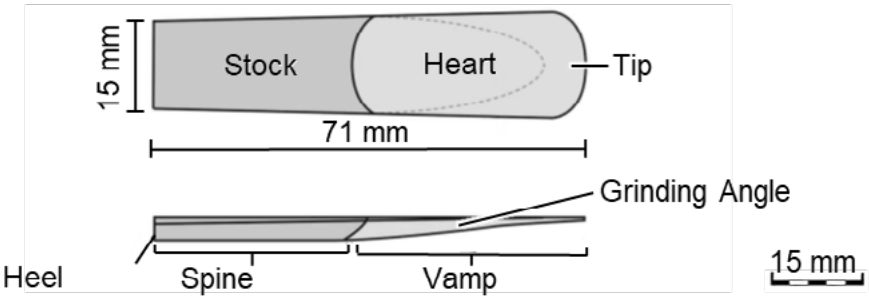

Figure 1: Construction of an alto saxophone reed

The reed is placed on the lower lip, with which the reed is bent towards the mouthpiece by exerting pressure. The mouth rim encloses the mouthpiece as airtightly as possible so that an overpressure is created when blowing. The playing end aims to form a small gap between the tip of the reed and the tip of the mouthpiece. The air flows through this gap in a controlled manner. This creates a pressure difference between the top and bottom of the reed. It begins to vibrate, alternately closing and opening access to the air column in the instrument, which in turn is stimulated to vibrate. The process is illustrated in Fig. 2.1. The tip of the reed must be very light and stiff in order to vibrate. At the same time, it needs a high degree of elasticity in the longitudinal direction so that it does not break. In the transverse direction, the reed must be flexible enough to allow the player to bend it airtight against the side rail of the mouthpiece through the pressure of the lips [UD20].

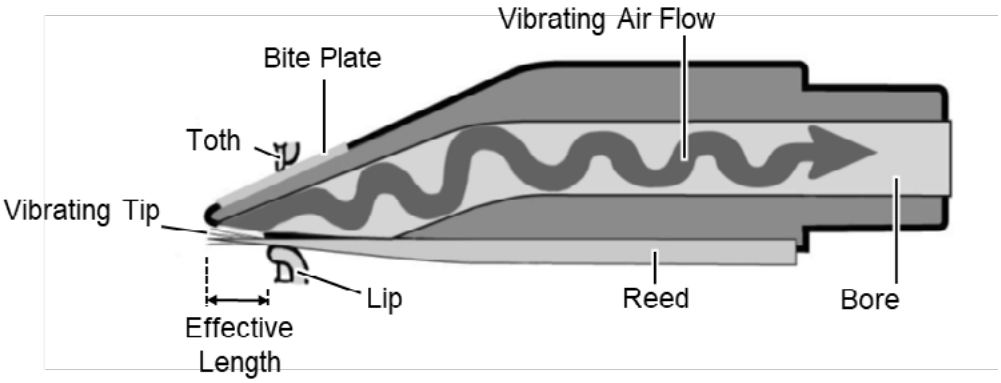

Figure 2: How the reed works on the mouthpiece

The wood of the giant reed Arundo Donax has traditionally been used as the raw material. The plant is an upright-growing, perennial reed with an inner cavity. It grows wild in warm, temperate regions and is cultivated specifically for reed production in certain European landscapes, particularly in France and Spain. The plant can grow to a height of 4 to 6 metres, with an outer diameter of about 2 to 4 cm and a diameter of the cane wall of 2 to 7 mm [Per58]. The reeds are produced by first cutting a cane into three or four strips in the longitudinal direction of the reed fibres. Each strip is cut straight on the inside and thinned on the outside with fine sandpaper to half its length towards the tip [Per58]. This removes the outer and middle layer so that the vibrating part of the leaf consists of the vascular bundles lying in the longitudinal direction.
When the leaf is bent by blowing and lip pressure, the fibres are stretched. This gives the wood a high degree of rigidity in the longitudinal direction. As there are no wood fibres in the transverse direction, only the matrix of parenchyma cells is bent when pressure is applied in this direction. It has a lower modulus of elasticity than the fibres. [UD20]

1.2. Composit materials used as saxophone reeds

Since around the middle of the 20th century, research has been carried out into replacement reeds made of polymer or composite materials. The aim is to guarantee musicians consistent quality and a longer reed life. [WLB+18; UD20] There are now a whole range of different saxophone reeds on the market that offer reeds made of plastics or fiber-reinforced plastics. An overview of the manufacturers can be found in the following table:

Table 1: Manufacturer of synthetic reeds

Manufacturer	Headquarter	Materials
Bari Woodwinds, Inc	Palmetto, Florida, USA	Twill 2/2-Fabric
D'Addario Woodwinds	Farmingdale, New York, USA	Twill 2/2-Fabric
Fibracell	San Marcos, Kalifornien, USA	Twill 2/2-Fabric
Forestone	Osaka, Japan	Twill 2/2-Fabric
Harry Hartmann Fiberreed	Oberaichen bei Stuttgart, Deutschland	Unidirectional
Légère Reeds LTD	Barrie, Ontario, Canada	Twill 2/2-Fabric Nonwoven
Silverstein Works	Ringefield, New Jersey, USA	Twill 2/2-Fabric Nonwoven
Yamaha Corporation	Hamamatsu, Japan	Twill 2/2-Fabric nonwoven

The current focus of most research projects is therefore on simulating the structure of Arundo Donax. These are mimicked, for example, by thermoset polymers filled with parallel glass or carbon fibers [Har22] or by the orientation of the polymer backbone of thermoplastic materials by stretching the polymer [Lég00; Lég22]. These sheets, compared to polycarbonate and polyacrylic, contain fibers that give them highly anisotropic elasticity parameters comparable to Arundo-Donax. [WLB+18]

2. Experimentation

2.1 Materials an Sample Preperation

Various semi-finished products available on the market based on hybrid yarns are used to manufacture the test specimens.

PP-Glass Prepreg:

The PP prepreg (polypropylene) used is a hybrid glass fabric pre-impregnated with PP from Comfil ApS (product number 30028-17). According to the manufacturer, the prepreg is easy to process, drapes well and has low porosity thanks to the 2/2 body weave. PP also has high chemical resistance. The basis weight is 700g/m² [Com21b; Com21a].

LPET-Glass Prepreg:

The LPET prepreg (modified polyethylene terephthalate) used is a hybrid glass fabric pre-impregnated with LPET from Comfil ApS (product number 30001-3). LPET is modified PET (polyethylene terephthalate), which is completely amorphous before and after the process. Due to the 2/2 body bond, the prepreg has the same properties as PP prepreg. LPET also has high chemical resistance and good wettability of the fibres. The basis weight is 750 g/m² [Com21b; Com21a]

PP-Flax Prepreg
The EcoRein F/PP 50 material selected for the three-point-bending tests is a bidirectional hybrid yarn fabric manufactured by BPREG Composites, Izmir, Turkey. The fabric consists of flax fibres and a polypropylene (PP) staple fibre yarn in a 50/50 ratio and has a 2x2 body weave. The manufacturer specifies a basis weight of 260 g/m2. Unidirectional semi-finished products of the manufacturer are specified with a recommended processing temperature of 190-210°C.

Table 2: Overview of the individual composite specimens

Specimen Type	*Material*	*Type*	*Supplier*	*Density* *[g/m³]*
1	Glas-PP	Twill 2/2-Fabric	Comfil 30028-17	1,49
2	Glas-LPET	Twill 2/2-Fabric	Comfil 30001-3	1,88
3	Flax-PP	Twill 2/2-Fabric	BPreg EcoRein F/PP 50	1,10
4	Flax-PP	Twill 2/2-Fabric	BPreg EcoRein F/PP 50	1,10
5	Flax-PP	Unidirectional	BPreg UD50	1,10

2.23-Point Bending Test
The three-point bending test is a method of destructive material testing used to determine the flexural modulus and flexural strength of the stress-strain relationship of thermoplastics or thermosetting plastics. These parameters are a measure of the stiffness or bending capacity of the material. The flexural modulus is defined as the slope of the curve in the stress-strain diagram in the linear elastic range. The ISO 14125 standard uses the three- and four-point method to determine the flexural properties of fibre-reinforced plastics. This standard is based on the contents of ISO 178, which applies to the determination of the flexural properties of plastics, but extends these to include the aspect of fibre reinforcement. [DIN11]

Testing machine
The testing machine must be designed in accordance with the ISO 5893 standard. The specimen is placed on two parallel supports and bent on the other side of the specimen using a compression fin. The compression fins and supports are arranged as shown in Figure 2.9. The radius of the supports depends on the thickness of the specimen. Measuring screws or equivalent measuring devices are used to record the measured values.

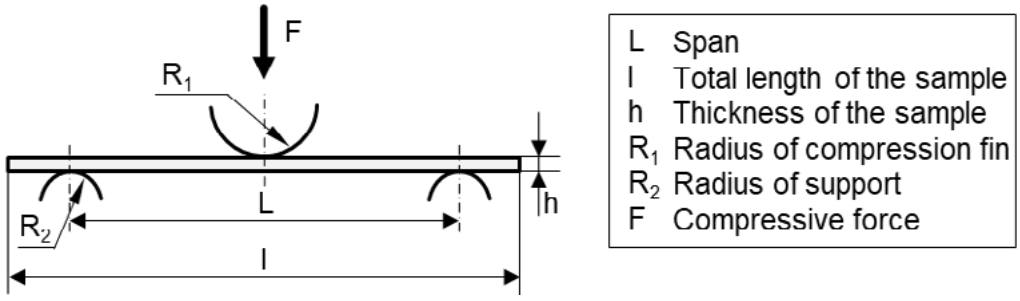

Figure 3: Geometry and arrangement of supports and compression fins based on [DIN11]

Specimen body
The specimen type has a rectangular cross-section without rounded edges. The preferred dimensions for a continuously reinforced, for example by fabric, plastic (type II) can be taken from the standard. The span and the total length are determined in relation to the thickness of the specimen. Specimens with dimensions deviating from the standard can lead to the results not being comparable. [DIN11]

Test method
The compression fin deforms the specimen at a constant speed. This occurs until the specimen breaks or reaches a required characteristic value. The deflection and the applied force are measured during the process with the aid of measuring equipment. The types of failure of a sample that can be analysed are those fractures that are triggered away from the support points by tensile or compressive stress. Failure due to interlaminar shear, as shown in Figure 2.10, is not acceptable. [DIN11]

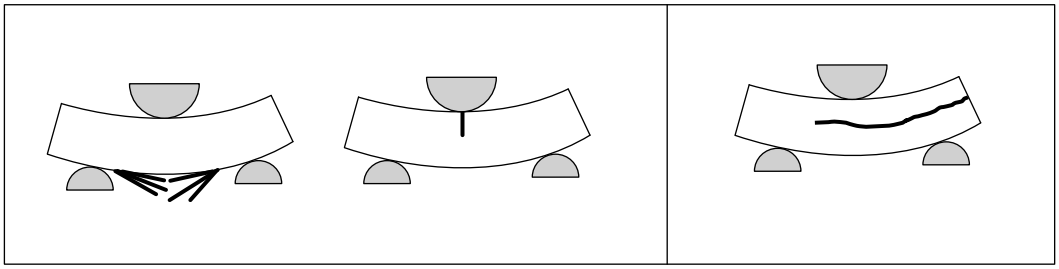

Figure 4: Fracture due to tensile and compressive stress, permissible (left); fracture due to interlaminar shear, not permissible (right) [DIN11].

3. Results
The bending properties are determined by a three-point bending test. The bending test determines the maximum bending stress and the bending modulus. The bending test provides information about the strength and stiffness both in the direction of the grain and perpendicular to the grain direction.

3.1 Glass
The following figure shows the results of the 3-point bending tests of the semi-finished glass products.

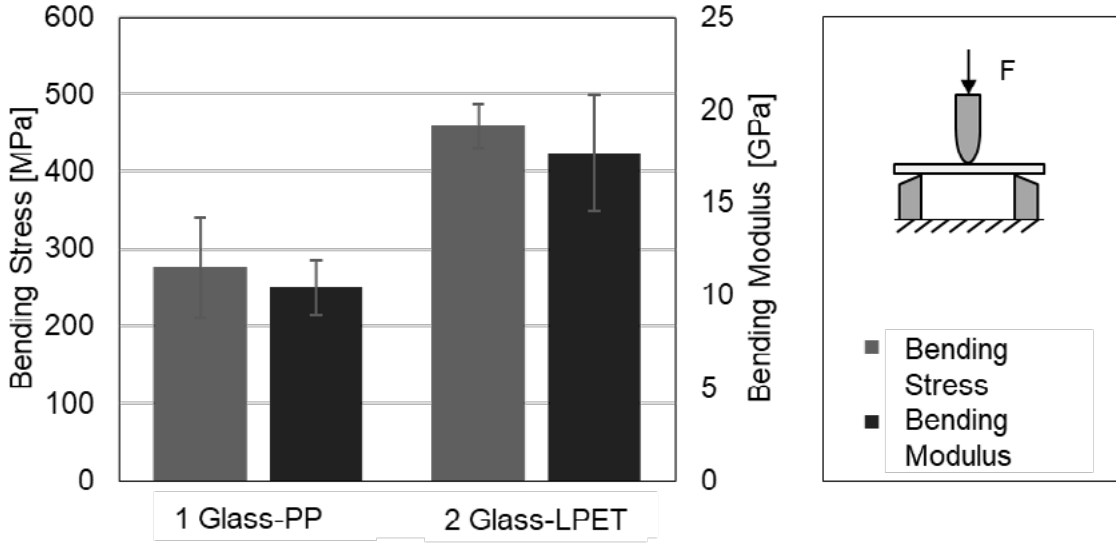

Figure 5: Tensile properties of the glass fibre test specimens

The test specimen made of glass and PP has a flexural rigidity of 276 MPa with a standard deviation of 65.1, while the flexural modulus is 10.4 GPA with a deviation of 1.44.At 459 MPa an a deviation of 28,3, glass-LPET has a 66% higher specific flexural strength and, at 17.7 GPa (deviation = 3,12), a 70% higher flexural modulus compared to glass-PP.

3.2 Flax

Figure 6 shows the flexural properties of the flax PP specimens. The unidirectionally reinforced test specimen (5) exhibits the highest specific flexural strength (52 MPa) and the highest specific modulus of elasticity (8.7 MPa).

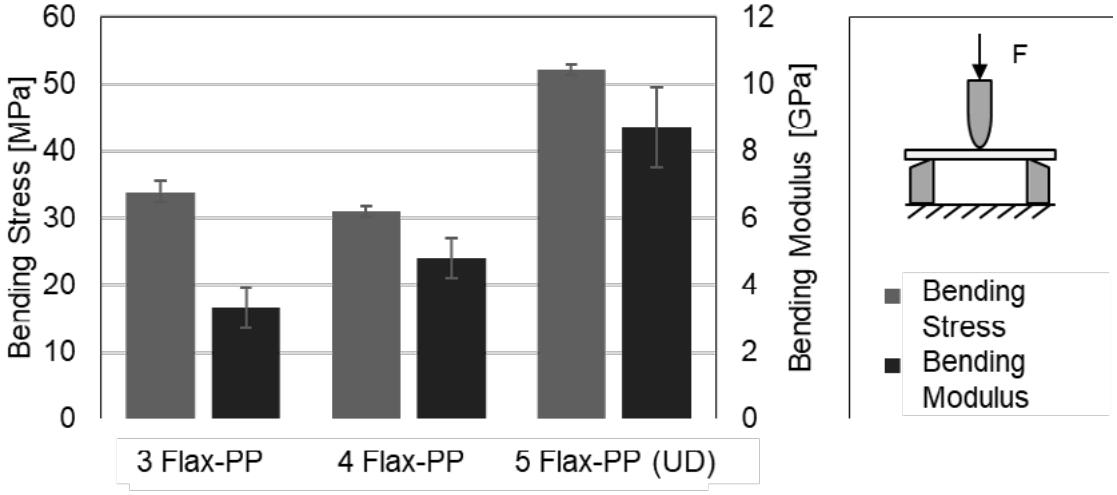

Figure 6: Bending properties of test specimens made from flax-PP semi-finished products

The fabric-based specimens 3 and 4 perform quite similarly. Specimen 3 has a flexural strength of 33.9 (standard deviation s = 1.67) and a flexural modulus of 3.33 GPa with a deviation of 0.62. The pre-consolidated specimen 4 has a lower flexural strength of 30.9 MPA (s = 0.758). However, it shows a higher flexural modulus of 4.79 GPa (s = 0.586).

3.3 Discussion

The functioning of a saxophone reed can be idealised as a harmonic oscillation. In this case, the undamped natural frequency is proportional to the square root of (D/m). D is the spring constant and thus proportional to the bending modulus E. m is the mass and can be seen as proportional to the density. This results in the following relationship.

$$f \sim \sqrt{\frac{D}{m}} \sim \sqrt{\frac{E}{\rho}} \tag{1}$$

For saxophone reeds, the Arundo Donax reed has established itself. All sound characteristics are adapted to this reed. For this reason it is necessary that the stiffness to mass ratio is as similar as possible. Sources show that in addition to vibration along the blade orientation, there are other vibration modes that depend on the modulus of elasticity transverse to the fibre direction. In this research work, however, only an idealised comparison is given in the most important vibration modes along the blade direction. Figure 7 shows an overview of the relationship between bending depth and density. Specimens A1-A5 are considered in relation to the benchmark of Arundo Donax (A6). According to the literature, Arundo Donax has a flexural modulus of 5.7 with a density of 0.75, resulting in a stiffness to mass ratio of 7.6 (light grey balance line). A comparison with the manufactured test specimens shows that the material combination A1 (flax-PP) and the material combination Flass + PP as unidirectional semi-tensile show great similarities in mass stiffness behaviour. Similar mirror properties can therefore be expected here.

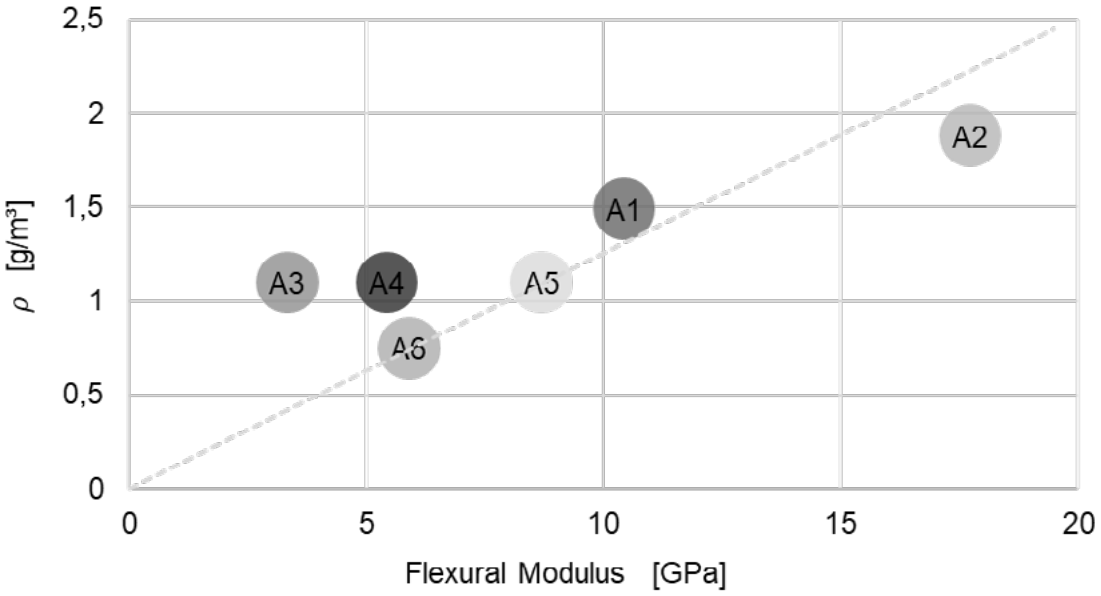

Figure 7: Flexural Modulus of different Materials

The test specimen blanks were successfully processed using conventional machines. The following illustration shows the realisation of test specimens 1, 2, 3 and 5.

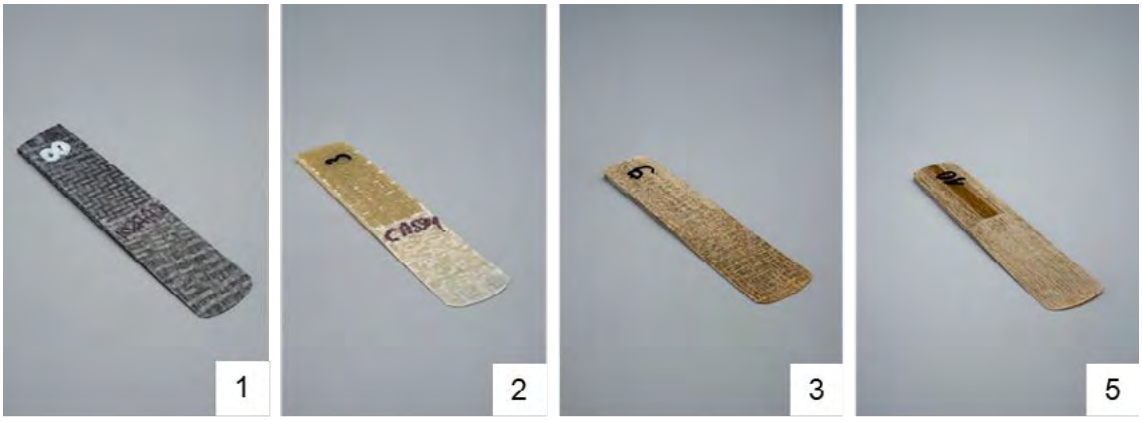

Figure 8: Overview of semi-finished products processed into saxophone reeds

Play tests were able to assign the best playing characteristics to sheets 1 and 5. However, an analysis within a scientific framework is still pending.

4. Conclusion

As part of this research work, saxophone reeds were produced on the basis of thermoplastic semi-finished products. Test specimens based on hybrid yarn semi-finished products made of glass and flax fibres were used for this purpose. In addition to the material pairings of glass-PP and glass-LPET, test specimens made of flax-PP were produced both on the basis of fabrics and on the basis of unidirectional semi-finished products. A subsequent investigation of the bending properties provided information about the bending modulus. Glass-LPET has the highest flexural modulus at 17.7 GPa. Glass-PP follows closely behind with 10.4 GPa. The unidirectional flax fibre semi-finished product (5) has a flexural modulus of 8.7 GPa. While the two flax fabric samples have the lowest flexural moduli of 3.33 and 4.79 GPa.

References

[1] E. Ukshini, J.J.J. Dirckx, Materials (Basel, Switzerland) 13 (2020).

[2] R.E. Perdue, Econ Bot 12 (1958) 368–404.

[3] B. Weidenfeller, O.A. Lambri, F.G. Bonifacich, U. Arlic, D. Gargicevich, Mat. Res. 21 (2018).

[4] Harry Hartmann's Fiberreed, Harry Hartmann's Fiberreed. fiberreed.de/en/the-idea/.

[5] G. Legere, Oriented polymer reeds for musical instruments. US19980075175P;US19990248902 G10D9/02;G10D9/02(US6087571 (A)), 1999.

[6] Légère Reeds Ltd., Why They Work. www.legere.com/need-to-know/why-they-work/.

[7] Comfil ApS, Fabric | Comfil. www.comfil.biz/comingled-composites/fabric/.

[8] DIN, DIN EN ISO 14125:2011-05, Faserverstärkte Kunststoffe - Bestimmung der Biegeeigenschaften (ISO_14125:1998_+_Cor.1:2001_+_Amd.1:2011); Deutsche Fassung EN_ISO_14125:1998_+_AC:2002_+_A1:2011, Berlin, Beuth Verlag GmbH, 10.31030/1753441.

CHARACTERIZATION OF MECHANICAL PROPERTIES OF A 3D-PRINTED CONTINUOUS BASALT FIBER REINFORCED COMPOSITE

Marco Zanelli[1], Giulia Ronconi[1], Valentina Mazzanti[1] and Francesco Mollica[1]

[1]Department of Engineering, University of Ferrara, Via Saragat 1, 44123 Ferrara, Italy
Email: marco.zanelli@unife.it

Keywords: Fused filament fabrication, Fused deposition modeling, Classical lamination theory

Abstract
A possible way to improve the mechanical properties of fused filament fabricated 3D printed materials is to use continuous fiber reinforcement. Recently, 3D printers that can print continuous fiber reinforced materials have appeared on the market, therefore it is interesting to test whether these materials possess mechanical characteristics, which render them suitable for structural applications. The tensile strength of a continuous basalt fiber reinforced 3D printed polyamide 12 is investigated. Since the material is anisotropic, methods that are typical of composite materials are utilized, in particular the ASTM D3039 standard was followed for specimens loaded along the longitudinal and transverse direction. Shear strength was estimated through tensile testing at a 10° loading direction. It was confirmed that the material is anisotropic and possesses quite a relevant strength in the longitudinal direction, while the properties in the transverse direction and at 10° are much lower. The reasons for these low properties in the transverse direction can be correlated to the voids that are inevitably introduced during printing. Therefore, such a material can be successfully used as a structural material, but care must be used in order to optimize the printing direction as a function of the applied external loading.

1. Introduction

Despite the continuously rising interest towards 3D printing technologies for manufacturing structural polymeric parts, it is still difficult to obtain a sufficient degree of reliability [1]. This is mainly due to the mechanical properties of the printed materials that are usually well below what can be expected from an injection molded or extruded part [2].

One possibility to obtain higher mechanical properties is to use short reinforcement fibers, as it is commonly done in traditional polymer processing techniques. Indeed, short fiber reinforced filaments to be used in Fused Filament Fabrication (FFF) are becoming more and more common for structural applications, nevertheless the gain in terms of stiffness and strength is quite limited. In order to increase such properties in a very substantial way, usage of longer fibers would be of course convenient, but in such a case it is quite clear that 3D printing cannot be performed with standard technologies.

Quite recently, novel 3D printing devices that are capable of manufacturing continuous fiber reinforced (CFR) polymers have appeared commercially. Examples are the Composer systems by Anisoprint (Luxembourg) and the X7 printer by Markforged (Walthan, MA, USA). For instance, the Anisoprint Composer printer works by co-extruding a polymeric filament and CFR together (Figure 1), using an ad-hoc developed slicing software.

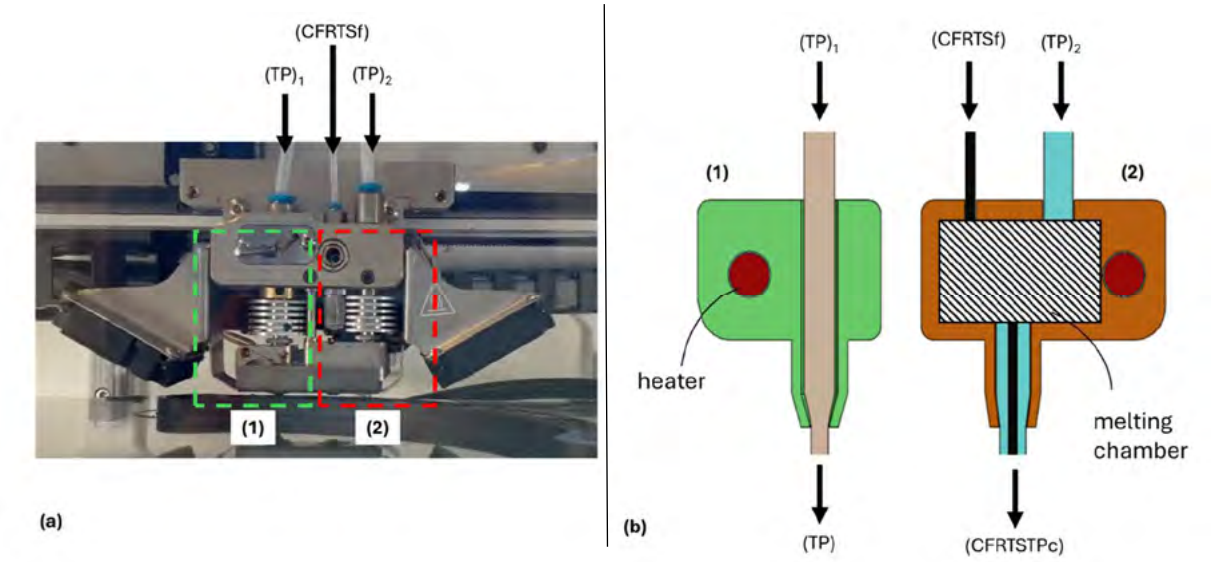

Figure 1. The printing head of the Anisoprint Composer A3. (a) Picture. (b) Operating scheme

The extent of reinforcement that can be achieved using CFR is clearly a subject of great interest in order to manufacture structural components by FFF 3D printing. In this paper, continuous basalt fiber will be employed to reinforce polyamide 12 (PA12) using an Anisoprint A3 3D printing apparatus. Basalt fibers are an attractive reinforcement: they belong to the class of natural fibers, despite being of mineral rather than vegetable origin, and possess properties that are analogous to traditional glass fibers. Moreover, much like in the case of glass fibers, sizing is necessary in order to increase interface properties [3].

Since the material that is obtained is actually a composite material, a marked anisotropy is to be expected both in stiffness and strength. As a result, methods that are typical of composites are often conveniently used to characterize 3D printed materials [1,4,5]. In this introductory paper only tensile strength characterization will be performed on 100% infill density continuous basalt fiber reinforced PA12, in order to measure longitudinal and transverse single layer properties. Shear properties will be obtained by assuming that the Tsai-Hill criterion holds for strength characterization of the single layer and performing tensile tests at a 10° angle with respect to the continuous fiber direction, following the methods of [1,4].

2. Theoretical foundations

Orthotropic materials that are loaded in plane stress can normally be characterized with 5 quantities: the longitudinal tensile strength S_L^+, the tranverse tensile strength S_T^+, the longitudinal compressive strength S_L^-, the transverse compressive strength S_T^- and the in-plane shear strength S_{LT}. Very often, though, it is assumed that the compressive and tensile strength are equal to each other, therefore strength characterization can be limited to the measurement of only 3 quantities, namely the longitudinal strength S_L, the transverse strength S_T and the shear strength S_{LT}. The first one can be obtained by tensile testing in the longitudinal direction (i.e. at 0° with respect to the deposition direction), the second one through tensile testing in the transverse direction (i.e. at 90° with respect to the deposition direction) and the last one using shear testing [6].

On the other hand, performing a characterization test in shear may be somewhat difficult, therefore in this introductory paper we will use a different methodology: after measuring S_L and S_T, specimens will be tested in tension at 10° with respect to the deposition direction. Then, the Tsai-Hill failure criterion will be used in order to estimate the critical load in shear using the following equation:

$$\frac{{S_{10}}^2 \cos^4 10}{{S_L}^2} - \frac{{S_{10}}^2 \sin^2 10 \cos^2 10}{{S_L}^2} + \frac{{S_{10}}^2 \sin^4 10}{{S_T}^2} + \frac{{S_{10}}^2 \sin^2 10 \cos^2 10}{{S_{LT}}^2} = 1 \quad (1)$$

in which S_{10} represents the failure stress at 10°, thus knowing S_L and S_T the only unknown is S_{LT}.

3. Materials and methods

Continuous basalt fiber filament was purchased from Anisoprint. This filament has a diameter of 0.2 mm and is already sized with an unspecified thermoset material to improve interfacial adhesion to polymeric matrices. The polyamide 12 filament named CFC PA was also purchased from Anisoprint. This filament has the standard 1.75 mm diameter. Rectangular specimens were printed using an Anisoprint Composer A3 at 100% infill density and at various raster angles, i.e. 0°, 90° and 10°. This printer has two different extruders arranged in parallel (Figure 1), one for printing thermoplastic materials only (TP1 in Figure 1) and the other one for the CFR co-extrusion. This accepts as input both the fiber filament (CFRTS in Figure 1) and an additional thermoplastic filament that is molten and coextruded with the fiber (TP2 in Figure 1). In this work, both basalt fiber and CFC PA were printed through this second extruder. Concerning the printing parameters, the layer height was 0.28 mm and a total of 10 layers were printed so that the total thickness of the specimens was 2.8 mm. At least 3 specimens per raster angle were printed and tested, the printing parameters are listed in Table 1.

Due to the very nature of the FFF process, the outer boundary of the specimens may result in geometric irregularities. This is especially true for 90° and 10° raster angles (Figure 2a). These may cause premature failure of the specimens due to stress concentration, therefore it was decided to enclose the composite specimens within 5 contour lines (Figure 2b). The contour lines were printed using the material named “Smooth PA” which was also purchased from Anisoprint. Smooth PA is a 10wt.% short carbon fiber reinforced polyamide 12 and was printed using the Anisoprint Composer A3 through the TP1 thermoplastic extruder. The final specimens were 200 mm long and 20 mm wide, including the continuous basalt fiber reinforced core and the Smooth PA contour lines. Tensile testing was performed at room temperature, using an INSTRON 34TM-30 dynamometer operated at a crosshead speed of 2 mm/min using a 30 kN load cell.

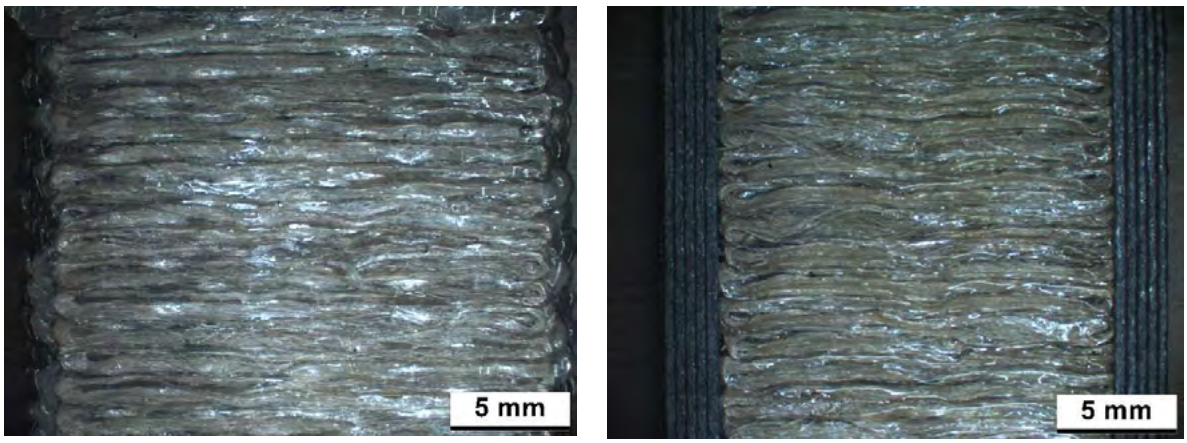

Figure 2. Transverse direction specimen: (a) without contour lines; (b) with contour lines

In order to obtain the mechanical properties of the basalt fiber reinforced composite, though, the properties of the Smooth PA contour lines must be subtracted. This can be done using the rule of mixtures as performed in [1]. Briefly, since the contour lines are arranged in parallel to the loading

direction, it can be assumed that the contour lines and the basalt fiber reinforced core are constrained to have the same longitudinal strain. If the strain at break of the basalt reinforced composite ε_{bc} is less than the strain at break of the contour lines for all raster angles, the strength of the contoured specimen S_{sp} will be given by:

$$S_{sp} = (1 - \Phi)\, S_{bc} + \Phi \sigma_{cl} = (1 - \Phi)\, S_{bc} + \Phi E_{cl} \varepsilon_{bc}, \tag{2}$$

in which Φ is the volume fraction of the contour lines in the contoured specimens, S_{bc} is the strength of the basalt fiber reinforced composite, while σ_{cl} is the stress in the contour lines when the basalt fiber reinforced composite breaks. This can be calculated as the Young's modulus of the contour lines E_{cl} times the strain at break of the composite.

Concerning the contour line volume fraction Φ, there are a total of 10 contour lines (5 lines on the left and 5 lines on the right). Since each contour line was 0.4 mm, the total width of the contour lines is 4 mm, therefore $\Phi = 4/20 = 20\%$. Now, if S_{sp} and ε_{bc} are measured during the tensile tests, Equation 2 can be used to obtain S_{bc}, provided that the longitudinal Young's modulus of Smooth PA is also known. Therefore, 3 specimens at 0° of Smooth PA were also printed through the TP1 extruder (Figure 1) using the printing parameters listed in Table 1. These specimens had the same length and width of the composite specimens, but were 4 mm thick, and were tested in tension in the longitudinal direction at the same crosshead speed and using the same load cell. Young's modulus was calculated using an INSTRON extensometer to measure longitudinal strain.

Table 1. The printing parameters used for composite and Smooth PA specimens.

		Layer height [mm]	Line width [mm]	Extrusion temperature [°C]	Printing speed [mm/s]
Smooth PA	TP ext.	0.2	0.4	265	40
	Composite ext.	/	/	/	/
Basalt fiber / PA12	TP ext.	0.28	0.4	265	40
	Composite ext.	0.28	0.6	250	30

4. Results

After performing tensile tests on the Smooth PA specimens in the longitudinal direction, it was found that the Young's modulus is 3.68 GPa with a standard deviation of 0.05 GPa. The strength in the longitudinal direction is 79.19 MPa with a standard deviation of 1.95 MPa, while the average strain at break was 0.032 mm/mm or 3.2%.

Considering now the contoured basalt fiber reinforced specimens, tensile strength results are listed in Table 2. Since these specimens are enclosed within the contour lines, the actual strength must be cleared of the contribution of the contour lines by using Equation 2. Taking into account that the contour line volume fraction amounts at 0.2, the net strength results of the basalt fiber reinfored composite can be easily calculated and are listed also in Table 2 in the last line.

Table 2. Tensile properties of the composites. Values in parentheses represent standard deviation.

	0°	**10°**	**90°**
Tensile strength [MPa]	236.08 (7.53)	83.63	27.92 (0.38)
Young's modulus [GPa]	14.61 (0.54)	3.81 (0.62)	1.01 (0.20)
Strain at break [mm/mm]	0.0169 (0.001)	0.022	0.0276 (0.005)
Corrected tensile strength [MPa]	279.5	84.30	9.51

As a result, the value of S_L and S_T can be obtained from Table 2 directly, and are 279.5 MPa and 9.51 MPa, respectively. The value of S_{LT} must be obtained from Equation 1, and this yields S_{LT} = 15.68 MPa.

5. Discussion and conclusions

As can be seen from the strength values, the material is highly anisotropic: for instance, the longitudinal strength is rather high, but the transverse strength is more than one order of magnitude less than the longitudinal strength. Also shear strength is not completely satisfactory for a truly structural material. It is very likely that such low values are caused by the unevitable presence of voids that are introduced during the printing process [2], therefore one possibility to improve the quality of the printed material is to optimize the printing parameters or performing post-treatments [2], in order to reduce the amount of voids as much as possible.

On the other hand, since it is rather unlikely that voids may be eliminated completely, the best design practice that can be adopted when 3D printing this material must be different. For example, optimizing the line deposition direction as a function of the expected external loadings, can be suitable to exploit the excellent longitudinal properties of this material.

Stiffness characterization of the materials was not included in this paper. Young's moduli of the basalt fiber reinforced materials could be measured and cleared of the effect of the contour lines in the same way as the strength values. On the other hand, a complete stiffness characterization requires measuring also the Poisson's ratio of the longitudinal specimens, which can be performed through strain gauge or Digital Imaging Correlation, and this will be performed in a forthcoming paper.

References

[1] L. Malagutti, V. Mazzanti and F. Mollica. Tensile properties of FDM 3D-printed wood flour filled polymers and mathematical modeling through classical lamination theory. *Rapid Prototyping Journal*, 28:1835-1842, 2022.
[2] L. Malagutti, G. Ronconi, M. Zanelli, F. Mollica and V. Mazzanti. A post-processing method for improving the mechanical properties of fused-filament-fabricated-3D printed parts. *Processes*, 10:2399, 2022.
[3] P. Russo, G. Simeoli, L. Vitiello, G. Filippone. Bio-polyamide 11 hybrid composite reinforced with basalt/flax interwoven fibers: a tough green composite for semi-structural applications. *Fibers*, 7:41 2019.
[4] C. Casavola, A. Cazzato, A. Moramarco and C. Pappalettere. Orthotropic mechanical properties of fused deposition modelling parts described by classical laminate theory. *Materials and Design*, 90:453-458, 2016.
[5] S. R. Rajpurohit, H. K. Dave and K. P. Rajurkar. Prediction of tensile strength of fused deposition modeling (FDM) printed PLA using classical laminate theory. *Engineering Solid Mechanics*, 10:13-24, 2022.
[6] R. F. Gibson. *Principles of Composite Materials Mechanics*. CRC Press, New York, 2016.

FABRICATION AND DAMPING CAPACITY OF SHORT ALUMINA FIBER AND VGCF HYBRID REINFORCED ALUMINUM ALLOY COMPOSITES

Kazunori Asano[1] and Yuki Fujioka[1]

[1] Department of Mechanical Engineering, Faculty of Science and Engineering, Kindai University, 3-4-1 Kowakae, Higashi-osaka, 577-8502, Japan
Email: asano@mech.kindai.ac.jp

Keywords: aluminum, hybrid composite, squeeze cast, microstructure, damping capacity

Abstract
The hybrid aluminum alloy composites, in which alumina short fibers with superior high-temperature strength and VGCF with small diameter and high thermal conductivity as the reinforcements, were fabricated by squeeze casting. Volume fraction of the VGCF was 0, 3, 6, and 9 vol% and that of alumina fibers was 5,10 and 15 vol%. Microscopy of the composites showed that the VGCF was dispersed among the alumina fibers in the composite and the agglomeration of VGCF was clearly observed when the volume fraction of VGCF was great and that of alumina fiber was small. Electron microscopy revealed that the microporocity was observed near the agglomeration area. Damping capacity of the alloy was improved by the reinforcement at every temperature measured. It would be due to the energy loss by shear at the reinforcement-matrix interface. The damping capacity of the composite was the highest when the volume fraction of VGCF and alumina fiber was 9 and 15 vol%, respectively. In addition to the energy loss due to the shear as mentioned above, the energy loss due to friction would be caused by the movement of the exposed VGCF in the microporocity near the agglomeration area, leading to the improvement.

1. Introduction

Aluminum, which is used as a lightweight material for equipment, has problems such as low high-temperature strength and wear resistance. For the machine parts, vibration and noise generation caused by weight reduction are also problems. Recently, reinforcement with the non-metallic fibers has attracted attention as a possible solution of these problems. The authors have shown that reinforcement with alumina short fibers improves the high-temperature strength of aluminum alloys [1], and that reinforcement with carbon fibers improves the wear properties and thermal conductivity of aluminum alloys [2-4]. The composites are also expected to improve the vibration damping capacity due to the energy loss associated with shear at the reinforcement-matrix interface [5]. We expected that the reinforcement with VGCFs, which are finer than carbon fibers, and alumina short fibers with aluminum alloys would provide the materials with high-temperature strength, high thermal conductivity, wear resistance, and high vibration damping capacity. This would lead to a possibility of the exploration of new markets as a metal matrix composite with high-durability at elevated temperature, such as the parts for electric vehicles or aerospace.

In this study, hybrid composites were fabricated by squeeze casting of molten aluminum alloy into preforms with various volume fraction of reinforcements, and the effects of the volume fraction of the reinforcements on the damping capacity of the composites were clarified.

2. Experimental Procedure

JIS-AC8A (Al-12Si-1Cu-1Ni-1Mg) alloy casting was used as the matrix of the composite. Alumina short fibers (4 μm diameter and 200 μm length) with superior high-temperature strength and VGCF (150 nm diameter and 4 μm length), high thermal conductivity were used as the reinforcements.

Preforms of the reinforcement were prepared as follows. The anionic polymer was used to charge the VGCF negatively, and the cationic polymer was used to charge the alumina fiber positively, and then they were mixed to fabricate the preform with VGCFs attached to the surface of alumina fibers.

Table 1 shows the volume fraction of the reinforcements in the preforms and composites. Preforms with different volume fraction were prepared by mixing VGCFs with volume fraction of 0, 3, 6, and 9 vol% and alumina short fibers with volume fraction of 5, 10 and 15 vol%.

Table 1. Volume fraction of the reinforcements in preforms and composites (AC8A is an unreinforced alloy).

Specimens	Volume fraction [vol%]	
	Al_2O_3	VGCF
AC8A	0	0
A15V0	15	0
A15V3		3
A15V6		6
A15V9		9
A5V6	5	6
A10V6	10	

Composites were fabricated by squeeze casting. The preforms were placed in a permanent mold that was preheated to 673 K. Molten JIS-AC8A alloy was poured into the mold at 973 K, and then the pressure (40 MPa for 60 s) was applied to accomplish the infiltration of the molten alloy into the preforms.

The reinforcement distribution in the preforms was observed by scanning electron microscopy (SEM), and the cross-sectional microstructure of the composites were observed using optical microscopy and SEM.

Test pieces of 50 mm long, 10 mm wide, and 1.5 mm thick was machined from the composites, and vibration damping capacity were measured. Measurements were made by fixing one end of the test pieces in the length direction, attaching a jig at the other end, and vibrating the jig with a magnetic force. Tests were conducted at 296-573 K with amplitude strains ε varying from 1×10^{-4} to 5×10^{-4}.

The logarithmic damping rate (δ), is expressed by the following equation (1).

$$\delta = \frac{1}{n}\ln\frac{A_0}{A_n} \tag{1}$$

where A_0 is the initial amplitude, and A_n is the nth vibration amplitude from origin of the vibration.

The loss factor (η) obtained in this test is expressed by the following equation (2).

$$\eta = Q^{-1} = \frac{\delta}{\pi} \quad (2)$$

where Q is the value related to the energy reduction in vibration absorption of elastic waves.

3. Results and Discussion

3.1. Microstructure

SEM images of the preforms are shown in Fig. 1. Although many VGCF were attached to alumina fiber surfaces when the volume fraction of VGCF was 3 vol%, the attachment to the fiber surfaces of the VGCF was slight (Fig. 1(b)), and the agglomeration of the VGCFs was clearly observed when the VGCF volume fraction was 6 vol% (Fig. 1(c-2), an enlarged view of (c)). the agglomeration was pronounced when the VGCF volume fraction was greater (9 vol%, Fig. 1(d)) or alumina fiber volume fraction was smaller (5 and 10 vol%, Figs. 1(e) and (f)).

Figure 2 shows the optical micrographs of the composites. Areas of agglomerated VGCF were observed in the composites with greater volume fractions of VGCF (circle areas in the Figs. 1 ((c)-(f)), especially in the composites A15V9, A5V6 and A10V6 (Figs. 1((d)-(f)). This results also indicate that the distribution of the reinforcements in the composites was caused by that in the preforms. Due to the increase in the VGCF and the decrease in the alumina fiber, attachment of the VGCF to the alumina fiber surface would be difficult and leading to the agglomeration of the VGCF among the alumina fiber.

As shown in Fig. 3, the microporosity was observed near the agglomerated area in the composites, indicating that the infiltration of the molten aluminum alloy into the agglomerated area would be imperfect. It should be noted that the VGCF surface (partially exposed VGCF) can be observed near the microporocity.

3.2. Damping Capacity

Relationship between ε and η of AC8A and composites at 296 K (ambient temperature) is shown in Fig. 4. The η value of the AC8A was increased by the reinforcement. The increase in the η value, that is, the improvement in the damping capacity due to the reinforcement, was considered to be due to the energy loss by the shear at the reinforcement-matrix interface. When the volume fraction of the alumina fiber

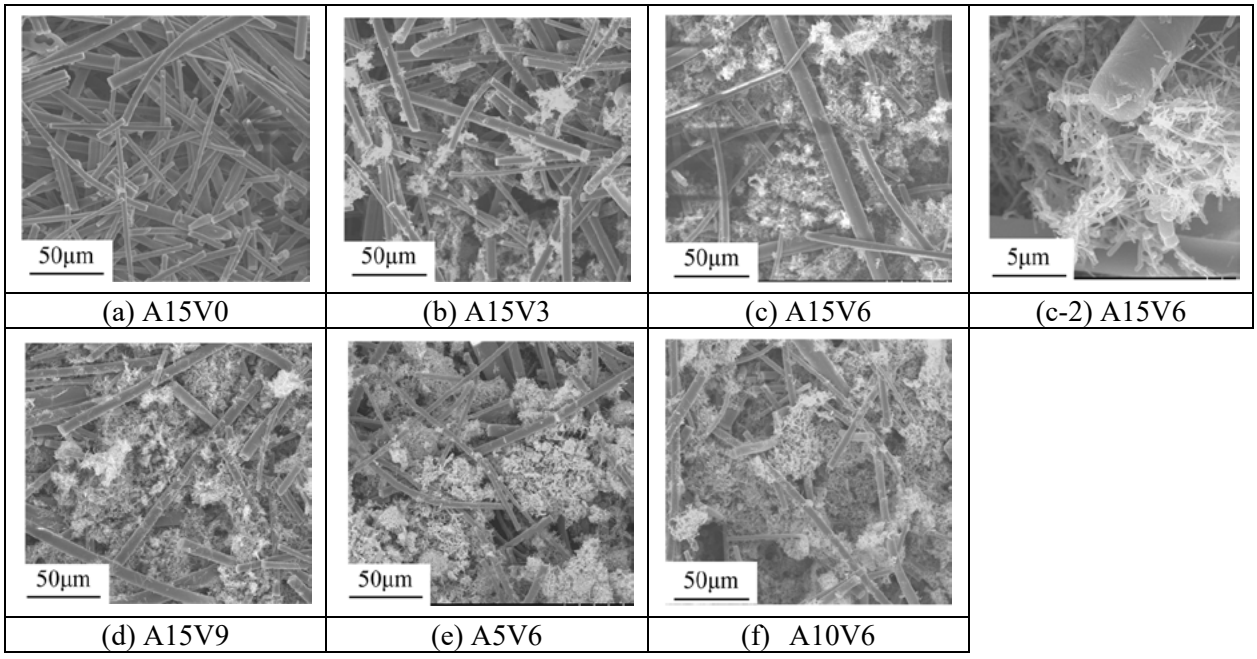

(a) A15V0 (b) A15V3 (c) A15V6 (c-2) A15V6

(d) A15V9 (e) A5V6 (f) A10V6

Figure 1. Secondary electron images of preforms ((c-2) is an enlarged view of A15V6).

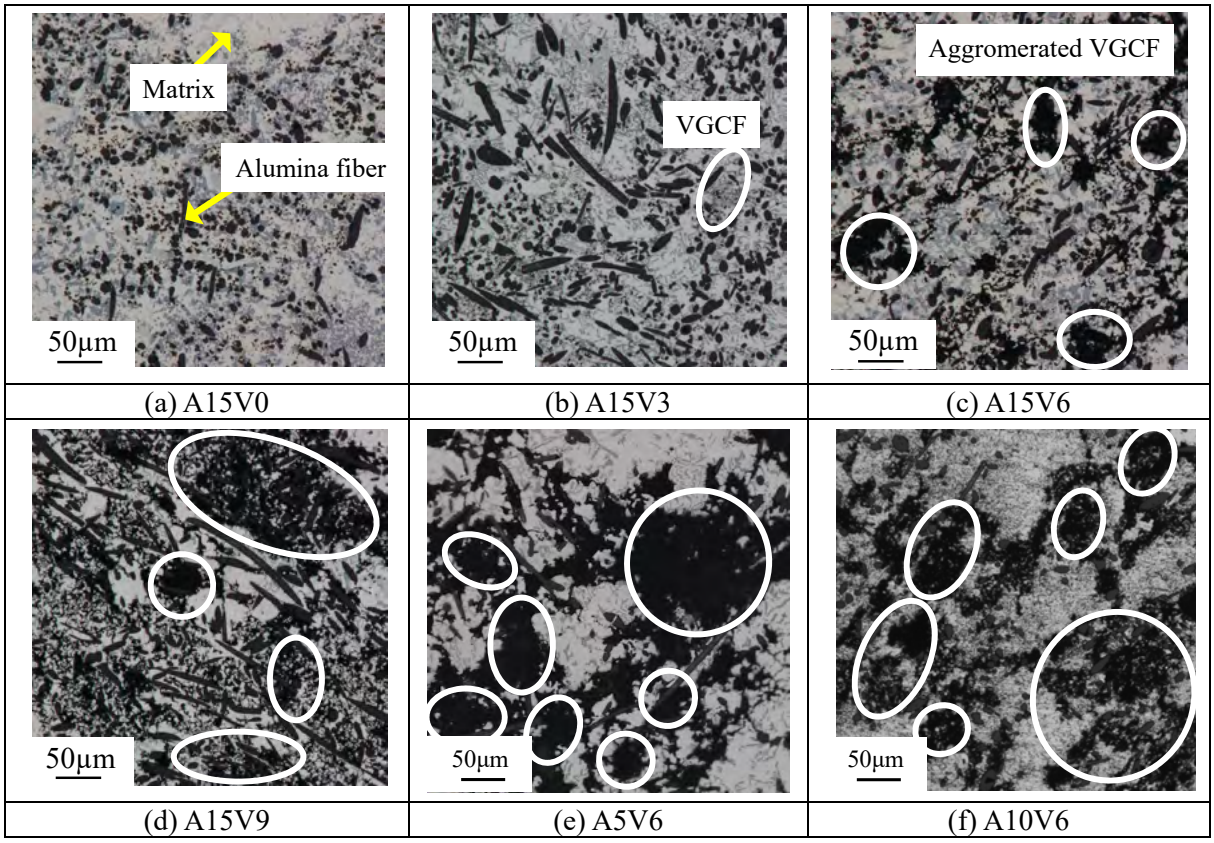

Figure 2. Optical micrographs of the composites.

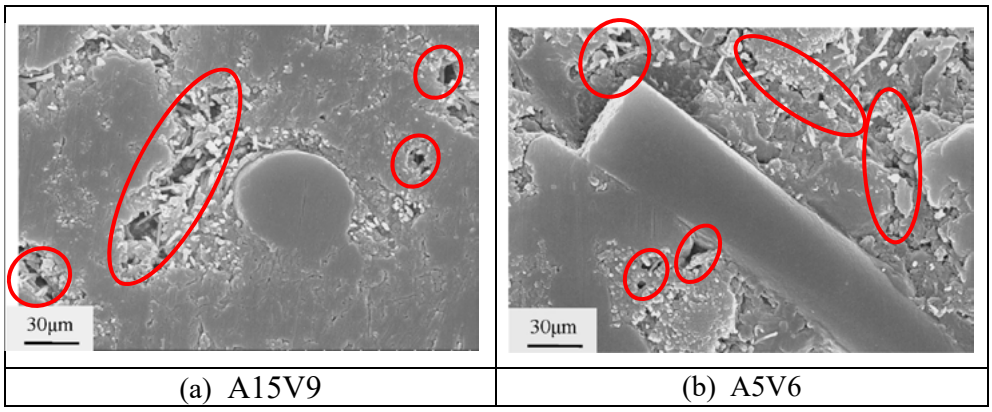

Figure 3. Secondary electron images of the composites, showing that the microporocity (circles in the images) was observed near the agglomerated area of VGCF.

was constant (15 vol%), η of the composites with 9 vol% VGCF (A15V9) was greater than that of the other composites and AC8A (Fig. 4(a)). When the volume fraction of the VGCF was constant (6 vol%), η of the composites with 5 vol% alumina fiber (A5V6) was the greatest (Fig. 4(b)). As shown in the Figs. 1 and 2, many agglomerations of the VGCF was observed. In the vicinity of the agglomeration of the fine VGCF, the melt infiltration would be difficult, and lead to the formation of microporocity with partially exposed VGCF (Fig. 3). The greater damping capacity of the two composites (A15V9 and A5V6) was probably due to the energy loss due to friction caused by the movement of the exposed VGCF at the agglomeration area when the vibration is applied.

Figure 5 shows the η of AC8A and composites at various temperatures. The η value of every specimen

increased as the temperature increased due to the softening of the AC8A matrix alloy. The η value of the composite was greater at the elevated temperature, as well as the ambient temperature.

To see if there is correlation between the volume fraction of microporosity and the η value, the relationship between the η value and the area fraction of microporosity in the composites (obtained with the image analyzer using the 10 views of secondary electron images with a magnification of 1,000) was obtained and shown in Fig. 6 ($\varepsilon = 1.0\times10^{-4}$). The correlation coefficient in this case was 0.87; The loss factor is positively correlated with the volume of the microporosity, and it can be controlled by changing the volume fraction of the alumina fiber and VGCF.

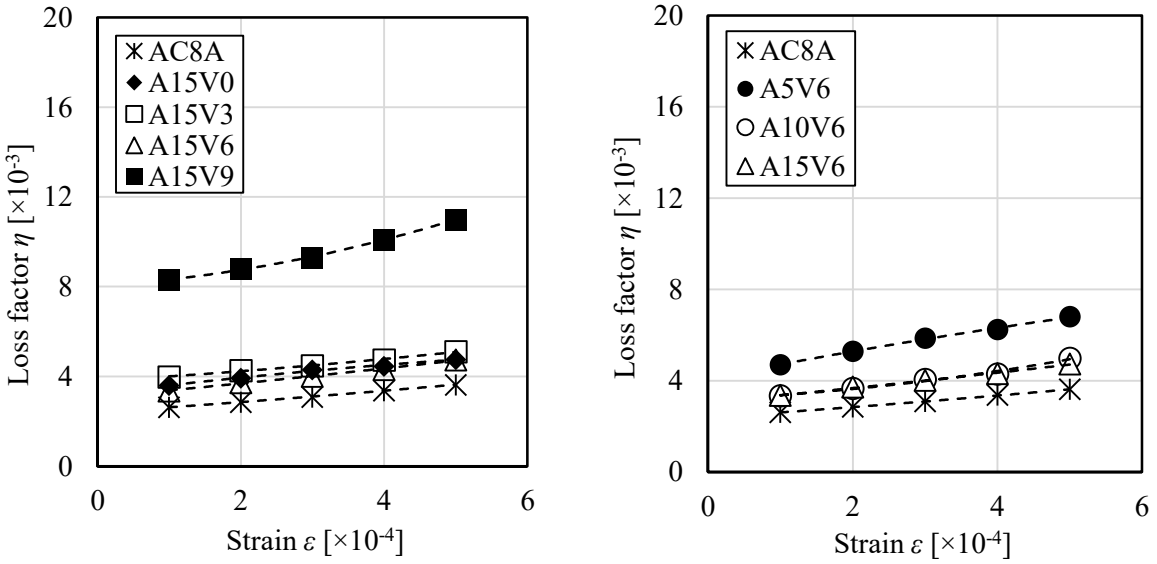

(a) Composites A15 (b) Composites V6

Figure 4. The loss factor of the unreinforced alloy and composites at ambient temperature (296 K).

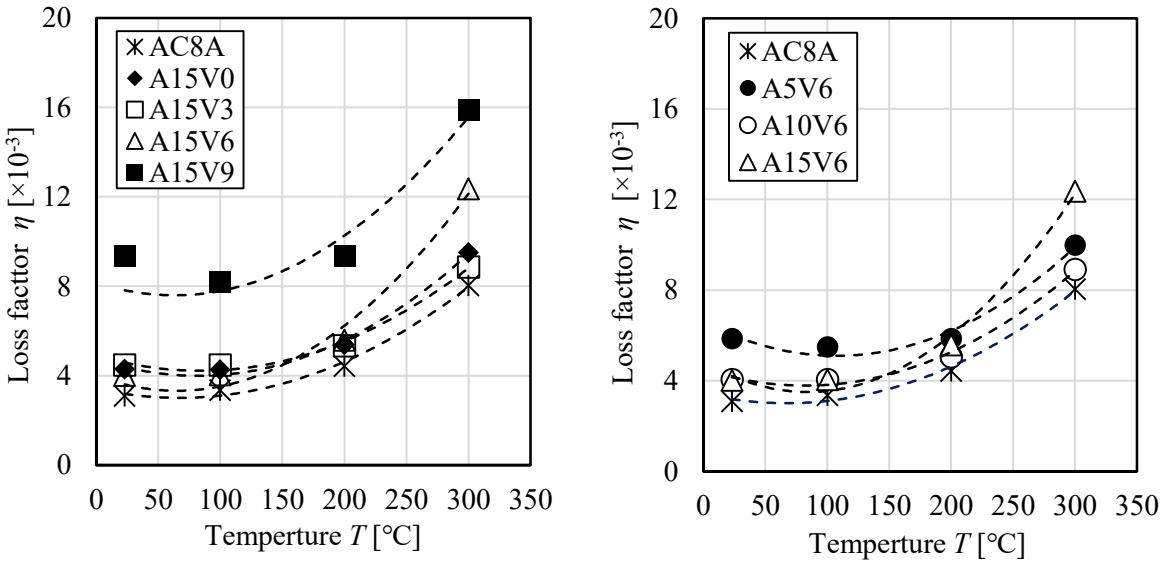

(a) Composites A15 (b) Composites V6

Figure 5. Relationship between the loss factor of the unreinforced alloy and composites and temperature ($\varepsilon = 3.0\times10^{-4}$).

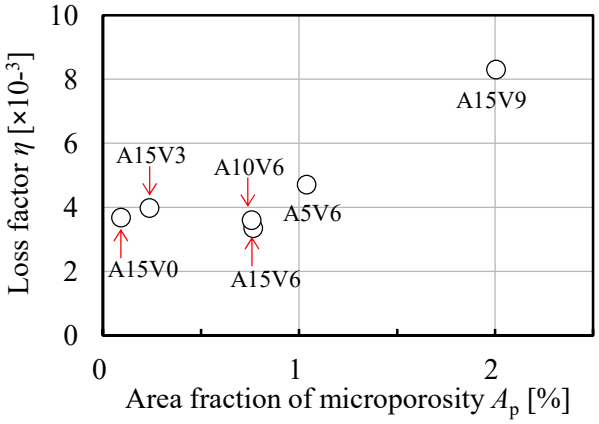

Figure 6. Relationship between the loss factor and the area fraction of microporosity in the composites ($\varepsilon = 1.0\times10^{-4}$).

4. Conclusions

In the composites, the VGCF was dispersed among the alumina fibers and the agglomeration of VGCF was pronounced as the volume fraction of VGCF increased and that of alumina fiber decreased.
Damping capacity of the alloy was improved by the reinforcement at every temperature. It would be due to the energy loss by shear at the reinforcement-matrix interface. The highest damping capacity was obtained by reinforcing with the combination of the 9 vol% VGCF and 15 vol% alumina fiber. The increase in the reinforcement-matrix interface and the increase in the microporosity with the partially-exposed VGCF in the composite improve the damping capacity of the aluminum alloy. Using the techniques proposed in this paper, the distribution of the reinforcements and the microporosity can be optimized to obtain the alloy composite having the high-damping capacity by controlling the volume of the alumina fiber and VGCF.

References

[1] K. Asano and H. Yoneda. Strength of AC8A aluminum alloy reinforced with alumina short fiber using alumina binder. *Journal of Japan Foundry Engineering Society*, 74(2): 109-115, 2002.
[2] K. Asano. Thermal conductivity and mechanical properties of pitch-based carbon fibre reinforced aluminium composites fabricated by squeeze casting. *International Journal of Cast Metals Research*, 31(1): 29-36, 2018.
[3] K. Asano. Thermal expansion behaviour of squeeze-cast aluminium matrix composites reinforced with PAN- and Pitch-based carbon fibres. *International Journal of Cast Metals Research*, 30(6): 365-373, 2017.
[4] K. Asano and M.F. Zainuddin. Wear behavior of pan- and pitch-based carbon fiber reinforced aluminum alloy composites under dry sliding condition. *Materials Transactions*, 58(6): 898-905, 2017.
[5] I. Shiota. Damping mechanism and properties of metal matrix composites. *Journal of the Japan Society for Precision Engineering*, 55(12): 2127-2130, 1989.

INFLUENCE OF THERMOPLASTIC FIBRE RATIO ON THE MECHANICAL PROPERTIES OF CARDED RECYCLED CARBON FIBERS WITH A WEIBULL STATISTICAL APPROACH

Jean Ivars[1], Ahmad Rashed Labanieh[1], Damien Soulat[1], Kim Phuc Tran[1]

[1]ENSAIT ULR 2461-GEMTEX–Génie et Matériaux Textiles, Université de Lille
2 Allée Louise et Victor Champier, F-59100 Roubaix, France
e-mail : jean.ivars@ensait.fr, ahmad.labanieh@ensait.fr, damien.soulat@ensait.fr and kim-phuc.tran@ensait.fr

Keywords: recycled carbon fibre, carding, Weibull, tensile properties

Abstract
By 2050, the aerospace industry alone is expected to produce approximately 34.2 ktons of carbon fiber reinforced plastic waste. Thermal and chemical recycling techniques are employed to recover and preserve the carbon fibers' mechanical properties. One of the main challenges is then to effectively realign and repurpose these fibers for high-performance applications. In this study, a carding machine is utilized for this purpose, investigating variations in the ratio of thermoplastic fibers mixed with recycled carbon fiber (rCF) in the produced web. The carded rCF fibers are tested to analyze the evolution of tensile properties based on the thermoplastic fiber ratio in the web. CF having a brittle fracture behavior, a common statistical method employed is the Weibull statistical model, which assesses the probability of failure across all tested samples. By comparing the values of the mechanical properties and the Weibull distributions, it was possible to highlight an optimum ratio of polypropylene (PP) fibre blended with rCF, and also to show that the damage to rCF passing the carding stage was controlled.

1. Introduction

Carbon fibres are high-performance fibres that are mainly used to reinforce composite materials in the aeronautics, aerospace and automotive sectors. However, these composite materials generate waste when they reach the end of their life. It is estimated that 34.2 ktonnes of carbon composite waste will need to be processed annually between now and 2050 in the aerospace sector alone [1]. In recent years, various processes for recycling this waste have been developed. Although they each have their own advantages and disadvantages, they all enable most of the initial properties of the virgin fibres to be recovered at fibre level [2–4].
The fibres produced by these different processes are discontinuous, and fibre continuity and alignment are among the factors that have the greatest impact on the mechanical properties of composite materials. The literature indicates an improvement in composite properties with recycled carbon fibres (rCF) longer than 50mm [5]. At the same time, fibre misalignment can significantly reduce the mechanical properties, stiffness and strength, of the composite, in the order of 50% for a unidirectional composite whose fibres are misaligned by 15° [6]. With a view to realigning the fibres, a number of studies have shown the possibility of carding discrete-length carbon fibres from production offcuts or cut tows [5,7–9]. Hengstermann et al. [5,14] were able to card 40mm and 60mm long rCF, and demonstrated the influence of fibre length at the card infeed. In another study a core-sheath yarn has been produced also with 60mm carded rCF in the core and co-polyamide as sheath [9]. This work investigates the influence of the proportion of thermoplastic fibre in the blend with rCF, reclaimed from steam-thermolysis process, on the mechanical properties of carbon fibres. The aim is to study the average tensile properties of these fibres after carding, and to analyse the underlying statistical distributions as a function of the proportion of thermoplastic fibres in the blend, using the 2-parameter Weibull statistic, commonly used for CF stress data, on the data for stress at break but also on the tensile modulus and elongation at break.

2. Materials and methods

The carbon fibres used in this study are SM carbon fibres reclaimed by steam thermolysis. The fibres are unsized and cut to a length of 60mm. Recovered rCF using this technique shows a slight degradation of its initial tensile properties, about 10% [10], a good surface condition [11] and a well-preserved diameter [12]. rCF before carding tensile properties are listed in (Table 1).
These values are extracted from 51 tensile tests performed using the protocol detailed in section 2.2.1. at a gauge length of 25mm. These values enabled us to classify these recycled carbon fibres as low-SM type fibres [13].

Table. 1 : Summary of rCF tensile properties

	Diameter (µm)		Tensile Strength (MPa)		Tensile modulus (GPa)		Elongation at break (%)	
	Mean	Std.	Mean	Std.	Mean	Std.	Mean	Std.
rCF bef.carding	7.41	0.25	3143	773	186.2	20.8	1.57	0.37

The thermoplastic fibres used in this study are popypropylene crimped fibres cut to 60mm.

2.1 Web manufacturing process with a carding machine

The global aim of the project is to develop carded webs and slivers by giving continuity and alignment to steam-thermolized recycled carbon fibres, and then to create rovings with properties that will enable them to be used in other textile technologies. This process eliminates very short fibres and aligns the fibres preferentially along the production axis through successive passes across toothed cylinders (To manufacture the web, rCF reclaimed from the steam thermolysis process are used alongside thermoplastic polypropylene fibres at different ratios. Polypropylene fibres are widely used in the textile industry due to its low-cost and processability as a matrix in thermoplastic composites.

) that open and comb the fibres. To manufacture the web, rCF reclaimed from the steam thermolysis process are used alongside thermoplastic polypropylene fibres at different ratios. Polypropylene fibres are widely used in the textile industry due to its low-cost and processability as a matrix in thermoplastic composites.

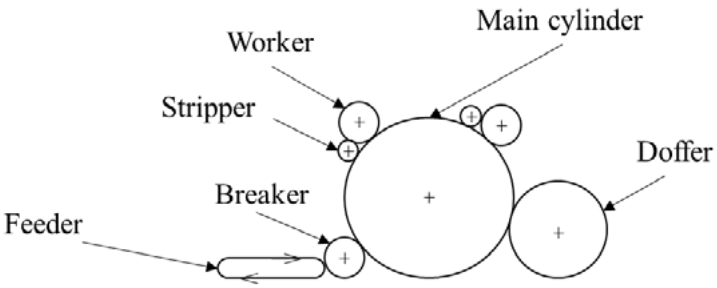

Figure. 1: Carding machine simplified schema

Also, it has been shown that crimped polypropylene helped mixing and carrying rCF, diminishing fibre breakage through the carding process [14]. This approach aligns with previous works where polyamide and polyester were used as carrier fibre in blend with with carbon fibre from manufacturing scraps [7]. It's been concluded that an rCF ratio of between 50 and 70% was the best trade-off between tenacity and the amount of carbon fibre in the ring-spun yarn produced.
Also, the morphological and mechanical properties of fibres and web are influenced by the parameters of the machine and the material used. For example, Manis et al. [15] were able to demonstrate that a

higher number of worker/stripper pairs led to a greater degradation of 60mm fibre length. Another study looked at the influence of the distance between the worker and the stripper on the length of the fibres leaving the carding machine [9]. A higher clearance between the worker/stripper led to fewer fibre length degradation.
In this study, four webs are manufactured with only changing the rCF/PP blend's ratio with respectively: 50/50%, 70/30%, 85/15% and finally 100/0%. Other parameters such as feeding density, speed or number of passes through the carding machine are fixed. From theses webs, carbon fibres are extracted and individualized to be tested mechanically on a tensile testing machine equipped for single fibre tensile testing.

2.2 Characterization method and data extraction

2.2.1 Fibre preparation and tensile tests

The tensile test measures stress evolution in a material under load to determine its strength, elongation at break, and stiffness. The standard used is NF ISO 11566 [16], which is specific to single carbon fibres. After individualization, a single fiber is fixed to a cardboard frame with cyanoacrylate glue and tested using an INSTRON MTS machine with a 10N load cell at 2mm/min. The standard recommends twenty measurements per fibre type. However, the inherent fragility of carbon fibres makes the preparation difficult, potentially leading to measuring errors. In addition, numerous studies have shown that a minimum number of tensile tests must be carried out to obtain robust data. Indeed, it has been shown that for 50 tensile tests on carbon fibre, the Weibull modulus could vary by +/- 1 [17].
Considering the number of webs and the time of preparation, it has been considered necessary to carry out a more thorough test procedure of at least sixty tests to ensure more sufficient and reliable data. For each tensile sample, diameter measurements are taken at five points along the fibre using an OLYMPUS DSX1000 microscope. This is done to derive stresses and tensile moduli from the force values together with elongation values. For these fiber tensile tests, a 25mm gauge length was chosen for two reasons: to align with the NF ISO 11566 standard and to minimize misalignment errors on the cardboard frame, which can affect measurements at shorter lengths. [18]. Cardboard frames were laser-cut to ensure accurate fiber length. Compliance values were not considered in this study.

2.2.2 Weibull statistical distribution

The brittle behaviour of carbon fibre can be depicted by the Weibull's statistic, which assumes that carbon fibre is an assembly of links. Tensile failure of the fibre then occurs when the weakest link in the assembly breaks [19]. The Cumulative Distribution Function (CDF) is used to represent the probability of failure P at a given value of σ the applied stress on the fibre following the Eq. (1), also known as the 3-parameters Weibull CDF:

$$P(\sigma) = 1 - e^{-\left(\frac{\sigma-\sigma_u}{\sigma_0}\right)^m} \quad (1)$$

With $\sigma_0 -$ scale parameter, $m -$ shape of the distribution, or Weibull modulus, $\sigma_u -$ location parameter $\sigma -$ applied stress
The location parameter σ_u in Eq. (1) can be set to zero in order to obtain a 2-paramters Weibull CDF. The choice of using a 2 or 3 parameters Weibull distribution was guided by the fitting results which showed the best p-values between the theoretical and experimental distributions on the 2-parameter Weibull fibre data, using the Kolmogorov-Smirnoff (K-S) test. This test assesses the fit between a sample of data and a reference distribution by measuring the maximum distance between their respective cumulative distribution functions. A p-value greater than 0.05 indicates that the hypothesis that the data do not follow the distribution cannot be rejected. It is therefore possible to choose the Weibull model best fitted to our data by comparing the value of the KS test and the associated p-value.

The experimental data is used to fit the distribution, determining the two parameters of the distribution for each batch of fibers extracted from the webs: the Weibull modulus, which measures the disparity of the variable under study, a lower Weibull modulus indicates a greater disparity; the scale parameter,

indicating variable's value at 63.2%. According to the different manufactured webs, these models are then compared with each other but also with recycled carbon fibre before carding. Comparisons are made on stress at break, but also on tensile modulus and elongation at break.

3. Tensile properties

Table. 2: Summary of fibre properties depending on webs fibre ratio

	Data points	Diameter (µm)		Stress at break (MPa)		Tensile modulus (GPa)		Elong. at break (%)	
	Numb.	Mean	S-E	Mean	S-E	Mean	S-E	Mean	S-E
100% rCF	45	7.36	0.45	3221	769	192.8	13.7	1.57	0.36
15-85% rCF	49	7.21	0.46	3406	741	195.5	12.1	1.57	0.29
30-70% rCF	47	7.18	0.34	3563	656	198.5	13.6	1.68	0.30
50-50% rCF	25	7.10	0.48	3413	685	206.4	15.9	1.53	0.27
rCF bef. Card.	51	7.41	0.25	3143	773	186.2	20.8	1.57	0.37

Before each tensile strength test, the fibre diameter is measured using an OLYMPUS DSX1000 optical microscope. In the case of these recycled carbon fibres, it is possible to guarantee a specific type of carbon fibre and specific fibre lengths, but no manufacturer's data was given for the diameter values. The diameters of the recycled carbon fibres measured for each batch showed a similar variability to virgin carbon fibres, with CV% ranging from 3.37 to 6.11% [17]. Post-carding, the average diameter slightly decreases while standard deviation increases, yet all values remain within comparable ranges, indicating minimal impact from carding on fiber diameter (see Table. 3). The tensile modulus is determined within the strain range of 0.1 to 0.6%.

3.1 Stress at break

Using the diameters for individual fibres, it is possible to determine the stress at break of the fibres in each batch by dividing the force at break by the cross-section of the fibre, which is assumed to be circular. The average stress at break for each batch of fibre has shown no significant change with regard to the standard deviations. Before carding, the average stress at break of the rCF was 3143 ± 773 MPa. All the stress-at-break values after carding, regardless of the proportion of polypropylene fibre in the blend, were within the standard deviation (Table. 3).

In order to determine the differences between the stress at break distribution according to the PP fibre ratio, these values are also studied using the 2-p Weibull modulus.
It can already be noted that the number of tests has a significant impact on the standard deviation of the Weibull modulus. In fact, for the 50-50 blend, whose data set contains 20 fewer usable trials than the 100% rCF, the standard deviation rises from 0.59 to 0.92 (Table. 4).
At the same time, Weibull modulus values increase with the carding process compared with fibres recycled before carding. This means a less consistent spread of stress-at-break data. In relation to the average values and Weibull moduli for each of the fibres extracted from the webs, it can be observed that on this criterion of stress at break, carding has no impact that would significantly damage the carbon fibres. This can be explained by three factors. Blending with crimped polypropylene fibres helps to protect the carbon fibre during carding, allowing it to move more easily over the different carding cylinders, limiting damage of the metal teeth they are fitted with. In addition, the components of the carding machine have been designed and selected for the use of carbon fibre.

Table. 3: 2p-Weibull modulus values of stress at break for each fibre ratio

	Points	**2p Weibull modulus**		**Kol. Smirn.**
		Mean	SE.	(p-value)
100% rCF	45	4,99	0,59	0,89
15-85% rCF	49	5,26	0,59	0,99
30-70% rCF	47	6,29	0,71	0,99
50-50% rCF	25	5,90	0,92	0,99
rCF bef. carding	51	4,48	0,47	0,99

The teeth's shape, the number of teeth per inch, and the spacing between the cylinders are adapted to the fineness carbon fibre in order to limit and control the creation of defects on the surface of the fibre. Finally, extracting the fibres from the web means recovering fibres longer than 25-30 mm for tensile strength testing. The fibre must therefore not have broken significantly during the carding process, which may involve a pre-selection of statistically less brittle fibres, where, prior to carding, any 60mm fibre is chosen. However, if the carded fibres are compared with and without PP, there is a significant difference in the Weibull moduli from 4.99 to 6.29, highlighting the action of the crimped polypropylene fibres on the carbon fibres during carding.

3.2 Tensile modulus

To avoid variations in stress due to the resolution of the force sensor, the tensile modulus is calculated by linear regression in the deformation range between 0.1 and 0.6%, in accordance with standard NF ISO 11566. The average tensile modulus of recycled fibres calculated before carding is equal to 186.2 ± 20.8 GPa (Table. 3).

Table. 4: 2p-Weibull modulus values of tensile modulus for each fibre ratio

	Points	**2p Weibull modulus**		**Kol. Smirn.**
		Mean	SE.	(p-value)
100% rCF	45	16.33	1.84	0,83
15-85% rCF	49	17.85	1.89	0,82
30-70% rCF	47	17.67	1.99	0,84
50-50% rCF	25	14.40	2.18	0,76
rCF bef. carding	51	10.99	1.18	0,74

This places this batch of recycled carbon fibre at the bottom end of the table compared with virgin Standard Modulus (SM) carbon fibre [13]. After carding, the tensile modulus slightly increases for fibres extracted from 100% rCF webs. But even more so with the gradual addition of PP fibre to the blend, reaching up to 206.4 GPa for fibres extracted from 50-50 webs.
In parallel with the increase in the tensile modulus values of carded fibres compared to fibres before carding, a corresponding increase in the Weibull modulus on the tensile modulus value is observed.
The heatmap shown in Figure 3 can be used to describe the relationships between two variables by calculating the Pearson coefficient. An absolute value close to 1 indicates a strong linear correlation

between two variables. The "Fibre_pct" variable corresponding to the fibre content in the web shows a strong and positive correlation, 0.89, with the value of the Weibull modulus, "Point Estimate" in the figure, in tensile modulus. This indicates a homogenisation of the tensile modulus values with carding on the one hand, but also with the increase in the PP ratio in the web where the fibres tested are extracted. The Weibull modulus values reaches a peak for blends 70-30% and 85-15% suggesting an optimum value of PP ratio in the webs produced.

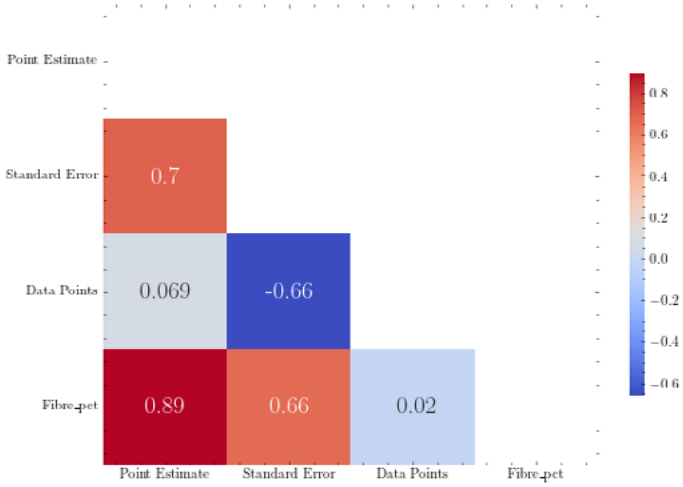

Figure. 2: Heatmap for Weibull modulus on the tensile modulus

This observation, along with the increase in modulus values, is highlighted by scientific studies documenting the phenomenon of stiffening of the carbon fibre, an increase in modulus value, either during the tensile test with the increase in deformation [20] or during fatigue tensile tests where a slight increase in the tensile modulus of the fibres was observed due to a realignment of the graphite crystal microstructure along the fibre axis [21].

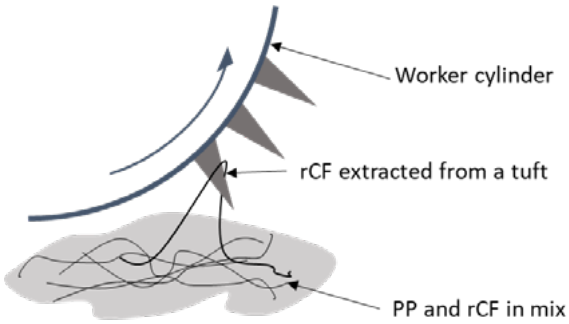

Figure 3: Fibre pull-out from tuft during carding

In the fibre extraction process through the carding machine, mechanisms of fibre rupture can occur. When a carding tooth catches a fibre loop (Figure 4), if the fibre is trapped at both ends within the fibre tuft, it breaks. Also, if the force applied to extract the fibre exceeds its resistance, the fibre will also break. The extracted fibre is subjected to successive tensile forces which can either cause it to break or extract it from a tuft of fibres. Linked to the observation made by Bunsell et al [21] on cyclic tensile tests for carbon fibres, this mechanism within the carding machine provides the beginnings of an explanation for the increase in tensile modulus values, stiffening, but also for the homogenisation of values resulting in an increase in Weibull modulus values.

3.3 Elongation at break

To complete this investigation, a study of elongation at break values was also carried out. Before carding, the average elongation at break value of the rCF was 1.57 ± 0.37 %.
Since carbon fibre is a rigid fibre, the trends shown for stress at break also apply to elongation at break. The average values of carded fibres, regardless of the level of PP fibre in the blend, remain stable and within the standard deviation of fibres recycled before carding (Table. 6).

Table. 5: 2p-Weibull modulus values of elongation at break for each fibre ratio

	Points	**2p Weibull modulus**		**Kol. Smirn.**
		Mean	SE.	(p-value)
100% rCF	45	5.24	0.62	0,99
15-85% rCF	49	5.87	0.64	0,43
30-70% rCF	47	6.36	0.69	0,96
50-50% rCF	25	6.94	1.10	0,96
rCF bef. carding	51	4.79	0.52	0,99

The Weibull modulus values show the same trend as for the stress at break values. A slight increase in Weibull modulus values was noted with carding and the addition of PP fibre to the blend. Rising from 4.79 for non-carded fibres to 6.94 for carded carbon fibres in a 50-50 mix, also showing a homogenisation of values with carding and the addition of PP fibres.

Conclusion

The influence of the proportion of thermoplastic polypropylene (PP) fibres on the mechanical properties of recycled carded carbon fibres (rCF) was investigated using a statistical Weibull approach. Four different web compositions were prepared with varying rCF/PP blend ratios (100/0%, 85/15%, 70/30% and 50/50%). The experimental results lead to the following conclusions. The addition of crimped polypropylene fibers during the carding process had no significant effect on the stress at break properties of the rCF. Tensile modulus values showed a slight increase post-carding, particularly notable in fibers extracted from 100% rCF webs, further enhanced with the gradual addition of PP fibers. This increase was accompanied by a rise in Weibull modulus, indicating a more consistent distribution of tensile modulus data with carding, especially evident in blends with higher PP ratios, notably 85-15% and 70-30%. Elongation at break values remained stable despite the addition of PP fibers and carding, with Weibull modulus values following a similar trend to stress at break, showing a slight increase with carding and higher PP ratios.
Overall, the study demonstrates the potential of carding rCF in conjunction with PP to produce carded webs. The Weibull statistical approach provided valuable insights into the variability and homogenization of mechanical properties. Finally, it can be concluded that the carding process, coupled with the use of crimped PP fibres, makes it possible to control the properties of carded recycled carbon fibres without degrading their tensile properties.
Future research could explore additional factors such as processing parameters to further optimize the mechanical properties of carded recycled carbon fibres with or without thermoplastic polypropylene.

References

1. Zhang, J.; Chevali, V.S.; Wang, H.; Wang, C.-H. Current Status of Carbon Fibre and Carbon Fibre Composites Recycling. *Composites Part B: Engineering* **2020**, *193*, 108053, doi:10.1016/j.compositesb.2020.108053.

2. Sukanto, H.; Raharjo, W.W.; Ariawan, D.; Triyono, J. Carbon Fibers Recovery from CFRP Recycling Process and Their Usage: A Review. *IOP Conf. Ser.: Mater. Sci. Eng.* **2021**, *1034*, 012087, doi:10.1088/1757-899X/1034/1/012087.
3. Pakdel, E.; Kashi, S.; Varley, R.; Wang, X. Recent Progress in Recycling Carbon Fibre Reinforced Composites and Dry Carbon Fibre Wastes. *Resources, Conservation and Recycling* **2021**, *166*, 105340, doi:10.1016/j.resconrec.2020.105340.
4. Pimenta, S.; Pinho, S.T. Recycling of Carbon Fibers. In *Handbook of Recycling*; Elsevier, 2014; pp. 269–283 ISBN 978-0-12-396459-5.
5. Hengstermann, M.; Hasan, M.; Abdkader, A.; Cherif, C. Development of a New Hybrid Yarn Construction from Recycled Carbon Fibers (rCF) for High-Performance Composites. Part-II: Influence of Yarn Parameters on Tensile Properties of Composites. *Textile Research Journal* **2017**, *87*, 1655–1664, doi:10.1177/0040517516658511.
6. Rimmel, O.; May, D.; Goergen, C.; Poeppel, A.; Mitschang, P. Development and Validation of Recycled Carbon Fiber-Based Binder Tapes for Automated Tape Laying Processes. *Journal of Composite Materials* **2019**, *53*, 3257–3268, doi:10.1177/0021998318820422.
7. Colombo, B.; Gaiardelli, P.; Dotti, S.; Caretto, F. An Innovative Spinning Process for Production and Characterisation of Ring-Spun Hybrid Yarns from Recycled Carbon Fibre. *Journal of Cleaner Production* **2023**, *406*, 137069, doi:10.1016/j.jclepro.2023.137069.
8. Miyake, T.; Imaeda, S. A Dry Aligning Method of Discontinuous Carbon Fibers and Improvement of Mechanical Properties of Discontinuous Fiber Composites. *null* **2016**, *2*, 117–123, doi:10.1080/20550340.2016.1265693.
9. Abdkader, A.; Bachor, S.; Hasan, M.M.B.; Cherif, C. Development of Yarns from Recycled Carbon Fiber Based on Friction Spinning Technology with Specific Properties for Thermoset Composites. *Textile Research Journal* **2023**, 00405175231198272, doi:10.1177/00405175231198272.
10. Jlassi, S. Composites à Fibres de Carbone Recyclées: Variabilité Des Sources et Optimisation Des Performances Mécaniques, Thèse de Doctorat de l'Université de Toulouse, 2019.
11. Boulanghien, M. Formulations de composites thermoplastiques à partir de fibres de carbone recyclées par vapo-thermolyse, Ecole Nationale Supérieure des Mines d'Albi-Carmaux, 2014.
12. Boulanghien, M.; Ye, S.; R'Mili, M.; Bernhart, G.; Soudais, Y.; Berthet, F. Recycling of Carbon Fiber Composites Using a Steam-Thermolysis Process.; June 2013.
13. Matsuhisa, Y.; Bunsell, A.R. Tensile Failure of Carbon Fibers. In *Handbook of Tensile Properties of Textile and Technical Fibres*; Elsevier, 2009; pp. 574–602 ISBN 978-1-84569-387-9.
14. Akonda, M.H.; Lawrence, C.A.; Weager, B.M. Recycled Carbon Fibre-Reinforced Polypropylene Thermoplastic Composites. *Composites Part A: Applied Science and Manufacturing* **2012**, *43*, 79–86, doi:10.1016/j.compositesa.2011.09.014.
15. Manis, F.; Stegschuster, G.; Wölling, J.; Schlichter, S. Influences on Textile and Mechanical Properties of Recycled Carbon Fiber Nonwovens Produced by Carding. *J. Compos. Sci.* **2021**, *5*, 209, doi:10.3390/jcs5080209.
16. AFNOR Détermination Des Propriétés En Traction Sur Éprouvette Monofilament, NF ISO 11566.
17. Mesquita, F.; Bucknell, S.; Leray, Y.; Lomov, S.V.; Swolfs, Y. Single Carbon and Glass Fibre Properties Characterised Using Large Data Sets Obtained through Automated Single Fibre Tensile Testing. *Composites Part A: Applied Science and Manufacturing* **2021**, *145*, 106389, doi:10.1016/j.compositesa.2021.106389.
18. Islam, F.; Joannès, S.; Laiarinandrasana, L. Evaluation of Critical Parameters in Tensile Strength Measurement of Single Fibres. *J. Compos. Sci.* **2019**, *3*, 69, doi:10.3390/jcs3030069.
19. ESPCI Paris - Université PSL Statistique à Rupture de Renforts Fibreux Fragiles.
20. Kant, M.E.; Crabtree, J.D.; Young, S.; Penumadu, D. Concept of Limit Stress for the Tensile Behavior of Carbon Fiber Composite Tows. *Composites Part B: Engineering* **2020**, *201*, 108384, doi:10.1016/j.compositesb.2020.108384.
21. Bunsell, A.R.; Somer, A. The Tensile and Fatigue Behaviour of Carbon Fibres. In *Plastics, Rubber and Composites Processing and Applications*; 1992; Vol. 18, pp. 263–267.

COMMON REED AS A NOVEL BIOSOURCE FOR COMPOSITE PRODUCTION

P. Linderbäck[1], S. Gebrehiwot [1], L. Montin[1], R. Björkvall[1], L. Suarez[2], J. Theis[3] and Z. Ortega[3]

[1] School of engineering, culture and wellbeing, Arcada University of Applied Sciences, Helsinki, Finland
Email: paula.linderback@arcada.fi, Web Page: http://www.arcada.fi
[2]Departamento de Ingeniería Mecánica, Universidad de Las Palmas de Gran Canaria, Campus universitario de Tafira, 35017, Las Palmas de Gran Canaria, Spain
Email: luis.suarez@ulpgc.es, Web Page: https://accedacris.ulpgc.es/cris/rp/rp02233/publicaciones.html
[3]Departamento de Ingeniería de Procesos, Universidad de Las Palmas de Gran Canaria, Campus universitario de Tafira, 35017, Las Palmas de Gran Canaria, Spain
Email: J.T.: jakobtheis.jt@gmail.com; Z.O.: zaida.ortega@ulpgc.es, Web Page: https://accedacris.ulpgc.es/cris/rp/rp00631/publicaciones.html

Keywords: common reed, composite, PE, sustainable, polymer

Abstract
The production of plastics has grown significantly in the last decades, and the trend is expected to continue, depending mainly on increasing demand from various industries, such as packaging, construction, and consumer goods. Today, researchers are looking for new biobased sources to replace fossil fuel-based plastics. Common reed bed along the coast in Baltic Sea present a sustainable resource that could play a role in the future circular economy, but the potential of reeds as an unused biological material, effectively binding nutrients and carbon, has been only partially identified. This study examines the potential of common reed as a sustainable, novel composite material. Common reeds were harvested both in summer and winter, and various blends were analyzed to determine their suitability for composite applications. The mechanical characterization shows that the integration of common reed fibers into polyethylene matrices has been shown to enhance crucial properties such as tensile strength and yield strength, demonstrating that common reed can be utilized in composite materials, thereby reducing reliance on fossil-based plastics.

1. Introduction

The path towards a circular economy for plastics and composite materials, while enhancing circularity, strongly focuses on phasing out fossil fuel-based plastics. A promising solution to the environmental issues is the shift towards biobased and/or biodegradable materials. Biobased plastics are made fully or partially from biobased resources, with the integration of biobased carbon being a crucial element.
Currently, bioplastics constitute only 1-2% of all plastics, yet there is potential to replace up to 90% of fossil-based plastics with them. Plastic and composites are used for several different sectors and articles, due to their high flexibility and endless possibilities due to the possibility to vary their mechanical properties over a wide range, at a reasonable cost [1]. An essential area for substituting fossil-based plastics with biobased alternatives is in short-term use products for consumers, such as packaging, which represents the most significant usage area for conventional plastics [2].

Cellulose-based reinforced composites have been of interest for researchers and engineers over the past years [3]. By adding biobased fibers to composite material it is possible to modify the mechanical properties and biodegradability or decreasing the carbon footprint of composite [4]. Various engineering

sectors, including automotive interiors, have been replaced by plant-based fibers, including sisal, hemp, kenaf, flax, ramie, jute and rice husk as examples, have showed good mechanical characteristics for fiber reinforced composites [5], [6], [7], [8]. The characteristics with low density, light weight, low cost, decent thermal, electrical and acoustic insulation properties combined with minimal health hazard and energy consumption makes these natural fiber-based composites attractive choices instead of conventional synthetic fibers [9].

Researchers around the world are actively searching for new novel natural fibers for solving the challenge of composites. One fiber that researchers have suggested as an interesting alternative to reinforce novel composites is *Arundo donax* L. [10], [11]. This interest in giant reed is not only due to the interesting mechanical features shown by these fibers [12], but also because of its fast growth, the possibility of cultivating it in marginal soils and with wastewaters. For instance, Suárez et al. studied the mechanical properties of giant reed fibers in thermoplastic composite materials [13]. They found that these composites show improvement in flexural and tensile elastic modulus and the use of *Arundo donax* L. shows great potential to be used as reinforcement in polymer composites. On the other hand, giant reed composites also provide some other interesting features, such as the increase in the biodisintegration rates when introduced into a PLA matrix [14]. The use of this plant within a biorefinery context for the obtaining of valuable compounds and materials [15] also provides added value to the use of natural sourced materials, as part of a strategy for the control of invasive plant, and finding a closed loop strategy for the use of waste, also useful for the remediation of polluted soils and the reduction of soil losses [16].

Another novel natural-based material, with closed-loop strategy for harvesting waste, is common reed. Common Reed (*Phragmites australis*) is a perennial grass growing in shallow waters, shores, and wetlands, forming dense stands 1–3 meters tall and spanning up to hundreds of hectares. Common reed bed along the coast in the Baltic Sea present a sustainable resource that could play a role in the future circular economy. Common reed beds have the capacity to sequester nutrients and carbon, which are the major contributors to the Baltic Sea Eutrophication and the climate crisis. A potential strategy to recycle nutrients and close the nutrient cycles in the Baltic Sea ecosystem is coastal management, aiming to remove nutrients by harvesting biomass. Significant amounts of nutrients accumulate in various parts of emergent or submergent macrophytes during the growing season, such as reeds [17].

Harvested biomass can be reused for nutrient recycling, thereby closing the loops by returning extracted nutrients to the ecosystem. Reed contains significant amounts of nutrients contributing to Baltic Sea eutrophication, with up to 10 kg of phosphorus and 100 kg of nitrogen per hectare. Harvesting reeds can remove nutrients from coastal ecosystems while providing a climate-friendly raw material for various purposes. By harvesting reed beds, nutrients can be removed from ecosystems with biomass. Despite the rapid proliferation of common reeds and their biological characteristics, there are still limited applications for them. While some research has been done on reed value chains, there are still gaps that require further research. The potential of reeds as an unused biological material, effectively binding nutrients and carbon, has been only partially identified.

In previous studies, value chains for reed have been identified, including products like biogas, composting, and cultivation materials. However, higher-value products have not yet found their place in functional value chains. Manufacturing products according to circular economy principles requires reducing waste, replacing fossil materials like plastics, and developing responsible and sustainable production processes. There's an increasing focus on renewable solutions, driven by the negative impacts of plastics and a growing awareness of global waste issues, pushing material producers and industries towards environmentally friendly solutions throughout a product's lifecycle.

Albretch et al. (2023) studied the mechanical characteristics of common reed stems in comparison to wood. They concluded that common reed is suitable raw material for bio-based load bearing structural materials [18]. Kraiem and collaborators produced composites based on HDPE at low loadings (maximum of 10 % by weight) and reprocessed them to simulate a recycling process; these authors

found that reprocessing resulted in a better dispersion of the filler within the matrix, as easily understood, therefore obtaining improved properties after three reprocessing cycles [19]. More interestingly, the incorporation of such low amounts of reed provided an improved behavior after reprocessing, due to a stabilization effect provided by the biomass. This has been recently pointed out in other research works, where the analysis of potential stabilizing and antioxidant behavior of lignocellulose is being analyzed. In a different approach, Albretch et al. proposed the use of common reed stems for the production of load-bearing applications, bringing them together with wood glue (polyurethane resin). According to these authors, reed stems are a promising source for obtaining building materials.

This study examines the potential of common reed as a sustainable, novel composite material. It shows the characterization of the common reed harvested at two moments (winter and summer) and provides a first approach to its use for high-loaded composites.

2. Materials and methods

2.1. Plant characterization

Common reeds were harvested and collected both in summer and winter, with stems of an average of 1 cm, in South Finland during 2023. The plants that were harvested at the end of the summer period were separated in three parts: stems, leaves and flowers for characterization tests. From the plants harvested during the beginning of winter period only stems were characterized.

The content in ashes, lignin, cellulose and hemicellulose were determined using standardized methods, briefly described. Lignin content was determined using the Klason method [20] by hydrolysis with H2SO4. Holocellulose content was obtained through a gravimetric method, by samples delignification with acetic acid and sodium chlorite, as described by Browning [21]. Total cellulose content was derived from the holocellulose sample by digestion of hemicellulose with NaOH [22]. Hemicellulose content was calculated by subtracting cellulose from holocellulose. Three replicates from different batches were used, and results are presented as average values with standard deviations.

The thermogravimetric tests were carried out in order to determine the thermal stability of the materials. These studies were performed in a TGA 4000 from Perkin Elmer, using a sample of nominally 10 mg, from 30 to 600ºC at a heating rate of 10 ºC/min in a nitrogen atmosphere. The surface composition analyses were performed by Fourier transform infrared spectroscopy (FTIR). FTIR spectra were obtained in a Perkin Elmer spectrum Two device (Perkin Elmer, Waltham, MA, USA) equipped with an attenuated total reflectance (ATR) device, from 4000 to 500 cm^{-1}, at a resolution of 16 cm^{-1}, obtaining each spectrum as the average of 16 scans.

2.2. Composites Obtaining and Characterization

Composites obtaining were carried out following: Mixed common reed with stems, flowers and leaves (A) entire stems for summer (B) or winter (C) were milled and sieved for fractions of 0.075-0.8 mm to produce natural fiber composites (NFC) by dry blending with polymeric matrics and subsequent compression molding/extruder-injection molding. Polyethylene (Revolve N-461) was used as a matrics polymer to produce the composites, and various blends were analyzed to determine their suitability for composite applications. These blends were processed using twin-screw extrusion and molded, with their thermal properties, thermogravimetric analysis, and mechanical characteristics being assessed.

2.3 Mechanical characterization

Quasistatic tension tests are used to characterize the mechanical properties of the four different sample categories that include the pure PE (0 % Reed), and the PE reinforced with 20% fiber loading of reed A, B and C. ISO 527-2: test guidelines and condition to conduct the experiments on specimen type 1B was followed for these tests. A test speed of 10 mm/ min was used for all studied sample categories. Five specimens from each sample category were tested, and the mean stress-strain data is used for the characterization. The analyses of required mechanical properties are based on the nominal stress-strain data.

3. Results

3.1. Plant characterization

Table 1 summarizes the results from the composition analyses performed to the different samples of reed. It can be observed that mixed reed shows the higher humidity and ashes contents, possibly due to the incorporation of leaves within this group. Leaves are known to store salts and minerals [23]. Lignin content in the plant is similar despite the season of harvesting, only resulting in lowered amounts for the mixed reed, due to the presence of leaves in this fraction; lowered lignin content in leaves has also been found for other species of reed [11]. Finally, holocellulose content is about 76% for the three different species, although with different carbohydrates depending on the fraction. Winter reed exhibits the higher cellulose fraction, while summer and mixed reeds provide a lower content of that compound, with an increased fraction of hemicellulose. Other authors have reported similar composition, i.e. about 40 % cellulose, 26 % hemicellulose and 12% for lignin [24]. Contents around 30% of lignin have been reported previously in literature for giant reed [23], [25], [26], [27], while this plant exhibits usually a lower cellulose content, thus making common reed (Phragmites australis) a promising source for cellulose compounds.

Table 1. Compositional results for the different samples of common reed (in %)

	Humidity	Ashes	Lignin	Hemicellulose	Cellulose
Winter reed	5.66±0.23	7.60±0.20	25.87±1.25	20.92±0.83	55.09±0.36
Summer reed	5.37±0.01	8.82±0.21	24.01±0.47	28.07±0.55	48.75±1.03
Mixed reed	7.41±0.13	12.83±0.32	21.29±0.51	25.38±0.14	48.87±0.32

3.2. FTIR spectroscopy

Figure 1 shows the recorded spectra for the different samples assessed. Typical bands for lignocellulosic materials can be observed, namely at 3000-3700 cm^{-1}, assigned to O-H stretching in biomass; a double peak at 2917-2850 cm^{-1}, attributed mainly to C-H aliphatic groups in hemicellulose [26]; 1733 cm^{-1}, attributed to C=O stretching in lignin and hemicellulose[28], [29]; broad intense peak centered at 1034 cm^{-1} is observed for all the samples; this is attributed to C=O stretching ring vibration in cellulose [30]. Summer reed shows more prominent bands on the areas related to hemicellulose, particularly in the double peak close to 2900 cm^{-1}, as also observed for the composition analysis. The higher hemicellulose content is related to a lower thermal stability, as also observed in thermogravimetric analysis.

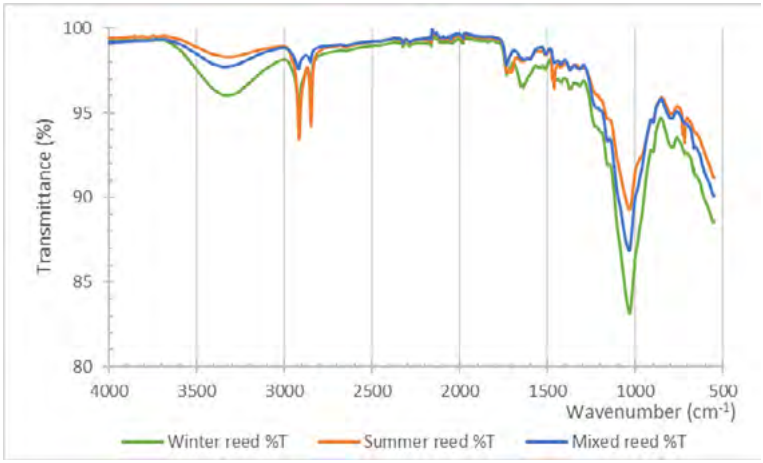

Figure 1. FTIR spectra for untreated reed samples

3.3. Thermogravimetric analysis (TGA)

From the thermogravimetric analysis the thermal stability of the different samples can be obtained. As observed from figure x, the winter reed shows more thermal stability than summer or mixed reeds, as explained above, due to the lower hemicellulose content. The mixed reed, on the contrary, shows a significantly lower onset temperature, due to the incorporation in this fraction of leaves, also exhibiting the higher amount of ashes (as usually minerals are stored there). This material exhibits three degradation steps, at the temperatures found in table 2. Remaining samples show the degradation occurring at two main moments, between 240-250 ºC, related to hemicellulose depolymerization [28] and at 270-290ºC (higher for winter reed samples).

Table 2. Results from TG analysis

	Onset (ºC)			Derivative peaks (ºC)			Ashes (%)
Winter harvested reed, stems		253.7	286.1		279.5	344.3	20.6
Summer harvested reed, stems		243.9	270.5		268.6	338.8	22.8
Mixed summer harvested reed	208.4	244.1	287.3	222.7	279.2	287.2	26.2

3.4. Mechanical characterization

The experimental stress-strain result shows that reed fiber-reinforcement decreased the ductility of the pure PE, however enhanced the key mechanical properties related to strength, as shown in figure. 2.

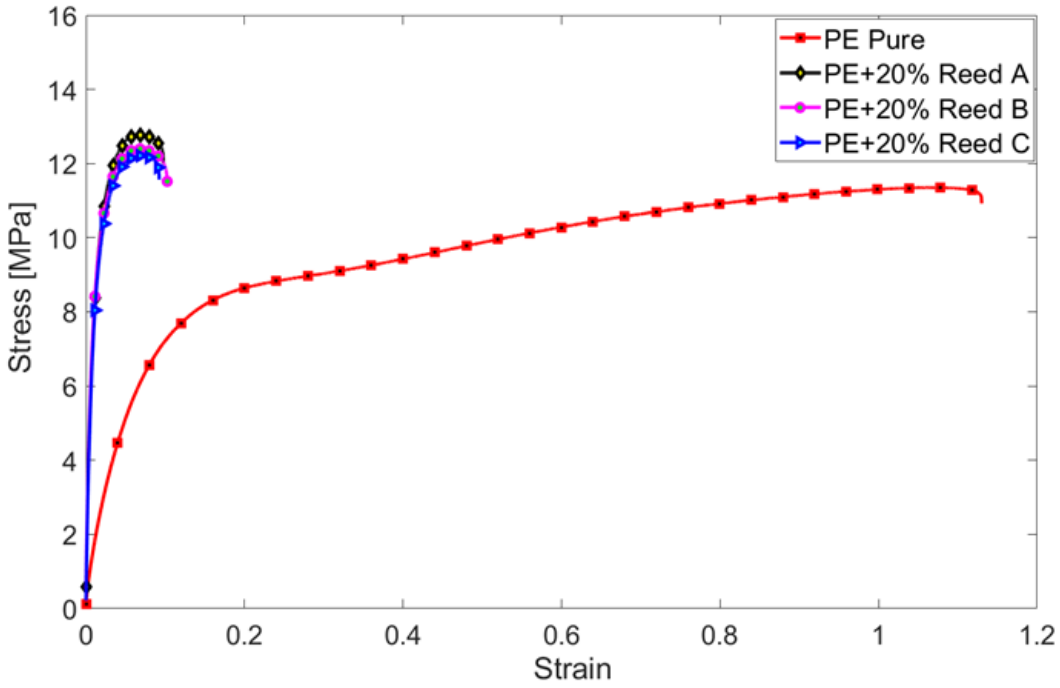

Figure 2. Experimental stress-strain relationship of the four sample variants

4. Conclusions

This study demonstrates that common reed can be utilized in composite materials, thereby reducing reliance on fossil fuel-based plastics. Additionally, it offers the potential for common reed to serve as a carbon sink in durable products. The analysis shows that common reed has a robust composition of lignocellulosic materials, and is suitable for various composite application, exhibiting comparable lignin and cellulose contents across different seasons. The higher cellulose fraction in winter-harvested reeds show seasonal variability also in material properties, which can be optimized for specific application. However, the determination of cellulse/lignin content should be determined further to be able to understand the variation of seasons or harvesting sites.

From the thermogravimetric analysis, the results shows that the thermal stability of reed-based composites can vary significantly depending on the blend and harvesting season. In thias study common reed were not treated chemically, which may lead to better thermal stability and should be studied further. The mechanical characterization shows that the integration of common reed fibers into polyethylene matrices has shown to enhance crusial properties such as tensile strenhgt and yield strength. While there are benefits achieved, a reduction of ductility is making composites stronger but less flexible.

The utilization of common reed, especially from dominant growth along the Baltic coast, could contribute positively to environmental management efforts by mitigating eutrophication through nutrient sequestration. This aligns well with circular economy principles and resource efficiency.

In conclusion, while promising, the application of common reed in biocomposites is still in the early stages. Future research should focus on optimizing harvesting times, blend proportions, and processing techniques to maximize the material´s functional properties and environmental benefits. This could create the way for a sustainable alternative to traditional fossil fuel-based plastics, contributing to a more resilient and environmentally conscious materials science landscape.

Acknowledge
We gratefully acknowledge the financial support from The Fund for Technical Education and Research,TUF, and the Central Baltic Interreg Programme.

5. References

[1] K. G. Satyanarayana, G. G. C. Arizaga, and F. Wypych, "Biodegradable composites based on lignocellulosic fibers—An overview," *Prog. Polym. Sci.*, vol. 34, no. 9, pp. 982–1021, Sep. 2009, doi: 10.1016/j.progpolymsci.2008.12.002.
[2] M. Lackner, A. Mukherjee, and M. Koller, "What Are 'Bioplastics'? Defining Renewability, Biosynthesis, Biodegradability, and Biocompatibility," *Polymers*, vol. 15, no. 24, p. 4695, Dec. 2023, doi: 10.3390/polym15244695.
[3] A. Bledzki, "Composites reinforced with cellulose based fibres," *Prog. Polym. Sci.*, vol. 24, no. 2, pp. 221–274, May 1999, doi: 10.1016/S0079-6700(98)00018-5.
[4] J. P. Correa, J. M. Montalvo-Navarrete, and M. A. Hidalgo-Salazar, "Carbon footprint considerations for biocomposite materials for sustainable products: A review," *J. Clean. Prod.*, vol. 208, pp. 785–794, Jan. 2019, doi: 10.1016/j.jclepro.2018.10.099.
[5] S. A. Pradeep, R. K. Iyer, H. Kazan, and S. Pilla, "Automotive Applications of Plastics: Past, Present, and Future," in *Applied Plastics Engineering Handbook*, Elsevier, 2017, pp. 651–673. doi: 10.1016/B978-0-323-39040-8.00031-6.
[6] P. R. Hornsby, E. Hinrichsen, and K. Tarverdi, "Preparation and properties of polypropylene composites reinforced with wheat and flax straw fibres: Part I Fibre characterization," *J. Mater. Sci.*, vol. 32, no. 2, pp. 443–449, 1997, doi: 10.1023/A:1018521920738.
[7] A. Shahzad, "Hemp fiber and its composites – a review," *J. Compos. Mater.*, vol. 46, no. 8, pp. 973–986, Apr. 2012, doi: 10.1177/0021998311413623.
[8] M. Poletto, H. Ornaghi, and A. Zattera, "Native Cellulose: Structure, Characterization and Thermal Properties," *Materials*, vol. 7, no. 9, pp. 6105–6119, Aug. 2014, doi: 10.3390/ma7096105.
[9] S. Mahmud, K. M. F. Hasan, Md. A. Jahid, K. Mohiuddin, R. Zhang, and J. Zhu, "Comprehensive review on plant fiber-reinforced polymeric biocomposites," *J. Mater. Sci.*, vol. 56, no. 12, pp. 7231–7264, Apr. 2021, doi: 10.1007/s10853-021-05774-9.
[10] V. Fiore, T. Scalici, and A. Valenza, "Characterization of a new natural fiber from Arundo donax L. as potential reinforcement of polymer composites," *Carbohydr. Polym.*, vol. 106, pp. 77–83, Jun. 2014, doi: 10.1016/j.carbpol.2014.02.016.
[11] L. Suárez, J. Castellano, F. Romero, M. D. Marrero, A. N. Benítez, and Z. Ortega, "Environmental Hazards of Giant Reed (Arundo donax L.) in the Macaronesia Region and Its Characterisation as a Potential Source for the Production of Natural Fibre Composites," *Polymers*, vol. 13, no. 13, p. 2101, Jun. 2021, doi: 10.3390/polym13132101.
[12] L. Suarez, "Use of giant reed (Arundo donax L.) for polymer composites obtaining: a mapping review," *Cellul. 2023 304793–4812*.
[13] L. Suárez *et al.*, "Influence of Giant Reed (*Arundo Donax L* .) Culms Processing Procedure on Physicochemical, Rheological, and Thermomechanical Properties of Polyethylene Composites," *J. Nat. Fibers*, vol. 21, no. 1, p. 2296909, Dec. 2024, doi: 10.1080/15440478.2023.2296909.
[14] L. Suárez, Z. Ortega, F. Romero, R. Paz, and M. D. Marrero, "Influence of Giant Reed Fibers on Mechanical, Thermal, and Disintegration Behavior of Rotomolded PLA and PE Composites," *J. Polym. Environ.*, vol. 30, no. 11, pp. 4848–4862, Nov. 2022, doi: 10.1007/s10924-022-02542-x.

[15] M. Villegas Calvo *et al.*, "Bioconversion of Giant Cane for Integrated Production of Biohydrogen, Carboxylic Acids, and Polyhydroxyalkanoates (PHAs) in a Multistage Biorefinery Approach," *ACS Sustain. Chem. Eng.*, vol. 6, no. 11, pp. 15361–15373, Nov. 2018, doi: 10.1021/acssuschemeng.8b03794.
[16] J. Andreu-Rodriguez *et al.*, "Agricultural and Industrial Valorization of *Arundo donax* L.," *Commun. Soil Sci. Plant Anal.*, vol. 44, no. 1–4, pp. 598–609, Jan. 2013, doi: 10.1080/00103624.2013.745363.
[17] C. Junli, G. Wang, Z. Fu, H. Qiao, and F. Liu, "Assessing wetland nitrogen removal and reed (Phragmites australis) nutrient responses for the selection of optimal harvest time," *J. Environ. Manage.*, vol. 280, Feb. 2021.
[18] K. Albrecht, F. Neudecker, S. Veigel, S. Bodner, J. Keckes, and W. Gindl-Altmutter, "The suitability of common reed (Phragmites australis) for load-bearing structural materials," *J. Mater. Sci.*, vol. 58, no. 39, pp. 15411–15420, Oct. 2023, doi: 10.1007/s10853-023-08996-1.
[19] D. Kraiem, S. Pimbert, A. Ayadi, and C. Bradai, "Effect of low content reed (Phragmite australis) fibers on the mechanical properties of recycled HDPE composites," *Compos. Part B Eng.*, vol. 44, no. 1, pp. 368–374, Jan. 2013, doi: 10.1016/j.compositesb.2012.04.062.
[20] "Standard Test. Methods for Lignin in Wood—D 1106-56." ANSI/ASTM, 1977a., 1977.
[21] Browning, B. L., "Methods of wood chemistry.," Volumes I&II vols., New York: John Wiley & Sons, 1967.
[22] "ANSI/ASTM, 1977b. Standard test methods for alpha-cellulose in wood D 1103-60."
[23] L. Suárez, M. Barczewski, P. Kosmela, M. D. Marrero, and Z. Ortega, "Giant Reed (*Arundo donax* L.) Fiber Extraction and Characterization for Its Use in Polymer Composites," *J. Nat. Fibers*, vol. 20, no. 1, p. 2131687, Apr. 2023, doi: 10.1080/15440478.2022.2131687.
[24] G. Başaran Kankılıç and A. Ü. Metin, "Phragmites australis as a new cellulose source: Extraction, characterization and adsorption of methylene blue," *J. Mol. Liq.*, vol. 312, p. 113313, Aug. 2020, doi: 10.1016/j.molliq.2020.113313.
[25] D. Barana, A. Salanti, M. Orlandi, D. S. Ali, and L. Zoia, "Biorefinery process for the simultaneous recovery of lignin, hemicelluloses, cellulose nanocrystals and silica from rice husk and Arundo donax," *Ind. Crops Prod.*, vol. 86, pp. 31–39, Aug. 2016, doi: 10.1016/j.indcrop.2016.03.029.
[26] M. D. L. Chikouche, A. Merrouche, A. Azizi, M. Rokbi, and S. Walter, "Influence of alkali treatment on the mechanical properties of new cane fibre/polyester composites," *J. Reinf. Plast. Compos.*, vol. 34, no. 16, pp. 1329–1339, Aug. 2015, doi: 10.1177/0731684415591093.
[27] A. A. Shatalov and H. Pereira, "Papermaking fibers from giant reed (Arundo donax L.) by advanced ecologically friendly pulping and bleaching technologies," *BioResources*, vol. 1, no. 1, pp. 45–61, Jul. 2006, doi: 10.15376/biores.1.1.45-61.
[28] W. Bessa *et al.*, "Characterization of raw and treated Arundo donax L. cellulosic fibers and their effect on the curing kinetics of bisphenol A-based benzoxazine," *Int. J. Biol. Macromol.*, vol. 164, pp. 2931–2943, Dec. 2020, doi: 10.1016/j.ijbiomac.2020.08.179.
[29] T. Scalici, V. Fiore, and A. Valenza, "Effect of plasma treatment on the properties of Arundo Donax L. leaf fibres and its bio-based epoxy composites: A preliminary study," *Compos. Part B Eng.*, vol. 94, pp. 167–175, Jun. 2016, doi: 10.1016/j.compositesb.2016.03.053.
[30] M. Martínez-Sanz, E. Erboz, C. Fontes, and A. López-Rubio, "Valorization of Arundo donax for the production of high performance lignocellulosic films," *Carbohydr. Polym.*, vol. 199, pp. 276–285, Nov. 2018, doi: 10.1016/j.carbpol.2018.07.029.

MULTISCALE MODELING OF 3D BRAIDED COMPOSITE WITH VOID DEFECTS USING MACHINE LEARNING METHOD

Xinyi Song[1], Jin Zhou[1,] *, Di Zhang[1] , Shenghao Zhang[1],

[1] School of Mechanical Engineering, Xi'an Jiao Tong University, Xi'an 710049, P. R. China
* Corresponding author (jin.zhou@xjtu.edu.cn)

Keywords: 3D braided composite, Micro-CT, Pore defect, Machine learning.

Abstract

A novel multiscale damage analysis approach is proposed for 3D braided composite with void defects, utilizing unsupervised machine method. To implement the multiscale damage model, a user-defined material subroutine (UMAT) is developed. Experimental validation demonstrates the accuracy of this approach in capturing damage modes. Furthermore, the framework predicts the mechanical properties of braided composites with various porosities. The relationships between porosity, modulus reduction, and strength reduction are established through rigorous statistical analysis. This method provides a valuable tool for the efficient visualization of mechanical analyses of 3D braided composite materials with void defects, based on accurate geometric information. This approach offers significant advancements in the field of composite material damage analysis for further research in this area.

1. Introduction

3D braided CMCs are gaining increasing attention in the field of the aeronautics and astronautics due to their low density, high mechanical properties, and near-net-shape forming ability [1-4]. The preparation and verification of 3D braided composites are time-consuming and costly[5-7]. The structure and damage mode of ceramic based braided composite materials have multi-scale characteristics[8, 9], coupled with unavoidable pore defects during the forming process, making it difficult to analyze the mechanical properties. Therefore, reconstructing a real geometry model and establishing an accurate and efficient trans-scale damage model for braided composite materials has been a challenge in the composite materials research.

The forming process inevitably gives rise to void defects and yarns deformation, resulting in the complex multiscale structure. The pore defects will significantly affect the mechanical properties and failure mechanism of the composites[10-12]. With the 3D image and data information provided by micro-CT, the actual parameters of the internal structure of the composites can be extracted [13-15]. This non-destructive inspection technique has been used to the 3D braided composites. Ge et al. [16] established the micro-CT based trans-scale finite element models. And he investigated the effects of interface strength by the progressive damage model and cohesive-zone model. Liu et al.[17] considered the fabric compaction and the axial yarn torsion and proposed a statistical approach to generate the meso-scale representative volume element (RVE) of 3D five-directional braided composites. Wang et al.[18] proposed a combination of parametric and statistical methods to establish the real meso-scale finite element model considering yarn shape and pore defects. Gao et al. [19] established the constitutive model and finite element model and predicted the evolution of the mechanical properties of 3D braided composite material with defects. The structure and damage evolution of braided composite materials have multi-scale characteristics, and directly incorporating high-precision microscopic models into large-scale calculations will lead to greatly reduce computational efficiency. Models incorporate machine learning to establish direct mappings between different scales a significantly reduced computational time. Bhaduri et al. [20] predicted the local stress field of fiber-reinforced matrix

composite material by using deep learning tools. Yang et al. [21] proposed a multi-scale damage model based on the parametric finite-volume direct averaging micromechanics theory, extended finite element method (XFEM), and a clustering algorithm to describe the progressive damage evolution of laminates. Sengodan [22] established a deep machine learning strategy that uses the statistical quantification and dimensionality reduction techniques to visualize and understand the distribution of microstructure-response data in the transformed dimensional space are presented in detail. As shown above, in terms of structural characterization, most prior studies using the geometrical parameters before the PIP (Precursor infiltration and pyrolysis) process[23], the voids and braiding characteristics are all assumed, bu

t the real structure after the manufacturing process is not considered. In terms of simulation, scholars have conducted extensive research on the multi-scale mechanical properties of braided materials, but have not utilized machine learning methods to reduce the computational dimensions of multi-scale analysis of braided composite, lacking efficient and visual methods for predicting mechanical properties.

This article proposes an unsupervised machine learning based method coupled with micro-computed tomography (micro-CT) and progressive damage analysis is proposed to conduct trans-scale damage of 3D braided CMCs with void defects. The 3D reconstruction is carried out to establish real microscale and mesoscale models, the unsupervised machine learning method is used to reduce the calculation dimension and data visualization analysis, combined with progressive damage analysis method to conduct trans-scale strength prediction and damage analysis, and verified by experiments. Mechanical properties of braided composites with different porosity are predicted. The pore content and the reduction ratio of modulus and strength is fitted.

2. Multi-scale parameter feature extraction based on micro-ct and sem

2.1 Statistical analysis of microscale

The microscale of 3D braided CMCs can be regarded as the scale of yarn which consists of filaments, intra-yarn voids and matrix. The specimens are polished to obtain clear images, and a scanning electron microscope (SEM) (Gemini SEM 500) is used to analyze the filaments' filling factor and cross-section. Fig. 1 shows the SEM image of the filaments, where the fiber and matrix are segmented.

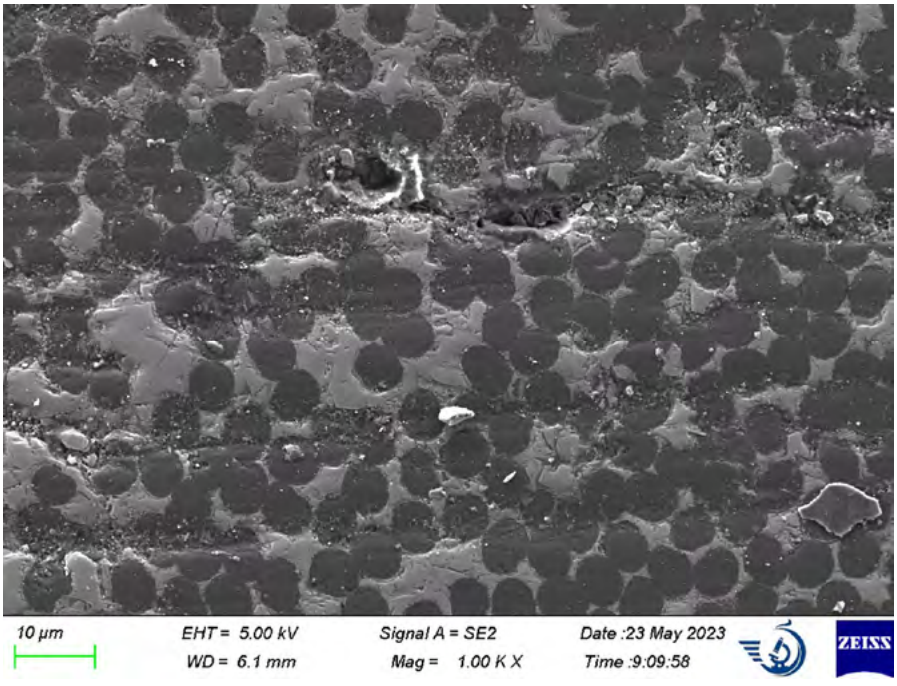

Figure 1. SEM images

A typical laboratory micro-CT system [25] involves an X-ray source [26], a rotation of the sample and a planar detector. This method allows for the visualization and analysis of internal details of materials in a non-destructive manner. A Xradia 610 Versa with a 20 × lens detector, is performed to scan samples of 3D braided composites, as shown in Fig. 2a. It is worth noting that using a smaller sample size can lead to higher resolution and scan quality [27]. Therefore, the sample was cut to a size of 0.81mm × 0.82 mm × 0.85 mm to achieve sufficient spatial resolution. were reconstructed using the Dragonfly software package. To reduce image noise, a 3D median filter was applied. For the segmentation of the full-size region, a scalable neural network was trained using image data from a small range of separated materials.

2.2 Experimental verification

In this paper, 3D braided preforms are fabricated by the 3D four-step braiding process[28]. The preform structure is composed of the braiding yarn made of carbon fiber tows (T700-12K, Toray®, Tokyo, Japan). The PIP process is employed to prepare the composites. The 3D braided CMC are cut into tensile specimens, and the specification of test samples are shown in Fig. 2. All tests are conducted on a DNS200 electromechanical testing machine, following the ASTM D3039 standards. The strain during the tests is measured by strain gage attached parallel to the axial direction on the surface of the specimens. The surface full-field strain of samples during axial tensile test was recorded by Digital Image Correlation (DIC)[29]. Three samples were tested to get the average value.

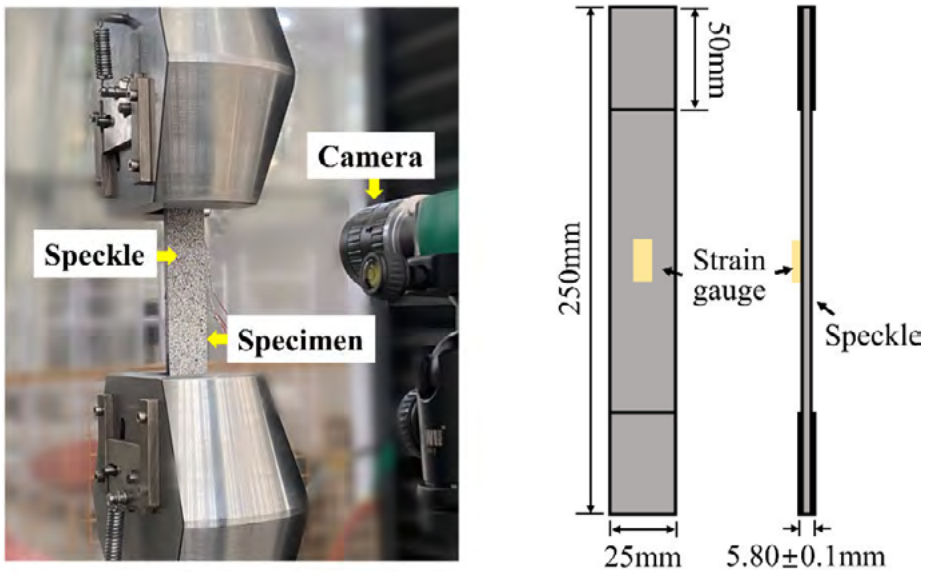

Figure 2. The schematic of micro-CT system.

3. Trans-scale damage analysis based on unsupervised machine learning

The mechanical properties and damage analysis of 3D braided composite are typical multi-scale problem. Based on the statistical results of SEM (figure. 3) and micro-CT. The inter-yarn voids are established by randomly choosing elements according to the micro-CT results. Periodic meshing is required before imposing periodic boundary conditions on the established microscale model. The meshed FE model contains 20784 nodes and 27068 C3D6 elements. If the microscopic unit cell model is directly embedded in the mesoscopic model which will bring great computational complexity to the calculation of the macroscopic model. Compared with the traditional k-means clustering method, the Uniform Manifold Approximation and Projection (UMAP) [30] clustering method is a more efficient unsupervised machine learning method in dealing with high-dimensional big data problems. In this

chapter, we proposes the Principal Component Analysis (PCA) [31] and UMAP clustering dimensionality reduction method, which puts sub-cell with similar mechanical behavior into the same category. The trans-scale damage analysis of braided composites is realized by using the failure theory to predict the tensile properties of braided composites and reveal the microscopic damage failure process.

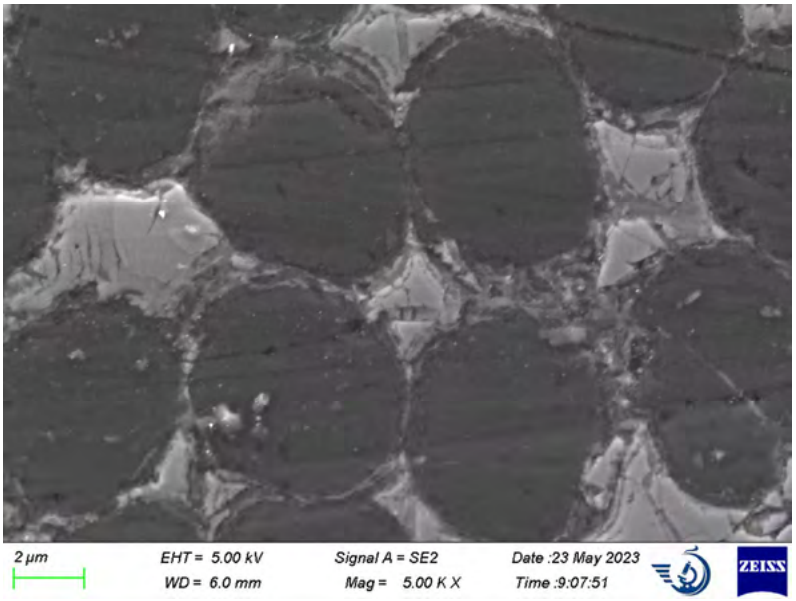

Figure 3. Establishment of microscale model

In order to realize the multi-scale analysis method based on the failure theory of micromechanics, the elastic analysis of the microscale model is required to obtain the stress under the unit strain. The strain relationship between microscale RVE and sub-cell can be established:

$$\varepsilon^{(k)} = \boldsymbol{A}^{(k)}\varepsilon \tag{1}$$

where $\varepsilon^{(k)}$ represents the average strain in the kth sub-cell, A(k)represents the strain amplification matrix of the kth sub-cell, ε represents the strain applied to the RVE.

The stress of each sub-cell can be expressed as:

$$\sigma^{(k)} = \boldsymbol{C}^{(k)}\varepsilon^{(k)} = \boldsymbol{C}^{(k)}\boldsymbol{A}^{(k)}\varepsilon = \boldsymbol{M}^{(k)}\varepsilon \tag{2}$$

where M(k) is the 6×6 strain-stress amplification matrix of the kth sub-cell, which represents the relationship between the strain ε and the stress response $\sigma^{(k)}$ in the kth sub-cell.

Based on volume averaging method, the stress relationship between microstructural RVE and sub-cell can be established:

$$\sigma = \frac{1}{V}\int \sigma(x)\mathrm{d}V = \frac{1}{V}\sum_{k=1}^{N_k}\int_{V_k}\sigma^{(k)}(x)\mathrm{d}V^{(k)} = \sum_{k=1}^{N_k} v^{(k)}\boldsymbol{M}^{(k)}\varepsilon \tag{3}$$

where Nk is the number of the sub-cell, $V^{(k)}$ and $v^{(k)}$ represents the total volume and the volume fraction of the kth sub-cell respectively.

Therefore, by applying periodic boundary conditions[32] and unit strain, the 6×6 strain-stress amplification matrix of the sub-cell M can be obtained to calculate the stress of the microscale RVE, which can be applied on mesoscopic analysis. But the data size of the unit cell representing one integration point will be 27068 × 6 × 6 in mesoscopic model. In this study, we use PCA-UMAP to reduce the dimensionality of data.

Primarily, mapping the 36-dimensional matrix M to low-dimensional space by using PCA method which requires finding a matrix W = [w1, w2,…,wd] , so that the low-dimensional data Y = WTM can retain the original structure of the original high-dimensional data.

$$\begin{aligned} \boldsymbol{W} &= \arg\max \sum_{i=1}^{n} \mathrm{y}_i - \overline{y}^2 = \arg\max \sum_{i=1}^{n} \boldsymbol{W}^{\mathrm{T}} \left(m_i - \overline{m} \right)^2 \\ &= \arg\max \sum_{i=1}^{n} Tr\left[\boldsymbol{W}^{\mathrm{T}} \left(m_i - \overline{m} \right) \left(m_i - \overline{m} \right)^{\mathrm{T}} \boldsymbol{W} \right] \\ &= \arg\max Tr\left[\boldsymbol{W}^{\mathrm{T}} \boldsymbol{X} \boldsymbol{W} \right] \end{aligned} \tag{4}$$

X is the total dispersion matrix, where $\boldsymbol{X} = \sum_{i=1}^{n} \left(\boldsymbol{m}_i - \overline{\boldsymbol{m}} \right) \left(\boldsymbol{m}_i - \overline{\boldsymbol{m}} \right)^{\mathrm{T}}$ .Thus, the dimensionality reduction matrix can be obtained by solving the eigenvector matrix of X. The dimension of compressed dataset Y is usually higher than 2 or 3, making it impossible to use 2D or 3D scatter plots for visual analysis.

Then the UMAP uses local manifold approximations and local fuzzy simplex set representations to construct topological representations of high-dimensional data[33]. The UMAP optimizes the layout of data representation in low dimensional space to minimize the cross entropy between two topological representations shown in Eqs. (5).

$$CE((\boldsymbol{Z}, \mu), (\boldsymbol{Z}, \nu)) \triangleq \sum_{a \in A} \left(\mu(a) \log\left(\frac{\mu(a)}{\nu(a)} \right) + (1 - \mu(a)) \log\left(\frac{1 - \mu(a)}{1 - \nu(a)} \right) \right) \tag{5}$$

where Z is the weighted adjacency matrix; ν And μ represent probabilities.

4. Results and discussion

4.1 Pore distribution on macro and microscale

Based on the scanning data, 3D reconstruction is performed at the microscale to obtain intra-yarn voids distribution. The intra-yarn void content is defined as the ratio of volumes of voids and yarns which is calculated about 1.52%and the void content statistics are shown in Fig. 4. Small voids (1 × 10-5~1 × 10-7mm3) accounts for over 90% of the inter-yarn voids, with pore volumes ranging from 10-6 to 10-5mm3 accounting for the most (58.91%). And the void content inside the yarn is higher than that near the edge of the yarn, which is caused by uneven ceramic deposition.

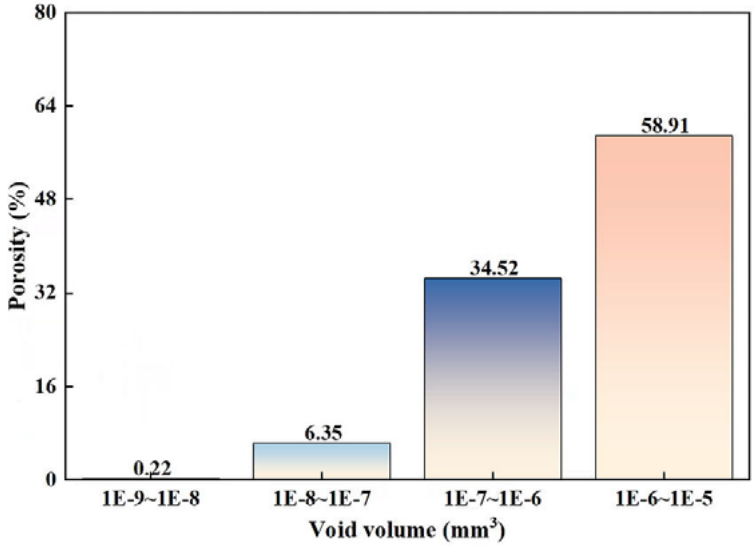

Figure 4. The characteristics of the intra-yarn voids in micro-scale.

At the microscale, the inter-yarn voids is defined as the ratio of the volumes of voids and the matrix which is 5.04%. Fig. 5 shows the voids distribution and the histograms of the cumulative probability of the void volume distribution ranging from 10^{-6} to 1 mm^3. The results show that the main defects in the composites between 10^{-5} and 10^{-4} mm^3, accounting for 67.54 %. The percentages of voids with the volume of 10^{-3}~0.01 mm^3, 0.01~0.1 mm^3 and 0.1~1 mm^3 are 2.28 %, 1.53% and 0.07 %, respectively. Obviously, the volume

content of small voids is much higher than that of large voids. The larger voids are distributed inside the sample, while the void volume around the sample is smaller. This is because during the deposition process of ceramics, the matrix is first formed externally, making it difficult for the gas-phase precursor to enter the center of the sample, resulting in a larger internal void volume.

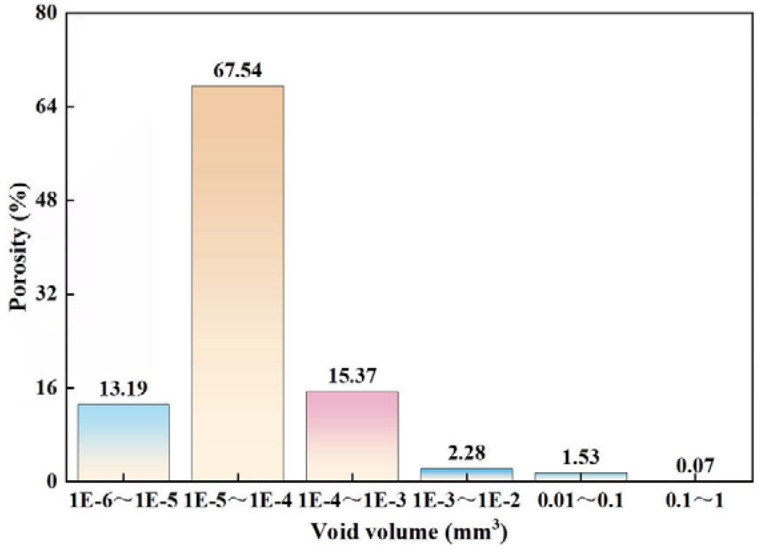

Figure 5. The characteristics of the inter-yarn voids in micro-scale.

4.2 Damage mechanisms analysis

According to the pore content results obtained in Section 4.1, the 1.52% intra-yarn porosity and the 5% inter-yarn porosity RVEs model was adopted for finite element simulation. As the number of clusters increases, more information of the microscopic model will be saved in the higher-scale model, which can predict the response results more accurately. But the number of databases increase will also reduce the efficiency. In order to ensure the accuracy of the test results, the convergence of the number of clusters was studied. The strain-stress curves of the 3D braided CMCs with different cluster numbers are plotted in Fig. 6.

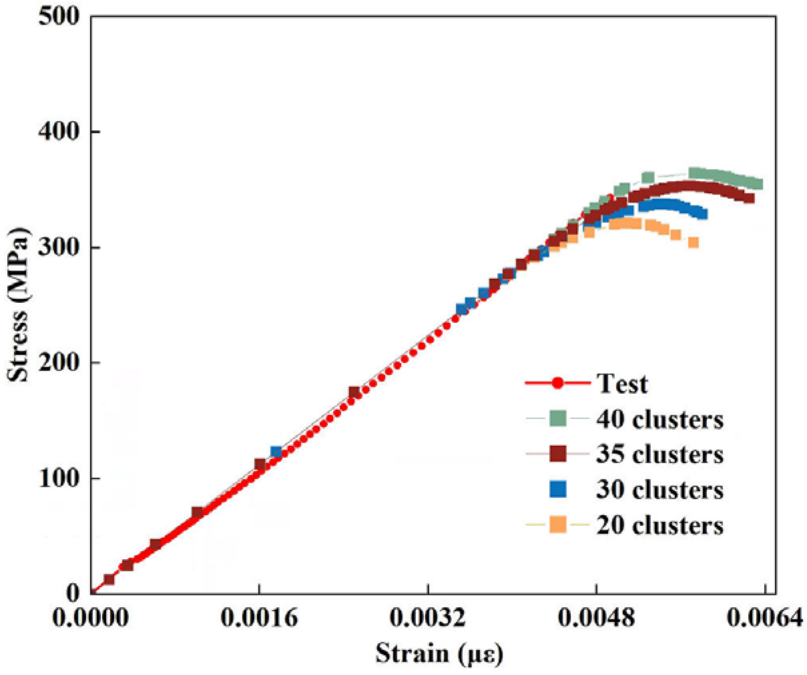

Figure 6. Stress-strain curves

5. Conclusions

We propose a method for analyzing the trans-scale damage of 3D braided ceramic matrix composites (CMCs) with void defects using unsupervised machine learning, micro-computed tomography (micro-CT). We first perform 3D reconstruction to establish real microscale models. The calculated contents of intra-yarn voids and inter-yarn voids are approximately 1.52% and 5.04%, respectively. To reduce the calculation dimension and visualize the data, we apply unsupervised machine learning and combine it with a progressive damage model for trans-scale damage analysis. Experimental results demonstrate that this approach, coupled with micro-CT technology and unsupervised machine learning for dimensionality reduction, effectively captures the void features. This scheme provides valuable insights into the efficient visualization of mechanical analysis of braided composite materials with pore defects, based on based on real geometric information.

Acknowledgment

This research was funded by National Natural Science Foundation of China [grant numbera12002265] and the National Key R&D Program of China [grant number 2021YFF0500100].

References

[1] Triantou, K.I., K. Mergia, B. Perez, S. Florez, A. Stefan, C. Ban, G. Pelin, G. Ionescu, C. Zuber, W.P.P. Fischer, J. Barcena, Thermal shock performance of carbon-bonded carbon fiber composite and ceramic matrix composite joints for thermal protection re-entry applications. Composites Part B: Engineering, 2017. 111: p. 270-278.
[2] Sciti, D., L. Zoli, T. Reimer, A. Vinci, P. Galizia, A systematic approach for horizontal and vertical scale up of sintered Ultra-High Temperature Ceramic Matrix Composites for aerospace – Advances and perspectives. Composites Part B: Engineering, 2022. 234: p. 109709.
[3] Yao, L., Z. Liu, Q. Song, B. Wang, Y. Cai, Prediction modelling of cutting force in rotary ultrasonic end grinding 2.5D woven SiO2f/SiO2 ceramic matrix composite. Composite Structures, 2023. 304: p. 116448.
[4] Lee, W., J. Hong, J. Song, W. Yang, J. Kim, Fabrication of high-performance thermally conductive phase change material composites with porous ceramic filler network for efficient thermal management. Composites Science and Technology, 2023. 240: p. 110092.
[5] Li, Y., X.J. Chen, J. Zhou, X. Liu, D. Zhang, F. Du, W. He, P. Jia, H. Liu, A review of high-velocity impact on fiber-reinforced textile composites: Potential for aero engine applications. International Journal of Mechanical System Dynamics, 2022. 2: p. 50 - 64.
[6] Han, J., R. Wang, D. Hu, J. Bao, X. Liu, X. Guo, A novel integrated model for 3D braided composites considering stochastic characteristics. Composite Structures, 2022. 286: p. 115309.
[7] Guo, J., Y. Ke, Y. Wu, B. Gu, B. Sun, Effects of defect sizes at different locations on compressive behaviors of 3D braided composites. Thin-Walled Structures, 2022. 179: p. 109563.
[8] Wang, B., G. Zhang, X. Nie, C. Wu, A multi-scale finite element approach for the mechanical behavior analysis of 3D braided composite structures. Composite Structures, 2022. 279: p. 114711.
[9] Tian, W., L. Qi, M.W. Fu, Multi-scale and multi-step modeling of thermal conductivities of 3D braided composites. International Journal of Mechanical Sciences, 2022. 228: p. 107466.
[10] Shen, X., X. Liu, S. Dong, L. Gong, RVE model with shape and position defects for predicting mechanical properties of 3D braided CVI-SiCf/SiC composites. Composite Structures, 2018. 195: p. 325-334.
[11] Fu, Y., X. Yao, X. Gao, Micro-mesoscopic prediction of void defect in 3D braided composites. Composites Part A: Applied Science and Manufacturing, 2021. 147: p. 106450.
[12] Arregui-Mena, J.D., T. Koyanagi, E. Cakmak, C.M. Petrie, W.-J. Kim, D. Kim, C.P. Deck, C. Sauder, J. Braun, Y. Katoh, Qualitative and quantitative analysis of neutron irradiation effects in SiC/SiC composites using X-ray computed tomography. Composites Part B: Engineering, 2022. 238: p. 109896.
[13] Holmes, J., S. Sommacal, R. Das, Z. Stachurski, P. Compston, Characterisation of off-axis tensile behaviour and mesoscale deformation of woven carbon-fibre/PEEK using digital image correlation and X-ray computed tomography. Composites Part B: Engineering, 2022. 229: p. 109448.

[14] Lim, H.J., H. Choi, G.J. Yun, Multiscale failure and damage analysis of sheet molding compound (SMC) composites using Micro-CT image-based reconstruction model. Composites Part B: Engineering, 2022. 231: p. 109593.
[15] Zhao, Q., Z. Gao, H. Wang, H. Wu, X. Chen, Z. Qu, T. Zhao, D. Fang, On accurate characterization of interfacial morphology and damage evolution of thermoplastic composite welded joints: A microscale study via in-situ micro-CT. Composites Science and Technology, 2023. 236: p. 110004.
[16] Ge, L., H. Li, J. Zhong, C. Zhang, D. Fang, Micro-CT based trans-scale damage analysis of 3D braided composites with pore defects. Composites Science and Technology, 2021. 211: p. 108830.
[17] Liu, X., D. Zhang, J. Sun, S. Yu, Y. Dai, Z. Zhang, J. Sun, G. Li, K. Qian, Refine reconstruction and verification of meso-scale modeling of three-dimensional five-directional braided composites from X-ray computed tomography data. Composite Structures, 2020. 245: p. 112347.
[18] Wang, Z., Q. Yuan, X. Wang, D. Zhang, Real meso-scale model reconstruction and tensile failure prediction of 3D braided PIP-SiCf/SiC composites considering pore defects. Composite Structures, 2023. 305: p. 116478.
[19] Gao, X., L. Yuan, Y. Fu, X. Yao, H. Yang, Prediction of mechanical properties on 3D braided composites with void defects. Composites Part B: Engineering, 2020. 197: p. 108164.
[20] Mendikute, J., M. Baskaran, I. Llavori, E. Zugasti, L. Aretxabaleta, J. Aurrekoetxea, Predicting the effect of voids generated during RTM on the low-velocity impact behaviour by machine learning-based surrogate models. Composites Part B: Engineering, 2023. 260: p. 110790.
[21] Yang, D., V. Wei, Z. Jin, Z. Yang, X. Chen, A UMAP-based clustering method for multi-scale damage analysis of laminates. Applied Mathematical Modelling, 2022. 111: p. 78-93.
[22] Ammasai Sengodan, G., Prediction of two-phase composite microstructure properties through deep learning of reduced dimensional structure-response data. Composites Part B: Engineering, 2021. 225: p. 109282.
[23] Fang, C., X. Yang, L. Chai, Z. Zhang, Y. Weng, L. Zheng, X. Luo, X. Zhang, Q. Huang, Ablation property and oxide scale evolution of Y2O3 modified C/C-SiC composites fabricating via precursor infiltration and pyrolysis method. Journal of the European Ceramic Society, 2023. 43(3): p. 842-852.
[24] Newbury, D.E., N.W. Ritchie, Performing elemental microanalysis with high accuracy and high precision by scanning electron microscopy/silicon drift detector energy-dispersive X-ray spectrometry (SEM/SDD-EDS). Journal of materials science, 2015. 50: p. 493-518.
[25] Zaw Thin, M., C. Moore, T. Snoeks, T. Kalber, J. Downward, A. Behrens, Micro-CT acquisition and image processing to track and characterize pulmonary nodules in mice. Nature Protocols, 2023. 18(3): p. 990-1015.
[26] Nugent, K.A., Coherent methods in the X-ray sciences. Advances in Physics, 2010. 59(1): p. 1-99.
[27] du Plessis, A., W.P. Boshoff, A review of X-ray computed tomography of concrete and asphalt construction materials. Construction and Building Materials, 2019. 199: p. 637-651.
[28] Bilisik, K., Three-dimensional braiding for composites: A review. Textile research journal, 2013. 83(13): p. 1414-1436.
[29] McCormick, N., J. Lord, Digital image correlation. Materials today, 2010. 13(12): p. 52-54.
[30] McInnes, L., J. Healy, J. Melville, Umap: Uniform manifold approximation and projection for dimension reduction. arXiv preprint arXiv:1802.03426, 2018.
[31] Maćkiewicz, A., W. Ratajczak, Principal components analysis (PCA). Computers & Geosciences, 1993. 19(3): p. 303-342.
[32] Henyš, P., L. Čapek, J. Březina, Comparison of current methods for implementing periodic boundary conditions in multi-scale homogenisation. European Journal of Mechanics-A/Solids, 2019. 78: p. 103825.
[33] Dorrity, M.W., L.M. Saunders, C. Queitsch, S. Fields, C. Trapnell, Dimensionality reduction by UMAP to visualize physical and genetic interactions. Nature communications, 2020. 11(1): p. 1537.

PERFORMANCE EVALUATION OF NOVEL BIOBASED THERMOPLASTIC COMPOSITES REINFORCED WITH DIFFERENT PLIES OF HEMP FABRICS

Vito Gigante[1], Laura Aliotta[2], Bianca Dal Pont[3], Pietro Russo[4], Jessica Passaro[5] and Andrea Lazzeri[6]

[1]Department of Civil and Industrial Engineering, University of Pisa, 56122 Pisa, Italy
Email: vito.gigante@unipi.it, Web Page: https://www.linkedin.com/in/vito-gigante-a40221237/
[2]1Department of Civil and Industrial Engineering, University of Pisa, 56122 Pisa, Italy
Email: vito.gigante@unipi.it, Web Page: https://www.linkedin.com/in/laura-aliotta-a91223237/
[3]Department of Civil and Industrial Engineering, University of Pisa, 56122 Pisa, Italy
Email: bianca.dalpont@phd.unipi.it, Web Page: https://www.linkedin.com/in/bianca-dal-pont-b29195275/
[4] Institute for Polymers, Composites and Biomaterials, National Research Council, Via Campi Flegrei 34, 80078 Pozzuoli, NA, Italy Email : pietro.russo@ipcb.cnr.it, Web Page: https://www.linkedin.com/in/russo-pietro-16088a82/
[4] Institute for Polymers, Composites and Biomaterials, National Research Council, Via Campi Flegrei 34, 80078 Pozzuoli, NA, Italy Email : jessica.passaro@ipcb.cnr.it, Web Page: https://www.linkedin.com/in/jessica-passaro-ph-d-17212ba6/
[1]Department of Civil and Industrial Engineering, University of Pisa, 56122 Pisa, Italy
Email: andrea.lazzeri@unipi.it, Web Page: https://www.linkedin.com/in/andrea-lazzeri-0b99184a/

Keywords: biocomposites, hemp fibers, water uptake, analytical model

Abstract

The combination of poly(lactic acid) (PLA)/poly(butylene succinate-coadipate) (PBSA) with hemp fabrics to produce thermoplastic based composite is a novelty. This necessity is pushed up by environmental issues but is important that also technological properties are comparable with bcurrent benchmarks. The aim of this work is to investigate the properties of a new biocomposite made by a biopolymeric blends as matric reinforced with different amounts of hemp fabrics for rigid trays.

The effects of different amounts of fibres were analysed using tensile, flexural, impact and HDT tests. Analytical prediction models were also used to predict the tensile and flexural properties of the biocomposites, emphasising the role of the fibres.The role of warp and weft fibres in determining the final mechanical properties. To better compare the results obtained with existing composites of reinforced hemp fabrics, a “Merit Index” was also calculated to evaluate the performance obtained with these new composites in terms of stiffness and lightness.

1. Introduction

The growing emphasis on sustainability has driven both academic and industrial sectors to explore the adoption of biobased renewable resources for composite material production. This imperative extends beyond environmental concerns to encompass technological advancements [1].
Sustainable biocomposites, featuring biobased and/or biodegradable thermoplastic matrices coupled with natural fibers, emerge as promising alternatives to current fossil-based composites. Their notable specific strength, stiffness, and lightweight properties make them well-suited for a wide array of applications [2].

Biocomposites consisting of a bio-based, biodegradable matrix and natural fibres make them ideal for various applications. However, to extend their use, several drawbacks must be overcome, such

as poor moisture resistance, incompatibility between fibres and matrix, flammability, processing difficulties and fibre variability [3].

In particular, fabric-based laminated composites have attracted much attention in recent years due to their properties, such as light weight, high strength and low cost compared to other reinforcements. There are several techniques for the production of fabric-based laminated composites, such as compression moulding, profiling, forming and machining. The use of thermoplastic resin and reinforcing fibres allows for easy processing and fast production, resulting in high mechanical performance and low weight. In addition, thermoplastic composites offer advantages over thermosets, such as high toughness, rapid production and recyclability [4]. The fibre and matrix coating method, followed by compression moulding, is one of the most popular and suitable production techniques for thermoplastic biocomposites.

The PLA/PBSA blend selected for this study was based on results from a previous work [5], where it was shown that adding 40 wt% of PBSA not only improved the PLA's flexibility and viscosity but also its processability. Although the correlation between processing, morphology, and properties is well known, the identification of optimal processing conditions, including screw speed, feeding rate, and shear rate, is still approached through trial and error. In this work the extrusion of the matrix has been optimized with a software tool to have control over the blend morphology since it profoundly affects the material properties [6].

As for the fiber reinforcement materials, hemp was chosen for its impressive mechanical properties, high cellulose content, and low cost. Additionally, hemp fibers are quite convenient to use since they're available globally, thanks to the environmental conditions needed for their growth, making it easy to cultivate them worldwide [7].

The goal of this project is to explore the mechanical properties of new PLA/PBSA fabric-based biocomposites with varying amounts of hemp fibers added. Our main aim is to investigate how the fiber volume fraction affects the thermal and mechanical behavior of PLA/PBSA composites reinforced with hemp fabric. Fiber volume fraction has been shifted from 30 to 50% and examined its impact on the composite properties using thermo-mechanical characterization combined with morphological analysis. Moreover, for improving the possibility of using simple predictive analytical models, like the mixture rule and modified mixture rule, to predict the tensile and flexural properties of the resulting composites.

2. Materials and Methods

- Poly(lactic) acid (PLA) with trade name Luminy LX175 was purchased by Total Corbion PLA. It is an extrusion PLA grade that contains about 4% of D-lactic acid units. [density: 1.24 g/cm^3; melt flow index (MFI) (210 °C/2.16 kg): 6 g/10 min].
- Poly(butylene succinate-co-adipate) (PBSA) with trade name BioPBS FD92PM was purchased from Mitsubishi Chemical Corporation. It is a ductile semicrystalline copolymer of succinic acid, adipic acid and butanediol. [density of 1.24 g/cm^3; MFI (190 °C, 2.16 kg): 4 g/10 min].
- Hemp twill fabric, trade name FIBER-MJ 401, purchased from Fibertech Group (Marnate (VA), Italy). It is a twill 2/2 fabric having a light brown colour, tending to yellow. The roll width is 1000 mm and the fabric thickness is of 0.34 mm. From the producer datasheet, the following information was provided: weigh ratio warp/weft: 50/50; weight: 350 g/m^2; density: 1.47 g/cm^3; elastic modulus of hemp yarn: 23.07 GPa; tensile strength of hemp yarn: 399.8 MPa. No sizing has been reported on the fibres which are in their natural status.

For the production of the thermolpastic based composites, the first step was the twin-screw extrusion by a semi-industrial Comac EBC 25HT (L/D = 44) (Comac, Cerro Maggiore, Italy) twin-screw extruder. This process is necessary to guarantee an optimized dispersive mixing of the two polymers with tailored processing parameters exploited with a simulation software. The achieved pellets were preliminarily transformed into films by a flat die extruder Teach-Line E 20-T (Collin GmbH, Ebersberg, Germany) equipped with a CR 72 T calender unit.

PLA/PBSA films with a thickness of about 150 µm were then stacked alternately with layers of hemp reinforcing fabric, and the superimposed system was finally subjected to hot-compaction using a lab-press Collin P400E (Collin GmbH, Ebersberg, Germany).
Specifically, setting a compaction temperature of 185 °C, laminates consisting of 2, 4 and 6 plies were obtained using a pressure profile specifically studied for decreasing the voids quantity.
All the pathway is shown in **Figure 1**.

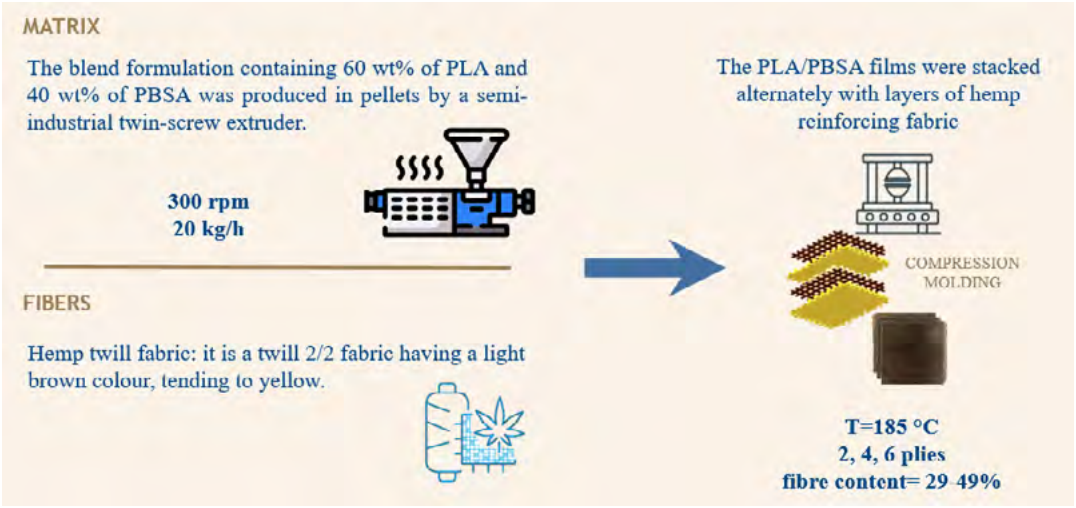

Figure 1. Composites preparation

The methodologies used in this work were:

Uniaxial tensile tests: Conducted on an MTS Criterion model 43 universal tensile testing machine equipped with a 10 kN load cell, at a crosshead speed of 10 mm/min. Specimens with rectangular sections measuring 80 × 110 mm were used.

Flexural tests: Carried out according to ASTM D790 via a three-point bending (3 PB) test on the same MTS machine, using a 10 kN load cell and a crosshead speed of 2 mm/min. A support span-to-size ratio of 20:1 was adopted, with rectangular specimens measuring 80 × 12.7 mm.

Charpy impact tests: Conducted at room temperature using an Instron CEAST 9050 machine equipped with a 15 J Charpy pendulum. Rectangular specimens measuring 80 × 10 mm were V-notched in the middle with a 45° V-notch, 2 mm deep, with a 0.25 mm radius of curvature at the base of the notch.

HDT measurements: Carried out with an HVT302B according to ISO 75-1 (method B). A parallelepiped with dimensions of 80 × 10 mm is immersed in a silicone oil bath and subjected to a flexural stress of 1.81 MPa. The bath heating rate was set at 120 °C/h.

Thermal analysis via DSC: Conducted using a DSC Q200 TA instrument to investigate the thermal properties of the pure matrix and laminated composites, following the conditions specified in the paper of Aliotta et al. [8].

SEM analysis: Performed on an EM-30 scanning electron microscope to observe the adhesion between the PLA/PBSA matrix and the hemp fibers.

3. Results

Starting from thermal characterizations, the incorporation of hemp fibers resulted in a decrease in the crystallinity degree of PLA, while leaving the PBSA crystallinity almost unchanged. A general reduction in the total crystallinity of the PLA/PBSA matrix was observed with the inclusion of hemp fabric layers. This phenomenon can be attributed to the addition of large quantities of long hemp fibers, which, although not chemically interacting strongly at the polymer interface, could physically impede

the reorganization of polymer chains during the hot macro- and micro-impregnation phases. Consequently, this hindered the overall degree of crystallization [9].
The addition of hemp fibers increased material stiffness, correlating with fiber content, as expected. This effect, commonly observed, is attributed to the higher stiffness of hemp fibers compared to the pure PLA/PBSA matrix. However, the increase in flexural modulus exceeded that of the elastic modulus, likely due to fiber arrangement and test type. During flexural tests, fiber orientation influences stresses, with fibers in both warp and weft directions contributing equally to modulus increase. Conversely, in tensile tests, only fibers aligned parallel to the load direction contribute significantly to stiffness enhancement. Despite modulus improvement, poor interlayer adhesion can lead to reduced flexural strength (**Figure 2**).

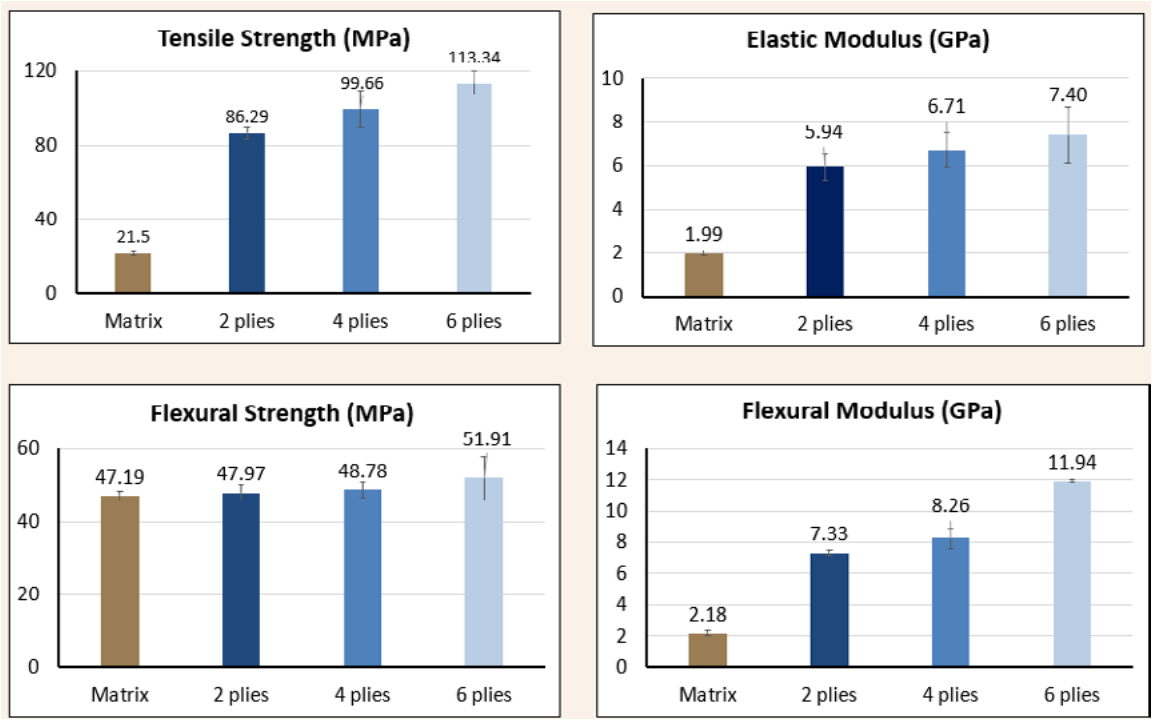

Figure 2. Mechanical properties of the composites with differen plies

The increase in tensile and flexural properties with higher volume fiber content is also attributed to the decrease in void content achieved by increasing the number of fabric layers. For instance, composites with six layers exhibit lower void content compared to those with two layers. This reduction in void content is facilitated by the higher pressure applied during fabrication. As the number of fabric layers increases, a gradual increase in compaction pressure becomes necessary at the same temperature. This ensures thorough impregnation of the innermost fiber layers by the matrix, potentially reducing the overall void content of the laminate. Optimizing process parameters, including pressure and holding time, improved interlayer adhesion with increasing ply number, this behavior is also confirmed by SEM micrographs (**Figure 3**).

Moreover, the addition of the fibres improves the thermal resistance, increasing the fibre content an increment of HDT was observed and increasing the number of plies a marked increment of the Charpy impact strength was achieved.

To comprehensively assess the potential of the new composite system, a "merit index" was computed to facilitate comparison with existing composite systems in terms of lightweight design and stiffness [10]. Various equations were employed to establish upper and lower bounds for the composite properties relevant to the merit index. **Figure 4** illustrates constant values of the E/ρ^3 ratio, representing the merit index, which should be maximized to achieve minimum component weight while maintaining permissible deflection for different shapes and loading scenarios. Increasing the merit index indicates superior lightweight and stiffness characteristics. The composites developed in this study exhibit a

comparable merit index, with an increase observed as the number of plies rises, resulting in enhanced stiffness and reduced weight. Comparing with other types of composite systems documented in the literature, it's noteworthy that the new composites show competitiveness, particularly when compared to thermoplastic composites featuring hemp fabric and PLA or PP matrix.

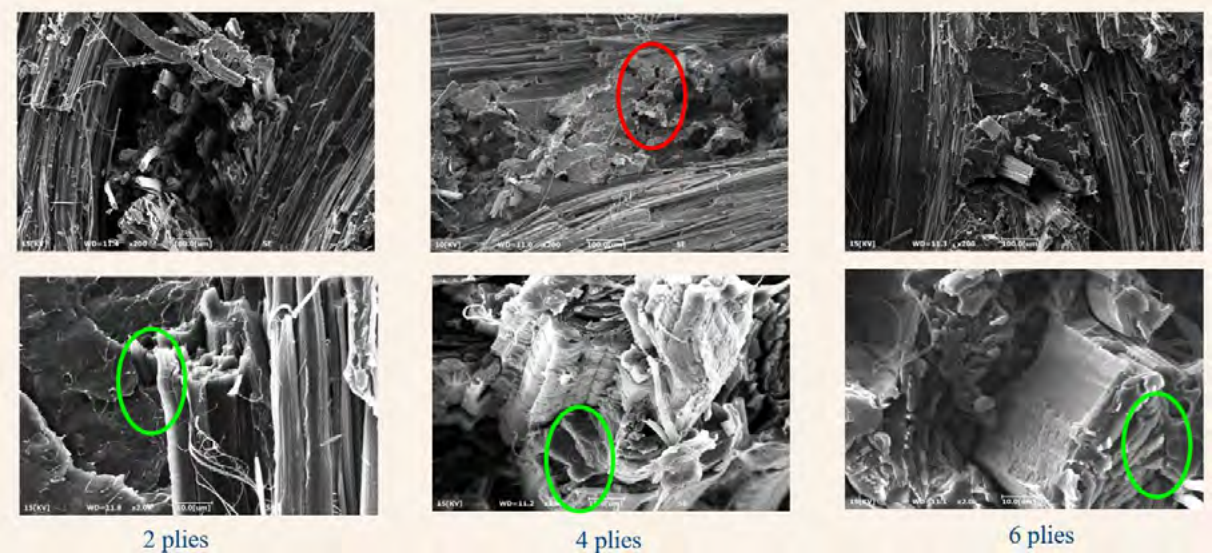

Figure 3. SEM micrographs of the biocomposites produced

Moreover, the utilization of biobased PLA and PBSA matrices in contrast to PP-based and partially biobased epoxy composites contributes to a reduced carbon footprint. Additionally, the end-of-life sustainability of the analyzed composite systems is enhanced. Incorporating PBSA into the matrix blend improves material eco-efficiency, Despite PBSA's higher cost compared to classical PP and biobased PLA, the favorable mechanical properties obtained broaden the application potential of these laminated composites, extending beyond conventional packaging applications typically associated with PBSA.

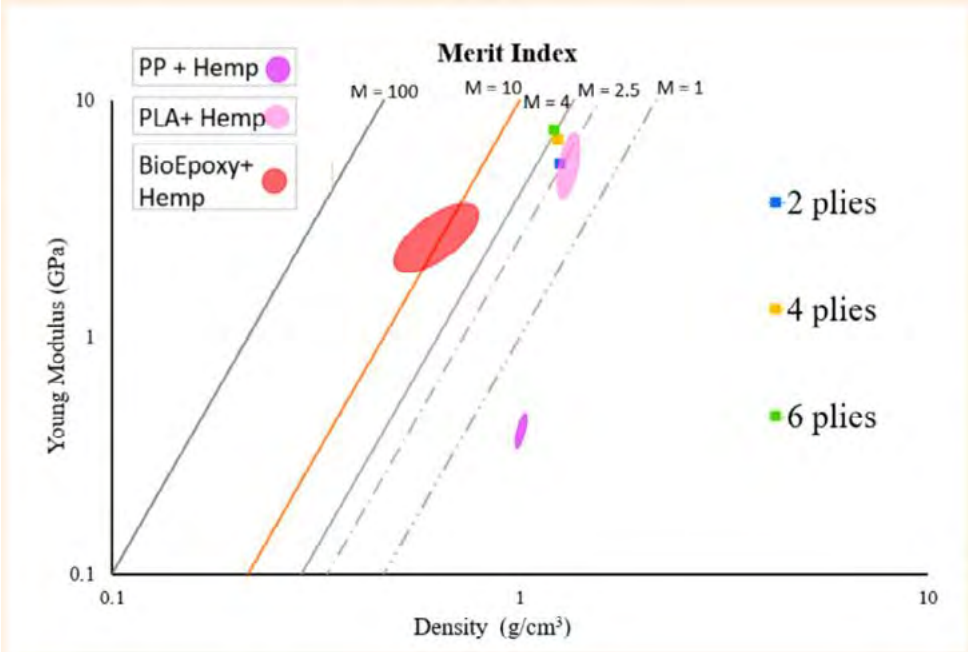

Figure 4. "Merit Index"

4. Conclusions

The laminated composites were obtained by hot compression moulding technique and, varying the number of hemp plies, laminated composites with different fibre volume fraction were produced (from 29 up to 49%). Increasing the fibre volume fraction, an increment of mechanical, flexural, impact and HDT properties were obtained. The good adhesion between the various layers, through the composites thickness, have been noticed through optical microscope and SEM analysis; no voids are present through the composites thickness and the different hemp twill fabric are well embedded to the polymeric matrix. To compare results with existing composites reinforced with hemp fabrics, a "merit index analysis" has been constructed to evaluate the efficiency of these new composites in terms of stiffness and lightweight. The merit index indicates encouraging stiffness values relative to the lightweight nature of the laminates, even when compared to typical fossil-based thermoplastic composites.
The excellent mechanical properties open possibilities for the application of these laminated composites in high-performance scenarios, contributing to the advancement of sustainable materials across various industries.

References

[1] Abdur Rahman, M. , Haque, S. , Athikesavan, M. M. , and Kamaludeen, M. B. A review of environmental friendly green composites: production methods, current progresses, and challenges. *Environmental Science and Pollution Research* **2023**, 30, 16905–16929.
[2] Rajeshkumar, L. , Ramesh, M. , Bhuvaneswari, V. , Balaji, D. , and Deepa, C. Synthesis and thermomechanical properties of bioplastics and biocomposites: a systematic review. *Journal of Materials Chemistry B* **2023**, 11, 3307–3337.
[3] Elfaleh, I. , Abbassi, F. , Habibi, M. , Ahmad, F. , Guedri, M. , Nasri, M. , and Garnier, C. A comprehensive review of natural fibers and their composites: An eco-friendly alternative to conventional materials. *Results in Engineering* **2023**, 19, 101271.
[4] Nabels-Sneiders, M. , Platnieks, O. , Grase, L. , and Gaidukovs, S. Lamination of Cast Hemp Paper with Bio-Based Plastics for Sustainable Packaging: Structure-Thermomechanical Properties Relationship and Biodegradation Studies. *Journal of Composites Science* **2022**, 6, 246.
[5] Aliotta, L. , Vannozzi, A. , Cinelli, P. , Coltelli, M.-B. , and Lazzeri, A. Essential Work of Fracture and Evaluation of the Interfacial Adhesion of Plasticized PLA/PBSA Blends with the Addition of Wheat Bran by-Product. *Polymers* **2022**, 14, 615.
[6] Gigante, V. , Aliotta, L. , Dal Pont, B. , Titone, V. , Botta, L. , Mantia, F. P. La , and Lazzeri, A. Tailoring morphology and mechanical properties of PLA/PBSA blends optimizing the twin-screw extrusion processing parameters aided by a 1D simulation software. *Polymer Testing* **2023**, 108294.
[7] Shahzad, A. Hemp fiber and its composites – a review. *Journal of Composite Materials* **2012**, 46, 973–986.
[8] Aliotta, L. , Dal Pont, B. , Gigante, V. , Russo, P. , Passaro, J. , and Lazzeri, A. Investigation of new Poly(lactic acid) (PLA)/Poly(butylene succinate-co-adipate) (PBSA) thermoplastic composites reinforced with different amount of twill hemp fabrics. *Journal of Materials Science* **2023**
[9] Salmins, M. , Gortner, F. , and Mitschang, P. Challenges in Manufacturing of Hemp Fiber-Reinforced Organo Sheets with a Recycled PLA Matrix. *Polymers* **2023**, 15, 4357.
[10] Ashby, M. F. Criteria for selecting the components of composites. *Acta Metallurgica et Materialia* **1993**, 41, 1313–1335.

Study on dispersion mixing of cellulose nanofiber reinforced polyvinyl chloride composites using a single screw extruder

Haruya Baba[1], Tatsuya Tanaka[2], Masahiro Sasada[3], Kana Miyamoto[4] and Hiroshi Ohsaki[5]

[1]Doshisha University/Kyoto, Japan
Email: ctwj0507@mail4.doshisha.ac.jp
[2]Doshisha University/Kyoto, Japan
Email: tatanaka@mail.doshisha.ac.jp
[3] Doshisha University/Kyoto, Japan
Email: msasada@mail.doshisha.ac.jp
[4] TOLI Co., Ltd./Hyogo, Japan
Email: kana_miyamoto@toli.co.jp
[5] TOLI Co., Ltd./Hyogo, Japan
Email: hiroshi_ohsaki@toli.co.jp

Keywords: Composites, Cellulose nanofibers (CNF), Single screw extruder, Extensional flow

Abstract
This study investigated the dispersion of sub-micron filler in a single screw extruder by using a newly developed extensional flow screw. Fillers were dispersed by passing the pellet mixture through a single-screw extruder with 30 holes and a $1mm$ diameter through-hole, hereafter referred to as XBD, to create the extensional flow. The experiments used materials with $1phr$, $5phr$, and $10phr$ of cellulose nanofiber added to the base material. Extrusion conditions were set at a temperature of 165℃ and a rotation speed of $40rpm$, and the pressure drop before and after XBD was measured. The results showed the large agglomerates were reduced when comparing kneading with and without XBD. The extensional flow of XBD increased the agglomerate area frequency from $4\mu m^2$ to $18\mu m^2$ and was also effective in breaking the agglomerates. The results also indicated that for extensional flow dispersion in a single screw extruder, it is important to keep the melt viscosity high, increase the feed rate and increase the pressure drop to improve dispersion.

1. Introduction

In recent years, the development of polymer composites has been promoted to achieve high performance and high functionality of materials by mixing polymers and fillers.
In this study, we focused on polyvinyl chloride resin (PVC) as the polymer and cellulose nanofiber (CNF) as the filler. PVC is made up of about 60% salt and has a lower environmental impact than other petroleum-based plastics. In addition, its mechanical and chemical stability and good moldability make it suitable for a wide range of applications, such as interior decoration, building materials, and agricultural materials. However, PVC has a low heat resistance temperature and there are concerns about thermal degradation and pyrolysis during processing. Therefore, a counter-rotating twin-screw extruder with a relatively low kneading capacity is often used, which can suppress heat generation, but it is not suitable for kneading with fillers.
Composites with CNF have attracted attention to improve the strength, thermal dimensional stability, and other properties of PVC. CNF is a sustainable natural resource characterized by its light weight, high strength [1] (2-3GPa), and low coefficient of thermal expansion [2] ($10^{-7}/K$). However, the small particle diameter, hygroscopicity, and high particle surface cohesion of CNF make the dispersive mixing of particle agglomerates an industrial challenge.

This study focused on the dispersion of filler using extensional flow as a method of both suppressing thermal degradation of PVC and breaking up agglomerates in the extruder. Shear flow, which is generally dominant in an extruder, is not suitable for filler dispersion in PVC due to the rotation of the filler, the high ratio of loss to given energy and the shear heating. Extensional flow is a flow in which the material is stretched in the direction of the principal stress. In the uniaxial extensional flow field of a Newtonian fluid, the extensional viscosity is three times the shear viscosity [3] , the stress acting on the filler is larger [4] , and heating is not easily generated, so the filler dispersion effect of extensional flow is expected.
Several kneading techniques using extensional flow have been studied [5-8].
Tanaka and Matsumoto installed a fixed multi-through-hole segment in a co-rotating twin-screw extruder and developed a segment that generates extensional flow by coughing up resin in front of the segment and pressurizing it [9-10]. By actively allowing the material to pass through the through-holes, resin leakage from the mesh area is suppressed, and the pressure drop across the segment is successfully improved by a factor of approximately 1.6.
In this study, we have applied this multi-hole segment to a single-screw extruder, to disperse filler by extensional flow suppressing thermal degradation of PVC.
The dispersion of CNF using extensional flow kneading was compared with full flight (FF) kneading in a single-screw extruder to assess the difference in dispersibility as a function of CNF concentration in the polymer, the pressure drop before and after the segment and feed rate.

2. Experimental samples and apparatus

2.1. Experimental samples

PVC (Shin Daiichi Enbi, degree of polymerization 800) was used as the matrix. Additives such as calcium carbonate, stabilizers and plasticizers were added, and the pellet mixture was used hereafter referred to as Standard1. CNF (nanoforest-PDP, Chuetsu Pulp & Paper Co., Ltd.) was used as filler. The addition of $1phr$, $5phr$ and $10phr$ of CNF to Standard1 was named as Standard2, Standard3 and Standard4, respectively. The measurements were carried out after hot air drying at 80℃ for at least 24 hours prior to extrusion.
Figure 1 shows a SEM image of 30-50μm in diameter CNF agglomerates, with submicron order fibers (0.13-13.8μm in diameter) physically entangled with each other.

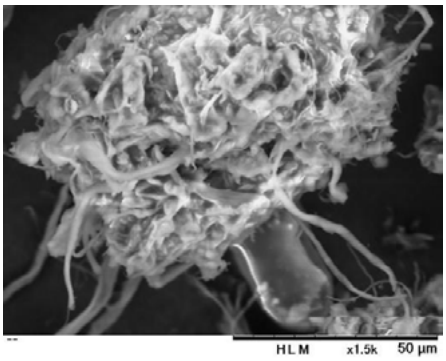

Figure 1. SEM image of cellulose nanofibers used in the experiment.

2.2. Single screw extruder

Figure 2 shows the multi-through-hole segment (XBD) used in the experiment, and Figure 3 shows the screw with and without the XBD attached. The XBD has 30 holes of diameter of $1mm$ and thickness of $3mm$. The XBD is motionless and it is connected to the rotating screw by a bearing. The XBD was used to partially slow the resin flow. The resin was then pressurized and extruded to create an extensional flow. Figure 4 shows a single-screw extruder (SS-24-24 Sanki) with the outlet barrel removed and a

cross-sectional view. This single-screw extruder has a L/D of 20 and a diameter of 24mm.The screw had two configurations: with the XBD to generate an extensional flow and without the XBD (FF), as shown in Figure 3. The pressure before and after the XBD was measured and the pressure drop difference ΔP was calculated.

Figure 2. XBD used in the experiment.

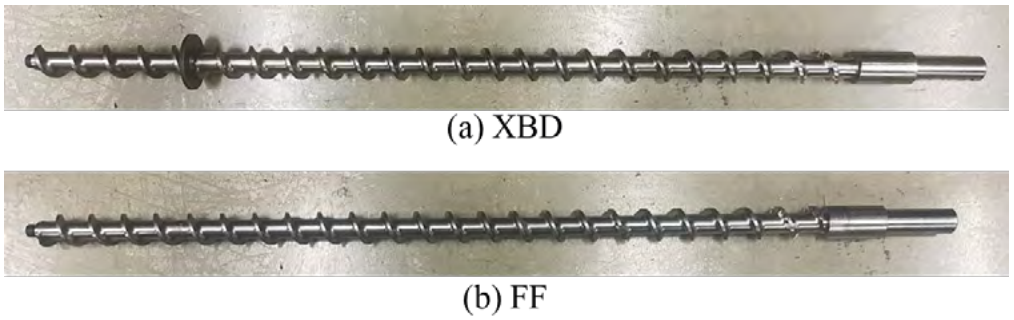

Figure 3. Screw used in the experiment: (a)screw with XBD, (b)screw without XBD.

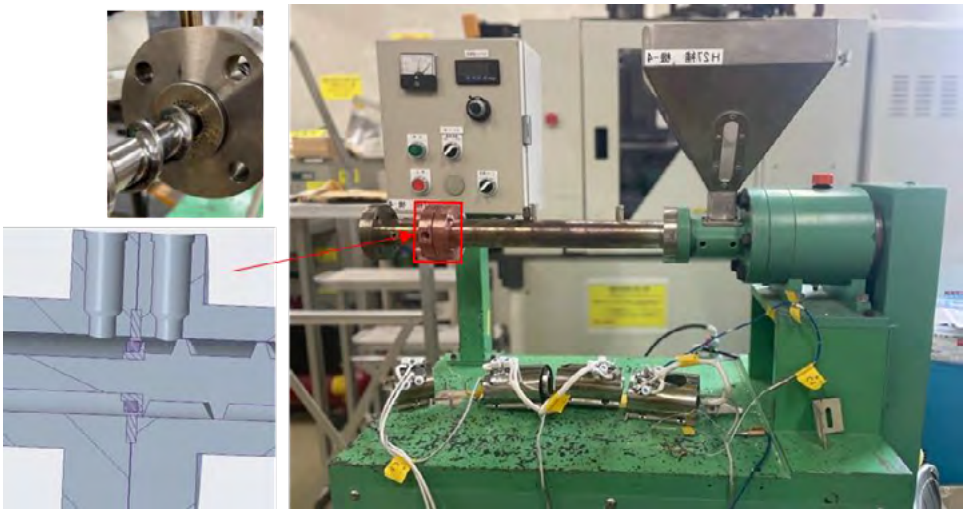

Figure 4. Single-screw extruder and a cross section.

3. Experimental procedure

3.1. Effects of CNF content on dispersibility

The effect of CNF content on dispersibility was investigated using a single-screw extruder with a die, a barrel temperature of 165℃, a rotation speed of 40rpm, and the materials Standard2, Standard3 and Standard4.

3.2. Effect of CNF content on pressure drop and feed rate

The effect of CNF content on pressure drop and feed rate was investigated using a single-screw extruder with a die, a barrel temperature of 165℃, a rotation speed of $40rpm$, and the materials Standard1, Standard2, Standard3, and Standard4. The feed rate was calculated from the amount extruded in 36 seconds.

4. Evaluation method

4.1. Dispersibility

Materials extruded by a single-screw extruder were heat-pressed at 165℃ and $10kN$ in a compression molding machine to produce sheets. They were observed with a SEM (Miniscope® TM3030Plus) at magnifications of 200x and 1000x. The observations at 1000x and 200x were used to measure the area distribution of fillers below and above $60\mu m^2$, respectively. As shown in Figure 5, fillers were detected as black spots and calcium carbonate as white spots. Sigma Scan Pro 5 (SYSTAT) was used to binarize the observed images and measure the area of the black spots to obtain the frequency distribution of the agglomeration area, as shown in Figure 6.

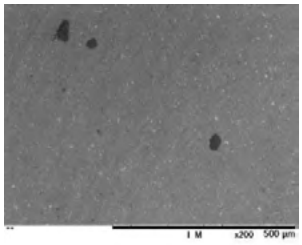

Figure 5. SEM image.

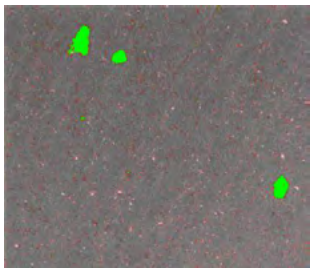

Figure 6. Binarization of a SEM image with Sigma Scan Pro 5.

5. Results and discussion

5.1. Relationship between CNF content and dispersibility

Figure 7 shows a comparison of the dispersibility for Standard2, Standard3, and Standard4 produced with screw configuration XBD and FF, with filler area below $60\mu m^2$, while Figure 8 shows a comparison for filler area above that. For Standard2, almost no difference in dispersibility between XBD and FF was measured. Comparing Standard3 and Standard4, the agglomerate area in the range $4\mu m^2$-$18\mu m^2$ increased, as shown in Table 1, indicating that the extensional flow is effective in breaking up the agglomerates.

As for in the comparison of the dispersibility of agglomerates larger than $60\mu m^2$, the agglomerates formed during the kneading Standard3 and Standard4 in FF were eliminated in XBD, and the average agglomerate area was reduced by 21.9% and by 31.3% in Standard3 and Standard4, respectively. In

particular, agglomerates larger than $725\mu m^2$ were eliminated in Standard4, indicating that XBD is effective in reducing large agglomerates.

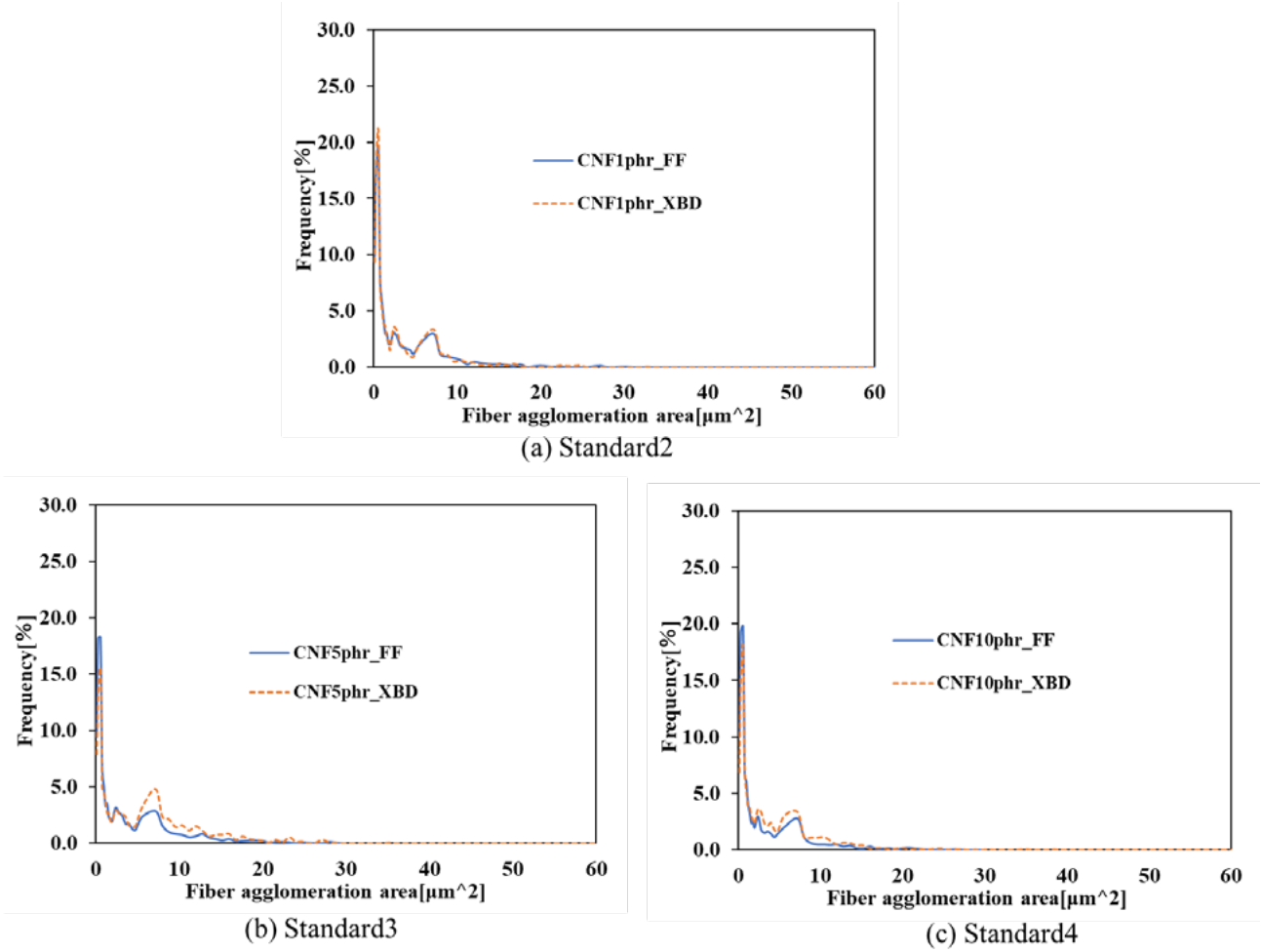

Figure 7. Comparison of the dispersion in Standard2, 3 and 4 produced with between XBD and FF.

Table 1. Cumulative frequency of $4\mu m^2 \sim 18\mu m^2$.

Sample type	Standard2		Stabdard3		Standard4	
Screw condition	FF	XBD	FF	XBD	FF	XBD
Cumulative area frequency of $4\mu m^2 \sim 18\mu m^2$ [%]	15.5	14.7	17.5	28.8	14.3	20.7

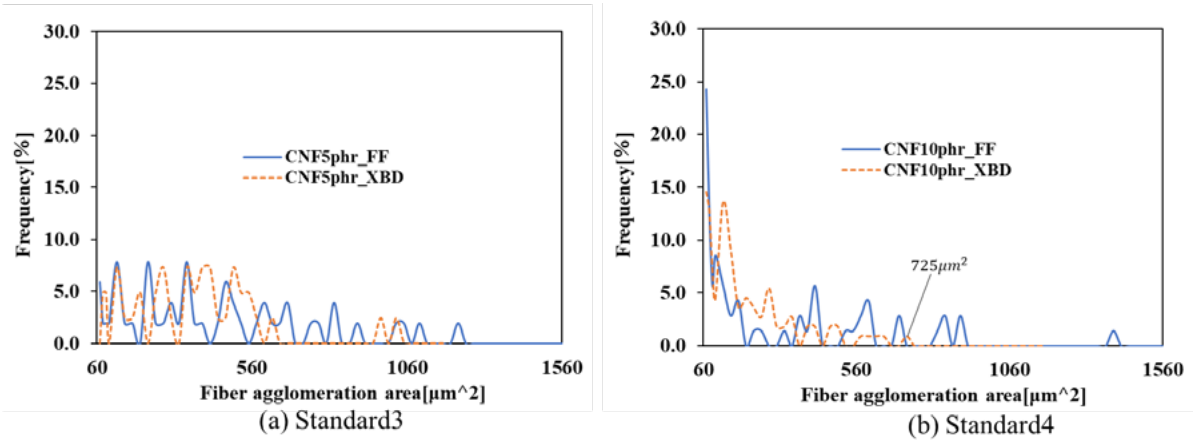

Figure 8. Comparison of the dispersion in Standard3 and Standard4 produced with XBD and FF.

5.2. Effect of CNF content on pressure drop and feed rate

Figure 9 shows the relationship between pressure drop and feed rate for each material. The figure shows that the pressure drop and feed rate decrease with the addition of CNF. This may be due to a decrease in viscosity caused by the addition of CNF.

Figure 10 shows the viscosity measurements on a capillary rheometer at a temperature of 165℃. The decrease in viscosity caused by the addition of CNF is thought to be due to the dispersant in the CNF. The addition of dispersant reduced the coefficient of friction between the inside of the barrel of the single-screw extruder and the resin, causing slippage, which reduced the feeding effect of the screw. As a result, the extrusion rate and the feed rate decreased, which is believed to be the reason for the decrease in pressure drop.

In addition, Table 2 show that the cumulative area frequency in the range $4\mu m^2$-$18\mu m^2$ and the pressure drop are positively correlated when attention is paid to Standard3 and Standard4. In other words, it is suggested that it is important to keep the viscosity high and increase the pressure drop by increasing the feed rate for this material as a condition for improving dispersibility.

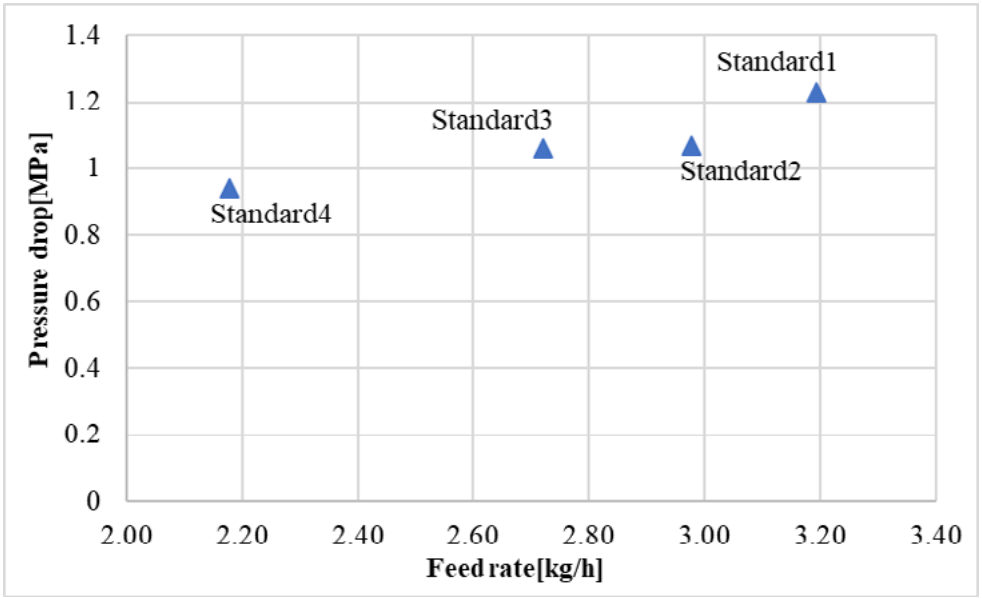

Figure 9. Relationship between pressure drop and feed rate each material.

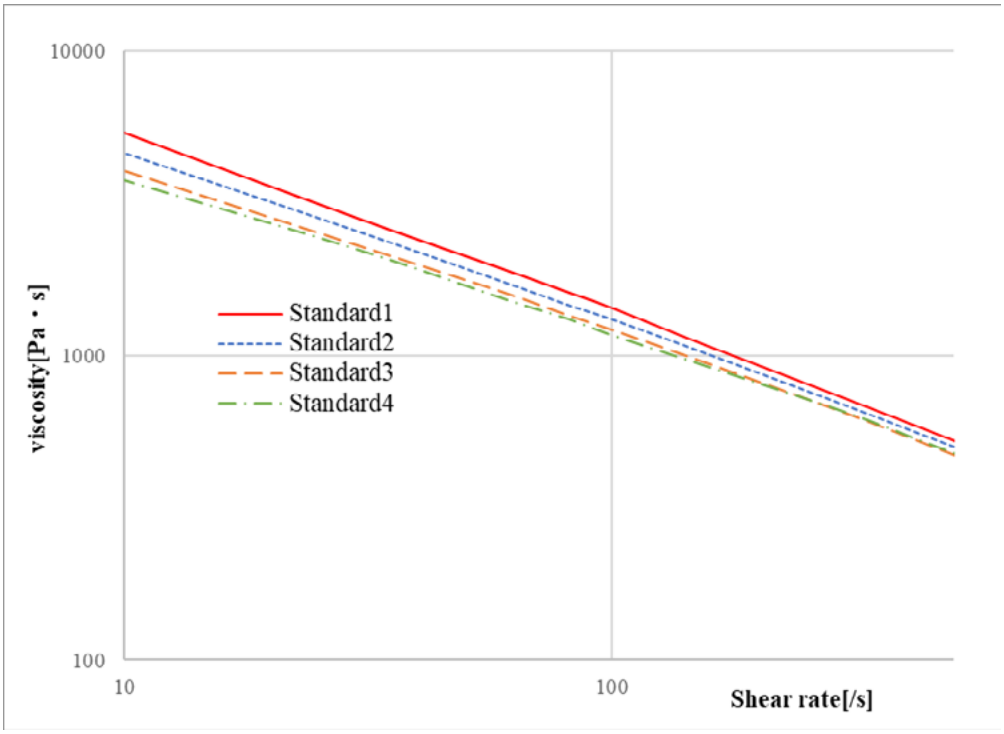

Figure 10. Viscosity measurement results with capillary rheometer.

Table 2. Relationship between cumulative frequency of $4\mu m^2 \sim 18\mu m^2$ and pressure drop.

Sample type	Standard3	Standard4
Screw condition	XBD	
Cumulative area frequency of $4\mu m^2 \sim 18\mu m^2$ [%]	28.8	20.7
Pressure drop $[MPa]$	1.06	0.94

6. Conclusions

The XBD was connected to a single screw extruder to create an extensional flow and the differences in dispersibility between kneading with XBD and kneading with FF(without XBD) were compared.

The material passing through the through-holes, and the cumulative area frequency in the range of $4\mu m^2$-$18\mu m^2$ was higher in the kneading produced with XBD. The XBD was also found to be effective in breaking up agglomerates.

The kneading produced with XBD had a decrease of the melt viscosity due to the reduction in the coefficient of friction between the inside of the barrel and the resin caused by the dispersing agent. It is suggested that this decrease in pressure drop may have affected the cumulative area frequency from $4\mu m^2$ to $18\mu m^2$.

In conclusion, the dispersibility of the filler was improved in the single-screw extruder with the extensional flow.

References

[1] Saito,T.; Kuramae, R.; Wohlert, J.; Berglund, L.; Isogai, A.: *Biomacromolecules*, **14**, 248(2013)
[2] Nishino, T.; Matsuda, I.; Hirao, K.: *Macromolecules*, **37**, 7683(2004)
[3] F.T. Trouyon, The Vapor Pressure in Equilibrium with Substances Holding Varying Amounts of Moisture, *Proc. Roy. Soc.*, Vol.77, No.517, (1906), pp.292-314
[4] Tadmor, Z. : Ind. Eng. Chem. Fundamen., 15, 346(1976)
[5] C. Rauwendaal, T. Osswald, P. Gramann and B. Davis, New Dispersion Mixers for Single Screw Extruders, *SPE/ANTEC 1998 Proceedings* (1998), pp.277-283
[6] S.O. Carson, J.A. Covas and J.M. Maia, A New Extensional Mixing Element for Improved Dispersion Mixing in Twin Screw Extrusion, Part1: Design and Computational Validation, *Adv. Polym. Technol.*,Vol.36(2017), pp.455-465.
[7] M. Tokihisa, K. Yakemoto, T. Sakai, L.A.Utracki, M. Sepehr, J. Li and Y.Simard, Extensional flow mixer for polymer nanocomposites, *Polym Eng Sci*., Vol.46(2006), pp.1040-1050
[8] R.I. G ó mez, R.Muller, M.Bouquey, J. Rondin, C.A. Serra, F. Hassouna, Y.E. Mouedden, V.Tpniazzo and D.Ruch, Processing of nanocomposites PLA/graphite using a novel extensional mixing device. *Polym.Eng. Sci.*, Vol.55(2015), pp.214-222.
[9] Matsumoto, K., Arao, Y. and Tanaka, T. : *WIT Trans*actions *on Modelling and Simulation*, **59**,33(2015)
[10] Tatsuya Tanaka, Koki Matsumoto, Method of manufacturing nanocomposites using a multi-spindle mixer and disk-shaped segments used in the method, Patent 6532628, 2019-5-31

POLYMERIC BIOCOMPOSITES FROM CACTUS PEAR BY-PRODUCTS: UTILIZING GLOCHIDS AND PEEL FOR SUSTAINABLE MATERIALS

L. Botta[1], M.C. Mistretta[1], G. Lamattina[1], F. Gargano[2] and G. Liguori[2]

[1]Department of Engineering, RU INSTM, University of Palermo, Viale delle Scienze, 90128 Palermo, Italy
Email: luigi.botta@unipa.it
[2]Department of Agricultural, Food and Forest Sciences, University of Palermo, Viale delle Scienze, 90128 Palermo, Italy

Keywords: Biocomposites, Polylactic acid (PLA), Food waste valorization, Opuntia ficus-indica

Abstract
This study explores the potential of cactus pear (Opuntia ficus-indica) by-products as sustainable fillers in polymeric biocomposites. Fruit processing generates significant by-products, including peel and glochids, which are often discarded. We investigated the incorporation of cactus pear peel and glochids into polylactic acid (PLA) matrices to produce biocomposites via melt compounding. Composites were formulated at 10% and 20% by weight for both fillers. Morphological, rheological, mechanical, and thermal characterizations were conducted to assess the properties of the resulting materials. The findings revealed that biocomposites filled with peel particles exhibited reduced viscosity compared to pure PLA, while those with glochids showed higher flow curves than that of PLA. Furthermore, biocomposites with glochids exhibited an increased elastic modulus proportional to filler content, surpassing both PLA and peel-filled biocomposites. The difference between the two fillers in affecting the properties of filled PLA was attributed to the observed degradation induced by peel, contrasting with the inert nature of glochids. This underscores the potential of glochids as effective reinforcement agents for PLA-based biocomposites, offering promising applications such as food packaging.

1. Introduction

Food waste is a pressing issue globally, with significant environmental, economic, and social implications. Approximately one-third of the initial mass of processed fruit is discarded as by-products during fruit processing operations. These by-products, including fruit skins, seeds, and fleshy parts, pose challenges for waste management and disposal. However, they also represent valuable resources that can be harnessed for sustainable applications.[1]

One promising approach to valorize fruit waste is the integration of by-products into polymeric materials as reinforcement fillers. This strategy not only reduces waste but also enhances the mechanical and functional properties of biocomposites. In this context, cactus pear (*Opuntia ficus-indica*) by-products present a compelling opportunity for sustainable materials development. Cactus pear is widely cultivated for fruit production, forage, and seed oil extraction in semi-arid areas in both hemispheres. Fruit peel, rich in fibers and bioactive compounds, and the glochids, tiny spines on the fruit's surface, are typically discarded during processing. However, these by-products possess unique properties that can be effectively utilized as fillers in biocomposite materials.[2]

Biodegradable polymers, such as polylactic acid (PLA), have emerged as a viable alternative to conventional oil-based polymers due to their renewable origin and favorable properties. PLA offers

excellent processability, mechanical strength, and biocompatibility, making it suitable for a wide range of applications, including packaging, biomedical devices, and automotive components. Furthermore, PLA demonstrates versatility in its ability to seamlessly integrate with various materials, making it an ideal candidate for blending with diverse substances or acting as a biodegradable polymeric matrix for biocomposites enriched with natural fillers.[3–6]

In this context, our research aims to further explore the potential of cactus pear by-products as sustainable fillers in PLA-based biocomposites. While some studies have explored the use of cactus cladodes as a fiber source for biocomposites, to the best of our knowledge, the peels and, particularly, the glochids have not yet been utilized for this purpose.[7–9] Through comprehensive morphological, rheological, mechanical, and thermal characterizations, we aim to elucidate the effects of filler incorporation on the properties of biocomposites and identify potential applications for various applications.

2. Materials and methods

2.1. Materials

The polymer used as the matrix for producing the biocomposites was a sample of Ingeo™ PLA 4032D, supplied by NatureWorks LLC (Minnesota, MN, USA), in the form of pellets.

The cactus pear by-products (peels and glochids) were kindly provided by a commercial orchard (Garufa) located in Roccapalumba, Palermo, Italy (37◦48′ N, 13◦38′ E, 350 m a.s.l). Specifically, the company supplied the peels generated during the processing stages of fruits destined for the fresh-cut industry, and the glochids, a by-product derived from the mechanical brushing of fruits done before marketing.

The cactus pear peel was processed into micrometric particles suitable for incorporation into the biopolymeric matrix through a two-stage procedure: drying and grinding. The drying process involved both conventional oven dehydration and freeze-drying. Specifically, after drying, the peels were finely ground using a homogenizer to attain a uniform consistency and particle sizes below 300 micrometers. Subsequently, the ground particles underwent freeze-drying to further reduce the water content.

For the glochids, which are naturally micrometric and oblong in shape, they were used as-is, although a selection process was conducted through sieving to eliminate larger lignocellulosic residues while preserving the smaller ones.

2.2. Processing of biocomposites

The biocomposites were prepared using a batch mixer (Brabender model PLE330,) at 190 °C with a mixing speed of 60 rpm for 5 minutes, with the simultaneous addition of filler and polymer matrix. Sample codes, along with their respective polymer and filler concentrations, are detailed in Table 1. Before processing, biopolymer pellets and both fillers were dried at 70 °C under vacuum overnight to prevent PLA hydrolysis phenomena during compounding.

Table 1. Formulation codes and compositions.

Sample code	*PLA (wt. %)*	*Peels (wt. %)*	*Glochids (wt. %)*
PLA	100	0	0
PLA+P_10%	90	10	0
PLA+P_20%	80	20	0
PLA+G_10%	90	0	10
PLA+G_20%	80	0	20

2.3. Characterization of biocomposites

The morphology of both the fillers and the biocomposites was evaluated through scanning electron microscopy (SEM) performed with a Phenom Pro X instrument from Thermo Fisher Scientific.

The rheological measurements were achieved with a ARES-G2 rheometer (TA instrument) equipped with parallel plates of 25 mm diameter and a gap distance of 1 mm. All materials were tested in frequency sweep mode at frequencies ranging from 0.1 to 100 rad/s. The temperature was set constant at 190°C during all measurements. The tests were carried out directly putting the pellets onto the lower plate.

Tensile tests were performed according to ASTM: D638 standard, using a Zwick-Roell Universal Testing Machine (UTM) equipped with a load cell of 5 kN. Seven Dumbbell samples for each composite were tested setting the crosshead speed equal to 5 mm/min.

Dynamic mechanical thermal analysis was performed using a Metravib DMA 50. The measurements were carried out at a constant frequency of ω = 1 Hz in a temperature range of 25 to 130 °C with a heating rate of 3 °C/min. Analyses were carried out on samples cut to the size of 10 × 30 × 0.45 mm before being mounted in the DMTA apparatus.

The intrinsic viscosity [η] was measured using an iVisc LMV 830 capillary viscometer (Lauda Proline PV 15,) equipped with a Ubbelohde capillary viscometer in a thermostated oil bath. To prepare the solution at a concentration of 0.2 wt%, each material was dissolved in tetrahydrofuran (THF). To evaluate the intrinsic viscosity of the composites, each composite was dissolved in THF, the solid fraction was removed with filter paper, the resulting solution was poured and a 0.2 wt% solution was prepared. Flow time measurements were performed in triplicate for each sample until the standard deviation was less than 0.5 s. The intrinsic viscosity values were calculated according to Solomon-Ciuta equation (Eq. 1)[10]:

$$[\eta] = \frac{\sqrt{2}}{c}\sqrt{\eta_{sp} - \ln \eta_{rel}} \tag{1}$$

where c is the concentration of the polymer solution, [η], η_{sp} and η_{rel} are the intrinsic, specific and relative viscosities, respectively. The viscosity average molecular weight (M_v) was calculated using the Mark-Houwink equation (Eq. 2):

$$[\eta] = KM_v^a \tag{2}$$

Depending on the specific polymer-solvent system, the parameter values of the Mark-Houwink constants, a and K, are different. For PLA-THF, $K = 1.74 \cdot 10^{-4}$ and a = 0.736.[11]

3. Results and discussion

In Figure 1, SEM micrographs at various magnifications of both the particles derived from the peels (Figure 1a and 1b) and the glochids in their natural state (Figure 1c and 1d) are depicted. SEM micrographs of the peels revealed the presence of irregular particles with varying sizes, ranging from 20 to 200 μm in diameter. Regarding the glochids, as previously demonstrated by other researchers [12] and clearly visible in the SEM images, they exhibit a conical shape with a surface covered by oriented retrorse barbs. Grooves appear to be more pronounced from the central portion to the base of the glochid.

The morphological analysis of the biocomposites revealed a uniform dispersion of the incorporated materials, although the heterogeneity in filler sizes was clearly visible. As illustrated in Figure 2a, peel-filled biocomposites exhibited a good interfacial adhesion between the polymer matrix and the filler,

indicating a strong interaction between the two components. Conversely, in the case of glochid-filled biocomposites (Figure 2b), the interfacial adhesion between the fibers and the matrix appeared to be fairly weak.

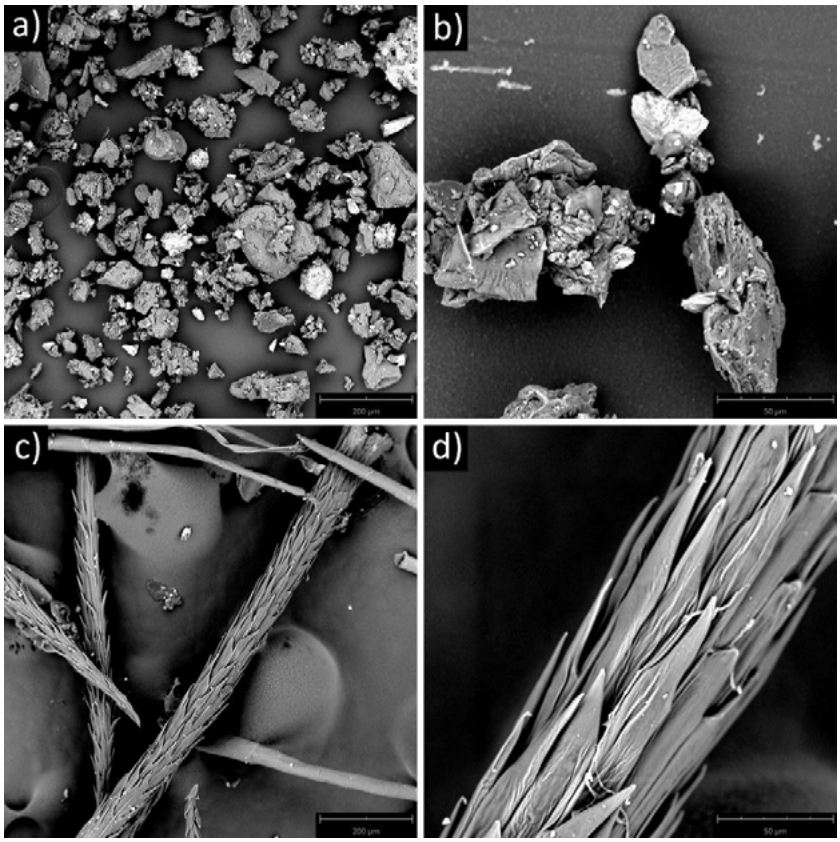

Figure 1. SEM micrographs of peels (a and b) and glochids (c and d) at two different magnifications

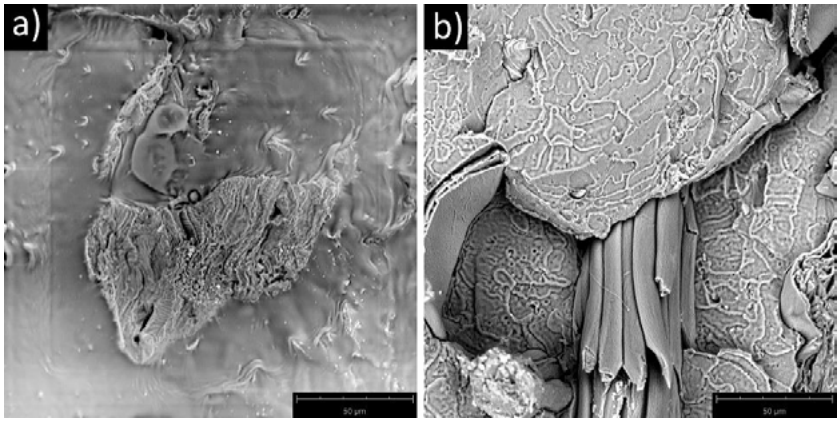

Figure 2. SEM micrographs of PLA+P_10% (a) and PLA+G_10%glochids (b)

The results of the tensile tests revealed a slight increase in the elastic modulus with the addition of peels, with the modulus growing from 10% to 20% filler content, as expected. A greater reinforcing effect was observed in biocomposites containing glochids, showing a modulus increase of approximately 30% for samples with 20% filler. However, this reinforcing effect was accompanied by a reduction in the elongation at break, which was more pronounced in the case of biocomposites containing peels. It is worth noting that the neat PLA is inherently brittle, thus remaining fragile even with lower elongation

values. The superior reinforcing capability of glochids was validated by DMA analysis, which also indicated a higher onset temperature of E' drop for the composites compared to pure PLA.

The rheological characterization of all materials was conducted through tests in oscillatory mode, and the complex viscosity as a function of frequency is depicted in Figure 3.

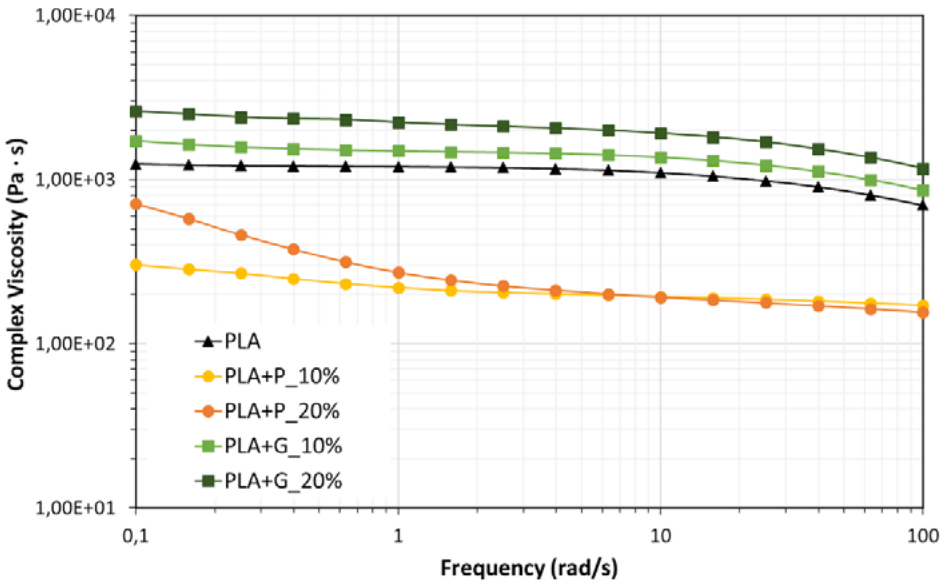

Figure 3. Complex viscosity as a function of frequency of neat PLA and all biocomposites

As evidenced by the curves, the incorporation of the two fillers results in distinct rheological characteristics. Specifically, in the case of glochids, the viscosity of the composites surpasses that of PLA, with the curve showing an upward trend with increasing filler content. Conversely, in biocomposites containing peels, there is a notable reduction in composite melt viscosity with a 10% filler content. Upon increasing the peel content to 20%, there is a slight upturn in viscosity compared to the 10% scenario, particularly evident at lower frequencies, accompanied by a more pronounced non-Newtonian behavior characterized by significant shear thinning. However, even with a 20% peel content, the viscosity curve of this composite material remains below that of pure PLA. The observed behavior in peel-based biocomposites is likely attributable to degradation phenomena occurring during processing, possibly due to the presence of specific molecules within the peels.

To investigate the hypothesis of potential degradation phenomena of PLA in the presence of peels, associated with a decrease in molecular weight, the intrinsic viscosity test was conducted on both PLA and the 20% weight filler biocomposites. This test enabled the determination of the intrinsic viscosity value, from which the viscosity average molecular weight can be derived through the Mark-Houwink correlation.

The findings revealed a significant decrease in the molecular weight of the biopolymeric matrix upon the addition of 20% peels, while the molecular weight of the matrix derived from the biocomposites with 20% glochids remained largely unaffected. This phenomenon is likely linked to the composition of the peels. Numerous studies in the literature highlight the presence of mono- and polyunsaturated compounds in peels, with linoleic acid, oleic acid, and palmitic acid being the most prominent among them. Linoleic acid received particular attention due to its behavior, which, based on scientific literature, appears analogous to that of citric acid. Acting as a catalyst, linoleic acid is believed to accelerate the depolymerization of PLA at elevated temperatures.

4. Conclusions

In this study, composites were fabricated by integrating cactus pear peel and glochids into a polylactic acid (PLA) matrix through melt compounding. Composites were formulated at 10% and 20% by weight for both peel and glochids. The cactus pear peel underwent a process of freeze-drying and grinding to attain micrometric particles suitable for incorporation into the biopolymeric matrix. Meanwhile, the glochids, naturally micrometric and oblong in shape, were utilized as they are. The resulting materials underwent comprehensive morphological, rheological, mechanical, and calorimetric characterizations.

The two fillers yielded distinct outcomes. Particularly, while both fillers served as reinforcements, the composites with glochids exhibited superior performance. In the case of peel-filled composites, a reduction in viscosity was observed, likely attributed to degradation phenomena caused by molecules present in the peels. Conversely, such degradation did not occur with glochids, indicating their potential as natural reinforcements without significant drawbacks.

Acknowledgments

Funded by the European Union – Next Generation EU - PNRR M4 - C2 -investimento 1.1: Fondo per il Programma Nazionale di Ricerca e Progetti di Rilevante Interesse Nazionale (PRIN) - PRIN 2022PNRR cod. P2022M3FTM_002 dal titolo " SUstainable routes to high PErformance and Recycling of BIOdegradable plastics for a circular economy - SuperBio" CUP B53D23027630001

References

[1] F. Dilucia, V. Lacivita, A. Conte, M.A. Del Nobile. Sustainable use of fruit and vegetable by-products to enhance food packaging performance. *Foods*, 9 (7), 2020.
[2] L. Klaai, D. Hammiche, A. Boukerrou, J. Duchet-Rumeau, J.-F. Gerard, N. Guermazi. On the use of prickly pear seed fibres as reinforcement in polylactic acid biocomposites. *Emergent Mater*, 5 (3): 859–872, 2022.
[3] L. Aliotta, V. Gigante, G. Molinari, R. D'Ambrosio, L. Botta, F.P. La Mantia, A. Lazzeri. Effect of biobased plasticizers, used as dispersing aids, on mechanical, rheological and thermal properties of micro fibrillated cellulose (MFC)/poly (lactic acid) (PLA) biocomposites over the time: how MFC controls the plasticizer migration? *Cellulose*, 30 (4): 2237–2252, 2023.
[4] V. Fiore, L. Botta, R. Scaffaro, A. Valenza, A. Pirrotta. PLA based biocomposites reinforced with Arundo donax fillers. *Compos Sci Technol*, 105: 110–117, 2014.
[5] L. Botta, V. Fiore, T. Scalici, A. Valenza, R. Scaffaro. New Polylactic Acid Composites Reinforced with Artichoke Fibers. *Materials*, 8 (11): 7770–7779, 2015.
[6] L. Botta, M.C. Mistretta, S. Palermo, M. Fragalà, F. Pappalardo. Characterization and Processability of Blends of Polylactide Acid with a New Biodegradable Medium-Chain-Length Polyhydroxyalkanoate. *J Polym Environ*, 23 (4): 478–486, 2015.
[7] A. Alane, I. Zembouai, A. Benhamida, L. Zaidi, N. Touati, M. Kaci. Opuntia ficus indica fibers as reinforcement in PHBV biocomposites. *Mater Today Proc*, 53: 218–222, 2022.
[8] A. Greco, A. Maffezzoli. Rotational molding of biodegradable composites obtained with PLA reinforced by the wooden backbone of opuntia ficus indica cladodes. *J Appl Polym Sci*, 132 (48): 42447, 2015.
[9] R. Scaffaro, A. Maio, E.F. Gulino, B. Megna. Structure-property relationship of PLA-Opuntia Ficus Indica biocomposites. *Compos B Eng*, 167: 199–206, 2019.
[10] A.-A.A. Abdel-Azim, A.M. Atta, M.S. Farahat, W.Y. Boutros. Determination of intrinsic viscosity of polymeric compounds through a single specific viscosity measurement. *Polymer* 39 (26): 6827–6833, 1998.
[11] J.R. Dorgan, J. Janzen, D.M. Knauss, S.B. Hait, B.R. Limoges, M.H. Hutchinson. Fundamental solution and single-chain properties of polylactides. *J Polym Sci B Polym Phys*, 43 (21): 3100–3111, 2005.
[12] Y.S. Masrahi. Glochids microstructure and dew harvesting ability in Opuntia stricta (Cactaceae). *J King Saud Univ Sci*, 32 (8): 3307–3312, 2020.

MECHANICAL AND ADSORPTION CHARACTERIZATION OF A CALCIUM LACTATE/S-PEEK COMPOSITE COATING FOR THERMOCHEMICAL ENERGY STORAGE

E. Previti[1], E. Mastronardo[1], C. Milone[1], L. Calabrese[1]

[1] Department of Engineering, University of Messina, Contrada Di Dio (Sant'Agata), 98166 Messina, Italy
Email: emanuele.previti@studenti.unime.it, emastronardo@unime.it; cmilone@unime.it; lcalabrese@unime.it Web Page: http://www.unime.it

Keywords: thermochemical energy storage; coatings; salt hydrate; sulfonated polyether ether ketone; aging.

Abstract
Thermochemical energy storage using salt hydrates is a promising way to store large amounts of heat for extended periods. It's ideal for incorporating renewable energy into traditional grids and optimizing energy usage. These hydrates undergo reversible reactions with water vapor, transitioning between hydrated and anhydrous states to release or absorb heat efficiently. Organic salts are also attractive for this purpose because of their high heat capacity, suitable temperatures for hydration/dehydration, non-toxicity, and resistance to deliquescence. This study examines a new composite coating for thermochemical energy storage, combining calcium lactate organic salt hydrate with a sulfonated polyether ether ketone matrix. All composite coatings were prepared through drop-casting on aluminum substrates and evaluated for adhesive strength. Hydration/dehydration cycles were simulated to assess material stability. Water vapor adsorption capacity was measured under various conditions to evaluate its potential in energy storage applications. Dynamic mechanical analysis performed in controlled environment revealed a large dependence of elastic properties of the composite materials with the water vapor partial pressure.

1. Introduction

Thermochemical energy storage (TES) employing salt hydrates offers a promising technique to store large volumes of heat for long periods of time, making it a viable option for integrating renewable energy sources into conventional energy grids and optimize the management of energy consumption [1]. These salt hydrates involve reversible chemical reactions with water vapor, suffering reversible phase transitions between hydrated and anhydrous states. This engages releasing or receiving heat during the process allowing for efficient energy storage and conversion.
In such a context, organic salts can be identified as promising thermochemical energy storage materials due to their high heat storage capacity, suitable hydration/dehydration temperatures, non- toxicity and resistance to deliquescence.
Some promising approaches were identified as suitable option to significantly improve TES technology i.e. encapsulation of salt hydrates within a porous matrix and composite sheets or coatings [2–4]. The latter option, especially, offers great potential for optimizing heat and mass transfer during hydration and dehydration processes. For TES applications, coupled to energy density and fast sorption/desorption process, a crucial property of the composite coating is its adhesion to the underlying substrate [5]. Strong adhesion safeguards the material from damage during handling, assembly, and operation. Additionally, it enhances durability and enables the system to withstand harsher operating conditions [6,7].
TES systems deployed in the field often encounter critical mechanical stress due to frequent hydrothermal stresses and/or mechanical shocks and vibrations throughout their service life [8]. This

significantly restricts their long-term stability and durability. Consequently, to develop an absorbent material with superior mechanical performance and strong adhesion to the metal substrate is critical for achieving a far more robust and stress-resistant TCM-based TES reactor.
In this concern, this research delves into the viability of an innovative composite adsorbent coating, performing calcium lactate (CaL) organic salt hydrate embedded within a sulfonated polyether ether ketone (S-PEEK) matrix, for thermochemical energy storage applications. A composite slurry adding a salt hydrate content equal to 50 wt.% CaL in the polymer matrix has been prepared. The coating is carefully prepared via a drop-casting technique depositing the composite slurry onto aluminum substrates and subsequent drying step at 60°C for 12h. All composite coatings were mechanically evaluated through scratch tests. The samples exhibit significant adhesive strength, demonstrating pull-off adhesion strength that exceeds that of conventional adsorbent composite coatings. Dynamic mechanical analysis performed in controlled environment revealed a large dependence of elastic properties of the composite materials with the water vapor partial pressure. To assess the material stability during service life, hydration/dehydration cycles, according to operating conditions, were applied. The adsorption and desorption capacity of the composite coating, by water vapor adsorption isobars, are measured at equilibrium at a pressure of 11 mbar across a temperature range of 30-120 °C, both for unaged and hydrothermally aged samples with the purpose to evaluate its potential applicability as an adsorbent composite coating in thermochemical energy storage field.

2. Experimental Part

2.1. Materials and coating preparation

At first, a polyether ether ketone (PEEK) pellets (Heroflon S.p.A., Italy) were modified through a sulfonation process to obtain a sulphonated polyether ether ketone (SPEEK), a polymer with high water vapor permeability. In particular, according to [9], the PEEK pellets were dissolved in concentrated sulfuric acid (98%, Sigma Aldrich) at 35°C for 48 hours. The resulting solution was then dripped slowly into an ice-cold bath of deionized water to induce polymer precipitation. The precipitated polymer was washed with distilled water and dried at 60°C for 24 hours. The final sulfonated PEEK granules exhibited a degree of sulfonation (DS) of around 40%, as determined by a titration procedure described elsewhere [10].
For the coating preparation, preliminary, 6061 aluminum plates (25 mm wide, 45 mm long, and 2 mm thick), used as metal substrate, are cleaned. This involves mechanical polishing with sandpaper (up to grade 800), washed in water, followed by degreasing in a mild alkaline solution (0.1 N sodium hydroxide) for 3 minutes. The plates are then rinsed with distilled water and finally with acetone. Next, the calcium L-lactate-SPEEK composite coatings are prepared. A specific amount of SPEEK polymer is dissolved in a solvent (N,N-Dimethylformamide, DMF) for 30 minutes with vigorous stirring. Once the SPEEK is completely dissolved, calcium L-lactate pentahydrate (CaLP) is added. A composite composition with CaLP weight ratio equal to 50% was produced, as detailed in Table 1. The specimens, were coded by a CS prefix, indicating their composite nature, followed by a numerical assignment which reflected the weight content of the adsorbent organic salt hydrate filler. As reference the unfilled coating (CS-0) was also produced.

Table 1. Codes and constituent's ratio of CaLP/SPEEK composite coating

Code	*DMF (wt.%)*	*SPEEK (wt.%)*	*CaLP (wt.%)*	*CaLP:SPEEK ratio*
CS-0	80	20	0	0:100
CS-50	80	10	10	50:50

The mixture CaLP and SPEEK mixture is stirred open to air and at room temperature until the CaLP is completely dissolved, until obtaining a clear liquid slurry. The liquid is then applied onto aluminum surfaces using drop casting technique. To prevent air bubbles or local defects due to slurry shrinkage,

the coated surfaces are gently dried in a vacuum oven at 60 °C for 12 hours. The final coating has a thickness of around 200±50 µm.

2.1. Coating characterization

The mechanical performance of the coating on the aluminum substrate was assessed using a scratch test. An Elcometer 3000 scratch tester was employed, by using loaded tip to progressively scratch the coating surface in six lines with increasing force. The scratch depth and width were then measured using a 3D optical microscope to quantify the coating's scratch resistance.
Rectangular-shaped specimens (11 x 5.0 x 0.1 mm³) were subjected to tensile dynamic mechanical analysis (DMA) using a DMA 242 E Artemis (Netzsch) in isothermal conditions (30°C) and varying water vapor partial pressure (0-90%). The tests were conducted at frequencies ranging from 0.5 to 100 Hz. Experiments were performed by using a maximum dynamic force of 2.2 N and a maximum sample amplitude of 35 µm.
The hydration/dehydration of the composite coating was studied using a thermogravimetric dynamic water vapor analyzer (DVS) with a microbalance (sensitive to 0.1 micrograms). Before testing, the coating was dried at 150°C for 2 hours under vacuum. The DVS measured mass changes during hydration/dehydration cycles at varying partial pressure at a constant temperature of 30°C (isotherm measurements).

3. Results and Discussion

Scratch testing can provide valuable insights into the relative adhesion capabilities of the composite coating, although it offers comparisons measurements of coupled cohesive and adhesive adhesion strength. **Figure 1** depicts the scratch width of coatings realized with pure S-PEEK and at different CaLP content at increasing scratching load. Scratches that leave a wider mark indicate a weaker scratch-resistant coating.

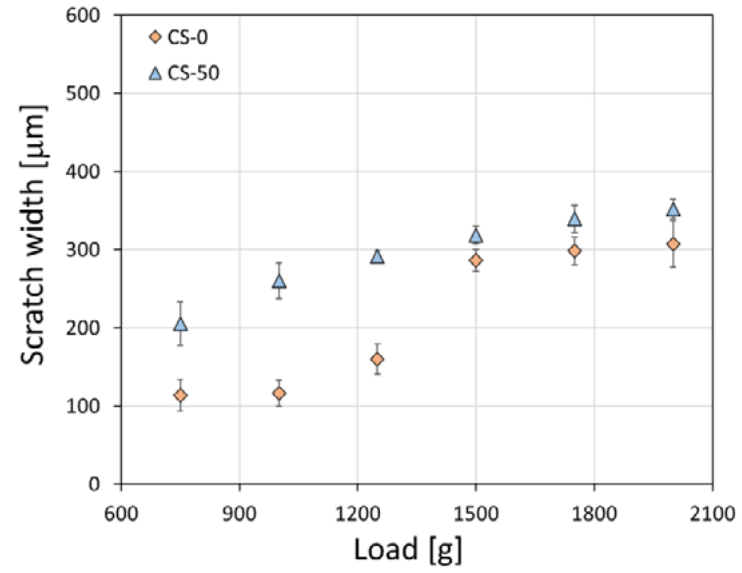

Figure 1. Scratch width of filled and unfilled composite coating (CS-50 and CS-0 batches, respectively)

Scratch test results reveal a clear dependence on the presence and content of filler. Comparing these data, it can be argued that the coupled adhesive and cohesive stresses applied during the scratch test consistently influence the mechanical stability of the coating, even for coatings characterized by high adhesion (CS-50 batch). This can lead to premature scratch-induced fracture at low scratch loads.
At low applied loads, coating without filler (CS-0 batch, unfilled S-PEEK) exhibits greater scratch resistance than CS-50, evidenced by lower width values. This suggests that the filler weakens the composite at these loads, although the adhesion performances evidenced by composite coating are

compatible to other composite coating [10]. A reversal of this trend is observed at higher loads (above 1300g), where composite coating demonstrates quite compatible scratch resistance to the unfilled one. This difference in behavior can be attributed to the distribution of the filler within the S-PEEK matrix. The composite coating a homogeneous distribution of the filler particles in the polymer, leading to an efficient transfer of stress between the filler and the matrix. This leads to a suitable cohesive force between the composite constituents, which is particularly important at low loads where the scratch depth is insufficient to reach the underlying aluminum substrate. In this regime, the scratch resistance is mainly related to the cohesive strength of the coating itself.
Conversely, at higher loads, the scratch can penetrate deeper up to reach the aluminum substrate. Here, the scratch resistance becomes more dependent on the coupled cohesive and adhesive strength between the coating and the metal substrate. The observed scratch tests at high loads are quite similar for all batches indicating that all coatings are characterized by similar scratch resistance strength in the aluminum substrate.
To see if this material can be used for thermochemical energy storage application, it is important to check that the CaL particles inside the plastic matrix are still able to adsorb water vapor from the surrounding air. In this concern, Figure 2 shows the water adsorption/desorption isotherms (at 30 °C) for CS-50 composite coating, and pure CaL powder.

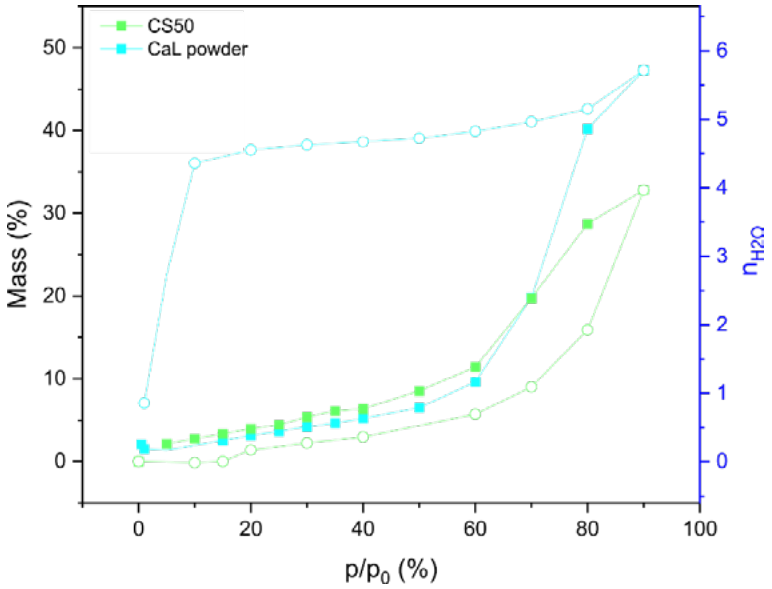

Figure 2. Isotherm adsorption/desorption tests on CaL powder and CS-50 composite coating.

Although the composite material exhibits lower adsorption performance across all pressure ranges compared to pure calcium powder due to the reduced organic salt hydrate content, it's noteworthy that the CS-50 batch achieved a maximum water adsorption of 32.8 wt.%. This value aligns well with the added filler content. The CaL powder batch, on the other hand, exhibited a maximum water uptake of 47.3 wt.% at a partial pressure of 90%. This suggests that the coating preparation improved the sorption capacity of the adsorbent filler, likely due to an optimal distribution that prevents agglomeration within the composite bulk. These results indicates that the binder doesn't impede water vapor adsorption/desorption, thanks to the S-PEEK's high permeability [11]. This allows even fully encapsulated salt hydrate to actively participate in the process, making the composite a promising candidate for TES applications due to its effective adsorption/desorption properties.
Further consideration can be argued evaluating the evolution storage and loss modulus (E' and E'', respectively) during an isothermal DMA test at 30°C on the composite coatings at varying relative humidity (**Figure 3**).

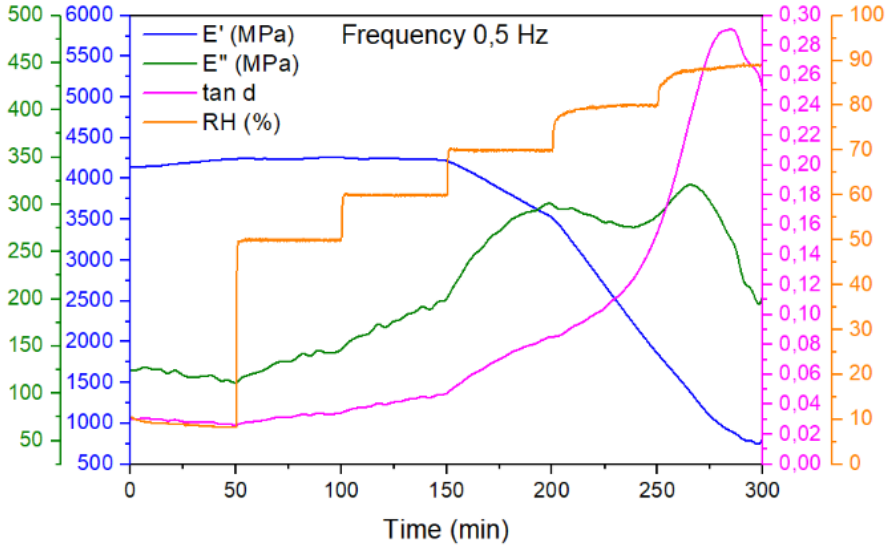

Figure 3. DMA results for on CS-50 composite coating

For clarity on the plot, only the results at 0.5 Hz are shown. A clear dependence of the E' at increasing RH can be identified. At low relative humidity, the storage modulus remains quite constant, exhibiting only a slight decrease as RH values approach 60-70%. When P/P_0 reaches 80%, an abrupt decrease in storage modulus is observed. The tanδ is characterized by a local peak, followed by a progressive increase with increasing time. At maximum water vapor partial pressure (P/P_0 = 90%), E' further decreases, evidencing a value about 70% lower than the initial one at the end of the test. This behavior can be attributed to the progressive hydration of calcium lactate which increases in volume during its hydration process, facilitating a softening action of the composite. This effect becomes relevant only for high partial pressures necessary to induce effective hydration of the organic salt (see **Figure 2**).
This study emphasizes the crucial issue regarding how the mechanical properties of the material can alter over time due to the extended periods of dehydration and hydration involved in a thermochemical energy storage and release process. Monitoring these changes throughout the cycles is essential to understand the overall performance and durability of the material in this process. The hygrothermal cycles create internal stresses that may lead to degradation through cracking within the material itself and at the interface with the support structure, potentially causing debonding. Dynamic mechanical analysis (DMA) under variable environmental conditions proves to be an effective method to assess the risk of degradation from hydration/dehydration cycles. This technique could provide valuable insights for designing durable TCM composites specifically tailored for enhancing performance in thermochemical energy storage applications.

4. Conclusions

In this manuscript it was investigated the potential of a new composite adsorbent coating for thermochemical energy storage. This coating incorporates calcium lactate (CaL) organic salt hydrate embedded within a matrix of sulfonated polyether ether ketone (S-PEEK).

- Mechanical tests showed CaLP content dependence. Scratch tests deeper extended the mechanical characterization of the coatings. Unfilled coating excelled in scratch resistance at low loads due to a regular structure, while at high loads, all coatings demonstrated similar behavior, showing suitable cohesion and adhesion with the substrate.
- Despite the reduction in water adsorption capacity compared to pure CaLP powder, the CS-50 composite coating achieved a significant water uptake (32.8 wt.%). This demonstrates that the S-PEEK binder doesn't hinder water vapor diffusion due to its high permeability, allowing the encapsulated CaLP to participate in the adsorption/desorption process.
- DMA tests highlights the detrimental effects of humidity on the mechanical properties of calcium lactate-based composites for thermochemical energy storage. By analyzing the changes in storage

modulus and tan δ, DMA proves to be a valuable tool for assessing material degradation risks under hygrothermal cycling. These findings emphasize the need for considering hygrothermal stability when designing TCM composites for long-term performance and durability in energy storage applications.

In summary, the study successfully developed CaLP/SPEEK composite coatings with tunable mechanical properties and demonstrates their potential for thermochemical energy storage applications due to the retained water adsorption/desorption capability. Moving forward, it is relevant to focus on enhancing the mechanical stability of the CaLP/SPEEK composite coatings and investigating their long-term performance under hydrothermal conditions. By further addressing these aspects, it can better understand the durability and reliability of these coatings for thermochemical energy storage applications. Analyzing how the materials respond to prolonged exposure to water adsorption and desorption will provide valuable insights into their operational capabilities and help optimize their efficiency and effectiveness for such applications.

Acknowledgments
This work has been partially funded by European Union (NextGeneration EU), through the MUR-PNRR project SAMOTHRACE (ECS00000022). The views and opinions expressed are those of the authors only and do not necessarily reflect those of the European Union or the European Commission. Neither the European Union nor the European Commission can be held responsible for them.

References

[1] J. Lin, Q. Zhao, H. Huang, H. Mao, Y. Liu, and Y. Xiao, Applications of low-temperature thermochemical energy storage systems for salt hydrates based on material classification: A review, *Solar Energy* 214, 149–178 2021.
[2] E. Mastronardo, E. La Mazza, D. Palamara, E. Piperopoulos, D. Iannazzo, E. Proverbio, and C. Milone, Organic Salt Hydrate as a Novel Paradigm for Thermal Energy Storage, *Energies* 15, 4339 2022.
[3] L. Calabrese, P. Bruzzaniti, D. Palamara, A. Freni, and E. Proverbio, New SAPO-34-SPEEK composite coatings for adsorption heat pumps: Adsorption performance and thermodynamic analysis, *Energy* 203, 117814 2020.
[4] Y. Zhang, D. Palamara, V. Palomba, L. Calabrese, and A. Frazzica, Performance analysis of a lab-scale adsorption desalination system using silica gel/LiCl composite, *Desalination* 548, 116278 2023.
[5] D. Palamara and L. Calabrese, Sulfonated-Recycled-PEEK as Matrix of Water Vapor Adsorbent SAPO-34 Based Composite Coatings for Adsorption Heat Pumps: Mechanical and Thermochemical Characterization, *Materials* 15, 8439 2022.
[6] Q. Zhao, J. Lin, H. Huang, Q. Wu, Y. Shen, and Y. Xiao, Optimization of thermochemical energy storage systems based on hydrated salts: A review, *Energy and Buildings* 244, 111035 2021.
[7] H. Yang, C. Wang, L. Tong, S. Yin, L. Wang, and Y. Ding, Salt Hydrate Adsorption Material-Based Thermochemical Energy Storage for Space Heating Application: A Review, *Energies* 16, 2875 2023.
[8] L. Calabrese, V. Brancato, and A. Frazzica, Experimental evaluation of the hydrothermal stability of a silicone/zeolite composite foam for solar adsorption heating and cooling application, *Journal of Applied Polymer Science* 137 2020.
[9] L. Calabrese, D. Palamara, P. Bruzzaniti, and E. Proverbio, Assessment of high performance SAPO-34/S-PEEK composite coatings for adsorption heat pumps, *Journal of Applied Polymer Science* 138 2021.

[10] D. Palamara, P. Bruzzaniti, L. Calabrese, and E. Proverbio, Effect of degree of sulfonation on the performance of adsorbent SAPO-34/S-PEEK composite coatings for adsorption heat pumps, *Progress in Organic Coatings* 154, 106193 2021.
[11] L. Jia, X. Xu, H. Zhang, and J. Xu, Sulfonation of polyetheretherketone and its effects on permeation behavior to nitrogen and water vapor, *Journal of Applied Polymer Science* 60, 1231–1237 1996.

SCALING UP A TWO-STEP PYROLYSIS OF CFRP: STUDY OF VALIDATION AND ROBUSTNESS

Corvo-Alguacil M.[1], Umeki K.[1] and Joffe R.[1]

[1]Department of Engineering Sciences and Mathematics, Luleå University of Technology, 971 87 Luleå, Sweden
Email: marina.corvo.alguacil@ltu.se, Web Page: http://www.ltu.se

Keywords: pyrolysis, carbon fiber, composites recycling, validation, robustness

Abstract
Demand for stiffer and lighter materials in various every-day applications is steadily increasing, making carbon fiber reinforced polymers (CFRP) gain significant popularity. However, the cost of carbon fibers (CF) remains high. Recovered fibers from composite waste can reduce the cost of these materials. Extending prior research on model composites recycled up to three times by a two-step pyrolysis-oxidation treatment [1], validation and robustness studies are carried out with the recycling process in use. Tensile properties of recovered fibers from composite laminates and two different model composites are compared. The validation study results illustrate the differences between model and laminate composites that forego the same treatment and mechanical characterization. With higher volume fraction, the laminates show less mass loss during recycling and recovered fiber are with smaller diameter with poorer mechanical performance, compared to fibers obtained from model composites. On the other hand, the robustness study evidences the negative impact of complex geometrical composite parts in the mechanical performance of recovered CF. These results contribute to the understanding of CFRP recycling from actual end-of-life composites, with the ultimate objective to work towards scaling up recycling from laboratory scale to industrial application.

1. Introduction

Carbon fiber reinforced polymers (CFRP) are highly valued for their lightweight and strength combination, and increasingly utilized in industries like transportation and energy [2]. Inopportunely, production cost of carbon fibers (CF) and their overall sustainability is hindering the expansion of these materials to other industrial sectors. One alternative to push both issues concurrently, is to recover CF from composite waste using a thermal treatment. At a reduced cost, recovered carbon fibers (rCF) with reasonable mechanical properties offer an innovative solution to the CFRP waste problem, offering more sustainable and cheaper CF [3]. The market for recycled CF is still in its early development stage with scattered material performance data and limited use in high-value applications. To unlock the full potential of the recycled CF market, further research is needed to understand the impact and feasibility of multiple recycling cycles on realistic end-of-life composite components. A logical next step in the sustainability journey of CF, is the investigation of potential of multiple recycling plus manufacturing cycles of rCF. The evolution of mechanical properties in such conditions is of great interest to fully assess the suitability of recovered CF for secondary applications. In addition, the realistic geometrical complexity of the CFRP waste needs to be studied and considered as an impactful factor.

This work focuses on the validation and robustness studies of a two-step pyrolysis-oxidation recycling process for CFRP waste. Model composites priorly used in an optimization study [4][5], commonly have low fiber volume fraction compared to industrially manufactured advanced composites. Therefore, lab-scale results must be validated on a larger scale, with material mimicking real-life composite. The

validation study presented in this article is performed on a CF composite laminate. Mechanical properties of recovered fibers are evaluated and compared to those of model composites that have undergone the same recycling path. Moreover, as composite part can vary in geometry, to ensure a robust recycling process that can accommodate complex shapes is important. Thus, the robustness study is also presented in this article, evaluating the influence of complex part geometries by recycling model composites with fibers bent at an angle close to 180 degrees.

2. Materials and methods

2.1. Materials

Two distinct types of materials have been manufactured and recycled and this work. For the validation study, a carbon fiber reinforced composite (CFRP) with $[0_4]_T$ layup manufactured by vacuum infusion is used. The reinforcement is an unidirectional (UD) carbon fabric from Porcher, Carbone-UD-4510 205gr/sqm. Nominal value for CF stiffness and strength are 213.2 ± 24 GPa and 3033.4 ± 502.5 MPa correspondently, from tensile tested single virgin fibers. As matrix, an epoxy system from Huntsman, Araldite LY1564/XB 3404-1 is used. Resin and hardener have a mix ratio of 100:36 by weight.

In the robustness study, and due to dimensional limitations related to the recycling setup, model composites are employed. These composites are manually assembled using the same raw materials as for the validation study. However, because of the repeated recycling cycles on a single specimen, ease of handling is a prerequisite. To that purpose, carbon fiber bundles are manually winded to a stainless steel metal grid (50x20mm, see Figure 1 (a)) prior to infusion. Bundles are separated from a stitched fabric, winded and held in place by chromnickel filament at both ends, see Figure 1 (b). Grids, filaments, and fibers are individually weighed. Resin impregnation is done by fully submerging the mounted grids into a container with the priorly mixed resin. Curing is carried out at 80 C for 8h as specified in the resin material datasheet. Cured specimens are presented in Figure 1 (c). More detailed information about the procedure can be found in [1].

2.2. Thermal Recycling: Pyrolysis-Oxidation

All composites in this work are thermally recycled through a two-step pyrolysis-oxidation process. A laboratory-scale setup composed by a tube furnace with an integrated thermogravimetric feature is utilized. Figure 1 (d) provides a schematic representation of the equipment. Flow rate, temperature, and mass loss are monitored throughout the experiments.

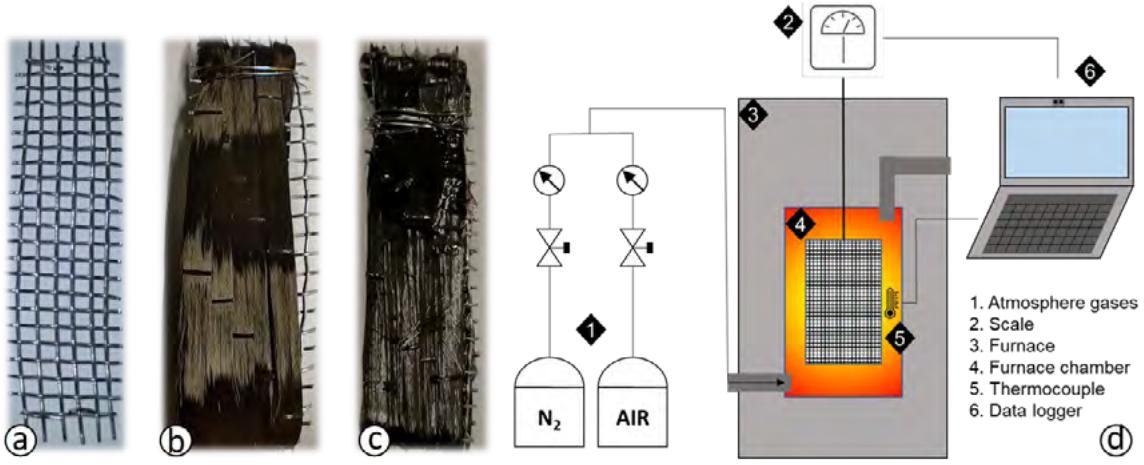

Figure 1. (a) empty metal grid, (b) dry bundles wrapped around the grid, (c) model composite after impregnation, (d) schema of the pyrolysis setup.

Two distinct recycling methods are carried out. Each method consists of two steps, pyrolysis under inert atmosphere and oxidation under air atmosphere. Process parameters are singular, temperature, residence times and heating rates for both methods are shown in Table 1. The six specimens of the robustness study undergo three consecutive manufacturing followed by recycling cycles, three per recycling method. The two methods intrinsic parameters are based on previous work [4][5], which focused on optimization of mechanical properties of recovered CF by two-step pyrolysis recycling treatment.

Table 1. Parameters of the two distinct recycling methods.

Method	T (°C)	Heating (°C/min)	Pyrolysis t_p (min)	Oxidation t_o (min)	Total t_T (min)
Rapid	550	N/A	5	10	15
Slow	500	10	30	30	60

2.3 Mechanical Characterization: Single Fiber Tensile Test (SFTT)

Recovered fibers were characterized by means of SFTT in an Instron 4411 testing machine. The single fibers were manually separated and mounted in paper frames. Using a light optic microscope (Nikon Eclipse MA200), individual diameters were measured. The tests were performed following the ASTM C1557-14 standard. To measure load, a 5N load cell was installed in the machine. For the validation samples, a 20mm gauge length was used. For the robustness samples the gauge length is increased to 80mm. In both cases the loading rate corresponds to 10%/min of the used gauge length (e.g. 2mm/min and 8mm/min), as specified in the standard.

In the test, the machine logged load and crosshead extension values. To determine the elastic modulus and tensile strength of the specimens the data was transformed into stress-strain curves, by using the priorly measured fiber diameters. Stiffness values were calculated using the curves slope in the linear region within a strain range of 0.05% to 0.25%. Furthermore, values were corrected using the compliance of the machine for this material. Average values presented here, exclude results from outlier fibers that exhibited non-linear behavior.

2.4 Optical characterization: Scanning Electron Microscope (SEM)

Surface analysis of virgin and recycled fibers was conducted using a Jeol JCM 6000 scanning electron microscope. In the case of recovered fibers, fibers were randomly chosen from the same bundle. All captured images adhered to consistent parameters, including 15kV voltage, high vacuum mode, secondary electron imaging mode and standard probe current.

3. Results and Discussion

As presented in the introduction, this work is divided into two studies. The validation study is a comparison between model composites and a laminate manufactured from the same raw materials and recycled through the same two recycling methods. Differences in the manufacturing process have a direct effect in the volume fraction of the samples and therefore, could have an impact on mass loss during recycling and the final mechanical properties. This validation study represents the first step to scaling up this recycling process. Secondly, the robustness study is a direct comparison to data obtained in prior work [1], where the same model composites undergo up to three manufacturing and recycling cycles. Complex geometries are simulated with model composites featuring virgin carbon fibers bent at

an angle close to 180 degrees. After each manufacturing and recycling loop, rCF are mechanically and optically characterized.

3.1 Validation study

3.1.1 Volume fraction

The fiber volume fraction of the laminate is calculated through its density. Two specimens were measured and the resultant value averaged. In the case of the model composites, the presence of the metal grid does not allow for the use of the same technique. However, the weights of every component are logged during the manufacturing and therefore, using the weight of the samples their volume fraction can be approximated. Values for both composite plate and model composites are presented in Table 2.

Table 2. Volume fraction of the carbon fiber in the laminate and model composite samples.

Sample	Volume fraction (%)
Laminate	45
Grid Slow	≈ 23
Grid Rapid	≈ 25

The difference on volume fraction between the composite laminate and the model composites is almost doubled in favor of the composite plate. Lower amounts of resin in the composite could have a negative effect in the general state of the recovered fibers. If the recycling process is tailored to clean a certain percentage of matrix, reproducing the process with a lesser amount of resin to degrade could provoke an early deterioration of the fiber's surfaces instead.

3.1.2 Mass loss

Throughout the recycling treatments, mass changes are registered and logged for further study. The initial weight of all specimens is known and the weight at the end of the pyrolysis and oxidation stages can be obtained from the logged data. The percentage of mass loss respect to the initial weight is shown in Table 3.

Table 3. Mass loss percentages throughout the recycling treatment. Divided in heating, pyrolysis and oxidation stages.

Sample	Initial weight (g)	Mass Loss *(%)*			
		Heating	Pyrolysis	Oxidation	Total
Lam_Slow	1.87	24.7	14.3	6.9	45.9
Lam_Rapid	1.55	-	27.5	4.8	32.3
Grid_Slow	1.46	73.5	5.5	0.8	79.8
Grid_Rapid	1.44	-	73.5	4.0	77.5

When comparing the total mass loss between the laminate samples and the model composites the difference is noticeable. The total percentage of mass loss is higher in the model composites compared to the laminates, almost double in the case of the Rapid method. This can be explained by the higher amount of resin in the model composites as they have a lower fiber volume fraction. However, according to the volume fraction values from Table 2, the total mass loss for the plate samples on both methods is

lesser than that of matrix in the composite. This could indicate incomplete resin degradation during the recycling process for the samples coming from the composite laminate. Higher char yield from pyrolysis stage is expected because of the secondary reactions. Volatiles from resin pyrolysis can meet several layers of CF, which can facilitate the secondary char formation. In addition, a large amount of char in tandem with multiple CF layers implies a risk of unconverted char due to scant residence time in the oxidation stage.

3.1.3 Diameter

The diameters of all mechanically tested fibers are measured by optical microscope. From the measurements take average and standard deviation are calculated and presented in Figure 2 (left).

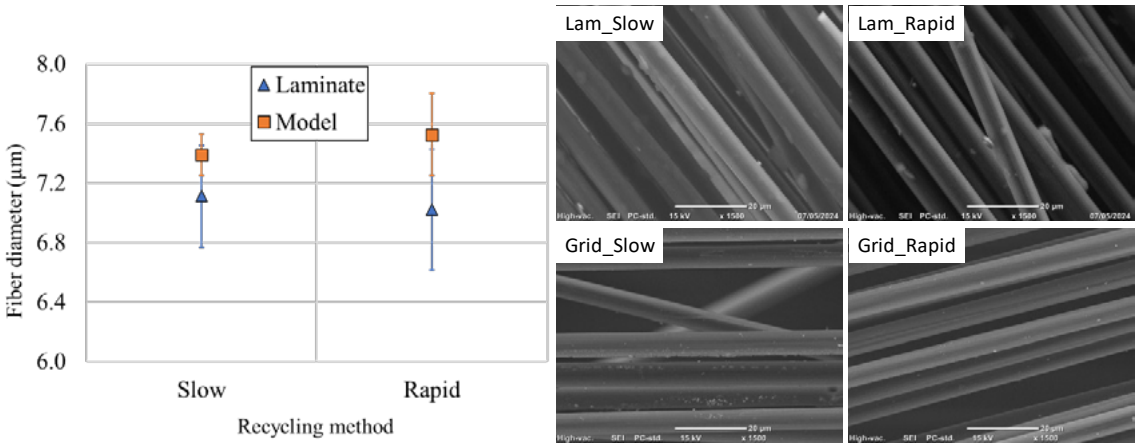

Figure 2. (left) Average and standard deviation of diameters for all fibers tested, (right) SEM images from all samples taken under same conditions.

Despite the lower amount of mass lost displayed by the samples from the composite laminate, their measured diameters are lower (by 3-7%) than those of the model composites. This trend is common for both recycling methods. However, the samples from the composite laminate also display a larger standard deviation. With ten diameters measured by sample and the overlapping produced by the standard deviations, the differences in diameters might not be statistically significant.

3.1.4 Surface Properties

Images obtained by scanning electron microscopy are presented in Figure 2 (right). All samples show clean and smooth fibers except the *Grid_Slow* sample (bottom left). Remnants of partially burnt resin are still attached to the recovered fibers. The other samples display clean fibers with rests of unburnt resin in the form of char laying on the fiber's surfaces. Char can be identified as bright spots laying on the fiber's surfaces. However, the char is not attached to the fibers. This might indicate insufficient residence time during the oxidation stage, the step where the char is removed by thermal degradation. Unclean fibers and the presence of foreign particles can hinder the adhesion of these fibers to a matrix when they are re-purposed into new composites.

3.1.5 Mechanical Properties

The elastic modulus and tensile strength of single fibers are obtained through single fiber tensile testing. The values are reported in Table 4, together with the calculation of the retention for both values with

respect to the nominal properties of the virgin fibers. Values from all samples have been corrected with the machine's compliance.

Table 4. Elastic Modulus and Tensile Strength values obtained by SFTT.

Sample	Elastic Modulus (GPa)	St Dev (GPa)	Retention (%)	Tensile Strength (MPa)	St. Dev. (MPa)	Retention (%)
Lam_Slow	197.3	10.3	92.6	1876	390	59.3
Lam_Rapid	198.6	18.5	93.1	1748	366	57.6
Grid_Slow	267.6	21.0	125.5	2181	179	71.9
Grid_Rapid	280.8	17.2	131.7	1675	285	55.2

The tensile values for the composite plate samples are consistently lower than the ones displayed by the model composites. This is especially patent for stiffness, being the difference less noticeable in tensile strength. It is apparent that the scale up from model composites to a composite laminate directly affects the recycling process and the mechanical properties of the recovered fibers.

3.2 Robustness Study

3.2.1 Mechanical Properties

As mentioned at the beginning of this section, for each recycling method three different samples are mechanically tested. To assess the effect of complex shapes of CFRP on the recycling process, longer and warped specimens are used in the *Complex* samples compared to shorter and straight fibers of the *Model* samples. Specimens belonging to the *Complex* samples have a testing gauge length of 80mm, compared to the 20mm gauge length of the *Model* specimens. All stiffness values have been corrected using the compliance value calculated for the same setup using virgin fibers. All values have been normalized to the nominal value from tested virgin fibers for comparison. Results are displayed in Figure 4. However, it is important to state the length difference between the samples, 20mm for the *Model* and 80mm for the *Complex*. This is relevant for the comparison of tensile strengths, as strength is strongly directed to surface imperfections. Longer testing length increases the probability of an imperfection that leads to early failure.

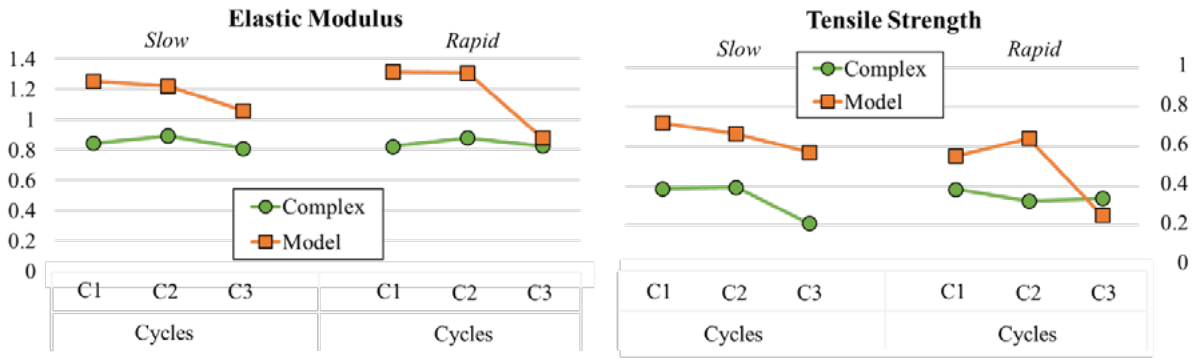

Figure 4. (left) Elastic Modulus normalized with the nominal values from virgin CF, (right) Tensile Strength values normalized with the nominal values from virgin CF.

In a general overview, the *Complex* samples from the robustness study show lesser mechanical properties than the Model composite samples. This difference is kept constant for both methods and all

cycles, except for the third recycling cycle of the rapid method. In this case, the values are almost the same for both sets, *Complex* and *Model*. The observed behavior could be an indication of complex shapes and sharp geometries in CFRP parts having a negative effect on final tensile properties after recycling. By the third recycling cycle, the fibers belonging to straight simple geometries have cumulated enough damage, produced by the recycling process itself, to fail at a similar load than the ones pertaining to more geometrically complex composite parts.

4. Conclusions

In this work, the validity and robustness of a lab-scale recycling process for CFRP waste was assessed by two separate studies. The validation study compares a laminate composite to a model composite when they both undergo the same recycling methods. The mass loss observed during the process are distinctly different. Higher resin content, consequence of lower fiber volume fraction in model composites leads to increased total mass loss percentage during recycling. In addition, mechanical performance displayed is reduced in the laminate composite, especially for the elastic modulus. Although the retention values are comparable to other pyrolysis-oxidation results in literature, the stiffness of the fibers is not boosted by the same identified process that occurs in the case of the model composite [5].

Furthermore, the robustness study shows a decrease of mechanical performance demonstrating the negative impact of complex geometries in CFRP waste. This trend is common to the first and second recycling plus manufacturing cycles. After the third recycling cycle, the damage introduced in the fibers by the recycling process itself in the straight model composites is equivalent to that present in bended model composites.

The presented results contribute to prove the potential for scaling up lab-scale recycling processes that will help CF to meet the current demands for environmentally sustainable and economically viable composites.

Acknowledgments
This work was supported by Createrity Graduate School at Luleå University of Technology.

References

[1] M. Corvo-Alguacil, K. Umeki, and R. Joffe, “Preservation of Mechanical Properties of Carbon Fibers after Multiple Pyrolysis Cycles,” in *Twenty-Third International Conference on Composite Materials (ICCM23)*, Belfast, UK, Aug. 2023.

[2] E. Witten and V. Mathes, “The European Market for Fibre Reinforced Plastics / Composites in 2021 Market developments, trends, challenges and outlook,” 2022. Accessed: Mar. 08, 2023. [Online]. Available: https://www.avk-tv.de/files/publications/files/avk_marketreport_final.pdf

[3] R. A. Witik, R. Teuscher, V. Michaud, C. Ludwig, and J. A. E. Månson, “Carbon fibre reinforced composite waste: An environmental assessment of recycling, energy recovery and landfilling,” *Compos Part A Appl Sci Manuf*, vol. 49, pp. 89–99, 2013, doi: 10.1016/j.compositesa.2013.02.009.

[4] M. Corvo-Alguacil, K. Umeki, and R. Joffe, “Retention of mechanical properties of carbon fibers after recovery by thermal treatment,” in *International Conference on Sustainable Wind Turbine Blades: New Materials, Recycling and Future Perspectives*, Roskilde, Denmark, Nov. 2022.

[5] M. Corvo-Alguacil, “Circularity in Thermal Recycling for Sustainable Carbon Fibers,” Licentiate Thesis, Luleå University of Technology, 2023.

©2024 | 2_CORVO ALGUACIL_Marina_KW4LO.pdf:8

INVESTIGATING LIGHTNING-INDUCED DAMAGE: A COMPARATIVE ANALYSIS OF CFRP SPECIMENS SUBJECTED TO MULTIPLE LIGHTNING STRIKES

Timothy M. Harrell[1], Ole T. Thomsen[2] and Janice M. Dulieu-Barton[2]

[1]Faculty of Mechanical Engineering, University of Bath, BA2 7AY, UK, Email: th2312 @bath.ac.uk
[2]Bristol Composites Institute (BCI), University of Bristol, Bristol, BS8 1TR, UK

Keywords: CFRP composites, Lightning Damage, Wind Turbine Blades, Thermal Imaging

Abstract
The impact of direct lightning strikes on Carbon Fiber Reinforced Polymer (CFRP) specimens is studied, with a focus on damage assessment through repeated strikes. Four CFRP specimens underwent repeated simulated lightning strikes. Visual inspections and dimensional analyses were performed and identified consistent damage characteristics. Intriguingly, additional lightning strikes did not result in proportional increases in damage, evident through stable damage areas and lengths. To probe sub-surface defects, 10 mm strips were cut from specimens, revealing distinct delamination at the edges. Thermal data indicated an exponential decay in maximum temperatures post-strike, with repeated strikes retaining heat for an extended duration, highlighting the consistency of fibre conduction paths after damage. The research described in the paper provides valuable insights into lightning-induced damage patterns in CFRP materials, explaining the damage relationship with strike frequency. The findings hold implications for designing resilient materials and protective measures against lightning-induced damage in composite structures.

1. Introduction

The introduction of CFRP composites in wind turbine (WT) blades has presented new challenges in protecting the structure from lightning. The semi-conductive nature of the CFRP leads to an additional path to ground for the electric current in the structure, and the anisotropic nature of the material thermal and electrical properties leads to large amounts of resistive heating (or Joule heating), especially in the through-thickness direction where the electric conductivity is the lowest. The heating causes elevated temperatures leading to damage in the forms of resin burn off, fibre breakage and delamination that effects mechanical behaviour and performance of the CFRP [1–9]. The main reasons for this are the limited electrical and thermal conductivities transverse to the fibers, the anisotropic material properties, and the integration of the CFRP into the overall WT blade or aerospace structures. With the progressive use of CFRP materials in WT blade structures, it is important to develop a full understanding of the effects of lightning strike induced damage on the material and the structural response.

The aerospace industry has implemented CFRP materials into structural components for decades and has explored different methods of reducing and/or mitigating the damage introduced by lightning interacting with CFRP materials. Much of the literature focuses on direct effects from a single direct lightning strike [3,10–16] because this is the most common scenario of electric current injection into CFRP on aircraft structures. This is an adequate approach for an aircraft that will be inspected after a lightning strike. WTs are often left to the elements where they may be exposed to more lightning strikes. Hence the work described in the present paper.

2. Methods

2.1. Specimen Manufacturing

For the repeated lightning strike test, the composite materials were made up of woven carbon fibre dry fabric (375 gsm) and epoxy resin. An eight-ply woven CFRP composite large plate with dimensions of 420mm x 420mm x 4.03mm was manufactured by vacuum liquid resin infusion. Four lightning strike specimens were cut from the large plate with dimensions 200 mm long x 200 mm wide x 3.90 mm thick. The individual specimens were chamfered along the four edges with an approximate 1:4 taper to expose the carbon fibres and to provide a connection to ground. Simulated lightning strikes were applied at the same location and all having a similar waveform. The repeated waveform was an approximate 18/150 µs oscillating with an approximate peak current of 38 kA. An example of the AE1-A-1 waveform is shown in **Figure 1**.

Table 1. Test parameters defined for the simulated lightning strike test AE1: peak current, waveform, charge, and specific energy applied to the specimens

Sample ID	Strike Attempt	Peak Current [kA]	Waveform Characteristics (Impulse $t_1/t_2/t_f$) [µs]	$\|Q\|$ [C]	AI [kJ/Ω]
AE1-A-1	1st strike	37.6	18/155/481	3.88	71
AE1-B-1	1st strike	35.7	17/159/354	3.69	63
AE1-B-2	2nd strike	38.7	17/142/341	4.00	79
AE1-C-1	1st strike	34.7	17/142/355	3.58	59
AE1-C-2	2nd strike	38.4	17/141/355	3.97	77
AE1-C-3	3rd strike	38.6	17/141/355	3.98	79
AE1-D-1	1st strike	38.1	17/142/345	3.94	72
AE1-D-2	2nd strike	37.7	17/145/355	3.89	75
AE1-D-3	3rd strike	38.4	17/142/355	3.97	76
AE1-D-4	4th strike	37.3	17/149/355	3.85	76
Q = 0 for oscillating waveform					

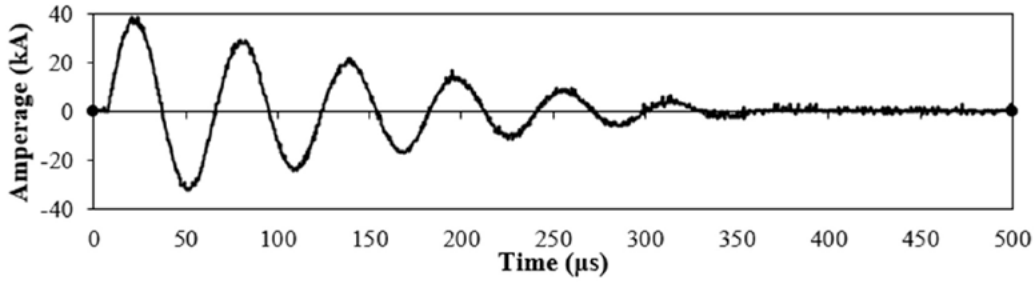

Figure 1. AE1-A-1 current waveform

3. Results

Four CFRP specimens were subjected to simulated lightning strike events for test AE1. The four specimens were struck with 1, 2, 3, and 4 lightning strikes respectively. For all AE1 specimens, the surface damage and charred damage were primarily in a circular shape; see **Figure 2a**. AE1-A through AE1-D had similar patterns of surface and damage shapes and sizes. The four specimens showed fiber breakage and resin burn off to previous research [3,10–16]. The damaged area did not significantly change with repeated lightning strikes despite the additional energy applied to the specimen. The areas are presented in **Figure 2b-c** which plots the damage area against the cumulative charge and specific energy.

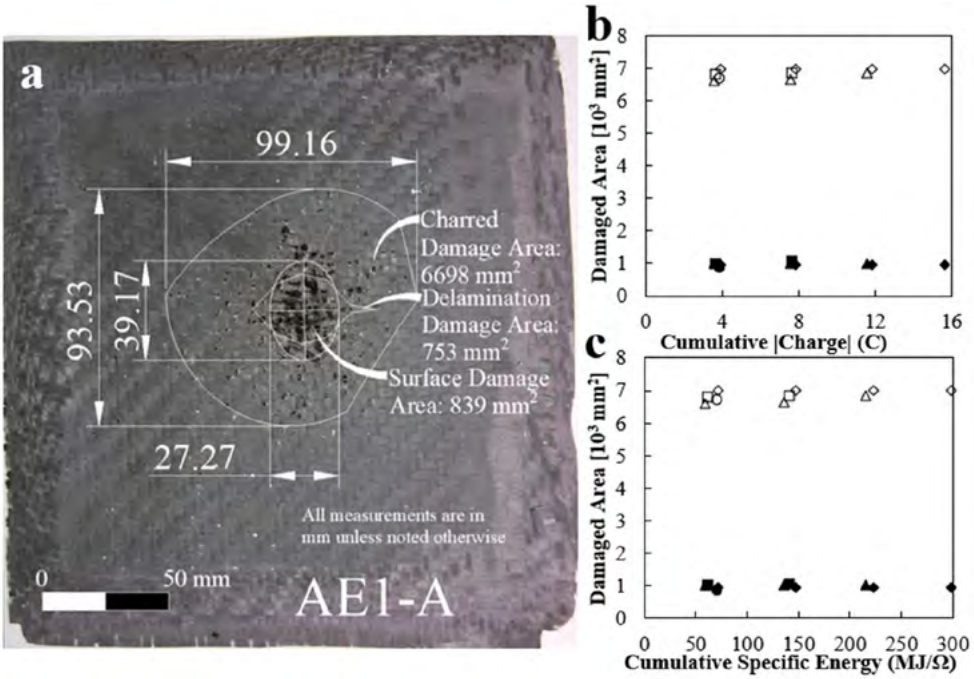

Figure 2. (a) Visual inspection AE1-A and the damage area compared to number of lightning strikes from AE1 against (b) cumulative |charge| and (c) cumulative specific energy

Examining the edges of the waterjet cut strips, each had clear delamination (**Figure 3a-d**). The delamination damage increased with each successive lightning strike. Each strip edge delaminated length was measured. The measured distances were added to a chart with the distance from the centre of the damage and provided a delaminated region. The coordinates of this region were used to calculate a delamination area. The delaminated areas are shown in **Figure 4a**. The total delamination area was compared against the cumulative specific energy in **Figure 4b**. Showing the delamination region for each sample grew in a linear fashion.

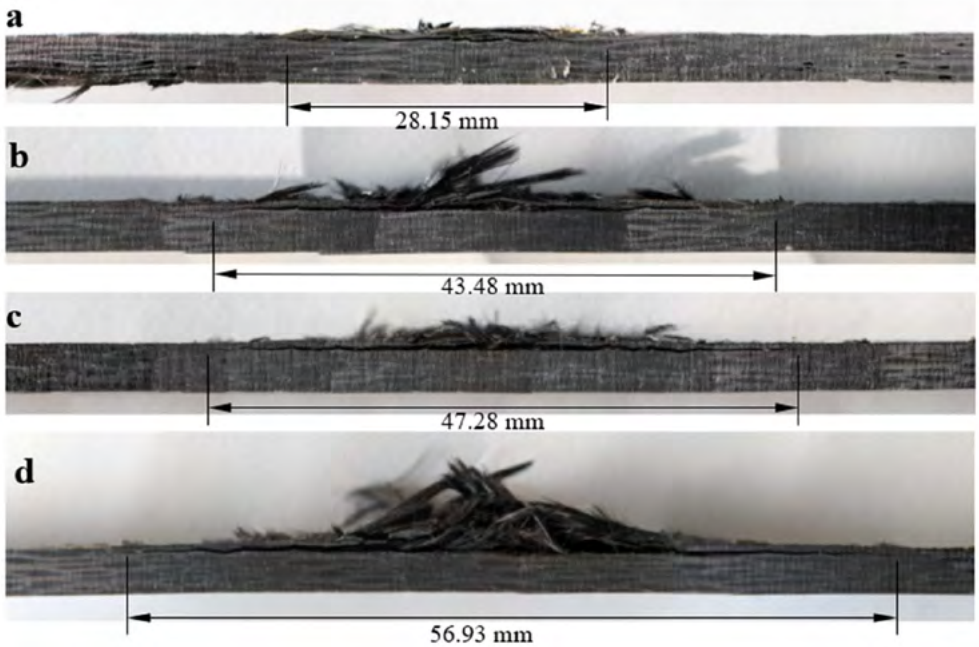

Figure 3. Microscopy images of (a) AE1-A, (b) AE1-B, (c) AE1-C, and (d) AE1-D

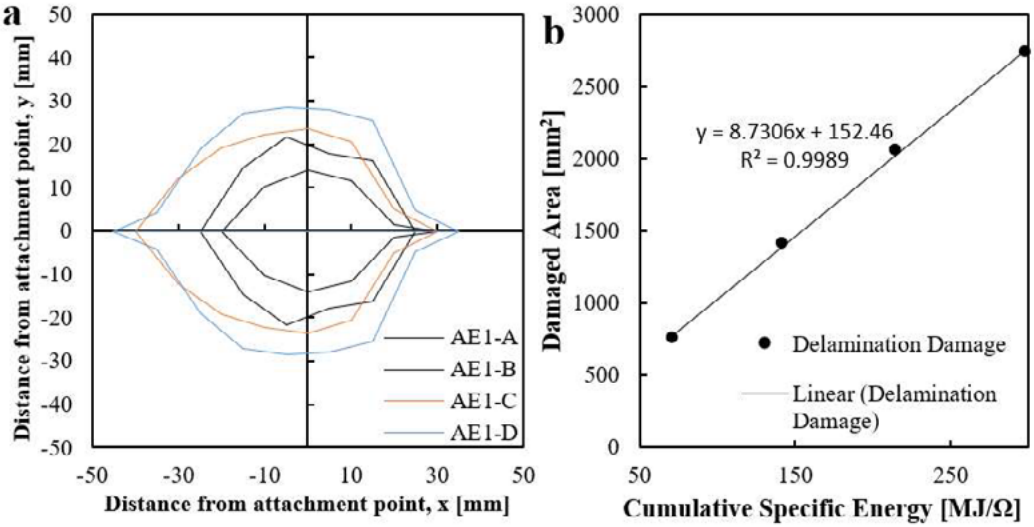

Figure 4. Delamination damage from specimens in test AE1 where (a) is an overview of the area and (b) is the total area compared to the cumulative specific energy

The thermal data were recorded via a thermal camera. The maximum temperature during the lightning strike tests were extracted from the data and is shown in **Figure 5**. During the lightning strike the heat was higher near the spark would result in a high maximum temperature, however this temperature is not recorded because the maximum recording temperature of the camera is 650°C and the rapidness of the strike did not allow the full thermal data to be recorded. However, the amount of time the heat took to dissipate is clearly shown in **Figure 5**. And the fact that the highest temperature always occurred directly after the lightning strike event and exponentially decayed afterwards. On all samples, the initial lightning strike thermal evolution decayed the fastest. The repeated lightning strikes held the heat longer. This would indicate either higher specific heat or lower electrical/thermal conductivities in the damaged region. The one outlier is the AE1-D-3 specimens because the maximum temperature occurred on a part of the specimen that ignited and burnt for approximately 6 seconds.

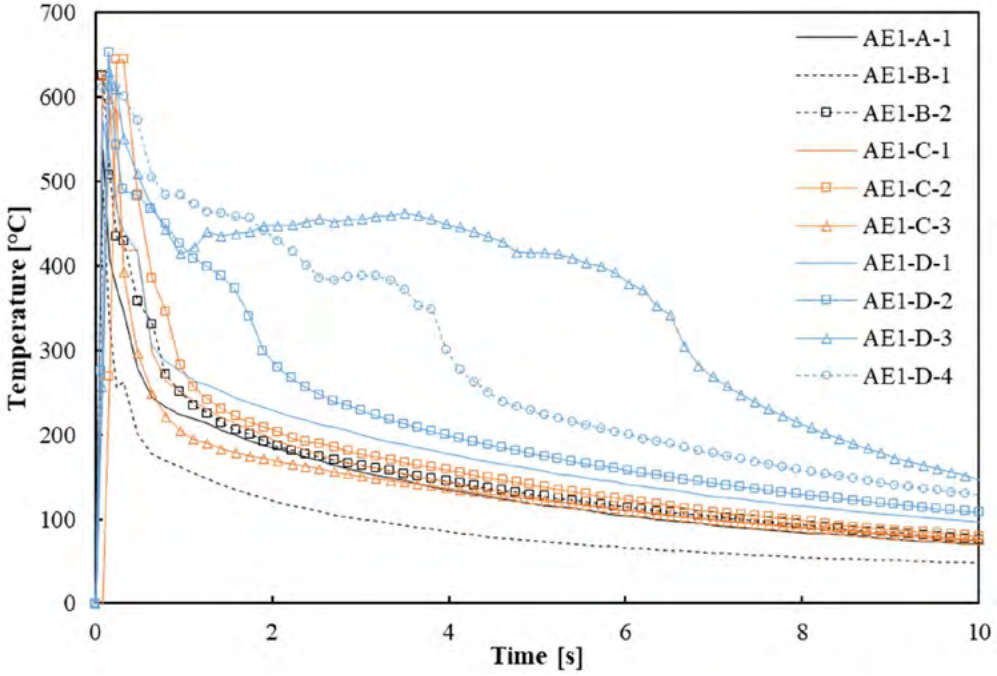

Figure 5. Maximum temperature evolution of AE1 tests

These results indicate that the current always takes the same path to ground even after damage. This would mean that the fibres are not damaged enough to stop or reduce the conduction of current.

3. Conclusions

The complex interaction between lightning strikes and CFRP materials in WT blades has been studied. By subjecting CFRP specimens to repeated simulated lightning strikes, an intriguing pattern emerges in damage accumulation and thermal behaviour. Contrary to expectations, additional lightning strikes did not proportionally increase damage on the surface, suggesting a potential threshold effect. However, the sub-surface delamination increased linearly in size. Thermal data further explained the post-strike temperature dynamics, indicating an exponential decay does not change with repeated lightning strikes. These findings underscore the need for a comprehensive understanding of lightning-induced damage in CFRP materials to ensure the structural integrity and reliability of WT blades in the face of repeated exposure to lightning strikes.

Acknowledgments
This work was sponsored by the Marie Skłodowska Curie Actions, Innovative Training Networks (ITN), Call: H2020-MSCA-ITN-2014, as part of the 642771 “Lightning protection of wind turbine blades with carbon fibre composite materials” SPARCARB project.

References

[1] H. Kawakami, P. Feraboli, Lightning strike damage resistance and tolerance of scarf-repaired mesh-protected carbon fiber composites, Compos. Part A Appl. Sci. Manuf. 42 (2011) 1247–1262. https://doi.org/10.1016/j.compositesa.2011.05.007.

[2] L. Chemartin, P. Lalande, B. Peyrou, A. Chazottes, P.Q. Elias, C. Delalondre, B.G. Cheron, F. Lago, Direct Effects of Lightning on Aircraft Structure : Analysis of the Thermal , Electrical and Mechanical Constraints, J. Aerosp. Lab (2012) 1–15.

[3] P. Feraboli, M. Miller, Damage resistance and tolerance of carbon/epoxy composite coupons subjected to simulated lightning strike, Compos. Part A Appl. Sci. Manuf. 40 (2009) 954–967. https://doi.org/10.1016/j.compositesa.2009.04.025.

[4] T.M. Harrell, O.T. Thomsen, S.F. Madsen, L. Carloni, Lightning protection of CFRP wind turbine blades - What is the dominant cause of failure : Specific Energy or Charge?, in: Int. Conf. Light. Static Electr., Nagoya, Japan, 2017: pp. 1–5.

[5] T.M. Harrell, O.T. Thomsen, J.M. Dulieu-Barton, S.F. Madsen, Damage in CFRP composites subjected to simulated lightning strikes - Assessment of thermal and mechanical responses, Compos. Part B Eng. 176 (2019) 107298. https://doi.org/10.1016/j.compositesb.2019.107298.

[6] C. Karch, W. Wulbrand, I.E. Works, Thermo-Mechanical Damage of Protected CFRP Structures Caused by Lightning Continuous Currents, in: Int. Conf. Light. Static Electr., Seattle, WA, USA, 2013: pp. 1–12.

[7] B. Lepetit, F. Soulas, S. Guinard, I. Revel, G. Peres, Analysis of composite panel damages due to a lightning strike: mechanical effects., in: Int. Conf. Light. Static Electr., Seattle, WA, USA, 2013: pp. 1–8.

[8] C. Karch, J. Steinwandel, K.W. Dittrich, R. Honke, Contributions of lightning current pulses to mechanical damage of CFRP structures, in: Int. Conf. Light. Static Electr. (ICOLSE 2015), Institution of Engineering and Technology, 2015: pp. 2 (8 .)-2 (8 .). https://doi.org/10.1049/ic.2015.0149.

[9] T.M. Harrell, O.T. Thomsen, J.M. Dulieu-Barton, Buckling Behaviour of UD Carbon/Epoxy Panels Subjected to Direct Lightning Strike, in: 22nd Int. Conf. Compos. Mater., Melbourne, AU, 2019: pp. 1–6.

[10] T. Ogasawara, Y. Hirano, A. Yoshimura, Coupled thermal-electrical analysis for carbon

fiber/epoxy composites exposed to simulated lightning current, Compos. Part A Appl. Sci. Manuf. 41 (2010) 973–981. https://doi.org/10.1016/j.compositesa.2010.04.001.

[11] G.W. Reid, Investigations Into the Damage for Various Types of Unprotected Carbon Fibre Composites With a Variety of Lightning Type Arc Attachments, in: Int. Conf. Light. Static Electr., Coca Beach, FL, 1991: p. 11.

[12] P. Feraboli, H. Kawakami, Damage of Carbon/Epoxy Composite Plates Subjected to Mechanical Impact and Simulated Lightning, J. Aircr. 47 (2010) 999–1012. https://doi.org/10.2514/1.46486.

[13] S. Kamiyama, Y. Hirano, T. Okada, T. Ogasawara, Lightning strike damage behavior of carbon fiber reinforced epoxy, bismaleimide, and polyetheretherketone composites, Compos. Sci. Technol. 161 (2018) 107–114. https://doi.org/10.1016/j.compscitech.2018.04.009.

[14] T.M. Harrell, J.M. Dulieu-barton, O.T. Thomsen, Identification of lightning strike damage using Pulse Thermography through integration of thermal data, in: Soc. Exp. Mech., Greenville, SC, 2018: pp. 1–3.

[15] T.M. Harrell, O.T. Thomsen, J.M. Dulieu-Barton, Predicting the effect of lightning strike damage on the structural response of CFRP wind blade sparcap laminates, Compos. Struct. 308 (2023) 116707. https://doi.org/10.1016/j.compstruct.2023.116707.

[16] T.M. Harrell, S.F. Madsen, O.T. Thomsen, J.M. Dulieu-Barton, On the Effect of Dielectric Breakdown in UD CFRPs Subjected to Lightning Strike Using an Experimentally Validated Model, Appl. Compos. Mater. (2022). https://doi.org/10.1007/s10443-022-10014-7.

Study on dispersion mixing of nano silica by extensional flow using a twin-screw extruder

Daisuke Higuma[1], Tatsuya Tanaka[2], Masahiro Sasada[3] and Hiroyuki Kitamura[4]

[1]*Doshisha University, Tataramiyakodani, Kyotanabe-city, Kyoto-fu, Japan*
Email: ctwj0514@mail4.doshisha.ac.jp, Web Page: https://www.doshisha.ac.jp
[2]*Doshisha University, Tataramiyakodani, Kyotanabe-city, Kyoto-fu, Japan*
Email: tatanaka@mail.doshisha.ac.jp, Web Page: https://www.doshisha.ac.jp
[3]*Doshisha University, Tataramiyakodani, Kyotanabe-city, Kyoto-fu, Japan*
Email: msasada@mail.doshisha.ac.jp, Web Page: https://www.doshisha.ac.jp
[4]*Mitsubishi Chemical Corporation, yokkaichi-city, Mie, Japan*
Email: hiroyuki.kitamura.ms@mcgc.com, Web Page: https://www.mcgc.com/index.html

Keywords: Twin-screw extruder, Nanocomposites, Extensional flow, Blister disk, Dispersion

Abstract
To further exploit the effects of nanocomposites, it is essential to establish a dispersion technique for nanofillers. Chemical dispersion methods, such as the use of compatibilizers and surface treatment, can increase costs and adversely affect the matrix. Mechanical methods are known to fail to achieve sufficient dispersibility. In this work, we aim to achieve the same dispersibility as the chemical methods using a mechanical method. It is based on a new segment in the extrusion process that creates an extensional flow. Preliminary extrusion experiments were dedicated to the effects of different parameters on the dispersibility of nano silica in the extensional flow. Based on the results, further experiments were carried out to compare the effect of an extensional flow segment and a conventional segment in a twin-screw extruder. It was found that the extensional flow segments improved the dispersibility while suppressing the increase in resin temperature, and the dispersibility was improved compared to the conventional segments. This mechanical process produced transparent PLA/nano silica pellets at 10 wt%, which was previously unattainable.

1. Introduction

In recent years, the development of polymer composites has been promoted to achieve high performance and high functionality. These mainly include composites in which fillers are mixed with polymers and blends in which different polymers are mixed [1]. They can be produced on twin-screw extruders capable of continuous production and high productivity [2]. Shear flow is generally the dominant flow in extruders, but it makes difficult to knead materials with small filler particle sizes or multiple resins. A good mechanical mixing process is mandatory to achieve a uniform distribution of the fillers to be effective in the composite [3]. Droplet splitting using a 4-roll type apparatus (including a shear flow field) was proposed in [4], where the extensional flow field is dominant and disperses droplets with lower energy.
In this work, the extensional flow is used, in which the material is stretched in the direction of the principal stress. The experiments were carried out using a segment in the extruder capable of generating extensional flow by passing the melted resin through a hole, based on the extensional flow theory proposed in [5]. Although this technology is effective for dispersion, it is still under

investigation and only a few applications are available [6]. To apply this technology to actual products, information on the effects of additive ratios and dispersion limits is also required.
Polyethylene terephthalate (PET) is used as the matrix and silica particles as the filler. Silica particle composites are attracting attention to improve the gas barrier properties of PET [7,8]. Fillers can be dispersed by chemical treatments to reduce their aggregation energy or by the use of compatibilizers, but this can increase cost and the adhesion to the matrix [9,10]. Chemical treatment of the particle during the synthesis stage or the dispersion of the filler in a solvent can led to uneven dispersion and removal of the treatment agent throughout the entire process to the final product [11]. It is therefore necessary to establish a mechanical dispersion method without pre-treatment to reduce process and material costs.
The aim of this work is to demonstrate the effectiveness of extensional flow in dispersing small particle size. To this end, preliminary extrusion experiments were carried out to investigate the effects of various parameters on the dispersibility of nano silica in extensional flow. Based on the results, further experiments were carried out to compare the effect of an extensional flow segment and a conventional segment in a twin-screw extruder. Feed rate and rotation speed were varied, and pressure drop, machine torque, resin outlet temperature and dispersibility were measured and compared between the two segments.

2. PET/silica preliminary extrusion experiments

To adapt the extensional flow mixing technology for composites with nanofillers to twin-screw extruders, the effect of various parameters such as feed rate, pressure drop and segment shape on dispersibility were investigated to understand the conditions for uniform dispersion.

2.1. Experimental Methods

PET (Mitsubishi Chemical Corporation, GM701S) was used as the matrix, and spherical silica particles with diameters of 0.3 μm (Nippon Shokubai, KE-S-30) and 10 nm (Admatechs, YA010C-SV1) were used as fillers. Silica particles with a diameter of 0.3 μm are hereafter named "submicron silica" and those with a diameter of 10 nm "nano silica".
Master batches (MB) were prepared using a co-rotating twin-screw extruder (Coperion, ZSK18 MEGAlab) with a feed rate of 2.5 kg/h, a rotation speed of 150 rpm, and a barrel temperature of 280 °C. The screw configuration was mainly full-flight (FF) with low mixing effect. MB were produced with different silica particle contents.
Samples were prepared by feeding MB into the extrusion equipment shown in Figure 1 and extruding the melted resin through the Blister Disk (BD) into the mold. The Blister Disk creates the extensional flow by passing the melted resin through a hole.

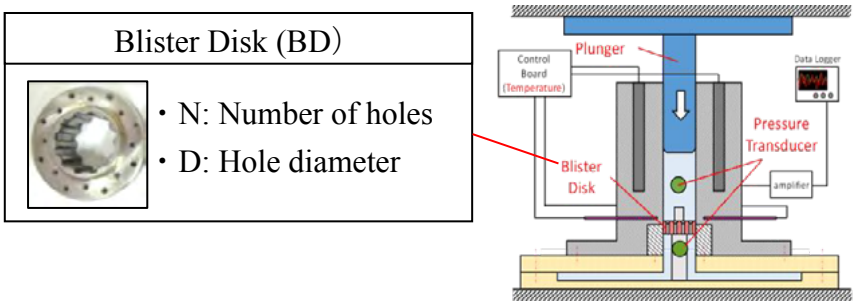

Figure 1. Image of self-designed extrusion equipment.

The extrusion equipment was connected to a servo press (TAIYO, PQCS2-60kN-FC) to control the extrusion speed. The extrusion temperature was set at 280°C. The Blister Disks were interchangeable. They have different number of holes N [-], hole diameter D [mm], and vary the

area ratio of the holes. The BDs used are shown in Table 1. A pressure transducer was set up to measure the pressure drop before and after the BD.

Table 1. Features of the blister disks.

	N16, D0.5	N8, D1.0	N16, D1.0	N32, D1.0
Number of holes [-]	16	8	16	32
Hole diameter [mm]	0.5	1.0	1.0	1.0
The area ratio of the holes [%]	1.23	2.47	4.94	9.88

Samples for morphological observations were prepared by cutting a portion of the extruded material and hot-pressing it at 10 kN and the same temperature as the extrusion to a film thickness of approximately 100 µm. Images were taken with a tabletop scanning electron microscope (@Hitachi High-Tech, TM3030Plus) at 5,000x magnification. To evaluate the dispersibility, the images were binarized using Sigma Scan Pro5 and the agglomeration area was measured.

2.2. Results and Discussion

Figure 2 shows the relationship between pressure drop and the area ratio of the holes. The pressure drop increased as the area ratio of the holes decreased and the feed rate increased. Figure 3 shows SEM images before and after extrusion. MB before extrusion had large agglomerates, but BD after extrusion had not such agglomerates, indicating that dispersion had improved. Thus, the greater the pressure drop, the smaller the average agglomerate area and the better the dispersibility of BD.

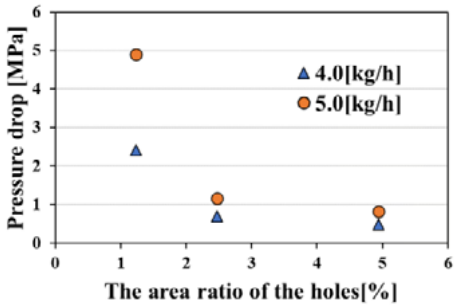

Figure 2 Relationship between pressure drop and percentage of through-hole area.

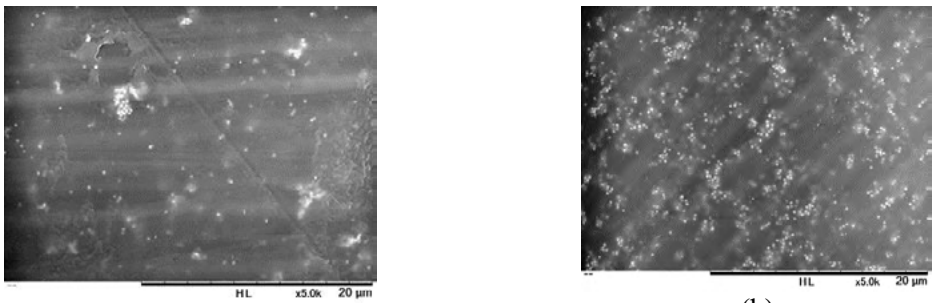

(a) (b)

Figure 3. SEM Image at 5,000x : (a) MB (b) BD.

For improved particle dispersion, based on Cogswell's extensional theory Eq. 1, it is assumed that the extensional stress increases with the pressure drop at the through-hole inlet, resulting in improved dispersion. This confirms that pressure drop is an indicator of dispersion, and that control of pressure is important for application to twin-screw extruders.

$$\sigma = \frac{3}{8}(n+1)\Delta P_0 \tag{1}$$

where ΔP_0 is the inlet pressure drop, σ is the extensional stress, and n is the power-law index of the viscosity curve.

3. PET/submicron silica twin-screw extrusion experiments

Preliminary extrusion experiments have shown that BD improves the dispersibility of nano silica in composites by generating extensional flow. Based on these results, BD was set up on a twin-screw extruder and the results were compared with a conventional shear kneading.

3.1. Experimental Methods

As detailed in section 2.1, PET was used as the matrix and submicron silica as filler at 10wt%. A co-rotating twin-screw extruder (Coperion, ZSK18 MEGAlab) was used with two types of screw configurations (see Figure 4): a KD (Kneading Disk) configuration, where shear flow is dominant, and an XBD (Fixed Blister Disk) configuration, where extensional flow is dominant.

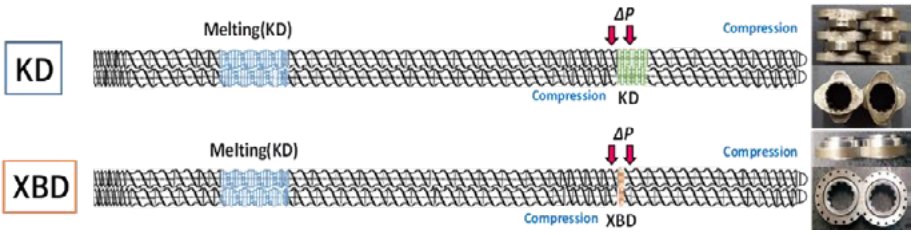

Figure 4. Schematic view of screw configuration.

The operating conditions are shown in Table 2. The barrel temperature was set at 280°C. The materials were pelletized using a pelletizer. Resin temperature, torque, and pressure were measured during the process, and pressure drop (ΔP), and specific energy (SME) were calculated. Extruded samples were observed and the dispersibility was evaluated.

Table 2. PET/submicron-silica mixing conditions.

	Feed rate Q [kg/h]	Screw speed N [rpm]	Q/N
1	2.0	150	0.013
2	3.0	150	0.020
3	3.0	300	0.010
4	3.0	500	0.006
5	4.0	150	0.027

3.2. Results and Discussion

3.2.1. Effect of Q/N (feed rate/screw speed) on SME and discharge resin temperature

Figure 5 shows the relationship between Q/N (feed rate/screw speed), the specific energy (SME), and discharge resin temperature.

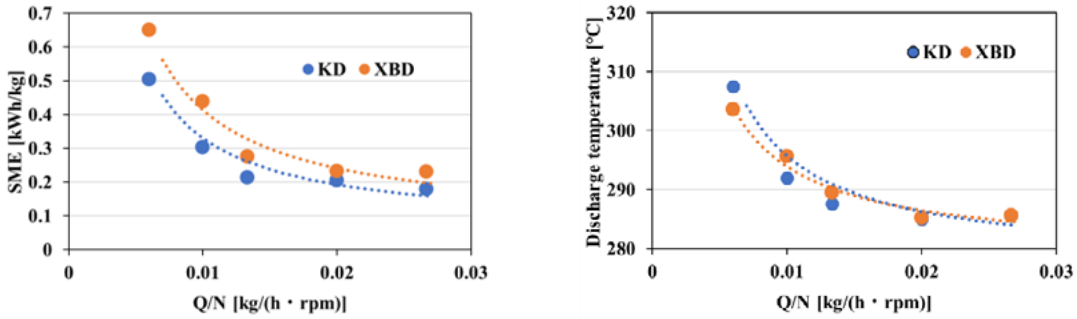

(a) (b)

Figure 5. Relationship between Q/N and (a) SME, (b) Discharge temperature.

Eq. 2 shows that the specific energy (SME) is inversely proportional to Q/N, and a similar trend was observed in the experiment. Figure 5(b) shows that the discharge resin temperature is also inversely proportional to Q/N. This indicates that the discharge resin temperature also increases with an increase in SME.

$$\mathrm{SME}\left[\frac{kWh}{kg}\right] = \frac{P_{mot}[kW]}{Q\left[\frac{kg}{h}\right]} = \frac{2 \times M_{VT} \times 1.05}{9550} \times \frac{N}{Q} \tag{2}$$

where P_{mot} is the motor power, Q is feed rate, M_{VT} is the torque per shaft, and N is screw speed.

3.2.2. Effect of Q/N on pressure drop

Figure 6 shows the relationship between pressure drop and Q/N. Figure 6 shows that pressure drop increases for both XBD and KD as Q/N increases. Eq. 3 shows the equation for the fill factor in the extruder. Eq. 3 indicates that a higher Q/N results in a higher fill factor in the extruder and therefore a higher pressure drop. In addition, the rate of increase in pressure drop is greater for the XBD than for the KD. This is due to the fact that the XBD has a structure that does not rotate and retains the melted resin, resulting in a greater increase in the fill factor.

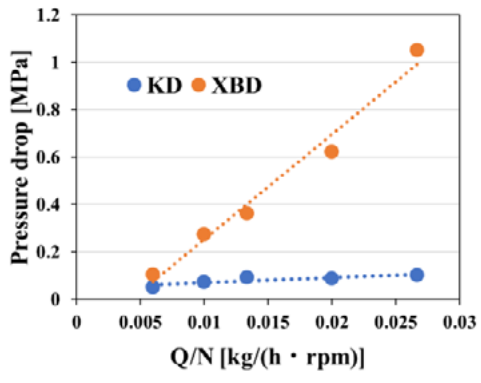

Figure 6. Relationship between Q/N and pressure drop.

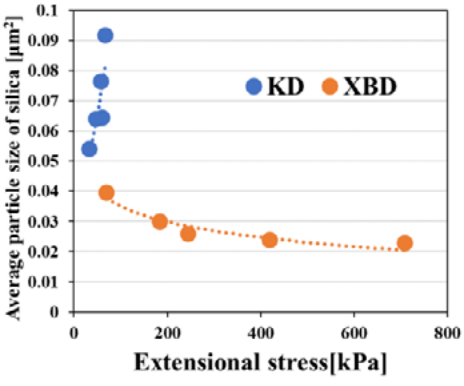

Figure 7. Relationship between extensional stress and dispersibility.

Figure 7 shows the relationship between the extensional stress, obtained from pressure drop and Eq. 2, and the average agglomeration area. For XBD, the average agglomeration area decreases with increasing extensional stress, and the dispersibility improves. For KD, the improvement in dispersion is not related to the extensional stress.

$$Q = fQ_d = \frac{fNAs}{2}$$
$$f = \frac{2}{As} \times \frac{Q}{N} \quad (3)$$

where Q is actual volume flow rate, Q_d is max volume flow rate, f is fill rate, A is cross-sectional area, s is spiral pitch length, N is screw speed.

3.2.3. Dispersibility evaluation results

Figure 8 shows the relationship between average agglomeration size and SME in KD and Figure 9 shows the relationship between average agglomeration size and pressure drop in XBD. Figure 10 shows the particle size frequency distributionand its cumulative frequency. In shear flow, the average agglomeration area decreases with increasing SME, indicating an improvement in dispersibility. In extensional flow, the average agglomeration area decreases with increasing pressure drop and the dispersibility is significantly improved. Compared to KD, the average agglomeration area of XBD is smaller, and under high pressure drop conditions, large agglomerates are eliminated, indicating that goodt dispersion has been achieved.

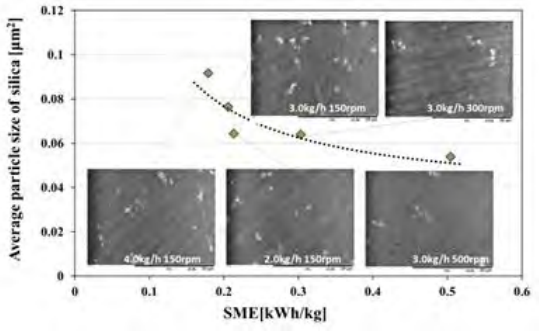

Figure 8. Relationship between average particle size and SME in KD.

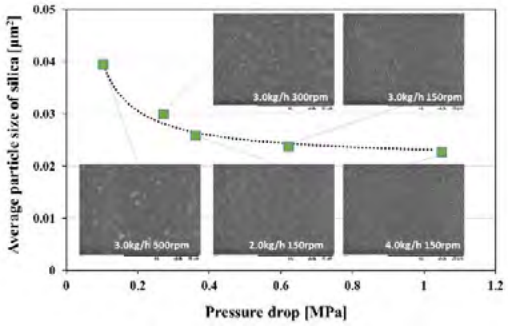

Figure 9. Relationship between average particle size and pressure drop in XBD.

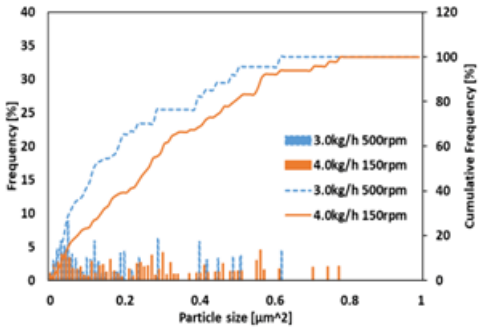

(a)

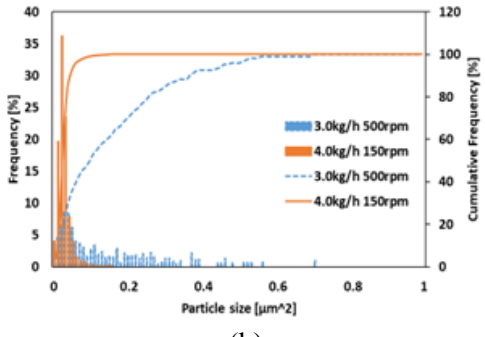

(b)

Figure 10. Frequency and cumulative frequency of agglomeration area: (a) KD (b) XBD.

3.2.4. Effect of Q/N on dispersibility and discharge resin temperature

Figure 11 shows the relationship between Q/N, dispersibility, and discharge resin temperature. In KD, decreasing Q/N increases SME and improves dispersibility, but also promotes shear heating. In general, increasing the SME reduces the mechanical properties of polymers due to degradation caused by the molecular weight reduction and heat generation, making it difficult to achieve both dispersibility and temperature control. In contrast, XBD improves dispersibility and suppresses shear heating by increasing Q/N, to increase pressure drop and decreasing SME. In other words, KD is a trade-off between improved dispersion and temperature reduction, whereas XBD can both improve dispersion and reduce temperature. These results confirm that Q/N and dispersibility are inversely correlated for KD and XBD. In addition, the average particle area is smaller for XBD than for KD for all conditions. Therefore, the use of extensional flow-generating segments improves dispersion more than general kneading segments, indicating the effectiveness of extensional flow.

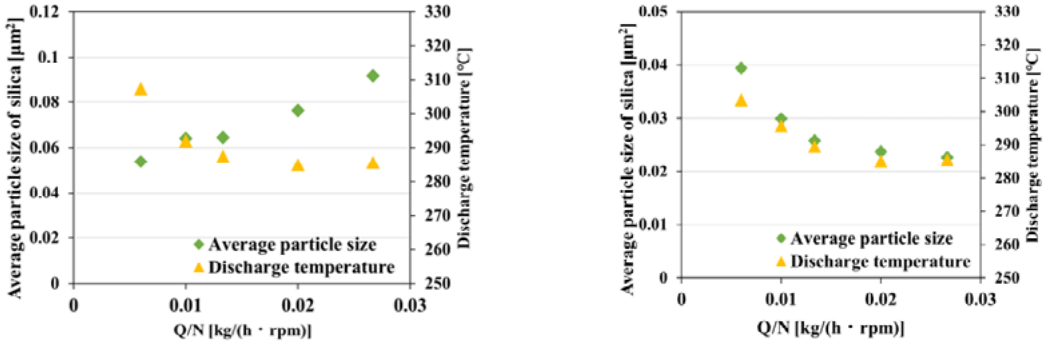

Figure 11. Relationship between dispersibility, discharge temperature and Q/N: (a) KD (b) XBD.

4. PLA/nano silica twin-screw extrusion experiment

Experimental results of twin-screw extrusion of PET/nano silica showed the effectiveness of extensional flow in twin-screw extruders. Based on these results, the extensional flow is used for the twin-screw extruder of PLA/nano silica.

4.1. Experimental Methods

PLA (Zhejiang Hisun Biomaterials, REVODE110) was used as the matrix and nano silica as the filler at 10 wt%. Experiments were carried out with XBD hole diameters of 0.5 mm and temperatures of 165°C. Observations were made using a TM3030Plus and a scanning electron microscope a JSM-7001F (JEOL) at magnifications of 5,000 to 50,000 times.

4.2. Results and Discussion

In order to increase the pressure drop, PLA, which has a melting point more than 100°C lower than that of PET and has the same ester bonding as PET, was used to increase the pressure drop. Figure 12 shows a MB with PLA produced with a feed rate of 3.5 kg/h, a rotation speed of 150 rpm, an XBD hole diameter of 0.5 mm and a pressure drop of 4.23 MPa, as well as an image of the pellets. MB has a large agglomerate of particles, whereas XBD has small particles of about 10 nm. MB is white, while XBD is transparent. This indicates that the aggregates of silica particles are smaller than the wavelength of visible light (400-700 nm).

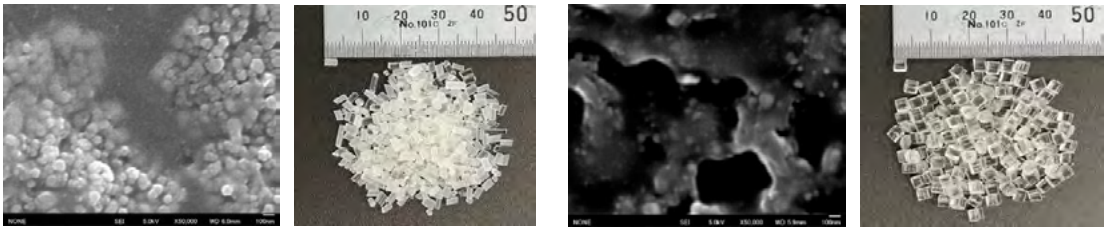

(a) (b)

Figure 12. Optical micrographs at 50,000x and Pellet image: (a) MB (b) XBD.

7. Conclusion

- In extensional flow segments , dispersibility was found to be improved by increasing the pressure drop before and after the BD.
- In twin-screw extruders, it was found that there is a trade-off relationship between improved dispersibility and reduction of discharge resin temperature using conventional segments, whereas extensional flow segments improve both dispersibility and reduce discharge resin temperature, as well as provide excellent dispersibility.
- In PLA/nano silica, transparent pellets were successfully produced by acting on the extensional flow.

References

[1] HIRANO.A, " Development of Nano-ZrO2 Dispersion Materials and its Applications" , Function & Materials, Vol35, No.11(2015) , p38-43(in Japanese).
[2] S.O. Carson, J.A. Covas and J.M. Maia, A New Extensional Mixing Element for Improved Dispersive Mixing in Twin-Screw Extrusion, Part 1: Design and Computational Validation, Adv. Polym. Technol., Vol.36 (2017), pp.455-465.
[3] MUTOU.H, " Electrostatic Adsorption assembly Technique of Nano-Materials to Development of Novel Composite materials" , Function & Materials, Vol35, No.11(2015) , p44-58(in Japanese).
[4] H.P. Grace, dispersion phenomena in high viscosity immiscible fluid systems and application of static mixers as dispersion devices in such systems, Chemical Engineering Communications, Vol.14(3-6) (1982), pp.225-277.
[5] F. N. Cogswell, converging flow of polymer melts in extrusion dies, Polymer Engineering and Science, vol12(1972), pp64-73.
[6] TANAKA.T, MATSUMOTO.K, Multi-axis kneading machine and method for producing nanocomposites using this multi-axis kneading machine and disk-type segments for these, Japanese Patent No. 6532628 (2019).
[7] TAKAKI.T and NISHIURA.K," Transparent Gas-barrier Organic-inorganic Nano-composite Materials" , Journal of the Adhesion Society of Japan, Vol.47, No.5(2011) , p198-202(in Japanese).
[8] KATSURA.T, Recent Trends in Gas-barrier Films and PET Bottles, Journal of the Japan Society of Polymer Processing, Vol.21, No.5(2009) , p234-240(in Japanese).
[9] Kim.Y, AKIYAMA.S, MATSUDA.A, Chemical Reactions and Phase Structures Induced in Polycarbonate (PC)/Nylon Alloys by Maleic Anhydride-Allyl Compatibilizers, Kobunshi Ronbunshu, Vol. 53, No. 3 (1996), pp. 169-75(in Japanese).
[10] MIYAZAKI.H, "Development and deployment of plastic additives for sustainable society," Plastics Age, Vol.68, No.4(2022), p.37-41(in Japanese).
[11] KAMIYA.H, " Resent Research Trend of Nanomaterial Dispersion and Aggregation Behavior Control" , Function & Materials, Vol35, No.11(2015) , p4-10(in Japanese).

CHARACTERIZATION AND OPTIMIZATION OF THE FORMING BEHAVIOR OF THE TEXTILE PREFORMS BY TRIMMING

Jian Hu[1], Xavier Legrand[1], Peng Wang[2]

[1]University of Lille, ENSAIT, GEMTEX, F-59056 Roubaix, France.
Email: jian.hu@ensait.fr, xavier.legrand@ensait.fr
[2]University of Haute Alsace, ENSISA, LPMT, F-68093 Mulhouse, France.
Email: peng.wang@uha.fr

Keywords: forming, textile, trimming, shear angle, wrinkling

Abstract

In industrial applications, the geometries of textile-reinforced composites are gaining increasing attention due to their high flexibility in fiber reinforcement. These composites can be directly manufactured into their final shape without the need for additional assembly operations. To optimize the manufacturing process of composite preforms reinforced by trimming, it is important to study the forming behavior of these trimmed preforms, particularly the influence of the trimming position. This paper aims to investigate the formability of different trimmed performs during hemispherical forming. Various forming defects, such as maximum material draw-in, shear angle, and wrinkling, were explored. The results indicate that different trimming methods have little impact on the punch force under the same pressure and can also decrease the shear angle in the corners. Additionally, different trimming methods affect the pressure dispersion in the non-forming area under the bland-holder, thereby influencing the maximum material draw-in. Suitable trimming methods have the potential to mitigate wrinkling defects.

1. Introduction

Glass fiber-reinforced composite materials have seen a significant increase in their industrial applications in recent years. This is primarily due to their exceptional characteristics, including high strength, lightweight construction, superior corrosion resistance, and remarkable durability [1, 2]. Glass fiber reinforcement composite materials are widely employed in the marine and piping industries due to their excellent environmental resistance, ability to recover from damage caused by impact loading, and high specific strength and stiffness properties [3, 4]. Overall, the Liquid Composite Molding (LCM) process has proven to be a viable and promising solution for cost-effective, high-volume production of composites. With its ability to produce complex shapes, reduce costs, and offer versatility, LCM has the potential to revolutionize the composite manufacturing industry [5–7]. Forming or preforming is a crucial initial stage in the LCM process for the production of textile-reinforced composites, performed before the resin infusion procedures [8]. Ensuring precise control over the orientation of fibers is crucial to prevent the occurrence of fiber misalignments and wrinkles. These imperfections can have a detrimental effect on the mechanical properties of the composite part [9, 10]. Therefore, the study of forming behavior has become an increasingly significant issue over the years in academic discourse.

The simulation of predicting the orientation stresses experienced by the material, and the occurrence of forming defects such as wrinkling, buckling, bridging, yarn sliding, and misalignment of yarns has gained widespread popularity in academic research. The collaborative efforts led by Philippe Boisse [11–15], Peng Wang [12, 16], Damien Soulat [17–19] and other team have significantly advanced the field of forming process simulation. Their work encompasses the development of various models aimed at predicting crucial parameters such as shear angle, wrinkling, maximum materials draw-in and more

throughout the forming process. However, the consideration of numerous material properties (including in-plane tension, in-plane shearing, transverse shearing, bending behavior, friction, and yarn orientation) alongside forming device parameters (such as punch speed, blank holder pressure, and punch shape and size) poses a challenge in accurately predicting forming defects [20,21]. Thus, depending on the type of preforms, the forming processes can range from simple and controlled methods to much more delicate processes which are still the subject of intensive research and discussion.

Therefore, numerous experiments are imperative to consider the impact of process parameters fully. Moreover, recent research has proposed novel forming strategies aimed at minimizing forming defects and enhancing stress and strain distributions within the material. For instance, the adoption of incremental shaping necessitates multiple punches for a single mold [20, 22]. Often, the employment of blank-holders can subject the reinforcement to cyclic loads as well. The findings indicate a significant reduction in forming defects compared to previous instances where a non-optimized blank holder set was utilized. Buckling of the tows was mitigated by decreasing tension in the vertical tows of the shape while increasing tension in the affected tows. While this process improved geometry, it also led to elevated characteristics such as shear angles, curvature, or fiber tension, potentially impacting the structural integrity of the final product. Additionally, multilayer preforms are particularly susceptible to interlayer slippage. Several numerical and experimental studies have demonstrated that employing various technologies, such as 3D weaving, stitching, tufting, and Z-pinning, can mitigate forming defects. Research on the impact of stitching patterns on forming behaviors has shown that a higher stitch density can decrease material draw-in measurements and fabric shearing. However, this technology is most suitable for multilayered reinforced preforms. In summary, adopting innovative approaches to optimize stress and strain distributions within the preform can effectively diminish forming defects.

This study aims to enhance comprehension regarding the impact of various trimming methods on the formability behaviors of preforms with distinct sequences. A novel approach is proposed to manipulate stress and strain distributions within the preform, thereby regulating local in-plane shear deformation and mitigating forming defects. Three different trimming methods, corresponding to hemispherical punch shapes, were evaluated to ascertain the necessity of specific trimming techniques.

2. Methods and materials

2.1. Materials

In the forming experiments, E-glass plain woven fabric with an areal density of 174 ± 3 g/m^2 was utilized. The preform selected for this study follows a sequence aligned with the orientation of yarns. The dimensions of the tested preforms measure 280×280 mm^2, with a thickness ranging from 1.2 ± 0.2 mm.

2.2. Trimming process

Trimming commonly denotes the procedure of removing surplus material or undesired edges from a fabric or textile item after its formation or sewing. This step is crucial for attaining the intended size, shape, and aesthetic of the ultimate textile product [23]. The trimming process, as employed in this study, involves a straightforward cutting method aligned with the yarn orientation to minimize forming defects. To preserve the integrity of the forming area, it's imperative to meticulously control the length of the trimming. The positioning of the trimming is determined by the maximum or minimum material draw-in and the shear angle of the preform. Fig. 1 illustrates the specific trimming methods and parameters utilized.

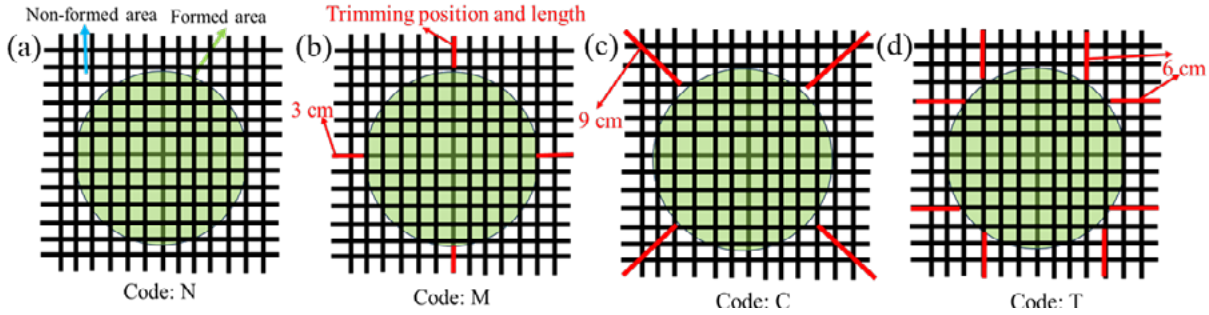

Fig. 1 Different trimming methods: (a) No trimming, (b) Trimming in middle, (c) Trimming in the corner, (d) Trimming around shear angle area

2.3. Forming process

To investigate the effects of trimming approaches on forming behavior, the hemispherical is chosen in this study. The main dimensions of these punches and their orientations to the fabrics have been shown in Fig. 2. The punch is controlled by an electric jack to reach its target location at a given speed. A load sensor (500 N ± 0.3%) records the variation of the punch load during the preforming. A continuous video to record the forming process is shot by a digital camera installed above the specimen. The maximum material draw-in used in this study can be measured by the image extracted from this video using ImageJ. The pre-tensioning system consists of four pneumatic jacks and two transparent blank-holders. This system permits to apply an adjustable pressure on the fabric. The picture of the forming device is shown in Fig. 2. In this study, the pressure of each pneumatic jack linked to the blank-holders is set to 0.05 MPa, and the bottom one used for forming is set to 0.15 MPa to ensure the punch has a constant forming speed of 40 mm/s. The punch pressure and the blank-holder pressure represent the values of the air pressure supplied to the punch and blank-holder respectively.

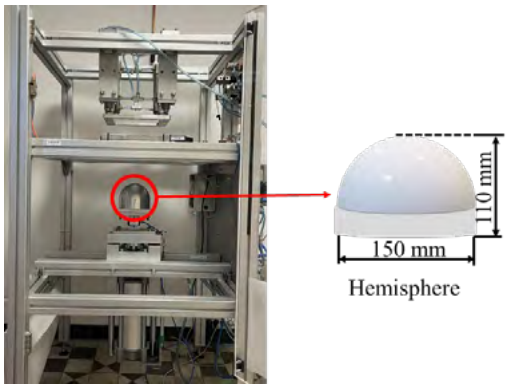

Fig. 2 Forming device

3. Forming results

Four samples of the deformed trimmed preforms post-forming are depicted in Fig. 3. Given that all specimens were arranged in the same sequence, the deformation pattern during forming was consistently quasi-symmetric and similar across samples. To quantify formability, indicators such as maximum punch force and maximum material draw-in on the surface were employed to assess the extent of global deformation. The maximum material draw-in was determined as the mean values at the center of the four sides in Fig. 3. To enhance our understanding of trimmed preforms and their formability during manufacturing, particularly, the investigation of the forming behavior of various trimmed preforms will be conducted by analyzing shear angle and wrinkling.

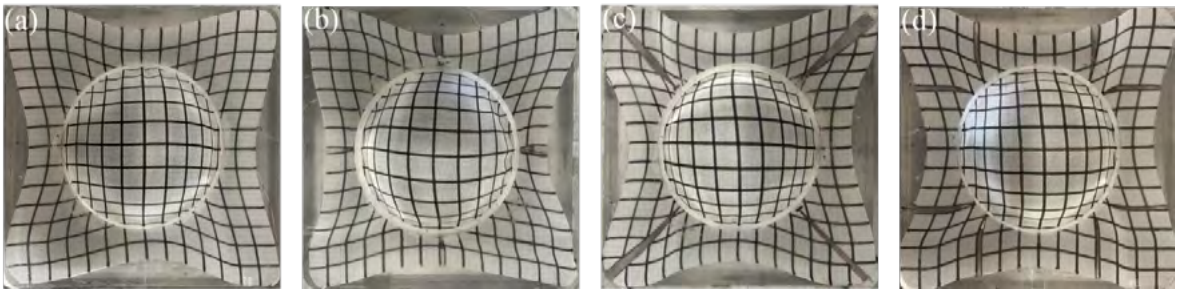

Fig. 3 Forming result: (a) Code N, (b) Code M, (c) Code C, (d) Code T

3.1. Maximum punch force

The maximum punch force for different samples is depicted in Fig. 4 (a). Under a blank-holder pressure of 0.05 MPa, there is minimal variation in the maximum punch force. Compared to Code N, the maximum punch force for Code C decreases by 1.08 N, while for Code T, it increases by 1.14 N. Similarly, there are no significant differences observed between Code T and Code C. This is because the blank-holder evenly distribute pressure across the unformed area, resulting in uniform pressure distribution over the punch, as illustrated in Fig. 4 (b). Consequently, it can be inferred that the impact of trimming approaches on the maximum punch force in hemispherical forming is only noticeable under low blank-holder pressure.

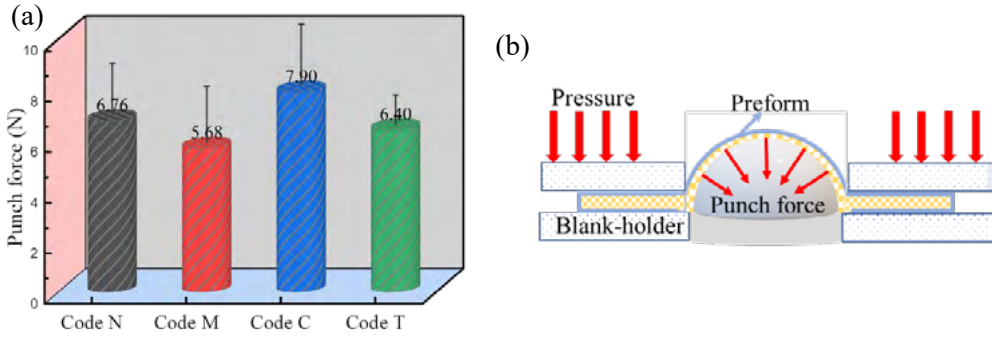

Fig. 4 Punch force: (a) Maximum punch force, (b) Schematic of punch force

3.2. Maximum materials draw-in

Material draw-in is typically assessed by measuring the change in the perimeter shape of the preform, serving as a comprehensive indicator of material deformation during forming [22]. The maximum draw-in is typically observed at the central point of the four sides of the 0°/90° ply. As depicted in Fig. 5 (a), the maximum material draw-in varies with different trimming approaches, with the trimmed preform of Code C exhibiting the smallest maximum draw-in compared to other trimming approaches. In areas where no forming occurs, material is drawn toward the maximum draw-in point. Therefore, aligning the trimming direction with the minimum draw-in helps evenly distribute the punch force. Different trimming methods influence the pressure distribution in the non-forming areas under the blank-holder, consequently affecting the maximum material draw-in.

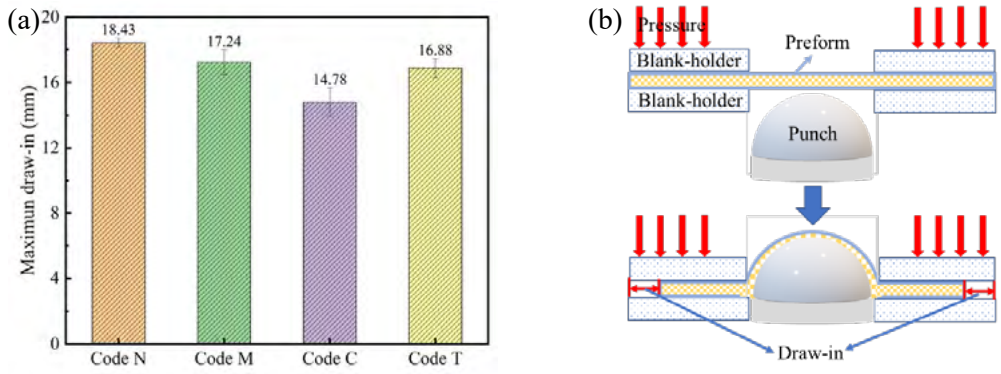

Fig. 5 Materials draw-in: (a) Maximum materials draw-in, (b) Schematic of draw-in

3.3. Shear angle

The shear angle was defined as an appropriate indicator to identify wrinkling defects in different material regions [24]. Fig. 6 shows the distribution of the shear angle under different trimming methods. The results show that the shear angle mainly appears at the four corners of the preform. Besides, the trimmed position of Code C reduces the shear angle at the corner. And shear angle could be increased at the non-forming area with the trimmed position of Code T. These results highlight the consequence of choosing an appropriate trimming method and emphasize the importance of developing a trimming method to reduce excessive shear deformation and decrease the shear angle at the non-forming area.

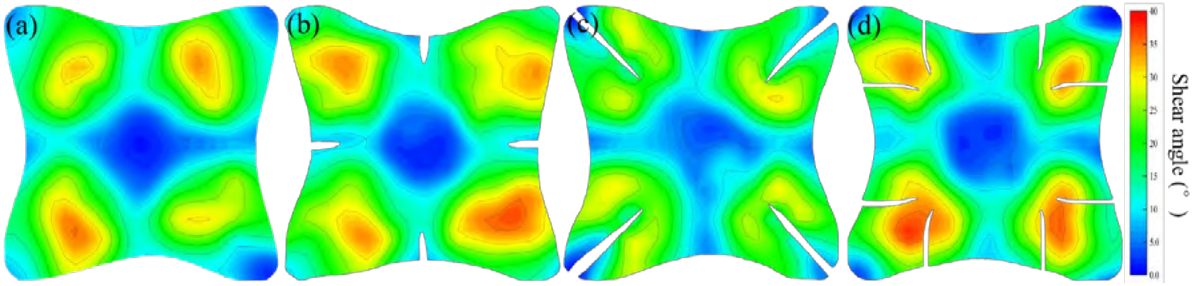

Fig. 6 Shear angle:(a) Code N, (b) Code M, (c) Code C, (d) Code T

3.4. Wrinkling

Wrinkling stands out as a prevalent issue encountered during the forming of textile composite reinforcements, posing a risk of diminishing the performance of the end product [25, 26]. This defect arises when the energy required for an out-of-plane deformation is lower than that for an in-plane deformation. Fig. 7 illustrates the characterization of wrinkling in our study. The features of wrinkles are assessed based on the number of wrinkles and the height of the deformation compared to the surface. The forming results depicting the wrinkling of various trimmed preforms are presented in the figure. Our findings reveal that different trimming approaches exert varying effects on wrinkles. For instance, in Code N without any trimming, large wrinkles with irregular shapes are observed. The middle trimming position effectively reduces wrinkles compared to Code N, as evidenced by the fewer weaves visible in Fig. 7 (b) compared to Fig. 7 (a). Moreover, the trimming approach of Code C leads to a decrease in the height of the wrinkle appearance by reducing the maximum shear angle. Notably, Code T demonstrates the most favorable forming result with fewer waves, indicating minimal wrinkling. Thus, trimming during the forming process of trimmed preforms can effectively modify the wrinkling phenomenon.

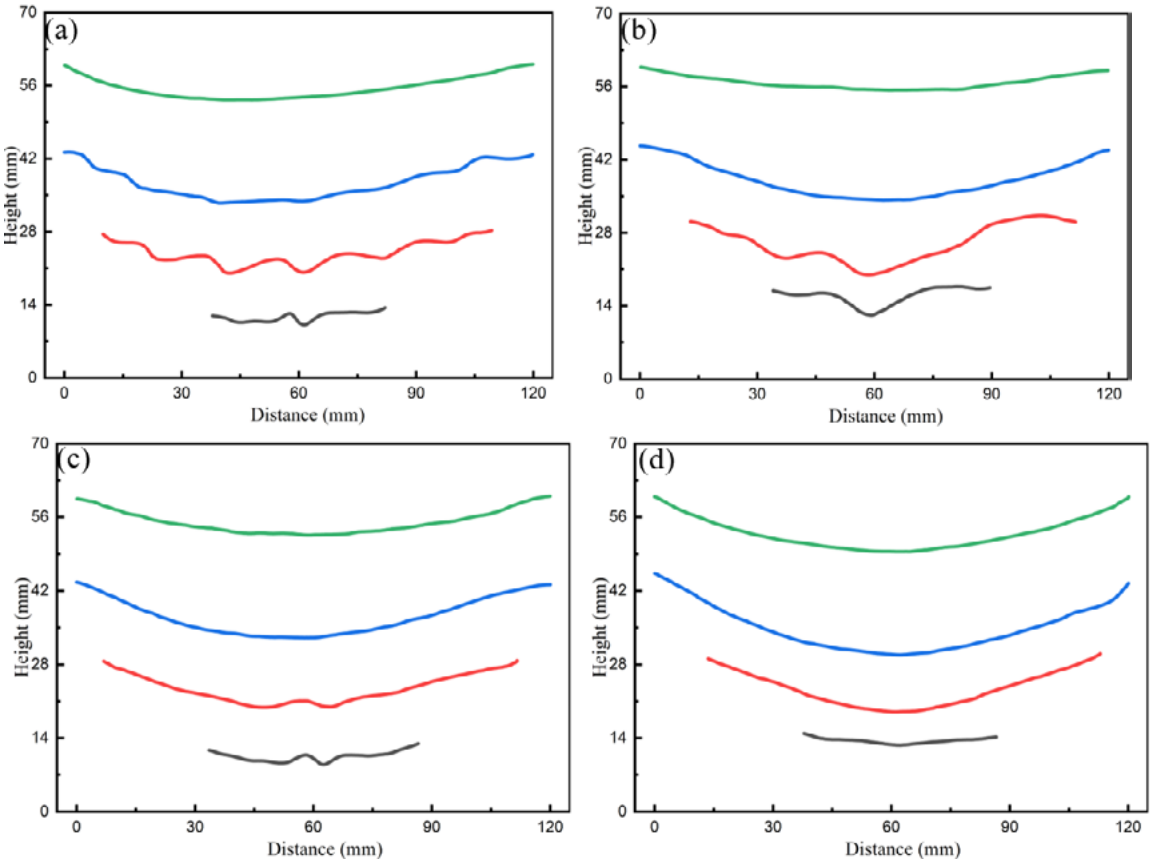

Fig. 7 Wrinkling:(a) Code N, (b) Code M, (c) Code C, (d) Code T

4. Conclusion

In this study, we investigated different trimming approaches applied to preforms aimed at reducing forming defects. A series of experimental investigations were conducted to assess the forming behaviors of the trimmed preforms at the dry fabric scale. Key parameters such as maximum punch force, material draw-in, shear angle, and wrinkling were quantified and evaluated to understand the forming process comprehensively. Our analyses focused on the hemispherical forming processes, revealing that the presence of trimming significantly modified the wrinkling and shear angle of the deformed preform. We observed changes in wrinkles, material draw-in, shear angle, and punch force as the trimming method varied. Suitable trimming methods proved effective in mitigating wrinkling defects. Additionally, the position of trimming influenced material draw-in. Our discussion highlighted the importance of consistent trimming positions, demonstrating that trimmed preforms effectively reduce forming defects. From an economic standpoint, trimming can reduce production costs for preforms with intricate shapes. Currently, our research focuses on trimmed single-layer fabrics, as trimmed multi-layer fabrics have not yet been explored. Therefore, future work will involve optimizing trimmed multi-layer fabrics to minimize forming defects, representing a crucial avenue for further investigation.

Acknowledgments
The research presented in this paper was gratefully acknowledged by financial support from the China Scholarship Council (CSC) (Grant CSC N° 202206920010).

References

[1] Morampudi, P. et al.: Review on glass fiber reinforced polymer composites. *Materials Today: Proceedings*, **43**, 2021, p. 314–319.

[2] Rajak, D.K. et al.: Manufacturing technologies of carbon/glass fiber-reinforced polymer composites and their properties: A review. *Polymers*, **13** (21), 2021, p. 3721.
[3] Stickel, J.M., Nagarajan, M.: Glass Fiber-Reinforced Composites: From Formulation to Application. *International Journal of Applied Glass Science*, **3** (2), 2012, p. 122–136.
[4] Sathishkumar, T. et al.: Glass fiber-reinforced polymer composites – a review. *Journal of Reinforced Plastics and Composites*, **33** (13), 2014, p. 1258–1275.
[5] Naresh, K. et al.: The use of X-ray computed tomography for design and process modeling of aerospace composites: A review. *Materials & Design*, **190**, 2020, p. 108553.
[6] Trochu, F. et al.: Advanced numerical simulation of liquid composite molding for process analysis and optimization. *Composites Part A: applied science and manufacturing*, **37** (6), 2006, p. 890–902.
[7] Rocha, H. et al.: Sensors for process and structural health monitoring of aerospace composites: A review. *Engineering Structures*, **237**, 2021, p. 112231.
[8] Seyednourani, M. et al.: A two-stage optimization methodology for gate and vent locations and distribution media layout for liquid composite molding process. *Composites Part A: Applied Science and Manufacturing*, **149**, 2021, p. 106522.
[9] Liang, B., Boisse, P.: A review of numerical analyses and experimental characterization methods for forming of textile reinforcements. *Chinese Journal of Aeronautics*, **34** (8), 2021, p. 143–163.
[10] Lin, H. et al.: Predictive modelling for optimization of textile composite forming. *Composites Science and Technology*, **67** (15–16), 2007, p. 3242–3252.
[11] Madej, L. et al.: *Material Forming: ESAFORM 2023*. Materials Research Forum LLC, 2023.
[12] Wang, J. et al.: Mesoscopic analyses of the draping of 3D woven composite reinforcements based on macroscopic simulations. *Composite Structures*, **250**, 2020, p. 112602.
[13] Bai, R. et al.: Physics-based evaluation of the drapability of textile composite reinforcements. *Composites Part B: Engineering*, **242**, 2022, p. 110089.
[14] Lahoud, P. et al.: Precision medicine using patient-specific modelling: state of the art and perspectives in dental practice. *Clin Oral Invest*, **26** (8), 2022, p. 5117–5128.
[15] Boisse, P. et al.: Advances in composite forming through 25 years of ESAFORM. *Int J Mater Form*, **15** (3), 2022, p. 39.
[16] Shen, H. et al.: Characterization of wrinkle morphologies by surface waviness evaluation method during deep forming of multilayer composite preforms. *Composite Structures*, **306**, 2023, p. 116586.
[17] Corbin, A.-C. et al.: Towards hemp fabrics for high-performance composites: Influence of weave pattern and features. *Composites Part B: Engineering*, **181**, 2020, p. 107582.
[18] Huang, J. et al.: Experimental and numerical analysis of textile composite draping on a square box. Influence of the weave pattern. *Composite Structures*, **267**, 2021, p. 113844.
[19] Li, M. et al.: Investigation of impact performance of 3-dimensional interlock polymer fabrics in double and multi-angle pass stabbing. *Materials & Design*, **206**, 2021, p. 109775.
[20] Capelle, E. et al.: Complex shape forming of flax woven fabrics: Design of specific blank-holder shapes to prevent defects. *Composites Part B: Engineering*, **62**, 2014, p. 29–36.
[21] Chen, S. et al.: Inter-ply stitching optimisation of highly drapeable multi-ply preforms. *Composites Part A: Applied Science and Manufacturing*, **71**, 2015, p. 144–156.
[22] Denis, Y. et al.: A dissipative model for deep-drawing simulations: Elastic springback prediction and incremental forming strategies. *Composites Part A: Applied Science and Manufacturing*, **149**, 2021, p. 106547.
[23] Nguyen, D. et al.: The effect of fiber orientation on tool wear in edge-trimming of carbon fiber reinforced plastics (CFRP) laminates. *Wear*, **450**, 2020, p. 203213.
[24] Boisse, P. et al.: Simulation of wrinkling during textile composite reinforcement forming. Influence of tensile, in-plane shear and bending stiffnesses. *Composites Science and Technology*, **71** (5), 2011, p. 683–692.
[25] Guzman-Maldonado, E. et al.: Experimental and numerical analysis of wrinkling during forming of multi-layered textile composites. *Composite Structures*, **208**, 2019, p. 213–223.
[26] Shen, H. et al.: Characterisation and optimisation of wrinkling during the forming of tufted three-dimensional composite preforms. *Composites Part A: Applied Science and Manufacturing*, **127**, 2019, p. 105651.

FIRST-PRINCIPLES STUDY ON THE MECHANICAL PROPERTIES OF CITRIC ACID-MODIFIED CELLULOSE COMPOSITE POLYMERIC MATERIALS

Takeru Komyo[1], Chao Luo[2], Yasutomo Uetsuji[2*]

1. Graduate school of engineering, Osaka Institute of Technology. Osaka, Japan
* m1m24412@st.oit.ac.jp
2. Department of Mechanical Engineering, Osaka Institute of Technology. Osaka, Japan
* yasutomo.uetsuji@oit.ac.jp

Keywords: reversible crosslinking, cellulose composites, first-principles calculations, hydrogen bonding, stress-strain relationships

Abstract
The mechanical properties of cellulose fiber-reinforced polymer composites with reversible cross-linking were investigated atomistically as a polymer material that simultaneously satisfies the two properties of sustainability and toughness. 2-hydroxypropyl acrylate and 2-methoxyethyl acrylate were employed as the primary and secondary polymers, respectively. Citrate-acid modified cellulose (CAC) was used as the reinforcing fiber, and reversible crosslinking with β-cyclodextrin as the host molecule and adamantane as the guest molecule was introduced to toughen the base material. First-principles calculations based on density functional theory were used to analyze the bonding forces between the constituent molecules in the CAC composite. The first-principles calculations were used to investigate the bonding forces between the guest-host structures, the effect of citric acid denaturation on the strength of the cellulose interface, and the compatibility between the parent polymers. First-principles calculations provided atomistically consistent explanations of the experimental results and elucidated the strengthening mechanism of the CAC composites.

1. Introduction

In recent years, environmental protection has been emphasized, and attempts have been made to reduce weight by using polymeric materials in the fields of automobiles and aircraft. At the same time, however, carbon cycling is an ideal goal we must achieve toward a carbon-neutral society, and the first step toward this goal is to reduce the number of petroleum-derived components. Cellulose fiber is a plant-derived, highly abundant biofiller. Cellulose has high stiffness and strength, making it an effective reinforcing material in polymer composites [1-2]. However, because cellulose is hydrophilic, surface modification is necessary for mixing with hydrophobic base polymers. Cellulose acetate, in which hydroxyl groups in cellulose are acetylated, and cellulose modified with citric acid (CAC), in which citric acid is substituted, are expected to improve compatibility with polymers and mechanical properties [3].

On the other hand, another approach to reduce the use of petroleum-based resources is to toughen polymeric materials to improve their durability. Polymeric materials can be toughened by energy dissipation mechanisms. Preparation of toughened polymeric materials based on various concepts incorporating supramolecular cross-linking, topological cross-linking, sacrificial bonding, structural uniformity, and a single cross-network of secondary permeable linear polymers has been conducted.

In this study, CAC was employed as the reinforcing material, 2-hydroxypropyl acrylate (HPA) as the primary polymer of the matrix and 2-methoxyethyl acrylate (MEA) as the secondary polymer. CAC was used as the reinforcing fiber, and β-cyclodextrin (βCD) as the host molecule and adamantane (Ad) as

the guest molecule were introduced as reversible cross-links to toughen the matrix. Reversible cross-links are formed by the inclusion of Ad, a cage-shaped molecule, in the vacancies of β-CD, which has a cyclic molecular structure. Therefore, the reversible cross-linking by host-guest interaction is expected to realize a longer service life as a material with self-healing properties that enables adhesion of fractured pieces without adhesives [4-5]. In a previous study [6], host-guest cross-linked CAC composites were created and the effect on mechanical properties was verified, but the mechanism is unknown. In this study, the mechanical properties of cellulose composites with movable cross-links were elucidated atomistically.

2. Methods

2.1 First-principles calculation

The calculations in this work were based on the DFT and employed the quantum mechanics calculation program, CASTEP [7] that use the Material Studio (Dassault Systems). A plane-wave basis set was utilized to expand the single-particle Kohn-Sham wave functions. The generalized gradient approximation of the Perdew-Burke-Ernzerhof (GGA-PBE) [8] was applied to estimate the exchange-correlation energy. The projector-augmented wave (PAW) [9] was employed to consider the interaction between the ion cores and valance electrons. The Monkhorst-Pack scheme [10] was used for the Brillouin zone (BZ) integration.

2.2. Method for evaluating bonding strength between constituent molecules

In this study, we clarify the intermolecular interactions that exist within CAC composites. First, the intermolecular forces, especially the cohesive energy between molecules interacting through hydrogen bonds, were evaluated. In general, the cohesive energy E_co is defined as the difference between the total energy E_ag when two molecules are cohesive and the total energy E_se when two molecules are well separated, and is calculated by the following equation.

$$E_{co} = E_{se} - E_{ag} \tag{1}$$

Next, a virtual force was applied to a local model of two molecules bound together to obtain an atomic-level stress-strain relationship. In the virtual loading test, one molecule was fixed and the other molecule was subjected to a forced displacement in the direction that pulled the two molecules apart. At each loading level, a stable configuration with minimum energy was searched for, and the stress was obtained as the partial derivative of the total energy with respect to the loading strain.

3. Results and discussion

3.1. Intermolecular interactions within the polymer matrix

The intermolecular interactions within the base polymer present in composite materials are evaluated based on the cohesive energy. For the first-principles calculations, we created a bonding structure in which dimers extracted from the molecular chain are ideally aggregated. Figure 1 shows three analytical models, and Figure 2 shows the calculated aggregation energies for these models. Figure 2 shows that the cohesive energy of HPA-HPA is the largest, followed by HPA-MEA and MEA-MEA. The binding energy of hydrogen bonding is known to be about 2eV. Based on the distance between the oxygen and hydrogen atoms in the model, it is assumed that hydrogen bonds are formed at two locations at the molecular interface in the HPA-HPA model and at one location in the HPA-MEA model. In both cases, the hydroxy group at the tip of the side chain of the HPA molecule forms the hydrogen bond. In the MEA-MEA model, on the other hand, no hydrogen bond is expected to form, and the presence of a methyl group at the end of the side chain prevents the formation of a hydrogen bond between the MEA molecules. The cohesive energy in Figure 2 can be explained by the hydrogen bonds formed at the molecular interface.

©2024 | 2_KOMYO_Takeru_8NQKR.pdf:2

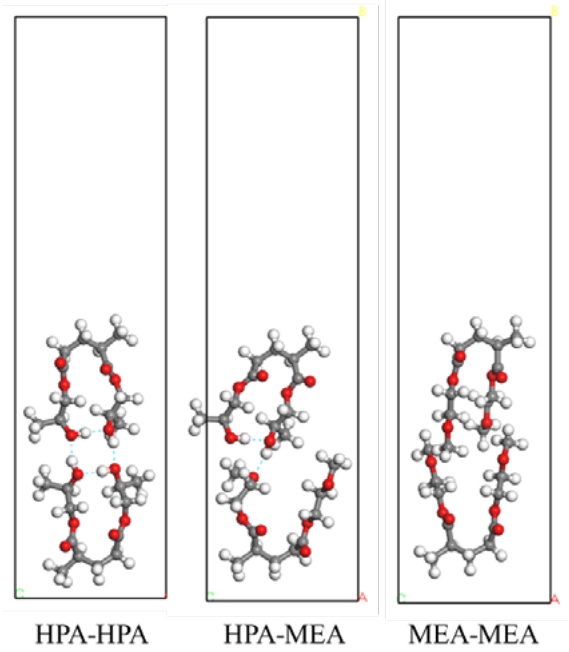

Fig.1 Molecular structures for different combination of matrix polymers

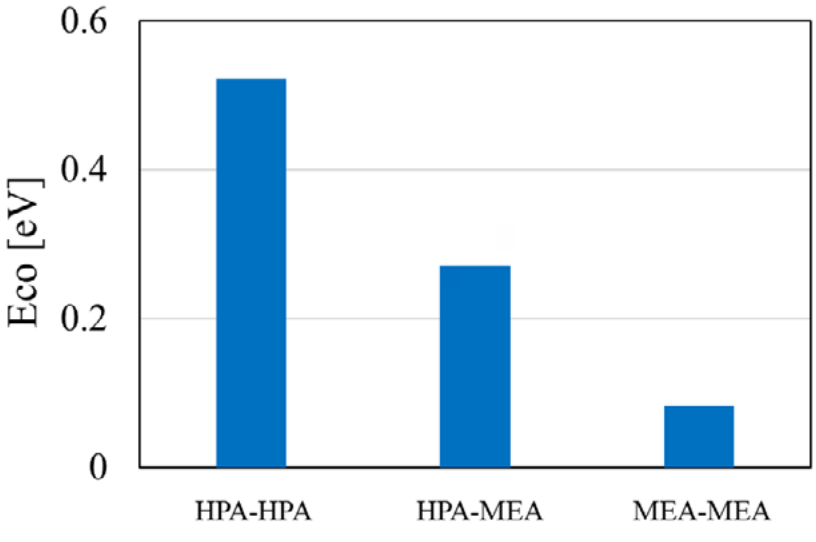

Fig.2 Comparison of cohesive energy among different combinations of matrix polymers

3.2. Citric acid denaturation of cellulose to polymer

To clarify the effect of citric acid denaturation on cellulose interfacial strength, virtual loading tests were performed on the four combinations shown in Figure 3 to compare stress-strain relationships. For the primary polymer, HPA, CNC-HPA is bonded to CNC without citrate denaturation, and CAC-HPA is bonded to CAC with citrate denaturation. Similarly, for the secondary polymer MEA, CNC-MEA is bound to CNC without citrate denaturation, and CAC-MEA is bound to CAC with citrate denaturation.

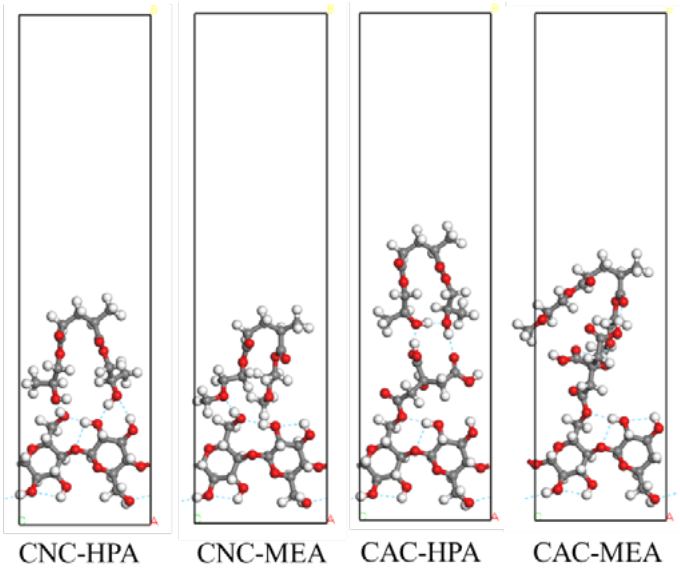

Fig.3 Molecular structures for cellulose interface with and without citric acid denaturation

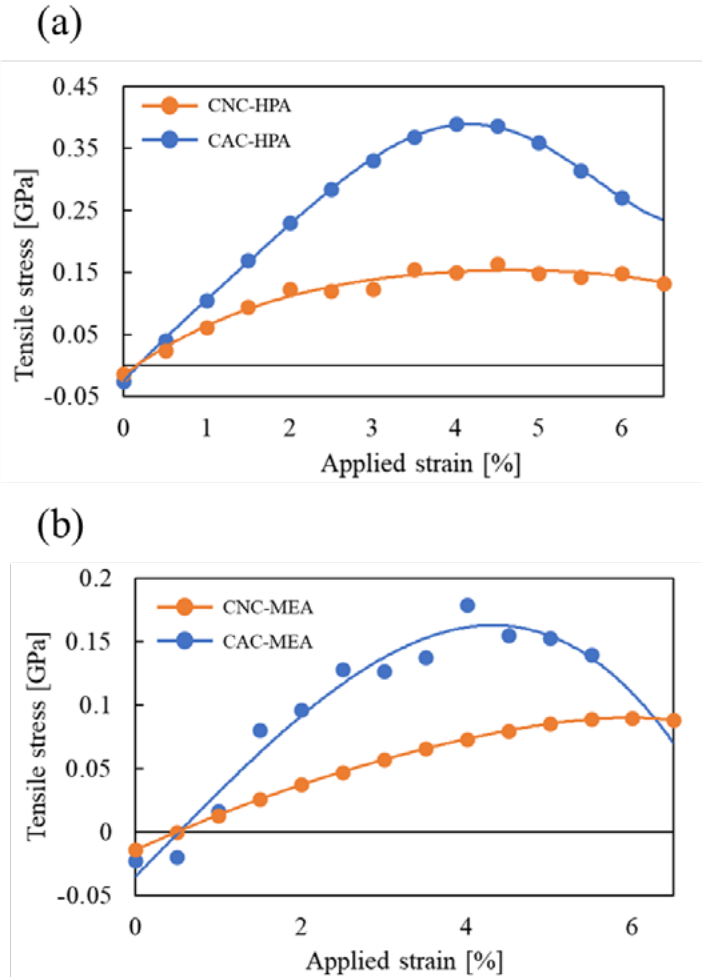

Fig.4 Comparison of stress-strain relation at cellulose interfaces with and without citric acid denaturation

Figure 4 shows the stress-strain relationship obtained from the virtual loading test. The vertical axis indicates the tensile stress of the entire bonded molecular model, and the horizontal axis indicates the applied strain. The results for (a) CNC-HPA and CAC-HPA, which are interaction models of the primary polymer with CNC and CAC, and (b) CNC-MEA and CAC-MEA, which are interaction models of the secondary polymer with CNC and CAC, are compared. CAC-HPA exhibited a maximum tensile stress of 0.390 GPa at 4.0 % applied strain, while CNC-HPA exhibited a maximum tensile stress of 0.163 GPa at 4.5 % applied strain. CAC-MEA and CNC-MEA exhibited a maximum tensile stress of 0.184 GPa at 4.0 % loading strain and 0.089 GPa at 6.0 % loading strain, respectively. The maximum tensile stress at applied strain is reduced.

4. Conclusion

The intermolecular interactions in polymer composites with reversibly cross-linked HPA as primary polymer, MEA as secondary polymer, and CAC as reinforcing fiber were analyzed atomistically based on first-principles calculations. The results showed that the cohesive energies of HPA-HPA, HPA-MEA, and MEA-MEA were smaller in that order and correlated well with the number of hydrogen bonds formed between the molecules. The interfacial strength of cellulose to HPA and MEA increased 2.4- and 2.1-fold, respectively, after citric acid denaturation. In other words, the effectiveness of citric acid denaturation for CNC was atomistically clarified.

References

[1] Akira Isogai, Cellulose Nanofiber, *Surface Technology*, Vol.71, No.6, 2020.
[2] Hiroyuki Yano, Production and Utilization of Cellulose Nanofibers, *Journal of Functional Paper Research Society*, No. 49, 15-20, 2020.
[3] Xinnan Cui, Toshiki Honda, Taka-Aki Asoh, et al. Cellulose modified by citric acid reinforced polypropylene resin as fillers, *Carbohydrate Polymers*, Vol.230, 115662, 2020
[4] Hinako Tsuchiya, Yuki Asaki, Garrry Sinawang, et al. Cellulose Nanofiber Composite Polymeric Materials With Reversible and Movable Cross-links and Evaluation of their Mechanical, *ACS Applied Polymer Materials*, 4, 403-412, 2021.
[5] Tommaso Auletta, Menno R. de Jong, Alart Mulder et al. β-Cyclodextrin Host-Guest Complexes Probed under Thermodynamic Equilibrium: Thermodynamics and AFM Force Spectroscopy, *Journal of the American Chemical Society*, 126(5): 1577-1584, 2004.
[6] Takuma Wada; Junsu Park, Kenji Yamaoka, Yuki Asaki, Akihide Sugawara, Ryohei Ikura, Yuya Takahashi, Naomi Takenaka, Yasutomo Uetsuji, Hiroshi Uyama, Yoshinori Takashima, “Material Design of Citric Acid-Modified Cellulose Composite Polymeric Materials with Both Tough and Sustainable Enhancement by Multiple Noncovalent Bonds”, ACS Applied Polymer Materials, 5 (2023-11) 10334-10341.
[7] Segall MD, Lindan PJD, Probert MJ, Pickard CJ, Hasnip PJ, Clark SJ, Payne MC (2002) First-principles simulation:ideas, illustrations and the CASTEP code. J Phys : Condens Matter 14 : 2717-2743
[8] Perdew JP, Burke K, Ernzerhof M (1996) Generalized Gradient Approximation Made Simple. Phys Rev Lett 77 : 3865.
[9] Kresse G, Joubert D (1999) From ultrasoft pseudopotentials to the projector augmented-wave method. Phys Rev B 59 : 1758
[10] Pack JD, Monkhorst HJ (1977) "Special points for Brillouin-zone integrations"—a reply. Phys Rev B 16 : 1748

TURNING MACHINABILITY OF CAST ALUMINUM ALLOY MATRIX COMPOSITES

Jinrong Liu[1], Kazunori Asano[1], Mutsuo Hayashi[2], Shuhei Katsumata[2] and Shogo Ochiai[2]

[1] Kindai University, Higashi-osaka, Osaka, 577-8502, Japan
[2]Advanced Composite Corporation, Fuji City, Shizuoka, 417-0801, Japan
E-mail: 2333330366d@kindai.ac.jp asano@mech.kindai.ac.jp
katsumata@advance-composite.co.jp m.hayashi@advance-composite.co.jp
ochiai@advance-composite.co.jp

Keywords: aluminum, composites, carbon fibers, SiC particle, machinability,

Abstract
The machinability of fiber-reinforced and particle-dispersed aluminum alloy composites were evaluated. PAN-based carbon fibers (CF) and silicon carbide particles (SiC_p) were used as the reinforcing materials. Aluminum alloy composites were fabricated by squeeze casting. Optical microscopy revealed that CF and SiC_p were randomly distributed within the alloy matrix. During the machining of CF-reinforced composites, the cutting resistance values show larger fluctuations compared to those of SiC_p-dispersed composites and the unreinforced alloy. An increase in the volume fraction of SiC_p results in higher cutting resistance. CF-reinforced composites offer lower average cutting resistance values than the unreinforced alloy. The roughness of machined surface tends to decrease due to the reinforcement; particularly, the reinforcement with fine-SiC_p enhances the smoothness of the surface. Observation of the machined surface indicated that the reinforcement suppressed the formation of built-up edge, leading to the smoother surface.

1.Introduction

Aluminum alloys are widely used in many industrial applications due to their light weight and excellent oxidation resistance. However, their use in components requiring high temperature strength, rigidity, wear resistance, and low thermal expansion is limited. To address these limitations, non-metallic fibers and particles have been proposed to reinforce aluminum alloys. Carbon fiber (CF), which has low density, high strength, high stiffness and low thermal expansion, would be one of the most promising reinforcement materials [1]. Silicon carbide particle (SiC_p) is also widely used as reinforcement materials. Studies have been carried out on the effects of Al_4C_3 formation at the fiber-matrix interface on the mechanical properties of composites prepared through melt infiltration techniques [2]. Although the microstructure [3], mechanical and thermal properties [4], and wear characteristics [5] of the composites have been investigated, the machinability, which is one of the most important properties for the industrial application of these composites, remains unclear.

In this research, PAN-based CF reinforced aluminum alloy composites were prepared using the squeeze casting and their machinability was compared with SiC_p -dispersed aluminum alloy composites and unreinforced aluminum alloys under various cutting conditions.

2. Experimental Procedure

The JIS-AC8A alloy (Al-12Si-1Cu-1Ni-1Mg-alloy casting) was used as the matrix, PAN-based short CF was used as the reinforcing material. The properties [6] of the CF and SiC_p are listed in

Table 1. To fabricate the fibrous preform, the CF were mixed with polyvinyl alcohol as an organic binder and silica sol as an inorganic binder in a water. The mixture was then pressed into a shape with a diameter of 50 mm and a height of 20 mm using a cylindrical mold at ambient temperature. The green compart was then dried at 453 K for 2 hours. The fiber volume fraction in the preform was controlled 25 vol%. SiC_p preforms were also formed using similar procedure.

The composite was fabricated by squeeze casting. The preform was horizontally placed in a permanent mold, and the molten AC8A alloy at 1073 K was poured into the mold (preheated to 673 K). A pressure of 40 MPa was applied rapidly and maintained until solidification was complete. The types and proportions of reinforcement materials for each composite are listed in Table 2.

Test piece with a diameter of 40 mm were machined from the composite, and their machinability during turning operations was examined by machining the surface of the pieces using a lathe. The cutting conditions are listed in Table 3. The cutting resistances (cutting force: F_x) were measured using the lathe equipped with an elastic disc-type tool dynamometer. The roughness of the machined surface (maximum height of profile, R_z) was measured using a laser scanning digital microscope, and the morphology of the chips was observed using SEM.

Table 1. Properties of the CF and SiC_p.

Reinforcement	Density (Mg/m^3)	Length (μm)	Diameter (μm)	Thermal conductivity (W/(mK))	Coefficient of thermal expansion(K^{-1})	Elastic modulus (GPa)
CF	1.76	130	7	10-15	-0.4×10^{-6}	230
SiC_p	3.16	-	4-25	60-200	4.0×10^{-6}	-

Table 2. The types and proportions of reinforcements for the composites.

	Reinforcement A	Reinforcement B	Particle size of A (μm)	Volume fraction of A (vol%)	Particle size of B (μm)	Volume fraction of B(vol%)
25PAN	PAN	-	-	-	-	-
No.5	SiC	A6061	4	32	20	27
No.10	SiC	A6061	25	30	20	25
No.5(2)	SiC	-	4	52	-	-
No.10(2)	SiC	-	25	52	-	-

Table 3. Dimensions of the tool and cutting conditions used.

Cutting tool	PCD
Nose radius (mm)	0.8
Rake angle (°)	+5
Installation angle (°)	15
Cutting depth t (mm)	0.2, 1.0
Feed rate f (mm/rev)	0.1, 0.2
Cutting speed v (m/min)	50, 100, 150

3. Results and Discussion

3.1 Microstructure

Figure 1 is the optical micrographs of the unreinforced alloy and composites, showing that the CF and SiC_p are randomly distributed within the alloy matrix.

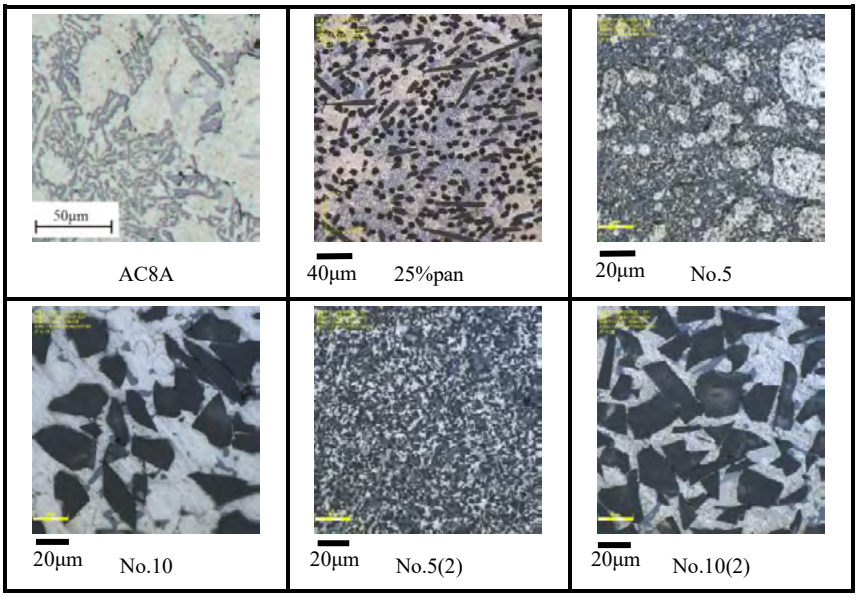

Figure 1. Optical micrographs of the unreinforced alloy and composites.

3.2 Cutting Resistance

Figures 2 is the waveforms showing the change in the cutting force (F_x) during the machining of the unreinforced AC8A alloy and composites at a cutting speed (v) of 150 m/min, a feed rate (f) of 0.2 mm/rev, and a cutting depth (t) of 1.0 mm. The fluctuation range of cutting force for the CF-reinforced composite was broader compared to that of the unreinforced AC8A alloy, although the average F_x is lower. In contrast, the fluctuation range for the SiC_p- dispersed composite (samples No. 5, 10, 5(2) and 10(2)) was narrower than that of the unreinforced alloy, although the average F_x is higher. No functional relationship between the range of cutting force fluctuations and the SiC_p size in the composites was observed. samples containing A6061 powder (samples No. 5 and 10) exhibited slightly larger fluctuations in F_x during cutting than those without A6061 powder (samples No. 5(2) and 10(2)).

Figure 3 is the average F_x of materials, showing that the reinforcement with the CF effectively

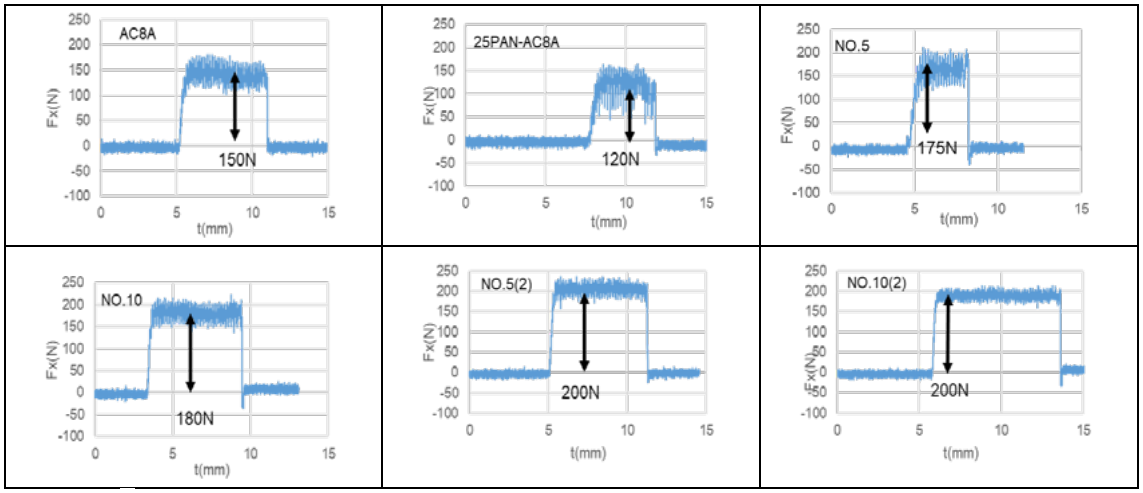

Figures 2. Waveforms showing the change in the cutting force (F_x) during the machining of the unreinforced AC8A alloy and composites at a cutting speed (v) of 150 m/min, a feed rate (f) of 0.2 mm/rev, and a cutting depth (t) of 1.0 mm.

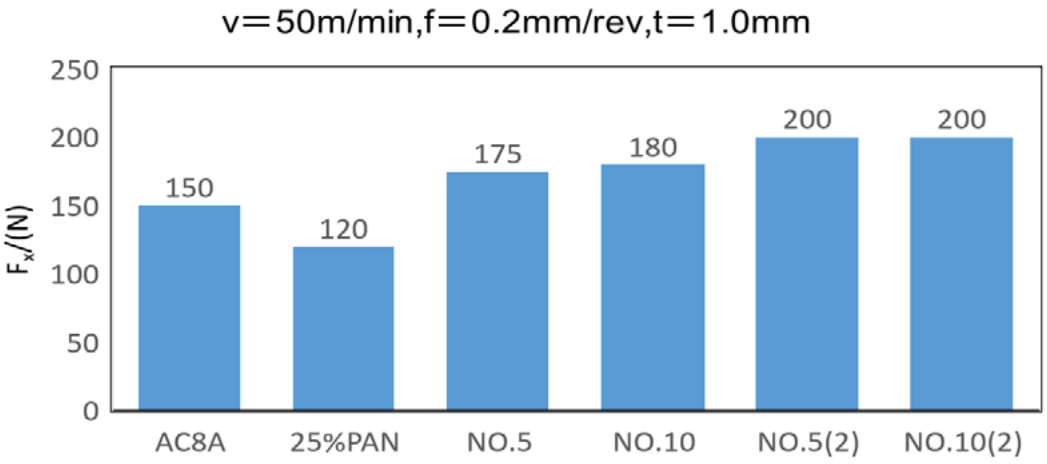

Figures 3. Average F_x of materials.

reduced the average F_x of the alloy, while SiC_p increased it.

The F_x values for various composites as well as the unreinforced alloy increased with the increase in cutting depth (t) and feed rate (f), while the effect of v on the F_x is smaller compared to the effects caused by the increases in the f and t.

3.3 Machined Surface

Figure 4 illustrates the waveform showing the change in the surface roughness (R_z) during the machining of the unreinforced AC8A alloy, CF-reinforced composite, and SiC_p-dispersed composite at a cutting speed (v) of 150 m/min, a feed rate (f) of 0.2 mm/rev, and a cutting depth (t) of 1.0 mm. The AC8A alloy exhibits a mixture of small and relatively large waves on its surface. The composites reinforced with CF and SiC_p tend to show smaller waveforms. Notably, with a high volume of fine SiC_p (samples No. 5(2)), the waveforms was smaller and the semicircular shape of the tool tip can be clearly seen. When comparing samples with a high volume fraction of SiC_p (samples 5(2) and 10(2)) to those with a lower SiC particle volume fraction (samples 5 and 10), the latter exhibited coarser small waves, either due to fewer particles or the inclusion of a softer reinforcement B (A6061) compared to AC8A.

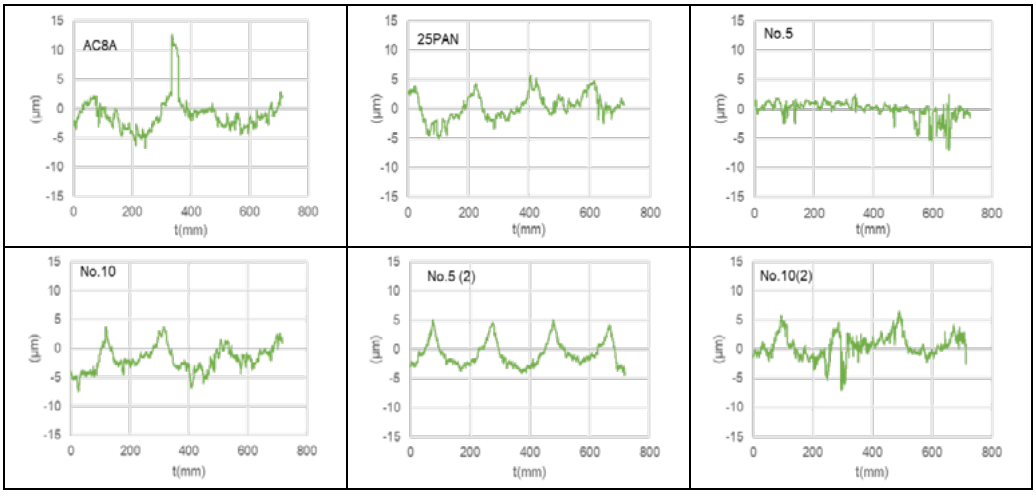

Figure 4 . Waveform diagrams of surface roughness during machining materials.

Figure 5 displays the comparison of surface roughness (R_z) among CF-reinforced composites, SiC_p-dispersed composites, and unreinforced AC8A aluminum alloy.The reinforcement with the CF and SiC_p leads to a reduction in the R_z of AC8A alloy. The R_z of CF composites are significantly smaller than that of SiC_p composites, and there is an obvious positive correlation between the SiC_p diameter, SiC_p volume ratio and surface roughness values among SiC_p composites.

The theoretical roughness can be geometrically calculated from the nose radius of the cutting tool and feed rate [7]. It can be written as

$$R_{th} = \frac{f^2}{8r}$$

where R_{th} is the theoretical roughness and r is the nose radius.

The experimental R_z value of the CF composite was the closest to the R_{th}, indicating that the CF reinforcement has the effect of reducing the formation of the built-up edge during the cutting. Although the R_z values of SiC_p-dispersed composites are higher than those of CF composites, they are still lower than that of unreinforced AC8A.

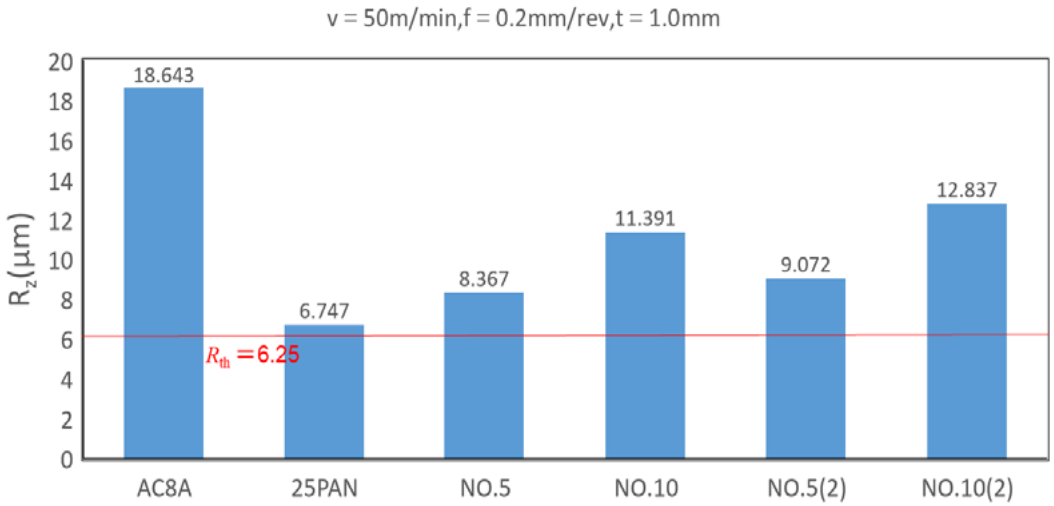

Figure 5. Comparison of surface roughness (R_z) among CF-reinforced composites, SiC_p dispersed composites, and unreinforced AC8A aluminum alloy.

Figure 6 presents the elemental distribution images in the chips of CF-reinforced composites, SiC_p-dispersed composites and unreinforced AC8A aluminum alloy. They reveal that the chips undergo the repeated shear deformations during the cutting. In the unreinforced alloy, this deformation leads to the fragmentation of eutectic silicon into small pieces. Similarly, in the composites, the CF and SiC_p were pulverized into fine fragments due to the repeated shear deformation, and these fragments were randomly distributed throughout the matrix.

4. Conclusions

(1) The fluctuation range of cutting force for the CF-reinforced composite was broader compared to that of the unreinforced AC8A alloy, although the average F_x for the CF-reinforced composite was lower. In contrast, the fluctuation range for the SiC_p-dispersed composite was narrower than that of the unreinforced alloy, although the average F_x is higher. No functional relationship

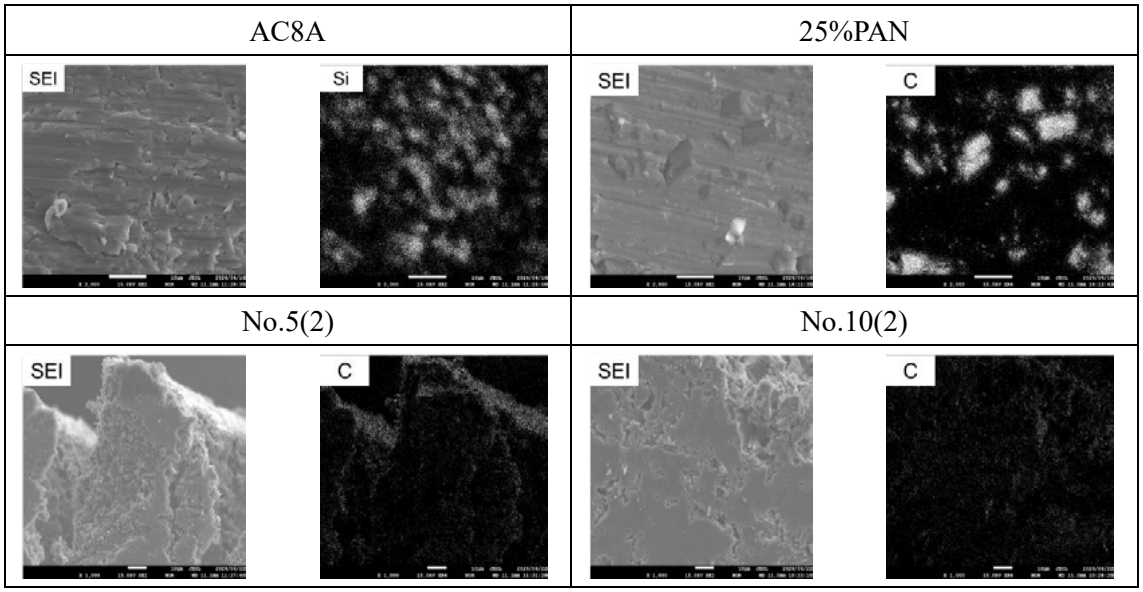

Figure 6. SE images and elemental distribution images within the chips of CF-reinforced composites, SiC_p dispersed composites, and unreinforced AC8A aluminum alloy.

between the range of cutting force fluctuations and the SiC_p size in the composites was observed. The cutting resistance values increased with the volume fraction of SiC_p.

(2) The waves on the surface roughness curves when machining unreinforced AC8A alloy became smaller due to the reinforcement, particurally when a quantity of fine SiC_p was incorporated. The finished surface of SiC_p-dispersed composites was somewhat rougher compared to that of CF-reinforced composites.The incorporation of composites would reduce the formation of built-up edge, resulting in a smoother finish.

References

[1] D. Jang, M. Lee, J. Choi, S. Cho and S. Lee. Strategies for the production of PAN-Based carbon fibers with high tensile strength. *Carbon*, 186: 644-677, 2022.
[2] Y. Zhang, G. Wu, Interface and thermal expansion of carbon fiber reinforced aluminum matrix composites. *Transaction of Nonferrous Metal Society of China*, 20: 2148–2151, 2010.
[3] M. Selvaraj, N. Rajesh and J. Hynes. Influence of processing conditions and issues in Machining of aluminum metal matrix composites. *Materials today proceedings*, 47: 7035-7040,2021.
[4] K. Asano. Thermal expansion behavior of squeeze-cast aluminum matrix composites reinforced with PAN- and Pitch-based carbon fibers. *International Journal of Cast Metals research*, 30: 365–373, 2017.
[5] K. Asano and Muhammad Faiz Bin Zainuddin. Wear Behavior of PAN- and Pitch-Based Carbon Fiber Reinforced Aluminum Alloy Composites under Dry Sliding Condition. *Materials Transactions*, 58: 898-905, 2017.
[6] Nippon Graphite Fiber Corporation: Data sheet for GRANOC, 2015.
[7] Ed.by Kikai Kosakugaku Henshu Iinkai: *Kikai Kosakugaku* (Sangyo Tosho), 148, 2003.

UNDERSTANDING THE SCALE DEPENDENT DUCTILITY OF EPOXIES

Janina Mittelhaus[1], Suprit P. Bhusare[2], Nazanin Pournoori[2], Matti Isakov[2], Turkka Salminen[3], Pekka Laurikainen[2,4], Essi Sarlin[2], Gaurav Mohanty[2], Bodo Fiedler[1]

[1]Institute of Polymers and Composites, Hamburg University of Technology, Denickestr. 15, 21073 Hamburg, Germany
Email: janina.mittelhaus@tuhh.de,
Web Page: https://www.tuhh.de/kvweb/en/institute/people/janina-mittelhaus
Email: fiedler@tuhh.de, Web Page: https://www.tuhh.de/kvweb/en/institute/people/bodo-fiedler
[2] Materials Science and Environmental Engineering, Faculty of Engineering and Natural Sciences, Tampere University, 33720 Tampere, Finland
Email: gaurav.mohanty@tuni.fi, Web Page: https://researchportal.tuni.fi/en/persons/gaurav-mohanty
Email: suprit.bhusare@tuni.fi, Web Page: https://researchportal.tuni.fi/en/persons/suprit-bhusare
Email: matti.isakov@tuni.fi, Web Page: https://researchportal.tuni.fi/en/persons/matti-isakov
Email: essi.sarlin@tuni.fi, Web Page: https://researchportal.tuni.fi/en/persons/essi-sarlin
Email: nazanin.pournoori@tuni.fi, Web Page: https://researchportal.tuni.fi/en/persons/nazanin-pournoori
[3]Tampere Microscopy Center, Faculty of Engineering and Natural Sciences, Tampere University, Korkeakoulunkatu 3, 33720 Tampere, Finland
Email: turkka.salminen@tuni.fi, Web Page: https://researchportal.tuni.fi/en/persons/turkka-salminen
[4]Materials processing and circular solutions, VTT Technical Research Centre of Finland, Visiokatu 4, 33720 Tampere, Finland
Email: Pekka.Laurikainen@vtt.fi, Web Page: https://cris.vtt.fi/en/persons/pekka-laurikainen

Keywords: Epoxy films, Size effect, Shear bands, Digital Image Correlation, Polarized Raman Spectroscopy

Abstract

The interconnecting (epoxy) matrix material in fiber reinforced polymers has a microscopic volume and therefore, different mechanical behavior than standard bulk epoxy samples. It has been found in previous studies that a decreased epoxy gauge volume leads to an increased deformation ability (necking and shear band formation). By using laser cutting to create dogbone samples from manufactured epoxy films, the gauge volume can be further reduced in comparison to previous studies and the ductility can be enhanced even further. To understand load-induced molecular mechanisms responsible for increase in ductility at macroscale, this study combines digital image correlation (DIC) with tension tests and precise force measurement. The global and local strains are generated from the DIC data and achieve values up to 80 % (global strains) and 120 % (local strains), respectively. These strain values are significantly more compared to archetypical brittle epoxy bulk samples (less than 10 %). Polarized Raman spectra show that load-bearing backbone molecules in deformed film samples are oriented in tensile load direction since the intensity there depends on the polarization direction. This might be due to unraveling of entanglements which can be seen as sudden decrease followed by subsequent rise in engineering stress values during deformation.

1. Introduction

Fiber reinforced polymers (FRPs) can often be found in industrial applications that require excellent mechanical performance at low weight, e.g. in aviation or automotive industry. The structure of FRP consists of oriented fibers surrounded by a matrix material, such as an epoxy resin system. This results in a structure with zones of interconnected matrix materials that are in the (sub-) micrometer range, such as resin-rich zones between fibers (around 1 – 25 µm, intralayer) and between reinforcing prepregs or layers (around 10 – 200 µm, interlayer) [1]. The standard characterization of matrix materials is usually performed using macroscopic test volumes such as those specified in the standardized test methods ASTM D638 or DIN EN ISO 527. However, often while modeling FRPs, it is considered that the matrix, containing an epoxy system, has bulk mechanical properties, which may not be true. The bulk mechanical parameters of standard specimens as input for microscale modeling of composite materials can lead to insufficient agreement between the modeled and experimentally observed behavior [1-4]. Beside geometrical constraints, this might be due to the deviation of the mechanical behavior of the microscopic matrix from the macroscopic standard bulk specimens. It has been shown in previous studies that the ductility and plasticity of an archetypical brittle epoxy matrix can be increased by reducing the gauge volume [1, 5]. Especially micro-scale epoxy films exhibit an increased deformation ability due to necking and the formation of shear bands under tension load [6]. However, to date, there is no complete physical, mechanochemical or molecular explanation for the observed size effect regarding the deformation ability and the mechanisms behind the shear band formation.

The mechanical properties of a material are a manifestation of the way in which individual bonds within the material respond to applied macroscopic stress [7]. For film samples, with a comparably small gauge volume, a very sensitive load cell and a suitable micro tension test device is necessary to investigate the mechanical behavior. Performing tension tests with an appropriate setup allows accurate measurement of changes in force (stress) due to molecular processes inside the epoxy material. The strain analysis can be done by applying the digital image correlation (DIC) technique, where the (surface) deformation of the test specimen is observed during the test based on tracking a random speckle pattern on the sample surface. This allows the observation of local deformation mechanisms which lead to the macroscopic measured mechanical parameters.

To study the molecular processes in epoxy materials, which leads to the local and global mechanical response to external stress, Raman spectra can be recorded, beside infrared (IR) spectra, to investigate load-bearing bonds [3, 5]. Both vibrational methods are complementary and allow an overall analysis of the molecular bonds inside the epoxy films. By performing polarized Raman measurements, load-induced molecular backbone orientations can be detected as well. This has been demonstrated for epoxy fibers [5]. Polarized Raman measurements can be performed in the shear bands and the necked region of the deformed and tensile-loaded specimens to analyze the increased local strains there. This facilitates the observation of presumed unraveling of entanglements and molecular alignment due to the tension load.

A combination of these methods will provide a detailed insight into the micromechanical properties of the thermoset matrix as a micro-component of composites. This is important for the optimization of the design and performance of polymeric composites with an epoxy matrix. Furthermore, as the multiscale modelling of composite materials becomes even more popular and essential for the industry, it is necessary to fully understand the required conditions for an increased deformation ability and the underlying mechanisms in epoxy.

Therefore, in this study, a combination of micro-scale tension tests with DIC followed by photoelastic imaging and polarized Raman spectra analysis of the deformed film specimen is used to visualize the deformation and to understand the associated molecular backbone movements and orientation as a result of the applied tension load. A low viscosity resin has been chosen for this study to produce thin epoxy film samples with a previous developed manufacturing method. The samples, which had dogbone geometry with a comparably small gauge volume, were created by a femto-second laser.

2. Materials and Methods

A low viscosity resin system consisting of EPIKOTE™ Resin MGS RIMR 135, which is based on diglycidyl ether of bisphenol A (DGEBA), combined with a liquid aliphatic diamine hardener, EPIKOTE™ Curing Agent MGS RIMH 137 (Westlake, International:USA/Europe) was used. Both components were mixed in a weight ratio of 100:30 in a mixer (SpeedMixer DAC 150.1 FVZ) at 3500 rpm for 5 min. The backbone of the epoxy or DGEBA contains aromatic rings, or more precisely para-phenylene groups, as shown in Figure 1.

2.1. Epoxy film samples

In a previous study, a new infusion manufacturing process was developed and optimized to produce thermoset films with a defined thickness [6]. By using the developed manufacturing method, epoxy films with a thickness of 32.36 ± 2.01 µm were created for this study in the same way. After this procedure, the selected thickness of the films was verified and the utilized dogbone geometry (see Figure 1) was created by femto-second laser cutting. A laser with a wavelength of 343 nm and a beam size (in focus) of approximately 10 µm was used. The cutting speed was set to 175 mm/s which amounts to pulse energy of 4.6 µJ.
The geometric dimensions of the cut dogbone samples deviate from the established standard DIN EN ISO 527-3, as they are predefined by the used microtest grippers for the tension tests and the gauge volume is further reduced in comparison to the previous studies [6] due to limitation in maximum force of the load cell. The gauge length was 4 mm and the gauge volume was about 0.06 mm³ for the chosen dogbone specimen geometry.

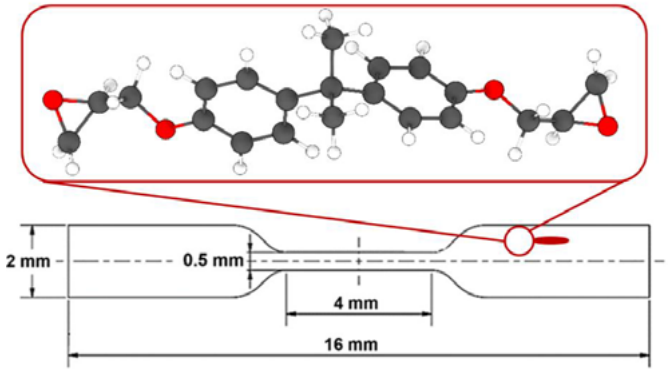

Figure 1. Dogbone sample geometry for tensile tests and chemical structure of DGEBA backbones (gray = carbon atoms, white = hydrogen atoms, red = oxygen atoms).

2.2. Tension tests and DIC analysis

An Alemnis in-situ nanoindenter was modified with grippers to perform tension tests (see Figure 2). Alemnis sample-side load cell (SLC-2.5) was used. This load cell has a load range of 2.5N and load resolution of <15µN. Therefore, all experiments were confined to less than 2N. The displacement was applied using the Z stage of the nanoindenter which is based on piezoactuation mechanism and has a resolution < 10nm. All tests were performed in displacement-controlled mode. A displacement rate of 0.3 mm/min was imposed resulting in a nominal strain rate of 10^{-3} s^{-1} to provide the epoxy material with sufficient time to undergo the (molecular) deformation processes. In total, six samples (three longitudinal and three transverse to the resin flow direction in the film manufacturing process samples) were tension tested with this setup. Supplementing the standard series of tension tests, a second set of tensions tests were carried out using the DIC analysis to obtain information about local strains. In preparation for these tests, some of the epoxy film samples were placed on a paper to color them with a fine stochastic speckle pattern using black spray paint. After the color had dried, the pattern was checked for DIC applicability under an optical microscope.

The samples with a feasible speckle pattern were used for the tension tests combined with DIC. In total, six samples (three longitudinal and three transverse to the resin flow direction in the film manufacturing process samples) with DIC pattern were tested in tension. For this purpose, the tension stage with the clamped sample was positioned under a stereo-optical microscope from Leica with a camera and a USB connection for video and images storage. The magnification was set so that optical resolution of ~0.1 mm/pixel at the gauge section was achieved. The DIC system was calibrated using a calibration plate (a glass plate with rectangular grid of dots placed at 0.5 mm from each other). During the mechanical loading of the samples, 15 images per second were recorded. For the DIC analysis and results presented in this study, every 100th image is used resulting in an effective frame rate of 0.15 images per second, which is considered sufficient for the present purposes. The DIC analysis was performed with LaVision DaVis 10.2.1 software with the following correlation parameters: correlation relative to first frame, 2nd order shape functions and subset size / step size ranging from 19/6 to 23/7 pixels. The resulting deformation data is analyzed in terms of strain fields obtained directly from the calculations as well as in terms of data obtained via post processing, that is virtual extensometer and strain along a line placed longitudinally on the gauge section.

2.3. Polarized Raman spectroscopy

The polarized Raman Spectroscopy measurements were performed with a Renishaw inVia Qontor Raman microscope using a 50x long working distance objective (NA 0.55). The laser wavelength was 532 nm and the spectrometer had a grating with 1200 grooves per millimeter (spectral resolution of 2 cm^{-1}).
The resolution was 0.5 µm in x- and y- direction. To achieve a strong Raman signal, a depth of 2-3 µm close to the surface was chosen.
Before mechanical testing, the six film samples (without DIC pattern) were analyzed in the as-produced state by the polarized Raman microscope to identify the initial molecular state. Therefore, polarized Raman spectra at 4 different sample positions in the gauge length are recorded. For every measurement position, measurements in polarization mode or setup XX and ZZ (see Figure 5 for directions) for 120 seconds were performed. After mechanical loading and final failure, Raman spectra was recorded in both different polarization modes in the visible deformed and necked sample regions with shear bands. The raw data was processed by a 4th order polynomial baseline correction.

3. Results and discussion

3.1. Tension tests and DIC analysis

Figure 2 shows a representative engineering stress-strain curve of an epoxy film specimen without a DIC pattern. The elongation at break is 74 % and the tensile strength is about 48 MPa. The latter is reduced in comparison to previous film sample geometries [6], but the global strain at break is significantly increased, especially in comparison to standard bulk samples (less than 10 %) and other epoxy film samples [6]. After yielding, the engineering stress decreases and the plastic deformation process starts. Especially around global strains of 35 %, 55 % and 70 %, the stress decreases suddenly followed by an increase with further tensile deformation. This macroscopic strain softening and hardening can be explained in the following manner. The global engineering stress decreases due to the presumed unraveling of entanglements and molecular alignments inside the material. After the stress is partially relaxed by the molecular movements and macroscopic visible shear bands are formed, the stress increases again due to the hardening effect of the molecules aligned in the tensile direction inside the deforming sample.

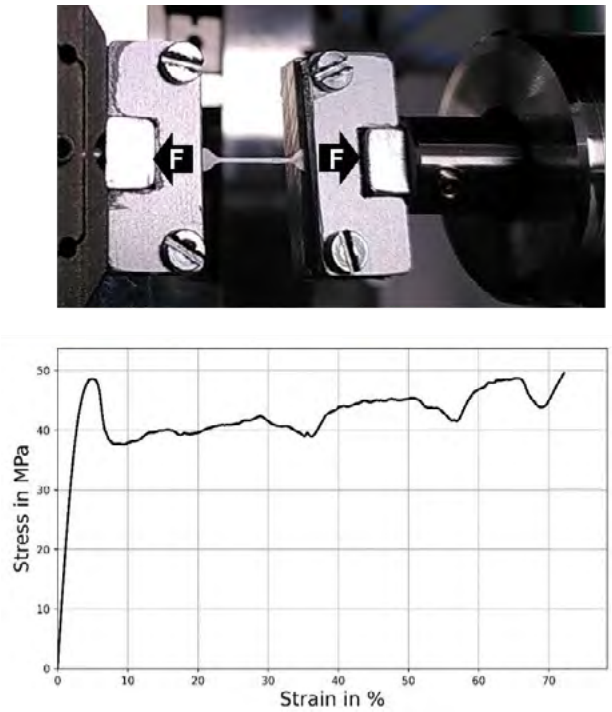

Figure 2. Tension test stage with a clamped epoxy film sample and a stress-strain curve of a representative epoxy film specimen.

The shear bands and necked gauge length of the specimens can be visualized in photoelastic digital microscope images, as can be seen in Figure 3, for a representative tension tested epoxy film sample.

Figure 3. Photoelastic image of a tension tested and deformed epoxy film sample.

The shear band orientation of 45-55 degrees to the tension direction and the necking can also be seen in the DIC deformation field data shown in Figure 4 (left). The local strain at the righthand part of the sample gauge section increases first during the tensile test after the yield point is reached. The maximum local strain reach values of 100 %. In general, necking and shear band formation can be clearly related to the local strain data. The local deformation phenomena are also evident in the global engineering stress-strain curve, as can be seen in Figure 4 (right). In sample regions with increased local strain values, shear band formation begins. This correlates with a decrease in global stress since the external mechanical energy is used for the molecular backbone movement processes, as it can be seen in the corresponding engineering stress-strain curve. During the formation and growth of local necked region, the stress remains relatively constant. After a critical threshold of molecular orientation is reached in the tensile direction, the stress increases and strain hardening takes place (approximately at 30 % global strain).

At about 35 % global strain, the stress decreases again and a second deformation localization zone within the gauge section forms. This probably takes place because the maximum possible amount of deformation for this stress level has been reached in the first necked region (on the righthand side). Thus, the formation of a new neck on the lefthand side of the specimen is energetically more feasible than a continued deformation in the first neck, where hardening resulting from local molecular reorientation has already taken place.

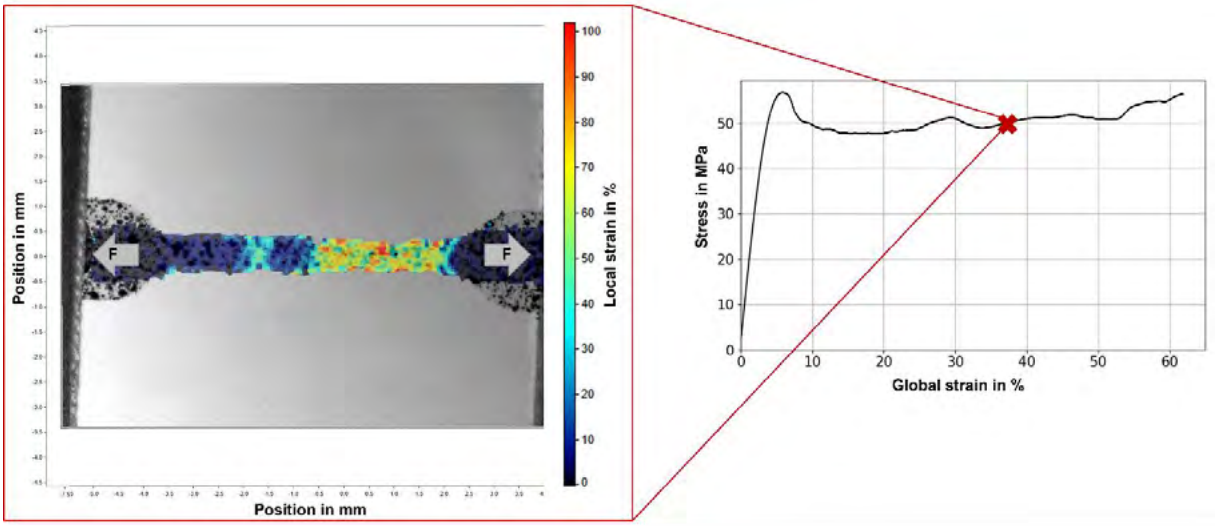

Figure 4. Visualized DIC data or image at a global strain of 37 % and the corresponding engineering stress-strain curve of a representative epoxy film sample.

3.2. Polarized Raman spectroscopy

The polarized Raman spectra of the initial or as-produced state show no polarization dependent intensity, which means that no molecular orientation from the film manufacturing process is evident. The polarized Raman spectra recorded in the necked and deformed sample region with shear bands after tension test and final failure, in contrast, show an increased intensity for a XX polarization mode (in tensile direction) and a decreased intensity for a ZZ polarization setup (perpendicular to tension direction), especially for backbone components, as can be seen in Figure 5. The different aromatic vibration modes (peaks at 1605, 1580, 1105 and 821 cm^{-1}) exhibit a significant increased intensity for the XX polarization in load direction. This leads to the conclusion that the molecular chains with the aromatic rings in the deformed sample areas or shear bands are oriented in tensile direction. As a component of the backbones, the aromatic rings or the para-phenylene groups are directly involved in the load transfer, especially in sample regions with high local strains. This is consistent with previous studies that have shown that the aromatic para-phenylene groups, as a load-bearing part of the backbones, are stretched [6] and a molecular environment change occurs in microscale epoxy samples [9]. In addition, a study by Sui et al. on necked epoxy fibers has shown that the side chains of the backbones are oriented in 90 degrees, i.e. perpendicular to the direction of tension [5]. This is in line with the presented results and the detection of load-induced molecular backbone orientation in tension direction.

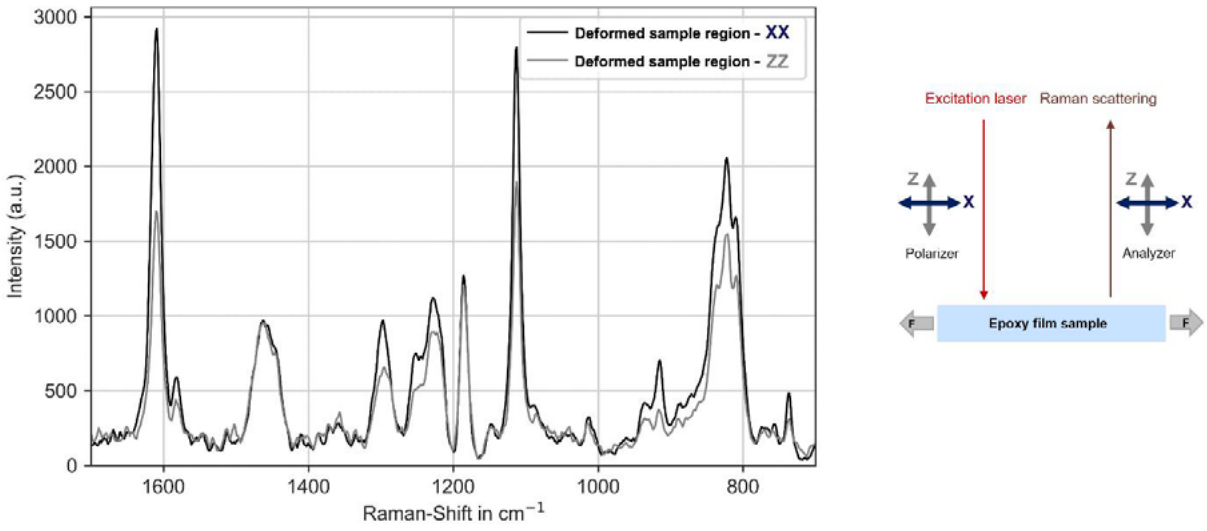

Figure 5. Polarized Raman spectra of a necked epoxy film sample region with shear bands for different polarization modes.

3. Conclusions

It has been shown that with a further decrease of the test volume of epoxy samples, the deformation ability and elongation at break (up to 80 %) in tension tests increases significantly and is remarkable for an archetypical brittle thermoset material, especially compared to standard bulk epoxy specimens. Shear bands and necking are clearly visible in the photoelastic images after tension tests and final failure.

The tensile test data with a very precise force recording and local strain determination via DIC, show an interplay of stress increase and decrease, even higher local strain values of up to 120% and the macroscopic formation of shear bands. The molecular processes like unraveling of entanglements and backbone stretching lead to a decrease of stress and strain softening. After the alignment of molecular backbones in load direction, a stress increase and strain hardening are recognizable in the engineering stress-strain curves. Polarized Raman measurements show, that in deformed and necked sample regions with shear bands, the molecular backbones are oriented and aligned in load direction.

This allows the conclusion, that at low strain rates for samples with microscale gauge volume, it is possible to reach high ductility and increased elongation at break as a result of molecular movements, even in a high-crosslinked epoxy material. High local strain values result in shear bands or sample regions with molecular oriented backbones, respectively.

Further experimental studies on epoxy films and epoxy simulations are planned in order to understand the molecular processes in detail and to gain an even better understanding of the necessary requirements for the increased ductility.

Acknowledgments
The research was done in collaboration with Tampere University and Hamburg University of Technology (Institute of Polymers and Composites) and the research strategy was a result of joint efforts. During the collaboration, J. Mittelhaus completed a 2 months' research visit at Tampere University funded by DAAD (German Academic Exchange Service). Before the visit, the epoxy film samples were manufactured at TUHH (M.Sc. J. Mittelhaus, M.Sc. J. Jacobs, M.Sc. P. Röttger). At Tampere University, there were two research groups involved in the work and a large group of scientists: the research group for Plastics and Elastomer Technology (Assoc. Prof. E. Sarlin, Dr. P. Laurikainen, M.Sc. N. Pournoori) and the Multiscale Mechanics of Materials Research Group (Asst. Prof. G. Mohanty, M.Sc. S. Bhusare), as well as Dr. T. Salminen from Tampere Microscopy Center and Dr. M. Isakov from Materials Science and Environmental Engineering. This work made use of H2MIRI and Tampere Microscopy Center research facilities at TAU.

This research at TUHH received funding from Grant No. 525597740 provided by the Deutsche Forschungsgemeinschaft (DFG, German Research Foundation). GM and SPM acknowledge partial funding from project DURATRANS (364408, 2024–2027, under the framework of M-ERA.Net).

References

[1] O. Verschatse et al., In-situ observations of microscale ductility in a quasi-brittle bulk scale epoxy, *Polymers*, 12 (11), 2581, 2020

[2] T. J. Vaughan et al., Micromechanical modelling of the transverse damage behaviour in fibre reinforced composites, *Composites Science and Technology*, 71(3), 388–396, 2011

[3] W. Tan et al., The role of interfacial properties on the intralaminar and interlaminar damage behaviour of unidirectional composite laminates: Experimental characterization and multiscale modelling, *Composites Part B: Engineering*, 138, 206–221, 2018

[4] M.-F. Ren et al., An integrated macro/micro-scale approach for in situ evaluation of matrix cracking in the polymer matrix of cryogenic composite tanks, *Composites Structures*, 216, 201–212, 2019

[5] X. M. Sui et al., A polarized micro-Raman study of necked epoxy fibers, *Polymer,* 230, 124034, 2021

[6] J. Mittelhaus et al., Investigation of the ductile deformation potential of microscale epoxy materials, *Polymer Testing*, 128, 108217, 2023

[7] A. J. Kinloch et al., A mechanism for ductile crack growth in epoxy, *Polymers,* 21, 1051–1056, 1986

[8] R. P. Wool, Mechanisms of frequency shifting in the infrared spectrum of stressed polymer, *Journal of Polymer Science: Polymer Physics Edition*, 13, 795–1808, 1975

[9] P. Laurikainen et al., Length-scale discrepancy in the properties of epoxy resin specimens, *Polymer*, 283, 126148, 2023

Advancements in MWCNT-Enhanced Porous Thermoplastic Elastomeric Composite Foam for Electromagnetic Radiation Suppression

Jasomati Nayak[1], Narayan Chandra Das[2]

Rubber Technology centre, Indian Institute of Technology, Kharagpur. India
[1]Email address: jasomatinayak@kgpian.iitkgp.ac.in
[2]Email address: ncdas@rtc.iitkgp.ac.in

Keywords: Microcellular foam, Thermoplastic elastomer,

Abstract
The proliferation of electronic devices has given rise to significant electromagnetic pollution, posing potential threats to communication systems and human well-being. Enhancing the conductivity of electromagnetic shielding materials is imperative to bolster their efficacy. However, challenges like impedance mismatch effects and secondary pollution complicate this endeavour. The study centered on creating microcellular nanocomposites by employing a blend of melt and solution mixing techniques, incorporating ethylene octane copolymer (EOC) and multiwall carbon nanotube (MWCNT). A chemical blowing agent was employed to introduce porous structures into the nanocomposite. The resultant distinct porous configuration achieved a low percolation threshold at 4 wt% and demonstrated outstanding shielding effectiveness of 25.5 dB in a 10 wt% MWCNT-loaded 2 mm thick nanocomposite. This performance, observed in the frequency range of 8.2–12.4 GHz, surpasses the criteria for electromagnetic interference (EMI) shielding materials in commercial applications. Moreover, the porous structure effectively addressed impedance mismatch concerns between the materials and the surrounding environment, leading to enhanced multiple reflections and subsequently increased absorption (96%). Additionally, these porous nanocomposite materials exhibit good thermal conductivity, contributing to better heat absorption capacity, a desirable trait for integrated electronics.

1. Introduction

The rapid advancement of gigahertz telecommunication equipment and fast processors has exacerbated electromagnetic pollution, posing significant challenges for electronic devices and human health[1]. To mitigate this, conductive polymer composites (CPC) have emerged as promising alternatives for electromagnetic interference (EMI) shielding due to their low density, cost-effectiveness, and corrosion resistance. Incorporating various conductive fillers into CPC enhances conductivity, although it may lead to density and flexibility trade-offs. Introducing cellular structures like foams offers benefits such as low density and enhanced material utilization efficiency. Methods like physical foaming and chemical foaming have been employed to create these structures, with chemical blowing agents gaining popularity for their efficiency in large-scale production. The porous nature of foam composites improves electromagnetic wave absorption, reducing reflection and minimizing interference[2]. This leads to improved impedance matching at the air-specimen interface, effectively reducing electromagnetic wave reflection[3].

The research presented a fresh approach to manufacturing nanocomposite foams containing segregated EOC/MWCNT. This method combines melt and solution mixing to achieve a uniform distribution of MWCNT within the EOC matrix. Additionally, a chemical blowing agent was incorporated to facilitate the foaming process during compression molding, resulting in the curing of the material and the creation of distinct porous structures. The primary focus of the study was on characterizing the morphological and microstructural properties to establish a correlation between the microstructure and the MWCNT content in the foamed EOC/MWCNT nanocomposites. Furthermore, a comprehensive analysis was

carried out to examine how the varying MWCNT content affects the mechanical, electrical, thermal, and EMI shielding properties of the foam nanocomposite. The EOC/MWCNT foam nanocomposite that is produced demonstrates a density of 0.53 gm/cm3 and showcases a tensile strength of 5.8 MPa. It also exhibits robust stability when subjected to compression forces. The elevated aspect ratio of MWCNT enables the formation of a conductive pathway within the nanocomposite, even at a low loading concentration of 4 wt%. This attribute not only contributes to an absorption-dominated EMI shielding effectiveness of 25.5 dB but also enhances its capacity for heat absorption.

2. Experimental Procedure

For this study nanocomposite foam are prepared by a blend of melt and solution mixing techniques. The preparation of the nanocomposite foam followed a structured process encompassing three key stages. Initially, the masterbatch was prepared mixing EOC material with a series of additives such as zinc oxide, stearic acid, paraffin oil, chemical blowing agent (DNPT), curing agent (DCP) by melt mixing procedure in a Brabender Plasticoder, ensuring uniform distribution and subsequently forming it into sheets. Following this, MWCNT was dispersed in toluene through sonication, subsequently blended with the masterbatch solution, and dried to yield a film-like substance. Finally, the compounds underwent compression molding, facilitated by a Moore Press at 170°C temperature and 20 MPa pressure for 8 mins, to achieve optimal curing and desired material properties[4]. Figure 1 provides a visual representation of the entire preparation procedure.

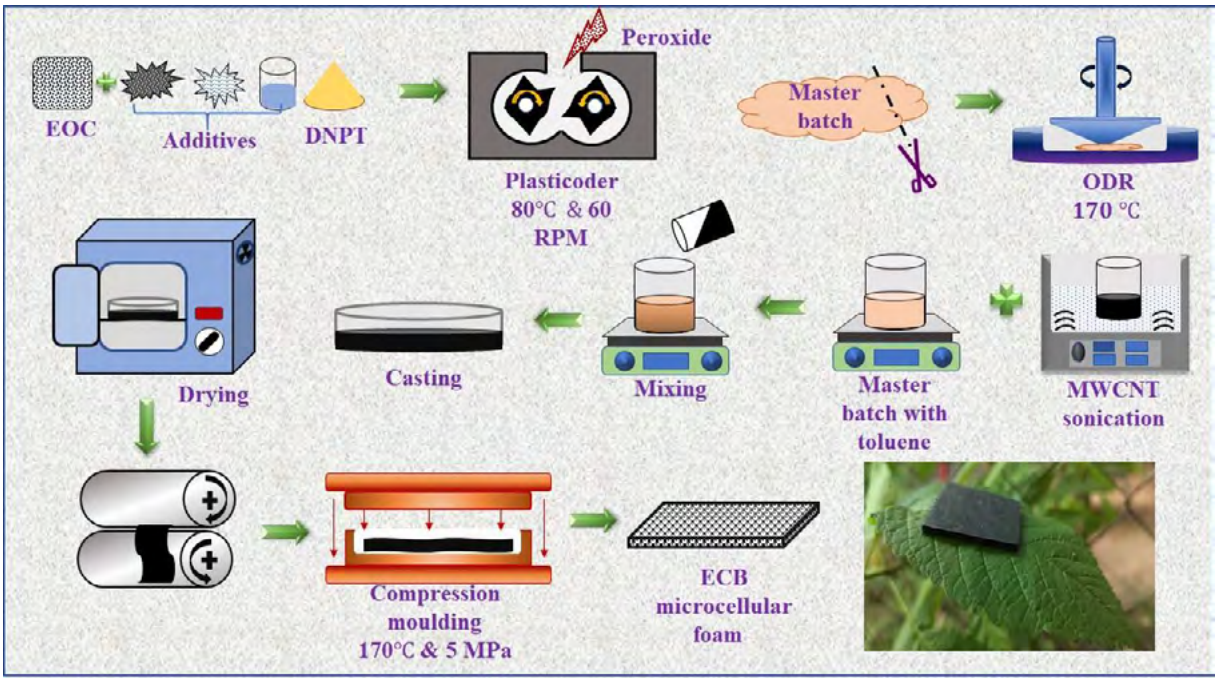

Figure 1: Schematic of fabrication procedure of EOC/MWCNT nanocomposite foam

3. Material Characterisation

Various characterization techniques were employed to evaluate the properties of the EOC nanocomposite foam with or without MWCNT. Foam density was determined using the water-displacement method according to ASTM D792, while expansion ratio (φ) was measured relative to the density of the solid nanocomposite precursor using Hildbrand's electronic densimeter H-300S. Surface morphology was observed using a Field Emission Scanning Electron Microscope (FESEM), with samples prepared by slicing and sputter-coating with a thin layer of gold nano dust. Mechanical characteristics such as tensile and compressive strength were evaluated using a Universal Testing

Machine (UTM) following ASTM standards. AC and DC conductivity measurements were performed using an AC impedance analyzer and Agilent equipment, respectively. Electromagnetic interference (EMI) shielding characteristics were assessed using a 2-port Vector Network Analyzer (VNA) in the X-band region.

4. Result and Discussion

4.1. Physical and Morphological characteristic

The density observations provided crucial insights into the foam characteristics, particularly concerning cell size, density, expansion ratio, and energy absorption capacity. Figure 2(a) illustrates the impact of MWCNT content on the density of MWCNT/EOC porous nanocomposites. It was observed that the introduction of MWCNT led to a significant decrease in density compared to pristine materials or solid nanocomposites. This decrease in density correlated with a reduction in expansion, indicating that MWCNT incorporation into the polymer matrix hindered the flexibility of the nanocomposite. The expansion ratio (φ) of the porous material, defined as the ratio of foam density (ρ_f) to solid nanocomposite density (ρ_s), decreased from 2.17 to 1.78 with the presence of MWCNT. Additionally, SEM images in Figure 2(c) revealed closed spherical or polygonal cells in all foams, with cell size decreasing and becoming more uniformly distributed as the amount of MWCNT increased. The mean pore diameter also reduced from 200 µm to 152 µm, attributed to MWCNT acting as heterogeneous nucleating agents in the polymer matrix, leading to increased cell density.

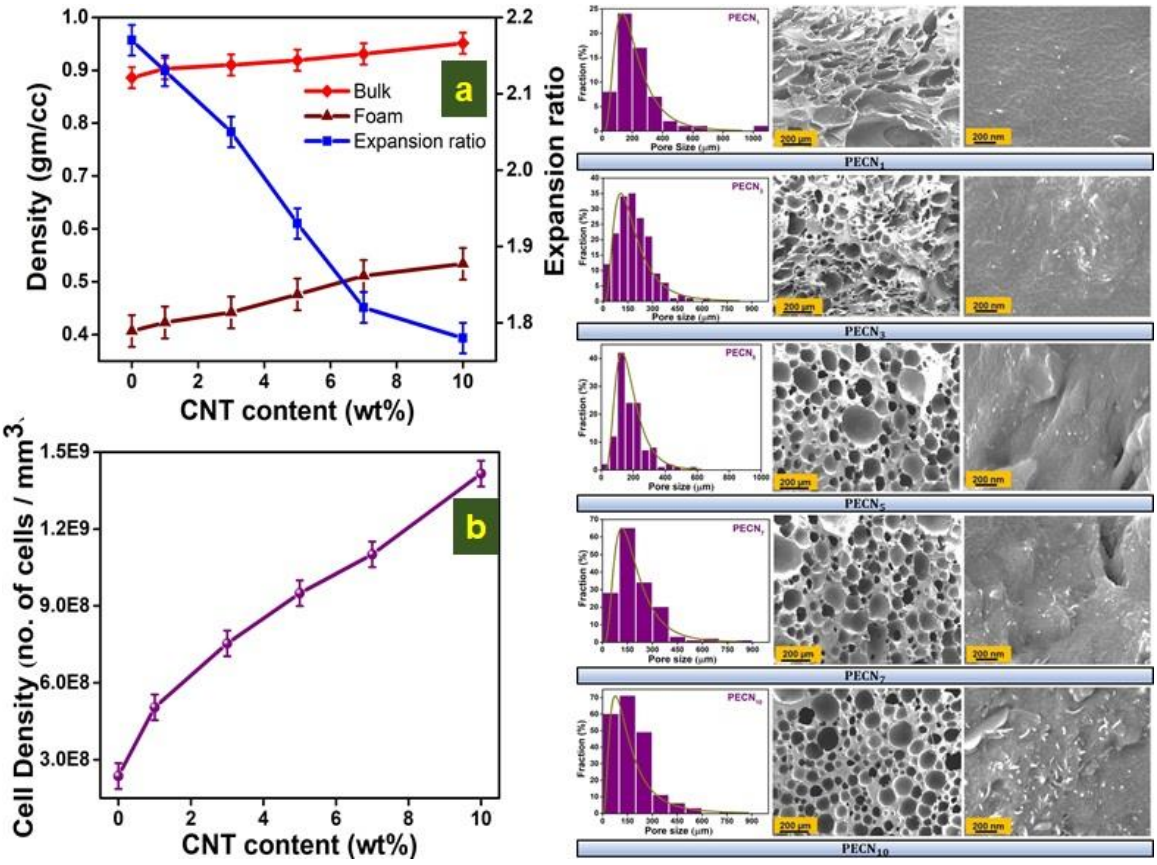

Figure 2: (a) Density and expansion ratio of EOC/MWCNT nanocomposite foam, (b) Cell density of EOC/MWCNT nanocomposite foam, (c) The FESEM image pores, histogram of the distribution of pores, and dispersion of MWCNT of EOC/MWCNT foam nanocomposite

Despite challenges in achieving homogeneous dispersion due to MWCNT clustering tendencies, sonication and a dual mixing procedure facilitated even filler distribution, as shown in Figure 2. Moreover, the non-deformability of MWCNT hindered cell expansion, contributing to the reduction in

cell size. These findings underscore the intricate interplay between MWCNT content and foam characteristics, elucidating the potential for tailored foam properties through controlled nanofiller incorporation and dispersion techniques

4.2. Mechanical characteristics:

Assessing the mechanical performance of EOC foam nanocomposites is essential for understanding their suitability for real-world applications, particularly in sealing and packaging electronic equipment[5,6]. In our study, MWCNTs acted as reinforcing nanofillers, leveraging their high aspect ratio, extensive surface area, and impressive mechanical properties. Figure 3(a) presents the classical tensile stress-strain plot for EOC nanocomposite foam loaded with MWCNTs. The elongation of PECN1 was notably higher than that of pristine EOC foam, ranging from 413% to 730%. With increased MWCNT concentration, a trend emerged where tensile strength increased while elongation decreased. This phenomenon can be attributed to factors such as heightened MWCNT affinity to coalesce, the formation of rigid structures reducing flexibility, and the incorporation of air leading to internal defects. Figure 3(b) demonstrates the impact of MWCNT content on compressive strength at a high strain of 90%, exhibiting typical behavior of "elastic-plastic" foams. Notably, as MWCNT content increased, a substantial enhancement in compressive stress was observed, reaching an impressive value of 38 MPa with 10wt% MWCNT. Figures 3(c)-(e) depict stress-strain curves for cyclic compression-release tests at compressive strains of 20%, 40%, and 50%, respectively. Despite gradual decreases in loading and unloading stresses with successive compressive cycles, excellent mechanical recovery was demonstrated by EOC/MWCNT nanocomposite foams, with recovery losses as low as 6.5%, 6.2%, and 5.3%, even after the 25th compression cycle. These findings underscore the remarkable potential of EOC/MWCNT nanocomposite foams for applications requiring robust mechanical performance and resilience.

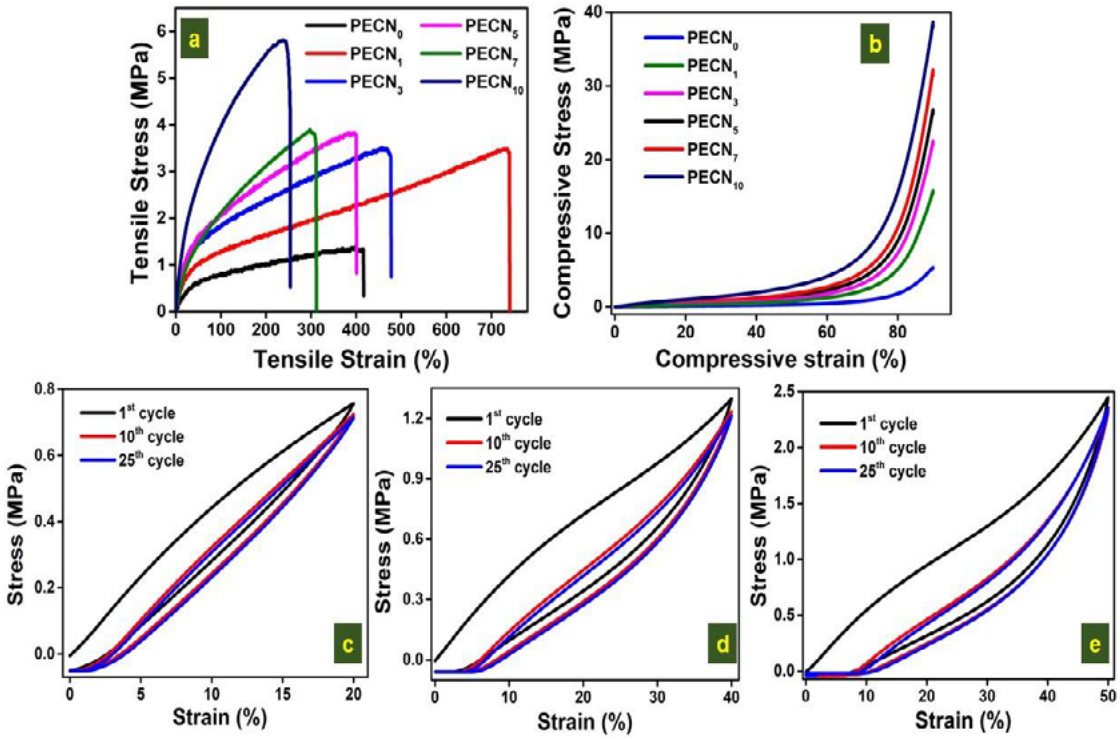

Figure 3: (a) Tensile stress-strain plot, (b) Compressive stress-strain plot of EOC/MWCNT foam nanocomposite. (c, d, e) Cyclic compression loading test of $PECN_{10}$ at 20 %, 40 %, 50 % strain respectively

4.3. Electrical characteristics:

Understanding the electrical conductivity of MWCNT/EOC nanocomposite foam is pivotal as it significantly influences their electromagnetic interference (EMI) shielding capabilities. Figure 4(a)

illustrates that the addition of MWCNTs notably increases the DC conductivity of pure EOC foam, creating a dense three-dimensional interconnected network within the matrix. This enhancement in conductivity is attributed to the extended-length MWCNTs facilitating enhanced electrical movement by establishing a conductive pathway for electron hopping. Percolation threshold analysis revealed a critical filler concentration at approximately 4 wt %, indicating the establishment of a 3-dimensional electrical network in the EOC matrix. AC electrical conductivity, evaluated across a frequency range from 1 to 107 Hz (Figure 4(c)), demonstrated an increasing trend with higher MWCNT concentrations, reaching up to 10 wt %. At lower MWCNT loadings, the nanocomposites exhibited frequency-dependent behavior due to limited interconnected conductive networks, while higher loadings showcased frequency-independent behavior, facilitated by the establishment of interconnected pathways for charged particle movement under an applied electric field. The remarkable AC electrical conductivity can be attributed to factors such as the intrinsic conductivity of MWCNTs, effective dispersion within the matrix, creation of a three-dimensional network, charge carrier displacement mechanisms, and the high surface area and extended length of MWCNTs promoting conductive contact points. These findings underscore the potential of MWCNT/EOC nanocomposite foams for EMI shielding applications, highlighting their versatile electrical properties and tailored conductivity behavior.

4.4. EMI shielding characteristics:

The electrical conductivity of carbon-polymer composites (CPCs) plays a crucial role in determining their electromagnetic interference shielding effectiveness (EMI SE)[7]. In this study, the exceptional EMI SE observed is attributed to the presence of effective conductive networks within the materials, leading to consistent increases in EMI SE as the MWCNT content rises. Figure 4(d) illustrates the EMI SE characteristics of MWCNT-filled ethylene octene copolymer (EOC) nanocomposite foam within the 8.2–12.4 GHz frequency range. Notably, the EMI SE remains independent of frequency but exhibits a pronounced dependence on MWCNT concentration, with the highest achieved value reaching approximately 25.5 dB, satisfying the commercial EMI shielding requirement of 20 dB.

The collective EMI SE is commonly regarded as the summation of absorption and reflection, resulting from multiple reflections being disregarded. The reflection phenomenon occurs due to an impedance mismatch between shields and air, while absorption is attributed to ohmic loss and polarization loss. Given the nonmagnetic attributes of EOC and MWCNT, this study focuses on EMI SE due to ohmic loss and polarization loss.

The EMI shielding performance of the EOC/MWCNT nanocomposite foam can be explained by the schematic depiction in figure 4(g), illustrating the dissipation of electromagnetic microwaves within the foam. In this representation, the foam exhibits reflection of incident waves at the interface between air and the shield due to an impedance mismatch. The porous structure of the foam provides numerous interfaces, facilitating constant reflection and absorption of electromagnetic waves, thereby enhancing EMI shielding effectiveness. Further analysis was conducted to understand the total SE (SET) in terms of absorption (SEA) and reflection (SER) at a frequency of 10 GHz. Figure 4(e) reveals a notable increase in SEA and SET values with MWCNT content compared to SER. Beyond the percolation threshold, the predominant role in EMI SE is played by microwave absorption, with a maximum absorption coefficient of 94±3%. Additionally, specific EMI SE of the foams with different MWCNT loadings at 10 GHz is represented in Figure 4(f), showing improvement with MWCNT loading, with a maximum specific EMI SE of 47.7 dBcm3/gm achieved.

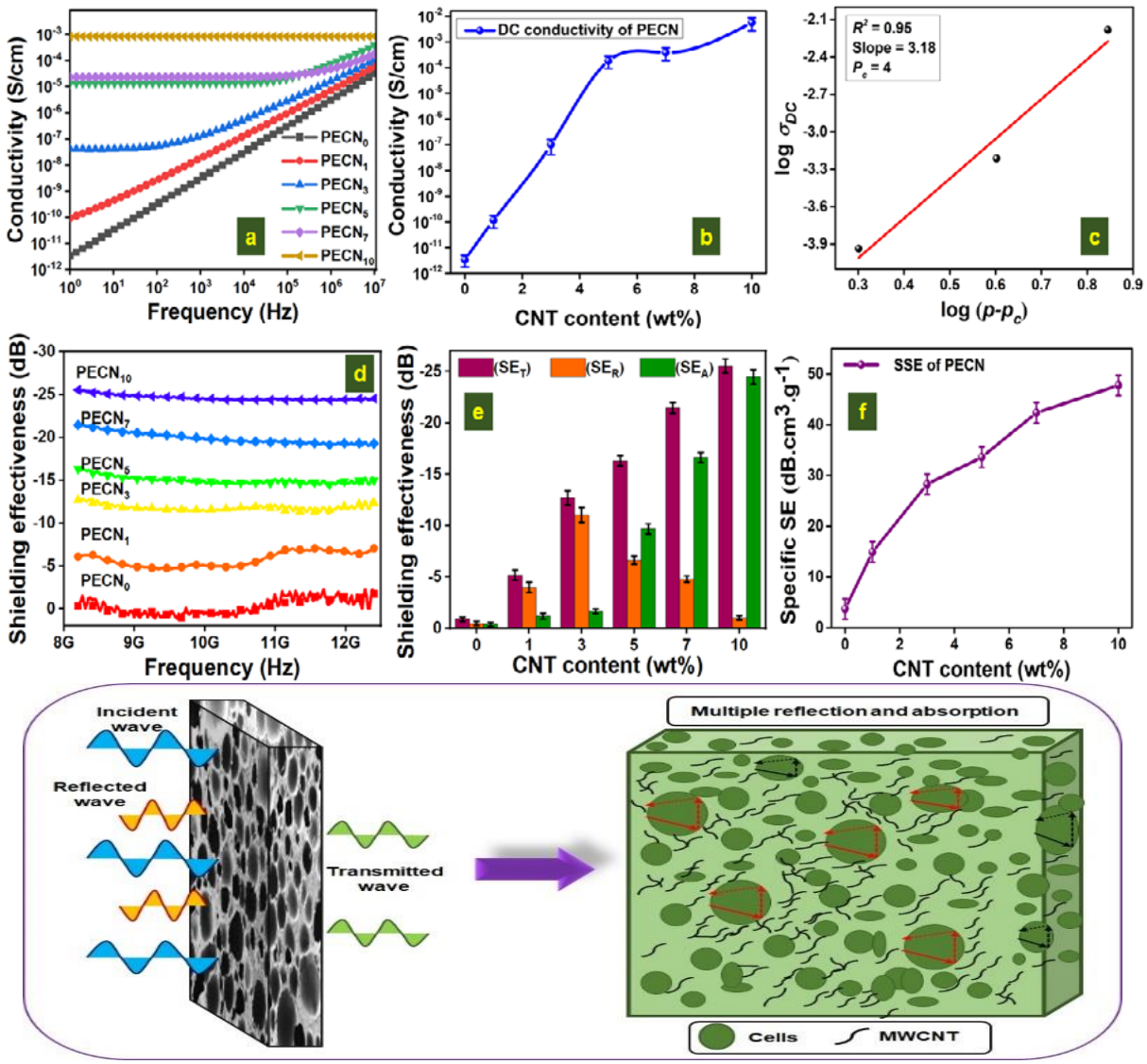

Figure 4: a) DC conductivity, (b) the log log plot of DC conductivity and ($p - p_c$), (c) AC conductivity of EOC/MWCNT foam nanocomposite, (d) Total SE of EOC/MWCNT foam nanocomposite in X-band region, (e) SE_T, SE_R, SE_A of EOC/MWCNT foam nanocomposite at 10 GHz frequency, (f) SSE of EOC/MWCNT foam nanocomposite, (g) Schematic of the shielding princlple of porous nanocomposite.

4.5. Thermal conductivity characteristics:

The rapid evolution of integrated electronics has accentuated the need for EMI-reducing materials, while concurrently addressing the issue of electronic device overheating[6]. Most reported CPC EMI shielding materials with porous structures exhibit thermal insulation, posing a challenge. Consequently, there is a growing interest in porous polymer nanocomposites that not only shield EMI but also possess good thermal conductivity to absorb the heat generated by devices. The thermal conductivity of virgin EOC foam demonstrated an initial value of 1.17 Wm-1K-1, depicted in Figure 5(a). As the MWCNT content increased, the thermal conductivity of the porous material steadily rose, reaching its peak value of approximately 0.2585 Wm–1K–1 at 10 wt% MWCNT, signifying a notable 53% increase. Three fundamental mechanisms influence the thermal conductivity of foam materials: conduction, convection, and radiation interactions. Given the material's thickness is smaller than the critical thickness of 4 mm, convection can be disregarded. The porous structure of polymer foams causes radiated heat to undergo multiple reflections within the cell walls, ultimately leading to heat absorption. Moreover, the dispersion

of MWCNTs forms an interconnected network inside the polymer matrix, enhancing total thermal conductivity due to MWCNTs' exceptionally high thermal conductivity. To evaluate the maximum heat absorption capacity, equivalent sections of the materials were subjected to a constant temperature of 70 ^{o}C on a hot plate, with thermal images captured at various intervals. Figure 5(c) demonstrates the temporal temperature evolution for nanocomposites with varying concentrations of modified MWCNTs, revealing improved heat absorption capacity with increased filler concentration. Figure 5(b) further illustrates temperature variations at the material center after 15 seconds, 60 seconds, and 100 seconds of heating, confirming the effective heat absorption capabilities of the EOC/MWCNT foam nanocomposite, notwithstanding its porous structures. These findings underline the promising potential of such nanocomposites in mitigating EMI and efficiently managing device-generated heat in electronic applications.

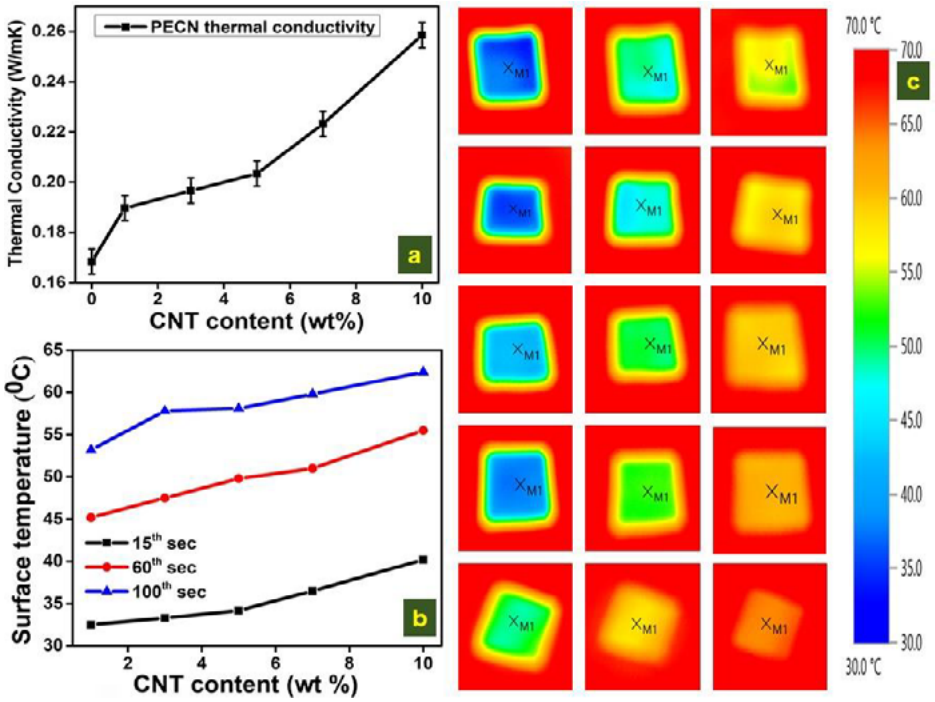

Figure 5 (a) Thermal conductivity of EOC/MWCNT foam nanocomposites, (b) Temperature recorded of the center of the upper surface of EOC/MWCNT foam nanocomposites at different times, (c) IR image of EOC/MWCNT foam nanocomposites.

5. Conclusion

In summary, A flexible and lightweight nanocomposite foam comprising EOC and MWCNT was successfully synthesized using a combination of solution and melt mixing techniques. The incorporation of a commonly used chemical blowing agent (DNPT) facilitated the creation of porous structures. MWCNTs served as nucleating agents, resulting in increased cell density and reduced cell size. The uniform dispersion of MWCNT particles on the surface formed a segregated structure, enhancing the conductive network and leading to remarkable conductivity with a low percolation threshold. The combined influence of the segregated MWCNT networks and microcellular structure yielded a high specific electromagnetic interference shielding effectiveness (EMI SE) value of 47.8 dB cm³/g, with absorption contributing to 96% of the shielding. Despite the presence of multi-walled carbon nanotubes (MWCNT) with inherently high thermal conductivity, the introduction of an air-filled cellular structure prevented a significant increase in thermal conductivity. However, the material demonstrated noteworthy heat absorption capacity. The nanocomposite material displayed low density and

exceptional tensile properties, including high tensile strength (5.8 MPa), elongation, and stability under intense compressive stresses. These characteristics make the material well-suited for EMI shielding material in sealing and packaging applications. The attributes of the EOC/MWCNT nanocomposite foam hold substantial potential for diverse applications in aerospace technology, military operations, smart-wearable technology, and portable electronic devices.

Acknowledgment
The author would like to acknowledge the Indian Institute of Technology, Kharagpur India for providing financial help and technical facilities for this research work.

References

1. Katheria A, Nayak J, Das NC. A journey of thermoplastic elastomer nanocomposites for electromagnetic shielding applications: from bench to transitional research. *Mater Adv*. 2022;3(6):2670-2691. doi:10.1039/D1MA00989C
2. Ameli A, Nofar M, Park CB, Pötschke P, Rizvi G. Polypropylene/carbon nanotube nano/microcellular structures with high dielectric permittivity, low dielectric loss, and low percolation threshold. *Carbon N Y*. 2014;71:206-217. doi:10.1016/J.CARBON.2014.01.031
3. Das P, Katheria A, Nayak J, et al. Stretchable and lightweight 2D MXene-based elastomeric composite foam for suppressing electromagnetic interference. *J Alloys Compd*. 2024;976:173011. doi:10.1016/j.jallcom.2023.173011
4. Nayak J, Das P, Katheria A, Giri S, Banerji P, Das NC. Fabrication of electrically conductive interconnected microcellular thermoplastic elastomeric foam composite for absorption dominating electromagnetic interference shielding with ultra low reflection. *Polym Eng Sci*. 2024;64(3):1194-1208. doi:10.1002/PEN.26607
5. Li J, Zhang G, Ma Z, et al. Morphologies and electromagnetic interference shielding performances of microcellular epoxy/multi-wall carbon nanotube nanocomposite foams. Published online 2016. doi:10.1016/j.compscitech.2016.04.003
6. Wang YY, Zhou ZH, Zhou CG, et al. Lightweight and Robust Carbon Nanotube/Polyimide Foam for Efficient and Heat-Resistant Electromagnetic Interference Shielding and Microwave Absorption. *Cite This: ACS Appl Mater Interfaces*. 2020;12:8712. doi:10.1021/acsami.9b21048
7. Chen J, Liao X, Xiao W, Yang J, Jiang Q, Li G. Facile and Green Method To Structure Ultralow-Threshold and Lightweight Polystyrene/MWCNT Composites with Segregated Conductive Networks for Efficient Electromagnetic Interference Shielding. Published online 2019. doi:10.1021/acssuschemeng.9b00678

INFLUENCE OF THE NUMBER OF PLIES ON THE STIFFNESS OF LAMINATED VENEER LUMBER

A. Peignon[1], J. Serra[1], A. Cantarel[1], F. Eyma[1] and B. Castanié[1*]

[1]Institut Clément Ader (ICA), University of Toulouse, CNRS UMR 5312, INSA, ISAE-Supaéro, INSA, IMT Mines Albi, UPS, Toulouse, France
Email: peignon@insa-toulouse.fr, joel.serra@isae-supaero.fr, arthur.cantarel@iut-tarbes.fr, florent.eyma@iut-tarbes.fr, castanie@insa-toulouse.fr

Keywords: Tensile Tests, Laminated Veneer Lumber, Poplar, Young's Modulus, Longitudinal, Transverse

Abstract
This research paper studies how changing the number of plies affects the mechanical properties, such as stiffness, in poplar Laminated Veneer Lumber (LVL) through tensile testing. Various configurations of LVL poplar specimens were manufactured and tested under uniaxial tensile test to assess both longitudinal and transverse stiffness. The findings reveal that the arrangement of plies significantly impacts mechanical properties. These outcomes offer crucial insights for enhancing the design and efficiency of laminated wood structures.

1. Introduction

The use of wood in transportation is not a recent development, yet it presents an encouraging solution to contemporary environmental challenges thanks to its affordability, minimal carbon emissions and lightweight nature [1,2]. Laminated Veneer Lumber (LVL) and plywood, both wood composites constructed from thin wood plies bonded with adhesive, exhibit mechanical properties comparable to or even surpassing those of solid wood. Recent research underscores LVL's potential in crash and impact scenarios [3,4]. However, these wood composites, and more generally, wood ply, exhibit heterogeneity, resulting in dispersion and variability in mechanical properties. Thus, a detailed analysis is imperative to consider their suitability as structural materials in transportation.

Studies indicate that the number of plies, within a fixed thickness of LVL, influences stiffness and strength [5]. This phenomenon is observed across shear, compression, tensile, and bending tests, with thinner plies yielding higher breaking strength and rigidity in LVL. Nonetheless, only limited research has explored the impact of the number of constant thickness plies on LVL properties [6]. In the case of Carbon Fiber Reinforced Polymer, the laminate theory model does not predict an increase in composite stiffness as the number of plies increases whereas experiments exhibit contradictory results[7].

The present study aims to continue the work carried out by ICA members since 2014 [8]. LVL made up of different poplar plies are being characterized through a series of uniaxial tensile tests. The aim of this campaign is to understand and identify the mechanical properties of poplar LVL and the influence of the number of plies on its behavior

2. Material and Methods

Tensile tests on 1-, 2-, 3-, 5-, 7-, and 9-ply of Koster poplar (*Populus x canadensis*) LVL were carried out to characterize the transverse and longitudinal stiffnesses of these laminates and the influence of the number of plies. Each ply used for the manufacturing of the tensile specimens was 1 mm thick. The

wood veneers were bonded together using Kleiberit 510 PUR 1C FIBERBOND adhesive, stacked, and subjected to a pressure of 10 bars at 25°C for 5 hours to form the LVL. The amount of adhesive applied, as per the manufacturer's recommendation, was 250 g/m^2. The density of the poplar veneers was 355 kg/m^3, with a Standard Deviation (SD) of 21 kg/m^3.
Six 0° unidirectional specimen configurations were used for this study: $[0°]$, $[0°]_2$, $[0°]_3$, $[0°]_5$, $[0°]_7$, and $[0°]_9$. Three 90° unidirectional specimen configurations were also studied: $[90°]_3$, $[90°]_5$, and $[90°]_9$. These series were used to evaluate the effect of the number of plies on the transverse stiffness of LVL. A total of 15 specimens, with rectangular geometry, were manufactured per configuration. The tensile specimens had nominal dimensions of 250×25×thickness of LVL mm^3. Tabs, 50 mm long, were added at each end to limit stress concentrations, and therefore breakage, in the jaws of the testing machine

Tensile testing was conducted under standard ambient conditions of temperature and humidity (23.6°C and 64.6% RH). Prior to testing, the wood samples were conditioned to achieve a moisture content of 9.8% (SD: 0.28%). The tests were performed using an Instron 5900 machine equipped with a 50 kN force cell, providing a measurement accuracy of 0.5 N. A cross-head displacement rate of 2 mm/min was applied during testing. Stereo Digital Image Correlation (DIC) was employed to monitor sample deformation, for which the specimens were coated with speckles to allow image correlation. The size of the speckle patterns was adjusted according to the experimental setup to ensure a minimum size of 3 pixels for each spot [9].

3. Results

3.1. Study of $[0°]_n$ specimens

Figure 1 illustrates the distribution of the mean Young's modulus for the $[0°]_n$ specimens. The variability in the longitudinal Young's modulus of the $[0°]_n$ specimens tends to diminish as the number of plies increases (Figure 1 (a)). Furthermore, there is an evident trend of stiffening in the LVL corresponding to the number of plies. A comparison among 2-, 3-, 5-, 7-, and 9-ply specimens reveals that the Young's modulus tends to escalate with an increase in the number of plies. However, the considerable variability observed in the $[0°]_1$ series precludes a direct comparison with the other series. This inclination towards increased stiffness is noteworthy and aligns with findings from Lechner and colleagues, who observed a similar trend in tensile tests involving 1-, 2-, and 4-ply specimens [6].

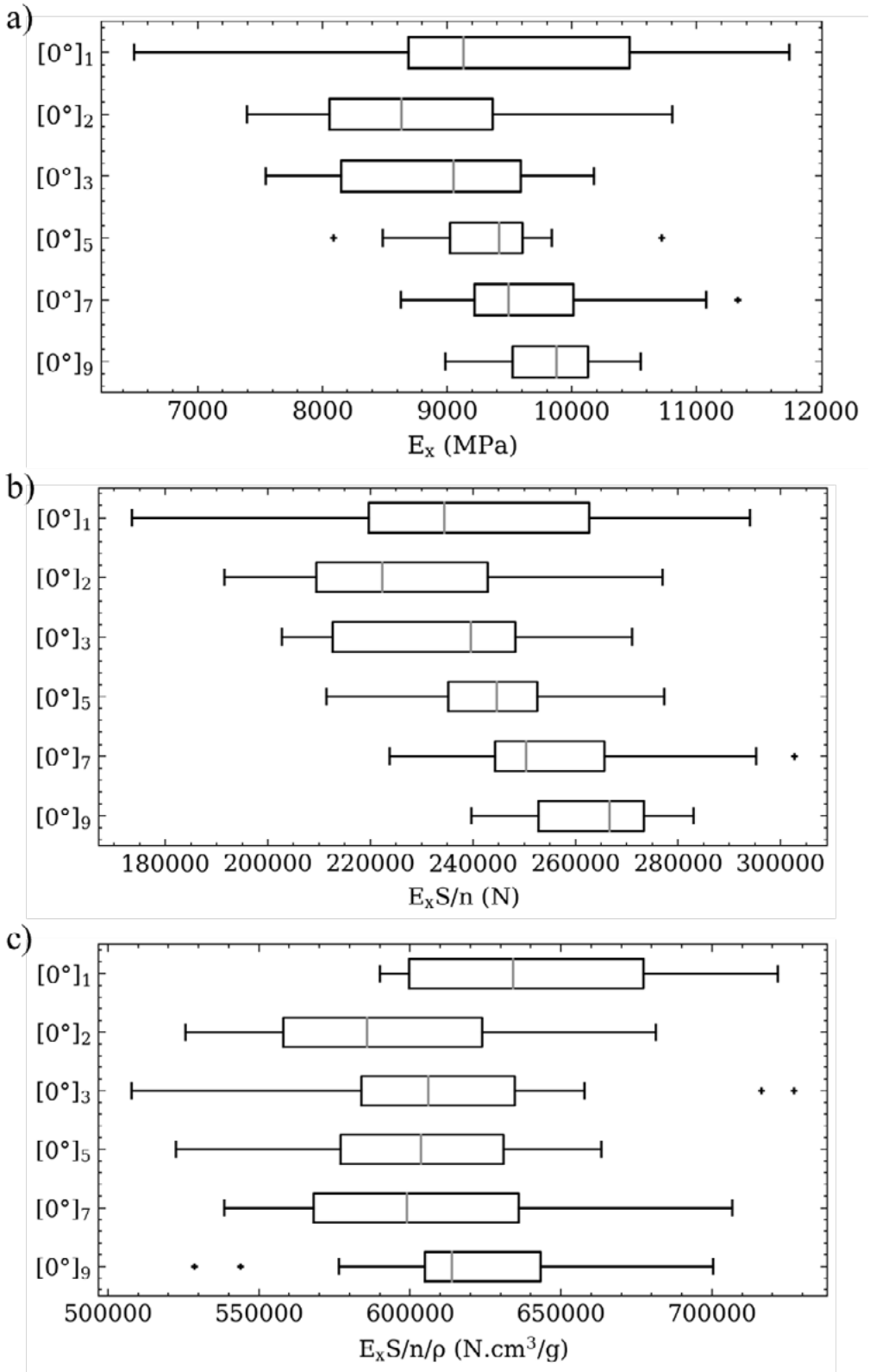

Figure 1. Distribution of the longitudinal Young's modulus by series (a), the Young's modulus multiplied by the cross-section and relative to the number of plies (b), and the specific Young's modulus multiplied by the cross-section and related to the number of plies (c)

It's important to acknowledge that when calculating the stress for determining LVLs stiffness, the cross-section measured on the tensile specimens is taken into account. However, the manufacturing process alters this cross-section (such as compression of the veneers during LVL plate pressing) and this change affects the specimen's cross-section, it may influence stress calculations too. To address this issue, comparing the Young's modulus of the specimens involves adjusting it by multiplying with the specimen's cross-section and dividing by the number of plies (for cross-series comparisons). Figure 1 (b) illustrates this distribution across different series. Despite this adjustment, a stiffening effect remains evident when comparing 2-, 3-, 5-, 7-, and 9-ply specimens.

To assess the impact of density on the results, the wood density of each specimen can be determined using the theoretical density of the wood it comprises. This density is calculated by subtracting the mass of glue from the total mass of the manufactured specimen and relating this to the specimen's volume, excluding the glue joints. It is assumed that the glue is uniformly distributed across all specimens within the same series.

Figure 1 (c) indicates that the distribution of the specific longitudinal Young's modulus, multiplied by the cross-section, relative to the number of plies in the specimens tends to follow a consistent trend with the number of plies. This observed increase in properties with the number of plies can be attributed to the phenomenon of densification associated with the LVL manufacturing process [10]. Consequently, the role of glue in this stiffness enhancement appears to be secondary.

However, as noted by some authors [5,11], the thinner the LVL veneers, the greater the relative amount of glue used to manufacture the LVL. For 2-ply specimens, glue represents 25% of the LVL mass, and it rise up to 37% for 9-ply specimens.

The ply number does not appear to affect the experimentally measured Poisson's ratio (ν_{lt}) values. However, there is a trend where increasing the number of plies decreases the variability in Poisson's ratio measurements, though it does not affect the mean values obtained. This decrease in variation can be attributed to the enhanced plane stability resulting from the increased number of plies, which in turn mitigates the occurrence of cupping in specimens [12].

3.2. Study of $[90°]_n$ specimens

The Young's moduli of the $[90°]_n$ specimens is also an increasing function of the number of plies. This stiffening is more marked than for $[0°]_n$ specimens. Figure 2 shows that, in contrast to the $[0°]_n$ series, specific transverse Young's moduli multiplied by the cross-section relative to the number of plies of the specimens is always an increasing function of the number of plies. The increase observed in properties with the increasing number of plies can then be explained by the presence of glue in the LVL. In this configuration, the glue has a non-negligible effect on the stiffening of the specimens.

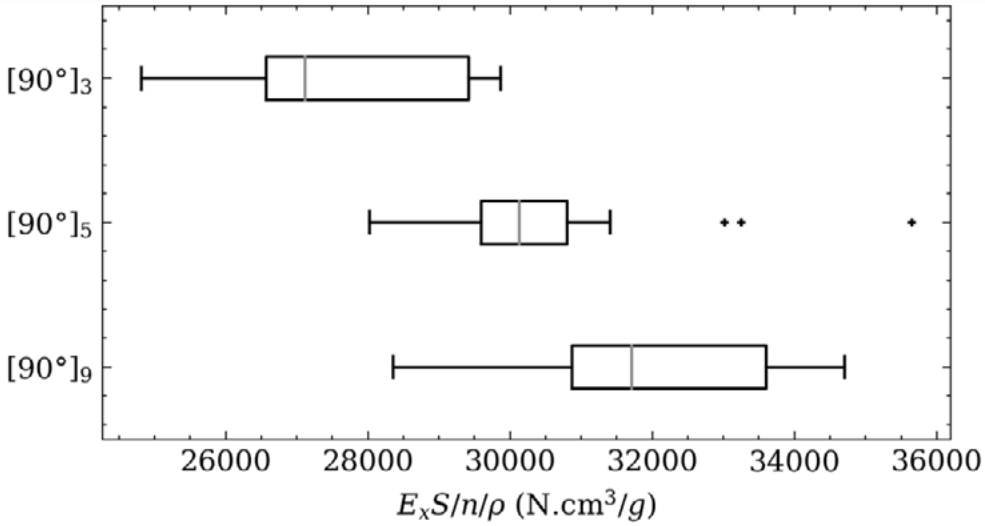

Figure 2. Distribution of specific transverse Young's modulus times the cross-section and relative to the number of plies per series

Since the transverse stiffness of poplar veneers is lower than the longitudinal stiffness, the stiffness of the glue added during the manufacture of LVLs plays a more important role in the total stiffness of the laminate.

4. Discussion and Conclusions

Tensile tests on 1-, 2-, 3-, 5-, 7-, and 9-ply poplar LVLs were carried out to characterize the transverse and longitudinal stiffnesses of these laminates and the influence of the number of plies. The results show that stiffness tends to increase when the laminate is composed of a sufficient number of plies. This observation is valid, not only for longitudinal stiffness but also for transverse stiffness, where the effect is even greater. Although Lechner et al. [6] had already been able to observe this phenomenon, they did not explain it. The explanations on the increase in stiffness put forward during this work are based on the LVL manufacturing process: when the number of plies is increased, the relative amount of glue in the laminate increases. For the $[0°]_n$ specimens, it's interesting to note that the more plies there were in an LVL, the more the variation of the elastic modulus seemed to decrease. The stiffness observed on tensile tests was more homogeneous.

Nevertheless, based on the findings presented, it's important to recognize that wood density, and consequently the densification of wood veneer during manufacturing, can also impact this phenomenon. However, measuring the densification of veneer during manufacturing poses considerable challenges. The stiffness of the adhesive, can also affect the analysis performed. However, the phenomenon of interaction between glue and wood is still considered complex, so it remains an area of active research even today.

Moreover, it's worth noting that the stiffness of the adhesive used is approximately 1.8 GPa (as identified in other studies not presented here). This stiffness of 1.8 GPa may help elucidate why the adhesive has a more pronounced effect on stiffening $[90°]_n$ specimens compared to $[0°]_n$ specimens. In the case of $[90°]_n$ specimens, the adhesive is nearly 12 times stiffer than the 90° plies, whereas for the $[0°]_n$ series, the 0° plies are 5 times stiffer than the adhesive.

Examining the stiffness of LVL based on the number of plies offers a deeper comprehension of the connection between manufacturing processes and the material's mechanical characteristics. This data appears pertinent for establishing an analytical or digital model for wood-based composites. Nonetheless, further investigation is warranted to discern the impact of the number of ply across diverse

orientations, materials, and adhesives. Incorporating factors such as local density or veneers' lathe checks could potentially elucidate some of the observed variability in these tests. Moreover, exploring different wood resources could corroborate the observed behavior in species beyond poplar.

Acknowledgments
The research that led to the results presented received funds from the French National Research Agency under the BOOST project (ANR-21-CE43-0008-01). The authors thank the LaBoMaP Laboratory, Cluny, France for providing the Poplar veneers used in this study, through the research project ANR BOOST.

References

[1] B. Castanié, A. Peignon, C. Marc, F. Eyma, A. Cantarel, J. Serra, R. Curti, H. Hadiji, L. Denaud, S. Girardon, B. Marcon, Wood and plywood as eco-materials for sustainable mobility: A review, *Compos. Struct.* 329, 2024. https://doi.org/10.1016/j.compstruct.2023.117790.
[2] B. Castanié, C. Bouvet, M. Ginot, Review of composite sandwich structure in aeronautic applications, *Compos. Part C* Open Access 1, 2020. https://doi.org/10.1016/j.jcomc.2020.100004.
[3] R. Guélou, F. Eyma, A. Cantarel, S. Rivallant, B. Castanié, Dynamic crushing of wood-based sandwich composite tubes, *Mech. Adv. Mater. Struct.* 29:7004–7024, 2022. https://doi.org/10.1080/15376494.2021.1991533.
[4] R. Guélou, F. Eyma, A. Cantarel, S. Rivallant, B. Castanié, Crashworthiness of poplar wood veneer tubes, *Int. J. Impact* Eng. 147, 2021. https://doi.org/10.1016/j.ijimpeng.2020.103738.
[5] Y. Kiliç, M. Colak, E. Baysal, E. Burdurlu, An investigation of some physical and mechanical properties of laminated veneer lumber manufactured from black alder (AInus glutinosa) glued with polyvinyl acetate and polyurethane adhesives, *For. Prod. Soc.* 56, 2006.
[6] M. Lechner, P. Dietsch, S. Winter, Veneer-reinforced timber – Numerical and experimental studies on a novel hybrid timber product, *Constr. Build. Mater.* 298, 2021. https://doi.org/10.1016/j.conbuildmat.2021.123880.
[7] F. Nardone, M. Di Ludovico, F.J. De Caso Y Basalo, A. Prota, A. Nanni, Tensile behavior of epoxy based FRP composites under extreme service conditions, *Compos. Part B* Eng. 43:1468–1474, 2012. https://doi.org/10.1016/j.compositesb.2011.08.042.
[8] J. Susainathan, F. Eyma, E. De Luycker, A. Cantarel, B. Castanié, Manufacturing and quasi-static bending behavior of wood-based sandwich structures, *Compos. Struct.* 182:487–504, 2017. https://doi.org/10.1016/j.compstruct.2017.09.034.
[9] P. Reu, All about speckles: Speckle Size Measurement, *Exp. Tech.* 38:1–2, 2014. https://doi.org/10.1111/ext.12110.
[10] R. Kurt, M. Cil, Effects of Press Pressures on Glue Line Thickness and Properties of Laminated Veneer Lumber Glued with Phenol Formaldehyde Adhesive, *BioResources* 7:5346–5354, 2012. https://doi.org/10.15376/biores.7.4.5346-5354.
[11] A. Daoui, C. Descamps, A. Zerizer, R. Marchal, B. Pałubicki, Variation de l'épaisseur du placage de déroulage des bois et son influence sur les caractéristiques mécaniques des panneaux LVL, *MATEC Web Conf.* 11, 2014. https://doi.org/10.1051/matecconf/20141101041.
[12] L. Blomqvist, D. Sandberg, J. Johansson, Influence of veneer orientation on shape stability of plane laminated veneer products, *Wood Mater. Sci.* Eng. 9:224–232, 2014. https://doi.org/10.1080/17480272.2014.919022.

DESIGNING STIFF AND TOUGH BIOCOMPOSITES BY HYBRIDIZATION OF FLAX AND SILK FIBRES: SCRUTINIZING THE EFFECTS OF FIBRE RATIO AND LAMINATE LAY-UP CONFIGURATION

Alexandros Prapavesis[1,*], Weijing Wu[1,2], Penelope Kopana[1], Kobe Schildermans[1], Yasmine Mosleh[3], Aart Willem van Vuure[1]

[1]Department of Materials Engineering, KU Leuven, Kasteelpark Arenberg 44, 3001 Heverlee, Belgium
Email: alexandros.prapavesis@kuleuven.be, penelope.kopana@student.kuleuven.be, kobe.schildermans@student.kuleuven.be
[2]College of Energy and Power Engineering, Nanjing University of Aeronautics and Astronautics, Nanjing 210016, China
Email: weijing.wu@student.kuleuven.be
[3]Biobased Structures and Materials Group, Department of Engineering Structures, Faculty of Civil Engineering and Geosciences, Delft University of Technology, Delft, the Netherlands
Email: y.mosleh@tudelft.nl

Keywords: Biocomposite, Hybrid composites, Ductility, X-ray Computed Tomography, Flax fibre, Silk fibre

Abstract
In this study, the hybridization of flax and silk fibre reinforced composites, at ply level, were studied and compared to their monolithic counterparts. Hybrid FRP laminates were produced via the film-stacking compression moulding method using the highly ductile thermoplastic high-density polyethylene grafted with maleic-anhydride as the matrix. The fibre volume fraction ratio between the two fibres and the lay-up configuration were studied, resulting in hybrid composites with different degrees of distribution of the flax and silk plies within the laminate. The results showed that more balanced properties in terms of stiffness, strength, strain to failure, and impact energy absorption can be achieved by varying those two parameters, thus increasing the designing freedom tailored to specific engineering applications. Additionally, the findings revealed that by optimizing those parameters, multiple fractures of the flax plies or "fragmentation" can be achieved as a toughening mechanism, leading to a pseudo-ductile hybrid composite with a gradual or delayed failure development. The fibre fragmentation mechanism, apart from the increased ductility, can be potentially used as a failure detection criterion for structural health monitoring.

1. Introduction

Flax fibre composites offer a sustainable alternative to traditional synthetic fibre-reinforced composites. Known for their relatively high stiffness and strength along with a low density, these composites find applications in industries such as automotive and construction, combining performance with eco-friendliness [1]. Additionally, flax fibres with negative CO2 emissions during their growth phase, are (potentially) low-cost and have additional outstanding physical properties such as remarkably good acoustic and mechanical vibrational damping and low coefficient of thermal expansion [2, 3]. As the demand for sustainable bio-based solutions grows, flax fibre composites present a compelling option for diverse applications.

However, flax fibre composites have limited impact resistance and toughness due to the intrinsic brittleness of the reinforcing fibres reaching a tensile strain at failure in the range of 1%-2% [4–6]. Therefore, this results in brittle catastrophic failure with little to no signs of failure before breakage and poor impact performance typically reaching energy values of around 4-6 J/mm (normalized to plate thickness, with a 16-20 mm diameter striker on a circular plate of diameter 80mm) [7]. On the other hand, silk, a protein-based (animal) natural fibre is attracting growing attention in the composites research community because it exhibits high ductility resulting in outstanding toughness and impact damage resistance.
In general, silk fibres can be divided based on their origin to spider or silkworm produced fibres with spider silk outperforming silkworm produced silk essentially in any mechanical property, often being described as a "super" fibre. This outstanding combination of properties is a result of continuous evolution by nature for 300-400 million years which allowed the development of fibres capable of stopping larger flying insects with high kinetic energy [8–10]. However, mass production of spider silk is not possible, particularly in the scale required for high performance composites due to the cannibalistic nature of the spiders to control their population dynamic in an area [11]. Therefore, hereafter any mention to silk will refer to silkworm produced silk, specifically produced by the *Bombyx mori* species, which can reach exceptionally high strain to failure of above 16% [12], remarkable toughness (70 MJ/m^3, surpassing traditional highly tough synthetic fibres like Kevlar 40 (50 MJ/m^3) [13, 14]), and high impact resistance [15].

Therefore, it seems promising to combine the high stiffness flax fibres together with the highly tough silk fibres to create a hybrid composite without compromising the bio-based nature of the composite, thus obtaining synergistic properties as well as introducing various modes of damage propagation which can affect the toughness and impact resistance. The two types of fibres can be combined in many different configurations, however the hybridization at the ply level, here indicated as interlayer configuration, where the different layers/plies of each fibre are stacked onto each other, has the advantage of the manufacturing simplicity and low cost for producing hybrid composites, compared to intralayer hybrids where the two fibres are combined within the same fabric and the yarn-to-yarn where the fibres are mixed at the fibre level [16]. The combinations of different lay-up stacking sequence reportedly have a strong effect on the resulting properties of the hybrid composites due to the degree of ply dispersion [17–19] between the two types of fabric layers as well as the fibre volume fraction (V_f) ratio between the fibres, thus resulting in different damage propagation mechanisms. Controlling these parameters in an intelligent combination can result in development of synergistic effects and in some cases appearance of pseudo-ductility [20].

In this study, silk fibres are combined with flax fibres in an interlayer configuration at different fibre volume fraction (V_f) ratios between the two fibres and different lay-up stacking sequences, thus resulting in a range of mechanical behaviour due to the resulting damage initiation and propagation. Both non-hybrid (monolithic) and hybrid laminates were subjected to tensile testing and low-velocity impact and were thereafter inspected using X-ray computed tomography (XCT) to observe the resulting characteristics of the failure modes.

2. Materials and Methods

2.1. Materials

Unidirectional flax fabrics with an areal density of 110 g/m^2 under the commercial tradename FlaxTape were sourced from Ecotechnilin, France and silk weave fabrics with an areal density of 200 g/m^2 were supplied by Sport Soie, France. The silk fabric was degummed by the supplier before used in the manufacturing of the composites. High density polyethylene grafted with maleic anhydride (HDPE-MA), grade Bynel 40E529 was select as the polymer matrix system which was provided by DuPont, Belgium and extruded by Amcor flexibles, Belgium in a thin film with thickness of 65 μm. The reasoning of the matrix selection system is the high strain to failure of above 200% which based on the results of [12, 21] is a crucial parameter to allow the silk fibres to reach their full potential in terms of tensile strain and impact resistance. Furthermore, the melting point of the matrix is around 135 °C, which

is positive since it is highly recommended that the processing temperature is kept below 160 °C due to the thermal degradation temperature of the silk, which is accompanied by a transition in colour of the fabric from white to yellow.

2.2. Composite manufacturing

Because of the hydrophilic nature of both types of fibres, all fabrics together with the matrix films were pre-dried at 60°C for 24h prior to the composite manufacturing step. If this is not done, this may result in high porosity due to the formation of steam because of the applied processing temperature. The composites were manufactured using the film stacking compression moulding method where polymer films of the matrix are stacked alternately between each fabric layer. The stacking of the layers occurs in a stainless steel frame, which is used to control the final thickness of the laminate, thus ensuring high control of the produced thickness of the laminate and hence precise control of the final fibre volume fraction (V_f), which was aimed to be close to 40% for the pure composites and for the hybrids (flax and silk). For the compression moulding process the stack was pressed in a pre-heated hydraulic hot press (Fontijne, Belgium) where pressure of 15 bar and temperature of 150 °C were applied for 15 min, followed by a cooling step to room temperature using the internal cooling system of the press with a cooling speed of approximately 30 °C/min. Both non-hybrid and hybrid composites were manufactured following the same process. The produced laminates were cut into testing coupons using a hydraulic guillotine knife.

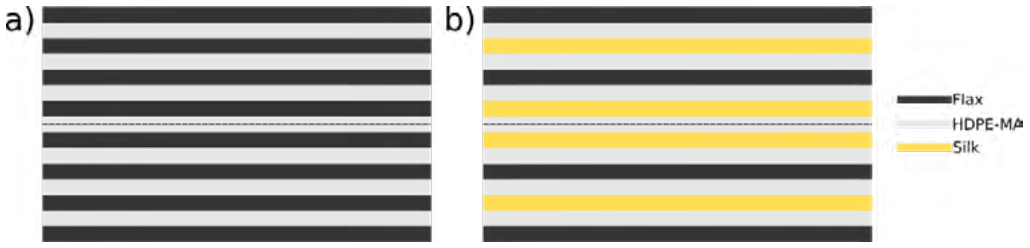

Figure 1. Representative manufacturing layup configurations of a) non-hybrid and b) hybrid composites.

2.3. Tensile testing

Tensile testing was performed using an INSTRON 5567 frame equipped with a 30 kN loadcell and an extensometer to measure the strain. The testing rate and dimensions of the produced specimens were in accordance with ASTM D3039. No end tabs were used apart of sandpaper, however the statistical majority of the specimens failed within the gauge length and samples failing within the gripping area were excluded from the analysis.

2.4. Low-velocity-impact testing

Impact properties were determined using an INSTRON CEAST 9350 following the falling weight impact method, where in this test specimens of 100×100 mm plates were punctured using a rail guided striker with a hemispherical head of 20 mm diameter. The combination of the striker mass and drop height resulted in a kinetic energy level before impact of 100 J. The composite plates were pneumatically clamped with a ring-shaped fixture with an inner diameter of 80 mm. The force was recorded using a 22 kN loadcell installed in the striker and the displacement was recorded using a laser device monitoring the position of the striker. Together with the monitoring of the time, force-displacement and displacement-time diagrams were used to determine the actual kinetic energy before impact and after impact, thus leading to a precise calculation of the absorbed impact energy. The specimens used for the impact testing had a crossply configuration to properly characterize the composite behaviour in impact.

2.5. X-ray computed tomography (XCT)

The post-impact inspection of the composites was performed using the XCT scanner TESCAN UniTom HR equipped with a 160 kV/25 W X-ray tube with a tungsten reflection target and a detector of 2916 x 2280 pixels, with a 50 µm pixel pitch. The scans were performed at 60 kV and 4 W with a voxel size of 4 µm for the tensile and 30 µm for the impact specimens, respectively. The reasoning behind the larger voxel size for the impact specimens is the need for a larger field of view due to the large area affected by the impact load. In total, 3000 radiographic projections were acquired over a 360° angle rotation of the sample each with a 210 ms exposure time and with a frame averaging set to 5. After acquisition, the radiographic projections were reconstructed to tomographic slices using the TESCAN reconstruction software Panthera, which is based on a filter back-projection algorithm. The results analysis and further 2D or 3D visualization were performed in the Avizo software (Thermo Fisher Scientific).

3. Results and discussion

The mechanical behaviour of the hybrid composites compared to the non-hybrid flax and silk composites is shown in Figure 1, using the representative stress-strain diagrams. The reference non-hybrid composite shows the reasoning behind the combination of these two fibres with flax being significantly stiffer and stronger but with a drastically lower tensile failure strain, whereas the silk is compliant but has a higher failure strain. It is observed that depending on the stacking sequence (Figure 1a) the hybrid composites achieve different behaviour and more noticeably strain to failure, despite having the same flax and silk ratio. When the silk fibres are positioned on the outside in a “sandwich” configuration with the flax fabrics on the inside, the composite exhibits sudden catastrophic failure when the hybrid composite reaches the failure strain of the flax composites. On the other hand, when the layers are positioned inversely, the hybrid shows an initial drop at the strain to failure level of flax composites, however then pseudo-ductility is noticed where the stress remains on a fairly stable level while the composite can reach nearly 5 times higher strain to failure than non-hybrid flax composites. This pseudo-ductility is a result of the damage mechanisms within the composite where after the initial fragmentation, delaminations develop and spread around the fragmented brittle fibre fabric [16, 20]. Additionally, the more dispersive configurations often showed a more classical hybrid behaviour where an initial drop is observed and is followed by a transition of the load to the remaining silk fabrics which to a little extent delays the failure of these hybrid composites.

Similarly, in Figure 1b, the effect of the V_f ratio between the two fibres on the mechanical response is presented. It is observed that at flax V_f level of above 21%, the failure of flax layers essentially determines the fracture of the hybrid composite, because the silk layers are getting damaged due to the energy release during the breakage of flax. However, this strain energy release due to flax fibre breakage can be avoided at lower flax V_f content, thus allowing the silk layers to survive since there are less flax layers failing, and thus keep carrying load. Moreover, at flax V_f content of 7%, the hybrids can retain almost all the strain to failure compared to the pure silk composites coupled with a noticeably higher stiffness due to the presence of the much stiffer flax layers leading to significant synergistic effect.

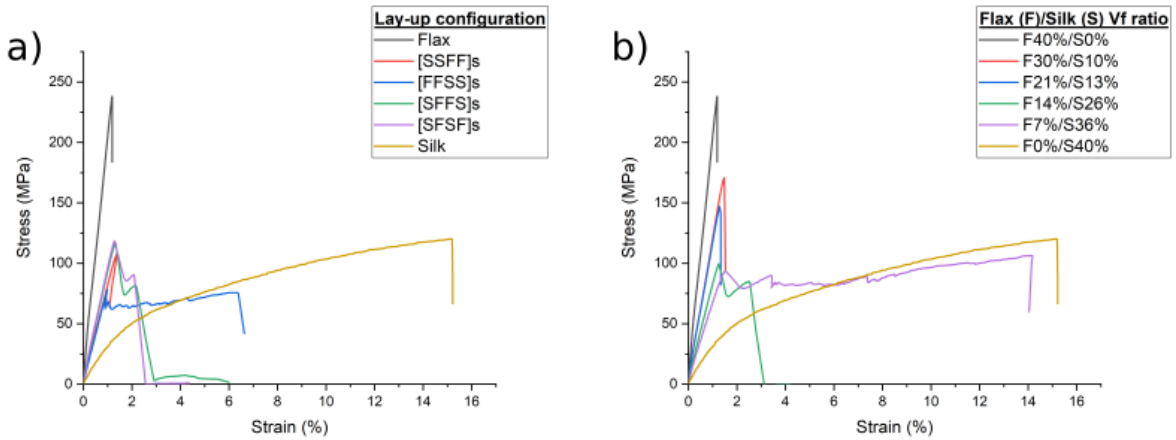

Figure 2. Representative stress-strain diagrams of hybrid composites and their non-hybrid counterparts: a) effect of layup configuration for the same V_f ratio of flax 14%/silk 26% and b) effect of the V_f ratio.

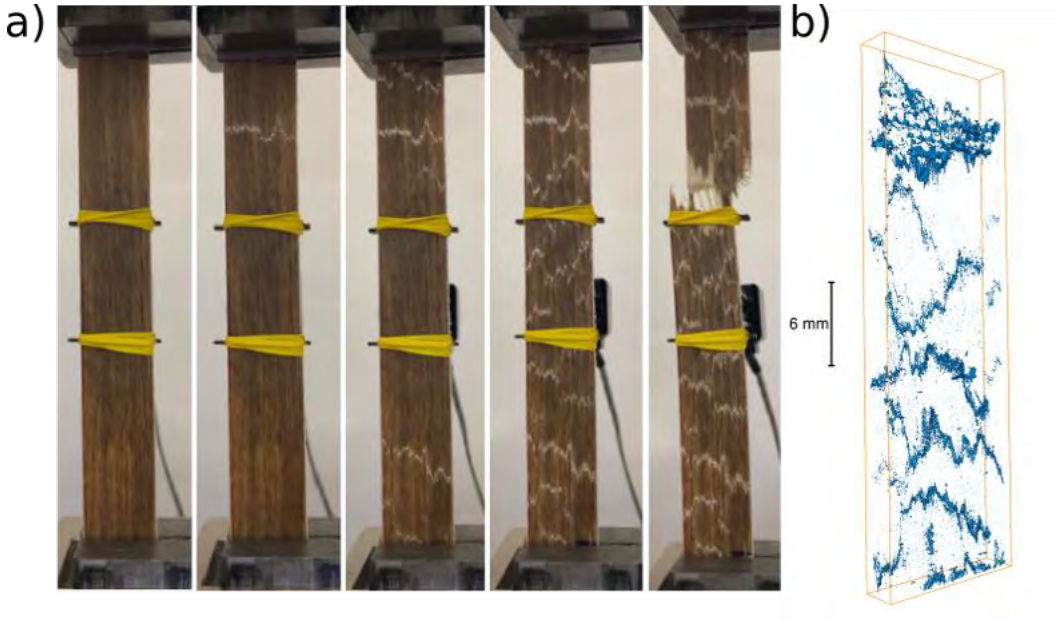

Figure 3. a) Visual development of the fragmentation process and b) internal image using XCT observation of the damage mechanism which resulted in the appearance of pseudo-ductile behaviour,

Multiple fractures of the flax layers were achieved in specimens by optimizing the combination of the two parameters of lay-up stacking sequence and V_f ratio between the two fabrics. The fragmentation behaviour (Figure 3a) starts with one fragment when the strain to failure of flax is reached, however with further increase of the strain the stress starts building up again resulting in the creation of follow up failures on the same flax layers, which are often accompanied by delamination of flax near the fragmented area (Figure 3b). The samples which exhibited this fragmentation process had a stress-strain curve where a pseudo-ductile behaviour was visible.

The impact resistance is one of the key reasons for performing hybridization in this study. Figure 4 shows the impact force-displacement recorded together with the low-velocity kinetic energy absorption at penetration. It can be seen that increasing the V_f content of silk higher than the flax content increases

the kinetic energy required for penetration. However, from the tensile stress-strain curve, it can be observed that this comes at a cost of primarily stiffness. Overall, the sandwich structure with flax at the outer layers showed consistently, for all V_f ratios, the best performance amongst the different stacking sequences. One potential explanation is that due to the stiff and strong fibres being on the outside, the bending stiffness of the laminate increases and since a bending moment is induced when the striker impacts the specimen, higher bending stiffness increases the resistance to the impact load.

Another observation is that when the flax/silk fibre content ratio increases from 14%/26% to 21%/13% and above, the impact energy absorption is practically the same as for the pure flax composites, which is rather limiting towards application of these materials where high stiffness is essential for the structure. Overall, the flax/silk system with a ratio of 14%/26% shows an in between behaviour with ~130% improvement in impact energy compared to the flax composites while retaining a stiffness higher than the silk composites, thus allowing more design freedom in the use of bio-based composites due to its more balanced properties.

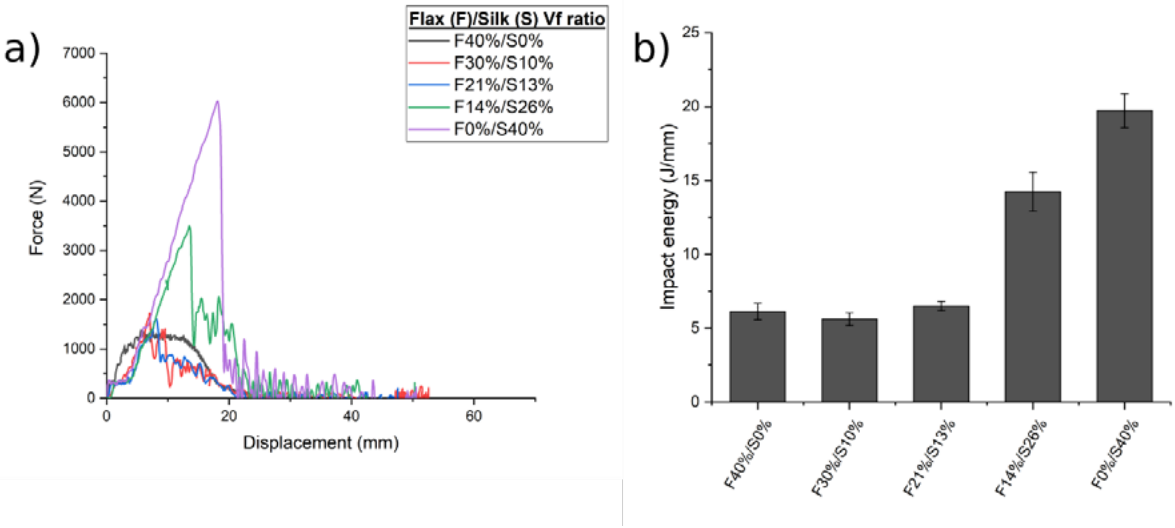

Figure 4. Impact properties of produced hybrids compared to non-hybrids: a) force-displacement representative curves and b) calculated impact energy absorbed normalized to laminate thickness.

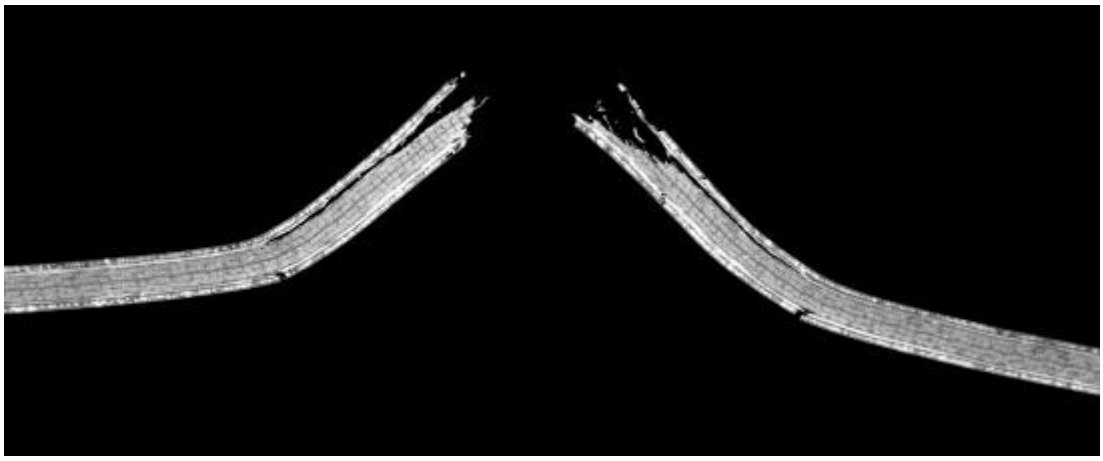

Figure 5. Internal damage observation of best performing hybrid (F14%/S26%) in impact using XCT.

Furthermore, XCT was used to study and explain the high, compared to non-hybrid flax, energy absorption in low-velocity impact of the F14%/S26% sandwich-type hybrids where the flax is located at the outer plies. Using this method the internal damage of the specimens is visualized in Figure 5 where the appearance of large delamination areas is observed indicating that this combination of design parameters for the hybrid material results in damage spreading over a larger area.

4. Conclusions

In this work, the interlayer hybridization of stiff and strong flax fibres with highly tough silk fibres was explored using different lay-up stacking sequences with a range of V_f ratios between the two fibres. By controlling these parameters, different stress-strain behaviours and balance in properties such as stiffness, strength, tensile strain to failure and impact energy absorption was achieved. It was noticed that when the fibre content of flax is higher than 21%, compared to the total 40%, the failure of flax fibres determines the failure of the hybrid composites due to the damage to the surrounding silk layers, explained by the violent nature and rapid energy release from the flax fibre breakage. Furthermore, in specific cases, namely F14%/S26%, only for the [FFSS]s configuration, and for the composites with volume fraction ratio F7%/S36%, the fragmentation of flax layers in multiple locations across the specimen's length was observed, which resulted in around 5 times higher strain to failure compared to flax fibre composites. This introduction of pseudo-ductility was further studied using XCT where flax delamination around the fragmented areas was observed, thus introducing a damage mechanism which can be used to control the materials' behaviour and additionally these local delaminations add to energy absorption mechanisms. Furthermore, laminates with fibre content of 14% flax/26% silk showed more than 130% increase in impact energy absorption compared to monolithic flax fibre composites while retaining a higher modulus than silk composites. This observation was explained using XCT suggesting that large delamination areas lead to spread of damage over a larger volume in this hybrid configuration.

References

[1] K.L. Pickering, M.G.A. Efendy, and T.M. Le, "A review of recent developments in natural fibre composites and their mechanical performance.," *Composites Part A: Applied Science and Manufacturing*. vol. 83, pp. 98–112, 2016.

[2] S. V. Joshi, L.T. Drzal, A.K. Mohanty, and S. Arora, "Are natural fiber composites environmentally superior to glass fiber reinforced composites?," *Composites Part A: Applied Science and Manufacturing*. vol. 35, no. 3, pp. 371–376, 2004.

[3] F. Duc, P.E. Bourban, C.J.G. Plummer, and J.A.E. Månson, "Damping of thermoset and thermoplastic flax fibre composites.," *Composites Part A: Applied Science and Manufacturing*. vol. 64, pp. 115–123, 2014.

[4] M.C. Symington, W.M. Banks, O.D. West, and R.A. Pethrick, "Tensile testing of cellulose based natural fibers for structural composite applications.," *Journal of Composite Materials*. vol. 43, no. 9, pp. 1083–1108, 2009.

[5] D.B. Dittenber and H.V.S. Gangarao, "Critical review of recent publications on use of natural composites in infrastructure.," *Composites Part A: Applied Science and Manufacturing*. vol. 43, no. 8, pp. 1419–1429, 2012.

[6] F. Bensadoun, I. Verpoest, J. Baets, et al., "Impregnated fibre bundle test for natural fibres used in composites.," *Journal of Reinforced Plastics and Composites*. p. 2017.

[7] F. Bensadoun, D. Depuydt, J. Baets, I. Verpoest, and A.W. van Vuure, "Low velocity impact properties of flax composites.," *Composite Structures*. vol. 176, pp. 933–944, 2017.

[8] W.A. Shear, J.M. Palmer, J.A. Coddington, and P.M. Bonamo, "A devonian spinneret: early evidence of spiders and silk use.," *Science (New York, N.Y.)*. vol. 246, no. 4929, pp. 479–481, 1989.

[9] R.J. Garwood, J.A. Dunlop, B.J. Knecht, and T.A. Hegna, "The phylogeny of fossil whip spiders.," *BMC Evolutionary Biology*. vol. 17, no. 1, pp. 1–14, 2017.

[10] D.P. Knight and F. Vollrath, "Liquid crystalline spinning of spider silk.," *Nature*. vol. 410, no. 6828, pp. 541–548, 2001.

[11] D.H. Wise, "Cannibalism, food limitation, intraspecific competition, and the regulation of spider populations.," *Annual review of entomology*. vol. 51, pp. 441–465, 2006.

[12] A.W. Van Vuure, J. Vanderbeke, Y. Mosleh, I. Verpoest, and N. El-Asmar, "Ductile woven silk fibre thermoplastic composites with quasi-isotropic strength.," *Composites Part A: Applied Science and Manufacturing*. vol. 147, pp. 1–28, 2021.
[13] Z. Shao and F. Vollrath, "Surprising strength of silkworm silk.," *Nature*. vol. 418, no. 6899, p. 741, 2002.
[14] J.G. Hardy, L.M. Römer, and T.R. Scheibel, "Polymeric materials based on silk proteins.," *Polymer*. vol. 49, no. 20, pp. 4309–4327, 2008.
[15] A.W. Van Vuure, Y. Mosleh, J. Vanderbeke, and I. Verpoest, "Highly Impact-Resistant Silk Fiber Thermoplastic Composites.," *Advanced Engineering Materials*. vol. n/a, no. n/a, p. 2300080,.
[16] Y. Swolfs, L. Gorbatikh, and I. Verpoest, "Fibre hybridisation in polymer composites: A review.," *Composites Part A: Applied Science and Manufacturing*. vol. 67, pp. 181–200, 2014.
[17] L. Onal and S. Adanur, "Effect of stacking sequence on the mechanical properties of glass-carbon hybrid composites before and after impact.," *Journal of Industrial Textiles*. vol. 31, no. 4, pp. 255–272, 2002.
[18] S.C. Amico, C.C. Angrizani, and M.L. Drummond, "Influence of the stacking sequence on the mechanical properties of glass/sisal hybrid composites.," *Journal of Reinforced Plastics and Composites*. vol. 29, no. 2, pp. 179–189, 2010.
[19] Y. Swolfs, R.M. McMeeking, I. Verpoest, and L. Gorbatikh, "The effect of fibre dispersion on initial failure strain and cluster development in unidirectional carbon/glass hybrid composites.," *Composites Part A: Applied Science and Manufacturing*. vol. 69, pp. 279–287, 2015.
[20] Y. Swolfs, Y. Meerten, P. Hine, I. Ward, I. Verpoest, and L. Gorbatikh, "Introducing ductility in hybrid carbon fibre/self-reinforced composites through control of the damage mechanisms.," *Composite Structures*. vol. 131, pp. 259–265, 2015.
[21] A.W. Van Vuure, Y. Mosleh, J. Vanderbeke, and I. Verpoest, "Highly Impact-Resistant Silk Fiber Thermoplastic Composites.," *Advanced Engineering Materials*. vol. n/a, no. n/a, p. 2300080, 2023.

RELATION BETWEEN PROCESS, MICROSTRUCTURE AND MECHANICAL PROPERTIES OF A CONTINUOUS CERAMIC FIBER UNDER DEVELOPMENT

J. Redonnet[1,2], S. Joannès[2], O. Francy[1], S. Pfeifer[3], B. Clauβ[3], M.H. Berger[2]

[1]Saint-Gobain Research Provence, 550 avenue Alphonse Jauffret,
CS 20224 – F 84306 Cavaillon Cedex France
Email: Juliette.Redonnet@saint-gobain.com, Olivier.Francy@saint-gobain.com
Web Page: https://www.saint-gobain.com/fr/saint-gobain-research-provence-cavaillon-france
[2] Mines Paris, Université PSL, Centre des Matériaux (MAT), CNRS UMR 7633,
Evry Cedex, BP 87 91003, France
Email: juliette.redonnet@minesparis.psl.eu, marie-helene.berger@minesparis.psl.eu,
sebastien.joannes@minesparis.psl.eu,
Web Page: https://www.mat.minesparis.psl.eu/
[3]German Institutes of Textile and Fiber Research (DITF),
Körschtalstraβe 26, 73770 Denkendorf, Germany
Email: stephanie.pfeifer@ditf.de, bernd.clauss@ditf.de, Web Page: https://www.ditf.de/en/

Keywords: ceramic fiber, mechanical characterization, uncertainties, failure control, critical defects

Abstract
The development of ceramic matrix composites is highly dependent on the availability of continuous and weavable ceramic fibers with increasingly high thermo-mechanical properties. The present study is part of a collaboration between Saint-Gobain Research Provence, the DITF (Deutsche Institute für Textil- und Faserforschung) and the Centre des Matériaux of Mines Paris within the framework of a PhD project. The goal is to develop continuous oxide ceramic fibers by studying the relationship between process, microstructure and thermo-mechanical properties. Mechanical characterization at the single fiber scale is challenging due to the very small size of a fiber, ten times thinner than a human hair, and many difficulties arise from its brittleness. Single fiber tensile test requires accurate evaluation of the uncertainties associated with the various steps from fiber extraction from the bundle to data storage. Many questions remain unanswered regarding the understanding of the monofilament behavior of a continuous ceramic fiber due to the fracturing of the fiber during a tensile test. Information such as failure location and failure surface observations are therefore inaccessible. Single fiber tensile tests in a viscous medium have overcome some of these difficulties.

1. Introduction

Continuous weavable oxide ceramic fibers constitute the architecture of many Ceramic Matrix Composites (CMC). The damage tolerant elastic behavior of CMC combined with the refractory properties of ceramics and their low densities, make them the best candidate to replace metal alloys operating in extreme environments in aeronautical and aerospace structures and land turbines. For such applications CMC can significantly increase turbine operating temperatures, thereby improving efficiency and reducing emissions of polluting gases.
There are two different types of CMC: non-oxide (C/C, C/SiC, SiC/SiC) and oxide (alumina/alumina, mullite/alumina, …). Non-oxide CMC show good mechanical properties at high temperature, but their durability is affected by their low oxidation resistance. In addition, the high cost of SiC fibers makes

non-oxide CMC expensive solutions. Oxide CMC, also referred to as O-CMC, are more suitable for oxidizing environment working at medium temperature. The development of these CMC is highly dependent on the availability of continuous ceramic fibers. Currently, no continuous weavable oxide fiber is produced and marketed in Europe. The market is dominated by the American leader 3M Company.

The DITF (Deutsche Institute für Textil- und Faserforschung) has published very promising pre-pilot scale results for the development of alumina-based fibers [1] and mullite fibers [2]. To address high-growth, high value-added markets and in line with its environmental commitments, Saint-Gobain has entered a collaboration with the DITF for the development and production of continuous oxide ceramic fibers. Through the Centre des Matériaux, Mines Paris - PSL University has more than forty years of experience in the microstructural and mechanical characterization of fibers. The aim of this tripartite partnership is to optimize, at the scale of a continuous pilot, an alumina fiber in order to achieve mechanical properties comparable to those of non-European manufacturers for the reinforcement of oxide matrices with a view to its industrialization.
Ceramic fibers are designed to reinforce critical structural parts. Since they are responsible for the mechanical strength of the composite, determining their performance is of paramount importance. Ceramic fibers are made from bundles of hundreds of fibers. Two types of mechanical tests can be used to evaluate their mechanical properties: bundle or single fiber tensile tests. Bundle tensile tests are easier to implement and give a quick idea of the strength of the bundles used in structures if the dimension of the failure surface can be reached. This is an initial approach that should be supplemented by single fiber tests. At the single fiber scale, it is possible to obtain information on the variability of strength within a bundle and thus correlate microstructural observations with mechanical properties.

Performing a single-fiber tensile test on a fragile filament that is ten times thinner than a human hair is not a simple matter. Although single fiber testing has been around for several decades, its implementation remains a real challenge, especially for such fine, fragile fibers. Many parameters and uncertainties must be taken into account to properly understand the mechanical behavior of such materials. Mechanical properties reported by different authors in the literature show significant differences in strength results [3]. In addition, during a single tensile test, ceramic fibers break into multiple pieces due to the release of stored energy and it is then impossible to locate the failure, recover the pieces, and observe the failure surfaces, which could provide information about critical defects.
Many questions arise: Is the flaw randomly distributed along the gauge length? How do we get access to the flaws? How can we trust the mechanical measurement if it cannot be verified?
We will first focus on the difficulties associated with mechanical characterization of ceramic fibers before attempting to understand how to overcome fiber breakage during tensile testing and how to access basic information such as failure location and failure surfaces.

2. Difficulties in testing single ceramic fibers

Due to their small size, cross-sectional diameter, morphological variations, and random sampling, mechanical tests on fibers require an appropriate protocol otherwise many uncertainties can introduce errors and affect the test accuracy. The various steps that must be considered throughout the process to obtain accurate mechanical data in single fiber tensile testing are described in Figure 1 and are applicable to many fiber types. For example, a single fiber tensile test, whether natural or synthetic fiber, begins with fiber sample preparation, as this first step is delicate and operator dependent, but very few studies have looked at and reported on the biases introduced during this stage.

Figure 1. The steps involved in generating mechanical fiber characterization raw data. This diagram is based on a collaborative work within the MecaFib Research Group (GDR CNRS)

Ceramic fibers present additional difficulties in single fiber testing. Two types of strength variability must be understood in order to estimate the uncertainties and interpret the results:

1. Uncertainties due to sample preparation which, as with any type of fiber, lead to variations in results. The brittleness of ceramic fibers introduces additional difficulties described below.
2. Strength variability within a ceramic fiber sample is high due to defect dispersion. A statistical dispersion model such as Weibull theory is used to describe the strength variability.

The brittleness of ceramic fibers makes them difficult to handle and requires special care during specimen preparation. Fiber mounting on the jaws and the arbitrary pre-selection affect the final strength values and variability [4].
Conventionally, a single filament tensile test starts by extracting a single filament from the bundle and then mounting this fiber on a cardboard frame, aligned in a straight line and glued at its ends. The fiber must be carefully prepared to be as aligned as possible with direction of loading to minimize angular misalignment [5]. The distance between the two glue points determines the gauge length and must be as accurate as possible since fiber strength depends on the length tested. The cardboard frame is then attached to the tensile machine with two holes, and the central part of the cardboard frame is removed by cutting, exposing the fiber for tensile testing. This method works properly but is operator dependent (especially for the fiber alignment), time-consuming and cumbersome [3]. Due to the strength variability, a large number of fibers must be tested to obtain the most representative fiber sample. Dia-Stron® has developed solutions to improve fiber testing instrumentation and reduce fiber breakage during setup on the tensile machine. Dia-Stron® have for example developed a unique sample mounting method to align the fibers and reduce handling as much as possible. A fiber is glued at its ends on two plastic tabs well positioned in a cassette and quickly secured with a UV-curing adhesive (Figure 2). Different gauge lengths can be chosen (4, 12, 20 or 30 mm) to suit a variety of applications. The sample can then be transferred to the machine with a pick-up pen or semi-automatic vacuum arm. This transfer

of fragile samples from the storage cassette to the tensile module is efficient and safe, allowing more fibers to be tested compared to traditional techniques.

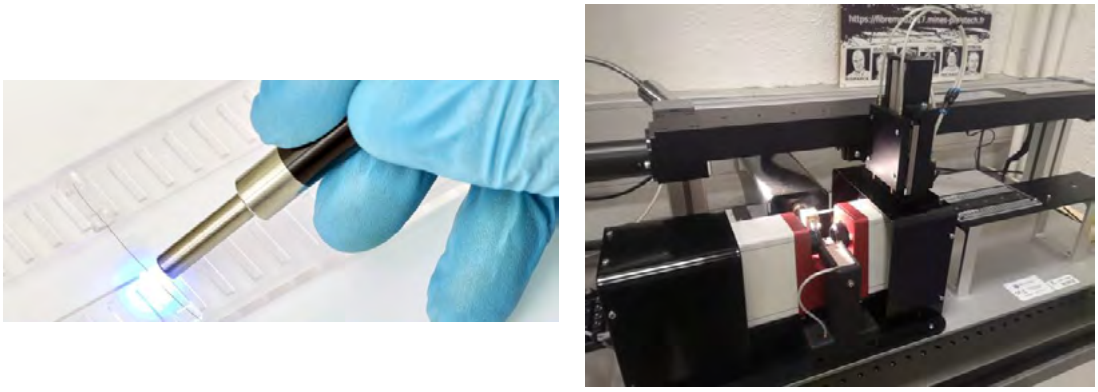

Figure 2. The Dia-Stron® sample mounting and machine [6]

During the preparation of a single fiber sample, the pre-selection effect is often underestimated. Indeed, during the fiber extraction from the bundle, some fibers may break and will not be tested. These are not necessarily the least resistant fibers, but those that "see" too much effort during extraction, either because of entanglement with other fibers or because of inappropriate effort (bending, twisting, etc.). Depending on the number of broken fibers during the extraction, the strength distribution is more or less truncated, resulting in non-linearities on the Weibull graph. As no solution can help to completely avoid pre-selection, proper treatment of these non-linearities is essential, and Bayesian statistical methods are well suited to analyze the results.

3. Multi-fragmentation in tensile testing: Controlling ceramic fiber fracture

Failure in ceramic fibers is initiated by the presence of critical defects of variable size, which are assumed to be randomly distributed. Fiber strength is generally described by a 2-parameter Weibull distribution [7], [8]. This statistical model, commonly associated to the concept of the weakest-link (a strong belief), is widely used in materials science. However, its application requires the utmost vigilance with respect to the underlying assumptions. For non-interacting defects randomly distributed in a stressed volume, the Weibull distribution correctly predicts the failure probability if and only if “the stress dependence of the probability that a flaw will be critical is a power law or can be approximated well by a power law” [9]. In particular, it is important to verify the nature of the defects and confirm the "locally initiated failure by flaws".

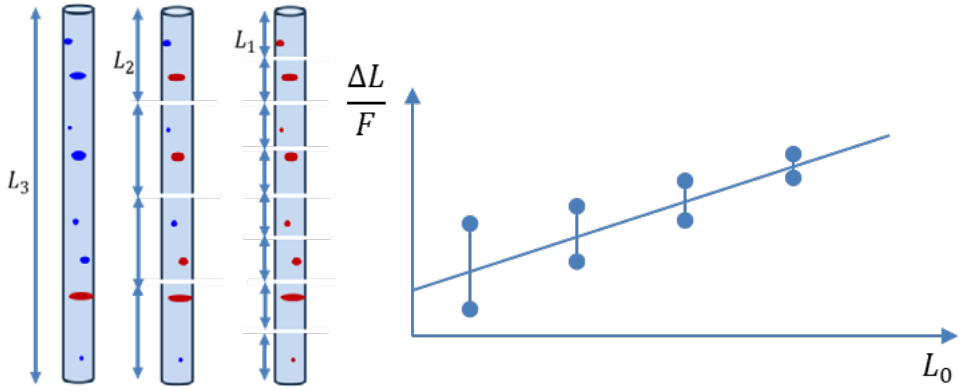

Figure 3. Distribution of critical defects (in red) size and location depending on the length considered. (Diagrams from (CMC)² Research Group)

Therefore, from an understanding standpoint, it is primordial to recover and observe the failure surfaces and thus identify the critical defects. From an industrial point of view, understanding the presence and distribution of these defects is also the key to the production of stronger fibers by avoiding their formation during the manufacturing process. However, during a tensile test, the release of stored energy causes the ceramic fiber to fracture into multiple pieces, resulting in a flexural secondary failure (Figure 4). It is then impossible to locate the primary failure, recover the pieces and observe the failure surfaces which could provide information about critical defects.

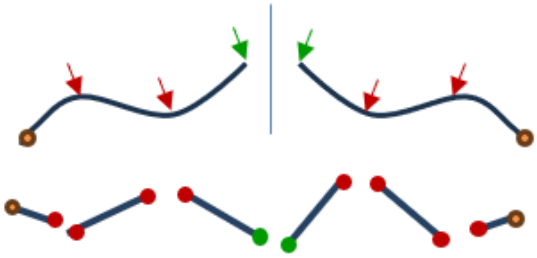

Figure 4. Multi-piece fracture of a ceramic fiber as a result of shock wave propagation. Green: Tensile primary failure, Red: Flexion secondary failure

The multi-piece fracture of a ceramic fiber, which is very difficult to observe, was tracked with a high-speed camera at a frequency of 75 000 frames per second (Figure 5).

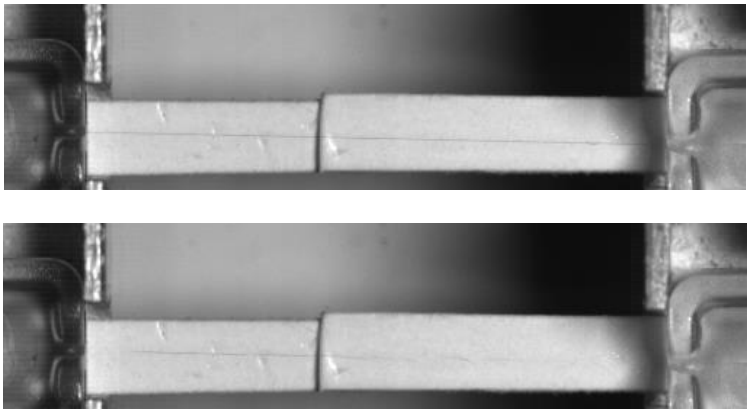

Figure 5. High Speed Camera images (75000 fps) of a ceramic fiber fracture during a tensile test. Top: Image before the failure, Bottom: Image just after failure

Even with such a high acquisition frequency, the primary failure is difficult to locate because the break is catastrophic. In the image immediately after the failure, many parts of the fiber have already disappeared. Either, the fracture was initiated at this point, or the shock wave propagation moved this part out of the focus of the camera. This method is quite limited but confirms the multi-piece fracture of the ceramic fiber during a tensile test.

In the literature, tensile tests have been performed in a viscous medium to absorb the shock wave and prevent the fiber from breaking into multiple pieces. Studies have used viscous media such as glycerin [10], grease [8] or petroleum jelly [11] to absorb the shock wave. The following section presents the experimental setup developed for this study.

3.1. Method

A special holder has been designed (Figure 6). The fiber is placed between the jaws shown at the top of the drawing. A support consisting of a 1 mm deep mini tank is placed under the fiber. This tank is then

carefully filled with glycerin using a pipette to cover the entire gauge length of the fiber. The viscous glycerin forms a bulge above the tank, allowing the fiber to be completely coated.
After the tensile test, only one break has occurred, and the two pieces of the fiber are still attached to the jaws. The ends of the fiber pieces are immersed in an ethanol bath to clean the glycerin and glued to a copper adhesive tape for SEM observation.

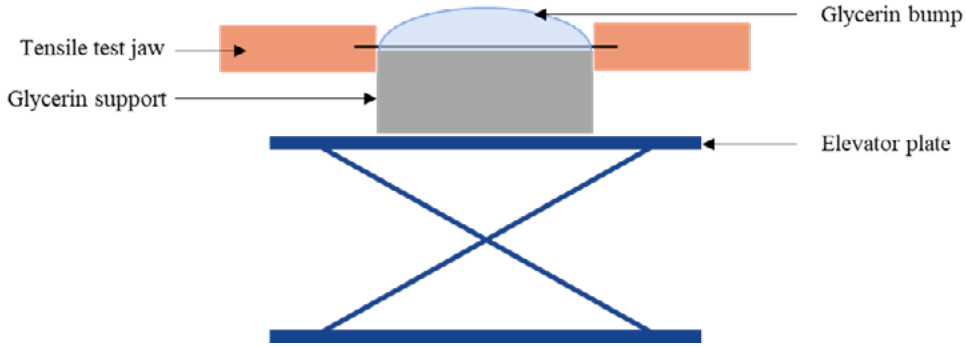

Figure 6. Experimental Mounting of glycerin single fiber tensile test

3.2. Results

This method allowed the failure to be located and the fracture surfaces to be observed. When the failure occurred between the jaws, the fracture is randomly distributed along the gauge length. However, 40% of the fibers tested broke in the jaws. Despite the optimization of the alignment and gluing steps, it was not possible to avoid some fiber failures in the jaws. The explanation for this phenomenon is still under investigation.
For the remaining fibers that broke between the jaws, most of the failure surfaces show a porous zone either in the core or on the surface of the fiber with poorly sintered grains inside. These defects lower the failure stress; the larger the defect, the lower the mechanical strength value.

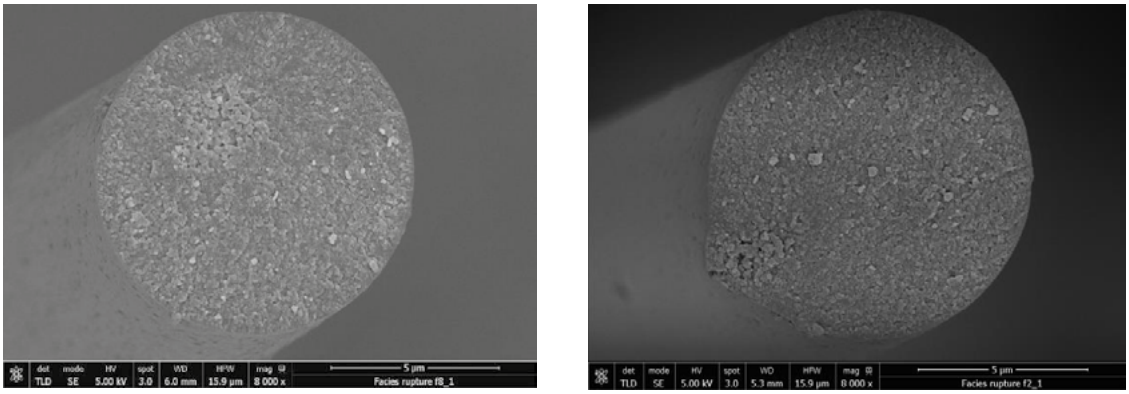

Figure 7. SEM images of the fracture surface recovered in a single fiber glycerin tensile test.

These defects have highlighted an inhomogeneity within the fibers that still needs to be related to the manufacturing process in order to maximize mechanical strength.
Further studies will focus on the possible influence of the glycerin on the strength values, a comparison with tensile tests performed in air will be done.

4. Conclusion

To produce high-resistance ceramic fibers with thermo-mechanical properties that meet the specifications required for O-CMC, the relationship between the manufacturing process parameters, the fiber microstructure, and their mechanical properties must be fully understood and controlled. However, access to accurate mechanical data on ceramic fibers is a real challenge. These 10 µm diameter brittle fibers require a specific protocol starting from sample preparation to overcome the various uncertainties that lead to strength variations. Solutions such as the Dia-Stron® machine have been developed to improve the fiber alignment, fiber loading and test convenience. The pre-selection effect remains an important error factor. Strength variability in ceramic fibers also results from the random flaw distribution along the fibers introduced during the manufacturing process. The multi-piece fracture of the ceramic fiber during a tensile test in air due to the release of stored energy prevents the recovery of the failure surfaces and access to the original microstructural information. Single fiber tensile tests performed in glycerin allowed recovery of the failure surfaces and observation of the critical defects leading to failure. These observations are key for understanding the critical defects and their origin in order to avoid them in the manufacturing process and to improve the failure stresses of the fibers.

Acknowledgments
This work would not have been possible without the collaboration instituted between Saint-Gobain Research Provence, the DITF and Mines Paris-PSL. The authors would particularly like to thank the colleagues from these institutions involved in the program for their support.

References

[1] Pfeifer, S., Demirci, P., Duran, R., Stolpmann, H., Renfftlen, A., Nemrava, S., Niewa, R., Clauß, B., & Buchmeiser, M. R. Synthesis of zirconia toughened alumina (ZTA) fibers for high performance materials. *Journal of the European Ceramic Society*, 36(3), 725-731, 2016
[2] Reinders, L., Pfeifer, S., Kröner, S., Stolpmann, H., Renfftlen, A., Greiler, L. C., Clauß, B., & Buchmeiser, M. R. Development of mullite fibers and novel zirconia-toughened mullite fibers for high temperature applications. *Journal of the European Ceramic Society*. 41(6) : 3570-3580, 2020.
[3] Joannès, S., Islam, F., and Laiarinandrasana, L. Uncertainty in Fibre Strength Characterisation Due to Uncertainty in Measurement and Sampling Randomness. *Applied Composite Materials*, 27(3):165–184, 2020.
[4] Berger, M. H. and Jeulin, D. Statistical analysis of the failure stresses of ceramic fibres: Dependence of the Weibull parameters on the gauge length, diameter variation and fluctuation of defect density. *Journal of materials science*, 38 : 2913-2913, 2003.
[5] Islam, Joannès, Laiarinandrasana. Evaluation of Critical Parameters in Tensile Strength Measurement of Single Fibres, *Journal of Composites Science*, 3: 69, 2019.
[6] https://www.diastron.com/
[7] Wolfenden, A. and van der Zwaag, S. The Concept of Filament Strength and the Weibull Modulus. *Journal of Testing and Evaluation*, 17(5):292, 1989.
[8] Wilson, D. Continuous oxide fibers. *Handbook of Properties of Textile and Technical Fibres*. Elsevier, 903–927, 2018.
[9] M.T. Todinov. Is Weibull Distribution the Correct Model for Predicting Probability of Failure Initiated by Non-Interacting Flaws? *International Journal of Solids and Structures* 46, nº 3-4: 887-901; 2009.
[10] Sawyer, L. C., Jamieson, M., Brikowski, D., Haider, M. I., and Chen, R. T. Strength, Structure, and Fracture Properties of Ceramic Fibers Produced from Polymeric Precursors: I, Base-Line Studies. *Journal of the American Ceramic Society*, 70(11):798–810; 1987.
[11] Cantonwine, P. E. Strength of thermally exposed alumina fibers. Part I Sinfle filament behavior. *Journal of materials science*, 38: 461-470, 2003.

INFLUENCE OF THE USE OF ADDITIVE PHASE CHANGE MATERIALS IN THE MATRIX OF FIBRE COMPOSITES ON THE ABLATIVE PROPERTIES

R. Szczepaniak[1*], P. Przybyłek[1], K. Krzysztofik[2], J. Masiewicz[1], M. Mucha[1], P. Sapiński[1], E. Kosicka[3]

[1] Faculty of Aviation, Polish Air Force University, Dywizjonu 303 Street No. 35, 08-521 Dęblin, Poland
[2] Institute of Navigation, Polish Air Force University, Dywizjonu 303 Street No. 35, 08-521 Dęblin, Poland
[3] Faculty of Mechanical Engineering, Lublin University of Technology, 20-618 Lublin, Poland
Email: r.szczepaniak@law.mil.pl

Keywords: composite, phase change material, ablative properties, ablative weight loss

Abstract

The need to provide thermal protection for sensitive aeronautical technology components exposed to high heat flux temperatures necessitates the emergence of new materials with high thermal protection properties. The research focused on a fiber composite consisting of 14 layers of aramid fabric and 6 layers of carbon fabric. Epidian 52 epoxy resin hardened at room temperature with TFF hardener was used as a matrix. The resin was modified with phase change material (PCM) in the form of Micronal DS5038X powder. Two series of 3 pieces each were prepared, differing in the amount of PCM in the composite matrix. The samples were exposed to a mixture of hot gases at a temperature of approximately 1100°C for 3 minutes. During the tests, the temperature of the material's ablation surface, the temperature of the back surface, as well as the temperature in 3 places of the composite up to half of its thickness from the back surface were read. A thermal imaging camera was used to verify the temperature distribution on the rear surface. After the tests, the ablation mass loss and mass ablation rate were also analyzed.

Analysing the experimental results, it was found that the use of phase change materials in the composite matrix would significantly affect the ablative properties of the material. The average value of the back wall surface temperature of the fibre composite without the addition of PCM after 180 seconds was about 168°C. The average back wall surface temperature of all composites with the addition of phase change material PCM was in the range of 96 ± 10°C after 180 seconds. The fibre composites with PCM addition reached a rear wall surface temperature of approximately 1000°C reduced from the ablative surface temperature. The ablative weight loss of the fibre composites without PCM addition was 31.7%. The relative ablative weight loss of the polymer composite with 16% PCM addition has a value of 32.9%. The addition of PCM to the composite resulted in an increase in ablative weight loss of approximately 1- 4 % (relative to the original weight of the material tested).

1. Introduction

Ablation is a self-regulating process of heat and mass exchange, resulting in irreversible structural and chemical changes to a material due to physical transformations and chemical reactions, with concomitant heat absorption. This process is initiated and sustained from external thermal energy sources. In the physical model of ablation, one can distinguish [1, 2]:

- the ablative surface,
- the ablative layer, located between the ablation front and the ablative surface,
- the ablation front, separating the ablation layer from the virgin material,
- the virgin material.

Through the ablative surface, which occurs at the interface between the gas and solid phases, heating takes place. Chemical processes take place in the ablative layer, which can be divided into the following groups [2, 3]:

- pyrolysis and chemical decomposition reactions,
- thermochemical transformations of solid and gaseous decomposition products,
- solid-phase chemical reactions between solid and gaseous decomposition products,
- phase transformations of undecomposed material components and chemical reaction products,
- transformations and reactions in the liquid phase.

Enhanced thermoprotective properties can be achieved by using composite polymer coatings with typical ablative composite matrices, such as or epoxy resins [4-7], and fillers to increase the thermal stability of the composite [8-12]. Interesting work on the use of Kevlar49 fibres was presented by Alagar et al. [13] and Minkook et al. who used aramid fibres in combination with a phenolic foam-filled honeycomb [14]. In their work [15], Kucharczyk et al. tested the ability of aramid fibres in thermo-protective ablative castings.

Another interesting direction of research is the use of Phase Change Materials (PCMs) in these systems and the evaluation of the possibility of using this additive in composites as well as attempts to estimate the effect of PMCs on the thermal resistance of such composites. There is little information in the available literature on the use of phase change materials in composites for high-temperature applications. Of the available studies, the works [16-20] are noteworthy.

2. Experiments

In view of the high demand for this type of material (resistant to degradation during long-term operation at elevated temperatures [11]), an attempt was made to determine the effect of the addition of PCM in the resin matrix on the thermal resistance of the polymer composite with fibre reinforcement. To determine the ablative properties of the tested sample structure, the testing process analysed:

- temperature of the rear surface of the test material Ts,
- temperature of the ablative surface Ta,
- relative ablative loss of mass Ma,
- relative speed of mass ablation ma,
- temperaturę wewnątrz materiału kompozytowego Ti.

2.1. Material for ablative research

For the purposes of the study, two different types of composites were made: without the addition of PCM in the matrix and with the addition of PCM in the amount of 16 wt.%. Epidian 52 epoxy resin was used as the matrix and TFF hardener produced by Zakłady Chemiczne "Organika - Sarzyna S.A. was used for crosslinking Epidian 52 at room temperature. A phase change material (PCM) in the form of MicronalDS5038X was used as a powder resin additive in one batch of samples. As reinforcement of the composite, 14 layers of aramid fibres in plain weave and 6 layers of carbon fibres in twill weave were used produskci G. Angeloni. The basic parameters of the materials used are shown in Table 1. The fibre-reinforced composite layer was created to ensure the stiffness and thermal stability of the polymer composite.

Table 1. Właściwości materiałów zastosowanych na kompozyt.

Epidian 52	density ρ (g/cm^3)	value pH	flash-point (°C)
	1.12 – 1.13	~7	64
Hardener TFF	density ρ (g/cm^3)	value pH	melting point (°C)
	1.15 – 1.20	~12	8
MicronalDS5038X	Bulk density (g/cm^3)	Particle size (µm)	Melting point/crystallisation temperature (°C)
	0.3 – 0.4	50 – 300	24/25

fibre	gramatura (g/m^2)	thickness (µm)	wide (mm)
carbon	160 ±5%	0.16 ±2.5%	1000±2.5%
aramid	220 ±5%	0.28 ±1.5%	1000±2.5%

The initial step in preparing the specimens for testing was to cut circular layers of carbon fibre and aramid fibre with a diameter of 35 mm. The composites in group 1 do not have the addition of the phase change material PCM (Phasne Change Materials) in the form of Micronal DS5038X, in order to see what effect the additive has on the ablative properties of the polymer fibre composites (Fig. 1). Group 2 composites, on the other hand, have this additive at 16 %. The hand-lay method was used to make the samples. The stacking order of the different fabric layers was also determined (Fig. 1).

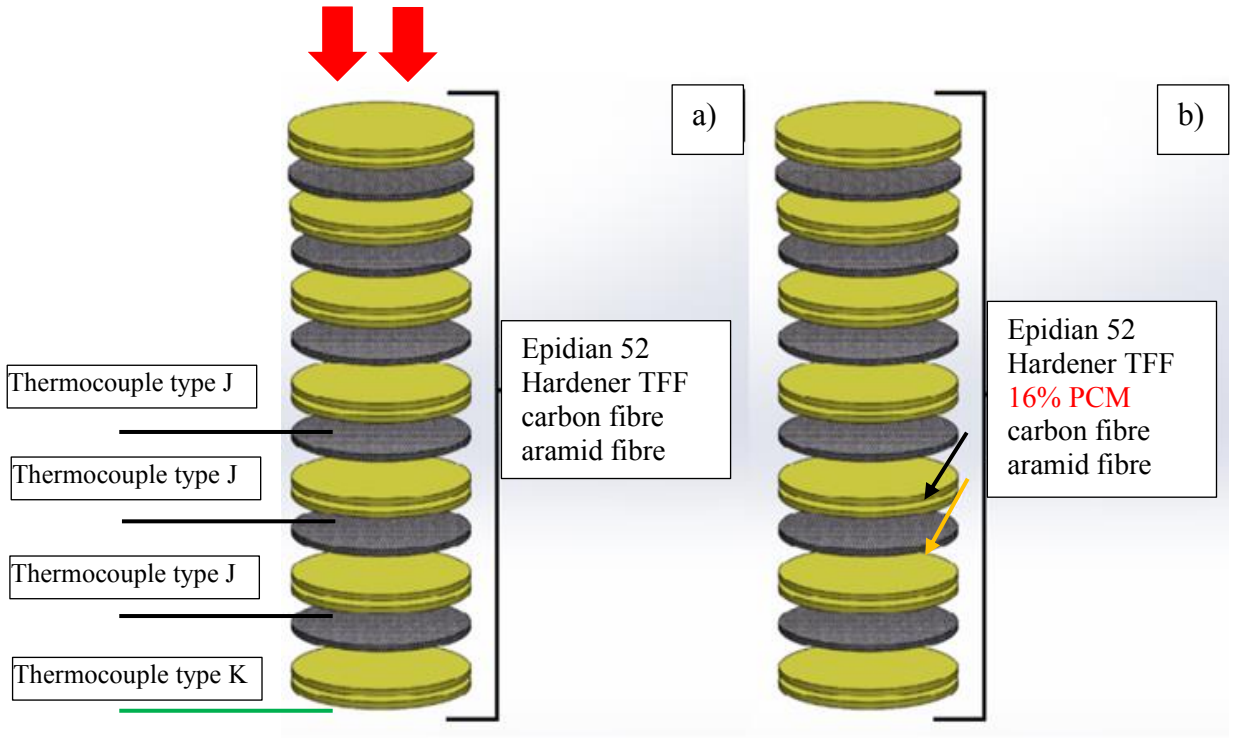

Figure 1. Schematic of the constructed composite with the location of the thermocouples measuring, a) without the addition of PCM b) with the addition of PCM in the matrix.

The samples prepared for testing were cylindrical in shape with a diameter of 35 mm and a thickness of about 10 mm and a weight of about 11 g. Once the samples were fabricated, they were left for 7 days to crosslink the resin. After previously fixing the thermocouples inside according to the scheme (Fig. 1). Each of the samples prepared in this way was built into a refractory casing made of plasterboard. If a gap was observed between the sample and the enclosure, Ceresit's high-temperature filler with a thermal resistance of up to 1500°C was used.

2.2. Test stand and research methodology

The manufactured samples were subjected to a high-temperature heat flux (approximately 1,000ºC) on the test stand developed by the authors (Fig. 2). Prior to the test, the measuring system was calibrated. Also the optimum distance from the ablation gun to the ablation surface was determined in order to obtain the temperature of approximately 1,000°C. The test duration time equalled 180 seconds for each sample. Due to the temperature range, the authors decided to measure the temperature on the rear surface of the composite sample wall, using K-type thermocouples and J-type thermocouples were used inside the composite. The temperature was registered by means of an SCB device produced by the National Instruments company and LAbVIEW software. The temperature of the ablation surface (exposed to a flame) of the tested sample was measured using a pyrometer made by Optris, model CT, along with a

head equipped with a laser pointer of the measurement place. In order to verify the homogeneity of the distribution field of the rear surface temperature, a thermal imaging camera FLIR i60 was used. On completion of the examination, the structure of the selected samples of the tested composite material was verified using the Olympus GX53 optical microscope in order to determine the structure of the composite as well as the effect of the flame on the material under scrutiny.

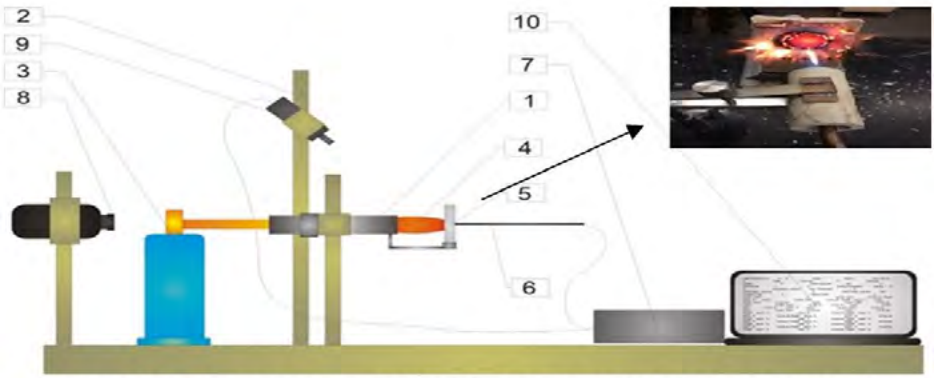

Figure 2. Laboratory research stand [2]

In the course of examining the ablative properties, the authors observed a delamination of the first layers of the fiber-reinforced composite (Fig. 3), resulting from an impact of a stream of hot gases on the material surface.

Figure 2. Exemplary photos of the ablation surface images of a material subjected to a stream of hot gases

3. Results and discussion

The ablative surface temperature was measured with the CT pyrometer and recorded every 10 seconds. The results obtained for all the tested samples are shown in Figure 3. The most important parameter for the analysis of the effect of powder additives on the ablative properties of the polymer composite with a fibre reinforcement was the temperature on the rear surface of the wall of the tested material Ts. Moreover, in order to compare the influence of powder additives, the authors recorded and presented in Table 2 the temperature Ts taken in the last second of the test (after 180 seconds). Also, a change in this temperature was illustrated during the test (an average value for three samples of the same series Figure 4).

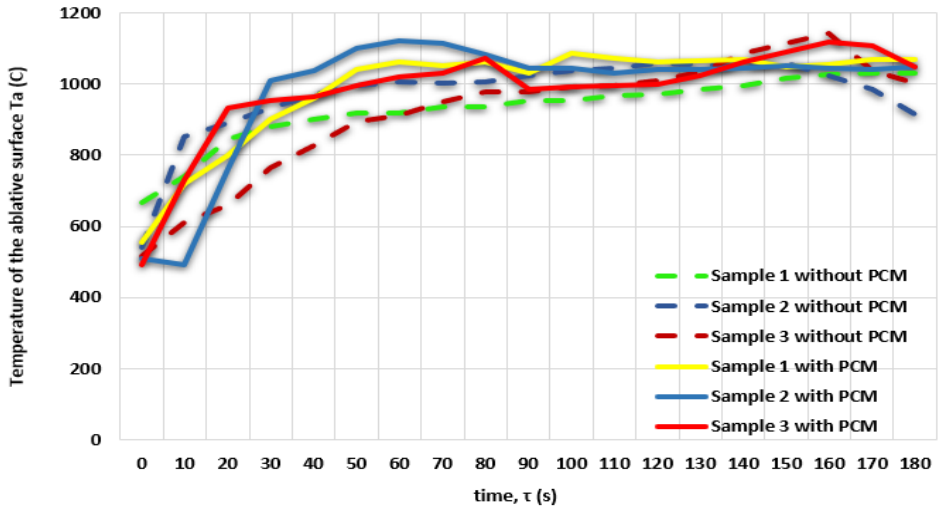

Figure 3. Ablative surface temperature of all tested composites

Table 2. Results of ablative properties testing of the examined composites.

Batch number	Sample number	Temperature Ts (°C)	Mass before test (g)	Mass after test (g)	Thickness before test (mm)	Thickness after test (mm)	Ablative mass loss (%)	Average mass ablation rate (mg/s)
1	1	164.6	10.92	7.73	10.52	9.53	31.7	18.8
	2		10.26	7.08	9.74	10.57		
	3		10.82	7.05	10.44	9.25		
2	1	106,1	11.78	8.07	11.23	9.35	32.9	21.8
	2		12.12	7.84	10.57	9.57		
	3		11.83	8.05	10.78	10.22		

On the basis of the obtained results, it can be concluded that the addition of the PCM phase change material to the composites results in a clear increase in their heat resistance (Fig. 4). The use of PCM in the vital signs resulted in a decrease in the average back surface temperature of the materials studied of approximately 60°C.

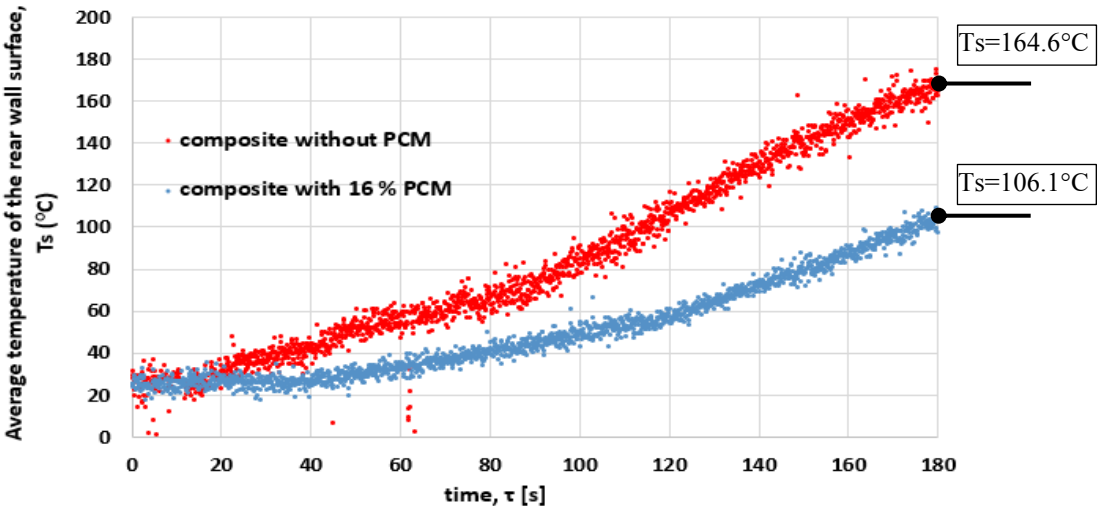

Figure 4. Average temperature of the rear wall surface Ts of the examined materials

Figure 5 shows an example of a set of temperature test results for sample 1.2 (epoxy resin without an addition of PCM).

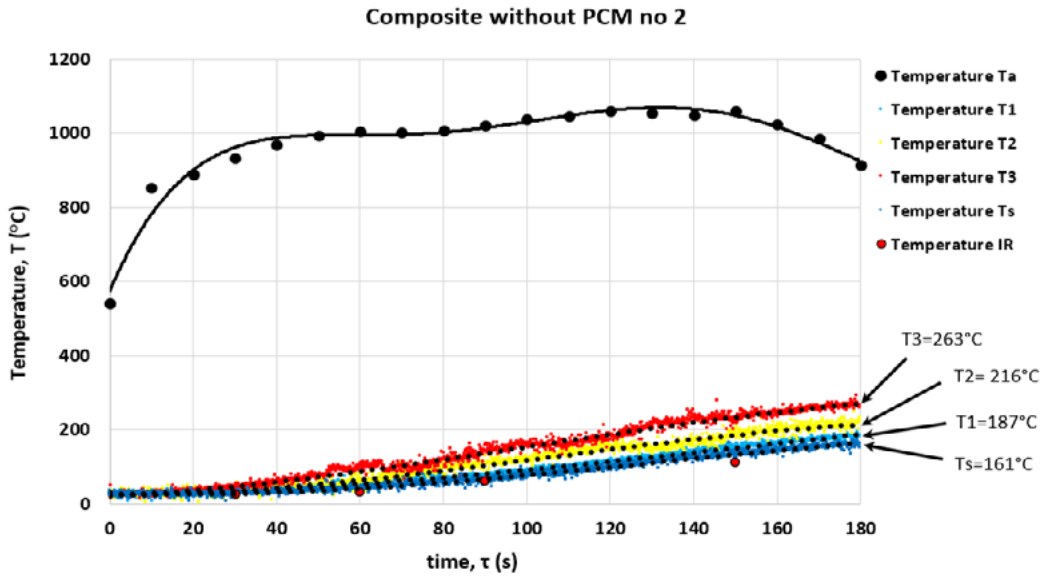

Figure 5. Exemplary temperature rises behind the fibre composite *Tf,* on the rear sample wall *Ts* and on the ablative surface *Ta,* and temperature inside the composite *Ti*

In order to monitor the uniformity of the temperature field distribution on the rear surface during the examination, a FLIR i60 thermal imaging camera was used, which allows contactless imaging of the temperature field. Figure 5 shows an example of the temperature distribution on the rear sample wall (sample 1.2 - composite without powder additives). On the basis of the photos taken by a thermal imaging camera, an assessment of the correctness of fixing the samples in the protective plate was made (Fig. 6 a - d). Temperature measurement with a thermal imaging camera from a point close to the centre of the sample (thermocouple temperature measurement point) was read every 30 seconds. Photographs of an example sample after ablative testing are also shown (Fig. 6 e).

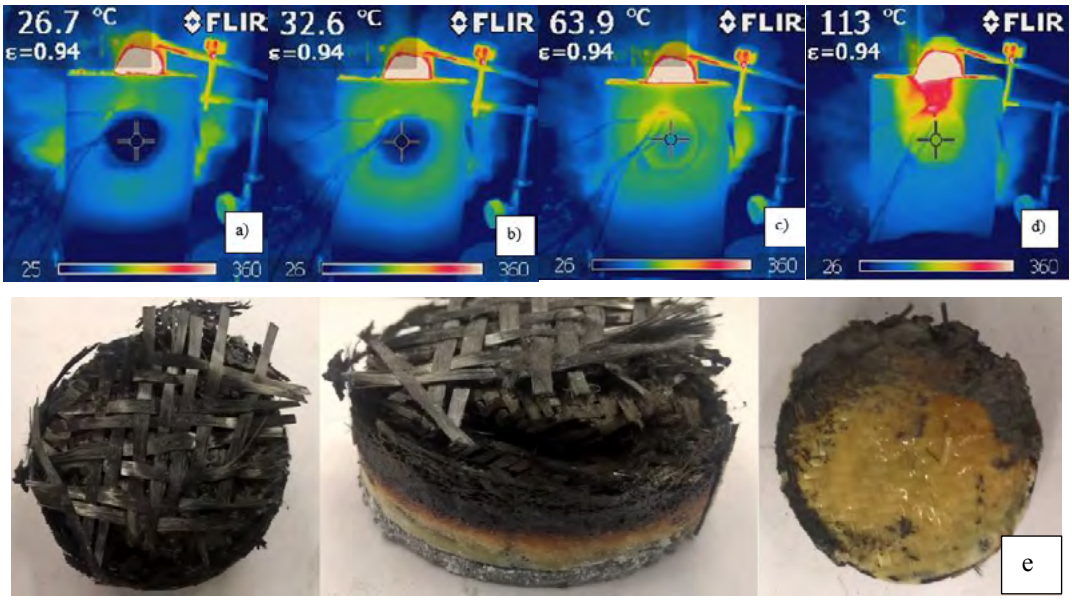

Figure 6. Measurement of the rear surface temperature using a thermal imaging camera a) at 30 seconds, b) at 60 seconds, c) at 90 seconds, d) at 150 seconds after the start of the heat flux on the front surface of the sample and photo of an example of a sample after an ablation test

Relative ablative loss of mass (percentage) was determined on the basis of an analysis of the changes in weight of the examined samples, before and after the heat resistance tests the results obtained are presented na figure 7 a and relative speed of mass loss (mg/s) illustrated at figure 7 b.

a) b)

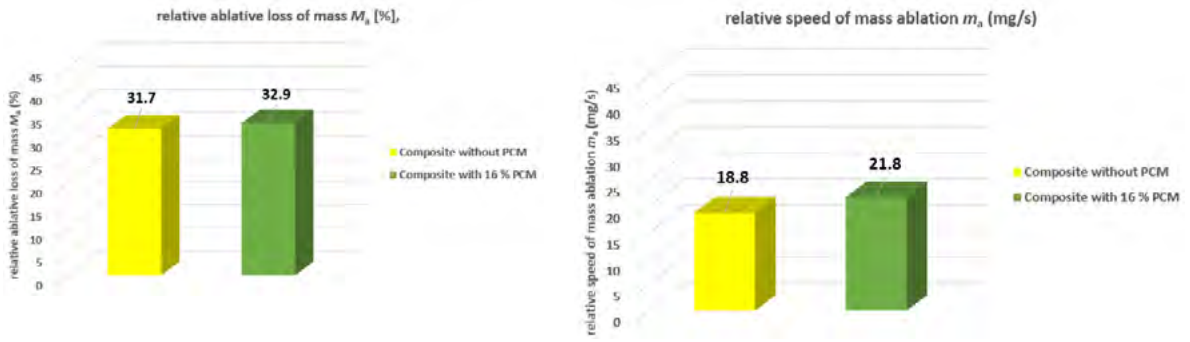

Figure 7. a) relative ablative loss of mass M_a (%), b) relative speed of mass ablation m_a (mg/s)

3. Conclusions

On the basis of the analysis of the obtained findings of experimental studies and the observation of the course of the examination (with phase change additive PCM in the resin matrix), the research led to the formulation of the following conclusions:

- During the test with the burner, the first layers (fibre reinforced polymer part of the composite) underwent aerodynamic erosion and were completely separated from the sample, which indicates ablative properties of the investigated materials.
- The distribution of temperature on the rear surface of the sample was roughly homogenous (Fig. 14); the occurring disturbances could have resulted from an uneven thickness of the sample, which did not considerably influence the final measurements;
- The application of the PCM (Phase Change Materials) additive "consumed" part of the energy supplied to the system into the phase change energy of the PCM material, which resulted in an improvement in the thermo-protective properties of the composite - it reduced the ablative mass loss to a small extent, but to a significant extent the temperature at the back surface of the tested composite decreased significantly from about 165°C for the composite without PMC to 106°C for composites with PCM additives).

References

[1] W. Kucharczyk. Thermo-protective ablation properties of polymer composites with pulveraceous fillers. *Problemy Techniki Uzbrojenia*, 36(101):151—158, 2007.
[2] W. Kucharczyk, A. Mazurkiewicz, W. Żurowski, *Nowoczesne materiały konstrukcyjne*, Politechnika Radomska, Radom, 2010.
[3] J. Izbicka and J. Michalski, Kompozyty, laminaty, tworzywa stosowane w technice, *Prace Instytutu Elektrotechniki*, 228:341-348, 2006.
[4] J.K. Chen, C.T. Sun and Chang C.I. Failure analysis of a graphite/ epoxy laminate subjected to combined thermal and mechanical loading. *Journal of Composite Materials,* 19:408–423, 1985.
[5] C.A. Griffis, J.A. Nemes, F.R. Stonesifer and C.I. Chang. Degradation in strength of laminated composites subjected to intense heating and mechanical loading. *Journal of Composite Materials*, 20:216–235, 1986.
[6] N. Dodds.A.G. Gibson, D. Dewhurst and J.M. Davies. Fire behaviour of composite laminates. *Composite Part A:Applied Science and Manufacturing*, 31(7):689–702, 2000.
[7] M. Bakar, W. Kucharczyk and S. Stawarz. Investigation of thermal and ablative properties of modified epoxy resins. *Polymers & Polymer Composites* 24(8):617-623, 2016.
[8] A.R. Bahramian, M. Kokabi, M.H.N. Famili and M.H. Beheshty. Ablation and thermal degradation behaviour of a composite based on resol type phenolic resin; process modelling and experimental, *Polymer* 47:3661–3673, 2006
[9] A.R. Bahramian and M. Kokabi. Ablation mechanism of polymer layered silicate nanocomposite heat shield, *Journal of Hazardous Materials*, 166(1):445-454, 2009

[10] W. Kucharczyk, P. Przybyłek and T. Opara. Investigation of the thermal protection ablative properties of thermosetting composites with powder fillers: the corundum Al2O3 and the carbon powder C. *Polish Journal of Chemical Technology*, 15(4):49-53, 2013.
[11] B.D. Butler, M. Winter, F. Panerai, A. Martin, S.C. Bailey, M. Stackpoole, P.M. Denehy and S. Splinter. Characterization of candidate materials for remote recession measurements of ablative heat shield materials, *54th AIAA Aerospace Sciences Meeting*, San Diego, California, USA, 2016.
[12] T. Czigany. Discontinuous basalt fibre-reinforced hybrid composites (in: polymer composites from nano- to macro scale), Springer, New York, 2005.
[13] M. Alagar, A. Ashok Kumar, K.P.O. Mahesh and K. Dinakaran. Studies on thermal and morphological characteristics of E-glass/Kevlar 49 reinforced siliconized epoxy composites. *European Polymer Journal*, 36:2449-2454, 2000.
[14] K. Minkook,C. Jaeheon and L. Dai Gil. Development of the fire-retardant sandwich structure using an aramid/glass hybrid composite and a phenolic foam-filled honeycomb. *Composite Structures*, 158:227-234, 2016.
[15] A. Krzyżak, W. Kucharczyk, J. Gąska and R. Szczepaniak. Ablative test of composites with epoxy resin and expanded perlite. *Composite Structures*, 202:978-987, 2018.
[16] X. Wu. J. Ding, Y. Kong, Z. Sun, G. Shao, B. Li, J. Wu, Y. Zhong, X. Shen and S. Cui S. Synthesis of a novel three-dimensional Na2SO4@SiO2@Al2O3-SiO2 phase change material doped aerogel composite with high thermal resistance and latent heat, Ceramics International 44(17):21855–21865, 2018.
[17] Y. Ren, P. Li, M. Yuan, F. Ye, C. Xu and Z. Liu. Effect of the fabrication process on the thermophysical properties of Ca(NO3)2–NaNO3/expanded graphite phase change material composites. *Solar Energy Materials and Solar Cells*, 200:110005, 2019.
[18] F. He, X. Wang and D. Wu. Phase-change characteristics and thermal performance of form-stable n-alkanes/silica composite phase change materials fabricated by sodium silicate precursor. *Renewable Energy*, 74:689-698, 2015.
[19] Y.H. Huang, Y.X. Cheng, R. Zhao and W.L. Chen. A high heat storage capacity form-stable composite phase change material with enhanced flame retardancy. *Applied Energy* 262:114536, 2020.
[20] R. Szczepaniak, G. Kozun. P. Przybylek, A. Komorek, A. Krzyzak and G. Woroniak. The effect of the applicaton of a powder additive od a phase change materials on the ablative properties of a hybrid composite. *Composite Structures*, 256:113041, 2021.

EFFECT OF MOISTURE CYCLING DURATION AND TEMPERATURE ON THE STRENGTHENING AND STIFFENING OF CYCLED FLAX FIBRES

Clare Garing[1,2], Yasmine Mosleh[3], and Aart Willem Van Vuure[3]

[1]Department of Materials Engineering, KU Leuven, Kasteelpark Arenberg 44, 3001 Leuven, Belgium
[2]Department of Engineering Science, College of Engineering and Agro-Industrial Technology, University of the Philippines Los Baños, Laguna 4031, Philippines
[3] Biobased Structures and Materials,Faculty of Civil Engineering and Geosciences, TU Delft, Kluyverweg 1, 2629 HS Delft, Netherlands
Email: clare.garing@kuleuven.be, y.mosleh@tudelft.nl, aartwillem.vanvuure@kuleuven.be

Keywords: bio-composites, moisture durability, natural fibre, flax, moisture cycling, pectin

Abstract
The aim of this study was to determine the effect of moisture cycling (environmental relative humidity cycles) on the durability of flax-epoxy composites and investigate the influence of cycling duration and temperature on the stiffening and strengthening of flax fibres. Four moisture cycling protocols for flax fibres were employed in this research which includes 4D21 (4days per cycle at 21°C), 4D60 (4days per cycle at 60°C), 3H27 (3hours per cycle at 27°C) and 3H60 (3hours per cycle at 60°C). To measure the impact of high-low humidity cycling at different cycling durations and temperature, tensile testing of impregnated fibre bundle test (IFBT) samples was done. Results of the back-calculated properties revealed that the applied cycling protocols enhanced both the tensile strength and modulus of the fibres. Better improvement of tensile properties was observed in fibres cycled at longer duration. The fibres undergoing 4 days of cycling at 21°C (4D21 fibres) showed the highest improvements in tensile strength (18%), as well as tensile moduli E1 (19%) and E2 (18%) after 10 cycles. Interestingly, all fibres showed increased stiffness (E1) in the range of 8-20% after 10 cycles and 4-8% after 20 cycles. This fibreimprovement in mechanical strength and stiffness of the fibres can possibly be attributed to a phenomenon similar to a hornification effect in wood or possibly by fibre repair due to pectin migration, which produces the strengthening and stiffening effect.

1. Introduction

Natural fibre reinforced polymer composites based on renewable sources such as flax fibres, present environmentally friendly solutions with notable specific mechanical properties. However, despite their advantages in lightweight design and cost-effectiveness, their inherent hydrophilic nature poses a significant challenge, leading to moisture absorption and subsequent performance degradation [1-7]. Previous studies have already made attempts to address this issue.

Some related studies investigated the effect of moisture cycling on plant fibre properties but mostly on wood fibres. These studies revealed that exposure to high-low humidity cycling can significantly change the mechanical and physical characteristics of the materials. For instance, research by Stamboulis et al. (2001), Scida et al. (2013) and Ferreira et al. (2017) have demonstrated that moisture cycling can induce a phenomenon known as "hornification" in natural fibres, which can result in increased stiffness and strength. Hornification, a term commonly used in the context of wood and lignocellulosic materials, refers to the irreversible changes in the structure and properties of natural fibres when subjected to drying

and rewetting cycles. This process can reduce the fibre's water-uptake capacity and enhance mechanical properties, as reported by several researchers [1,3-10].

This study will aim to investigate the effect of different moisture cycling regiments on the evolution of properties of flax fibre epoxy composites (particularly fibre stiffness and strength). This includes the influence of cycling duration and temperature on the stiffening and strengthening of flax fibres after exposure to alternating relative humidities, based on a recent study [1]. Subsequently, we will aim to unravel the underlying mechanisms behind the previously observed stiffening of the lignocellulosic flax fibres after moisture cycling.

The acquired understanding will pave the way for the development of strategies to further improve the durability of flax fibre reinforced composites when subjected tohigh enviromental humidity variations. Furthermore, the findings of this study can help optimize the performance and long-term reliability of flax-based biocomposites, paving the way for their increased adoption in various applications.

2. Materials and Methods

2.1. Materials

FlaxTape™200, a unidirectional flax fibre tape with an areal density of 200g/m^2 and measuring 400mm in width, was procured from EcoTechnillin. The epoxy resin employed in the research was Epikote™ 828 combined with 1-2-diaminocyclohexane hardener in a ratio of 100 parts resin to 15.2 parts hardener. The potassium salts utilized for the long-duration moisture cycling were sourced from Sigma-Aldrich.

2.2. Moisture Cycling

FlaxTape200 was subjected to alternating high (wetting phase, 85% RH) and low (drying phase, 23% RH) relative humidities. Four moisture cycling protocols (4D21, 4D60, 3H27, 3H60) were implemented to investigate the effect of temperature and duration of cycling on the tensile strength and modulus of flax fibres. The long duration cycling (4 days per cycle, 4D) was done inside salt boxes with standard potassium salt solutions while the short duration cycling (3 hours per cycle, 3H) was done inside a Weiss Technik WKL64 humidity chamber. For the moisture cycling protocol at a lower temperature of 21ºC and 4 days per cycle (4D21), the wetting condition was controlled using potassium chloride, and potassium acetate for the drying step. At an elevated temperature of 60ºC (4D60), high relative humidity was maintained using potassium nitrate, and potassium acetate for the low relative humidity condition. Due to the limitations of the humidity chamber, the shorter duration cycling at lower temperature was set to 27ºC (3H27) instead of 21ºC to attain the same level of low relative humidity (23% RH). The high temperature - short duration protocol (3H60) was maintained at 60°C with the same alternating humidity conditions. The process was repeated for the designated number of cycles for all moisture cycling protocols: C0 (uncycled), C1 (1 cycle), C5 (5 cycles), C10 (10 cycles) and C20 (20 cycles). After each set of cycles, the samples were stored in a conditioned room set at 21ºC and 50% RH.

2.3. Impregnated Fibre Bundle Test (IFBT) Method

The fibre properties were determined through a back-calculation method after impregnating flax fibre bundles within an epoxy matrix based on the rule of mixtures. This method, along with sample preparations, was adapted from ASTM D2343 [1,12]. Flax fibres underwent a pre-drying stage at 60°C for at least 24h. The fibres were cut into 25 cm lengths, and weight measurements were noted to determine the actual fibre volume fraction (v_f) of each specimen after processing using Eq. 1. In the equation below, m_f denotes the mass of the fibre, ρ_f stands for the density of the fibres (1.45 g/cm^3), m_c is the mass of the composite, and ρ_m indicates the density of the epoxy matrix (1.16 g/cm^3). The targeted v_f for each test sample was 40%.

$$v_f(\%) = \frac{\frac{m_f}{\rho_f}}{\frac{m_f}{\rho_f}+\frac{m_c-m_f}{\rho_m}}\ x\ 100 \quad (1)$$

A thin coating of release agent (Chemtrend Chemlease® PMR 90 EZ) was applied on the IFBT moulds, countermoulds, vacuum films and metals spacers before usage for easy removal and to prevent damage of the composites when demoulding the samples afterwards. The pre-conditioned fibres were placed inside the mould cavities lined with vacuum film. Homogenized epoxy resin was poured onto the fibres ensuring it thoroughly saturated the entire bundles. A counter mould was applied on each cavity and metal spacers were placed at both ends of the mould cavities to maintain a consistent composite thickness of 2mm. Curing was carried out at 70°C for 1 hour, followed by post-curing at 150°C for another hour. Then, the samples were allowed to cool down before removing from the mould to prevent any thermal effects. The cured IFBT samples were then conditioned at standard conditions of 21ºC and 50% RH for at least a week before undergoing mechanical testing [1]. All tests were conducted on six samples, and mean values were computed.

2.4. Tensile Test

ASTM 3039 standard was used as basis for performing the tensile tests on the IFBT samples (250 mm × 10 mm × 2 mm) with a gauge length of 150 mm. The impregnated fibres were tested using a universal testing machine (Instron 5567) equipped with a 30 kN load cell and operated at a cross-head speed of 2 mm/min. To prevent slippage, rectangular end tabs were put at the ends of the specimens using Araldite® epoxy adhesive. Strain measurement was facilitated using an extensometer with a 50 mm gauge length. Tensile modulus and tensile strength for each cycled fibre were back-calculated using Equations 2 and 3, employing the rules of mixtures. E_f represents the stiffness of the fibre in the longitudinal direction, E_C is the modulus of the composite, and E_m signifies the stiffness of the matrix. Additionally, σ_f is the longitudinal strength of the fibre, and σ'_m represents the stress in the matrix at the failure strain, where $\sigma'_m = E_m * \varepsilon_c$. Furthermore, σ_c and ε_c are the strength and strain at failure of the composite, respectively. For tensile modulus, both E1 (Young's modulus) and E2 (elastic modulus associated with non-linear behavior) were computed [1,12-13].

$$E_f = \frac{E_c - E_m*(1-v_f)}{v_f}\ x\ 100 \quad (2)$$

$$\sigma_f = \frac{\sigma_c - \sigma'_m*(1-v_f)}{v_f}\ x\ 100 \quad (3)$$

2.4. Scanning Electron Microscopy

Scanning electron micrographs were taken to analyze the fibre microstructure, topography and internal features of a fractured C10 IFBT composite. The sample was examined using a Philips XL-30 FEG scanning electron microscope. Before SEM analysis, the sample was first degassed and coated with gold using a plasma sputter coater to enhance its conductivity. High-resolution images were obtained using a 10kV acceleration voltage and a back-scattered electron (BSE) detector. The BSE detector aided in achieving excellent image contrast and depth analysis.

3. Results and Discussion

3.1. Tensile Properties

Tensile testing was performed after each set of moisture cycles (C0, C1, C5, C10 and C20) to assess its impact on the durability of flax fibres. Results of the impregnated fibre bundle tests, used to back-calculate the tensile properties of the flax fibres, demonstrated significant stiffening and strengthening of the moisture-cycled fibres after several cycles. Figure 1 summarizes the tensile strength of the fibres while Figure 2 shows tensile moduli from the four moisture cycling protocols.

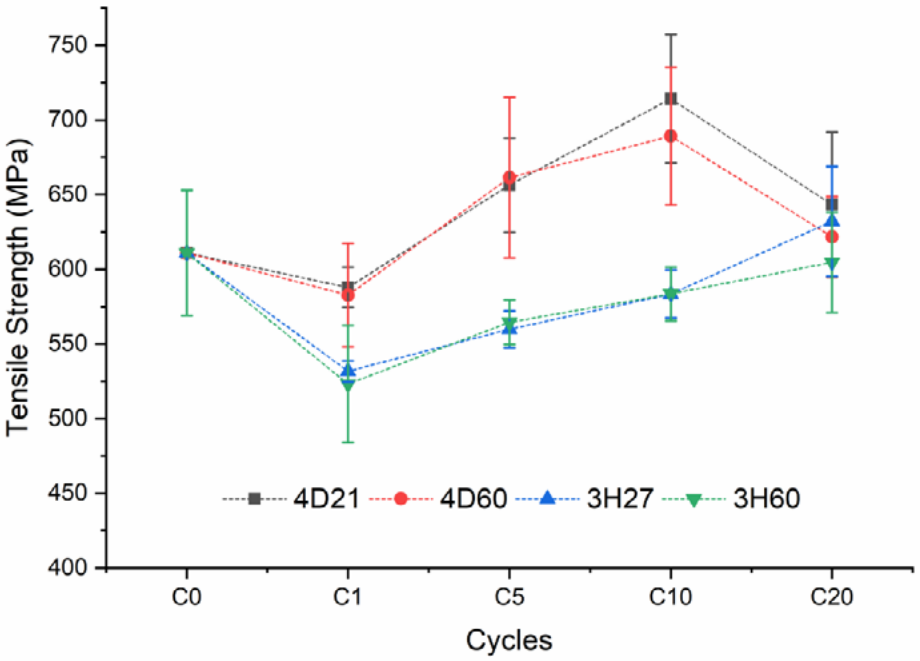

Figure 1. Tensile strength of moisture-cycled flax fibres.

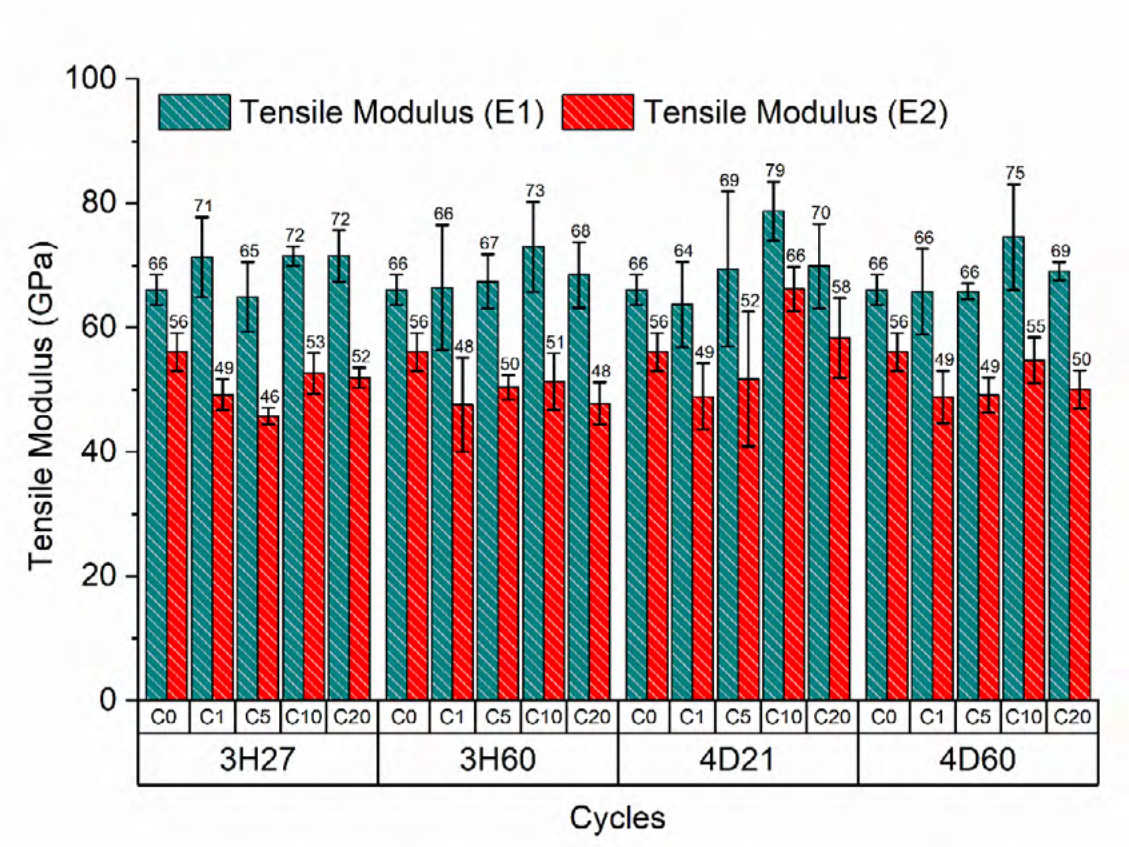

Figure 2. Tensile moduli of moisture-cycled flax fibres.

After one high-low relative humidity cycle, there is a noticeable decrease in the tensile strength which is due to the damage caused by the swelling and shrinking of fibres [2]. Interestingly, subjecting the fibres to repeated cycles of high and low humidity environments led to a phenomenon akin to "fibre repair" on both stiffness and strength. After some time, the fibre properties exhibited an upward trend. Figure 1 demonstrates the remarkable increase in fibre strength, with enhancements of 18% (C10-4D21) and 13% (C10-4D60) after ten cycles. An increase of 7% (C10-4D21) and 8% (C10-4D60) were also observed after five cycles. Moreover, even after twenty cycles, the fibers continued to show indications of repair, ranging from 2 to 5 percent. It shows that 10 cycles is the optimum number of high-low humidity cycles for 4D flax fibres. This result is similar to the research findings of Ferreira et. al (2017) on sisal fibres after wetting (water immersion, 22°C, 3h) – drying (oven-drying, 80°C, 16h) treatments which improved its bond mechanisms. For overall mechanical performance, they concluded that 5 cycles for both curaua and sisal fibres produce enhanced properties [5]. It is also apparent from Figure 1 that longer duration cycling (4D) results in greater improvements in tensile strength. It is possible that 1.5h at high %RH and 1.5h at low %RH of the 3H moisture cycling protocols is insufficient to prompt the fibre repair effect. Moreover, while an increase in temperature might have been expected to affect this phenomenon, the results contradicted this hypothesis. While temperature elevation enhance diffusion, the damage caused by the increased water uptake was balanced by the fibre repair effect. In a related study, Scida and colleagues observed a marginal increase in mechanical property reduction of flax-epoxy composites after hygrothermal ageing (40°C, 90%RH, around 40 days) [4]. In this study, 4D21 fibres showed higher improvements in tensile properties than 4D60 due to more degradation at higher temperature. During shorter duration cycling, the effects were not significant because of the brief exposure to high relative humidity conditions.

Figure 2 clearly illustrates significant improvements in tensile modulus (E1) of all moisture cycled fibres and is independent on both temperature and cycling duration. For all moisture cycling protocols, highest E1 improvements were observed after ten cycles. The fibres exhibited stiffness enhancements of 20% (C10-4D21), 13% (C10-4D60), 11% (C10-3H60) and 8% (C10-3H27) after ten cycles. Furthermore, twenty cycles of exposure to high-low relative humidities produced an improvement of 8% (C10-3H27), 6% (C10-4D21), 5% (C10-4D60) and 4% (C10-3H60). The observed increase in stiffness values and strength is similar to improvements during wood hornification which is attributed to increased hydrogen bonding in literature. This increase in hydrogen bonding results to increase in dimensional stability of the fibres [5].

The observed strengthening and stiffening effect could be due to changes in the distribution and chemistry of the primary constituents of flax, such as pectin, cellulose, lignin, and hemicellulose, accompanied by changes in the microstructure of the flax fibres. It is known from wood hornification that lignin and hemicellulose inhibits this phenomenon by preventing hydrogen bond formation affecting the cross-linking between the cellulose microfibrils [8-9]. The role of pectin in this strengthening and stiffening effect is also considered. Hornification in flax fibres may be linked to the migration of pectin, which fills gaps and defects within the fibres. This process contributes to the fibre repair effect observed after exposure to high-low humidity cycling. It was also found in a recent study that residual pectin improved the storage modulus of cellulose nanofibril dispersions from ramie fibres indicating more rigidity and better mechanical strength [14]. The reason for the improvement in stability and strength is the possible formation of pectin-hemicellulose/lignin-cellulose composite nanostructure.

3.2. Fibre Microstructure

Figure 3a shows perfectly straight and well-aligned fibres within the composite which could possibly explain the remarkable tensile strength and modulus of C10 fibres [1]. This good orientation of the fibres might have facilitated better load transfer and uniform load distribution. Additionally, it reveals properly impregnated fibres, suggesting the possibility of good adhesion between the fibers and the matrix. Future research will aim to validate this through adhesion tests. Figure 3b shows fibre shear failure due to misalignment caused by the force from matrix cracking (shown in Figure 3c) in the surrounding region.

But no obvious differences between samples subjected to the various regimes of cycling could be seen, so the exact mechanism of the fibre improvement upon cycling stays as yet elusive, and is subject to further research.

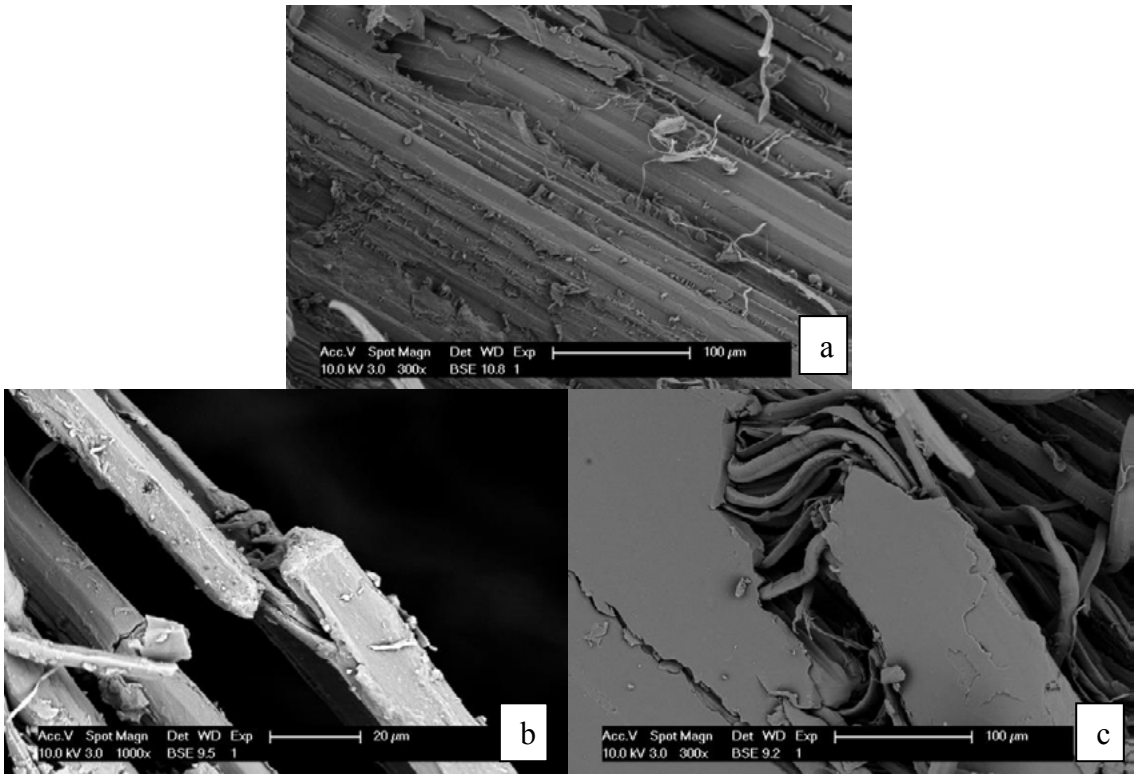

Figure 3. C10 IFBT composite (a) straight and aligned fibres, (b) fibre failure, (3) matrix crack.

Conclusion

This research employed the Impregnated Fibre Bundle Test (IFBT) method to determine fibre stiffness and strength using a fibre volume fraction of approximately 40%. Four moisture cycling protocols: 4D21(4days per cycle at 21°C), 4D60 (4days per cycle at 60°C), 3H27 (3hours per cycle at 27°C) and 3H60 (3hours per cycle at 60°C) were implemented in this study. Flax fibres were subjected to different number of cycles (C0, C1, C5, C10 and C20) of alternating high (85%) and low (23%) humidities. Analysis of the back-calculated properties from flax-epoxy composites revealed that the applied cycling protocols enhanced both the tensile strength and modulus of the fibres. The apparent fibre repair effect on tensile strength is more pronounced at longer duration cycling after 10 cycles with values of 18% (C10-4D21) and 13% (C10-4D60). Even after 20 cycles, good improvements were still observed compared to untreated fibres C0. For tensile modulus, all cycling protocols produced significant increase in stiffness. The improvement in stiffness values is in the range of 8-20% and 4-8% after 10 and 20 cycles, respectively. This strengthening and stiffening is comparable to wood hornification which is attributed to increased and permanent hydrogen bonds as mentioned in previous studies. Alternatively, the role of pectin migration contributing to a fibre repair effect will be the subject of future studies. The strengthening and stiffening effect could be due to changes in the distribution and chemistry of the primary constituents of flax, such as pectin, cellulose, lignin, and hemicellulose, accompanied by changes in the microstructure of the flax fibres.

Acknowledgments
The authors would like to acknowledge the financial support of the University of the Philippines – PhD and Master's Fellowship Program for Faculty and REPS, KU Leuven – Belgium, and Technische Universiteit Delft – Netherlands for this study.

References

[1] MM. Lu and AW. Van Vuure. Long-term moisture cycling performance and unexpected strengthening of non-dry flax fibre composites. *Industrial Crops and Products*, Volume 195: 116486, 2023.
[2] MM. Lu and AW. Van Vuure. Moisture sorption and swelling of flax fibre and flax fibre composites. *Composites Part B*, Volume 231: 109538, 2022.
[3] J. Claramunt, M. Ardanuy and J.A. Garcia-Hortal. Effect of drying and rewetting cycles on the structure and physicochemical characteristics of softwood fibres for reinforcement of cementitious composites. *Carbohydrate Polymers*. Volume 79, Issue 1: 200-205, 2010.
[4] D. Scida, M. Assarar, C. Poilane and R. Ayad. Influence of hygrothermal ageing on the damage mechanisms of flax-fibre reinforced epoxy composite. *Composites Part B: Engineering*, Volume 48: 51-18, 2013.
[5] SR. Ferreira, F.D. Silva, PR.L. Lima and R.DT. Filho. Effect of hornification on the structure, tensile behavior and fibre matrix bond of sisal, jute and curauá fibre cement based composite systems. *Construction and Building Materials*. Volume 139: 551-561, 2017.
[6] H. Ventura, J. Claramunt, A. Navarro, M.A. Rodriguez-Perez and M. Ardanuy. Effects of Wet/Dry-Cycling and Plasma Treatments on the Properties of Flax Nonwovens Intended for Composite Reinforcing. *Materials*, Volume 9, 92: 93, 2016.
[7] A. Stamboulis, C.A. Baillie, S.K. Garkhail, H.H.H. Van Melick and T. Peijs. Environmental Durability of Flax Fibres and their Composites based on Polypropylene Matrix. *AppliedComposite Materials*. Volume 7: 273-294, 2000.
[8] A.M. Scallan and G.V. Laivins. The mechanism of hornifi cation of wood pulps. *Products of Papermaking*, 1235–1260, FRC, Manchester, 2018.
[9] W. Mo,, K. chem, X. Yang, F. Kong, J. Liu and B. Li. Elucidating the hornification mechanism of cellulosic fibres during the process of thermal drying. *Carbohydrate Polymers*. Volume 289: 119434, 2022.
[10] S. Aghajanzadeh, G. Fayaz, Y. Soleimanian, A.M. Ziaiifar, S.L. Turgeon and S. Khalloufi. Hornification: Lessons learned from the wood industry for attenuating this phenomenon in plant-based dietary fibres from food wastes. *Comprehensive Reviews in Food Science and Safety*, Volume 22: 4-45, 2023.
[11] E.E. Thybring, L.G. Thygesen and I. Burgert. Hydroxyl accessibility in wood cell walls as affected by drying and re-wetting procedures. *Cellulose*. Volume 24: 2375-2384, 2017.
[12] F. Bensadoun, I. Verpoest, J. Baets, J. Mussig, N. Graupner, P. Davies, M. Gomina, A. Kervoelen and C. Baley. Impregnated fibre bundle test for natural fibres used in composites. *Journal of Reinforced Plastics and Composites*, Volume 36: 942-957, 2017.
[13] A. Pisupati, A. ayadi, M. Deleglise-Lagardere and C.H. Park. Influence of resin curing cycle on the characterization of the tensile properties of flax fibres by impregnated fibre bundle test. *Composites Part A*, Volume 126: 05572, 2019.
[14] W. Yu, Y. Yi, H. Wang, Y. Yang, C. Xing, L. Zeng, J. Tang and Z. Tan. Effects of residual pectin composition and content on the properties of cellulose nanofibrils from ramie fibres. *Carbohydrate Polymers*. Volume 298: 120112, 2022.

THE TRANSITION FROM THERMOSET TO THERMOPLASTIC COMPOSITES

David Leach

Thermoplastic Composite Specialists, Walnut Creek, CA 94598 USA
Email: dleach539@yahoo.com

Keywords: Thermoplastics, Thermosets, Properties, Processing, Adoption.

Abstract
The first thermoset composites were developed in the early 1900s and high-performance thermoplastic composites followed much later in the 1970s with the development of advanced polymers and composite manufacturing methods. Thermoplastics composites have many advantages in processing and performance, but their adoption has been relatively slow. This paper will explore the attributes of both classes of materials, the factors which have influenced materials selection and the future direction.

1. Introduction

The first modern composites were developed in the early 1900s using thermosetting resins such as phenolics and polyesters. Epoxy resins were developed in the 1930s and provided a significant increase in temperature resistance, strength and stiffness [1]. The first use in long fiber composites was with flax fibres in the 1930s and these composites were used in aircraft in World War 2 [1]. The resins were readily available, simple to formulate and more importantly had low viscosities and therefore were easy to impregnate into high fiber volume composites. Glass fibres (GF) were developed in the 1930s and carbon fibres (CF) in the 1960s and the demand for lightweight, high strength materials grew considerably with their availability, particularly in sporting goods and aircraft applications. Epoxy resins provided high mechanical strength and service temperature for aerospace but were brittle. Through the 1970s epoxy resin composites were used increasingly in commercial aircraft secondary structures such as fairings and control surfaces with glass fibres, and in defense applications with carbon fibres.

Thermoplastic polymers were developed from the 1930s to 1970s with increasing thermal and mechanical performance. While a wide range of thermoplastic polymers were developed most had relatively low glass rubber transition temperature (Tg) and hence service temperature, and low strength and stiffness. These aspects were offset by high toughness and the ability mould parts quickly as there is no chemical reaction during part fabrication [2]. As a result, unreinforced and short fibre reinforced thermoplastics became widely used in commodity applications. Higher performance amorphous and semi-crystalline polymers were developed in the 1980s including poly(aryl-ether-sulphone) (PAES) family, poly(ether-imide) (PEI) both amorphous, and poly(phenyl-sulphide) (PPS) and Poly(aryl-ether-ketone) family (PAEKs) both semi-crystalline. The semi-crystalline polymers had Tgs more than 90°C, and amorphous polymers Tgs over 200°C. In the early 1980s poly(ether-ether-ketone) (PEEK), a member of the PAEK family, was commercialized and this combined the benefits of crystalline polymers, with increased service temperature (Tg of 140-150°C), and high toughness. Thermoplastic polymers displaced thermosetting resins in unreinforced and short fiber applications due to the ease of molding and short cycle times, but the viscosity of thermoplastic polymers presented a major challenge to wetting out highly reinforced composites.

This paper will consider the performance and fabrication methods for the two types of materials which has led to the gradual transition from thermosetting to thermoplastic matrices in high performance composite materials.

2. Composite Materials

A wide range of thermoplastic polymers are available but high-performance applications have been limited to a small number of polymers [3]. The main polymers and their characteristics are summarized in Table 1.

Table 1. Thermoplastic polymers for high performance composites [3].
Tg: Glass-rubber transition temperature. Tm: Melt temperature. Tp: Typical processing temperature.

Polymer	Morphology	Polymer Structure	Tg °C	Tm °C	Tp °C
PESU Poly(ether-sulfone)	Amorphous	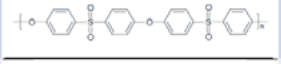	220	-	360
PEI Poly(ether-imide)	Amorphous	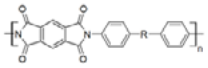	217	-	332
PPS Poly(phenylene-sulfide)	Semi-Crystalline		93	280	329
PEEK Poly(ether-ether-ketone)	Semi-Crystalline	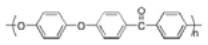	143	343	390
PEKK Poly(ether-ketone-ketone)	Semi-Crystalline	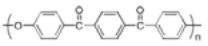	159	337	380
Low Melt PAEK LM-PAEK	Semi-Crystalline	PEEK – PEDEK Copolymer	147	305	350

The performance of thermoplastic composites (TPCs), and particularly their toughness, has been widely characterized [3, 4]. For example, residual compression strength after impact of a PEEK/carbon fibre composite has been shown to be up to three times that of an epoxy matrix composite as shown in Figure 1. Toughness is one of the major performance benefits of TPCs, and others include flammability resistance, insensitivity to moisture, and high resistance to aggressive fluids for semi-crystalline polymers.

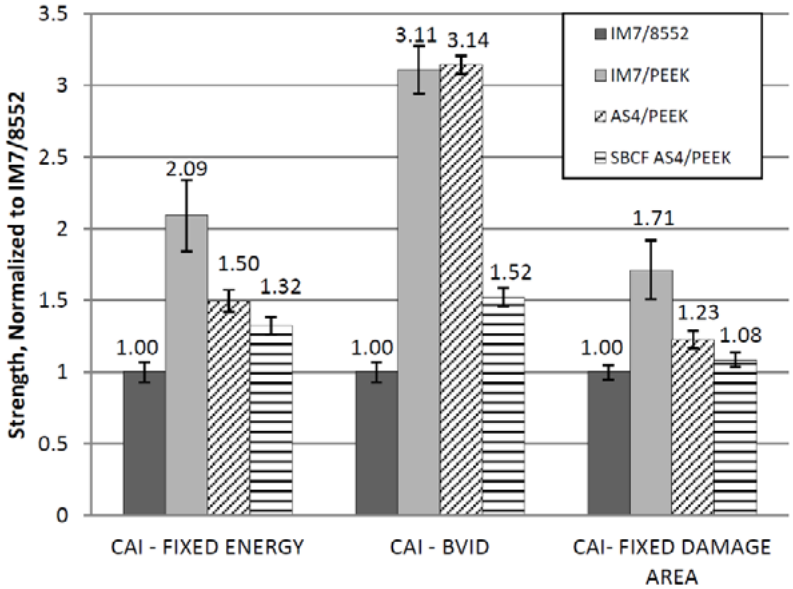

Figure 1. Residual compression strength after impact (CAI) for thermoplastic (PEEK) and thermoset epoxy (8552) composites.
BVID: Barely Visible Impact Damage. SBCF: Stretch Broken Carbon Fibre.

3. Part Fabrication and Assembly

Continuous fibre reinforced thermosetting composites are typically laid-up ply-by-ply on the part tool and then cured in an oven or autoclave. This is a time-consuming process, and thermoset materials also require frozen storage and have a short working life at room temperature. In contrast TPCs can be prepared and consolidated using highly automated processes and can be rapidly formed into a finished part using techniques such as stamp forming. A frequently used illustration is shown in Figure 2 showing that the fabrication time for TPC parts can be around 10% that of a thermoset [6].

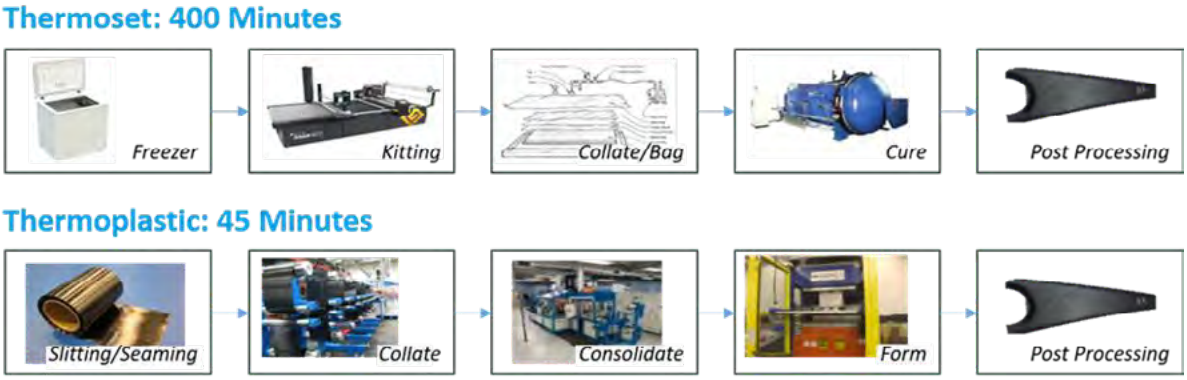

Figure 2. Part processing times for thermoset and thermoplastic composite parts [6].

The short process times can have a significant impact on recurring part cost particularly for small to medium sized parts where the rapid forming and high degree of automation that can be used with thermoplastics can give lower part cost compared to thermoset prepregs, thermoset resin infusion and even metallic parts as shown in Figure 3 [7].

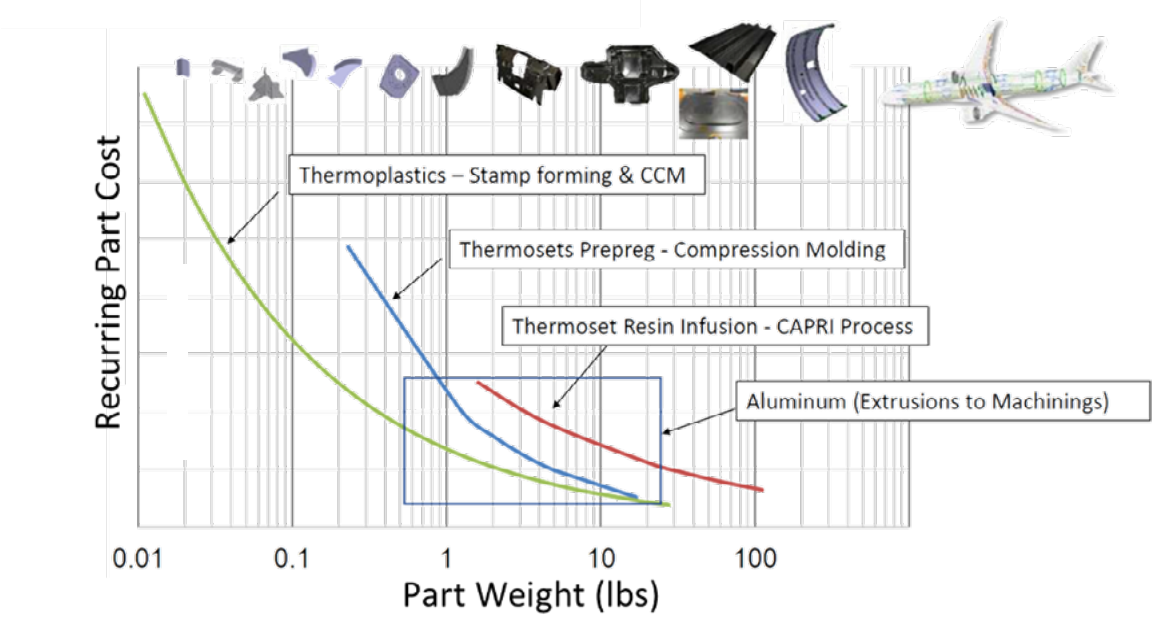

Figure 3. Recurring aircraft part cost by component size [7].

Fabrication cycle times of TPCs can be very short, but high process temperatures are required, generally 300 – 400 °C, compared to thermosets at 180 °C. One of the challenges in TPC fabrication is that different methods and equipment are required to realize the benefits of rapid processing compared to thermoset composites. This can present a significant barrier to change due to the need to invest in new equipment and apply different fabrication techniques.

4. Thermoset to Thermoplastic Transition Experience

While glass and carbon fibres provide high stiffness and strength at low densities compared to metals, they must be supported using a matrix resin. If we were to start over today and propose that these matrices need frozen storage, have a working life of a few days at room temperature, require cure cycles of many hours and have a significant reduction in service temperature in the presence of moisture, it would be difficult to convince designers of the benefit of these resins. However, when the reinforcing fibers became available the thermosetting resins were the only viable option, and a whole infrastructure developed around the use of these materials. The steps in the adoption of TPCs composites are shown in Figure 4 [8].

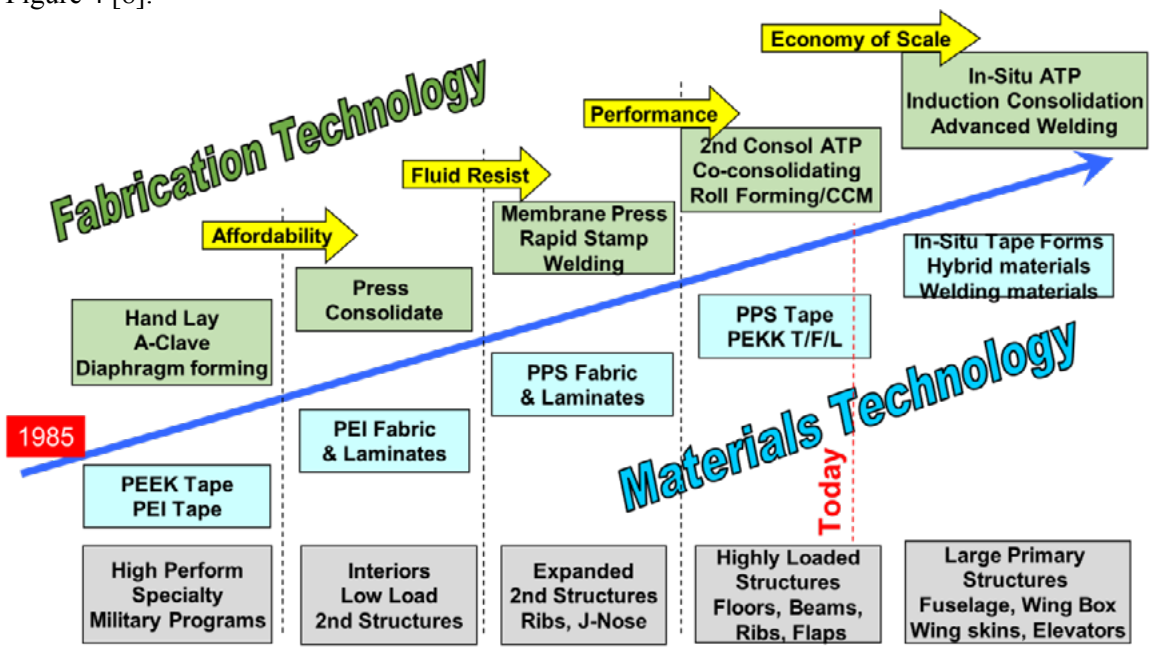

Figure 4. Thermoplastic composites adoption curve [8].

By the early 1980s there was a demand for composites with high toughness and ease of fabrication. This led to the development and commercialization of TPCs in the form of unidirectional (UD) tapes by ICI (now Syensqo) and fabric reinforced materials by TenCate (now Toray).

Thermoplastic composites offered increased performance in critical areas compared to the available thermoset composites. Several initial applications were driven entirely by performance and the defense industry was willing to pay a high premium to reach performance goals. Two early production applications are shown in Figure 5. On the Lockheed-Martin F-22 the forward fuselage and weapons bay doors were manufactured using PEEK/CF UD tapes [9]. This was driven by the need for high toughness in these parts and the limited toughness of thermoset composites. In the Dassault Rafale the use of TPCs in the central fuselage section was driven by the need for high temperature and flammability resistance of PEEK/CF UD tape [10]. These applications met performance requirements but the fabrication methods were not optimized for TPCs and the structures were relatively high cost.

To realize the processing benefits of TPCs it was necessary to move from thermoset fabrication technologies, such as autoclave, to rapid fabrication and assembly methods including stamp-forming, fiber placement and welding. Initial work to develop these technologies was performed in the 1990s. TenCate (now Toray) supplied fully impregnated laminates (‘organo-sheets’) which could be rapidly formed into a part using a hot stamp forming process. Due to lower performance requirements and high part count some of the initial applications using these materials and techniques were in aircraft interior applications using PEI/glass fabric laminates. An example of a high-volume application is the smoke detector pan which is used throughout the cargo hold of commercial aircraft, shown in Figure 6. This utilized the benefits of rapid forming and flammability resistance of PEI [11].

a b

Figure 5. a. Lockheed-Martin F-22 with PEEK/CF forward fuselage and weapons bay doors [9]. b. Dassault Rafale with PEEK/CF central fuselage structure [10].

Figure 6. High-volume smoke detector housings for commercial aircraft cargo area fabricated using PEI/glass fabric [11].

During the late 1980s and 1990s the toughness of epoxy-based composites was increased considerably through mechanisms such as thermoplastic toughening, the development of semi-interpenetrating approaches and interleaving [12]. This negated one of the benefits of TPCs, and thermoset fabrication methods were already widely available including increasing use of automated processes such as advanced fibre placement (AFP) and automated tape laying (ATL). Some TPC applications emerged, but widespread adoption of high-performance TPCs was not realized and thermosets became the established technology.

A major step in TPC applications was the fabrication of Airbus A340 and A380 leading edges using PPS/GF materials. These developments were led by GKN Fokker and combined many of the TPC forming advantages including stamp forming of ribs, and welding of the ribs to the aerodynamic skins [13]. These production applications successfully showed that larger scale TPC assemblies were feasible and demonstrated both weight and cost saving using a combination of fabrication and assembly methods. As such they were an important pathfinder in the transition of aircraft structures to TPCs.

a b

Figure 6. a. Airbus A340 leading edge fabricated by GKN Fokker using PPS/glass fabric composite. b. Airbus A340 and A380 leading edges in flight [13].

Opportunities came in the 2000s with increased use of composites in commercial aircraft, notably the Boeing 787 [7] and Airbus A350 [14]. Both these aircraft make extensive use of thermoset composite structures and this drove the desire to use composites in detailed parts which would have previously been made using aluminium. If these parts had remained aluminium then considerable mitigation would have been needed to avoid galvanic corrosion with CF composites. TPCs offered cost saving vs thermosets in smaller detailed parts and weight savings compared to metallic solutions. This provided a platform for development of cost-effective fabrication methods such as continuous compression molding and stamp forming, and of material databases and processing methodology. The A350 uses 5,000 clips with more than 2,000 designs, manufactured using carbon fabric with PPS or PEEK in a stamp-forming process [14]. Typical applications are shown in Figure 7. This has been a further major step in the use of TPCs, including in primary structural applications, although these parts are still limited in size, typically less than 1 m in size.

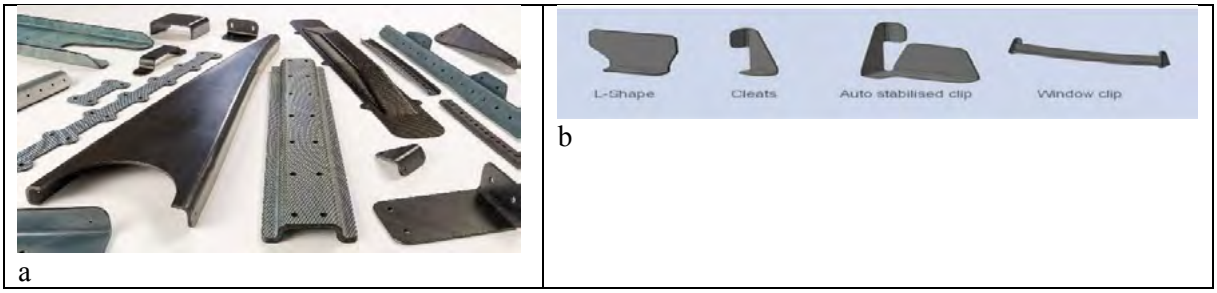

a b

Figure 7. a. Structural aircraft components using carbon fibre TPC UD tapes and fabrics [11]. b. Airbus A350 Frame Clips [14].

A further step in the adoption of TPCs came in the late 2000s with the development of welded assemblies for the Gulfstream G650 control surfaces fabricated by GKN Fokker using PPS/CF fabric materials shown in Figure 8 [15]. These assemblies use a combination of different fabrication technologies including autoclave consolidation of the skins and spar, stamp forming of the ribs and induction welding of the ribs to the skins. There is now more than 12 years of in-service experience for these structures which demonstrated 20% cost reduction and 10% weight reduction compared to the previous thermoset composite solution.

Figure 8. Gulfstream G650 rudder fabricated by GKN Fokker using PPS/CF fabric [15].

Moving into the 2020s there is great interest in TPCs for structural applications. Transportation is committed to achieve net-zero by 2050 which requires lightweight materials, TPCs are sustainable in that materials and parts can be recycled or downcycled, and applications demand high volume and high-rate. These include commercial aircraft, advanced air mobility, unmanned air vehicles and electric vehicles. This is driving the readiness of high-rate manufacturing for large scale parts and assemblies, for example through the Clean Aviation program in Europe, and in the NASA High Rate Composites Manufacturing program in the USA. The TPC multi-functional fuselage demonstrator manufactured using TPCs through the Clean Aviation programme is shown in Figure 9 [16].

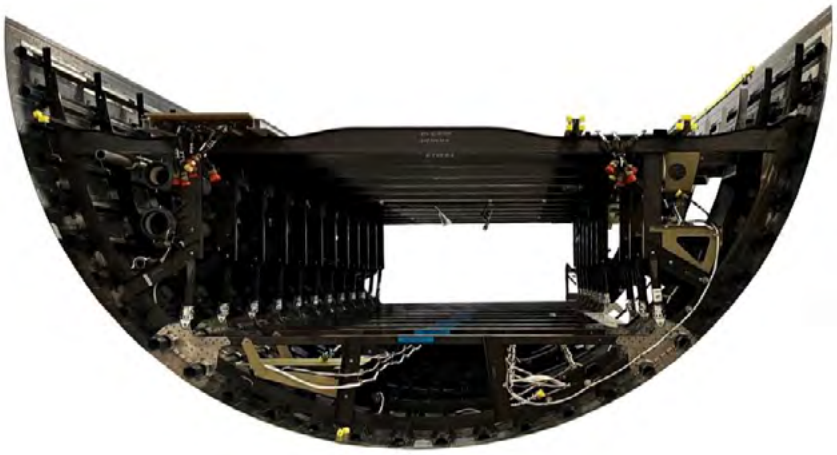

Figure 9. Multi-Functional Fuselage Demonstrator [16].

5. Conclusions

The transition of aerospace structures from thermoset to thermoplastic composites has been an incremental process, and the adoption has taken much longer than originally anticipated. Aerospace structures are highly regulated and considerable supporting information is required, even for non-structural applications. This includes material and process specifications, design allowable data as well as the availability of process equipment and maturity of fabrication methods. As such the implementation of TPCs has been incremental, initially driven by performance, then by cost and rate, starting with low risk, lightly loaded structures and gradually moving to more highly loaded, primary structure components and assemblies. The opportunity to assemble parts using welding has a multiplicative effect. While the benefits of thermoplastics may appear to be compelling, there are many barriers to change. The development of toughened thermosets and the fact that the whole supply chain and infrastructure for thermoset composites was already created major delays in the adoption of

thermoplastics. This reflects that a complete transition is needed in capital equipment and manufacturing approaches for the adoption of a new technology such as thermoplastics. This only occurs when there are new programmes which require new investment. The next generation of aircraft will make much more use of composites, and thermoplastic composites will be key to achieving the targets.

Acknowledgments
I would like to thank Advanced Thermoplastic Composites (ATC Manufacturing) for the use of material developed during my employment there.

References

[1] I Verpoest. History of Composites Volume 1 – Milestones in the History of Composites, JEC, https://www.jeccomposites.com/discover-composites/about-composites/, accessed 20 April 2024.
[2] I Verpoest. 'History of Composites Volume 2 – The Last 50 Years & The Future', JEC, https://www.jeccomposites.com/discover-composites/about-composites/, accessed 20 April 2024.
[3] D Leach, J Pratte. Overview of High Performance Thermoplastic Composites. ASM Handbook, Volume 21, Composites, ASM International, Materials Park, Ohio USA, 2024.
[4] F N Cogswell. Thermoplastic Aromatic Polymer Composites. Butterworth Heinemann, Oxford UK, 1992.
[5] S Levin, D Dequine, B Lamm, J Crocco. Damage Tolerance of Thermoplastic Stretch-Broken Carbon Fiber Prepreg vs Continuous Carbon Fiber Pre-preg. In proc SAMPE Conference 2013, Long Beach CA, 6-9 June, 2013.
[6] N Melillo. Thermoplastics Manufacturing Technologies for Aerospace Applications. Aerodef Satellite Session, 20 January 2021. Society of Manufacturing Engineers, Southfield, Michigan USA,
[7] R Wilkerson. Aerospace Applications for High Performance Thermoplastic Composites. ACMA Thermoplastic Composites Conference, Virtual, March 2020, American Composite Manufacturers Association, Arlington, VA USA.
[8] D Leach, J Pratte. Creating Successful Product/Market Combinations with an Aligned Material System. ACMA Thermoplastic Composites Conference, San Diego, March 2024, American Composite Manufacturers Association, Arlington, VA USA.
[9] S Black. Thermoplastic Composite Wings on the Horizon. https://www.compositesworld.com/articles/thermoplastic-composite-wings-on-the-horizon CompositesWorld, 9 May 2016, Accessed 2 May, 2024.
[10] S Dellus. Thermoplastic Developments at Dassault Aviation. Proc Composites in Manufacturing '92, Society of Manufacturing Engineers, Paper EM92-107, 7-8 January 1992. Society of Plastics Engineers, Danbury, Connecticut USA.
[11] D Leach. High Performance Thermoplastic Composites - Opportunities and Challenges. SPE Auto EPCON, 14 May 2024, Troy Michigan, Society of Plastics Engineers, Danbury, Connecticut USA.
[12] G Almen, P MacKenzie, V Malhotra, R Maskell, P McGrail, M Sefton. Thermoset/Thermoplastic Alloys: An Approach to Tough, High Performance Resin Matrices. Proc 20th International SAMPE Technical Conference p 46-59. 1988. Society for the Advancement of Material and Process Engineering, Covina, California USA.
[13] A Offringa. Thermoplastics, From Press Forming to Co-Consolidation. Proc SAMPE Technical Conference, Seattle WA, 31 Oct – 3 Nov 2005. Society for the Advancement of Material and Process Engineering, Covina, California USA.
[14] A Miaris, K Edelmann, M von Hayek Boelingen. A350 WXB: Thousands of Thermoplastic Composite Parts in an FRP Aircraft - The Breakthrough to a Highly Automated Composite Manufacturing. SAMPE Conference Proceedings. Seattle, WA, 2-5 June 2014. Society for the Advancement of Material and Process Engineering, Covina, California USA.
[15] J Ingen, A Buitenhuis, M van Wijngaarden, F Simmons III. Development of the Gulfstream G650 Induction Welded Thermoplastic Elevators and Rudder. SAMPE Conference, Seattle, WA, 2010, Society for the Advancement of Material and Process Engineering, Covina, California USA.
[16] https://www.clean-aviation.eu/clean-sky-2/key-demonstrators/multi-functional-fuselage-demonstrator. Accessed 2 May 2024.

MULTIFUNCTIONALITY OF HIGH VOLUMEHIGH-VOLUME-FRACTION ALIGNED CARBON-NANOTUBE/BISMALEIMIDE NANOCOMPOSITE LAMINATES

Carina Xiaochen Li[1], Erick Gonzalez[2], Aniruddha Ghosh[3], Yuying Lin[4], Jingyao Dai[5], Luiz Acauan[6], Brian L. Wardle[7]

[1]Department of Aeronautics and Astronautics, Massachusetts Institute of Technology, Cambridge, MA, USA, 02139
Email: carinali@mit.edu
[2] Department of Aeronautics and Astronautics, Massachusetts Institute of Technology, Cambridge, MA, USA, 02139
Email: egonza@mit.edu
[3] Department of Media Arts and Sciences, Massachusetts Institute of Technology, Cambridge, MA, USA, 02139
Email: ghoshani@mit.edu
[4] Department of Aeronautics and Astronautics, Massachusetts Institute of Technology, Cambridge, MA, USA, 02139
Email: yuyingl@mit.edu
[5] Department of Aeronautics and Astronautics, Massachusetts Institute of Technology, Cambridge, MA, USA, 02139
Email: jydai@mit.edu
[6] Department of Aeronautics and Astronautics, Massachusetts Institute of Technology, Cambridge, MA, USA, 02139
Email: lacauan@mit.edu
[7] Department of Aeronautics and Astronautics and Department of Mechanical Engineering, Massachusetts Institute of Technology, Cambridge, MA, USA, 02139
Email: wardle@mit.edu

Keywords: nanocomposites, current carrying compacity, ampacity, sheet resistance, TCR, BNL, electrical property

Abstract
We fabricated a novel, high volume fraction (> 50 vol%) aligned carbon nanotubes (A-CNTs) reinforced polybismaleimide (BMI) bulk nanocomposite laminate (BNL), specifically engineered to achieve high mass-specific mechanical properties. This bulk aligned nanocomposite has ideal morphology for mechanical benefit of aligned CNTs and demonstrates potential for multifunctional applications, including in electrical and thermal properties. In this study, the current carrying capacity of the BNL composite was measured, revealing an ampacity four orders of magnitude higher than that of low CNT fraction buckypaper composites and traditional carbon fiber-reinforced polymers (CFRP). A modified Wesscher and Montgomery 4-probe method was employed to measure the sheet resistance of the BNL at both room and elevated temperatures, assessing the temperature dependence of the electrical properties. No increase in ply-level sheet resistance was observed, indicating that the polymer matrix between the CNTs and in the interlaminar region had minimal impact on the CNT-CNT junctions and sheet resistance. Anisotropy in the electrical properties was noted in the longitudinal and transverse directions of the BNL. With several noted mechanical benefits and the multifunctionality offered by

aligned CNTs, this BNL composite holds significant promise for applications in the electronics, energy storage, and aerospace industries.

1. Introduction

Nanocomposites incorporating carbon nanotubes, nanowires, graphite, and nanowalls demonstrate superior and unique mass-specific thermal, electrical, and mechanical properties[1–7]. Previous research showcased a high-volume- fraction (50%) bulk nanocomposite laminate (BNL), leveraging the high axial strength of CNTs and the effective load-transferring capabilities of aerospace-grade polymer systems, to achieve remarkable specific strength and modulus[8–11]. A polymer infusion process was developed to create horizontally aligned CNT (HA-CNT) polymer nanocomposites using aerospace-grade polybismaleimides (BMI), followed by densification through heated pressing to fully cure the matrix and secure the HA-CNTs. The resulting cured PNCs maintained the alignment of CNTs and displayed enhanced anisotropic mechanical properties[10].

Graphite and CNTs, as carbon allotropes, are excellent electrical conductors due to their sp^2-bonded hexagonal carbon atom networks, making them ideal for electrodes and electronic device applications [5,12,13]. CNTs, seamless tubes derived from rolled graphene sheets, can display either metallic or semiconducting behavior depending on their rolling angle. Factors such as impurities, defects, and the number of walls significantly affect their conductivity. Despite challenges in achieving uniform dispersion and high volume fractions, our use of a content exceeding 50 vol% and an aligned distribution of CNTs suggests potential for unique electrical properties in these A-CNT nanocomposites, marking a significant step in translating individual CNT electrical characteristics to macroscopic scales.

In this study, to further explore the multifunctionality of the BNL composite, current carrying capacity tests were conducted and a square 4-point probe method was employed, based on the modified Wesscher and Montgomery technique, to measure sheet resistance at both room and elevated temperatures. The BNL exhibited an ampacity four orders of magnitude higher than that of low CNT fraction buckypaper composites and traditional carbon fiber-reinforced polymers (CFRP) [14]. Additionally, it demonstrated low sheet resistance and high anisotropy compared to other fiber-based and nanofiber-based composites. Our findings indicated that the polymer matrix in the inter- and intra-laminar region had a negligible impact on the electrical resistance. Furthermore, the BNL's resistance showed a temperature-dependent decrease, indicative of non-metallic behavior, as expected[13]. These advantageous electrical properties highlight the potential of BNL composites for multifunctional applications, including in sensors, detectors, flexible electronics, thermal management, and energy storage systems.

2. Experiments and Results

2.1. BNL Fabrication

Figure 1 illustrates the fabrication process of the as-grown, vertically aligned CNT (VA-CNT) arrays produced via the CVD method [9]. Initially, these CNT arrays underwent a "knock-down" process to increase their density. The BMI solution was prepared by dissolving BMI resin in acetone and subjecting it to ultrasonication for approximately 10 minutes. This solution was then applied to the dry 2-ply HA-CNT laminates using a pipette, followed by spin-coating at 4000 RPM for 30 seconds. Excess acetone was removed by drying the laminates in an 80°C oven for 2 hours under vacuum conditions. Subsequently, these dried 2-ply HA-CNT laminates underwent further densification through hot-pressing at 120°C for 10 minutes. The densified 2-ply laminates served as free-standing "prepregs" used to construct thicker laminates with various lay-up configurations. Eight-ply unidirectional BMI laminates were created by stacking four of these 2-ply "prepregs." These 8-ply laminates were then hot-pressed for curing and subsequently post-cured on a hot plate. The CNT volume fraction was calculated based on densities and Thermogravimetric Analysis (TGA) results to be ~50 vol%. The cured BNL was then cut into the required dimensions for different measurements.

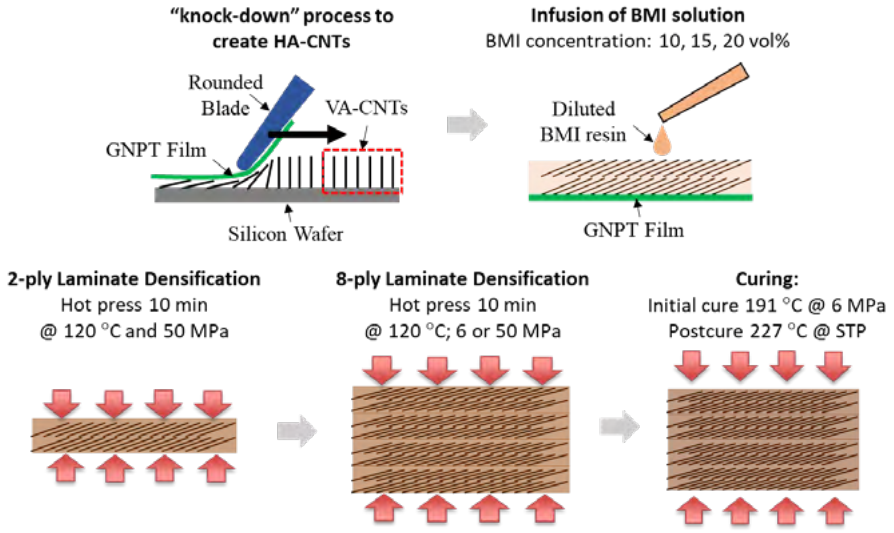

Figure 1: Fabrication schematics of high- volume- fraction aligned carbon-nanotube/Polybismaleimide nanocomposite laminates, including: knock-down of vertically-aligned CNTs into horizontally-aligned (HA-CNTs), infusion of the BMI solution, densification of the 2-ply and 8-ply laminate, and final cure & post-cure [9,11].

2.2. Current Carrying Capacity of BNL

The maximum current carrying capacity, or ampacity, of materials is crucial for the longevity and efficiency of electronic devices. As device sizes decrease, the channels that transport current to these components also become smaller, leading to higher current densities in conductors. In the aerospace industry, the use of carbon-fiber-reinforced polymers (CFRPs) poses significant safety and durability challenges related to lightning strike protection, especially since commercial aircraft typically endure 1-2 lightning strikes per year. Carbon nanotubes (CNTs) have proven effective in improving the current carrying capabilities of traditional electronics metals like copper and aluminum, as well as enhancing CFRPs used in aerospace, owing to their superior ampacity [15,16]. In this study, the current carrying capacity and the ampacity of the high volume fraction CNT composites with BMI matrix was experimentally measured, with schematics shown in Figure 2.

For the current carrying capacity test, BNL samples were cut into 30x5 mm rectangles along the CNT knockdown direction. These samples were secured in a custom sample clamp and a good electrical connection was ensured using silver paste. They were connected to a direct current source and the voltage was recorded. Current measurements were taken using a digital multimeter (Keysight, 34461A). Three specimens were tested, with the voltage incrementally raised by 0.2 V every 10 seconds. Using the measured voltage, current, and dimensions of the specimen, the current density, resistance, and resistivity were calculated. The ampacity was defined as the current density at which the sample began to burn.

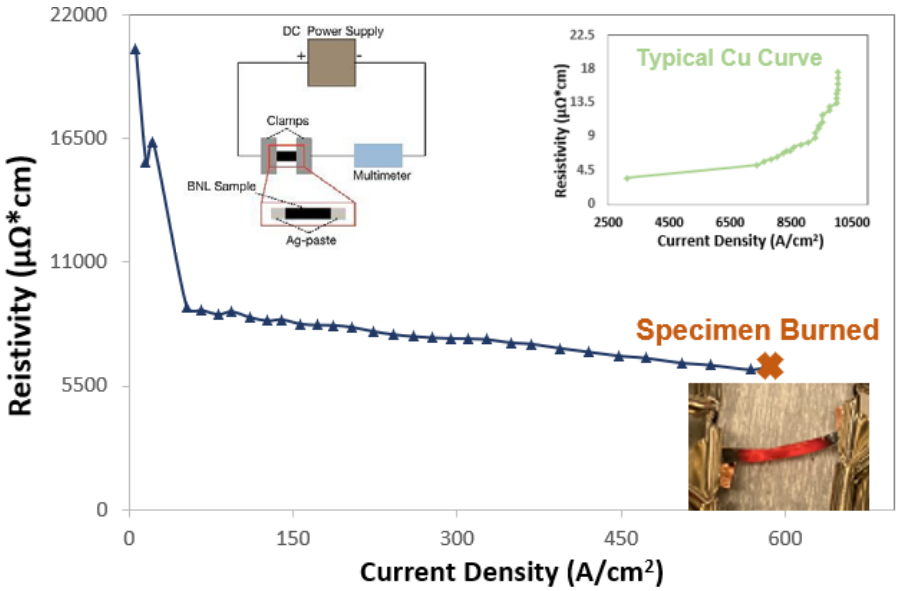

Figure 2. Representative Resistivity vs. Current Density Curve for BNL. Resistivity decreased with increasing current density, showing an opposite trend compared to typical metal behavior.

The representative resistivity versus current density curve for BNL, exhibiting non-metallic behavior is shown in Figure 2: different from typical metals such as copper, as the current density increases, causing a rise in temperature, the resistivity decreases. This is consistent with the negative temperature coefficient of resistance found in dry aligned CNTs, as demonstrated by Lee et al [13]. This effect is primarily due to the temperature-dependent functionality of the CNT-CNT junctions following the fluctuation induced tunneling conduction (FITC) model. The maximum current density the specimens reached before burning was 555.3 ± 25.6 A/cm^2. Azamian et al. reported that the ampacity for CFRP was 200 * 10^{-4} A/cm², and for MWCNT-epoxy composites with a CNT weight fraction ranging from 1 wt%-5 wt%, the ampacity was between 500-600 * 10^{-4} A/cm² [16]. Both ampacity values are 4 orders of magnitude lower than ampacity of BNL, indicating the effective enhancement of electrical properties by the high volume fraction of aligned CNTs.

2.3. Sheet Resistance and Temperature Dependence of BNL

The sheet resistance of BNL was measured using a square 4-point probe tester following the modified Wesscher and Montgomery method [17,18]. BNL composites were cut into 0.5 cm × 0.5 cm squares and measured with the 4-point probe test, which eliminates contact resistance. In this section, the footnotes 'L' and 'T' were used to clarify the measurement direction, indicating the CNT knockdown direction (L) and the transverse direction (T), respectively, for both dry-CNT and the BNL laminate. To measure the temperature dependence of the sheet resistance, the specimen was placed on a programmable hot plate for testing.

Table 1 displays the sheet resistance of the dry CNTs and 8-ply BNL. To explore the effect of the polymer matrix on the CNT-CNT junction, the sheet resistance and anisotropy (R_{sh_T}/R_{sh_L}) of both dry HA-CNTs and the BMI BNL were analyzed. The BNL demonstrated a lower sheet resistance, attributable to its 8-ply configuration providing more pathways for electrons, and a higher anisotropy ratio (2.1 vs. 1.2). This indicates that the hot-pressing process to manufacture the BNL samples, in conjunction with the polymer matrix's retaining effect, enhances the material's anisotropy by confining the fibers. In the longitudinal direction, the normalized single-ply BNL sheet resistance showed no statistically significant differences when compared to dry CNTs, indicating that the polymer matrix didn't affect the in-plane conductivity of CNTs. The conductivity calculated from the resistance was 1.46 * 10^4 S/m, about one order of magnitude higher than the conductivity of Buckypaper (2-6 * 10^3 S/m), demonstrating effective conduction of the high CNT volume fraction.

Table 1. Sheet resistance of dry CNT and the processed BNL in the longitudinal and transverse direction, measured with the modified Montgomery method.

Specimen Type	R_{sh_T} (Ω/sq) Avg ± SE	R_{sh_L} (Ω/sq) Avg ± SE	R_{sh_T} / R_{sh_L}
Dry CNT (1ply, 600 μm)	6.41 ± 0.55	7.72 ± 0.66	1.2
BNL (8 plies, ~100 μm)	0.75 ±0.06	1.56 ±0.21	2.1

The temperature dependence of resistance significantly influences the efficiency and reliability of electronic devices, impacting their performance across various temperatures. Metals typically exhibit a positive temperature coefficient of resistance (TCR). To explore the temperature dependence of electrical properties, resistance measurements of BNL were performed at temperature ranging from room temperature to 200 °C. Figure 3 shows a decrease in sheet resistance with rising temperature in both longitudinal and transverse directions, indicative of non-metallic behavior characterized by a negative TCR. This trend is attributed to the increased mobility of charge carriers in both the carbon nanotube and BMI matrix materials. These results are consistent with observations from the current carrying capacity test and previous studies [13], suggesting enhanced electron transport activation through tunneling effect in the CNT-CNT junctions with increased temperature.

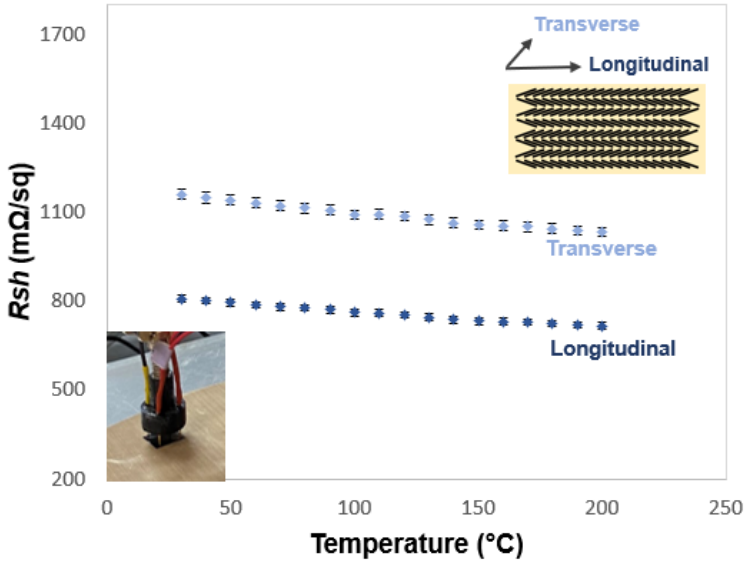

Figure 3. Representative temperature dependence of sheet resistance of BNL measured with the modified Montgomery Method: increasing temperature leads to decrease in sheet resistance.

3. Conclusions

This multifunctionality study of the BNL composites revealed an ampacity four orders of magnitude higher than traditional CFRP and low CNT fraction buckypaper composites. Additionally, the BNL demonstrated low sheet resistance and anisotropy in electrical conductivity, underscoring its suitability as an exceptional material for advanced engineering applications. The polymer matrix's minimal impact on both the interlaminar and intralaminar conductivity emphasizes the effective integration of the BMI with the CNT framework. This integration preserves the inherent electrical properties of the CNTs. At elevated temperatures, BNL exhibited a negative temperature coefficient of resistance (TCR), highlighting the non-metallic behavior of the composites, and indicative of the fluctuation-induced tunneling conduction (FITC) mechanism. These attributes underscore the BNL's potential for advanced applications in aerospace, electronics, and energy storage.

Acknowledgments

This work was supported by Airbus, ANSYS, Boeing, Embraer, Lockheed Martin, Saab AB, and Teijin Carbon America through MIT's Nano-Engineered Composite aerospace STructures (NECST) Consortium, and partially supported by the U.S. Army Research Laboratory and the U.S. Army Research Office through the Institute for Soldier Nanotechnologies (ISN) under contract number W911NF-13-D-0001 and the U.S Office of Naval Research (ONR) under grant/contract number N00014-22-1-2203. This material is based upon work supported in part by the U. S. Army Research Office through the Institute for Soldier Nanotechnologies at MIT, under Cooperative Agreement Number W911NF-18-2-0048. Micro-computed tomography instrumentation support by the Office of Naval Research (ONR) under grant number ONR.N000141712068 through the Defense University Research Instrumentation Program (DURIP) is gratefully acknowledged. The authors gratefully acknowledge the members of necstlab at MIT for technical support and advice.

References

[1] Ebbesen TW, Lezec HJ, Hiura H, Bennett JW, Ghaemi HF, Thio T. Electrical conductivity of individual carbon nanotubes. Nature 1996;382:54–6. https://doi.org/10.1038/382054a0.
[2] Garrett MP, Ivanov IN, Gerhardt RA, Puretzky AA, Geohegan DB. Separation of junction and bundle resistance in single wall carbon nanotube percolation networks by impedance spectroscopy. Appl Phys Lett 2010;97:163105. https://doi.org/10.1063/1.3490650.
[3] Salvato M, Cirillo M, Lucci M, Orlanducci S, Ottaviani I, Terranova ML, et al. Charge Transport and Tunneling in Single-Walled Carbon Nanotube Bundles. Phys Rev Lett 2008;101:246804. https://doi.org/10.1103/PhysRevLett.101.246804.
[4] Sakurai S, Kamada F, Futaba DN, Yumura M, Hata K. Influence of lengths of millimeter-scale single-walled carbon nanotube on electrical and mechanical properties of buckypaper. Nanoscale Res Lett 2013;8:546. https://doi.org/10.1186/1556-276X-8-546.
[5] Nirmalraj PN, Lyons PE, De S, Coleman JN, Boland JJ. Electrical Connectivity in Single-Walled Carbon Nanotube Networks. Nano Lett 2009;9:3890–5. https://doi.org/10.1021/nl9020914.
[6] Berber S, Kwon Y-K, Tománek D. Unusually High Thermal Conductivity of Carbon Nanotubes. Phys Rev Lett 2000;84:4613–6. https://doi.org/10.1103/PhysRevLett.84.4613.
[7] Dhakate SR, Subhedar KM, Singh BP. Polymer nanocomposite foam filled with carbon nanomaterials as an efficient electromagnetic interference shielding material. RSC Adv 2015;5:43036–57. https://doi.org/10.1039/C5RA03409D.
[8] Kaiser AL. Interfacial and Physical Confinement Effects on the Structure and Properties of Aligned Carbon Nanotube Architectures. PhD Thesis. Massachusetts Institute of Technology, 2021.

[9] Lin Y, Li C, Dai J, Acauan L, Wardle BL. Fabrication and Characterization of Carbon Nanotube/Poly(methyl) Methacrylate Nanocomposite Laminates. ASC, Woburn, MA: 2023.
[10] Curtis-Smith C, Rogers M, Dai J, Gonzalez E, Li CX, Lin Y, et al. Fabrication and Characterization of Carbon Nanotube/Bismaleimide Nanocomposite Laminates with Ultrahigh Nanofiber Volume Fraction. AIAA SCITECH 2023 Forum, National Habor: 2023. https://doi.org/10.2514/6.2023-2031.
[11] Kaiser AL, Chazot CAC, Acauan LH, Albelo IV, Lee J, Gair JLJr, et al. High-Volume-Fraction Textured Carbon Nanotube–Bis(maleimide) and −Epoxy Matrix Polymer Nanocomposites: Implications for High-Performance Structural Composites. ACS Appl Nano Mater 2022;5:9008–23. https://doi.org/10.1021/acsanm.2c01212.
[12] Tehrani M. Advanced Electrical Conductors: An Overview and Prospects of Metal Nanocomposite and Nanocarbon Based Conductors. Phys Status Solidi A 2021;218:2000704. https://doi.org/10.1002/pssa.202000704.
[13] Lee J, Stein IY, Devoe ME, Lewis DJ, Lachman N, Kessler SS, et al. Impact of carbon nanotube length on electron transport in aligned carbon nanotube networks. Appl Phys Lett 2015;106:053110. https://doi.org/10.1063/1.4907608.
[14] Li CX, Gonzalez E, Ghosh A, Lin Y, Dai J, Acauan L, et al. Multifunctionality of High Volume Fraction Aligned Carbon-Nanotube/Bismaleimide Nanocomposite Laminates. AIAA SCITECH 2024 Forum, American Institute of Aeronautics and Astronautics; 2024. https://doi.org/10.2514/6.2024-0764.
[15] Subramaniam C, Yamada T, Kobashi K, Sekiguchi A, Futaba DN, Yumura M, et al. One hundred fold increase in current carrying capacity in a carbon nanotube–copper composite. Nat Commun 2013;4:2202. https://doi.org/10.1038/ncomms3202.
[16] Azamian P, Park JG, Liang Z, Wang B, Zhang C. High current-carrying capacity study of CNT enhanced composites. 18th International Conference on Composite Materials, Jeju Island: 2011.
[17] dos Santos CAM, de Campos A, da Luz MS, White BD, Neumeier JJ, de Lima BS, et al. Procedure for measuring electrical resistivity of anisotropic materials: A revision of the Montgomery method. Journal of Applied Physics 2011;110:083703-083703–7. https://doi.org/10.1063/1.3652905.
[18] Miccoli I, Edler F, Pfnür H, Tegenkamp C. The 100th anniversary of the four-point probe technique: the role of probe geometries in isotropic and anisotropic systems. J Phys: Condens Matter 2015;27:223201. https://doi.org/10.1088/0953-8984/27/22/223201.

COMPOSITE HYDROGELS BASED ON MODIFIED CHITOSAN WITH HAEMOSTATIC AND ANTIMICROBIAL ACTIVITY

Zoi Terzopoulou, Ioanna Koumentakou, Rizos Bikiaris

Laboratory of Polymer and Colors Chemistry and Technology, Department of Chemistry, Aristotle University of Thessaloniki, 54124 Thessaloniki, Greece;
Email: terzozoi@chem.auth.gr

Keywords: chitosan, haemostatic, antimicrobial, nanoparticles, wound care

Abstract
Chitosan (CS) has gained prominence in developing haemostatic products due to its cationic polysaccharide nature, offering bactericidal, renewable, biodegradable, and hydrophilic properties. This study aims to enhance haemostatic CS-based materials with improved antimicrobial features, biocompatibility, and rapid clotting abilities. A grafted chitosan copolymer with [2-(N-morpholino) ethanesulfonic acid (MES)] was synthesized, yielding CS-g-MES porous sponges via modified thermal-induced phase separation. Heparin was encapsulated within poly(butylene) succinate (PBSu) nanoparticles to augment haemostatic potential. Nanoparticles, prepared using dichloromethane (DCM) and polyvinyl alcohol (PVA), showed increased size with heparin loading. Analysis confirmed successful synthesis and thermal stability. These advancements culminated in a chitosan-based composite dressing integrating nanoparticles, exhibiting haemostatic and improved antimicrobial properties. Characterization involved FT-IR, XRD, and SEM imaging. Biological studies affirmed antibacterial effects and haemostatic activity, indicating the potential of this composite as a multifunctional wound care solution.

1. Introduction

The objective of this work is the development of new hemostatic products with the application of innovative solutions that will give them faster and more effective hemostasis in order to fill an important gap in health and the market of pharmaceutical products, that of effective, cheap hemostatics without unwanted side effects. The is the development of hemostatic products that will have the ability to:
1. clot formation in the injured vessel and in the cases of patients who are already subject to some medical treatment with anticoagulant agents
2. maximum effectiveness with the use of a smaller amount of product
3. application to all kinds of wounds, in any part of the body and in any shape of wound
4. avoiding any kind of side effect such as further thrombosis and the creation of infections.

To achieve these goals, hemostatic chitosan powder with antimicrobial properties was prepared through its chemical modification. Also, the method proposed to dissolve the clots that form in unwanted parts of the body is an original approach. Hydrophilic antithrombotic heparin, was encapsulated in polymer nanoparticles.

The nanoparticles are composed of biodegradable poly(butylene succinate PBSu). PBSu is a biocompatible polymer with a fast biodegradation rate. So with the use of this polymer, it is proposed to prepare nanoparticles that will release the heparin at the right time, not too soon, so that the clot can form in the injured vessel, but not too late, so that it immediately dissolves any clots that may form inside the vessels that can cause a problem. This approach has not yet been applied to another hemostatic formulation.

2. Results

2.1. Functionalization of Chitosan

The synthesis was carried out by the mechanism of free radical polymerization. Specifically, medium molecular weight chitosan powder was gradually added under continuous stirring in a volumetric flask together with H_2O and aqueous acetic acid solution 2% (v/v). After its complete dissolution, 2-(N-morpholino)ethanesulfonic acid (MES), shown in Figure 1, and the initiator (potassium persulfate) were added. The reaction was carried out at 60°C for 2 hours under a nitrogen atmosphere. After 2 hours, the chitosan derivative was placed in the freezer for 25 hours and then in a lyophilizer to remove moisture. In order to remove any by-products the unreacted amount of monomer was purified in a Soxhlet apparatus with a flask and the use of acetone for 5 hours. After cleaning the polymer was left on filter paper for complete drying.

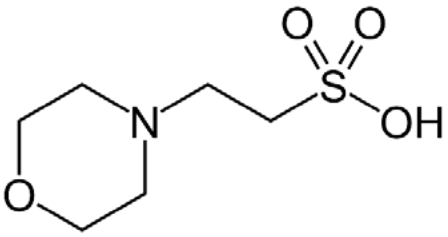

Figure 1. The chemical structure of 2-(N-morpholino)ethanesulfonic acid (MES).

In the FTIR spectrum of MES (Figure 2a) we observe a broad peak at 3380 cm^{-1} due to the hydroxyl strain vibration of the sulfate group, a sharp peak at 1185 cm^{-1} due to the amide bond (C-N) of the heterocyclic ring, as well as the characteristic peaks at 1080 cm^{-1} and 1133 cm^{-1}, which are due to S=O bonds. In the CS-MES spectrum of the modified chitosan it was observed that there were shifts of the characteristic peaks of pure chitosan, from 3444 to 3334 cm^{-1}, from 1656 to 1649 cm^{-1} and from 1584 to 1542 cm^{-1}. These shifts indicate the formation of hydrogen bonds between pure chitosan and MES. In Figure 2b we see the XRD graohs of the chitosan, MES and the modified chitosan CS-MES. MES, as a crystalline monomer, showed in its diffractogram sharp peaks of high density at angles 2θ=12, 17, 19, 21, 24, 31 and 32. The modification of chitosan with MES, resulted in a amorphous product with a single broad peak at 22°. In Figure 2c, it is shown that the swelling ration of CS-MES reaches 3500%, which is a necessary feature for its use in haemostatic wound dressings.

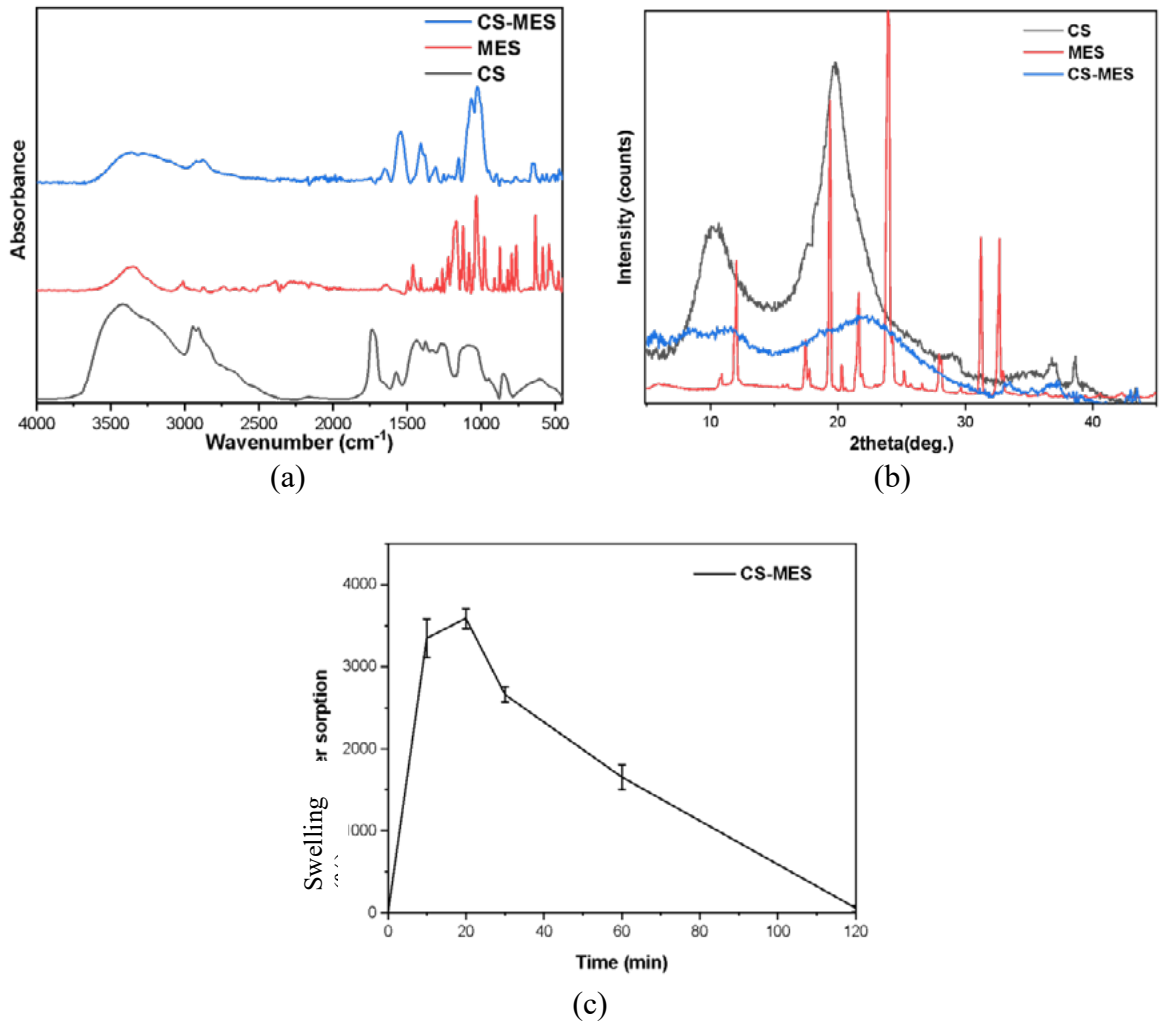

Figure 2. (a) FTIR spectra of CS, MES and CS-MES, (b) XRD patterns of CS, MES and CS-MES and (c) % swelling of CS-MES in aqueous buffer with pH=5.6.

2.2 Preparation of heparin-loaded PBSu nanoparticles

The nanoparticles were prepared by the spray drying technique. In a first step, three (3) different PBSu nanoparticles were prepared, using for each a 1%, 2% and 4% w/v solution of PBSu in dichloromethane. This procedure was done to find the optimal concentration of PBSu which will be used for the subsequent preparation of heparin-encapsulated nanoparticles.

The operating conditions of the spraying drying during the procedure were Aspirator 100%, Gas input 5-6 bar (atmospheric air $O_2 + N_2$), and Q flow 30%. The inlet temperature was 80°C, while the external one (outlet) was stabilized in the region of 50 ± 2 °C, while the time needed for the complete spraying of the solution was 4.5 ± 0.3 min. The best results were presented by the solution with 2 wt% PBSu which was used to prepare nanoparticles with encapsulated heparin following the same manufacturing method. Specifically, 0.5 g of PBSu and 50 mg of heparin were dissolved in 25 mL of dichloromethane (2 wt% PBSu and 0.2 wt% heparin) and the spraying procedure was carried out as mentioned above. SEM image of the resulting particles (Figure 3) shows that after heparin encapsulation in PBSu nanoparticles, well-shaped nanoparticles are still formed, larger in size, which is expected due to heparin encapsulation, as also confirmed by DLS measurements (692 nm to 797 nm).

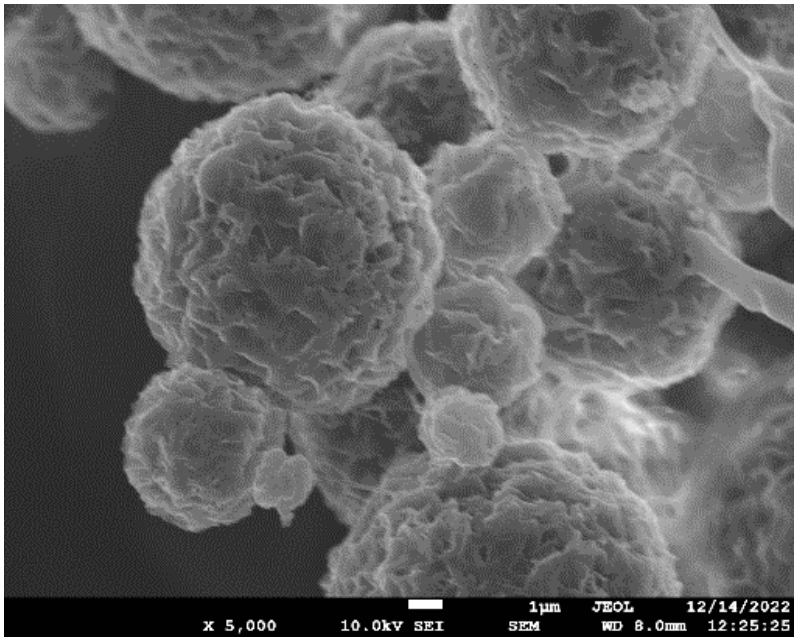

Figure 3. SEM image of the Heparin-loaded PBSu nanoparticles.

2.3 Characterization of chitosan-based composite dressing

To prepare the dressings, first, an appropriate amount of heparin-encapsulated PBSu nanoparticles was dispersed in water using high-speed stirring (1150 rpm) for 2 consecutive minutes. Then, an appropriate amount of protamine sulfate, vitamin K, and iron sulfate was added and stirring was carried out for five hours. After stirring the mixture, an appropriate amount of modified chitosan (CS-MES) was added, left under stirring for 50 min to uniformly disperse the chitosan in the mixture, and finally acetic acid (1% v/v) was added to synthesize a high-viscosity hydrogel. The prepared hemostatic hydrogel was left under agitation for 24 hours, then the amount was placed on suitable drying surfaces and dried at 40°C for 24h. The resulting solid was triturated to prepare the final hemostatic product, containing 10 wt% PBSu nanoparticles, and abbreviated as CS-MES-10%.

The FTIR spectra of the prepared dressings are presented in Figure 4. The Heparin-loaded PBSu nanoparticles (blue spectrum) show the characteristic peaks of the polymer's carbonyl group, the C-H stretching and a broad hydroxyl absorption band, arising from the hydroxyls of both heparin as well as the terminal hydroxyls of PBSu. Adding the nanoparticles in CS-MES (green spectrum), the carbonyl band emerges and the hydroxyl band becomes larger in intensity and area, in comparison with CS-MES, and its peak position shifts to higher wavenumbers. This indicates that interactions such as hydrogen bonding took place between the heparin-loaded PBSu nanoparticles and the CS-MES hydrogel.

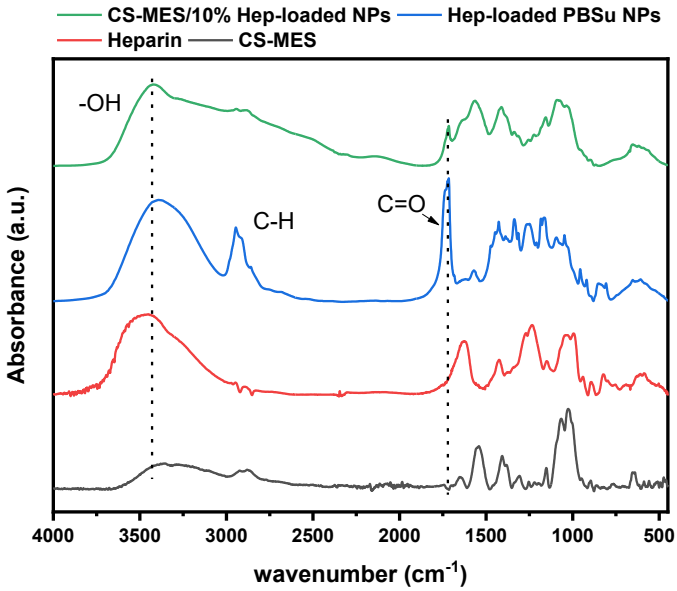

Figure 4. FTIR spectra of neat CS-MES, neat Heparin, Heparin-loaded PBSu nanoparticles and the final composite dressing (CS-MES/10% Hep-loaded NPs).

X-Ray diffraction patterns are presented in Figure 5. The heparin-loaded PBSu nanoparticles display some crystalline peaks owning the semicrystalline nature of the polymer PBSu. On the other hand, both CS-MES and amorphous. After the addition of the heparin-loaded PBSu nanoparticles in the CS-MES hydrogel (green curve), the typical halos of chitosan change and crystalline peaks starts to emerge, confirming the preservation of the structure of the nanoparticles.

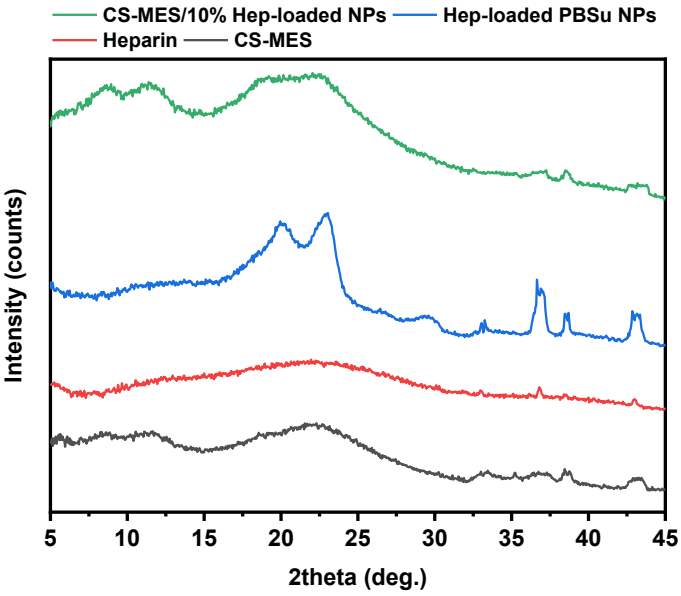

Figure 5. XRD patterns of neat CS-MES, neat Heparin, Heparin-loaded PBSu nanoparticles and the final composite dressing (CS-MES/10% Hep-loaded NPs).

3. Conclusions

In conclusion, this study successfully developed composite hydrogels based on modified chitosan (CS-MES), suitable for wound care applications. The innovative approach involved grafting chitosan with 2-(N-morpholino)ethanesulfonic acid (MES) to create a porous sponge structure and encapsulating heparin within poly(butylene succinate) (PBSu) nanoparticles to optimize haemostatic efficacy.

Characterization through FT-IR, XRD, and SEM confirmed the successful preparation of the composite material. Biological evaluations demonstrated effective antimicrobial activity and rapid clot formation, highlighting the potential of these composite hydrogels as multifunctional wound dressings. These findings suggest that the developed materials could fill a critical gap in the market for effective, affordable, and safe haemostatic agents.

Acknowledgments
The authors wish to acknowledge co-funding of this research by European Union-European Regional Development Fund and Greek Ministry of Education, Research and Religions/EYDE-ETAK through program EPANEK 2014- 2020/Action "EREVNO-DIMIOURGO-KAINOTOMO" (project T2EΔK-00275).

IN-SITU X-RAY NANOIMAGING OF FRACTURE MECHANISMS IN CNT YARN REINFORCED PLASTIC COMPOSITES

Go Yamamoto[1], Sojun Nakano[2], Okamoto Shugo[3] and Yoshinobu Shimamura[4]

[1]Department of Aerospace Engineering, Tohoku University, 6-6-01 Aramaki-Aza-Aoba, Aoba-ku, Sendai 980-8579, Japan
gyamamoto@tohoku.ac.jp, http://www.yamamotolab.mech.tohoku.ac.jp/
[2]Department of Aerospace Engineering, Tohoku University, 6-6-01 Aramaki-Aza-Aoba, Aoba-ku, Sendai 980-8579, Japan
nakano.sojun.q2@dc.tohoku.ac.jp, http://www.yamamotolab.mech.tohoku.ac.jp/
[3]Department of Aerospace Engineering, Tohoku University, 6-6-01 Aramaki-Aza-Aoba, Aoba-ku, Sendai 980-8579, Japan
shugo.okamoto.r2@dc.tohoku.ac.jp, http://www.yamamotolab.mech.tohoku.ac.jp/
[4] Department of Mechanical Engineering, Shizuoka University, 3-5-1, Johoku, Chuo-ku, Hamamatsu, 432-8561, Japan
shimamura.yoshinobu@shizuoka.ac.jp, https://mechmat.eng.shizuoka.ac.jp/

Keywords: Fiber reinforced composites, CNT yarn, Polymer environment, Fracture mechanisms

Abstract
Carbon nanotubes (CNTs) having a high elastic modulus and tensile strength are anticipated for use as a reinforcing agent in fiber reinforced composites. Recently, the focus has shifted to investigating the fracture mechanisms of CNT spun yarns, which are twisted together to form long threads of CNTs, particularly in a polymer matrix environment. A sequence of failure events of CNT spun yarns in a polymer matrix environment under tensile loading were investigated by the synchrotron radiation (SR) X-ray computed tomography (CT) using dumbbell-shaped composites with two yarns embedded in parallel. X-ray CT imaging revealed that the yarns fractured closely together in the direction of the long axis of the yarns. The fact that yarn breakage took place close to each other suggests that one yarn initially fractured following the statistical distribution of yarn strength, and the adjacent yarn failure immediately afterward occurred as a result of the initial yarn break. Our findings revealed that stress concentration is expected to occur on the adjacent yarn, providing valuable insight into the similarity of the failure mechanisms between plastic composites reinforced by CNT spun yarns and unidirectional carbon fiber reinforced plastics.

1. Introduction

Carbon nanotubes (CNTs) offer superior strength and stiffness relative to their weight compared to conventional fibrous materials. Consequently, they are being increasingly used in various industries, including sports, aviation, and industrial applications. Recently, the focus has shifted to investigating the fracture mechanisms of CNT spun yarns, which are twisted together to form long threads of CNTs [1], particularly in polymer matrix environments [2]. The failure of unidirectional carbon fiber reinforced plastics (CFRPs) under longitudinal loading conditions comprises a sequence of microscopic events, which can include fiber failure, matrix cracking, interfacial debonding, and formation of clusters of broken fibers, each of which impacts the stress distribution of the constituents around fiber break points [3]. These events continue until a critical condition is reached, resulting in the overall failure of the unidirectional CFRP composites. Consequently, the investigation of stress distribution around fiber fractures remains a central focus in research aimed at predicting the tensile strength of unidirectional CFRPs [3–5]. To date, few studies have been published on epoxy-based composites using

unidirectionally aligned CNT spun fibers [6–13]. Unfortunately, previous studies have not completely demonstrated the potential of CNT spun yarns as preforms for epoxy-based composites. This may be due to the lack of understanding of how CNT spun yarns break in a polymer matrix environment. A sequence of failure events of CNT spun yarns in a polymer matrix environment under tensile loading were investigated by the synchrotron radiation (SR) X-ray computed tomography (CT) using dumbbell-shaped composites with two yarns embedded in parallel.

2. Methods

Cabon nanotube forest was synthesized using the chloride-mediated chemical vapor deposition method [14], and subsequently CNT spun yarns were produced through a dry-spinning method without the use of any binder material [14]. Epoxy resin was used as matrix material for preparation of double-fiber composites. A sequence of microscopic failure events of CNT spun yarns in the polymer matrix environment under tensile loading were investigated by synchrotron radiation (SR) X-ray computed tomography (CT) and polarized-light microscopy using dumbbell-shaped double-fiber composites with two CNT spun yarns embedded in parallel. This approach enables the examination of the interaction between fibrous materials and localized fracture processes in polymer matrix environments. Details on the composite preparation is provided in Refs. [3–5]. In brief, two CNT spun yarns were glued in parallel on two pieces of heat-resistant tapes attached to a heat resistant glass mold. The yarns were bridged between the two tapes with a gap of approximately 60 mm. Subsequently, a preheated and degassed epoxy resin was poured into the preheated glass mold in which the yarns were bonded. Finally, the specimens were cured in an air oven at 50°C for 5 h. The specimens were then cooled in the oven to room temperature before being cut into dumbbell shape. As precise control of inter-yarn spacing is formidable task, numerous double-fiber specimens were prepared, and those with predefined inter-yarn spacings were subjected to fragmentation experiments.

A combination of micro- and nano-CT systems, called multiscale CT [15], at the BL20XU beamline of the large SR facility SPring-8 was used for observing nano/micro-scale damage events of the CNT spun yarns in the polymer matrix environment. Double-fiber fragmentation tests were performed by using the multiscale CT equipped with a custom-made tensile loading apparatus. The displacement was applied to the specimen by manually rotating a shaft on top of the apparatus. A strain gauge was attached on the surface of the double-fiber composite subjected to tensile loading to monitor the tensile strain applied to the composite. The strain level was maintained under predetermined conditions, and evolutions in morphology of the CNT spun yarns with increased strain were observed.

3. Results and discussion

Figure 1 illustrates the positional relationship of failures of the CNT spun yarns in two specimens, each experiencing maximum fiber strains of approximately 0.70% (Fig. 1a) and 0.73% (Fig. 1b) under SR X-ray CT observation, respectively. Their inter-yarn spacings were approximately17.8 μm and 15.2 μm, respectively, which are approximately 1.1 and 0.9 times the average fibre diameter. A total of 12 yarn breaks, indicated by white arrows, were observed, and these breaks appear to form pairs of break points, as observed in double-fiber fragmentation tests of carbon fibers with fiber-fiber interactions [3,4].

The SR X-ray CT observations revealed the sequence of microscopic failure events of CNT spun yarns in the polymer matrix environment. Figure 2 shows a series of micro-CT images depicting the failure events with increasing tensile strain, captured at yarn break points #5 and #6. Yarn breaks, which were not observed under the 0.36% yarn strain condition, were observed for both yarns under the 0.46% condition. The fact that yarn breaks took place close to each other suggests that one yarn initially fractured following the statistical distribution of strength, and the adjacent yarn failure immediately afterward occurred as a result of the initial yarn break. When the yarn strain increased from 0.46% to 0.70%, delamination at the fiber/matrix interface, along with matrix crack propagation in the yarn's radial direction, was observed. Even in the unloaded condition, gaps were observed in each broken yarn, indicating that the polymer matrix near the break point yielded due to the increased local stress under X-ray irradiation conditions. Similar observations have been made at different break points.

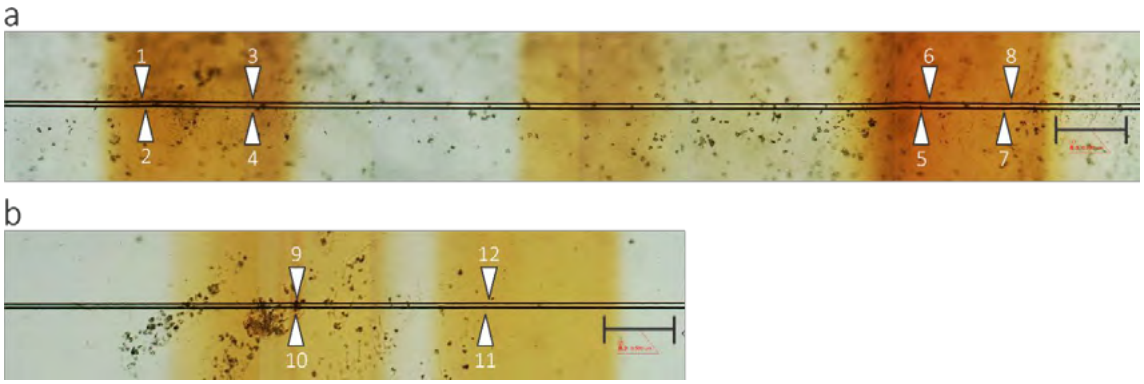

Figure 1. Optical microscope images showing the positional relationship of failures of the CNT spun yarns in two double-fiber composites. Scale bar, 0.5 µm.

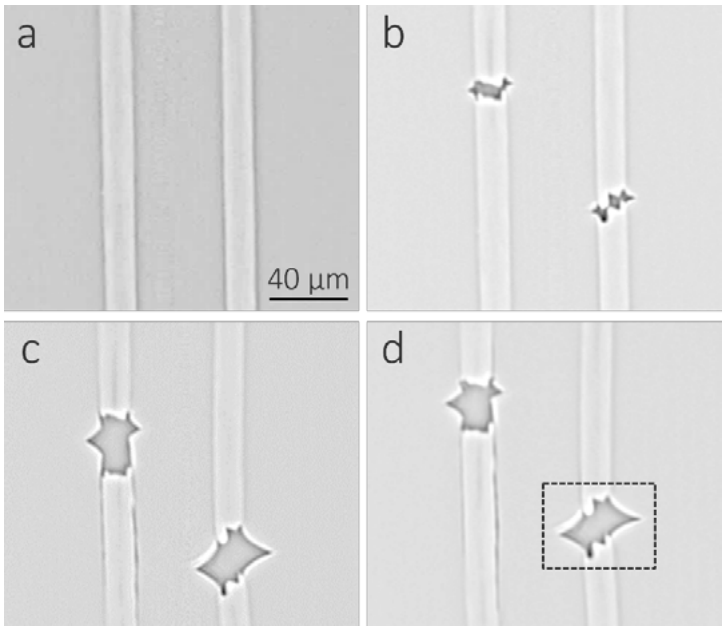

Figure 2. Micro-CT images showing the evolution of yarn breakage with increasing strain. Yarn strains, (a) 0.36%, (b) 0.46%, (c) 0.70%, and (d) 0%.

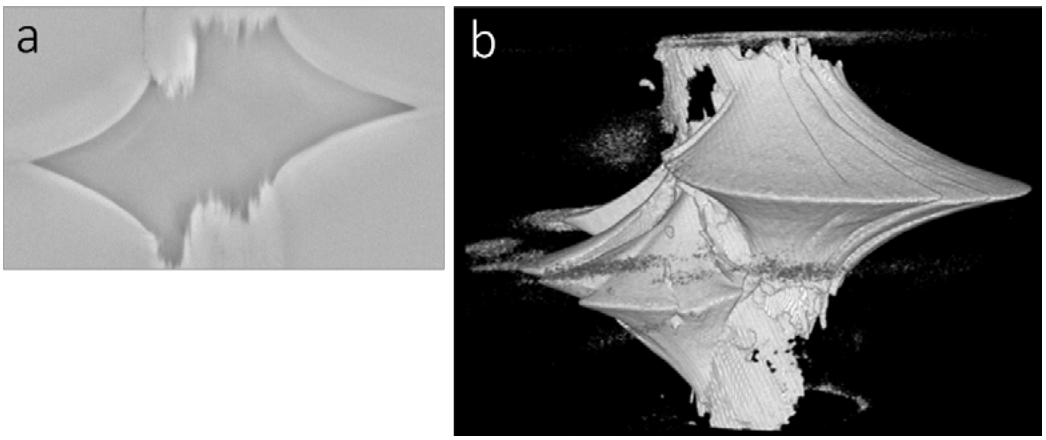

Figure 3. Nano-CT imaging extracted from the area surrounding the dashed line in Fig. 2(d).

An interesting fracture structure was observed in the nano-CT observations of yarn breakage points. As shown in Fig. 3(a), the fracture surface of CNT spun yarn was not smooth but rather showed irregularities, suggesting that breakage of the CNT spun yarns occurred due to the relative slipping of CNT bundles. Furthermore, spiral-shaped cracks propagating through the epoxy matrix can be observed from Fig. 3(b). The difference in failure morphologies between CNT spun yarns and carbon fibers in polymer matrix environments is expected to be due to the twisted structure of CNT spun yarns, which consist of a large number of CNTs, whereas carbon fibers undergo failure in a brittle manner. The impact of matrix cracks propagating spirally and breakage from relative slippage on additional stress concentration acting on adjacent CNT spun yarns needs to be investigated in future study.

4. Conclusion

The fracture process of CNT spun yarns in the epoxy matrix environment was investigated using X-ray CT at the BL20XU beamline of the large SR facility SPring-8. Double-fiber composites were prepared by embedding two CNT spun yarns parallel to each other in the epoxy matrix. This study successfully achieved three-dimensional and sequential observation of the fracture process of CNT spun yarns in the polymer matrix environment, which was difficult with conventional observation methods. The fracture morphology of CNT spun yarns and the crack propagation in the epoxy matrix were different from those observed in unidirectional carbon fiber reinforced plastics. On the other hand, the fracture mechanisms of CNT spun yarn/epoxy composites and unidirectional CFRP were observed to be similar. This is evidenced by the fact that the fractures of the two CNT spun yarns occurred in close proximity to each other along the long axis of the yarns, resulting in stress concentration on adjacent yarns.

Acknowledgments

The authors thank Prof. K. Takahashi of the Division of Mechanical and Aerospace Engineering, Hokkaido University for technical support in the synchrotron radiation X-ray computed tomography observation. This work was partly supported by TOYOTA MOTER CORPORATION, and JSPS KAKENHI [grant number 22H01351].

References

[1] M. Beese, X. Wei, S. Sarkar, R. Ramachandramoorthy, M. R. Roenbeck, A. Moravsky, M. Ford, F. Yavari, D. T. Keane, R. O. Loutfy, S. T. Nguyen and H. D. Espinosa. Key factors limiting carbon nanotube yarn strength: Exploring processing-structure-property relationships. *ACS Nano*, 8(11):11454–11466, 2014.

[2] Y. Shimamura, D. Miao, K. Tohgo and T. Fujii. Elastic analysis of tensile behavior of a composite using unidirectionally aligned staple-spun yarn preform. *Text Res J*, 86(4):440–448, 2016.

[3] G. Yamamoto, M. Onodera, K. Koizumi, J. Watanabe, H. Okuda, F. Tanaka and T. Okabe. Considering the stress concentration of fiber surfaces in the prediction of the tensile strength of unidirectional carbon fiber-reinforced plastic composites. *Compos Pt A-Appl Sci Manuf*, 121:499–509, 2019.

[4] G. Yamamoto, K. Koizumi, T. Nakamura, N. Hirano and T. Okabe. Tensile-strength-controlling factors in unidirectional carbon fiber reinforced plastic composites. *Compos Pt A-Appl Sci Manuf*, 140:106140, 2021.

[5] G. Yamamoto, K. Oshima, R. A. Ramadhan, T. Lim, Y. T. Megra, J. W. Suk, J. Watanabe, H. Okuda and F. Tanaka. Tensile strength prediction of unidirectional polyacrylonitrile (PAN)-based carbon fiber reinforced plastic composites considering stress distribution around fiber break points. *Compos Pt A-Appl Sci Manuf*, 183:108234, 2024.

[6] W. Ma, L. Liu, Z. Zhang, R. Yang, G. Liu, T. Zhang, X. An, X. Yi, Y. Ren, Z. Niu, J. Li, H. Dong, W. Zhou, P. M. Ajayan and S. Xie. High-strength composite fibers: realizing true potential of carbon nanotubes in polymer matrix through continuous reticulate architecture and molecular level couplings. *Nano Lett*, 9(8):2855–2861, 2009.

[7] R. J. Mora, J. J. Vilatela and A. H. Windle. Properties of composites of carbon nanotube fibres. *Compos Sci Technol*, 69:1558–1563, 2009
[8] A. E. Bogdanovich and P. D. Bradford. Carbon nanotube yarn and 3-D braid composites. Part I: Tensile testing and mechanical properties analysis. *Compos Pt A-Appl Sci Manuf*, 41:230–237, 2010.
[9] Y. Shimamura, K. Oshima, K. Tohgo, T. Fujii, K. Shirasu, G. Yamamoto, T. Hashida, K. Goto, T. Ogasawara, K. Naito, T. Nakano and Y. Inoue. Tensile mechanical properties of carbon nanotube/epoxy composite fabricated by pultrusion of carbon nanotube spun yarn preform. *Compos Pt A-Appl Sci Manuf*, 62:32–38, 2014.
[10] C. E. Evers, B. Vondrasek, C. N. Jolowsky, J. G. Park, M. W. Czabaj, B. E. Ku, K. R. Thagard, G. M. Odegard, and Z. Liang, Scalable High Tensile Modulus Composite Laminates Using Continuous Carbon Nanotube Yarns for Aerospace Applications. *ACS Appl. Nano Mater*, 6:11260−11268, 2023.
[11] J. W. Kim, J. M. Gardner, G. Sauti, R. A. Wincheski, B. D. Jensen, K. E. Wise and E. J. Siochi. Multi-scale hierarchical carbon nanotube fiber reinforced composites towards enhancement of axial/transverse strength and fracture toughness. *Compos Pt A-Appl Sci Manuf*, 167:107449, 2023.
[12] A. Naderi, A. Tarafdar, W. Lin and Y. Wang. Tensile Properties of Unidirectional Polymer Composites Reinforced by Aligned Carbon Nanotube Yarns. In *Proceedings of the American Society for Composites - 38th Technical Conference*, 1178–1188, 2023.
[13] J. G. Park, C. Evers, C. Jolowsky, B. Vondrasek, K. Thagard, M. Czabaj, B. Ku, Y. Wang, T. Dumitrică, G. M. Odegard and Z. Liang. Gamma-ray irradiation to achieve high tensile performance of unidirectional CNT yarn laminates. *Carbon*, 216:118530, 2024.
[14] Y. Inoue, K. Hayashi, M. Karita, T. Nakano, Y. Shimamura, K. Shirasu, G. Yamamoto and T. Hashida. Study on the mechanical and electrical properties of twisted CNT yarns fabricated from CNTs with various diameters. *Carbon*, 176:400–410, 2021.
[15] K. Takahashi, R. Shoya, T. Matsuo, W. Sato, T. Nakamura, A. Takeuchi, M. Uesugi and K. Uesugi. X-ray nanoimaging of a transversely embedded carbon fiber in epoxy matrix under static and cyclic loads. *Sci Rep*, 12:8843, 2022.

OPTIMIZING OF STABILIZATION AND CARBONIZATION PROCESSES FOR SUSTAINABLE LIGNIN-DERIVED CARBON FIBER PRODUCTION

Silvia Zecchi[1], Stavros Anagnou[2], Mattia Bartoli[3], Stefania Termine[2], Alberto Tagliaferro[1], Costas A. Charitidis[2]

[1]Department of Applied Science and Technology, Politecnico di Torino, Corso Duca degli Abruzzi 24, 10129 Turin, Italy, silvia.zecchi@polito.it, alberto.tagliaferro@polito.it, https://www.polito.it/
[2] R-Nano Lab, School of Chemical Engineering, National Technical University of Athens, Heroon Polytechniou 9, 15780 Zografou, Greece, sanagnou@chemeng.ntua.gr, stermine@chemeng.ntua.gr, charitidis@chemeng.ntua.gr, www.r-nano.gr
[3] Istituto Italiano di Tecnologia, Center for Sustainable Future Technologies - CSFT@POLITO, via Livorno 60, Torino 10144, Italy, mattia.bartoli@iit.it, https://www.iit.it/

Keywords: lignin, PA11, aphthalic anhydride, stabilization, CF

Abstract

Carbon fibers, renowned for their exceptional strength-to-weight ratio and versatile applications, have long been pivotal in various industries. As interest grows in sustainable and cost-effective carbon fiber production, lignin emerges as a promising precursor due to its abundance from the paper and pulp industry, offering an eco-friendly alternative to petroleum-based sources. This research focuses on the crucial stabilization process for carbon fiber production. Phthalic anhydride is used as a cross-linker on extruded fibers, demonstrating effective chemical modification. Continuous research and optimization of thermal process parameters are essential for emulating a semi-continuous stabilization process, thus contributing to the efficient utilization of industrial waste streams and aligning with circular economy principles.

1. Introduction

Carbon fibers, renowned for their exceptional strength-to-weight ratio and versatile applications, have long been an integral component of advanced materials in various industries. In recent years, there has been a growing interest in exploring sustainable and cost-effective sources for carbon fiber production. Carbon fibers derived from lignin offer a pathway for sustainable and cost-effective manufacturing, leveraging the surplus of lignin derived from the paper and pulp industry [1]. The utilization of lignin as a precursor for carbon provides an eco-friendly alternative to traditional petroleum-based precursors [2]. This research contributes to the efficient utilization of industrial waste streams and aligns with the principles of a circular economy. Lignin's properties, such as its extent of hydrolytic degradation, chemical functionalities, and molecular weight, are intricately tied to processing conditions and the biomass source's characteristics [3]. Lignin's structure is notably complex, primarily comprising three main monomers: coniferyl alcohol, sinapyl alcohol, and p-coumaryl alcohol [4]. This structural complexity presents challenges in the extrusion process and subsequent stabilization and carbonization stages necessary for carbon fiber formation. To facilitate extrusion, it is common to create blends with materials like polyamides. Stabilization is a crucial step involving the gradual oxidation and cross-linking of the material to elevate or eliminate its thermal transition points. This process prevents the fibers from melting during carbonization. Although lignin lacks a distinct melting point, its glass transition temperature (Tg) significantly impacts its mobility and thermal behaviour [5]. Both lignin and most carbon fiber precursors have Tg values lower than their thermal decomposition temperatures. Thus, the initial processing step involves thermally stabilizing the material to prevent fiber softening and fusion before carbonization. Chemical pretreatment can enhance thermosetting by promoting material cross-linking. Phthalic anhydride, for instance, has been successfully used in lignin treatments before extrusion. In our study, phthalic anhydride was chosen for post-extrusion treatment, aligning with sustainability principles as it can be derived from lignin oxidation.

2. Materials and methods

2.1. Materials

The fiber used in this study is composed of 40% lignin (Hardwood) and 60% PA11. The fibers were provided by Centelbex and consist of 24 filaments. Phthalic anhydride used for the chemical pre-treatment of the fiber was purchased from Chembiotin. Additionally, acetonitrile used for the fiber pre-treatment was acquired from Sigma Aldrich.

2.2. Methods

2.2.1. Chemical treatment of the fiber

The fiber underwent a chemical treatment using phthalic anhydride to act as a cross-linker within the fiber structure [6]. Phthalic anhydride was dissolved in acetonitrile to form a solution. The fibers were then immersed in the solution at a ratio of fiber to phthalic anhydride of 1:2 [7]. The immersed fibers were maintained at 75°C for 4 hours. Subsequently, three cycles of washing with acetonitrile were conducted, followed by drying the fibers at 50°C overnight.

2.2.2. Thermal treatment of the fiber

The fiber was subjected to thermal treatment using a tubular furnace, with a weight of 2 g applied to simulate tension [8]. The thermal process was conducted in ambient air. Initially, the sample was isothermally treated at 180°C for 2 hours, following a heating ramp from room temperature to 180°C at a rate of 3°C/min. Subsequently, the samples underwent natural cooling before being heated to 220°C

at a rate of 3°C/min and maintained at this temperature for 1 hour. Finally, a temperature boost to 240°C was applied for 30 minutes. Natural cooling was again employed after the thermal treatment.

2.2.3. Characterization of the fiber

2.2.3.1. Optical microscopy

Images of the fibers were obtained with the Olympus BX53M microscope using a brightfield observation method, with a camera resolution of 5760 x 3600 pixels. The Olympus Stream Motion software was used for capturing and analysing images.

2.2.3.2. FTIR

Fourier-transform infrared (FT-IR) spectroscopy was conducted with an Agilent Cary 630 spectrometer FT-IR from 550 cm^{-1} to 4000 cm^{-1}.

2.2.3.3 Thermal analysis

The thermal stability was studied by thermal gravimetric analysis (TGA) through a Jupiter STA 449 F5 instrument (Jupiter, Germany). To this end, samples of fibers were heated in alumina crucibles at 10 °C min^{-1} from 25 to 700 °C under nitrogen atmosphere (50 mL/min). The analysis was performed in accordance with ISO 11358.

The thermal behaviour of the fiber was assessed by using a Mettler DSC-822 apparatus. DSC analyses were carried out by heating about 10 mg of sample from 25 °C to 250 °C at a rate of 10 °C/min; the glass transition temperature (T_g) was taken by applying the first derivative method. Calibration was performed using indium as standard (T_m = 156.4 °C; ΔH_m = 28.15 J/g).

3. Results

3.1. Optical microscopy

In the optical microscopy analysis of the precursor material composed of 40% lignin and 60% PA11, several observations were made. In the untreated precursor Figure 1.a, variations in fiber diameters were evident both between individual fibers and within the same fiber. The diameters range between 70 to 120 µm, likely due to the production process, particularly during extrusion where swelling may occur. The uneven diameters within filaments can create challenges during the stabilization process. Variations in diameter can lead to non-uniform heat transfer and diffusion rates during stabilization, potentially resulting in inconsistent reactions and properties across the material. Additionally, the rough surface observed on the fibers can amplify these issues by providing more surface area for reaction, further complicating the stabilization process.

Upon chemical and thermal stabilization treatments, the treated fibers exhibited reduced diameters of about 20-30% as can be seen in Figure 1.b. This reduction in diameter is a common phenomenon observed during stabilization processes. The heat treatments facilitate the removal of volatile components and induce structural rearrangements, leading to shrinkage and densification of the precursor material. Therefore, it is expected to observe a decrease in fiber diameter after stabilization treatments.

Comparatively, precursors for carbon fibers derived from PAN (polyacrylonitrile) typically have smaller diameters of about a quarter of the diameter of the fiber considered for this work. Decrease in fiber diameter is known to increase the mechanical properties of carbon fibers [9]. This variation can be attributed to the differences in molecular structure and processing conditions between lignin-based and PAN-based precursors. PAN precursors offer advantages such as higher carbon yield and better mechanical properties due to their more uniform and controlled molecular structure. However, extruding precursors containing lignin presents challenges, as lignin is more complex and prone to degradation at high temperatures, making it difficult to reduce extrusion hole diameters. This technical limitation in reducing extrusion hole diameters imposes constraints on lignin-based precursor production and contributes to the observed differences in fiber diameters compared to PAN-based precursors.

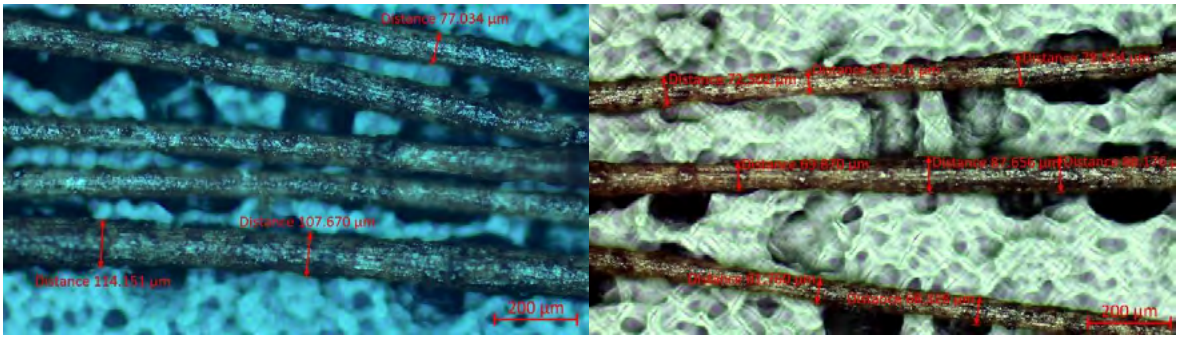

Figure 1. Optical microscopy images: a) Pristine fiber; b) Fiber treated with chemical and thermal process.

3.2. FT-IR

The Figure 2 show the FT-IR analysis performed on three samples. One spectrum is related to the untreated fiber, one to the fiber chemically treated with phthalic anhydride, and one to the fiber treated both chemically and thermally (as previously described). The spectroscopic pattern remained consistent across the samples, except for a notable peak rising at 800 cm^{-1} in the spectrum of the chemically treated fiber, which became more pronounced in the spectrum of the fiber treated both chemically and thermally. This rising of a peak at 800 cm^{-1} was due to the ortho substitution of aromatic compounds (indicating aromatic out-of-plane $\delta_{C\text{-}R}$), corresponding to the esterification of functionalities of lignin during the reaction with the phthalic anhydride [10]. Consequently, the lignin component act as an anchoring point within the fiber matrix, contributing to its stabilization through the formation of esteric linkages promoted by both the temperature and the oxidative atmosphere used.

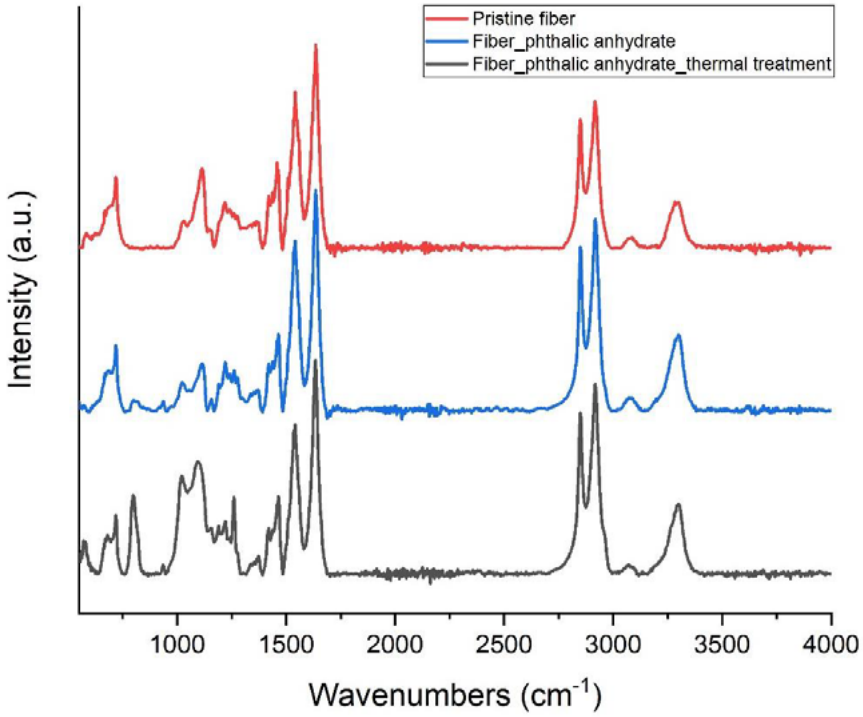

Figure 2. FT-IR spectra of the fiber at each phase of the process.

3.3. Thermal analysis

In the thermogravimetric analysis (TGA) showed in Figure 3 and Figure 4, two distinct weight loss profiles were observed for the untreated and chemically treated fibers. In the TGA curve of the untreated fiber, three mass losses were detected. The first onset at 247.8°C, accounting for about 7% mass loss, corresponds to the decomposition of labile functional groups, which could include aliphatic groups. These aliphatic groups may be present as side chains or as part of the polymer backbone and are susceptible to thermal degradation at relatively low temperatures. The second mass loss onset at 350°C, also contributing to about 7% of the total mass loss, may correspond to the degradation of additional aliphatic groups or other labile components. This further decomposition process could involve the breaking of weaker bonds within the polymer structure, leading to the release of volatile components and subsequent weight loss. The major weight loss, with an onset at 383.8°C and constituting 67.41% of the total mass loss, likely reflects the decomposition of polyamide (PA11) and the aromatic portion of lignin. Polyamide decomposition typically occurs at elevated temperatures, where the polymer chains break down into smaller molecular fragments. Similarly, the aromatic components of lignin are thermally stable but can undergo degradation at elevated temperatures, leading to the release of volatile by-products and carbonaceous residues. This significant loss reflects the decomposition of the polymer matrix, where the breaking of one bond may lead to the collapse of the entire structure.

In the TGA of the untreated fiber, the observed weight loss profiles can be attributed to various chemical processes occurring within the precursor material. The single mass loss peak observed with an onset at a higher temperature (417.8°C), accounting for an 81.55% mass loss, indicates significant thermal stability imparted by the cross-linking reaction. The cross-linking process involves the formation of covalent bonds between functional groups of lignin and PA11, resulting in the creation of branching points within the polymer matrix. The enhancement of cross-links improved the mechanical properties of the fiber by increasing its structural integrity and resistance to thermal degradation.

Furthermore, the absence of weight loss at 210°C indicates the successful removal of adsorbed phthalic anhydride, confirming the completion of the cross-linking reaction. This thorough washing ensures that any residual chemical species are effectively removed, leaving behind a stable cross-linked structure.

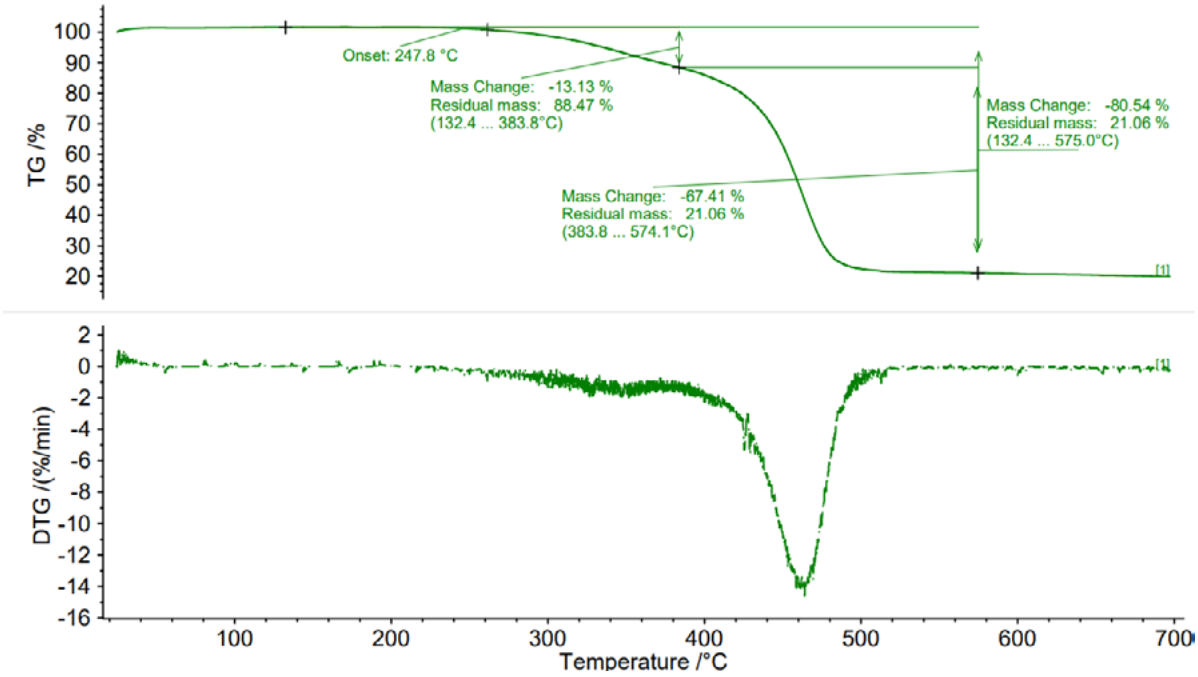

Figure 3. TGA/DTG pristine fiber.

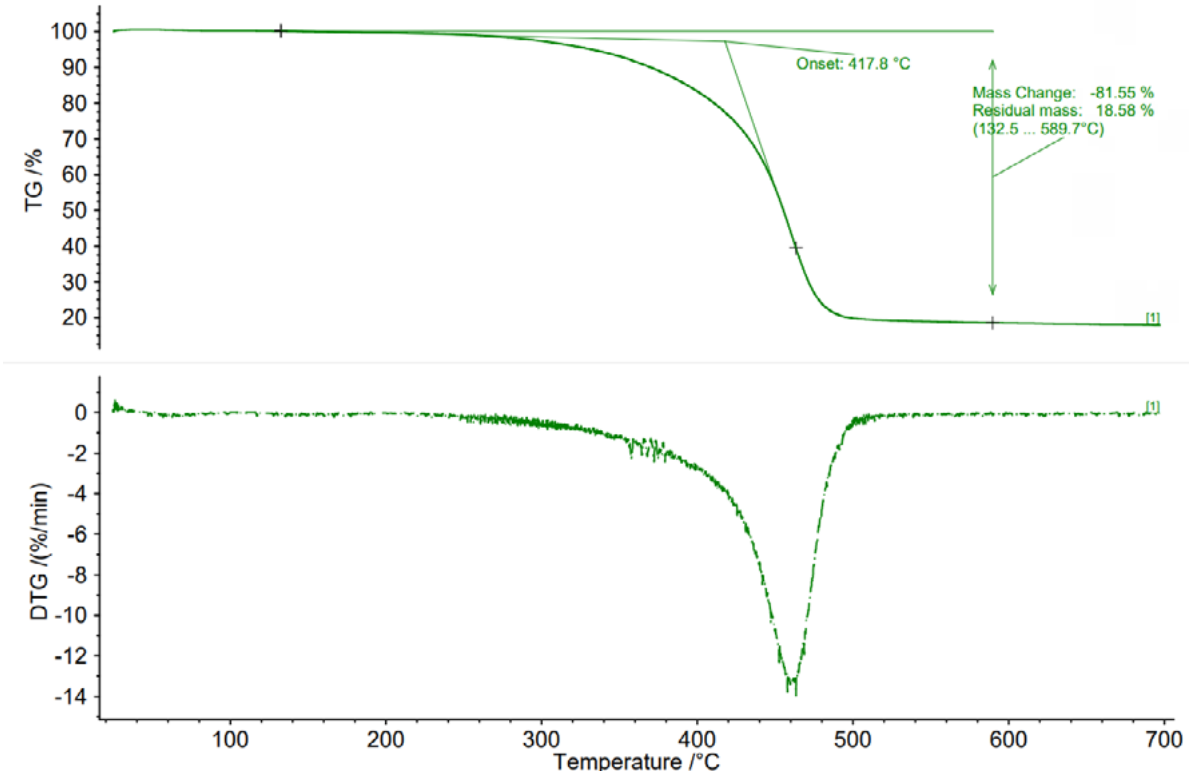

Figure 4. TGA/DTG fiber treated with phthalic anhydrate.

In the differential scanning calorimetry (DSC) analysis, the chemical and thermal treatments on the fibers were evaluated to understand their effect on thermal stabilization. In the untreated fiber, a low

glass transition temperature (Tg) around 37°C and a double melting peak were observed. The presence of two endothermic peaks is commonly reported for polyamide materials such as PA11 [11] and PA12 [12]. The onset of the first peak at 180°C and the second at 188°C corresponds to the melting of different crystalline phases of PA11. The smaller, less intense peak is attributed to the melting of less stable crystals formed during cold crystallization or the transformation of α-PA11 to γ-PA11, while the more intense peak corresponds to the melting of crystals in the γ phase.

In the DSC curve of the chemically and thermally treated fiber, the Tg disappeared, indicating a successful chemical pre-treatment. This phenomenon can be attributed to the successful cross-linking induced by the chemical treatment, which creates branching points within the polymer matrix. These branching points, formed through the breaking of PA11 chains and the creation of bridges between fibers, enhance mechanical properties while maintaining elasticity. Although endothermic peaks are still present in the chemically and thermally treated fiber, notably the first peak is almost disappeared. This suggests progress in stabilization, as the disappearance of these endothermic peaks indicates complete thermal stabilization.

4. Conclusions

Despite facing significant challenges inherent to the precursor material, including non-uniform diameters, a small number of filaments of about 24, and complexities in processing, the study has demonstrated the effectiveness of the chemical treatment with phthalic anhydride. It is noteworthy that while phthalic anhydride is typically employed for cross-linking lignin prior to fiber extrusion, its application directly to the fiber precursor in our study yielded successful results. This was evident through comprehensive analyses including FTIR and TGA, which confirmed the desired chemical modifications and thermal stability achieved. However, the presence of residual endothermic peaks in the DSC suggests that complete stabilization has not yet been achieved, indicating the need for extended thermal treatment durations to allow for further structural modifications. Overall, the preliminary results are promising, but further optimization of thermal treatment times may be necessary to achieve complete stabilization.

Acknowledgments

This work has been funded by the European Union's Horizon Europe research and innovation program "SUSPENS" under Grant Agreement No. 101091906

References

1. Yao, M., et al., *Recent advances in lignin-based carbon materials and their applications: A review.* International Journal of Biological Macromolecules, 2022.
2. Soulis, S., et al., *Strategies towards Novel Carbon Fiber Precursors: The Research Results on the Synthesis of PAN Copolymers via AGET ATRP and on Lignin as a Precursor.* NanoWorld Journal, 2015. **1**(2).
3. Poursorkhabi, V., et al., *Processing, carbonization, and characterization of lignin based electrospun carbon fibers: a review.* Frontiers in Energy Research, 2020. **8**: p. 208.
4. Fang, W., et al., *Manufacture and application of lignin-based carbon fibers (LCFs) and lignin-based carbon nanofibers (LCNFs).* Green Chemistry, 2017. **19**(8): p. 1794-1827.
5. Braun, J., K. Holtman, and J. Kadla, *Lignin-based carbon fibers: Oxidative thermostabilization of kraft lignin.* Carbon, 2005. **43**(2): p. 385-394.

6. Chatterjee, S., et al., *Conversion of lignin precursors to carbon fibers with nanoscale graphitic domains.* ACS Sustainable Chemistry & Engineering, 2014. **2**(8): p. 2002-2010.
7. Chatterjee, S., et al., *Synthesis and characterization of lignin-based carbon materials with tunable microstructure.* Rsc Advances, 2014. **4**(9): p. 4743-4753.
8. Muthuraj, R., et al., *Effect of compatibilizers on lignin/bio-polyamide blend carbon precursor filament properties and their potential for thermostabilisation and carbonisation.* Polymer Testing, 2021. **95**: p. 107133.
9. Shirolkar, N., et al., *Continuous small diameter carbon fibers.* Carbon, 2023. **201**: p. 1193-1199.
10. Bengtsson, A., et al., *Carbon fibers from lignin-cellulose precursors: effect of stabilization conditions.* ACS Sustainable Chemistry & Engineering, 2019. **7**(9): p. 8440-8448.
11. Androsch, R., K. Jariyavidyanont, and C. Schick, *Enthalpy relaxation of polyamide 11 of different morphology far below the glass transition temperature.* Entropy, 2019. **21**(10): p. 984.
12. Lupone, F., et al., *Selective Laser Sintering versus Multi Jet Fusion: A Comprehensive Comparison Study Based on the Properties of Glass Beads-Reinforced Polyamide 12.* Advanced Engineering Materials, 2024. **26**(3): p. 2301345.

FINITE ELEMENT ANALYSIS OF MICRO PEEL TEST FOR EVALUATING PULP FIBRE INTERFACIAL ADHESION

Junaid Zubair[1], Royson Dsouza[2], Farzin Javanshour[3], Jarno Jokinen[1], Pasi Kallio[4], Essi Sarlin[1], Mikko Kanerva[1]

[1]Materials Science and Environmental Engineering, Tampere University, 33014 Tampere, Finland
[2]VTT Technical Research Centre of Finland, Espoo, Uusimaa, Finland
[3]VTT Technical Research Centre of Finland, Visiokatu 4, FI-33720, Tampere, P.O. Box 1300, Finland
[4]Faculty of Medicine and Health Technology, Tampere University, 33014 Tampere, Finland

E–Mail: mikko.kanerva@tuni.fi and junaid.zubair@tuni.fi.

Keywords: Advanced composite, Micromechanical testing, Interfacial Adhesion, Micro peel test, Pulp-PLA composites, FEA

Abstract

The study uses finite element analysis of micro peel tests to examine the interfacial adhesion between pulp fibres and polylactic acid matrix. Two pulling angles, also known as the load angles of 45° and 90° are used and the embedding angles of the fibre from 0° to 10° are studied to understand their impacts on interfacial stress states. The reason to have the different embedding angles is the fact that the fibre can partly sink into the matrix droplet in reality. For pulp fibres, the embedding angle can vary due to waviness and the challenging sample preparation. The results indicate that, in comparison to a 90° load angle, a 45° load angle produces a more even distribution of stress across various embedding angles. This result emphasizes how important it is to know the load angle carefully when assessing interfacial adhesion. The work provides important understandings into optimizing micro peel tests for assessing fibre-matrix interfacial adhesion.

1. Introduction

Interfacial adhesion between reinforcing fibres and matrix in composite materials is challenging to determine due to the small dimensions, especially the diameter, of single fibres. There are extensive reviews [1] of possible micromechanical tests. One of the methods is the micro peel test [2,3]. The peel test is challenging for short and relatively weak fibres, such as natural fibres. However, in the peel test, it could be possible to control the fracture mode mixity during the testing by changing the fibre pulling angle by a sophisticated micro test device.

Understanding the basic interactions between fibres and matrix in composite materials is important, but estimating and identifying the adhesion between fibre and matrix is a complicated process. Hence using different micromechanical testing, it is possible to study the adhesion between the fibre and matrix. The mechanical characteristics and performance of the composite, such as strength, and durability, are directly influenced by the strength of the fibre-matrix interaction. Efficient distribution of stress from the matrix to the reinforcing fiber is ensured by a strong fibre-matrix interface, which improves the composite material's overall structural integrity and load-bearing capability.

This work focuses on finite element analysis (FEA) for the micro peel test to study the effects of fibre embedding angle from 0° till 10° and fibre pulling angles which is also the load angle of 45° and 90° on the interface stress state. The materials considered in this FEA are pulp fibre and the matrix substrate which is a polylactic acid (PLA).

2. Micro peel test

The micro peel test involves the separation of a bonded interface, typically with one fibre being peeled away from the matrix at the certain pulling angle. Figure 1 below illustrates the setup and procedure of a typical micro peel test. Initially, a fibre is set on the surface of droplet, and the system is allowed to solidify. Subsequently, a pulling force is applied on the fibre, which simulates the peeling of the fibre from the matrix. During this peeling process, the force required to create fracture and the displacement of the fibre being pulled are carefully measured. By analyzing the force and displacement curve, the interfacial fracture energy can basically be determined. This provides valuable information about the strength of the bond between the fibre and matrix, which is crucial for understanding the mechanical properties and performance of composite materials.

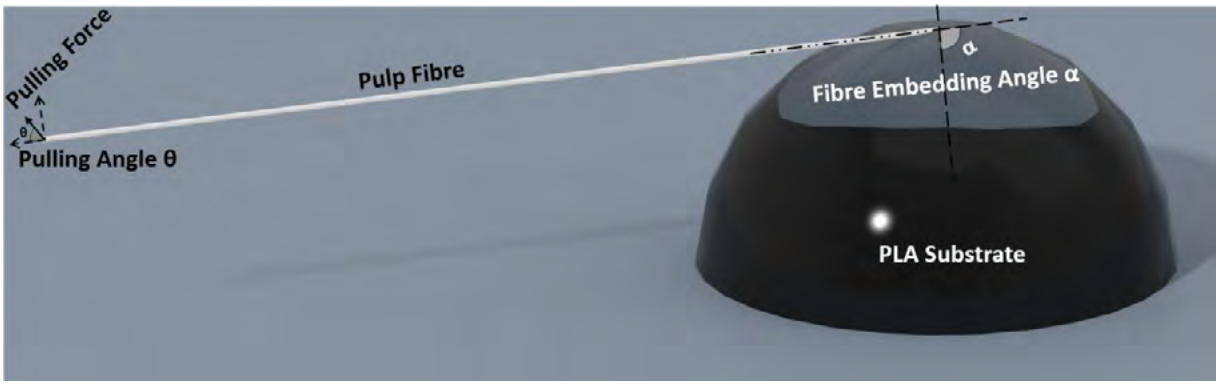

Figure 1: Schematic design of a micro peel test.

3. Finite element analysis

Representing the groove that forms when setting fibre on resin surface, and fibre shape appropriately is a major task in FE modeling of micro peel tests. This is because the groove is irregular creating a variety of angles, making it difficult to examine. Hence to tackle this, finite element models are made as shown in Figure 2. The fibre is embedded in the matrix with the first model configuration with $\alpha = 0°$ angle, in which the fibre is above the cubic-estimated matrix, and the final model configuration with $\alpha = 10°$ angle. The micro peel test in this work is modeled and simulated using Abaqus/Standard 2023 learning edition (Dassault Systemes). This indicates that a structural model supports a maximum of 1000 nodes. Firstly, the entire model is a three-dimensional assembly which includes the fibre and the matrix. Secondly, it is anticipated that the fibre is a linear elastic model, the matrix (cube) is an elastic model for $\alpha = 1°$ to $\alpha = 9°$ models, and elastic-plastic for $\alpha = 0°$ and $\alpha = 10°$ model. Thirdly, the angle representations for the embedding angle and the pulling angle are Greek letter alpha (α) and theta (θ). And finally, the fibre matrix interfacial adhesion is a tie constraint in the models having the embedding angles from $\alpha = 1°$ to $\alpha = 9°$. Additionally, the model with the embedding angle $\alpha = 0°$ which is the reference model and $\alpha = 10°$ are studied with cohesive zone model (CZM).

The fibre is designed as a simple circular cylinder with a diameter of 20 μm [4], making it easier to model analytically and computationally for finite element analysis (FEA) while minimizing issues at the edges. The matrix cube is given a dimension of 400 μm each side. The approximate seed size in the slot during meshing is kept 50 μm with element type of 8-node linear brick. Details of the mechanical properties and mesh are provided in Table 1 below.

Table 1: Properties of the FE modelling

Components	Young's Modulus (GPa)	Poisson's ratio	Plastic Strain (MPa)
Pulp Fibre	50 [5]	0.169 [6]	-
PLA Matrix	3.145 [7]	0.33 [7]	60 [8]

3.1 Assembly and interaction of the fibre and matrix

The target is to achieve the stress profile for all these angles using two different loading angles θ, that are 45° and 90° which will be further explained in the boundary condition section. Figure 2 below shows the assembly.

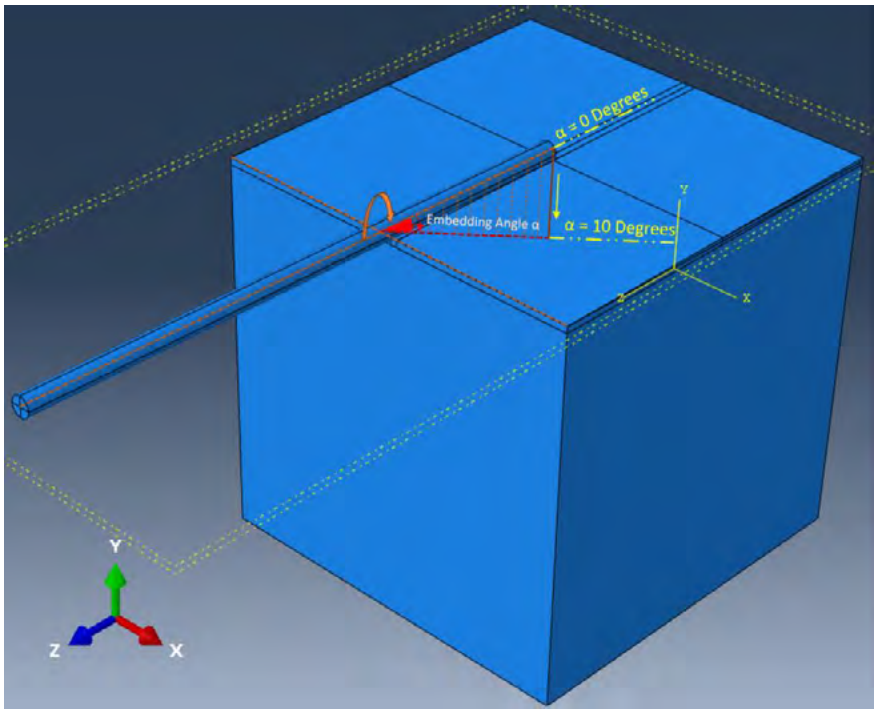

Figure 2: The assembly of the model with a fibre and cube of PLA matrix**.**

Figure 2 represents how the embedding angle will rotate the fibre towards the cubic matrix starting from 0° and ending with the last model having the embedding angle of 10°. This means that excluding the reference model, ten model configurations are made for each embedding angle and each model is then tested with both pulling angles. It is crucial that fibre-matrix interaction is modeled accurately as that is the area in which we are interested. Figure 3 below shows the interaction surfaces of the reference model and the model having the embedding angle of 10°.

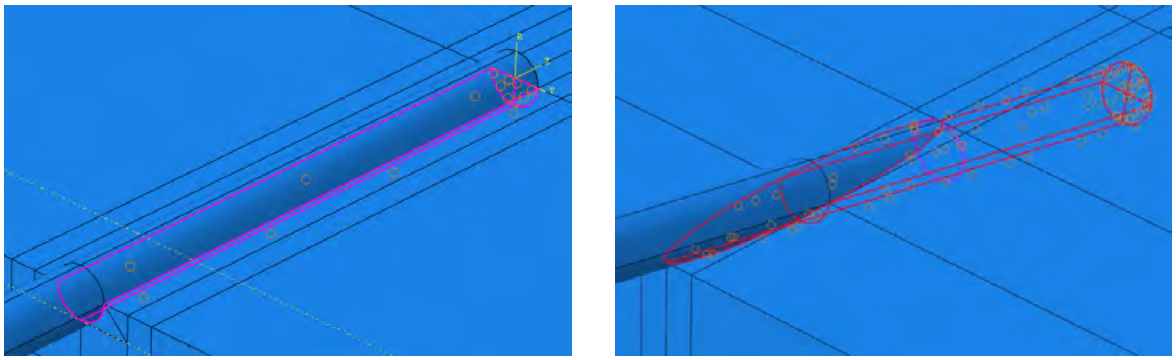

(a) (b)

Figure 3: Interaction surfaces (a) Reference model (α = 0°) and (b) Model with α = 10°**.**

The interaction between the fibre and matrix interface is modeled using the tie constraint except the reference and the model with α = 10°, which is modeled using the (CZM). By imposing tie constraint, it makes sure that there is no relative slip or separation between the fibre and matrix at their interface.

CZM is implemented and compared to the models with different embedding angles. CZM uses a traction separation law which refers to the relationship of cohesive stiffness (K), contact separation (δ) and overall traction. This relationship is better explained in Figure 4.

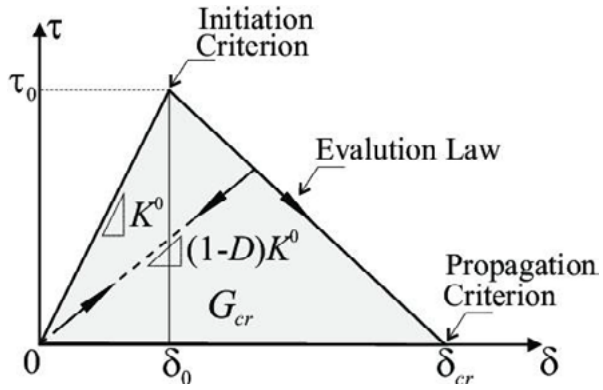

Figure 4: Typical bi-linear traction separation law [9].

The interface model with cohesive zone model (CZM) properties are stated in table below. The criterion used for the damage initiation is quadratic stress criterion and for damage evolution, power law is used for fracture criterion having linear type exponent of 1 for all the fracture modes.

Table 2: Cohesive zone properties

Cohesive stiffness	$10^{13}\ \frac{N}{m^3}$	[8]
Critical traction (all modes)	10 MPa	[10]
Fracture toughness (all modes)	$85\ \frac{J}{m^2}$	[10]

3.2 Boundary conditions

Boundary conditions play a critical role in FEA as they define the external constraints applied to the model. In micro peel testing, boundary conditions dictate how the fibre, and the matrix are loaded and constrained during the peeling process. The boundary conditions include fixed displacements and loads applied to specific regions of the fibre, which represents the clamping or gripping mechanisms used in experimental setups. The load applied in our case is achieved by giving displacement to the fibre tip. The direction at which the displacement is given defines the pulling angle, which is of 45°, and 90° respectively. This angle is made with the vertical axis meaning that θ = 90° is vertically parallel to the y-axis. Figure 5 represents the applied boundary condition. The model represented here is at the embedding angle 10° and the applied boundary condition is for 45° pulling angle. The bottom of the cube is fixed whereas the displacement is applied to the tip of the fibre.

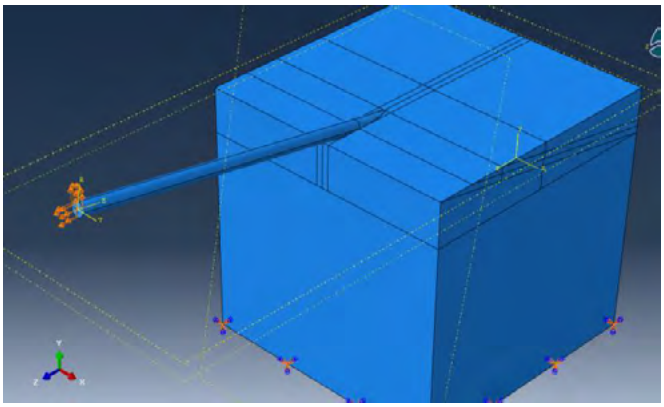

Figure 5: Boundary conditions.

4. Results and Discussion

The number and size of elements are carefully adjusted to remain as consistent as possible across the various geometries, ensuring comparable results for each configuration. Each geometry is subdivided into five sections, depicted in Figure 6, facilitating a structured analysis and comparison.

4.1 Interfacial stress behavior across the sections

Figure 6 represents stress contours with red color indicating the maximum stress locations and blue is indicating the minimum stress locations. The nodal points which are used to calculate the average von Mises stresses per section can also be seen in Figure 6, which are indicated by red dots.

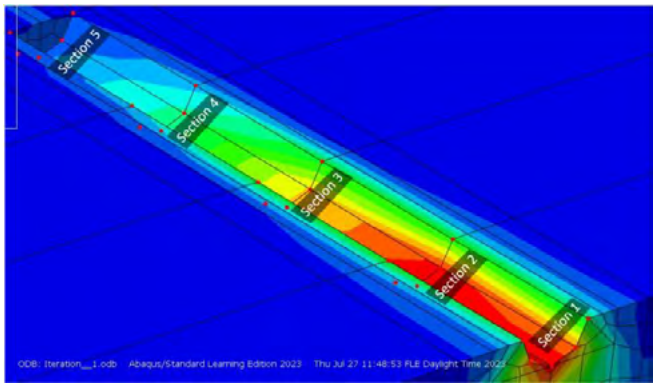

(a)

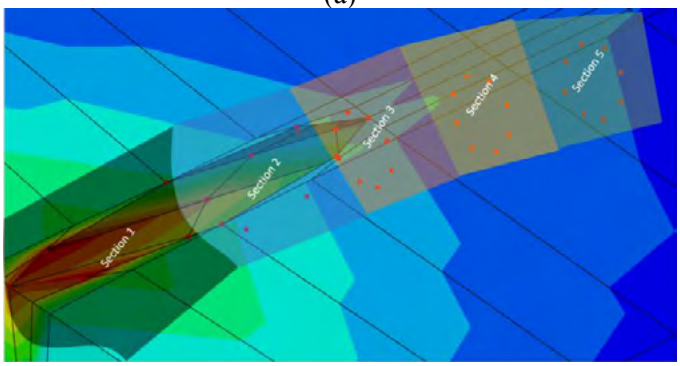

(b)

Figure 6: Sections (a) Reference model with α = 0° and (b) Model with α = 10°.

Average von Mises stresses are calculated using the FEA for all the sections to see how the stress at the groove varies when the fibre is peeled at a certain angle. Variation of the stresses along the sections for the embedding angle $\alpha = 10°$ is compared to the reference model in Figure 7 below at the pulling angles $\theta = 45°$.

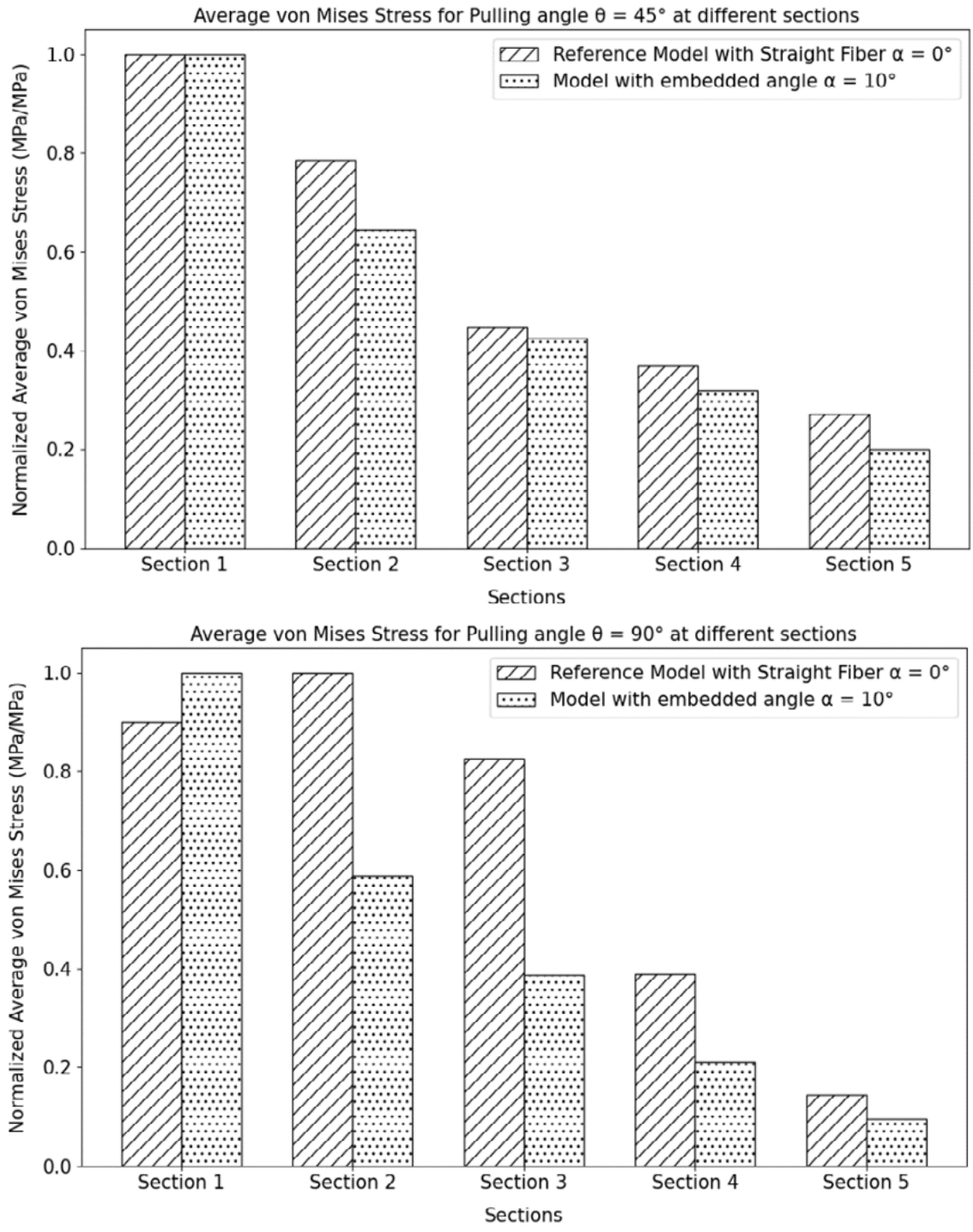

Figure 7: Average von Mises stress comparison at each section interface for $\theta = 45°$ & $\theta = 90°$

Figure 7 illustrates the normalized data represented along the y-axis, with sections progressing along the x-axis. It is observed that as we move along the sections on the x-axis, the normalized values decrease.

This trend suggests a decrease in average stress across the sections. Comparatively, for puling angle of 45°, the decrease in the normalized average stress value is around 80 percent from section 1 to section 5 whereas when the pulling angle is increased to 90°, the difference between the normalized average stress is even much higher exceeding 90 percent between section 1 and section 5. This suggests that the change at which the normalized average stress decreases is more when the pulling angle is 90°. The comparison between the model with $\alpha = 0°$ (considered as the reference model) and the model with $\alpha = 10°$ for the normalized average stress suggests that, on a per-section basis, the difference in stress is more pronounced when the pulling angle θ is 90°. This observation suggests the importance of considering both α and θ angles in understanding stress distribution across the groove.

4.2 Interfacial stress behavior across the models ($\alpha = 0°$ to $\alpha = 10°$)

All the models from the embedded angle $\alpha = 0°$ to the embedded angle $\alpha = 10°$ are simulated for both the pulling angles and are compared to the reference model which is half dipped with the embedded angle of 0°. The model with fibre embedded at $\alpha = 1°$, 2° and 3° had small area embedded into the matrix cube, which could not give proper total average stress values hence these models are excluded, and the rest of the model's results are shown in Figure 8 below. The average von Mises stress values in Figure 8 are taken from the nodal values of all the sections in the groove for each model.

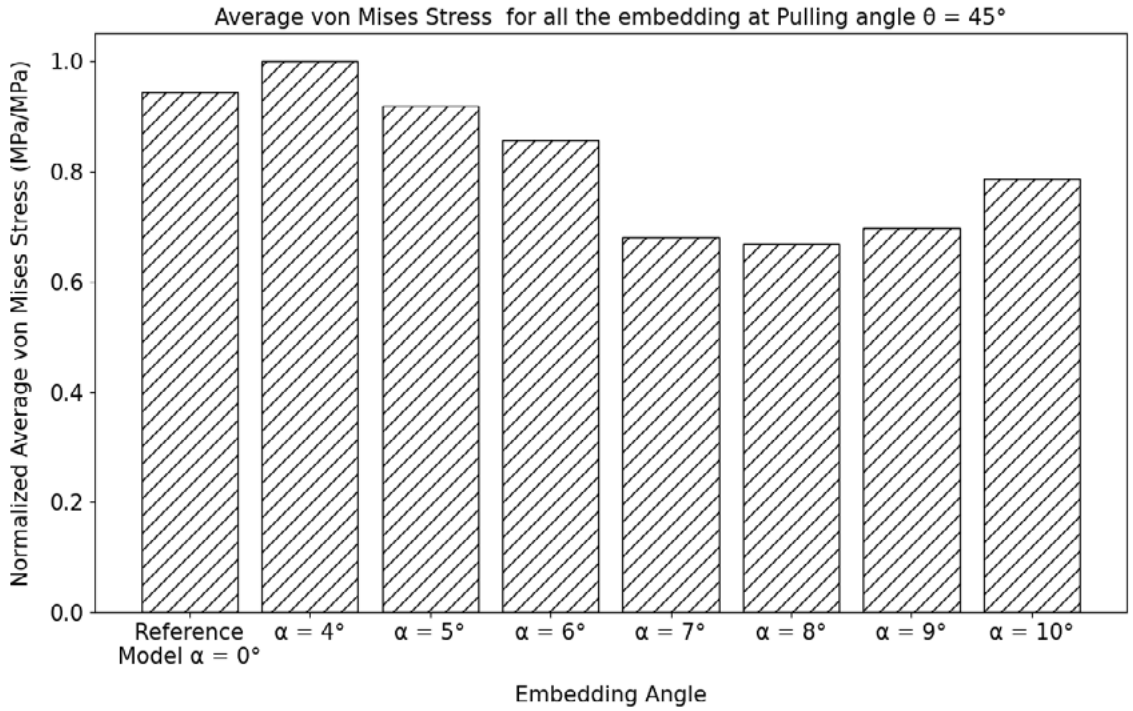

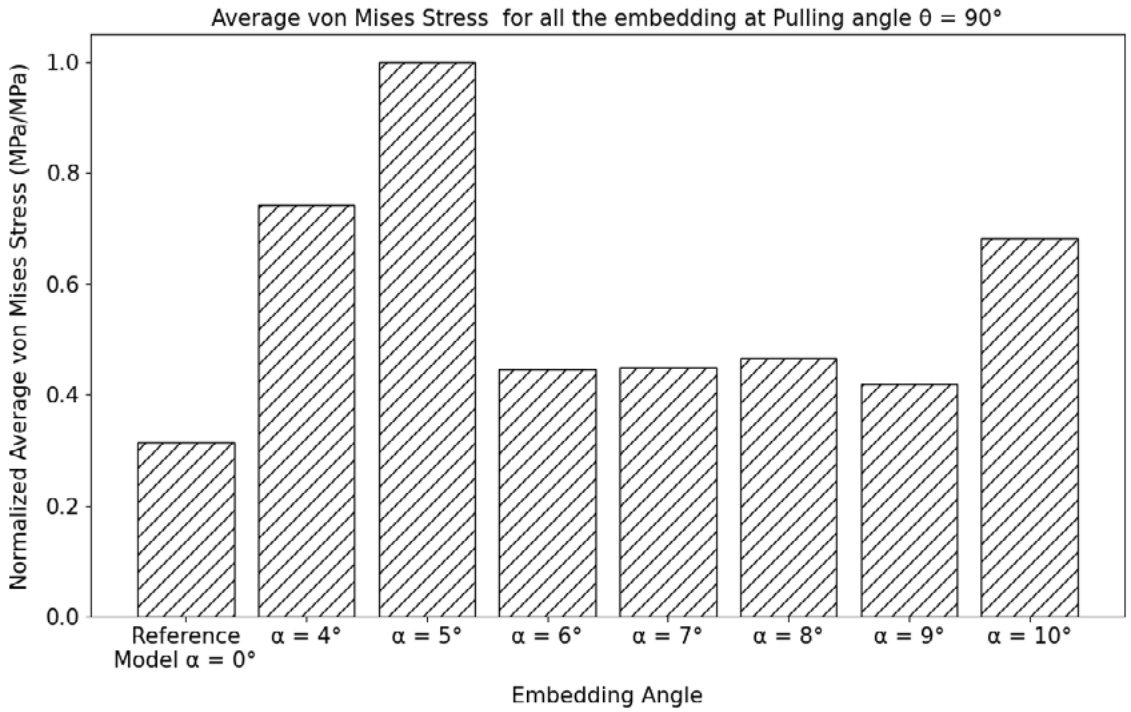

Figure 8: Average von Mises stress comparison at interface for all fibre embedded angles at θ = 45° and θ = 90° pulling angles

Interesting results can be seen in Figure 8. It clarifies how the stress levels are affected by the fibre embedded angles for simulated load angle values. What is particularly interesting is how the fibre's exit from the matrix, often referred to as the "meniscus" effects the results. The meniscus is the curvature of the groove, which is caused by the fiber embedding on the matrix. From Figure 8, the fibre embedded angle increases, there is no monotonic trend in total average stress. Figure 8 shows the significance of the fibre pulling angle as when the pulling angle is of 45°, it yield more uniform stress distribution (with a variance of approximately -18% to +22% from the overall average) across the models with varying the embedding angles (ranging from α = 0° to α = 10°), as opposed to using a 90° pulling angle, which exhibits a wider range of stress differences (from -21% to +77%).

4.3 Load and displacement curves using CZM

Two graphs were plotted to compare force and displacement curves for models with different embedding angles (α = 0° and α = 10°) and for the pulling angle (θ) of 90°. These graphs examine the differences between the two interactions, that are tie constraint and CZM. In Figure 9, arrows indicate where the cohesive bond starts to fail on the force and displacement curve of the cohesive interaction.

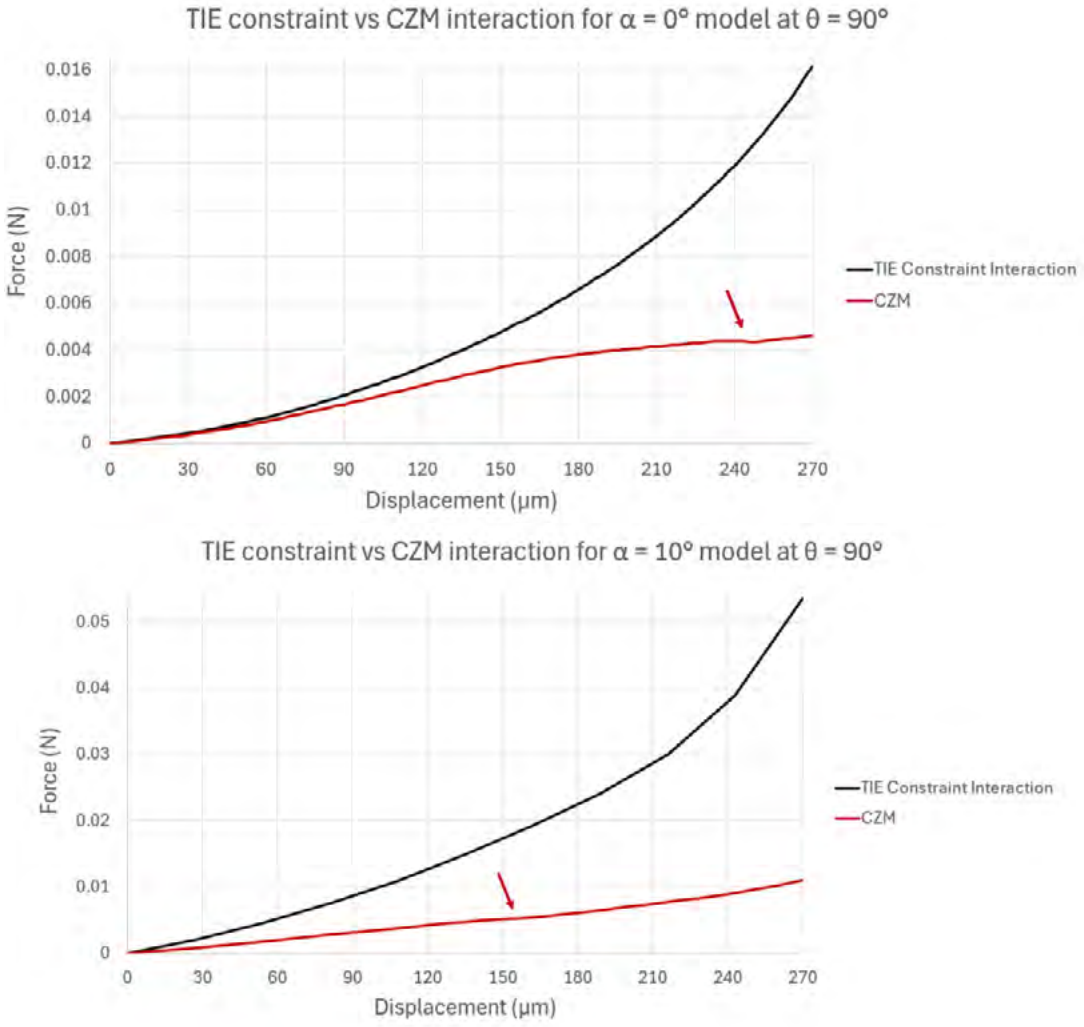

Figure 9: Force and displacement curve for tie interactions and CZM.

Figure 9 shows how much difference can be generated when the surface interactions change. The tie constraint keeps increasing the force exponentially as the displacement increases whereas CZM curve changes its slope as the displacement starts to increase. The crack onset on CZM graph occurs at the point indicated by an arrow. At this point, a noticeable change can be observed in curve slope, and after that, the next section starts to resist the peel hence the force increases again.

5. Conclusions

The study describes the key factors affecting interfacial adhesion in pulp fibre-PLA composite materials. It clarifies the implications of changing the embedding and load angles on interfacial stress states using FEA of micro peel tests. According to this research, the average stress decreases along the groove in the matrix but as the pulling angle increases, the variation between the stress at the initial of the groove to the end of the groove increases indicating mores stress at the initial sections. This finding suggests how crucial it is to choose the load angle carefully when using the micro peel test. Further research in this direction holds promise for advancing our understanding about the cohesive interactions between the fibre and the matrix.

Acknowledgments

This research was made in the ABCmodels project (https://www.tuni.fi/en/research/abcmodels) funded by Research Council of Finland. The authors gratefully acknowledge the help by Fibrobotics (Tampere, Finland), especially researchers M. Kakkonen and O. Tanhuanpää. Also, researchers from VTT (Finland) and KTH (Stockholm, Sweden) acknowledged for the support towards the research.

References

[1] S. AhmadvashAghbash, I. Verpoest, Y. Swolfs and M. Mehdikhani. Methods and models for fibre–matrix interface characterisation in fibre-reinforced polymers: a review. *International materials reviews*, 68(8): 1245–1319, 2023.
[2] M. A. Alimuddin and M. R. Piggolt. Fracture toughness of fiber-polymer interfaces estimated from single fiber peel test. *Polymer composites*, 20: 655–663, 1999.
[3] D.J.H Cederlof and B. F. Sorensen. Characterisation of fibre/matrix interfacial fracture energy using the single fibre peel experiment. *IOP Conference series: Materials Science and Engineering*, 942: 1–10, 2020.
[4] H. M. Brodowsky and A. Hennig. Micromechanical tests on natural fibre composites with enzymatically enhanced fibre–matrix adhesion. *Material circular economy*, 4: 1–11, 2022.
[5] R. C. Neagu, E. K. Gamstedt, and F. Berthold. Stiffness contribution of various wood fibers to composite materials. *Composite material*, 40: 663–699, 2006.
[6] G. Hua, M. Yang, W. Fei, and F. Lu. Poisson's ratios of molded pulp materials by digital image correlation method and uniaxial tensile test. *Journal of Engineered Fibers and Fabrics*, 15: 1–10, 2020.
[7] V. S. Vakharia, L. Kuentz, A. Salem, M. C. Halbig, J. A. Salem, and M. Singh. Additive manufacturing and characterization of metal particulate reinforced polylactic acid (PLA) polymer composites. *Polymers*, 13: 1–15, 2021.
[8] R. Dsouza, J. Jokinen, E. Sarlin, P. Antunes, and M. Kanerva. Future microbond testing – finite element simulation of optical fibers for strains. *ICCM22*, v1, 1–12, 2019.
[9] V. N. Burlayenko and S. Tomasz. FE modeling of delamination growth in interlaminar fracture specimens. *Budownictwo i Architektura*, 2: 95–109, 2008.
[10] R. Dsouza, P. Antunes, M. Kakkonen, J. Jokinen, E. Sarlin, P. Kallio and M. Kanerva. 3D interfacial debonding during microbond testing: Advantages of local strain recording. *Composites Science and Technology*, 195: 1–9, 2020.

Improved curing and reduced moisture sensitivity of structural composites based on active cellulose nanofibril fibres and epoxy resin

Sabrina Assenheimer[1a], Karl Håkansson[2], Mats Johansson[3] and Malin Åkermo[1b]

[1]Department of Engineering Mechanics, KTH Royal Institute of Technology, Stockholm, Sweden
[a]Email: sabass@kth.se
[b]Email: akermo@kth.se
[2]CelluXtreme AB, Stockholm, Sweden
Email: karl@celluxtreme.com, Web Page: https://www.celluxtreme.com/
[3]Department of Fibre and Polymer Technology; KTH Royal Institute of Technology, Stockholm, Sweden, Email: matskg@kth.se

Keywords: cellulose nanofibrils (CNF), CNF fibre, biocomposite, cure behaviour, interface

Abstract

Previous research could show CNF as nanofillers reinforced in epoxy influence the curing of epoxy and increase strength and stiffness. In this study, a new type of man-made bio-based cellulose nanofibril (CNF) fibres are utilised as reinforcement. The aim of this study was to investigate if the fibres with a significantly lower surface area compared to pure CNFs influence the curing. Therefore, composites altering in the fibre pretreatment, fibre diameter and fibre weight fraction were produced. Results from calorimetry and infrared spectroscopy also show a change in the cure behaviour of the CNF fibres. The experimental data indicates that the pretreatment of the CFNs with TEMPO oxidation, a smaller fibre diameter and a higher fibre weight fraction in particular lead to a greater shift in the endothermic cure peak temperature. The binding effects of the fibre surface hydroxyl- and carboxyl groups with epoxides are discussed.

1 Introduction

Natural fibres (NF) have received more and more attention in recent years within the context of the production of low-emission structural parts. The advantages of these fibres are their low density, comparable specific mechanical properties to glass fibres, low costs, as well as good recyclability and biodegradability [1, 2]. However, natural fibres also present challenges due to their variable properties, relatively large diameter, which vary along the fibre, and finite length [3]. In addition, the hydrophilic surface of those fibres contains many hydroxyl groups (OH). This can lead to poor adhesion between the fibres and conventional, mostly hydrophobic, matrix systems [3]. The surface hydroxyl groups also attract and absorb water.

Multiple studies have shown that Cellulose nanocellulose fibrils (CNFs) own unique properties, such as stiffness in the range of 78 GPa to 143 GPa, a strength up to 3000 GPa and a low density of $1.5\ \mathrm{g/cm^3}$ [4, 5]. CNFs have a diameter ranging from 4 nm to 20 nm in diameter and a length of $0.5 - 2\mu$m [6–8]. Recent developments in the field of extracting CNFs out of plant fibres and the associated cost reduction and availability [9] have led to a growing number of publications focusing on reinforced CNFs in thermosets, particularly as nanofillers [10–13]. Previous research has shown that 15 vol% of enzymatic pretreated CNFs in the form of a porous network lower the activation energy and increase the curing rate of epoxy resin [10]. It is assumed that the OH groups of the CNFs support the ring opening of the oxirane ring of the functional group of the epoxy resin. As a result, the CNFs crosslink with the matrix and a chemical interface can be formed. This leads to excellent adhesion, resulting in improved strength compared to pure epoxy.

However, so far, only porous networks or films have been infiltrated with epoxy resin or the CNFs have been added to before curing, but not in fibre form as reinforcement. A novel type of man-made bio-

based fibre has been developed, based on CNFs extracted from wood. The CNFs are stored in dispersion and spun to a continuous gel thread using a microfluidic flow-focusing technique [5]. This technique allows for precise control of the internal structure of the nanocellulose dispersion. The gel thread is subsequently dried into a continuous small and controllable diameter CNF fibre with specific properties, comparable to those of conventional advanced fibre systems [5]. Furthermore, the spinning technique enables the adjustment of properties such as strength, stiffness and fibre diameter [14]. However, the spinning process also reduces the surface area compared to pure CNFs and, at the same time, reduces the number of hydroxide groups on the surface, contributing to strong bonding with the epoxy resin.

This study set out to investigate the impact of CNF fibres by altering their pretreatment, fibre diameter and fibre weight fraction on the curing behaviour of epoxy. The question to be answered is whether observations on previous CNF composites can be transferred to composites with a high volume fraction of CNF fibres, which offers significant improved structural properties. A prepreg material based on epoxy reinforced with CNF fibre was produced. The curing of the pure epoxy and the fibre-reinforced epoxy was analysed through dynamic Differential Scanning Calorimetry (DSC). Furthermore, the functional groups of the cured laminates were analysed using Fourier Transform Infrared Spectroscopy (FTIR).

2 Materials and methods

2.1 Cellulose nanofibril (CNF) fibres

The CNFs were produced from a dissolving pulp made from wood. The pulp was chemically treated with either a 2,2,6,6-tetramethylpiperidinyl-1-oxyl (TEMPO) oxidation reaction or carboxymethylation (CM) before a mechanical treatment was used to delaminate the pulp fibres into CNFs. The TEMPO pretreatment results in the replacement of the primary hydroxyl groups of the repeated β-1,4-linked anhydroglucose unit with a carboxyl group [7], thereby charging the surface with 1000 µekv/g. The CM pretreatment, in contrast, introduces an additional ether bond between the glucose units and the carboxyl group, which raises, in this case, the surface charge to 600 µekv/g. The CNFs are oriented using a double-flow focusing technique, followed by alignment in a dispersion gel [15]. For this paper, two TEMPO-CNF fibre patches with fibre diameters of 21 μm and 25 μm and one CM-CNF batch with a fibre diameter of 21 μm were provided by the company CelluXtreme [16].

2.2 Cotton and Flax fibre

For comparative purposes, a commercially available cotton fabric in the form of a woven fabric and a flax fabric ampliTex 5057 from Bcomp [17] were employed.

2.3 Polymer Matrix System

In this study, the epoxy film AX 201-XL from Axiom [18] with an area weight of 25 g/m^2 was utilised. One advantage of this epoxy film is that it exhibits a low curing temperature of 120°C. Epoxy resin systems for structural components are often cured at 180 °C. It is important to note that the application of high temperatures can result in alterations in the properties of the natural fibres. The major components of the epoxy film are epoxy phenol novolac resin, 2,2-Bis[4-(glycidyloxy)phenyl]-propane (DGEBA) and DGEBA-oligomers. Based on the datasheet, cationic polymerisation is assumed at this point. An inhibitor is triggered by heat and releases protons, which, as illustrated in Figure 1, lead to the protonation of the O-atom of the oxirane ring. This initiates chain growth by adding further monomers (option I) through a nucleophilic attack of the next chain element until the polymerisation is stopped as soon as all the reactants have been consumed. Hydroxyl groups (option II) or carboxyl groups (option III), which are present on the surface of the CNF fibres, can also contribute to the chain growth and, in this way, bind the fibres covalently to the matrix.

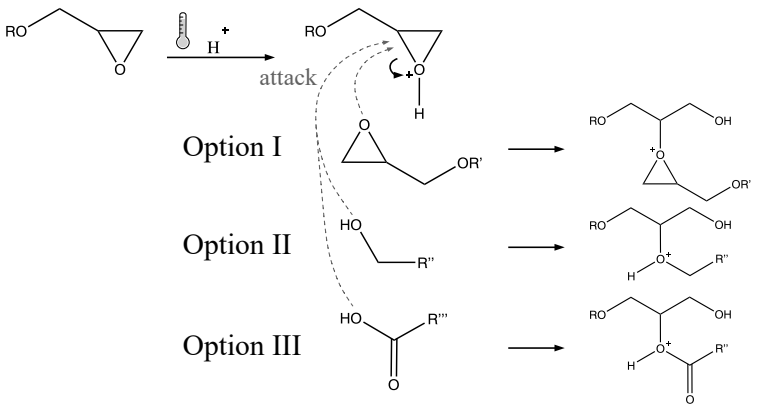

Figure 1: Cationic Polymerisation: Step 1 - an epoxide is protonated due to heat; Step 2 - The positively charged oxirane ring is attacked by another epoxide (option I), a hydroxide group (option II) or a hydroxide group of a carboxyl group (option III), the opening of the ring occurs with the formation of an OH group and a transfer of the charge to the attacking O atom; Step 3 - Chain growth until the reaction is stopped due to lack of residual reaction partners

2.4 Preparation of prepregs and curing

A series of different prepregs was manufactured manually for this study. The CNF fibres are aligned in a unidirectional (UD) direction and held in place by tapes at their ends. The fibres were accurately placed between two epoxy tapes. In the final step, the prepreg is consolidated under a vacuum at a temperature of 65 °C for 10 minutes and stored at -18 °C. Each prepreg differed in the type of used fibre (TEMPO, CM), the diameter (D21, D25) and the amount of reinforced fibres (17wt.%, 33wt,%, 50wt.% and 67 wt.%). The prepreg allows for straightforward handling of the curing process between flat, heated plates, thereby enabling relatively homogeneous fibre distribution. The flax and cotton composites were similarly produced and the 50 wt.% target was attempted. Table 1 provides an overview of all produced prepregs. To produce laminates, one-layer prepregs are stacked together to a UD-laminate with six plies. The prepregs are cured under a vacuum in a hot press (Fontune Presses, LabEcon600). A pressure of 4.5 bar is applied. The material is subjected to a temperature programme, starting at room temperature and increasing at a rate of 2 K/min until reaching 120°C, where it is held for a period of two hours.

2.5 Characterization methods

2.5.1 Differential Scanning Calorimetry (DSC)

A Mettler Toledo DSC5+ was utilized for the DSC measurements. All samples with a weight of 8 mg $\pm$ $0,2$ mg were placed in a 40 μl aluminium crucible with a perforated lid and analysed in a nitrogen atmosphere at a flow rate of 50 ml/min. The dynamic temperature programme for the pure epoxy and composite samples consisted of two parts. In the first part, the samples were ramped from -35 °C to 250 °C with 2 K$/$min to study the curing kinetics. Subsequently, the samples were rapidly cooled to room temperature and heated again at a rate of 2 K$/$min to detect the glass transition temperature T_{g}. The collected data were normalised by the sample weight.

2.5.2 Fourier transform infrared spectroscopy (FTIR)

An attenuated total reflection (ATR) Fourier transform infrared (FTIR) analysis was performed using a Perkin Elmer Spectrum 1000 with a triglycine sulfate (TGS) detector. The aim of this technique was to study the changes in the functional groups of epoxy and fibre-reinforced epoxy. The spectra were collected in absorption mode in between the range of 4000 cm^{-1} and 600 cm^{-1} with a resolution of

2 cm^{-1}. All samples were measured after curing, with the exception of the epoxy, which was also measured in an uncured state.

2.5.3 Microscopy

To study the cross-section shape distribution of fibres in the laminate, the cross-section of a six-plies laminate is analysed with a Light Microscope (Olympus BX53M, Japan). The samples are first embedded in an epoxy resin mixture (100:45, EpoThin^{TM} 2 Epoxy Resin and Hardener), trimmed (Metkon Micracut 152, Turkey) and finally polished (QATM, Qpol 300 A1 ECO+, Germany).

3 Results and discussion

3.1 Composite structure

To begin this section, a look should be taken at the cross-sectional area of the composite, presented in Figure 2. It is noticeable that the CNF fibres (a-c) have an almost homogeneous, repeatable shape and size, is also relatively homogeneously distributed and has no lumen, especially in comparison to flax (e), but also visible in cotton (d). There is no noticeable difference between the fibres based on TEMPO-CNFs and CM-CNFs. A statement about the interface between the CNF fibre and the matrix can only be made to a limited degree. The fibres are surrounded by the matrix and do not indicate any open porosity.

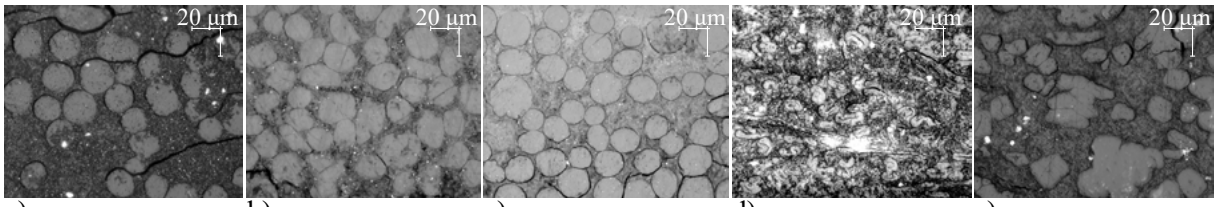

Figure 2: Cross-section with 50x magnification of a) TEMPO-CNF50.%-D21 b) TEMPO-CNF50.%-D25 c) CM-CNF50.%-D21 d) Cotton50wt.%, d) flax50wt.%

3.2 Kinetic effects of CNF fibres on cure behaviour of epoxy

The results for the curing influences study are presented in Figure 3 and shown for CNF fibre/epoxy with TEMPO and CM pretreatment, flax/epoxy and cotton/epoxy composites an endothermic peak between 40 °C and 110 °C and all material combinations an exothermic peak ranging from 90 °C to 200 °C.

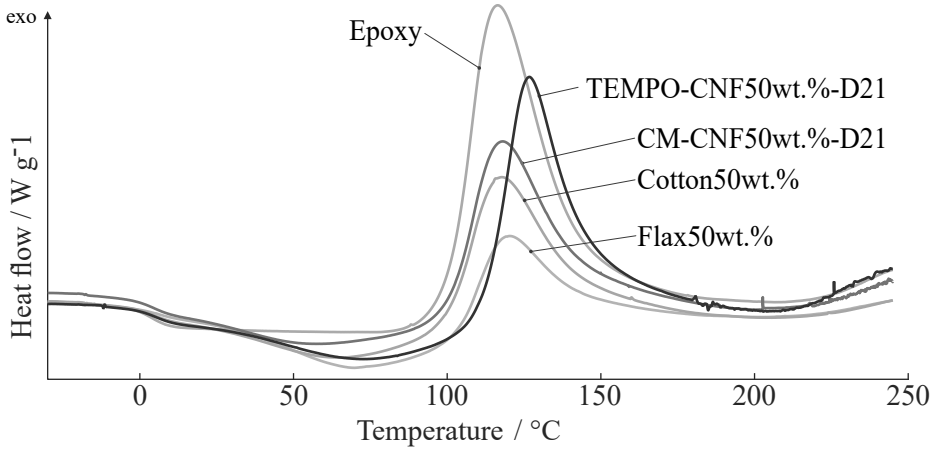

Figure 3: Cure behaviour of pure epoxy compared to CNF, flax and cotton-fibre reinforced epoxy

The endothermic peak can be attributed to absorbed moisture by the fibres, which are dissolved within the specified temperature range. What stands out in this figure is the difference in the temperatures of the onset T_{on} and peak maxima T_{max} of the exothermic peaks, both provided in Table 1. The most significant shift of about 6°C is reached with the TEMPO-CNF50wt.%-D21 configuration. However, the TEMPO samples with a larger diameter and the CM samples also show a small shift. It is also interesting to note that cotton also causes a small shift, but this is significantly smaller. The onset begins at higher temperatures compared to the pure epoxy resin.

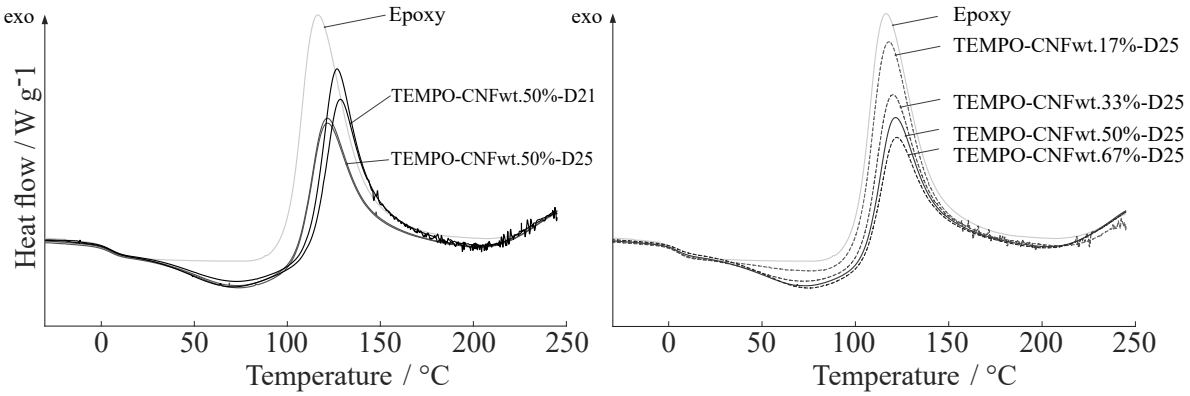

Figure 4: Cure behaviour of TEMPO-CNF fibre as a function of the fibre diameter (left) and as a function of the fibre weight fraction for TEMPO-CNF-D25 μm (right)

Another parameter that was investigated in this paper was the fibre diameter. Two TEMPO-pretreated CNF fibres with 50 wt.% FWF and two different diameters, 21 μm and 25 μm, were utilised. Looking at Figure 4 left, it is apparent that the smaller fibre diameter results in a significantly larger shift in the maximum peak to higher temperatures. The result can be explained in part by considering the active interface area. The composite with the smaller fibre diameter exhibits a larger interface area, which allows for a greater number of functional groups to react with the oxirane ring of the epoxy resin and form a three-dimensional network. In a further study, the fibre weight fraction was now varied. The results, provided in Figure 4 in the right plot, show that with an increased fibre weight fraction, a stronger shift of T_{on} and T_{max} is measured.

Table 1: Summary of the results obtained after curing.

Pretreatment	Fibre	FWF (wt.%)	D (μm)	T_{max} (°C)	T_{on} (°C)	spez. E_C (mJg^{-1})	spez. E_{EP} (mJg^{-1})	T_g (°C)
Epoxy AX201-XL				115,57	77,62	279,25	279,25	117,58
	cotton	50	10,5	120,52	81,11	63,01	31,61	113,71
	flax	50	19,7	117,76	106,60	137,91	68,96	115,83
TEMPO	CNF	50	21	126,20	105,31	176,14	88,07	112,14
TEMPO	CNF	17	25	119,01	92,52	242,23	201,05	116,10
TEMPO	CNF	33	25	120,13	100,05	174,44	147,03	115,75
TEMPO	CNF	50	25	121,62	110,51	141,09	106,11	114,90
TEMPO	CNF	67	25	122,06	106,51	117,06	77, 13	113,52
CM	CNF	50	21	118,11	96,64	174,07	87,03	117,56

3.3 Chemical analysis of the functional groups

The following section will provide more detailed information about the chemistry reactions behind the cure kinetics of epoxy. Figure 5 shows two extracts from the FTIR analyses. A brief look should first be taken at the spectrum around the wavelength of 915 cm^{-1}, attributed to the C-O deformation of the oxirane group [19]. A clear peak can be seen there for the uncured epoxy, which has disappeared after curing for the pure epoxy and all composite samples besides from TEMPO-50wt.%-D21. Interestingly, in this sample, a residual peak is left, which can be concluded that it has not undergone complete curing, although all samples were exposed to the same temperature-pressure cycle at the same time. If we turn now to the spectra in the range 1690 cm^{-1} and 1760 cm^{-1}, the interaction of the carboxyl groups of the CNF fibre with epoxy can be studied. If the peaks for the fibres and those of the fibres embedded in epoxy at 50wt.% are compared, a small shift in the peak can be detected for TEMPO-CNF50wt.%-D21 and also, but to a lesser and smaller amount, for TEMPO-CNF50wt.%-D25. No shift is detectable for the CM sample. This shift is an indicator that the carboxyl group of the fibres has reacted with the epoxy resin by forming an ester. The limited number of carboxyl groups present on the surface of the fibre, in comparison to those contained inside, results in the inability to observe a complete conversion. Consequently, only a trend is recognisable.

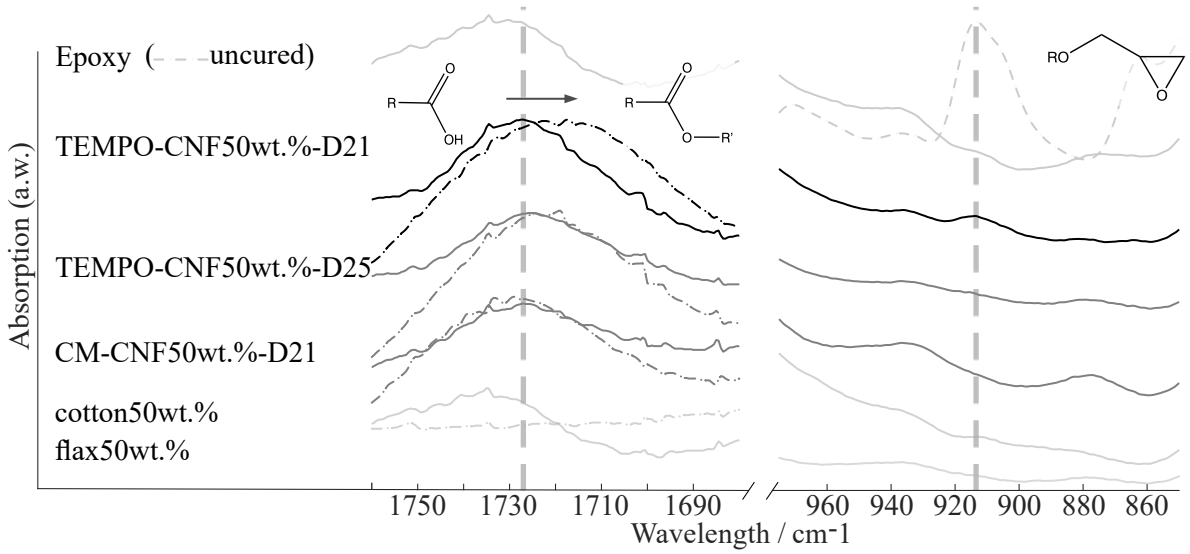

Figure 5: FTIR spectra of pure epoxy and composites in the range of 1690 cm^{-1} to 1760 cm^{-1} compared to the pure fibre (dashed lines), and around 915 cm^{-1} in comparison with uncured epoxy (dashed line)

Assuming that cationic polymerisation is present, it can be concluded from the DSC and FTIR data that the polymer epoxides can react with the OH-groups under acid conditions. It could be shown that the epoxides can directly react with carboxylic acids and hydroxyl groups of the fibres. Moreover, the fibres interact with the curing, but they do not inhibit the process. A decrease in the activation energy, as reported before, can not be confirmed. The results give the possibility for a strong indication that the fibres are covalently bonded to the epoxy resin, which can lead to good mechanical properties that should be investigated in further studies. Since the fibres take an active part in the resin curing in the future, this might enable tailoring of the epoxy resin towards less added reactants.

3.4 Glass Transition Temperature

The determination of the glass-transition temperature T_g after curing was not straightforward, so only trends can be identified from the data in Table 1. The T_g has the highest value for epoxy and is up

to 4 °C lower in the presence of the fibres. What stands out from the data is the low glass-transition temperature for TEMPO-CNF-50wt.%-D21. This material parameter is a function of the molecular structure, the degree of cure and the type of curing [20]. As already discussed above, the FTIR analysis, see Figure 5, showed that this sample configuration is not fully cured. This leads to a lower glass transition temperature. It can also be seen that a higher fibre volume fraction lowers the T_g. Several studies [10, 11, 21] investigating the T_g of epoxy resin with CNFs as nanofillers report an increase in T_g, which could not be confirmed here. This can be attributed to the lower reactive surface area of the fibres. In addition, as can be seen in the micrograph in Figure 2, the epoxy resin of the matrix is in large parts unaffected, so that even if T_g increases around the fibres, this effect is so small in terms of quantity that it has no influence on the measurement.

4 Conclusion

This project was undertaken to design a composite with a high fibre volume fraction of a novel type of bio-based CNF fibres and evaluate the influence of the curing due to the active surface of the fibres, based on the reported positive influences of CNFs as nanofillers in epoxy. The new fibre type based on CNFs could be successfully used as reinforcement in epoxy with high fibre weight fractions. The cross-section pictures show a homogeneous, repeatable shape and size of the CNF fibres. The cure-kinetic study has examined the impact of the pretreatment of CNFs, the fibre diameter and the fibre weight fraction. In general, the results of this investigation have shown that TEMPO CNF pretreatment, smaller fibre diameter and higher fibre weight fraction increase the curing interaction by elevating the reaction start temperature T_{on}, and the maximum peak temperature T_{max}. FTIR analysis showed that TEMPO pre-treatment with a small diameter resulted in incomplete curing and provided strong evidence that the carboxyl groups react with epoxides. Compared to pure epoxy, the glass transition temperature shows no significant change due to fibre reinforcement. Taken together, the results of this first report on CNFs in the form of fibres as reinforcement in composites indicate that the active surface of the fibres interacts with epoxides to form a covalent bond. Further work is required to ensure that the expected good mechanical properties are achieved.

Acknowledgements
The authors acknowledge the funding from Vinnova and Formas through the strategic innovation programme LIGHTer and LIGHTer Academy. The authors thank Anna Wiberg, Jakob Redlinger-Pohn and Mathias Kvick for valuable inputs and discussions. Tijana Todorovic is acknowledged for providing help with FTIR measurements.

References

[1] H. Ku et al. “A review on the tensile properties of natural fiber reinforced polymer composites”. In: *Composites Part B: Engineering* 42.4 (2011), pp. 856–873. DOI: 10.1016/j.compositesb.2011.01.010.

[2] “Investigation of the curing behaviour of carbon fibre epoxy prepreg by Dynamic Mechanical Analysis DMA”. In: *Polymer Testing* 32.2 (2013), pp. 231–239. DOI: 10.1016/j.polymertesting.2012.11.004.

[3] Chioma Ifeyinwa Madueke et al. “A review on the limitations of natural fibres and natural fibre composites with emphasis on tensile strength using coir as a case study”. en. In: *Polymer Bulletin* 80.4 (2023), pp. 3489–3506. DOI: 10.1007/s00289-022-04241-y.

[4] Tsuguyuki Saito et al. “An Ultrastrong Nanofibrillar Biomaterial: The Strength of Single Cellulose Nanofibrils Revealed via Sonication-Induced Fragmentation”. In: *Biomacromolecules* 14.1 (2013), pp. 248–253. DOI: 10.1021/bm301674e.

[5] Nitesh Mittal et al. "Multiscale Control of Nanocellulose Assembly: Transferring Remarkable Nanoscale Fibril Mechanics to Macroscale Fibers". In: *ACS Nano* (2018). DOI: 10.1021/acsnano.8b01084.

[6] Caitlyn M. Clarkson et al. "Melt Spinning of Cellulose Nanofibril/Polylactic Acid (CNF/PLA) Composite Fibers For High Stiffness". In: *ACS Applied Polymer Materials* 1.2 (2019), pp. 160–168. DOI: 10.1021/acsapm.8b00030.

[7] Shuji Fujisawa et al. "Preparation and characterization of TEMPO-oxidized cellulose nanofibril films with free carboxyl groups". In: *Carbohydrate Polymers* 84.1 (2011), pp. 579–583. DOI: 10.1016/j.carbpol.2010.12.029.

[8] Hayaka Fukuzumi et al. "Transparent and High Gas Barrier Films of Cellulose Nanofibers Prepared by TEMPO-Mediated Oxidation". In: *Biomacromolecules* 10.1 (2009), pp. 162–165. DOI: 10.1021/bm801065u.

[9] Fleur Rol et al. "Recent advances in surface-modified cellulose nanofibrils". In: *Progress in Polymer Science* 88 (2019), pp. 241–264. DOI: 10.1016/j.progpolymsci.2018.09.002.

[10] Farhan Ansari et al. "Cellulose nanofiber network for moisture stable, strong and ductile biocomposites and increased epoxy curing rate". In: *Composites Part A: Applied Science and Manufacturing* 63 (2014), pp. 35–44. DOI: 10.1016/j.compositesa.2014.03.017.

[11] Mohan Turup Pandurangan et al. "Study of Curing Characteristics of Cellulose Nanofiber-Filled Epoxy Nanocomposites". In: *Catalysts* 10.8 (2020), p. 831. DOI: 10.3390/catal10080831.

[12] N. Saba et al. "Thermal and dynamic mechanical properties of cellulose nanofibers reinforced epoxy composites". In: *International Journal of Biological Macromolecules* 102 (2017), pp. 822–828. DOI: 10.1016/j.ijbiomac.2017.04.074.

[13] N. Saba et al. "Mechanical, morphological and structural properties of cellulose nanofibers reinforced epoxy composites". In: *International Journal of Biological Macromolecules* 97 (2017), pp. 190–200. DOI: 10.1016/j.ijbiomac.2017.01.029.

[14] Karl M. O. Håkansson. "Effect of carboxymethylated cellulose nanofibril concentration regime upon material forming on mechanical properties in films and filaments". en. In: *Cellulose* 28.2 (2021), pp. 881–895. DOI: 10.1007/s10570-020-03566-z.

[15] Karl Håkansson. "Orientation of elongated, macro and nano-sized particles in macroscopic flow". PhD thesis. Stockholm: KTH Royal Institute of Technology, 2014.

[16] *CelluXtreme*. Oct. 2024. URL: https://www.celluxtreme.com/.

[17] *Bcomp - Sustainable Lightweighting to Decarbonise the World*. URL: https://www.bcomp.com/ (visited on 05/14/2024).

[18] *AXIOM Materials | Advanced Composites Manufacturer*. URL: https://axiommaterials.com/ (visited on 05/14/2024).

[19] María González et al. "Applications of FTIR on Epoxy Resins - Identification, Monitoring the Curing Process, Phase Separation and Water Uptake". In: *Infrared Spectroscopy - Materials Science, Engineering and Technology*. 2012. ISBN: 978-953-51-0537-4. DOI: 10.5772/36323.

[20] Bamdad Barari et al. "Mechanical, physical and tribological characterization of nano-cellulose fibers reinforced bio-epoxy composites: An attempt to fabricate and scale the 'Green' composite". In: *Carbohydrate Polymers* 147 (2016), pp. 282–293. DOI: 10.1016/j.carbpol.2016.03.097.

[21] Shikha Shrestha et al. "Surface hydrophobization of TEMPO-oxidized cellulose nanofibrils (CNFs) using a facile, aqueous modification process and its effect on properties of epoxy nanocomposites". In: *Cellulose* 26.18 (2019), pp. 9631–9643. DOI: 10.1007/s10570-019-02762-w.

FIBRILLATION - IMPROVING THE FIBRE/MATRIX ADHESION OF LYOCELL FIBRES FOR USE IN SHORT FIBRE-REINFORCED AND 3D PRINTED COMPOSITES

Graupner, N.[1], Gauss, C.[2]; Pickering, K.L.[2], Schmidt, S.[3] and Müssig, J.[1]

[1]HSB – City University of Applied Sciences, The Biological Materials Group, Bremen, Germany
ngraupner@hs-bremen.de, jmuessig@bionik.hs-bremen.de
[2]School of Engineering, The University of Waikato, Hamilton, New Zealand
cgauss@waikato.ac.nz, kim.pickering@waikato.ac.nz
[3]Leibniz-Institut für Verbundwerkstoffe GmbH, Kaiserslautern, Germany
stefan.schmidt@ivw.uni-kl.de

Keywords: regenerated cellulose, fibrillation; fibre/matrix adhesion; additive manufacturing

Abstract
This study investigates the influence of fibrillation of lyocell fibres on the mechanical properties of compression moulded polylactide (PLA), polypropylene (PP) composites, and 3D printed PLA composites. Fibrillation was shown to reduce the strength and elongation at break of the fibres without affecting the Young's modulus compared to untreated fibres. Nevertheless, fibrillation in composites resulted in a 1.15 higher strength for PP composites and 1.62 for PLA composites. Young's modulus and impact strength were increased by factors of 1.41 and 1.38 for PP composites and 1.2 and 1.23 for PLA composites. Applying the fibrillated fibres in 3D printed PLA shows a significant increase in the mechanical properties. For example, with a fibre mass fraction of 30%, the tensile strength of the composites with fibrillated fibres was increased by a factor of 1.18 compared to composites with untreated fibres. The use of maleic anhydride in the PLA matrix in combination with composite heat treatment further increased the strength by a factor of 1.46. With a strength of 85 MPa, a Young's modulus of 7.2 GPa and an elongation at break of 3.2%, these are some of the highest values reported for this kind of 3D printed materials.

1. Introduction

Using regenerated cellulose fibres, especially lyocell fibres, in composite applications is not new. Lyocell fibres are particularly characterised by their high toughness compared to plant bast fibres (see, e.g., [1]). Improving the adhesion between the generally hydrophobic matrix and the hydrophilic fibre is important. Besides using adhesion promoters [2], alternative approaches involve modifying the fibre surface, e.g. by plasma treatment, enzymatic processes, ultrasound or chemical treatment methods. One method for significantly increasing the specific surface area and, thus, the bonding surface between the matrix and the fibre is fibrillation. While fibrillation is unwanted in textile applications and makes processing more difficult, this process can offer distinct advantages in fibre-reinforced composites. Similar to a plant root system, the nanofibrils can intertwine with the matrix, making them more resistant to detaching from the matrix when force is applied [3].

In this study, fibrillation was deliberately induced to improve the reinforcing effect of short and randomly oriented lyocell fibres in a PLA and PP matrix produced by compression moulding [4] and to improve the properties of short fibre-reinforced, 3D printed PLA materials [5]. In a previous study, it was shown that improved adhesion affects especially short fibre-reinforced materials. Material extrusion

processes, particularly fused deposition modelling (FDM), are one of the most commonly used methods for 3D printing with polymers or polymer composites due to their simplicity and low operating costs [6]. Therefore, the present study investigated compression moulded and 3D printed composites with short fibre reinforcement and random fibre orientation. Additionally, the use of maleic anhydride (MA) on the properties of PLA and as a potential adhesion promoter between cellulose fibre and matrix is being investigated. This approach to improve fibre/matrix adhesion has already been tested [7]. Some materials were also subjected to heat treatment to increase the crystallinity of the PLA.

2. Materials & methods

Lyocell fibres with a fineness of 15.0 dtex and a length of 90 mm were used to produce the compression-moulded samples (Lenzing AG, Lenzing, Austria). The matrices used were PLA (SLN 2660 D Ingeo fibres from Eastern Textile Ltd. (Taipei, Taiwan) with a fibre fineness of 6.0 dtex and a staple fibre length of 64 mm) and PP fibres (lot no. PP-N08 with a diameter of approx. 35 µm without adhesion promoters supplied by Nafgo GmbH, Dötlingen-Neerstedt, Germany). For the 3D printed materials, lyocell fibres with a fineness of 1.3 dtex (FCP400) with a nominal length of 400 µm (Lenzing AG, Lenzing, Austria) and as matrix PLA (grade 2003D from NatureWorks®) were used.

The fibres were fibrillated in an ultrasonic bath (Emmi-H22, EMAG AG, Mörfelden-Walldorf, Germany, operating frequency of 40 kHz and an ultrasonic power of 120 W) in a multi-stage treatment with demineralised water for 30 min, isohexane for 60 min, acetone for 60 min and demineralised water for 15 min. The fibres were dripped onto cellulose paper for 5 min between the treatment steps. To measure the fibre width of lyocell 15.0 dtex fibres and the length of lyocell 1.3 dtex fibres, the FibreShape software (IST AG, Vilters, Switzerland) was used. Fibres were conditioned at 20 °C and 65% relative humidity. For untreated and fibrillated fibres, 3 slide frames of each sample (Gepe Produkte AG, Zug, Switzerland) were prepared with fibre snippets and scanned with a slide scanner (CanoScan FS 4000US, Canon Deutschland GmbH, Krefeld, Germany; transmitted light mode with a resolution of 4000 dpi). The influence of fibrillation on the mechanical properties of the lyocell fibres was analysed using 15.0 dtex lyocell fibres in fibre tensile tests (clamping length 20 mm, test speed 10 mm/min, test conditions: 20 °C, 65% rel. humidity; test device Fafegraph M testing machine, Textechno, Mönchengladbach, Germany; equipped with a pneumatic clamping system and a 100 cN load cell). The influence of fibrillation on fibre/matrix adhesion was investigated using microbond tests. For this purpose, individual lyocell fibres with a fineness of 15.0 dtex were placed in a perforated aluminium frame, and, in the case of the PLA matrix, 2-3 PLA fibres were knotted around a single lyocell fibre; for PP, one fibre was knotted around one lyocell fibre. The ends of the polymer fibres were cut off close to the lyocell fibre, and the aluminium frame was treated in an oven for 5 minutes at 185 °C to melt the polymers. The embedding length of the fibres was measured under a microscope and the fibres were then pulled out of the matrix in a universal testing machine at a test speed of 1 mm/min and a free gauge length of 5 mm with a self-developed test device for a Zwick/Roell Z020 universal test machine (Zwick/Roell GmbH, Ulm, Germany; load cell 5 N). The forces were measured to determine the shear strength (test conditions: 23 °C, 50% rel. humidity).

For the compression moulded composites, lyocell 15.0 dtex fibres were carded with PLA or PP fibres to blend them using a manual roller card (Standard 46 tpi, fleece size 78 x 19 cm², Louët, Lochem, The Netherlands). The fibre content was set to 30 vol.-%. The multilayer webs were cut to a size of approx. 200 x 200 mm² and dried for 18 h in an oven at 60 °C. The fibres were then pressed to a thickness of 1 mm using 1 mm thick spacers at a temperature of 185 °C and a pressure of 15 bar for 2 minutes (LaboPress P200S, Vogt Labormaschinen GmbH, Berlin, Germany). The sheets were shredded (shredder type EBA 2326C, Krug & Priester GmbH & Co. KG, Balingen, Germany) into pellets and then pressed again to a thickness of 1 mm. In order to ensure a higher homogeneity of the random fibre-oriented composites, a further shredding process was applied. Afterwards, the granules were pressed to a thickness of 2 mm using 2 mm thick spacers at a temperature of 185 °C and a pressure of 15 bar for 5 min. The test specimens for the tensile and impact tests were produced from these sheets with a band saw.

A fibre content of 30 mass% was used for the 3D printing materials. The PLA matrix and fibres were blended at 180-195 °C with a Sigma blade-type compounder for 10 min. Compounds were produced with and without maleic anhydride (MA). For the materials with MA, 2% MA in relation to the PLA mass and 10% dicumyl peroxide in relation to the MA mass were added during the compounding process. 3D printing wires with a diameter of 1.7 mm were produced from the granulates manufactured. After compounding, the composites were granulated into particles of < 4 mm using a Moretto GR knife mill (Mercer County, PA, USA). The particles were vacuum dried at 60 °C for 4 h and extruded using a Filabot EX2 single screw extruder (Barre, VT, USA) at 180-185 °C. An air cooling system was used to cool the thermoplastic wire. The 3D printing was carried out using a fused deposition modeling (FDM) process with a MakerGear™ M2 desktop 3D printer (Beachwood, OH, USA) using the Simplify 3D® software package for slicing the CAD files and controlling the 3D printer. Before printing, all the wires were vacuum-dried at 50 °C for 2 h. All samples were printed using a perimeter (shell) of one printing line (approx. 0.75 mm). After 3D printing, one set of samples for each formulation was heat treated at 105 ± 2 °C for 2 h in a laboratory oven.

Tensile characteristics of compression moulded composites (n=6; dimensions 200 x 15 x 2 mm³) were tested at a clamping length of 125 mm and a test speed of 2 mm/min with a universal testing machine type Zwick Z020 (Zwick/Roell GmbH, Ulm, Germany) equipped with a 20 kN load cell and a pneumatic clamping system (clamping pressure: 1 - 2 bar) at a crosshead speed of 2 mm/min. The elongation was determined using a video extensometer (VideoXtens, Zwick/Roell GmbH, Ulm, Germany; measuring mark distance 80 mm). The impact properties were investigated using unnotched Charpy impact tests (n=8; dimensions 80 x 10 x 2 mm³; pendulum device type 5102, Zwick GmbH, Ulm, Germany) with a bearing distance of 40 mm and broadside impact.

The 3D-printed tensile test specimens (n=5; ASTM D638 type V samples, dimensions 10.96 x 3.18 x 1.2 mm³) were tested in an Instron® 5982 universal testing machine (Norwood, MA, USA) equipped with a 5 kN loadcell) using a crosshead speed of 2 mm/min. The elongation was measured with a 10 mm clip-on extensometer.

SEM investigations were done with a JSM 6510 scanning electron microscope (Jeol, Eching, Germany) operating with secondary electrons. Prior to SEM investigations, the samples were sputtered with a gold layer for 90 s under a current of 56 mA using a Bal-Tec sputter coater type SCD 005 (Bal-Tec, Liechtenstein).

More details on the materials and methods used are described in previous publications [4, 5].

3. Results & discussion

3.1 Effect of fibrillation on fibre surface and mechanical characteristics

Figure 1 shows the influence of the surface treatment on the lyocell fibres with a fineness of 15.0 dtex. The fibres are clearly fibrillated due to swelling and ultrasonic treatment. It becomes apparent that the fibres are only fibrillated in the outer areas, whereas the fibre core has remained intact. The measured nanofibrils have widths between ~100 and ~400 nm. It is to be expected that the fibrils lead to better bonding to the matrix in a composite material due to the increase in surface area, similar to a plant root system in the soil. The fibre width did not change significantly as a result of the treatment and resulted in mean values of 36.0 ± 5.6 µm (median value: 36.0 µm) for the untreated fibre and 35.7 ± 5.4 µm (median value: 35.6 µm) for the fibrillated fibre. Results show good agreement with the calculated equivalent diameter of 35.7 µm.

It was shown that fibrillation slightly reduces the tensile strength and elongation at break of the fibres, while it does not affect Young´s modulus. A median value of 251 MPa was determined for the tensile strength of the untreated fibre and 192 MPa for the fibrillated fibre. The fibrillation did not significantly influence Young's modulus, as it is determined in the linear-elastic initial slope, and the influence of possible defects is lower. The Young´s modulus resulted in a median value of 6.47 GPa for the untreated

fibre and 6.25 GPa for the fibrillated fibre. The elongation at break was reduced by the defects on the fibre surface, from a median value of 12.1% for the untreated fibre to 8.5% for the fibrillated fibre.

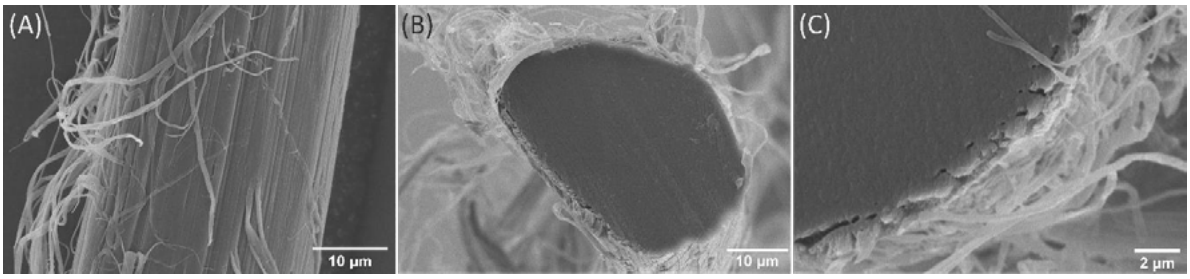

Figure 1: Fibrils on a lyocell fibre surface (A) in cross-section (B) and in detail in cross-section (C)

3.2 Influence of fibrillation on the fibre/matrix adhesion in a PLA and PP matrix and

The fibre/matrix adhesion of lyocell fibres with a fineness of 15.0 dtex was tested in a PLA and PP matrix using microbond tests. The median interfacial shear strength could be increased from 3.3 to 4.4 MPa in a PP matrix and from 7.1 to 8.2 MPa in a PLA matrix using fibrillated fibres compared to untreated fibres (Figure 2 A&B). Better adhesion of lyocell in PLA than in a PP matrix is achieved. The improvement in IFSS is not significant from a statistical point of view. It should be noted that only individual fibres are tested in the microbond test, whereas a large number of fibres are present in a composite, and the effects of the improved adhesion are more pronounced. It is assumed that individual fibrils anchor themselves in the matrix and thus, lead to a larger specific bonding area between fibre and matrix, which improves the shear strength. In addition, fibrillation leads to a higher roughness of the fibre surface, which can increase friction and mechanical interlocking. At the same time, fibrillation significantly reduces the critical fibre length, which means that a shorter fibre length can have a reinforcing effect in a composite. Analogous to the better adhesion in the PLA matrix, it was found that the critical fibre length for PLA composites is lower than for PP-based composites (Figure 2 C&D). This is particularly interesting when short fibres with lengths around the critical fibre length are used, e.g. in injection-moulded or 3D printed composites.

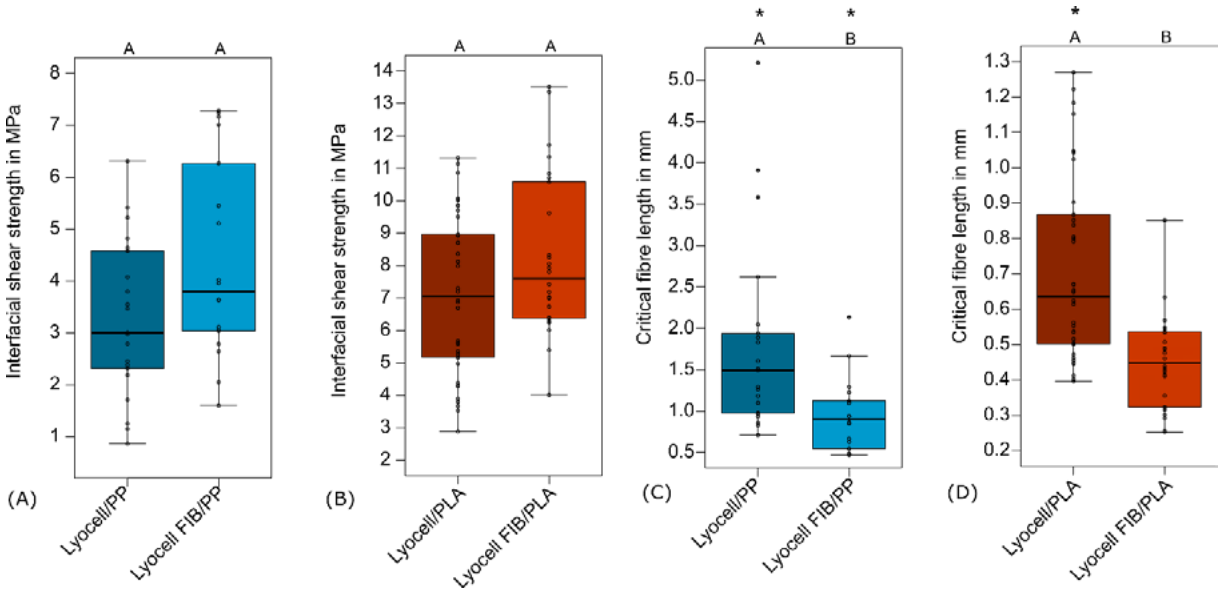

Figure 2: Box-Whisker plots of the interfacial shear strength of lyocell fibres embedded in a PP matrix (A) and a PLA matrix (B) and the critical fibre length in a PP matrix (C) and PLA matrix (D) (results that do not comply with a normal distribution are marked with an asterisk, significant differences between median values are labelled with different letters; figure reproduced from [4])

3.3 Influence of fibrillation on compression moulded short fibre-reinforced PLA and PP composites

Composites with short fibres and random fibre orientation were produced by compression moulding to evaluate whether fibrillated lyocell fibres can improve the mechanical properties in a PP and PLA matrix. Figure 1 shows that fibrillation only takes place on the fibre surface, and the core of the fibre is hardly affected. Despite the lower tensile strength of the fibrillated lyocell fibres, the strength of the composites was increased by a factor of 1.15 for PP and 1.62 for PLA compared to the composites produced with untreated fibres (Figure 3 A&D). The Young´s modulus of the composites was increased by a factor of 1.41 for PP and 1.20 for PLA with fibrillated fibres (Figure 3 B&E). The increase in strength can be explained by an improvement in adhesion due to anchoring effects caused by the larger specific fibre surface area as described by Karlsson et al. [3].

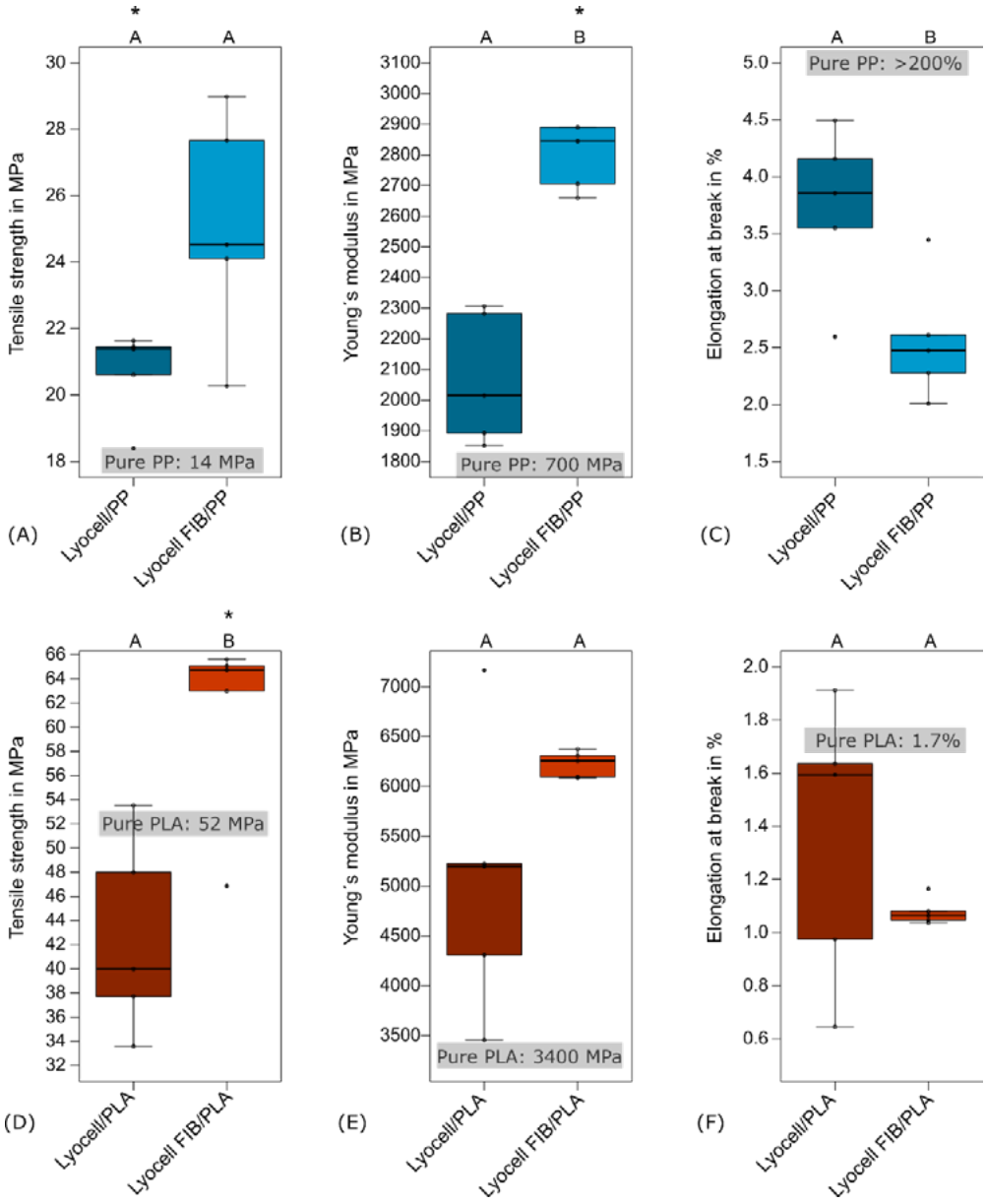

Figure 3: Box-Whisker plots of the tensile characteristics of lyocell/PP composites (A-C) and lyocell/PLA composites (D-F) (results that do not comply with a normal distribution are marked with an asterisk, significant differences between median values are labelled with different letters; figure reproduced from [4])

SEM analyses indicate that the improved adhesion between the fibrillated lyocell fibres and the PP and PLA matrices, as demonstrated by the results of the microbonding tests, can be transferred to the composites. Figure 4 shows an example of a fracture surface of a composite made with fibrillated lyocell fibres. A ripped lyocell fibre can be seen on which fibrils are visible; a broken lyocell fibre coated with PP matrix is visible on the right. At the point of breakage, fibrils protrude from the matrix and bridge the crack, delaying it. The fibrils serve as a kind of anchor within the matrix. Since the Young's modulus of the fibres was not significantly influenced by the fibrillation, structural effects must be a reason for the increased Young's modulus of the composites. Only the main fibre is tested when measuring the fibre Young's modulus. The nanofibrils cannot be measured and, therefore, do not influence the measured Young's modulus. However, in a composite, they are embedded in the matrix and contribute significantly to the stress transfer from the matrix to the fibre. It is assumed that the individual nanofibrils embedded in the matrix contribute to an increase in Young's modulus. Due to the increased adhesion of the nanofibrils, the elongation at break of the composite is reduced. While the elongation at break of the PLA matrix is barely affected by the lyocell fibres, the very high elongation at break of the PP matrix (>200%) is significantly reduced by the considerably lower elongation of the fibres (Figure 3 C&F).

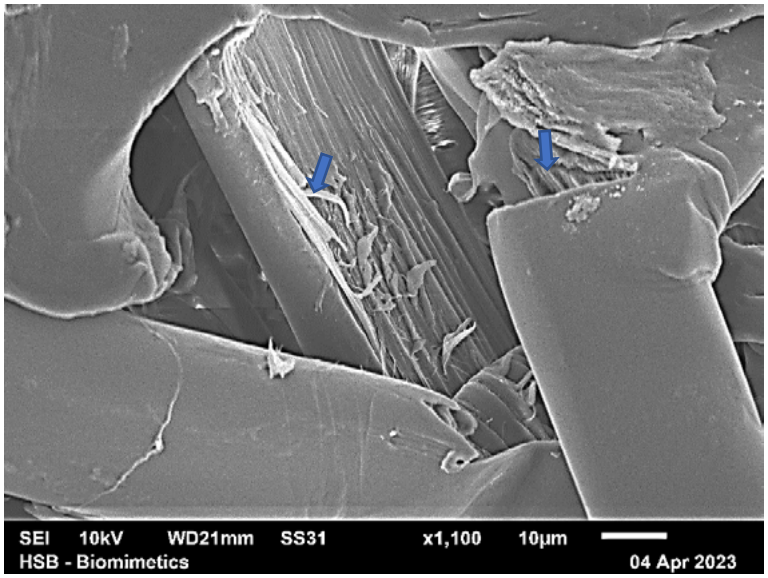

Figure 4: Fracture surface of a lyocell/PP composite (fibrils are marked with blue arrows)

For both the PLA and the PP matrix, the impact strength could not be improved with the lyocell fibres. The reason for this is the use of short fibres with random orientation. These fibres prevent the energy-absorbing fibre pull-outs. Using longer and oriented fibres leads to significantly improved energy absorption by fibre pull-outs when the material breaks. However, the use of fibrillated lyocell fibres results in a significant increase in impact strength compared to untreated fibres. The unnotched Charpy impact strength was improved by a factor of 1.38 for PP composites and 1.23 for PLA composites by using fibrillated fibres.

3.4 Influence of fibrillation on 3D printed short fibre-reinforce PLA composites

As improved fibre/matrix adhesion has a more significant effect on the mechanical properties of short fibre-reinforced materials compared to long fibre-reinforced composites, fibrillated lyocell fibres were used to produce 3D printed PLA composites [5]. In order to increase the aspect ratio of the short lyocell fibres, 1.3 dtex fine lyocell fibres were used instead of the coarse lyocell 15.0 dtex fibres. Fibrillation was carried out as described for the 15.0 dtex lyocell fibres. An analysis of the fibre lengths (extracted fibres from composites) after compounding, wire production and 3D printing revealed fibre lengths for the different formulations between 116 and 134 µm and, thus, similar fibre length distributions. An influence of different fibre lengths can therefore be excluded [5].

The tensile properties of 3D-printed composites are summarised in Table 1. The formulation of fibrillated lyocell fibres and PLA show an improvement by factor 1.18 for tensile strength and 1.14 for Young's modulus compared to the composite with unmodified fibres and has similar tensile properties to the lyocell-reinforced maleic anhydride modified PLA (PLA-MA). The combination of the fibrillated fibres and the MA-modified PLA further improved the tensile properties, resulting in a tensile strength of 76.6 MPa, Young's modulus of 6.44 GPa, and elongation at break of 3.7%. These results represent an improvement of 1.31 in tensile strength and 1.28 in Young's modulus compared to the composite with untreated lyocell fibres and unmodified PLA matrix.

Table 1: Tensile properties of lyocell-reinforced composites produced by 3D printing

Composite	*Tensile strength in MPa*	*Young´s modulus in MPa*	*Elongation at break in %*
PLA	65.3	3460	6.7
PLA-MA	57.2	3320	4.0
30% lyocell 1.3 dtex/PLA	58.4	5050	2.9
30% fibrillated lyocell 1.3 dtex/PLA	69.2	5760	3.4
30% fibrillated lyocell 1.3 dtex/MA-PLA	76.6	6440	3.7
30% fibrillated lyocell 1.3 dtex/MA-PLA + heat treatment	85.0	7180	3.2

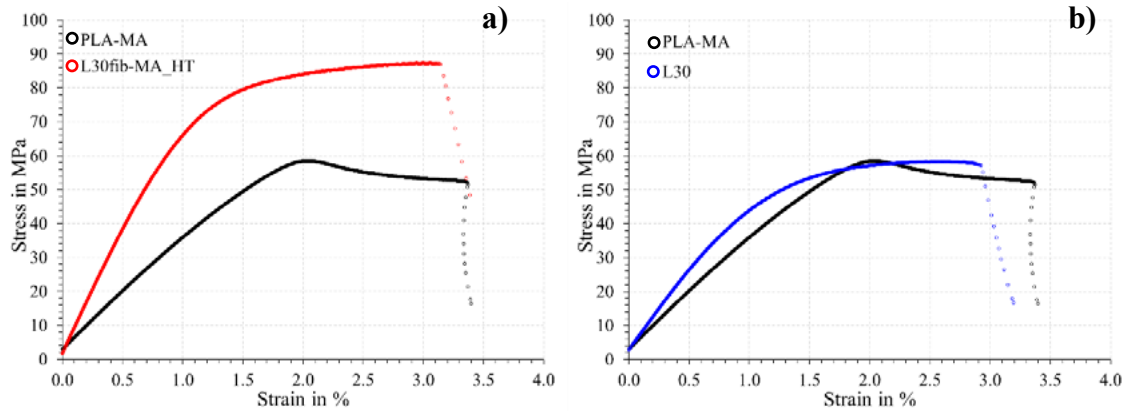

Figure 5: Stress-strain curves of the 3D printed composites produced from fibrillated lyocell/PLA (L30fib-MA_HT) after heat treatment (HT) (a) and untreated lyocell/PLA (L30) (b) samples in comparison with PLA-MA (figure reproduced from [5])

The mechanical properties of the composites with a high proportion of lyocell fibres can be further improved by increasing the PLA crystallinity through heat treatment (HT). Heat treatment was beneficial for all formulations, and the combination of fibre fibrillation, matrix modification (MA treatment) and heat treatment can achieve very promising mechanical properties such as a tensile strength of 85 MPa, a Young's modulus of 7.18 GPa and an elongation at break of 3.2% (see Table 1 and Figure *5*). These values correspond to an improvement by factor 1.30 in tensile strength and by 2.11 in Young's modulus compared to 3D printed pure PLA (1.49 and 2.12, respectively, compared to PLA-MA), without significantly affecting the elongation at break. Additionally, it has been demonstrated that increasing PLA crystallinity, when combined with reinforcing lyocell fibres, significantly enhances the thermo-mechanical stability of the composite. This is evidenced by a storage modulus at 80 °C that is up to 200 times higher than that of neat PLA [5].

4. Conclusions

The results show that the fibrillation of lyocell fibres positively affects adhesion in both a PP and a PLA matrix. The fibrillation process reduced the strength and elongation at break of the lyocell fibres while the Young's modulus remained constant. Despite the lower fibre strength, the tensile strength of compression moulded short fibre-reinforced PLA and PP composites was significantly increased by using fibrillated lyocell fibres in both matrices compared to the use of non-fibrillated fibres. The tensile modulus of the composites was also improved. Despite reducing the elongation at break of the composites, the fibrillated lyocell fibres significantly improved the impact strength. The use of fibrillated lyocell fibres in 3D printed PLA composites was tested, as it has been shown that an improvement in adhesion has a particular effect on short fibre-reinforced composites. The shear forces during extrusion and 3D printing allow the short fibres to partially align and split off nanofibrils from the main fibre, resulting in a significant increase in fibre surface area and fibre aspect ratio, which could significantly increase the reinforcing effect. The micro- and nanofibrils can anchor themselves in the matrix, similar to a plant root system. Fibrillated lyocell fibres could be successfully processed with a PLA matrix in 3D printing and showed a considerably increased tensile strength compared to materials made from untreated lyocell fibres. The mechanical properties were significantly increased by using maleic anhydride and heat treatment resulting in a tensile strength of 85 MPa, a Young's modulus of 7.2 GPa and an elongation at break of 3.2%. This class of materials has some of the highest characteristic values currently known in the literature for short fibre-reinforced 3D printing (fused deposition modeling - FDM) materials.

References

[1] R.-B. Adusumali, M. Reifferscheid, H. Weber, T. Roeder, H. Sixta, and W. Gindl. Mechanical properties of regenerated cellulose fibres for composites. *Macromolecular Symposia*, 244(1):119–125, 2006.

[2] Y. Borja, G. Rieß, and K. Lederer. Synthesis and characterization of polypropylene reinforced with cellulose i and ii fibers. *Journal of Applied Polymer Science*, 101(1):364–369, 2006.

[3] J.O. Karlsson, J.-F. Blachot, A. Peguy, and P. Gatenholm. Improvement of adhesion between polyethylene and regenerated cellulose fibers by surface fibrillation. *Polymer Composites*, 17(2):300–304, 1996.

[4] N. Graupner, S. Schmidt, C. Gauss, and J. Müssig. Making positive use of the fibrillation of lyocell fibres in composite materials. *Composites Part C: Open Access*, 11:100359, 2023.

[5] C. Gauss, K.L. Pickering, N. Graupner, and J. Müssig. 3d-printed polylactide composites reinforced with short lyocell fibres - enhanced mechanical properties based on bio-inspired fibre fibrillation and post-print annealing. *Additive Manufacturing*, 77:103806, 2023.

[6] L.P. Muthe, K. Pickering, and C. Gauss. A review of 3d/4d printing of poly-lactic acid composites with bio-derived reinforcements. *Composites Part C: Open Access*, 8:100271, 2022.

[7] L. Petersson, K. Oksman, and A. P. Mathew. Using maleic anhydride grafted poly(lactic acid) as a compatibilizer in poly(lactic acid)/layered-silicate nanocomposites. *Journal of Applied Polymer Science*, 102(2):1852–1862, 2006.

RUBBERY NANOFIBERS VIA BLEND AND EMULSION ELECTROSPINNING FOR STRUCTURAL MODIFICATION OF COMPOSITE LAMINATES

Emanuele Maccaferri[a,b,c], *Laura Mazzocchetti*[a,b,c], *Tiziana Benelli*[a,b,c], *Tommaso Maria Brugo*[b,d], *Andrea Zucchelli*[b,d], *Loris Giorgini*[a,b,c]

a: Department of Industrial Chemistry "Toso Montanari", University of Bologna, Viale Risorgimento 4, 40136 Bologna, Italy – emanuele.maccaferri3@unibo.it
b: Interdepartmental Center for Industrial Research on Advanced Applications in Mechanical Engineering and Materials Technology, CIRI-MAM, University of Bologna, Viale Risorgimento 2, 40136 Bologna, Italy.
c: National Interuniversity Consortium of Materials Science and Technology (INSTM), 50121 Florence, Italy
d: Department of Industrial Engineering, University of Bologna, Viale Risorgimento 2, 40136 Bologna, Italy.

Keywords: Blend electrospinning; Emulsion electrospinning; Elastomer; Nanofiber; Delamination; CFRP

Abstract

FRP laminates, especially Carbon Fiber Reinforced Polymer (CFRP) ones, are currently replacing metals for lightning where weight reduction is a key factor. However, they suffer from delamination due their laminar structure, thus limiting employment. Solutions for reducing the risk of delamination are welcoming. In this context, polymeric electrospun nanofibers, especially rubbery ones, are valid for hindering delamination. The present work illustrates the production and use of rubber-based nanofibers to improve some structural properties, such as the interlaminar fracture toughness, of CFRP laminates. Single-needle electrospinning of Nitrile Butadiene Rubber (NBR) mixed with suitable thermoplastic polymers is exploited to fabricate dimensionally stable rubbery mats made of nanofibers. In particular, blend electrospinning of NBR and poly(e-caprolactone) (PCL) and emulsion electrospinning of NBR and the polyaramid Nomex are effective approaches for obtaining stable nanomats without the need for a crosslinking step. In addition, the effect of their integration into epoxy Carbon FRP (CFRP) laminates on delamination resistance is investigated. Results demonstrate that rubbery nanofibers can significantly improve the interlaminar fracture toughness (up to 4-5 times) with limited impact on the other laminates' thermal and mechanical properties, paving the way for their use for improving the service life and safety of components made of composite laminates.

1. Introduction

Thermosetting Fiber Reinforced Polymer (FRP) laminates are valid for reducing components' weight while retaining high specific mechanical properties. However, their laminar structure leads to an intrinsic delamination weakness [1] triggered by out-of-plane loads (impacts), fatigue, or a combination thereof.

Adding toughеners to the bulk resin is a well-known solution to limit delamination by increasing the interlaminar fracture toughness [2–6]. However, the addition of toughеners, such as elastomers, may result in a loss (even significant) of the laminate's thermomechanical properties. On the contrary, the modification of localized interlaminar regions where stresses are concentrated the most (holes, free edges, etc.) limits the overall impact on the other materials' properties.

The integration of electrospun nanofibrous mats represents a valid solution for improving delamination resistance [7–10] and, in some cases, even the material damping, with reduced impact on the laminate's strength and stiffness.

Besides common nanomats, mainly made of Nylons and polycaprolactone (PCL), rubber-based nanofibrous mats have been recently proposed for hindering delamination. While the latter are very promising nanomaterials, shaping rubbers straightforwardly into nanofibers is prevented by their low glass transition temperature (Tg): just the formation of a bulk film can be attained due to the rubber cold flow. Two main different approaches can be addressed for maintaining the nanofibrous structure: i) coaxial electrospinning and ii) single-needle electrospinning of polymeric blends. The first approach, besides requiring a more complicated electrospinning setup, provides poor control over the produced nanofibers due to feeding two distinct solutions (the "core" rubber solution and the "shell" one containing a polymer with a Tg higher than room temperature). The second way exploits the common and simple single-needle electrospinning process, enabling even precise control of the rubber content in the nanofiber.

The present work illustrates the production and use of rubber-based nanofibers to improve some structural properties, such as the interlaminar fracture toughness, of CFRP laminates. Single-needle electrospinning of Nitrile Butadiene Rubber (NBR) mixed with suitable thermoplastic polymers is exploited to fabricate dimensionally stable rubbery mats made of nanofibers. In particular, blend electrospinning of NBR and poly(-caprolactone) (PCL) and emulsion electrospinning of NBR and the polyaramid Nomex are effective approaches for obtaining stable nanomats without the need for a crosslinking step. In addition, the effect of their integration into epoxy Carbon FRP (CFRP) laminates on delamination resistance is investigated. Results demonstrate that rubbery nanofibers can significantly improve the interlaminar fracture toughness (up to 4-5 times), paving the way for their use for improving the service life and safety of components made of composite laminates.

2. Materials and methods

2.1 Materials

The elastomer used is Nitrile Butadiene Rubber (NBR), Nipol 1072CGX, Zeon Chemicals, containing 68 %mol of butadiene, 28 %mol of acrylonitrile, and 4 %mol methacrylic acid. The polycaprolactone (PCL), Sigma-Aldrich, has a molecular weight of 70-90 kDa. The polyaramide used is poly(m-phenylene isophtalamide) (Nomex), Sigma-Aldrich. Lithium chloride (LiCl), N,N-dimethylacetamide (DMAc), N,N-dimethylformamide (DMF) and chloroform ($CHCl_3$) were used without any preliminary treatment. Plain weave carbon fabric, 200 g/m2, in epoxy matrix prepreg for composite production was supplied by G. Angeloni s.r.l., Venezia, Italy.

2.2 Solution preparation and nanofibrous mat production

The starting rubber solutions (NBR 10% wt) were prepared in DMAc and CHCl3. The starting solutions made of thermoplastic polymers were prepared in solvent systems suitable for next mixing with the starting rubber solution. PCL (10% wt) was solubilized in CHCl3/DMF 1:1 wt; Nomex (10% wt) was dissolved in N,N-dimethylacetamide with lithium chloride (3.5% wt with respect to the total solution weight). Polymeric solutions were stirred at room temperature until formation of homogeneous solutions. The polymeric solution blends were prepared by mixing the NBR solution with the PCL or Nomex solution in a weight ratio 60:40 to obtain rubbery nanofibers (NBR/PCL and NBR/Nomex) constituted by 60% wt of rubber. Detailed procedures for producing both rubbery nanofibrous mat types are reported in [11] and [12]. The NBR/PCL and NBR/Nomex nanofibrous mats were produced via single-needle electrospinning, using a 4-needles machine (Spinbow®). Nanofibers were collected on a drum rotating at a tangential speed of 0.4 m/s. The rubbery mats (approx. 15 × 25 cm) have a grammage of (10 ± 2) and (5 ± 1) g/m2. The electrospinning process parameters are listed in Table 1 (ambient conditions: 25 °C and 25-30 % relative humidity).

Table 1: Process parameters used for single-needle electrospinning.

Nanofibrous mat	Flow rate [mL/h]	Potential [kV]	Distance [cm]
NBR/PCL	0.55	18	13
NBR/Nomex_*f*	0.20	25	18
NBR/Nomex _c	1.10	25	11

Scanning Electron Microscopy (SEM, Phenom ProX) was used for evaluation of nanofibers' morphology. In the case of NBR/Nomex rubbery nanofibers, the morphology was deeply investigated even after the removal of the NBR fraction via its dissolution in chloroform (2 consecutive washes, 1 h each).

2.3 Production and characterization of rubbery-modified CFRP laminates for delamination tests

In the case of NBR/Nomex nanofibers, prior the integration into CFRP the nanofibrous mat was washed in water to remove lithium chloride. Laminates for Double Cantilever Beam (DCB) were produced by stacking 14 plies of prepreg via hand lay-up, and inserting the electrospun mat in the middle plane together with a Teflon film with appropriate length. For the sake of comparison, unmodified specimens were produced too. Laminates underwent autoclave curing according to the following procedure: i) pre-treatment of 2 h at 45 °C under vacuum to favour nanofibers impregnation; ii) curing cycle in autoclave for 2 h at 135 °C, under vacuum, 6 bar external pressure, heating/cooling ramp 2 °C/min).

DCB tests were carried out using a universal testing machine (Remet TC-10) equipped with a 1 kN load cell, 3 mm/min cross-head separation rate.

The energy release rate in Mode I loading (G_I) was calculated according to the equation [13]:

$$G_{\mathrm{I}} = \frac{3P\delta}{2ba} \qquad (1)$$

where P is the load, δ the cross-head displacement, a the crack length, b the specimen width.

3. Results and discussion

Shaping liquid rubbers, i.e. not crosslinked, into nanofibers is a complicated task due to the occurring rubber cold flow at room temperature. Such a behaviour prevents the production of dimensionally stable nanostructure [14], as NBR nanofibers, leading to film formation (Figure 1), as previously assessed by electrospinning of NBR-only solution [12].

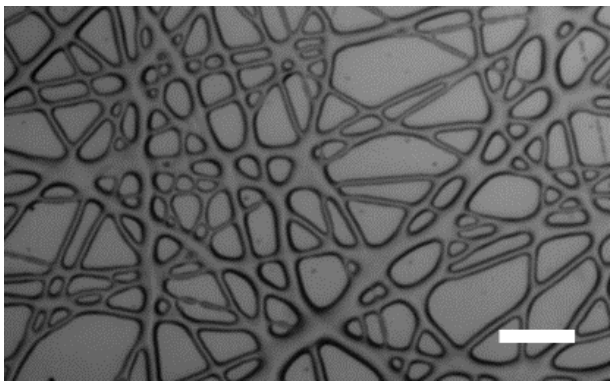

Figure 1. Film formation derived from plain NBR electrospinning, scale bar 10 μm [12].

For this reason, smart solutions must be taken to overcome this detrimental phenomenon that leads to film formation, thus leading to lose the benefits of a highly porous structure for better impregnation of the laminate resin and, in turn, optimal integration into CFRP laminates.

A viable way to by-pass the problem is crosslinking the rubber [15], but it involves an additional crosslinking step. Another solution may be the coaxial electrospinning [16], but it is tricky to have an accurate control of the rubber fraction in the polymer pair, besides a more complicated setup.

Rubber blending with a suitable thermoplastic polymer was proposed [11,12,17] as a smart approach to solve the rubber cold flow of uncrosslinked rubbers when shaped into nanofibers via single-needle electrospinning of polymeric blends/emulsions.

The elastomer used for producing rubbery nanofibers via single-needle electrospinning is nitrile rubber together with suitable thermoplastics, PCL and Nomex. NBR/PCL and NBR/Nomex nanofibers were electrospun to obtain two different mat grammages to evaluate their effect on the interlaminar fracture toughness.

While NBR/PCL electrospinning produces a polymeric blend, as previously assessed, the NBR/Nomex electrospinning generates a sort of “composite” nanofibers made of distinct phases of the two polymers. The latter behaviour derives from the fact that the starting solution is not a blend, but an emulsion that translates the heterogeneity even into the final nanofibers.

Both the produced nanofiber types are dimensionally stable over time without the need for rubber crosslinking. NBR/PCL nanofibers (mean diameter: 250 nm) have a smooth surface, as NBR/Nomex ones (mean diameter: 450 nm). However, after removal of the NBR fraction in the latter nanofibers, the heterogeneous structure (whose morphology depends just only to processing

conditions, is clearly revealed. In particular, a low flow rate leads to a "fibril-like" morphology made of Nomex, while electrospinning at a higher flow rate generates a morphology resembling a quasi-core–shell one, with the rubber located in the inner channel (Figure 2).

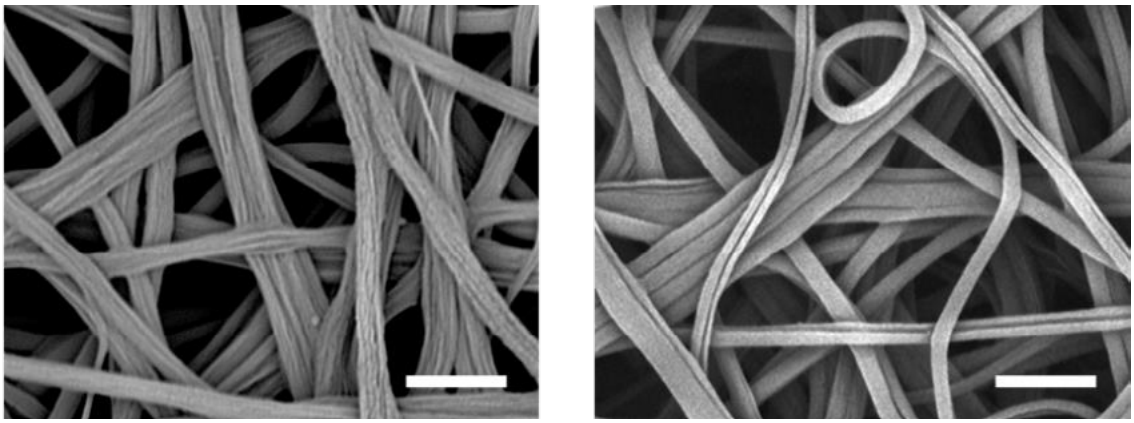

Figure 2. NBR/Nomex mats after washings in chloroform for NBR removal: NBR/Nomex_f (sx) and NBR/Nomex_c (dx), scale bar 2 µm.

3.1 Mode I interlaminar fracture toughness

Double Cantilever Beam (DCB) tests have been carried out to evaluate the interlaminar fracture toughness in Mode I (G_I).

All the rubbery-modified CFRPs show higher G_I than unmodified laminate (Figure 3 and Table 2).

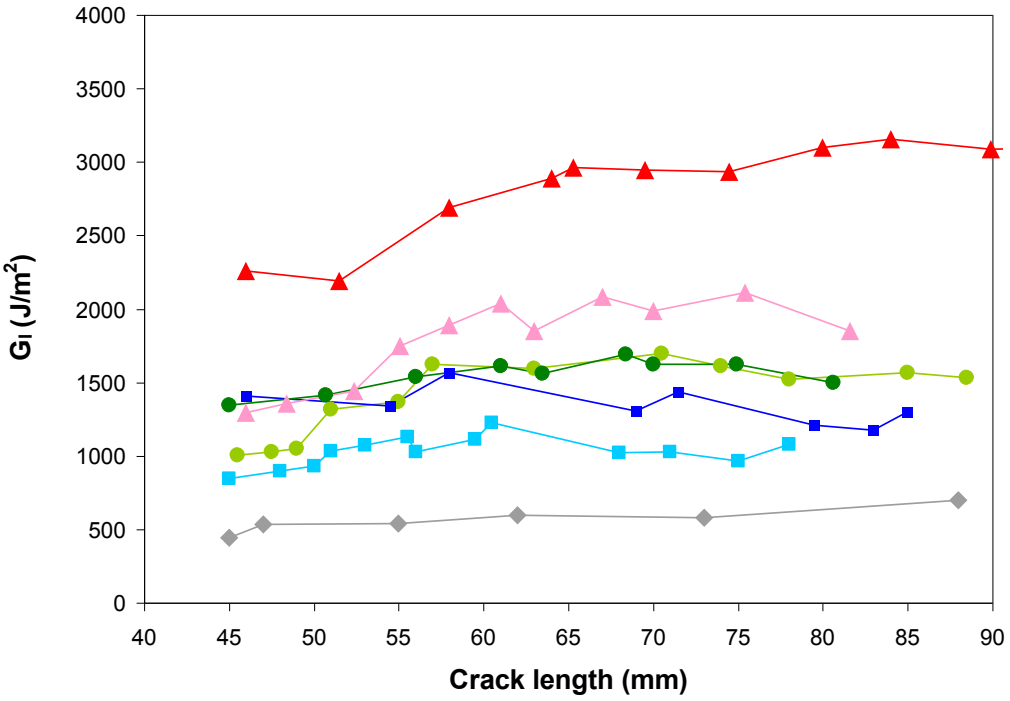

Figure 3. Results obtained from DCB test: G_I vs. crack length trends (R-curves). Colors: grey for Reference, pink for NBR/PCL_10, red for NBR/PCL_20, cyan for NBR/Nomex_f_10, blue for NBR/Nomex_f_20, light green for NBR/Nomex_c_10, dark green for NBR/Nomex_f_20.

The NBR/PCL and NBR/Nomex_c mat at the highest grammage (samples NBR/PCL_20 and NBR/Nomex_*c_20*) provide the maximum delamination hindering (up to +450% for NBR/PCL and +200% for NBR/Nomex). Regarding the different morphologies obtained for electrospun NBR/Nomex nanofibers, the quasi-core–shell mat provide best performance with respect to the fibril-like membrane (at the same grammage).

The use of doubled grammage generally improve the Mode I interlaminar fracture toughness.

Table 2: Results obtained from DCB test.

CFRP laminate	Total mat grammage	$G_{I,C}$ [J/m^2]	$G_{I,R}$ [J/m^2]
Reference	0	523 ± 134	569 ± 81
NBR/PCL_10	10	1283 ± 28	2122 ± 469
NBR/PCL_20	20	2234 ± 194	3129 ± 370
NBR/Nomex_*f_10*	10	910 ± 55	1161 ± 155
NBR/Nomex_*c_10*	10	1102 ± 107	1559 ± 238
NBR/Nomex_*f_20*	20	1346 ± 144	1403 ± 208
NBR/Nomex_*c_20*	20	1458 ± 184	1663 ± 188

4. Conclusions

Rubbery nanofibers, produced via single-needle electrospinning of NBR/PCL blend and NBR/Nomex emulsion, are very effective at hindering delamination in Mode I. The interlaminar fracture toughness improve up to +450%. Such results pave the way for the use of rubbery nanofibers for improving the service life and safety of components made of composite laminates.

5. Acknowledgments

This research was funded by the European Union - NextGenerationEU (National Sustainable Mobility Center CN00000023, Italian Ministry of University and Research Decree n. 1033 - 17/06/2022, Spoke 11 - Innovative Materials & Lightweighting) and Project Ecosyster—Ecosystem for Sustainable Transition in Emilia-Romagna, Project funded under the National Recovery and Resilience Plan (NRRP), Mission 04 Component 2 Investment 1.5 – NextGenerationEU, Call for tender n. 3277 dated 30/12/2021, Award Number: 0001052 dated 23/06/2022, within Spoke 1 activities—Materials for sustainability and ecological transition—(CUP J33C22001240001).

6. References

1. Wu X-F, Yarin AL. Recent progress in interfacial toughening and damage self-healing of polymer composites based on electrospun and solution-blown nanofibers: An overview. *Journal of Applied Polymer Science* 2013; **130**: 2225–37.
2. Wise CW, Cook WD, Goodwin AA. CTBN rubber phase precipitation in model epoxy resins. *Polymer* 2000; **41**: 4625–33.
3. Riew CK, Siebert AR, Smith RW, Fernando M, Kinloch AJ. Toughened Epoxy Resins: Preformed Particles as Tougheners for Adhesives and Matrices. *Toughened Plastics II*. Vol252. American Chemical Society, 1996: 33–44.
4. Bagheri R, Marouf BT, Pearson RA. Rubber-toughened epoxies: A critical review. *Polymer Reviews* 2009; **49**: 201–25.
5. Caldona EB, De Leon ACC, Pajarito BB, Advincula RC. A Review on Rubber-Enhanced Polymeric Materials. *Polymer Reviews* 2017; **57**: 311–38.
6. Williams RJJ, Rozenberg BA, Pascault J. *Reaction-Induced Phase Separation in Modified Thermosetting Polymers*., 1997.
7. Palazzetti R, Zucchelli A. Electrospun nanofibers as reinforcement for composite laminates materials – A review. *Composite Structures* 2017; **182**: 711–27.
8. Zheng N, Liu H-Y, Gao J, Mai Y-W. Synergetic improvement of interlaminar fracture energy in carbon fiber/epoxy composites with nylon nanofiber/polycaprolactone blend interleaves. *Composites Part B: Engineering* 2019; **171**: 320–8.
9. Daelemans L, van der Heijden S, De Baere I, Rahier H, Van Paepegem W, De Clerck K. Damage-Resistant Composites Using Electrospun Nanofibers: A Multiscale Analysis of the Toughening Mechanisms. *ACS Applied Materials & Interfaces* 2016; **8**: 11806–18.
10. Daelemans L, Kizildag N, Van Paepegem W, D'hooge DR, De Clerck K. Interdiffusing core-shell nanofiber interleaved composites for excellent Mode I and Mode II delamination resistance. *Composites Science and Technology* 2019; **175**: 143–50.
11. Maccaferri E, Mazzocchetti L, Benelli T, Brugo TM, Zucchelli A, Giorgini L. Self-Assembled NBR/Nomex Nanofibers as Lightweight Rubbery Nonwovens for Hindering Delamination in Epoxy CFRPs. *ACS Applied Materials & Interfaces* 2022; **14**: 1885–99.
12. Maccaferri E, Mazzocchetti L, Benelli T, Brugo TM, Zucchelli A, Giorgini L. Rubbery nanofibers by co-electrospinning of almost immiscible NBR and PCL blends. *Materials and Design* 2020; **186**: 108210.
13. ASTM D5528-13 - Standard Test Method for Mode I Interlaminar Fracture Toughness of Unidirectional Fiber-Reinforced Polymer Matrix Composites. *American Society for Testing and Materials*2013; doi 10.1520/D5528-13.2.
14. Zhang X, Chase GG. Electrospun elastic acrylonitrile butadiene copolymer fibers. *Polymer* 2016; **97**: 440–8.
15. Thielke MW, Bruckner EP, Wong DL, Theato P. Thiol-ene modification of electrospun polybutadiene fibers crosslinked by UV irradiation. *Polymer* 2014; **55**: 5596–9.
16. Wu H, Hu Q, Zhang L, Fong H, Tian M. Electrospun composite nanofibers of polybutadiene rubber containing uniformly distributed Ag nanoparticles. *Materials Letters* 2012; **84**: 5–8.
17. Saghafi H, Ahmadi I, Khamedi R et al. The thickness effect of rubbery nanofibrous mat on modes I–II fracture mechanism of composite laminates. *Thin-Walled Structures* 2024; **196**: 111556.

Digital volume correlation analysis of carbon fibre-reinforced thermoplastic sheet moulding compounds

S.E. Madi*‡ [1], Y. Wan**‡ [2], K. Madi[3], J. Soete[1], S.V. Lomov[1], Y. Swolfs[1]
[1] Department of Materials Engineering, KU Leuven, Kasteelpark Arenberg 44 bus 2450, Belgium
[2] Department of Systems Innovation, School of Engineering, The University of Tokyo, 337, Eng. Bldg. 3, 7-3-1, Hongo, Bunkyo-ku, Tokyo 113-8656, Japan
[3] 3Dmagination Ltd. Atlas Building, Fermi Avenue, Harwell Oxford, Didcot OX110QX United Kingdom
* salaheddineemine.madi@kuleuven.be, Tel: 0032467029781
** wan-yi@cfrtp.t.u-tokyo.ac.jp, Tel: 0081358410865
‡These authors contributed to the work equally and should be regarded as co-first authors

Abstract
The mechanical characterisation of carbon fibre-reinforced thermoplastic sheet moulding compound (CFRTP-SMC) materials has gained a lot of attention thanks to its growth. Mechanical simulations deliver poor results for this material, mainly because of its complex internal geometry. *In-situ* X-ray Computed Tomography (XCT) testing coupled with digital volume correlation (DVC) is a powerful alternative experimental method for characterising the mechanical behaviour of composite materials such as CFRTP-SMC materials, in direct relation to its local reinforcement geometry. Within this study, the focus was on the failure behaviour during the loading of this material. The *in-situ* XCT test, conducted at the KU Leuven XCT Core Facility encompassed three loading steps leading to material failure, with scans performed after each load level, involving five samples to validate the experimental method, and assess the influence of fibre length on the internal geometry and failure characteristics of CFRTP-SMC.

The DVC results have enabled a new path to segment damage based on the correlation residual maps and investigate damage mechanisms in this type of material by linking the microstructure with the strain localisations and the microcrack initiation area. Successful tests were conducted on all the samples, resulting in 3D quantitative data and visual output on the evolution of the microstructure of the material, such as displacement and strain maps, fibre/strand orientations and porosity.

Keywords: Composites, *In-situ* testing, Digital volume correlation

1. Introduction

Carbon Fibre Reinforced ThermoPlastics (CFRTP) are crucial in developing lightweight structures for high-volume production, essential for achieving sustainable green transformation and carbon neutrality. Carbon Fibre Sheet Moulding Compounds (CF-SMCs) combine the high performance of long-fibre prepregs with the ability for complex shape moulding, making CFRTP-SMC widely used in structural components, especially in automotive and sports industries. Compression moulding of CF-SMC results in tape deformation and changes in fibre orientation, leading to complex internal geometries and significant variations in mechanical properties [1]. A thorough understanding and accurate prediction of this material's performance require comprehensive research due to its intricate internal structure [2].

An extensive analysis of CF-SMC's mechanical properties was conducted with a focus on internal morphology [3-5]. Despite efforts to incorporate features like fibre orientation into modelling to improve prediction accuracy, a persistent mismatch between simulations and experiments remains, largely due to the complexity of internal morphology. Various studies have aimed to uncover CF-SMC's failure mechanisms. *In-situ* X-ray computed tomography (XCT) mechanical testing [6, 7] offers a promising approach to capture its complex micro- and meso-structures, although quantitative assessments remain limited. This study conducts microfocus *in-situ* XCT tensile tests on high-performance CFRTP-SMC, capturing internal morphologies at different stress levels. DVC [8-10] analysis enables a detailed examination of spatial strain distribution, defect distribution, crack initiation processes, and their correlations with material microstructure, aiming to provide profound insights into CFRTP-SMC failure mechanisms.

2. Materials and methods

2.1 Materials

The CFRTP-SMC utilised in this study consists of randomly oriented prepreg unidirectional tapes. These tapes are manufactured using spread carbon fibre tow (TR50S, Mitsubishi Rayon Co., LTD.) and polyamide-6 (PA6, DIAMIRON™ C, Mitsubishi Plastics, Inc.). The fibre volume fraction of the CFRTP-SMC averages 50%. The ultra-thin prepreg tapes employed here have an average thickness of 50 μm, thinner than conventional tapes which are typically 150 μm or thicker. The tapes were cut into rectangles measuring 5 mm wide and 30 mm long.

For the moulding process, the tapes were randomly distributed in-plane and moulded using a hydraulic compression machine. The moulding conditions involved 30 minutes of compression at a pressure of 5 MPa and a temperature of 270 °C, followed by an air-water hybrid cooling process at a cooling rate of 20°C/min. Subsequently, after the formation of CFRTP-SMC plates, specimens were prepared for *in-situ* tensile XCT testing. The geometry of these specimens was specifically tailored to fit the tensile rig utilised in this study (**Figure 1**).

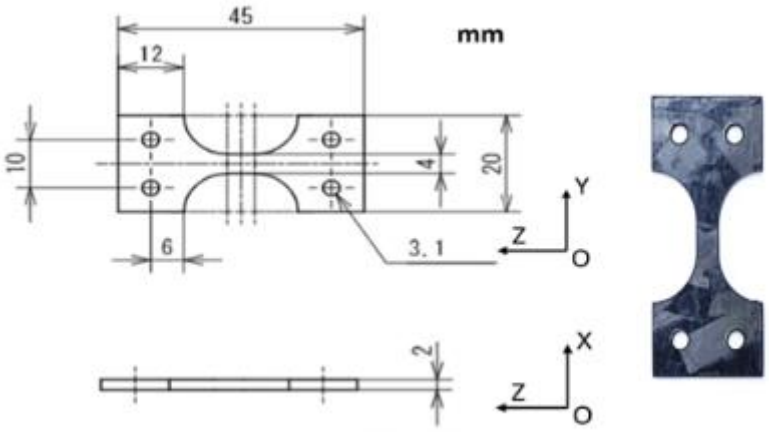

Figure 1. Geometry of the *in-situ* tensile 4D-XCT specimens.

2.2 In-situ tensile 4D-XCT after relaxation

A modified loading rig (Deben CT5000) with a 5 kN load cell (with an overall uncertainty of ±1 % of the full scale) was employed to apply load to the specimen. The specimens were secured in serrated tensile clamps using screws to prevent slippage, and stability was further ensured by pinning the specimen to the clamps with four steel pins. Modifications to the rig included incorporating modular spacers to accommodate different specimen lengths, ranging from 5 mm to 35 mm. Additionally, a long (150 mm) carbon fibre composite tube was installed to absorb the force applied to the sample, reduce X-ray attenuation and allow operation at smaller source-to-object distances, resulting in higher magnification and reduced scan time. The motor drives the lower jaw, while the upper jaw remains stationary, fixed to the composite tube.

At the beginning of the experiment, a preload of 150 N was applied, and the specimen was scanned twice. The two preload repeat scans were utilised to evaluate the precision and accuracy of DVC by examining the measurement error. XCT scan parameters (TESCAN UniTOM XL, with a 230 kV/300 W X-ray tube) were set at a tube voltage of 60 kV, a current of 250 µA, and an isotropic voxel with an edge size of 4 µm, utilising 1920 x 1896 pixels on the detector. Subsequently, *in-situ* stepwise tensile tests were conducted at three displacement-controlled loading steps (0.65 mm, 0.75 mm, and 0.93 mm) with a constant displacement rate of 0.1 mm/min. After each step, the specimen was first allowed to relax for 15 minutes to prevent movement during XCT acquisition. The scan duration was approximately 1 hour 30 minutes, with an additional 15 minutes for reconstruction from 2000 angular projections, utilising a 10% Gaussian filter with the TESCAN Panthera software. Image processing was carried out using Thermo Scientific Amira-Avizo 2023.1 software.

For the XCT data analysed in this study, a consistent coordinate system was established: the X-axis was perpendicular to the in-plane direction of the specimen, the Y-axis aligned with the specimen's width, and the Z-axis corresponded to the loading direction (length direction of the specimen), as illustrated in **Figure 2.b**. Before DVC analysis, 3D datasets were filtered using a 3D Gaussian filter with a small kernel size of 1 (standard deviation: 1 pixel) to remove high-frequency noise and enhance the correlation process. The XCT data were converted to 8-bit to expedite DVC calculations.

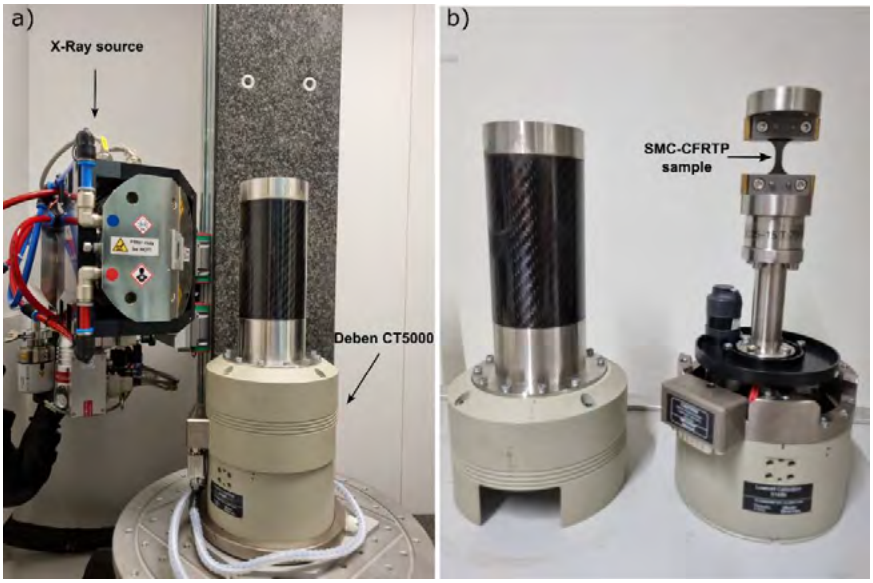

Figure 2. *In-situ* test equipment: a) XCT *in-situ* testing setup as mounted during the scan, b) Deben CT5000 rig with the top cap removed and the SMC specimen fixed in the tensile clamps.

2.3 Image processing and digital volume correlation

The DVC and image processing parts were realised in the Thermo Scientific Amira-Avizo2023.1 software. A robust DVC strategy, implemented in the XDigitalVolumeCorrelation module of Avizo, was utilised to compute displacements and strains at various loading steps. A global finite element (FE)-based correlation algorithm analysed the entire volume of interest, minimising the sum of squared differences between reference and deformed images, known as the correlation residual. Results were considered reliable when the standard deviation of residuals matched image noise. Compared to subset-based local DVC methods, this approach ensured displacement continuity, yielding more robust and accurate results.

An unstructured mesh comprising four-node tetrahedrons (T4 elements) was generated from the specimen shape to measure DVC displacements. Green-Lagrange strain formulation derived strains from displacements. The mesh generator, part of the XDigitalVolumeCorrelation module, employed a tetrahedral meshing approach tailored for DVC applications. Optimal mesh size balanced spatial resolution and measurement uncertainties. Element size adjustment, correlated with two repeat scans, maintained uncertainty levels by incrementally varying element size (50 to 140 voxels). Standard displacement and strain uncertainties were measured relative to mean values, with systematic errors calculated from spatial averages of displacements/strains.

To quantify microcrack progression, the first principal strain map at loading step 3 was correlated with initial local pore density and fibre orientation near damaged zones. Correlation residuals were used to segment the microcracks and dilated by 10 voxels to define damaged zones. Data were remapped onto a refined tetrahedral grid mesh for comparison. Tensile strain, calculated by rig displacements, was compared with average axial strain from DVC measurements. Python scripts collated relevant data into spreadsheets, excluding nodes outside damaged zones. Based on the generated 2D scatter plots within damaged zones, we explored the causes of progressive damage development.

3. Results and discussion

3.1 Measurement uncertainties

During the DVC analysis, the entire deformed series was referenced to the first preload scan volume. Deformed XCT datasets were initially aligned with the reference dataset using registration techniques to mitigate rigid body motion. A consistent reference mesh (mesh size: 90 voxels) was employed for all DVC computations, with displacements from each step initialising subsequent computations. Larger displacements observed between the first step and reference necessitated utilising displacements obtained on a coarser mesh (mesh size: 200 voxels) as an initial guess for the final FE DVC analysis on the reference mesh. Successful convergence of all DVC analyses occurred after 96-124 iterations, resolving the matrix inversion problem.

Cracks often violate continuity across the cracked surface, visible in the residual image, aiding crack detection. A non-local means filter was employed to denoise the correlation residuals image, and a combination of black top-hat and region-growing algorithms was utilised to segment microcracks. To better understand damage mechanisms, DVC strain maps were correlated with initial local pore density and fibre orientation, calculated using custom Python plugins in Avizo.

3.2 Strain map

Figure 3.a illustrates the full-field axial strain maps at the last loading step, offering a comprehensive visualisation of strain distribution during loading. The average axial strain was computed from the loading rig displacement (pre-relaxation) and DVC measurements (post-relaxation) for each loading step, with the corresponding stress-strain correlation plotted using experimental stress data. The average axial strain derived from DVC measurements notably differs from that calculated from loading rig displacement, aligning more closely with behaviours observed in standard tensile tests.

Compared to the average failure strain of 1.1% observed in standard tensile tests of the same CFRTP-SMC, the principal strains after relaxation are slightly higher. This discrepancy primarily stems from two factors. Firstly, *in-situ* compared to standard tests, the smaller size of specimens used in *in-situ* XCT may not consistently reflect average mechanical performance due to variations in fibre orientation caused by strand distribution. Secondly, conventional tensile tests typically measure surface strain, capturing only average strain across the measured area. At the same time, DVC analysis reveals detailed strain distribution within the entire 3D observation area, including strain concentrations induced by internal defects or oriented strands. This comprehensive measurement approach may contribute to relatively higher strains reported in DVC results.

Figure 3.c illustrates the full-field first principal strain maps generated at the last loading step, which are crucial for analysing potential strain concentrations and the likelihood of initial microcrack formation within the specimen. The local strain concentrations, reaching approximately 2.5%, were observed. Compared to the average axial strain, the first principal strain exhibits a higher maximum value, primarily due to significant local strain concentration resulting from heterogeneity induced by the random distribution of strands and other internal structural defects.

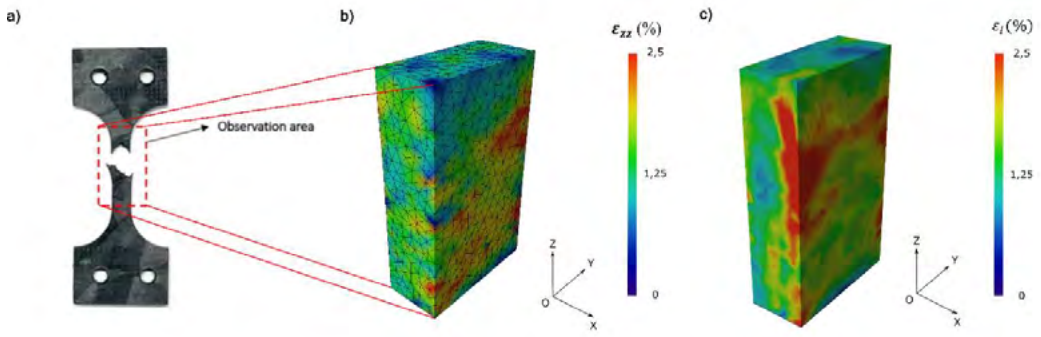

Figure 3.a) Fracture of the specimen, b) Step 3 Z -axial strain, c) 3D visualisation of the first principal strain (step 3)

4. Conclusion

This study presents findings from *in-situ* tensile XCT tests on CFRTP-SMC specimens and subsequent DVC analysis, a novel approach for this material. Key conclusions are as follows:

- DVC analysis addressed measurement uncertainty, enhancing quantification reliability and XCT image data resolution.

- Strain distribution observations under increasing loading unveiled correlations with pore density, strand orientation, and microcrack formation, elucidating microcrack initiation mechanisms.
- Improving internal morphology regularities could enhance material mechanical performance, as microcrack propagation indicates final fracture. These insights signify a significant stride in comprehending CFRTP-SMC's mechanical behaviours and failure mechanisms.

5. Acknowledgements

The authors acknowledge the KU Leuven XCT Core facility for their assistance with 3D image acquisition and post-processing tools (https://xct.kuleuven.be/). Additionally, this work received partial support from JSPS KAKENHI Grant Number JP23K13556.

6. References

[1] Wan et al., "Stochasticity modeling and analysis of elastic modulus of randomly oriented strands," *Adv Compos Mater,* vol. 30(3), 2021.

[2] Bing Xiao et al., "Characterization and elastic property modeling of discontinuous carbon fiber reinforced thermoplastics prepared by a carding and stretching system using treated carbon fibers," *Composites Part A: Applied Science and Manufacturing,* vol. 126:105598, 2019.

[3] Wan et al., "Tensile and compressive properties of chopped carbon fiber tapes reinforced thermoplastics with different fiber lengths and molding pressures. ," *Composites Part A: Applied Science and Manufacturing,* vol. 87, pp. 271-281, 2016.

[4] Li et al., "Experimental investigation of randomly-oriented tow-based discontinuous composites and their equivalent laminates," *Composites Part A: Applied Science and Manufacturing,* vol. 102, pp. 64-75, 2017.

[5] Tyler Cleveland Paolo Feraboli, Patrick Stickler, John Halpin, "Stochastic laminate analogy for simulating the variability in modulus of discontinuous composite materials," *Compos Part a-Appl S,* vol. 41, 2010.

[6] Holmes et al., "Digital image and volume correlation with X-ray micro-computed tomography for deformation and damage characterisation of woven fibre-reinforced composites," *Compos. Struct.,* vol. 279 p. 114775, 2022.

[7] A. Buljac et al., "Digital Volume Correlation: Review of Progress and Challenges," *Exp. Mech.,* vol. 58, 2018.

[8] Madi et al., "In situ characterization of nanoscale strains in loaded whole joints via synchrotron X-ray tomography," *Nat. Biomed. Eng.,* vol. 4, 2020.

[9] Madi et al., "Computation of full-field displacements in a scaffold implant using digital volume correlation and finite element analysis," *Med Eng Phys,* vol. 35, 2013.

[10] Mehdikhani et al, "Digital volume correlation for meso/micro in-situ damage analysis in carbon fiber reinforced composites " *Compos Sci Technol,* vol. 213, 2021.

APPLICATIONS OF PLASMA TREATMENT OF RECYCLED CARBON FIBRES

NOVOTNÁ Jana[1], TOMKOVA Blanka[2], JELÍNEK ŠOURKOVÁ Hana[3]

[1] Faculty of Textile engineering, Department of Material Engineering, Technical University of Liberec, Studentská 2, Liberec, Czech Republic
Email: jana.novotna3@tul.cz, Web Page: www.ft.tul.cz
[2] Faculty of Textile engineering, Department of Material Engineering, Technical University of Liberec, Studentská 2, Liberec, Czech Republic
Email: blanka.tomkova@tul.cz, Web Page: www.ft.tul.cz
[3]Faculty of Mechatronics, Informatics and Interdisciplinary Studies, Technical University of Liberec, Studentská 2, Liberec, Czech Republic
Email: hana.sourkova@tul.cz, Web Page: www.tul.cz

Keywords: recycled carbon fiber, plasma treatment, epoxy composites

Abstract

To improve the mechanical properties of the epoxy resin, short recycled carbon fibers with a length of 100 µm were used as a filler in this study. To improve the compatibility of the recycled fibers with the epoxy matrix, a plasma treatment was used as the surface treatment of the carbon fibers. Surface functionalization was by XPS analysis, SEM and WCA. For comparison, composite samples filled with recycled carbon fibers with and without plasma treatment were prepared at low concentrations (1 wt% and 2.5 wt%) and high concentrations (20 wt% and 30 wt%) by weight ratio. Mechanical properties were analyzed on these samples. Improved impact strength, increased modulus of elasticity, and improved flexural stress occurred in composite samples with a low concentration (1 wt%) of plasma-treated fibers compared to samples with untreated fibers. At higher fiber concentrations, the plasma treatment worsened the mechanical properties of the composite samples compared to the samples with untreated fibers. However, there was a slight reduction in the variance of measured values quantities in the samples filled with plasma-treated fibers for all types of measurements.

1. Introduction

Epoxy resins have many excellent utility properties; they excel in good adhesion to a wide range of materials, good chemical and thermal resistance after curing. They are dimensionally stable and shrink little during the production preparation process [1]. The low molecular weight of uncured epoxy resins in the liquid state leads to high molecular mobility during processing and leads to good wettability on the surface of carbon fibers [2,3]. The crosslinking reactions continue to proceed rapidly, and as a result, high crosslinking densities are decided, making epoxy resins more brittle. This brittleness (toughness) can be influenced by suitable filling [4-6]. Various materials can be used as fillers for epoxy matrices, such as carbon-based materials; short recycled carbon fibers are selected in this study. The selected epoxy resin affects the viscosity, which is particularly advantageous if it consists entirely of short fibers since low viscosity leads to good wettability of the fibers. Casting technology was used to produce the experimental samples, as this method of production does not cause any damage to the fibers, unlike injection molding technology.

When preparing two-component composites with filler, the filler must be well mixed with the epoxy resin. The epoxy resin consists of two components - epoxy and hardener. The epoxy part has a higher viscosity; the hardener has a lower viscosity. From a technological point of view, it is easier to mix short fibers first into the hardener and add epoxy. At higher fiber concentrations, it is difficult to mix a mixture of hardener and filler into the epoxy; stirring with a magnetic stirrer is impossible due to the mixture's high viscosity; it is necessary to stir by hand. Surface plasma treatment of fibers was chosen as a possible solution. Several plasma treatments of carbon fibers are available [7, 8]. As these were recycled fibers, it had to be considered that the treatment chosen was sufficiently "gentle" on the fibers, as the recycling process itself could affect the surface of the recycled fibers compared to the original carbon fibers [9]. In Lee [10] and Altay [11], plasma treatment is recommended for short recycled fibers. Both studies confirmed the effects of plasma on PAN-based recycled carbon fibers. There was a slight deepening of the corrugated fiber surface, the increased surface roughness of treated fibers, and improved composites' flexural strength and modulus filled with plasma-treated recycled carbon fibers. The interface between the fibers and resin plays a key role in fiber-reinforced composites [12]. Appropriate chemical modification of the surfaces can make the fibers easily wettable, thereby reducing cavities and bubbles in composites, especially at the fiber-resin interface. The application of plasma treatment to functionalize the surface of recycled carbon is advantageous over other treatments, mainly due to the possibility of precise setting of treatment parameters (type of gas, power, type of source) [13]. Moreover, the plasma treatment time is relatively short. The type and concentration of functional groups depending on the properties of the plasma used. They most often form hydroxyl, and carboxyl groups [14-17]. In particular, after treatment fibers showed significantly more COOH groups, which are removed during recycling [10]. For carbon fibers, the surface roughness usually increases during plasma treatment [18]. Disadvantages of plasma treatment include that plasma-treated surfaces can be deactivated when exposed to air due to recombination of radicals and must be immediately incorporated into the matrix [19, 20]. One possible reason for the loss of efficiency of plasma carbon fiber treatment after prolonged storage, the adhesion depends on the active chemical groups of the outer surface of the fibers. Long-term exposure of these sites to air leads to surface reorganization, reducing total surface energy [21]. Plasma treatment can induce deeper local oxidations leading to changes in surface topography as revealed by SEM were also considered, as reported, for example, by Donnet [22].

This study analyzes the mechanical properties of carbon fiber reinforced RCF/EP epoxy composites at low concentrations (1 wt% and 2.5 wt%) and high concentrations (20 wt% and 30 wt%) at the following concentrations: (a) recycled RCF short carbon fibers, (b) plasma-treated recycled RCF short carbon fibers. The mechanical properties were analyzed using the impact toughness and flexural strength test. These tests were chosen because, based on knowledge of fiber-reinforced composite materials, it can be assumed that the test specimens have low ductility. During tension, the applied tensile force would act mainly on the material matrix, and the reinforcement from short fibers would not significantly help the tensile strength. The effect of plasma on recycled carbon fibers was analyzed by XPS analysis, WCA, and SEM scanning electron microscopy.

2. Experiment

2.1. Materials

An epoxy matrix system made from bisphenol A-based low-viscosity epoxy resin LR 285 was used, along with cyclic-aliphatic polyamine curing agent H 508, with a mixing ratio 100:40 by weight [4]. The density of the resin was 1.200 kg/m^3, and the density of the hardener was 1.030 kg/m^3. The specimens were filled with low (1 wt% and 2.5 wt%) and high (20 wt% and 30 wt%) concentrations of RCFs. Commercially available PAN-based Carbiso Milled Carbon Fibers (RCF), with a density of 1.800 kg/m^3, were obtained. Because the fibers were recycled, they were without sizing. They have diameters of approximately 7.0 ± 0.3 μm and lengths of 100 ± 9 μm [5].

2.2. 1. Plasma treatment of recycled carbon fibers

RCFs were placed in a plasma reactor (SurfaceTreat LA 400) with a special mixing mechanism designed for loose materials. The reactor includes a plasma aluminum chamber. On top of the chamber is a 2.45 MG plasma generator with 1 kW of power. A duty cycle of 70%, which has the ideal O-atom density, was used for the plasma treatment. The bottom of the mixing pot was placed 15 cm from the MG plasma generator. Working gases were brought into the chamber with a flowmeter (O_2/H_2, 99.5/99.9), and the pressure in the chamber was specified using a Pirani vacuum gauge regulated by a butterfly valve set to 10^2 Pa.

2.2. 2. Characterization of recycled carbon fibers

SEM. Characterization of the effect of plasma treatments on recycled carbon fibers was performed using scanning electron microscopy (SEM; VEGA 3 TESCAN); the images are shown in Figure 3.
WCA. Wettability measurements were performed by determining the water contact angle (WCA). It was measured using a DSA30 droplet shape analyzer (Krüss) with a water volume of 3 µl; the RCF was spread on adhesive tape to measure the contact angle. Drops were applied to each prepared sample, and then the approximate WCA value was calculated. The measurement results are shown in Figure 4.
X-ray photoelectron spectroscopy. The spectra were measured in the spectrometer analysis chamber under a residual gas pressure of 10^{-8} Pa. The spectra in the binding energy range 0–1000 eV were measured, and spectral regions containing C 1s, O 1s, and N 1s electron lines were measured at room temperature. The chemical compositions of the samples' surface layers were calculated using the integrated intensities of the photoemission lines after a nonlinear background reading. To fit and quantify the spectra and thus correct the transmission function, XPSPEAK4.1 and Casa XPS were used. The measurement results are shown in Figure 5.

2.2. 3. Preparation of composite samples RCF / EP

The mixture of epoxy, hardener, and fibers was stirred at room temperature for 10 minutes using a magnetic stirrer. At higher concentrations above 10 wt%, it was impossible to use a magnetic stirrer due to the high viscosity of the resulting mixture. After the use of plasma treatments, the possibility of mixing was significantly improved; with the use of plasma-treated recycled fibers, it was possible to use magnetic stirring up to 20 wt% of the fibers. Samples with higher concentrations were mixed manually. The mixture was then poured into pre-separated glass molds and allowed to stand for 24 hours at room temperature. After curing, the mixture was left in an oven for 15 hours at 60 ° C. The thickness of each sample varied, ranging from 2 to 3.10 mm. The overall sample preparation process is shown in [23].

3. Results and discussion

3.1. Analysis and morphology of fibers

SEM images. If we compare the SEM images of the recycled carbon fibers in Fig. 1, we see the defects in the plasma-treated fibers during the plasma treatment. Donnet [20] also draws attention to the possibility of these defects. It can be assumed that massive defects of the surface layers of the basal planes can adversely affect the mechanical properties of composites prepared from these fibers, especially at higher concentrations. The surface morphology of the recycled carbon fibers is characterized by grooves arranged along the fiber axis resulting from the fiber manufacturing process. After plasma treatment, these features deepened, and the number of small particles irregularly distributed on the surface of the fibers was reduced.

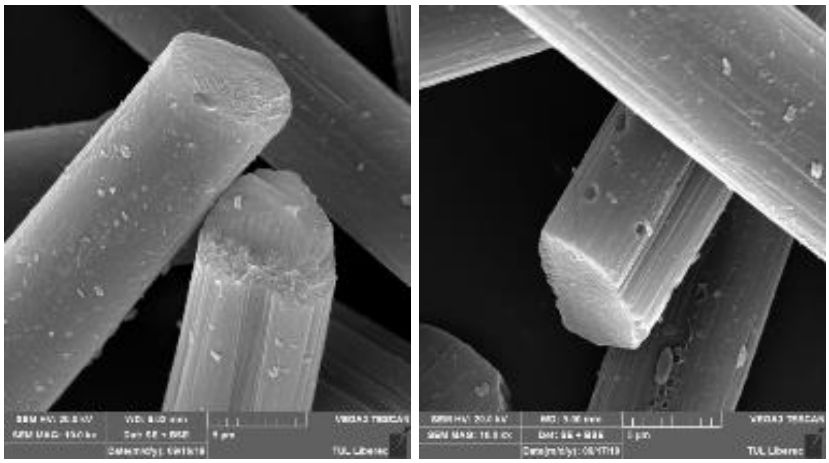

(a) (b)

Figure 1. SEM images of used RCF: (a) RCF, (b) plasma treated RCF

The contact angle WCA is strongly influenced by the surface roughness of the fibers; however, it also displays signs of plasma treatment. Fig. 2 shows that it can be observed that plasma treatment has a significant influence on the changes in hydrophobic character of RCFs. Non-treated fibers show hydrophobic behavior, while plasma-treated fibers show hydrophilic behavior. The increased hydrophilicity of the fibers is probably caused by the binding of oxygen groups on the fibers' surfaces; this is likely also the cause of the increased surface roughness.

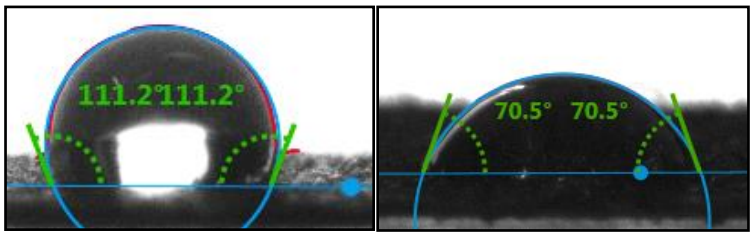

(a) (b)

Figure 2. WCA of used RCF: (a) RCF, (b) plasma treated RCF

X-ray photoelectron spectroscopy. In addition to the most intense components belonging to sp2 and sp3 hybridized carbon (89% of the total carbon), on the Figure 5, the electron spectra *C1s* also contain less intense components belonging to -C-O, -C=O, and -O-C=O bonds, in accordance with the literature [24]. The electron spectra *C 1s* are identical in both samples, which, together with the results presented in Table 1, show that plasma treatment under the studied conditions led to changes in the chemical composition of the surface layers.

Table 1. Concentration of carbon, oxygen, and nitrogen in fiber calculated from integrated electron emission intensities

Element	C	O	N
RCF [atomic %]	84.9 ± 1.1	11.4 ± 0.2	3.7 ± 0.1
plasma treated RCF [atomic %]	81.4 ± 0.9	14.3 ± 0.3	4,3 ± 0.2

Table 2. Comparison of plasma treatment conditions in this study, and in reference articles

References	Samples	Power	Time	Source type	Condition	Atomic ratio O/C
this study	RCF	-	-	-	-	0.13
this study	RCF + plasma	100W	10min.	MW	atmospheric	0.18
Altay [11]	RCF	-	-	-	-	0.20
Altay [11]	RCF + plasma	100W	70s	MW	atmospheric	0.33
Altay [11]	RCF + plasma	200W	70s	MW	atmospheric	0.43
Altay [11]	RCF + plasma	300W	70s	MW	atmospheric	0.58
Lee [10]	RCF	-	-	-	-	0.12
Lee [10]	RCF + plasma	800W	0.5s	RF	atmospheric	0.25

If we compare the results of the O / C ratios given in Table 2, we see that in all studies, the 0 / C ratio of plasma-treated fibers increased. This is a general trend, with the O / C ratio also increasing with increasing source power used, as confirmed in [25-26].

3.2. Characteristics of RCF / EP composites

The dispersion of the fibers in the matrix was evaluated. From the morphology of fiber composites, we see that dispersed RCF fibers can transmit stresses that lead to the absorption of external energy during the mechanical test. When cracks form in the composite, destruction of the composite can be prevented by the scattered fibers. We see evident differences if we compare images of composites filled with RCF and plasma-treated RCF, especially at low fiber concentrations (1 wt% and 2.5 wt%).

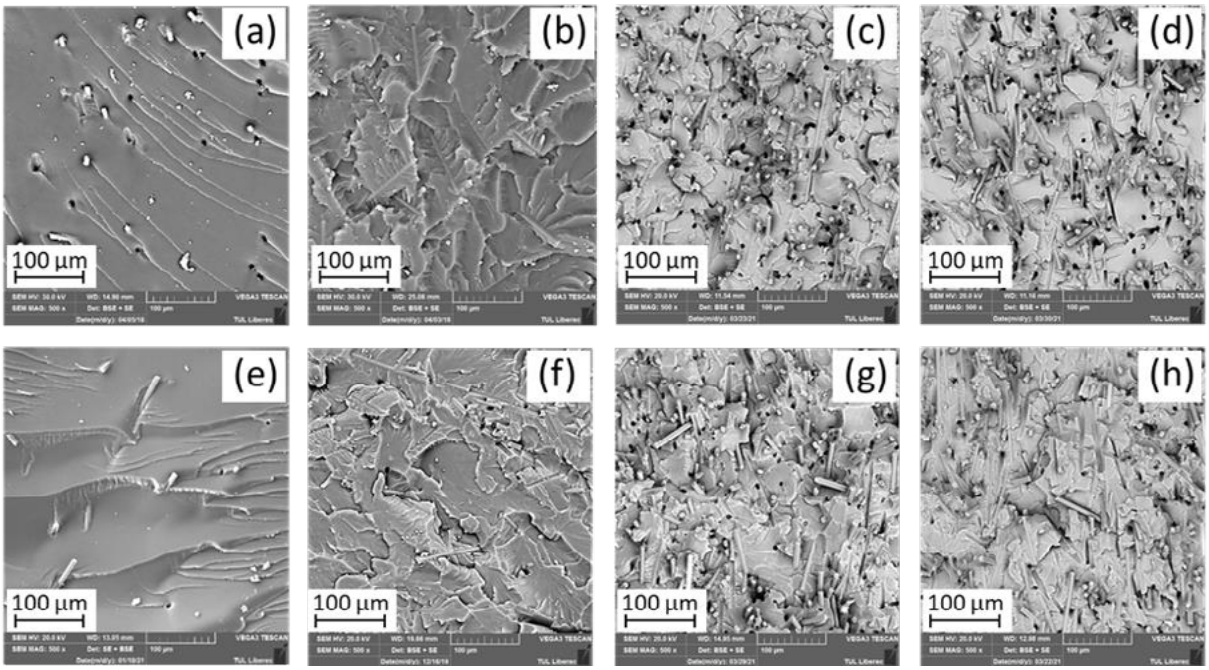

Figure 3. SEM images of fracture surfaces of composite samples: composites filled with recycled carbon fibers (a) 1 wt%, (b) 2.5 wt%, (c) 20 wt% (d) 30 wt%, composites filled with plasma-treated recycled carbon fibers (e) 1 wt% , (f) 2.5 wt% (g) 20 wt% (h) 30 wt%

The impact strength of RCF / EP composites. Figure 4 shows significant differences in the mechanical properties of composites presented as a result of impact strength. By comparing the measured values with the impact strength of pure resin (A = 37.4 J/m^2, marked with a red dashed line in Figure 4), it is clear that plasma treatments improve the impact resistance of samples. Samples with low filler concentrations have higher impact strength, while samples with high filler concentrations have lower impact strength. Low fiber concentrations (1 wt% and 2.5 wt%) increased the mechanical properties of the tested composites compared to the mechanical properties of the unfilled resin. The impact strength was improved in composite samples with low concentration (1 wt%) of plasma-treated fibers by 35% and 20% in fibers without plasma treatment. The variance of impact values is lower for plasma-treated fiber samples than for untreated fiber samples.
Booroj [17] confirmed that ILSS epoxy composites from plasma-treated carbon fibers show good interfacial adhesion between carbon fibers and epoxy resin, which increased after plasma modification. However, long plasma exposure time and high performance can partially destroy carbon fiber surface (as seen in this study in Figure 1). That could also be the reason for reducing impact values for composite samples with higher concentrations of plasma-treated recycled carbon fibers.

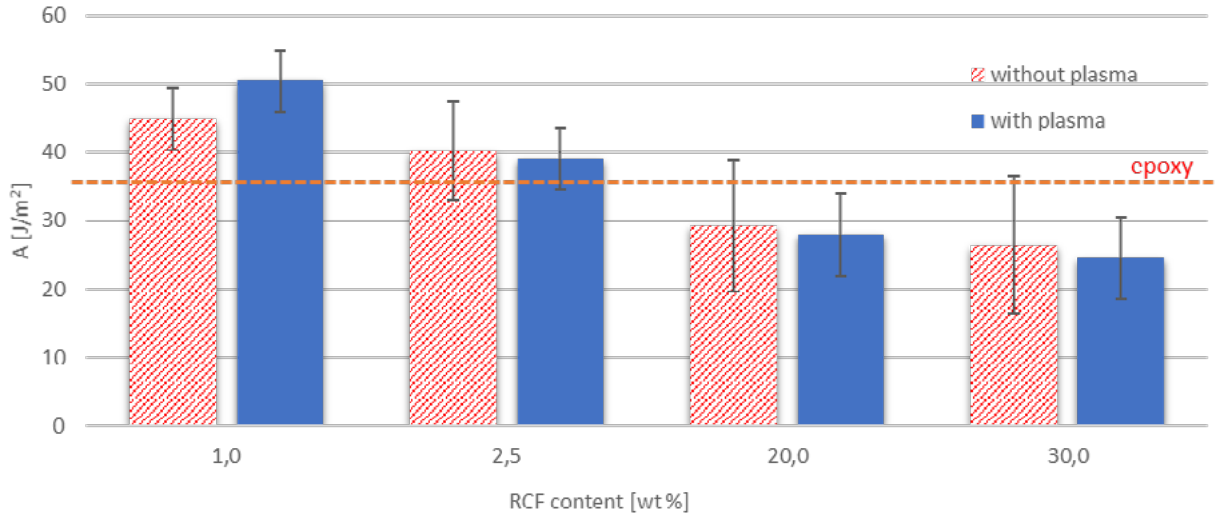

Figure 4. Impact toughness of RCF / EP composites

Three-point bending. Figure 5 show the values of modulus of elasticity and flexural stress of the tested composite samples. When comparing the values of pure resin (E = 3000MPa, σ = 11MPa, indicated by a red line in Fig. 8), the composites use the modulus of elasticity and the bending stress at all fiber concentrations. Plasma treatments improve the impact resistance of samples with low filler concentrations on the contrary for samples with high filler concentrations. The modulus of elasticity determined by three-point bending increased in composite samples with low concentrations (1 wt%) of plasma-treated fibers and by up to 20% and 10% in fibers without plasma treatment. The bending stress was improved by composite samples with fibers concentrations (1 wt%) of plasma-treated fibers and by 27% and 15% for fibers without plasma treatment. The variance of impact values is lower for plasma-treated fiber samples than for untreated fiber samples.
Comparing the results obtained with the results reported in Lee [10] and Altay [11], there were similar changes in the surface of recycled carbon fibers. However, in these studies, there was an improvement in the flexural strength of composite samples at 20 wt% fiber concentrations, while this work did not show this improvement. In [7-8], PP, which is a thermoplastic, is used as the matrix, while in this study, an epoxy matrix is used, known as a thermoset.

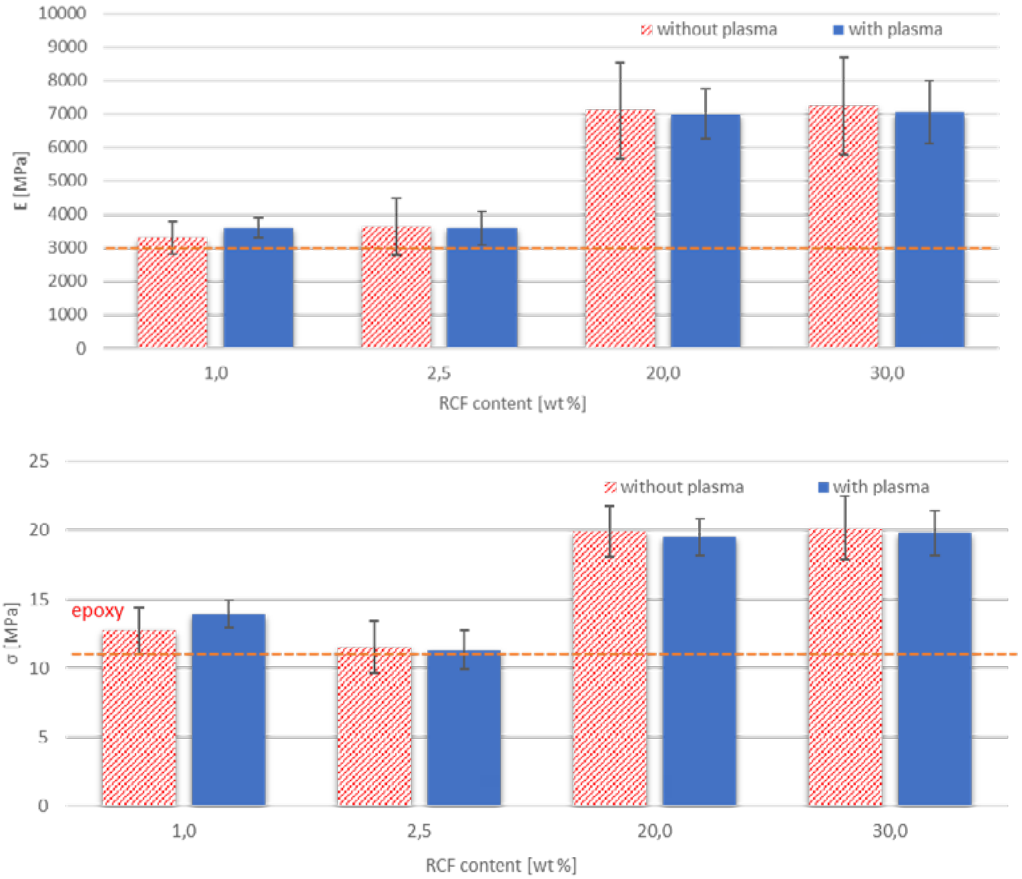

Figure. 5 Flexural strength RCF / EP

4.Conclusion

It has been confirmed that plasma treatments alter the surface layers of carbon fibers, as demonstrated in various studies [10-11]. This study showed the effect of plasma on short recycled CF. The plasma treatment used is of practical importance in processing plasma-treated short carbon fibers into epoxy resins. It contributes to significantly better fiber handling during the preparation of composite samples. The functionality of the plasma treatment was further verified by mechanical tests performed on composite samples prepared from these fibers. There was an increase in impact resistance, increased bending stress, and modulus of elasticity in samples with low filler concentrations (1 wt%). At the same time, the plasma treatment of recycled carbon fibers reduces the variability of the measured mechanical properties of the epoxy composites filled with these fibers, indicating that the use of plasma improves the dispersibility of the fibers in the epoxy matrix.
The following conclusions regarding the mechanical properties of RCF / EP are based on this study:
The small amount of RCF fibers in the epoxy has a strong effect on both the impact strength and the flexural strength of the composites. Epoxy composites filled with RCF showed brittle behavior after the addition of higher concentrations of filler. Thus, it can be said that at higher concentrations of filler in RCF / EP composites, agglomeration of particles is likely to occur, which may be the reason for the deteriorated impact strength of composites, as stated by Oszoy [27]. Plasma treatment applied to the surfaces of recycled carbon fibers is important for using RCF fibers in epoxy composites for applications at low concentrations of recycled carbon fibers.

Acknowledgements
Authors are grateful for the financial support from the Student research project 2019 No. 21308 supported by Czech Ministry of Education, and by Faculty of Textile, Technical University of Liberec.

References:

[1] MLEZIVA, Josef a Jaromír ŠŇUPÁREK. *Polymery*. 2000. ISBN 80-85920-72-7.
[2] VAN KREVELEN, D. W. a Klaas TE NIJENHUIS. *Properties of Polymers*. 2009. ISBN 9780080548197. doi:10.1016/B978-0-08-054819-7.X0001-5
[3] THOPPUL, S. D., A.J. FINEGAN a R. F. GIBSON. Mechanics of mechanically fastened joints in polymer-matrix composite structures - A review [online]. 2009, **69**, 301–329.
[4] DRZAL, Lawrence T., Michael J. RICH a Pamela F. LLOYD. Adhesion of Graphite Fibers to Epoxy Matrices: I. The Role of Fiber Surface Treatment. *Journal of Adhesion Science and Technology*.1983.
[5] TANG, Long Gui a John L. KAROOS. A review of methods for improving the interfacial adhesion between carbon fiber and polymer matrix. *Polymer Composites*. 1997. ISSN 02728397.
[6] CHUNG, Deborah D. L. *Composite Materials: Science and Applications*. 2010. ISBN 9781848828308. doi:10.1007/978-1-84882-831-5_1
[7] TIWARI, S. a J. BIJWE. Surface Treatment of Carbon Fibers - A Review. *Procedia Technology* [online]. 2014. ISSN 22120173. doi:10.1016/j.protcy.2014.08.064
[8] YUAN, L. Y., S. S. SHYU a J. Y. LAI. Plasma surface treatments on carbon fibers. II. Mechanical property and interfacial shear strength. *Journal of A. P.* 1991. ISSN 10974628.
[9] KUMAR, Sudheer a Sukhila KRISHNAN. Recycling of carbon fiber with epoxy composites by chemical recycling for future perspective: *Chemical Papers*. 2020, **74**, 3785–3807. ISSN 13369075.
[10] LEE, Hooseok, I. OHSAWA a J. TAKAHASHI. Effect of plasma surface treatment of recycled carbon fiber on carbon fiber-reinforced plastics interfacial properties. *Applied S. Science*. 2015. ISSN 01694332.
[11] ALTAY, Lutfiye, E. BOZACI, M. ATAGUR, K. SEVER, G. Se. TANTUG, M. SARIKANAT a Y. SEKI. The effect of atmospheric plasma treatment of recycled carbon fiber at different plasma powers on recycled carbon fiber and its polypropylene composites. *Journal of A.P. Science*. 2019. ISSN 10974628.
[12] DRZAL, Lawrence T. *Epoxy Resins and Composites II,*. Berlin: Springer-Verlag, 1986.
[13] DILSIZ, Nursel. Plasma surface modification of carbon fibers: A review. *Journal of Adhesion Science and Technology* [online]. 2000. ISSN 15685616. doi:10.1163/156856100743013
[14] SMILEY, R.J. a W.N. DELGASS. AFM, SEM and XPS charakterization of PAN-based carbon fibres in oxygen plasma. *J. Mater.Sci.* 1993, **288**, 3601–3611.
[15] TAKADA, T., M. NAKAHARA, H. KUMAGAI a Y. SANADA. Surface modification and characterisation of carbon black with oxygen plasma. *Carbon*. 1996. ISSN 00086223.
[16] SCHEFFLER, C., E. WÖLFEL, T. FÖRSTER, C. POITZSCH, L. KOTTE a G. MÄDER. Influence of microwave plasma treatment on the surface properties of carbon fibers and their adhesion in a polypropylene matrix. In: *IOP C. Series: Materials Science and Engineering*. 2016. ISSN 1757899X.
[17] BOROOJ, M.B. SHOUSHTARI, A.M., A. HAJI a E. N. SABETA. Optimization of plasma treatment variables for the improvement of carbon fibres/epoxy composite performance by response surface methodology. *Journal of Adhesion Science and Technology*. 2016.
[18] BISMARCK, Alexander, M. Emin KUMRU a J. SPRINGER. Influence of oxygen plasma treatment of PAN-based carbon fibers on their electrokinetic and wetting properties. *Journal of Colloid and Interface Science* [online]. 1999. ISSN 00219797. doi:10.1006/jcis.1998.5912
[19] HOECKER, F. a J. KARGER-KOCSIS. Surface energetics of carbon fibers and its effects on the mechanical performance of CF/EP composites. *Journal of A.P. Science*. 1996. ISSN 00218995.
[20] DONNET, J. B., M. BRENDLE, T. L. DHAMI a O. P. BAHL. Plasma treatment effect on the surface energy of carbon and carbon fibers. *Carbon* [online]. 1986. ISSN 00086223.
[21] BASCOM, W. D. a W. J. CHEN. Effect of plasma treatment on the adhesion of carbon fibers to thermoplastic polymers. *The Journal of Adhesion* [online]. 1991. ISSN 15455823.
[22] DONNET, J. B., T. L. DHAMI, S. DONG a M. BRENDLE. Microwave plasma treatment effect on the surface energy of carbon fibres. In: *Journal of Physics D: Applied Physics*. 1987. ISSN 00223727.
[23] NOVOTNÁ, Jana, Jana MÜLLEROVÁ, Miroslava PECHOČIAKOVÁ a Jiří MILITKÝ. *Influence of Filler Size and Structure on the electrical Properties of Carbon fiber reinforced composites*.
[24] HINTERREITER, A. P., J. DUCHOSLAV, M. KEHRER, T. TRUGLAS, A. LUMETZBERGER, C. UNTERWEGER, C. FÜRST a D. STIFTER. Determination of the s. chemistry of ozone-treated carbon fibers by highly consistent evaluation of X-ray photoelectron spectra. *Carbon*. 2019. ISSN 00086223.
[25] PROCTOR, Andrew a Peter M. A. SHERWOOD. X-ray photoelectron spectroscopic studies of carbon fibre surfaces. I. *Journal of E. S. and Related Phenomena*. 1982, **27**(1), 39–56.
[26] WANG, Yu-Qing, Feng-Qiu ZHANG a Peter M. A. SHERWOOD. X-ray Photoelectron Spectroscopic Study of Carbon Fiber Surfaces. *Chemistry of Materials*. 1999, **11**(9), 2573–2583.
[27] OZSOY, Iskender, A. DEMIRKOL, A. MIMAROGLU, H. UNAL a Z. DEMIR. The Influence of Micro- and Nano-Filler Content on the Mechanical Properties of Ep. Composites. *Journal of Mechanical Engineering*. 2015, **61**(10), 601–609.

ADDITIVE MANUFACTURING AND MECHANICAL TESTING OF INTERPENETRATING METAL COMPOSITES

Frederik Siegmund[1], Quirin Schneider[1], Joél Schukraft[1] and Kay A. Weidenmann[1]

[1]Institute of Materials Resource Management, Chair of Hybrid Composite Materials, University of Augsburg, Am Technologiezentrum 8, 86159 Augsburg, Germany
Email: frederik.siegmund@mrm.uni-augsburg.de, Web Page: uni-augsburg.de/mrm/hybw/

Keywords: multi-material, fused-filament-fabrication, metal-metal-composite, compression testing, triply periodic minimal surface

Abstract
Interpenetrating metal composites were created using a sub-process of Fused Filament Fabrication (FFF) called material extrusion additive manufacturing of highly filled polymers (MEAM-HP). The filament used is similar to pellets in metal injection molding (MIM) and consists of a thermoplastic matrix, which is filled to a high degree with metal powder. The two-step debinding and sintering process converts the green body into an interpenetrating metal composite without reaching the molten phase.
Three different triply periodic minimal surface (TPMS) structures, including gyroid, Schwarz-P, and Schwarz-D, each consisting of a 1:1 ratio of copper and stainless steel were manufactured.
Micrographs were prepared to identify flaws and cracks that occurred during sintering due to the different shrinkage of each phase. These results were then compared to the amount of open porosity from density measurements. Mechanical testing was conducted in the form of compression tests to investigate how the structure affects the results. The samples behave rather similar in the elastic regime, except for the Schwarz-P structure, a structural influence could be seen clearly in the plastic regime.
The influence of the microstructure and its pre-damage were compared to the obtained mechanical properties. The approach in this work allows interpenetrating structures with a minimal wall thickness of 0.21 mm and layer heights of 0.12 mm.

1. Introduction

In recent years, modern industrial applications, especially in the aerospace sector, have demanded the capability to combine disparate mechanical, chemical, and physical properties within a single structure [1, 2]. Some heavily stressed components require the integration of tailored properties which cannot be found within one material only, such as high thermal conductivity and thermal insulation, corrosion and oxidation resistance at elevated temperatures, yet maintaining adequate mechanical strength at lower temperatures, electrical conductivity, and thermal conductivity [3, 4].
Consequently, manufacturing additive multi-material structures out of metal is a viable solution for the required tasks and can produce more complex parts than classic multi-material manufacturing processes of plastic deformation like rolling, extruding and deep drawing or welding processes like explosion welding or friction stir welding. Metal additive manufacturing has been the subject of intensive research in recent years, both in terms of the materials that can be used and the possible process designs. Nevertheless, the range of materials is still limited, particularly with regards to the simultaneous use of several metallic materials in 3D [5]. Mainly laser powder bed fusion (L-PBF) and direct energy deposition (DED) are the focus of scientific research [6, 7]. With L-PBF, this resulted in commercial machines, which are capable of depositing metal powders selectively within a layer, allowing three-dimensional interpenetrating structures. Material combinations that have been successfully manufactured with L-PBF are for example stainless steel – nickel alloy [8], stainless steel – copper alloy [9] and steel – steel composites [10].
All processes that use the molten phase, including L-PBF and DED are dependent on the metallurgical compatibility of the constituent, or else unwanted alloys form at the interface and effects like the

Marangoni convection appear [8–11]. The transition area between the two alloys can be in the range of 300 µm [10] to 500 µm [9]. Furthermore, oxidated areas can be found within the material [12] or unwanted isolated islands of one alloy surrounded by the other alloy [9]. The occurrence of thermal expansions and intermetallic phases can give rise to the formation of cracks in the transition area [10]. Due to the differing thermal conductivities of the materials, the laser power must be optimally adjusted to the material to be lasered, as well as to the existing layer underneath. The dissipation of heat differs between materials, and thus the laser power must be adjusted accordingly. [13]
The transition to the filament-based MEAM-HP process (material extrusion additive manufacturing of highly filled polymers), as used by the authors, where a filament containing metal powder and a polymer binder, similar to pellets for metal injection molding (MIM), is printed with fused filament fabrication (FFF) and the absence of a molten phase when sintering afterwards, results in the absence of many of the aforementioned reaction-related structural characteristics. An additional advantage of using the MEAM-HP process is the ability to produce closed cavities within the component, improving its lightweight construction potential. Furthermore, the investment costs for these systems are lower compared to L-PBF and DED. The MEAM-HP process enables simple material changes within a layer, thus allowing the production of interpenetrating composites. In the field of ceramic materials, this process has already been researched for the depiction of complex components, as the necessary sintering is an elementary process step in ceramic production technology. The MEAM-HP process is well-suited to tool-free processing in small series, as demonstrated by the successful production of multi-material filaments on modified standard 3D printers [14]. The printer itself plays a subordinate role in the process, with the debinding and sintering process being of greater importance. Once the shrinkage rates and sintering kinetics have been adjusted, only the printing parameters need to be optimized in order to meet the requirements of the filaments. This approach enabled the production of delamination-free ceramic components that exhibited cracks only after sintering in complex geometries. As demonstrated by Clemens et al. [15], the use of filament printers with multiple print heads enables the production of ceramic multi-material composites or functionally graded composites. This approach was implemented by Wick-Joliat et al. [16] using a pellet-based method based on differently colored zirconium oxide for a molybdenum disilicide/alumina/feldspar composite. The material-related challenges are essentially the same: the formulations (in particular, the filament powder contents and powder particle sizes) must be coordinated in order to achieve comparable shrinkage in the individual components and thus prevent stress cracks during sintering. It is essential that the particle sizes are as homogeneous as possible and adapted to the diameter of the nozzle. Furthermore, it is necessary to select sintering progression curves and sintering end temperatures in such a way that all components are able to sinter.
The aim of the presented work is to show that it is possible to manufacture interpenetrating metal-metal composites with the MEAM-HP approach. By arranging multiple materials in a three-dimensional interpenetrating manner, functional and structural characteristics can be combined flexibly, leading to enhanced mechanical and thermal properties. Given that the process-structure-property relationships of additively manufactured hybrids, such as interpenetrating composites, are not only largely determined by the spatial arrangement of the constituents but can also be controlled within a wide range of parameters, homogeneity, anisotropy, and grading can be adjusted as desired within the process limits, the resulting structures can be largely optimized for the specific use case.

2. Materials and methods

The interpenetrating structures investigated were the so called triply periodic minimal surfaces (TPMS) Schwarz-D, Schwarz-P and Gyroid after Schoen [17]. One volume described by these surfaces was filled with copper (99.8% purity), the other with 17-4PH stainless steel leading to a completely filled interpenetrating composite. Both, copper, and steel filaments were produced by Markforged Inc., Watertown, USA and are commercially available. The structures and their copper and stainless steel phases can be seen in Figure 1. The gyroid structure is commonly used as an infill in FFF, as it has almost isotropic properties. The Schwarz-D structure has a higher stiffness and can absorb more energy than Schwarz-P [18]. Because of its homogeneous curvature and structure, Schwarz-P can achieve the highest compressive strengths of all three structures [19, 20].

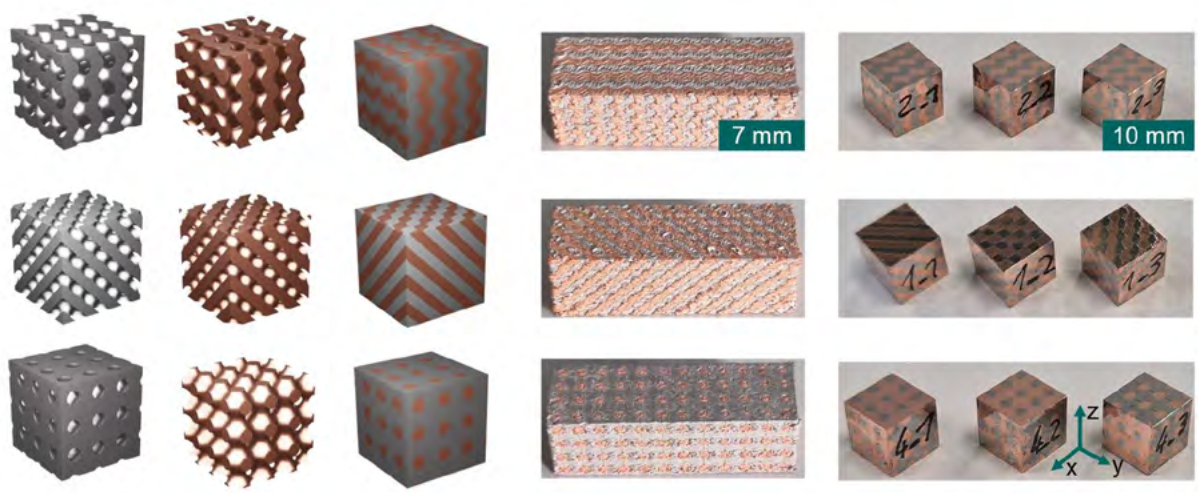

Figure 1. Gyroid, Schwarz-D and Schwarz-P structure rendering with the separated phases below (left) prepared samples (middle) and after sintering (right).

2.1. Sample manufacturing

The samples were printed using a converted Prusa i3 MK3S+ (Prusa a.s., Prague, Czech Republic). The printer was equipped with a Bondtech LGX extruder (Bondtech AB, Värnamo, Sweden) and a Mosquito hotend (Slice Engineering LLC, Gainesville, USA). Furthermore, a hardened TwinClad nozzle (Micro Swiss LLC, Ramsey, USA) with a diameter of 0.25 mm had also been installed.
The filament was manually changed between copper and steel. In order to facilitate the cleaning of the nozzle following each layer and filament change, a wire brush was attached to the printer. The printing platform consisted of the printer's smooth polyetherimide (PEI) printing plate to which a Metal X printing paper (Markforged Inc., Watertown, USA), was bonded with a conventional adhesive. The slicing process was conducted using the PrusaSlicer 2.6.1 software. Prior to the start of the printing process, the optimal filament temperatures were determined, the filament changes and automatic nozzle cleaning were programmed, and all other process parameters were set.
The green bodies produced in the printing process were subjected to a chemical debinding process for a period of 24 hours in a heated solvent bath filled with 3M Novec 73DE (3M Corp., Saint Paul, USA), in accordance with the specifications provided by the filament manufacturer. Subsequently, the components were subjected to thermal debinding in the Sinter-1 furnace (Markforged Inc., Watertown, USA) and sintered using the sintering program for the lower-melting metal, which in this case is copper. The height in which the samples were printed was designated z-direction, resulting that layers were printed in x- and y-direction. The samples after sintering can be seen in Figure 1.

2.2. Sample preparation and experimental procedure

To investigate the different structures experimentally, the specimens underwent cutting on a QATM Qcut 200 A (ATM Qness GmbH, Mammelzen, Germany), a cutting machine equipped with a CBN cut-off wheel. The rotational speed was 4000 rpm, and the feed rate was 0.05 mm/s.
The specimens were then ground to a final size of 7x7x7 mm using a Tegramin 25 preparation system (Struers GmbH, Willich, Germany) in an automatic specimen holder and a specially manufactured clamping device. Initially, this involved grinding with P80 and P500 grit. The sample was subsequently polished on the xz-side for the microscopic analysis. The polishing program is analogous to the one proposed by Struers for copper, but the times had to be extended to 5 min each, which was described in detail in [21]. Following each stage of the process, the samples were subjected to ultrasonic cleaning in water. The finished samples were coated with a thin layer of wax to prevent oxidation.
In the end, batches of three samples of each structure (Schwarz-D, Schwarz-P, Gyroid) were manufactured. As a comparison, a batch of a hollow gyroid structure from stainless steel and a batch each of 100% stainless steel and 100% copper were printed and prepared with the same procedure as well. The unit cell of all structures was set to an equal size with an edge length of approximately 2.24 mm after sintering. The prepared samples are shown in Figure 1.

Microscopic analysis
The microscope images were captured using a Keyence VHX 7000 (Keyence Corp., Osaka, Japan) on the polished xz-side of the sample.

Density measurement
The density was determined by two different methods: Geometrically as a total bulk density ρ_t and with gas pycnometry as a skeletal density ρ_s. For the first method, the samples were measured with a Tesa µHite height measuring device (TESA Technology, Renens, Switzerland) in all four corners of each surface, with the height then being averaged over the four corners. The measuring device has an inaccuracy of 1 µm. The weight of the samples was then determined using an Explorer EX225D precision scale (OHAUS Europe GmbH, Nänikon, Switzerland), with the deviation being 10 µg. A density was calculated from mass divided by the averaged heights, assuming a perfectly cubed sample with a perfectly flat surface.
As a comparison, the volume without open pores and open cracks (skeletal volume) was also determined by helium gas pycnometry using a micrometrics AccuPyc II 1340 (Micrometrics Instrument Corp., Norcross, USA). Each sample was measured three times in accordance with ISO 12154:2014 [22]. Helium gas pycnometry determines the change in pressure when filling a previously evacuated crucible with the pressure p_1 containing the sample with a known empty volume V_c with Helium from a known reference volume V_r:

$$V_s = V_c + \frac{V_r}{1 - \frac{p_1}{p_2}} \tag{1}$$

With the resulting pressure p_2, the sample's skeletal volume V_s can be calculated. [22] The resulting volume of the sample is therefore the volume where Helium was not able to get to, or, in other words, all open cracks and pores are not considered part of the sample volume with this method. Hence, from both densities, the amount of open porosity Φ can be calculated [23]:

$$\Phi = 1 - \frac{V_t}{V_s} = 1 - \frac{\rho_t}{\rho_s} \tag{2}$$

With the index t describing the geometrically determined total bulk density/volume and s describing their skeletal counterparts from gas pycnometry.

Setup for compression testing
The mechanical testing procedure was oriented on DIN 50106:2023-02 [24]. All experiments were carried out on a universal testing machine of the type "1464" (ZwickRoell GmbH und Co. KG, Ulm, Germany) with a calibrated Xforce K 50 kN load cell. Strain was measured through the travel of the machine traverse. Testing was aborted once the force was below 80% of the maximum force Two compression stamps made from plane turned and polished hardened machine screws of grade 12.9 with a tensile strength of 1200 N/mm² and a yield strength of 1050 N/mm² have been used. Strain was measured. Prior to testing, an initial preload of 30 N was applied to the samples. Testing was executed path-controlled with a calculated nominal compressive strain rate of 10^{-3} 1/s. The stiffness of the machine setup was determined beforehand and later subtracted. All samples were tested in z-direction.

Ultrasonic phase spectroscopy
The Young's modulus was determined by ultrasonic phase spectroscopy (UPS) prior to mechanical testing as described in [25], but without determination of the whole C-matrix.

3. Results
The results of the experiments are presented in the following sections.

3.1. Initial sample quality
The sample quality after preparation can be seen in Figure 2. The stainless steel shows areas of porosity in each sample, the sintering quality of the copper is fine. All structures except the hollow gyroid show

regular cracks in the steel phase. Crack widths of the gyroid structures are in the range of 10-40 µm, Schwarz-D samples are in the range of 10-20 µm. Schwarz-P samples show wider cracks between 70-80 µm. As the filaments flow into remaining voids during printing, zig-zag lines appear when viewing the samples from the side (here in xz-direction). Also, defects from printing are visible, in general the Schwarz-P structure was the most difficult to print, which can be seen by the large number of defects.

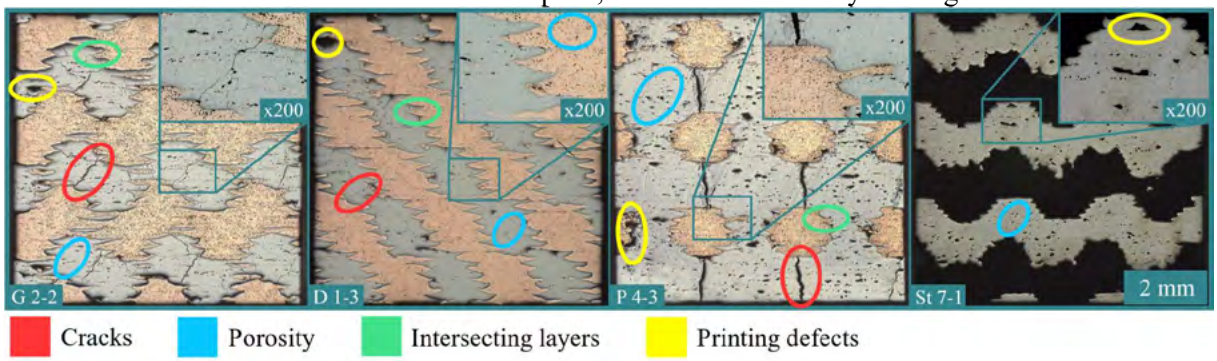

Figure 2. Microscopy images of gyroid, Schwarz-D, Schwarz-P and hollow gyroid (from left to right).

3.2. Density

The results of the density measurements are shown in Figure . As a comparison, a range of literature values of casted copper and bulk 17-4PH stainless steel were included from Granta Edupack [26]. From the average value for the materials, a value for a 1:1 volume mixture was calculated and given as a reference. All measured densities of the printed parts lie below the solid materials. The relative density of pure copper is at about 97% compared to cast material, and the density of pure steel is at about 96% of bulk material, not depending on the type of measurement. The hollow steel gyroid is less dense with a relative density of 95%, when measured with gas pycnometry. A geometrical measurement is not included, as it is not feasible. When looking at the copper-steel samples, the differences in the measurement methods become obvious. As the Helium gas can fill all open pores and cracks, the skeletal volume of the sample is lower in gas pycnometry, increasing the density value when using this method compared to a geometrical total bulk density. Skeletal densities for the three TPMS structures are between 93.7% and 94.6% with the lowest density being the Schwarz-P samples at 7884 kg/m³, followed by the Gyroid samples at 7904 kg/m³ and the Schwarz-D samples at 7929 kg/m³. Total bulk densities are lower between 90.5% and 92.7% with the Schwarz-P structure being at 91.1% or 7652 kg/m³ with a large standard deviation of 52 kg/m³, followed by Schwarz-D and Gyroid at 7773 kg/m³ and 7774 kg/m³

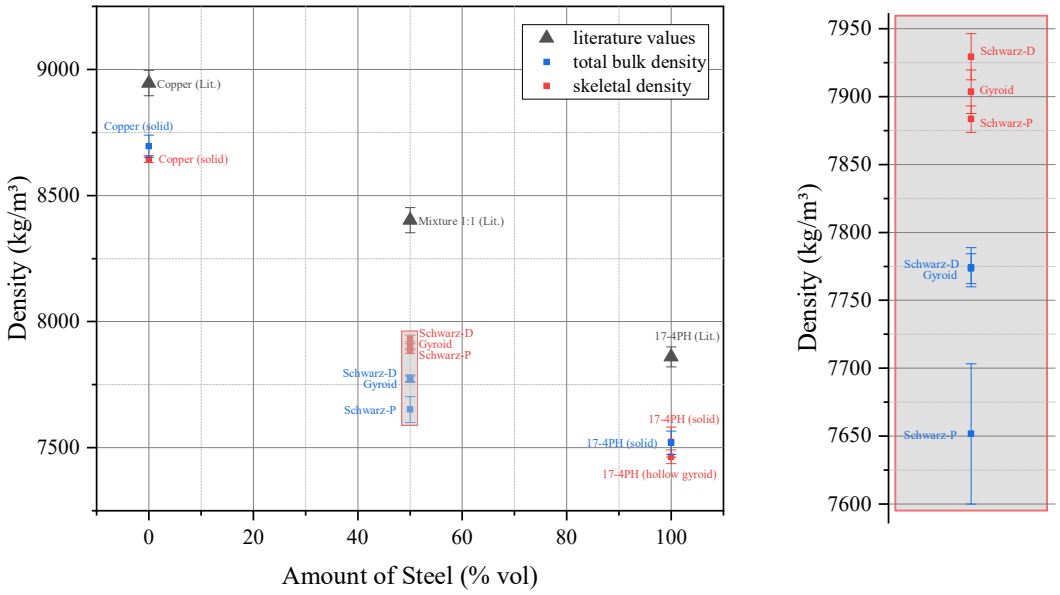

Figure 3. Total bulk and skeletal density of the samples compared to bulk material from literature.

or 92.5% relative, with deviations of 11 kg/m³ to 14 kg/m³. Overall, density results from gas pycnometry seem to be more precise with smaller deviations. With equation 2, the open porosity was determined at 1.64% for gyroid, 1.97% for Schwarz-D and 2.94% for Schwarz-P samples.

3.3. Compression testing

The stress nominal strain curves are shown in Figure 43. Each curve is the average of the three tests performed. The stainless steel curves show the highest slope and values. The interpenetrating samples can only be differentiated in the plastic regime, where the Schwarz-P structure can maintain the highest compressive loads, followed by gyroid and Schwarz-D at almost the same values. The hollow structure collapses fatally once it enters the plastic regime. The solid copper shows almost no elastic regime and immediately plastifies at low loads.

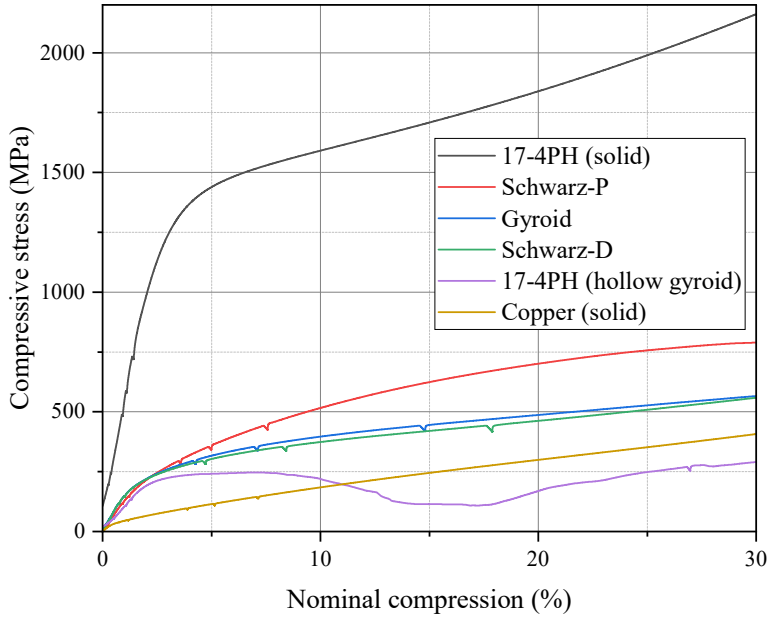

Figure 43. Representative stress - nominal compression curves of each structure

From the data, the compressive yield strength was determined according to DIN 50106:2023-02 [24]. The results are shown in Table 1 together with the results from UPS. The highest yield strength of around 1030 MPa was found for the solid 17-4PH sample, followed by the interpenetrating structures and the hollow gyroid structure again at very similar values of on average 182-183 MPa. The cross-sectional area of the hollow gyroid was plotted as if it was filled completely, including the air. Far below that are the solid copper samples with a yield strength of 46 MPa. The same increments can be seen in the moduli. Moreover, the modulus of the Schwarz-P structure is clearly lower than gyroid and Schwarz-D.

Table 1. Young's Modulus and compressive yield strength

Pattern	Young's modulus in z-direction from UPS (GPa)	Compressive yield strength in z (MPa)
17-4PH (solid)	170.5 ± 3.9	1030 ± 38
Schwarz-P	106.0 ± 4.8	182 ± 4
Schwarz-D	118.8 ± 5.6	183 ± 11
Gyroid	121.4 ± 2.6	182 ± 6
17-4PH (hollow gyroid)	not applicable	183 ± 14
Copper (solid)	113.8 ± 7.2	46 ± 9

4. Discussion

Although the two materials sinter into one, form-fit solid piece, cracks appear during sintering, which is due to the different shrink rates of the two constituents and not because of too low sintering temperatures,

for example, as the hollow gyroid samples do not show cracks at all. The cracks of the Schwarz-D and gyroid samples are rather similar in size, the Schwarz-P structure shows wider cracks. Due to its geometry, it is less suitable for this manufacturing method, and seems to be very susceptible to cracks caused by uneven shrinkage. The bad manufacturability could also be observed during printing, as the quality of the layers was not as perfect as with the other structures. The wider cracks and the higher amount of print defects could also be validated by the density measurements, where the amount of open porosity is the highest for the Schwarz-P structure, whereas gyroid and Schwarz-D show smaller amounts.
As already found by Restrepo et al. [20] the Schwarz P structure can withstand the highest compressive loads which could also be seen in this work. This is noteworthy, as this structure has the highest number of defects and porosity. Furthermore, there is almost no difference between the gyroid and Schwarz-D structure in the obtained data, which is plausible, as the structures mathematical equations to determine the surface are closely related to each other. Interestingly the strength of the crack-free hollow gyroid is also similar to the aforementioned structures, resulting in the conclusion, that the copper's impact on the interpenetrating structure to strength is balanced out by the cracks in these samples. The copper phase becomes relevant in the plastic regime, where it prohibits a more spontaneous failure than was observed with the hollow gyroid samples.

5. Conclusion

Despite the significant differences in sintering temperatures, structurally stable interpenetrating samples with relative densities between 94% and 95% were successfully produced. This approach enables the fabrication of structures with minimum extrusion widths of 0.21 mm and layer heights of 0.12 mm after sintering. Overall, cracks have a rather small, but noticeable influence on the stability. For a further investigation, tensile tests and computer tomography measurements would be of use, to improve the understanding of the composites.

Acknowledgements

The present work has been conducted within the framework of a publicly funded project, which is a collaboration between the Technical University of Applied Sciences Augsburg and the University of Augsburg and is funded by the Bavarian Government (Bayerisches Staatsministerium fuer Wirtschaft, Landesentwicklung und Energie, StMWi), identification code HAM-2109-0043 / HAMI21-016-A.

References

[1] R. R. Boyer, J. D. Cotton, M. Mohaghegh, and R. E. Schafrik, "Materials considerations for aerospace applications," *MRS Bull.*, vol. 40, no. 12, pp. 1055–1066, 2015, doi: 10.1557/mrs.2015.278.
[2] M. Moore, "Aviation Frontiers - On Demand Aircraft," in *Aviation Technology, Integration, and Operations (ATIO) Conferences: 10th AIAA Aviation Technology, Integration, and Operations (ATIO) Conference*, Fort Worth, Texas, 2010.
[3] J. Haynes and J. Karthikeyan, "Cold Spray Copper Application for Upper Stage Rocket Engine Design," in *Thermal Spray 2003: Proceedings from the International Thermal Spray Conference*, Orlando, Florida, USA, 2003, pp. 79–83.
[4] J. S. Shelley, R. LeClaire, and J. Nichols, "Metal-matrix composites for liquid rocket engines," *Jom*, vol. 53, no. 4, pp. 18–21, 2001, doi: 10.1007/s11837-001-0140-6.
[5] Y. Wang, Y. Gao, Y. Li, W. Zhai, L. Sun, and C. Zhang, "Review of preparation and application of copper–steel bimetal composites," *Emerging Materials Research*, vol. 8, no. 4, pp. 538–551, 2019, doi: 10.1680/jemmr.17.00008.
[6] D. R. Feenstra, R. Banerjee, H. L. Fraser, A. Huang, A. Molotnikov, and N. Birbilis, "Critical review of the state of the art in multi-material fabrication via directed energy deposition," *Current Opinion in Solid State and Materials Science*, vol. 25, no. 4, p. 100924, 2021, doi: 10.1016/j.cossms.2021.100924.
[7] C. Wei and L. Li, "Recent progress and scientific challenges in multi-material additive manufacturing via laser-based powder bed fusion," *Virtual and Physical Prototyping*, vol. 16, no. 3, pp. 347–371, 2021, doi: 10.1080/17452759.2021.1928520.

[8] V. Errico, P. Posa, A. Fusco, A. Angelastro, and S. Luisa Campanelli, “Intralayer multi-material structure stainless-steel/nickel-superalloy fabricated via laser-powder bed fusion process,” *Manufacturing Letters*, vol. 35, pp. 11–15, 2023, doi: 10.1016/j.mfglet.2022.11.004.
[9] Y. Bai, J. Zhang, C. Zhao, C. Li, and H. Wang, “Dual interfacial characterization and property in multi-material selective laser melting of 316L stainless steel and C52400 copper alloy,” *Materials Characterization*, vol. 167, p. 110489, 2020, doi: 10.1016/j.matchar.2020.110489.
[10] L. Langer, M. Schmitt, J. Cuesta Aguirre, G. Schlick, and J. Schilp, “Hybrid additive manufacturing of hot working tool steel H13 with dissimilar base bodies using Laser-based Powder Bed Fusion,” *IOP Conf. Ser.: Mater. Sci. Eng.*, vol. 1135, no. 1, p. 12012, 2021, doi: 10.1088/1757-899X/1135/1/012012.
[11] Venkata Karthik Nadimpalli, Thomas Dahmen, Emilie Hørdum Valente, Sankhya Mohanty, and David Bue Pedersen, “Multi-material additive manufacturing of steels using laser powder bed fusion,” *Proceedings of the 19th International Conference and Exhibition (EUSPEN 2019)*, pp. 240–243, 2019. [Online]. Available: https://orbit.dtu.dk/en/publications/multi-material-additive-manufacturing-of-steels-using-laser-powde
[12] E. Louvis, P. Fox, and C. J. Sutcliffe, “Selective laser melting of aluminium components,” *Journal of Materials Processing Technology*, vol. 211, no. 2, pp. 275–284, 2011, doi: 10.1016/j.jmatprotec.2010.09.019.
[13] C. Tang, L. Yao, and H. Du, “Computational framework for the simulation of multi material laser powder bed fusion,” *International Journal of Heat and Mass Transfer*, vol. 191, p. 122855, 2022, doi: 10.1016/j.ijheatmasstransfer.2022.122855.
[14] F. J. Clemens and A. Kerber, “FDM/FFF an Alternative to CIM Manufacturing of Prototype and Small Quantities of Ceramic Part,” *Ceram Appl*, vol. 8, pp. 27–31, 2020.
[15] F. Clemens, F. Sarraf, A. Borzì, A. Neels, and A. Hadian, “Material extrusion additive manufacturing of advanced ceramics: Towards the production of large components,” *Journal of the European Ceramic Society*, 2022, doi: 10.1016/j.jeurceramsoc.2022.10.019.
[16] R. Wick-Joliat, M. Schroffenegger, and D. Penner, “Multi-material ceramic material extrusion 3D printing with granulated injection molding feedstocks,” *Ceramics International*, vol. 49, no. 4, pp. 6361–6367, 2023, doi: 10.1016/j.ceramint.2022.10.170.
[17] A. H. Schoen, “Infinite periodic minimal surfaces without self-intersections,” *NASA Technical Note*, TN D-5541, 1970.
[18] H. Niknam and A. H. Akbarzadeh, “Graded lattice structures: Simultaneous enhancement in stiffness and energy absorption,” *Materials & Design*, vol. 196, p. 109129, 2020, doi: 10.1016/j.matdes.2020.109129.
[19] N. Soro, H. Attar, X. Wu, and M. S. Dargusch, “Investigation of the structure and mechanical properties of additively manufactured Ti-6Al-4V biomedical scaffolds designed with a Schwartz primitive unit-cell,” *Mater. Sci. Eng. A*, vol. 745, pp. 195–202, 2019, doi: 10.1016/j.msea.2018.12.104.
[20] S. Restrepo, S. Ocampo, J. A. Ramírez, C. Paucar, and C. García, “Mechanical properties of ceramic structures based on Triply Periodic Minimal Surface (TPMS) processed by 3D printing,” *J. Phys.: Conf. Ser.*, vol. 935, p. 12036, 2017, doi: 10.1088/1742-6596/935/1/012036.
[21] F. Siegmund, Q. Schneider, J. Schukraft, and K. A. Weidenmann, “Herstellung und Analyse von additiv gefertigten Metallverbunden,” in *Abstract Band: 24. Symposium Verbundwerkstoffe und Werkstoffverbunde - Verbund 2024*, Freiburg, 2024, pp. 76–78.
[22] *ISO 12154:2014-4, Determination of density by volumetric displacement Skeleton density by gas pycnometry*, Geneva, 2014.
[23] Y. Salissou and R. Panneton, “Pressure/mass method to measure open porosity of porous solids,” *J. Appl. Phys.*, vol. 101, no. 12, 2007, doi: 10.1063/1.2749486.
[24] *DIN 50106:2023-02, Testing of metallic materials - Compression test at room temperature*, Berlin.
[25] J. Schukraft, J. Roßdeutscher, F. Siegmund, and K. A. Weidenmann, “Thermal expansion behavior and elevated temperature elastic properties of an interpenetrating metal/ceramic composite,” *Thermochimica Acta*, vol. 715, p. 179298, 2022, doi: 10.1016/j.tca.2022.179298.
[26] Ansys Inc., *Granta EduPack*, 2020.

EVALUATION ON ABLATION BEHAVIOR OF ZrO_2 NANOPARTICLE-DISPERSED POROUS CARBON COMPOSITES

Hiroya Taniguchi[1],Yutaro Arai[1] and Yasuo Kogo[1]

[1]Department of Materials Science and Technology, Tokyo University of Science, 6-3-1, Niijuku, Katsushika-ku, Tokyo, Japan
Email: 8223547@ed.tus.ac.jp, Web Page: https://www.tus.ac.jp

Keywords: porous carbon, ablator, zirconia, carbon monolith, nano particle dispersion

Abstract

Ablators are well-known as one of thermal protection systems (TPS) protected spacecraft from aerodynamic heating during re-entry and composed of carbon-based materials and impregnated resins. A porous carbon has been selected as a substrate for ablator. carbon monolith is a porous carbon with a three-dimensional continuous struts and open pores and an attractive candidate for the substrate. Carbon monolith is prepared by carbonization of porous phenolic resin (phenolic monolith) with the same structure as carbon monolith. Since phenolic monolith is fabricated by using polymerization induced phase separation (PIPS), it makes the addition of second phase and the design of structure possible. In the present study, ZrO_2 nano particle dispersed carbon monolith (ZCM) is prepared as a resin free ablator because of compatibility of lightweight and mechanical reliability. The ablation behavior of them is evaluated by arc-wind tunnel test simulated for a re-entry environment. the result shows mechanical properties of ZCM is similar to conventional porous carbon in spite of the addition of second phase and surface recession of ZCM by the formation of ZrO_2 region on the surface is observed, whereas selective surface recession is also observed. The relationship between recession behavior and ZrO_2 content is discussed.

1. Introduction

During atmospheric re-entry, vehicles are exposed to high temperatures owing to aerodynamic heating and a thermal protection system (TPS) is required for re-entry vehicles [1][2]. The ablator is one of representative TPS, which combines carbon substrates and resins that protect the vehicles through endothermic decomposition of the resin and its own recession. The decomposition of the resin forms a rigid carbonized layer on the surface and it makes the recession of ablator suppressed. The resin decomposition also prevents the increase of surface and internal temperature. In addition, the decomposed gases pass through the carbonized layer and emit toward the surface and they also prevent the exposure of high-temperature gases to the surface. A Report for thermal insulation of ablator indicates that the temperature of bottom surface maintains ~50℃, while the sample surface temperature of ablator by approximately 30 mm thick reaches 2900℃ [2]. Recently, the compatibility of lightweight and mechanical reliability is required for ablators.

Previous studies have prepared a porous phenolic resin (hereafter denoted as phenolic monolith) fabricated by polymerization induced phase separation (PIPS). By the carbonization of phenolic monolith, carbon monoliths are obtained as a material for ablator. Carbon monolith has a similar structure to phenolic monolith and a three-dimensional continuous struts and open pores are notable feature of them. The fabrication process of carbon monolith and the evaluation of its structure and mechanical properties have been studied. Since the addition of second phase and the design of structure of phenolic monolith is possible, various design of carbon monolith is also available. the recession behavior of carbon monolith by arc-wind tunnel test simulated a re-entry environment have been evaluated in a previous study and revealed that the higher internal temperature is observed compared to traditional porous carbons, whereas the recession of carbon monolith is suppressed in comparison with

conventional porous carbons. In addition, carbon monolith ablators (CMA), in which carbon monoliths are impregnated with acrylic resin, have also shown a decrease in surface temperature [3]. In the present study, ZrO_2 particles are added to carbon monolith to reduce thermal conduction and it proposes as a resin free ablator. ZrO_2, is well known as a material for thermal barrier coatings in gas turbine engines [4] and has a significantly low thermal conductivity (~2.5 W/m・K) and high melting point (2680℃). ZrO_2 is also known to be dispersible in many solvents [5][6]. However, the addition of a second phase to the phenolic monolith precursor inhibits phase separation, and a method to maintain the monolith structure while dispersing particles has not been established. The relationship between the structure and mechanical and thermal properties of ZrO_2 dispersed carbon monolith also remains unexplored. Thus, the objective of this study is to establish the fabrication processes for ZrO_2 nanoparticle-dispersed phenolic monolith (ZPM) and carbon monolith (ZCM), and evaluate the relationship between particle content and the mechanical properties, thermal properties, and recession behavior of the monoliths as a resin free ablator.

2. Experimental procedures

2.1. Fabrication of ZrO_2 Particle Dispersed Monolith

As the precursor of carbon monolith, a phenolic monolith was prepared. Then, the monomer concentration (ω, wt%) was defined as the ratio of resin and curing agent to solution by the following equation:

$$\omega = \frac{W_{resin}+W_{cure}}{W_{solution}} \tag{1}$$

$$W_{solution} = W_{resin} + W_{cure} + W_{solvent} \tag{2}$$

W_{resin}, W_{cure}, $W_{solution}$ and $W_{solvent}$ were the weight of phenolic resin, curing agent, solution, and solvent, respectively. A resol-type phenolic resin (PL2407 by Gunei Chemical, Japan), concentrated sulfuric acid, and ethylene glycol were used as resin, curing agent and solvent. These were mixed in a weight ratio of 13:1:21(hereafter as the mixed solution) in a beaker. ZrO_2 particles (KZ-0Y-LSF, particle size: 80-120 nm, KCM Corporation, Japan) were used as the particles. The mixed solution was held at 40℃ in an ambient atmosphere for 12 h to cure by using an oven (DRN320DE, ADVANTEC TOYO KAISHA, LTD. Japan). After 4 h from the beginning of curing, ZrO_2 particles were added by 3.1, 6.1, or 9.2 vol% to mixed solution. The solution was stirred and held under a reduced pressure of about -0.08 MPa for 30 minutes using a rotary pump to remove air bubbles. After 12 h, the temperature was increased to 180℃ and held for 2 h. After that, samples were cooled to room temperature (25℃) over ~12 h. After curing, the solvent in the samples were removed in water at 80℃ for 72 h and dried in the oven at 80℃ for 72 h to obtain the ZrO_2 dispersed phenolic monolith (hereafter denoted as ZPM). ZPM was carbonized at 950℃ for ~4 h in an atmospheric furnace (FT-POT-300, Fulltech) under an Ar atmosphere to obtain the ZrO_2 particle dispersed carbon monolith (hereafter denoted as ZCM). ZCM with ZrO_2 particles by 3.1, 6.1, and 9.2 vol% were defined as 3.1 ZCM, 6.1 ZCM and 9.2 ZCM, respectively.

2.2. Basic characterization of structures for ZPM and ZCM

ZPM and ZCM were cut into three layers and defined as top layer, intermediate layer and bottom layer as shown in Figure 1. The bottom of the beaker used in the fabrication was set as the xy plane and the center of the xy plane in the second layer along the z-axis was used for the observation by a scanning electron microscope (SEM). In addition, the density of each layer was measured to evaluate the dispersion of particles.

2.3. Evaluation of mechanical properties for ZCM

ZCM was cut into rectangular blocks with size of 10×10×20 mm and 8×8×30 mm. The latter shaped continuously into a dumbbell with a cross-section of 5×8 mm in the center. The shapes of both compression test specimens are shown in Figure 2. Compression tests were conducted using a universal testing machine (5967 model, INSTRON, The U. S.), with a crosshead speed of 0.1 mm/min. The load was recorded using a 30 kN load cell, and displacement was measured using a extensometer attached to the compression jig. From these values, the Young's modulus and compression strength were evaluated.

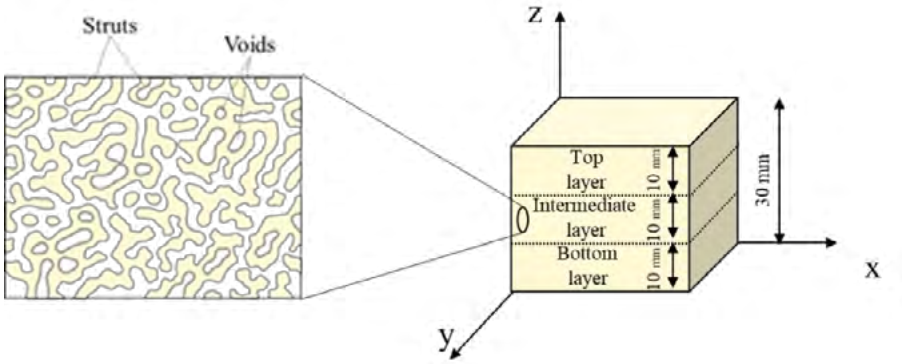

Figure 1. Schematic diagram of the sample

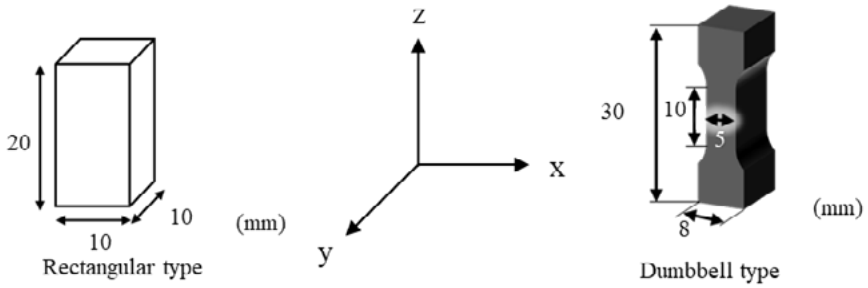

Figure 2. Shape of compression specimen

2.3. Arc-wind tunnel test

Arc-wind tunnel tests were conducted to evaluate the ablation behaviors of ZCM. The tests used a 1 MW class arc heater at Japan Aerospace Exploration Agency/Institute of Space and Astronautical Science (JAXA/ISAS) in their arc-wind tunnel. In the tests, the high-enthalpy flow heated by arc heater is emitted from the nozzle into the chamber, allowing for simulated testing of atmospheric re-entry conditions. The appearance of the test specimens before and during the test in the arc heating wind tunnel were shown in Figure 3. By varying the distance between the air nozzle and the test specimen, the heat flux and dynamic pressure at stagnation point were adjusted. The size of specimens and specimen holder were exhibited in Figure 4. The specimen surface was Φ50 mm and set to bakelite holder. Nozzle distances were set at 150 mm, 100 mm, or 80 mm. The specimen surface was exposed for 30s by high enthalpy flow. The surface temperature was measured during heating by using radiation thermometer (emissivity ε = 0.90). The internal temperature was measured during heating and until 20 min after heating. Internal temperature was measured by inserting a type K thermocouple at 20 mm and 30 mm depth from the surface. After arc-wind tunnel test, the recession length of surface was measured by using a laser displacement sensor (LK-G155, KEYENCE CORPORATION, JAPAN).

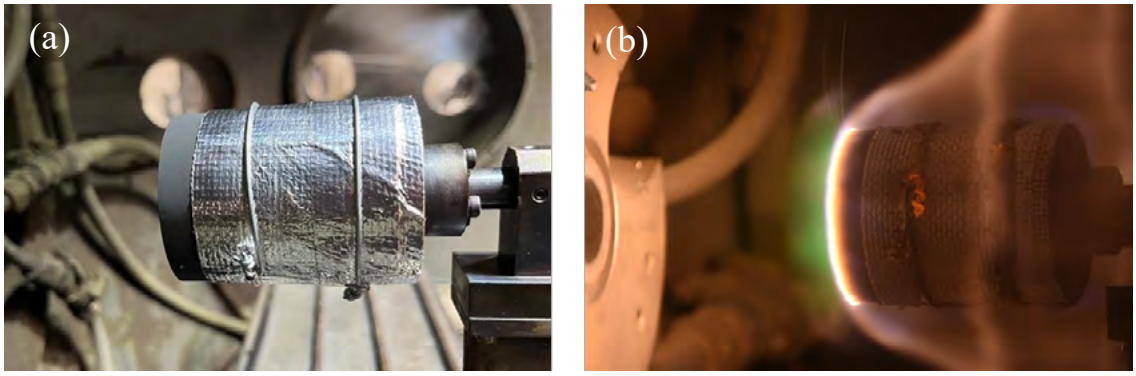

Figure 3. A typical appearance of the specimen: (a)Before test, (b)During test

Table 1. Test conditions

Test	Specimen	Nozzle distance (mm)	Exposure time (s)	Emissivity	Heat flux (MW/m^2)	Dynamic pressure (kPa)
A	3.1 ZCM 6.1 ZCM 9.2 ZCM	150			2.05	1.95
B	3.1 ZCM 6.1 ZCM 9.2 ZCM	100	30	0.90	3.95	10.50
C	3.1 ZCM 6.1 ZCM 9.2 ZCM	80			6.27	20.25

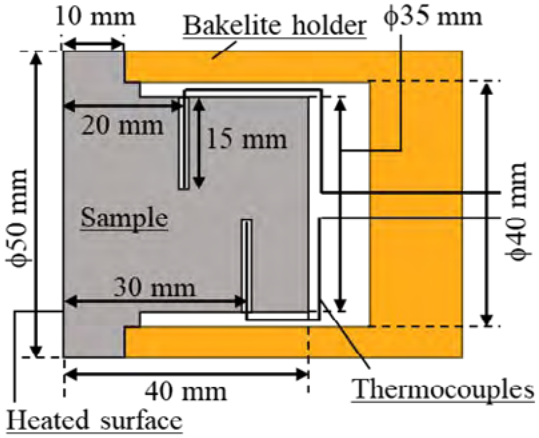

Figure 4. Cross section of arc wind tunnel specimen

3. Results and Discussion

3.1. Density of ZPM

The density of each layer for ZPM was shown in Table 2. Since the density of ZrO2 (5.67g/cm^3) is much higher than that of phenolic resin (~1.3g/cm^3), the density of the bottom layer is the highest. On the other hand, the result indicates that ZrO_2 particles are roughly dispersed in ZPM because the density increased in each layer as the ZrO_2 additive amount increased. ZCM is made by carbonizing ZPM and is considered to be coarsely dispersed in ZCM as it retains its structure

Table 2. Relationship between ZrO_2 concentration and density

ZrO_2 concentration [vol%]	Density [g/cm^3]		
	Bottom layer (z = 0-20 mm)	Intermediate layer (z = 20-40 mm)	Top layer (z = 40-60 mm)
0		0.403	
3.1	0.582	0.533	0.570
6.1	0.584	0.579	0.623
9.2	0.680	0.636	0.661

3.2. Structural Observation

Microstructures of ZPM and ZCM was presented in Figure 5. The monolith structure, which is a typical microstructure of monolith, is maintained even with the addition of ZrO_2 particles. Notably, agglomerate of ZrO_2 particle with the size of ~2.3-3.0 μm were observed for 9.2 ZPM and 9.2ZCM. The result clearly shows that ZrO_2 contained monolith is successfully prepared by material process proposed in the present study.

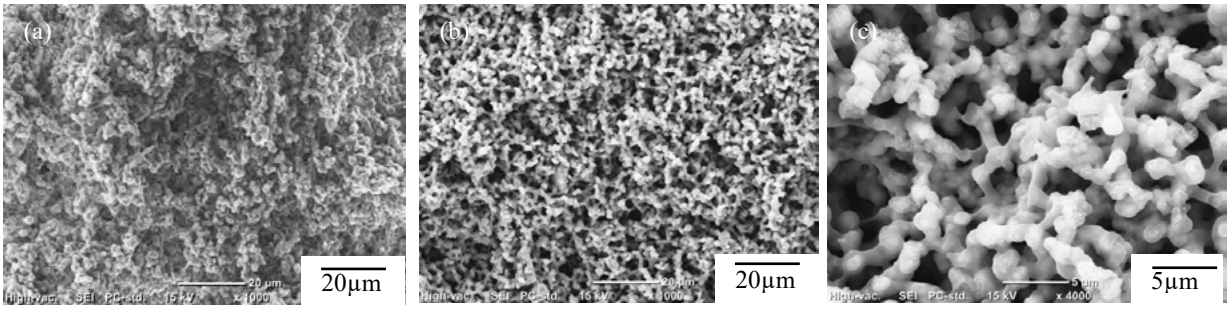

Figure 5. Typical microstructures of ZrO_2 particle containing monoliths:(a)9.2 ZPM, (b)9.2 ZCM, (c)9.2 ZCM (An enlarged view)

3.3. Evaluation of Mechanical Properties

The compression strength was 108.9±1.34 MPa for 0 vol% ZrO_2 (carbon monolith), 27.72±4.16 MPa for 3.1 ZCM, 20.52±0.89 MPa for 6.1 ZCM, and 15.51±1.41 MPa for 9.2 ZCM. The Young's modulus was 7.17±0.10 MPa for 0 vol%, 1.99±0.20 MPa for 3.1 ZCM, 1.86±0.20 MPa for 6.1 ZCM, and 1.22±0.09 MPa for 9.2 ZCM. These results show the compression strength and Young's modulus decrease with increase of the ZrO_2 particles. However, compression strength for 3.1 ZCM is comparable to conventional porous carbons (~25MPa) used in previous studies [7]. The decrease in mechanical properties was attributed to the agglomeration of ZrO_2 nanoparticles. As a further study, the improvement of dispersion of ZrO2 nano particles are required to improve mechanical properties of ZCM.

3.4. Arc Heating Wind Tunnel Test

The specimens after arc-wind tunnel test are shown in Figure 6. After the tests, the surface is covered with white compounds. The recession at near the center is more severe than edges after the test at 6.0MW/m^2. Large holes (drastic recession) are formed in the center of the 3.1 ZCM and 6.1 ZCM in the 6.0 MW test. Notably, holes are not observed for 9.2 ZCM and a melting trace is observed. The relationship between surface temperature and heat flux during test is shown in Figure 8. The surface temperature reaches at 2206, 2464 and 2817°C for test at 1.8, 3.2 and 6.0 MW/m^2, respectively. Since these temperature is measured by radiation thermometer (ε =0.9), it is considered that actual temperature is higher than measured temperature because the emissivity of ZrO_2 is ~0.4 for IR with the wavelength of 1 μ m at 1727°C◦ [8]. The result shows that the surface temperature tested at 6.0MW/m^2 reaches above melting point of ZrO_2 and the surface is melted. The internal temperature measured from 20 mm and 30 mm depths up to 1200 s from the beginning of heating is shown in Figure 9. The result indicates that the maximum internal temperature decreases with the increase of ZrO_2 content. Furthermore, the maximum internal temperature for 9.2 ZCM is almost the same for all tests. These results reveal that the thermal insulation by ZrO_2 particles occur for ZCM.

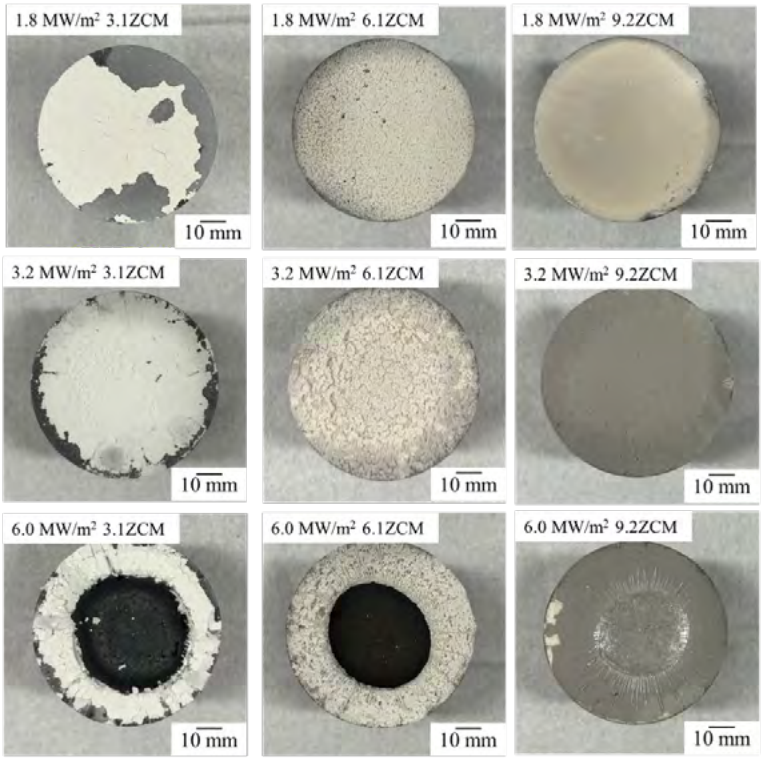

Figure 6. Specimens after arc wind tunnel test

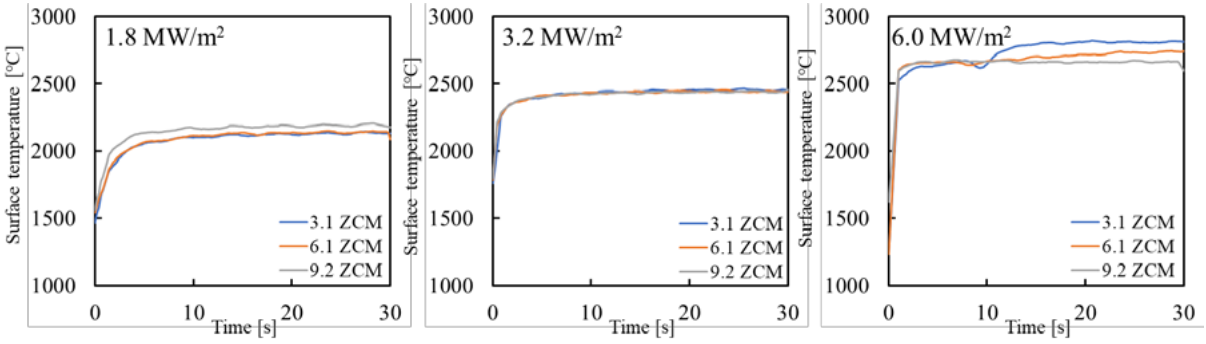

Figure 7. Temperature history of surface temperature (ZCM)

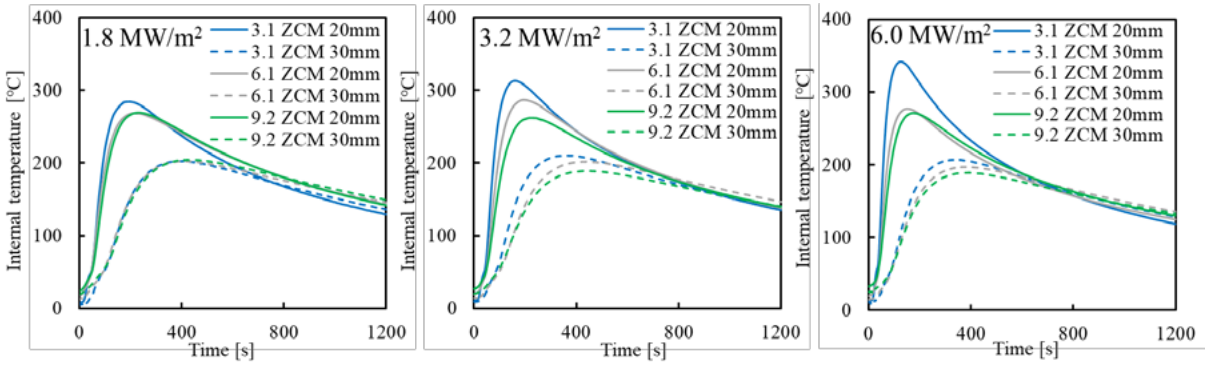

Figure 8. Temperature history of internal temperature (ZCM)

4. Conclusion

In the present study, ZrO_2 containing carbon monolith (ZCM) was obtained by carbonization of ZrO_2 containing phenolic monolith (ZPM) prepared by polymerization induced phase separation (PIPS) and the design of materials process of them was established. The density of ZPM increased by up to 60% compared to samples without ZrO_2. In all samples, the density at the bottom layer (z = 0-20 mm) was approximately 10% higher than at the surface, and some agglomerate particles were observed. The compression strength and Young's modulus of ZCM decrease with the increase of ZrO_2 content and the uniform dispersion of ZrO_2 nano particles is required. Arc-wind tunnel tests clearly revealed that recession of samples was prevented for all samples for test at 1.8 and 3.0MW/m^2. However, drastic recession occurs for 3.1 and 6.1 ZCM for test at 6.0MW/m^2, whereas drastic recession did not occur for 9.1 ZCM. The evaluation of relationship between ZrO_2 content and recession behaviors are required as a further study.

References

[1] Brody K. Bessire et.al, ACS Appl. Mater. Interfaces 2015, "*Pyrolysis of Phenolic Impregnated Carbon Ablator (PICA)*", vol. 7, pp. 1383–1395. 2015.

[2] Tetsuya Yamada et.al., J. Plasma Fusion Res. "*Plasma Phenomena during Re-entry of the Hayabusa Capsule into the Earth's Atmosphere and its Surroundings*", 82, pp. 370-371, 2006. (in Japanese)

[3] Rina Ono, Kenjiro Tsukamoto et al, MRS Advances, "*Experimental and analytical evaluation of an aerospace thermal protection system: Carbon monolith ablator*", 2024

[4] R.J. Takahashi et.al, J. Mater. Res. Technol. "*Thermal conductivity study of ZrO_2-$YO_{1.5}$-$NbO_{2.5}$ TBC*", 19, pp. 4932-4938, 2022

[5] Sho-Hsun Wang et al, Journal of Colloid and Interface Science. "*Hansen solubility parameter analysis on the dispersion of zirconia nanocrystals*", 407, pp. 140-147, 2013.

[6] G. Pulci et.al, Composites Part A: Applied Science and Manufacturing. "*Low density ablative materials modified by nanoparticles addition: Manufacturing and characterization*", 109, pp. 330-337 ,2018.

[7] Y. Kubota et.al., Journal of the Japan Society for Aeronautical and Space Sciences "*Development of Lightweight Ablator Using Porous Carbon Material*", 64, pp. 24-29, 2016.

[8] Stanislav M Avdoshenko and Alejandro Strachan, Modelling and Simulation in Materials Science and Engineering. "*High-temperature emissivity of silica, zirconia and samaria from ab initio simulations: role of defects and disorder*", 22, 2014.

TANNIC ACID: AN INTERESTING NATURAL FILLER FOR HDPE

Myrto Tara,[1] Christina Samiotaki,[1] Evangelia Tarani,[2] Alexandra Zamboulis,[1] Konstantinos Chrisafis,[2] and Dimitrios Bikiaris[1]

[1]Laboratory of Polymer Chemistry and Technology, Department of Chemistry, Aristotle University of Thessaloniki, Thessaloniki, Greece
Email: myrtotara@chem.auth.gr, christinasamiotaki@gmail.com, azamboulis@gmail.com, dbic@chem.auth.gr
[2]Laboratory of Advanced Materials and Devices, Department of Physics, Aristotle University of Thessaloniki, Thessaloniki, Greece
Email: etarani@physics.auth.gr, hrisafis@physics.auth.gr

Keywords: Tannic acid, HDPE, natural filler, antioxidant activity

Abstract
Due to the environmental crisis experienced by our modern societies in the 21st century, alternatives to the linear model of production and consumption established in the 20th century are sought. One of the most popular approaches to improve the sustainability of our products and reduce their environment footprint, is the valorization of renewable resources. In this context, natural fillers are extensively investigated and polymeric composites with a variety of natural fillers have been reported. Tannin has recently attracted significant interest as an inexpensive biobased renewable resource that is worth investigating. In the present work, tannic acid was used as a biobased filler to confer, among others, antioxidant properties to HDPE. HDPE/tannic acid composites were prepared through melt-mixing and characterized. The antioxidant activity will be further evaluated by monitoring the reduction rate of the DPPH• radical in the composites presence via UV-visible spectroscopy, and ageing studies will be conducted.

1. Introduction

Polyolefins are a class of materials that, due to their low cost and good performances, are indispensable in daily life, satisfying the needs of a rapidly expanding global population. They are versatile polymers, finding diverse applications, from packaging for safe storage of food, to lightweight engineering plastics for automotive and architectural uses, textiles, rubbers, electrical and thermal insulation, pipes for water and gas transportation, just to name a few. Among them, high-density polyethylene (HDPE) holds a prominent position. HDPE is a semicrystalline thermoplastic synthetic polymer, characterized by limited branching, high crystallinity, and rapid crystallization kinetics. These characteristics contribute to the formation of a dense, rigid yet ductile, polymer network, rendering HDPE highly relevant for various technological applications.

Polymer composites are advanced, high-performance materials that combine the properties of the polymer matrix and the filler. In the context of the environmental crisis that our modern societies are going through, the valorization of biomass and wastes for the preparation of composites with natural fillers has attracted a great deal of attention. Plant fibers are well-known for reinforcing polymers, while lignin particles and cellulose fibers and crystals are among the most studied fillers. Tannins, a common class of natural polyphenols, with diverse molecular structures, well-known in oenology and for their applications in the tanning industry, are emerging as a novel class of abundant inexpensive natural fillers. Tannic acid, Figure 1, is a commercially available tannin, and, in the present study, it was investigated as a filler for HDPE. Structurally, tannic acid is described as a decagalloyl glucose, i.e., a glucose ester, containing ten galloyl groups, but in fact it is as a mixture of galloyl esters with various

galloyl moieties. In any case, tannins and tannic acid are characterized by the presence of numerous phenolic OH groups. They exhibit various interesting properties such as superior antioxidant activity, UV protection effects, they are non-toxic and biocompatible, while also presenting antibacterial properties. Various research groups have investigated tannin as a filler for PLA. Tannin was found to act as a nucleating agent, while endowing the composites with antioxidant and antibacterial properties [1–4], nevertheless to the best of our knowledge there are no reports of HDPE/tannic acid composites.

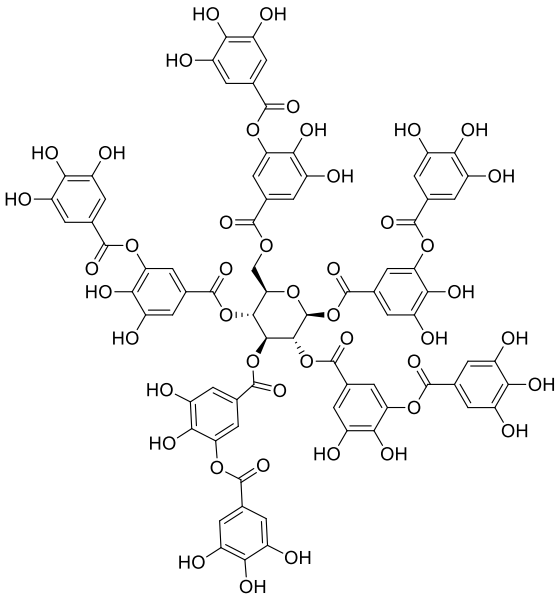

Figure 1. Chemical structure of tannic acid.

The present research work focuses on HDPE/tannic acid composites. Composites containing 1%, 5%, 10%, 15%, and 20% w/w of tannic acid were prepared via melt mixing, and further studied. Herein, preliminary results obtained from this study will be presented.

2. Materials and methods

2.1 Materials

HDPE LITEN MB 71 was donated by SILON s.r.o. Tannic acid was provided by Thermoscientific.

2.2 Preparation of HDPE - tannic acid composites

HDPE composites were prepared by melt-mixing at 190 °C. HDPE and tannic acid were dried before use. Composites with a tannic acid content of 1%, 5%, 10%, 15%, and 20% by weight were prepared. Hereafter, these composites will be denoted as "TAx," with 'x' representing the percentage of tannic acid in the composite (TA0 refers to neat HDPE).

2.3 Fourier transform infra-red spectroscopy (FTIR)

FTIR spectra were recorded using potassium bromide discs or thin composite films. Spectra were collected in the range from 4000 to 450 cm^{-1} using a resolution of 4 cm^{-1}. The spectra were baseline corrected and normalized.

2.4 Mechanical Properties

Tensile tests were performed in accordance with ASTM D882, using a 2 kN load cell and a crosshead speed of 5 mm/min, on dog bone specimens (central portions 5 × 0.5 mm thick, 22 mm gauge length).

3. Results and discussion

A series of five high-density polyethylene (HDPE) composites, with a tannic acid (TA) content ranging from 1% to 20%, were prepared via melt mixing, following the procedure outlined in the experimental section. The resulting composites exhibited a deep brown color, except for TA1, which appeared lighter. The tannic acid was effectively dispersed within the matrix, even at the higher concentration, showing no apparent signs of aggregation.

The chemical structure of the composites was examined by infra-red spectroscopy (Figure 2). The characteristic absorbances of HDPE (asymmetric and symmetric stretching vibrations of the C-H bonds (2919 and 2847 cm^{-1}), CH_2 bending and rocking deformation vibrations 1472/1461 cm^{-1} and 730/717 cm^{-1}) are clearly observed in all spectra [5]. When it comes to the composites, in TA1, due to the low tannic acid content, signals attributed to TA are not clearly detected. When the TA content increases over 5%, the corresponding signals increase, confirming TA has been successfully incorporated in the HDPE matrix.

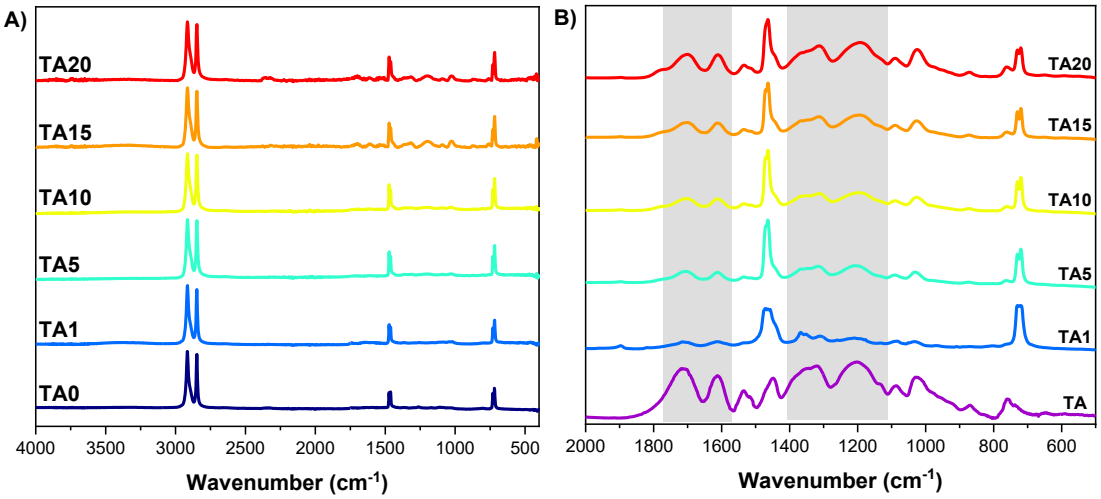

Figure 2. FTIR spectra of the prepared composites.
A) Full spectra, and B) Zoom in the 500-2000 cm^{-1} region.

Mechanical properties were evaluated by tensile testing, as illustrated in Figure 3. Interestingly, Young's modulus (Figure 3B) initially increased (up to a 10% TA content) before decreasing when TA content is further increased; overall the Young's modulus of the composites is similar or slightly improved compared to neat HDPE (TA0). Stress at break and elongation at break exhibit a progressive deterioration with the increase of tannic acid content. These observations indicate that the composites are stiffer than HDPE, which is consistent with the introduction of a rigid filler.

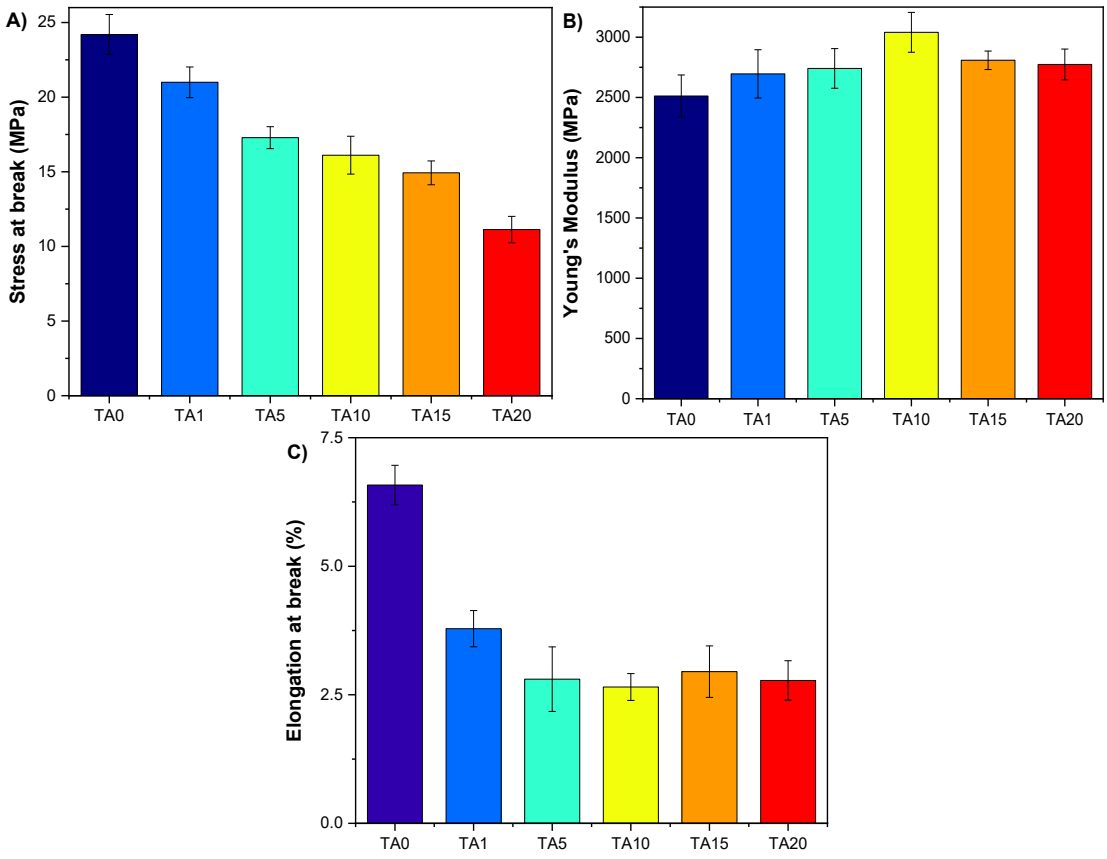

Figure 3. Mechanical properties of HDPE/TA composites.
A) Stress at break, B) Young's modulus, and C) Elongation at break.

4. Conclusions

A series of HDPE composites containing commercial tannic acid were prepared to explore its influence on HDPE behavior. Tannic acid was smoothly incorporated to HDPE, yielding dark brown materials. The incorporation of tannic acid was confirmed by IR. Young's modulus showed a slight improvement up to 10% tannic acid content, followed by a decrease, while other mechanical properties exhibited a declining trend with increasing tannic acid content. Antioxidant potential of the composite will be further assessed and if promising, aging studies will be conducted.

Acknowledgments

This project has received funding from the European Union's Horizon Europe Framework Programme under Grant Agreement No 101058449. Views and opinions expressed are however those of the author(s) only and do not necessarily reflect those of the European Union or HADEA. Neither the European Union nor the granting authority can be held responsible for them.

5References

[1] M. Ma, Z. Jiang, Z. Liu, B. Huang, N. Sun, S. Chen, Y. Shi, H. He, Y. Zhu, and X. Wang. Toward Flame Retardancy, Antimelt Dripping, and UV Resistance Properties of Polylactic Acid Based on Eco-Friendly Core–Shell Flame Retardant. *ACS Appl Polym Mater*, 6(7): 3814–3825, 2024.
[2] Y. Liu, B. Xia, R. Zhao, M. Qin, X. Weng, Z. Zeng, K. Deng, and H. Jiang. Automatic in situ short-distance deposition of PLGA/PLLA composite nanofibrous membranes for personalized wound dressings. *Nanoscale*, 16: 8546-8562, 2024.

[3] K. P. Črešnar, A. Zamboulis, D. N. Bikiaris, A. Aulova, and L. F. Zemljič. Kraft Lignin/Tannin as a Potential Accelerator of Antioxidant and Antibacterial Properties in an Active Thermoplastic Polyester-Based Multifunctional Material. *Polymers* (Basel), 14(8): 1532, 2022.
[4] K.P. Črešnar, P.A. Klonos, A. Zamboulis, Z. Terzopoulou, E. Xanthopoulou, L. Papadopoulos, A. Kyritsis, K. Kuzmič, L.F. Zemljič, D.N. Bikiaris. Structure-Properties relationships in renewable composites based on polylactide filled with Tannin and Kraft Lignin - Crystallization and molecular mobility. *Thermochim Acta*, 703: 178998, 2021.
[5] J. V Gulmine, P.R. Janissek, H.M. Heise, and L. Akcelrud. Polyethylene characterization by FTIR. *Polym Test*, 21(5): 557–563, 2002.

INVESTIGATION OF NOVEL POLY(LACTIC ACID) (PLA)/ HAZELNUT SHELL POWDER BIOCOMPOSITES FOR 3D PRINTING APPLICATIONS

L.Aliotta[1], C. Sergi[2], B. Dal Pont[3], M.B. Coltelli[4], V.Gigante[5] and A.Lazzeri[6]

[1]Department of Civil and Industrial Engineering, University of Pisa, 56122 Pisa, Italy
Email: laura.aliotta@unipi.it, Web Page: https://www.linkedin.com/in/laura-aliotta-a91223237/
[2]Department of Chemical Engineering Materials Environment, Sapienza Università di Roma and UdR INSTM, Via Eudossiana 18, 00184 Rome, Italy
Email: claudia.sergi@uniroma1.it, Web Page: https://www.linkedin.com/in/claudia-sergi-380a97165/
[3]Department of Civil and Industrial Engineering, University of Pisa, 56122 Pisa, Italy
Email: bianca.dalpont@phd.unipi.it, Web Page:
[4]Department of Civil and Industrial Engineering, University of Pisa, 56122 Pisa, Italy
Email : maria.beatrice.coltelli@unipi.it, Web Page: https://www.linkedin.com/in/maria-beatrice-coltelli-01b50532/
[5]Department of Civil and Industrial Engineering, University of Pisa, 56122 Pisa, Italy
Email : vito.gigante@unipi.it, Web Page: https://www.linkedin.com/in/vito-gigante-a40221237/
[6]Department of Civil and Industrial Engineering, University of Pisa, 56122 Pisa, Italy
Email : andrea.lazzeri@unipi.it, Web Page: https://www.linkedin.com/in/andrea-lazzeri-0b99184a/

Keywords: Biocomposites, Additive Manufacturing, Circular Economy, keyword 4, keyword 5

Abstract
The use of fillers from agricultural waste to obtain bio composites, has been widely adopted in literature essentially to reduce the materials costs. In this work the valorisation of hazelnuts shell powder (HSP) has been investigated. Different HSP amounts (from 10 up to 30 wt.%) were added in a poly(lactic acid) (PLA) matrix, by extrusion compounding, to obtain novel formulations to be used by FDM 3D printer for design applications (like jewellery and home accessories). The FDM manufactured bio composites were mechanically characterized (by flexural, tensile and impact tests) and the results compared with the same bio composites obtained by classical injection molding technique. The specimen's roughness was also measured to identify the best 3D printing configuration in terms of surface finishing. The effect of three different raster angles (0, 90 and ± 45°) on the final mechanical properties was also analyzed and to conclude, 3D printed jewelry (in real dimension) and home furniture (in scale) were produced as "validated objects".

1. Introduction

The adoption of circular economy models has gained much interest in the last decade [1]. In particular, the attention has been dedicated to the recovering of resources, to the reduction of raw materials coming from non-renewable resources and to the waste valorization [2]. In this work the attention has been focused on the valorization of agricultural wastes to obtain novel biocomposites formulation for 3D printing applications.
The choice of using hazelnut agriculture waste lies in its large availability. In fact, the European hazelnut (*Corylus avellana L.*) is one of the most produced tree nut crops worldwide, exceeding 700,000 tons/year in the past ten years [3]. Starting from the hazelnut shells, thanks to grinding, it is possible to obtain different granulometries of hazelnut shell powder (HSP) that can be used as filler in thermoplastic matrices. In literature several biocomposites containing HSP have been investigated; however, the low aspect ratio and the irregular shape of grinded HSP has led to poor mechanical results. Consequently, this filler has been used as low added value filler to reduce the costs for the production injection molded

object with low added value (for example agricultural pots and mulching films) [4]. In this work the HSP valorization for design applications with Fused Deposition Modeling (FDM) technique has been investigated. In literature several studies can be found that investigate biocomposites made of poly(lactic acid) (PLA) and natural short fibers (like wood, waste eggshells, almonds shells etc..[5–8]. However, the excessive filament stiffness achieved with the filler addition to the PLA matrix and the difficulties encountered in reaching a constant filament diameter limited the processability of these biocomposites by FDM technique. To avoid both the problem related to the filament production and to reduce the costs, in this work PLA/HSP biocomposites have been studied by 3D printing using a pellets 3D printer. The final applications for the PLA/HSP biocomposites are design applications like to take advantage of the woody aesthetic effect provided by the natural HSP color.
Three HSP amount (from 10 up to 30 wt.%) were investigated and once that the best composition was selected, a design of experiment was carried out to generate response surfaces able to identify the best printing conditions for optimize the mechanical properties.

2. Materials and methods

Poly (lactic acid) (PLA), trade name 3052D purchased by Natureworks (Minnesota, USA), was used. This PLA grade was chosen for its high fluidity [density: 1.24 g/cm^3; MFR (210 ◦C, 2.16 kg): 14 g/10min]. Kern hazelnut shell powder, trade name HM200 were kindly provided by Arianna Fibers (Pistoia, Italy) [ρ = 0.954–1.08 g/cm^3 with HR 5–30% and average particle diameter of 25.8 μm]. Pure PLA and PLA/HSP biocomposites Bio composites formulations containing different HSP amount (from 10 up to 30 wt%) were obtained in granules by extrusion compounding technique using a Comac EBC 25HT (L/D = 44) (Comac, Cerro Maggiore, Italy) twin screw extruder. In Table 1 the formulation obtained, and their names have been reported.

Table 1. Formulations name and composition

Name	*PLA (w.%)*	*HSP (wt.%)*
PLA_10	90	10
PLA_20	80	20
PLA_30	70	30

The printing process of the 3D samples was carried out using a NX Pro pellets 3D printer (Tumaker, Gipuzoka, Spain). A 3D models of ISO527-1A dog bone specimen (useful length: 80 mm, width:10 mm, thickness: 4 mm) and ISO 179 parallelepiped specimens (80 x 10 × 4 mm) were produced and then the specimens were mechanically tested (by uniaxial tensile tests, flexural tests and Charpy impact tests). As comparison, the specimens were also produced by injection molding (IM) technique using a Megatech injection molding machine (TECNICA DUEBI s.r.l., Fabriano, Italy). The 3D specimens were produced with a 0.8 mm nozzle diameter, 0.2 mm layer thickness, 100% infill density and 55°C of build plate temperature. To select the best HSP composition firstly the nozzle temperature and the printing speed were fixed at 220°C and 25mm/s respectively. Once that the best HSP composition was selected, to optimize the mechanical performance of the 3D printed components, two main printing parameters (extrusion temperature and printing speed), were identified and the Design of Experiment (DoE) technique was applied. A surface response analysis to identify the optimum 3D printing parameters which maximize material mechanical properties was identified. The function adopted was the following (Eq.1):

$$Y(T,t) = a + bT + cS + dTS + eT^2 + fS^2 \quad (1)$$

where Y is the mechanical property under consideration, T the extrusion temperature and S the printing speed.

3. Results and conclusions

The main mechanical properties of the 3D printed biocomposites are summarized in Figure 1; moreover, the comparison with the injection molded materials is also reported.

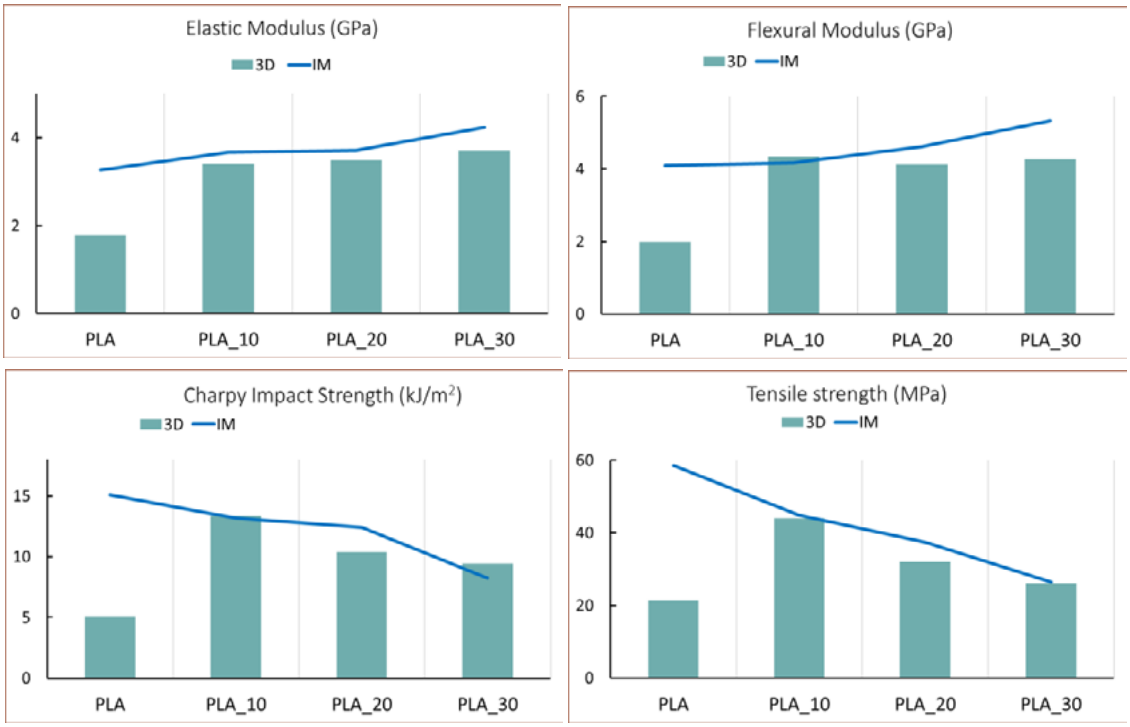

Figure 1. Mechanical properties of IM and 3D printed materials

As it could be expected the addition of a rigid filler has led to an increment of the material stiffness that is confirmed by the increment of both tensile and flexural modulus with the HSP content. The tensile stress reaches the maximum value at an HSP content of 10wt.% then the excessive filler amount and its agglomeration tendency caused a decrement of the tensile stress. Comparing the results of injection molded materials with the 3D printed ones, a general improvement of the mechanical properties was registered respect to the pure PLA matrix respect to the injection molded (IM) bio composites where a worsening of the mechanical performances respect to pure PLA was observed. The main reason for the improved properties for the 3D printed biocomposites respect to the PLA matrix, is correlated to the final porosity reached. In fact, the porosity measurements revealed that the HSP addition has reduced the final porosity of the 3D printed materials respect to pure PLA. The best HSP content was identified to be 10 wt.% for which the DOE analysis was carried out.

In Figure 2 are reported the response surfaces of the main mechanical properties (tensile and flexural modulus, tensile and flexural strength and Charpy impact strength). Equation 1 was adopted for the evaluation of the response surfaces. It can be observed that the optimum printing configuration that is able to guarantee the best mechanical performances is the one with the highest extrusion temperature (220 °C) and the lowest printing speed (25 mm/s). The analysis of SEM images confirmed the results obtained and it has been revealed that this configuration guarantees the best layers adhesion and the lowest specimens porosity. Other important results can be obtained from Figure 2. It can be observed that, also adopting the highest extrusion temperature, a progressive decay of the mechanical performance was registered increasing the printing speed. This phenomenon can be ascribed to the low viscosity of the molten polymer that caused dragging phenomena with the increment of the printing speed. This phenomenon has led to poor layers adhesion and thus to a decay of the mechanical properties [9]. On the other hand, this effect becomes less marked at the lower printing temperatures where a continuing decline in mechanical performance gap between 25 and 50 mm/min was observed.

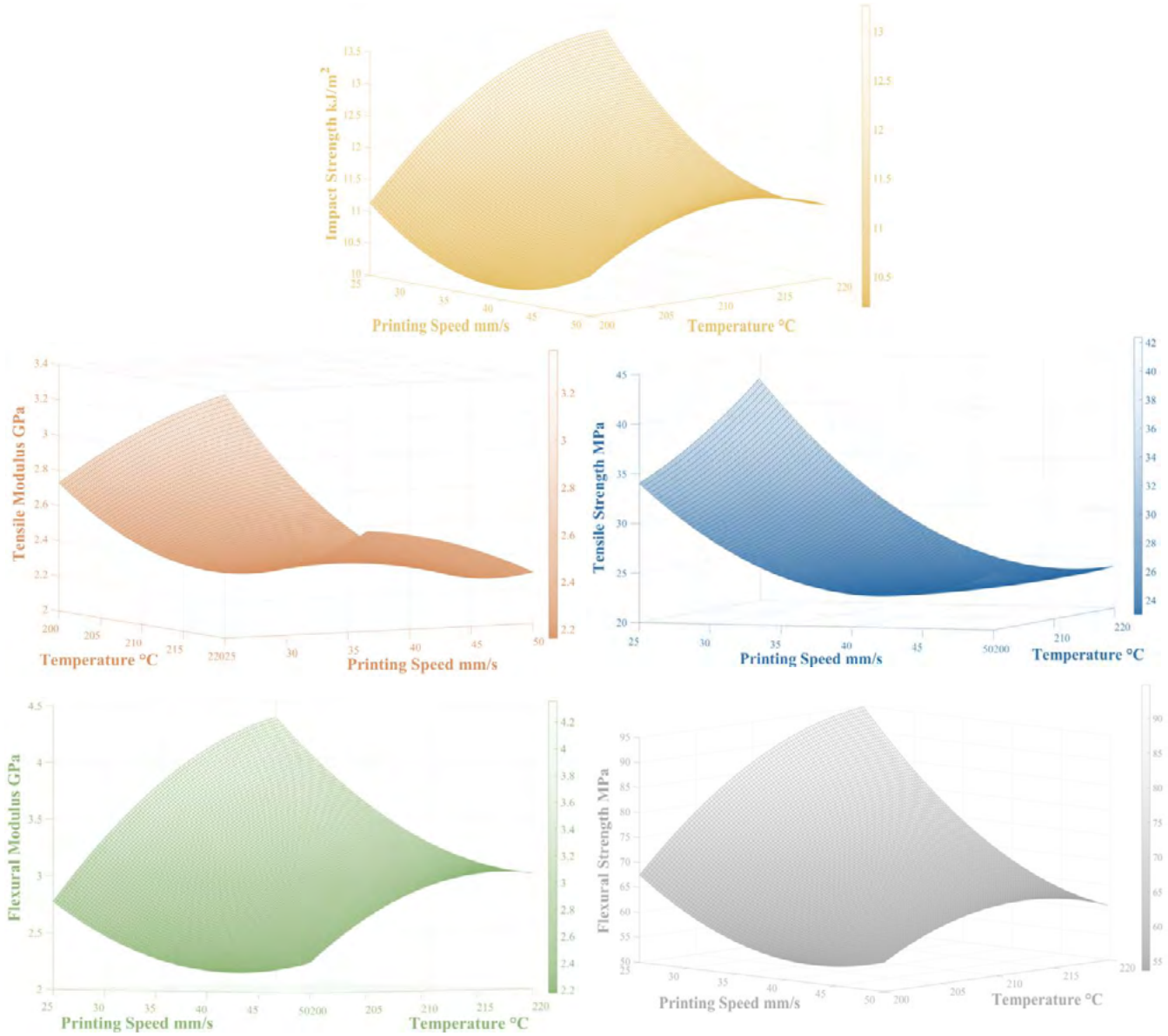

Figure 2. Response surfaces of the main mechanical properties

The analysis of the surface response confirmed that the best printing configuration was achieved with a nozzle temperature of 220°C and 25mm/min of printing speed.
Based on the results obtained some prototypes have been created to demonstrate the potentiality of HSP to produce biocomposites useful for 3D printed tailor-made applications.

References

[1] J. Kirchherr, N.-H.N. Yang, F. Schulze-Spüntrup, M.J. Heerink, K. Hartley, Conceptualizing the Circular Economy (Revisited): An Analysis of 221 Definitions, Resour Conserv Recycl 194 (2023) 107001. https://doi.org/10.1016/j.resconrec.2023.107001.

[2] J. Korhonen, C. Nuur, A. Feldmann, S.E. Birkie, Circular economy as an essentially contested concept, J Clean Prod 175 (2018) 544–552. https://doi.org/10.1016/J.JCLEPRO.2017.12.111.

[3] A. Solís, S. Rocha, M. König, R. Adam, H.O. Garcés, O. Candia, R. Muñoz, L. Azócar, Preliminary assessment of hazelnut shell biomass as a raw material for pellet production, Fuel 333 (2023). https://doi.org/10.1016/j.fuel.2022.126517.
[4] R.A. Fuentes, J.A. Berthe, S.E. Barbosa, L.A. Castillo, Sustainable Materials and Technologies 30 (2021) e00338 Development of biodegradable pots from different agroindustrial wastes and byproducts, (2021). https://doi.org/10.1016/j.susmat.2021.e00338.
[5] D. Veeman, S. Palaniyappan, Process optimisation on the compressive strength property for the 3D printing of PLA/almond shell composite, Journal of Thermoplastic Composite Materials 36 (2023) 2435–2458. https://doi.org/10.1177/08927057221092327.
[6] S. Kain, J. V. Ecker, A. Haider, M. Musso, A. Petutschnigg, Effects of the infill pattern on mechanical properties of fused layer modeling (FLM) 3D printed wood/polylactic acid (PLA) composites, European Journal of Wood and Wood Products 78 (2020) 65–74. https://doi.org/10.1007/s00107-019-01473-0.
[7] H.G. Hanumantharaju, K.P. Prashanth, B. Ramu, N. Venkatesh, G.R. Chethan, 3D Printing of Biopolymer Composites Investigation on Effect of Egg Shell Particles on Polylactic Acid Matrix, Biointerface Res Appl Chem 13 (2023). https://doi.org/10.33263/BRIAC133.251.
[8] G.S. Sivagnanamani, S.R. Begum, R. Siva, M.S. Kumar, Experimental Investigation on Influence of Waste Egg Shell Particles on Polylactic Acid Matrix for Additive Manufacturing Application, J Mater Eng Perform 31 (2022) 3471–3480. https://doi.org/10.1007/s11665-021-06464-y.
[9] L. Aliotta, C. Sergi, B.D. Pont, M.-B. Coltelli, V. Gigante, A. Lazzeri, Sustainable 3D printed poly (lactic acid) (PLA)/Hazelnut shell powder bio composites for design applications, Materials Today Sustainability 26 (2024) 100780. https://doi.org/10.1016/j.mtsust.2024.100780.

TAILORED HYBRID COMPOSITE PREFORMS BY AUTOMATED FIBRE PLACEMENT OF POWDER EPOXY-BASED TOWPREGS

Murat Çelik[1,2], Arun Kumar Alapati[1], James Davidson[3], Hanisa Hasrin[3], David May[4], Colin Robert[3], Conchúr Ó Brádaigh[3]
[1]School of Engineering, Institute for Materials and Processes, University of Edinburgh, EH9 3FB, Edinburgh, Scotland, UK
Email: M.Celik@ed.ac.uk
[2]Engineering Faculty, Erciyes University, 38280, Kayseri, Türkiye
[3]Department of Materials Science and Engineering, University of Sheffield, S1 3JD, Sheffield, UK
Email : c.robert@sheffield.ed.ac.uk
[4]Leibniz-Institut für Verbundwerkstoffe GmbH, 67663, Kaiserslautern, Germany
Email : David.May@ivw.uni-kl.de

Keywords: Powder epoxy, solid resin, towpregs, hybrid composites, AFP

Abstract

Hybrid composites, which combine different fibre reinforcement types in a single matrix, aim at enhancing and tailoring mechanical properties for specific applications. The use of powder epoxy can be attractive for hybrid composites, due to its exceptional characteristics. At room temperature, powder epoxy is solid, and it undergoes melting at around 45°C. Powder epoxy-based towpregs have been successfully developed for use in automated composite manufacturing techniques. These towpregs do not need to be stored at refrigerated conditions, resulting in a significant reduction in transportation and storage costs and also ecological impact. Automated fibre placement (AFP) processing can be employed to produce reshapable, hybrid composite preforms from powder epoxy-based towpregs. In this study, a corresponding concept is proposed, where the target is to combine carbon and glass fiber in a single matrix. The primary objective of the study is to assess the potential of utilising powder epoxy-based towpregs in AFP applications for the production of composite parts that are specifically customised to particular applications. For this, carbon fibre towpregs made from powder epoxy are laid on dry glass fibre fabrics using an AFP head, with the towpregs undergoing partial curing. Subsequently, the preform is fully cured via compression moulding, with additional powder epoxy being introduced during this process to impregnate the dry glass fiber. Mechanical tests are carried out to characterise the hybrid composite. The interply hybrid samples displayed a quasi-linear stress-strain relationship, with an ultimate tensile strength (UTS) of 531.73±42.71 and an interlaminar shear stress (ILSS) of 17.67±2.99 for 0° fibre orientation, which are consistent with the values reported in the literature. Dynamic mechanical analysis (DMA) results indicate a good adhesion between the matrix and fibres. Scanning electron microscopy (SEM) revealed a good consolidation is achieved in both glass and carbon fibre.

1. Introduction

In recent decades, there has been an increase in the adoption of automated composite production techniques. These techniques offer several benefits, including repeatability, accuracy, as well as reduced labour and material scrap [1]. Particularly, the aerospace industry extensively utilises the automated fibre placement (AFP) process, in which narrow tapes are laid onto a tool with a gantry or robotic system, in a layer-by-layer fashion. It is expected that AFP technology will experience substantial growth in the next two decades [2]. Tapes for AFP applications can be fabricated from thermosetting or thermoplastic

materials, while the former requires special conditions for storage and processing to avoid premature curing.

Powder epoxy, also referred to as solid resin, has been shown to be a promising alternative to conventional thermosetting prepreg systems [3]. Powder epoxy is solid at room temperature; hence, it has a virtually indefinite shelf life. Unlike other thermosetting prepreg systems, powder epoxy prepregs or towpregs (prepreg tapes) do not require refrigerated storage, which reduces transportation and storage costs considerably. This feature not only presents economic advantages, but also contributes to reducing the carbon footprint associated with refrigeration, aligning with current environmental sustainability concerns. Thanks to the heat-activated curing agents present in the powder epoxy, significant curing does not occur until elevated temperatures (>100°C) are reached. This characteristic effectively provides the ability to create consolidated, uncured solid preforms that can be reshaped multiple times, similar to thermoplastic materials. These preforms enable the co-curing of multiple components, eliminating the need for adhesives. Furthermore, low curing exotherms and little to no volatile organic compound (VOC) release are some other advantages of powder epoxies [4].

Hybrid composites exploit the advantages of various reinforcement or matrix systems. As far as weight and cost are concerned, carbon and glass reinforcements can be incorporated to tailor the desired properties. For instance, hybridisation can yield pseudo-ductility due to synergistic effects, from the integration of constituent components that individually exhibit brittleness [5]. In terms of hybrid composites, combining powder epoxy-based towpregs with the AFP process can present opportunities for many applications, where localised strengthening is necessary while the cost and weight are major parameters. This study aims to utilise AFP technology with powder epoxy-based towpregs to produce locally reinforced hybrid composites. To achieve this goal, firstly, powder epoxy-based carbon fibre towpregs were produced in a towpregging line. Produced towpregs were then laid onto a dry glass fibre bed to produce intermediate preforms. The resulting preforms were consolidated with powder epoxy to create fully cured hybrid composite plates through compression moulding. Tensile and interlaminar shear tests were carried out to investigate the mechanical behaviour of the produced specimens. To gain insights into the viscoelastic behaviour, dynamic mechanical analysis (DMA) test was carried out. Fractographic surfaces are investigated using scanning electron microscopy (SEM). The results suggest that powder epoxy-based hybrid composites can be produced by integrating AFP with further manufacturing technologies.

2. Experimental

2.1. Materials

For towpregs, Toray T700S-24 K-50C (1% sizing) carbon fibre tow was impregnated with powder epoxy (PE6405, 1220 kg/m^3, supplied by FreiLacke and designed by Swiss CMT AG) in an automated towpregging line. Glass fibre used was biaxial stitched SAERTEX X-E-444g/m^2.

2.2. Hybrid composite specimen production

The first step of the study involved the production of powder epoxy-based towpregs. Figure 1 illustrates the towpreg production process, which begins with the introduction of carbon fibre tows to the towpregging line through a series of rollers. Powder epoxy is then applied on the surfaces of the tow with an electrostatic powder gun. Subsequently, the tows, now coated with powder epoxy, proceed into a heating section equipped with an infrared lamp. The radiation emitted by the infrared lamp melts the powder epoxy on the tow surfaces, initiating the impregnation of the tow. Once the impregnation is complete, the towpreg is cooled and wound onto spools. Production speed, tension or temperature are monitored with the sensors and control units on the line throughout the process. It is possible to control the fibre volume fraction by adjusting the production speed and electrostatic deposition parameters. Details of the system are given in Refs. [6], [7]. Using the towpregging line, towpreg spools with a target FVF of 36%, and a width of 6.35 mm were produced at a production speed of 3.2 m/min, at 120°C.

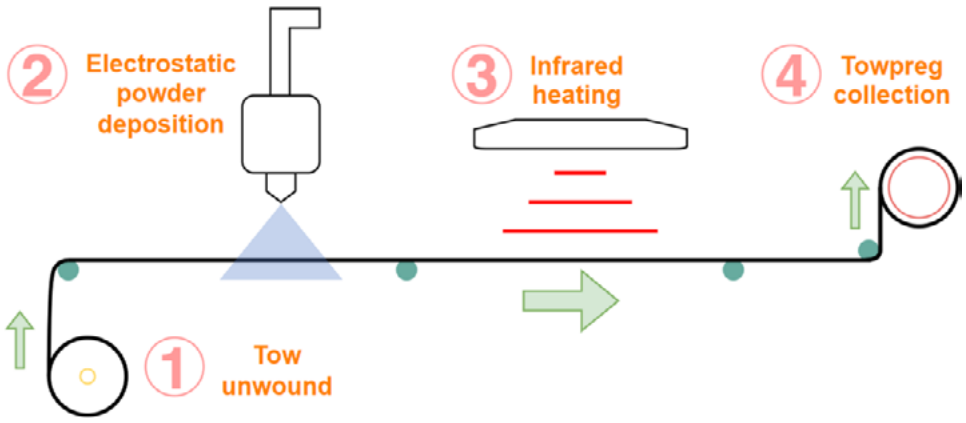

Figure 1. Towpregging process

After the production of towpregs, an AFP machine (EVO I) was used to deposit them onto a glass fibre fabric at Leibniz-Institut für Verbundwerkstoffe GmbH (IVW), Germany. The AFP system at the IVW features a specialised AFP head equipped with a hot gas torch to provide heating during the layup. To ensure a proper consolidation, a consolidation force of 200 N and a torch flow rate of 3 SLPM were used for the layup process. The AFP head moved at a speed of 20 m/min, while a consolidation roller was used, which was actively cooled down to room temperature. The relatively faster layup speed (20 m/min) was adopted to demonstrate the capability of processing towpregs at considerable speeds without encountering issues. Moreover, the higher speed proved useful in preventing overheating risks associated with the hot gas torch system. Figure 2 displays the AFP process, wherein one layer of towpreg strips are laid onto the glass fabric side by side in the same direction.

Figure 2. AFP process of the powder epoxy-based towpreg onto glass fibre

The hybrid preforms, consisting of AFP-laid carbon fibre on glass fibre, were then cured in a compression moulding process to obtain fully cured hybrid composite samples, with the manual addition of extra powder epoxy on the dry glass fabric based on the target FVF to also impregnate it (Figure 3). The curing cycle involved an isothermal dwell at 120°C temperature and 3 bar pressure for 2 hours. This

dwell period was aimed at providing a good wetting of the glass fibre, due to the low viscosity of powder epoxy at these temperatures. Subsequently, curing was finalised with another 2-hour isothermal dwell at 180°C and 1 bar. A heating rate of 1°C/min was maintained in all ramp periods. After the curing, the samples were cut with a wet saw for the mechanical tests, according to the required dimensions defined by standards.

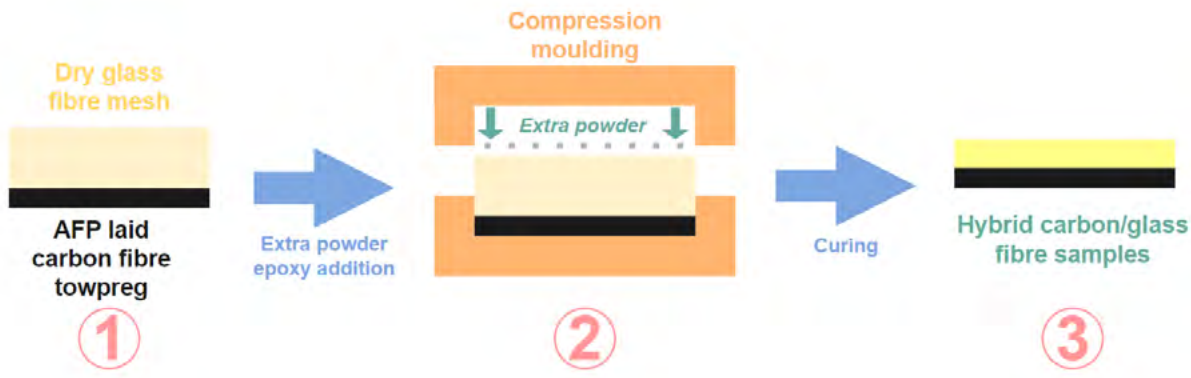

Figure 3. Hybrid composite sample production from preforms

2.3. Tests

Tensile and interlaminar shear stress tests were carried out for the samples to determine the mechanical behaviour. Tensile tests were done according to ISO 527-5:2009 standard, with a crosshead speed of 2 mm/min. As only one layer of carbon fibre is laid onto a layer of glass fibre, cured samples are quite thin (~1 mm). Short beam interlaminar shear stress (ILSS) tests were carried out according to ISO 14130 standard. The co-curing ability of the powder epoxy has been demonstrated previously, enabling the production of multiple-component composites without the adhesives [8]. For ILSS tests, two preforms were cured together in a [G/C/C/G] arrangement to explore the viability of joint curing of multiple preforms. This arrangement can be potentially useful in thermoforming applications, in which a seamless integration of multiple fibre types is needed.

A dynamic mechanical thermal analyzer (TA Instruments Discovery DMA 850) was used to measure glass transition temperature (Tg) and damping (tan delta). The measurements were performed in a dual cantilever beam setup using a heating rate of 3 °C/min, in an oscillatory temperature ramp, at temperatures ranging from 20 to 180 °C, at an amplitude of 20 µm, and at a test frequency of 0.1, 1, 3, 7, and 10 Hz. The specimen dimensions were 35mm in length, 13mm in width and 1mm in thickness. The dynamic glass transition temperature was determined at the peak value of the mechanical damping tan delta.

3. Results and discussion

The mechanical test results of an interply hybrid sample are displayed in Figure 4. The stress-strain graph reveals a quasi-linear relationship, indicative of a brittle behaviour. For this specific sample, the ultimate tensile strength (UTS) is 561.69 MPa. Figure 4 (b) illustrates the ILSS results for all the samples at 0 and 90° orientation. The average ILSS is 17.67±2.99 and 8.28±2.10 MPa for 0 and 90 deg samples, respectively. Due to the fibre directions of glass and carbon fibres (±45° glass fibre and unidirectional carbon fibre) and single-layer layup, the ILSS of 0° samples is 113.4% higher than that of 90° samples. A summary of mechanical test results for all samples is provided in Table 1. The average UTS for all

the samples is 531.73±42.71 MPa, whereas the average modulus is 40.09±2.3 GPa. The mechanical test results demonstrate that the proposed novel processing strategy provides mechanical properties comparable to existing methods and has no negative effects on the mechanical behaviour [9][10].

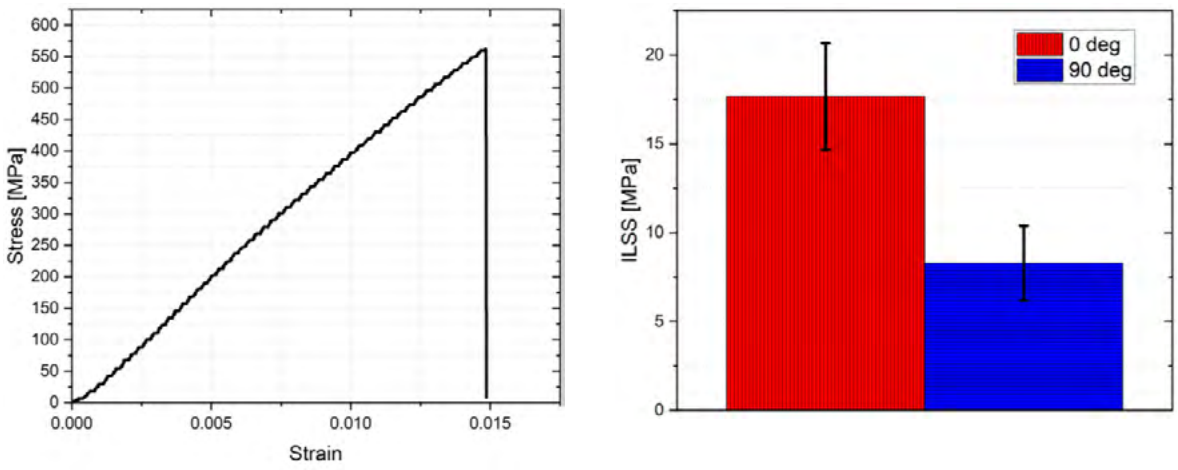

Figure 4. (a) Stress-strain graph of a tensile 0 degree sample **(b)** ILSS test results

Table 1. Tensile and ILSS test results for the hybrid composite samples

Sample FVF (%)	Tensile Strength (MPa)	Tensile Modulus (GPa)	ILSS (0°) (MPa)	ILSS (90°) (MPa)
36	531.73±42.71	40.09±2.35	17.67±2.99	8.28±2.10

Viscoelastic and thermomechanical properties of the samples were analysed through DMA. Figure 5 shows the storage modulus and tan delta of the samples across different frequency rates. The frequency dependency of glass transition temperature (Tg) can be observed. At higher frequencies, the reptation of polymer chains within the material is hindered, leading to a delay in the onset of molecular motion and consequently a higher observed Tg. At 10 Hz frequency, the Tg_{peak} of the samples is around 120°C. Storage modulus values surpass 15,000 MPa at 3 Hz frequency, indicating a good adhesion between the matrix-fibre interfaces [11]. However, it is noticeable that at higher frequencies (7 and 10 Hz) the modulus value is reduced, likely due to both the stiffness and the fibre orientation mismatches between carbon and glass fibres, leading to poorer stress transfer at high frequencies.

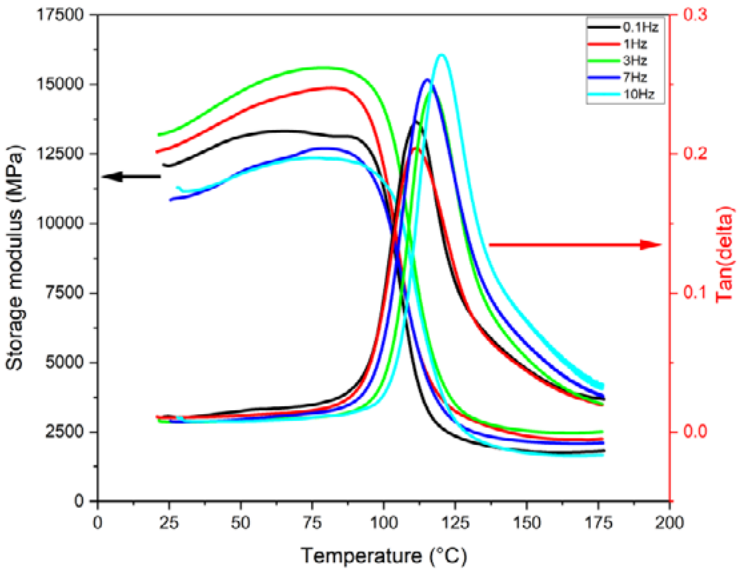

Figure 5. DMA scan of a sample for different frequencies

The SEM images of the failed tension test samples reveal a few key features of the produced hybrid composites. Figure 6 (b) shows the different regions of the sample, with the dashed line encompassing the glass fibre region. It can be seen that generally the carbon fibre part of the samples exhibits a better homogeneity, compared to the glass fibre part, partly due to the unidirectional fibre arrangement. Both fibre types have undergone good consolidation, resulting in a cohesive structure. However, resin-rich regions are observed within the carbon fibre part, indicating potential areas of concern for optimisation to achieve more uniform resin distribution in the towpregging and AFP process. There is evidence of better fibre wetting in the carbon fibres laid by AFP compared to the glass fibres, which are consolidated via compression moulding. Fracture surfaces have relatively low roughness, indicating smooth crack propagation, which suggests a potential weakness at the glass-carbon fibre interface.

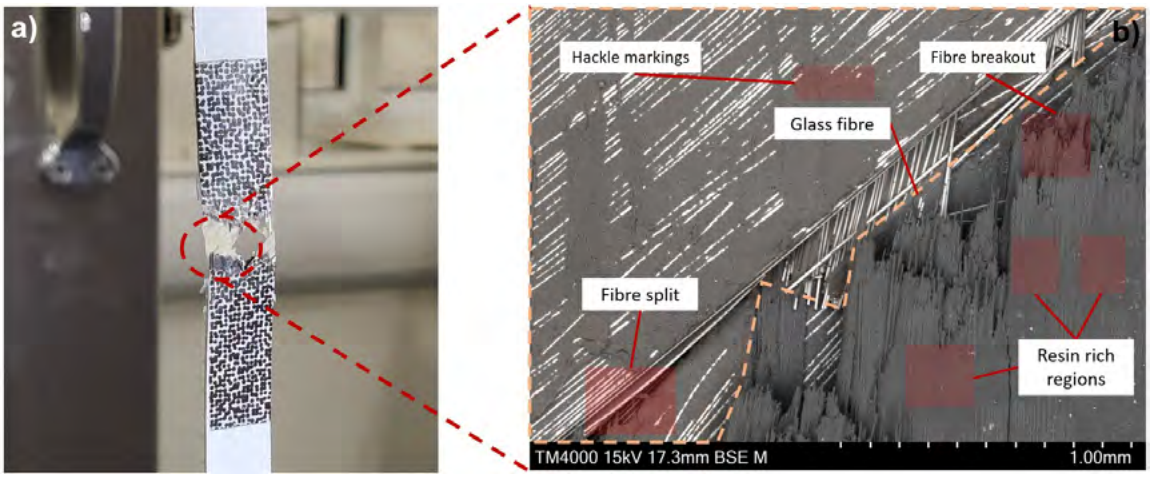

Figure 6. (a) Fracture of a sample during tensile testing **(b)** SEM images of a fracture surface (dashed line encompasses the glass fibre part)

4. Conclusions

This preliminary study demonstrates the successful implementation of a novel processing strategy for producing interply hybrid composites. The results suggest that the AFP process can be effectively utilised to create hybrid preforms, thanks to the superior characteristics of powder epoxy-based towpregs. Processing at decent output rates is possible without any damage of the towpregs. The mechanical performance of the produced hybrid composites is consistent with the reported values in the literature. The intermediate preforms can be further processed to produce locally strengthened, cost-effective hybrid composites. Future research should extend the investigation to compare the performance of full-scale functional parts with alternative production systems. Optimising powder distribution is essential both during towpreg production and manual dispersion during compression moulding. A more homogenous powder distribution can reduce the number of resin-rich areas and enhance the interfaces between different fibre phases, thus improving overall composite performance. Furthermore, the long processing times can be alleviated by altering the resin formulation, which would facilitate the adoption of powder epoxy-based hybrid composites in various industries.

References

[1] E. Oromiehie, B. G. Prusty, P. Compston, and G. Rajan, “Automated fibre placement based composite structures: Review on the defects, impacts and inspections techniques,” Compos. Struct., vol. 224, p. 110987, Sep. 2019.

[2] A. Brasington, C. Sacco, J. Halbritter, R. Wehbe, and R. Harik, “Automated fiber placement: A review of history, current technologies, and future paths forward,” Compos. Part C Open Access, vol. 6, p. 100182, Oct. 2021.

[3] J. M. Maguire, P. Simacek, S.G. Advani, and C.M. Ó Brádaigh, “Novel epoxy powder for manufacturing thick-section composite parts under vacuum-bag-only conditions. Part I: Through-thickness process modelling,” Compos. Part A Appl. Sci. Manuf., vol. 136, p.105969, May 2020.

[4] D. Mamalis, T. Flanagan, and C. M. Ó Brádaigh, “Effect of fibre straightness and sizing in carbon fibre reinforced powder epoxy composites,” Compos. Part A Appl. Sci. Manuf., vol. 110, pp. 93–105, Jul. 2018.

[5] P. Zuo, D. V. Srinivasan, and A. P. Vassilopoulos, “Review of hybrid composites fatigue,” Compos. Struct., vol. 274, p. 114358, Oct. 2021.

[6] M. Çelik, T. Noble, F. Jorge, R. Jian, C. M. Ó Brádaigh, and C. Robert, “Influence of Line Processing Parameters on Properties of Carbon Fibre Epoxy Towpreg,” J. Compos. Sci. 2022, Vol. 6, Page 75, vol. 6, no. 3, p. 75, Mar. 2022.

[7] M. Çelik, J. M. Maguire, T. Noble, C. Robert, and C. M. Ó Brádaigh, “Numerical and experimental investigation of Joule heating in a carbon fibre powder epoxy towpregging line,” Compos. Part A Appl. Sci. Manuf., vol. 164, p. 107285, 2023.

[8] T. Noble et al., “Powder Epoxy for One-Shot Cure, Out-of-Autoclave Applications: Lap Shear Strength and Z-Pinning Study,” J. Compos. Sci. 2021, Vol. 5, Page 225, vol. 5, no. 9, p. 225, Aug. 2021.

[9] Y. I. Tsai, E. J. Bosze, E. Barjasteh, and S. R. Nutt, “Influence of hygrothermal environment on thermal and mechanical properties of carbon fiber/fiberglass hybrid composites,” Compos. Sci. Technol., vol. 69, no. 3–4, pp. 432–437, 2009.

[10] P. W. Manders and M. G. Bader, “The strength of hybrid glass/carbon fibre composites - Part 1 : Failure strain enhancement and failure mode P.W.,” J. Mater. Sci., vol. 16, no. 8, pp. 2233–2245, 1981.

[11] T. Brocks, M. O. H. Cioffi, and H. J. C. Voorwald, “Effect of fiber surface on flexural strength in carbon fabric reinforced epoxy composites,” Appl. Surf. Sci., vol. 274, pp. 210–216, Jun. 2013.

BETA-PHASE INDUCED POLY(3-HYDROXYBUTYRATE-CO-3-HYDROXYVALERATE) NANOFIBERS SYNERGIZED BY VAPOR SOLVENT INTERFIBER WELDING FOR SELF-REINFORCING EFFECT

Pejman Heidarian[1], Shazed Aziz[2], Peter Halley[3], Tony McNally[4], Ton Peijs[5], Luigi Vandi[6] Russell J. Varley[7]

[1]Carbon Nexus at the Institute for Frontier Materials, Deakin University, Geelong, Victoria 3216, Australia
Email: p.heidarian@deakin.edu.au, Webpge: https://www.deakin.edu.au/about-deakin/people/pejman-heidarian
[2]School of Chemical Engineering, University of Queensland, St Lucia, 4072, Australia
Email: shazed.aziz@uq.edu.au, Webpage: https://researchers.uq.edu.au/researcher/24393
[3]Centre for Advanced Materials Processing and Manufacturing AMPAM, The University of Queensland, St Lucia, 4072, Australia
Email: p.halley@uq.edu.au, Webpage: https://researchers.uq.edu.au/researcher/333
[4]International Institute for Nanocomposite Manufacturing (IINM), WMG, University of Warwick, Coventry, CV4 74L, United Kingdom
Email: t.mcnally@warwick.ac.uk, Webpage: https://warwick.ac.uk/fac/sci/wmg/about/our-people/profile?wmgid=946
[5]Materials Engineering Centre, WMG, University of Warwick, Coventry, CV4 74L, United Kingdom
Email: t.peijs@warwick.ac.uk, Webpage: https://warwick.ac.uk/fac/sci/wmg/about/our-people/profile?wmgid=1864
[6]School of Mechanical and Mining Engineering, University of Queensland, St Lucia, 4072, Australia
Email: l.vandi@uq.edu.au, Webpage: https://researchers.uq.edu.au/researcher/2503
[7]Carbon Nexus at the Institute for Frontier Materials, Deakin University, Geelong, Victoria 3216, Australia
Email: russell.varley@deakin.edu.au, Webpge https://www.deakin.edu.au/about-deakin/people/russell-varley

Keywords: Poly(3-hydroxybutyrate-co-3-hydroxyvalerate); Electrospinning; Self-reinforcing effect; β-phase; Vapor solvent interfibre welding

Abstract
In this study, we explore an approach to enhance the mechanical performance of Poly(3-hydroxybutyrate-co-3-hydroxyvalerate) (PHBV) by utilizing the self-reinforcing effect of β-phase induced PHBV electrospun nanofibre mats. This involves electrospinning combined with low-temperature post-spun vapor solvent interfibre welding. Scanning electron microscopy (SEM) imaging confirmed fibre alignment, while XRD diffraction revealed the presence of both α and β crystalline phases under optimized electrospinning conditions. The resulting composite exhibited significant improvements in mechanical properties attributed to the formation of more perfectly structured α and β polymorphs and enhanced interfacial adhesion of electrospun nanofibres after vapor solvent treatment. This approach offers entirely recyclable and biodegradable materials, presenting the potential for a new family of sustainable bioplastics.

1. Introduction

In recent years, there has been growing concern about the impact of petroleum-based plastic waste on the environment, leading to an urgent need for sustainable and biodegradable alternatives [1-3]. Among the diverse array of bio-based polymers, bacterial aliphatic polyester polyhydroxyalkanoates (PHAs)

have emerged as promising alternatives to traditional petroleum-based plastics due to their biodegradability, biocompatibility, and similar hydrophobicity and mechanical properties to most common polyolefins, such as polyethylene and polypropylene [4-6]. The categorization of PHAs relies on the composition of the monomers forming the polymer backbone. These include polyhydroxybutyrate (PHB), polyhydroxyvalerate (PHV), polyhydroxybutyrate-co-valerate (PHBV), poly(3-hydroxybutyrate-co-3-hydroxyhexanoate) (PHBH), polyhydroxyhexanoate (PHHX), and polyhydroxyoctanoate (PHO). Amongst the family PHAs, PHBV has recently gained interest as a biodegradable and versatile thermoplastic. However, PHBV has limitations such as lower tensile toughness and stiffness compared to petroleum-based plastics and some aliphatic biodegradable polyesters [7-12].

One approach to improve the mechanical performance of PHBV is to fabricate fully biodegradable PHBV composites either using sustainable fillers, such as natural fibres [13-15] or utilize a self-reinforcing approach. The self-reinforcing effect relates to the reinforcement of polymers with highly oriented films, fibres, or particles from the same polymer. Of particular interest is the ability of PHBV to crystallize into α and β polymorphs, with the β phase standing out for its highly ordered crystalline structure. The β phase in PHBV is formed from the orientation of free chains between the α-form lamellar crystals, exhibiting a twisted planar zigzag conformation with a higher crystal lattice modulus. The β phase in PHBV exhibits a highly ordered crystalline structure and superior mechanical properties, with a high potential for self-reinforcing, but compared to the α phase, preserving the β phase is challenging due to its lower melting temperature [16-18].

In this research, to preserve the β-phase and achieve strong bonding at the fibre intersections, a low-temperature post-spun vapor solvent interfibre welding was utilized. This combined approach seeks to fabricate PHBV composites with enhanced mechanical properties appealing to diverse applications, including medical devices, long-term drug delivery platforms, sustainable packaging, and biomedical devices. The orientation of polymer chains along the fibre axis and the formation of α and β crystalline phases were confirmed through XRD diffraction confirming that vapor solvent welding allowed for the preservation of the β-phase. DSC experiments provided insights into the thermal behaviour of the fibres, and tensile test were conducted to evaluate their mechanical performances.

2. Materials and Methods

Poly(3-hydroxybutyrate-co-3-hydroxyvalerate) (PHBV) powder under the trade name of ENMAT Y1000 with 1 mol% 3-(hydroxyvalerate) (HV) content, was generously provided by TianAn Biopolymer (ENMAT), Zhejiang Province, China. Chloroform and DMF were used as received, as solvents for electrospinning.

2.1. Preparation of PHBV solution and Electrospinning of PHBV Nanofibres

The PHBV polymer was added to chloroform and stirred until the complete dissolution of the polymer was achieved. Subsequently, DMF was added to the solution as a co-solvent and stirred to achieve a homogeneous solution. The resulting solution consisted of 8 wt% PHBV in a 90/10 chloroform/DMF co-solvent [19]. The solution of 8 wt% PHBV in a 90/10 chloroform/DMF co-solvent was loaded into a 20 mL syringe with a blunt-tipped needle (25 g). The syringe was mounted onto a commercial electrospinning system (HOLMARC HO-NFES-043, Kerala, India). To generate polymer jets in the electrospinning process, three different source-to-target distances were selected: 15 cm, 20 cm, and 25 cm. To maintain a constant electric field intensity of 1 kV/cm, voltages of 15 kV, 20 kV, and 25 kV were applied, respectively. The electrospinning process was conducted at a flow rate of 1 mL/h at room temperature, while the collector was rotated at speeds of 300, 600, and 1200 rpm.

2.2. Post-spun treatment by solvent vapor interfibres welding

After the electrospinning process, the collected PHBV nanofibre mats were subjected to solvent vapor interfibre welding to weld loosely packed electrospun nanofibres at their junction points. Samples were placed into a sealed glass desiccator at room temperature and exposed to saturated DMF vapor at different times 60, 120, and 180 min.

2.3. Characterization

Scanning electron microscopy (SEM, Zeiss, Supra, Oberkochen, Germany) was employed to assess the morphology, alignment, and welding of PHBV nanofibress. Image analysis was performed using ImageJ software. Crystalline structures were assessed using an analytical XPert Powder diffractometer equipped with a Copper X-ray target and wavelength of 1.54A operating at 40kV and 30 mA. The samples were scanned in the 2θ range from 5° to 40° at a scanning rate of 5° per min. Thermal properties were then assessed using a differential scanning calorimeter (DSC, 214, Netzsch). To assess the quasi-static mechanical properties of the samples, tensile tests were performed using an Instron Universal testing machine equipped with a 50 N load cell at the strain rate of 2 mm/min.

3. Results and Discussions

3.1. Morphology, Crystallinity, and Thermal Properties

Figures 1a-i show the morphology of electrospun PHBV nanofibres mats collected under nine different rotational speeds and source-to-target distance conditions. At a rotational speed of 300 rpm and three different source-to-target distances, misalignment is evident, see SEM images in Figure 1a-c. Increasing the rotational speed to 600 and 1200 rpm across all source-to-target distances resulted in improved fibre alignment, attributed to the heightened stretching forces acting along the fibre axis. Moreover, the influence of the source-to-target distance on fibre alignment also revealed that longer distances provided more elongation to the polymer solution, leading to a higher degree of fibre alignment. Increasing the distance to 25 cm and the speed to 1200 rpm resulted in the optimum electrospinning condition for aligning PHBV nano fibres with a diameter of 530 ± 41 nm.

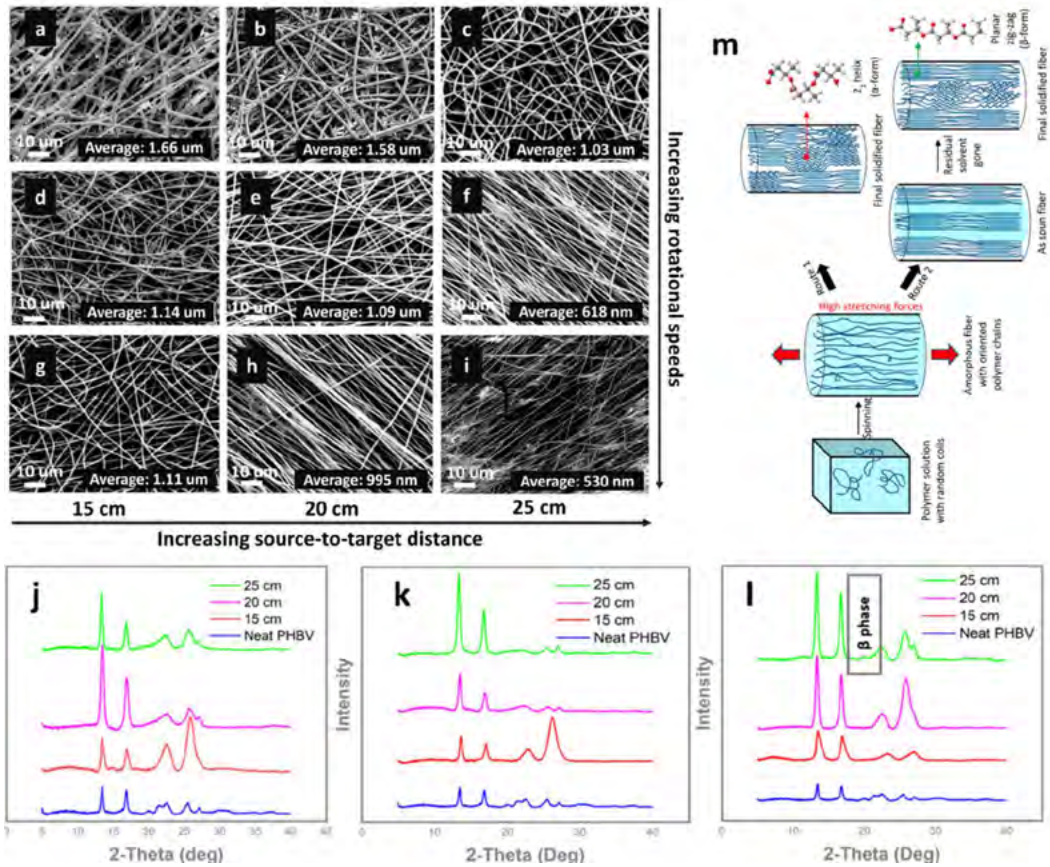

Figure 1. SEM images of PHBV nanofibress at the rotational speed of 300 rpm and source-to-target distances of (a) 15 cm (b) 20 cm and (c) 25 cm; the rotational speed of 600 rpm and source-to-target distances of (d) 15 cm (e) 20 cm (f) 25 cm; and rotational speed of 1200 rpm and source-to-target distances of (g) 15 cm, (h) 20 cm, (i) 25 cm, XRD analysis of PHBV nanofibre at (j) 300 rpm, (k) 600 rpm, (l) 1200 rpm, and (m) potential routes for the formation of α- and β-form crystal structures during the electrospinning [20].

Figures 1j-k display the XRD patterns of different electrospun fibres collected under nine different rotational speeds and source-to-target distance conditions. Within these patterns, two distinctive diffraction peaks at 13.7° and 17.1° corresponding to (020)α and (110)α reflection planes were identified that are related to the α-form [21, 22]. Notably, the intensity and sharpness of these peaks were observed to increase, as the rotational speed and source-to-target distance were elevated. In addition to the presence of orthorhombic α-form crystals displaying a helical chain arrangement [45], electrospun PHBV fibres aligned under rotational speeds of 1200 rpm and a source-to-target distance of 25cm exhibited a unique diffraction peak at a 2θ angle of 19.95°, corresponding to a planar zigzag conformation of (110)β planes. The subtle emergence of β-form crystals confirms substantial chain stretching within the amorphous region positioned between the α-crystalline lamellae. This observation reveals that the interconnected chains between the α-form crystalline lamellae experienced further elongation during the jet-whipping process, ultimately resulting in the formation of both α and β crystalline polymorphs.

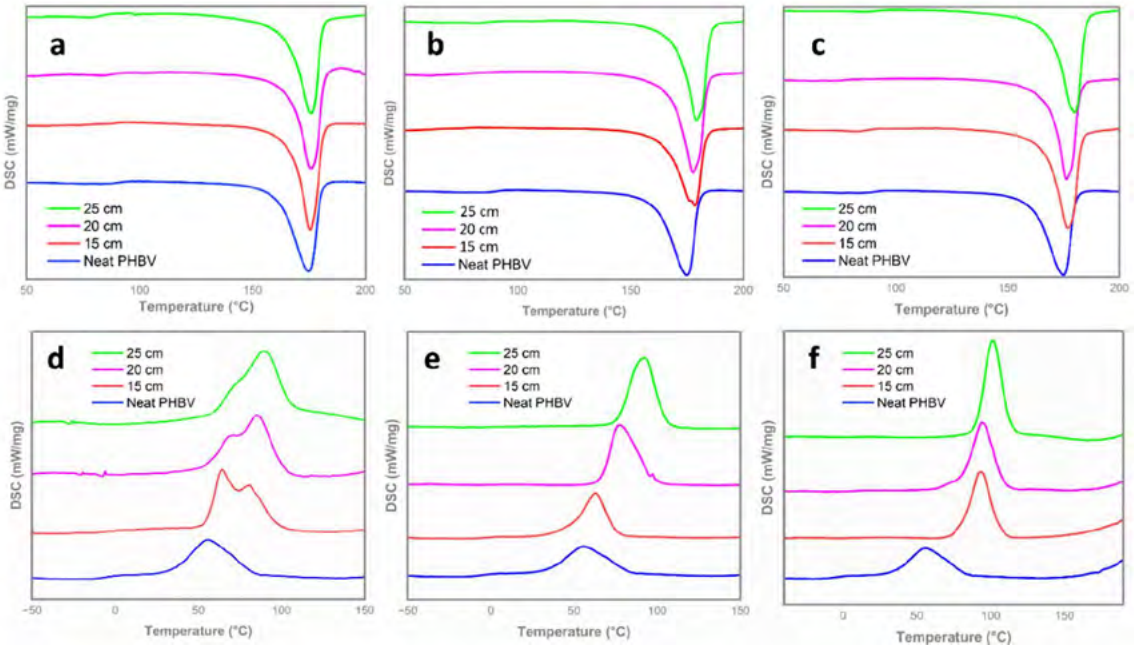

Figure 2. DSC analysis of electrospun PHBV nanofibre and the first melting run at (a) the rotational speed of 300 rpm; (b) the rotational speed of 600 rpm; (c) rotational speed of 1200 rpm at source-to-target distances of 15 cm, 20 cm, 25 cm; the cooling run at (d) the rotational speed of 300 rpm; (e) the rotational speed of 600 rpm; (f) rotational speed of 1200 rpm at source-to-target distances of 15 cm, 20 cm, 25 cm.

3.2 Effect of solvent vapor-induced interfibre welding on the morphology and crystallinity

Retaining the β crystalline phase during thermal processing is relatively challenging due to its lower melting temperature and instability compared to the α crystalline phase. Processes that require high temperatures to bond the fibres to the matrix clearly will likely destroy the β phase rendering a homogeneous composite [23-26]. To preserve the self-reinforcement effect of the β phase and reduce the delamination of PHBV nanofibres therefore, the β phase-induced PHBV nanofibres were exposed to DMF vapor for different exposure times. During a 60-min exposure, only minimal welding was observed at the nanofibre intersections, as can be seen in Figure 3a-c. Extending the exposure time to 120 min led to improved fusion between the intersecting nanofibres due to some dissolution of the polymer at the intersections of the fibres, without impacting the overall structure of the electrospun nanofibre mats. A 180 min exposure to solvent vapor led to significant fusion effects compared to the shorter exposure at the cross points. As can be observed in Figure 3d and e after a solvent exposure time of 180 min, the β phase in PHBV remained intact confirmed by the existence of the peak at 2θ angle of

19.95°, corresponding to a planar zigzag conformation and an observed shift in the C=O stretching in the FTIR spectrum.

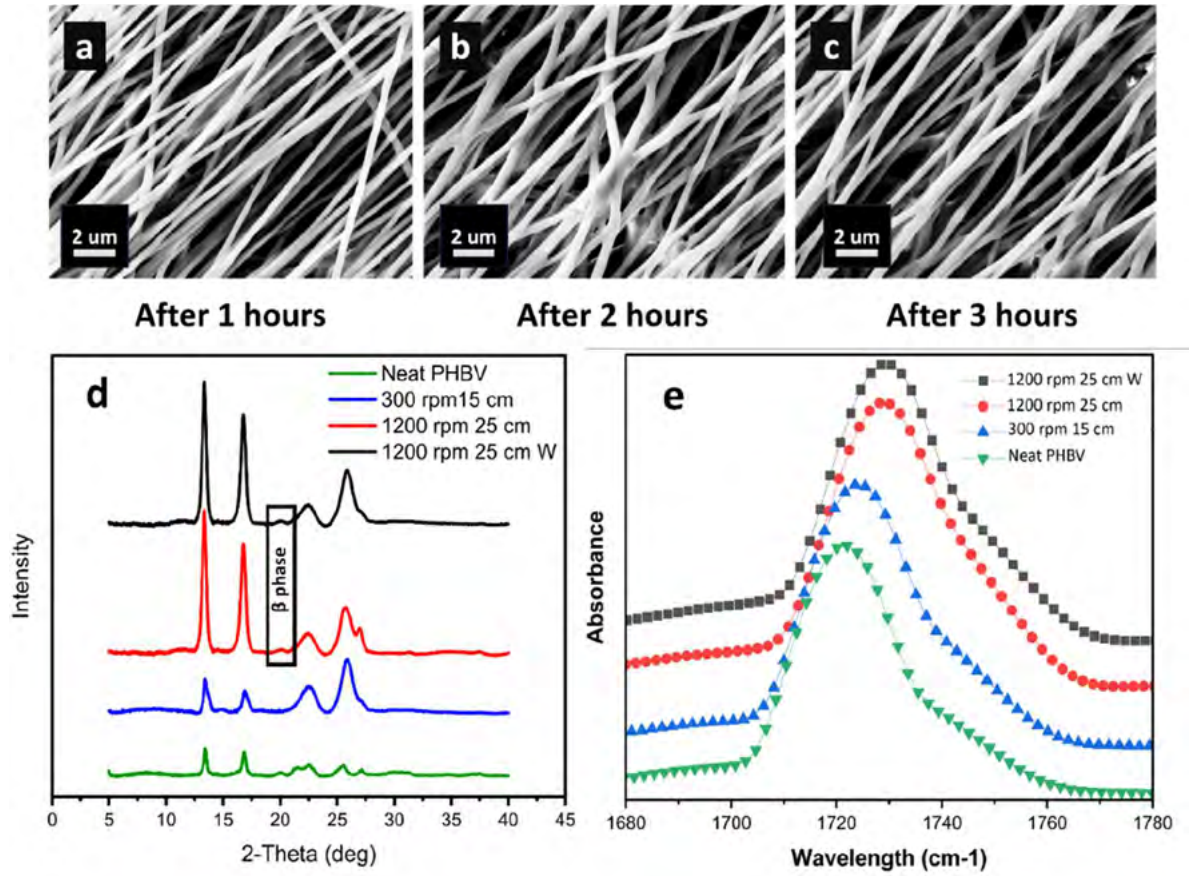

Figure 3. Exposing the β-phase reinforced electrospun PHBV nanofibres to DMF vapor under different exposure times: (a) 60 min, (b) 120 min, (c) 180 min; (d) XRD and (e) FTIR of welded (W) and non-welded PHBV nanofibres to confirm the existence of a planar zigzag conformation and shift in the C=O stretching vibration.

3.2 Mechanical Properties of Non-Welded and Welded Electrospun Nanofibre Mats

The UTS, determined from tensile testing (Figure 4a-d), showed an increase from 878 MPa to 1454 MPa at 300 rpm, representing a 65.2% increase. This shows that the source-to-target distance is an important consideration in achieving enhanced mechanical properties. At a constant source-to-target distance (e.g., 25 cm), an increase in rotational speed also results in notable increases in UTS results. For instance, the UTS increases from 1454 MPa at 300 rpm to 6095 MPa at 1200 rpm, indicating the largest enhancement due to the coexistence of α and β crystalline polymorphs and the self-reinforcing effect of the β phase. Based on the tensile results, a consistent improvement in the UTS was observed as both the source-to-target distance and rotational speed increased due to the enhanced fibre alignment. It was demonstrated that vapor solvent interfibre welding can lead to localized welding at the loose junctions between fibres with minimal impact on the surrounding morphology of the aligned electrospun fibre mats. To further assess the impact of vapor solvent bonding on the mechanical properties and the self-reinforcing effect of the β phase, tensile test was conducted. The results indicated that interfibre welding resulted in enhanced UTS values. For instance, after 2h welding, the UTS values increased further to 8650 MPa, corresponding to 41.8% enhancement, respectively. With 3h of welding, the UTS value further increased to 1080 MPa, respectively. This represents a continued rise of approximately 87.5% compared with the values obtained after 2h welding. These findings suggest that longer welding time can indeed enhance the mechanical properties of PHBV due to the β phase-induced nanofibres.

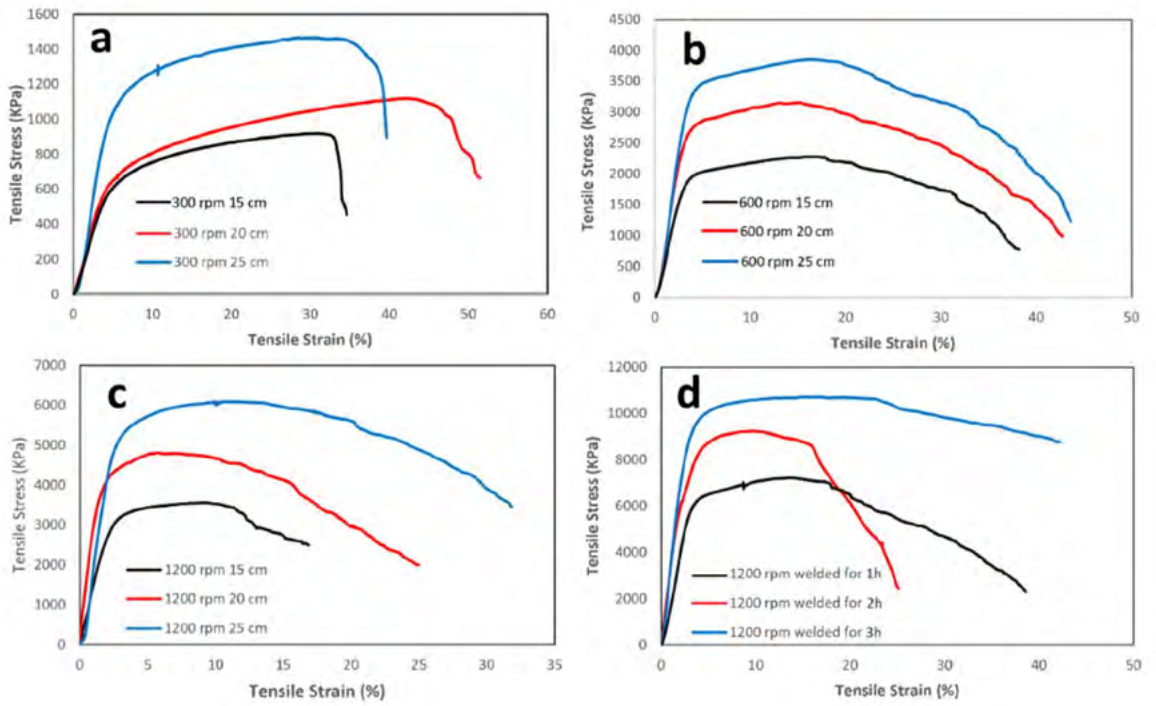

Figure 4. Tensile analysis of aligned electrospun PHBV nanofibre mats at source-to-target distances of 15 cm 20 cm and 25 cm and (a) the rotational speed of 300 rpm; (b) rotational speed of 600 rpm (c) rotational speed of 1200 rpm, and (d) rotational speed of 1200 rpm, source-to-target distances of 25 cm, solvent vapor welding of 1h, 2h, and 3h.

4. Conclusion

In this study, an approach to enhance the mechanical performance of PHBV was explored by the self-reinforcing effect of β-phase-induced aligned PHBV electrospun nanofibre mats, combined with low-temperature post-spun vapor solvent interfibre welding. Results indicated that vapor solvent interfibre welding can result in localized welding at the junctions between fibres while minimally impacting the surrounding morphology of the electrospun fibrous mats. The resulting composite demonstrated improvements in mechanical properties probably due to more perfectly formed α and β crystalline polymorphs and improved interfibre welding of loosely packed electrospun nanofibres. This method offers fully recyclable and biodegradable polymers, paving the way for the emergence of a novel category of environmentally friendly bioplastics.

Acknowledgment
This work was supported by an Australian Research Council Discovery grant (DP220100845).

References
[1] Haider TP, Völker C, Kramm J, Landfester K, Wurm FR. Plastics of the future? The impact of biodegradable polymers on the environment and on society. *Angewandte Chemie International Edition.* 2019;58(1):50-62.
[2] Millican JM, Agarwal S. Plastic pollution: a material problem? *Macromolecules*. 2021;54(10):4455-69.
[3] Wurm FR, Spierling S, Endres HJ, Barner L. Plastics and the environment—current status and challenges in Germany and Australia. *Macromolecular rapid communications*. 2020;41(18):2000351.
[4] Anjum A, Zuber M, Zia KM, Noreen A, Anjum MN, Tabasum S. Microbial production of polyhydroxyalkanoates (PHAs) and its copolymers: a review of recent advancements. *International journal of biological macromolecules*. 2016;89:161-74.

[5] Muhammadi, Shabina, Afzal M, Hameed S. Bacterial polyhydroxyalkanoates-eco-friendly next generation plastic: production, biocompatibility, biodegradation, physical properties and applications. *Green Chemistry Letters and Reviews.* 2015;8(3-4):56-77.
[6] Melendez-Rodriguez B, Reis MA, Carvalheira M, Sammon C, Cabedo L, Torres-Giner S, et al. Development and characterization of electrospun biopapers of poly (3-hydroxybutyrate-co-3-hydroxyvalerate) derived from cheese whey with varying 3-hydroxyvalerate contents. *Biomacromolecules*. 2021;22(7):2935-53.
[7] Kiruthika A. PHBV based blends and composites. *Biodegradable Polymers, Blends and Composites*: Elsevier; 2022. p. 283-308.
[8] Melendez-Rodriguez B, M'Bengue M-S, Torres-Giner S, Cabedo L, Prieto C, Lagaron JM. Barrier biopaper multilayers obtained by impregnation of electrospun poly (3-hydroxybutyrate-co-3-hydroxyvalerate) with protein and polysaccharide hydrocolloids. *Carbohydrate Polymer Technologies and Applications*. 2021;2:100150.
[9] Ibrahim MI, Alsafadi D, Alamry KA, Hussein MA. Properties and applications of poly (3-hydroxybutyrate-co-3-hydroxyvalerate) biocomposites. *Journal of Polymers and the Environment.* 2021;29:1010-30.
[10] Ashori A, Jonoobi M, Ayrilmis N, Shahreki A, Fashapoyeh MA. Preparation and characterization of polyhydroxybutyrate-co-valerate (PHBV) as green composites using nano reinforcements. *International journal of biological macromolecules.* 2019;136:1119-24.
[11] Gupta A, Lolic L, Mekonnen TH. Reactive extrusion of highly filled, compatibilized, and sustainable PHBV/PBAT–Hemp residue biocomposite. *Composites Part A: Applied Science and Manufacturing*. 2022;156:106885.
[12] Barkoula N, Garkhail S, Peijs T. Biodegradable composites based on flax/polyhydroxybutyrate and its copolymer with hydroxyvalerate. *Industrial Crops and Products.* 2010;31(1):34-42.
[13] Mook Choi W, Wan Kim T, Ok Park O, Keun Chang Y, Woo Lee J. Preparation and characterization of poly (hydroxybutyrate-co-hydroxyvalerate)–organoclay nanocomposites. *Journal of Applied Polymer Science.* 2003;90(2):525-9.
[14] Varghese SA, Pulikkalparambil H, Rangappa SM, Siengchin S, Parameswaranpillai J. Novel biodegradable polymer films based on poly (3-hydroxybutyrate-co-3-hydroxyvalerate) and Ceiba pentandra natural fibers for packaging applications. *Food Packaging and Shelf Life.* 2020;25:100538.
[15] Guo Y, Wang L, Chen Y, Luo P, Chen T. Properties of luffa fiber reinforced PHBV biodegradable composites. *Polymers.* 2019;11(11):1765.
[16] Kabe T, Tanaka T, Marubayashi H, Hikima T, Takata M, Iwata T. Investigating thermal properties of and melting-induced structural changes in cold-drawn P (3HB) films with α-and β-structures using real-time X-ray measurements and high-speed DSC. *Polymer*. 2016;93:181-8.
[17] Hufenus R, Reifler FA, Fernández-Ronco MP, Heuberger M. Molecular orientation in melt-spun poly (3-hydroxybutyrate) fibers: Effect of additives, drawing and stress-annealing. *European Polymer Journal.* 2015;71:12-26.
[18] Westlie AH, Quinn EC, Parker CR, Chen EY-X. Synthetic biodegradable polyhydroxyalkanoates (PHAs): Recent advances and future challenges. *Progress in Polymer Science*. 2022:101608.
[19] Yu W, Lan C-H, Wang S-J, Fang P-F, Sun Y-M. Influence of zinc oxide nanoparticles on the crystallization behavior of electrospun poly (3-hydroxybutyrate-co-3-hydroxyvalerate) nanofibers. *Polymer*. 2010;51(11):2403-9.
[20] Gong L, Chase DB, Noda I, Liu J, Martin DC, Ni C, et al. Discovery of β-form crystal structure in electrospun poly [(R)-3-hydroxybutyrate-co-(R)-3-hydroxyhexanoate](PHBHx) nanofibers: From fiber mats to single fibers. *Macromolecules*. 2015;48(17):6197-205.
[21] Xu Y, Zou L, Lu H, Wei Y, Hua J, Chen S. Preparation and characterization of electrospun PHBV/PEO mats: The role of solvent and PEO component. *Journal of Materials Science*. 2016;51:5695-711.
[22] Gong L, Chase DB, Noda I, Marcott CA, Liu J, Martin DC, et al. Polymorphic distribution in individual electrospun poly [(R)-3-hydroxybutyrate-co-(R)-3-hydroxyhexanoate](PHBHx) nanofibers. *Macromolecules*. 2017;50(14):5510-7.

[23] Kabe T, Tanaka T, Marubayashi H, Hikima T, Takata M, Iwata T. Investigating thermal properties of and melting-induced structural changes in cold-drawn P(3HB) films with α- and β-structures using real-time X-ray measurements and high-speed DSC. *Polymer*. 2016;93:181-8.
[24] Hufenus R, Reifler FA, Fernández-Ronco MP, Heuberger M. Molecular orientation in melt-spun poly(3-hydroxybutyrate) fibers: Effect of additives, drawing and stress-annealing. *European Polymer Journal.* 2015;71:12-26.
[25] Perret E, Reifler FA, Gooneie A, Chen K, Selli F, Hufenus R. Structural response of melt-spun poly(3-hydroxybutyrate) fibers to stress and temperature. *Polymer*. 2020;197.
[26] Laycock B, Halley P, Pratt S, Werker A, Lant P. The chemomechanical properties of microbial polyhydroxyalkanoates. *Progress in Polymer Science.* 2013;38(3-4):536-83.

PLASMA-ENHANCED GROWTH OF CARBON NANOTUBES WITH IN-SITU CATALYST GENERATION FOR MULTIFUNCTIONAL BASALT FABRICS

Ginevra Lalle[1], Ilaria Rago[2], Ravi P. Yadav[3], Gianluca Cavoto[2-3], Francesco Pandolfi[2], Maria Paola Bracciale[1], Giovanni Sotgiu[4], Irene Bavasso[1], Elisabetta Petrucci[1], Fabrizio Sarasini[1] and Jacopo Tirillò[1]

[1] Department of Chemical Engineering Materials Environment, 'Sapienza' Università di Roma, Roma, Italy
Email: ginevra.lalle@uniroma1.it
[2] INFN Sezione di Roma, Roma, Italy
[3] Dipartimento di Fisica 'Sapienza' Università di Roma and INFN Sezione di Roma, Roma, Italy,
[4] Department of Industrial, Electronic and Mechanical Engineering, Roma Tre University, Rome, Italy

Keywords: Basalt fiber, Carbon nanotubes, Plasma-enhanced chemical vapour deposition, Interface, Electrochemical properties

Abstract
Hierarchical reinforcements offer the opportunity to produce high-performance composite materials with multifunctional properties. In this work, the growth of carbon nanotubes (CNTs) is achieved on basalt fabrics at low temperatures (400-600 °C) without the addition of any external catalyst by combining *in-situ* catalyst generation and plasma assistance. First, an alkaline etching pre-treatment is performed to promote the segregation of the native iron oxides of basalt to be exploited as catalysts upon thermal annealing in H_2 atmosphere. Afterwards, a plasma-enhanced chemical vapour deposition (PE-CVD) technique is employed for the synthesis of CNTs at low temperatures to mitigate the well-known degradation of the fibre strength following high-temperature exposure in traditional thermal CVD. As a result, SEM investigation revealed an abundant growth of vertically aligned CNTs at 585 °C, with catalyst activation through H_2-annealing pre-treatment at temperatures as low as 485 °C. At lower temperatures (440-500 °C), only short and sparse CNTs were obtained. Moreover, the CNT-modified basalt fabric, in combination with a conductive polymer, showed promising responses in the electrochemical characterization, opening for possible applications as electrochemical devices, such as energy harvesting devices, to be further investigated in future research.

1. Introduction

Nowadays, the use of glass fibre within polymer matrix composite materials occupies a prominent slice of the global composite market, gaining attention due to the limited end-life disposal options of these materials. In this context, natural fibres of mineral origin, such as basalt fibres, are regarded as a promising greener alternative to glass fibres, thanks to their mechanical properties comparable to those of glass fibres and superior resistance to chemical agents, to high temperatures, and lower moisture absorption compared to natural fibres of vegetal origin [1]. Unfortunately, the widespread use of basalt fibre reinforced composites is hindered by the weak interface between the fibres and the polymer matrices. Among the strategies explored by the scientific community for interphase optimization in fibre reinforced composites, the production of hierarchical reinforcements offers the opportunity to improve the mechanical properties of basalt fibre composites while implementing additional functions for a wider class of industrial applications.
Significant research activity adopted chemical vapour deposition (CVD) to directly grow high loadings of carbon nanostructures, particularly carbon nanotubes (CNTs), on the surface of reinforcing fibres,

thus enhancing the interfacial adhesion with the polymer matrix and providing additional functions, such as damage sensing [2], electromagnetic wave absorption [3], and electrochemical properties [4]. The CVD method generally requires the presence of metal catalysts, commonly based on Fe, Ni and Co, which act as nucleation sites for the growing CNTs. While the addition of an external catalyst precursor is required for most fibre substrates, *in-situ* catalyst generation has been demonstrated for basalt fibres by promoting the microstructural segregation of iron oxides via basic or acidic pre-etching and the subsequent reduction in hydrogen atmosphere to nanocrystalline metallic iron. This approach, reported for the first time by Forster et al. [5], was employed for the growth of high density vertically aligned (VA)-CNTs by Sarasini et al. [6]. However, the high temperatures used for the process (above 700 °C) caused a significant deterioration of the fibre mechanical properties, with a reported strength loss of 39%.
In this work, a plasma-enhanced CVD (PE-CVD) technology is proposed as an alternative to thermal CVD. Thanks to a high energetic plasma, which supplies some of the energy for hydrocarbon decomposition and CNT formation, the PE-CVD method allowed lower operating temperatures which can mitigate the loss of mechanical strength of the substrate fibres. Moreover, a preliminary assessment of the electrochemical response of the CNT-modified basalt fabric has been carried out to investigate its potential as multifunctional fabric for applications in the field of electrochemical sensors and supercapacitors.

2. Materials and methods

2.1. Materials

A commercially available basalt woven fabric (220 g/m^2) was provided by Basaltex (BAS 220.1270.P). Individual fibres were coated with an epoxy-compatible sizing. NaOH (by Sigma Aldrich, reagent grade ≥98%) was dissolved in water for chemical pre-treatment of the basalt fabric.

2.2 CNT synthesis procedure

Prior to the CVD process, a chemical pre-treatment was carried out in a NaOH 2M aqueous solution for 3 hours at room temperature. The CNT synthesis was performed at the Sapienza-INFN CVD facility equipped with a RF-plasma module with a gas-shower cathode.
The basalt substrate (20 mm × 20 mm) was placed on the heating element of the high vacuum reaction chamber and thermally annealed in hydrogen atmosphere for 8 minutes to reduce the iron oxides to active metallic iron and promote the formation of nanoparticles catalysing the growth of CNTs. Afterwards, acetylene was introduced in the chamber as the carbon feedstock for CNT synthesis for 14 minutes while a plasma power of 45 W was employed. Finally, the samples were allowed to cool down to room temperature under the base pressure. These growth parameters were tuned based on the CVD protocol previously reported by Sarasini et al. [6] for the growth of VA-CNTs on basalt fabric via thermal CVD, which was replicated for the assessment of the electrochemical properties of the CNT-modified fabric. The temperature was measured with two thermocouples: one placed inside the heating element and the other anchored to the top surface of the fabric substrate. As the focus of the work is to reduce the temperature experienced by the fibre substrate, the substrate temperatures will be addressed. Two different temperature conditions were investigated, as reported in Table 1.

Table 1. Substrate temperatures investigated for the growth of CNTs on basalt fabric via PE-CVD.

Process	Annealing Temperature (°C)	Growth Temperature (°C)
PE-CVD-1	485	585
PE-CVD-2	440	500

2.3 Characterization techniques

A Mira3 field emission scanning electron microscope (FESEM) by Tescan was used for the morphological investigation of CNT-modified basalt fabric.

All electrochemical measurements were conducted by using an Autolab PGSTAT204 apparatus. The setup for the measurements consisted of two CNT-modified basalt electrodes separated by a conductive polymer synthesized by solvent casting from starch and an ionic liquid.

3. Results and discussion

The aim of this work is to investigate the use of PE-CVD for the low temperature growth of CNTs on basalt fibres. Based on a previous work by our group [6], an innovative approach of exploiting the native iron oxides of basalt fibres as catalysts was used for the growth of CNTs. An alkali etching pre-treatment was therefore carried out on the basalt fabric samples before the CVD process to promote the exposure of iron oxides on the surface of basalt fibres. In fact, the corrosive attack experienced by basalt in alkaline environment involves the breaking of the siloxane bonds and consequent silicates migration in the solution, thus exposing calcium, titanium, and iron oxides on the fibre surface. This iron content can seed the growth of CNTs from the basalt surface upon reduction during the H_2-pre-synthesis annealing treatment. Whereas in the previous work both annealing and growth steps were conducted at typical thermal CVD temperatures (above 700 °C) at the expense of a severe fibre strength loss, in this work a plasma-enhanced CVD technique was used to achieve a lower temperature growth.

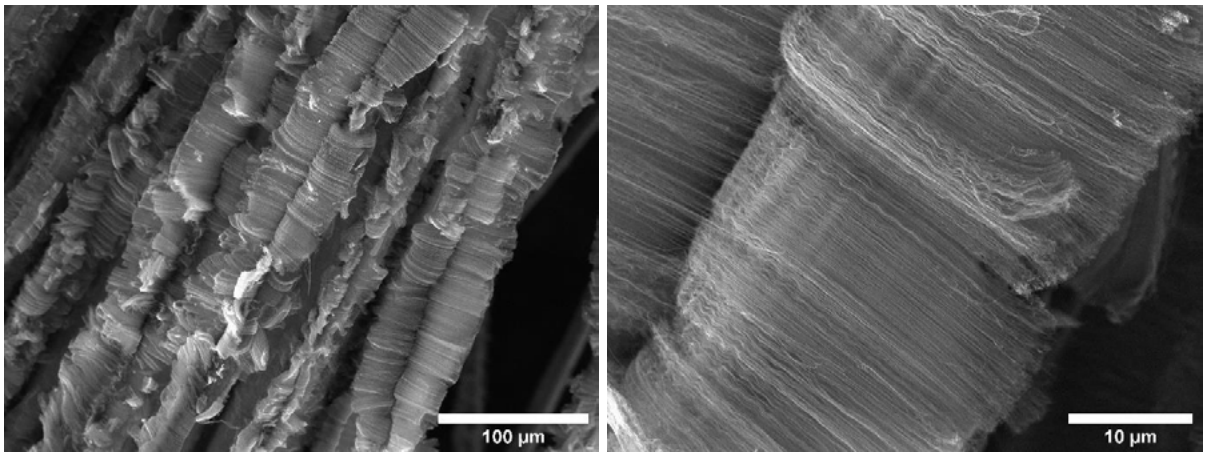

Figure 1. SEM micrographs of basalt fibres following the PE-CVD process at 485-585 °C.

As shown in the representative SEM micrographs reported in figure 1, the PE-CVD-1 process led to an abundant growth of dense VA-CNTs arrays, with lengths ranging from 30 to 40 µm. Such morphology is completely comparable to the one obtained via thermal CVD at temperatures above 700 °C, demonstrating that the plasma power introduced during the growth step was able to compensate entirely for the temperature difference in terms of energy needed for the growth. Moreover, the obtained morphology demonstrates that the native iron oxides exposed on the fibre through the alkaline etching can be reduced to a uniform and dense distribution of iron catalyst nanoparticles at temperature as low as 485 °C. In fact, a dense distribution of nucleation sites is required to generate proximity effects and force the tubes to grow in a common direction due to van der Waals interactions between nearby CNTs [7]. As observed by Tolga Gul [8], the density of the catalyst nanoparticles also affects the tortuosity of individual tubes in the VA-CNT forest. By comparing the higher magnification SEM micrograph in figure 1 to the one reported by Sarasini et al. [6], it can be assumed that in both cases the density of nanoparticles was sufficient to guarantee the growth of well-aligned CNTs.

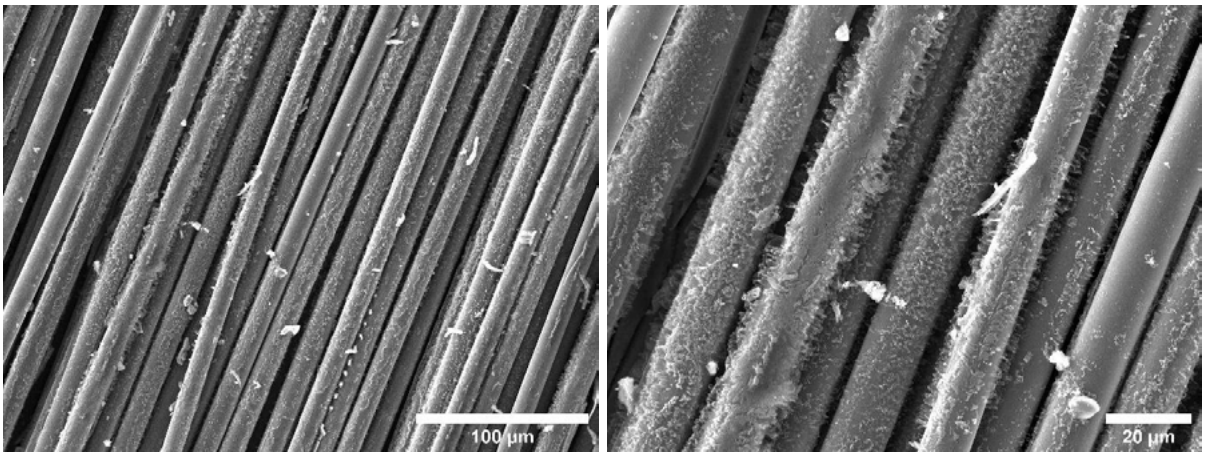

Figure 2. SEM micrographs of basalt fibres following the PE-CVD process at 440-500 °C.

A further reduction of process temperatures was made for the PE-CVD-2 process. The SEM investigation (figure 2) revealed the growth of sparse and much shorter CNTs (~3 µm). As opposed to the previous process, the poor coverage indicates that the lower temperature annealing was probably not sufficient to completely activate the iron catalyst into suitable-sized and evenly distributed nanoparticles. It is worth noting that, despite the low density, the CNTs grew with a radial orientation and relatively low tortuosity. The radial orientation and low waviness of the tubes in this case is mainly determined by the plasma which, along with the catalyst distribution, contributes to the final CNT morphology and orientation. As reported by Bower et al. [9], in fact, the interaction with the electric field during the growth tends to align the CNTs perpendicularly to the fibre surface in the direction of the electric field lines.

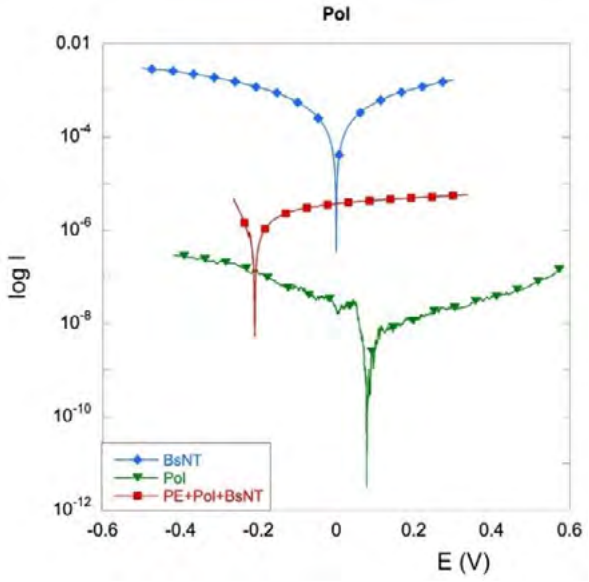

Figure 3. Polarization curves of the materials tested individually and in combination.

In contrast to conventional silane-based sizing coatings, CNTs directly grown on basalt fabrics might provide enhanced interfacial adhesion with the polymer matrix as well as multifunctional opportunities. In addition to the electrical conductivity measured in [6], a preliminary assessment of the electrochemical response of the material was carried out in this work. Fig. 3 illustrates the potentiodynamic polarization curves of basalt with nanotubes and the polymer alone at a scan rate of 1

mV/s. The combined system presents an intermediate current value compared to the individual components and stability in the potential range investigated. This behaviour opens possibilities for applications in the field of electrochemical devices, such as those for energy harvesting.

4. Conclusions

The *in-situ* growth of CNTs without external catalyst was investigated at low temperatures (400-600 °C) by means of a PE-CVD technique. Two synthesis processes were conducted at different temperatures to highlight the potential of this technique for temperature reduction and the resulting CNT morphologies were compared to the thermal counterpart from a previous work performed at temperatures above 700 °C [6]. The PE-CVD-1 process (485-585 °C) allowed to achieve a CNT morphology completely comparable to the thermal one with a consistent temperature reduction which is expected to mitigate the strength loss experienced by the basalt substrate. On the other hand, the PE-CVD-2 process (440-500 °C) led to a non-uniform coverage of short CNTs, identifying a lower temperature limit under the selected process conditions. Future works will be focused on the proper tuning of the process parameters in the identified temperature range to further investigate the low temperature opportunities of PE-CVD on basalt fabrics.
Moreover, the electrochemical investigation carried out in this work showcases promising potential for the application of hierarchical basalt fabrics in the field of electrochemical devices, such as supercapacitors, to be further investigated in future works.

References

[1] V. Fiore, G. Di Bella, and A. Valenza. Glass-basalt/epoxy hybrid composites for marine applications. *Mater. Des.*, 32(4): 2091–2099, 2011.

[2] H. G. De Luca, D. B. Anthony, E. S. Greenhalgh, A. Bismarck, and M. S. P. Shaffer. Piezoresistive structural composites reinforced by carbon nanotube-grafted quartz fibres. *Compos. Sci. Technol.*, 198: 108275, 2020.

[3] D. K. Kim, W. Han, K. W. Kim, and B. J. Kim. Electromagnetic Interference Shielding Effectiveness of Direct-Grown-Carbon Nanotubes/Carbon and Glass Fiber-Reinforced Epoxy Matrix Composites. *Materials (Basel).*, 16(7): 2604, 2023.

[4] Y. Zhao, Z. Yang, W. Fan, Y. Wang, G. Li, H. Cong and H. Yuan. Carbon nanotube/carbon fiber electrodes via chemical vapor deposition for simultaneous determination of ascorbic acid, dopamine and uric acid. *Arab. J. Chem.*, 13(1): 3266–3275, 2020.

[5] T. Förster, B. Hao, E. Mäder, F. Simon, E. Wölfel, and P. C. Ma, CVD-Grown CNTs on basalt fiber surfaces for multifunctional composite interphases. *Fibers*, 4(4): 28, 2016.

[6] F. Sarasini, J. Tirillò, M. Lilli, M. P. Bracciale, P. E. Vullum, F. Berto, G. De Bellis, A. Tamburrano, G. Cavoto, F. Pandolfi, I. Rago. Highly aligned growth of carbon nanotube forests with in-situ catalyst generation: A route to multifunctional basalt fibres. *Compos. Part B Eng.*, 243: 110136, 2022.

[7] P. Sharma, V. Pavelyev, S. Kumar, P. Mishra, S. S. Islam, and N. Tripathi. Analysis on the synthesis of vertically aligned carbon nanotubes: growth mechanism and techniques. *Journal of Materials Science: Materials in Electronics,* 31(6): 4399-4443, 2020.

[8] O. T. Gul. Decoupling the catalyst reduction and annealing for suppressing Ostwald ripening in carbon nanotube growth. *Appl. Phys. A Mater. Sci. Process.*, 127(10):1–11, 2021.

[9] C. Bower, W. Zhu, S. Jin, and O. Zhou. Plasma-induced alignment of carbon nanotubes. *Appl. Phys. Lett.*, 77(6):830–832, 2000.

MULTISCALE NATURAL FIBRE-REINFORCED THERMOPLASTIC COMPOSITES TOWARDS ENHANCED MECHANICAL COMPOSITES

Luís Nobre[1*], Dina Esteves[1], Ângela Pinto[1], Carlos Mota[1], João Bessa[1], Fernando Cunha[1], Raúl Fangueiro[1, 2]

[1]Fibrenamics, Institute of Innovation on Fibre-Based Materials and Composites, University of Minho, 4800-058 Guimarães, Portugal; [*]luisnobre@fibrenamics.com (L. N.); dinaesteves@fibrenamics.com (D.E.); angelapinto@fibrenamics.com (A.P.).
[2]Department of Textile Engineering, University of Minho, Azurém Campus, 4800-058, Guimarães, Portugal

Keywords: flax fibres, surface treatments, functionalization, thermoplastic resin, mechanical performance

Abstract
This study aims to investigate the behaviour of thermoplastic composites reinforced with natural fibres. Composite materials were developed using reactive methyl methacrylate (MMA) resin, commercially known as Elium®, with incorporation of cellulose nanocrystals (CNCs), dispersed in the matrix at different concentrations. Natural fibres, such as flax, were chemically treated by immersion in an aqueous solution based on $NaHCO_3$, during different periods of exposure. After this treatment, flax fibres were washed with distilled water and dried. The degree of fibre surface tension was measured by contact angle. Then, cellulose nanocrystals were incorporated and mixed in the thermoplastic resin and the samples were developed via the incorporation of intercalated layers of treated flax fibres. The composites were produced using compression moulding. After that, the samples were evaluated, regarding their mechanical performance and morphology. The research results show that flax fibres treated with 9 wt.% $NaHCO_3$ for 48 hours improve the flexural strength by removing impurities and introducing hydroxyl groups. The incorporation of 1% CNCs into thermoplastic resin significantly enhances the fibre/matrix interface, resulting in a remarkable 38.04% increase in flexural strength. These findings demonstrate the effectiveness of using treated natural fibres and CNCs to improve composites' performance.

1. Introduction

Global concern for sustainability and the environment has propelled the development of products and solutions that minimize environmental impact. As traditional materials raise concerns about resource depletion and pollution, there's a growing demand for eco-friendly alternatives. This shift towards sustainability extends to various industries, including the field of composite materials.
Composite materials can generally be defined as heterogeneous materials comprising the synergistic combination of two or more materials [1,2]. The reinforcement and matrix are the two main components of any composite material. The reinforcement serves as the primary load-bearing component, carrying the majority of applied forces. It is characterized by its need for hardness, brittleness, and high strength to effectively bear these loads. Conversely, the matrix acts as a supportive medium, enveloping and safeguarding the reinforcement. The properties of composite materials are influenced by various factors, including the type and characteristics of both reinforcement and matrix, their arrangement and dispersion within the composite structure, the volume fraction of reinforcement, and the manufacturing processes employed [3].
The reinforcement constituent is commonly in the form of fibres/fabrics or particles/fillers. As for fibre-reinforced composites (FRCs), they can be reinforced by synthetic fibres or natural fibres. Synthetic fibres have long been used in polymer matrix composites (PMCs) to create lightweight materials that

are stronger and more rigid. However, the environmental ramifications associated with the production, disposal, and recycling of these synthetic fibre-based composites have prompted a shift towards more sustainable solutions. As a result, there's a growing interest in using natural fibres as an environmentally friendly alternative. These natural fibres are now being increasingly considered for a range of applications across various industries, including automotive, marine, chemical, infrastructure, and sporting goods [4].

Natural fibres have many advantageous properties such as recyclability, eco-friendliness, nominal cost, low density, high specific strength, high impact resistance, and high flexibility, low specific gravity, less abrasiveness to equipment, less health hazards, process-friendly, lower greenhouse emissions and CO2 neutral [3,5]. Despite of all the advantages, there are also some drawbacks associated with the usage of this type of fibre. The hydrophilic nature of natural fibres poses a challenge to their application as reinforcement in polymeric composites [3]. This property leads to poor interfacial adhesion between the fibres and the matrix. The surface of natural fibres comprises oils, cellulose, hemicellulose, lignin, and a waxy layer, all of which pose challenges to achieving effective interfacial bonding. Having strong adhesion between the fibre and matrix plays a crucial role in enhancing both the thermal and mechanical characteristics of the composite [6]. The quality of the interfacial bonding between fibre and matrix alongside the strength of fibre are parameters that influence the overall strength of composite materials [3].

Hence it is critical to enhance the adhesion between fibre and matrix when producing natural fibre reinforced composites. Besides the hydrophilic character of natural fibres other challenges commonly encountered include thermal degradation, and biodegradation [7]. To tackle these issues effectively, a range of chemical or physical treatments can be performed to modify the reinforcing fibre's surface [8]. Mercerization is an alkali treatment method of partially physical and chemical nature, in which natural fibres are immersed in a highly concentrated aqueous sodium hydroxide solution at a given temperature, during a specific time, endorsing the ionization of the hydroxyl groups present on fibres to alkoxides [7,9]. This treatment proves effective in providing natural fibres with a rough surface topography, that results in better fibre matrix interface adhesion and increased mechanical properties of the fibre and the resulting composite [7]. However, mercerization wastewater is extremely alkaline [10]. Highly alkaline wastes can have a significant and long-term negative impact on terrestrial and aquatic environments [11].

Alternatively, studies report the use of sodium bicarbonate ($NaHCO_3$) for natural fibre treatment as a means of achieving better fibre/matrix adherence [12–14]. $NaHCO_3$ is an environmentally friendly product with a slightly alkaline nature which can dissolve in water up to a maximum concentration of 10% [12,13]. It is commonly used for a variety of purposes, including cooking, gardening, cleaning and even medicine, without harming public health or the environment [12]. In addition, Das P. et al. developed a study in which the environmental impact of two surface modification treatments of natural plant fibres is comparatively analysed, one of them carried out in an NaOH aqueous solution and the other carried out in an $NaHCO_3$ aqueous solution. The results show that the pH of the residual chemical solution following the sodium bicarbonate treatment of the fibres was found to be neutral, suggesting its disposal poses minimum or no harm to the environment. In contrast, the pH of the sodium hydroxide solution was strongly alkaline, indicating potential adverse effects in disposal areas [13]. Surface modification treatments utilizing environmentally friendly products like $NaHCO_3$ on natural fibres could hold significant promise for polymeric composites across various applications.

On the other hand, in the last few years, fibre-reinforced polymer composites (FRPCs), made by reinforcing polymeric resins with high-strength fibres, exhibit enhanced and unique properties that are not achievable by either component. FRPCs could be manufactured using either thermoset (TS) or thermoplastic (TP) polymeric resins. Recent progress in this area has been achieved with the development of new reactive TP resins such as Elium®, Arkema's novel liquid methyl methacrylate (MMA) thermoplastic resin which shows promising characteristics for various applications. This resin can be cured at room temperature using a mixture of MMA monomer and initiator, presents low-viscosity liquids (100 Pa.s), and is suitable for processing by using liquid composite infusion techniques or compression moulding process [15]. One of its key features is to offer recyclability benefits, making it environmentally friendly. According to recent research, Elium® is actively investigated for its recycling ability and can be recycled by two methods, mechanically or chemically, to produce recycled

composite parts. In industry, this thermoplastic resin has been utilized in the fabrication of composite sandwich structures, showcasing improved mechanical properties compared to traditional epoxy resins, namely, with significant enhancements in flexural and flatwise strength [16].
Various studies report the use of cellulose particles as nanofillers to reinforce different kinds of composite materials [15–18]. In the field of composite production nanocellulose has emerged as a prominent choice for reinforcing polymer matrices. These composites consist of polymeric matrices fortified with nanocellulose fillers. The utilization of nanocellulose crystals in this role has attracted considerable interest owing to their intrinsic properties and potential applications. Cellulose is a material extracted from abundantly available natural resources such as plants, algae, fungi and bacteria. It is characterised by being the most affluent bio-based polymer, eco-friendly, toxic free, and biodegradable [19]. Such properties make it compelling to be explored extensively in the preparation biomaterials, namely bio composites.

2. Materials and Methods

2.1. Materials

The natural fibres selected for the experimental study were a non-crimp unidirectional flax fabric with fibres oriented at 0°, supplied by Bcomp, Switzerland. The flax fibres were treated using $NaHCO_3$ purchased from Nogueira – Materiais de Construção, Portugal. The acrylic polymer used for the composite preparation was a liquid reactive MMA thermoplastic resin (Elium® 151 XO/SA), supplied by Arkema, France. The Elium® 151 XO/SA resin system is made of 3 components with resin 151 XO, accelerator 151 SA and peroxide initiator. When all 3 components are mixed, radical polymerisation occurs to produce poly(methylmethacrylate) (PMMA) TP matrix. The initiator used in this research work was Butanox® M-50, a medium-reactive, general purpose methyl ethyl ketone peroxide (MEKP), a solution in dimethyl phthalate, purchased from Ecocompósitos, SA, Portugal. Cellulose nanocrystals (CNCs) were supplied by CelluForce, Canada. This nanoscale (10^{-9} m) particles are derived from cellulose, a natural polymer found in plant cell walls, and were used to functionalise the TP matrix.

2.2. Fibre treatment

The flax fabric was dipped in an aqueous solution of $NaHCO_3$ at a concentration of 9 wt% for four different periods of time: 24, 48, 72 and 96 hours. The treatment was carried out at room temperature. Once the treatment times had elapsed, the fibres were removed from the treatment solution and rinsed in distilled water. The samples were then dried in an oven at 50ºC for approximately 18 hours. The effectiveness of the treatment was assessed through the fibres contact angle analyses as well as with flexural testing performed on the resulting composites, which will be discussed in detail in the subsequent sections.

2.3. Matrix functionalization

In a first phase, the required amount must be dried in an oven at 60°C for 24 hours. After drying, the CNC powder should be thoroughly mixed with MMA resin. CNCs were added to the MMA resin in varying weight percentages of 1.0%, 2.5%, 5.0% and were stirred manually for 5 to 10 minutes until no lumps are visible. The suspension was later treated with ultrasonication using an Ultrasonic Cleaners serie EP S3, from Soltec, Italy. Operation mode was at a frequency of 40 kHz and a power of 180 W for 30 minutes. Afterward, a calculated amount of 1.5 wt% of initiator was mixed with the CMC-dispersed resin suspension, taking in account a quantity of resin.

2.4. Preparation of composites

In the first step, 12 layers of flax were cut with dimensions 100 mm x 120 mm, according to the following directional angles: [-45°/0°/45°/-45°/90°/45°/-45°/0°/45°/-45°/90°/45°]. Then, it was necessary to weigh 12 flax sheets, which correspond to 40% of the total weight of Elium® 151 SA/XO resin. After the functionalization of the matrix, referred on previous paragraph 2.3, the final mixture was applied sequentially on the various layers of the linen fibrous structure using hand lay-up technique. Compression moulding press (model LabManual 300, purchased from Fontijne, The Netherlands) was

turned on at a temperature of 60 °C and the sample was placed on the between the two heated plaques, for 10 minutes, at 1 bar. After this time, the pressure was increased to 9 bars for 35 minutes to prepare the final samples, presented below in Table 1.

In Table 1, presented below, is shown a description of all developed samples.

Table 1. Plan of the experiments.

Sample code	Surface treatment	Matrix functionalization
S1	Untreated flax fibres	-
S2	Surface treatment of flax fibres with 9 wt% of $NaHCO_3$, at 24 hours	-
S3	Surface treatment of flax fibres with 9 wt% of $NaHCO_3$, at 48 hours	-
S4	Surface treatment of flax fibres with 9 wt% of $NaHCO_3$, at 72 hours	-
S5	Surface treatment of flax fibres with 9 wt% of $NaHCO_3$, at 96 hours	-
S6	Surface treatment of flax fibres with 9 wt% of $NaHCO_3$, at 48 hours	1.0 wt% CNCs
S7	Surface treatment of flax fibres with 9 wt% of $NaHCO_3$, at 48 hours	2.5 wt% CNCs
S8	Surface treatment of flax fibres with 9 wt% of $NaHCO_3$, at 48 hours	5.0 wt% CNCs

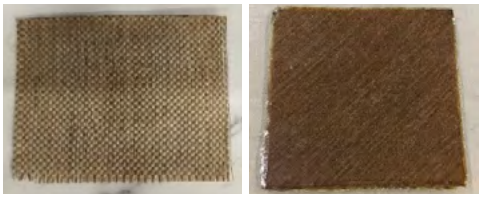

Figure 1. Fibrous structure of flax and sample S1.

2.5. Contact angle

In order to verify whether the treatment influenced the hydrophilicity of the flax fibres, the fibres were subjected to a contact angle measurement. The contact angle is a measurement that describes how a liquid interacts with a solid surface. It quantifies the wettability of a solid surface by a liquid based on the Young equation. This procedure can be performed using water or a variety of other liquids.
For this purpose, flax fibres and fibres treated during the different time periods had their contact angles estimated at room temperature using an optical contact angle goniometer. To do this, 10 drops of water of approximately 5 µL each were placed on randomly selected spot on each flax fabric sample. The average contact angle for each sample was calculated from the multiple measurements to ensure accuracy and reliability of the results. The contact angles were then recorded and estimated immediately after drop contact with the surface, using the goniometer video drop shape analyser OCA15. Special care was taken to ensure that the fibres were laid flat and free of wrinkles or folds that could affect the accuracy of the measurements.

2.6. Flexural testing

The tensile tests were carried out being based to the EN ISO 178:2003 standard, using a H100KS Hounsfield Universal Testing Instrument. The test was performed at room temperature, with a 5 kN load cell, at a 5 mm/min speed. 5 specimens with dimensions of 10 mm x 80 mm and a thickness ranging from 2.5 mm to 5 mm were tested. Various properties of the flexural stress/strain relationship were determined, including flexural strength, flexural modulus, and flexural strain.

2.7. SEM/EDS analysis

The morphologies and microstructures of all samples were examined using a Leica M125 microscope, a Hitachi FlexSem 1000 II scanning electron microscope to perform SEM studies, and a Bruker Quantax 80 energy dispersive X-ray spectrometer.

3. Results and discussion

3.1. Contact angle

The results obtained for the contact angle measurement are summarized in Table 2.

Table 2. Contact angle (CA) measurement results of flax fibres before and after chemical treatment with $NaHCO_3$ for different periods of time: 24 hours (T=24h), 48 hours (T=48h), 72 hours (T=72h) and 96 hours (T=96h).

Specimen Type	*Untreated*	*T=24h*	*T=48h*	*T=72h*	*T=96h*
CA (°)	135.99	141.67	142.21	143.76	143.94

Notably, there was a clear tendency for the contact angle to increase with increasing treatment time. The untreated fibres exhibited the lowest contact angle, while the fibres treated for 96 hours recorded the highest contact angle. These results indicate a slight increase in the hydrophobicity of flax fibres after treatment with $NaHCO_3$, whereby the longer the treatment time, the greater the contact angle. The preparation of an aqueous $NaHCO_3$ solution involves the formation of carbonic acid (H_2CO_3) and hydroxide ion (OH^-), which makes it slightly alkaline. Besides, based on the predominance of alcoholic hydroxyl groups (which are weak acids) in the fibres, it is reasonable to suggest that the interaction resembles what occurs in a conventional mercerization treatment [20]. For this reason, it is plausible to assume that similarly to mercerization, the $NaHCO_3$ pre-treatment reduces fibre diameter, which increases the aspect ratio which leads to the development of a rough surface topography [20,21]. The increase in the roughness of the fibre surface may explain the increase in the contact angle.

On the other hand, this test showed that although the flax fibres treated with $NaHCO_3$ had a higher contact angle than the untreated flax, the water droplets were absorbed over time, while the untreated flax, despite having a slightly lower contact angle, the droplets remained on the sample without being absorbed, regardless of the time elapsed. Fourier-transform infrared spectroscopy (FTIR) analyses carried out by Fiore V. et al. on sisal fibres before and after treatment with an aqueous $NaHCO_3$ solution reveal that by pre-treating lignocellulosic fibres with $NaHCO_3$, it is possible to achieve the removal of hemicellulose and the reduction of lignin from the surface fibres [20]. The removal of these compounds, as well as other impurities, usually results in an improvement in the fibres' ability to absorb moisture, which may explain the phenomenon described above.

3.2. Flexural testing

3.2.1 Influence of fibre treatment and matrix functionalization on flexural properties

To assess the impact of surface treatment of flax fibres and matrix functionalization on flexural properties, figure 2, presented below, illustrates the correlation between each sample and its mechanical performance.

Table 3. Evaluation of mechanical performance by flexural properties.

Sample code	Flexural Strength (MPa)	Flexural Modulus (MPa)	Flexural Strain (%)
S1	72.1	2.8	7.5

S2	92.8	3.6	5.9
S3	114.1	5.8	4.6
S4	82.4	4.1	5.2
S5	77.1	2.9	7.8
S6	157.5	15.8	2.1
S7	125.9	4.0	5.1
S8	115.3	4.3	3.6

Based on Table 3, treating flax fibres with 9 wt% $NaHCO_3$, and after 48 hours of exposure to $NaHCO_3$ solution (S3), significantly improved the flexural strength of the composites by 58.25% when compared to untreated sample (S1). However, a noticeable decrease in flexural strength and flexural modulus and an increase of flexural strain was observed after 72 and 96 hours of treatment, related to samples S4 and S5, respectively. Using $NaHCO_3$ as a surface treatment can degrade flax fibres due to its alkaline nature which dissolves the hemicellulose and lignin regions in the flax fibres, weakening their structure. This dissolution process breaks down the fibre components, making it more susceptible to degradation. Additionally, alkaline conditions hydrolyze the hemicellulosic and lignin areas in the fibres, further contributing to their degradation.

After being exposed the fibrous structure to a 9% $NaHCO_3$ solution for 48 hours, and functionalizing the matrix with CNCs, samples S6, S7, and S8 exhibited a significant improvement in mechanical properties. This increase was particularly pronounced for sample S6, which was functionalized with 1.0% of CNC, showing a 38.04% increase in flexural strength, 172.41% increase in flexural modulus and a decrease of 119 % related to flexural strain, in comparison to sample S3, without functionalization. The mechanical performance of the samples was greatly improved by adding CNCs. This advancement was achieved by enhancing interactions within the matrix and improving interfacial interactions. The dispersion of CNCs within the Elium® resin significantly enhanced the compatibility between flax fibres and the matrix, resulting in a significant improvement of fibre/matrix interfacial properties [23]. However, for CNC concentrations equal to or greater than 2.5 wt%, related to samples S7 and S8, a decrease in mechanical performance is evident in comparison to S6. Higher concentrations of CNCs can lead to a reduction in the mechanical properties of composites. This is due to the potential agglomeration of CNCs within the polymer matrix at elevated concentrations. This phenomenon can result in non-uniform dispersion of CNCs, leading to localized stress concentrations and weak points in the composite structure, ultimately compromising its mechanical performance [17,19].

3.3. SEM/EDS analysis

In Figure 4, presented below, scanning electron microscopy (SEM) images reveal the microstructures formed within by the cross-section and at the surface of the samples S1, S3, S5, S6 and S8.

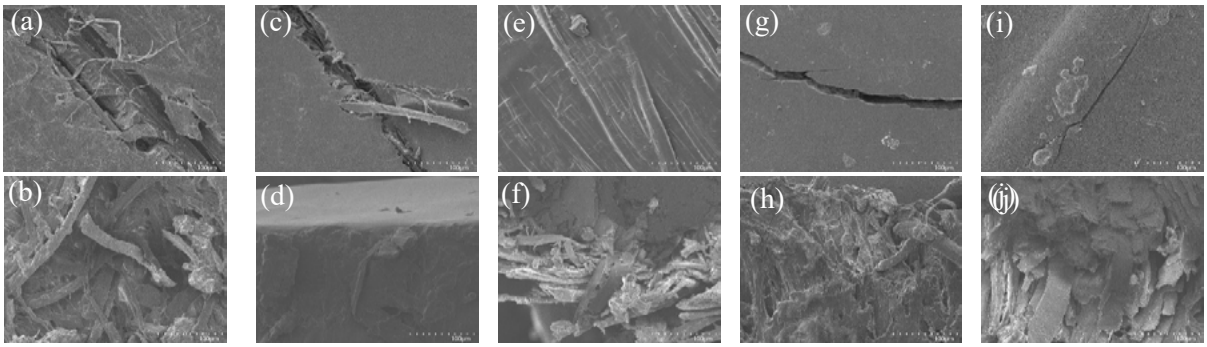

Figure 4. SEM images of surface of S1 (a), cross section of S1 (b), surface of S3 (c), cross section of S3 (d), surface of S5 (e), cross section of S5 (f), surface of S6 (g), cross section of S6 (h), surface of S8 (i) and cross section of S8 (j).

Figure 4 shows a significant improvement in surface quality after treatment with $NaHCO_3$ for samples S3, S5, S6 and S8. In this case, untreated sample S1 displays poor adhesion between fibre and matrix, as shown in Figure 4(a) and Figure 4(b). This surface treatment aids in the removal of impurities like lignin and hemicellulose, enhancing the biodegradability of cellulose fibres and improving their adhesion.
However, after exposure to $NaHCO_3$ for longer time, up to 96 hours, as shown in Figure 4e) and in Figure 4f), the adhesion between the flax fibres and the matrix appears to be weaker compared to sample S3, which was exposed for 48 hours.
In Figure 4(j), it is evident that there is some rigidity in the fibres in the cross-section of sample S8. When a higher amount of CNCs is dispersed in the matrix, it can lead to degradation in properties attributed to the rigid and crystalline nature of CNCs, making the composite more brittle and less resilient.

4. Conclusions

To improve the quality of TP composites using $NaHCO_3$ in flax fibres, surface modification is essential. Alkaline treatments like $NaHCO_3$ can effectively remove impurities and enhance the surface roughness of fibres, promoting better adhesion with the Elium® resin. This treatment improves bonding and enhances mechanical properties by exposing more hydroxyl groups for interlocking with the matrix, leading to improved fibre-matrix adhesion. The use of $NaHCO_3$ can result in increased flexural strength, flexural modulus and a decrease of flexural strain of the composites, ultimately enhancing their overall performance. However, the time of exposure needs to be well controlled to avoid some degradation of flax fibres. The alkaline environment created by $NaHCO_3$ facilitates the breakdown of the fibre structure, ultimately leading to the degradation of flax fibres. After considering the latest developments, it has been determined that exposing the fibres to a 9 wt% NaHCO3 solution, for 48 hours, is the most effective approach.
On the other hand, the functionalization of the TP matrix with CNCs improves its mechanical performance, including flexural strength, flexural modulus, and flexural strain. The CNC structure has a large number of hydroxyl groups on its surface, making it ideal for reinforcement. Additionally, the addition of cellulose nanocrystals can strengthen the fibre-matrix interface, increase the stiffness of the composite, and enhance its overall performance.
When higher concentrations of CNCs, are added to functionalize the TP matrix, up to 1 wt%, it can reduce the effective interaction between the CNCs and the polymer matrix. This diminishes the ability of CNCs to strengthen the composite and improve its mechanical properties. Therefore, it is crucial to optimize the CNC concentration to prevent clustering and ensure even dispersion in order to maximize the mechanical properties of the composite. Based on this research findings, the optimal concentration for maximizing composite mechanical performance is 1 wt% of CNCs.

Acknowledgments

The authors extend their gratitude to Center for Science and Technology (2C2T), Guimarães, Portugal, for generously granting us access to their SEM/EDS equipment, which was instrumental in conducting the SEM/EDS analysis of the composites. We are particularly grateful to Diana P. Ferreira and Diego Chaves for their invaluable assistance throughout the acquisition of SEM images.

References

[1] S. Erden and K. Ho. Fiber reinforced composites. *Fiber Technology for Fiber-Reinforced Composites*: 51–79, 2017.
[2] P. S., K. M. S., N. K., S. S. Fiber Reinforced Composites - A Review. *Journal of Material Science & Engineering*, 06, 2017.
[3] L. Kerni, S. Singh, A. Patnaik, N. Kumar. A review on natural fiber reinforced composites. *Materials Today: Proceedings*, 28: 1616–1621, 2020.
[4] S. Begum, S. Fawzia, M. S. J. Hashmi. Polymer matrix composite with natural and synthetic fibres. *Advances in Materials and Processing Technologies*, 6: 547–564, 2020.

[5] P. Sahu, M. K. Gupta. A review on the properties of natural fibres and its bio-composites: Effect of alkali treatment. *Proceedings of the Institution of Mechanical Engineers, Part L: Journal of Materials: Design and Applications*, 234: 198–217, 2020.
[6] K. Seisa, V. Chinnasamy, A. U. Ude. Surface Treatments of Natural Fibres in Fibre Reinforced Composites: A Review. *Fibres and Textiles in Eastern Europe*, 30: 82–89, 2022.
[7] Ali, K. Shaker, Y. Nawab, M. Jabbar, T. Hussain, J. Militky, V. Baheti. Hydrophobic treatment of natural fibers and their composites—A review. *Journal of Industrial Textiles*, 47: 2153–2183, 2018.
[8] S. Rana and R. Fangueiro, R. (2016). *Science and Clothing Technology Fibrous and Textile Materials for Composite Applications*. Springer, 2016.
[9] C. L. Luchese, J. B. Engel, I. C. Tessaro. A Review on the Mercerization of Natural Fibers: Parameters and Effects. *Korean Journal of Chemical Engineering*, 41: 571–587, 2024.
[10] M. Zebić Avdičević, K. Košutić, S. Dobrović. Effect of operating conditions on the performances of multichannel ceramic UF membranes for textile mercerization wastewater treatment. Environmental Technology (United Kingdom), 38: 65–77, 2017.
[11] H. I. Gomes, W. M. Mayes, M. Rogerson, D. I. Stewart, I. T. Burked. Alkaline residues and the environment: A review of impacts, management practices and opportunities. *Journal of Cleaner Production*, 112: 3571–3582, 2016.
[12] A. Belaadi, S. Amroune, M. Bourchak. (2020). Effect of eco-friendly chemical sodium bicarbonate treatment on the mechanical properties of flax fibres: Weibull statistics. *International Journal of Advanced Manufacturing Technology*, 106: 1753–1774, 2020.
[13] P. P. Das, A. Manral, F. Ahmad, B. Sharma, V. Chaudhary, S. Gupta, P. Gupta. Environmentally sustainable chemical treatment of plant fibers for improved performance of polymeric composites. *Polymer Composites*, 43: 7155–7169, 2022.
[14] J. C. Dos Santos, P. R. Oliveira, R. T. S. Freire, L. M. G. Vieira, J. C. C. Rubio, T. H. Panzera. The Effects of Sodium Carbonate and Bicarbonate Treatments on Sisal Fibre Composites. *Materials Research*, 25, 2022.
[15] W. F. Stanley, A. K. Bandaru, S. Rana, S. Parveen, S. Pichandi. Mechanical, dynamic-mechanical and wear performance of novel non-crimp glass fabric-reinforced liquid thermoplastic composites filled with cellulose microcrystals. *Materials and Design*, 212, 2021.
[16] R. Manaii, S. Terekhina, L. Chandreshah, N. Shafiq, D. Duriatti, L. Guillaumat. Influence of fibre orientation, moisture absorption and repairing performance on the low-velocity impact response of woven flax/Elium® thermoplastic bio-composites. *Journal of Composite Materials*, 57: 3601–3618, 2023.
[17] K. Bandaru, S. Pichandi, H. Ma, M. Panchal, R. Gujjala. Effect of microcrystalline cellulose on the mechanical properties of flax reinforced methylmethacrylate and urethane acrylate composites. *Journal of Materials Science*: 2872–2892, 2024.
[18] C. Calvino, N. Macke, R. Kato, S. J. Rowan. Development, processing and applications of bio-sourced cellulose nanocrystal composites. *Progress in Polymer Science*,103, 2020.
[19] C. Zinge and B. Kandasubramanian. Nanocellulose based biodegradable polymers. *European Polymer Journal*, 133, 2020.
[20] V. Fiore, T. Scalici, F. Nicoletti, G. Vitale, M. Prestipino, A. Valenza. A new eco-friendly chemical treatment of natural fibres: Effect of sodium bicarbonate on properties of sisal fibre and its epoxy composites. *Composites Part B: Engineering*, 85: 150–160, 2016.
[21] S. Kalia, B. S Kaith, I. Kaur, I. Pretreatments of natural fibers and their application as reinforcing material in polymer composites-a review. *Polymer Engineering and Science*, 49: 1253–1272, 2009.

Investigation of the piezoresistivity of CNT/PLA nanocomposite with an improved solvent-casting process

Zhenghao. Zhang[1], Vito. Tagarielli[2] and Qianqian. Li[3*]

[1]Department of Aeronautics, Imperial College London, Exhibition Road, United Kingdom
Email: zhenghao.zhang19@imperial.ac.uk
[2]Department of Aeronautics, Imperial College London, Exhibition Road, United Kingdom
Email: v.tagarielli@imperial.ac.uk
[3] Department of Aeronautics, Imperial College London, Exhibition Road, United Kingdom
Email: qianqian.li@imperial.ac.uk

Keywords: Carbon nanotubes, PLA, Piezoresistivity

Abstract
Conductive polymer composites (CPCs) reinforced with multi-walled carbon nanotubes (CNTs) have attracted much attention over the past decades as a new functional material due to their excellent mechanical, electrical and thermal properties. In this paper, multi-walled carbon nanotubes (MWCNTs) reinforced poly(lactic acid) (PLA) nanocomposites were manufactured via a solution-casting and hot-pressing method. The fundamental material properties of nanocomposites, including mechanical and electrical properties, were characterized. After the incorporation of CNTs, the mechanical and electrical properties of PLA were improved at different scales. The piezoresistive response of the nanocomposite was also studied and the 1wt% PLA/CNT nanocomposite sample demonstrated good sensitivity to small strain change.

1. Introduction

Composite materials, especially polymer composites, have been widely researched and applied in industrial sectors like aerospace, automotive, and sports [1] as structural components because of their superior properties like high specific strength, good corrosion and fatigue resistance compared with traditional materials. Besides conventional fibre reinforcements like carbon and glass fibres, nano-size reinforcements like carbon nanotubes have received widespread attention over the last two decades since the first documented discovery by Iijima [2]. The tubular, large aspect-ratio structure of CNTs provides them with excellent mechanical, electrical and thermal conductivities [3-6]. The addition of CNTs can transfer polymer from insulator to conductive polymer composite by constructing conductive networks inside the matrix via the direct contact among CNTs and the quantum tunnelling effect [7]. In addition, this network can be affected by external stimuli like chemical vapours [8, 9], thermal [10] and strain fields [11, 12], making CPC promising in various sensing applications. For instance, Christ et al. [13] 3D printed thermoplastic polyurethane/multiwall CNT (TPU/MWCNT) strain sensors with a high gauge factor (GF) up to 176 under 100% applied strain. Hwang et al. [14] incorporated poly(3-hexylthiophene) (P3HT) wrapped MWCNT into polydimethylsiloxane (PDMS) to make composites for finger-sensing devices.

Poly(lactic acid) or Polylactide (PLA) is one of the most promising bio-friendly thermoplastic polymers which can be produced from renewable resources such as starch and corn [15, 16]. Moreover, owing to its good mechanical properties and processibility [17], PLA was widely chosen as the polymer matrix for nanocomposites and used for various applications such as organic vapour sensors [8], 3D-printed actuators [18], EMI shielding [19] and strain sensors [20].

CNT dispersion status in the polymer matrix, including its uniformity, the orientation of CNTs and an efficient interfacial bonding between the nanofiller and the matrix, has a significant impact on the performance of CPC. Various methods were applied to mix CNTs into PLA, and these dispersion techniques can generally be divided into two categories, which are solvent-free and solvent-involved methods. Solvent-free methods typically disperse the nanofillers directly in the molten polymers. These methods are prevalent and preferred for potential industrial manufacture since removing organic solvents is time-consuming. Single and twin-screw extruders [21-23] are often applied to mix and disperse CNTs in PLA through shear flows. Other techniques like melt stirring [24], powder blending [25] and co-axial eccentric melt mixing [12] are also used to mix CNTs with PLA. Solvent-involved methods need to dissolve PLA in organic solvents, and the dispersion process happens in the aqueous form via stirring or ultrasonication. These methods are more suitable for lab-scale production and less dependent on the manufacture facilities. Moreover, researchers have compared these two techniques and found that the solvent-involved method could achieve a better CNT dispersion result at low CNT concentrations [26]. Therefore, the solution-mixing method was selected to disperse nanocarbons into the polymer matrix. In this paper, the MWCNTs and PLA were mixed in acetone and dispersed via an ultrasonication process. Basic characterisations were applied to the nanocomposite samples and the results showed a significant increase in electrical conductivity and piezoresistivity.

2. Experimental

In this project, CNT/PLA nanocomposite plates were manufactured via a solvent-casting and hot-pressing process. Dried PLA pellets (PLA 4043D, NatureWorks) were first dissolved in a low-toxic organic solvent, acetone. Multi-walled CNTs (MWCNTs, NC7000, NanoCyl®) were mixed with acetone and ultrasonicated for initial dispersion. This mixture was then added to PLA/acetone solution and ultrasonicated again. Next, the entire mixtures underwent solvent evaporation, casting, vacuum degassing, and hot-pressing processes to become CNT/PLA nanocomposites for further measurements.

The mechanical properties of nanocomposites of dog-bone shaped samples were measured by tensile tests on a universal testing machine (Instron 5969 50kN) based on the ASTM D638 standard. A video gauge system (Imetrum Limited, equipped with a general-purpose lens) was applied to measure specimens' strain changes during the tests. Small, rectangular plates were cut from the nanocomposites for the electrical property measurement. The sides of the samples were first brushed with conductive silver paint (RS Pro, 186-3600). Then, tinned copper wires were attached to them by conductive adhesives (RS Pro silver conductive epoxy). The electrical conductivity of CNT/PLA nanocomposites was measured by a digital multimeter (Keysight 34465A) with a 2-wire set-up. The electrical conductivity is calculated by Equation (1):

$$\sigma = \frac{l}{RA} \tag{1}$$

Where σ is the electrical conductivity, [S/m]; l is the length of the specimen, [m]; A is the cross-section area of the specimen, [m^2]. Dog-bone shaped specimens were also prepared similarly for the piezoresistivity measurements. Other characterisations such as DSC, TGA, SEM and more were also conducted.

3. Results

According to the mechanical tests, the tensile strength and elastic modulus of PLA could be improved by 18.3% and 20.7% by adding only 0.5 wt% MWCNTs. The electrical conductivity of PLA was significantly improved after the addition of MWCNTs. Figure 1 shows that the conductivity of PLA is increased by over 7 orders of magnitude with the help of 0.1wt% MWCNTs. Nanocomposite could achieve a good electrical conductivity of 0.32 S/m at 1wt% concentration. The percolation threshold and critical component of the nanocomposite were calculated as 0.48 wt% and 1.61 according to the traditional percolation theory.

The piezoresistive responses of nanocomposites under different strain fields were measured and analysed. Since the percolation threshold was around 0.5 wt%, 1 wt% CNT/PLA nanocomposite was used in further piezoresistivity measurement because of its balance between sensitivity and high electrical conductivity. One example of the piezoresistive response CNT/PLA nanocomposite is shown in Figure 2. The resistance change of CNT/PLA nanocomposite was responsive under different cycles, indicating the composite had good sensitivity to small strain change and could be useful in strain sensing application.

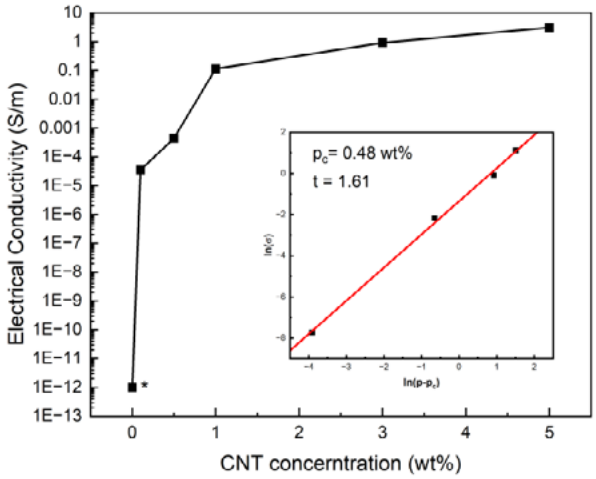

Figure 1. Electrical conductivity of PLA 4043D (* data from [27]) and CNT/PLA nanocomposites. The calculated percolation threshold and critical component are presented in the small graphs.

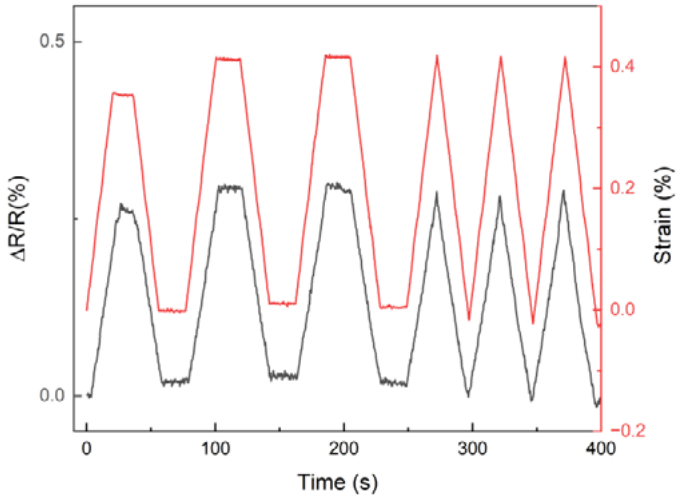

Figure 2. Example of the piezoresistivity measurement of 1wt% CNT/PLA nanocomposite under tension-relaxation cycles.

4. Conclusions

In conclusion, the CNT/PLA nanocomposites were successfully manufactured via an improved solution-casting and hot-pressing method. The tensile strength and elastic modulus of PLA were increased by around 20% after the addition of 0.5 wt% MWCNTs. The electrical conductivity of PLA was obviously enhanced with the help of nanocarbons, and the nanocomposite could achieve a high conductivity value of 0.32 S/m at 1wt% concentration. The nanocomposites also demonstrated decent piezoresistive response under repeated small deformation, which showed their potential in applications like strain sensing and structural health monitoring. More detailed works will also be presented on the conference presentation session.

References

[1] Andrews, R. and M.C. Weisenberger, Carbon nanotube polymer composites. Current Opinion in Solid State and Materials Science, 2004. 8(1): p. 31-37.
[2] Iijima, S., Helical Microtubules of Graphitic Carbon. *Nature*, 1991. 354(6348): p. 56-58.
[3] Harris, P.J.F., Carbon nanotube composites. *International Materials Reviews*, 2013. 49(1): p. 31-43.
[4] Shimamura, Y., et al., Tensile mechanical properties of carbon nanotube/epoxy composite fabricated by pultrusion of carbon nanotube spun yarn preform. *Composites Part a-Applied Science and Manufacturing*, 2014. 62: p. 32-38.
[5] Ando, Y., et al., Physical properties of multiwalled carbon nanotubes. *International Journal of Inorganic Materials*, 1999. 1(1): p. 77-82.
[6] Yang, D.J., et al., Thermal and electrical transport in multi-walled carbon nanotubes. Physics Letters A, 2004. 329(3): p. 207-213. Kobayashi, S. and K. Müllen, *Encyclopedia of Polymeric Nanomaterials*. 2015.
[7] Castro, M., et al., Novel e-nose for the discrimination of volatile organic biomarkers with an array of carbon nanotubes (CNT) conductive polymer nanocomposites (CPC) sensors. *Sensors and Actuators B-Chemical*, 2011. 159(1): p. 213-219.
[8] Wan, X., et al., CNT-based electro-responsive shape memory functionalized 3D printed nanocomposites for liquid sensors. *Carbon*, 2019. 155: p. 77-87.
[9] Chen, D., et al., 4D Printing Strain Self-Sensing and Temperature Self-Sensing Integrated Sensor-Actuator with Bioinspired Gradient Gaps. *Adv Sci (Weinh)*, 2020. 7(13): p. 2000584.
[10] Park, K., et al., Coupled health monitoring system for CNT-doped self -sensing composites. *Carbon*, 2020. 166: p. 193-204.
[11] Yuan, Q.W., et al., Efficient fabrication of highly stretchable and ultrasensitive thermoplastic polyurethane/carbon nanotube foam with anisotropic pore structures for human motion monitoring. *Journal of Materials Chemistry A*, 2023. 11(14): p. 7447-7456.
[12] Christ, J.F., et al., 3D printed highly elastic strain sensors of multiwalled carbon nanotube/thermoplastic polyurethane nanocomposites. *Materials & Design*, 2017. 131: p. 394-401.
[13] Hwang, J., et al., Poly(3-hexylthiophene) wrapped carbon nanotube/poly(dimethylsiloxane) composites for use in finger-sensing piezoresistive pressure sensors. *Carbon*, 2011. 49(1): p. 106-110.
[14] Murariu, M. and P. Dubois, PLA composites: From production to properties. *Adv Drug Deliv Rev*, 2016. 107: p. 17-46.
[15] Tümer, E.H. and H.Y. Erbil, Extrusion-Based 3D Printing Applications of PLA Composites: A Review. *Coatings*, 2021. 11(4).
[16] Rodriguez-Panes, A., J. Claver, and A.M. Camacho, The Influence of Manufacturing Parameters on the Mechanical Behaviour of PLA and ABS Pieces Manufactured by FDM: A Comparative Analysis. *Materials (Basel)*, 2018. 11(8).
[17] Liu, Y., et al., Remotely and Sequentially Controlled Actuation of Electroactivated Carbon Nanotube/Shape Memory Polymer Composites. *Advanced Materials Technologies*, 2019. 4(12).

[18] Yu, B.W., et al., Fabrication of PLA/CNC/CNT conductive composites for high electromagnetic interference shielding based on Pickering emulsions method. *Composites Part a-Applied Science and Manufacturing*, 2019. 125.
[19] Hu, C., et al., Comparative assessment of the strain-sensing behaviors of polylactic acid nanocomposites: reduced graphene oxide or carbon nanotubes. *Journal of Materials Chemistry C*, 2017. 5(9): p. 2318-2328.
[20] Liu, S., et al., Degradation Behavior In Vitro of Carbon Nanotubes (CNTs)/Poly(lactic acid) (PLA) Composite Suture. *Polymers (Basel),* 2019. 11(6).
[21] Pinto, V.C., et al., Dispersion and failure analysis of PLA, PLA/GNP and PLA/CNT-COOH biodegradable nanocomposites by SEM and DIC inspection. *Engineering Failure Analysis*, 2017. 71: p. 63-71.
[22] Pandey, V. and J.M. Maia, Extension-dominate improved dispersive mixing in single-screw extrusion. Part 1: Computational and experimental validation. *Journal of Applied Polymer Science*, 2020. 138(4).
[23] Logakis, E., et al., Highly conducting poly(methyl methacrylate)/carbon nanotubes composites: Investigation on their thermal, dynamic-mechanical, electrical and dielectric properties. *Composites Science and Technology*, 2011. 71(6): p. 854-862.
[24] Zhang, X., N.Q. Zhao, and C.N. He, The superior mechanical and physical properties of nanocarbon reinforced bulk composites achieved by architecture design - A review. *Progress in Materials Science*, 2020. 113.
[25] Rhim, J.W., et al., Effect of the processing methods on the performance of polylactide films: Thermocompression versus solvent casting. *Journal of Applied Polymer Science*, 2006. 101(6): p. 3736-3742.
[26] Sui, G.P., et al., The dispersion of CNT in TPU matrix with different preparation methods: solution mixing vs melt mixing. *Polymer*, 2019. 182.
[27] Lebedev, S.M., et al., Poly(lactic acid)-based polymer composites with high electric and thermal conductivity and their characterization. *Polymer Testing*, 2017. **58**: p. 241-248.

TOWARD ADHESIVES-FREE BIO-BASED COMPOSITES VIA UV-ASSISTED INTERFACIAL CROSS-LINKING

R. Bade[1], B. Gebert[2], L. Tsarkova[2], D.Koch[3] & J. Müssig[1*]

[1] The Biological Materials Group, Dept. of Biomimetics, HSB – City University of Applied Sciences Bremen, Neustadtswall 30, D-28199 Bremen, Germany
Email: Venkata-Rajasekhara-Reddy.Bade@hs-bremen.de, (*) Email : jmuessig@bionik.hs-bremen.de
Web Page: https://www.hs-bremen.de
[2] German Textile Research Center North-West gGmbH, Germany
Email: tsarkova@dtnw.de, Web Page: https://www.dtnw.de/en
[3] Institute of Materials Resource Management, University of Augsburg, D-86135 Augsburg, Germany
Email: dietmar.koch@mrm.uni-augsburg.de, Web Page: https://www.uni-augsburg.de

Keywords: Adhesive-free composites, UV irradiation, Regenerate cellulose fibres, polyolefins, stress-relaxation tests

Abstract
The performance of fibre-reinforced composites (FRC) depends crucially on the quality of the fibre-matrix adhesion. The basic idea of the presented project concerns photo-induced interfacial crosslinking using UV irradiation of absorbent viscose fibres through a transparent polyolefin polymer matrix. This radically driven process creates an intermediate layer bonded to the fibre without an additional adhesion promoter. The fatigue results of the composites show about 20 % improvement in fatigue strength UV irradiation. The results of the stress-relaxation and tensile tests on irradiated single layer composites revealed that a second thermal pressing is necessary to transform the formed interfacial layer into a strong adhesive contact between fibres and the polymer matrix. The unique perspective of the method lies in the use of industrially produced bio-based reinforcing fibres and the absence of adhesion-promoting additives, which also opens up opportunities for easier recycling.

1. Introduction

The use of bio-based fibres, e.g., regenerated cellulose or polylactic acid fibres, in fibre-reinforced composites (FRC) makes it possible to avoid the use of petroleum-based fibres and also eliminates the well-known problem of the variability of the properties of natural plant fibres. However, the mechanical properties of the resulting FRC must meet the product requirements. Increasing efforts are also being made to reduce the use of potentially harmful chemical ingredients and additives, opening up opportunities for economic recycling. The food and pharmaceutical industries consider it desirable to use pure ingredients without chemical additives, which are increasingly on the banned list. Polyolefins such as polyethylene (PE) and polypropylene (PP) offer several advantages when used as matrix polymers. These include their low cost, chemical inertness and anti-adhesive properties, as well as their beneficial behaviour concerning contamination and decontamination. In the long term, these commodity polymers are also envisaged to be used in their bio-based form. In principle, the fibre surface and the matrix can be modified to improve fibre-matrix adhesion. Extensive research has been conducted on this topic, either by modifying the fibre surfaces, adding additives, or treating entire composite structures. In order to improve adhesion, the additive or component applied to the fibre surface must react with the OH groups of the cellulose on the one hand and with the non-polar chain of the polyolefin on the other [1].

The present research uses industrially manufactured continuous regenerated cellulose fibres woven to a fabric and polyethene powder to manufacture adhesive-free single-layer composites. The manufactured single-layer composites were irradiated using a UV broadband lamp with a wavelength spectrum from 250 to 300 nm (UVACUBE 2000, Dr Hönle, Munich, DE). The irradiation dose was varied by the exposure time while maintaining a consistent specific power of 50 W/cm. The distance between the lamp and the sample was kept constant to 10 cm. The samples were exposed for three minutes (UV_3) and eight minutes (UV_8) on each side. The concept in the present study implies the UV-activated formation of covalent bonds between UV-transparent polymer and UV-absorbing fibres. The positive influence of UV treatment on fibre-matrix adhesion was demonstrated through single fibre fragmentation, tensile, and double-notch tensile tests. Samples for tensile and double-notch tensile tests were prepared by compacting multiple stacks of single-layer composites at 180 °C [3].

Enhanced fibre-matrix adhesion is expected to impact long-term properties positively. The influence of UV treatment on long-term stability, including fatigue tests on multi-layer composites and stress-relaxation tests on the single-layer composites, was investigated. Single-layer composites were aged in a climatic chamber at 80 °C and 80 % relative humidity for 12 days for the stress-relaxation test. Additionally, the effects of UV treatment with and without a second compaction cycle were examined. In the first scenario, untreated and UV-treated single-layer composites underwent a second compaction cycle at 180 °C. In the second scenario, the single-layer composites underwent only one compaction cycle, followed by tensile testing.

2. Methods

2.1. Fatigue test

The fatigue behaviour of the Un, UV_3 and UV_8 multi-layer composite samples (each a stack of five single-layer composites) was evaluated under different ageing conditions. Stress-controlled fatigue tests under tension-tension loading ranged from 10^3 to 10^6 cycles, with data analysed and presented in Wöhler diagrams. Strip-shaped tensile test specimens (10 mm x 100 mm) were clamped in an MTS testing machine (858 Mini Bionix II, MTS Systems Corporation, Eden Prairie, USA). Cyclic tests were performed under tension-tension loading (R = 0.1) with force control at specific upper and lower forces. The "bead chain method" ensured comprehensive coverage across 10^3 to 10^6 cycles, and testing continued until specimen failure or one million cycles at a frequency of 5 Hz.

2.2. Stress-relaxation

The relaxation tests were conducted using a universal testing machine (EZ 50, Zwick/Roell GmbH, DE) with a gauge length of 135 mm and a crosshead speed of 2 mm/min. A preload of 5 N was applied, and the maximum elongation was set to 0.6 %. The samples (single-layer composites) were clamped using mechanical clamps, with measurement precision ensured by a thickness gauge (+/- 0.01 mm) and a digital calliper/screw (+/- 0.001 mm). Applied strains were selected to remain within the elastic range of each material's stress-strain curve, specific to each material. The strain was held for 5 minutes during the relaxation tests. Each result was averaged over five repeat measurements. The measurements included relaxation (stress (σ) in N/mm² over time (t)) and hysteresis (stress (σ) in N/mm² versus elongation (%L) for remaining elongation). Cross-sections were considered for all materials tested. Before testing, samples were conditioned for 24 hours at 23 °C and 50 % relative humidity.

2.3. Tensile test

Tensile tests were carried out according to the DIN standard 527-4 (Type 1B) [2]. Specimens were prepared using a CO_2 laser (150 W, Sabko GmbH, Trierweiler, DE). Before testing, specimens were conditioned for 24 hours at 23 °C and 50 % rel. Humidity. The test was performed with a Zwick universal testing machine (Z020 Zwick/Roell, Ulm, DE) at 2 mm/min crosshead speed. The strain was optically determined via a video extensometer (Zwick/Roell, Ulm, DE) with a distance between the measuring marks of 50 mm.

2.4. Artificial aging

To simulate the long-term use of composites under application conditions, the single-layer composites (each untreated and UV-irradiated) were tested under defined climatic conditions. Ageing was conducted in a climate chamber WK1 340 (Weiss Technik GmbH, Reiskirchen, DE) at 80 °C and 80 % relative humidity for 12 days. The samples were placed horizontally on a grid to minimise damage caused by condensation. At the end of the treatment, the humidity was also reduced to 40 % relative humidity to avoid condensation. Before the test, all aged samples were conditioned in a climate chamber at 20 °C and 65 % relative humidity. The aged samples were then analysed regarding their mechanical properties (relaxation tests).

2.5. Statistical analysis

The statistical evaluation of the tensile test results was evaluated with the open-source software R (R studio 1.4.1103/ R version 4.0.3). The data's normal distribution ($\alpha = 0.05$) was checked using the Shapiro-Wilk test. The Tukey–Kramer HSD test ($\alpha = 0.05$) was performed to check the significant differences among normally distributed data. A Wilcoxon test ($\alpha = 0.05$) was performed in the case of not normally distributed data. The results were shown as Box-Whiskers plots, with the median and the standard deviation. An asterisk (*) represents the results that do not follow a normal distribution, and different letters are used to indicate significant differences between median values.

3. Results

3.1. Fatigue test

The fatigue strength measurements of untreated, UV_3 and UV_8 multi-layer composites (each a stack of five single-layer composites) are presented as Wöhler curves in Figure 1. The evaluation of cyclic strength refers to the fatigue strength determined at a cycle count of 106 cycles and is designated as the fatigue limit $\Delta\sigma$ (N = 106) along with the slope (-d log N / d log $\Delta\sigma$) of the Wöhler curve.

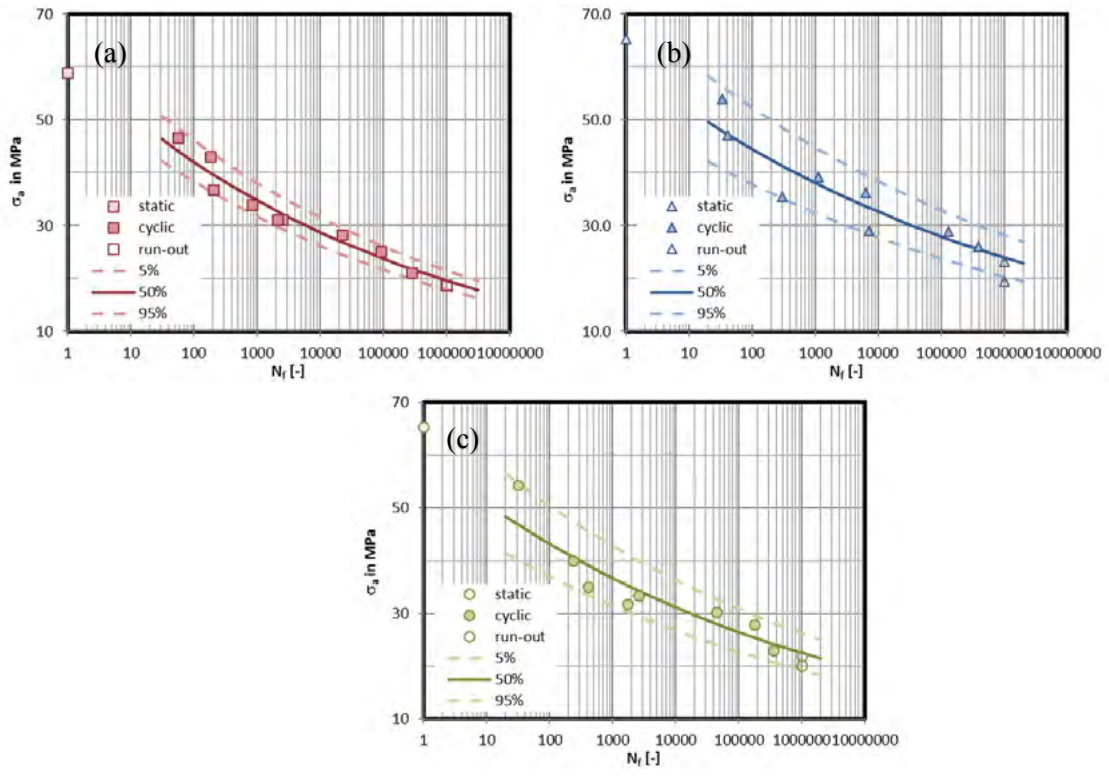

Figure 1. Wöhler curves of the untreated (a) and (b, c) UV-treated (UV_3 & UV_8) viscose/HDPE composites

Statistical analysis is performed to evaluate fatigue strength, providing the median as well as the 5 % and 95 % quantiles. Additionally, the static strength R^m_{stat} and the limits $\Delta\sigma$ (N = 1) of the Wöhler curve for a single cycle are given as references. Table 1 provides a comparative overview of the cyclic properties of all three examined composites. For all samples, a similar extrapolated value of the Wöhler curve for the static load case N = 1 was observed, around σ_a = 61 MPa, with only minor fluctuations within a consistent scatter band. The fatigue strength at a cycle count of N = 10^6 for the Un, UV_3 and UV_8 samples are 19,6 MPa, 24 MPa, and 22.5 MPa, respectively. The UV_3 and UV_8 samples showed a 23 % and 18 % improvement in fatigue strength compared to the untreated ones, with the UV_3 samples exhibiting the highest average fatigue strength with σ_a (N = 10^6) = 24.0 MPa. Therefore, moderate UV irradiation positively influences both fatigue properties and quasi-static tensile strength.

Table 1. Characteristic values of the Wöhler curves

Samples	R^m_{stat} in MPa	σ_a (N=1) in MPa			σ_a(N=10^6) in MPa			-d log N / d log
		5 %	50 %	95 %	5 %	50 %	95 %	
Ub	131,0	56,2	61,6	67,5	17,9	19,6	21,5	12,1
UV-3	145,0	51,6	60,6	71,3	20,4	24,0	28,2	14,9
UV-8	145,0	51,2	59,8	69,8	19,2	22,5	26,2	14,1

More prolonged irradiation is believed to be contra productive presumably because of partial damage of the regenerate cellulose fibers as a result of high energy absorption. To get more insights into possible mechanisms behind additives-free improvement of the interfacial adhesion of the composites under UV-irradiation, additional studies have been performed on single-layer composites (prepregs).

3.2. Stress-relaxation test

The relaxation curves of the single-layer composites, which were initially stretched at an elongation of 0.6 % for 5 min, are shown in Figure 2. The discussion refers to the comparison of the loss of stress after 120 s to the maximum stress (in %) (Table 2). The greater the ratio, the faster the stress of the samples was relaxed. The comparison of unirradiated aged and non-aged single-layer composites (black lines in Figure 2) shows that ageing has a significant influence on the strength of the single-layer composites. The aged UV-irradiated samples also show lower strength and more pronounced plastic behaviour compared to the non-aged samples, as seen in Table 2.

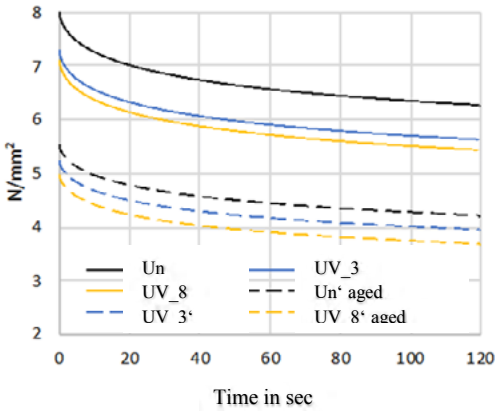

Figure 2. Relaxation mean value curves of the single-layer composites. The untreated, UV-treated (UV_3 and UV_8) samples are shown as solid lines, and the corresponding aged samples as dashed lines.

Surprisingly, UV irradiation on single layer composites did not positively influence the relaxation properties, contrasting with the findings from tensile, double-notch, and fatigue tests. A key factor contributing to this discrepancy is the testing conditions: while the single-layer composites were tested directly after irradiation, samples for tensile, double-notch [3], and fatigue tests underwent an additional compaction cycle at 180 °C to achieve the desired thickness. The UV treatment of single-layer composites not only results in covalently bonded interfaces but also leads to the formation of voids at the interface due to moisture loss and volume changes in the regenerated cellulose fibres. The subsequent section reports on the influence of a second compaction cycle after irradiation.

Table 2. Stress loss after 2 min compared to maximum stress in %.

Single-layer composites					
Non-aged samples			Aged samples		
Un	UV_3	UV_8	Un‘	UV_3‘	UV_8‘
22	23	23	24	25	26

3.2. Tensile test

The tensile strength of single-layer composites subjected to one and two pressing steps is presented in Figure 3. Figure 3a illustrates the impact of UV irradiation on the manufactured single-layer composites, while Figure 3b displays the influence of the second compaction cycle on the tensile strength of the UV-treated samples. Irradiation of the single-layer composites after their manufacturing did not result in notable changes in the tensile strength. Interestingly, these findings contradict the analysed tensile strength, interlaminar shear strength, and fatigue strength, where single layer-composites were irradiated and stacked to achieve the desired thickness [3].

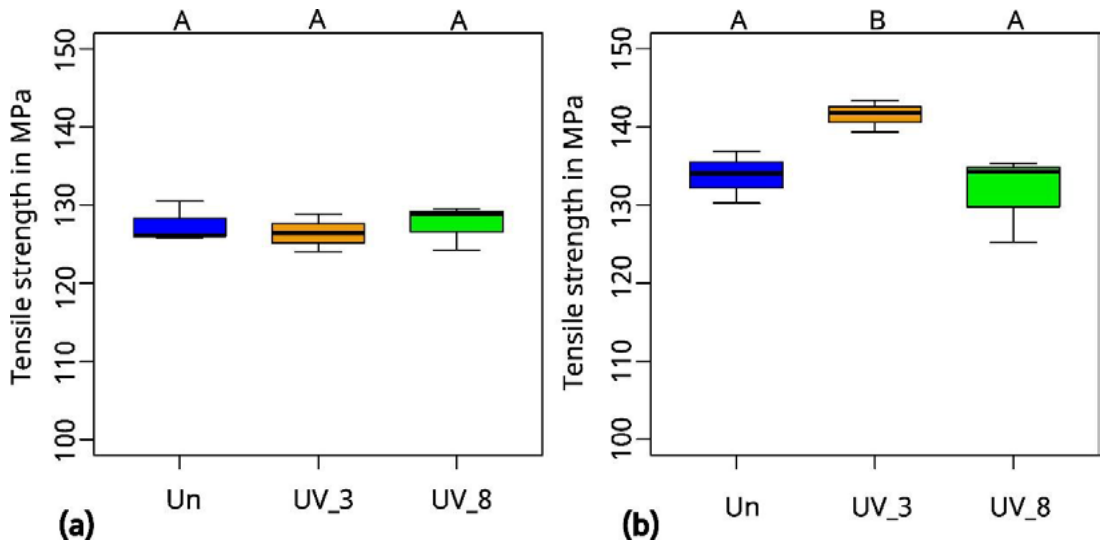

Figure 3. Tensile strength of the direct irradiated single-layer composites (a); single-layer composites that went through a second-compaction cycle after irradiation (b)

This prompts discussion regarding the observed discrepancy, highlighting that the samples showing positive interfacial property influences underwent a second compaction cycle. It is speculated that alongside UV-induced covalent bonding between fibres and the matrix, moisture loss and fibre shrinkage occur during UV irradiation of the single-layer composites, leading to a heterogeneous interface with voids. The subsequent pressing process eliminates this interlayer inhomogeneity. The results from Figure 3b support the assumption that a second compaction after UV irradiation of single-layer composites mitigates the inhomogeneity induced by moisture loss at the fibre-matrix interface. The UV_3 samples showed an 8 % increase in the tensile strength compared to untreated samples, whereas UV_8 samples showed no improvement and no further increase in the tensile strength. Prolonged irradiation is believed to be contra productive presumably because of partial damage of the regenerate cellulose fibers as a result of high energy absorption.

4. Conclusions

This study demonstrates the notable positive influence of UV irradiation on the fatigue performance of composites comprising regenerated cellulose fabric and a polyethylene matrix. UV-induced crosslinking between the fibre and matrix enhances the material's resistance to fatigue, contributing to its overall durability. However, it is essential to acknowledge that UV irradiation also induces moisture loss in the fibres, leading to the formation of voids at the interface. Consequently, our findings underscore the importance of a second compaction cycle post-UV treatment to address interface inhomogeneities caused by moisture loss, thereby further optimising the composite's tensile strength and long-term performance.

Acknowledgements

The research project IGF-Nr. 21818 N was funded by the German Federation of Industrial Research Associations (AiF) within the program for sponsorship by the Industrial Joint Research (IGF) of the German Federal Ministry of Economic Affairs and Climate Action based on an enactment of the German Bundestag. We are grateful to Cordenka GmbH (Obernburg, DE), Kelheim Fibres GmbH (Kelheim, DE) and LyondellBasell Industries (Rotterdam, NL) for providing material for the experiments.

References

[1] Müssig J, Kelch M, Gebert B, Hohe J, Luke M, Bahners T. Improvement of the fatigue behaviour of cellulose/polyolefin composites using photo-chemical fibre surface modification bio-inspired by natural role models. Cellulose 2020; 27(10):5815–27.

[2] DIN EN ISO 527-4:1997-07, Plastics - Determination of tensile properties - Part 4: Test conditions for isotropic and anisotropic fibre-reinforced plastic composites (ISO 527-4:1997); German version EN ISO 527-4:1997, Beuth Verlag GmbH, Berlin.

[3] Bade R, Gebert B, Tsarkova L, Bahners T, Müssig J (2023): Toward adhesives-free bio-based composites via UV assisted interfacial cross-linking. Fangueiro, Raul (Ed.) In: 6th International Conference on Natural Fibers - ICNF, 19. - 21. June, 2023, Funchal, Madeira, Portugal, p. 131-132, ISBN: 978-989-54808-8-3.

RESOURCES FROM SUSTAINABLE LAND USE FOR NATURAL FIBRE COMPOSITE INJECTION MOULDING

Jonas-Rumi Baumann[1], Andreas Hellmann[2], Colja Beyer[2] and Jörg Müssig[1]

[1]The Biological Materials Group, Biomimetics, City University of Applied Sciences, Neustadtswall 30, 28199 Bremen, Germany
Email: joerg.muessig@hs-bremen.de, Web Page: http://www.hs-bremen.de

[2]3N Kompetenzzentrum Niedersachsen e.V., Kompaniestraße 1, 49757 Werlte, Germany
Email: beyer@3-n.info, Web Page: https://www.3-n.info/

Keywords: short-fibre reinforced polymer, paludiculture, nettle, mechanical properties

Abstract
This study delves into the innovative use of biomass from land unsuitable for food cultivation to create sustainable materials. Stinging nettle (*Urtica dioica* L.) was found to thrive on marginal lands, presenting a unique opportunity. Biomass from nettle and various plant species cultivated through paludiculture was used as reinforcement material in short-fibre composites, a novel approach in material science. Paludiculture refers to the sustainable agricultural or forestry use of wet and rewetted peat soils, conserving peat and minimising greenhouse gas emissions. Suitable species for these conditions include cattail (*Typha latifolia*), reed (*Phragmites australis*), reed canarygrass (*Phalaris arundinacea*), and sedges (*Carex acutiformis*). These biomasses were compounded with PLA as a matrix polymer and processed via injection moulding for mechanical characterisation. The results from tensile testing revealed homogenous compounds with small variances in mechanical properties. Notably, compounds reinforced with decorticated nettle fibres exhibited high tensile properties. *Typha* and *Phragmites* showed the most promising results for use in short-fibre reinforced composites among the different biomasses from paludiculture. This research underlines the potential of biomass from non-arable lands to meet the growing demand for bio-based materials, contributing to the development of sustainable materials.

1. Introduction

Natural fibre-reinforced composite materials can be an essential part of the development towards a more sustainable future [1]. Established natural fibres, such as hemp, flax, and cotton, have already been processed with bio-based polymers in various studies to create natural fibre composite materials for injection moulding processing (e.g., [2]). Injection moulding is an important process for producing components from compound materials, as large quantities can be achieved with short processing times. Although the natural fibres are considerably shortened during the compounding and injection moulding process, the mechanical properties can be significantly increased by using natural fibres as reinforcement compared to pure polymers. In [3], losses from the hackling process of long hemp were compounded with a PLA matrix. With a fibre mass fraction of 20 %, the tensile strength and Young's modulus could be significantly increased compared to the raw polymer, while the unnotched Charpy impact strength was higher in the pure polymer.

A potential problem in the utilisation of plant biomass for technical applications such as materials or energy production is the possible competition in land use. Suitable soils and areas for cultivation are not infinitely available, so conflicts with other land use alternatives such as food production can arise. To avoid these conflicts, areas that are not suitable for food cultivation, in particular, could be selected to cultivate biomass for technical applications like fibre-reinforced composites. Such areas are, for

example, marginal land that is not available for the cultivation of food crops due to contamination from industrial wastewater.

In this study, the biomass from land not available for food cultivation was utilised as a resource for sustainable materials. The Stinging Nettle *Urtica dioica L.* was found to grow spontaneously on phytomanaged marginal land sites contaminated by traces of metal [4]. Further, the biomass from different plant species from the cultivation in paludiculture was used as reinforcement material. Paludiculture describes the sustainable agricultural or forestry use of wet and rewetted peat soils under peat-conserving conditions and minimising greenhouse gas emissions [5]. Only certain plant species can be grown in such wet soils. Biomass from cattail (*Typha latifolia*), reed (*Phragmites australis*), reed canarygrass (*Phalaris arundinacea*), sedges (*Carex acutiformis*) and stinging nettle (*Urtica dioica L.*, clone L18*)* were compounded with poly(lactic acid) (PLA) as matrix polymer. The compounds were processed via injection moulding to produce specimens for mechanical characterisation.

2. Materials & Methods

Composites with different biomass as reinforcement and PLA as matrix were produced and characterised. The goal was to evaluate the potential biomass use of plants from paludiculture and nettle biomass from contaminated soils. The complete plant of the different species was cut into chunks with a length of 5-10 cm. For the nettle, the leaves were removed from the stems before cutting.

Additionally, the nettle biomass was processed using a laboratory-scale breaking unit (Worthmann Maschinenbau GmbH, Barßel, Germany). Each stem was passed through the breaking unit three times, with the thicker end first. The resulting fibre bundles were manually cleaned from shives and used for compounding.

2.1 Production of bio-based composites

Composite granules with different types of biomass were produced by compounding at 3N in Werlte, Germany. Each reinforcing material was compounded with PLA (Ingeo 3251D, NatureWorks, Plymouth, USA) after drying both for 24 h at 80 °C. Details on the compounding concept are found in [6]. Paludiculture biomass (*Typha, Phalaris, Carex* & *Phragmites)* was used to produce compounds with 20 % and 30 % biomass content. With the two types of nettle biomass (whole stem & decorticated fibre bundles), only compounds with a mass fraction of 30 % were produced.

Dog bone-shaped tensile test specimens from the composite granules were manufactured by injection moulding at NHL Stenden, Netherlands. Before processing, the granules were dried at 105 °C for at least 24 h hours. The injection moulding for all granules was done using an Engel e-mac injection moulding machine (ENGEL AUSTRIA GmbH, Schwertberg, Austria). The temperatures in the screw were set to 150 °C, 165 °C and 175 °C and the temperature in the injector was set to 175 °C. A dwell pressure of 70 MPa for 25 seconds and a cooling time of 30 seconds were applied.

2.2 Characterisation of bio-based composites

Before the mechanical characterisation, the composite specimens were conditioned 24 h at 23 °C and 50 % relative humidity according to DIN EN ISO 291 (2008). Tensile tests were performed following DIN EN ISO 527 (1996) using a universal testing machine type Zwick Z 020 (Zwick/Roell GmbH & Co.KG, Ulm, Germany) working with a load cell of 20 kN and a Zwick/Roell pneumatic clamping system (clamping pressure: 1–2 bar). Seven specimens per composite were preloaded with 5 N and then tested at a speed of 2 mm/min. The displacement for calculating Young's modulus and the strain was measured using an optical contactless extensometer (VideoXtens, Zwick/Roell GmbH & Co. KG, Ulm, Germany).

3. Results & Discussion

The production of compounded granules and the injection moulding of dog bone-shaped test specimens could be successfully accomplished. Aesthetically appealing materials based on visual control were produced.

The measured Young's moduli of the compounds from tensile testing can be seen in Figures 1 and 2. A significantly higher modulus compared to pure PLA was measured for all tested composites, while no statistical difference between the compounds with 20 wt% biomass could be found. From the compounds reinforced with 30 wt% of biomass, using the decorticated nettle fibre bundles led to the highest measured modulus with a value of 7.23 GPa. This is an increase of 101 % per cent compared to the pure polymer. Interestingly, the second highest modulus was found in the compound reinforced with 30 wt% of *Phragmites*-biomass, which also exceeds the compound reinforced with the whole nettle stems.

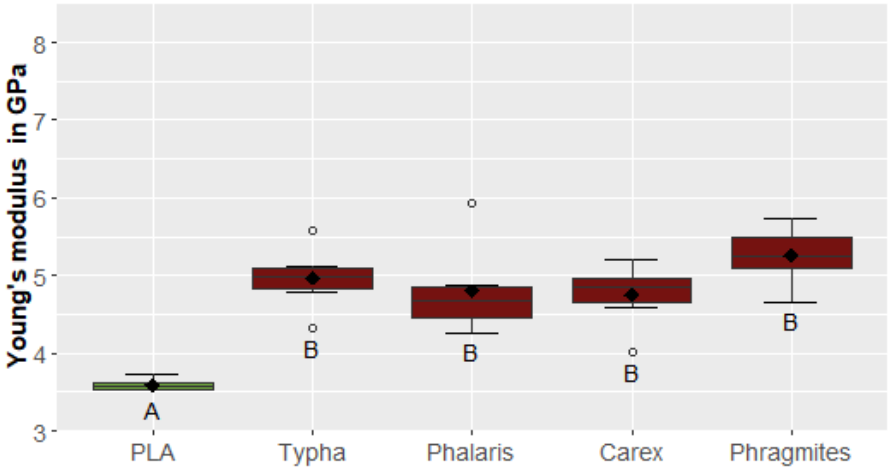

Figure 1. Box-Whisker-plot of Young's modulus of the compounds with 20 wt% of biomass.

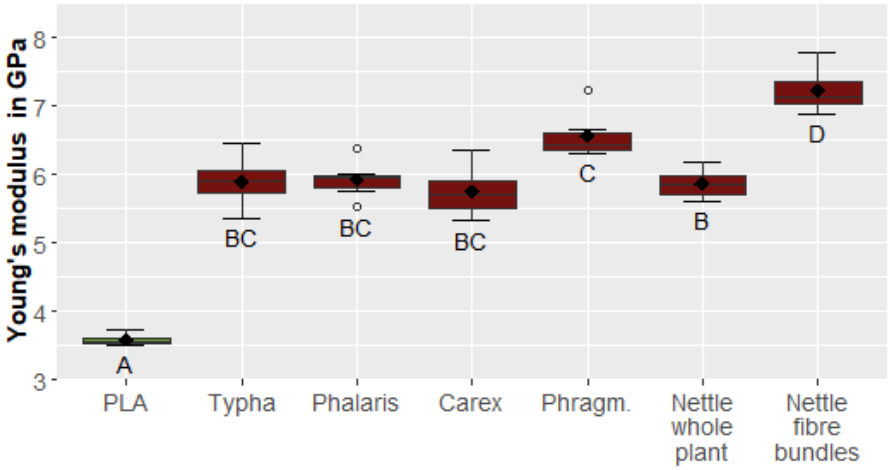

Figure 2. Box-Whisker-plot of Young's modulus of the compounds with 30 wt% of biomass.

Figures 3 and 4 show the measured tensile strength of the composites. It can be seen, that the strength was statistically significantly lower for all tested compounds except for the one compounded with decorticated nettle fibres. Among the whole plant-reinforced compounds, the compound with 20 wt% of *Typha* and 30 wt% of *Phragmites* and nettle showed the smallest drop in the tensile strength.

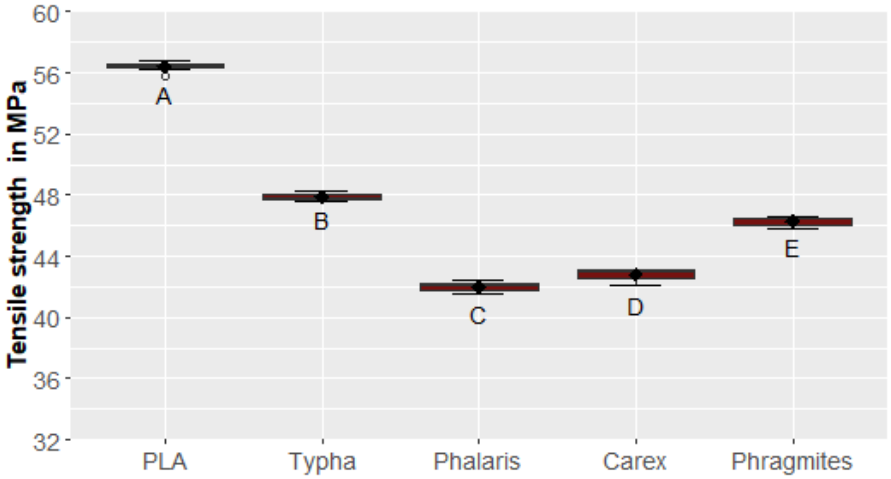

Figure 3. Box-Whisker-plot of the tensile strength of the compounds with 20 wt% of biomass.

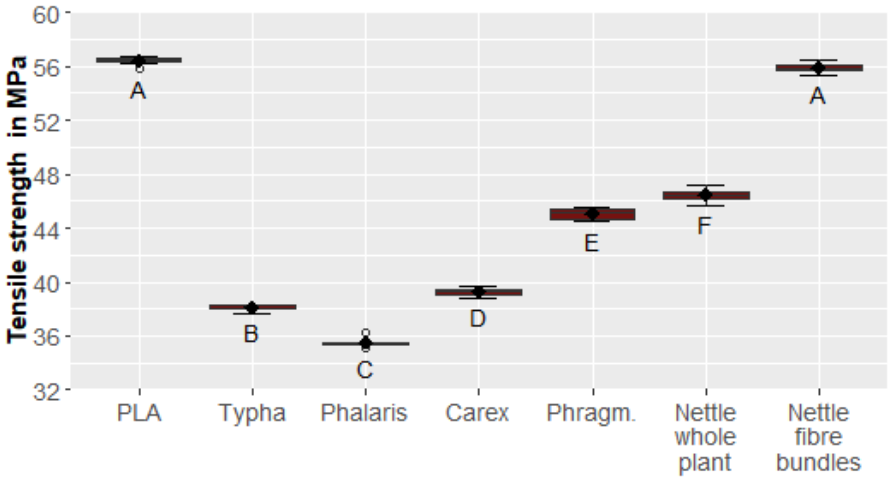

Figure 4. Box-Whisker-plot of the tensile strength of the compounds with 30 wt% of biomass.

In general, the results from tensile testing show only a small scattering in the mechanical properties, which indicates that homogenous compounds could be successfully produced with the different types of biomass. The comparably high tensile properties of the compound reinforced with decorticated nettle fibres were to be expected since stinging nettle is a fibre crop with a long history of use in textiles [7, 8]. Also, nettle fibres have already been used in fibre-reinforced composites because of the interesting fibre properties of high tensile strength and stiffness values [9].

Among the different types of biomass from paludiculture, the use of *Typha* and *Phragmites* showed the most promising results for the application in short-fibre reinforced composites. In the work of Maharani et al. [10], the biomass of *Phragmites* was used as a reinforcement of polypropylene. Using a coupling agent, it was possible to increase the Young's modulus and the tensile strength of the composite compared to pure PP.

4. Conclusions

The biomass from lands unavailable for food crop cultivation was used for the production of short-fibre reinforced composites with a bio-based polymer as a matrix. The compounded granules could be processed via injection moulding. The Young's modulus was significantly increased by using all the different types of biomass, while the tensile strength dropped for almost all the compounds compared to the pure polymer. Due to the increasing demand for bio-based materials, this work can be seen as part of a fundament in research into renewable resources for raw materials for the use of sustainable materials.

Acknowledgements

The NAPALU project, "Sustainability of Paludicultures with particular consideration of the matter balance" (funding code: 2221MT010G), financed by the Fachagentur Nachwachsende Rohstoffe eV (FNR) is funded by the Federal Ministry of Food and Agriculture based on a resolution of the German Bundestag.

References

[1] R. Dunne, D. Desai, R. Sadiku and J. Jayaramudu. A review of natural fibres, their sustainability and automotive applications. *Journal of Reinforced Plastics and Composites*, 35(13):1041-1050, 2016.

[2] V. Röhl, C. van Noordenne-Bos, H. Wieland, N. Graupner, M.L. Rottmann-Meyer and J. Müssig. Effect of Different Natural Fibers on Mechanical and Disintegration Properties of Compostable Biobased Plastics. *Journal of Natural Fibers*, 20(2), 2023.

[3] J. Müssig, K. Haag, S. Musio, M. Bjelková, K. Albrecht, B. Uhrlaub, S. Wang, H. Wieland and S. Amaducci. Biobased 'Mid-performance' composites using losses from the hackling process of long hemp–A feasibility study as part of the development of a biorefinery concept. *Industrial crops and products*, 145, 2020.

[4] T. Jeannin, L. Yung, P. Evon, L. Labonne, P. Ouagne, M. Lecourt, D. Cazaux, M. Chalot and V. Placet. Are nettle fibers produced on metal-contaminated lands suitable for composite applications? *Materials Today: Proceedings*, 31:291-295, 2020.

[5] W. Wichtmann, C. Schröder and H. Joosten (Edt.). *Paludiculture - Productive Use of Wet Peatlands. Climate Protection, Biodiversity, Regional Eco-nomic Benefits*. Schweizerbart Science Publishers, Stuttgart, Germany, 2016.

[6] J. Müssig. Natural Fibre Composites and their Processing. In *Processing of fibre composites – challenges for maximum materials performance – 34th Risø International Symposium in Materials Science*, pages 73-92, 2013.

[7] C. Viotti, K. Albrecht, S. Amaducci, P. Bardos, C. Bertheau, D. Blaudez, L. Bothe, D. Cazaux, A. Ferrarini, J. Govilas, et al. Nettle, a Long-Known Fiber Plant with New Perspectives. *Materials*, 15, 2022.

[8] G. Bredemann. *Die große Brennnessel Urtica dioica L. Forschung über ihren Anbau zur Fasergewinnung*. Akademieverlag, Berlin, Germany, 1959.

[9] E. Bodros and C. Baley. Study of the tensile properties of stinging nettle fibres (*Urtica dioica*). *Materials letters*, 62(14):2143-2145, 2008.

[10] M. Maharani, S. Soundararajan,K. Palanivelu and D.H. Raiker. Study of mechanical and thermal properties of natural fiber reinforced polypropylene composites. *Journal of Polymer Materials*, 30(3):349-404, 2013.

TOWARDS IMPROVING THE FIBRE-MATRIX ADHESION IN OLEAGINOUS FLAX FIBRE POLYLACTIDE (PLA) COMPOSITES

Alexander Behrens[1], Regine Hirschberg[2], Giulia Ronconi[3], Sebastian Drabben[4], Pia Borelbach[5] and Jörg Müssig[6]

[1]Biological Materials Group, Faculty 5 Dep. 2, City University of Applied Sciences Bremen, Neustadtswall 30, 28199 Bremen, Germany
Email: alexander.behrens@hs-bremen.de, Web Page: https://www.hs-bremen.de
[2]Biological Materials Group, Faculty 5 Dep. 2, City University of Applied Sciences Bremen, Neustadtswall 30, 28199 Bremen, Germany
Email: regine.hirschberg@hs-bremen.de, Web Page: https://www.hs-bremen.de
[3]Department of Engineering, University of Ferrara, Via Saragat 1, 44122 Ferrara, Italy
Email: giulia.ronconi@unife.it, Web Page: https://www.hs-bremen.de
[4] Fraunhofer Institute for Environmental, Safety and Energy Technology UMSICHT, Department Circular and Bio-based Plastics, Osterfelder Str. 3
46047 Oberhausen, Germany
Email: sebastian.drabben@umsicht.fraunhofer.de, Web Page: https://www.umsicht.fraunhofer.de
[5]Fraunhofer Institute for Environmental, Safety and Energy Technology UMSICHT, Department Circular and Bio-based Plastics, Osterfelder Str. 3
46047 Oberhausen, Germany
Email: pia.borelbach@umsicht.fraunhofer.de, Web Page: https://www.umsicht.fraunhofer.de
[6]Biological Materials Group, Faculty 5 Dep. 2, City University of Applied Sciences Bremen, Neustadtswall 30, 28199 Bremen, Germany
Email: joerg.muessig @hs-bremen.de, Web Page: https://www.hs-bremen.de

Keywords: oleaginous flax, fibre-matrix adhesion, biocomposite, sustainable materials

Abstract
This study gives an outlook for utilising the valorisation potential in the by-product of linseed cultivation through the usage of the unused stems in flax fibre-reinforced poly(lactic acid) (PLA) composites. Thus, providing the outlook towards a bio-based and recyclable composite material. The focus is in determining the adhesion properties between the two raw materials and the improvement of the adhesion through the functionalisation by using a coupling agent (maleic anhydride) as well as the fibre functionalisation (ethanol). Microbond test were performed to characterise the interfacial shear strength (IFSS) between the fibre and matrix. However, due to the low rate of successfully tested samples, double-notch tests were performed, thus providing insight towards the interlaminar shear strength (ILSS) between the two materials.

1. Introduction

Sustainability, from an ecological and economic point of view, is of great importance for mitigating climate change. Especially natural fibres have great reinforcing potential in more sustainable composites [1]. Accordingly, flax shows excellent specific mechanical properties for lightweight composite applications whilst being an eco-friendly reinforcing material. However, flax varieties are classified into textile and oleaginous flax species, where the textile flax is cultivated towards higher quality fibres and higher amounts of fibres per plant. On the contrary, oleaginous flax is harvested for the linseed and cultivated accordingly. The worldwide cultivation area of oleaginous flax far outweighs the area for

textile flax with an approx. area of 1.7 Mha [2]. Typically, after harvesting the seeds, the plant's stem is unused [3]. Therefore, a huge sustainable valorisation potential lies in the unused crop of the oleaginous flax plant. Using the reinforcing properties of the oleaginous flax fibres in combination with a biodegradable polylactide (PLA) matrix provides a bio-based and recyclable composite with a wide field of possible applications.

However, to utilise the potential of the composite, the mechanical properties, which are heavily dependent on the adhesion between the fibre and the matrix, have to be determined [4]. The adhesion between fibre and matrix depends on the mechanical, physical and chemical interaction. Whereas surface roughness is the main driving factor for mechanical adhesion, physical and chemical adhesion depends on the bonding between the two materials, which has proven difficult because of the polar fibres interacting with a nonpolar matrix [5]. Whilst the adhesion properties between flax and polyolefins have been researched extensively, very little research has been conducted on the adhesion between oleaginous flax and PLA. To improve the adhesion between fibre and matrix, either the fibre can be treated, or the matrix can be altered.

The conducted research presents approaches towards using maleic anhydride grafted PLA to change the matrix and treat the fibres with ethanol, thus offering a holistic approach to improve the adhesion between oleaginous flax fibre and a biobased PLA matrix.

2. Materials and Methods

2.1. Microbond Test

The preparation of the specimens for the microbond specimens is shown in Figure 1. A singular flax fibre or fibre bundle from the variety Agram (AGRITEC, výzkum, šlechtění a služby, s.r.o., Czech Republic) respectively Lincore (R-Lincore 1000 tex, Groupe Depestele, France) is extracted from the bundle, respectively roving and fixed to the metal frame with adhesive tape. Afterwards, a PLA fibre, which is drawn from the compounded granulates (NatureWorks Ingeo 3251D Injection Grade PLA, NatureWorsk LLC, USA & Scona TPPL 1112 PA) at a temperature of 180 °C on a heating plate (Stuart CB162, Cole-Parmer Instrument Company, LLC, USA), is being knotted around the flax fibre/fibre bundle. The specimens are being placed in a drying oven (Memmert UN450, Memmert GmbH + Co.KG, Germany) to melt the fibre and create a droplet around the fibre/fibre bundle (180 °C for 5 min). The fibres are then cut behind the droplet and glued into plastic tabs with a UV-hardening glue (Dymax 3193 Dymax Europe GmbH, Germany; coolLED pE-100, 15% intensity, CoolLED Limited, UK). The prepared specimens are placed under a microscope (ADL-601P, Bresser GmbH, Germany). Images to measure the size of the embedding length of the droplet around the fibre and the diameter of the fibre are being taken. The measurements are being carried out using the open-source software ImageJ (ImageJ 1.53T, Wayne Rasband and contributors National Institutes of Health, USA).

The microbond test was done with a Dia-Stron tensile testing unit (Dia-Stron LEX820, Dia-Stron, UK) using a shear plate with a slit width of 80 µm. The setup is schematically shown in Figure 2. The test was carried out with a testing speed of 10 mm/min. The measured force is then used to calculate the IFSS using the following equation, where τ is the IFSS, F_{MAX} is the maximum measured force, d_f is the diameter of the fibre and l_{ef} the embedded length of the fibre by the droplet:

$$\tau = \frac{F_{MAX}}{d_f \pi l_{ef}} \quad (1)$$

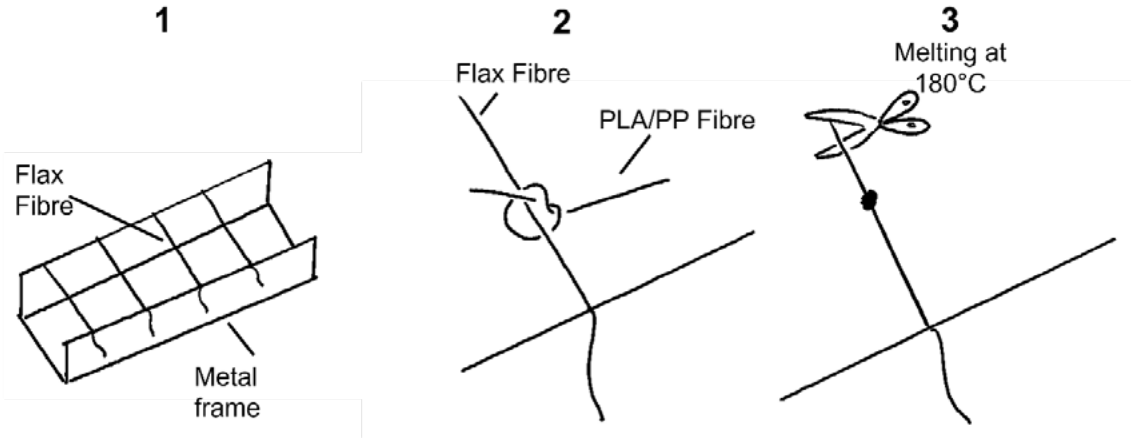

Figure 1. Schematic showing the sample preparation consisting of 3 steps. 1 – extracting single fibres or fibre bundles and placing them on a metal frame. 2 – drawing PLA fibres from granulates and knotting the fibre around the flax fibre. 3 – melting the PLA fibre to create a droplet and cutting off the fibre.

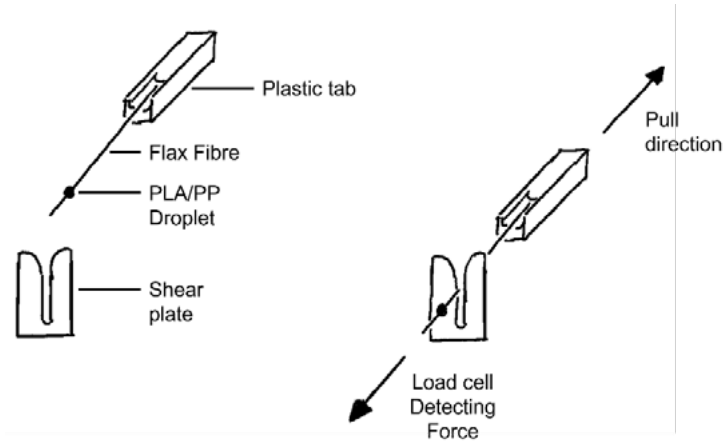

Figure 2. Schematic overview of the microbond experimental setup. The fibre with the droplet is placed into the slit of the shear plate and, through the extension, peeled off from the fibre.

$$w_2 = 0.1915 w_1 + 0.0192 \quad (2)$$

2.2. Double-notch test

The double-notch tensile test specimens were produced through a winding process. Therefore, PLA sheets were produced from the granulate by hot pressing the sheets at 180 °C for 5 min with a systemic pressure of 10 bar on a pressing area of 250 x 250 mm² (Vogt Laborpresse LaboPress P200S, Vogt Maschinenbau GmbH, Germany). The produced sheets were cut into rectangles of 150 x170 mm². The sheets were placed between the wound roving layers (R-Lincore 1000 tex, Groupe Depestele, France) and fixated using adhesive tape. The number of plates and layers was previously calculated to obtain a plate of 4 mm thickness with a fibre volume fraction of 30 %. The number of plates varies depending on the respective mass. The mandrel used for the winding process was an aluminium plate of 2 mm thickness. The layup of the roving was done using the X-Winder 4-axis Model 4X-23 (X-Winder LLC,

USA). The winding angle was set to 90 ° using the X-Winder Designer (X-Winder LLC, USA), but is object to the width of the roving. The width of the roving influences the winding angle slightly because of the spacing between each line to create a fully covered layer. The schematic overview of the process is shown in Figure 3.

After the winding process, the specimens were dried using a drying oven at 60 °C for at least 16 h. The plate was then pressed under temperature using spacers on each side of the plate. The pressing was done in 4 phases: a pre-heating phase, a first pressing phase (185°C for 5 min, 10 bar systemic pressure), a second pressing phase (185°C for 5 min, 30 bar systemic pressure) and cooling under pressure (30 bar systemic pressure). The pre-heating was done without pressure by driving the pressing surfaces as closely together as possible without generating pressure on the specimen. The distance was adjusted periodically during the pre-heating phase.

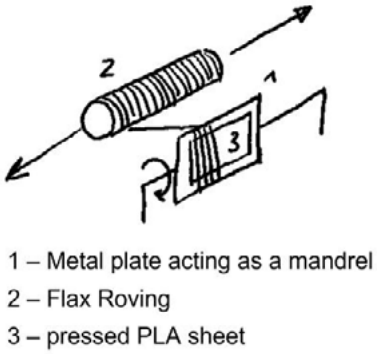

Figure 3. Schematic overview winding setup. The roving (2) is placed on the mandrel (1). Between each full layer of roving, the pressed PLA sheets (3) are placed and fixated on the mandrel.

3. Results and Discussion

The calculated interfacial shear strength of the Agram-PLA and Lincore-PLA samples with differing coupling agent concentrations can be seen in Figure 4. There is no significant difference between the different series. However, it can be observed that the mean and median values of the series with the 2 % coupling agent are higher compared to the reference, and that series showing a smaller deviation in the IFSS compared to the other samples. Nevertheless, due to the low rate of successfully tested samples, the results are not conclusive. Due to the Lincore-PLA showing a similar IFSS compared to the Agram-PLA as well as the comparably small difference in tensile properties in the respective fibres, shown in Table 1, the double-notch specimens were prepared and tested. The difference between the samples induced by the difference in fibre extraction, quality and the processed roving compared to the extracted fibres is acknowledged. However, due to the preparation of the specimen for the double-notch requiring a roving, the differences are acquiesced based on the shown similarity in fibre properties and IFSS.

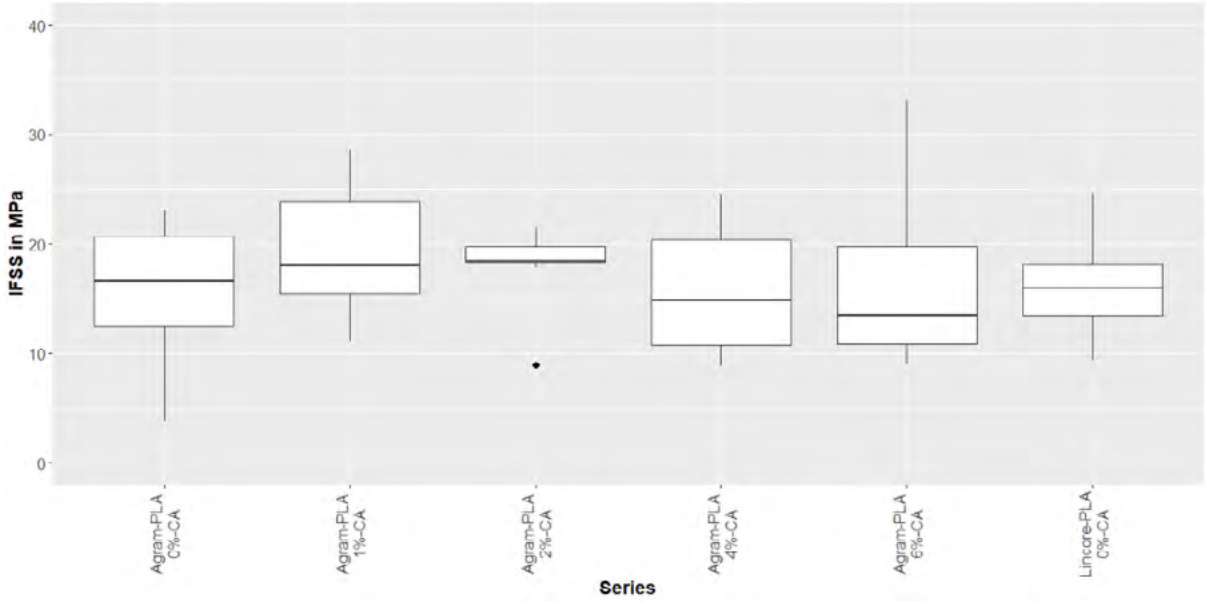

Figure 4. The calculated interfacial shear strength from the Agram flax adhering to the PLA compounded with differing concentrations of coupling agents.

Table 1. Tensile properties of the varieties Agram and Lincore (single fibre bundles).

Specimen Type	Young's Modulus in GPa	Tensile strength in MPa	Elongation in %
Agram	25.8 ± 12.6	448 ± 256	2.25 ± 0.97
Lincore	25.3 ± 11.5	456 ± 257	1.95 ± 0.61

The ILSS for each specimen is shown in Figure 5; on the left side, the Lincore-PLA composites with differing coupling agent concentrations are shown. The difference in ILSS is statistically not significant for the differing coupling agent concentrations. However, the same trend seen for the IFSS can be observed, as the Lincore-PLA with a coupling agent concentration of 2 % has a smaller deviation compared to the Lincore-PLA series, as well as slightly elevated mean and median.

The prior treatment of the roving with ethanol showed an improvement in the ILSS compared to the Lincore-PLA series. However, the ethanol-treated roving paired with the 2 % and 4 % coupling agent concentrations did not show any improvement in the ILSS.

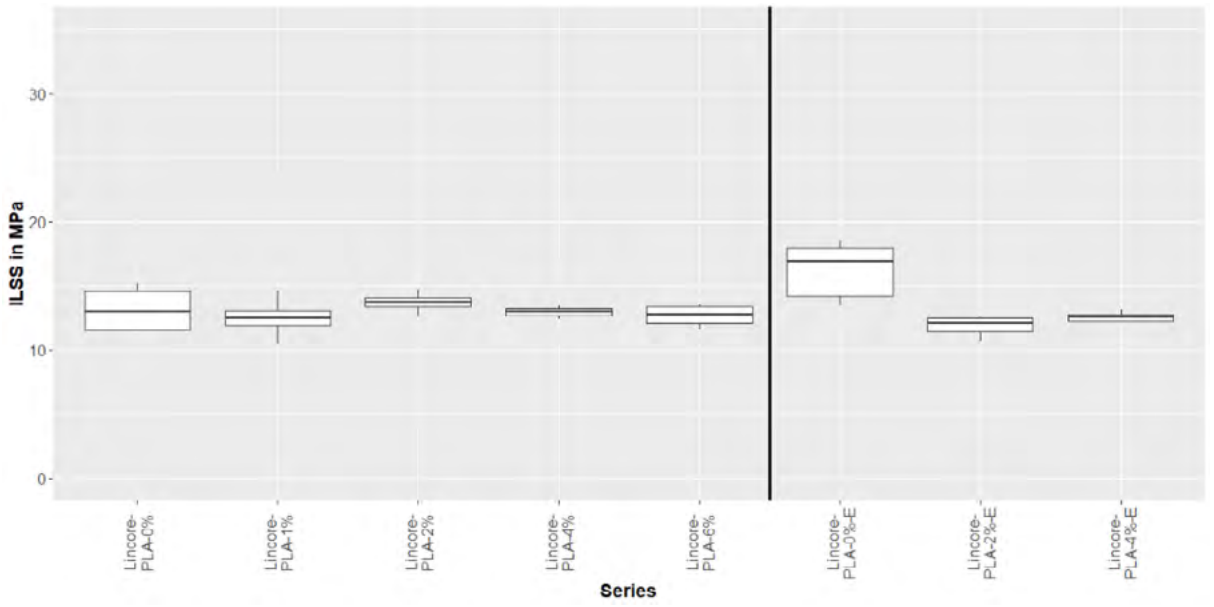

Figure 5. The interlaminar shear strength was calculated from the double-notch test. The differing coupling agent concentrations are shown on the left and the ethanol treatment of the samples is shown on the right.

The purpose of the maleic anhydride grafted PLA is to provide covalent binding sites for the fibre and matrix. Therefore, the polymer used as the coupling agent has to provide polar and non-polar binding sites to bind to the non-polar matrix and the polar natural fibre. However, since there is only a slight improvement through the use of the coupling agent compared to the reference sample without a coupling agent the question arises whether covalent bindings are formed, or if they are formed, whether there are enough covalent binding sites utilized to influence the adhesion.

4. Conclusions

The adhesion properties of the oleaginous flax Agram and PLA have been investigated. Fibre and matrix have undergone functionalizations in order to improve the adhesion between fibre and matrix. Summarized it can be said that:

1. No improvement of the adhesion through the coupling agent could be achieved.
2. Ethanol treatment of the roving showed an improvement in the adhesion between fibre and matrix. However, the additional usage of the coupling agent decreased the ILSS compared to the ethanol treatment and pure PLA.
3. The question arises whether the use of a coupling agent is needed. The adhesion properties are adequate and the potential usage of a coupling agent contradicts the economical benefit of using the byproduct of the linseed industry.

Our hypothesis is that due to the prior compounding of the maleic anhydride grafted PLA with the virgin PLA covalent bonds are formed between the coupling agent and the PLA. Due to the binding between the materials the polymeric chain of the maleic anhydride grafted PLA could potentially be oriented, hence hindering the binding between the fibre and the binding site of the maleic anhydride.

Acknowledgements

The Federal Ministry for Economic Affairs and Energy (Berlin, Germany) funded the German part of the transnational CORNET project "Using agro-waste flax to upgrade recycled plastics" (IGF project no.: 308 EN) based on a resolution of the German Bundestag.

References

[1] S. U. Khan and M. Bar and P. Evon and L. Labonne and P. Ouagne. Development of 100% Linseed Flax Yarns with Improved Mechanical Properties and Durability for Geotextiles Applications. *Fibers*, 10(12), 102, 2022

[2] P. Ouagne and B. Barthold-Malat and P. Evan and L. Labonne and V. Placet. Fibre extraction from oleaginous flax for technical textile applications: influence of pre-processing parameters on fibre extraction yield, size distribution and mechanical properties. *Procedia Engineering*, 200:213-220, 2017.

[3] H. Rennebaum and E. Grimm and K. Warmstorff and W. Diepenbrock. Fibre quality of linseed (Linum usitatissimum L.) and the assessment of genotypes for use of fibres as a by-product. *Industrial Crops and Products*, 16(3):201-215, 2022.

[4] J. Müssig and N. Graupner. Test methods for fibre/matrix adhesion in cellulose fibre-reinforced thermoplastic composite materials: A critical review. *Progress in Adhesion and Adhesives*, 6:69-130, 2021

[5] X. Xia and W. Liu and L. Zhou and Z. Hua and H. Liu. Modification of flax fiber surface and its compatibilization in polylactic acid/flax composites. *Iranian Polymer Journal*, 25:25-35, 2016.

[6] K. Haag and J. Müssig. Scatter in tensile properties of flax fibre bundles: influence of determination and calculation of the cross-sectional area. *Journal of Materials Scienc*e, 51:7907-7917, 2016.

MICROSTRUCTURAL ANALYSIS AND MECHANICAL BEHAVIOUR OF OXIDE/OXIDE CMCS PREPARED BY CONTINUOUS TOW IMPREGNATION

Z. Borius[1, 2, 3], A. Debarre[1], M. Singlard[2], T. Cutard[3] and A. Julian-Jankowiak[1]

[1]ONERA, DMAS, Université Paris-Saclay, F-92322 Châtillon, France
[2]IRT Saint-Exupéry, F-33405 Talence, France
[3]ICA, Université de Toulouse, CNRS, IMT Mines Albi, INSA, ISAE-SUPAERO, UPS, Campus Jarlard, F-81013 Albi, France

Keywords: Ceramic Matrix Composite, boehmite, microstructure, tensile tests, bending tests

Abstract
This paper focuses on the analysis of the mechanical behaviour of alumina/alumina ceramic matrix composites (CMCs) developed by a continuous tow impregnation method, in relation to their microstructures. The influence of the aqueous slurry formulation on the microstructures of the materials and their tensile and bending properties is studied. A combination of a hygroscopic plasticizer (glycerol) and a gelling powder (boehmite) within the slurry is needed to obtain a good interply cohesion in the composite. A large amount of glycerol (20 wt.% relative to the alumina mass) allows a fine-scale porosity distributed throughout the matrix with few large pores which allows to reach a high Young's, around 130 – 150 GPa. Moreover, reducing the plasticizer amount induces the apparition of delaminations and defects appear the microstructure, hence decreasing the stiffness. Then, increasing the boehmite amount (from 5 wt.% to 10 wt.%), the damage tolerance is enhanced, likely due to a higher densification level induced by the presence of the boehmite powder.

1. Introduction

Oxide/oxide ceramic matrix composites (CMCs) are being explored for continuous thermomechanical applications within the temperature range of 800 to 1000 °C, under moderate mechanical loads. They could allow both the required increase in operating temperatures in aeronautical propulsion systems and a weight reduction, due to their low density. In particular, oxide/oxide CMCs stand out for their ability to operate in oxidising atmospheres without the need for fibre coating. One of the main challenges of these recent materials is to automate their production processes and to control their heterogeneous microstructures and properties.

Since fibres provide the mechanical resistance of composites, it is necessary to avoid the propagation of matrix cracks through the fibres in order to induce a certain damage tolerance behaviour. It can be realized through two methods: introducing a weak interface between the fibres and the matrix, or employing a weak matrix, which is characterized by controlled and fine-scale porosity [1]. In particular, the weak matrix concept is interesting for oxide/oxide CMCs, as the fibres are resistant to oxidation [1–3]. A high porosity level matrix (~30-40 vol.%) [4] results in a matrix with low fracture toughness in which crack deflection is favoured, leading to non-simultaneous fibre failures.

The elaboration process of oxide/oxide CMCs usually includes liquid impregnation of the fibres with an aqueous slurry. Conventionally, a 2D fibre fabric is used for impregnation, then comes a shaping and drying step, followed by a high temperature sintering [5–8]. A partial sintering is prefered in order to prevent complete densification of the matrix and hence, maintain a high level of porosity. However,

these processes are non-automated and costly, particularly regarding fibres, which account for up to 70 % of the raw material cost [9].

A significant cost reduction approach is the use of fibre tows instead of fibre fabrics, as it eliminates the need for weaving. Also tows with higher filament counts are now available and less expensive. Coupled with Automated Fibre Placement (AFP), it enables both the reduction of the fibre costs, and the manufacturing of complex parts [10]. Very few studies focused on this method for oxide/oxide CMCs. Indeed, 3M is the only company providing an experimental product that is an impregnated tow (tow-preg) with Nextel^{TM}610 spread tow impregnated with an aqueous alumina slurry.

The present work involves developing alumina/alumina CMCs through a continuous fibre tow impregnation process with an aqueous slurry, and to study the mechanical behaviour of the obtained CMCs, in relation to their microstructures. Thus, the influence of the slurry composition on the microstructures and the mechanical properties of alumina/alumina composites has been evaluated. The spatial distribution of pores was studied through X-ray tomography and scanning electron microscopy (SEM) observations. The mechanical behaviour of CMCs plates was characterized at room temperature with both four-point bending and tensile tests.

2. Materials and methods

2.1. Raw materials and slurries

Nextel^{TM} roving of alumina fibres N610 (20 000 denier, 3M, USA) with polyvinyl alcohol (PVA) coating was chosen as the fibre reinforcement. These fibres are pure α-alumina ones, with a filament diameter of 12 µm, a density of 3.9 g.cm^{-3} and a filament tensile modulus of 370 GPa. The tow has a nominal filament count of 5100, and a linear weight of 0.0022 kg.m^{-1}.

The high-purity α-alumina powder SM8 (Baïkowski, France, d_{50}=0.2 µm, S_{BET}=10 m^2.g^{-1}), was used as the raw oxide powder for the aqueous slurry in this study. Besides, a boehmite powder was also introduced as a gelling agent. The water dispersible boehmite Disperal P2 (Sasol, Germany) with a median granule size of 45 µm, a crystallite size of 4.5 nm and a specific surface area of 260 m^2.g^{-1} was used. During the sintering heat treatment, boehmite will undergo various transformations, and convert into α-alumina around 1200°C [11–13].

Regarding the organic additives, a polyvinyl alcohol-based binder Optapix PAF 35 (Zschimmer & Schwarz, Germany) was chosen. The amount of PVA was not studied in this study and the same ratio of PVA to alumina powder is conserved for all slurries. Glycerol (Sigma-Aldrich, USA), which is a highly hygroscopic plasticizer of the PVA, was added to the slurry in order to give to the impregnated tows sufficient powder hold, flexibility and tack for composite manufacturig.

Different slurries were formulated with various amounts of glycerol and boehmite powder (Table 1). The mass contents of plasticizer and boehmite powder are calculated as mass ratios to the alumina mass. First, a slurry containing only glycerol at 20 wt.% (G20) was formulated. B5G20 and B10G20 slurries contain the same amount of glycerol, and also 5 wt.% and 10 wt.% of boehmite powder, respectively. B10G10 contains 10 wt.% of boehmite and 10 wt.% of glycerol, in order to reduce organic content by replacing it with boehmite powder.

Table 1: Slurry formulations; $w_{plasticizer}$ and $w_{boehmite}$ are the mass ratios (in wt.%) to the alumina mass of plasticizer and boehmite powder, respectively.

Slurry	*G20*	*B5G20*	*B10G20*	*B10G10*
$w_{plasticizer}$	20	20	20	10
$w_{boehmite}$	0	5	10	10

2.2. Manufacturing process

The automated impregnation line (Huguet Ingénierie, France) used for tow impregnation in this work is depicted
Figure 1. Initially, the tow extracted from the as-received roving is unwound and directed into a tubular furnace to remove fibre sizing. Then, the cleaned tow is spread out by multiple rollers before the impregnation bath, which is a metal container filled with the slurry. Afterward, the impregnated tow undergoes drying in a convective heating furnace with forced airflow to evaporate the water content from the impregnated slurry. The tow then passes through a series of rollers (tractor) to regulate speed throughout the line. Finally, at the end of the line, the dried tow is wound onto a mandrel, resulting in a product called "tow-preg". Several parameters can be monitored on the impregnation line, such as tension, roving speed, drying temperature and air flow. The processing speed was set at 0.5 m.min^{-1}, and the tension at 8 N. The drying parameters were optimized depending on the drying behaviour of each tested slurry. A square mandrel with sides of 125 mm was chosen to obtain unidirectional plies.

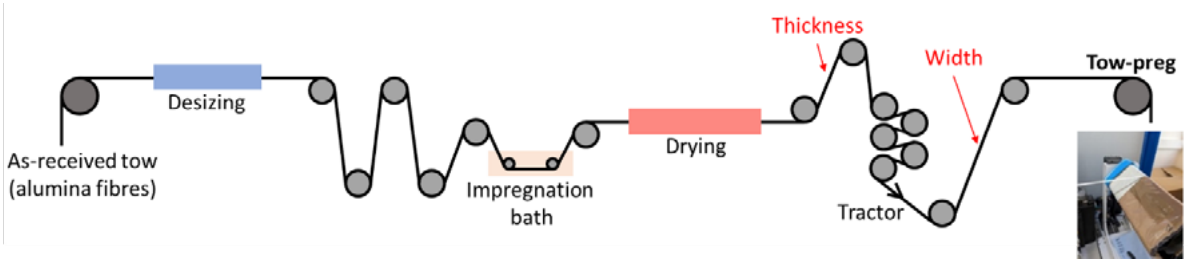

Figure 1: Schematic view of the impregnation line.

The plies are moisture-conditioned at RH=85% to reactivate a certain tack thanks to the presence of hygroscopic plasticizers. Then, they are layered to form a symmetric $[0/90/0/90]_s$ laminated composite plate and placed into an autoclave. Temperature-vacuum-pressure cycles in the autoclave were defined for each organic plasticizer, which are present in large quantities in tow-pregs. The aim is to initiate their degradation slowly while increasing the vacuum level simultaneously, to limit the volume of gas produced during their pyrolysis [13]. An isothermal dwell is then maintained to complete degradation. Finally, a partial sintering at 1200°C is applied so as to keep a high porosity level within the matrix.

2.3. Microstructural characterisations

The porosity of the as-processed composite plates was measured by the Archimede's method. The fibre volume content is then calculated, knowing the fibre length contained in the material, the linear density of the fibres, and the apparent density of the material.

Finally, the microstructure of materials is studied by scanning electron microscopy (SEM, MIRA TESCAN) and X-ray tomography (RX Solutions EasyTom 230) on cut samples of 20 x 20 mm^2. Then, the images from tomography were segmented using Otsu thresholding technique [14] to differentiate material and porosity areas, in order to determine a porosity level.

2.4. Mechanical characterisations

In-plane mechanical properties of the composites were studied through uniaxial monotonic tensile tests at room temperature, using a Z150 Zwick/Roell Materials testing machine. The tests were performed with a controlled displacement rate of 0.5 mm.min^{-1}. Straight-sided specimens, 120 mm x 16 mm x *composite thickness* with a gauge length of 50 mm were used. Pure aluminium annealed thin foils (0.2 mm thick) are used as tabs to ensure load transfer to the specimen, without damage. A two FLIR cameras system with a resolution of 9 MPx recorded the test at 5 Hz and the images are used to perform stereo digital image correlation (DIC, VIC-3D™). Acoustic activity such as matrix cracking or fibre failure is recorded during the test using a Nano03 sensor (Physical Acoustics Corporation).

Flexural strength was evaluated using four-point bending tests conducted using a Z010 Zwick machine (1 kN) running at a cross-head speed of 1 mm.min^{-1} and with outer and inner spans of 64 and 32 mm, respectively. Straight-sided specimens, 75 mm x 13 mm x *composite thickness* were used. A LVDT sensor is in contact with the underside of the specimen, at its centre, to measure the maximum value of the deflection during the test. Only one previously described FLIR camera recorded the test at 5 Hz.

3. Results and discussion

3.1. Influence of slurry composition on the CMCs microstructures

The morphological characteristics of the 8 plies CMCs plates are summed up in Table 2. The CMC prepared with the glycerol-only slurry (G20) exhibits a high porosity level of 34 vol.%. Combining glycerol and boehmite powder allows to decrease the porosity level to 23-26 vol.%. Indeed, thanks to its gelling properties, the boehmite powder increases the tow-pregs tack when moisture-conditioned, and favours inter-ply cohesion, resulting in composites that are denser and with higher fibre volume fraction. Prabhakaran et al. [15] found out that boehmite acts not only as a binder in an aqueous alumina slurry, but also as a sintering aid, that could explain the reduction in porosity.

Table 2: Morphological characteristics of 8 plies CMCs plates.

Material	*G20*	*B5G20*	*B10G20*	*B10G10*
Porosity (vol.%)	34	23	23	26
Fibres (vol.%)	41	52	57	55
Thickness (mm)	2.49 ± 0.12	2.48 ± 0.13	2.00 ± 0.09	2.02 ± 0.10

The ability of boehmite powder to increase interply cohesion is confirmed by the microstructures of the materials, displayed in Figure 2. Indeed, large delaminations between plies without boehmite powder can be observed in G20 microstructure. These defects, measuring a few millimeters, explain the high porosity of G20 plate. For materials containing both glycerol and boehmite, no delamination was observed. However, B5G20 and B10G20 exhibit about the same pores distribution, with a strong inter-ply bonding, while B10G10 presents more porosity and cracks within the matrix.

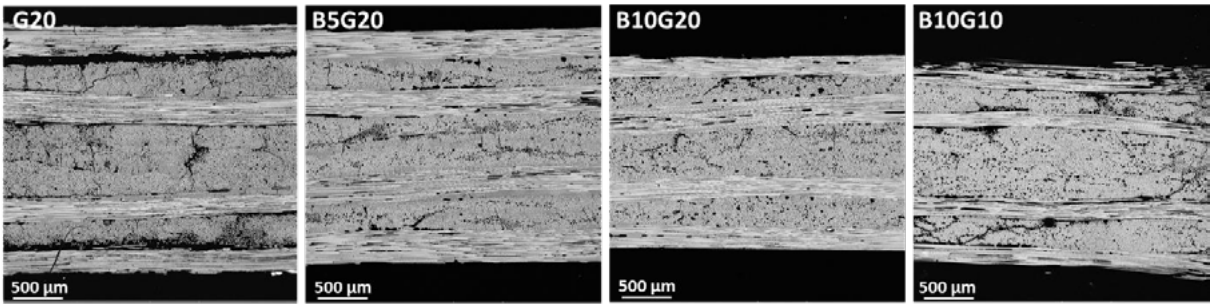

Figure 2: Microstructures of 8 plies CMC plates (SEM cross-sections).

Specimens of 20 x 20 mm^2 were cut for X-ray tomography analysis. Their porosities were measured with Archimede's method, to compare with the entire plates. The analysed area measures 20 mm^3 with a voxel size of 5 µm. The 2D porosity is detected (for pores larger than 25 µm^2) by image segmentation using Otsu thresholding method. Then, the porosity level in the volume of the specimen is calculated. As the pores are cylindrical, an ellipse is fitted around each pore, and the length of its largest dimension is extracted.

C. Ben Ramdane et al. [16] proposed a classification of the pores of 2D Nextel^{TM}610/alumina CMCs depending on their diameters, when considered spherical, into three domains: the macroporosity (diameter superior to 10 µm), the microporosity (diameter between 0.1 and 10 µm) and the nanoporosity

(diameter inferior to 0.1 µm). Nanopores are located within the matrix, micropores corresponds to small pores or microcracks, and macropores are located between plies or inside a ply, and can be prejudicial for the mechanical resistance of the composite. They studied the pore size distribution by mercury intrusion porosimetry, assuming pores are spherical. They concluded that the nanoporosity is the most significant, constituting 13 % of the total 25 % porosity measured by Archimed's method. In our work, the X-ray tomography analysis does not detect the micro or nanoporosity, but they are included in the total porosity measured by Archimede's method as well.

Table 3 sums up the total porosity of the specimens measured with Archimede's method, as well as the macroporosity volume fraction and the number of macropores determined by images segmentation from X-ray tomography. All specimens exhibit a porosity very close to that of the whole plates. Although the specimens B5G20, B10G20, and B10G10 have the same total porosity, they have different pore size distribution. B10G10 exhibits a higher amount of macropores (7.4 vol.%) compared to the two other compositions (4 – 5 vol.%), and a smaller number of detected pores. Hence, B10G10 contains both more large sized pores, and less fine porosity within the matrix. Figure 3 displays a view of the detected macropores and their largest dimension distribution for the composition B5G20. For all samples, the pores are cylindrical and along the fibres. Moreover, some delaminations can be observed for B10G10 composition when visualising the 3D pores distribution. SEM images reveal finer pores within the matrix on the cross section, while X-ray tomography images allow to depict the macropores in 3D.

Table 3: Porosity analysis of 20 x 20 mm^2 specimens. The total porosity is measured by Archimede's method, the macropores are detected by X-ray tomography images segmentation.

Specimens	*B5G20*	*B10G20*	*B10G10*
Total porosity (vol.%)	22	22	22
Macroporosity (vol.%)	4.3	4.9	7.4
Number of macropores (x 10^6)	3.1	3.0	2.4

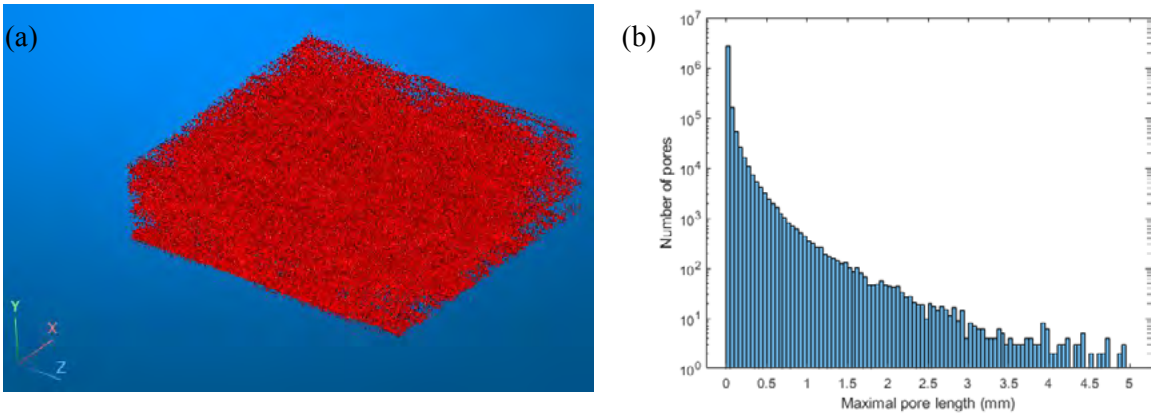

Figure 3: X-ray tomography pores visualisation (a) and distribution (b) for a 20 x 20 x *thickness* mm^3 B5G20 specimen.

3.2. Study of the mechanical behaviour of CMCs in relation to their microstructures

Tensile and four-points bending tests were conducted on at least 3 specimens per composition. Their porosities have been measured, and the results on the cut specimens were similar the those carried out on the whole plates (Table 2). Figure 4 illustrates a representative stress-strain curve for each composition, while Table 4 sums up the following mechanical properties: stiffness, stress and strain at failure (σ_f and ε_f).

With 20 wt.% of glycerol, when raising the boehmite content, the stiffness remains the same while damage tolerance increases, highlighted by higher stress and strain values at failure in both tensile and bending tests. Indeed, B5G20 exhibits a tensile failure stress $\sigma_f = 197 \pm 9$ MPa and a tensile fracture strain $\varepsilon_f = 0.17 \pm 0.01$ % while the values for B10G20 increase up to $\sigma_f = 266 \pm 36$ MPa and $\varepsilon_f = 0.28 \pm 0.06$ %. The Young's modulus E is not affected by the difference in fibre volume fraction between B5G20, that has 52 vol.% fibres and B10G20, that has a higher fibre volume fraction of 57 vol.%. Their total porosities as well as their pores distributions are equivalent.
On the contrary, when reducing the glycerol content, the stiffness drops: from 115 ± 7 GPa to 94 ± 13 GPa for tensile tests, and from 149 ± 8 GPa to 134 ± 9 GPa for bending tests. The failure stress and strain in tensile tests are reduced by 22 % and 8 % respectively, while they drop more drastically in bending tests: they are reduced by 57 % and 39 % respectively.

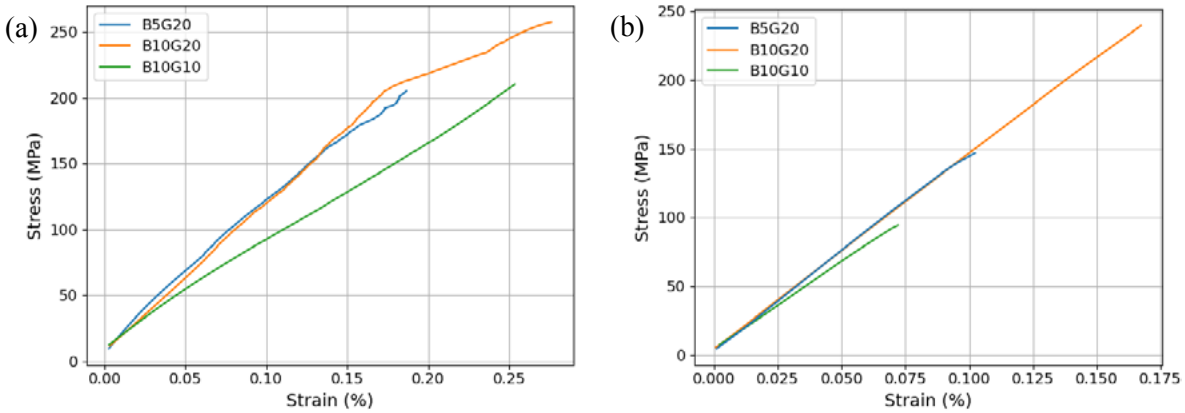

Figure 4: Mechanical behaviour of CMCs: (a) in tensile testing and (b) in four-points bending testing.

Table 4: Mechanical properties of the tested CMCs.

Material	*B5G20*	*B10G20*	*B10G10*
Tensile E (GPa)	126 ± 16	115 ± 7	94 ± 13
Tensile σ_f (MPa)	197 ± 9	266 ± 36	207 ± 27
Tensile ε_f (%)	0.171 ± 0.014	0.281 ± 0.055	0.259 ± 0.033
Bending E (GPa)	150 ± 5	149 ± 8	134 ± 9
Bending σ_b (MPa)	147 ± 36	238 ± 29	103 ± 25
Bending ε_b (%)	0.098 ± 0.020	0.161 ± 0.019	0.099 ± 0.034

For a 12 plies composite 2D Nextel™610/alumina under tensile loading, with 49 % fibres and 24 % porosity, C. Ben Ramdane et al. [16] measured a failure stress of 260 ± 37 MPa, a failure strain of 0.30 ± 0.09 % and an elastic modulus of 134 ± 19 GPa. The values obtained in this work for B10G20 composition are similar. Nevertheless, the two materials are different: ours consists of the layering of 8 unidirectionnal plies while the 2D Nextel™610/alumina composite is made of 12 2D plies. The fibre fraction volume for the 2D fabric composite is lower (49 vol.% versus 57 vol.%), and because of the weaving we can assume that the proportion of the fibres in the loading direction is even smaller. Under bending loading, A. Debarre et al. [7] observed for the 2D Nextel™610/alumina a quasi-linear behaviour as well. They measured higher failure resistance: 337 ± 57 MPa for the stress, and 0.29 ± 0.06 % for the strain, that could be due to the 2D structure of each ply, that creates a stronger bond between the fibres at 0° and 90°. In our case, the 0° and 90° fibres are only bonded by the matrix, which may reduce the interply shear strength.

The damage tolerance of the CMCs is evident when looking at the tensile stress-strain curve, as a change in the slope of the behaviour curve is observed (Figure 4 (a)). For bending tests, the behaviour appears

more linear (Figure 4 (b)). However, damage before the total failure of the material can be highlighted by focusing on acoustic events register throughout the test. Figure 5 displays the cumulative energy of acoustic events registered during bending testing for B5G20 and B10G10 CMCs only (as B10G20 presents the same behaviour than B5G20). The cumulative energy starts to increase at a stress value of 20 MPa that represents the first matrix cracks, which do not affect the mechanical strength of the materials. After this damage threshold, the energy gradually increases as both stress and strain rise. For B5G20, a jump in energy is observed at $\sigma = 140$ MPa, that corresponds to a significant crack of the matrix or several fibres breaks, which implies a load transfer to the fibres. Both the strain and stress continue to increase after this event, thus revealing the damage tolerance behaviour. This phenomenon is also revealed by looking at the images of the specimen's cross-sections taken from the FLIR camera during the test. Some cracks initiation and propagation in the matrix can be observed for B5G20 and B10G20, while the load continues to increase, until inter-ply delamination or multiple fibre failure occur, leading to a drop in stress and thus the failure of the CMC. Similar observations were made by C. Ben Ramdane et al. [16] when studying the acoustic emission of an 2D Nextel^{TM}610/alumina CMC through tensile/compression testing. They determined a higher damage threshold of 48 MPa. If the loading is below this value, the acoustic activity is negligible. The quasi-linear segment in their strain-stress curves corresponds to a small and regular activity, afterwards the activity increases due to fibre failures, up to the final CMC failure. In the case of B10G10, the jump in the cumulative energy occurs at the same time as the failure of the material, showing a brittle behaviour. This, as well as the drop in bending properties for B10G10, could be explained by the fact that in bending tests, the loaded section is smaller than in tensile tests, and the presence of delaminations (seen in B10G10 microstructure) in this section would result in early and more brittle material failure.

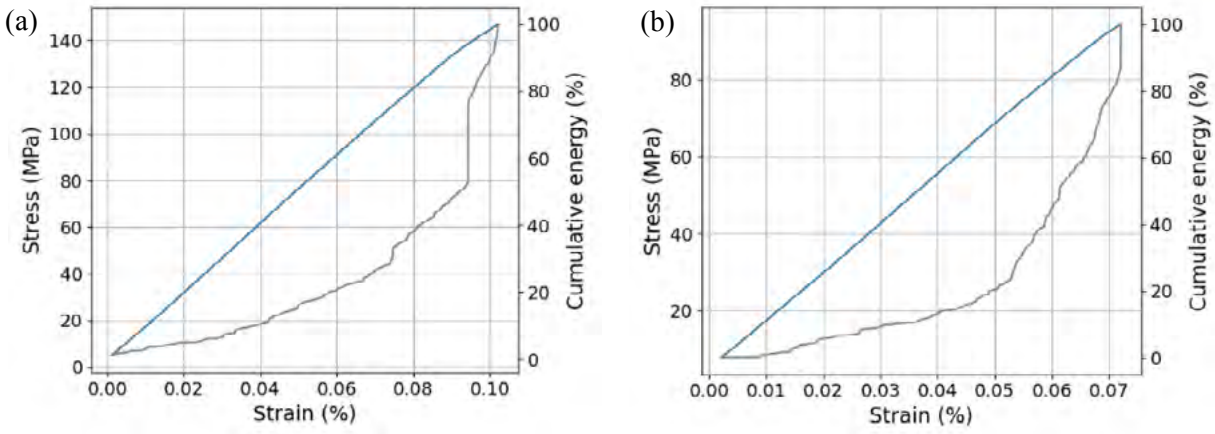

Figure 5: Acoustic activity registered during four-points bending tests of: (a) B5G20 and (b) B10G10 CMCs. (Blue: stress and grey: cumulative energy).

3. Conclusions

The manufacturing of oxide/oxide CMCs by continuous tow impregnation offers a cost reduction and a process automation that could limit heterogeneities in theses materials' microstructures. However, it requires a slurry that provides impregnated tows with sufficient flexibility and tackiness to produce composites. In this work, a combination of a hygroscopic plasticizer, glycerol and a gelling powder of boehmite, in an aqueous alumina slurry was found to be suitable for achieving interply cohesion.

A large amount of glycerol (20 wt.% relative to the alumina mass) results in a CMC with a fine-scale porosity distributed throughout the matrix with few large pores. This type of CMC microstructure ensures a damage tolerance behaviour, and a high Young's modulus, around 130 – 150 GPa. Moreover, reducing the plasticizer amount induces the apparition of delaminations and defects in the microstructure, hence decreasing the CMC stiffness. Also, it reduces damage tolerance and results in a more fragile fracture. Finally, when the boehmite amount is increased from 5 wt.% to 10 wt.%, the CMC

damage tolerance is enhanced, likely due to a higher densification level induced by the introduction of the boehmite powder.

Acknowledgments
The authors would like to thank Katia Dennis for her assistance with samples preparation, Anne Mavel, Céline Le Sinq and Sarah Boukobza for conducting the mechanical tests and Frédéric Laurin for his help with X-ray tomography images analysis.

References

[1] Zok FW, Levi CG. Mechanical Properties of Porous-Matrix Ceramic Composites. Adv Eng Mater 2001:9. https://doi.org/10.1002/1527-2648(200101)3:1/2<15::AID-ADEM15>3.0.CO;2-A.
[2] Mechnich P, Welter M. Porous Oxide Ceramic Matrix Composites – Properties, Manufacturing, and Applications. Encycl. Mater. Compos., Elsevier; 2021, p. 48–54. https://doi.org/10.1016/B978-0-12-819724-0.00073-2.
[3] Simon RA. Progress in Processing and Performance of Porous-Matrix Oxide/Oxide Composites. Int J Appl Ceram Technol 2005;2:9. https://doi.org/10.1111/j.1744-7402.2005.02016.x.
[4] Mattoni MA, Yang JY, Levi CG, Zok FW. Effects of Matrix Porosity on the Mechanical Properties of a Porous-Matrix, All-Oxide Ceramic Composite. J Am Ceram Soc 2001;84:9. https://doi.org/10.1111/j.1151-2916.2001.tb01059.x.
[5] Guglielmi PO, Nunes GF, Hablitzel M, Hotza D, Janssen R. Production of Oxide Ceramic Matrix Composites by a Prepreg Technique. Mater Sci Forum 2012;727–728:556–61. https://doi.org/10.4028/www.scientific.net/MSF.727-728.556.
[6] Ben Ramdane C. Etude et modélisation du comportement mécanique de CMC oxyde/oxyde. Université de Bordeaux, 2014.
[7] Debarre A. Comportement mécanique à haute température d'un composite alumine/alumine. Université PSL, 2021.
[8] Puchas G, Möckel S, Krenkel W. Novel prepreg manufacturing process for oxide fiber composites. J Eur Ceram Soc 2020;40:5930–41. https://doi.org/10.1016/j.jeurceramsoc.2020.06.064.
[9] Pritzkow WEC, Almeida RSM, Mateus LB, Tushtev K, Rezwan K. All-oxide ceramic matrix composites (OCMC) based on low cost 3M Nextel™ 610 fabrics. J Eur Ceram Soc 2021;41:3177–87. https://doi.org/10.1016/j.jeurceramsoc.2020.05.070.
[10] Arrabiyeh PA, May D, Eckrich M, Dlugaj AM. An overview on current manufacturing technologies: Processing continuous rovings impregnated with thermoset resin. Polym Compos 2021;42:5630–55. https://doi.org/10.1002/pc.26274.
[11] Ananthakumar S, Menon ARR, Prabhakaran K, Warrier KGK. Rheology and packing characteristics of alumina extrusion using boehmite gel as a binder. Ceram Int 2001;27:231–7. https://doi.org/10.1016/S0272-8842(00)00070-5.
[12] Zargar HR, Fard FG, Rezaie HR. The influence of nano boehmite on spinel formation in the alumina-magnesia system at low temperatures. Journal of Ceramic Processing Research 2008;9:46–51.
[13] Borius Z, Débarre A, Singlard M, Cutard T, Julian-Jankowiak A. Impact of additives on the quality of oxide/oxide tow-pregs obtained by continuous fibre impregnation. Compos Part Appl Sci Manuf 2024;184:108238. https://doi.org/10.1016/j.compositesa.2024.108238.
[14] Otsu N. A Threshold Selection Method from Gray-Level Histograms. IEEE Trans Syst Man Cybern 1979;9:62–6. https://doi.org/10.1109/TSMC.1979.4310076.
[15] Prabhakaran K, Ananthakumar S, Pavithran C. Gel Casting of Alumina using Boehmite as a Binder. J Eur Ceram Soc 1999;19:2875–81. https://doi.org/10.1016/S0955-2219(99)00075-8.
[16] Ben Ramdane C, Julian-Jankowiak A, Valle R, Renollet Y, Parlier M, Martin E, et al. Microstructure and mechanical behaviour of a Nextel™610/alumina weak matrix composite subjected to tensile and compressive loadings. J Eur Ceram Soc 2017;37:2919–32. https://doi.org/10.1016/j.jeurceramsoc.2017.02.042.

CELLULOSE NANOCRYSTALS AS REINFORCEMENTS IN THERMOPLASTIC COMPOSITES: PROCESSING ROUTES AS KEY

Bugaut M. [1,*], Le Moigne N.[1], Heuzey M.-C.[2], Carreau P.J. [2], Taguet A.[1]

[1]Polymers Composites and Hybrids (PCH), IMT Mines Alès, Alès, France
mathieu.bugaut@mines-ales.fr; nicolas.le-moigne@mines-ales.fr; aurelie.taguet@mines-ales.fr
[2]Chemical Engineering, CREPEC, Polytechnique Montréal, Montréal, CANADA
marie-claude.heuzey@polymtl.ca; pierre.carreau@polymtl.ca

Keywords: Cellulose nanocrystals, Thermoplastic polymer, Melt processing, Rheology, Microstructure

Abstract

A comparison of the different processing routes to produce thermoplastic composites reinforced with cellulose nanocrystals (CNC) has been studied, focusing on key steps to improve the mechanical properties of the final composite. The rheological behaviour of the composites is studied in relation to CNC dispersion. The elastic properties of the composites are modelled with the Halpin-Tsai micromechanical model. The solvent-based route gives the best mechanical results, the prior ultrasonication step appearing essential to ensure good CNC dispersion in the solid state. On the other hand, melt and combined solvent-melt processing routes lead either to thermal degradation of the matrix, or to possible re-agglomeration of the CNC during melt processing. Future work is suggested to investigate other processes that could be up-scalable.

1. Introduction

Cellulose nanomaterials (CNM), such as cellulose nanocrystals (CNC) and cellulose nanofibrils (CNF), are expected to play a major role in the current environmental and societal transition towards a greater use of bioresources for material applications. Due to their low density, high specific surface area and high Young's modulus, these nanomaterials have a great potential as sustainable, high-performance fillers for the development of materials with tunable rheological, thermo-mechanical, optical and barrier properties [1]. They are currently used mainly in paper manufacturing, packaging, membranes and bioengineering.

As with other nanoparticles, the dispersion of CNM in thermoplastic polymers remains a huge challenge for the development of high-performance polymer nanocomposites. In the literature, several processing routes have been studied to improve their dispersion and the mechanical properties of the nanocomposites, using solvent-based, melt processes and innovative processes such as chilled extrusion or wet compounding with various thermoplastic polymers as well as physico-chemical and processing aids [2], [3]. As shown in Figure 1, the choice of the processing route appears to have a significant impact on mechanical improvements (Young's modulus and yield strength), and therefore potentially on the CNM dispersion.

In this work, thermoplastic hydrosoluble polyvinyl alcohol (PVA) and CNC are used to study the effect of operating conditions for different processing routes, i.e. solvent, melt and hybrid solvent-melt. Dispersing CNC in thermoplastic polymers by melt-processing is indeed an interesting approach that could potentially facilitate the preparation steps and avoid the use of harmful solvents.

The objective is to identify the key processing steps for obtaining a good CNC dispersion that best improves the mechanical properties of the final composite. The impact of the processing conditions on

CNC dispersion in PVA is discussed, in particular by means of rheological and mechanical of PVA/CNC composites.

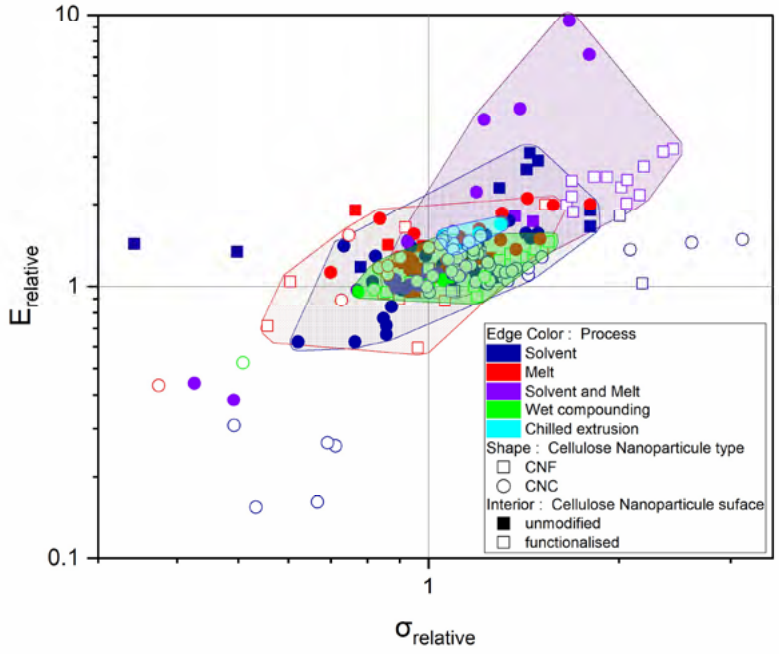

Figure 1. Ashby diagram for the relative Young's modulus, $E_{relative}$, versus relative yield strength, $\sigma_{relative}$, for nanocomposites based on modified and raw CNC and CNF: effect of processing methods. reproduced from [3].

2. Materials and methods

2.1. Materials

Cellulose nanocrystals (CNC) were obtained by acid hydrolysis of wood pulp and provided in spray-dried powder by CelluForce (Quebec, Canada). CNC lateral dimensions: 2−5 nm; CNC length: 50−110 nm; CNC surface charge density: 0.023 mmol/g; Crystalline fraction: 0.88. Polyvinyl alcohol (PVA), grade Mowiflex C30, was purchased from Kuraray (melting point =175°C; Density 1.28 g.cm^{-3}). Distilled osmosis water was produced in the laboratory.

2.2. Processing of PVA/CNC composites

Solvent-cast (SC) composite specimens were prepared starting from a CNC water suspension by first mechanical stirring (65°C, 750 rpm, 2h) then probe ultrasonication, based on the protocol proposed by Girard et al. [4]. Then PVA was dissolved in the CNC water suspension by mechanical stirring (65°C, 500 rpm, 1h), and the resulting mixture was cast into moulds under laboratory hood for 72h, then into a vacuum oven for 12h (80°C, 100mbar) to finalize water evaporation. The obtained films were then cut into small pieces prior to injection moulding using a Zamak Mercator press.
Solvent-cast without sonication (SC w/o S) composite specimens were also prepared following the same processing steps, but without the ultrasonication step.
Melt Mixing (MM) composite specimens were prepared using a DSM 15cc micro compounder with a T_{barrel} of 205°C and 5 min mixing time (2 min introduction of PVA pellets and CNC powder at 60rpm / 2min mixing at 120rpm / ~ 1min extrusion at 60rpm). The resulting compounds were then injected following the same parameters as the SC composites.

Finally, combining Solvent-Cast and Melt Mixing processes, (SC-MM) composite specimens were prepared by successively following the SC and MM protocols prior to injection moulding.

2.3. Characterization of PVA/CNC composites

Rheological properties of the composites were measured with a controlled stress Anton Paar MCR301 rheometer equipped with a parallel plate geometry with a diameter of 25 mm and a gap of 1 mm. The rheological tests were carried out under nitrogen, in molten state at 200°C. Prior to rheological tests, disk shape samples were conditioned overnight in vacuum oven at 80°C, 100 mbar. Time sweep measurements showed that the viscoelastic properties of PVA/CNC composites were stable at 200°C for 10 min. Frequency sweep tests were conducted from 300 to 0.1 rad.s^{-1}. All rheological data were reproductible to ±10%.

Tensile properties of the composites were measured with a Zwick TH 010 testing machine equipped with an Zwick "clip-on" extensometer for the determination of the Young's modulus (ISO 527 standard). The crosshead speed was fixed at 1 mm/min for the determination of the Young's modulus and 50 mm/min for the determination of the ultimate tensile properties. Prior to tensile tests, specimens were conditioned for 24 hours at 24°C, 50%HR. A minimum of five samples per formulation were tested and standard deviations are given for each mechanical property.

3. Results and Discussion

3.1. Rheological behaviour of the PVA/CNC composites

Based on frequency sweep tests, relative storage modulus G' at 1 rad.s^{-1} were plotted as a function of CNC volume fraction for all formulations (Figure 2).

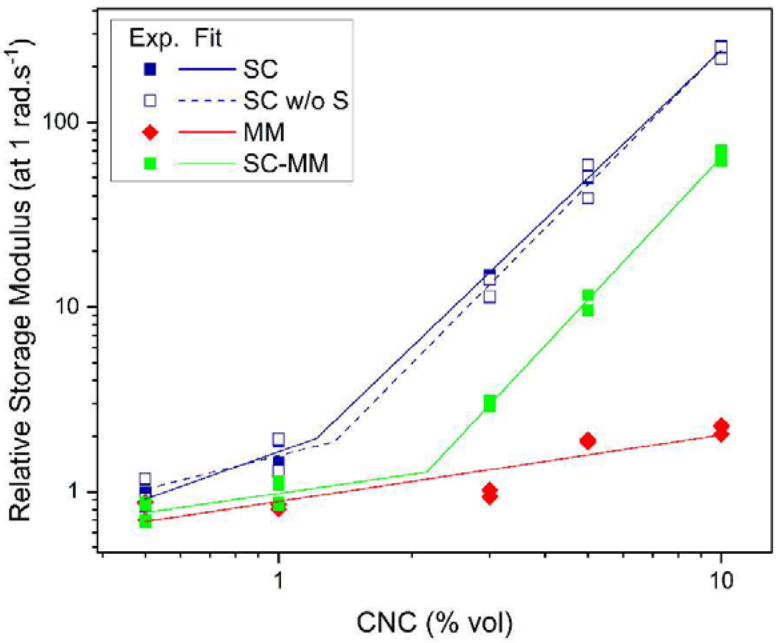

Figure 2. Influence of the processing routes and CNC volume fraction on the relative storage modulus G' of PVA/CNC composites at 1 rad.s^{-1} and 200°C.

From these data, two regimes can be determined by linear extrapolation, a dilute regime at lower concentration; a critical concentration, known as the percolation threshold C*; and a semi-dilute or concentrated regime at higher concentration. From this concentration, rheological percolation models

[5], [6] can be used to derive an average aspect ratio of the dispersed objects (Table 1) for the different processing routes.

Table 1. Influence of the processing routes on the percolation threshold C* and calculated aspect ratio of the dispersed CNC.

Process	Percolation threshold C*	Calculated aspect ratio (Ouali et al, 1991) [5]	Calculated aspect ratio (Favier et al, 1997) [6]
SC	1.22	37.7	57.5
SC w/o S	1.34	33.9	51.9
MM	≥ 10	≤ 1.5	≤ 7.0
SC-MM	2.16	20.3	32.4

Composites prepared by the solvent-cast route (SC and SC w/o S) show the highest calculated aspect ratios ranging from 35 to 58 depending on the model used and being consistent with the aspect ratio of individual CNC reported in the literature (10 to 55). On the other hand, composites prepared by the melt-mixing route (MM) show low aspect ratio not exceeding 7. The combined processing route (SC-MM) gives interesting results with aspect ratio ranging from 20 to 32. This suggests that the sole extrusion step does not allow the CNC to disperse properly and may cause re-agglomeration and/or thermo-degradation of the matrix that limit CNC dispersion. Besides, the ultrasonication step have only a minimal effect on the rheological behaviour of the composites and the calculated aspect ratios of CNC, although the appearance of the samples was noticeably different, showing opacification and bubble formation.

3.2. Tensile mechanical properties of PVA/CNC composites

By studying the tensile mechanical behaviour of the composites, in particular the change in Young's modulus (Figure 3), general trends can be drawn on the dispersion state of CNC, supported by previous rheological analyses. The Halpin-Tsai anisotropic model (Equation 1) is a micromechanical model classically used to predict the Young's modulus E_c of composite materials reinforced with various fillers:

$$E_C = E_m\left(\frac{3}{8}\left(\frac{1+\xi\eta_L V_f}{1-\eta_L V_f}\right)+\frac{5}{8}\left(\frac{1+2\eta_T V_f}{1-\eta_T V_f}\right)\right) \quad (1)$$

$$with:\ \xi = 2\,l/d\ ;\ \eta_L = \frac{E_f/E_m-1}{E_f/E_m+\xi}\ ;\ \eta_T = \frac{E_f/E_m-1}{E_f/E_m+2}$$

With V_f the volume fraction of the CNC, E_m = 1.1GPa the measured modulus of the matrix, E_f = 145 GPa the theoretical modulus of the CNC [3], and L/d = 1.5 to 37.7 the aspect ratio calculated with Ouali model in table 1. From this model, it is possible to make assumptions about the quality of CNC dispersion in the composites, i.e. a response close to the model is characteristic of a composite with micrometric dispersion, while a response greater than the model could indicate nanometric dispersion of CNC.

As observed for the rheological analyses, the processing route has little impact on the pure matrix. In contrast with rheological results, the ultrasonication step has a strong effect on composites Young's modulus. With ultrasonication (SC), Young's modulus are above those predicted by the Halpin-Tsai model for lower concentration, with improvements ranging from 1.47 to 2.47 times the young's modulus of PVA processed in the same conditions for CNC volume fractions ranging from 0.5 to 5 %vol. Without ultrasonication (SC w/o S), the response is well below the model, with Young's modulus of 0.65 to 1.85 times the one of PVA.

The melt-mixing route (MM) does not provide sufficient energy to break the CNC aggregates to achieve nanometric dispersion, giving a response close to the Halpin-Tsai model. With changes in Young's modulus ranging from 0.62 to 1.77 times the matrix modulus.
Finally, the combined solvent-cast and melt-mixing route (SC-MM) shows that the extrusion step alters the final tensile properties compared with the solvent route, either due to thermal degradation of the CNC and/or the matrix and/or re-agglomeration of the CNC. Changes in Young's modulus ranging from 0.80 to 2.01 times the matrix modulus.
These mechanical results corroborate the trends observed with rheological analyses regarding the effect of the processing route on CNC dispersion and the resulting aspect ratios. Concluding, the solvent route gives the best dispersion and tensile modulus, the melt route the worst, and the combined solvent and melt-mixing route, intermediate dispersion quality and tensile modulus of the composites.

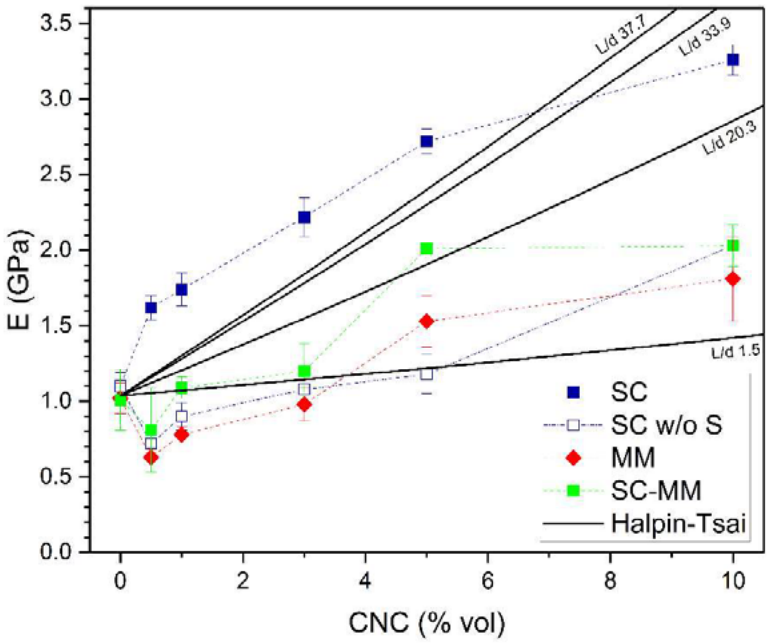

Figure 3. Influence of the processing routes on the evolution of Young's modulus of PVA/CNC composites with increasing CNC volume fractions.

4. Conclusion

Several process routes were studied, and a good correlation between the results of rheological tests (storage modulus G') and tensile tests (Young's modulus E) was observed.
The solvent route with the proper sonication step is the only way studied in this work to obtain what seems to be a nanocomposite. Whereas the other processes: solvent casting without sonication, melt mixing and solvent casting followed by melt mixed give results indicating instead that we have micro composites for different reasons: either the lack of sonication step; or the extrusion step which is insufficient to break CNC aggregates, and probably leads to a CNC re-agglomeration and/or a thermal degradation of PVA and/or CNC. Other characterisations are needed to understand the impact of extrusion step on CNC dispersion and mechanical properties.
Finaly, other possible key steps, like the solvent evaporation protocol, and processes, like master batch approach prepared by solvent route or wet compounding, need to be investigated to have a fuller view.

[1] T. Li *et al.*, "Developing fibrillated cellulose as a sustainable technological material," *Nature*, vol. 590, no. 7844, pp. 47–56, Feb. 2021, doi: 10.1038/s41586-020-03167-7.

[2] X. Ma, Y. Wang, Y. Shen, J. Huang, and A. Dufresne, "Current Status of Nanocellulose-Based Nanocomposites," in *Nanocellulose*, Wiley, 2019, pp. 155–200. doi: 10.1002/9783527807437.ch6.

[3] G. Banvillet, M. Bugaut, E. Doineau, A. Taguet, N. Le Moigne, and O. J. Rojas, "Advances in the Production of Cellulose Nanomaterials and Their Use in Engineering (Bio)Plastics," 2023, pp. 333–393. doi: 10.1007/978-981-99-2473-8_12.

[4] M. Girard, F. Bertrand, J. R. Tavares, and M. C. Heuzey, "Rheological insights on the evolution of sonicated cellulose nanocrystal dispersions," *Ultrason Sonochem*, vol. 78, Oct. 2021, doi: 10.1016/j.ultsonch.2021.105747.

[5] N. , C. J. Y. , P. J. Ouali, "Elastic, viscoelastic and plastic behavior of multiphase polymer blends," *Plastics, Rubber and Composites Processing and Applications*, vol. 16, no. 1, pp. 55–60, 1991.

[6] V. Favier', R. Dendievel', G. Canova', J. Y. Cavaille', and P. Gilormini', "Simulation and modeling of three-dimensional percolating structures: case of a latex matrix reinforced by a network of cellulose fibers," Ada Metallurgica Inc, 1997.

Title:

Sustainable method of chemical recycling of epoxy resin using microwaves

Authors:

Fabrizio Cafaro[1], Gloria Anna Carallo[1], Francesca Ferrari[1], Antonio Greco[1], Alfonso Maffezzoli[1]

[1] Department of Engineering for Innovation – University of Salento – Lecce (Italy)
Web page: https://www.dii.unisalento.it/web/ingegneria

E-mail: fabrizio.cafaro@unisalento.it, gloriaanna.carallo@unisalento.it, francesca.ferrari@unisalento.it, antonio.greco@unisalento.it, alfonso.maffezzoli@unisalento.it

Keywords:

Microwave, chemical recycling, epoxy resin, composites, green chemistry, zero waste

Abstract:

This work proposes a low cost, and efficient method for the recycling of the Glass Fiber and Carbon Fiber reinforced epoxy matrix composites, based on a microwave-assisted chemical oxidation method. Low processing time, low energy consumption and the use of green solvents, significantly reduces the environmental impact of the disposal of composite materials.
Several approaches were explored in order to optimize the recycling of epoxy waste, finding the best conditions in a single-step process using microwave heating, a mixture of hydrogen peroxide (H_2O_2) as a green oxidiser and tartaric acid (TA) as a natural organic acid. The optimized process allowed the decomposition of the epoxy matrix leading to a mix of compounds that can be again used in composite matrix formulations. Moreover, the use of microwave irradiation determined a reduction of both recycling time and energy consumption in comparison to oven heating.
The chemical residue (CR) obtained after the recycling process was first characterized by FTIR and DSC analysis. Then, the CR was mixed with virgin resin (VIR) for the production of new thermosetting composite matrices whose thermal and mechanical properties were measured. The role of the CR in this reaction was also evaluated.

Introduction and related work:

One of the most prominent applications of epoxy resin, is their use as matrix material in fiber-reinforced composites, widely used as composite matrices for wind turbine blades and in aerospace and ship building applications. Epoxy resin finds many other applications, such as

paints, adhesives and many others, because of its light weight, high strength, good corrosion resistance and excellent adhesion [1-5].

Market reports have stated that the global glass and carbon fiber reinforced epoxy polymer (GFRP - CFRP) composites market is likely to grow at a steady pace as the material finds an increasing number of applications [6-10]. This growth in the composites market creates a sustainability problem, as there is no efficient strategy for recycling or reusing thermosetting matrix composite material waste at the end of its life [11].

Thermosetting resins, epoxy in particular, are the preferred choice for continuous fiber reinforced composites in aircraft and car structures, for their good properties as composite material matrices and the low initial viscosity, which involves an easier processing before the cure [12]. The epoxy-based materials are different from disposable plastics, in that they have a long lifetime so that their recycling has not aroused enough attention in the last decades. The problem is becoming imperative with the massive decommissioning of the composite materials in recent years [3, 13-18], driven by the end-of-life of many wind blades. Recovering discarded composite materials, as well as being an environmental imperative, is also becoming increasingly important from an economic point of view [19, 20]. Furthermore, European legislation and that of other countries, try to push in this direction [10-12, 21].

Recycling technologies developed for thermoset composite materials comprise fundamentally three categories of recycling processes: mechanical, thermal and chemical [9]. Mechanical recycling is a low cost technology process based on grinding which dramatically reduces the aspect ratio of the fibers and so their mechanical performances [22]. Thermal recycling processes are aimed to recover the fibers: pyrolysis or fluidized bed reactors removed the resin releasing highly toxic gases and are high energy consumption processes [23]. For the reasons mentioned above, in recent years attention has been paid to chemical recycling processes. Some conventional chemical recycling processes, used in the past, involve the use of sulfuric and nitric acids, especially for the recovery of fibres. Some attempts have been made using supercritical fluids [12]. But this kind of methods involve harsh chemicals and/or the application of high temperatures and pressures, and consequently they are not in line with the principles of green chemistry [22, 24]. Apart from this, mechanical and chemical process also involve a significant degradation of the property of the fibers, due to physical (size reduction) and chemical (fiber oxidation) reasons. In contrast, some new approaches [11, 20, 22, 25-28] can preserve the mechanical and physical properties of the fibers.

In several works related to chemical recycling, microwaves were used to reach different objectives. Tavares de Moraes et al. in [6] used the microwaves to carry out pyrolysis and reduce the volume of waste to be disposed by 73%. Rani et al. in [25] used microwaves to super-heat the fibers which promotes fiber/matrix detachment. Zabihi et al. in [22, 24-26] and Yuwei Long et al. in [3] used microwaves to recover glass and carbon fibers from composites with good results in terms of the strength of the recovered fibers. Some attempts to recover resin from composites have been made by Mohan Das et al. in [20], Xu Zhao et al. in [27] and Kaiyou Huang et al. in [28], but most of the works focus on the recovery of the fibers and do not give indications on the possible recovery of the matrix.

This work is focused on the possibility of recovering and reusing epoxy resin from end-of-life composite materials, following the principles of green chemistry [24]. A one-step

chemical/physical recycling method without using chemical products dangerous or harmful to the environment and humans, is proposed. At the same time, the aim of this work is to drastically reduce the energy consumption by replacing conventional oven heating with microwaves. Furthermore, tartaric acid, yeast and hydrogen peroxide were used as green reagents. The characterization of the recycled materials was then carried out and a way of reusing them was proposed.

Materials and Methods:

Materials

Hydrogen peroxide (H_2O_2, 35 wt%, 130 V) and pure L-Tartaric Acid (TA, food additive E334) were purchased from Sigma Aldrich. Yeast (food grade) was produced by Cameo s.p.a. (Brescia, Italy). An epoxy resin based on Diglycidyl Ether of Bisphenol-A, Polar Bear provided by R*Concept (Barcelona, Spain), and characterized by a biocarbon content of 28% deriving from pine oils (expressed as a fraction of the total organic carbon content), was used. It is liquid at room temperature, hence making easy mechanical mixing process with the curing agent [29]. This resin was chosen because it is not recyclable, although a certain amount is of natural origin. Isophorone diamine (IPDA), supplied by Sigma Aldrich, was used as curing agent for the epoxy resin.

Methods

Preparation of samples

After mixing virgin epoxy resin (VIR) with 22 phr of IPDA, it was poured in a mold (35 x 10 x 2 mm) and cured in vented oven at 80°C for 2 hours and then post-cured at 120°C for 1 hour. The recycled resin samples containing the chemical residue (CR) coming from the chemical recycling were prepared by manually mixing CR and VIR in various ratios, as reported in Table 1. Then, 22 phr of IPDA, calculated on the amount of VIR used, were added to the mixture [29]. The cure and post-cure cycles were the same used for the virgin resin bars.

Tab 1: Composition of samples containing the chemical residue

SAMPLES	VIR [wt%]	CR [wt%]	IPDA [phr]
VIR_CR_1	90	10	22
VIR_CR_2	80	20	22
VIR_CR_3	70	30	22
VIR_CR_4	60	40	22

In order to evaluate the effect of the recycling procedure compared to using the cured virgin resin as a filler, samples were produced with the same composition as the previous ones, but virgin resin cured and then ground (GR) was added instead of CR (as reported in Table 2).

Tab 2: Composition of samples containing the ground virgin epoxy resin

SAMPLES	VIR [wt%]	GR [wt%]	IPDA [phr]
VIR_GR_1	90	10	22
VIR_GR_2	80	20	22
VIR_GR_3	70	30	22
VIR_GR_4	60	40	22

Recycling process

First step: evaluation of H_2O_2 / TA ratio

To prepare the solution used in the recycling process 35 wt% hydrogen peroxide and tartaric acid were mixed at room temperature using a magnetic stirrer at 3,000 rpm for 30 minutes. Two different ratios between hydrogen peroxide and TA were tested, 3:1 as indicated by Zabihi et al. [22, 25] and 4:1, in order to use a less concentrated solution of hydrogen peroxide. A resin sample of 0.81 g was immersed in 9 g of solution (corresponding to 1:11 weight ratio) so that the sample is completely immersed in the solution. Then the mixture was mixed gently and placed in the microwave oven (800 W) and heated for 1.5 minutes. Three recycling cycles were run in sequence, and in each cycle the solution completely evaporated, which required its replacement at the beginning of each cycle. In order to evaluate the weight loss that occurred, the resin sample was recovered at the end of the three cycles, washed in distilled water and dried for 24 hours at 50°C.

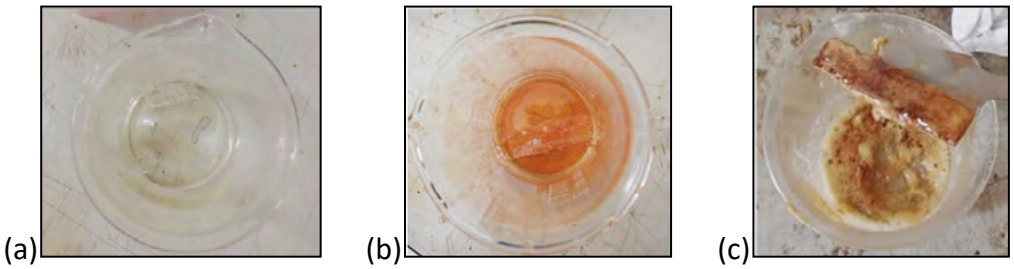

Fig 1: Before (a), during (b) and after (c) first cycle of the recycling process

The sample weight loss (WL) was calculated (Eq. 1) by measuring the weight of the sample after the recycling test (RW) made up of three cycles in relation with the initial weight of the virgin one (IW):

$$WL\ \% = (RW / IW) * 100 \quad (1)$$

Second step: evaluation of resting time

With the same procedure, the effect of resting time between subsequent cycles was evaluated. Resting could be useful both to lower the temperature of the solution in order to delay its evaporation in the following cycles and to continue the dissolution of the resin once the reaction is triggered. Three possibilities of resting time between one cycle and another were considered: 0 min (no resting time), 10 min, 15 min.

Third step: evaluation of microwave power and use of yeast

The microwave power was tailored in order to reduce energy consumption and the number of process cycles, and to avoid too fast evaporation of the hydrogen peroxide. Some tests were conducted at 20% - 30% - 40% - 50% of the maximum power of the microwave (800 W). By reducing the power of the microwaves, the dissociation reaction of the hydrogen peroxide would start later (increasing the process times) therefore, in order to speed up the reaction a food grade yeast, as natural catalyst, was added to the mixture. The yeast allows shortening the reaction time, thus promoting the dissociation of the hydrogen peroxide which would otherwise only occur through thermal activation (when approximately 80°C is reached). The yeast (1.5 wt% solution) was therefore added to the recycling solution, mixing it gently before placing everything in the microwave oven. The reaction progress is evidenced by a rapid evolution of O_2 and CO_2 bubbles.
To evaluate the process time saved with the use of yeast, once the optimal microwave power was chosen, the same test was also conducted without the use of yeast.

Fourth step: microwave vs conventional oven

Furthermore, a comparison between microwave (Sharp Corporation, Japan – max power 800 W) and conventional oven was also performed. Tests were carried out at different temperatures (150°C - 100°C) using a vented oven (Carbolite – max power 3,000 W). The duration of each cycle at 150°C is 15 minutes, at 100°C 30 minutes; at the end of each cycle weight loss was calculated.

It is important to point out that, in all tests carried out, the resin sample was not previously ground, because the objective of this research work is to recycle CFRP or GFRP while also recovering the fibers, without deterioration of their mechanical and physical properties.

Testing methods

Fourier transform infrared spectroscopy (FT-IR) analysis, performed with a FT-IR Jasco 6300 spectrometer (JASCO Corporation, Tokyo, Japan), was used to characterize the chemical residue obtained after the recycling process and to evaluate its behavior in samples obtained after the recycling process. Infrared spectra were recorded in the wavelength range between 550 and 4,000 cm^{-1}, 50 scans, and 4 cm^{-1} of resolution, by using ATR Pro One X with ZnSe crystal.

Differential scanning calorimetry (DSC) analysis was performed on a Mettler Toledo 822 (Mettler Toledo, Greifensee, Switzerland). The samples are first cured heating from 0°C to 150/200°C (at 10°C/min) followed by a two-minute temperature hold and then by cooling at 10°C/min back to starting temperature. A second heating scan, again performed at 10°C/min, was used to measure the glass transition temperature of the various cured samples.

The flexural properties of each cured sample were measured using a dynamometer, Lloyd LR5K, according to ASTM D790 (ASTM D790-17, 2017) (three-points bending). Four replicates were performed on each sample.

Results:

Recycling process

First step: evaluation of H_2O_2 / TA ratio

As reported in Table 3, the highest weight loss, and hence degradation of the virgin resin, was obtained with the 3:1 weight ratio between hydrogen peroxide and TA, therefore, it was decided to discard the possibility of using the 4:1 ratio.

Tab 3: First test to choose the hydrogen peroxide / TA ratio to be used in the recycling procedure

H_2O_2 : TA	Test time [min] (cycles x min)	WL [%]
3:1	4.5 (3 x 1.5)	23.06
4:1	4.5 (3 x 1.5)	19.98

Second step: evaluation of resting time

From the data reported in the Table 4, the resting time has no effect on weight loss, therefore we choose to eliminate the resting time between one cycle and another; this also involves a clear reduction in process time.

Tab 4: Second test to choose the right resting time to be used in the recycling procedure

H_2O_2 : TA	Resting time [min] (cycles x min)	Test time [min] (cycles x min)	WL [%]
3:1	0 (3 x 0)	4.5 (3 x 1.5)	23.15
3:1	30 (3 x 10)	4.5 (3 x 1.5)	23.06
3:1	45 (3 x 15)	4.5 (3 x 1.5)	22.87

Third step: evaluation of microwave power and use of yeast

The recycling process until complete degradation of the resin was studied. Compared to previously reported tests, in the following the aim is to completely recover the matrix, whereas in 1st and 2nd step, a partial recover was obtained. For each microwave power, the holding time of the solution was limited by its complete evaporation. Therefore, at 20, 30, 40 and 50 % of the maximum power, the maximum holding time in each step was calculated to be respectively 11.5, 5.5, 3.3 and 2.6 minutes. In order to obtain complete dissolution of the matrix, the number of required cycles is, for any microwave power except 50%, equal to 10. Therefore, the time for complete dissolution of the sample is reported in Table 5. Only for the microwave power of 50%, the very short holding time required an additional cycle to achieve complete sample dissolution.
In this process, after each cycle the solution was refilled to compensate its evaporation: for even cycles (2, 4, 6, 8 and 10) only hydrogen peroxide was added. For odd cycles, the complete solution, including TA and yeast, was instead added. This was done in order to reduce the amount of tartaric acid used.

Tab 5: Total process time (with yeast) and number of cycle as a function of microwave power

Microwave Power [%]	Total process time [min]	Number of cycles
20	115	10
30	55.5	10
40	33	10
50	28.5	11

From the data reported in Table 5, 40% was chosen as the optimal power, because it allowed to reduce the number of cycles required to obtain complete degradation of the resin, and therefore the consumption of hydrogen peroxide, TA and yeasts.

Once the 40% of maximum power was chosen, a single test was performed following the same procedure, without addition of yeast. In this case, an increase of 3.3 minutes was observed for complete dissolution.

Fourth step: microwave vs conventional oven

Regarding the comparison between microwaves and conventional heating, the same procedure was carried out in a vented oven: at 150°C almost complete degradation of the resin is achieved after 90 minutes (weight loss = 95.7%, the unreacted resin can be seen in Figure 2), while at 100 °C with the same processing time, a weight loss of 36.8% was observed.

Fig 2: Unreacted resin fragments (4.3 wt%)

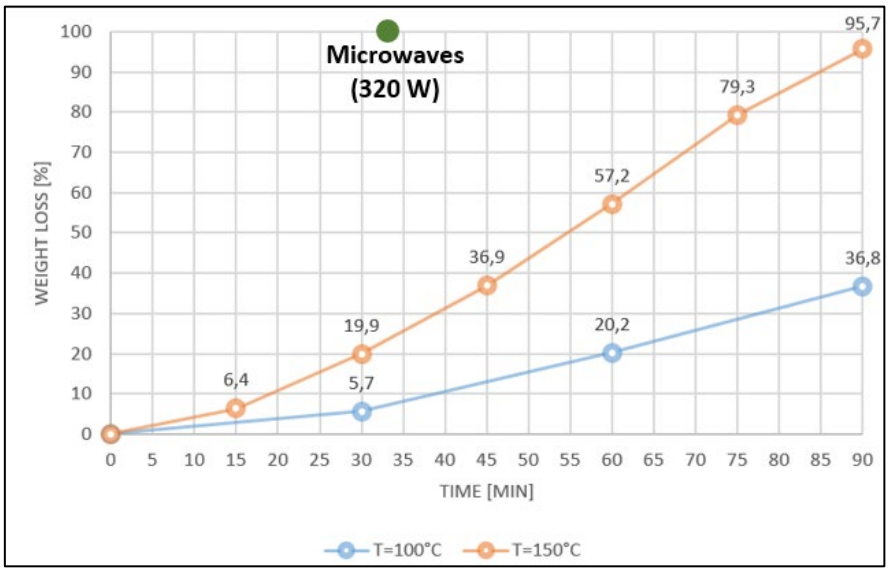

Fig 3: Weight loss trend of the resin during the test with conventional heating compared to the results obtained using microwave heating at 320 W

From data reported in Fig 3 it is clear that the microwave allowed reducing the recycling process times and consequently, also considering the powers of the two ovens used, energy consumption.

FTIR analysis

After completion of the recycling process, all the residue (degraded resin and precipitated tartaric acid) was collected, dried (24h at 50°C) and analysed by FT-IR. No waste products were eliminated.

(a)

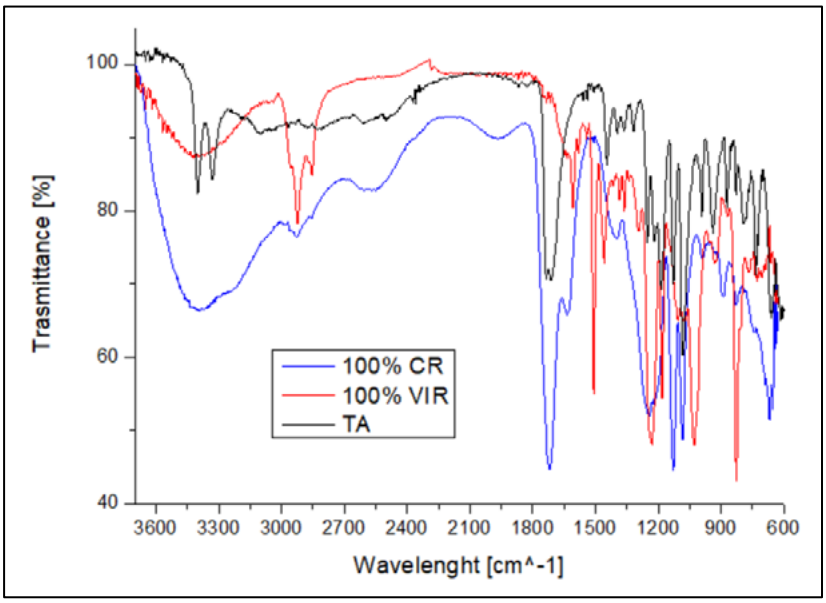

(b)

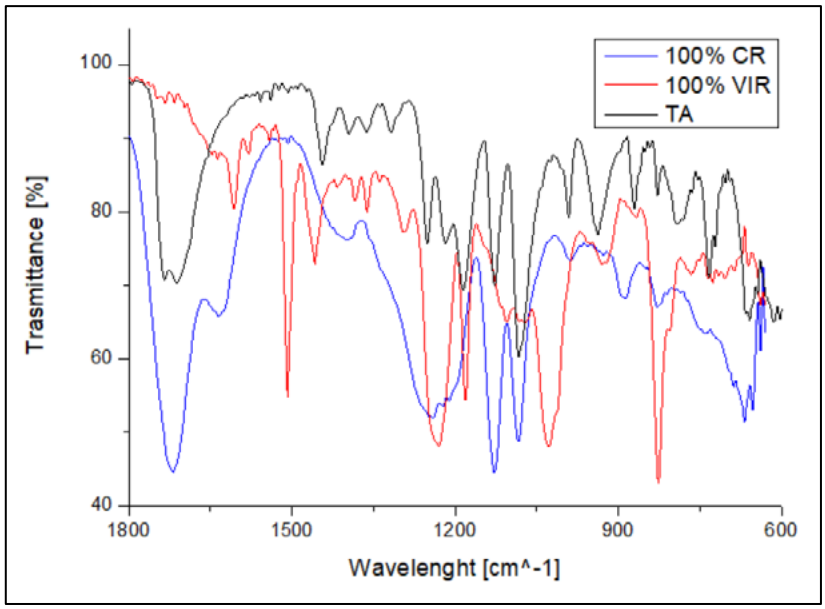

Fig 4a, 4b: Comparison between FT-IR spectra of 100% VER - 100% residue - TA

Figures 4a and 4b report the FTIR spectra of chemical residue in comparison with that of the TA and VIR. As expected the FT-IR spectra of CR and TA are very similar and this shows that the chemical residue is mainly made up of tartaric acid.

Some characteristic peaks have been identified on these spectra which it is considered useful to analyze in detail:

3500-3250 cm^{-1}: OH stretching band on 100% VIR and 100% CR; on TA there are two peaks, always relating to OH stretching; on the 100% VIR it could indicate the presence of NH stretching;

3000-2700 cm^{-1}: CH_3 - CH_2 stretching on all spectra;

2750-2500 cm^{-1}: CH stretching on 100% CR;

2000 cm^{-1}: CH stretching only on 100% CR; there is no peaks on 100% VIR and this indicates a complete cure of the sample;

1720 cm^{-1}: C=O stretching on 100% CR and TA;

1640 cm^{-1}: C=C stretching on 100% CR, this peak could indicate a certain reactivity of the chemical residue;

1500 cm^{-1}: NO stretching only on 100% VIR;

1450 cm^{-1}: CH bending on 100% VIR;

1250 cm^{-1}: band on 100% CR, which may likely be due to stretching of the epoxy (it indicates residual reactivity);

1105 cm^{-1}: CN stretching only on 100% VIR;

890 cm^{-1}: peak present only on 100% CR, also attributable to the presence of epoxides.

To evaluate whether the CR participates in the reaction or only acts as a filler, FTIR analyses were performed on the samples containing the CR (VIR_CR_1, VIR_CR_2, VIR_CR_3, VIR_CR_4) and on the samples containing the ground virgin resin (VIR_GR_1, VIR_GR_2, VIR_GR_3, VIR_GR_4). No differences were detected within the two categories: the spectra of the samples containing CR are very similar to each other as are those containing GR. Furthermore, the FTIR spectra containing GR are very similar to that of 100%VIR.

Given the previous considerations, we chose to compare the spectra of the 100% VIR sample, the one containing 10% GR (VIR_GR_1) and the one containing 10% CR (VIR_CR_1). As can be seen from the Figure 5, in the VIR_CR_1 spectra we notice that some peaks disappear (around 1600 – 1300 – 1100 - 900 cm^{-1}). This probably demonstrates that the CR, unlike the GR, participates in the reaction with the virgin resin.

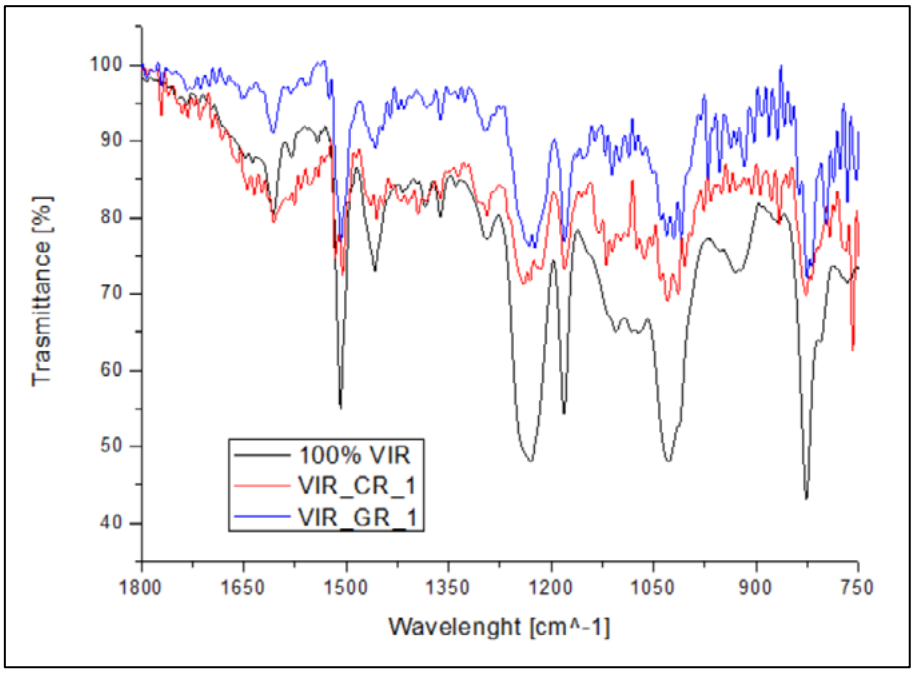

Fig 5: Comparison between FT-IR spectra of 100% VIR – VIR_CR_1 – VIR_GR_1

Thermal characterization

DSC analysis was performed on the CR in order to evaluate the thermal properties of the material. As shown in Fig 6, a very low T_g value at about 32.6°C is obtained. The low T_g value suggests the possibility that the CR can be mixed with virgin resin to obtain a material with higher T_g. Therefore, as reported in Table 1, virgin resin was mixed with CR, then the curing agent (IPDA) was added for the production of recycled specimens.

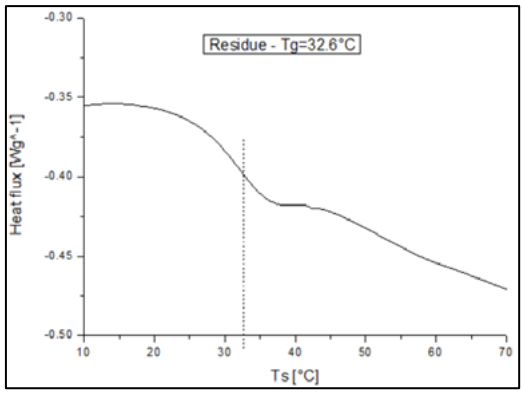

Fig 6: DSC analyses of the chemical residue

DSC analysis, carried out on the samples containing CR (as reported in Table 6), shows a decrease in the glass transition temperature as the CR content from the recycling process increases. However, the glass transition temperature measured for the composition with 40%

of CR (VIR_CR_4) is still high (about 82°C), thus highlighting good thermal properties, which makes the material suitable for further applications.

The glass transition temperatures of the samples containing GR were also evaluated: they are lower than that of the 100% VIR sample but increases as the GR content increases, contrary to what happens in the samples containing the residue. This could be another proof of the different behavior that GR and CR have when mixed with virgin resin.

Tab 6: Tg values found with DSC analysis

SAMPLES	Tg [°C]
100% VIR	157.2
VIR_CR_1	110.3
VIR_CR_2	91.5
VIR_CR_3	85.1
VIR_CR_4	82.3
VIR_GR_1	132.6
VIR_GR_2	139.6
VIR_GR_3	141.7
VIR_GR_4	142.5

Mechanical characterization

To complete the characterization and to evaluate the mechanical properties of the materials produced, the various samples were tested with a three-point bending test. Table 7 and Figures 7a-7b-7c show the average values of flexural strength, strain at break and modulus. Despite a very low change in the Young modulus for every composition, a reduction in bending strength and deformation were detected with increasing of CR content. Therefore, although good thermal properties were found even with high CR contents (40% - VIR_CR_4), only small amount of recycled filler (VIR_CR_1, VIR_CR_2) can be used in order to avoid strong decays in mechanical behavior.

The bending tests to determine the mechanical properties of the samples containing GR were not performed because we are not interested in the mechanical recycling of the resin (grinding) because this work also aims at the recycling of long fiber composite materials and therefore aims to keep unchanged the mechanical properties of the fibers even after the recycling process.

Tab 7: Results of the three-point bending test

SAMPLES	σ_r [MPa]	ϵ_r [%]	E [GPa]
100% VIR	75.8 ± 6.1	3.9 ± 0.8	1.9 ± 0.2
VIR_CR_1	42.6 ± 4.8	2.2 ± 0.3	2.1 ± 0.3

VIR_CR_2	25.9 ± 4.4	1.3 ± 0,2	1.8 ± 0.4
VIR_CR_3	6.7 ± 0.6	0.5 ± 0,1	1.3 ± 0.2
VIR_CR_4	5.2 ± 1.1	0.3 ± 0,1	1.7 ± 0.3

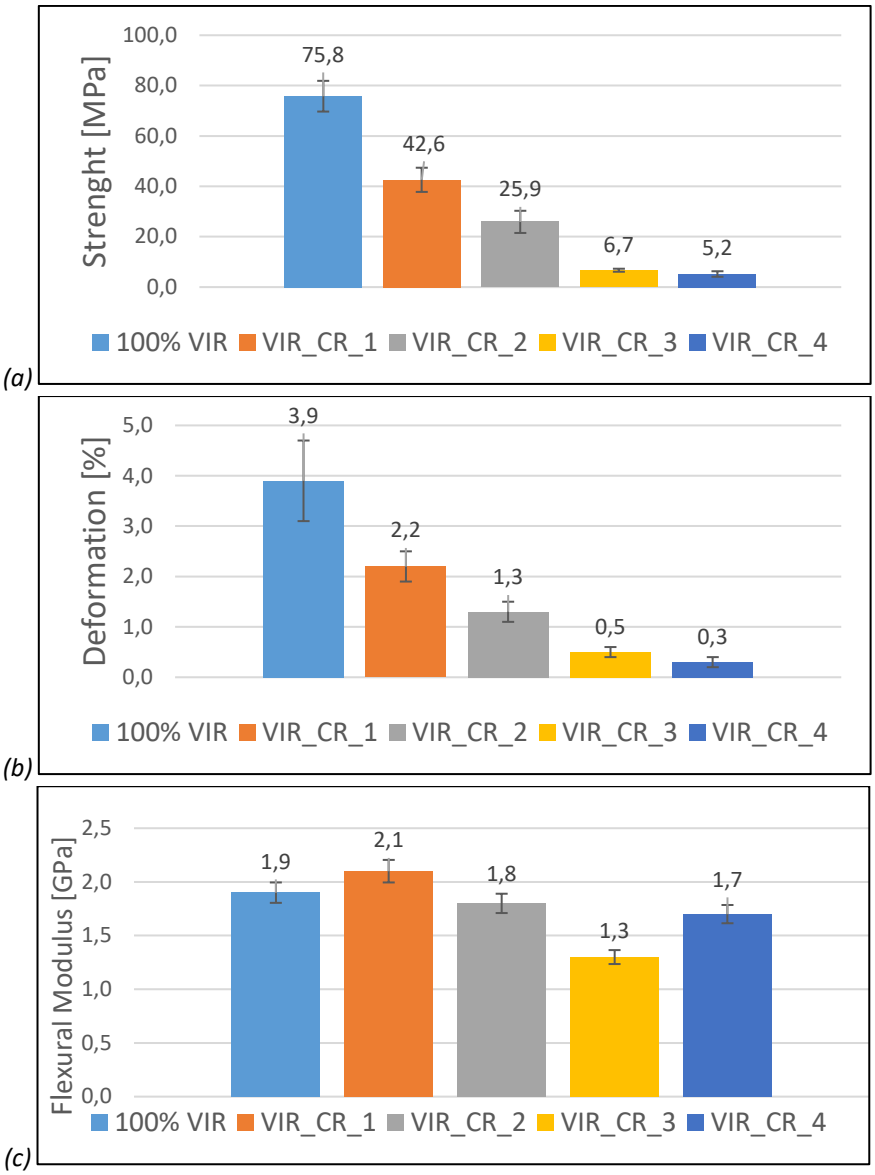

Fig 7: Results of the three-point bending test (a-Strenght, b-Deformation, c-Flexural Modulus)

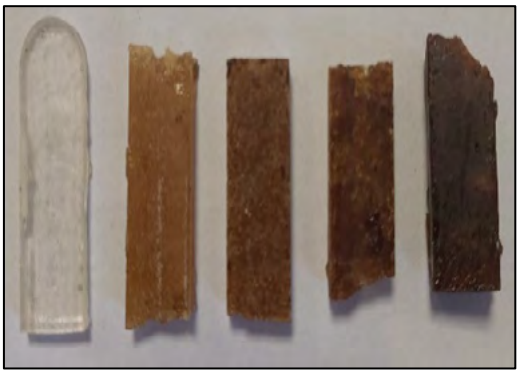

Fig 8: Samples after flexural test (to the left: 100% VIR, VIR_CR_1, VIR_CR_2, T VIR_CR_3, VIR_CR_4)

Conclusions:

This work was aimed to the development of an innovative method for the recovery of GF and CF epoxy matrix. To this purpose, different approaches were investigated, in order to optimize the yield of the recycling process and to minimize the recycling time and the energy consumption. The best recycling conditions were obtained with the use of a solution (3:1 weight ratio) of 35 wt% hydrogen peroxide (H_2O_2) as a green oxidiser, and tartaric acid (TA), catalysed by yeast (1,5 wt%) and activated by microwave radiation (40% - 320 W).

The chemical residue of the recycling process, once collected and desiccated, was characterized by FTIR analysis, which revealed the presence of epoxy and C=C reactive groups. The behaviour of the CR in the reaction is not yet clear but, as demonstrated by FTIR and DSC analyses, the CR takes part in the reaction and therefore does not act as a filler.

Several mixtures of virgin resin and CR were then produced and the thermal and mechanical behavior was studied after the addition of amine curing agent and the curing cycle. DSC analysis, carried out on the samples produced with different amount of CR, showed good thermal properties, even with high quantities of CR. On the other hand, significant reduction in bending strength was detected with increasing recycling chemical residue content.

Please note that this work focuses on the recycling of the epoxy matrix of a composite material, while the tests were carried out on samples of matrix only, without fibres. This is a worsening condition compared to the recycling of composite materials (matrix and fibres), both because for the same weight the composite material contains less matrix to be recycled, and because the presence of fibers inside the matrix and the use of microwaves generate super-heating [25] which further facilitates and speeds up the recycling process.

Next works will be focused on the optimization of the mechanical properties after the chemical residue addition to the virgin resin. Also, since different reactive groups were detected by FTIR analysis on the recycled resin, the chemical reaction of the residue after the addition of a curing agent, for the production of recycled epoxy sample, will be studied.

References:

[1] F.-L. Jin, X. Li and S.-J. Park, *J. Ind. Eng. Chem., 2015, 29, 1– 11*

[2] K. Yang, S. Wu, J. Guan, Z. Shao and R. O. Ritchie, *Sci. Rep., 2017, 7, 11939–11947*

[3] Yuwei Long, Fei Tian, Lan Bai, Wenli An, Xu Zhao, Rongcheng Du, Xuehui Liu, Xuelian Zhou, Shimei Xu and Yu-Zhong Wang., *Green Chem., 2022, 24, 7082–7091*

[4] Al-Lami A., Hilmer P., Sinapius M., *Aerosp. Sci. Technol. 2018, 79, 669–678*

[5] Leon Klose, Neele Meyer-Heydecke, Sasipa Wongwattanarat, Jennifer Chow, Pablo Pérez García, Camille Carré, Wolfgang Streit, Garabed Antranikian, Ana Malvis Romero and Andreas Liese, *Polymers 2023, 15, 2653*

[6] Viviane Tavares de Moraes, Luiz Alberto Jermoloviciusb, Jorge Alberto Soares Tenórioc, Susana Marraccini Giampietri Lebrãoa, Guilherme Wolf Lebrão, *Materials Research. 2020; 22(suppl. 1): e20190389*

[7] Mazumdar S., State of the Industry Report: the glass fiber market. *Composites Manufacturing [Internet] 2019*.

[8] Sokoli HU, Simonsen ME, Nielsen PR, Arturi KR, Sogaard EG. *Fuel Processing Technology. 2016; 149:29-39*

[9] Zhu, J.H.; Chen, P.Y.; Su, M.N.; Pei, C.; Xing, F. *Green Chem. 2019, 21, 1635–1647*

[10] Pi-Yu Chen, Ran Feng, Ying Xu and Ji-Hua Zhu, *Polymers 2023, 15, 3508*

[11] Carlos A. Navarro, Elyse A. Kedzie, Yijia Ma, Katelyn H. Michael, Steven R. Nutt, Travis J. Williams, *Topics in Catalysis (2018) 61:704–709*

[12] A.D. La Rosa, D.R. Banatao, S.J. Pastine, A. Latteri, G. Cicala, *Composites Part B 104 (2016) 17-25*

[13] S. Karuppannan Gopalraj and T. Kärki, *SN Appl. Sci., 2020, 2, 433–453*.

[14] J. Zhang, V. S. Chevali, H. Wang and C.-H. Wang, *Composites, Part B, 2020, 193, 108053–108067*.

[15] S. Kumar and S. Krishnan, *Chem. Pap., 2020, 74, 3785– 3807*.

[16] C. A. Navarro, C. R. Giffin, B. Zhang, Z. Yu, S. R. Nutt and T. J. Williams, *Mater. Horiz., 2020, 7, 2479–2486*.

[17] M. Shen, H. Cao and M. L. Robertson, *Annu. Rev. Chem. Biomol. Eng., 2020, 11, 183–201*.

[18] J. M. Garcia and M. L. Robertson, *Science, 2017, 358, 870– 872*.

[19] Marsh G., Recycling Carbon Fiber Composites. *Materials Today, April 22, 2009*

[20] Mohan Das, Rinu Chacko, and Susy Varughese, *ACS Sustainable Chem. Eng. 2018, 6, 1564−1571*

[21] Jianying Deng, Lei Xu, Jianhua Liu, Jinhui Peng, Zhaohui Han, Zhigang Shen, Shenghui Guo, *Polymer Degradation and Stability 182 (2020) 109419*

[22] Omid Zabihi, Mojtaba Ahmadi, Chao Liu, Roya Mahmoodi, Quanxiang Li, Minoo Naebe, *Composites Part B 184 (2020) 107750*

[23] S.R. Naqvi, H. Mysore Prabhakara, E.A. Bramer, W. Dierkes, R. Akkerman, G. Brem, *Resources, Conservation & Recycling 136 (2018) 118-129*

[24] Paul Anastas and Nicolas Eghbali, *Chem. Soc. Rev., 2010, 39, 301–312*

[25] Manjeet Rani, Priyanka Choudhary, Venkata Krishnan, Sunny Zafar, *Conservation & Recycling 179 (2022) 106107*

[26] Omid Zabihi, Mojtaba Ahmadi, Chao Liu, Roya Mahmoodi, Quanxiang Li, Minoo Naebe, *Sustainability 2020, 12, 641*

[27] Xu Zhao, Xiong-Lei Wang, Fei Tian, Wen-Li An, Shimei Xu and Yu-Zhong Wang, *Green Chem., 2019, 21, 2487*

[28] Kaiyou Huang, Jiongli Zheng, Wenyi Yuan, Xiaoyan Wang, Qingbin Song, Ying Li, John C. Crittenden, Lincai Wang, Jingwei Wang, *Waste Management 124 (2021)*

[29] Lorena Saitta, Giuliana Rizzo, Claudio Tosto, Gianluca Cicala, Ignazio Blanco, Eugenio Pergolizzi, Romeo Ciobanu and Giuseppe Recca, *Polymers 2023, 15, 2809*

BIO-BASED SANDWICH PANELS FOR SUSTAINABLE BUILDING CONSTRUCTION AND REHABILITATION

M. Helena C. Teixeira[1,*], Susana Sousa[1,2], Raquel Santos[1,2] and Andreia Araújo[1,2]

[1]INEGI - Institute of Science and Innovation in Mechanical and Industrial Engineering, Materials and Composite Structures Unit, Rua Dr. Roberto Frias, 4200-465 Porto, Portugal
[2]LAETA - Associated Laboratory for Energy, Transports and Aeronautics, Faculty of Engineering, Porto University, Porto, Portugal
[*]Email: hteixeira@inegi.up.pt

Keywords: Sandwich Panels, Bio-Based Composites, Sustainability, Building Construction, Rehabilitation

Abstract
In the current global context, climate changes, ecological degradation and the consumption of fossil fuels present significant challenges to the world. Moreover, the building industry consumes a large amount of energy and materials to provide thermal comfort. These challenges, combined with the need for lightweight structures, have spurred a surge in the scientific investigation of composite sandwiches with bio-based materials. The combination of natural materials provides several environmental advantages owing to their thermal and sound absorption properties, biodegradable nature, cost-effectiveness, and ease of accessibility. In the present work, different materials have been studied for developing composite sandwich panels, produced by combining core materials with vacuum-infused composite laminates. The aim was to compare their mechanical and thermal properties and select the most suitable solution for the construction sector. The density and fibre volume fraction of the laminates were determined, and the mechanical and thermal properties were evaluated to assess the core strength, the core//laminate interface properties, and the thermal insulation capacity of the samples. The studied sustainable materials presented higher or equal thermal properties in comparison with the commercial synthetic counterparts, however, the mechanical properties were slightly lower due to the intrinsic properties of the core materials.

1. Introduction

Significant challenges arise from the consumption of fossil fuels, climate changes, ecological degradation and resource overuse [1,2]. In fact, energy production accounts for approximately 80 % of fossil fuel consumption due to the reliance on non-renewable sources [1]. The building industry is a highly demanding energy sector to provide thermal comfort, however, a careful selection of materials can significantly reduce this consumption [2]. Thereby, this sector has exhibited a strong interest towards integrating advanced and sustainable materials characterised by lightweight, high strength and stiffness, among others [3]. Moreover, the development of new material structures with improved insulation characteristics can contribute to a more sustainable and energy-efficient construction that provides long-lasting comfort by minimising both energy loss and, consequently, the need for extra heating or cooling sources [4]. Besides addressing sustainability concerns, conventional construction materials, including concrete and steel, exhibit major limitations regarding weight, maintenance costs, and susceptibility to corrosion [5]. Therefore, several studies have successfully investigated the replacement of partition and external non-structural walls in buildings by composite sandwich panel solutions, particularly when lightweight construction is imperative [6]. Moreover, composite sandwich panels exhibit great potential

in rehabilitating degraded buildings, as they can be manufactured off-site, allowing for faster installation while minimising disruptions to occupants. The versatility of production of these structures in different shapes, sizes and configurations offers several advantages, making them excellent candidates for further use in building construction and rehabilitation [5].

Composite sandwich panels are typically constituted by two stiff laminates bonded to a soft and lighter core. Synthetic fibres, such as glass and carbon, are commonly used as skin reinforcement, and aluminium honeycomb, polyurethane (PU) and polystyrene (PS) foams as core [2,6,7]. Still, their production from non-renewable resources contributes significantly to global warming as it requires a huge amount of energy, and emits carbon dioxide and other greenhouse gases [3,7]. Nevertheless, the poor fire resistance of the polymers (epoxy resins, PS, and PU), limits their applicability in numerous scenarios [6]. Flax, hemp, jute, sisal or basalt fibres, and natural cores like cork, bamboo, coir, stone wool and recycled foams are promising sustainable materials that can offer several economic and ecological benefits [8]. Therefore, by combining different materials, several structures can be produced to meet different project requirements depending on the specific needs [9].

Basalt fibres, a natural and inert material, exhibit favourable strength and stiffness properties, high resistance to acids or solvents, low water absorption, and good heat and sound insulation properties [10]. The manufacturing process of basalt fibres consumes minimal energy and does not involve any additives or hazardous materials. Compared to carbon and glass fibres, basalt fibres offer a superior balance between quality and cost [10,11].

Since foams are synthetic materials, the application of recycled ones can be a suitable approach for reducing the environmental footprint of the final product. Moreover, cork is an excellent natural substitute for synthetic foams composed of suberin, lignin, and cellulose [12,13]. Its honeycomb-like cellular structure strongly influences the mechanical properties of its products [12]. The use of cork as a core in sandwich structures has many advantages, including excellent thermal, acoustic and electrical insulation properties, good mechanical performance, as well as strong compatibility with thermoset matrices and traditional production processes, such as hand lay-up and vacuum infusion [13,14]. On the other hand, stone wool can be recycled by manufacturers and it is commonly used as insulation material, providing fire safety properties owing to its non-flammable nature and resistance to humidity [4].

Therefore, this work aims to evaluate and compare the mechanical and thermal performances of different composite sandwich panels produced by using more sustainable materials. The laminate skins of all panels are composed of basalt fibres and a bio-based epoxy resin, while the core material was varied. The four different types of core materials used were: recycled expanded polystyrene (EPS) foam, expanded cork and stone wool (more sustainable ones), and extruded polystyrene (XPS), which is a conventional synthetic material, for comparison purposes.

2. Materials and Methods

2.1. Materials

The laminates of the composite sandwich panels were produced with basalt fibres (450 $g \cdot m^{-2}$, Castro Composites, Spain) and a bio-based epoxy resin containing approximately 38 % carbon derived from plants (SR InfuGreen 810 + SD 8825.2, Sicomin, Rebelco, Portugal). Different core materials with 2 cm thickness were used: XPS (ifoam®, IMPERALUM, Portugal), recycled EPS (Bewi, Portugal), stone wool (Rocterm+, Termolan, Portugal), and expanded cork (kindly offered by Amorim Cork Insulation, Portugal).

2.2. Experimental Procedure

To mitigate challenges related to the high resin absorption by the cork and stone wool cores during the vacuum infusion process, encountered in preliminary studies, a two-step process was used to manufacture the composite sandwich panels. The first step comprises the vacuum infusion of the laminate, followed by the bonding of the laminates to both sides of the core. During the first step, after

applying the release agent, 2 layers of basalt fabric were arranged in a ± 45° orientation, followed by the positioning of the peel ply, infusion mesh, spiral, tube, vacuum bag and sealant tape. The resin system was prepared using the producer's technical data sheet (mixing ratio recommendations), and the mixture was degassed for approximately 10 minutes to minimise the presence of air bubbles and potential defects. A vacuum pressure of 500 mbar was applied to the vacuum infusion setup and, after confirming that there were no leaks, the inlet valve was opened allowing the resin to flow through the layers of fibres. Afterwards, the laminates were cured for 10 h at 70 °C.

In the second step, the composite laminates were bonded to both sides of the core material using the same resin system applied in the vacuum infusion process. The resin was carefully applied on the core and the laminate, followed by the application of vacuum pressure to ensure a good bonding between the two parts.

Figure 1 shows a schematic representation of the produced composite sandwich panels.

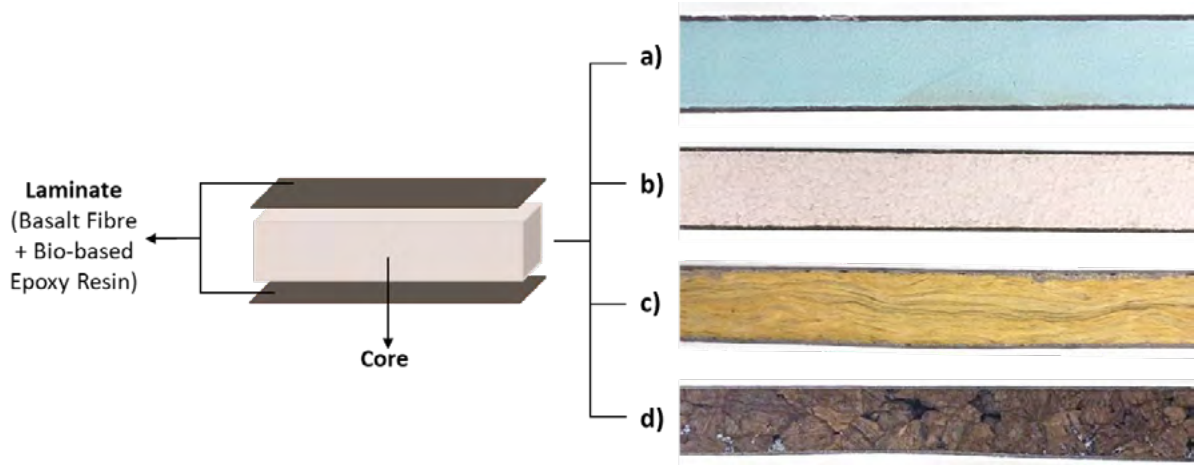

Figure 1. Produced composite sandwich panels with basalt laminates and different core materials: a) XPS, b) recycled EPS, c) stone wool, and d) cork.

2.3. Test Procedures

Aiming to characterise the laminates, the density was measured according to Method A of ASTM D 792, and the fibre volume fraction and void content were determined following ASTM 3171 – G. The thermal stability of the materials was determined using thermogravimetric analysis, performed with a Simultaneous Thermogravimetric Analyzer (STA) NEXTA STA300 (Hitachi). The test was conducted in a ceramic crucible at a heating rate of 10 °C·min^{-1}, ranging from 25 to 800 °C, with a nitrogen (N_2) flow rate of 100 mL·min^{-1}. The reproducibility of the test for each material was accessed by performing two samples for each one. The thermal conductivity tests were conducted at room temperature (RT) with a Hot Disk Thermal Constants Analyser, following ISO 22007-2. Since some of the tested materials are anisotropic, it was necessary to determine the volumetric specific heat, which was done using the differential scanning calorimetry (DSC) technique in a Q20 model calorimeter (TA Instrument), according to ASTM E1269 – 11.

The mechanical properties of the composite sandwich panels were assessed by applying two methods: *i)* three-point flexural test, and *ii)* edgewise compression test, following ASTM standards C 393/C393M and C364/C364M, respectively. The tests were performed using an Instron 5900R Universal Testing Machine with a 100 kN load cell. The flexural tests were carried out at a constant loading rate of 6 mm·min^{-1}, using specimens of 200 mm × 75 mm, to determine the core shear ultimate stress, the facing bending stress, and the modulus of elasticity in bending. In the compression tests, specimens measuring 160 mm × 40 mm were subjected to a compression force parallel to the plane of the laminates at a speed of 0.5 mm·min^{-1} to determine the ultimate strength.

3. Results and Discussion

The main goal of this research was to compare the performance of different core materials in bio-based composite sandwich panels for sustainable building construction and rehabilitation. The thermal stability of the produced materials is an important parameter to test, since it safeguards the structural integrity of the structures, allowing materials to resist high temperatures without compromising the building's construction. The results for the thermal stability of the laminates and core materials were compared, and the overall analysis is presented in Table 1.

Table 1. Results from the STA tests.

Properties	XPS Panel	Recycled EPS Panel	Stone Wool Panel	Cork Panel	Basalt Laminate
Initial Degradation Temperature / °C	282.5 ± 2.1	323.5 ± 2.1	-	291.5 ± 2.1	278.8 ± 0.0
Temperature of Maximum Velocity Degradation / °C	410.4 ± 0.5	408.1 ± 1.4	-	413.5 ± 2.3	353.2 ± 2.4
Total Weight Loss / %	99.2	99.4	3.9	75.0	25.7

A minor weight loss of approximately 1.0 % up to 200 °C was found for all analysed materials, corresponding to moisture evaporation and elimination of other volatile contents. In the basalt laminate, degradation started at 279 °C until reaching 500 °C, and the weight loss was around 25.1 %. In the results for the bio-based epoxy resin, the degradation of the material started at 280 up to 495 °C, with an overall mass loss of 94.0 %. Since the weight percentage of resin in the laminates was approximately 29 %, it can be concluded that the weight lost in the basalt laminate corresponds, essentially, to the epoxy resin.

Regarding the core materials, the stone wool presented high thermal stability with constant behaviour and a total weight loss of 3.9 % for the tested temperature range, showing its potential as an excellent fire-retardant candidate. With the derivative STA curves, the major degradation temperature occurs at 410.4, 408.1, and 413.5 °C for the XPS, recycled EPS and cork cores, respectively. The weight loss of XPS and EPS is related to the volatile gases generated by the solid material [15]. In the case of the cork, the weight loss between 291 and 536 °C is attributed to the degradation of organic substances or the combustion of hemicellulose, cellulose and lignin [16]. It is important to point out that the natural-based cores present higher thermal stability, with lower weight loss up to the final tested temperature when compared to the XPS and recycled EPS, making them more appealing for the construction sector, in terms of carbon footprint and performance.

When it comes to energy savings in buildings and minimising the need for extra heating or cooling systems, the use of insulating materials is crucial. In composite sandwich panels, the core material has a higher impact on the insulating capacity of the global structure, and the value of thermal resistance can be adjusted to different climatic zones by changing the core thickness. In this context, preliminary studies were focused on the thermal conductivity of the different core materials. The experimental tests were conducted at 24 ± 1 °C, and it was found that all the core materials presented similar values of thermal conductivity, including 0.038, 0.036, 0.046 and 0.035 $W \cdot m^{-1} \cdot K^{-1}$ for the XPS, recycled EPS, expanded cork and stone wool, respectively.

From the obtained results, it can be concluded that the thermal conductivity of the stone wool panel is similar to the XPS and recycled EPS, being an excellent substitute for conventional materials. The value presented by the stone wool-based panel is mainly promoted by air trapped within the material's physical structure, which provides conductive resistance for heat flow. Moreover, it is important to note that the analysis with a hot disk is influenced by the contact between the sensor and the material, which in the case of the cork could have affected the results since the surface was not smooth.

Regarding the mechanical properties, 3-point bending and edgewise compression tests were performed to assess the core strength and core//laminate interface properties. Figure 2 depicts the mechanical properties of the composite sandwich panels, which were calculated based on the average and standard deviations for five valid results. In addition, the density, fibre content, void volume, and thickness of each laminate were analysed. The average results and standard deviation for three valid tests are displayed in Table 2.

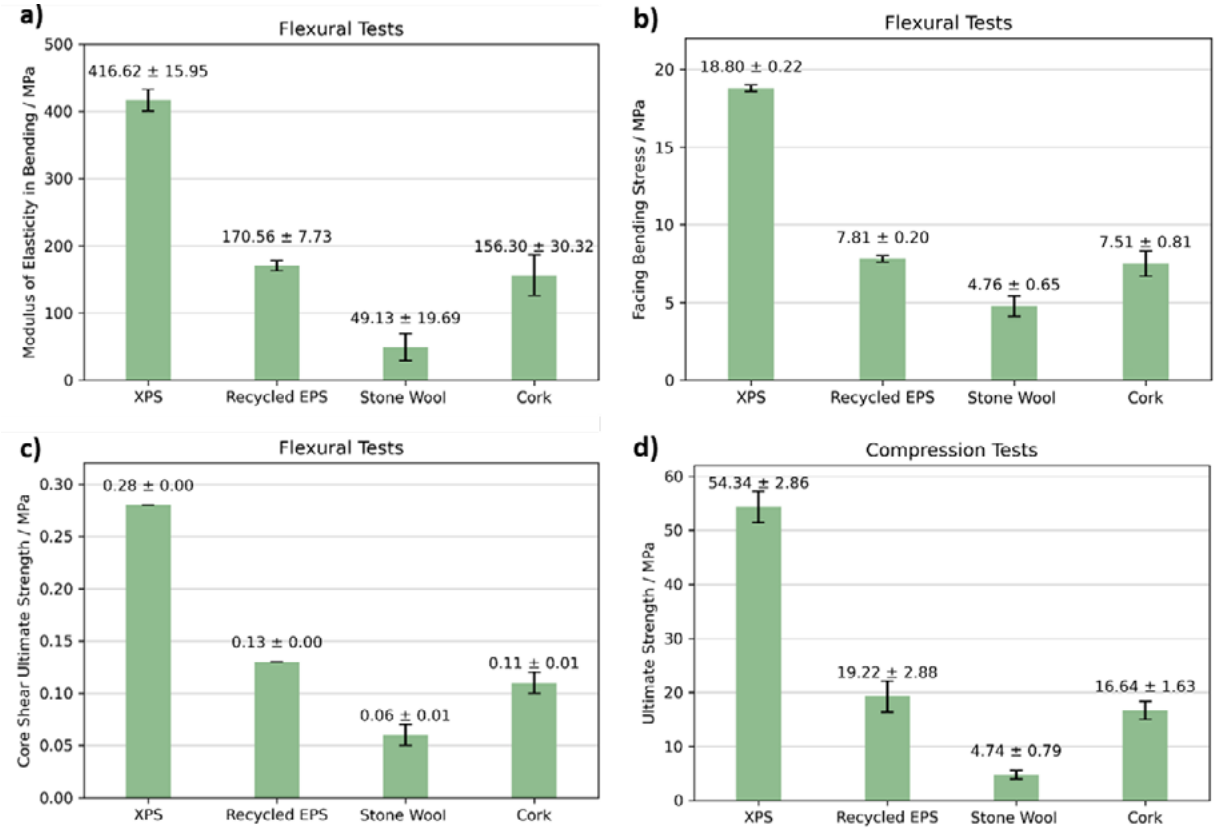

Figure 2. Mechanical properties of the different panels obtained by 3-point bending: a) modulus of elasticity in bending, b) facing bending stress, and c) core shear ultimate strength, and by edgewise compression tests: d) ultimate strength.

Table 2. Laminates' properties of each panel.

Panel Core Material	Laminate's properties			
	Density / g·cm^{-3}	Void Volume / %	Fibre volume fraction / %	Thickness / mm
XPS	1.92 ± 0.01	3.65 ± 0.45	53.01 ± 0.39	1.17 ± 0.04
Recycled EPS	1.90 ± 0.04	2.87 ± 1.83	51.06 ± 1.15	1.20 ± 0.04
Stone Wool	1.83 ± 0.02	2.89 ± 1.71	46.64 ± 0.17	1.04 ± 0.23
Expanded Cork	1.88 ± 0.01	1.53 ± 0.50	48.97 ± 0.59	1.03 ± 0.10

Analysing the mechanical properties of the different composite sandwich panels, it was found that the panels with XPS core presented values around 60 % higher for all the measured properties, probably due to the higher fibre volume fraction and laminate thickness (2 to 7 % and 15 % higher, respectively), as it can be seen in Table 2. Regarding the other properties (density and void volume), the small variations observed are not significant and allow the further comparison of the produced panels. The

sustainable panels, comprising cork or recycled EPS cores, presented similar values, i.e., a difference ranging from 4 % for the facing bending stress to 18 % for the core shear ultimate stress. However, a poor performance was obtained for stone wool-based panels (~84 % lower than the XPS core, and an average of 55 % lower than the cork core), being the material of least interest for the application.

These results evidence that the dimensions of the core and laminates can be optimised to attain better mechanical properties. Increasing the thickness of the laminates can enhance the stiffness of the panel. Additionally, Colomina *et al.* [17] stated that the increase of 4 to 10 mm in the core thickness has led to a decrease in the core shear ultimate stress (from 12.07 to 4.84 MPa). In this way, sustainable materials could be excellent candidates for composite sandwich panels applied in the building industry, if the materials' dimensions and properties were properly selected and optimised.

In Figure 3 the different failure modes observed for the flexural tests are shown.

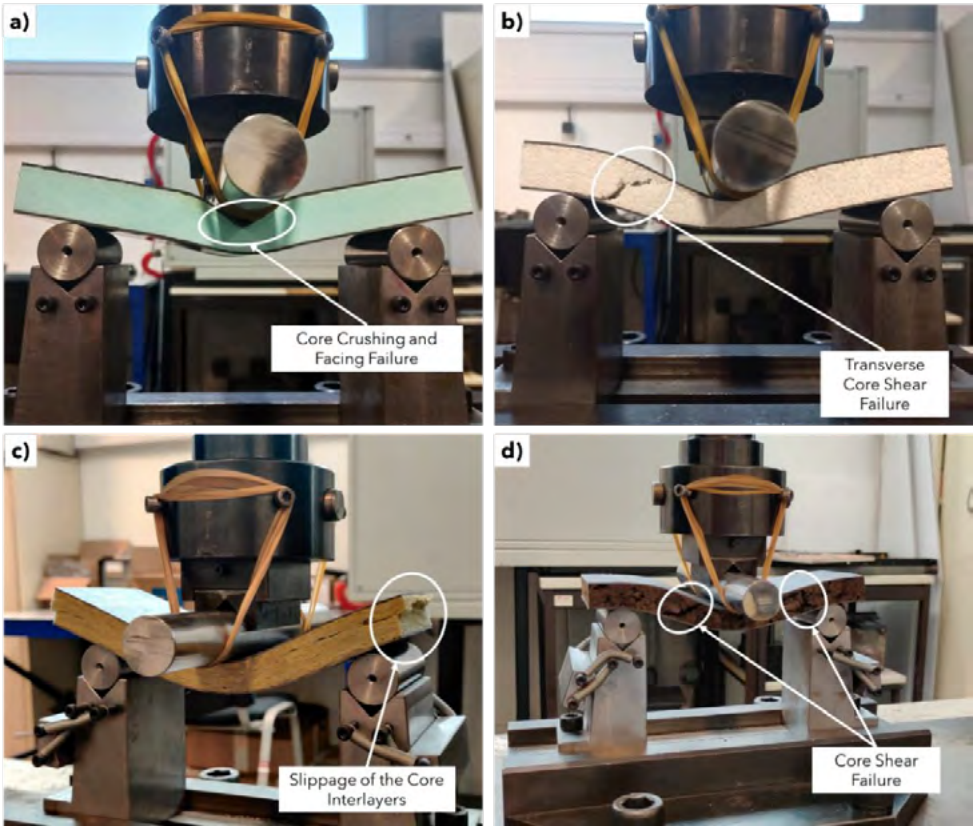

Figure 3. Photographs of the 3-point bending tests of the a) XPS, b) recycled EPS, c) stone wool, and d) cork panels.

XPS panels presented core crushing and facing failure, while for the recycled EPS, transverse core shear and, in some cases, core crushing and facing failure were observed. For both cork and stone wool panels, the failure was influenced by the nature of the core. In the cork-based panels, the failure was due to the shearing of the core between the granules of the material. On the other hand, for the stone wool panels, the main issue and cause of the failure was the detachment and slipping of the core interlayers. Although the bending tests are essentially used to obtain the interface properties of the composite sandwich panels, the failures have occurred due to fractures in the core and not due to interface problems, evidencing a good bonding between the laminates and the core. These conclusions align with those found in the literature, Jiang *et al.* [18] produced panels with hybrid skins composed of recycled carbon and flax fibres and recycled poly(ethylene terephthalate) (PET) foam as core, and Lakreb *et al.* [19] manufactured panels of wood veneer and cork. Both studies only detect core shear failures, which have proved the

good adhesion between the several components of the panel. However, complementary studies need to be performed to achieve a composite sandwich panel with improved performance.

The failure modes in the compression tests were very similar for all types of cores. In the recycled EPS and cork panels the failure was only core shear, while for the XPS panels, the failure was core shear and, in some cases, facesheet buckling. Finally, for the stone wool, a mix between compression and slippling of the core interlayers was observed.

4. Conclusion

Composite sandwich panels with different core materials (XPS, recycled EPS, stone wool and expanded cork) were proposed as a sustainable product for the construction sector. In this work, the mechanical and thermal performances of the developed solutions were studied. To be competitive in the construction market, a good performance with higher mechanical properties, lower values of thermal conductivity, and higher thermal stability should be achieved. In summary, the concluding remarks can be stated as:

- All the materials presented higher thermal stability with a minimal weight loss until 200 °C. In terms of the laminate, the weight lost between 25 and 800 °C was essentially due to the bio-epoxy resin present. Regarding to the core materials, the stone wool showed an overall mass loss of 3.9 % being the most stable at higher temperatures. The XPS, recycled EPS and stone wool present the maximum degradation temperature around 410.4, 408.1, and 413.5 °C, respectively.
- For the thermal conductivity tests, the stone wool core presented a value of 0.035 $W \cdot m^{-1} \cdot K^{-1}$, similar to XPS and recycled EPS cores, being a promising substitute to the conventional insulating materials used. However, the results for the cork core could have been influenced by the nature of the test and the characteristics of the material.
- The mechanical properties of the XPS panel were higher than the sustainable-based ones. Among these sustainable materials, the cork and recycled EPS panels presented similar values and were around 60 % lower than the conventional panels. The properties of the panel with stone wool were less interesting, ~84 % lower than the panel with the XPS core.
- The predominant failure modes observed were associated with the core materials, particularly in the case of stone wool and cork cores. In stone wool, mainly due to the direction of the fibres that constitute the material, and in cork, owing to the gaps and size of the granules.
- No debonding between the facings and the core has occurred, which evidences the good adhesion between the different materials.

The results revealed that it is possible to produce panels with natural materials with promising properties, being the panel with basalt fibre laminates and cork core the most interesting solution for the building industry. The dimensions of both laminates and core need to be adjusted, to maximise the mechanical properties of the panels. Furthermore, future investigations could explore variations in core densities, grain sizes and porosity. Additionally, alternative natural fibres, such as flax fibres, could be tested to find a more economical solution.

Acknowledgements

This work is supported by the “Alliance for Energy Transition” (56) project co-funded by the PRR - Recovery and Resilience Plan by the European Union.

References

[1] Prabhakaran, S., S. Sharma, A. Verma, S.M. Rangappa, and S. Siengchin. Mechanical, thermal, and acoustical studies on natural alternative material for partition walls: A novel experimental investigation. *Polymer Composites*, 43(7): p. 4711-4720, 2022.

[2] Manobala KS, Prabhakaran S, Ramji Gautham DR, Sathish Kumar M, Bala Ganesan, and N. C. Investigation of mechanical and thermal behaviour of natural sandwich composite materials for partition walls. *International Journal of Research and Review*, 7(5), 2020.

[3] Prabhakaran, S., V. Krishnaraj, S. Sharma, M. Senthilkumar, R. Jegathishkumar, and R. Zitoune. Experimental study on thermal and morphological analyses of green composite sandwich made of flax and agglomerated cork. *Journal of Thermal Analysis and Calorimetry*, 139(5): p. 3003-3012, 2020.

[4] Danaci, H.M. and N. Akin. Thermal insulation materials in architecture: a comparative test study with aerogel and rock wool. *Environmental Science and Pollution Research*, 29(48): p. 72979-72990, 2022.

[5] Mazzuca, P. Flexural behaviour of GFRP sandwich panels with eco-friendly PET foam core for the rehabilitation of building floors. *Structures*, 60: p. 105815, 2024.

[6] Ferreira, R., D. Pereira, A. Gago, and J. Proença. Experimental characterisation of cork agglomerate core sandwich panels for wall assemblies in buildings. *Journal of Building Engineering*, 5: p. 194-210, 2016.

[7] Prabhakaran, S., V. Krishnaraj, K. Shankar, M. Senthilkumar, and R. Zitoune. Experimental investigation on impact, sound, and vibration response of natural-based composite sandwich made of flax and agglomerated cork. *Journal of Composite Materials*, 54(5): p. 669-680, 2019.

[8] Oliveira, P., M. May, T. Panzera, and S. Hiermaier. Bio-based/green sandwich structures: A review. *Thin-Walled Structures*, 177: p. 109426, 2022.

[9] Frigione, M. and M. Lettieri. Durability issues and challenges for material advancements in frp employed in the construction industry. *Polymers*, 10, 2018.

[10] Su, B., T. Zhang, S. Chen, J. Hao, and R. Zhang. Thermal properties of novel sandwich roof panel made of basalt fiber reinforced plastic material. *Journal of Building Engineering*, 52: p. 104478, 2022.

[11] Jamshaid, H. and R. Mishra. A green material from rock: basalt fiber – a review. *The Journal of The Textile Institute*, 107: p. 1-15, 2015.

[12] Sadeghian, P., D. Hristozov, and L. Wroblewski. Experimental and analytical behavior of sandwich composite beams: Comparison of natural and synthetic materials. *Journal of Sandwich Structures & Materials*, 20(3): p. 287-307, 2016.

[13] Lakreb, N., U. Şen, E. Toussaint, S. Amziane, E. Djakab, and H. Pereira. Physical properties and thermal conductivity of cork-based sandwich panels for building insulation. *Construction and Building Materials*, 368: p. 130420, 2023.

[14] Mancuso, A., G. Pitarresi, and D. Tumino. Mechanical behaviour of a green sandwich made of flax reinforced polymer facings and cork core. *Procedia Engineering*, 109: p. 144-153, 2015.

[15] Hossain, D.*, et al.* Thermal and pyrolysis kinetics analysis of glass wool and xps insulation materials used in high-rise buildings. *Fire*, 6: p. 231, 2023.

[16] Todescato, D.*, et al.* Use of cork granules as an effective sustainable material to clean-up spills of crude oil and derivatives. *Environmental Science and Pollution Research*, 27(1): p. 366-378, 2020.

[17] Colomina, S., T. Boronat, O. Fenollar, L. Sánchez-Nacher, and R. Balart. High renewable content sandwich structures based on flax-basalt hybrids and biobased epoxy polymers. *AIP Conference Proceedings*, 1593(1): p. 467-470, 2014.

[18] Jiang, Q.*, et al.* Sustainable sandwich composites manufactured from recycled carbon fibers, flax fibers/pp skins, and recycled pet core. *Journal of Composites Science*, 5, 2021.

[19] Lakreb, N., B. Bezzazi, and H. Pereira. Mechanical behavior of multilayered sandwich panels of wood veneer and a core of cork agglomerates. *Materials & Design (1980-2015)*, 65: p. 627-636, 2015.

©2024 | 2_CARVALHO TEIXEIRA_Maria Helena_FZKM6.pdf:8

INVESTIGATION OF THE THERMOVISCOELASTIC BEHAVIOR OF A CLOSED-CELL POLYMER STRUCTURAL FOAM UNDER PRESSURE FOR PROCESSING IN HYBRID LCM PROCESSES

Sarah Dietrich[1], Christina Dohmen[1], Felix Frölich[1], Alexander Jackstadt[1], Florian Wittemann[1], Luise Kärger[1]

[1]Karlsruhe Institute of Technology (KIT), Institute of Vehicle System Technology - Lightweight Engineering, Rintheimer Querallee 2, 76131 Karlsruhe, Germany.
Email: sarah.dietrich@kit.edu, Web Page: https://www.fast.kit.edu/english/lbt/

Keywords: Dynamic Mechanical Analysis (DMA), PET Foam, compression-mode

Abstract
In order to accurately capture foam core deformations during manufacturing of sandwich structures in Liquid Compression Molding (LCM), in this work, the thermoviscoelastic behavior of a closed-cell Polyethylene terephthalate (PET) structural foam is investigated in compression mode. Three different densities of a closed-cell PET foam by AIREX® are considered: T92.80 with a density of $\rho \approx 85\,\mathrm{kg/m^3}$, T92.100 with $\rho \approx 100\,\mathrm{kg/m^3}$ and T92.130 with $\rho \approx 135\,\mathrm{kg/m^3}$. The foam exhibits a transversely isotropic material behavior due to its manufacturing in strangextrusion process. Compression tests are carried out in the temperature range between 30 °C and 150 °C on a Dynamic Mechanical Analysis (DMA) 242 E Artemis machine from NETZSCH. A strong decrease in storage modulus above the glass transition temperature T_g is observed, as well as an unexpected increase in storage modulus with increasing temperature below T_g. Various influences of the foam structure such as surface effects, orientation effects due to extrusion or the expansion of blowing agent residues on the observed increase in stiffness are investigated as potential causes for the stiffness increase below T_g.

1. Introduction

Structural polymer foams are gaining importance for sandwich components due to their potential to reduce weight and CO_2 emissions while maintaining good flexural stiffness. For a targeted and accurate design of the structural behavior and the manufacturing process of composite sandwich structures, for example in liquid compression molding (LCM), it is necessary to understand and model the time- and temperature-dependent structural behavior of the foams.

Investigations on the influence of temperature on shear and compression behavior of PET and Polyurethane (PUR) structural foams have been performed by Garrido et al. [1] and Mazzuca et al. [2], observing a strong degradation of stiffness and toughness with increasing temperature. Rezaei et al. [3] and Seuffert [4] also show in quasi-static compression tests, that the mechanical properties decrease when the glass transition temperature is exceeded. In addition to the density of the structural foam, the temperature has the greatest influence on the material behavior.

The thermoviscoelastic behavior of thermoplastic closed-cell structural foams has been investigated by Garrido et al. [1] in bending mode, and by Santo et al. [5] and Denay et al. [6] in compression mode. While Garrido et al. [1] report a continuous decrease in storage modulus in the measured temperature

range in dual cantilever mode, similar to homogeneous materials, the DMA tests in compression mode by Santo et al. [5] on PET foam and by Denay et al. [6] on PUR foam show an increase in storage modulus with increasing temperature in the range below the glass transition temperature. Santo et al. [5] justify the measured increase in storage modulus with the collapse of foam cells and Denay et al. [6] argue that it is a structural effect of the foam due to a morphological change.

The cell morphology of the AIREX® T92 series under investigation has been analyzed by Fathi [7]. He shows in his work that the process-related cell morphology has a strong effect on the anisotropy and mechanical behavior of strand foams. The foams of the AIREX® T92 series have hexagonal strands of different sizes and differ in the wall thickness of the strand border zone. The T92.100 foam exhibits the highest strand bulk cell diameter and lowest strand border cell diameter amongst the three considered foam densities.

Static characterization test results are obtained by Seuffert [4] for the structural foam of the AIREX® T92 series, which provide material parameters for the behavior at individual temperatures. However, the stiffness of the foam core as a function of temperature is important for mapping the thermomechanical behavior during manufacturing in an LCM process. For this purpose, the viscoelastic behavior of the closed-cell AIREX® PET structural foam is investigated in this work, using DMA in compression mode.

2. Experimental setup

Three densities of a closed-cell PET structural foam by AIREX® are studied: T92.80 with $\rho \approx 85$ kg/m^3, T92.100 with $\rho \approx 100$ kg/m^3 and T92.130 with $\rho \approx 135$ kg/m^3. The foams have been manufactured in a strangextrusion process and thus, show a transversally isotropic behavior as they exhibit a hexagonal honeycomb structure with elongated cells and aligned monomer chains in extrusion direction.

The experiments are performed on a DMA 242 E Artemis machine by NETZSCH in compression mode in a parallel plate measurement system. A temperature range from 30 °C to 150 °C is tested with a heating rate of 1 K/min between the isothermal steps every 5 K and sample dimensions of 7.5 mm diameter and a height of 3 mm. The material behavior is determined in the frequency range between 0.1 Hz and 50 Hz. The setup of the compression DMA is represented in Figure 1 along with the acting forces. A constant static force is used to ensure that the sample is in contact with the load-introducing stamp at all times. The static force is superimposed by a dynamic force resulting from a fixed defined amplitude and an additional static force due to a proportionality factor $p > 1$ applied to the dynamic force. The load specifications are defined based on preliminary stress sweeps and cyclic tests.

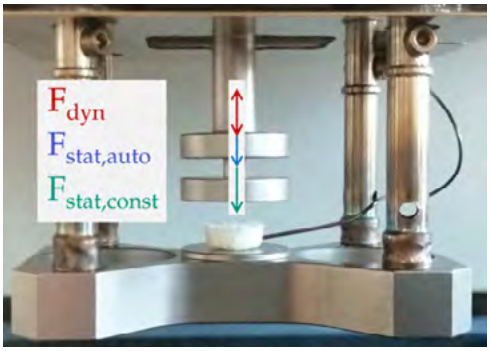

Figure 1: Sample holder of the NETZSCH 242 E Artemis DMA in pressure mode with representation of the force direction and superposition. An AIREX® T92.100 foam sample with a diameter of 7.5 mm and a height of 3 mm is placed on the sample holder.

The loads are summarized in Table 1 for the different foam density types. The amplitude is chosen

smaller for higher densities due to the maximum force of the used DMA machine. The dynamic load F_{dyn} is determined by the prescribed amplitude A and limited by the maximum dynamic load $F_{\mathrm{dyn,max}}$ due to machine specifications. The additional static load $F_{\mathrm{stat,auto}} = p\,F_{\mathrm{dyn}}$ is the dynamic load multiplied by the proportionality factor.

Table 1: Load specifications for the three investigated foam density types.

		T92.80	T92.100	T92.130
$F_{\mathrm{stat,const}}$	Static Force	1.5 N	2 N	3 N
A	Amplitude	19 µm	13 µm	10 µm
p	Proportionality Factor	1.3	1.3	1.3
$F_{\mathrm{dyn,max}}$	Maximum Dynamic Force	8 N	7.69 N	6.9 N

In order to investigate a possible expansion of blowing agent residues or water solved in the polymer with increasing temperature, a second campaign is performed, where the samples are tested cyclic. After the first test cycle, they are tempered for 10 hours at 150 °C, then cooled down with 2 K/min and tested a second time with the same test specifications. The second cycle is stopped when reaching a temperature of 110 °C because the range of interest is located between 30 °C and 80 °C. Another sample is tempered at 150 °C for 116 hours to ensure diffusion of blowing agent remains out of the polymer foam. In a next step, the open cells at the bottom and top of the samples are filled with fine filler to improve load introduction and investigate the influence of the open boundary cells due to cutting. The samples are tested in the extrusion direction by default. However, isolated tests are performed vertically to the extrusion direction to analyze the influence of the material orientation on the viscoelastic behavior.

3. Results

The storage modulus and loss factor of the untreated samples, tested in extrusion direction, are represented in Figure 2 for the structural foams T92.130, T92.100 and T92.80, respectively. The loss factor shows a peak between 75 °C and 97 °C, depending on frequency and density, corresponding to the softening range of PET. For the storage modulus, an increase with increasing temperature is observed between 30 °C and $65-75$ °C and a strong decrease for temperatures above. The same increase of storage modulus with rising temperature below T_{g} was reported in literature [5, 6]. The increase in storage modulus is highest for T92.100, which was reported by Fathi [7] to have the highest cell diameters, which, in conjunction with a medium density, leads to higher thickness of the cell walls compared to cell size. The same behavior is observed for samples tested vertically to the extrusion direction.

The results of the cyclic tests in the second campaign are shown in Figure 3. In the second cycle, after tempering fo 10 h at 150 °C a slight shift of the maximum of the loss factor towards higher temperatures can be observed, which is explainable by diffusion of water or blowing agent residues during tempering. However, the increase in storage modulus remains within the same order of magnitude. The observed increase in the second cycle is less pronounced for temperatures between 30 °C and 50 °C than in the first cycle and T_{g} is shifted towards higher temperatures. The same behavior is observed for samples, tempered for 116 hours at 150 °C and tested afterwards. The storage modulus is lower for the tempered samples, which can be explained by starting degradation of the polymer due to the heat treatment or different foam structures in the compared (tempered and untreated) samples (more or less strand bulk cells), but the increase below T_{g} remains unchanged. Moreover, the cyclic tests show, that the stiffness increase is a reversible phenomenon, because it occurs in a similar way in the second cycle. Thus, the storage modulus increase below T_{g} cannot be traced back to a collapsing cell structure as stated by Santo et al. [5].

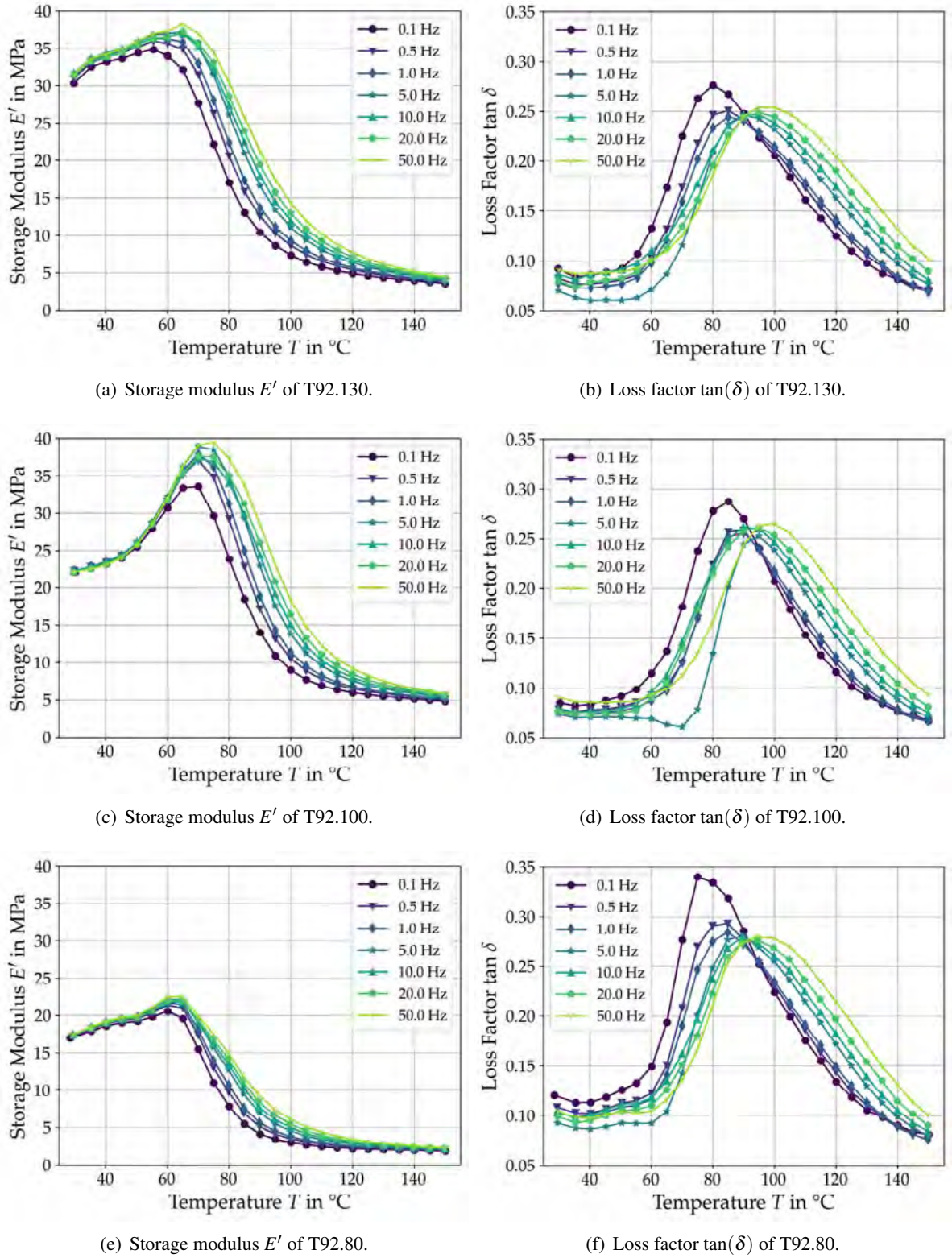

(a) Storage modulus E' of T92.130.

(b) Loss factor $\tan(\delta)$ of T92.130.

(c) Storage modulus E' of T92.100.

(d) Loss factor $\tan(\delta)$ of T92.100.

(e) Storage modulus E' of T92.80.

(f) Loss factor $\tan(\delta)$ of T92.80.

Figure 2: Storage modulus (a, c, e) and loss factor (b, d, f) of the foams T92.130 (a, b), T92.100 (c, d) and T92.80 (e, f), at different frequencies tested in step-wise isothermal mode every 5 K, showing an increase of storage modulus between 30 °C and 65 °C before the softening range while the loss factor shows one peak between 75 °C and 97 °C, depending on frequency and density, corresponding to the softening range.

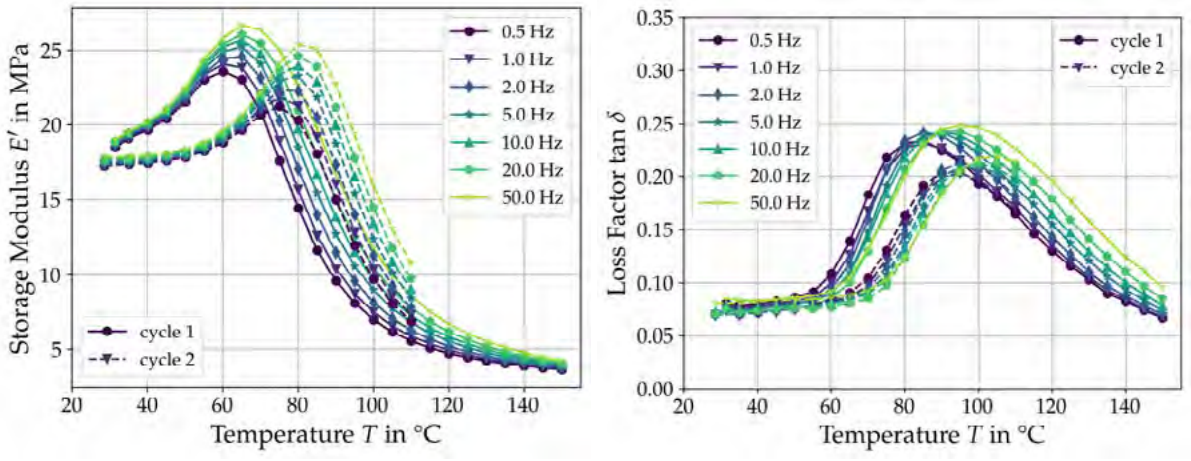

(a) Storage modulus E' of T92.130.

(b) Loss factor $\tan(\delta)$ of T92.130.

Figure 3: Storage modulus (a) and loss factor (b) of one sample of T92.130 tested twice in step-wise isothermal mode in one clamping. After the first DMA cycle (cycle 1), the sample is held at 150 °C for 10 h without loading and then cooled down with 2 K/min. Afterwards, the test is run a second time with the same loads (cycle 2).

Another possible explanation for the observed effect is, that the force is not introduced homogeneously into the samples. As the specimen are cut from a closed-cell foam, in the boundary area lower stiffness is expected, because the cells are cut open there. A possible effect could be, that in the beginning, the tips of the open cell walls are tested, which soften with rising temperature and are compacted more and more, introducing part of the load into the closed-cell structure in the progress. Therefore, tests have been performed on specimens with filled cells on top and bottom as shown in Figure 4 in order to introduce the load more direct into the closed-cell part of the foam.

Figure 4: Foam sample filled at the top and bottom surface with fine filler for better load distribution and introduction into the closed-cell inner section of the foam.

However, Figure 5 shows, exemplary for foam T92.100, that the increase in storage modulus persists with filled boundary cells. The overall stiffness increases, but the relative change in storage modulus below T_g stays the same. Thus, the open boundary layer can be excluded as cause for the observed increase in storage modulus with increasing temperature.

In compression mode, thermal expansion of the polymer could be another possible explanation for measuring an increase in storage modulus with increasing temperature, as the thermal expansion imposes an additional pressure against the compression direction. However, an upwards estimation of thermal strain leads to results that are smaller than the measured phenomena and cannot be correlated to the results for the different foam densities. The T92.100 foam shows the highest increase in storage modulus, although

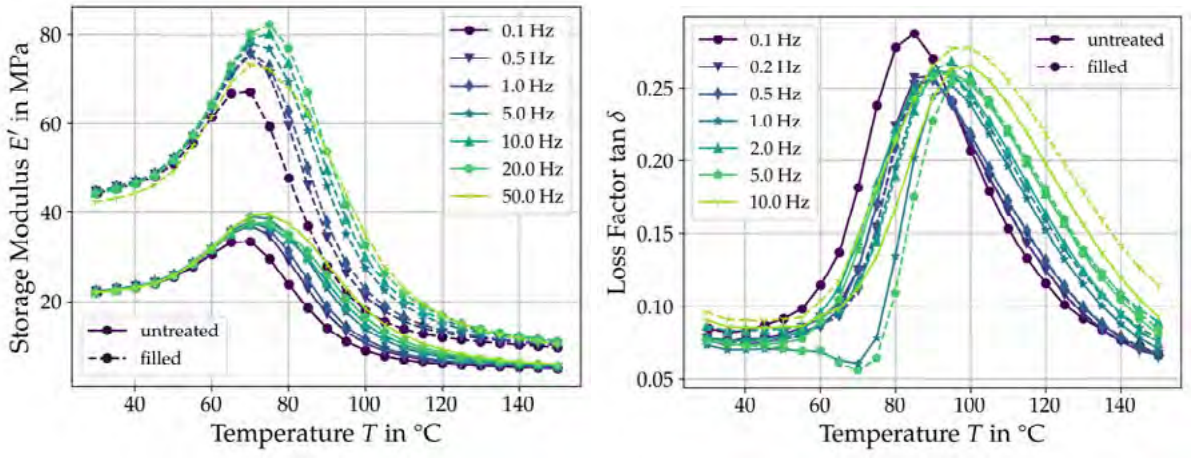

(a) Storage modulus E' of T92.100.

(b) Loss factor tan(δ) of T92.100.

Figure 5: Comparison of storage modulus (a) and loss factor (b) of T92.100 at different frequencies tested in step-wise isothermal mode every 5 K for an untreated and a surface-filled sample. The solid lines show the results for an untreated sample as in Figure 2 (c), (d) and the dashed lines for a sample with filled surface.

T92.130 has the highest density and thus, should have the highest thermal strain. Moreover, as the loss factor does not show unexpected behavior, the observed effect is likely to be due to the foam structure and not due to material effects of the PET.

Since in literature, the increase of storage modulus below T_g was only observed in compression and not in bending mode, a possible reason for the measured stiffness increase, is the static force, which is necessary in compression mode to ensure that the sample is in permanent contact with the stamp. As the static force is independent of the material stiffness, the softening of the polymer material due to higher temperatures might lead to a shift towards higher total strains, where the foam structure shows a non-linear stress-strain-relation due to the cell morphology and thus, a higher storage modulus is measured. However, this hypothesis has to be verified still.

4. Conclusion

In this work, different DMA campaigns in compression mode have been performed on a closed-cell PET foam by AIREX® in three different densities to analyze the thermoviscoelastic behavior. Specifically the observed increase in storage modulus below glass transition temperature has been investigated, which was also reported in literature for comparable foams tested in compression mode. Post-expansion of blowing agent residues as well as additional gas pressure in the cells due to temperature increase and evaporating water could be excluded as cause by cyclic tests and tempered samples. Moreover, surface effects were studied and did not show an effect on the observed increase in storage modulus, either. The effect was observed to be independent of material orientation.

However, the reason for the stiffness increase could not yet be clearly determined. Collapsing foam structure could also be excluded as cause for the observed effect, as the increase in storage modulus with rising temperature below T_g was shown to be reversible in cyclic tests. Morphological changes of the foam structure seem to be a more reasonable explanation. The static force was identified as possible cause for morphological changes leading to a nonlinear stress-strain-relation. As a next step, DMA tests are planned with varying static forces to further investigate this hypothesis.

Acknowledgments
The funding by the German Research Foundation (DFG) within the project "Modelling of the fluid-structure interaction in mold filling processes for an intrinsic manufacturing of fiber-reinforced composite sandwich components (FSI-Sandwich)" (project KA 4224/9-1 and HE 6154/8-1) is gratefully acknowledged. A special thank goes to the Institute for Pulsed Power and Microwave Technology (IHM) for providing the DMA machine.

References

[1] M. Garrido, J. R. Correia, and T. Keller. Effects of elevated temperature on the shear response of PET and PUR foams used in composite sandwich panels. *Construction and Building Materials*, 76: 150–157, 2015. ISSN 0950-0618. doi: 10.1016/j.conbuildmat.2014.11.053.

[2] P. Mazzuca, J. P. Firmo, J. R. Correia, and E. Castilho. Mechanical behaviour in shear and compression at elevated temperature of polyethylene terephthalate (PET) foam. *Journal of Building Engineering*, 42:102526, 2021. ISSN 2352-7102. doi: 10.1016/j.jobe.2021.102526.

[3] M. Rezaei, V. Karatzas, C. Berggreen, and L. A. Carlsson. The effect of elevated temperature on the mechanical properties and failure modes of GFRP face sheets and PET foam cored sandwich beams. *Journal of Sandwich Structures & Materials*, 22(4):1235–1255, 2020. ISSN 1099-6362. doi: 10.1177/1099636218781995.

[4] J. Seuffert. *Mold-filling Simulation of Resin Transfer Molding with Fluid-Structure Interaction*. Doctoral Thesis, Karlsruher Institut für Technologie (KIT), Karlsruhe, 2022. doi: 10.5445/IR/1000144393.

[5] L. Santo, D. Bellisario, and F. Quadrini. Shape Memory Behavior of PET Foams. *Polymers*, 10(2): 115, 2018. doi: 10.3390/polym10020115.

[6] A.-G. Denay, S. Castagnet, A. Roy, and G. Alise. Creep compression behaviour of a polyurethane foam from cryogenic temperatures: Size effect and long-term prediction. *EPJ Web of Conferences*, 6:25006, 2010. doi: 10.1051/epjconf/20100625006.

[7] A. Fathi. *Mechanical Properties of Strand PET Foams at Different Length Scales*. PhD thesis, Bayreuth, 2018.

©2024 | 2_DIETRICH_Sarah_U5DDE.pdf:7

CONTROLLING DUAL SCALE MORPHOLOGIES OF EPOXY AND POLY(ETHERIMIDE) TOWARDS IMPROVED INTERLAYER TOUGHENING OF COMPOSITES

U. Farooq, J. Teuwen and C. Dransfeld

Faculty of Aerospace Engineering, Delft University of Technology, Kluyverweg 1, Delft, The Netherlands
Email: c.a.dransfeld@tudelft.nl

Keywords: Diffusion, Interphase, Phase Separation, Toughening, Fracture

Abstract
A common approach to toughen epoxy matrix systems is to dissolve a thermoplastic phase, in the uncured thermosetting monomers. These can interdiffuse within the thermoplastic, followed by reaction-induced phase separation, leading to intricate graded morphologies with a high fracture toughness. Here, we first architect the thermoplastic phase, made of poly(etherimide) films as a macroscopic layered scaffold, and infiltrate it by an epoxy system, leading to dual-scale morphologies with distinct spatial control of morphological feature at the microscopic and macroscopic scale. The fracture toughness of the modified epoxy system is investigated as a function of varying cure temperature (120–200 °C) for interphase formation and poly(etherimide) film thickness (50–120 µm). Results show that the fracture toughness of the heterogeneous system is mainly controlled by the macroscopic feature, the final PEI layer thickness. Remarkably, as the PEI layer thickness exceeds the plastic zone around the crack tip, around 60 µm, the fracture toughness of the dual scale morphology surpasses the property of bulk PEI. Additionally, decreasing the gradient microscale interphase morphology triggers higher crack tortuosity, which seems to be the dominating mechanism for the synergistic toughening. Ultimately, this knowledge will lead to novel toughening approaches to increase the damage tolerance of fibre reinforced composites by suppressing delamination damage modes.

1. Introduction

In structural applications, fibre reinforced polymers are subjected to high static and dynamic loadings that call for a high damage tolerance and fracture toughness. However, epoxy-based thermosetting matrix systems have high cross-link densities to achieve sufficiently high glass transition temperatures, which generally leads to low fracture toughness. Therefore, many methods are thought of to improve its fracture toughness. Bulk resin modification is the process of adding a second phase—such as rubber, inorganic nanoparticles, or thermoplastics—to the epoxy matrix via a variety of techniques [1]. During the epoxy curing step, these tougheners typically create morphologies that improve the system's fracture toughness. Unfortunately, adding a tough phase to the epoxy system can limit the system's end-use temperature and lower the system's total modulus for elastomeric tougheners. In addition, bulk resin modification—mainly through thermoplastics—may also cause the resin system's processing viscosity to drastically rise, rendering them inappropriate for liquid composite moulding.

Various approaches have been explored to toughen brittle materials on different scales: One macro-scale approach consists of introducing ductile interlayers into brittle materials, leading to toughening through the *inhomogeneity effect*. This effect involves spatial variations in material properties influencing crack propagation. Ductile interlayers act as crack arresters, significantly increasing fracture toughness without a substantial loss in strength. Studies by Sistaninia et al. [2] demonstrate the effectiveness of this approach, emphasizing the importance of heterogeneous materials architectures to enhance fracture toughness.

At the microscale, toughening of epoxy systems is mostly achieved by adding an amorphous thermoplastic like poly(etherimide) (PEI) or poly(ethersulfone) (PES). This addition leads to the dissolution, followed by phase separation induced morphologies within the epoxy, resulting in a significant increase in fracture toughness by the intrinsic contribution of the tougher thermoplastics and also by crack deflection in the phase-separated systems. Alternatively, using a thermoplastic film or discrete powder deposition as an interlayer in prepregs allows for the diffusion of reactive monomers into the thermoplastic with spatial control, inducing phase separation and creating a gradient morphology in the interfacial zone [3], thus overcoming processability constraints.

The aim of this study was to investigate heterogeneities of PEI at the macro and microscale in a brittle epoxy system to deconvolute their respective effects on fracture toughness. With this objective PEI scaffolds with periodic arrangement of film were infiltrated with a brittle epoxy system and subjected to different cure cycles leading to varying degrees of dissolution and micro-scale gradients. The cured sample here is characterized through a single edge notched beam test.

2. Materials and Methods

Films of poly(etherimide) (ULTEM 1000, SABIC, Saudi Basic Industries Corporation), with a molecular weight 55,000 g/mol, and a glass transition of Tg = 217 °C, with thicknesses of 50, 60, 90, and 120 μm), were used as the tough phase. The epoxy systems was formulated as a blend of M-(2,3-epoxypropoxy)-N,N-bis(2,3- epoxypropyl)aniline (TGMAP, Araldite MY 0610 CH), and bisphenol-F epoxy resin monomer (DGEBF, Araldite PY 306 CH). 3,3′-sulfonyldianiline (DDS, Aradur 9719-1) all supplied by Huntsman Advanced Materials, Switzerland, resulting in a high Tg (around 200 °C).

First, PEI scaffolds were prepared by stacking the PEI films periodically in a 1:2 ratio of equal thickness as obtain scaffolds with 33 vol % fraction of PEI, respectively, with a porosity of 66% to be infiltrated by the epoxy system. Then, the epoxy system was then infused into the PEI. Infiltration occurred dominantly spontaneously through capillary action. Once the infiltration step was completed, samples were placed in a preheated oven at a selected cure temperature. The dimensions of the scaffolds were as follows: length = 120 mm, width = 26.4 mm, and thickness = 6 mm. Each scaffold allowed to extract nine samples, which were used for further analysis.

The experimental principle is represented in Figure 1 and shows an arrangement of the scaffold in respect to principal crack direction. Table 1 lists all configurations between original film thickness and curing cycles, note that the PEI volume fraction was kept constant for all experiments.

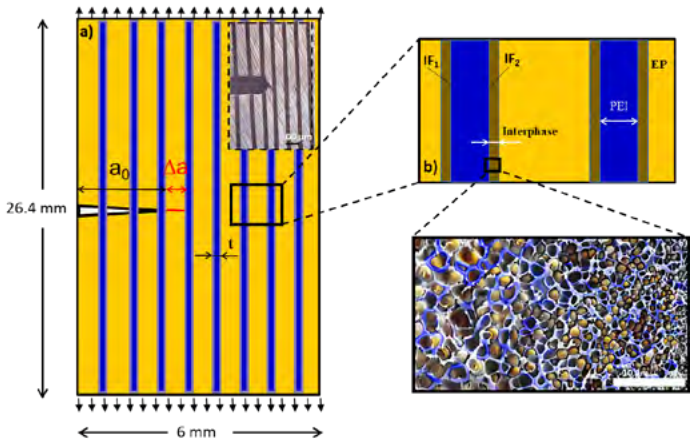

Figure 1 – (a) schematics of the experimental variables, including original PEI film thickness t with a constant pitch of 3t, and cure depending on interphase dimensions and morphology. (b) representation of different regions in the multilayered sample; PEI = poly(ether imide) (blue) EP = epoxy (yellow), IF1 = interface 1, and IF2 = interface 2.

The fracture toughness of the specimens was determined by single-edge notched bending (SENB) testing according to the ASTM D5045-99 standard. The dimensions of the SENB sample had a length = 26.4 mm, a width = 6 mm, and a thickness = 3 mm.

Table 1 Scaffold and curing parameters investigated [4]

PEI Thickness (µm)	*Cure Temperature (°C)*	*Sample ID*	*Number of PEI layers*	
50	120 140 160 180 200	5P12 5P14 5P16 5P18 5P20	40	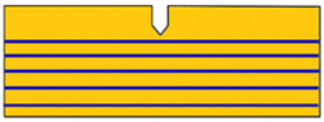
60	120 140 160 180 200	6P12 6P14 6P16 6P18 6P20	33	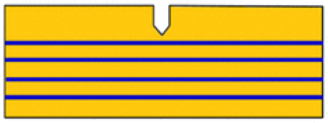
90	120 140 160 180 200	9P12 9P14 9P16 9P18 9P20	22	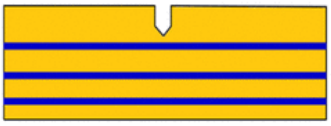
120	120 140 160 180 200	12P12 12P14 12P16 12P18 12P20	17	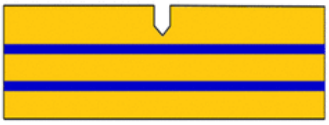

Specimen features, such as crack path and phase morphology were investigated with confocal laser scanning microscopy (CLSM) and scanning electron microscopy (SEM) at higher resolutions.

3. Results

CLSM and SEM were used to study the interphase development of epoxy and PEI at various cure temperatures. Figure 3 illustrates a multilayer sample with a 90 µm PEI layer that was cured at 160 °C (1st dwell temperature). The sample's CLSM image (Figure 3a) shows that the brittle epoxy contains parallel PEI layers that are uniformly dispersed. Simultaneously, Figure 3b displays a magnified SEM picture of two successive PEI layers and two interphase regions, each with a thickness of roughly 61 µm. Figure 3c shows a noticeable gradient in morphology between the pure epoxy (left) and pure PEI (right) interfaces. A noticeable morphological gradient has formed in Figure 3c between the interface of the epoxy system (left) and PEI (right). It shows the occurrence of epoxy-rich droplets in a continuous PEI matrix near the pure epoxy interface. They shrink gradually near the pure PEI region due to the rise in PEI concentration. Similar results were also obtained for the other temperatures.

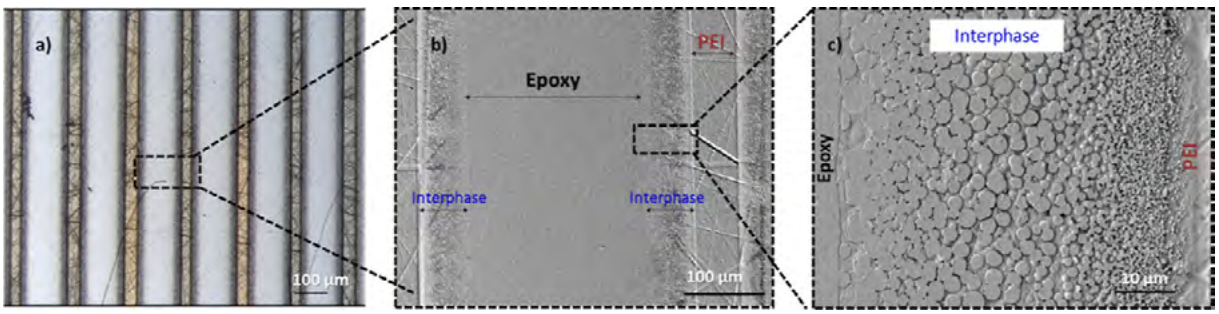

Figure 2 – Microscopic analysis reveals the dual-scale heterogeneous architecture at various scales [4]

The fracture toughness of the SENB samples is reported in Figure 3a, the low toughness of the pure epoxy system seems to be independent of the examined cure temperatures. However, the toughness of

the heterogeneous systems seems to decrease with increasing curing temperature. A correlation to the initial film thickness seems less conclusive. Interestingly, samples cured at lower temperatures seem to surpass the fracture toughness values of the tougher constituent, pure PEI. All reported values seem to be above a linear rule of mixture between the brittle epoxy system and the tough PEI.

These observations lead to an interest in the scaffold geometry after interphase formation: For a given scaffold film thickness, increasing the curing temperature leads to an increased diffusion and interphase dimension, resulting in a reduction of the remaining (final) PEI film thickness, as can be seen in Figure 3b. It also became apparent that the rate of dissolution vs temperature seems larger at lower temperature and seems to somewhat saturate at higher temperatures. The very thin PEI films of 50 µm do, however entirely dissolve at a curing temperature of 200°C.

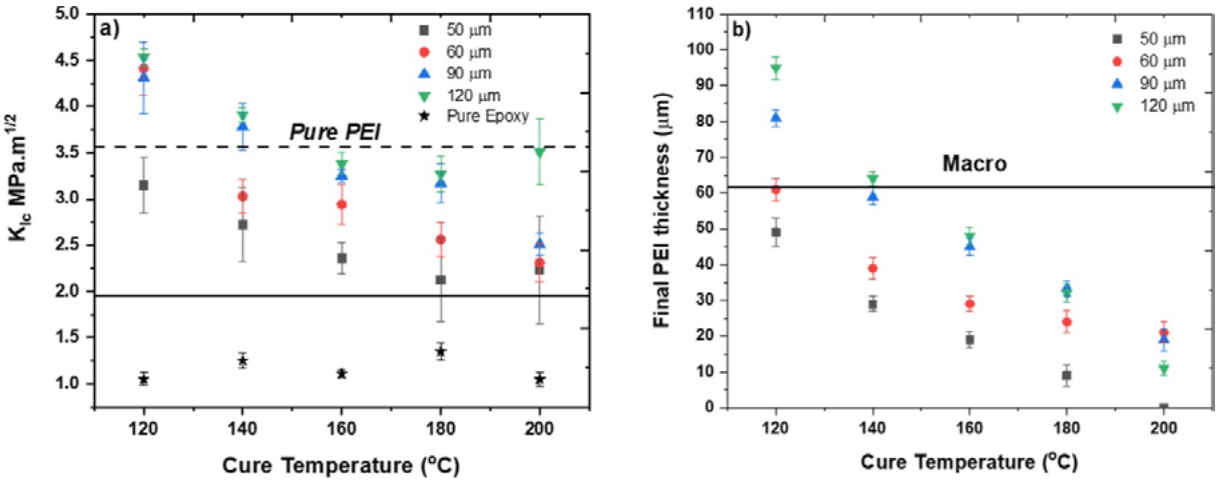

Figure 3 – Left: Fracture toughness (KIc) of SENB specimen made from different PEI film thickness with varying cure temperature, the dashed line represents the fracture toughness of pure PEI, while the solid line represents the corresponding target value in a simple rule of mixture. Right: Resulting PEI film thickness after partial dissolution as a function of cure temperature, the solid line represents the size of the plastic zone for pure PEI [4]

4. Discussion

To better understand the effect of scales of the heterogeneous architecture, the size of the plastic zone of the tough PEI phase was estimated, according to Irwin, for plane strain conditions to be about 62 µm

$$Plastic\ zone\ size = \frac{1}{6\pi}\frac{k^2}{\sigma^2} \quad (1)$$

Assuming a stress intensity factor k of 3.45 MPa.m$^{1/2}$ and a yield stress σ of 105 MPa for PEI. Representing the fracture toughness versus the macroscopic feature of the heterogeneity, the remaining (final) PEI films thickness, as shown in Figure 4, a clear trend emerges: The fracture toughness seems to correlate to the dimension of the tougher phase. Already at small final PEI thickness, the fracture toughness seems to exceed a simple rule of mixture expected for a homogeneous blend. It is hypothesized that the phase separated micro-scale heterogeneity is already contributing to the dissipative mechanism here. More interestingly, when the PEI film thickness exceeds the size of the plastic zone, the system fracture toughness exceeds the fracture toughness of the pure bulk PEI. The fracture path undergoes macroscopic change, which was captured by determining the crack tortuosity τ, which is a dimensionless expression of crack pat length with respect to its shortest path.

$$\tau = \frac{macroscopic\ crack\ length}{sample\ height} \quad (2)$$

With the final PEI thickness exceeding the size of the plastic zone, as shown in Figure 5, the macroscopic crack morphology gradually evolves to very high crack tortuosity values τ up to 2, the significant extension of the crack path is the root of the synergistic toughening effect leading to a higher fracture toughness than its tougher constituents.

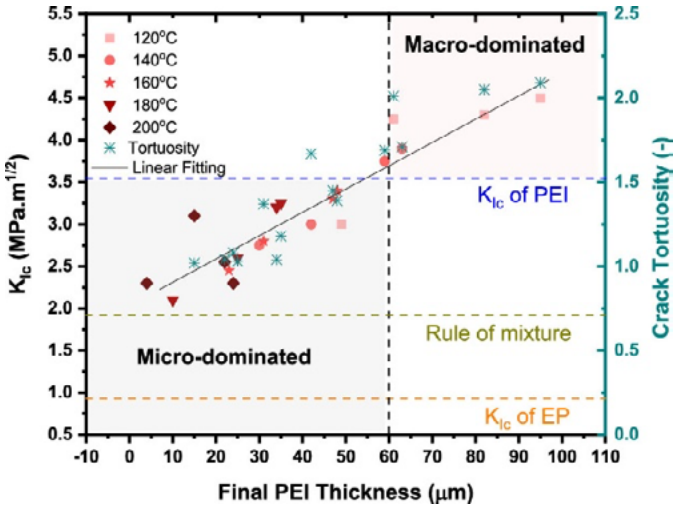

Figure 4 - Fracture toughness (KIc) and crack tortuosity as a function of the final PEI thickness obtained after curing. The vertical dashed line represents the size of the plastic zone (rp = 62 µm) of PEI; the horizontal blue and orange lines represent the fracture toughness of the bulk PEI and Epoxy systems, respectively [4]

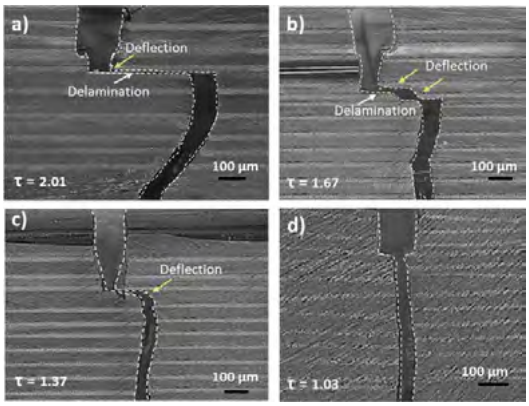

Figure 5 – Crack tortuosity analysis: CLSM images of a PEI/epoxy system with a 60 µm PEI layer cured at (a) 120 °C, (b) 140 °C, (c) 160 °C, and (d) 180 °C, corresponding to reducing final PEI thickness. Yellow arrows represent deflection, and white arrows show delamination. τ is the crack tortuosity [4]

5. Conclusion

It has been observed in nature, that principles of tailoring heterogeneous brick and mortar systems [5] allow to reach significant synergies in strength and damage tolerance. However, these effects refer to the contrasting stiffness of the brick and the soft mortar. Here, we have demonstrated that systems have the very similar elastic modulus but contrasting fracture toughness, interesting architecting option can be put into practice.

In choice of architecture, the size of the fracture process zone of the tougher phase is a relevant dimension and dictates the scale of the dominant heterogeneity. In a layered heterogeneity, the penetrating work of fracture must be high enough to promote deviatoric or delamination work of

fracture, leading to significant crack tortuosity. Hence, further controlling the balance of these failure modes will require more attention in future work.

References

[1] U. Farooq, J. Teuwen, and C. Dransfeld, "Toughening of Epoxy Systems with Interpenetrating Polymer Network (IPN): A Review," (in eng), *Polymers (Basel),* vol. 12, no. 9, Aug 24 2020, doi: 10.3390/polym12091908.

[2] M. Sistaninia, R. Kasberger, and O. Kolednik, "To the design of highly fracture-resistant composites by the application of the yield stress inhomogeneity effect," *Composite Structures,* vol. 185, pp. 113-122, 2017, doi: 10.1016/j.compstruct.2017.10.081.

[3] J. Cugnoni *et al.*, "Towards aerospace grade thin-ply composites: Effect of ply thickness, fibre, matrix and interlayer toughening on strength and damage tolerance," *Compos. Sci. Technol.,* vol. 168, pp. 467-477, 2018/11/10/ 2018, doi: 10.1016/j.compscitech.2018.08.037.

[4] U. Farooq, E. Sakarinen, J. Teuwen, R. Alderliesten, and C. Dransfeld, "Synergistic Toughening of Epoxy through Layered Poly(ether imide) with Dual-Scale Morphologies," *ACS Applied Materials & Interfaces,* 2023/11/02 2023, doi: 10.1021/acsami.3c10096.

[5] M. Grossman, D. Pivovarov, F. Bouville, C. Dransfeld, K. Masania, and A. R. Studart, "Hierarchical Toughening of Nacre-Like Composites," *Adv. Funct. Mater.,* vol. 29, no. 9, p. 1806800, 2019, doi: 10.1002/adfm.201806800.

DO BASALT FIBERS CORRODE IN HIGHLY ALKALINE ENVIRONMENTS?

Susana Garcia-Mayo[1,2], Hubert Rahier[2] and David Seveno[3]

[1]Department of Materials Engineering, KU Leuven, Kasteelpark Arenberg 44, 3001 Leuven, Belgium
Email: susana.garciamayo@kuleuven.be
[2]Research Group of Physical Chemistry and Polymer Science, Department of Materials and Chemistry, Vrije Universiteit Brussel, Pleinlaan 2, B-1050, Brussels, Belgium
Email: hubert.rahier@vub.be
[3] Department of Materials Engineering, KU Leuven, Kasteelpark Arenberg 44, 3001 Leuven, Belgium
Email: david.seveno@kuleuven.be, Web Page: https://complexurf.be/

Keywords: basalt, corrosion, textile-reinforced concrete, fibers

Abstract
The construction industry is moving towards sustainability, by reducing CO_2 emissions and resource consumption. Textile Reinforced Concrete (TRC) is emerging as a sustainable alternative to traditional materials, offering reduced weight and improved mechanical properties. The choice of textile is crucial for the composite's final properties. Basalt fibers arise as a promising alternative for their ability to maintain mechanical properties at high temperatures and their corrosion resistance, essential in hars environments, though their performance in alkaline conditions is debated. Our research corrosion effects on basalt fibers and the role of the sizing. We have employed physico-chemical methods including XRF, and SEM for composition and surface analysis, alongside wettability and tensile tests. Results showed basalt fibers retain their mechanical strength after 72 and 168 hours in alaline conditions at room temperature, indicating good resistance. However, both pristine and desized fibers weaked when boiled in alkaline solutions for 30 minutes. Understanding basalt fiber's properties and corrosion influence is vital for their optimal use in cement-based structures.

1. Introduction

In recent years, basalt fibers have become prominent as an eco-friendly inorganic material due to their widespread availability, good mechanical properties, chemical resistance, and high-temperature resistance. The latter is of particular importance when discussing structural applications, as basalt fibers retain a significant portion of their mechanical properties when exposed to elevated temperatures. After being exposed to 600 C, basalt fibers retain up to 90% of their tensile strength at normal temperatures [1], in comparison to s-glass and carbon fibers, retaining around 50%[1], [2]. This property has focused attention on its potential application in the construction sector, in the role of fiber reinforcement for textile-reinforced concrete (TRC), which emerges as a sustainable alternative to conventional construction materials, due to their potential material usage reduction and weight decrease [3]. Besides the inherent benefits of using TRCs, i.e. increase in the load-bearing capacity, and increase in resistance to cracking and spalling, basalt fibers would provide the necessary structural integrity at high temperatures, such as in the event of a fire [4].

One of the primary requirements for fibers used in TRCs is the chemical resistance. The aggressive environment associated with the high alkalinity of concrete matrices results in the corrosion of traditional reinforcement alternatives, such as steel bars. However, the chemical resistance of basalt fibers remains a topic of discussion. While certain studies suggest remarkable resistance of basalt fibers to corrosion [1],[5], others indicate potential changes in the fiber structure when exposed to highly alkaline conditions [6], [7], [8]. A plausible reason for this difference in results could be caused by the

impact of the sizing commonly present in commercial basalt fibers and the lack of a standardized test to corrode the fibers that could make the results from different studies comparable.

Therefore, this study aims to shed light on the corrosion resistance of basalt fibers and the possible divergences caused by the lack of a standardized approach and the impact of the different sizings.

2. Experimental

Basalt fiber samples used in this study were supplied by Basaltex (Wevelgem, Belgium). The chemical composition of the commercial fibers was determined by X-ray fluorescence and is detailed in Table 1. Additional traces of MnO and P_2O_5 were found in quantities lower than 0.5wt%.

Table 1. Chemical composition (wt%) of the basalt fiber sample.

SiO_2	Al_2O_3	Fe_2O_3	CaO	MgO	Na_2O	K_2O	TiO_2
53.10	15.60	12.10	9.12	3.75	2.57	1.79	1.33

2.1. Desizing process

Commercially available basalt fibers are usually coated with a layer of sizing agent. Primarily, the fibers' sizing was removed by immersing them in acetone at room temperature and sonicating them in an ultrasonic bath for 4 hours. The acetone was refilled every hour to compensate for evaporation.

2.2. Corrosion tests

For studying the impact of the different corrosion tests on both pristine and desized fibers, the samples were immersed in a 1 M NaOH aqueous solutions for different periods of time and at different temperatures, detailed in Table 2. The solutions were not renewed during the experiment and no stirring was used.

Table 2. Corrosion tests.

NaOH concentration (mol/L)	*Time (hours)*	*Temperature*
1	72	Room T
1	168	Room T
1	0.5	Boiling
1	1	Boiling

2.3. Characterization techniques

Both pristine and desized sample diameters of a minimum of 10 single fibers were measured using a Dia-Stron FDAS770 (Dia-Stron Ltd, Hampshire, UK), equipped with a high-frequency laser scanning micrometer. The diameter of each fiber was measured at three axial positions on the fiber and three angular positions of the laser.

The sample mechanical properties were measured with the Dia-Stron LEX820 linear extensometer (Dia-Stron Ltd, Hampshire, UK). The tests were performed according to ASTM C1557-14, using a gauge length of 12 mm and a speed of 1.5 mm/min.

Contact angles of 5 single fibers per sample were measured with a Krüss K100SF high-precision force tensiometer (Krüss GmbH, Hamburg, Germany), with a weight resolution of 0.1 µg. During the experiments, a single basalt fiber was attached to the sample holder and set perpendicular to the surface of the test liquid. The instrument allows for characterizing the wettability of single fibers according to

the Wilhelmy method [9]. The fibers were washed in milliQ water at room temperature for 5 minutes to obtain clean surfaces without affecting the sizing typically present on commercial basalt fibers. The main properties of the test liquids (*n*-hexane, VWR Chemicals; ultrapure water, RephiLe Bioscience Ltd.,) are listed in Table 3.

Table 3. Liquid/vapor surface tension and density of the probe liquids.

Liquid	γ_{LV} (mN/m)	ρ (g/cm^3)
n-hexane	18.4	0.659
Ultrapure water	72.8	0.98

Scanning electron microscopy (SEM) analysis was performed using a Philips XL 30 FEG apparatus, using secondary emitted electrons (SE) for studying the topography of the samples, at 10 kV acceleration voltage. The fibers were sputter-coated with a 5 nm layer of Pt/Pd to avoid surface charging.

3. Results

3.1. Impact of the sizing

Figure 1 shows the mechanical properties of the commercial basalt fibers pristine and after being desized. The results show that the desizing process has no impact on the mechanical properties of the fibers. Commercial fibers commonly contain a sizing that varies from 0.4 to 1%. Combined with the fibers' diameter variability due to the manufacturing spinning or extrusion process [10], makes it impossible to detect a diameter variation between pristine and desized fibers.

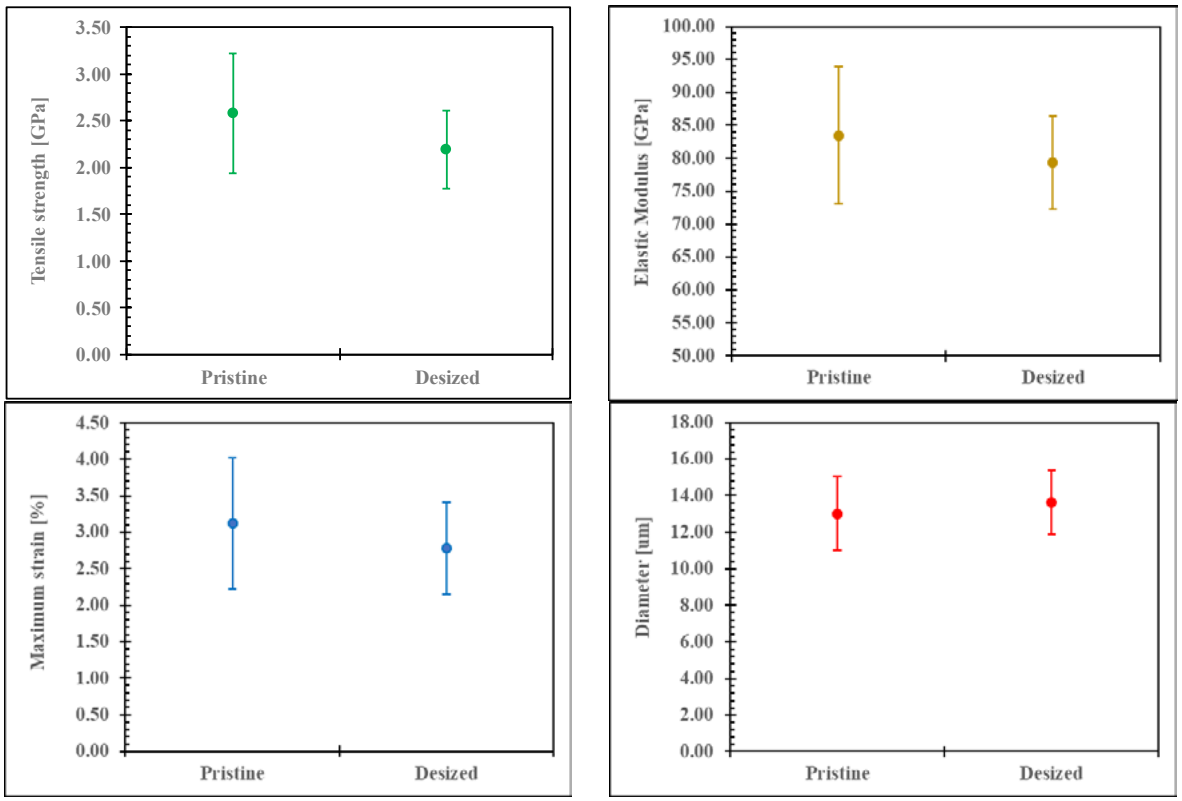

Figure 1. Mechanical properties of pristine and desized basalt fibers.

As shown in Figure 2, there is a decrease in the wettability of the fibers as the contact angle increases from 72.2° for pristine fibers to 85.8° upon removal of the sizing. This may be caused by the surface's chemical composition change, as the naked surface of basalt is exposed once the sizing is removed. Also, the SEM images (Fig 2.b and c) show a smoother surface once the fiber is desized, which translates into a decrease in rugosity that increases the contact angle displayed.

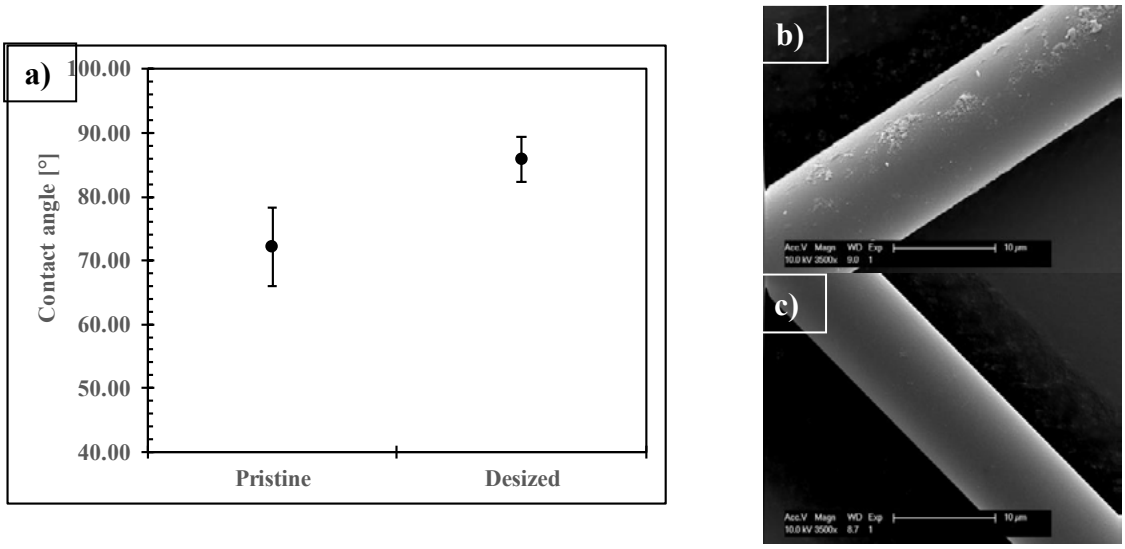

Figure 2. a) Contact angle measurement of pristine and desized basalt fibers, and SEM images of b) pristine and c) desized fibers.

3.2. Corrosion tests

Mechanical properties of pristine and desized fibers after being exposed to a highly alkaline environment for 72 and 168 hours are shown in Figure 3. The parameters evaluated do not show any statistically significant difference between pristine and desize fibers, suggesting that either of the samples is being corroded.

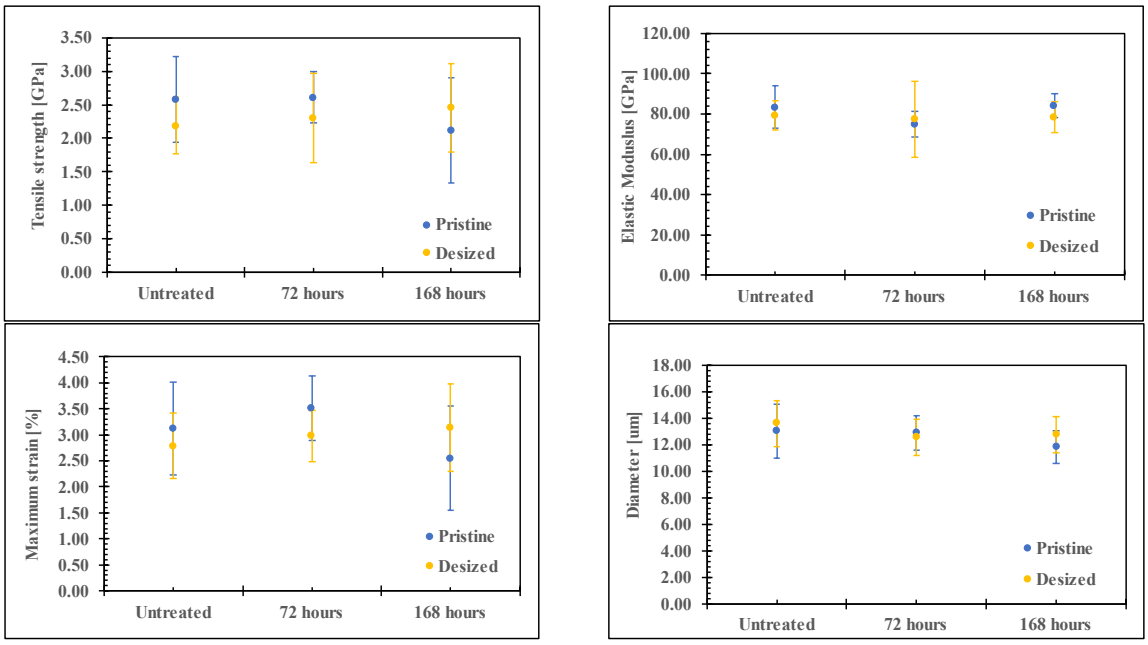

Figure 3. Mechanical properties of pristine and desized basalt fibers after exposure to a highly alkaline environment for 72 and 168 hours.

Changes in the wettability, shown in Figure 4, suggest a corrosion process ongoing on the pristine fiber's surface. After 72 hours immersed in 1 M NaOH solution at room temperature, pristine fibers show an increase in the contact angle from 71.27° to 86.06°. However, the contact angle increase is not present in the desized fibers, implying that the fiber's sizing is affected by the alkaline solution.

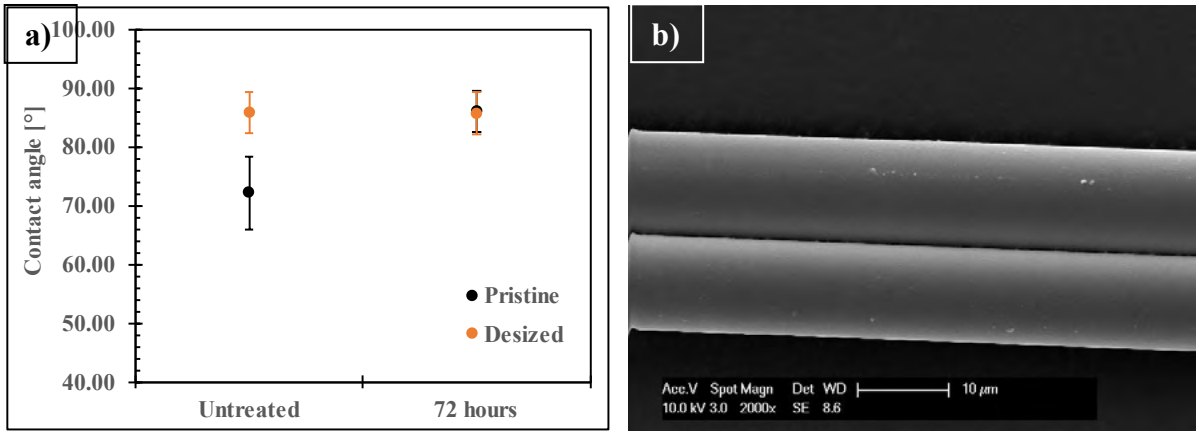

Figure 4. a) Contact angle of pristine and desized basalt fibers and b) SEM image of a pristine fiber after being exposed for 72 hours to a highly alkaline environment at room temperature.

Temperature acts as an accelerator as higher temperatures increase the rate of the chemical reactions involved in the corrosion process. Figure 5 shows the variation of the mechanical properties after the samples were exposed to a highly alkaline aqueous solution in boiling conditions. After 30 minutes of the fibers being immersed in a boiling alkaline solution, pristine and desized fibers show a 32.2% and 20.6% decrease of the initial tensile strength, respectively, which remain unchanged after 1 hour. While the elastic modulus is unaffected, there is also a significant decrease of the maximum strain percentage in both samples that ranges between 39.6 and 44.9%. Pristine and desized fibers show no statistically significant difference in their mechanical properties during corrosion, suggesting that this sizing did not act as a protective layer against corrosion for the fiber.

Diameter measurements follow a decreasing trend for both pristine and desized fibers, although not being statistically different due to the heterogeneity of the manufactured fiber diameter values.

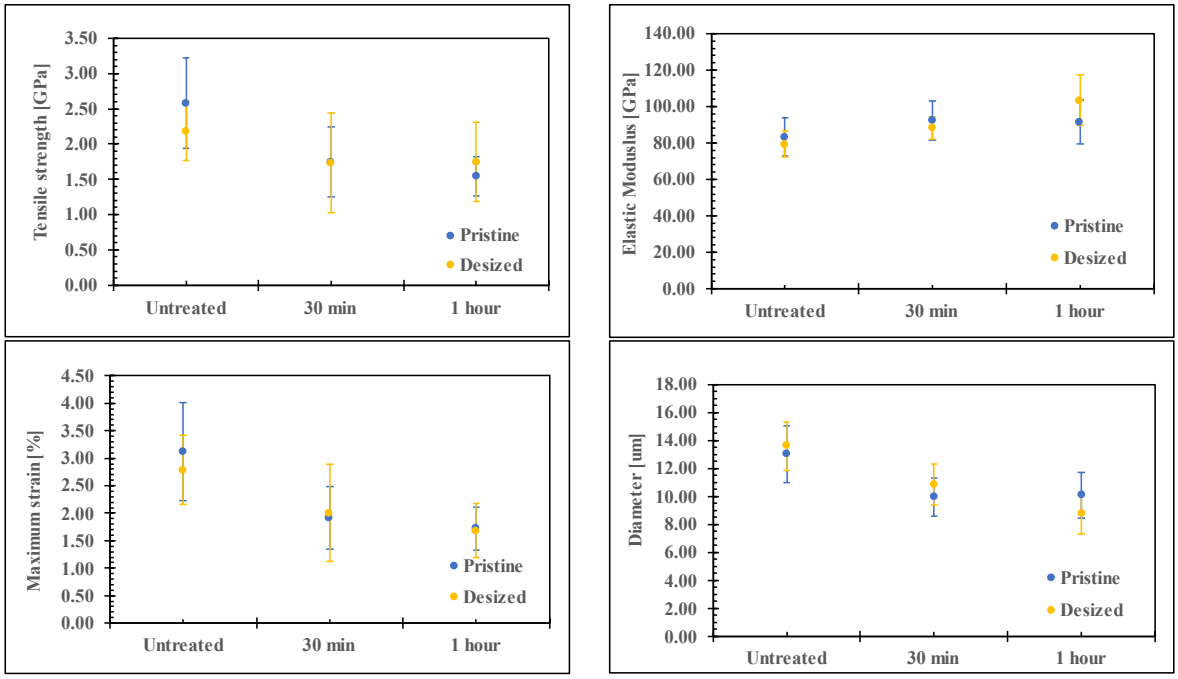

Figure 5. Mechanical properties of pristine and desized basalt fibers after exposure to a highly alkaline environment for 72 and 168 hours.

Figure 6 shows the corroded surface of a previously desized fiber. The corrosion has affected its previously smooth surface and pinholes and rugosity is visible.

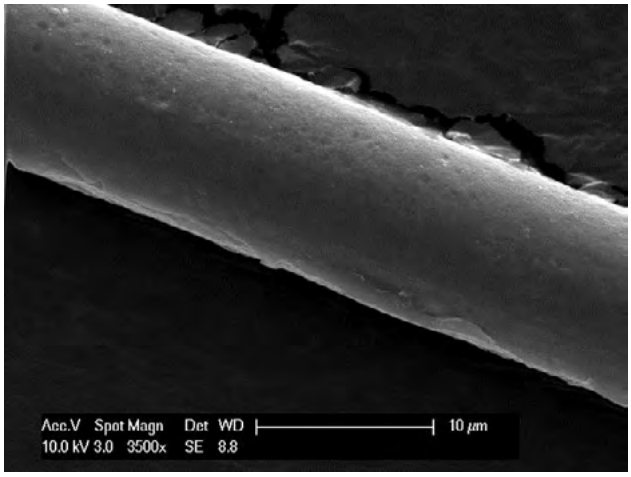

Figure 6. SEM image of a desized fiber's surface after being exposed for 1 hour to a boiling highly alkaline solution.

4. Conclusions

The impact of the sizing on the corrosion of commercial basalt fibers was studied in this paper.

- The sizing present in commercial fibers was successfully removed with acetone and did not show any significant influence in the basalt fibers' mechanical properties. However, the contact angle of the fibers increased upon desizing due to the changes in the chemical composition of the surface and its roughness.

- The corrosion solution at room temperature did not affect the basalt fibers' mechanical properties when exposed up to 168 hours.
- The corrosion solution in boiling conditions had a negative impact on the tensile strength and maximum strain of the basalt fibers. The sizing present in this sample did not act as a protective layer against corrosion.

References

[1] J. Sim, C. Park, and D. Young Moon, Characteristics of basalt fiber as a strengthening material for concrete structures, *Composites Part B: Engineering,* Vol. 36, Issues 6-7, pp. 504-512, 2005.
[2] S. Feih and A. P. Mouritz, Tensile properties of carbon fibres and carbon fibre–polymer composites in fire, *Compos Part A Appl Sci Manuf*, Vol. 43, No. 5, pp. 765–772, 2012.
[3] V. Afroughsabet, L. Biolzi, and T. Ozbakkaloglu, High-performance fiber-reinforced concrete: a review, *J Mater Sci*, vol. 51, No. 14, pp 6517-6551, 2016.
[4] Y. Li *et al.*, A review on durability of basalt fiber reinforced concrete, *Compos Sci Technol*, vol. 225, pp. 109519, 2022.
[5] S. Ying and X. Zhou, Chemical and thermal resistance of basalt fiber in inclement environments, *Journal Wuhan University of Technology, Materials Science Edition*, vol. 28, no. 3, pp. 560–565, 2013.
[6] B. Ding, L. Zhang, and J. Liu, The difference in weather resistance and corrosion process for different types of basalt fiber, *J Non Cryst Solids*, vol. 590, p. 121678, 2022.
[7] G. Wu, X. Wang, Z. Wu, Z. Dong, and G. Zhang, Durability of basalt fibers and composites in corrosive environments*, Journal of Composite Materials*, Vol. 49, Issue 7, 2014.
[8] Q. Wang, Y. Ding, and N. Randl, Investigation on the alkali resistance of basalt fiber and its textile in different alkaline environments, *Construction and Building Materials,* Vol. 272, pp 121670, 2020.
[9] S. Qiu, C. A. Fuentes, D. Zhang, Aart, W. Van Vuure, and D. Seveno, Wettability of a Single Carbon Fiber, *Langmuir*, Vol 32, Issue 38, pp 9697-9705, 2016.
[10] F. Bauer, M. Kempf, F. Weiland, and P. Middendorf, Structure-property relationships of basalt fibers for high performance applications, *Composites Part B: Engineering,* Vul 145, pp 121-128, 2018.

ADVANCED POLYETHYLENE TEREPHTHELATE (PET) AEROGELS AND THEIR COMPOSITES FROM PLASTIC WASTE FOR LOAD BEARING THERMAL INSULATION AND RADIATIVE COOLING APPLICATIONS

Xue Yang Goh[1,2], Jaesuk Hwang[3], Kaiting Guo[1], Luon Tan Nguyen[1], Ren Hong Ong[1], Tianliang Bai[1], Xinying Deng[2], and Wern Sze Teo[2]

[1]Department of Mechanical Engineering, National University of Singapore, 9 Engineering Drive 1, #07-26 EA, Singapore 117575, Singapore
Email: goh.xueyang@u.nus.edu
[2]Singapore Institute of Manufacturing Technology (SIMTech), Agency for Science, Technology and Research (A*STAR), 2 Fusionopolis Way, #08-04 Innovis, Singapore 138634, Republic of Singapore.
[3]Centre for Quantum Technologies, National University of Singapore, 3 Science Drive 2, Block S15, Singapore 117543 Singapore

Keywords: PET aerogel, PET aerogel composite, radiative cooling, thermal management, mechanical property

Abstract
Environmental issues brought about by waste polyethylene terephthalate (PET) calls for an alternative recycling solution. PET aerogel (PA) made from waste plastic bottles presents a good avenue for recycling as they can be used in thermal management solutions. However, the lack of structural rigidity makes PA susceptible to deformation which can negatively impact its performance. To circumvent this issue a honeycomb structure is incorporated within the PA to create PET aerogel composite (PAC). The developed PACs achieves the low density of 0.042 – 0.072 g/cm^3 and low thermal conductivity of 0.033 – 0.038 W/m·K. The PAC with 1-cm cell size achieved a compressive modulus of 15.30 MPa in the out-of-plane direction, and 0.070 – 0.128 MPa in the in-plane directions, highlighting its enhanced stiffness. The thermal performance of the PA is shown through its use as a concurrent radiative cooler and thermal insulator. With its highly emissive nature within the sky window (8 – 14 µm), and its highly insulative capabilities, the PA within the PAC is able to passively cool an object directly underneath via radiative cooling. Despite the unfavourable conditions of a warm Singapore night sky with high downwelling of 420 W/m^2, the PA can achieve a 2 °C sub-ambient temperature.

1. Introduction

The average global temperature of Earth has been rising at an alarming rate [1]. According to NOAA's 2022 annual climate report, the top 9 warmest years recorded since 1880 is occupied by the last 9 years of the decade, with the 10th being relatively recent itself in 2010 [2]. This is of major concern as the rise in temperature have detrimental impacts on the environment. With the average global temperature increase of approximately 1 °C since 2000, sea levels are rising, and several flora and fauna species face extermination [3]. Hence, it is importance to address such issues before irreversible damages occur.

Greenhouse gas emissions is one of the key contributors to rising temperatures [4, 5]. One of the major greenhouse gas emissions comes from the thermal management of buildings, particularly due to the large energy consumption of conventional compressor-based cooling systems such as air conditioners [6]. Additionally, instead of the removal of heat, such cooling systems only transfer heat from one

location to another. To mitigate such drawbacks, it is important to deploy effective thermal insulators to supplment prevalent cooling system [7].

Aerogels are a super insulator material due to its low density, high porosity, and extremely low thermal conductivity, achieving values as low as 0.01 W/m·K [8]. Despite its benefits, a major limitation is in its structural rigidity. Since its performance is primarily based on its porous nature, the deformation of its porous network hinders its effective performance. The PET aerogels (PA) developed in particular are generally soft and flexible [9]. To ensure effective application of the material, it is paramount to maintain its structural integrity especially in load bearing applications. While this can be done through chemically strengthening the network of the aerogel [10], a simpler and more macro approach can be used to provide the necessary stiffness.

For the first time, highly promising aerogels made from recycled PET fibres and PVA are used as an integrated thermal management solution. On top of its excellent thermal insulation, PA can be used as a radiative cooler to passively cool an object underneath without the need for electricity. The PAs are further enhanced by incorporating a honeycomb frame (HF) during fabrication, to develop the hybrid PET aerogel composite (PAC). The panels of PAC protects the aerogels within the cells of the honeycomb to retain its functionality. The development of PAC provides a simple and environmentally friendly solution to supplement current cooling systems and reduce greenhouse gas emissions. At the same time it provides an alternative to the recycling of waste PET.

2. Materials and methods

2.1. Materials

The PET film (Melinex ST506, 125 micron) is purchased from Innox Higa Singapore Pte Ltd. Ethyl cyanoacrylate (3M Scotch Super Glue Liquid in Precision Applicator) is purchased from Popular Holdings Limited (Singapore). Recycled polyester fibres (PET, 3D Denier, 64mm length) are purchased from Jiangsu Yangshuo Nonwoven technology Pte Ltd, China. Polyvinyl Alcohol cross-linker (PVA, Molecular weight ~89,000 – 98,000, ≥99% hydrolysed)is purchased from Merch, Sigma Aldrich Pte Ltd. (Singapore). All reagents are used as-received, with not further purification. All solutions are used with Deionised (DI) water unless otherwise stated.

2.2. Fabrication of PAs and PACs

The PET HF is fabricated by folding strips of PET (width of 2 cm) as shown in Figure 1a. The front edge of the strip is first folded in a single direction. Next, two folds opposite from the front edge are done. This two-fold in alternating sequence from the previous folds is repeated until the desired length of the PET strip is obtained. To end off, the PET strip is folded once in the same direction as the front edge. To form the HF, the folded PET strips are adhered with ethyl cyanoacrylate as seen in Figure 1b.

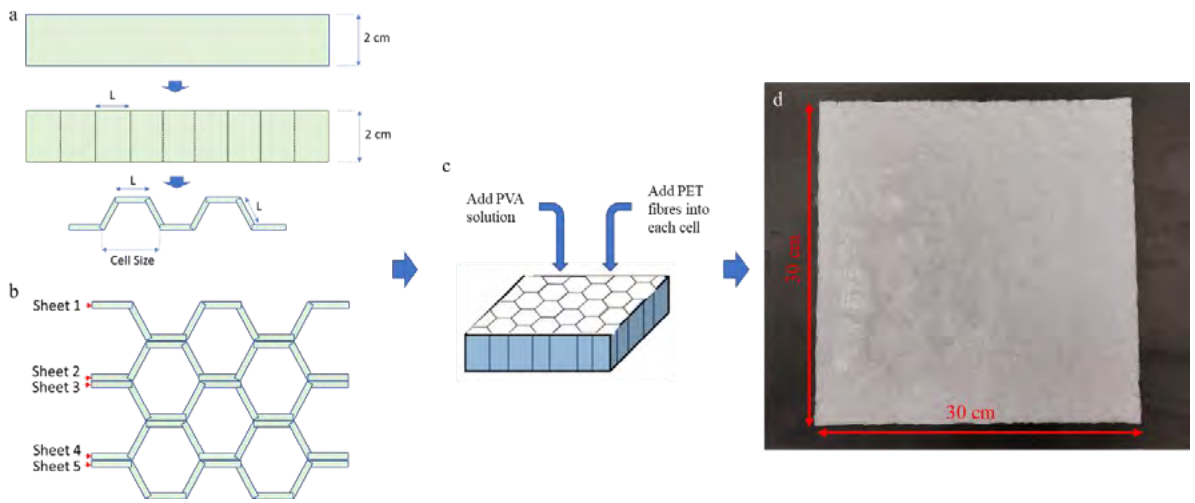

Figure 1. PET strips folded to form the cell walls of the HF (a), bonding the cell walls to form the HF (b), adding PVA and PET to create the PAC (c), and a PAC panel measuring 30 x 30 x 2 cm (d).

To create the PAC, The PVA crosslinking solution is first prepared by adding PVA powder into warm DI water gradually. With a magnetic stirrer, the solution is stirred until the powders are completely dissolved. The prepared solution is added into a mould with the fabricated PET HF. The solution is filled filled in the mould until its level is above the PET HF. Next, the PET fibres are filled into each cell of the PET HF shown in Figure 1c. The prepared hydrogel is then transferred to a freezer where it is frozen at -18 °C for at least 8 hours. Subsequently, it is freeze-dried at approximately -70 °C, 1 mbar, for 2 days to obtain the PAC. The fabrication of the PA can be done in a similar manner, excluding the use of the PET HF. An illustration of a large sized PAC panel measuring 30 x 30 x 2 cm can be seen in Figure 1d.

3. Results and discussion

The SEM image of the PA within the PAC can be seen in Figure 2a. The PVA crosslinker are dispered across the fibres forming the physical crosslinks of the PET fibre matrix to create the 3D open-porous structure of the aerogel. The bonding between the PA and the HF can be seen in Figure 2b. The PVA is well-bonded with the fibres and cell wall of the HF to create the composite unit. This could be due to hydrogen bonding between the PVA crosslinker, PET fibres and the HF as illustrated in Figure 2c. [11, 12].

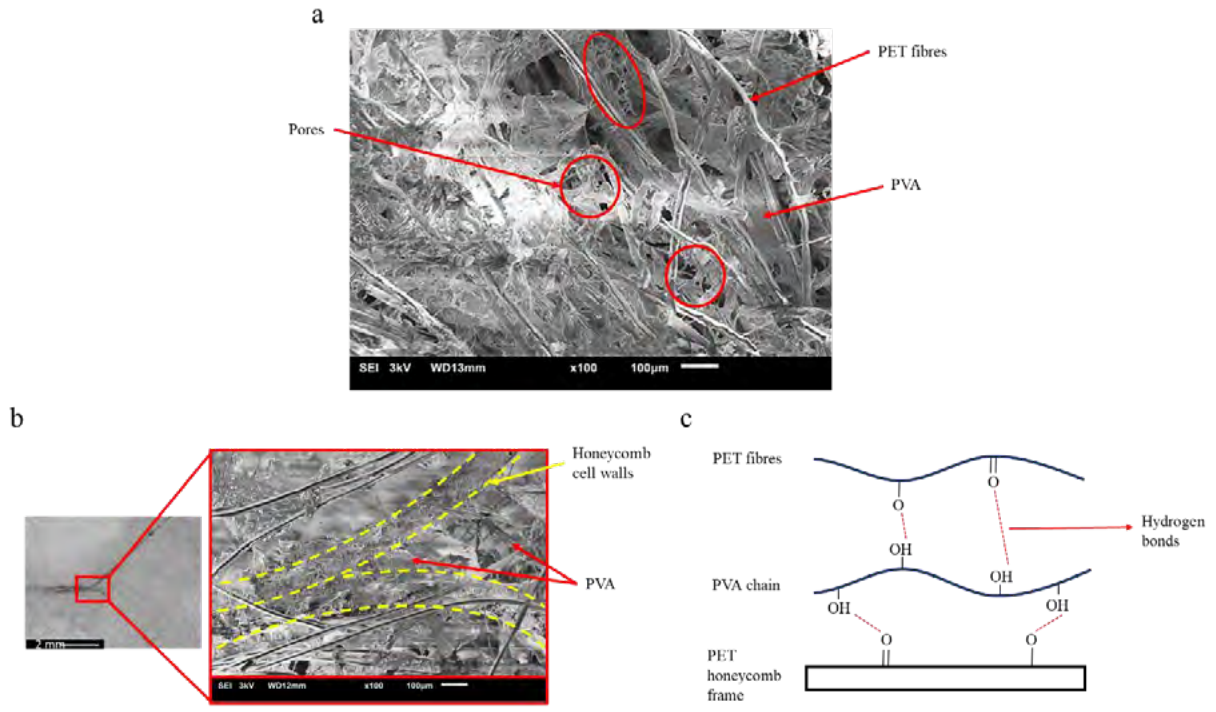

Figure 2. SEM image of PA (a), stereoscopic and SEM image of PAC (b), and schematic of suggested hydrogen bonding within PAC (c).

The properties of the PAC with varying cell sizes, and PET fibre content within the PET aerogels are summarised and tabulated in Table 1. When larger HF cell sizes are used in the fabrication of the PAC (1.0 – 2.0 cm), the density of the PAC decreased (0.070 – 0.041 g/cm^3). The reduction in density can be attributed to the lesser amount of solid bulk PET strips used in during its fabrication. Meanwhile, increasing the PET fibre ratio in PAC5-1 to that in PAC20-1, increases the density of the PAC from 0.042 – 0.062 g/cm^3. This happens due to the increased density of the aerogel fabricated alongside the HF when more fibres are added within the similar volume of cell wall.

Table 1. Properties of the PACs with various cell size and aerogel composition.

Sample	Cell size (cm)	PA ratio		Density (g/cm^3)	K-value (W/m·K)	Compressive modulus (MPa)		
		PET	PVA			Out-of-Plane (OOP)	In-Plane (IP) X-axis	In-Plane (IP) Y-axis
PAC10-1_CS1.0	1.0	10	1	0.072 ± 0.002	0.037 ± 0.001	15.30 ± 4.17	0.128 ± 0.023	0.070 ± 0.010
PAC10-1_CS1.5	1.5	10	1	0.047 ± 0.001	0.036 ± 0.001	8.07 ± 0.18	0.047 ± 0.007	0.031 ± 0.002
PAC10-1_CS2.0	2.0	10	1	0.041 ± 0.002	0.035 ± 0.001	4.29 ± 1.42	0.032 ± 0.005	0.021 ± 0.004
PAC5-1_CS1.5	1.5	5	1	0.042 ± 0.002	0.033 ± 0.001	7.94 ± 0.43	0.043 ± 0.007	0.028 ± 0.003
PAC20-1_CS1.5	1.5	20	1	0.062 ± 0.002	0.037 ± 0.001	8.20 ± 0.50	0.056 ± 0.009	0.054 ± 0.007

3.1. Mechanical properties

The compression curves of the PAC, PA, and HF can be seen in Figure 3. Notably, the PAC's compression behavior follows closely to that of the PET HF when compressed in the Out-of-Plane (OOP) axis as seen in Figure 3a. Meanwhile, the compressive behavior of the PAC in In-Plane (IP) axis (both X and Y-axis) is characteristic of an elastomer, similar to that of the PA, albeit at different magnitudes as illustrated in Figure 3b. Notably, the compressive Young's modulus of the PACs in the IP X-axis is observed to be consistently higher than that in the IP Y-axis as seen from Table 1. The difference can be attributed to the difference in configuration of the cell wall and its behaviour during compression.

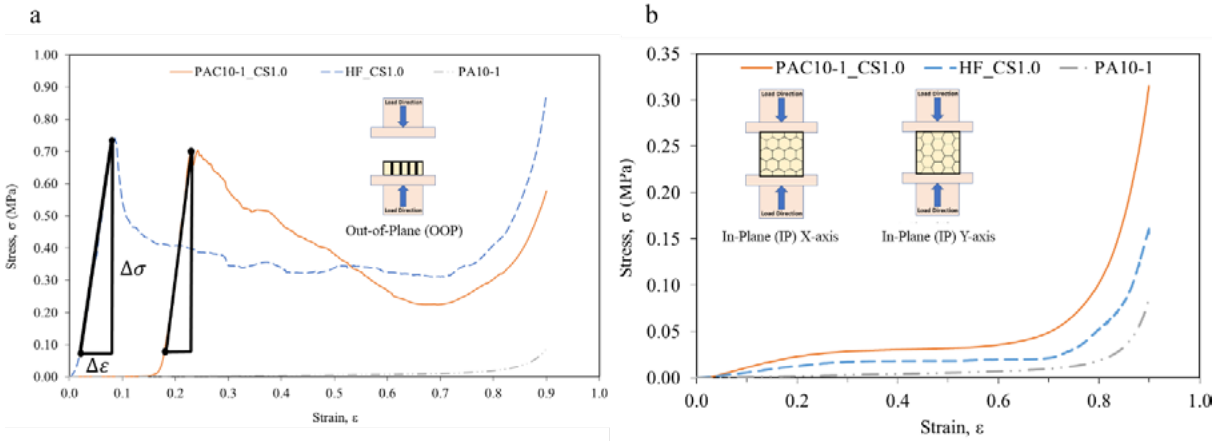

Figure 3. Stress-strain curve of the PAC, PA, and HF in the OOP compression (a), and IP X-axis compression (b).

From the compressive Young's modulus, it is clear that the HF embedded within the PA significantly enhances the stiffness of the PA as shown in Figure 4 and Table 1. When the cell size of the PAC is

reduced, the moduli of the PACs in all axis of compression is enhanced, albeit in different magnitutdes. For instance, the PAC10-1_CS2.0 with 2.0 cm cell size exhibits a stiffness of 4.29, 0.032, and 0.021 MPa in contrast to that of PAC10-1_CS1.0 with 15.30, 0.128, 0.070 MPa in the OOP axis, IP X-axis, and IP Y-axis, respectively. Overall the reduction in cell size enhances the stiffness of the PAC by approximately 3.6, 4.0, and 3.3 times OOP axis, IP X-axis, and IP Y-axis.. This can be attributed to the strengthening the HFs, when smaller cell sizes are fabricated, resulting in larger loads and stress required to deform the HF [13].

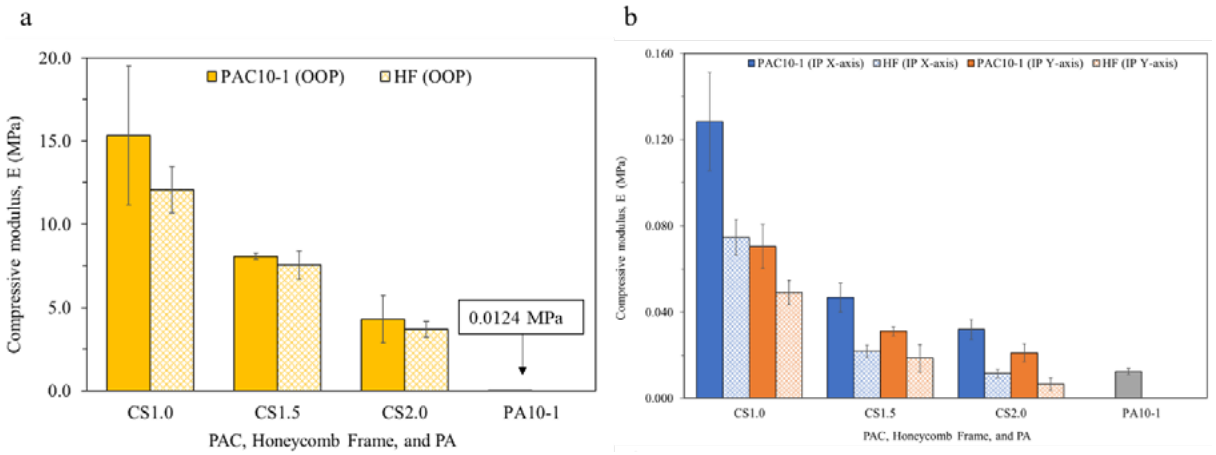

Figure 4. Compressive moduli of the PAC with varying cell sizes in the OOP compression (a), and the IP compressions (b).

Varying the composition of the PA within the PAC also affects the composite's compressive modulus where the increase in PET amount enhances the PAC's stiffness. This effect can be seen from the compressive modulus of PAC5-1_CS1.5 with the compressive modulus of 7.94, 0.043, and 0.028 MPa compared to that of PAC20-1_CS1.5 with 8.20, 0.056, and 0.054 MPa in the OOP, IP X-axis, and IP Y-axis, respectively as shown in Table 1. The marginal difference in stiffness in the IP X-axis and Y-axis from PAC20-1_CS1.5 suggest stiffness contributions from the PA. This implies that the enhancement in stiffness in the IP directions can be attributed from both the cell size and aerogel's composition. Nevertheless, the overall enhancement in stiffness of the PAC is more prevalent with the variation in cell size as opposed to varying the composition of the PA.

3.2. Thermal properties

PAC with larger cell sizes, increasing from 1.0 – 2.0 cm, tends to exhibit lower values of thermal conductivity, decreasing from 0.037 – 0.035 W/m·K, respectively as seen in Figure 5 and Table 1. The reduction in thermal conductivity can be attributed to the decrease in solid bulk PET content used for the strips of PET for the HF. The lesser use of solid bulk materials reduces the pathways for heat transfer, effectively enhancing its insulation performance. The change in thermal conductivity is more significantly affected by the composition of the PA within the PAC rather than that of the cell sizes. For example, a significant increase in thermal conductivity was observed when contrasting between PAC5-1_CS1.5 (0.033 W/m·K) to that of PAC20-1_CS1.5 (0.037 W/m·K). This is due to the increased density PA fabricated when the PET fibres are increasingly packed within the HF cells. Contrasting common insulating materials, the thermal insulation performance of PAC5-1_CS1.5 (0.033 W/m·K) is comparable to Foamex VVH38 (0.033 W/m·K [14]), and superior to EPS70 (0.039 W/m·K [15]). Moreover, it surpasses other composite materials such as silica aerogel composites (0.040 W/m·K [16]).

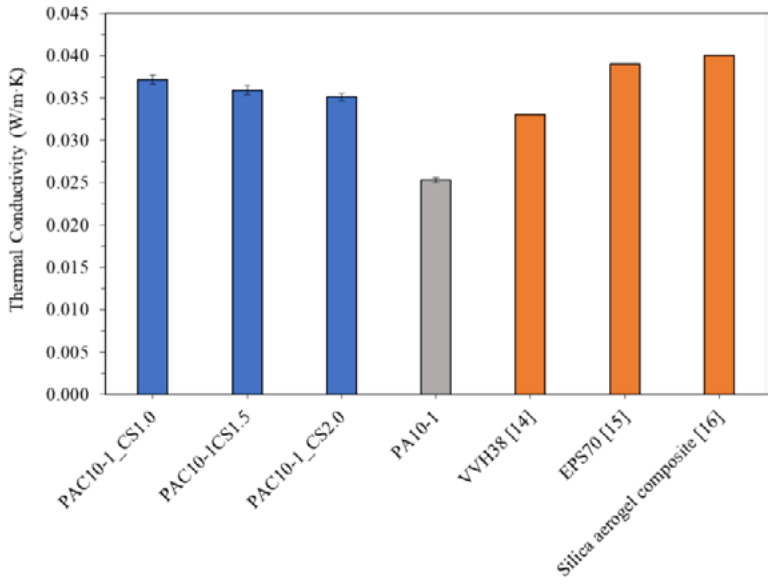

Figure 5. Thermal conductivity of the PACs with varying cell size compared with other products.

3.3. Radiative cooling performance

The working principle of radiative cooling is illustrated by the schematic shown in Figure 6. Placing the PAC or PA above an object, the object directly below and in contact with the PA can be cooled. Radiative cooling occurs when outgoing thermal radiation is larger than the heat gain from the incoming solar radiation and parasitic heat gain. Since the performance of the radiative cooler is primarily dependent on the surface exposed to the sky, and that the surface is predominantly made up of PA, the performance of the radiative cooler is largely contributed by the exposed PA. The inclusion of the PET HF within the PA, only serves to provide structural rigidity for the PA for practical application.

The nighttime radiative cooling performance of the PA5-1 and PA20-1 samples can be seen from Figure 7. Prior to measurement, the sample's was shielded from the sky by placing an aluminium plate above the PA. Once all the temperature readings stablises to that of the ambient temperature (~30 °C), the plate is removed to begin radiative cooling. In general, all PA samples cooled to temperatures below ambient, albeit at varying rates. The temperatures of PA5-1 thin and PA20-1 thin samples achieve the steady state temperature, ~2 °C below ambient temperature, within 20 minutes. Meanwhile, PA5-1 thick and PA20-1 thick samples experienced a gradual reduction throughout the duration of the measurements, eventually achieveing ~1 °C below ambient temperature. Despite superior thermal insulation from the thicker samples, the results showcase the potential for PA to concurrently work as both a radiative cooler and thermal insulator.

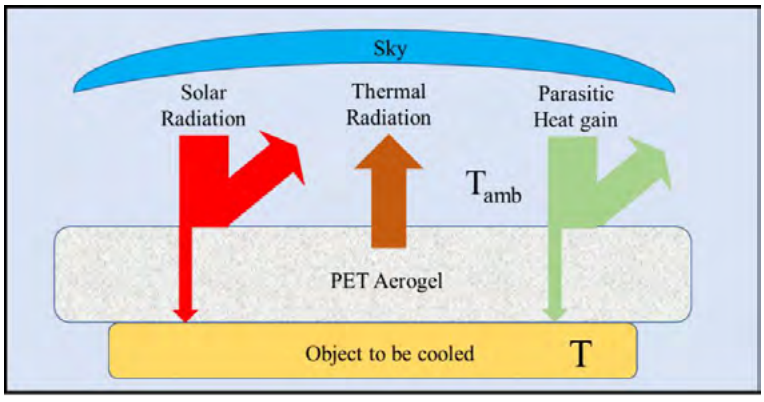

Figure 6. Schematic of the radiative cooling principle of the PET aerogel.

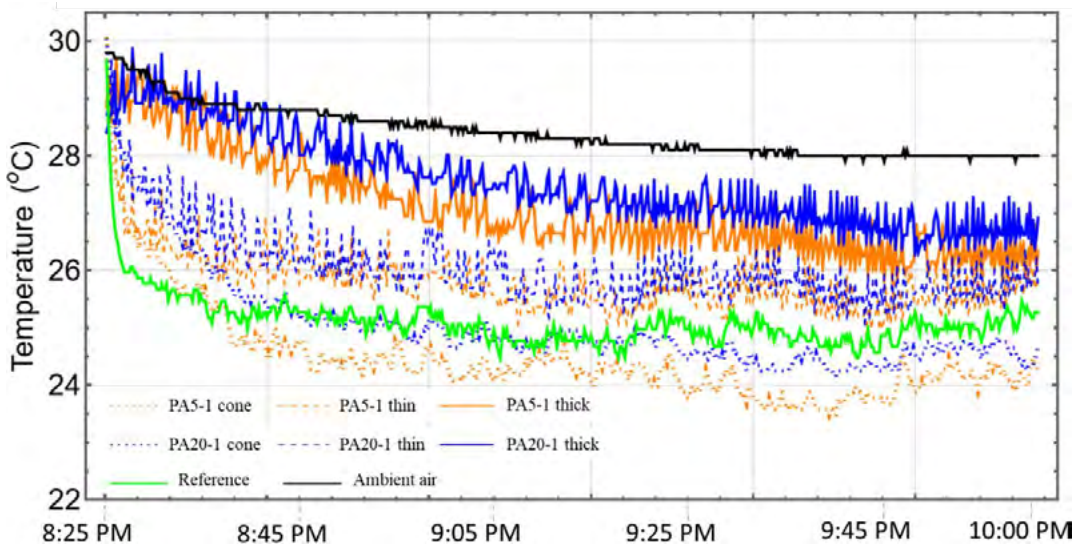

Figure 7. Radiative cooling performance during nighttime conditions.

It is important to note that the cooling performance of the PA is reportedly conservative. Radiative cooling performance can be significantly affected by the ambient conditions during the experiment. In night sky of Singapore, with 88% humidity, the downwelling was measured to be more than 420 W/m^2. These conditions reduces the effectiveness of radiative cooling. For comparison, the cooling performance of the reference sample in Singapore achieved a temperature of 3 °C below ambient temperature, only 1 °C lower than that of the PA setup. Contrasting a similar experimental set up, a temperature of 7 °C below ambient temperature was obtained when the experiment was done in Los Angeles, California with humidity around 26% [17]. Hence, similar to the reference sample, in more favourable climates, the cooling performance of the PAs can be improved.

4. Conclusions

Aerogels are well-known for its thermal insulative properties, which stems from its unique porous structure. Although the thermal properties of PA is excellent, its generally soft nature makes it susceptible to deformation and densification. One way to mitigate this limitation is to develop a hybrid composite by introducing a honeycomb structure. The developed PACs achieved low densities of 0.042 – 0.072 g/cm^3 with low thermal conductivities of 0.033 – 0.038 W/m·K. The PAC with 1-cm cell size achieved a compressive modulus of 15.30 MPa in the Out-of-Plane direction, and 0.070 – 0.128 MPa in the In-Plane directions, effectively enhancing its stiffness up to 2,550x greater than that of the PA equivalent.

In application, despite Singapore's challenging ambient conditions, the PA is able to cool to 2 °C below ambient temperature via its radiative cooling and thermal insulation capabilities. However this performance can be impacted with the deformation of the material. Hence, embedding aerogels within the honeycomb frames to preserve the structure and performance of the PA is suggested.

Acknowledgments

Authors would also like to thank Agency of Science Technology and Research (A*STAR) for the scholarship of Xue Yang Goh (SIMT/U20-Q2-018SU). Authors would also like to thank Associate Professor Duong Hai Minh, and Temasek Laboratories @ NUS, R-265-000-682-720 (Mapletree Gift), R-265-000-682-114 (MOE Tier 1 FRC), R-265-000-682-133 (ODPRT) and R-265-000-682-731 (ME) for the financial support.

References

[1] J. Tollefson, "How hot will Earth get by 2100," *Nature,* vol. 580, no. 7804, pp. 443-445, 2020.
[2] "Monthly Global Climate Report for Annual 2022," 2023. [Online]. Available: https://www.ncei.noaa.gov/access/monitoring/monthly-report/global/202213
[3] J. Hansen, M. Sato, R. Ruedy, K. Lo, D. W. Lea, and M. Medina-Elizade, "Global temperature change," *Proceedings of the National Academy of Sciences,* vol. 103, no. 39, pp. 14288-14293, 2006.
[4] K. Kurniawan, J. Supriatna, J. Sapoheluwakan, T. E. B. Soesilo, S. Mariati, and G. Gunarso, "The analysis of forest and land fire and carbon and greenhouse gas emissions on the climate change in Indonesia," *AgBioForum,* vol. 24, no. 2, pp. 1-11, 2022.
[5] L.-C. Lu, S.-Y. Chiu, Y.-h. Chiu, and T.-H. Chang, "Sustainability efficiency of climate change and global disasters based on greenhouse gas emissions from the parallel production sectors–A modified dynamic parallel three-stage network DEA model," *Journal of Environmental Management,* vol. 317, p. 115401, 2022.
[6] N. Wang, J. Zhang, and X. Xia, "Energy consumption of air conditioners at different temperature set points," *Energy and Buildings,* vol. 65, pp. 412-418, 2013.
[7] E. Bobrova, A. Pilipenko, and A. Zhukov, "Insulating sheath system and energy efficiency of buildings," in *E3S Web of Conferences*, 2019, vol. 91: EDP Sciences, p. 02019.
[8] X. Lu, M. Arduini-Schuster, J. Kuhn, O. Nilsson, J. Fricke, and R. Pekala, "Thermal conductivity of monolithic organic aerogels," *Science,* vol. 255, no. 5047, pp. 971-972, 1992.
[9] X. Y. Goh, X. Deng, W. S. Teo, R. H. Ong, L. T. Nguyen, T. Bai, and H. M. Duong, "Scale-up fabrication and advanced properties of recycled polyethylene terephthalate aerogels from plastic waste," *Polymer Engineering & Science,* 2024.
[10] X. Y. Goh, K. Guo, L. T. Nguyen, R. H. Ong, and H. M. Duong, "Fabrication and properties of polyethylene terephthalate (PET) aerogel composites from plastic bottle waste," *Materials Today Communications,* vol. 37, p. 107625, 2023.
[11] H. W. Koh, D. K. Le, G. N. Ng, X. Zhang, N. Phan-Thien, U. Kureemun, and H. M. Duong, "Advanced recycled polyethylene terephthalate aerogels from plastic waste for acoustic and thermal insulation applications," *Gels,* vol. 4, no. 2, p. 43, 2018.
[12] F. Naeem, S. Khan, A. Jalil, N. M. Ranjha, A. Riaz, M. S. Haider, S. Sarwar, F. Saher, and S. Afzal, "pH responsive cross-linked polymeric matrices based on natural polymers: effect of process variables on swelling characterization and drug delivery properties," *BioImpacts: BI,* vol. 7, no. 3, p. 177, 2017.
[13] V. Crupi, G. Epasto, and E. Guglielmino, "Collapse modes in aluminium honeycomb sandwich panels under bending and impact loading," *International Journal of Impact Engineering,* vol. 43, pp. 6-15, 2012.
[14] *Styroboard EPS - Thermal Resistance*, 2023. [Online]. Available: https://www.foamex.com.au/images/pdf/StyroBoard_EPS_R_Values.pdf. Accessed: April 2023.
[15] K. Voith, B. Spisák, M. Petrik, Z. Szamosi, and G. L. Szepesi, "Non-Conventional Reinforced EPS and Its Numerical Examination," *Processes,* vol. 11, no. 1, p. 12, 2022.
[16] M. Schwan, M. Rößler, B. Milow, and L. Ratke, "From fragile to resilient insulation: synthesis and characterization of aramid-honeycomb reinforced silica aerogel composite materials," *Gels,* vol. 2, no. 1, p. 1, 2015.
[17] X. Huang, J. Mandal, and A. P. Raman, "Do-it-yourself radiative cooler as a radiative cooling standard and cooling component for device design," *Journal of Photonics for Energy,* vol. 12, no. 1, Jan 2022, Art no. 012112, doi: 10.1117/1.Jpe.12.012112.

ADVANCED CHARACTERIZATION AND THERMOMECHANICAL MODELING OF PP/PE BLENDS FOR INNOVATIONS IN RECYCLED COMPOSITES

P. Hao[1], C. Siebers[2], K. Ragaert[2] and F. A. Gilabert[1]

[1]Department of Materials, Textiles and Chemical Engineering (MaTCh), Mechanics of Materials and Structures (MMS), Ghent University, Technologiepark Zwijnaarde 46, 9052, Zwijnaarde, Belgium
Email: pei.hao@ugent.be, fran.gilabert@ugent.be Web Page: https://materialmodels.ugent.be
[2]Circular Plastics, Department of Circular Chemical Engineering, Faculty of Science and Engineering, Maastricht University, Urmonderbaan 22, 6167 RD Geleen, The Netherlands
Email: charmayne.siebers@maastrichtuniversity.nl, k.ragaert@maastrichtuniversity.nl

Keywords: Thermomechanical constitutive modeling, Recycled plastics, Thermoplastics, Rate-dependence, RVE

Abstract
The non-biodegradable thermoplastic waste poses environmental threats and requires resource-intensive production processes. However, thanks to their melt-reshapability, these materials could be fully integrated in the production cycle of advanced composites. Currently, mechanical recycling is the most common method for recycling thermoplastics, valued for its efficiency and low cost. However, this method often fails to produce high-purity recyclates from a single polymer type. Classified bales usually contain small amounts of other polymers as contaminants, resulting in downcycled materials with reduced quality and utility. The complex nature and microstructure of polymer blend matrices complicate the thermomechanical characterization, which is crucial for assessing their suitability for being used in composites. To address this, an advanced model based on a unified constitutive formulation originally developed for pure polymers has been created to analyze various mix compositions of polymer blends. This model enables the investigation of the rate-sensitivity of the blend, as well as self-heating and thermal softening effects. After validating the polymer blend model through tensile tests using high-speed 3D stereo Digital Image Correlation (DIC) and infrared thermography, micromechanical models based on the Representative Volume Element (RVE) approach were employed for numerical simulations. The goal is to assess the overall behavior of polymer blend-based unidirectional (UD) composites using homogenization techniques.

1. Introduction

In pursuit of a circular economy, thermoplastics emerge as a prominent solution thanks to their reshape ability. Nowadays, pure and mixed blends of thermoplastics are being considered to be employed in the production of composites, showcasing their potential in advancing sustainability efforts [1-4]. The thermomechanical behavior of these composites might be influenced by the response of the polymer blend matrices, which gathers several load and environmental dependencies [5-7]. A recent study on polymer blends under tensile load reveals that the mechanical response is significantly influenced by the nature of the material and microstructure [8]. This presents substantial challenges in characterizing recycled polymer blends for the following reasons: (i) mechanically recycled polymer blends (or contaminated polymers) are not pure; (ii) most thermoplastic-based blends are semi-crystalline, inherently bi-phasic, comprising both amorphous and crystalline phases; (iii) the interactions between these phases, including their compatibility and interface bonding, are not fully understood in terms of mechanical response. As a result, these post-consumer plastics often lead to downcycled materials with

noticeable diminished quality and utility. This diminishes their acceptance in secondary markets and hinders the recycling of polymers and the usage of polymer-based composites.

This work presents a modeling-based methodology for predictive assessment of the performance of recycled plastics, focusing on the effect of using blends in UD composites. A state-of-the-art experimental investigation was conducted to capture the thermomechanical response of polyolefins and their blends under tension at various loading speeds. Numerical simulations using micromechanical models based on the Representative Volume Element (RVE) approach were performed to evaluate the overall behavior of UD composites using these blends. The primary objective of this research is to compare the performance of composites made from recycled plastics with those made from virgin materials. The information from this comparison will help to evaluate the feasibility of using recycled polymer blends in composites from a perspective of mechanical response. The ultimate goal is to promote eco-friendly designs by optimizing the mechanical properties of recycled-based composites and providing essential data to improve the mechanical recycling process. These advancements are expected to enhance the usability of post-consumer plastics and contribute to reducing plastic waste.

2. Advanced experimental characterization of PP/PE blend

In this study, high-density Polyethylene (PE) and Polypropylene (PP) were provided by SABIC, The Netherlands. A polyolefin blend containing 10 wt% PP was compounded using a Collin co-rotating twin screw extruder. The extruded strand was immersed in a cooling water tank and subsequently cut into pellets measuring 3 – 4 mm in size. Tensile test specimens (ISO 527, type-1A) were molded using a Boy E35E injection molding machine.

2.1. Experimental set-up and synchronization procedure

Experiments were conducted following ISO 527-1:2012 using an electromechanical Instron ElectroPuls E10000 tensile apparatus equipped with a 10 kN static load cell and pneumatic grips. Figure 1 presents the tensile apparatus equipped with a high-speed 3D stereo Digital Image Correlation (DIC) system and an infrared (IR) camera for the full field measurement. Loading speeds of the cross-head were chosen from 1 to 40 mm/min at room temperature (RT). For optimal accuracy, a random speckle pattern was applied to the specimen's surface using speckle stamps from Correlated Solutions, Inc.

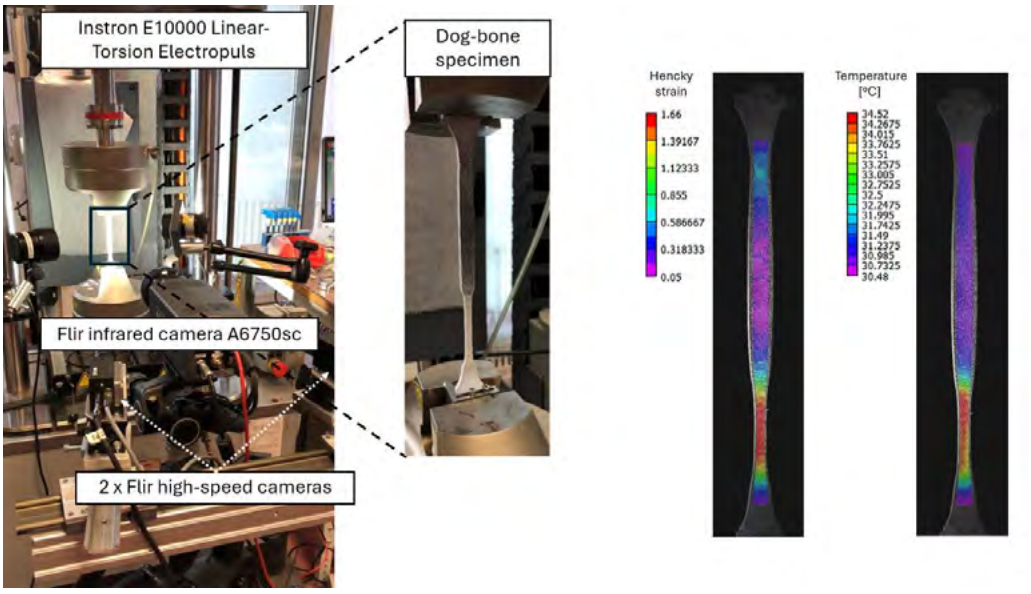

Figure 1. (Left) Instron ElectroPuls tensile experiment set-up equipped with Stereo DIC system and IR thermography. (Right) Synchronization of temperature field to DIC measurements during post-processing.

The research group developed a LabVIEW code and integrated it with corresponding hardware to synchronize the triggering of three cameras and the acquisition of force and displacement signals from the test bench. Data was captured at adjustable frequencies, ensuring 2,000 frames during a single tensile test. The IR camera captured temperature variations in the specimens during the test, and the results were synchronized with DIC measurements at the same frequency.

2.2. Experimental assessment of rate-dependence and self-heating of the polymer blend

Figure 2 plots the engineering stress-strain curves of PP/PE along with peak temperature evolution. The thermomechanical coupling effect of the PP/PE blend is illustrated using two distinct loading speeds, 2 and 20 mm/min, providing insights into its behavior under both isothermal and thermally coupled conditions, respectively. The stress-strain response of the PP/PE blend shows rate-dependence, with the peak yield stress increasing from 16.5 to 20 MPa as the loading speed is increased from 2 mm/min to 20 mm/min. Within this range of loading speeds, the viscoelastic response is barely observed. The stress-strain curves reveal distinct phases during tensile deformation, including elastic, visco-plastic, peak yield, initiation of necking, and stabilization of necking.

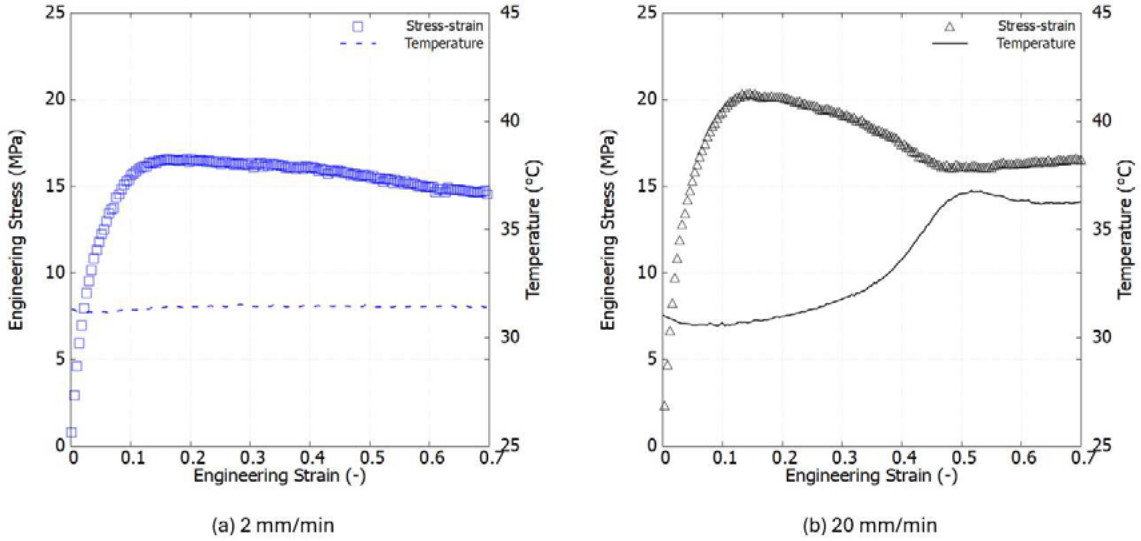

Figure 2. Experimental engineering stress–strain curves and peak temperature evolution for PP/PE blend at two loading speeds.

The synchronization of strain and temperature measurements enables a comprehensive quantitative examination of self-heating and thermal softening phenomena. Notably, the shape of stress-strain curve at a high loading speed of 20 mm/min, within the strain range of 0.2 to 0.45, shows a declining trend that tends to converge with the curve obtained at a lower strain rate. This behavior is attributed to thermal softening, a result of the inherent thermal sensitivity of polymers. During high-speed loading, self-heating causes a rapid temperature increase from 31 to 36 °C. However, the brief duration of this temperature rise is inefficient for efficient heat dissipation, leading to the degradation of material properties, particularly initiated at a strain of 0.1. Consequently, the thermal softening effect accelerates the progression of necking in the material.

3. Thermomechanical modeling of PP/PE blend

In this section, an advanced polymer constitutive model originally developed to characterize pure semi-crystalline polymers (SCP) was applied to the studied PP/PE blend. The thermal and mechanical properties of this binary blend are treated as those of a unified single continuum with an SCP structure [5].

3.1. Constitutive model

Polymers are widely recognized for their pronounced sensitivity to loading rate and temperature variations. The true stress-strain curve of the PP/PE blend closely resembles that of pure PE due to the small weight fraction of PP contamination. The double yield phenomenon, commonly observed in semi-crystalline thermoplastics and marked by two distinct turning points in the true stress-strain curves, can be effectively characterized using a recently introduced polymer model designed to encompass a variety of thermosets and thermoplastics [6]. The key time evolution of athermal strength is described as follows

$$\dot{s} = H_1(\bar{\varepsilon}) \cdot \left(1 - \frac{s}{s_1}\right) \cdot \dot{\bar{\varepsilon}} + H_2(\bar{\varepsilon}) \cdot \left(1 - \frac{s}{s_2}\right) \cdot \dot{\bar{\varepsilon}} + H_3(\bar{\varepsilon}) \cdot \left(1 - \frac{s}{s_3}\right) \cdot \dot{\bar{\varepsilon}} \tag{1}$$

A comprehensive evaluation and identification of the characteristic stresses s_i and functions $H_i(\bar{\varepsilon})$ (i=1,2,3) controlling the hardening evolution is described in Ref. [5]. To accurately depict the intricate interplay between thermal and mechanical coupling in capturing the self-heating effect, the heat equation is required [9-11]. In this work, the dissipation is assumed completely converted to heat according to the following relationship

$$\rho \, c_p \frac{\partial \theta}{\partial t} = \boldsymbol{\sigma} : \boldsymbol{F}_I^e \boldsymbol{L}_I^p (\boldsymbol{F}_I^e)^{-1} + \nabla \cdot \left(k \frac{\partial \theta}{\partial \boldsymbol{x}}\right) \tag{2}$$

where ρ is the polymer blend density, c_p constant thermal specific heat and k thermal conductivity. The 2nd-order tensors $\boldsymbol{F}_I^e$ is the elastic deformation gradient acting on the intermolecular resistance component shown in the rheological analog of Figure 3(left). The plastic velocity gradient expressed in the relaxed configuration is denoted by $\boldsymbol{L}_I^p$. More details on the methodologies employed to address this coupling can be consulted in Ref. [6].

3.2. Model validation

To accurately characterize the thermomechanical behavior of the PP/PE blend, it is essential to decouple the intrinsic material behavior from the 'necking' effects arising from geometric nonlinearity in the dog-bone specimen. The experimental true stress-strain curves, represented by the symbols in the middle plot of Figure 3, were derived using the Hencky strain extraction within the necking zone and true stress approximation methods, under the assumption of incompressibility and isotropy. This approach holds for highly stretchable polymers [5]. Currently, there is no consensus on how to determine true strains in these materials to provide a reliable measure for modeling and simulation frameworks. Accurate constitutive responses of the polymer are essential, for instance, in micromechanical modeling of composites using RVE-based approach.

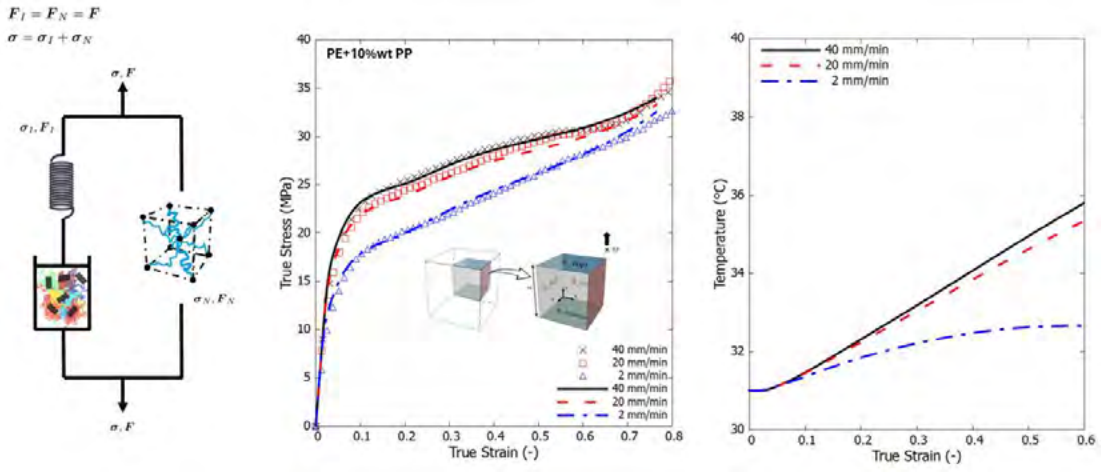

Figure 3. (Left) Rheological model for the characterization of PP/PE blend. (Middle) Model validation performed for PP/PE blend across different loading speeds. (Right) Prediction of temperature increase resulting from self-heating.

Unlike the engineering stress-strain curves with a cold draw during the necking stabilization stage, the true stress–strain curves display a distinct trend indicating a monotonic increase in stress at high strain levels. This hyperelastic-like behavior arises from the rubbery effect, wherein the reorientation of polymer chains predominates along the response of the material. The model effectively captured the rate-dependence, with the initial peak yield stress at a strain of 0.13 increasing from 18.7 MPa to 22.7 MPa and then to 24 MPa as the loading speed increased from 2 mm/min to 20 mm/min and then to 40 mm/min. The stress drops beyond a strain of 0.3 at higher loading speeds are attributed to thermal softening, highlighting the significant impact of heat generated from plastic dissipation. Additionally, the predicted temperature evolution versus true strain of PP/PE blend was plotted at different loading speeds. As the loading speed increased from 2 to 20 to 40 mm/min, experimental measurements at the strain of 0.6 showed a corresponding rise in peak temperature from 31.4 to 34.2 to 36.3 °C. Simulations indicated temperatures increasing from 32.6 to 35.3 to 35.8 °C, respectively. This temperature escalation is effectively captured by the thermomechanical coupling framework.

4. Application of RVE simulation for blend-based composites

The identified material model was subsequently employed to simulate the transverse compression of UD composites at two different loading rates: 10 and 100 s^{-1}. To quickly assess the UD composites with pure PE and compare them with those using a PP/PE blend, RVE simulations were conducted using four fibers under specific loading conditions. The load was applied symmetrically, with the lateral displacement of the surfaces perpendicular to the x-axis considered as "free on-plane" conditions (see Figure 4). The "free on-plane" enables the surfaces to move freely along the x-axis, but it is assumed that both the nodes of the fiber and the matrix remain in the same plane at all times. The carbon fibers were modeled as transversely isotropic, and a traction-separation law was applied to the interface using the same parameters specified in Ref. [12]. The homogenized true stress-strain response of three different carbon fiber (CF) reinforced polymers indicated that this boundary condition aligns well with the RVE undergoing periodic boundary conditions (PBCs) but is less computationally demanding [12]. The adoption of these non-periodic boundary conditions circumvents the periodic enforcement of potential sources of damage in UD composites under transverse loading, especially when small “exploratory” RVE models are used for quick evaluations on the material response.

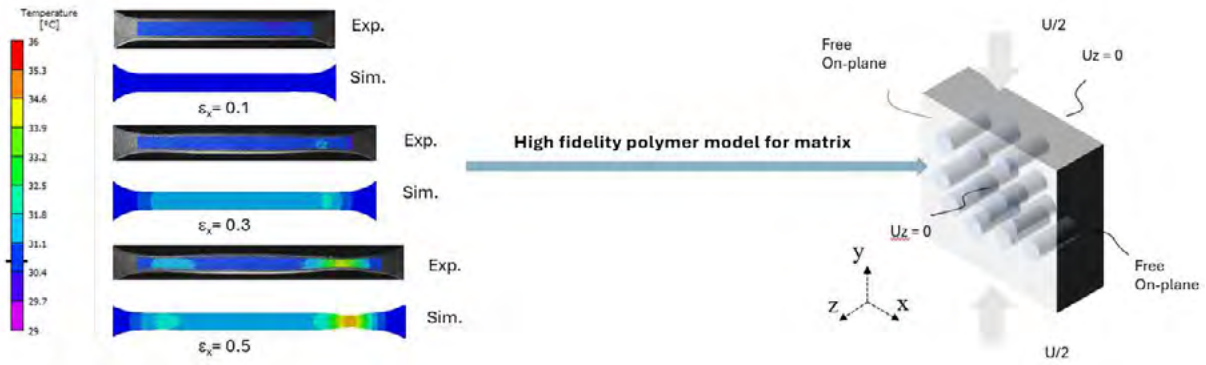

Figure 4. (Left) Comparison of temperature fields between experimental and simulated tensile test on polymer blend dog-bone. (Right) Illustration of the RVE settings for applying a blend in UD composites.

The engineering stress–strain curves were obtained by tracking the force and displacement of reference points attached to the top and bottom surfaces. Figure 5 shows curves from two material systems at two loading speeds, along with the local maximum principal strain field. The curves clearly present three phases: elastic, interface debonding and strain hardening. The plots indicate that the strain rate dependence is not evident in the stress-strain response or in the contour pattern of the local principal strain field. The maximum strain consistently occurs at the same location within the same UD composite

system but with a higher value at a lower strain rate. For instance, in the CF-PP/PE composite at a strain rate of 10 s^{-1}, the maximum principal strain is 0.15, located at the rightmost fiber. At a strain rate of 100 s^{-1}, the strain decreases to 0.133 at the same location. A similar trend is observed in CF/PE composite. This is attributed to the rate-dependence of the polymer matrix: as strain rates increase, the yield stress also rises (as depicted in Figure 3), making the deformation more difficult.

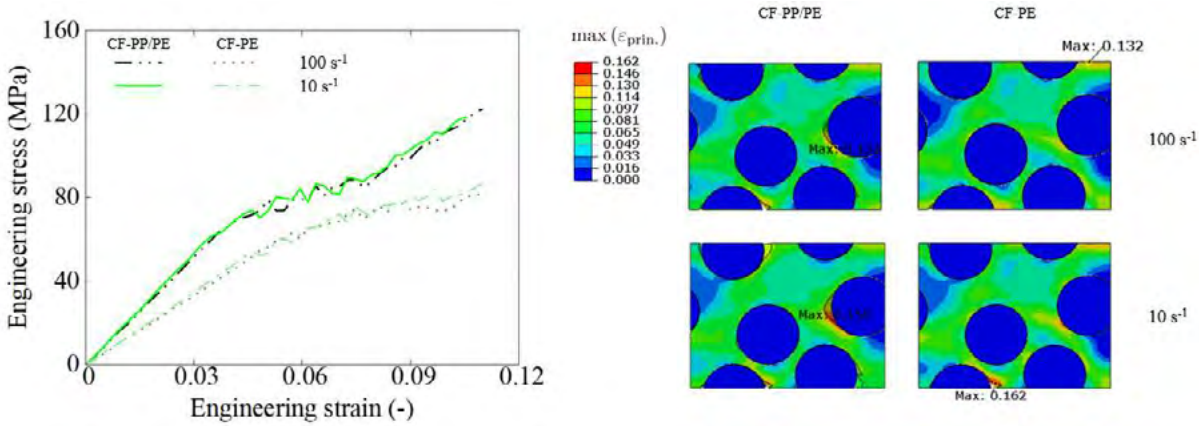

Figure 5. (Left) Stress–strain curves of RVE under transverse compression at strain rates of 10 and 100 s^{-1}. (Right) Principal strain profiles with a scale factor of three.

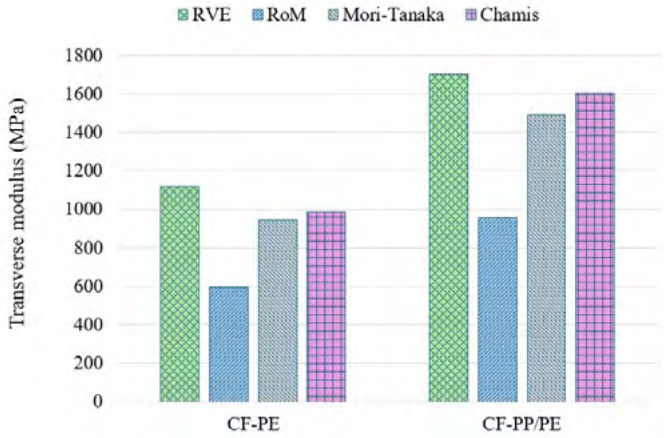

Figure 6. Transverse modulus of UD composites with pure PE and PP/PE blend matrices.

It is noteworthy that with just a 10 wt% addition of PP contaminant, the transverse modulus of CF-PP/PE, as calculated via RVE simulations, reaches 1700 MPa, marking a 34% increase compared to its CF/PE counterpart. Theoretical predictions also exhibit a similar trend, with the Chamis method closely aligning with the simulated RVE results, differing by 11.6% in CF-PE and 5.6% in CF-PP/PE. The incorporation of PP not only streamlines the sorting process for plastic waste during recycling but also enhances mechanical performance.

5. Conclusions

This study presents exploratory research that combines advanced constitutive material modeling for recycled polymer blends, experimental validation, and micromechanical simulations. It aims to explore the mechanical effects of using contaminated thermoplastics as matrices in UD composites under compression. To do this, a binary polymer blend of PP/PE underwent compounding and characterization using the advanced experimental methodologies. Integration of a 3D stereo digital image correlation (DIC) system with an Infrared (IR) thermography unveiled the self-heating effects on mechanical performance. Predictions from the constitutive model within the thermomechanical coupling framework closely aligned with observed mechanical behavior and temperature evolution, affirming its fidelity in

capturing intrinsic stress-strain behavior and the underlying physical mechanisms of polymer blends as a unified continuum.

The characterized intrinsic thermomechanical response of the PP/PE blend enabled the study of the rate-dependence of UD composites under transverse loading, providing insights into self-heating and thermal softening effects induced by the polymer blend matrix. RVE analyses showed the nonlinear response due to visco-plastic behavior and fiber debonding, resulting in strain localization within the polymer matrix and higher local strains compared to limited global strain levels. The rate-dependence is not evident in the UD composites and the limited heat associated with plastic dissipation was absorbed quickly into the carbon fibers with high thermal conductivity. The comparison between pure and blend-based composites highlighted increased stress levels and transverse modulus with the presence of traces of PP in the PE bulk.

Acknowledgments
P. Hao acknowledges the funding support from Ghent University's Special Research Fund ("Bijzonder Onderzoeksfonds", BOF) program under grant number BOF23/PDO/037.

References
[1] D. Maldas and B. V. Kokta. Recycled Thermoplastic–Woodflour Composites. *International Journal of Polymeric Materials*, 26: 69–78, 1994.
[2] Q. Yuan, D. Wu, J. Gotama and S. Bateman. Wood Fiber Reinforced Polyethylene and Polypropylene Composites with High Modulus and Impact Strength. *Journal of Thermoplastic Composite Materials*, 21(3): 195–208, 2008.
[3] K. Englund and V. Villechevrolle. Flexure and water sorption properties of wood thermoplastic composites made with polymer blends. *Journal of Applied Polymer Science*, 120(2): 1034–1039, 2011.
[4] G. M. Arifuzzaman Khan, M. S. Alam Shams, Md. R. Kabir, M. A. Gafur, M. Terano and M. S. Alam. Influence of chemical treatment on the properties of banana stem fiber and banana stem fiber/coir hybrid fiber reinforced maleic anhydride grafted polypropylene/low-density polyethylene composites. *Journal of Applied Polymer Science*, 128(2): 1020–1029, 2013.
[5] P. Hao, C. Siebers, K. Ragaert and F. A. Gilabert. Advancing the Characterization of Recycled Polyolefin Blends with a Combined Experimental and Numerical Approach to Thermomechanical Behavior. *Polymers*, 16(8): 1153, 2024.
[6] P. Hao, Z. Dai, V. Laheri and F. A. Gilabert. A unified amorphous–crystalline viscoplastic hardening law for non-isothermal modelling of thermoplastics and thermosets. *International Journal of Plasticity*, 159: 103469, 2022.
[7] E. M. Arruda, M. C. Boyce and R. Jayachandran. Effects of strain rate, temperature and thermomechanical coupling on the finite strain deformation of glassy polymers. *Mechanics of Materials*, 19: 193–212, 1995.
[8] R. Demets, M. Grodent, K. Van Kets, S. De Meester and K. Ragaert. Macromolecular Insights into the Altered Mechanical Deformation Mechanisms of Non-Polyolefin Contaminated Polyolefins. *Polymers*, 14: 239, 2022.
[9] D. Garcia-Gonzalez, R. Zaera and A. Arias. A hyperelastic-thermoviscoplastic constitutive model for semi-crystalline polymers: Application to PEEK under dynamic loading conditions. *International Journal of Plasticity*, 88: 27–52, 2017.
[10] P. Hao, S. W. F. Spronk, W. Van Paepegem and F. A. Gilabert. Hydraulic-based testing and material modelling to investigate uniaxial compression of thermoset and thermoplastic polymers in quasistatic-to-dynamic regime. *Materials & Design*, 224: 111367, 2022.
[11] F. Shen, G. Kang, Y. C. Lam, Y. Liu and K. Zhou. Thermo-elastic-viscoplastic-damage model for self-heating and mechanical behavior of thermoplastic polymers. *International Journal of Plasticity*, 121: 227–243, 2019.
[12] P. Hao, S. W. F. Spronk, R. D. B. Sevenois, W. Van Paepegem and F. A. Gilabert. Characterizing Pure Polymers under High Speed Compression for the Micromechanical Prediction of Unidirectional Composites. *Polymers*, 15(5): 1262, 2023.

METAL-EPOXY-MATRIX CARBON-FIBRE HYBRIDS FOR FUNCTIONAL AND STRUCTURAL APPLICATIONS

Hengli Cao[1], Shimeng Qian[2], Dominic Palubiski[1], Emile Greenhalgh[2], Xiaochuan Sun[3], Luiz F. Kawashita[1], Dmitry S. Ivanov[1]

[1]Bristol Composites Institute, School of Civil, Aerospace and Mechanical Engineering, University of Bristol, UK
[2]Department of Aeronautics, Imperial College London, South Kensington, London SW7 2AZ, UK
[3]National Composites Centre, Bristol and Bath Science Park, Emersons Green, Bristol BS16 7FS, UK

Email: Hengli.Cao@Bristol.ac.uk, Web Page: Hengli Cao — University of Bristol
Email: shimeng.qian21@imperial.ac.uk, Web Page: (32) Shimeng Qian | LinkedIn
Email : dominic.palubiski@bristol.ac.uk, Web Page : Dr Dominic Palubiski - Our People (bristol.ac.uk)
Email: e.greenhalgh@imperial.ac.uk, Web Page: Home - Professor Emile S Greenhalgh (imperial.ac.uk)
Email: ric.sun@nccuk.com, Web Page: (32) Ric Sun | LinkedIn
Email: luiz.kawashita@nccuk.com, Web Page: Dr Luiz Kawashita - Our People (bristol.ac.uk)
Email: Dmitry.Ivanov@Bristol.ac.uk, Web Page: https://www.bristol.ac.uk/people/person/Dmitry-Ivanov-092fdf5f-d92a-4931-bcb9-d13a72130d00/

Keywords: Metal matrix composites, functional composites, induction heating, stress concentrators

Abstract

The paper explores manufacturing and properties of a new form of hybrid composites combining metal and polymer matrices. These composites present unique architecture where metal matrix occupies inter-yarn space whereas the fibre bundles are impregnated with thermosetting matrix. The targeted placement of metals within the composite grants improvement of both structural and functional properties. It has been shown that a local incorporation of metal around stress concentrators can increase the strength of woven quasi-isotropic carbon-epoxy composite by 15%. On functional side, the stripes of metal built into woven preform double the current collection capabilities. To design and predict the performance of these novel architectures we explore the application embedded finite-element techniques allowing to reconcile the deeply intertangled scales of stress concentrator, heterogenous woven architecture with complex distribution of metal phase, and the geometry of metal patches.

1. Introduction

The drive for efficiency and functionality of composite materials pushes the need for new systems where various domains of an integral structure play different roles. Multi-Matrix Continuously-Reinforced Composites (MMCRC) [1,2] is a new class of composites hybrids where domains infused with conventional matrices share continuous reinforcement and hence reliably connected. Fibre bridging provides reliable integration of the domains which allows creating functional patches without disruption to the load flow.

The integration of metal in composites reinforcement may appear counter-intuitive. The weight was always considered to be the crucial advantage of the composites and adding heavy component seemingly defeats the key benefits. This is true when thinking of a whole structure made with metal-enhanced material. In this paper, we discuss the possibility of local doping with metals which is placed only where

it can change a certain aspect of composite behaviour but does not impose considerable weight penalty overall. This is where the concept of MMCRC becomes particularly relevant.

One such aspect is improving the behaviour of structures with features such as holes for bolted joints. The polymer composite matrices are known for being brittle and for their poor performance in the presence of multi-axial straining characteristic for stress concentrators, which results in early damage occurrence. The length at which the stresses experience rapid increase is often less than the size of the feature causing it – for bolted holes it is at the scale of millimetres. When metal is added locally and tailored to a specific stress concentrator geometry it does not create significant weight penalties but prompts the properties that polymers cannot achieve.

We hypothesise that the main property of metal that could help to tackle the stress concentration is its stiffness. Stiffness of even low melting temperature the metals, such as Tin (Sn), is of an order magnitude higher than the properties of any high-performance polymer. The introduction of metal at the location of high stress peak can help to redistribute stresses and decrease load in fibres. There are evidences that the incorporation of stiff elements around open hole may be important in improving the strength of structures. Stanier et al [3] showed that the Carbon-Nano-Tube (CNT) suspension can help to boost the strength in non-structural glass-epoxy composites. Liu et al [4], using embedded finite element formulation, explored the feasibility of improving strength of pure polymer by CNT introduced around hole in a specific pattern and confirmed that this could be a promising route. It has to be considered that the improving stiffness in structural carbon composites would require much greater boost in patch stiffness than CNT or any other additives can provide. Hence, the metals as the candidates for patching seems particularly attractive. In addition, lower threshold for initiating damage in Tin and plastic deformation may contribute to the improvement in such performance.

Another benefits of introducing the metal matrix is to enhance the current collection properties of the composites. While carbon composites are electrically conductive and enable functions such as energy storage [5] or resistive heating [6], the large contact resistance between the electrodes and the carbon preform creates substantial difficulty in exploiting the full potential of the material. Rather than bonding electrodes and relying on stochastic contact of fibres with metal, what if we could deeply integrated them into the depth of the woven architecture? Our hypothesis is that we can increase the electrical performance. This paper makes a first step towards validating this idea in experimental trials.

Hence, the main requirements to manufacturing are the locality of metal integration, the good control of electrodes/patch shapes, and the deep integration/infusion of metal into the textile architecture. Previously, we explored the feasibility manufacturing procedures and examined the structural behaviour in open-hole tests [7]. These observations are briefly iterated in the current paper for completeness. We proceed to exploring the functional behaviour of metal MMCRC in resistive tests and examine modelling tools to describe the structural behaviour for the new material system.

2. Manufacturing of metal-epoxy MMCRC

The manufacturing was implemented in two steps. In the first step, the tin foils cut to patch/electrode shape were placed between each layer of dry textile preforms (2×2 twill carbon preform with a weight of 210 g/m², composed of 3K yarns of T300 fibres). The preform was then packed into a vacuum bag to avoid oxidation while melting. The procedure hinged on tunning of process window to implement tin melting and preform impregnation before the heat reached temperature-sensitive consumables. Thermal insulation boards were included in the vacuum bagging preventing heat to reach the bag instantly. In a variation of this process the high-temperature consumables were sufficient to withstand processing temperature on their own. Thermocouples integrated in close proximity of the patch were used to control the process and by doing so to achieve various degrees of metal impregnation and composite morphologies. Temperature of the vacuum bag was monitored by thermal camera to prevent it from overheating and bursting. The process area was surrounded by EMI shielding material limiting the exposure of the material outside the patch area to magnetic field. Induction was applied using 10 kW

work head, which operated with frequencies ranging from 150-400 kHz. Novel cellular coils [2, 8] were used for electrodes and conventional pancake coils for strength patches. Applied current ranged from 80 to 250 A depending on targeted temperature, which was trialled in the range of 180°C-310°C – Figure 1.

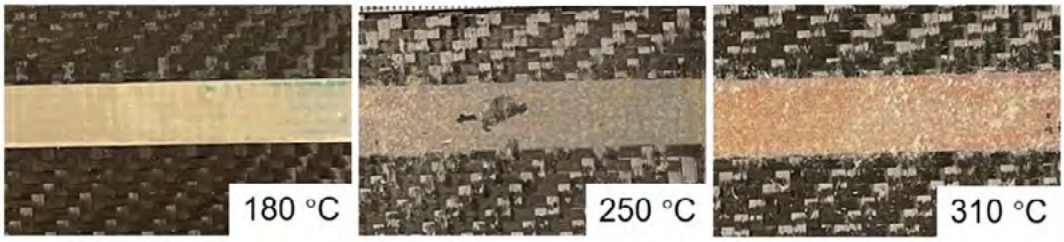

Figure 1. Various degrees of Sn integration into woven carbon preform using different process temperatures [7].

As the result of the trials it was found that holding temperature above 250°C for 5 minutes resulted in better outcomes in terms of depth impregnation and minimising oxidation. The second step involved conventional flexible bag infusion process using Prime 27 resin system.

The morphology of the material within the patch appeared to be rather unusual. Despite low viscosity of molten tin, the metal did not propagate through the fibre bundles and covered the inter-yarn / inter-ply space. The subsequent infusion impregnated the fibre bundle integrating the composite structure inside and outside of the patch – Figure 2. Both phases appeared to be practically void free with no sign of damage or delaminations at the yarn interface. This peculiar material distribution had some promising features. The new architecture did not interfere with the epoxy-carbon interfaces already optimised for good bonding and stress transfer. The metal enveloped fibre bundles providing good contact surface and creates integral percolative paths through thickness of the laminate.

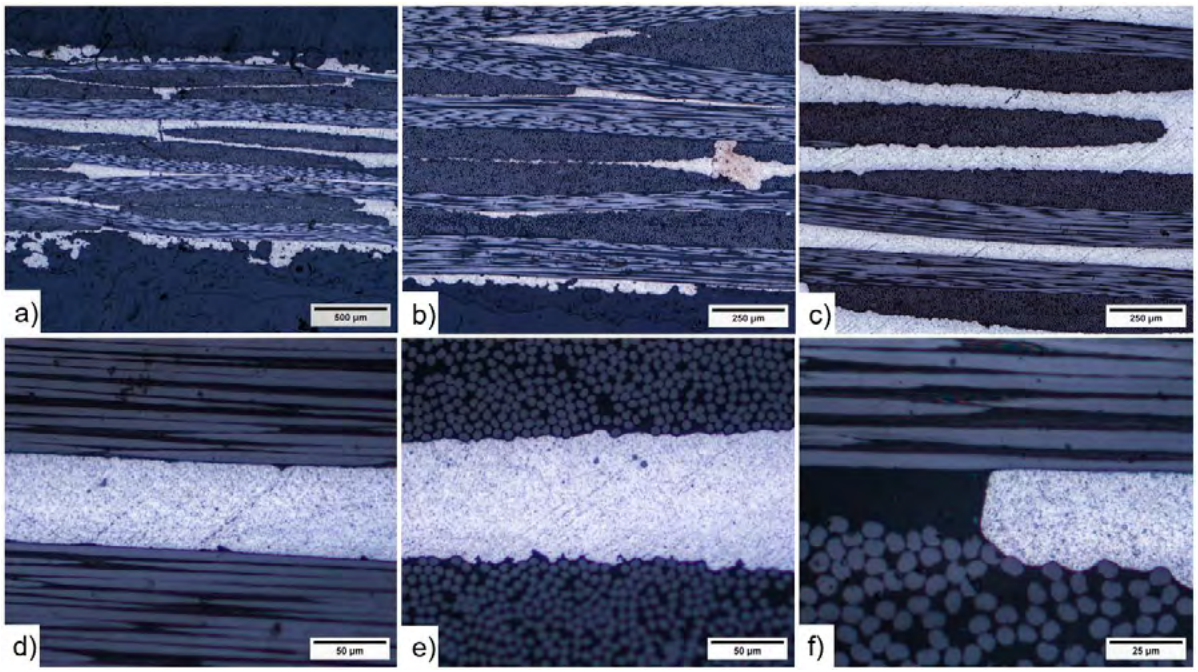

Figure 2. Microstructure of the metal-CFRP hybrid (light colour – Sn, dark grey – epoxy).

3. Experimental observations

3.1 Structural behaviour of metal-patched composites

Based on the initial numerical optimisation [7], it was found that the patch shape matters for releasing stress concentration and the most promising patch shape is a "butterfly" with the rays of R=14 mm in length – Figure 3. 6-mm hole was then drilled through the centre of the patch for the open hole tests. The test was conducted in line with ASTM D5766/D5766M-11 [9] standards using an Instron 8801 with a 100 kN load cell at a quasi-static rate of 2 mm/min. The tests were accompanied by DIC to explore both local and global deformation history and strain distribution maps.

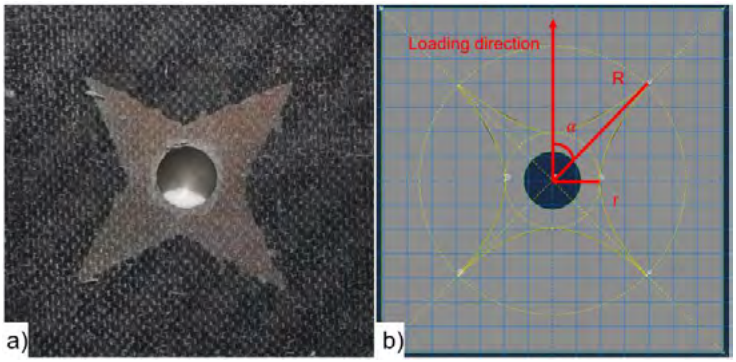

Figure 3. (a) Butterfly metal patch in CFRP, (b) parametrisation of patch shape to explore optimum geometry [7].

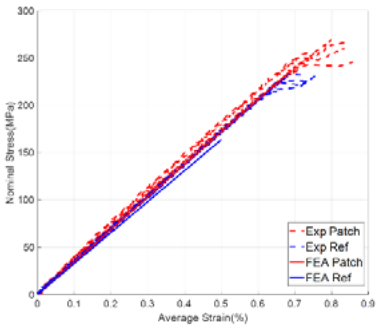

Figure 4. Stress-strain response of the reference and patched CFRP (dashed lines – experiments, solid – FEA).

The results of testing show 15% improvement in strength and 16.6% in failure strain of metal-patched samples compared to the reference configuration. The local strain histories recorded at the location of maximum stress concentrators show the signs of both – the stiffer response (lower local strain at given load compared to the reference configuration) and plastic yielding of metal matrix leading to strain redistribution mechanisms (non-linear response of local strain vs applied strain).

3.2 Functional behaviour of the hybrids

Tin foil stripes were merged into the twill woven fabric to produce electrodes 10 mm in width and 60 mm in length. Four electrodes were placed at a distance of 40 mm between them with their tip extending beyond the preform edge for clip attachment – Figure 5. Measurements were performed using Keysight 34465A 6.5 digital multimeter in the 4-wire resistance mode with a Keysight 11059A kelvin probe connecting to the tip of the electrodes– Figure 6. All measurements were conducted over the resistive range of 100 Ω with 10 NPLC (Number of Power Line Cycles), leading to a resolution of 0.01 mΩ. Transmission Line Method was used to evaluate the contact resistance. The total resistance, measured as the function of the distance between electrodes, allowed to estimate the contact resistance by extrapolating this function to zero electrode spacing. The obtained value was the double of contact resistance between the electrodes and the fabric. The slope of the curve on the other hand was proportional to the in-plane resistance of the fabric. Once resistances was evaluated, it was translated into the correspondent conductivities.

The measurements for the preform with the tin electrode were compared with the conventional copper tape electrodes. These electrodes, 35 µm with a one-sided layer of 25 µm electrically conductive pressure-sensitive acrylic adhesive, were cured at 120°C for 2 h under a 0.8 bar vacuum via a heated vacuum table to ensure the adhesion between the woven fabrics and electrode. The results showed that the contact conductivity increased from 0.66 ± 0.05 S/cm^2 (copper electrodes) to 2.0 S/cm^2 (tin electrodes). Interestingly, the in-plane conductivity also went up from 114 ± 1.5 S/cm to 249 S/cm probably owing to the enhanced in-plane conductivity under the surface of electrodes and leakage of the tin outside the electrode zone. While more research is needed to compare the current method with other available configurations (e.g. enhancing the contact with other conductive pastes) and measurement

methods (e.g. under controlled level of pressure), the initial results confirm our research hypotheses and indicate a certain promise of this direction.

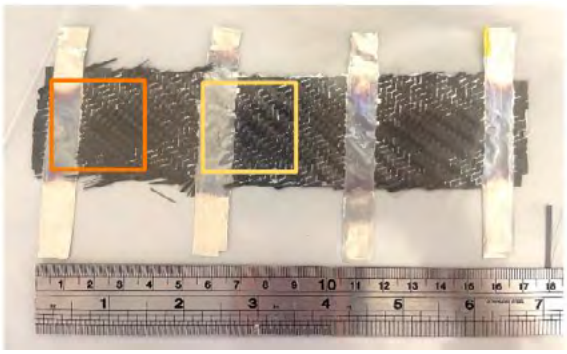

Figure 5. Tin stripes merged into woven fabric

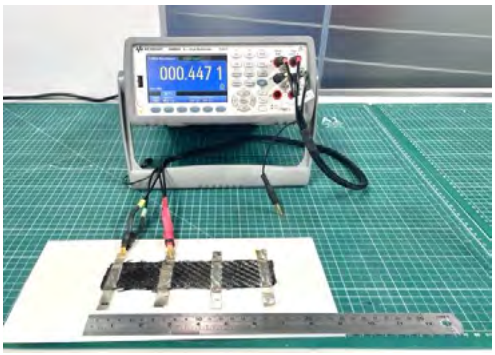

Figure 6. Set-up for evaluating in-plane and contact resistances.

4. Model of metal-patched composites

Modelling MMCRC presents a challenge for the conventional modelling approaches as there is a complex interaction of different heterogeneities at different scales: patch, yarns, and stress concentrator. This and the sharp stress peak in the hole vicinity makes the scale separation in multi-scale modelling problematic. On the other hand, the direct yarn-scale modelling may be prohibitive for the modelling approach or at least it cannot be deployed as the pragmatic design tool. To resolve this conundrum, we attempted to deploy the embedded element approach where the yarns and matrix are meshed independently and then "stitched" through constraints equations. To compensate for the volumes occupied by both the yarns and the matrix, the yarns were assigned reduced properties, i.e. the stiffness of the composite matrices are subtracted from the stiffness of yarns. The simplicity of the yarn meshing allows to avoid the issues with inter-yarn matrix region with complex distorted geometries and by doing that to reduce the overall mesh density and simplify the mesh in yarns. Such an approach has been successfully trialled for modelling composites enhanced with CNT [10] and woven composites [11]. It showed good computational efficiency while retaining sensible predictive capacity despite certain issues with the numerical noise, the complexities in justifying the mesh parameters, and the intricacies of pre- and post-processing.

A single ply of woven 2×2 twill carbon preform was modelled using WiseTex software and then transferred to Abaqus [12]. The solid geometry was then trimmed and operated to create open hole. Each yarn in this assembly presented independent geometric entity held together only by the matrix mesh. The matrix box with the in-plane dimensions of 36mm by 36mm was modelled independently of yarns with a butterfly patch (R=14 mm, r =7 mm) and the 6-mm hole located at the centre. The thickness of the matrix box matched the characteristic thickness of the fabric – 0.25 mm. The yarns and matrix were discretized using hex 3D element with 8 nodes (C3D8) to avoid hourglassing. The characteristic sizes of matrix elements in the patch zone was 0.125 mm and in the yarns was 0.25 mm – Figure 7.

The properties of the yarns were calculated using the micro-mechanical chess model [13], with a fibre volume fraction of 70%, characteristic input properties of T300 carbon fibres (longitudinal Young's modulus of 230 GPa), the properties of the matrix corresponded to Prime-27 epoxy (3.3 GPa Young's modulus, 0.35 Poisson's ratio), and the patch was assigned the properties of tin (41.6 GPa Young's modulus, 0.33 Poisson's ratio). The engineering constants were transformed into the stiffness matrix and the epoxy or tin were subtracted from the properties of yarns in the correspondent bulk and patch regions. Traction free boundary conditions were applied at the lateral edges to ensure free contraction and symmetry conditions applied to outer surfaces of the sample.

Modelling using embedded approach exhibited good predictive capability. The main peculiarity of using embedded elements was that the stiffness of the tin matrix within the patch was substantially higher than

the transverse stiffness of the yarns. This led to a negative "subtracted" stiffness of the yarns for the stiffness components responsible for transverse and shear deformation. This in turn results in irregular deformations of elements, particular on the patch interface, high distortions and noisy stress/strain output – Figure 8a. To obtain consistent results, all the negative components of the stiffness matrix were zeroed, which did improve the quality of the numerical response – Figure 8b. Stiffness was predicted to be 35.7 GPa for the patched samples and 32.6 GPa for the reference samples compared to 35.2 GPa for the patched samples and 34.3 GPa for the reference samples measured experimentally (Figure 4). Failure, predicted using the maximum strain criterion (translating to the longitudinal strain in fibres) in the fiber/loading direction, occurred at 0.68% applied strain for the patch model, compared to the experimentally measured 0.65-0.75%. For the reference model, failure was predicted at 0.50% applied strain, versus the experimental range of 0.60-0.65%. Even though the failure predictions in the reference sample are underestimated, the model showed good potential in capturing the main features of composites deformation and the improvement in the MMCRC as observed experimentally.

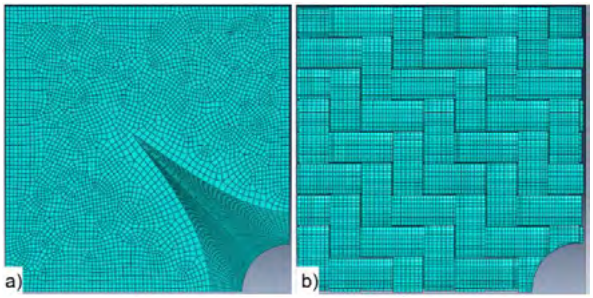

Figure 7. Superimposed mesh of (a) matrix (the ray in the right bottom corner is the metal patch) and (b) yarns. Only one quarter of the whole sample is shown.

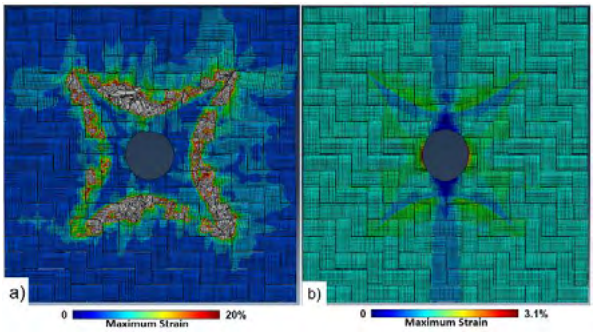

Figure 8 Direct strain in the loading direction at 1% applied strain (a) with negative stiffness elements of the stiffness matrix, (b) with negative stiffness zeroed.

4. Conclusions

In this work we explored metal MMCRC with the composites architectures that, to the best knowledge of the authors, were never created and explored before. We envisage a strong potential for this material configuration in both structural and functional behaviour of composite structures. Manufacturing method to produce these materials deployed conventional consumables typical for liquid moulding. The only aspect that stood out from the common manufacturing method is the application of induction heating and managing the heat transfer and process control. The obtained samples were manufactured with minor weight penalties (6-7% for the open-hole samples) and very local interference to the composite structure, which were the good match to the scales of characteristic stress concentrations.

We saw a good potential in deploying the methods such as the embedded element for the design of metal MMCRC. The peculiarities of the pre-processing of material properties led to the issues with mesh distortions and required certain stabilisation of the results. These numerical problems were managed by zeroing the negative stiffness matrix elements. The model showed sensible prediction capability of stiffness and failure although more work needs to be done regarding the potential mesh sensitivity.

Acknowledgments

The work has been supported by EPSRC grants EP/W03526X/1 and EP/W035219/1 "Realising Structural Power: Addressing the Manufacturing Challenges". The work of Hengli Cao was supported by the China Scholarship Council through the University of Bristol.

References

[1] Radhakrishnan A., Georgillas I., Hamerton I., Shaffer MSP., Ivanov DS Manufacturing multi-matrix composites: Out-of-vacuum bag consolidation, Journal of Manufacturing Science and Engineering, 145, 111003, 2023.

[2] Palubiski DR, Longana ML, Dulieu-Barton JM, Hamerton I, Ivanov DS. Multi-matrix continuously-reinforced composites: A novel route to sustainable repair of composite structures. Mater Des 2023;235:112446. https://doi.org/10.1016/J.MATDES.2023.112446.

[3] Stanier D, Radhakrishnan A, Gent I, Roy SS, Hamerton I, Potluri P, Scarpa F, Shaffer M, Ivanov DS. Matrix-graded and fibre-steered composites to tackle stress concentrations. Composite Structures 2019;207:72-80.

[4] Liu Q, Lomov SV, Gorbatikh L. Spatial distribution and orientation of nanotubes for suppression of stress concentrations optimized using genetic algorithm and finite element analysis. Materials & Design 2018;158:136-46.

[5] Asp LE, Greenhalgh ES Structural power composites, Composites Science and Technology 101 (2014) 41-61.

[6] Kwok N, Hahn T Resistance Heating for Self-healing Composites, Journal of composite materials, Vol. 41, No. 13/2007

[7] Cao H, Sun X, Kawashita LF, Ivanov DS New Metal-epoxy-matrix carbon-fibre hybrids to tackle stress concentration, Composites Part A (in print).

[8] Uzzell J.P.N, Pickard L.R., Hamerton I., Ivanov D.S. Novel cellular coil design for improved temperature uniformity in inductive heating of carbon fibre composites, Materials & Design 237 (2024) 112551.

[9] ASTM D5766/D5766M-11 Standard Test Method for Open-Hole Tensile Strength of Polymer Matrix Composite Laminates. 2011.

[10] Romanov VS, Lomov SV, Verpoest I, Gorbatikh L. Modelling evidence of stress concentration mitigation at the micro-scale in polymer composites by the addition of carbon nanotubes. Carbon 2015;82:184-94.

[11] Tabatabaei S.A., Lomov S.V., Verpoest I. Assessment of embedded element technique in meso-FE modelling of fibre reinforced composites, Composite Structures 107 (2014) 436–446.

[12] Lomov S.V., Verpoest I., Cichosz J., Hahn Ch., Ivanov D.S., Verleye B. Meso-level textile composites simulations: open data exchange and scripting, Journal of Composite Materials, 48(5): 621-637, 2014.

[13] Green S. D., Matveev M. Y., Long A. C., Ivanov D.S,, Hallett S. R., Mechanical modelling of 3D woven composites considering realistic unit cell geometry, Composite Structures, 118 (2014): 284- 293.

EFFECT OF CARBON BLACK AS A CONDUCTIVE FILLER ON THE ELECTRICAL, THERMAL AND MECHANICAL PROPERTY OF EPOXY

Bibhuti Bikash Kagyung[1], Chandra Sekher Yerramalli[2]

[1]Aerospace Engineering Department, Indian Institute of Technology, Bombay, Mumbai, India
Email: 204010009@iitb.ac.in
[2]Aerospace Engineering Department, Indian Institute of Technology, Bombay, Mumbai, India
Email: chandra@aero.iitb.ac.in

Keywords: Polymer composites, Matrix modification, nano-fillers, characterization

Abstract

This paper studies the variation of mechanical, electrical and thermal properties of epoxy resin mixed with Carbon Black (CB) nano-fillers. The average size of the CB nano fillers was 30 nm. Microscopic images of the powders were taken using Transmission Electron Microscope (TEM). A solvent-dispersion method was used to homogenously distribute the nano-fillers in the matrix. Tensile tests showed that the best mechanical properties were achieved at 4% to 6% filler addition. Electrical conductivity tests showed that at just 2% filler addition, the conductivity of the neat epoxy rose by 8 orders of magnitude. However, further addition does not cause much difference to the electrical conductivity. Thermal characterization was done using TGA and DSC studies. Glass transition temperature reduces upon addition of nano-fillers. However, there is an increase in T_g at 10% filler weight fraction. Based on the characterization tests, it was concluded that addition of a filler content of 4% to 6% weight fraction is ideal for lightning strike applications.

1. Introduction

Fiber-reinforced polymer matrix composites have widespread applications in various fields of engineering like in the aerospace industry, energy sector, automobiles, etc. They have numerous advantages over conventional metals, in terms of superior strength-to-weight ratio, superior stiffness-to-weight ratio, corrosion resistance, etc. Epoxy is one of the most commonly used thermosetting polymer in Carbon Fiber Reinforced Polymer (CFRP) composites for structural applications. Epoxies offer superior properties in comparison to other thermosetting polymers. These include high stiffness, high adhesion strength and low shrinkage in cure. Aircraft companies adopt such lightweight structures to minimize fuel consumption. Research is ongoing to replace traditional metals with these lightweight materials as much as possible. Despite the numerous advantages, epoxies are insulating by nature. This makes them susceptible to damage in case of a transient electrical energy discharge like in the case of a lightning strike phenomenon.

A lightning strike is a phenomenon in which huge amount of electric discharge takes place between clouds or from clouds to ground. When an airplane passes through the clouds during such an event, the lightning bolt attaches itself to one of the outer extremities like the nose, wing tip or rudder. The lightning channel then moves through the aircraft due to aerodynamic flow effect and exits through another extremity [1]. This is known as the swept stroke of the lightning discharge. Aircraft companies usually employ lightning strike protection systems to deter any damage from such events. The most conventional way is to use a metallic mesh like copper or aluminum mesh [2] on the outer skin of the aircraft. These meshes can dissipate the current from a lightning strike on the surface forming a Faraday cage and protecting the passengers inside. However, these protective meshes add to the overall weight

of the structure leading to increased fuel consumption. Researchers are on the lookout for better lightweight alternatives.

Carbon-based nanomaterials like Carbon nanotubes (CNTs), graphenes, carbon black (CB), etc are being extensively researched to be used either as conductive matrix or as a coating on composite laminates [3-7]. They have proven to enhance the electrical and thermal properties of epoxy matrices. These nano-materials have promising aspects to be used as lightning strike protection systems in aircrafts. However, there are few hurdles that it needs to overcome like operator-dependance, overall maintenance cost and large-scale manufacturing difficulties. This paper attempts to fabricate a conductive epoxy system by addition of CB nanofillers. Filler weight fractions ranging from 2% to 10% are being fabricated. A solvent dispersion method is employed to have a near-homogenous mixture of the nano-fillers in the epoxy matrix. Mechanical, thermal and electrical characterizations are done to determine the optimal filler weight fraction.

2. Experimental methodology

2.1. Materials used

Diglycidyl Ether of Bisphenol-A (DGEBA) type epoxy resin under the brand name of Lapox L-12 supplied by Atul Chemicals is used. An amine-based hardener (Lapox K-6) is used with it in a mixing ratio of 10:1 by weight. Acetylene black grade of Carbon Black was purchased from Otto Chemie Pvt Ltd. The average particle size was around 30 ± 2 nm.

2.2. Fabrication of CB/epoxy composites

A solvent dispersion method has been used for the fabrication of the nano-composites. This method has proved to give a better dispersion of the nano-fillers in epoxy matrix [8]. Figure 1 below shows a schematic of the fabrication technique.

The CB fillers were initially kept in an oven for 2 hours at 50° C to remove any moisture present. The CB fillers are then mixed in acetone (99.9% purity) with the help of a magnetic stirrer for 30 minutes at 400 RPM. It is then kept in an ultrasonic bath for 30 minutes to break down any remaining agglomerates. 75 grams of epoxy are separately heated at 120 ° C to make it less viscous. This is done so that the nano-fillers easily mix up in the resin. The CB-acetone mixture is then poured into the epoxy resin. The mixture is then heated and simultaneously stirred using a magnetic stirrer till all the acetone present in the mixture evaporates. A uniform dispersion of the CB nano-fillers in epoxy is thus obtained. Due to the continuous stirring and ultrasonication, numerous air bubbles get trapped inside the resin leading to micro pores in the cured epoxy samples. This is not desirable as it reduces the strength of the resin and also hampers the electrical and thermal properties. For this reason, the CB-epoxy mixture is kept in a vacuum chamber and degassed. This removes most of the air bubbles trapped inside the resin. The hardener is then mixed with the epoxy in a ratio of 10:1. It is then slowly stirred till the hardener completely mixes with the epoxy. The mixture is then again kept in a vacuum chamber and degassed for a few minutes. It is then poured into molds of required shapes and kept for 24 hours at room temperature for curing.

©2024 | 2_KAGYUNG_Bibhuti Bikash_XOZNN.pdf:2

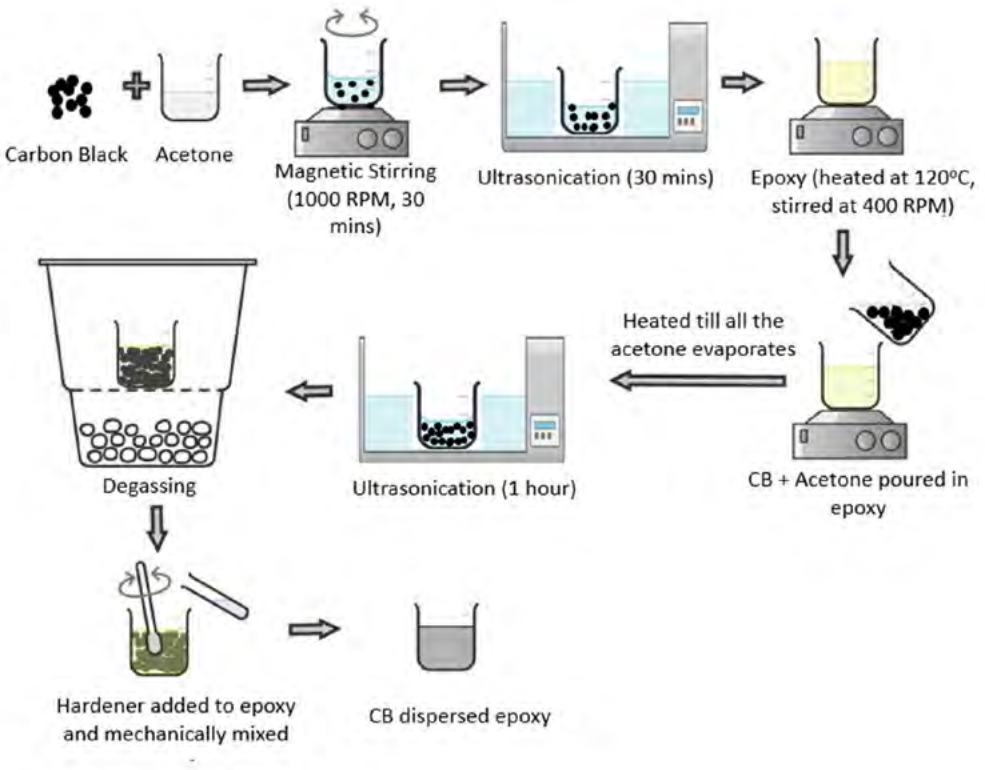

Figure 1. Solvent dispersion method

2.3. Material characterization

2.3.1 Morphological characterization

Transmission Electron Microscopic (TEM) images were taken of the powdered CB sample to understand its morphology. A small amount of the sample was mixed in acetone. A single drop of the sample is then injected on a carbon coated copper grid. The grid is then inserted in the microscope to analyze the sample. A FEI Tecnai G2, F30 model was used for the TEM study.

2.3.2 Mechanical characterization

Dog-bone samples were prepared for tensile tests according to ASTM D638 to determine the effect of nano-filler addition on the yield strength and Young's modulus of the pristine epoxy. A 30 kN capacity UTM (MTS E-44 model) was used for the tensile tests. Strain gauges were attached to the samples to get accurate strain readings. 3 samples for each configuration were tested to get a mean value of the yield strength and the Young's modulus.

2.3.3 Electrical characterization

The main purpose of the matrix modification is to make the epoxy electrically and thermally conductive. So, it is very important to understand the effect of nano-filler addition on the conductivity of epoxy. The electrical conductivity measurements were done using a Wayne Kerr 6500B Impedance Analyzer. The sample dimension was 10 mm x 10 mm x 1 mm. The opposite faces of the samples were coated with a conductive paste to create a channel for the current to pass through. Frequency range from 100 Hz to 1 MHz were analyzed. The lowest frequency tested was assumed to be the DC current.

2.3.4 Thermal characterization

Thermo-gravimetric analysis (TGA) was done for the samples to study the heat Vs mass loss for different filler weight fraction. Also, Differential Scanning Calorimetry (DSC) measurements were done for the samples to analyze the change in glass transition temperature (Tg) for the epoxy samples with different filler weight fractions. Powdered samples of around 30 milligrams were used for both TGA and DSC measurements. A Hitachi NEXTA STA 300 model and DSC 7020 model was used for the TGA and DSC measurements respectively.

3. Results and discussions

3.1 Morphology

Figure 2 below show the TEM image for the CB fillers. The average diameter of the fillers was found to be 30 nm. It is also observed that the nano-fillers tend to form agglomerates. This is due to the small size and high surface energy of CB [9]. This is why it is necessary to perform ultrasonication of the CB nano-fillers to breakdown the clustering.

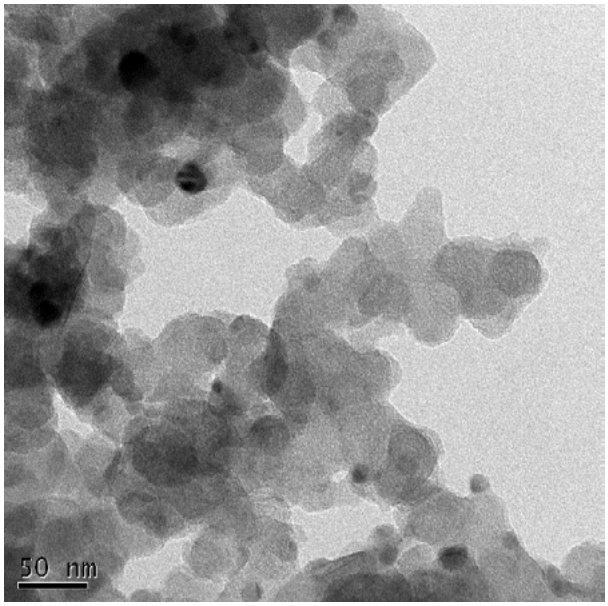

Figure 2. TEM image of CB nano-fillers

3.2 Mechanical characterization

Figure 3 and 4 shows the variation of yield strength and Young's modulus respectively with varying filler weight fraction. The yield strength of the samples slightly decreased upon addition of nano-fillers. 2% weight fraction of the nano-fillers showed the lowest yield strength, however for 4% and 6% weight fraction, the samples show the same strength as the neat epoxy. Again for 8% and 10% weight fraction, the strength reduces slightly. Similarly, for the modulus, 2% weight fraction of the nano-fillers showed the least stiffness. Overall, the stiffness reduces for all the samples except at 6% weight fraction which showed an increase in the Young's modulus.

It has to be noted the failure also depends on the percentage of voids present in the matrix. Higher percentage of voids leads to pre-mature failure of the samples. This drastically reduces the strength of the samples. This is why utmost care has to be taken while fabricating these samples to prevent voids.

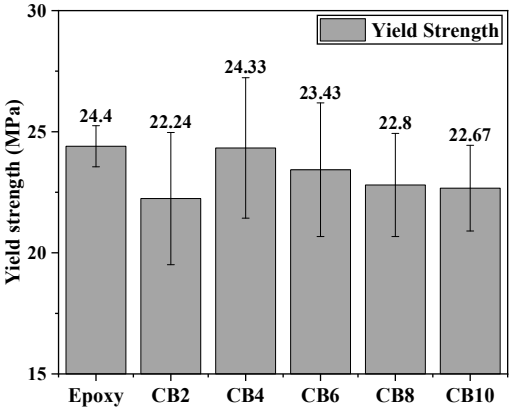

Figure 3. Yield strength Vs Filler weight fraction

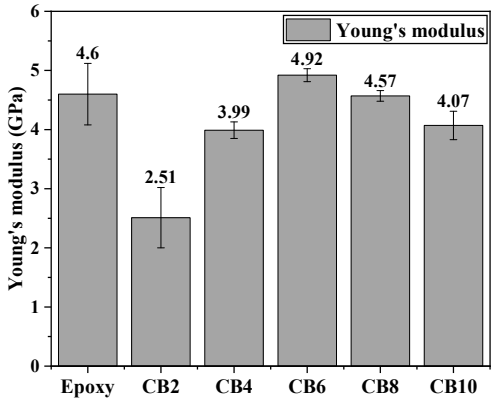

Figure 4. Young's modulus Vs Filler weight fraction

3.3 Electrical characterization

For nanocomposites, it is essential to understand the percolation threshold of the material. It is defined as the filler concentration at which the nanofillers form a conductive network in the insulating matrix and thus the material changes from an insulator to a conductor [10]. Adding further nanofillers beyond this point does not have any significant effect on the electrical conductivity of the material. Figure 5 below shows the variation of electrical conductivity with varying filler weight fraction. At just 2% filler weight fraction, the electrical conductivity of the pristine epoxy increased from 8.33E-15 to 1E-7. The conductivity increased by 8 orders. However, further addition did not cause any significant increase in the electrical conductivity. The electrical conductivity almost remains the same. This might be due to the reason that at higher filler weight fraction, there is a higher chance of agglomeration of the nano particles leading to more gaps in the matrix. Thus, the conductive network might get disrupted. However further addition will fill those gaps in the conductive network leading to a continuous network of the nano fillers. At 10% filler weight fraction, the electrical conductivity takes another jump by an order of one. It is also to be noted that it is essential to understand at which the conductivity takes a jump from the base matrix value to a semi-conductor range. For this, lower weight fraction of fillers in epoxy needs to be fabricated and tested.

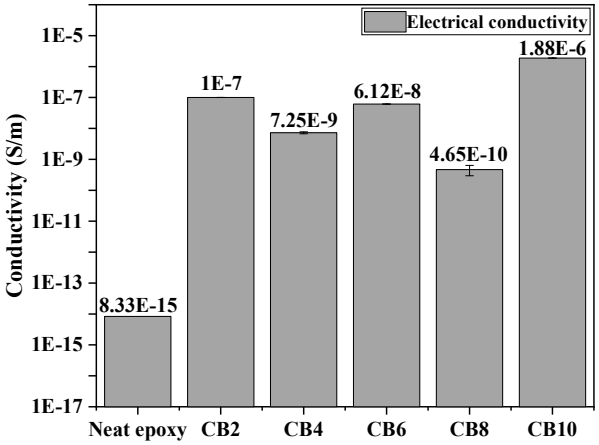

Figure 5. Electrical conductivity Vs Filler weight fraction

3.4 Thermal characterization

TGA and DSC analysis were done for the samples. Figure 6 and 7 below shows the TGA and DSC plots respectively for CB-epoxy samples from 2% to 10%. The TGA curve shows that the decomposition temperature for all the samples almost remains the same. However, the residual weight of the samples increase as the filler content increases. This can be attributed to the fact that the decomposition temperature for carbon black is higher than that of epoxy. The epoxy decomposes first leaving a residue of carbon particles. The initial 3-4% weight loss might be due to moisture content present in the samples. The DSC curve shows the heat flow Vs temperature for the samples. It has been observed that at lower filler weight fractions, the glass transition temperature (T_g) reduces. For the neat epoxy, it was around 59°C. Initial addition of nano-fillers reduces the T_g up to around 54°C. However, at 10% filler addition, the T_g takes a jump upto around 62°C.

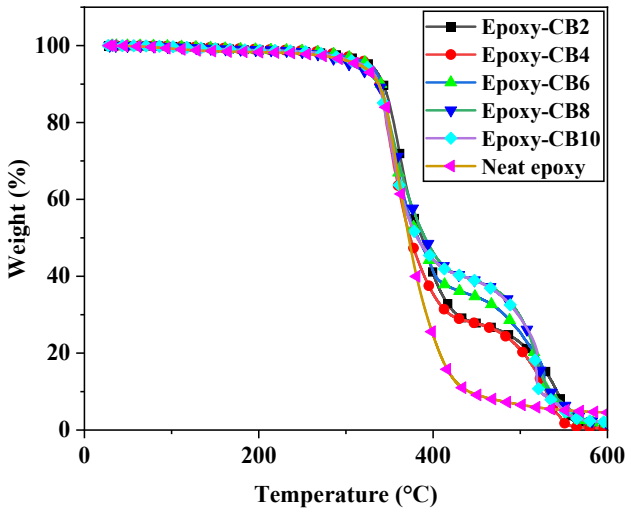

Figure 6. TGA curves for neat epoxy and CB filled epoxy resins

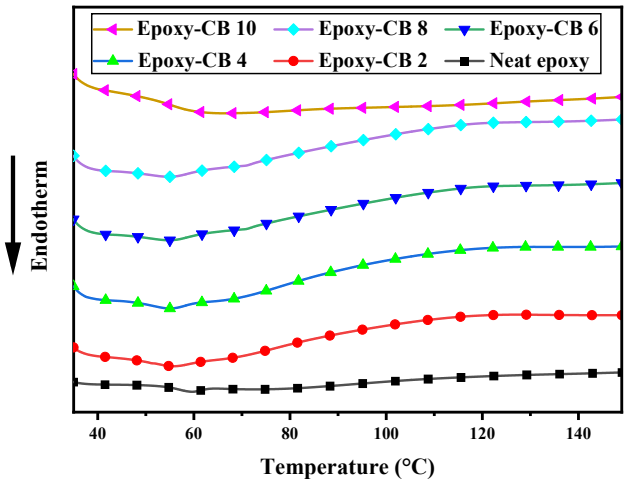

Figure 7. DSC curves for neat epoxy and CB filled epoxy resins

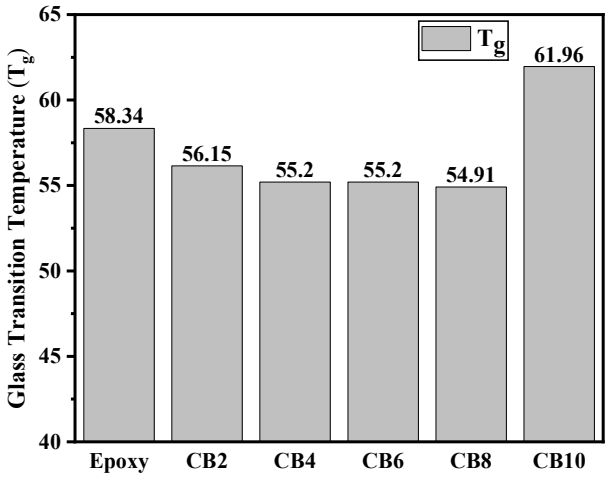

Figure 8. Tg Vs Filler weight fraction

4. Conclusions

The variations in the mechanical, electrical and thermal properties of epoxy resin upon addition of CB nano-fillers has been studied in this paper. CB nano-fillers ranging from 2% to 10% filler weight fraction were added to the matrix. A solvent dispersion method was employed to uniformly disperse the nano-fillers in the matrix. 4% weight fraction of the nano-fillers showed the best yield strength properties in comparison to the neat epoxy. However, it is to be noted that it is still less than the neat epoxy. 6% weight fraction showed the best stiffness properties. For the electrical properties, it has been observed that at just 2% filler addition, the electrical conductivity jumps by 8 orders from the neat epoxy conductivity. However, further filler addition does not affect the conductivity a lot. The TGA curve shows that the residual weight after decomposition increases with increasing filler weight fraction. This

is due to the presence of more CB fillers at higher concentrations. The DSC curve shows the variation of glass transition temperature (T_g) with varying filler weight fraction. The T_g decreases with increasing filler content. However, at 10% filler weight fraction, it slightly increases more than the neat epoxy. This paper has tried to study the variations in properties of epoxy resin with different concentrations of CB fillers to reach at an optimum filler concentration for applications in lightning strike protection systems. Based on the results, there is not a particular filler concentration at which all the properties showed optimum results. A trade-off has to be done. Based on the results, a filler weight fraction between 4% to 6% can be considered for further applications.

Acknowledgments

The authors would like to acknowledge the National Aerospace Laboratories (NAL), Bangalore for allowing them to use their facility for conducting experiments.

References

[1] Xiangteng MA, Fusheng Wang, Han Chen, Donghong Wang and Bin Xu. Thermal damage analysis of aircraft composite laminate suffered from lightning swept stroke and arc propagation. Chinese Journal of Aeronautics. Volume 33(4): 1242-1251, 2020
[2] T.M. Dhanya and Chandra Sekher Yerramalli. Lightning strike effect on carbon fiber reinforced composites – effect of copper mesh protection. Materials Today Communications. Volume 16: 124-134, 2018.
[3] Wenhua Lin, Yeqing Wang, Kamran Yousefpour, Chanyeop Park and Vipin Kumar. Evaluating the Lightning Strike Damage Tolerance for CFRP Composite Laminates Containing Conductive Nanofillers. Applied Composite Materials. Volume 29: 1537-1554, 2022.
[4] Tanusree Bera, S.K. Acharya and Punyapriya Mishra. Synthesis, mechanical and thermal properties of carbon black/epoxy composites. International Journal of Engineering. Volume 10(4):12-20, 2018.
[5] Florian H. Gojny , Malte H.G. Wichmann, Bodo Fiedler, Ian A. Kinloch, Wolfgang Bauhofer, Alan H. Windle and Karl Schulte. Evaluation and identification of electrical and thermal conduction mechanisms in carbon nanotube/epoxy composites. Polymer. Volume 47(6):2036-2045, 2006.
[6] Frank Gardea and Dimitris C. Lagoudas. Characterization of electrical and thermal properties of carbon nanotube/epoxy composites. Composites Part B: Engineering. Volume 56:611-620, 2014.
[7] A comprehensive review on the thermal, electrical, and mechanical properties of graphene-based multi-functional epoxy composites.
[8] Shubham, Palak Bharti, Rajesh Kumar Prusty and Bankim Chandra Ray. Tribological, Mechanical, and Thermal Behavior of Titanium Dioxide and Graphene Nanoplatelet Embedded Epoxy Based Hybrid Nanocomposite. Polymer Science, Series A. Volume 64:504-518, 2022.
[9] Shangyong Zhang, Ruipeng Zhong, Ruoyu Hong and David Hui. On factors affecting surface free energy of carbon black for reinforcing rubber. Nanotechnology Reviews. Volume 9(1):170-181, 2020.
[10] V. I. Irzhak. Percolation Threshold in Polymer Nanocomposites. Colloid Journal. Volume 83:64-69, 2021.

PHOTOCATALYTIC AND BIOCIDAL PROPERTIES OF BACTERIAL CELLULOSE-SILVER PHOSPHATE NANOCOMPOSITE

Amruth Kaitheri[1], Sudipto Pal[1], Sanosh Kunjalukkal Padmanabhan[1], Matteo Calcagnile[2], Antonio Licciulli[1]

[1]Department of Engineering and Innovation, University of Salento, Lecce 73100, Italy

[2]Disteba, University of Salento, Lecce 73100, Italy

Email: amruth.kaitheri@unisalento.it; sudipto.pal@unisalento.it; sanosh.padmanabhan@unisalento.it; matteo.calcagnile@unisalento.it; antonio.licciulli@unisalento.it,

Keywords: BC-AgP nanocomposite; photocatalyst; antibacterial

Abstract

In this study, we report the synthesis and properties of a bacterial cellulose-silver phosphate nanocomposite aimed at environmental and antibacterial applications. The bacterial cellulose/ silver phosphate nanocomposite had a weight ratio of 1:4. The visible light photocatalytic activity was investigated by the degradation of methylene blue and rhodamine B dyes. The size of silver phosphate particles on bacterial cellulose fibres was controlled by using the cationic surfactant cetyltrimethylammonium bromide (CTAB) and exhibited superior performance as compared to its counterpart without using CTAB. The reduction in particle size is directly correlated with an increase in photocatalytic efficiency, as it provides a larger surface area for the photocatalytic reactions to occur. The antibacterial activity of the composite was experimentally confirmed by performing halo test on *Escheria coli* indicating its potential dual functionality. The findings suggest that the bacterial cellulose-silver phosphate nanocomposite, particularly with the addition of cationic surfactants, holds great promise as an efficient and multifunctional material for environmental remediation and antibacterial applications.

1. Introduction:

The discharge of wastewater with toxic dyes and chemicals into aquatic ecosystems has raised a dire need for effective treatment methodologies [1]. Silver phosphate stands at the forefront for its renowned photocatalytic efficiency [2,3]. Its unique properties, such as low toxicity, wide photo response range, and commendable photocatalytic performance, makes it an ideal candidate for environmental remediation efforts [4].

The antibacterial properties of silver have been known for centuries [5]. Silver compounds are effective antiseptics due to their capacity to irreversibly damage key enzyme systems in pathogens' cell membranes [6]. Silver ions readily bind to bacterial cell walls and membranes, impeding the respiratory chain and disrupting vital cellular processes [7]. Although the exact mechanism is unknown, recent

research suggests that silver ions cause paired strands of DNA in bacteria to separate, weakening the binding between proteins and DNA, eventually leading to bacterial inhibition [8].

The integration of bacterial cellulose into silver phosphate nanocomposites could amplify the photocatalytic activity and it can be a biocompatible and eco-friendly dimension to the treatment process [2]. Surfactants like Cetyltrimethylammonium bromide (CTAB), Sodium Lauryl Sulphate (SLS), Pluronic F127 are commonly used to reduce the particle size of a material by preventing agglomeration and improving the dispersion [2,9,10].

In this work a bacterial cellulose-silver phosphate (BC-AgP) nanocomposite in a weight ratio of (1:4) was synthesised. The efficiency of the material as a visible light photocatalyst to treat the wastewater from textile industries were evaluated by performing dye degradation tests using Rhodamine B and methylene blue. The samples were prepared with and without CTAB to investigate the influence of particle size on material properties. Also, the antibacterial activity of these nanocomposites is studied offering a dual function of pollutant degradation and microbial inhibition, which is interesting for the prevention of pathogen growth in water bodies. BET, UV-Visible spectrophotometry, SEM, and antibacterial tests were carried out to characterise the material properties.

2. Materials

Silver nitrate ($AgNO_3$) was purchased from J.T Baker, Potassium phosphate dibasic trihydrate ($HK_2O_4P.3H_2O$) was purchased from sigma Aldrich and CTAB (1-Hexadecyl) trimethylammonium bromide, 98 % ($CH_3(CH_2)_{15}N(CH_3)_3Br$) was purchased from Alfa aeser. Black tea bags (Sir Bolton Company), commercial sucrose, commercial vinegar and Kombucha tea were purchased from a local market. The whole synthesis process was carried out using distilled water.

2.1 Method

2.1.1 Preparation of Bacterial cellulose-silver phosphate nanocomposite.

The synthesis of bacterial cellulose pulp was described in our previous works [2,11]. 4 grams of BC pulp (0.2 g dry weight) was added to 50ml of distilled water and allowed to stir for a while. A definite amount of silver nitrate was added on to the solution and kept under stirring overnight. Meantime, a fixed amount of dipotassium hydrogen phosphate and trimethylammonium bromide were added to a 50ml of distilled water and stirred overnight. The solution containing $HK_2O_4P.3H_2O$ and CTAB were added dropwise to the solution containing bacterial cellulose and silver nitrate, forming a yellow-coloured solution which confirms the formation of silver phosphate particles. This solution was decanted, and the sediment was washed using distilled water and kept for drying at 70°C overnight to obtain bacterial cellulose-silver phosphate (BC-AgP) nanocomposite. Silver phosphate without bacterial cellulose was also made in this similar way by omitting the inclusion of bacterial cellulose. Similarly, BCAgP nanocomposite without adding CTAB was also prepared to characterise.

2.2 Characterisation of the photoactivity

Photocatalytic activity of BCAgP was evaluated by dye degradation tests. A tungsten lamp of 300W (Sanolux, Radium Lampenwerk, Irradiance 41.4 W m^{-2} at 380–700 nm wavelength) was used as a solar light simulator inside a closed chamber. 100 ml of 5ppm Rhodamine B(RhB) and Methylene Blue (MB) were taken and 0.1 g of photocatalyst were added on it and stirred for almost an hour before turning on the light to maintain the absorption-desorption equilibrium.

2.3 Halo test

Esc*herichia coli* FB8 was grown on solid LB plates (composition per liter: 10 g Tryptone, 10 g NaCl, 5 g Yeast Extract, 18 g Agar) for 24 h at 37°C. The following day a colony was collected and resuspended in a 0.85% NaCl solution. The concentration of bacterial suspension was then adjusted to achieve a final inoculum with an OD at 600 nm of 0.06 (equivalent to 0.5 McFarland, 1 x 10^8 CFU/mL). The susceptibility test was performed on LB agar. Inoculation was carried out by immersing a sterile swab in the inoculum, removing excess fluid by pressing and turning the swab against the inside of the tube, and then swiping the swab in three directions on the agar surface. Finally, disks were firmly applied to the surface of the inoculated agar plate. The inoculum and medium were prepared following the EUCAST guidelines (EUCAST, 2024).

3. Results

3.1 SEM

Figure 1 shows the SEM images of BC-AgP (a), (b) and BC-AgP/CTAB (c), (d) in different magnifications. Silver phosphate particles are well attached onto the bacterial cellulose fiber which ensures the role of bacterial cellulose as a support material. Also, there is a considerable difference in the particle size of silver phosphate, as we can see more agglomeration in figure (a) and figure (b), compared to figure (c) and figure (d). The silver phosphate particles have medium particle size of 60-70 nm where CTAB is used and approximately 250-300 nm where CTAB is not used. This accounts the role of CTAB as a capping agent which prevents the silver phosphate agglomeration and facilitates a lower particle size for the material.

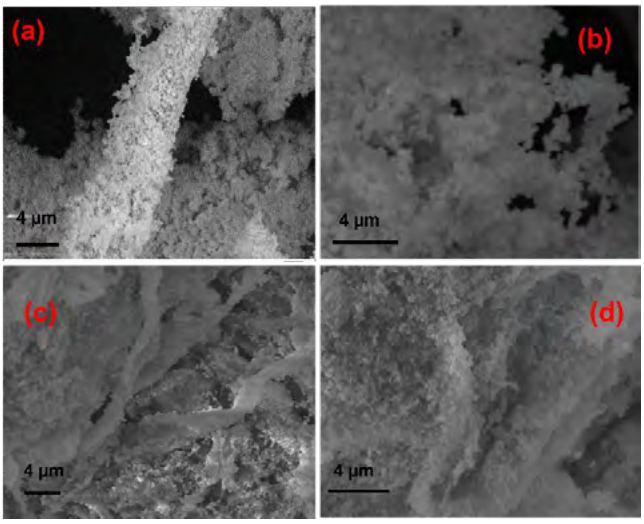

Figure 1. SEM images of BC-AgP (a), (b) and BC-AgP/CTAB (c), (d) with different magnifications.

3.2 BET

The BET of both samples showed a type (II) isotherm. The specific surface area, pore volume and pore diameter of all the samples are reported in table 1. There has been a significant decrease of specific

surface area (SSA) of BC-AgP when CTAB is not used. The SSA has reduced approximately 5 times compared to the sample with CTAB which emphasis the role of CTAB as a capping agent. Also, the pore volume of BC-AgP has decreased 6 times than that of BC-AgP/ CTAB.

Table 1. The BET specific surface area, pore diameter and pore volume of the samples are showed in the table below.

Sample	Specific surface area (m2/g)	Pore volume (cc/g)	Pore diameter (nm)
BC-AgP	3.68	0.01	3.78
BC-AgP/ CTAB	14.27	0.06	3.8

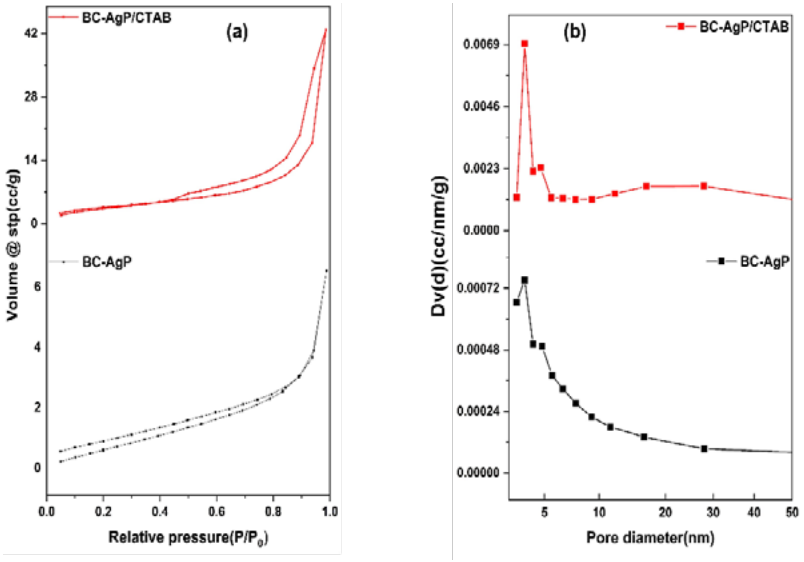

Figure 2. The Nitrogen sorption isotherms (a) and BJH pore size distribution (b) of BC-AgP and BC-AgP/CTAB

3.3 Photocatalytic studies

The photocatalytic efficiency of the samples was evaluated by calculating the rate constant (k) by using the second order rate law equation.

$$kt = -\ln([C]/[C_0]) \quad (1)$$

where [C] represents the reactant concentration at time t, $[C_0]$ is the initial reactant concentration, k is the rate constant, and ln is the natural logarithm. The rate constant of both samples in RhB and MB is tabulated in table 2. The rate constant of BC-AgP in both dyes are lesser than the rate constant of BC-AgP/CTAB, ie, the sample with CTAB has more photoactivity than the sample without CTAB. This can be because of the reduction of particle size of the material due to the addition of CTAB onto it. The C/C_0 v/s irradiation time and $-\ln C/C_0$ v/s irradiation time of both samples in RhB and MB were plotted and depicted in figure3.

Table 2. The rate constant of all the samples in RhB and MB

Sample	Rate constant (min^{-1})	
	RhB	**MB**
BC-AgP	**0.124**	**0.087**
BC-AgP/CTAB	**0.173**	**0.122**

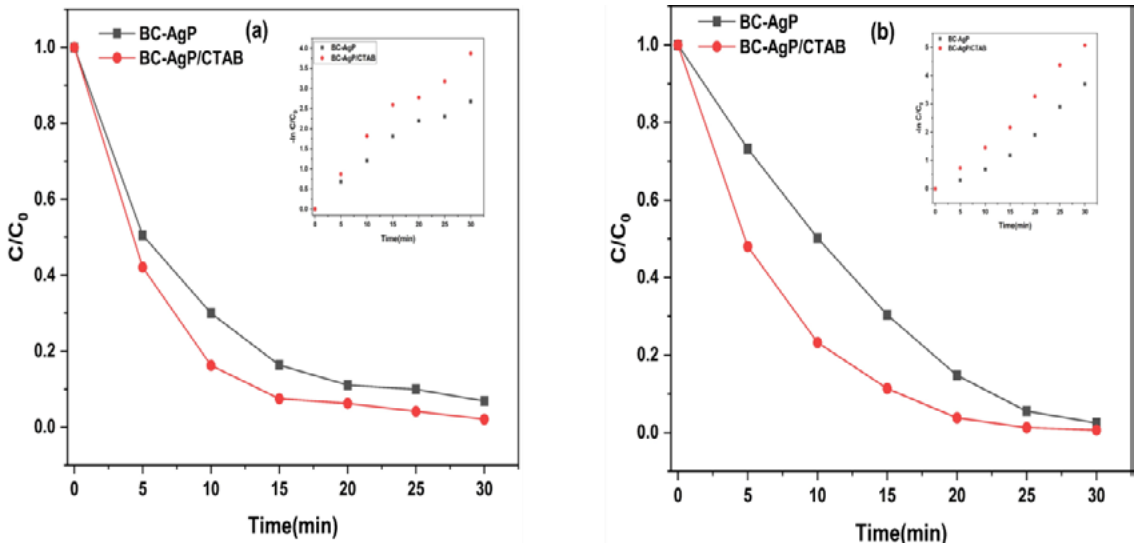

Figure 3. (a) C/C_0 v/s Irradiation time of 5 ppm MB in BC-AgP and BC-AgP/CTAB, and -ln C/C_0 v/s Irradiation time of the same in present in the inset (b) C/C_0 v/s Irradiation time of 5 ppm RhB in BC-AgP and BC-AgP/CTAB, and -ln C/C_0 v/s Irradiation time of the same in present in the inset**.**

3.4 Anti-bacterial test

The antibacterial susceptibility test was carried using bacterial cellulose, BC-AgP and BC-AgP/CTAB films in dark and in the light. Escheria coli (E. coli) was used as the bacterium. The halo formation was observed around the samples except for the bacterial cellulose on agar plates. The halo represents the area where bacterial growth is inhibited by the tested substances. Notably, BC-AgP/CTAB exhibited a larger halo of an approximate thickness of 2 mm, indicating stronger antibacterial activity compared to BC-AgP (halo of thickness of around 0.5 mm). Most importantly, the thickness of halo is more in the presence of light, which is around 4 mm for BC-AgP/CTAB and around 1 mm for BC-AgP. This indicates the increased efficiency of the material as a photocatalyst. When irradiated using light, there will be electron-hole pairs generated in the samples as its band gap energy (2.4 eV) is in the range of visible light [2]. When AgP interacts with E. coli, it leaches silver ions (Ag^+). Ag^+ ions disrupt bacterial cell membranes, causing increased permeability and leakage of cellular components [7]. They also bind to proteins, inhibit enzymes, and produce reactive oxygen species (ROS), which can cause oxidative damage. These ROS can interfere with adenosine triphosphate (ATP) production, disrupting critical cellular processes. Furthermore, silver ions can bind to bacterial DNA, impairing DNA replication and inhibiting ribosomes' ability to transcribe messenger RNA into essential proteins.

[12]. The inclusion of CTAB should have enhanced the antibacterial property of the material by increasing the surface area, and the silver phosphate may interact with the bacterial cell membranes, thus disrupting their metabolism and structure [13]. The images of antibacterial activity in the light and in the dark of bacterial cellulose, BC-AgP and BC-AgP/CTAB are shown in figure 4.

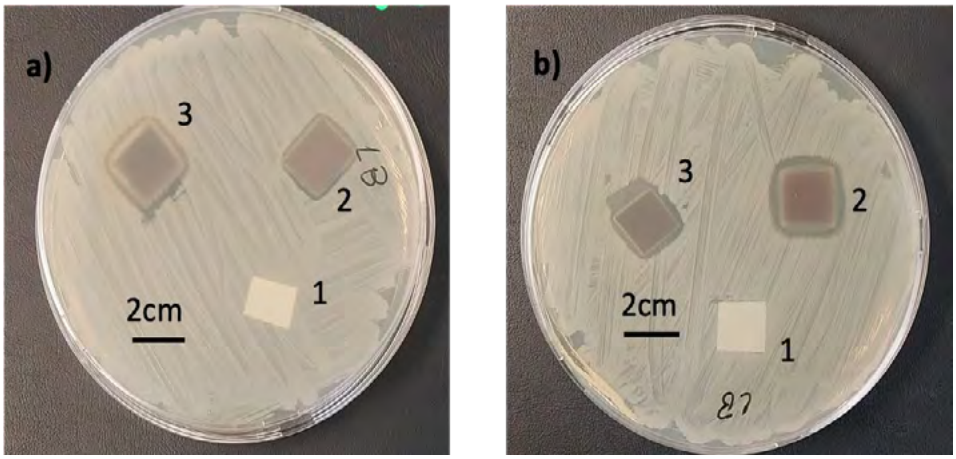

Figure 4. The image of anti-bacterial performance of bacterial cellulose, BC-AgP with and BC-AgP/CTAB in the dark (A) and in the light (B).

4. Conclusion.

Bacterial cellulose supported silver phosphate nanocomposite (BCAgP) with and without the surfactant CTAB were synthesised by an in-situ approach. The role of CTAB in determining the photocatalytic efficiency and the antibacterial property of the material was studied. The SEM images reveals that the inclusion of CTAB into the BC-AgP can prevent the agglomeration of the silver phosphate particles that are attached onto the bacterial cellulose fibres and reduce the particle size to a considerable margin. Also, the BET test shows that the specific surface area of BC-AgP/CTAB is higher (14.27 m^2/g) as compared to BC-AgP without CTAB (3.68 m^2/g). The photocatalytic efficiency of the samples was analysed using a UV-Visible spectrophotometer and the rate constant of BC-AgP/CTAB shows a higher value of 0.173 min^{-1} and 0.122 min^{-1} in 5ppm RhB and MB respectively as compared to BC-AgP, which was only 0.124 min^{-1} and 0.087 min^{-1} for the same concentration of RhB and MB, respectively. The antibacterial test results also shows that BC-AgP/CTAB can potentially kill more E. coli bacteria than BC-AgP and the bacterial cellulose. Also, the anti-bacterial activity of both BC-AgP/CTAB and BC-AgP was better in the presence of light, which highlights the multi-dimensional property of the BCAgP nanocomposites. BC-AgP/CTAB shows superior photoactivity and anti-bacterial property than BC-AgP, which shows the importance of particle size determining the efficiency of a material.

5. References

[1] G. Samchetshabam, A. Hussan, T. Gon Choudhury, S. Gita, P. Soholars, A. Hussan, Impact of Textile Dyes Waste on Aquatic Environments and its Treatment, (2017).

[2] A. Kaitheri, S. Kunjalukkal Padmanabhan, S. Pal, M. Stoppa, A. Licciulli, Silver phosphate–bacterial cellulose nanocomposites as visible light photocatalyst for wastewater purification,

Carbohydrate Polymer Technologies and Applications 6 (2023) 100365. https://doi.org/10.1016/j.carpta.2023.100365.

[3] S. Pal, S.K. Padmanabhan, A. Kaitheri, M. Epifani, A. Licciulli, Efficient Solar Light Photocatalyst Made of Ag3PO4 Coated TiO2-SiO2 Microspheres, Nanomaterials 13 (2023) 588.

[4] X. Li, P. Xu, M. Chen, G. Zeng, D. Wang, F. Chen, W. Tang, C. Chen, C. Zhang, X. Tan, Application of silver phosphate-based photocatalysts: Barriers and solutions, Chemical Engineering Journal 366 (2019) 339–357. https://doi.org/10.1016/j.cej.2019.02.083.

[5] G.A. Martínez-Castañón, N. Niño-Martínez, F. Martínez-Gutierrez, J.R. Martínez-Mendoza, F. Ruiz, Synthesis and antibacterial activity of silver nanoparticles with different sizes, J Nanopart Res 10 (2008) 1343–1348. https://doi.org/10.1007/s11051-008-9428-6.

[6] B. Le Ouay, F. Stellacci, Antibacterial activity of silver nanoparticles: A surface science insight, Nano Today 10 (2015) 339–354. https://doi.org/10.1016/j.nantod.2015.04.002.

[7] M. Guzman, J. Dille, S. Godet, Synthesis and antibacterial activity of silver nanoparticles against gram-positive and gram-negative bacteria, Nanomedicine: Nanotechnology, Biology and Medicine 8 (2012) 37–45. https://doi.org/10.1016/j.nano.2011.05.007.

[8] C.G.A. Das, V.G. Kumar, T.S. Dhas, V. Karthick, K. Govindaraju, J.M. Joselin, J. Baalamurugan, Antibacterial activity of silver nanoparticles (biosynthesis): A short review on recent advances, Biocatalysis and Agricultural Biotechnology 27 (2020) 101593. https://doi.org/10.1016/j.bcab.2020.101593.

[9] E. Nirmala, S. Dhivya, S. Sarojini, S. Duraivel, A REVIEW ON SODIUM LAURYL SULPHATE- A SURFACTANT, World Journal of Pharmaceutical Research (n.d.).

[10] M.S. Bakshi, S. Sachar, Influence of hydrophobicity on the mixed micelles of Pluronic F127 and P103 plus cationic surfactant mixtures, Colloids and Surfaces A: Physicochemical and Engineering Aspects 276 (2006) 146–154. https://doi.org/10.1016/j.colsurfa.2005.10.032.

[11] S. Kunjalukkal Padmanabhan, L. Lamanna, M. Friuli, A. Sannino, C. Demitri, A. Licciulli, Carboxymethylcellulose-Based Hydrogel Obtained from Bacterial Cellulose, Molecules 28 (2023) 829. https://doi.org/10.3390/molecules28020829.

[12] G. Lofrano, F. Ubaldi, L. Albarano, M. Carotenuto, V. Vaiano, F. Valeriani, G. Libralato, G. Gianfranceschi, I. Fratoddi, S. Meric, M. Guida, V. Romano Spica, Antimicrobial Effectiveness of Innovative Photocatalysts: A Review, Nanomaterials (Basel) 12 (2022) 2831. https://doi.org/10.3390/nano12162831.

[13] S. Pal, R. Nisi, M. Stoppa, A. Licciulli, Silver-Functionalized Bacterial Cellulose as Antibacterial Membrane for Wound-Healing Applications, ACS Omega 2 (2017) 3632–3639. https://doi.org/10.1021/acsomega.7b00442.

INFLUENCE OF THE PREPREG MORPHOLOGY ON THE PROPERTIES OF OOA CONSOLIDATED COMPOSITES

Karine LABASTIE[1], Laurent PUECH[1], Grégory ERB[1]

[1] IRT SAINT EXUPERY (https://www.irt-saintexupery.com/)
bâtiment B612, 3 rue Tarfaya, 31405 Toulouse cedex 4, France
karine.labastie@irt-saintexupery.com,
laurent.puech@irt-saintexupery.com,
gregory.erb@irt-saintexupery.com

Keywords: Thermoplastic composite, Prepreg, Out of Autoclave consolidation, PAEK resin,CFRP composite.

Abstract
Compared to other material solutions, thermoplastic composites present interesting properties to produce low environmental impact aerostructures. Nevertheless, the processing temperatures of these materials are higher than the thermoset ones, thus their energy consumption during the production of composite parts is higher, impacting significantly their Life Cycle Analysis (LCA). For this reason, out of autoclave consolidation processes have been investigated for this class of composites. However some difficulties remain to obtain composite parts with low residual porosity. Our study, through the production of different morphologies of HR carbon fiber/PAEK resin prepregs, highlights the key mophological paramaters that influence the ability of a prepreg to be well consolidated into an Out Of Autoclave consolidation process (OOA). The improvement of the quality of the laminates has been evaluated through microcopy, NDT analysis and mechanical evaluation. The results of this study confirm that the prepreg morphology has a significant impact on their processability in an out of autoclave consolidation process.

1. Introduction

To face the challenges of decarbonisation of the aviation sector for 2030, manufacturers are studying several solutions to reduce the VOC emissions from their aircrafts. Among them, composites have been identified for a long time as a relevant solution to radically reduce the weight of aerostructures. Up to now, mainly applications with thermoset composites have been developed. Nevertheless, this class of materials is difficult to repair, and poorly suited to automation and increased production rates. Thermoplastic composites can overcome these constraints as by their chemistry, they can be reprocessable and are suited for automating production processes. However, their main inconvenience is their higher processing temperatures that impact their production costs. For these reasons, out of autoclave consolidation processes has been pushed for this class of composites nevertheless difficulties remain with this process to obtain composite parts with low residual porosity [1], [2].

The goal of our study is to identify the morphological parameters of a high performance thermoplastic carbon prepreg influencing the final quality and performance of the associated laminate consolidated in oven under a vacuum-bag only process. To do this, a methodology based on an internal iterative loop (Figure 1) has been implemented at the IRT SAINT EXUPERY, starting from the production of different prepreg morphologies (thanks to the thermoplastic impregnation line installed at the IRT SAINT EXUPERY) up to the evaluation of the mechanical properties of the laminates, going through a complete characterisation of the prepreg and laminate morphology.

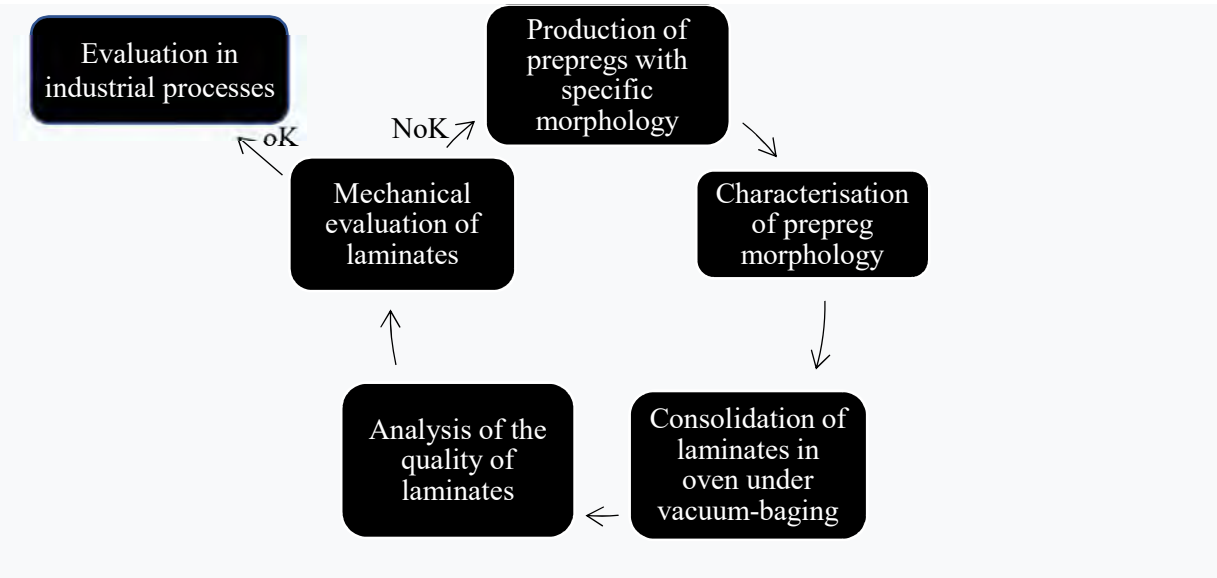

Figure 1: Methodology to evaluate the relation between prepreg morphology and its behavior in an oven consolidation process.

This study has been done with raw materials (carbon fiber / matrix) well known from the aeronautic market. During this study, mainly the influence on the laminate performances of the repartition of the resin between the core and the surface of the prepreg as well as their total resin content have been studied. To be able to modify the morphology of the prepreg, an impregnation process coupling different water based technologies has been developed at the IRT SAINT EXUPERY. In parallel, methods of analysis and digital tools have been developed to characterise the prepreg morphology, based on the analysis of pictures of the cross section and the surface of the prepregs, respectively obtained by optical and scanning electron microscopies. Similar approach, combining experimental analyses and digital tools, has been implemented to evaluate and quantify the quality of the laminates using c-scan and microscopy analysis. This work has confirmed that the prepreg morphology has strong influence on the quality of the OOA laminates. In addition, the association of the prepreg morphology analysis with the quality of the final laminates made it possible to define an optimum prepreg morphology for OOA application for the carbon fibre/matrix couple studied.

2. Experimental

2.1. Materials and laminates manufacturing

All prepregs of this study have been produced thanks to the IRT SAINT EXUPERY 's thermoplastic impregnation line, using a modified slurry process. They are composed of a HR carbon fiber and a PAEK resin. The different prepregs have been produced with different morphologies but similar targeted fiber area weight (FAW = 194g/m²), width (82±5mm) and mass resin content (34±2%).
320x320mm laminates have been handlaid with the different prepregs produced at IRT SAINT EXUPERY with two different stacking sequences $(0/90°)_{2s}$ and $(0°)_{10}$. All composites plates have been consolidated by IRT SAINT EXUPERY in an oven using an identical vacuum bagging and pressure/thermal cycle to be able to highlight the influence of the morphological prepreg parameters on their consolidation behaviour keeping identical the manufacturing parameters.

2.2. Characterisation

2.2.1. Prepreg morphology

The morphology of the different prepregs produced for this study, is characterized by its fiber area weight (FAW), residual porosity, mass resin content and surface resin content. In addition, the global

morphology of the prepreg is also evaluated by optical microscopy, through a picture (x200 zoom) of all the transversal section of the prepreg.

The Fiber Area Weight (FAW) of the prepreg expressed in g/m² are calculated from the number of yarn composing the prepreg multiplied by their theoretical lineic mass divided by the average width of the prepreg measured during its production.

The residual porosity (%s) of the prepreg is determined from optical microscopy pictures of their cross section done with a x500 zoom and a digital tool developed at IRT SAINT EXUPERY. The digital tool is based on a binarisation method using an OTSU model to identify resin and fiber content. The residual porosity is calculated as the surface fraction on the image not identified as resin or fiber.

The mass resin content (w(%)) of the prepreg is an average value calculated with Eq.1 by weighing of at least 10 prepreg samples of 320mm long ($M_{p.}$ Average value) taking into account the mass of dry fiber (M_F) contained in the prepreg calculated using their theoretical linear mass (g/mL):

$$\boldsymbol{w}(\%) = \frac{(\boldsymbol{M_p - M_F})\boldsymbol{x100}}{\boldsymbol{M_p}} \quad (1)$$

The surface resin rate of the prepregs (%s) is determined from pictures obtained by Scanning Electron Microscopy (SEM) of the surface of the prepreg coupled with a digital tool developed at IRT SAINT EXUPERY. The digital tool uses similar binary approach based on an OTSU model that the one developed to calculate the residual porosity of the prepreg. To use binary approach, specific analysis parameters to catch scanning electronic microcopy pictures are used to reveal the resin in white color. By this way, the surface resin ratio of the prepregs corresponds to the fraction of the surface having a white color. The fraction resin is an average values obtained from analysis done on almost 14 SEM pictures of prepreg samples. A mass surface resin content (%m) is also determined by difference of weight during the manufacturing step between the final prepreg and the prepreg without resin on the surface.

2.2.2. Quality control of the laminates

First, the global quality of each laminate is defined by a c-scan analysis. This analysis is done at IRT SAINT EXUPERY using an OMNIscan SX from Olympus with a 5 MHz sensor. The quality of the laminate is evaluated through the analysis of the response in amplitude of the US signal all over the plate evaluated on a 12 colors scale. The criterion to define an acceptable consolidation is to have a reflected signal with an amplitude of at least 50% of the incident signal. A digital tool developed at IRT SE allows to quantify the consolidation rate of the laminates by quantifying the surface rate of the laminate presenting an US response with an amplitude over 50% of the initial signal. This consolidation rate allows to have a quantitative comparison between the different laminates. Following this NDT analysis, two samples are cutted in specific areas to evaluate by optical microscopy respectively the quality of the consolidation and the nature of the defect inducing a bad c-scan response (amplitude of the reflected signal <50% of the initial signal). During this analysis, the cross section of the taken samples is observed with a x200 zoom to evaluate the size, amount and localization of the defects (inter or intralayer porosity).

The mechanical performances of the laminates are evaluated at IRT SAINT EXUPERY using a MTS electromechanical equipment. All the mechanical analysis are performed at room temperature and the results given for each reference are an average of five samples tested. Two types of mechanical tests have been done, according to the composite plates: In plane Shear (IPS) on laminates (0/90°) and 3-points bending test on lamiantes (0°).

Differential scanning calorimetry analysis (DSC) have been performed at IRT SAINT EXUPERY on composite samples to evaluate the potential degradation of the PAEK resin according to the

manufacturing parameters used, evaluating its physico-chemistry properties (T_g: glass transition temperature, T_f: melting temperature, T_c: crystallization temperature and crystallinity rate) in comparison with the data from literature. These analysis are done with a DSC25 from TA Instruments under nitrogen atmosphere at a heating rate of 10°C/min between room temperature and 400°C. The values given are average values of three analysis done on 3 different samples.

Only the analysis of the resin content and the residual porosity of the laminates measured by digestion according to the standard NF EN 2564 have been done in an external laboratory during this study.

2.3. Results and discussion

Six different prepreg morphologies have been produced thanks to the IRT SAINT EXUPERY's impregnation line. The technologies used to produce these prepregs are combined slurry technologies making it possible to control the quantity of resin at the core and on the surface of the prepregs. The morphology 0384-T1 is defined as the reference morphology in our study, as it is the morphology obtained with our standard slurry process. Among the different morphologies of prepreg produced, the morphology 0384-T2 has been duplicated with prepreg 0384-T3 to check the reproducibility of the process developped. The main differences between the prepreg morphologies in Table 1 are located on their surface and global mass resin contents. A screening of 6 different surface resin rates between 0 and 11.6%m have been done during this study for a global mass resin modified in the range [32.7 to 36.5]%m in correlation with the specification 34±2%.

Table 1: Morphological properties of carbon.PAEK prepreg produced for the study.

Prepreg Reference	FAW (g/m²)	Porosity (%s)	Mass resin content (%m)	Surface resin content (%m)	Surface resin content (%s)
0384-T1	187,5 ± 5,7	5,5 ± 2,7	35,5 ± 2,1	0	21,5 ± 4,7
0384-T2	192,4 ± 3,8	5,0 ± 2,1	35,1 ± 0,6	3	44,3 ± 5,1
0384-T3	192,1 ± 3,6	5,1 ± 2,4	34,6		42,2 ± 3,6
0384-T30	189,3 ± 5,1	5,9 ± 3,7	35,7 ± 0,3	8,1	50,1 ± 6,6
0384-T32	194,9 ± 3,5	4,9 ± 3,1	36,5 ± 0,2	9	62,7 ± 5,7
0384-T36	205,6±4,2	5,6±2,4	35,3±0,7	11,6	22,7±5,9
0384-T43	205,3±2,7	4,5±2,5	32,7±0,4	10,1	

The SEM analyses of the surface of the prepregs 0384-T1, 0384-T2 and 0384-T36 (Figure 2) confirm the different amount of their surface resin content in agreement with their properties in Table 1. Additionally, the pictures show that the technology used to enrich the surface resin content of the prepregs does not induce a uniform resin deposition.

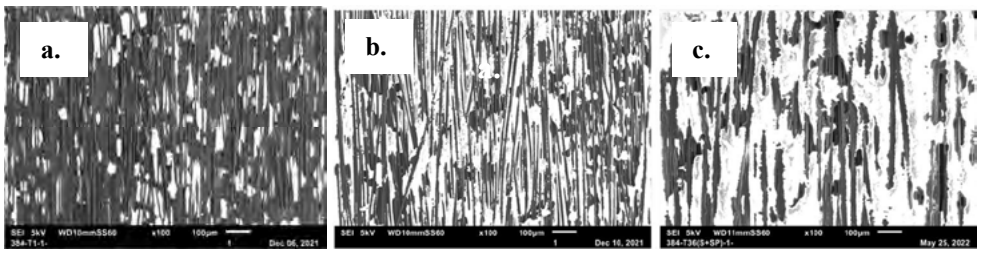

Figure 2 : SEM Analysis of the surface of the prepregs a) 0384-T1, b) 0384-T2 and c) 0384-T36.

The optical microscopy analyses of the cross section of the prepregs 0384-T1 and 0384-T36 (Figure 3), presenting the highest gap of surface resin content, show that the higher surface resin content of the prepreg 0384-T36 induced more resin on the edges and less independent fibers on the surface of the prepreg (Figure 3, b. in comparison with Figure 3 a.). Furtermore, they show that over the range of surface resin mass content [0; 11.6%]%m, a good balance on the surface/core distribution of the resin

can be maintained as no significant higher residual porosity is measured (Table 1). It is true that a limitation on the core/surface resin balance is expected, for a given global resin content, if a low residual porosity in the core of prepreg is required.

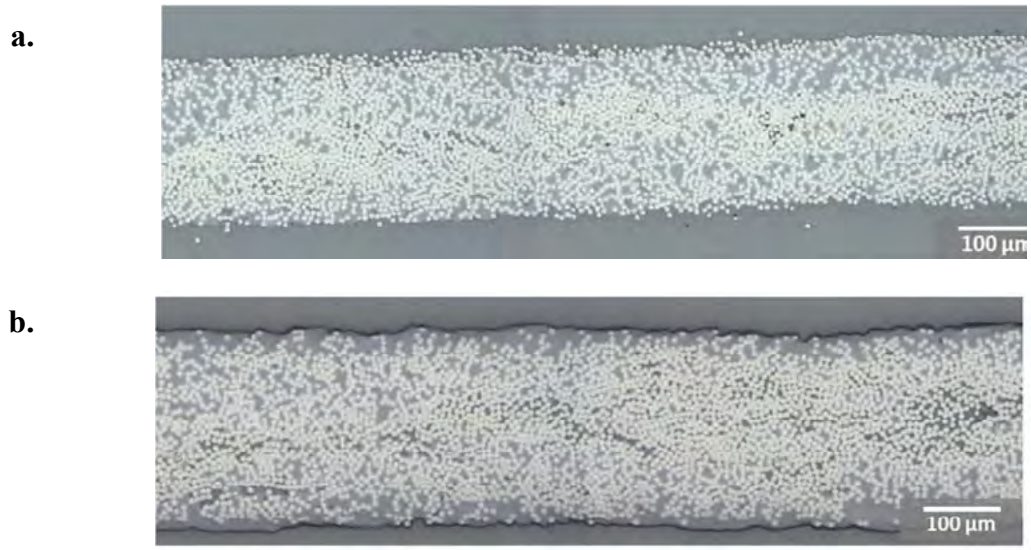

Figure 3 : Micrograph of the cross section of prepregs a) 0384-T1, b) 0384-T36.

From the six prepreg morphologies presented in Table 1, nine laminates $(0/90°)_{2s}$ or $(0°)_{10}$ have been manufactured to evaluate the influence of the prepreg morphology on its behaviour in an oven consolidation process (Table 2). The mass and volume resin contents as well as the residual porosity measured according to NF EN 2564 on each laminate are indicated in Table 2 except for the laminates 0384-L26, 0384-L36 and 0384-L44 for which the mass resin content has been determined using Eq.1. The results show a global resin content in line with the values measured on prepreg (Table 1) except for laminate 384-L25 that present a higher expected resin content taking into account the resin content on the prepreg 0384-T32 used to produce it. Additionally, the results highlight that the residual porosity of the laminates (0/90°) drops below 1% only for laminates produced with surface-enriched prepreg morphologies.

Table 2: Main properties of laminates produced with the different prepreg morphologies measured according to NF EN 2564.

Prepreg Reference	Laminate reference	Stacking	Volume resin content (%v)	Volume fiber content (%v)	Residual Porosity (%v)	Density	Masse resin content (%m)	Mass fiber content (%m)
0384-T1	0384-L1	$[(0°/90°)_2]_s$	42,5 ± 1,1	55,2 ± 0,2	2,1 ± 1,3	1,5 ± 0,0	35,5 ± 0,5	64,5 ± 0,5
	0384-L7	$(0°)_{10}$	43,6 ± 0,6	55,9 ± 0,4	0,5 ± 0,5	1,6 ± 0,0	36,0 ± 0,4	64,0 ± 0,4
0384-T2	0384-L5	$[(0°/90°)_2]_s$	42,9 ± 0,9	56,1 ± 0,5	1,0 ± 0,6	1,6 ± 0,0	35,5 ± 0,7	64,5 ± 0,7
	0384-L6	$(0°)_{10}$	43,7 ± 0,6	55, ± 0,4	0,5 ± 0,2	1,6 ± 0,0	36,0 ± 0,5	64,0 ± 0,5
0384-T30	0384-L24	$[(0°/90°)_2]_s$	44,4 ± 0,9	55,3 ± 1,1	0,3 ± 0,3	1,56 ± 0,0	36,7 ± 0,9	63,3 ± 0,9
0384-T32	0384-L25		45,5 ± 0,8	53,9 ± 0,6	0,6 ± 0,4	1,55 ± 0,0	37,9 ± 0,7	62,1 ± 0,7
	0384-L26	$(0°)_{10}$					36,5±0,2*	
0384-T36	0384-L44	$[(0°/90°)_2]_s$					35,3±0,7*	
0384-T43	0384-L36						32,7±0,4*	

*Values measured by Eq. 1.

The differential scanning calorimetry analyses carried out on samples taken from each laminate confirm that the processing parameters used do not impact the glass transition, melting and crystallisation temperatures of the PAEK resin contained in the composites compared to the intrinsic properties of the resin (Figure 4). The crystallisation rate of the laminates is between 20-25%, taking into account the

standard deviation obtained, these values can be considered in line with the intrinsic properties of the PAEK resin even if they are in the low trend of the values obtained in literature at 10°C/min [3].

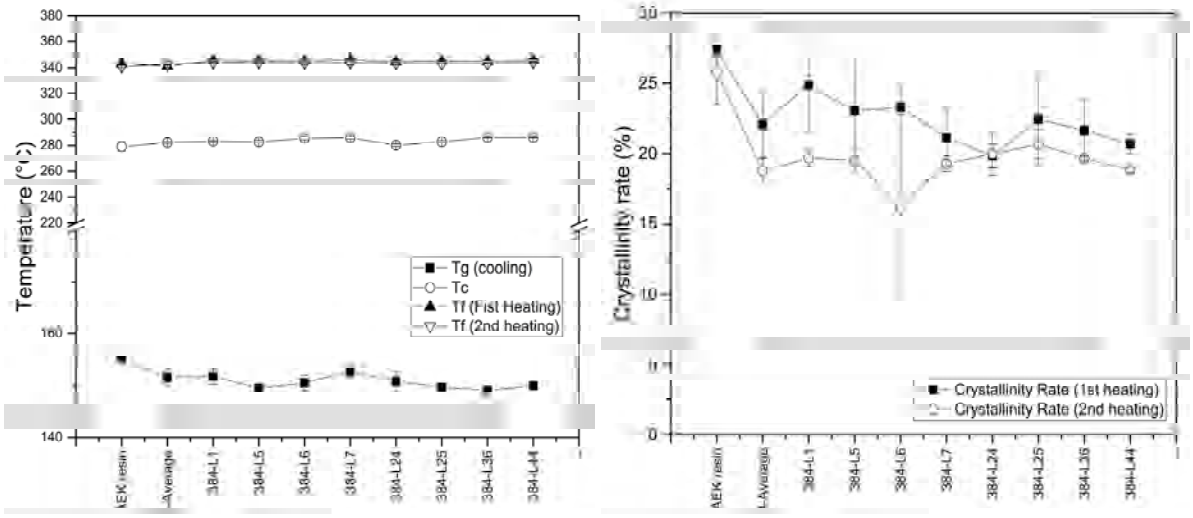

Figure 4: Analyses by differential scanning calorimetry of the different HR carbon/resin PAEK laminates. Left, glass transition, melting and crystallization temperatures/Right, crystallization rate.

The quality of the consolidation of the laminates were evaluated by c-scan analysis (Figure 5) and optical microscopy observations of the cross section of samples taken from the laminates (Figure 6). The best consolidation rate is obtained on the laminate 0384-L25 laid-up from the prepreg morphology 0384-T32 (Table 2) defined by a global mass resin content in the upper limit of the specification defined 34±2%w for this study and a surface resin content around 9%m.

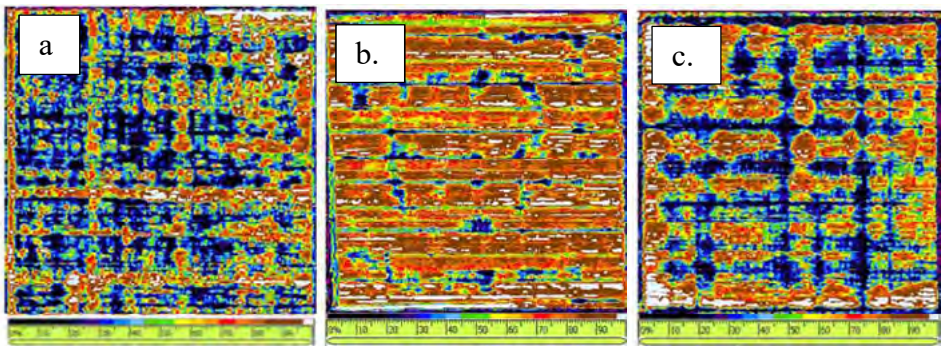

Figure 5: Analysis in amplitude by c-scan of the laminates a) 0384-L1 (consolidation rate 49%), b) 0384-L25 (consolidation rate 80%), c) 0384-L44 (consolidation rate : 56%).

The micrograph of the cross section of the laminates underline that in the laminate 0384-L1 the bad consolidation is mainly linked to interlayer porosity whereas in the laminate 0384-L44 produced with the prepreg 0384-T36, presenting the highest surface resin content, it looks mainly linked to intralayer porosity. In agreement with the c-scan analysis of the laminate 0385-L25, the interlayer as well as intralayer porosity (Figure *6* b.) is very low.

Figure 6: Micrograph of the cross section of the laminates a) 0384-L1, b) 0384-L25, c) 0384-L44.

The analysis of the relationship between of the three following parameters : total resin content and surface resin mass content of prepreg and the c-scan consolidation rate (Figure 7 a.) of the associated laminates shows that the best laminate consolidation in oven is obtained with prepreg having a total resin content of 36-37%m and a surface resincontent of around 9%m. These results confirm that a good balance between the core/surface resin content of the prepreg is required to have a good consolidation in an oven consolidation process: a lack of resin on the surface induce interlayer porosity whereas an excess induced a intralayer residual porosity difficult to remove in a oven consolidation process [4]. In parallel, a higher global resin content induce an easiest optimization of the core/surface resin content of the prepreg. Reproducibility on the c-scan consolidation rate done on two different laminates laid up with the same prepreg (Figure 7 b.) or similar prepreg morphology confirmed the results.

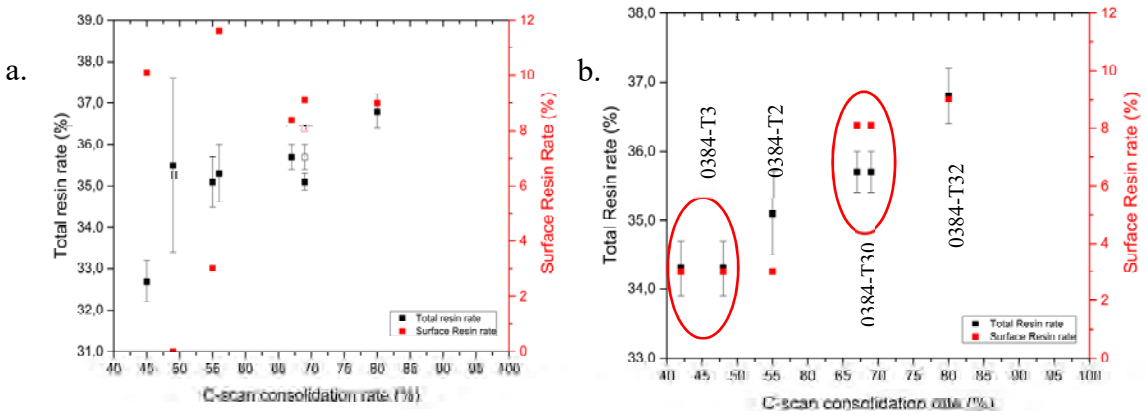

Figure 7: a. Relation between the total resin content and the surface resin content of prepreg versus the c-scan consolidation rate of laminates. b. Reproducibility on the c-scan consolidation rate for two laminates consolidated with the same prepreg and process parameters.

Futhermore, the impact of the improvement of the laminates consolidation according to their prepreg morphology has been evaluated through IPS and 3 points bending tests. The results (Table 3) show an increase respectively by around +36% and +16.5% on the maximal IPS and flexural stress values. This

confirms the significant improvement of the quality of the laminates highlighted by NDT and microcopy analysis by only modifying the morphology of the prepreg keeping identical the manufacturing and analysis parameters.

Table 3: In plane shear and 3 point bending results on laminates according to its prepreg morphology.

Prepreg Reference	Laminates Reference	IPS maximal stress (MPa)		IPS modulus (GPa)		3 point bending maximal stress (MPa)		3 point bending modulus (GPa)	
		Average	Standard deviation	Average	Standard deviation	Average	Standard deviation	Average	Standard deviation
0384-T1	0384-L1	114,0	3,1	5,0	0,1				
	0384-L7					1490,0	63,7	108,0	12,4
0384-T2	0384-L5	126,0	1,9	5,1	0,1				
	0384-L6					1650,0	76,7	109,0	6,2
0384-T30	0384-L24	141,1	2,1						
0384-T32	0384-L25	155,2	2,39	5,0	0,1				
	0384-L26					1736	36	123,5	4,5

3. Conclusion

Through the development of a specific impregnation process, on-demand prepreg morphologies controlling mainly their core/surface resin ratio and their global resin content in the range 34±2% could be produced at IRT SAINT EXUPERY. Additionally, based on an internal loop starting from the analysis of prepreg morphology up to the analysis of laminates quality, it has been underlined that prepreg morphology has a significant impact on the quality of laminates consolidated in oven under a vacuun bagging process. Mainly, it has been showed that, to have a good consolidation, prepreg morphology should have a good repartition of its core/surface resin content. This balance is easier to achieve with a high resin content around 36%. In this case, an improvement of around 36% can be measured on the IPS stress values of the laminates and around 16,5% on its flexural stress. At this stage, it seems interesting to duplicate this study on other fiber/matrix couples to check if similar optimization of prepreg morphology is obtained.

Acknowledgments
The authors thanks the French National Research Agency (ANR) as well as the industrial partners of the IRT SE compINNOVTP 2 project, Airbus Operations, Aviacomp, Huntchinson, Technocentre Airbus Atlantic, for their financial support.

References

[1] D. Zhang, « Void consolidation of thermoplastic composites via non-autoclave processing », University of Delaware, 2017. Consulté le: 17 avril 2024. [En ligne]. Disponible sur: http://udspace.udel.edu/handle/19716/23026
[2] J. N. Swamy, W. J. Grouve, S. Wijskamp, et R. Akkerman, « Vacuum-bag-only consolidation of C/PEKK fiber placed preforms with engineered gas evacuation channels », *Journal of Thermoplastic Composite Materials*, vol. 37, nº 4, p. 1309-1326, avr. 2024, doi: 10.1177/08927057231177571.
[3] T. Choupin, « Mechanical performances of PEKK thermoplastic composites linked to their processing parameters », These de doctorat, Paris, ENSAM, 2017. Consulté le: 25 janvier 2023. [En ligne]. Disponible sur: https://www.theses.fr/2017ENAM0043
[4] S. Boztepe *et al.*, « Effect of the initial resin distribution in partially impregnated thermoplastic prepregs on consolidation », *Composites Science and Technology*, vol. 225, p. 109488, juill. 2022, doi: 10.1016/j.compscitech.2022.109488.

Surface functionalized pyrolytic carbon composites

Lucija Pustahija[1], Sayed Ali Ahmad Alem[2], Christine Bandl[3], Wolfgang Kern[4]

[1-4]Institute for the Chemistry of Polymers, Montanuniversität Leoben, Otto-Glöckel Straße 2/4, 8700 Leoben, Austria

[1] lucija.pustahija@unileoben.ac.at

[2] ahmad.alem@unileoben.ac.at

[3] christine.bandl@unileoben.ac.at

[4] wolfgang.kern@unileoben.ac.at

Keywords: pyrolytic carbon, surface modification, solvothermal oxidation, reduction, silanization with APTMS and GPTMS, composites with BADGE

Abstract

The concept of using carbon black (CB), a by-product of the pyrolysis of methane and biomass, was sparked by the growing interest in producing sustainable composites. CB finds versatile applications among which it can serve as an adsorbent in wastewater treatment, but faces challenges due to its low dispersibility, caused by low surface polarity and agglomeration. Surface functionalization is a common approach to enhance material polarity. Silanes are typically coupled to carbon´s surface to alter its chemistry by serving as coupling agents which are forming bridges between an inorganic material (carbon) and a polymer matrix (e.g., epoxy). This work focuses on the modification of the surface of carbon black (CSC), employing amino- and glycidoxyorganosilanes (APTMS and GPTMS). The process includes (1) solvothermal and plasma oxidation of CB, followed by (2) a reduction using lithium aluminium hydride ($LiAlH_4$). This yields a transformation of C=O to -OH groups that can react with organosilanes and create stable Si-O-C bonds. The modified carbon black was characterized and used in the production of composites with bisphenol-A-diglycidyl ether (BADGE), where the resin acted as a binder for the carbon particles. The mechanical properties of these composites were assessed.

1. Introduction

Carbon black is a highly versatile material with a wide range of applications, primarily due to its high surface area [4,5]. While it is most famous for being produced from biomass resources, novel green technologies—such as methane pyrolysis—generate valuable carbon black as a side product during hydrogen production [1–3]. One of the ways to store and utilize carbon black effectively is through surface modification. By modifying its surface properties, its compatibility with other materials can be improved. One well-known method is oxidation, which introduces oxygen groups that serve as anchor points for other molecular entities. An example of this is the silanization of the carbon surface, achieved through covalent bonding between hydroxyl groups on the carbon surface and alkoxy groups on organosilanes [6–10]. When modified in this way, carbon black can be utilized in the production of carbon composites. The bond between the polymer and carbon is achieved through the terminal groups of organosilanes, such as epoxy resin. The combination of carbon black and organosilanes opens up exciting possibilities for creating efficient wastewater treatment materials. As a result, this investigation focused on (i) investigating the possibilities of solvothermal and plasma oxidation in the pre-activation of carbon surfaces, (ii) silanizing them with 3-(aminopropyl)trimethoxysilane (APTMS) and 3-

glycidyloxypropyl) trimethoxysilane (GPTMS), and (iii) producing stable carbon/epoxy (BADGE) composites [7,9,11,12]. All modified carbons were subjected to a three-point bending test after being prepared in this fashion.

2. Experimental

2.1. Materials

The carbon (CSC; YP-80F activated carbon powder, Kuraray, Japan) was wet oxidised in autoclave processes using a diluted solution of concentrated HNO_3 (65%). The autoclave, which held 100 millilitres, was purchased from Carl Roth GmbH in Germany and had a heating jacket and magnetic stirring gear. A low-temperature plasma reactor (Diener) with argon (99,9 %) and oxygen (99,9 %) was used for plasma treatments. Using $LiAlH_4$ (1.0 M $LiAlH_4$ solution in THF) and concentrated (37 %) HCl, the oxidised carbon surface was reduced. To achieve secondary functionalization, CB was further reacted with APTMS (97%) and GPTMS (≥ 98 %) using acetic acid (≥ 99.7%) as a catalyst. For the fabrication of composites a BADGE in combination with a room-temperature curing agent, diethylenetriamine (DETA), was applied.

2.2. Methods

2.2.1. Solvothermal oxidation and plasma-assisted oxidation

In an autoclave, pressureless processes were carried out for solvothermal oxidation [13–15]. The used components were 100 mg of CSC to 10 mL of 1M HNO_3. After first being sonicated for one hour, the mixture was heated for two hours at 120 °C. After being vacuum-filtered, the reaction mixture was cleaned with distilled water until its pH was neutral and then dried at 110 °C (>12h). In contrast to the wet-oxidation method, two steps were involved in the plasma-assisted oxidation process[16]. First, the carbon was preactivated for 10 minutes using argon gas (Ar, 10 sccm) at 100 W, and then it was oxidised for 20 minutes using an argon and oxygen mixture ($Ar+O_2$, 110 sccm) at 900 W. Dry oxidised carbon was directly used in the consequent reduction experiments.

2.2.2. Reduction of carbonyl-rich surface

Following their oxidation, the wet and dry oxidized CSC were reduced via $LiAlH_4$ [17,18]. The samples were dispersed in a 0.1 M solution of $LiAlH_4$. 100 mg of oxidised samples were vigorously stirred for an hour at room temperature. After centrifuging the reaction mixture, 1 mL of HCl was added to the carbon that had been distributed in a new 9 mL of THF to remove excess $LiALH_4$. In addition, the mixture was stirred for thirty minutes. The material was centrifuged, washed with THF, and dried at 110 °C.

2.2.3. Organosilane coupling to the carbon surface

The coupling of APTMS and GPTMS to the reduced carbon surfaces (wet and dry oxidized) was performed in an autoclave [6–8,10,19]. For wet-oxidized and reduced carbon (CSC ox.-R), a 1:1 by weight solution of water and ethanol was applied, including 100 mg of pre-activated carbon, 100 µL of organosilane, and 10 µL of catalyst (acetic acid). In the case of dry-oxidized and reduced carbon (900 W-20 min-R), the components were dissolved in distilled water (no ethanol added). One hour of sonication and six hours of constant stirring in an autoclave at 80 °C were the two steps in the silanization process. After centrifugation, the modified samples were repeatedly cleaned with distilled water and dried at 110 °C.

2.2.4. Production of carbon-BADGE composites

To find the minimum quantity of resin needed to create a stable carbon/epoxy composite [7,9,11,12], pristine, oxidised, reduced, and silanized carbons were dispersed in an acetone solution of BADGE (3 mL), and sonicated until the solvent had evaporated. Afterwards, 700 µL of 100 mg/mL DETA in acetone

was added. The slurries were vigorously stirred for a few minutes and carefully poured into acrylic-coated silicone moulds. Since DETA is a room-temperature curing agent, the specimens were allowed to dry for more than 12 hours. After curing, the composite specimens were removed from silicon moulds and subjected to tensile testing.

2.3. Results and Discussion

Surface modification of carbon black was performed in three following stages steps: (i) oxidation, (ii) reduction and (iii) silanization. Successfully modified carbons underwent the production of carbon/epoxy composites.

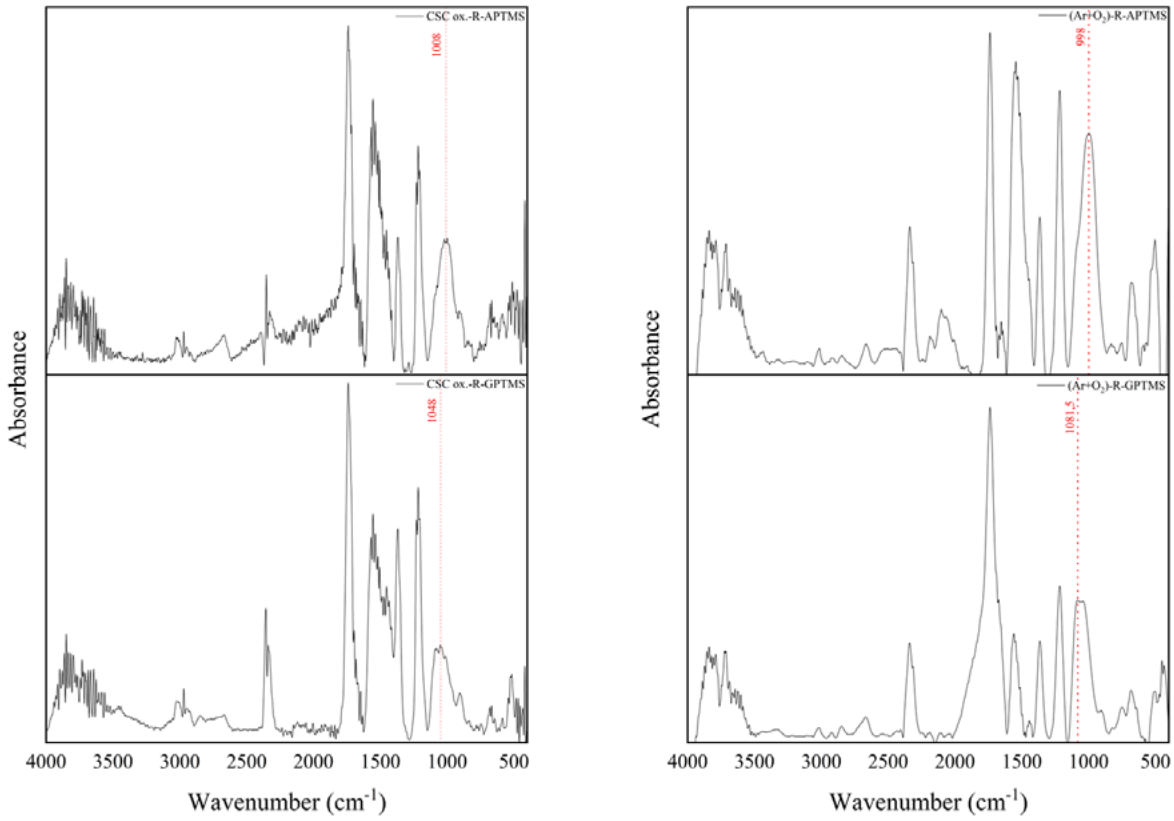

Figure 1. FTIR spectra of carbons functionalized with APTMS (top) and GPTMS (bottom). Left side: wet-oxidized carbon; right side: and dry-oxidized carbon.

The pre-activation of the surface resulted in an increased amount of oxygen at the surface (up to approx. 20 at.% according to XPS) in comparison to pristine carbon, both after wet- and dry-oxidation procedures. As mentioned above, these steps resulted in the formation of some C=O groups on the carbon surface. The oxidized carbons were further reacted with $LiAlH_4$ which resulted in the formation of the desired -OH groups. Those were detected by FTIR (signal around 3800 cm^{-1}) and XPS with a BE of 285.9-286.6 eV. The successfully prepared carbon was then reacted with organosilanes APTMS and GPTMS. Their presence was indicated by the observation of a Si-O-C bond at 1040 cm^{-1} (FTIR) and the presence of a C-Si bond in C1s spectra (XPS), a significant amount of Si (4,18 at. %-5,10 at. % for APTMS and 1.88 at. % - 2.75 at. % for GPTMS modified wet- and dry-oxidized CSCs) and showing a BE around 283.3 eV (see Table 1).

Table 1. Percentage of carbon atoms attached to Si (C-Si)

	C-Si/283.3-283.37 eV
CSC pristine	-
CSC ox.-APTMS	0.98
CSC ox. GPTMS	0.95
CSC (Ar+O_2) APTMS	2.36
CSC (Ar+O_2) GPTMS	1.39

The following step was done to utilize a modified carbon in the production of carbon/epoxy composites (Fig. 2.). It was found that a stabile composite can be produced with a minimum amount of 4 wt. % of epoxy resin, cured at room temperature. The bending test results suggest that the pristine carbon specimen with 4.5% epoxy content, the dry-oxidized specimen with 4.0% epoxy content have values of Young´s modulus from 692,47 to 725,31 MPa which exhibit greater strength and resistance to bending and stretching compared to other prepared specimens which happen to bend when the force is applied.

Figure 2. Carbon/epoxy composite.

3. Conclusions

The following findings were made during the step-by-step alteration of carbon surfaces and the processing of carbon/epoxy composites. Pre-activation of the carbon surface was accomplished by increasing the amount of oxygen groups via two types of oxidation. The wet-oxidation technique (also known as solvothermal oxidation) resulted in a permanently oxidized carbon surface. However, these reactions are time-consuming and require the employment of harsh chemicals, but a completely and permanently oxidized carbon surface is obtained. On the other hand, the dry-oxidation strategy (i.e., plasma-assisted oxidation) is faster and easier to apply, but it has the disadvantage of merely affecting the very top layer of the carbon surface.

The challenge of using wet- and dry-oxidized carbon for subsequent silanization reactions was solved by the reduction of carbonyl-rich surfaces. Reduction with $LiAlH_4$ resulted in the formation of -OH groups, which are required for the condensation of APTMS and GPTMS in the next phase of surface functionalization. After successfully reducing the carbonyl-rich surfaces, APTMS and GPTMS were coupled to the carbon surface, as evidenced by FTIR (Si-O-C bond at approx. 1040 cm^{-1}) and XPS. C1s detail spectra revealed that C-Si units are generated with a binding energy of approx. 283.3 eV. With APTMS, 4.18 and 5.10 at.% Si was found at the carbon surface (wet- and dry-oxidized carbon, resp.).

The use of GPTMS yielded a silicon content of 1.88 and 2.75 at.% at the surface (wet- and dry-oxidized carbon, resp.). It was also observed that these organosilanes can be coupled to a pre-activated carbon surface in an aqueous environment. Autoclaves are recommended to be used due to their convenience of handling, increased safety during experiment conduction, quick and continuous heating, and protection against solvent evaporation.

In the final stage of this investigation, silanized carbons, as well as pristine, oxidised, and reduced carbon types, were used to fabricate carbon composites. It was determined that at least 4 wt.-% of the epoxy resin is required to obtain mechanically stable carbon composites. The bending test results display that the pristine carbon specimen with 4.5% epoxy content and the dry-oxidized specimen with 4.0% epoxy content have Young's modulus values ranging from 692.47 to 725.31 MPa, indicating greater strength and resistance to bending and stretching than other prepared specimens that bend when a force is applied.

4. Acknowledgments

L. Pustahija would especially like to thank Montanuniversität Leoben for the possibility of pursuing Ph.D. studies at the Institute of Chemistry of Polymers. Special thanks go to C. Bandl and A. Alem for XPS experiments and evaluation. We are very grateful to C. Mitterer, A. Hofer-Roblyek and K-H. Pichler (Institute of Material Science at MU Leoben) for allowing the utilisation of their plasma reactor as well as M. Feuchter and Matthias Pferschy (Institute of Materials Science and Testing of Polymers at MU Leoben) who performed mechanical tests of produced composites.

This research has received funding from the European Innovation Council (EIC) under grant agreement No 101115293 (VanillaFlow).

5. References

[1] N. Sanchez-Bastardo, R. Schlögl, H. Ruland, Methane Pyrolysis for CO2-Free H2 Production: A Green Process to Overcome Renewable Energies Unsteadiness, Chem. Ing. Tech. 92 (n.d.) 1596–1609. https://doi.org/10.1002/cite.202000029.

[2] A.H. Khoja, A.K. Azad, F. Saleem, B.A. Khan, S.R. Naqvi, M.T. Mehran, N.A.S. Amin, Hydrogen Production from Methane Cracking in Dielectric Barrier Discharge Catalytic Plasma Reactor using a Nanocatalyst, Energies 13 (n.d.) 5921. https://doi.org/10.3390/en13225921.

[3] M. Gautier, V. Rohani, L. Fulcheri, Direct decarbonization of methane by thermal plasma for the production of hydrogen and high value-added carbon black, Int J Hydrogen Energy 42 (n.d.) 28140–28156. https://doi.org/10.1016/j.ijhydene.2017.09.021.

[4] B.K. Kwiecińska, S. Pusz, Pyrolytic carbon — Definition, classification and occurrence, International Journal of Coal Geology 163 (2016) 1–7. https://doi.org/10.1016/j.coal.2016.06.014.

[5] B. Reznik, K.J. Hüttinger, On the terminology for pyrolytic carbon, Carbon 40 (2002) 621–624. https://doi.org/10.1016/S0008-6223(01)00282-2.

[6] J. Kathi, K.-Y. Rhee, J.H. Lee, Effect of chemical functionalization of multi-walled carbon nanotubes with 3-aminopropyltriethoxysilane on mechanical and morphological properties of epoxy nanocomposites, Composites Part A: Applied Science and Manufacturing 40 (2009) 800–809. https://doi.org/10.1016/j.compositesa.2009.04.001.

[7] J.C. Hoepfner, S.H. Pezzin, Functionalization of carbon nanotubes with (3-glycidyloxypropyl)-trimethoxysilane: Effect of wrapping on epoxy matrix nanocomposites, Journal of Applied Polymer Science 133 (2016). https://doi.org/10.1002/app.44245.

[8] C. Velasco-Santos, A.L. Martinez-Hernandez, V.M. Castano, Silanization of Carbon Nanotubes: Surface Modification and Polymer Nanocomposites, in: S. Yellampalli (Ed.), Carbon Nanotubes - Polymer Nanocomposites, InTech, 2011. https://doi.org/10.5772/17274.

[9] Y. Lu, H. Li, M. Lin, W. Ng, H. Liu, Mechanical properties of 3-glycidoxypropyltrimethoxysilane functionalized multi-walled carbon nanotubes/epoxy composites cured by electron beam irradiation, Journal of Composite Materials 47 (2013) 1685–1694. https://doi.org/10.1177/0021998312450927.

[10] Z.-Q. Yu, S.-L. You, H. Baier, Effect of organosilane coupling agents on microstructure and properties of nanosilica/epoxy composites, Polymer Composites 33 (2012) 1516–1524. https://doi.org/10.1002/pc.22281.
[11] I. Rafique, A. Kausar, B. Muhammad, Epoxy Resin Composite Reinforced with Carbon Fiber and Inorganic Filler: Overview on Preparation and Properties, Polymer-Plastics Technology and Engineering 55 (2016) 1653–1672. https://doi.org/10.1080/03602559.2016.1163597.
[12] A. Uthaman, G. Xian, S. Thomas, Y. Wang, Q. Zheng, X. Liu, Durability of an Epoxy Resin and Its Carbon Fiber- Reinforced Polymer Composite upon Immersion in Water, Acidic, and Alkaline Solutions, Polymers 12 (2020) 614. https://doi.org/10.3390/polym12030614.
[13] E. Suvaci, E. Özel, Hydrothermal Synthesis, in: M. Pomeroy (Ed.), Encyclopedia of Materials: Technical Ceramics and Glasses, Elsevier, Oxford, 2021: pp. 59–68. https://doi.org/10.1016/B978-0-12-803581-8.12096-X.
[14] Q. Wang, B. Zhu, D.S. Su, Hydrothermal method oxidized carbon nanotube: Properties and performances in epoxy composite, Diamond and Related Materials 114 (2021) 108321. https://doi.org/10.1016/j.diamond.2021.108321.
[15] S. Morales-Torres, T.L.S. Silva, L.M. Pastrana-Martínez, A.T.S.C. Brandão, J.L. Figueiredo, A.M.T. Silva, Modification of the surface chemistry of single- and multi-walled carbon nanotubes by HNO3 and H2SO4 hydrothermal oxidation for application in direct contact membrane distillation, Phys. Chem. Chem. Phys. 16 (2014) 12237–12250. https://doi.org/10.1039/C4CP00615A.
[16] R. Laurano, M. Boffito, A. Torchio, C. Cassino, V. Chiono, G. Ciardelli, Plasma Treatment of Polymer Powder as an Effective Tool to Functionalize Polymers: Case Study Application on an Amphiphilic Polyurethane, Polymers 11 (2019) 2109. https://doi.org/10.3390/polym11122109.
[17] A. Ambrosi, C.K. Chua, A. Bonanni, M. Pumera, Lithium Aluminum Hydride as Reducing Agent for Chemically Reduced Graphene Oxides, Chem. Mater. 24 (2012) 2292–2298. https://doi.org/10.1021/cm300382b.
[18] H.C. Brown, N.M. Yoon, Selective Reductions. X. Reaction of Aluminum Hydride with Selected Organic Compounds Containing Representative Functional Groups. Comparison of the Reducing Characteristics of Lithium Aluminum Hydride and Its Derivatives, J. Am. Chem. Soc. 88 (1966) 1464–1472. https://doi.org/10.1021/ja00959a027.
[19] Q. He, Y. Xu, C. Wang, S. She, S. Zhou, R. Wang, Silane modification and characterization of activated carbon, Adsorption 18 (2012) 23–29. https://doi.org/10.1007/s10450-011-9377-8.

COMPARISON OF HIGH-PERFORMANCE MATRIX MATERIALS AS CANDIDATES FOR ADDITIVE PROCESSES

Melany McBean[1], Nan Yi[1], Adam Chaplin[2] and Oana Ghita[1]

[1]Centre for Additive Layer Manufacturing (CALM), Faculty of Environment Science and Economy, University of Exeter, Stoker Road EX4 4PY, United Kingdom
Email: msm221@exeter.ac.uk
[2]Victrex Manufacturing Limited, Hillhouse International, Thornton Cleveleys, Lancashire FY5 4QD, United Kingdom

Keywords: High temperature thermoplastics, Polyaryletherketone, Rheology, Composites, Crystallisation kinetics, Matrix materials, Material Extrusion, Additive Manufacturing.

Abstract
High performance thermoplastics such as Polyaryletherketones (PAEK) are gaining interest due to their potential applications in composite filaments and granules in additive manufacturing, where they are being increasingly considered as replacements for traditional thermosetting matrix materials. This is due to their superior properties, and ability to be reshaped, remoulded, or recycled. Despite their improved properties, PAEK printed parts can suffer from warpage and shrinkage, making their application a challenge. In additive manufacturing there are two methods that can be implemented to reduce the level of shrinkage in printed parts: adding fibres to a base polymer or altering the chemistry of the matrix material. In PAEK polymers the differences in the ratio and structure of the ether and ketone groups can influence their thermal and rheological properties, and therefore the overall printed part performance. The aim of this study was to present and compare the crystallisation kinetics and rheological properties of three high performance semi-crystalline PAEK grades, each with differing molecular chemistry, in order to understand their behaviour in the Material Extrusion (MEX) printing process.

1. Introduction

Due to the high demand for advanced materials, complex structures, and functionalities in the electrical, automotive, and aerospace industries, high temperature thermoplastics are gaining interest as potential replacements for thermosetting polymers as composite matrix materials. Candidates to replace thermosets include Polyaryletherketones (PAEKs): a family of semi-crystalline high-performance thermoplastic polymers which possess a unique combination of thermal and physical properties. These include: (i) high glass transition and operating temperatures, (ii) high mechanical performance including stiffness, strength, and toughness, (iii) chemical and solvent resistance. In addition, they have the advantageous properties inherent to thermoplastics, which include recyclability, indefinite shelf life, and ability to repair and remelt.

Despite their benefits and excellent mechanical performance, semi-crystalline parts can suffer from high shrinkage rates and warpage when melt processed. The complex thermal profiles of some of the manufacturing processes, combined with increasingly demanding and complex geometries, makes the use of semi-crystalline polymers with fast crystallisation kinetics challenging. Driven by the need for materials with low shrinkage and warpage rates, 3D printing has made significant progress in understanding the requirements for processing and has led to the development of new semi-crystalline matrix materials with tailored processing behaviour. This study presents the differences in rheological and crystallisation kinetics of three high performance semi-crystalline PAEK grades and how these differences affect their processability in the Material Extrusion (MEX) additive manufacturing process. These are: Victrex PEEK 450G, Victrex AM200, and Arkema Kepstan PEKK-A. Victrex PEEK 450G

©2024 | 2_MCBEAN_Melany_JDXHV.pdf

is a fast-crystallising grade used extensively in conventional manufacturing processes such as injection moulding, while also being available as a grade for the MEX process. Conversely, Kepstan PEKK-A and AM 200 are known as slow crystallising grades, each with unique molecular architectures designed specifically for additive processes. For these materials, the difference in the ratio and structure of the ether and ketone groups influences the melting and glass transition temperatures.

In order to reduce shrinkage and warpage in printed composite parts, the rheological and crystallisation kinetics need to be considered at every stage of the printing process. Figure 1 shows a schematic of a standard MEX printer and the areas in which rheology and crystallisation influence printing dynamics. To be considered as a viable matrix material for composite filaments and granules, a polymer must meet several criteria: it should be extrudable through a nozzle, hold its shape upon deposition, and generate strong bonds with adjacent filament strands. Within the nozzle, pressure-driven flow leads to the shear thinning of the melt. As the material is extruded, its viscoelastic properties cause radial expansion. During deposition, its viscosity influences the strength of the bonds between adjacent filaments. Upon solidification, the crystallinity determines the overall mechanical properties of the part. Thus, rheology and crystallinity are crucial in determining the suitability of a matrix material. In this study, rotational rheometry was used to measure the rheological profile of samples over a range of angular frequencies, whilst Differential Scanning Calorimetry (DSC) was used to determine the half time of crystallisation.

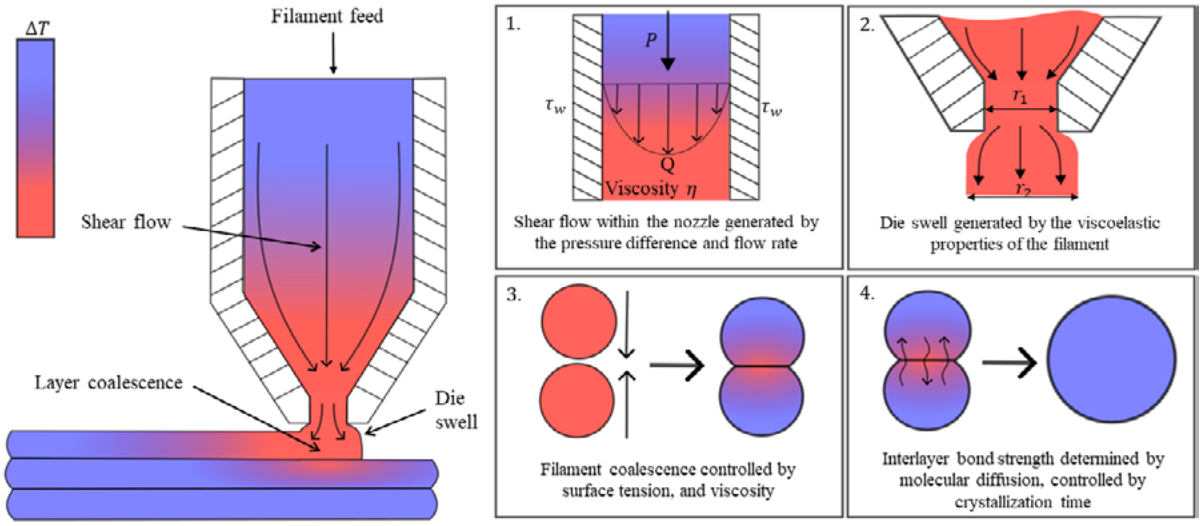

Figure 1. Stages of MEX where rheology and crystallisation influence the properties of printed parts.

2. Materials and preparations

Three PAEK grades have been used in this study: 1) Victrex PEEK 450G, 2) Victrex AM 200 and 3) Arkema Kepstan PEKK-A. The properties of these materials are displayed in Table 1. PEEK 450G and AM 200 were supplied by Victrex, whilst PEKK-A was purchased from 3D GBIRE. For the rotational rheology tests, 450G and AM200 were in granule form, whilst PEKK-A was in chopped filament. Prior to testing, the samples were dried at 110°C for at least 4 hours in order to remove moisture.

Table 1. Properties of 450G, AM 200 and PEKK-A [1], [2], [3]. *Average value in XY orientation.

Specimen name	Manufacturer	PAEK type	Glass transition temperature (°C)	Melting temperature (°C)	Nozzle temperature (°C)	Elastic Modulus (MPa)
450G	Victrex	PEEK	143	339	340-450	4000
AM200	Victrex	Copolymer	156	303	380-400	2600*
PEKK-A	Arkema	PEKK	162	305	350-400	2510

3. Methods

3.1. Rotational Rheology

A TA Instruments Discovery HR 1 rotational rheometer was used to characterize the rheological properties of 450G, AM200 and PEKK-A. Tests were conducted using a 25mm stainless steel parallel plate geometry, at a 1mm test gap within an inert nitrogen atmosphere. Using a standardized loading procedure, the samples were loaded at the test temperature and allowed to acclimatize prior to testing.

Two types of rheological tests were performed: The oscillatory amplitude tests for determining the Linear Viscoelastic Region (LVER), and the oscillation frequency sweep for measuring the storage and loss moduli. In order to avoid structural damage during oscillatory tests, the critical strain of the LVER was identified for each sample. It is important that any oscillation frequency tests are conducted within this region, as otherwise it can lead to sample fracture and inaccurate results. The LVER was obtained by conducting oscillatory amplitude test at the lowest possible temperature and the highest possible frequency. Due to the axial force limits on the rotational rheometer, the oscillation amplitude tests were conducted at 350, 310, and 315°C for 450G, AM200, and PEKK-A respectively. All samples were tested at a frequency of 500 Rad·s^{-1}. Based on the tests conducted to determine the LVER, oscillation frequency tests for viscosity were conducted at 1% for each sample. Oscillation frequency tests were conducted on the polymeric samples at standard nozzle temperatures: 400-420°C for 450G, 380-400°C for AM200 and PEKK-A over an angular frequency range of 0.5-500 Rad·s^{-1}.

3.2. Differential Scanning Calorimetry (DSC)

Protocols of using conventional Differential Scanning Calorimetry (DSC) and Flash DSC to track the isothermal crystallisation at the low, medium, and high temperature regions have been established prior to this work [4]. In this study, the isothermal crystallisations of 450G and AM200 between 170-190°C were measured via the cold-crystallisation isothermal test protocol [4], and between 250-290°C via the isothermal form melt test protocol [4]. These tests were conducted using a Mettler Toledo DSC 1 under an inert Nitrogen flow of 50ml/min. For the test, each sample had a mass of approximately 10mg, which was packed and encapsulated into a standard DSC Aluminium pan and lid. Isothermal crystallisations of 450G, AM200, and PEKK-A between 200-240°C were measured using the discontinuous isothermal test protocol [4] on a Mettler Toledo Flash DSC2+ with UFS 1-type chip sensors. For each chip sensor, a polymer piece with an approximate diameter of 50µm was placed into the membrane using a brush pen hair, followed by a pre-melt heating ramp at 0.5°C/s to 310°C to fixate the particles. All flash tests were purged by a Nitrogen flow of 80ml/min.

4. Results and discussions

4.1. Material feed and melting

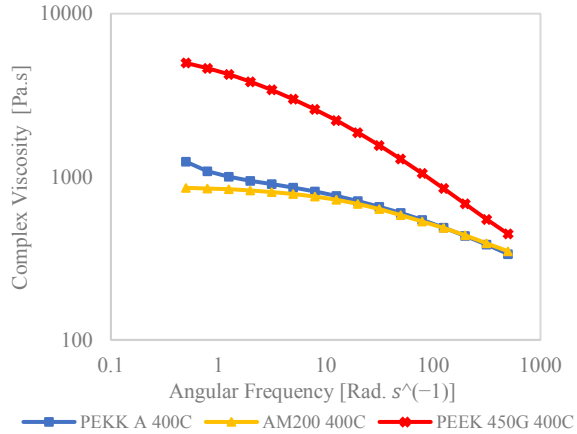

Figure 2. Complex viscosity of 450G, AM 200 and PEKK-A at 400°C over an Angular frequency range of 0.5-500 Rad·s^{-1}

Figure 2 presents the viscosities of PEEK 450G, AM 200 and PEKK-A at 400°C over an angular frequency range of 0.5-500 Rad·s^{-1}. The power law was applied to each PAEK grade viscosity curve in order to obtain the power law index. The power law index (n) and complex viscosities (η) for each sample are demonstrated in Table 2 and used for the calculations of the pressure drop within the nozzle.

In a standard MEX printer, filament is fed from a spool to the nozzle using a pinch roller mechanism. As it enters the nozzle it undergoes a phase change from solid to liquid, with the incoming solid portion acting as a piston [5]. The extrusion generates a pressure drop (Δp) between the melt and the atmosphere, causing the polymer to flow. The flow rate can be estimated using the printing speed and the extruded strand geometry according to Equation 1 [6].

$$Q = w_b \cdot h_b \cdot v_{print} \quad [1]$$

Where w_b and h_b are the width and height of the extruded bead, and v_{print} is the velocity of the print head. The flow rate of a polymer during printing is dependent on its melt viscosity at a given pressure generated by the feed rate of the filament [7]. However, the compression on the molten polymer enforced by the feed rollers places a limit on the pressure drop which is related to a materials elastic modulus [6]. Printing above this critical pressure limit increases the risk of non-flow and filament buckling [7]. An approximation of the critical pressure that can be placed on the filament by the feed rollers can be described by Eulers buckling analysis [8]:

$$P_{cr} = \frac{\pi^2 E d_f^2}{16 L_f^2} \quad [2]$$

Where E is the elastic modulus of the filament, d_f is filament diameter, and L_f is the distance between the feed rollers and the entrance of the liquefier [6]. Equation 3 describes the shear rates ($\dot{\gamma}$) present in the nozzle for a given flow rate (Q) [7], nozzle radius (R), and power law index (n). Using the shear rates, the corresponding viscosity (η) can be obtained from Figure 2 which can then be used to calculate the overall pressure drop (Δp) for a given nozzle length (L) and radius (R). Values relating to printing hardware were obtained from a 3D Gence F340 MEX printer.

$$\dot{\gamma} = \frac{4Q}{\pi R^3} \cdot \left(\frac{3n+1}{4n}\right) \quad [3]$$

$$\Delta p = \frac{8 \eta Q L}{\pi R^4} \quad [4]$$

Table 2. Typical printing values, critical pressure, shear rate, and pressure drop calculations. *Denotes values obtained from Figure 2.

Parameter	Symbol	Units	450G	AM200	PEKK-A
Bead width	w_b	mm		0.4	
Bead height	w_h	mm		0.2	
Print speed	v_f	mm/s		20	
Volume Flow rate	$\boldsymbol{Q}$	$\mathbf{mm^3/s}$		**1.6**	
Filament diameter	d_f	mm		1.75	
Roller to nozzle length	L_f	mm		145	
Critical pressure	$\boldsymbol{P_{cr}}$	**MPa**	**0.36**	**0.23**	**0.23**
Power law index*	n	–	0.554	0.755	0.792
Liquefier Radius	R	mm		0.875	
Shear rate	$\boldsymbol{\dot{\gamma}}$	$\mathbf{s^{-1}}$	**3.65**	**3.29**	**3.24**
Viscosity*	η	Pa·s	3200	800	900
Nozzle length	L	mm		25	
Pressure drop	$\boldsymbol{\Delta p}$	**MPa**	**0.56**	**0.14**	**0.16**

From calculations in Table 2, the pressure drop caused by 450G within the nozzle exceeds its critical pressure. Therefore, at a print speed of 20mm/s, 450G will have a greater risk of non-flow and buckling. An additional consideration regarding the critical pressure is the addition of fillers as this can increase the viscosity of the base polymer for all shear rates [9]. Therefore, a material with an initially high viscosity and shear thinning degree such as 450G could suffer in extrusion performance, leading to further risk of buckling and non-flow.

4.2. Extrusion

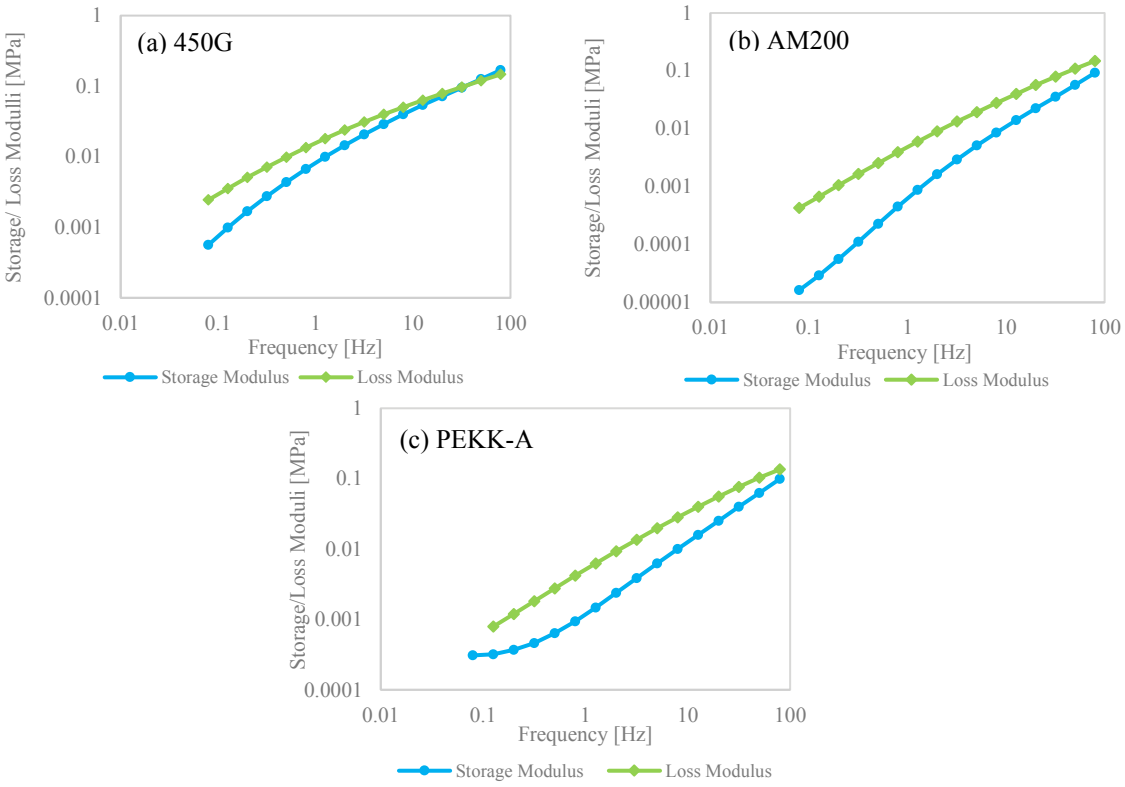

Figure 3. Loss and Storage moduli of 450G, AM 200 and PEKK-A

In MEX, the precise placement and dimensions of extruded tracks is critical to printing a high-fidelity part capable of fitting specified tolerances [10]. However, polymers are viscoelastic materials, demonstrating behaviour that is between that of an ideal Newtonian fluid (viscous) and an ideal solid (elastic). Therefore, as the filament is extruded from a larger diameter channel through a smaller diameter orifice it stores elastic energy which is then released in the form of radial expansion as it exits the orifice. This generates an extruded path with a greater diameter than the nozzle: referred to as die swell [5]. This phenomenon can be mitigated by controlling the feed rates and nozzle dimensions. However, die swell is also influenced by viscoelastic properties, namely the relaxation time, which is directly proportional to the ratio of die swell [5].

Viscoelastic properties can be described using the complex modulus (G^*) which is a quantitative measure of a materials resistance to deformation. The elastic and viscous contributions to the complex modulus are referred to as the storage modulus (G') and the loss modulus (G'') respectively. In an oscillatory frequency test, the frequency at which the storage and the loss moduli cross is equal to $1/\tau$, where τ is the relaxation time. Figure 3 (a)-(c) show the loss and storage moduli of 450G, AM 200 and PEKK-A obtained at 400°C over an angular frequency range of 0.5-500 Rad·s^{-1}. From the results, 450G is the only sample with a cross-over frequency within the test range. Therefore, the cross over frequency was extrapolated for AM 200 and PEKK-A. Table 3 details the cross-over frequency and relaxation time for each sample.

Table 3. Cross-over frequency and relaxation time for 450G, AM 200 and PEKK-A

Material	Cross-over Frequency (Hz)	Relaxation time (ms)
450G	35	28.6
AM 200	300	3.3
PEKK-A	180	5.6

From the calculated values in Table 3, 450G has the longest relaxation time when compared to AM 200 and PEKK-A. Therefore, upon extrusion, 450G will demonstrate a much greater radial expansion than AM 200 and PEKK-A for the same nozzle dimensions and filament feed rate. Meaning that out of the PAEK grades in this study, AM 200 will demonstrate the highest dimensional accuracy.

4.3. Filament bonding

As filament exits the nozzle, it is extruded onto a previously deposited layer, to which it bonds before solidifying together. The formation of bonds between two filaments can be broken down into three stages: 1) surface contact, 2) neck growth and 3) molecular diffusion at interface [11]. Once contact has been established, a 'neck' grows between the filaments marking the initiation of polymer chain diffusion. Neck growth is described by the ratio between the filament and contact area radii, with a ratio tending towards 1 leading to improved mechanical properties and reduced delamination [12], [13]. The ratio between the filament radius (a) and the neck radius (x) is governed by material surface tension (γ), neck growth time (t) and Newtonian viscosity and can be described using Equation 5 [14].

$$\frac{x}{a} = \sqrt{\frac{3\gamma t}{2\eta}} \quad [5]$$

Whilst this equation was primarily designed for use in particle sintering, the mechanism driving the bonding between two filaments is similar. From Equation 5, assuming the same filament diameter, a high viscosity will lead to a reduction in the neck growth ratio. However, whilst high viscosity may risk poor filament coalescence, it is also correlated to improved tensile properties due to the high molecular weight [15]. Therefore, a moderate viscosity ensures coalescence, mechanical strength, and allows the melt to retain its shape upon extrusion. From Figure 2, the Newtonian viscosities of the PAEK grades at 400°C are 6000, 855, and 1300 Pa·s for 450G, AM 200, and PEKK-A respectively. Therefore, comparing extruded filaments of the same diameter, 450G will have the lowest neck growth ratio, and AM 200 the highest. Adding fillers to a base polymer leads to an increase in viscosity at all shear rates [9]. This would cause 450G to have a further decrease in neck growth ratio, leading to a further reduction in filament coalescence and hence reduced mechanical properties.

4.4. Crystallisation

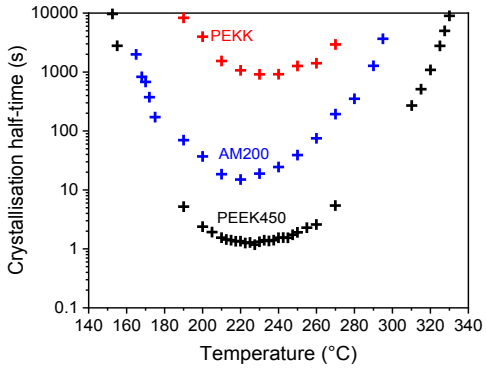

Figure 4. Crystallisation half-time of 450G, AM 200 and PEKK-A as a function of isothermal temperature.

In MEX, after contact between adjacent filaments has been established, molecular diffusion must take place across the interface such that it dissolves, enabling the bond to reach bulk properties [16], [17]. In order for this to occur, the molecular chains must be given sufficient time to diffuse, however, in semi-crystalline polymers, the rapid onset of crystallisation and nucleation limits molecular diffusion due to the restriction of chain mobility by crystalline structures [16]. Therefore, polymers with a slower crystallisation time are capable of delaying nucleation, thus allowing for longer diffusion times. A slower crystallisation time is therefore related to obtaining a greater interlayer strength and reduced anisotropy [18]. However, a polymer with a slower crystallisation time may still lead to the same degree of crystallisation as a fast-crystallising grade, with a higher crystallinity linked to increased rates of shrinkage and warpage. This is caused by the reduction in volume experienced by the crystalline structures when compared to amorphous polymer chains [19]. It is assumed that the path and speed of crystal formation for slow crystallising grades has an influence in reducing shrinkage and warpage. The addition of fillers to a base polymer further influences its crystallisation kinetics, with the total time of crystallisation reducing with the addition of fillers. This is caused by the fillers acting as nucleation sites on the melt. Therefore, when considering a matrix material, a slower crystallising grade may prevent a reduction in interlayer strength.

Figure 4 shows the crystallisation half time of 450G, AM 200 and PEKK-A, obtained from the exothermic heat flow integration in isothermal thermograms across a temperature range of 150-300°C. From the results, 450G is shown to have the fastest crystallisation time when compared to AM 200, with PEKK-A being the slowest crystallising grade. Therefore, upon extrusion PEKK-A molecular chains will have a greater time to diffuse and coalesce, potentially leading to stronger interlayer bonds and reduced part anisotropy. Additionally, PEKK-A will be more capable of countering the reduction in crystallisation time upon the addition of fillers.

5. Conclusions

This study presented and compared the rheological and crystallisation kinetics of three different PAEK grades: Victrex PEEK 450G, Victrex AM 200 and Arkema Kepstan PEKK-A, in order to determine their suitability as matrix materials in composite filaments and granules in MEX manufacturing. Rotational rheology was used to characterise the viscosity and complex moduli over a range of shear rates, whilst isothermal crystallisation was used to calculate the crystallisation half times. From the PAEK grades 450G was found to be the least suitable grade as a matrix material for MEX manufacturing due to its high viscosity and short crystallisation time. The effect of viscosity and crystallisation time on the printing performance and part properties were considered at different stages of the printing process: flow within the nozzle, extrusion, filament contact, and filament coalescence. Within the nozzle, a high viscosity requires a greater printing pressure, and if this exceeds the system capabilities it can lead to filament buckling. Upon extrusion, a high relaxation time is proportional to an increase in radial expansion (die swell), causing parts with poor dimensional fidelity. Upon filament contact, a high viscosity is linked to a reduction in neck growth ratio and therefore a reduction in part mechanical properties. Once contact has been established, a slow crystallisation time is required in order to allow sufficient time for molecular diffusion at interface.

When selecting a matrix material, further considerations need to be taken when selecting filler type and quantity. Adding fillers to a base polymer leads to an increase in viscosity for all shear rates, which increases with increasing quantity of filler, influencing not only the extrusion pressure, but also the filament coalescence. This can be mitigated by tailoring the grade to account for the increase in viscosity. Furthermore, the addition of fillers leads to a reduction in crystallisation time, which is required for molecular diffusion and strong interlayer bonds. Therefore, a matrix material requires a polymer with a low viscosity and relaxation time, and slow crystallisation kinetics.

References

[1] 'VICTREX AM™ 200 FIL', Victrex Technical Datasheets. Accessed: May 13, 2024. [Online]. Available: https://www.victrex.com/en/downloads/datasheets/victrex-am-200-fil

[2] 'VICTREX AM™ 450 FIL', Victrex Technical Datasheets. Accessed: May 13, 2024. [Online]. Available: https://www.victrex.com/en/downloads/datasheets/victrex-am-450-filament
[3] 'Kimya PEKK-A Amber 1.75mm', 3DGBIRE Kimya Filament. Accessed: May 13, 2024. [Online]. Available: https://3dgbire.com/products/kimya-pekk-a-amber-1-75mm-500g
[4] N. Yi, R. Davies, A. Chaplin, P. McCutchion, and O. Ghita, 'Slow and fast crystallising poly aryl ether ketones (PAEKs) in 3D printing: Crystallisation kinetics, morphology, and mechanical properties', *Addit Manuf*, vol. 39, p. 101843, Mar. 2021, doi: 10.1016/J.ADDMA.2021.101843.
[5] M. Elbadawi, 'Polymeric Additive Manufacturing: The Necessity and Utility of Rheology', in *Polymer Rheology*, J. Luis Rivera-Armenta and B. Adriana Salazar Cruz, Eds., London: IntechOpen, 2018, pp. 43–63. doi: 10.5772/INTECHOPEN.77074.
[6] B. N. Turner, R. Strong, and S. A. Gold, 'A review of melt extrusion additive manufacturing processes: I. Process design and modeling', *Rapid Prototyp J*, vol. 20, no. 3, pp. 192–204, Mar. 2014, doi: 10.1108/RPJ-01-2013-0012/FULL/PDF.
[7] C. Duty *et al.*, 'What makes a material printable? A viscoelastic model for extrusion-based 3D printing of polymers', *J Manuf Process*, vol. 35, pp. 526–537, Oct. 2018, doi: 10.1016/J.JMAPRO.2018.08.008.
[8] M. Atif Yardimci, T. Hattori, S. I. Guceri, and S. C. Danforth, 'Thermal Analysis Of Fused Deposition', in *International Solid Freeform Fabrication Symposium*, Texas, 1997, pp. 689–698. doi: 10.15781/T2M61C92N.
[9] V. Kishore *et al.*, 'Additive manufacturing of high performance semicrystalline thermoplastics and their composites', in *Solid Freeform Fabrication Symposium*, Austin, 2016, pp. 906–915. Accessed: May 30, 2023. [Online]. Available: https://repositories.lib.utexas.edu/handle/2152/89642
[10] M. E. Mackay, 'The importance of rheological behavior in the additive manufacturing technique material extrusion', *J Rheol (N Y N Y)*, vol. 62, no. 6, pp. 1549–1561, Nov. 2018, doi: 10.1122/1.5037687.
[11] Q. Sun, G. M. Rizvi, C. T. Bellehumeur, and P. Gu, 'Effect of processing conditions on the bonding quality of FDM polymer filaments', *Rapid Prototyp J*, vol. 14, no. 2, pp. 72–80, Oct. 2008, doi: 10.1108/13552540810862028.
[12] P. K. Gurrala and S. P. Regalla, 'Part strength evolution with bonding between filaments in fused deposition modelling', *Virtual Phys Prototyp*, vol. 9, no. 3, pp. 141–149, May 2014, doi: 10.1080/17452759.2014.913400.
[13] M. H. Khaliq, R. Gomes, C. Fernandes, J. M. Nóbrega, O. S. Carneiro, and L. L. Ferrás, 'On the use of high viscosity polymers in the fused filament fabrication process', *Rapid Prototyp J*, vol. 23, no. 4, pp. 727–735, 2017, doi: 10.1108/RPJ-02-2016-0027.
[14] J. Frenkel, 'Viscous Flow of Crystalline Bodies under the Action of Surface Tension', *J. Phys. (U. S. S. R)*, vol. 9, no. 5, p. 385, 1945, Accessed: May 13, 2024. [Online]. Available: https://cir.nii.ac.jp/crid/1570009749754474496.bib?lang=en
[15] P. Chen *et al.*, 'Recent Advances on High-Performance Polyaryletherketone Materials for Additive Manufacturing', *Advanced Materials*, vol. 34, no. 52, p. 2200750, Dec. 2022, doi: 10.1002/ADMA.202200750.
[16] P. Consul, A. Chaplin, N. Tagscherer, S. Zaremba, and K. Drechsler, 'Interlaminar strength in large-scale additive manufacturing of slow crystallizing polyaryletherketone carbon composites', *Polym Int*, vol. 70, no. 8, pp. 1099–1108, Dec. 2021, doi: 10.1002/PI.6168.
[17] C. A. Butler, R. L. Mccullough, R. Pitchumani, and J. W. Gillespie, 'An analysis of mechanisms governing fusion bonding of thermoplastic composites', *Journal of Thermoplastic Composite Materials*, vol. 11, no. 4, pp. 338–363, 1998, doi: 10.1177/089270579801100404.
[18] Q. Xu *et al.*, 'Enhanced interlayer strength in 3D printed poly (ether ether ketone) parts', *Addit Manuf*, vol. 55, Apr. 2022, doi: 10.1016/J.ADDMA.2022.102852.
[19] L. Benedetti, B. Brulé, N. Decreamer, K. E. Evans, and O. Ghita, 'Shrinkage behaviour of semi-crystalline polymers in laser sintering: PEKK and PA12', *Mater Des*, vol. 181, p. 107906, Jun. 2019, doi: 10.1016/J.MATDES.2019.107906.

The effect of fibre alignment on the fatigue behaviour of unidirectional flax fibre composites

Ali Moghimi-ardekani, Jan Ivens, Aart Willem van Vuure
KU Leuven, Department of Materials Engineering, , Kasteelpark Arenberg 44, 3001 Leuven, Belgium

Email (1st author): Ali.moghimiardekani@kuleuven.be

Email (2nd author): jan.ivens@kuleuven.be

Email (3rd author): aartwillem.vanvuure@kuleuven.be

Keywords: Fatigue, Fibre alignment, Flax fibre composites

Abstract

The influence of fibre alignment on fatigue behaviour of unidirectional flax fibre composites was studied using X-ray computed tomography. The tension-tension fatigue of flax fibre composites with epoxy matrix was evaluated, which were prepared by the impregnated fibre bundle method. A better understanding of manufacturing-related factors such as fibre alignment allows us to assess the reliability of the manufacturing process. Fatigue results indicate the extent to which natural fibre composites with highly oriented fibres in the loading direction show better fatigue performance, higher stiffness and lower permanent strain.

1. Introduction

In recent years, the use of natural fibres in fibre-reinforced composites has been considerable. Lightness, lower environmental impact, and high specific mechanical properties are some important parameters that distinguish natural fibre composites (NFCs) from glass and carbon fibre-reinforced polymers [1]. Among various types of natural fibres, bast fibres, particularly flax fibres, have become popular not only because of their favourable specific mechanical properties but also because their fatigue properties demonstrate a level of competitiveness comparable to that of glass fibre composites [2].

Fibre alignment is crucial in determining the mechanical properties of composite materials. Brahim et al. [3] observed a decrease in the elastic modulus and tensile strength of Alfa fibre/polyester composites

by 5% and 30%, respectively, as fibre angle increased from 0° to 10°. Fedulov et al. [4] reported a 16% reduction in compressive strength with fibres misaligned at 5°. Justo et al. [5] noted that the strength of graphite/epoxy composites diminished by 17% during fatigue loading as the fibre angle increased from 0° to 15°.

While there has been significant research into the influence of fibre alignment on mechanical properties, and the results for properties such as tensile stiffness are anticipated, the effect on fatigue behaviour in NFCs utilizing non-dried unidirectional fibres remains to be assessed. Fibres were intentionally not dried prior to production based on previous findings indicating improved moisture durability [1], as well as savings in cost and effort. Consequently, these conditions may closely reflect realistic industrial conditions.

2.Materials and Method

2.1. Materials

The unidirectional flax fabrics, with an areal density of 200 g/m^2, were supplied by Ecotechnilin, France. Epoxy resin, Bisphenol-A from Hexion, with 1,2-diaminocyclohexane as a hardener, was obtained from Sigma-Aldrich. The mixing ratio was 100 parts resin to 15.2 parts hardener.

2.2. Composite manufacturing method

The NFCs were prepared using the impregnated fibre bundle (IFBT) method, based on ASTM D2343 [6], to achieve a NFC with a 40% fibre volume fraction.

Flax fabric layers were conditioned at 65% RH to have non-dried fibres prior to the manufacturing of the NFCs.

Two material configurations were prepared with a different level of control over the longitudinal fibre orientation.

2.3. X-ray computed tomography (XCT)

The scanning was done with a Phoenix NanoTom S scanner, General Electric Germany. The scans were performed at 40 kV and 210 µA voltage and current respectively, with a 4.5 µm voxel size. The VoxTex software was used to evaluate the fibre alignment, as described in [7,8].

2.4. Fatigue test

Load-controlled tension-tension fatigue testing on longitudinal UD NFCs was conducted in accordance with ASTM D3479. A Schenck machine with a 120 kN load cell was utilised. R-ratio and frequency were 0.1 and 5 Hz, respectively. The maximum applied stress normalised to UTS (S/S0) ranged from 0.3 to 0.9. The strain was measured using a dynamic extensometer with a gauge length of 50 mm.

3.Results and discussion

The post processing of XCT images using Avizo software showed that the fibre volume fraction and void content in both prepared samples were 38% ± 1% and 0.3% ± 0.05%, respectively. As shown in Figure 1, the VoxTex software observations depict that the fibre in specimen IFBT_1st is oriented at 88.9° ± 7.5°, while the fibre direction in sample IFBT_2nd deviates by 89.1° ± 1.9° from the main direction (90°). This shows that the fibres in the first sample had a lower fibre alignment.

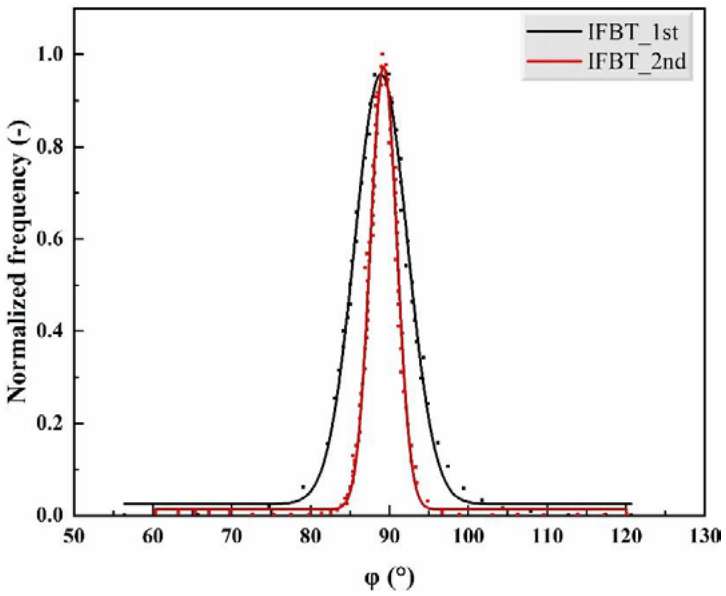

Figure 1: In plane fibre orientation of studied NFCs using VoxTex software.

Figure 2 shows the normalised S-N curve for both IFBT samples. The number of cycles to failure at each stress level for the NFC with better fibre alignment (IFBT_2nd) is higher than for the IFBT_1st. Since the fibre and void content in the studied NFCs are consistent, the reduced fatigue life found in IFBT_1st is likely due to the presence of misaligned fibres. Thus, long-term exposure to the fatigue load may cause a variety of internal defects, including matrix cracks and fibre-matrix debonding.

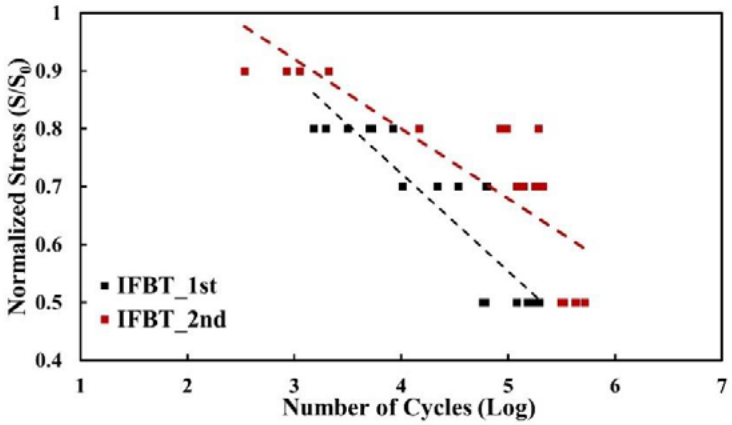

Figure 2: Normalized S-N curve.

Permanent/residual strain and stiffness are two crucial parameters that can be measured during fatigue loading as described in [9] and were reported in this research for a stress level at 30% of UTS. These factors are shown in Figure 3a and Figure 3b. Results indicate that there is an increase in permanent strain by 65% when fibres are aligned at an angle of 88.9° ± 7.5°, relative to samples with fibres deviated by 89.1° ± 1.9° °, as represented in Figure 3a. Thus, more plastic deformation and/or damage activity [10] are likely to occur in IFBT_1st in comparison with IFBT_2nd. As shown in Figure 3b, the stiffness during fatigue initially increases slightly (Region I), which might be attributed to fibre alignment [9,10], and then levels off in Region II. Moreover, the stiffness of IFBT_1st during fatigue is almost 22 GPa, and this value for IFBT_2nd after 1 million cycles is about 17% higher. In other words, a 6-degree difference in fibre orientation results in a 17% drop in the stiffness of these NFCs.

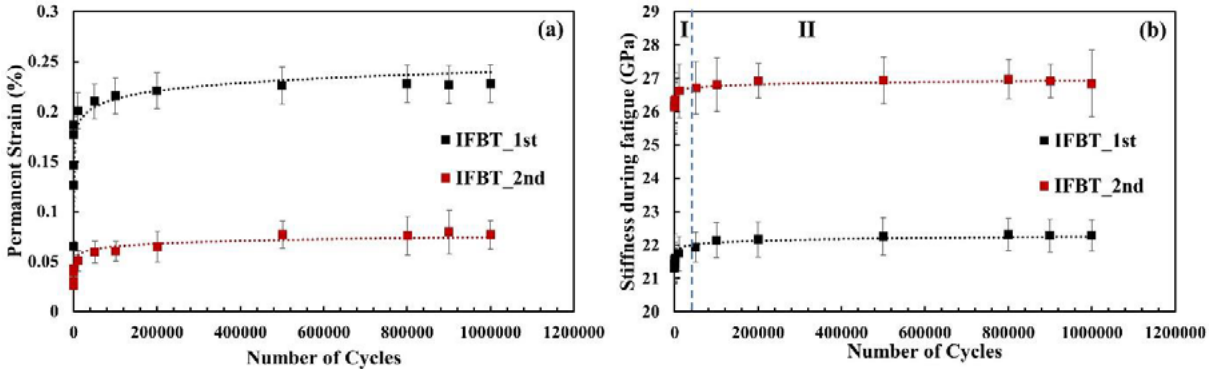

Figure 3: Fatigue parameters, (a) Permanent Strain, and (b) Stiffness during fatigue.

4.Conclusions

This study aims to focus on the impact of fibre alignment on the fatigue behaviour of NFCs, which were prepared using the IFBT method and evaluated for fibre orientation using XCT.

The VoxTex software observations using XCT images reveal that the fibres in IFBT_1st deviate by about 8° (88.9° ± 7.5°), while all the fibres in IFBT_2nd are oriented at 89.1° ± 1.9°.

Fatigue results indicate that IFBT_1st, with higher misalignment of fibre relative to the main load direction has higher permanent/residual strain, which may represent more plastic deformation and crack evolution during fatigue, as well as lower stiffness during fatigue in comparison with IFBT_2nd. These findings likely resulted in poorer fatigue performance for IFBT_1st.

References

[1] M.M. Lu, A.W. Van Vuure. Improving moisture durability of flax fibre composites by using non-dry fibres. *Compos. Part A Appl. Sci. Manuf.*, 123: 301–309, 2019.

[2] L. Yan, N. Chouw, K. Jayaraman. Flax fibre and its composites - A review. *Compos. Part B Eng.*, 56: 296–317, 2014.

[3] S. Ben Brahim, R. Ben Cheikh. Influence of fibre orientation and volume fraction on the tensile properties of unidirectional Alfa-polyester composite. *Compos. Sci. Technol.,* 67: 140–147, 2007.

[4] B.N. Fedulov, F.K. Antonov, A.A. Safonov, A.E. Ushakov, S. V. Lomov. Influence of fibre misalignment and voids on composite laminate strength. *J. Compos. Mater.* 49: 2887–2896, 2015.

[5] J. Justo, J.C. Marin, F. París, J. Cañas. The effect of frequency on fatigue behaviour of graphite-epoxy composites. *16th Eur. Conf. Compos. Mater. ECCM 2014.,* 22–26, 2014.

[6] F. Bensadoun, I. Verpoest, J. Baets, J. Müssig, N. Graupner, P. Davies, M. Gomina, A. Kervoelen, C. Baley. Impregnated fibre bundle test for natural fibres used in composites. *J. Reinf. Plast. Compos.,* 36: 942–957, 2017.

[7] I. Straumit, S. V. Lomov, I. Verpoest, M. Wevers. Determination of the local fibers orientation in a composite material from micro-ct data. *TEXCOMP-11 Conf.,* 11–15, 2013.

[8] I. Straumit, S. V. Lomov, M. Wevers. Quantification of the internal structure and automatic generation of voxel models of textile composites from X-ray computed tomography data. *Compos. Part A Appl. Sci. Manuf.,* 69: 150–158, 2015.

[9] F. Bensadoun, K.A.M. Vallons, L.B. Lessard, I. Verpoest, A.W. Van Vuure. Fatigue behaviour assessment of flax-epoxy composites. *Compos. Part A Appl. Sci. Manuf.,* 82: 253–266, 2016.

[10] T. Jeannin, X. Gabrion, E. Ramasso, V. Placet. About the fatigue endurance of unidirectional flax-epoxy composite laminates. *Compos. Part B Eng.,* 165: 690–701, 2019.

INVESTIGATING THE INFLUENCE OF FLAX SHIVES FRACTIONATION ON TENSILE PROPERTIES OF THERMOPLASTIC BIO-COMPOSITES USING 3D MICROSTRUCTURAL ANALYSIS

A. Nour El Dein[1,2,3], N. Le Moigne[2], M.F. Pucci[1], A. Barbuleé[3], O. Gamond[4] and A.S. Caro[1]

[1] LMGC, IMT Mines Ales, Univ Montpellier, CNRS, Ales, France
Email: ali-al-hadi.nour-el-dein@mines-ales.fr
[2] Polymers Composites and Hybrids (PCH), IMT Mines Ales, Ales, France
Email: nicolas.le-moigne@mines-ales.fr
[3] DEPESTELE, Teillage Vandecandelaere, 5 rue de l'Eglise, 14540 Bourguébus, France
Email: abarbulee@depestele.com
[4] AG PLAST, Route de Matafelon, 01460 Nurieux-Volognat, France
Email: olivier.gamond@agplast.fr

Keywords: Flax shives, injected bio-composites, mechanical properties, Mori-Tanaka modelling, microstructural analysis.

Abstract
This study aims to investigate the reinforcement potential of flax shives (FS) in thermoplastic composites. The influence of FS initial granulometry on the microstructure of the composites and their tensile properties is studied. Various FS granulometries were prepared. Polypropylene (PP) composites reinforced with 10% to 40%wt. of FS for each granulometry were manufactured using twin-screw extrusion and injection-moulding processes with Maleic Anhydride Polypropylene (MAPP) as a compatibilizer. Microstructural analysis was carried out using 2D scanner after fibre extraction and X-ray tomography on composites. The 3D microstructural parameters were used to model the elastic properties of the composite using Mori-Tanaka model. Our results revealed that FS-200-315 achieved maximum aspect ratio after processing, with granulometry deviations reducing aspect ratio. Additionally, medium size particles tend to be more oriented toward the injection flow compared to larger particles. These findings are consistent with the tensile properties of the composites. PP composites reinforced with FS-200-315 exhibit a 20% and 25% increase in Young's modulus and ultimate tensile strength, respectively, compared to those reinforced with FS-800-1600. The Mori-Tanaka model shows that there is a variation in the back-calculated FS Young's modulus as a function of granulometry, within a range between 14 and 28 GPa.

1. Introduction

Flax fibres have become increasingly popular as a reinforcement in polymer-based composite materials due to their attracting stiffness and strength properties that can compete to those of glass fibres [1]. As the demand for sustainable materials continues to grow, there is a notable increase in the utilization of flax fibres for various applications.

During flax fibre production, several byproducts are generated, with FS being the primary one. FS derives from the wood part of the flax stem (xylem) [2] and constitutes approximately 50% by weight of the dry flax stem. FS has been used in various applications, as in animal bedding [3] and particle board production [4]. However, its high availability, relatively low cost and low density make it an attractive option for reinforcement in composite materials.

Previous studies have shown promising reinforcement potential for FS in injected thermoplastic biocomposites [5,6]. However, the reinforcing capacity of FS is highly dependent on its initial granulometry prior to composite processing. Previous studies have shown that the microstructure of the composites has a significant impact on its mechanical properties, for instance, an increase in the

mechanical properties of wood flour composites is closely linked to the increase in the aspect ratio of its particles [7]. In addition, fibre orientation within the composite can have a substantial effect on its mechanical properties [8]. However, there is a lack in the literature regarding the relationship between FS granulometry, composite microstructure and the resulting tensile properties.

This study aims to investigate the influence of FS granulometry on the microstructure and resulting tensile properties of PP/MAPP injected composites reinforced with various FS granulometry and weight fractions. FS granulometry was assessed before and after processing using a 2D scanner, while X-ray tomography was employed to analyse fibre orientation in the composite. The effect of FS granulometry on composite tensile properties was investigated, followed by back-calculation of FS Young's modulus using micromechanical modelling with the Mori-Tanaka model. This comprehensive approach provides insights into the relationship between FS characteristics, composite microstructure and their mechanical properties, offering valuable guidance for the optimization of composites reinforced with FS and similar plant reinforcements.

2. Experimental

2.1. Materials

2.1.1. Reinforcement

Various granulometries of FS (FS-0-200, FS-200-500, FS-500-800 and FS-800-1600 µm), originating from the same batch, were industrially prepared by Depestele company (France). These FS groups were obtained by sieving the particles from both the bottom and the top using a specific mesh size. For instance, in FS-200-500, 200 and 500 µm represents the mesh opening size of the bottom and top mesh, respectively. Additional groups of FS (FS-200-315 and FS-315-500 µm) were prepared at a laboratory scale by further sieving FS-200-500 with a 315 µm mesh.

2.1.2. Polymer and compatibilizer

The thermoplastic polymer employed in the composite was PP homopolymer (PPH) 9020, supplied by Total Petrochemicals, which has a melting point of 165°C, a density of 0.905 g/cm^3 (ISO 1183) and a melt flow rate of 25 g/10 min at 230°C and 2.16 kg (ISO 1133). As the compatibilizer between the reinforcing material (FS) and PP polymer in the composites, Arkema supplied MAPP OREVAC® CA100 with a melt flow rate = 10 g/10 min at 230°C and 0.225 kg (ISO 1133), a melting point 167°C (ISO 11357-3) and a density of 0.905 g/cm^3 (ISO 1183). PP and MAPP were dried mixed prior to extrusion.

The optimal quantity of MAPP in a composite is proportional to the fibre weight fraction [9,10]. In this study, for each 10%wt. of FS, 2%wt. of MAPP was utilized, except when 40%wt. of FS was used, where it was found that 6%wt. of MAPP was sufficient to enhance the tensile properties of the composite.

2.2. Methods

2.2.1. Composite preparation

Different fibre weight fractions of composites were prepared (10, 20, 30 and 40%) using various particle granulometries. Initially, FS was dried for 24 hours at 80°C, after that it was compounded with PP/MAPP using co-rotating twin screw extrusion BC-2, featuring dimensions of 900 mm in length, 25 mm in width and an aspect ratio of 36. The polymer melting temperature was set at 200°C, this value decreased to 180°C upon introducing the fibres. The rotation speed and flow rate were maintained at 250 rpm and 3 kg/h, respectively. Following extrusion, the extruded line was cooled by immersion in a water bath and then grinded into pellets sized between 3 and 4 mm. The extruded pellets were further dried at 80°C in a vacuum oven for 72 hours before being injected using Krauss-Maffei (KM50-180CX). The injection barrel temperature and its screw rotation speed were adjusted at 180°C and 120 rpm, respectively. The prepared composites were in the form of ISO 527-2 type 1A tensile specimens.

©2024 | 2_NOUR EL DEIN_Ali Al Hadi_QH5CY.pdf:2

2.2.2. Fibre extraction

To analyse the fibre size distribution after processing, Decalin® (decahydronaphthalene) solvent supplied by Thermo Scientific (France) was employed to dissolve PP/MAPP allowing the fibre extraction from the composite, as suggested in [11]. Initially, the composite was introduced into a preheated Decalin® at temperatures ranging from 150°C to 155°C. Once the PP/MAPP had dissolved, stirring in the solution was ceased, allowing the fibres to undergo sedimentation. The PP/MAPP mixture was then diluted by replacing the Decalin®/PP/MAPP solution by pure Decalin®. The fibres were subsequently separated from the solution using filter paper, followed by washing with hot Decalin® and boiling Acetone.

2.2.3. Fibre granulometry analysis

2D scanner Epson perfection V850 Pro was used to characterise the fibre dimensions before and after processing. The extracted fibres were dispersed on a transparent sheet atop the scanner making sure that there is no contact or overlapping between the fibres. The resolution of the scanner was 3200 dpi, except for finer particles (FS-0-40), for which 6400 dpi was employed. Subsequently, the images were analysed using Fiji software [12]. After applying a two-pixel median filter to the images, the length and width of the particles were measured using maximum feret's diameter and minimum feret's diameter, respectively. The aspect ratio (AR) of the particles was determined by dividing the length (L) by the width (W). These measurements were conducted based on surface weighted distribution.

2.2.4. X-ray Tomography

To investigate the effect of fibre granulometry on the composite microstructure, X-ray tomography was employed. Analysis was done on composites reinforced with 10%wt. of FS-200-500 and FS-800-1600. The specimens used were the middle bars of the tensile specimens, however, they were cut in half to obtain a higher resolution of 4 µm. The EasyTom 150 kV system was used to perform X-ray tomography, with the X-ray source operating at a peak voltage of 40 kV, a current of 50 µA and a power of 2 W. The total acquisition time was 2 hours, with one projection image captured every 0.25°. The captured height of the specimens was approximately 5.4 mm.

Following the reconstruction of the projected images, the resulting 3D images were imported into Dragon fly software version 2022.2 (Canada) [13]. The particles were then separated from each other by removing the connected regions manually using a 20 µm sphere. For computational efficiency, particles with a volume less than 100 voxels (≈ 6742 µm³) were removed from the measurement, representing less than 1% of the total fibre volume. Subsequently, the images were loaded into 3D slicer software [14], where the length, width, thickness, orientation and position of each particle were measured using the minimal oriented bounding box (MOBB) through the Labelmap plugin in the segment statistics module. The volume weighted distribution was used to conduct the measurement, and particles touching the boundaries were eliminated.

2.2.5. Tensile test

Tensile tests were conducted using a Zwick TH 010 testing machine equipped of 2.5 kN load probe in a controlled environment of temperature 23°C and relative humidity of 50%. An extensometer, specifically Zwick "clip-on", was employed to determine the tensile modulus. The displacement speeds for measuring the tensile modulus and the tensile strength were set at 1 mm/min and 10 mm/min respectively, following the guidelines of the ISO 527 standard. The tensile modulus was determined as the slope of the linear trend line measured between 0.05% and 0.25% elongation. At least 5 samples were tested for each composite. The specimens were stored in a conditioned environment with a temperature of 23°C and 50% relative humidity for at least a week before the test. The actual dimensions of each specimen were measured before the test.

3. Micromechanical modelling

The micromechanical properties of composites reinforced with various granulometry of FS were modelled using the Mori-Tanaka approach, following the derivations of Fisher and Brinson [15] and Lee [16] for multiphase composite with aligned inclusions. The material consists of N phases, with the polymer matrix as the 0 phase and the rest $(N-1)$ phases are denoted as inclusions r. The dilute strain concentration factor for the rth inclusion is described by A_r^{dil} as shown in Eq. 1.

$$A_r^{dil} = [I + S_r C_0^{-1}(C_r - C_0)]^{-1} \tag{1}$$

Where I is the fourth order identity tensor and S_r is the Eshelby tensor assuming ellipsoidal inclusions described by their circular cross sections with AR. C is the stiffness matrix with the subscripts 0 and r corresponding to the matrix and the rth inclusion, respectively. A_0, which represents the strain concentration factor considering inclusion interactions by relating the average matrix strain to the uniform applied strain, is presented in Eq. 2.

$$A_0 = \left[v_0 I + \sum_{r=1}^{N-1} v_r A_r^{dil} \right]^{-1} \tag{2}$$

Where v corresponds to the volume fraction. The non-diluted strain concentration factor A_r for the rth inclusion phase is then presented by Eq. 3.

$$A_r = A_r^{dil} A_0 \tag{3}$$

The composite effective stiffness C for a unidirectional aligned inclusion is described in Eq. 4.

$$C = \left[v_0 C_0 + \sum_{r=1}^{N-1} v_r C_r A_r^{dil} \right] A_0 \tag{4}$$

The 3D particle orientation measured through X-ray tomography was then used to consider the effect of particle orientation on the composite tensile properties by employing the method proposed by Advani and Tucker [17].

4. Results

4.1. Fibres granulometry by 2D scanner

The aspect ratios of the FS across various granulometries before and after processing for composites reinforced with 30%wt. of FS, measured using the 2D scanner relative to their corresponding median width, are shown in Figure 1. The results indicate that the initial aspect ratio of the particles is dependent on the particle size. As the particle size increases, the aspect ratio of the particles also increases, reaching its maximum at FS-200-315 with a median aspect ratio of 3.4. Further increase in the particle size results in a decrease in its aspect ratio until it reaches a plateau between FS-200-500 and FS-800-1600, with a median aspect ratio of 2.7.

However, what really affects the mechanical properties of the composite is the size and shape of the particles inside the composite (after processing). The results show that the aspect ratio of the particles after processing decreases across the different granulometry. A relatively low aspect ratio, i.e. 1.9, is found for fine particles FS-0-200. As the size of the particles increases, their aspect ratio also increases, reaching its maximum at FS-200-315 with an aspect ratio of 2.6. However, additional increase in the particles size lead to a decrease in aspect ratio until it reaches 1.9 for FS-500-800 and FS-800-1600.

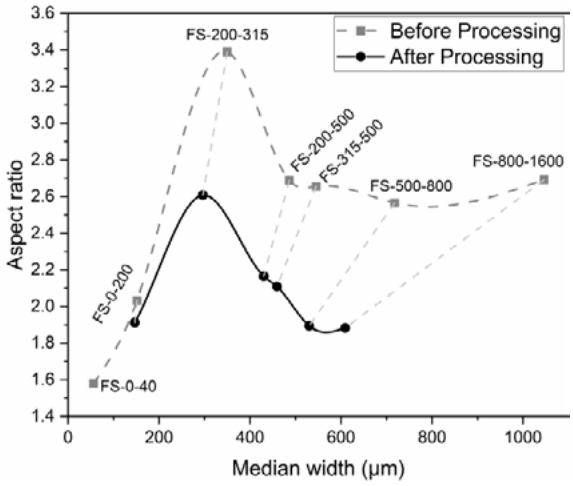

Figure 1. Flax shives (FS) median aspect ratio before and after processing for composites reinforced with 30%wt. of FS with respect to its corresponding median width. The measurements are based on surface weighted distribution.

4.2. Fibre orientation by X-ray Tomography

Figure 2 (a) presents the 3D microstructure for composite reinforced with 10%wt. of FS-200-500 after segmentation. Meanwhile, Figure 2 (b) presents the FS orientation relative to the tensile direction in composites reinforced with 10%wt. of FS-200-500 and FS-800-1600, as measured using X-ray tomography. The orientation values are based on volume weighted distribution. The findings reveal an influence of fibre granulometry on fibre orientation within the composite. Specifically, FS-200-500 particles exhibit a median orientation angle of 16°, whereas FS-800-1600 have a median orientation angle of 23°. Additionally, it is observed that 90% of FS-200-500 particles possess an orientation angle below 59°, while for FS-800-1600, 90% of particles have an orientation angle below 70°. Consequently, the results suggest that medium sized particles (FS-200-500) exhibit a better orientation towards the tensile direction compared to larger particles (FS-800-1600).

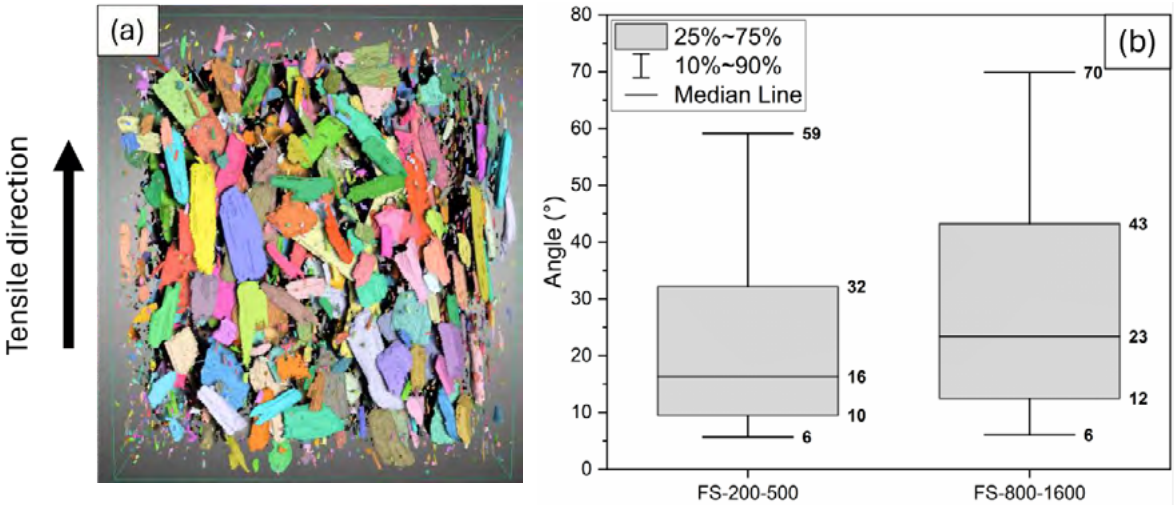

Figure 2. (a) 3D microstructure for PP/MAPP composite reinforced with 10%wt. of FS-200-500 after segmentation. (b) FS orientation distribution with respect to the tensile direction for composites reinforced with 10%wt. of FS-200-500 and FS-800-1600.

4.3. Composite tensile properties

Figure 3 displays the Young's modulus and Ultimate Tensile Strength (UTS) of PP/MAPP composites reinforced with various granulometries of FS across different fibre weight fractions (10, 20, 30 and 40%). These results show the significant influence of initial FS granulometry on the tensile properties of the composite. As the fibre weight fraction increases from 10% to 40%, a significant difference in tensile properties emerges between FS-0-200 and FS-200-500 on one hand, and FS-500-800 and FS-800-1600 on the other hand.

Comparing the Young's modulus of the composites reveals consistent patterns: FS-0-200, FS-500-800 and FS-800-1600 exhibit similar values for the different fibre weight fractions, while FS-200-500 consistently yields the highest values among the main FS fractions. In terms of UTS, FS-500-800 and FS-800-1600 consistently have the lowest values, with FS-0-200 displaying the highest value, closely followed by FS-200-500. This can be attributed to the superior dispersion of FS-0-200, which provides better interfacial bonding between the FS and the matrix, resulting in higher UTS.

Further analysis focused on composites reinforced with 30%wt. of FS-200-315 and FS-315-500. Results indicate that FS-200-315 exhibits superior tensile properties compared to other granulometries, with an increase in Young's modulus and UTS by 20% and 25%, respectively, compared to composite reinforced with 30%wt. of FS-800-1600. Hence, optimizing the FS granulometry evidently enhances its reinforcement potential.

Furthermore, these findings are consistent with previous research [2,5], which have shown that medium-sized FS particles (sieved below 500 µm) provide higher tensile properties compared to fine particles (particles sieved below 250 µm) and large particles (particles sieved with a mesh size higher than 500 µm).

A clear correlation emerges between the composite microstructure and its tensile properties, being consistent with the aspect ratio trend (section 4.1). Increasing the aspect ratio of FS will increase the tensile properties of the composite as observed in FS-200-315 and FS-200-500, while decreasing FS aspect ratio will eventually decrease the composite tensile properties as noticed for FS-500-800 and FS-800-1600. Additionally, tensile properties correlate with the FS orientation within the composite, i.e. fibres oriented more toward the tensile direction lead to better tensile properties, as observed for FS-200-500, compared to those oriented less toward the tensile direction, as seen for FS-800-1600 (section 4.2).

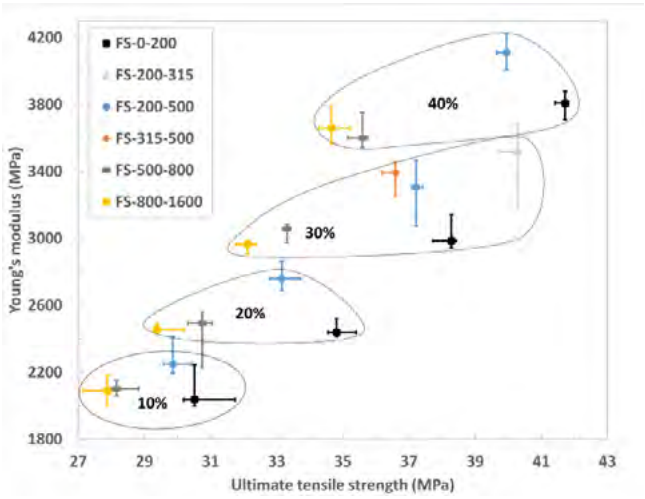

Figure 3. Young's modulus vs Ultimate tensile strength for PP/MAPP composites reinforced with various granulometries of flax shives and different fibre weight fractions. The margins indicate the minimum and the maximum points, with the median value positioned in the middle.

4.4. Mori-Tanaka micromechanical modelling

The Young's modulus of FS for varying granulometries was determined through back calculation using the Mori-Tanaka model, as detailed in Table 1. A noticeable difference in the Young's modulus of FS was observed relative to its initial granulometry. The results can be categorized into two groups: the first comprises FS with medium granulometry (FS-200-500, FS-200-315, and FS-315-500), exhibiting estimated Young's modulus values ranging from 27.1 GPa to 28.3 GPa. Conversely, the second group consists of fine particles (FS-0-200) and coarser particles (FS-500-800 and FS-800-1600), with estimated Young's modulus values ranging from 13.6 GPa to 15.3 GPa. These results are in the same order of ones existing literature, where the estimated FS Young's modulus was reported as 27.9 GPa [2] and 22.2 GPa [18] based on analytical modelling.

Various hypotheses can be formulated to elucidate the difference in FS Young's modulus. One possibility is variations in biochemical composition among the different FS fractions. In addition, the model lacks the consideration of the FS cell walls and porous microstructure, knowing that around 20% to 40% (depending on the FS granulometry and the fibre weight fraction) of the elliptical FS volume fraction comprises matrix/void within the composite, with a moderate porosity volume fraction (less than 3%) in the composite. This structure could enhance the interfacial area between FS and the matrix, consequently increasing its tensile properties.

Table 1. Young's modulus for different granulometry of FS estimated using back calculation Mori-Tanaka modelling.

FS Granulometry (µm)	0-200	200-315	200-500	315-500	500-800	800-1600
$E_{Mori\text{-}Tanaka}$ (GPa)	13.6	28.3	27.1	28.1	15.3	14.1
Standard deviation (GPa)	4.9	-	4.1	-	1.5	2

5. Conclusions

This study investigated the influence of flax shives (FS) granulometry on the microstructure and tensile properties of FS reinforced PP/MAPP composites. Our findings revealed significant variations in Young's modulus and ultimate tensile strength (UTS) across different FS granulometries and fibre weight fractions. Notably, medium-sized FS particles sieved between 200 µm and 500 µm exhibited relatively superior tensile properties, with FS-200-315 exhibiting the highest performance compared to fine particles (FS-0-200) and coarse particles (FS-500-800 and FS-800-1600). These results were consistent with the microstructural analysis of the composite, which highlighted that increasing the aspect ratio of the particles led to enhance tensile properties, as observed in FS-200-315 and FS-200-500. Additionally, composites featuring fibres oriented toward the tensile direction demonstrated better tensile properties (FS-200-500) compared to those with less orientation (FS-800-1600).

Furthermore, back-calculation of FS Young's modulus using the Mori-Tanaka model revealed significant differences with modulus ranging from 14 to 28 GPa. Medium granulometry particles exhibited higher values than fine and coarse ones. Possible explanations for these variations include differences in FS composition and cell wall microstructure as well as interfacial bonding with the matrix. Further investigations must be done to explain this phenomenon.

Acknowledgments

We acknowledge the MRI platform member of the national infrastructure France-BioImaging supported by the French National Research Agency (ANR-10-INBS-04, «Investments for the future»), the labex CEMEB (ANR-10-LABX-0004) and NUMEV (ANR-10-LABX-0020).

References

[1] L. Yan, N. Chouw, and K. Jayaraman, 'Flax fibre and its composites - A review', *Compos B Eng*, vol. 56, pp. 296–317, 2014, doi: 10.1016/j.compositesb.2013.08.014.

[2] L. Nuez *et al.*, 'Flax xylem as composite material reinforcement: Microstructure and mechanical properties', *Compos Part A Appl Sci Manuf*, vol. 149, no. December 2020, 2021, doi: 10.1016/j.compositesa.2021.106550.

[3] M. D. S. Borhan, S. Rahman, and C. Hammer, 'Water absorption capacity of flax and pine horse beddings and gaseous concentrations in bedded stalls', *J Equine Vet Sci*, vol. 34, no. 5, pp. 611–618, 2014, doi: 10.1016/j.jevs.2013.11.011.

[4] S. Sam-Brew and G. D. Smith, 'Flax and Hemp fiber-reinforced particleboard', *Ind Crops Prod*, vol. 77, pp. 940–948, 2015, doi: 10.1016/j.indcrop.2015.09.079.

[5] L. Nuez *et al.*, 'The potential of flax shives as reinforcements for injection moulded polypropylene composites', *Ind Crops Prod*, vol. 148, no. February, 2020, doi: 10.1016/j.indcrop.2020.112324.

[6] L. Nuez *et al.*, 'Determinant morphological features of flax plant products and their contribution in injection moulded composite reinforcement', *Composites Part C: Open Access*, vol. 3, no. October, 2020, doi: 10.1016/j.jcomc.2020.100054.

[7] N. M. Stark and R. E. Rowlands, 'Effects of wood fiber characteristics on mechanical properties of wood/polypropylene composites', *Wood and Fiber Science*, vol. 35, no. 2, pp. 167–174, 2003.

[8] E. Laranjeira, L. H. De Carvalho, S. M. D. L. Silva, and J. R. M. D'Almeida, 'Influence of fiber orientation on the mechanical properties of polyester/jute composites', *Journal of Reinforced Plastics and Composites*, vol. 25, no. 12, pp. 1269–1278, 2006, doi: 10.1177/0731684406060577.

[9] A. K. Rana, A. Mandal, B. C. Mitra, R. Jacobson, R. Rowell, and A. N. Banerjee, 'Short jute fiber-reinforced polypropylene composites: Effect of compatibilizer', *J Appl Polym Sci*, vol. 69, no. 2, pp. 329–338, 1998, doi: 10.1002/(sici)1097-4628(19980711)69:2<329::aid-app14>3.0.co;2-r.

[10] M. H. B. Snijder and H. L. Bos, 'Reinforcement of polypropylene by annual plant fibers: Optimisation of the coupling agent efficiency', *Compos Interfaces*, vol. 7, no. 2, pp. 69–75, 2000, doi: 10.1163/156855400300184235.

[11] N. Le Moigne, M. Van Den Oever, and T. Budtova, 'A statistical analysis of fibre size and shape distribution after compounding in composites reinforced by natural fibres', *Compos Part A Appl Sci Manuf*, vol. 42, no. 10, pp. 1542–1550, 2011, doi: 10.1016/j.compositesa.2011.07.012.

[12] J. Schindelin *et al.*, 'Fiji: An open-source platform for biological-image analysis', *Nat Methods*, vol. 9, no. 7, pp. 676–682, 2012, doi: 10.1038/nmeth.2019.

[13] 'Dragonfly 2022.2'. Comet Technologies Canada Inc., Montreal, Canada. [Online]. Available: https://www.theobjects.com/dragonfly.

[14] A. Fedorov *et al.*, '3D Slicer as an image computing platform for the Quantitative Imaging Network', *Magn Reson Imaging*, vol. 30, no. 9, pp. 1323–1341, 2012, doi: 10.1016/j.mri.2012.05.001.

[15] F. T. Fisher and L. C. Brinson, 'Nanomechanics of Nanoreinforced Polymers', *Volume 8 of Handbook of Theoretical and Computational Nanoscience*, pp. 253–360, 2006.

[16] D. Lee, 'Local anisotropy analysis based on the Mori-Tanaka model for multiphase composites with fiber length and orientation distributions', *Compos B Eng*, vol. 148, no. April, pp. 227–234, 2018, doi: 10.1016/j.compositesb.2018.04.050.

[17] S. G. Advani and C. L. Tucker, 'The Use of Tensors to Describe and Predict Fiber Orientation in Short Fiber Composites', *J Rheol (N Y N Y)*, vol. 31, no. 8, pp. 751–784, Nov. 1987, doi: 10.1122/1.549945.

[18] S. Verstraete, B. Buffel, D. Madhav, S. Debruyne, and F. Desplentere, 'Short Flax Fibres and Shives as Reinforcements in Bio Composites: A Numerical and Experimental Study on the Mechanical Properties', *Polymers (Basel)*, vol. 15, no. 10, 2023, doi: 10.3390/polym15102239.

APPROACH TO REDUCE ENVIRONMENTAL IMPACT OF FIBER REINFORCED PLASTIC BY USING FLAT GLASS FIBER

Yosuke Nukui[1]

[1]Nittoboseki Co., Ltd, Fukushima, Japan
Email: nukuiy@nittobogrp.com

Keywords: :Glass Fiber, Flat glass fiber, Environmental impact (CFP reduction, Recycling)

Abstract

In recent years, there has been a strong demand to reduce the environmental impact (CO_2 emisson, recycling), and the glass fiber used in fiber-reinforced plastic is also required to contribute to this demand. Glass fiber is originally a low environmental impact material, and it is known that the carbon foot print (CFP) is about 1.5 kg CO_2 eq, which is lower than other reinforced fiber (ex: Carbon fiber: about 20) and matrix resin (ex: PA6 about 4.5). In this study, we report the potential to reduce the CFP of fiber-reinforced plastic and to add value to the materials when they are recycled by using the flat glass fiber.

1. Introduction

In recent years, there has been a strong demand to reduce the environmental impact (CO_2 emisson, recycling) in all industries. Among them, the demand for the plastic industry is very strong because of the high use of fossil fuels and not low CO_2 emissions. The major effort for the environmental impact is using bio material, recycling, using renewable energy and mass balance approach. The situation for the fiber renforced plastic(FRP/FRTP) is also the same, and the glass fiber used for the composite is also required to contribute to this demand.

2. The environmental impact of the glass fiber pruduction

Glass fiber is a representative example of a reinforced fiber, it has the good balance of cost, property, supply volume, etc. Additionally, the glass fiber is originally a low environmental impact material. Table 1 shows the Carbon foot print (CFP) values (kg CO_2 eq) of the glass fiber and other typical materials. The glass fiber's CFP is very low compared to other marerials (Carbon fiber, resin) which are used for fiber renforced plastic. Also, the balance with its density is excellent, thus there is the significant possibility to contribute to the final product's design of a low CFP and reasonable property.

As another aspect, the glass fiber is produced from sustainable materials. Table 2 shows the material list used for the glass fiber production. Basically, the glass fiber is made from natural mineral raw materials which totally exist in the earth. In addition to this, it is possible to use the blast furnace slug which is the byproduct from iron ore manufacturing and a reasonable percent of the recycled material from the glass fiber manufacturing.

3. Motivation of this study

The flat glass fiber (FF) is a specialized material with the cross section shape of a rectangle. Due to this characteristic shape, various composite properties are improved, for example, low warpage, anisotropy reduction, good flowability and higher mechanical property for high glass contents.[5][6] In this study, we report the following two investigations to reduce the composite's environmental impact by applying FF features.

- Composite's CFP reduction possibility by using flat glass fiber
- Second time use of flat glass fiber composite

Table 1. Carbon foot print of various materials

		CFP (kg/CO_2 eq)	Density (g/cm^3)
Reinforcing Fiber	Glass Fiber [1] (Dry Chopped strand)	1.57	2.6
	Carbon Fiber [2]	24.4-31	1.8
Thermoplastic [3]	PA6	4.52	1.2
	PC	3.4	1.2
	PP	1.63	0.9
Thermoset [2]	Epoxy	4.7-8.1	1.1-1.4
Metal [4]	Steel	2.3	8
	Aluminum	16.5	2.7
GF-Composite ※Calculated value	PA6-GF30wt%	3.6	1.6
	Epoxy-GF70wt%	5.0	2.2
CF-Composite [4]	Epoxy-CF70wt%	22	1.6

Table 2. Materials for glass fiber production

Category	Example
Mineral Raw Material	Clay, Colemanite, Dolomite Calcium carbonate
Byproduct material	Blast-furnace slag (GGBFS)
Recycled material	Recycled glass fiber (Post Industrial) Recycled slaked lime

4. Composite's CFP reduction possibility by using flat glass fiber

4.1. CFP calculation of some composite conditions

Table 3 shows the calculated CFP, weight, etc of some composite conditions based on the data from table1's values, and the composite size was 50cm*50cm. From these caliculated results, by decreasing the thickness and amount of material, the CFP values significantly decreased. On the other hand, the balance of the thickness and the composite's mechanical maximum load are an issue, the reasonable action to solve this is increasing the glass fiber content. As already mentioned, the glass fiber is a low CFP material, thus by increasing the glass fiber contents, the composite application's CFP value would also decrease.

Table 3. Calculated CFP of some composite conditions

No.	Thickness mm	GF wt%	Density g/cm^3	Weight g	CFP CO_2 kg/1kg
① (BM)	3.0mm	30%	1.36	1,022	3.71
②	2.5mm	30%	1.36	852	3.10
③	2.5mm	35%	1.41	882	3.08
④	2.5mm	40%	1.46	914	3.05
※Calculate setting composite size:50cm*50cm Resin:PA6					

4.2. Experimental method

Table 4 shows the glass fiber specification for this study. We used the two types, one is the FF, and the other is a conventional round (dimaeter:11um) fiber. The resin used for the matrix is PA6 (1015B, UBE Corporation). The pellet was produced by using a twin-screw kneader and we made plate type (150mm*175mm*2.5mm or 3mm) test pieces by injection molding to evaluate the mechanical property and warpage.

We measured the flexural property(ISO178) both in the molding direction and traverse direction by cutting the test piece from the plate. The warpage was measured using the floating height of the plate test pieces.

Table 4. Glass fiber square face used in this study

	Round fiber (RF)	Flat Fiber (FF)
Fiber square face	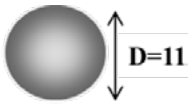	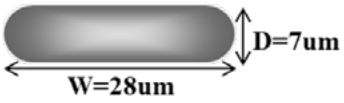
Ratio (W/D)	1	4
Fiber diameter	11um	15um (Round conversion)
Surface treatment	Suitable for matrix resin Same category treatment	

4.3. Composite property

Table5 and Figure1 shows the flexural test result for both the molding direction(MD) and traverse direction(TD) of No. ①,③, and ④. The test composite size was 150mm*175mm, the flexural test pieces were cut in each direction, the test method is ISO178, the composite No ①'s glass fiber is a round fiber(RF), while ③ and ④'s are a flat glass fiber(FF). Based on these results, in the MD, it would be possible to maintain the same maximum load for about 0.5mm thickness decreasing by 5% to 10% the glass fiber content increase. Additionally, in the TD, there shown an obvious advantage by using the FF. If the design basis values are the traverse direction values, there would be the possibility of being much thinner.

Table4 shows the warpage of each composite. The warpage is a big concern for the thinner composite, but from this result, the FF obviously shows a big advantage for this issue.

Also, the flowability is another issue, but it is known that the FF has a better flowability than RF, thus we assume that increasing the glass fiber content is relatively easily.[5][6]

Table 3. Flexural test result of condition ①③④

No.		Strength MPa	Modulus GPa	Max Load N	Thickness mm	GF wt%
① BM	MD	250	7.8	775	3.00	RF 30wt%
	TD	153	4.5	476		
③	MD	255	8.9	734	2.63	FF 35wt%
	TD	185	6.3	525		
④	MD	276	10.2	794	2.64	FF 40wt%
	TD	191	6.9	552		
Test composite size:150mm*175mm						

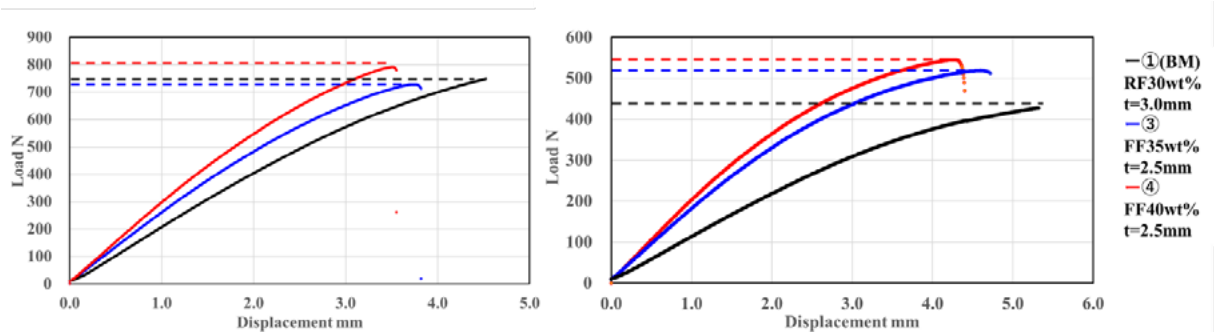

Figure 1. Flexural test Load-displacement curve (L:MD R:TD)

Table 4. Warpage of conditions ①,③ and ④

No	Warpage mm
①(BM) RF30wt% t=3.0mm	8.4
③ FF35wt% t=2.5mm	0.9
④ FF40wt% t=2.5mm	0.9

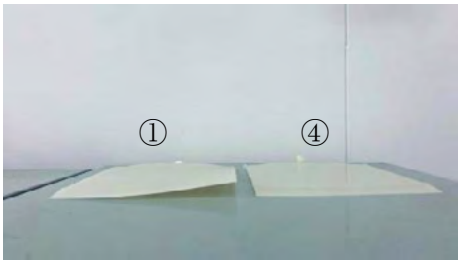

5. Second time use of flat glass fiber composite

5.1. Experimental method

We used two types, one is the FF, and the other one is a conventional round (diameter:13um) fiber. The resin used for the matrix is polypropylene (NOBLEN U-501E, SUMITOMO CHEMICAL Co., Ltd.) and modifier additives. Figure 2 shows the test outline. The virgin material pellet is produced by using a twin-screw kneader. The recycled material is produced by crushing the test pieces and spools made from injection molding which used virgin material. By using these materials, we made the plate type (80mm*60mm*2mm or 1mm) test pieces by injection molding to evaluate their mechanical property and warpage.

We measured the flexural property(ISO178) both in the molding direction and traverse direction by cutting a 2mm thick test piece from the plate. The warpage was measured using the floating height of the 1mm thick plate test pieces.

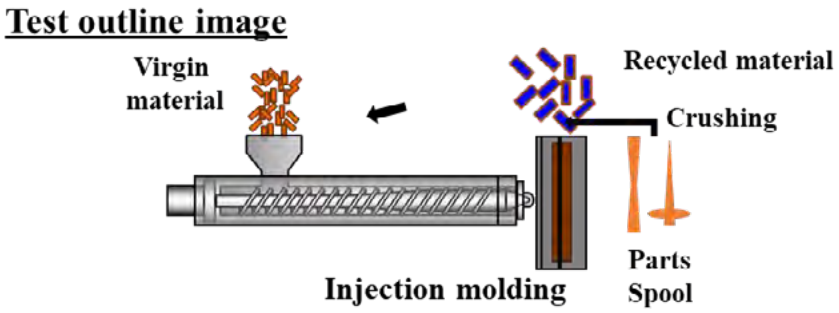

Figure 2. Test Outline

5.2. Result

Table7 shows the test results. As a result, even for the second time use, the FF's features, which are a low warpage and anisotropy reduction, are significantly effective. Generally, with more and more repeated recycling, the remaining fiber length would be shorter and the mechanical property would lower, but in these situations, the FF has a significant potential to contribute to other aspects.

Table 5. Recycled GF-PP composite property

Ⓐ Virgin Material	Ⓑ Recycled Material	Ⓐ : Ⓑ	Warpage mm	Flexural Strength MPa		Flexural Modulus GPa	
				MD	TD	MD	TD
RF 40wt%	-	-	14	120	94	5.2	3.2
FF 40wt%	-	-	4	140	144	4.9	4.6
RF 40wt%	FF 40wt%	50%:50%	9	126	107	5.6	4.1
FF 40wt%	FF 40wt%	50%:50%	5	128	133	5.2	4.8
Test composite size:80mm*60mm							

6. Conclusions

The approach of a thinner composite and increasing glass fiber content shows the possibility of reducing the CFP by 15-20% while maintaining its mechanical properties and composite weight. It was also shown that concerns, such as warpage due to thinner fiber – reinforced composites, can be eliminated by using the Flat Glass Fiber.

Also, the recycled resin pellets using the flat glass fiber were shown to have an improved dimensional stability and reduced anisotropy, the same as the virgin pellet using the flat glass fiber.

In conclusion, the glass fiber with a deformed cross section, i.e, the Flat Glass Fiber, has a significant potential to make a great contribution to the CFP reduction and recycling for the design of composite materials.

References

[1] Glass Fiber Europe, Life cycle assessment of CFGF –Continuous Filament Glass Fiber Products (2023)
[2] Becham et al, Environmental analysis of innovative sustainable composites with potential use in aviation sector—A life cycle assessment review, SCIENCE CHINA, September 2017 Vol.60 No.9:1301–1317
[3] Plastics Europe, Eco-profile
[4] World Auto Steel
[5] Koichi Nakamura, General Properties and Recent Research Results of Glass Fiber [Translated from Japanese], Journal of Textile Engineering, Vol.67 No.7 Page.413-420 (2014.07.25)
[6] Shunsuke Harashima et al, Influence of glass fiber with flat cross section on fiber-reinforced composites [Translated from Japanese], REINFORCED PLASTICS, Vol.65 No.12 Page.506-507 (2019.12.23)

SIMULATING THE CRYSTAL GROWTH OF PPS USING MOLECULAR DYNAMIC METHODS

H. Omichi[1], R. Higuchi[2], Y. Oya[3], J. Koyanagi[4], T. Yokozeki[5], T. Aoki[6]

[1]Department of Materials and Technology, Tokyo University of Science, Tokyo, Japan
Email: 8223516@ed.tus.ac.jp
[2]Department of Aeronautics and Astronautics, The University of Tokyo, Tokyo, Japan
Email: higuchi@aastr.t.u-tokyo.ac.jp
[3] Department of Materials and Technology, Tokyo University of Science, Tokyo, Japan
Email: oya@rs.tus.ac.jp
[4] Department of Materials and Technology, Tokyo University of Science, Tokyo, Japan
Email: koyanagi@rs.tus.ac.jp
[5] Department of Aeronautics and Astronautics, The University of Tokyo, Tokyo, Japan
Email: yokozeki@aastr.t.u-tokyo.ac.jp
[6] Department of Aeronautics and Astronautics, The University of Tokyo, Tokyo, Japan
Email: aoki@aastr.t.u-tokyo.ac.jp

Keywords: thermoplastics, PPS, Molecular Dynamic simulation

Abstract
In recent years, carbon fiber-reinforced thermoplastics (CFRTP) have garnered global interest, notably in the aerospace and automotive industries. The crystallinity of thermoplastic resin, influenced by modeling conditions such as pressure and cooling rate, impacts material properties by forming chain-folded polymer lamellae. We conducted all-atom MD simulations on a single PPS chain, focusing on the structural transition in the crystal structure. The comparison with PE is also made to show the difference in crystal structure depending on the composition. At the selected length of polymer, PPS would collapse into a non-structure as the polymer is being cooled from 400 K to 300 K while PE would form a stable structure after dropping below 300 K. Various methods such as calculating the radius of gyration and introducing gyration tensors were used to evaluate the results seen in the snapshots.

1. Introduction

Carbon Fiber Reinforced Plastics (CFRP) are expected to be a material that can solve problems in the automotive industry, such as reducing fuel consumption and extending service life by reducing the weight of the car body. The base material of CFRP, which is commonly used in aircraft, is thermosetting resin, mainly epoxy resin. Still, its application to general vehicles has not progressed due to economic concerns and mass production technology. In addition, thermosetting resin composite materials are difficult to recycle after use. As a solution to these problems, it is expected that thermoplastic resins, which have excellent properties such as impact resistance, recyclability, and short molding cycles, can be used as the base material of CFRP. Hereafter, CFRP using thermoplastic resin as the base material is referred to as carbon fiber-reinforced thermoplastic resin (CFRTP).

Thermoplastic resins are classified into amorphous and crystalline resins. Crystalline resins have a property called semi-crystallinity, in which the entire resin area does not crystallize even after reaching the crystallization temperature, but crystalline and amorphous portions are mixed [1] (Figure 1). It has been reported that the crystalline structure and degree of crystallinity of semi-crystalline polymers change depending on molding conditions such as cooling rate and pressure, affecting various material

properties such as stiffness and strength [2,3,4]. These are explained by the folding of polymer chains. Sequentially folded polymer chains become lamellar structures, which are the main building blocks of polymeric materials, and their spatial distribution governs all physicochemical properties of the materials. Therefore, it is an important issue to elucidate the crystal structure and crystallization mechanism.

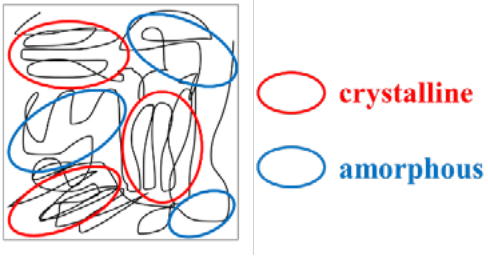

Figure 1. Schematic of thermoplastic resin crystals at the molecular scale

Although information on the crystallization of polymers at the nanoscale has been obtained by experimental techniques such as transmission electron microscopy and atomic force microscopy [5,6,7], information on the crystallization of polymers at the atomic scale has not been obtained. Over the past few decades, molecular dynamics (MD) and Monte Carlo (MC) simulations have improved our understanding of polymer crystallization. Sundararajan et al [8,9] used MD simulations to show that polymer chain folding is controlled by van der Waals intermolecular forces. Various methods have been proposed to analyze crystal structures, and Yamamoto [10,11,12,13] studied crystallization using local order parameters to simulate crystal growth on a substrate. Fujiwara [14,15] et al. analyzed bond orientation ordering and conformational defects based on successive trans segments, and Hagita [16] studied the structure formation of single polymer chains under different cooling rates. However, many of these simulations used the United Atom (UA) or coarse-grained (CG) model to simplify the chemistry of the repeating units, thereby reducing computational cost. In contrast, the all-atom (AA) model is more computationally expensive, but it is ideal for studying crystal structures and mechanical responses; Song [17] et al. used the CHARMM32 force field to study the folding structure of polyethylene oxide chains, and Trigg [18] et al. investigated the crystal structure of functional polyethylene chains using the LOPLS-AA force field. Jiang [19] et al. studied the effects of cutoff distance and molecular chain length on the crystal structure and state transitions of a single polyethylene chain using the OPLS-AA force field.

Conventional MD simulations mainly targeted general-purpose plastics such as polyethylene (PE), while thermoplastic resins used as base materials for CFRTP, which is applied to aircraft, are polyphenylene sulfide (PPS), polyether ether (PEEK), polyaryl ether ketone (PAEK), and other super engineering plastics have not yet been subjected to MD simulations.

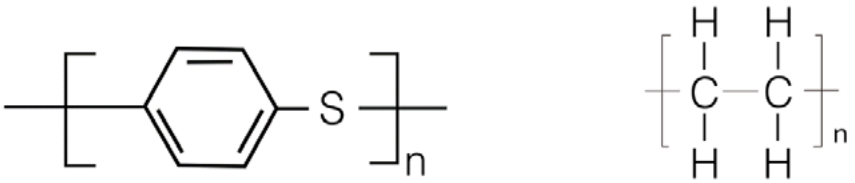

Figure 2. PPS monomer (left) and PE monomer (right)

Among the super engineering plastics, PPS is the subject of analysis in this study. In this paper, we simulate the cooling process of a single chain of PPS using all-atom MD simulation and focus on the structural transition in the crystal structure. The comparison with PE is also made to show the difference in crystal structure depending on the composition.

2. Model and Methods

2.1. Simulation Details

In this study, the AA model is used to simulate the cooling process of single chains of PPS and PE. All MD simulations are performed with J-OCTA, using the Nose-Hoover method, a NVT ensemble, and the OPLS-AA force field [20,21,22]. The cutoff distances for both Lennard-Jones (LJ) and Coulomb interactions are 0.65 nm, while electrostatic potential charges obtained from density functional theory calculations using B3LYP/6-31G (Hamiltonian/basis set) are set for each atom to reproduce the electrostatic field around each molecule.

A single chain with $N_s = 22$ $(n = 22)$ was used in the PPS simulations. The chains were held at 800 K for 5 ns before being cooled to 100 K at a cooling rate of 10 K/ns, i.e., the cooling time was 70 ns. The same simulations were also performed for PE to compare the results with those obtained from the PPS simulations; the PE simulations used a single chain with $N_c = 100$ $(n = 50)$. The PE chain was cooled from 600 K to 100 K at a cooling rate of 10 K/ns after being held at 600 K for 5 ns. This time, the cooling time was 50 ns. 15 independent samples were used for each chain in this study. Note that aligning the length of the molecular chains was the purpose for the selected degree of polymerization.

2.3. Gyration Tensor

To determine the structural features of the polymer single chain, the gyration tensor of a single chain was calculated using the following equation

$$S_{\alpha\beta} = \frac{1}{2N^2}\sum_{i=1}^{N}\sum_{j=1}^{N}\left(r_\alpha^{(i)} - r_\alpha^{(j)}\right)\left(r_\beta^{(i)} - r_\beta^{(j)}\right) \tag{6}$$

where N is the number of atoms of the target element present in the polymer chain, N_s representing the number of sulfur atoms in a PPS chain while N_c is representing the number of carbon atoms in a PE chain. α , β are the x, y, z directions, respectively. $r_\alpha^{(i)}$ is the α component of the position vector $r^{(i)}$ for the ith particle. The diagonalizing the gyration tensor $\boldsymbol{S}$ transforms it into the principal axis with the relative eigenvalues as in equation (7).

$$\boldsymbol{S} = \mathrm{diag}(\lambda_1\,, \lambda_2\,, \lambda_3) \tag{7}$$

In this case, the eigenvalues of $\boldsymbol{S}$ are sorted in descending order $(\lambda_1 \geq \lambda_2 \geq \lambda_3)$. The shape descriptors derived from the gyration tensor and its eigenvalues are used to analyze the conformation of the polymer chain. The shape parameters K_1 , K_2 [23] and the relative shape anisotropy parameter κ^2 [23] are used in this study. The shape parameters K_1 and K_2 are defined as Eqs. (8) and represent the shape of the polymer chain from the combination of $(K_1\,, K_2)$.

$$K_1 = \frac{\lambda_2 + \lambda_3}{\lambda_1 + \lambda_2}\,,\quad K_2 = \frac{\lambda_1 + \lambda_3}{\lambda_1 + \lambda_2} \tag{8}$$

Note that $K_2 \geq K_1\,, K_2 \geq 0.5$ always holds. The polymer chain becomes spherical when $(K_1\,, K_2)$ is approaching $(1\,, 1)$, rod-like shape when approaching $(0\,, 1)$, and disk-like shape when approaching $(0.5, 0.5)$. Other pairs represent intermediate shapes between these conformations. The relative shape anisotropy parameter κ^2, indicating the degree of anisotropy of the polymer chain, is defined as Equation (9).

$$\kappa^2 = \frac{3}{2}\frac{{\lambda_1}^2 + {\lambda_2}^2 + {\lambda_3}^2}{(\lambda_1 + \lambda_2 + \lambda_3)^2} - \frac{1}{2} \tag{9}$$

The range of κ^2 is $\kappa^2 \in [0\,,\,1]$, indicating that the polymer chain is spherically symmetric when approaching 0 and linear when approaching 1. The radius of gyration (R_g) was also obtained by equation (10).

$$R_g = \sqrt{{\lambda_1}^2 + {\lambda_2}^2 + {\lambda_3}^2} \tag{10}$$

3. Results and Discussion

Snapshots during the cooling process are shown in Figure 4 and Figure 5, displaying the conformational changes of a single chain at various temperatures. We could see that while PE showed a chain-folded structure at the end of the simulation, the same could not be said for PPS, crumbling into a spherical shape.

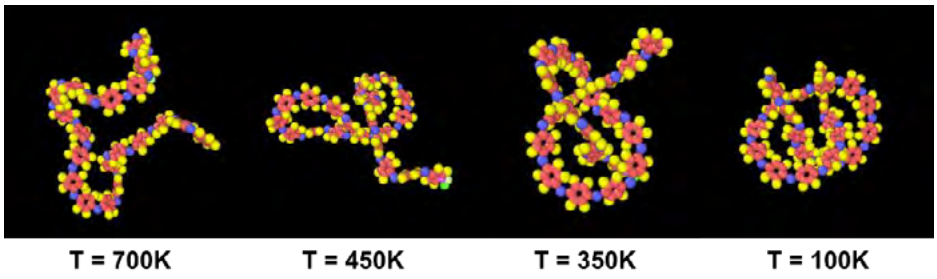

Figure 4. Snapshots of the PPS ($N_s = 22$) cooling process

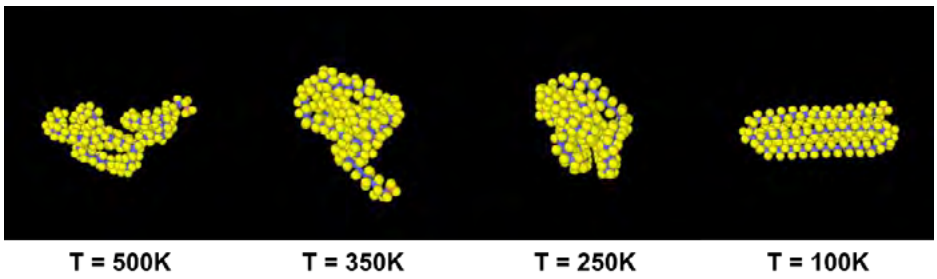

Figure 5. Snapshots of the PE ($N_c = 100$) cooling process

By looking at the snapshots, the difference between the dispersion can also be explained. The snapshots of all 15 cases after 300 K were near identical graphically for PPS while the PE had a few cases where the polymer chain showed different appearances after 200 K, for example cases B and C in Figure 6. Rather than a clear chain-folding structure, case B seemed to have spherical shape at the end of the chain-folding structure while case C was a thick disk-like shape. We strongly believe that these cases had a great attribution in increasing the standard deviation while also lowering the κ^2 under 0.6.

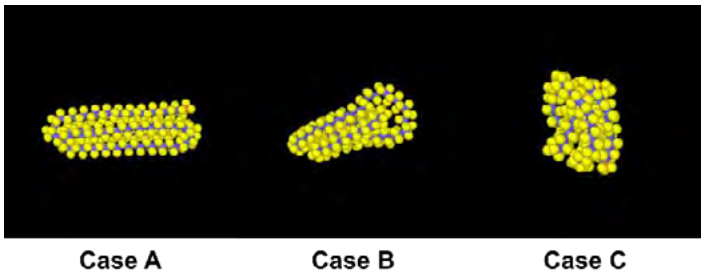

Figure 6. Different cases of PE ($N_c = 100$) at 150 K

The results of the current simulations give a systematic description of the natures between single chain short length PE and PPS during a cooling process. At this length, PE may or may not fold into a rod-like shape while PPS constantly becomes a disordered structure.

The shape parameters K_1 , K_2 and the relative shape anisotropy parameter κ^2 are shown in Figure 7 and Figure 8. The dark colors represent the average of 15 cases, while the area between the bright colors is within one standard deviation of the mean. When comparing these figures, we can see that the PPS data has less dispersion compared to those of PE, especially in the low temperatures. It also shows the difference in the change of K_1 , K_2 and κ^2, indicating that at this length, PE and PPS forms into different shape while cooling. For PPS, (K_1 , K_2) shifts from $(0.26 , 0.86)$ to $(0.50 , 0.78)$ while κ^2 shifts from 0.45 to 0.16 during cooling, transforming into a spherically symmetric disk-like shape. However, PE transforms into a more anisotropic rod-like shape as (K_1 , K_2) shifts from $(0.35 , 0.82)$ to $(0.22 , 0.95)$ while κ^2 shifts from 0.36 to 0.56. Focusing on the cooling process, a rapid change of the parameters could be seen after being cooled down to a certain temperature, i.e., 400 K for PPS and 300 K for PE.

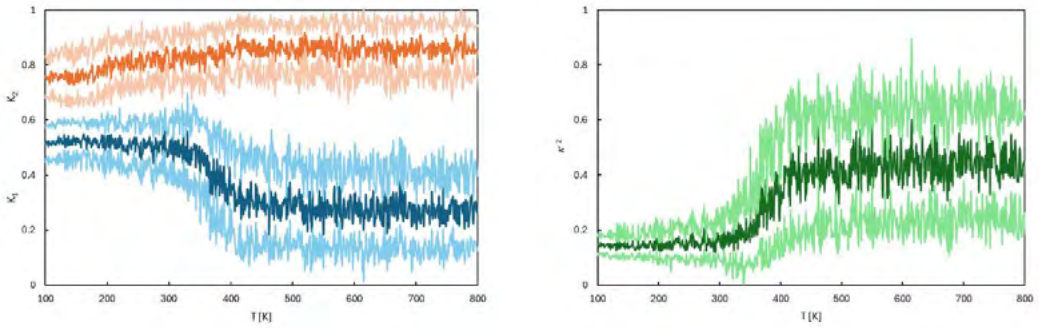

Figure 7. K_1 , K_2 and κ^2 during the cooling process of PPS ($N_s = 22$)

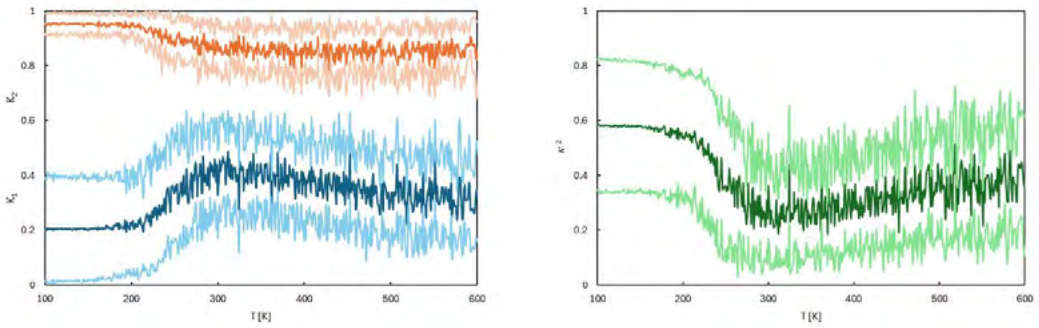

Figure 8. K_1 , K_2 and κ^2 during the cooling process of PE ($N_c = 100$)

The average of the torsion energy, van der Waals (vdW) energy, and the radius of gyration of the chains are also shown in Figure 9 and Figure 10. It is clearly visible that for the PPS chain of $N_s = 22$, R_g is held within a certain range before being dropping at 400 K, followed by another constant holding at another value from 300 K. We could see that R_g had a higher fluctuation before the drop from 400 K. During this time, we could see that the torsion energy and vdW energy are constantly decreasing at a specific slope, the torsion energy with a steep slope while the vdW energy has a very loose slope. In contrast of the PPS chain, the PE chain of $N_c = 100$ shows a different characteristic. Rather than showing a significand drop at a specific temperature, R_g decreases at a certain rate from 600 K to 300 K, followed by a slight increase until 200 K, and staying the same after 200 K. We can also see that the torsion energy and the vdW energy shows a similar outline, shifting from a convex upward to a convex downward at around 250 K.

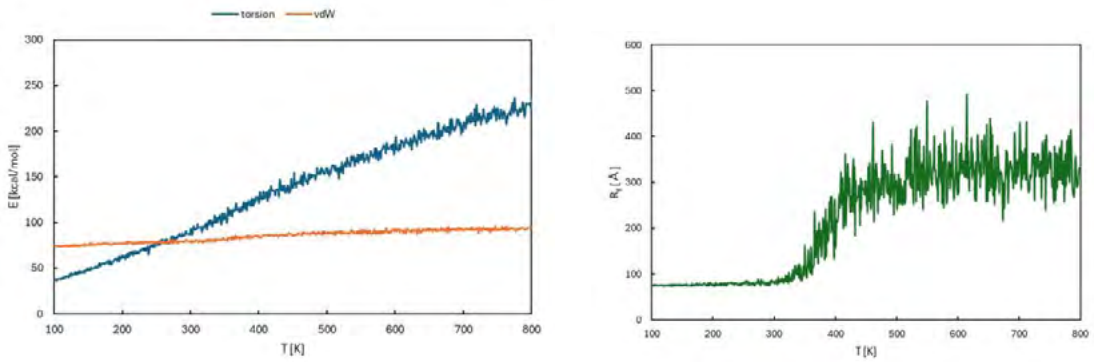

Figure 9. Variations of torsion energy, vdW energy and R_g of PPS ($N_s = 22$)

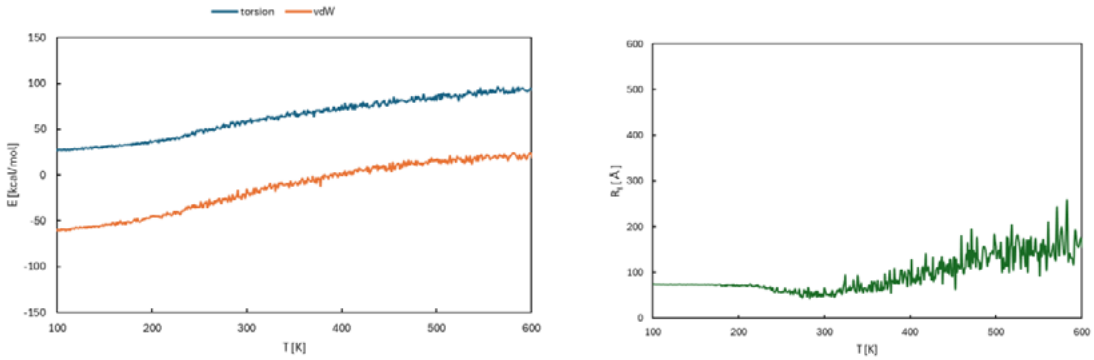

Figure 10. Variations of torsion energy, vdW energy and R_g of PE ($N_c = 100$)

4. Conclusions

A systematic description of the different natures between single chain short length PPS and PE during the cooling process was given from the simulation results. At the length selected for this study, PPS constantly becomes a disordered structure while PE may or may not fold into a rod-like shape while. To clearly observe the chain-folding structure for PPS, the simulation should be conducted with a much longer chain length, determining the minimum length needed for PPS to fold into an ordered structure on the way. The molecular structure of the polymer chains should also be taken into consideration, especially after finding out that the van der Waals energy showed different results. However, this theory cannot be confirmed at the moment without further results from different length of polymer chains. In future studies, not only would we like to conduct more simulations with longer polymer length but also considering using different cooling rates to understand the chain-folding sequence of PPS.

References

[1] H. Suemasu, Mechanics of Composite Materials Introduction to Engineering Beginners, Baifukan, Tokyo, 2009.
[2] S. L. Gao and J.K. Kim. Cooling rate influences in carbon fiber/PEEK composites. Part I: Crystallinity and interface adhesion, *Composites Part A*, 31: 517-530, 2000.
[3] S. L. Gao and J.K. Kim. Cooling rate influences in carbon fiber/PEEK composites. Part II: interlaminar fracture toughness, *Composites Part A*, 32: 763-774, 2001.
[4] S. L. Gao and J.K. Kim. Cooling rate influences in carbon fiber/PEEK composites. Part III: impact damage performance, *Composites Part A*, 32: 775-785, 2001.
[5] P. Yang, Y. Song, W. Feng, W. Zhang. Unfolding of a single polymer chain from the single crystal by air-phase single-molecule force spectroscopy: Toward better force precision and more accurate description of molecular behaviors, *Macromolecules*, 51: 7052−7060, 2018.

[6] Y. Song, Z. Ma, P. Yang, X. Zhang, X. Lyu, K. Jiang, W. Zhang. Single-molecule force spectroscopy study on force-induced melting in polymer single crystals: The chain conformation matters, *Macromolecules*, 52: 1327−1333, 2009.
[7] K. Liu, Y. Song, W. Feng, N. Liu, W. Zhang, X. Zhang. Extracting a single polyethylene oxide chain from a single crystal by a combination of atomic force microscopy imaging and single-molecule force spectroscopy: toward the investigation of molecular interactions in their condensed states, *J. Am. Chem. Soc*, 133: 3226−3229, 2011.
[8] T. Kavassalis, P. Sundararajan. A molecular-dynamics study of polyethylene crystallization, *Macromolecules*, 26: 4144−4150, 1993.
[9] P. Sundararajan, T. Kavassalis. Molecular dynamics study of polyethylene chain folding: the effects of chain length and the torsional barrier, *J. Chem. Soc. Faraday Trans*, 91: 2541−2549, 1995.
[10] T. Yamamoto. Molecular dynamics modeling of polymer crystallization from the melt, *Polymer*, 45: 1357−1364, 2004.
[11] T. Yamamoto. Molecular dynamics simulation of polymer crystallization through chain folding, *J. Chem. Phys*, 107: 2653−2663, 1997.
[12] T. Yamamoto. Molecular-dynamics simulation of polymer ordering. I. Crystallization from vapor phase, *J. Chem. Phys*, 109: 4638−4645, 1998.
[13] T. Yamamoto. Molecular dynamics simulation of polymer ordering. II. Crystallization from the melt, *J. Chem. Phys*, 115: 8675−8680, 2001.
[14] S. Fujiwara and T. Sato. Structure formation of a single polymer chain. I. Growth of trans domains, J. Chem. Phys, 114: 6455−6463, 2001.
[15] S. Fujiwara and T. Sato. Molecular dynamics simulations of structural formation of a single polymer chain: Bond-orientational order and conformational defects. *J. Chem. Phys*, 107: 613−622, 1997.
[16] K. Hagita, S. Fujiwara, N. Iwaoka. Structure formation of a quenched single polyethylene chain with different force fields in united atom molecular dynamics simulations. *AIP Adv*, 8: 115108, 2018.
[17] Y. Song, W. Feng, K. Liu, P. Yang, W. Zhang, X. Zhang. Exploring the folding pattern of a polymer chain in a single crystal by combining single-molecule force spectroscopy and steered molecular dynamics simulations, *Langmuir*, 29, 3853−3857, 2013.
[18] E. B. Trigg, M. J. Stevens, K. I. Winey. Chain folding produces a multilayered morphology in a precise polymer: simulations and experiments, *J. Am. Chem. Soc*, 139: 3747−3755, 2017.
[19] S. Jiang, Y. Lu, C. Luo. State Transitions and Crystalline Structures of a Single Polyethylene Chain: MD Simulations, *J. Phys. Chem. B*, 126: 964−975, 2022.
[20] W. L. Jorgensen, J. D. Madura, C. J. Swenson. Optimized intermolecular potential functions for liquid hydrocarbons, *J. Am. Chem. Soc*, 106: 6638–6646, 1984.
[21] W. L. Jorgensen, D. S. Maxwell, J. Tirado-Rives. Development and testing of the OPLS all-atom force field on conformational energetics and properties of organic liquids, *J. Am. Chem. Soc*, 118: 11225–11236, 1996.
[22] S. Nose. Constant-temperature molecular dynamics. *J. Phys.: Condens. Matter*, 2: 115-119, 1990
[23] H. Arkın, W. Janke. Gyration tensor based analysis of the shapes of polymer chains in an attractive spherical cage. *J. Chem. Phys*, 138: 054904, 2013.

MECHANICAL PROPERTIES OF 3D-PRINTED PLA COMPOSITES REINFORCED WITH CARBON-BASED FILLERS

Zaki Echcherki[1], Yasith S. Perera[1] and Chamil Abeykoon[1]

[1] Northwest Composites Centre, Aerospace Research Institute, and Department of Materials, Faculty of Science and Engineering, The University of Manchester, Oxford Road, M13 9PL, Manchester, UK
Email: zaki.echcherki@postgrad.manchester.ac.uk, yasith.perera@manchester.ac.uk, chamil.abeykoon@manchester.ac.uk

Keywords: 3D printing, Composites, Carbon fibres, Graphene, PLA

Abstract
This study investigates the mechanical properties of 3D-printed polylactic acid (PLA) composites reinforced with milled carbon fibres (mCFs) and graphene nanoplatelets (GNPs). The composites were produced through melt blending using a twin-screw extruder with different filler fractions (ranging from 3 wt.% to 15 wt.%) of mCF and GNP. 3D printing filaments manufactured using the developed composites were used to produce 3D-printed specimens using the fused deposition modeling technique with three different raster angles (i.e., [0°], [45°], and [0°, 90°]). The addition of mCF and GNP fillers improved the tensile and flexural properties of PLA, with mCF-reinforced PLA exhibiting better mechanical performance than GNP-reinforced PLA. In general, the tensile and flexural modulus of the specimens were found to increase as the filler fraction increased. Moreover, the raster angle was also found to have a significant influence on the mechanical properties, where a raster angle of [0°] generally exhibited the highest mechanical properties, followed by raster angles of [0°, 90°] and [45°]. The findings of this study should be invaluable for optimizing and tailoring 3D-printed carbon-based filler-reinforced PLA composites for a wide range of engineering applications.

1. Introduction

Three-dimensional (3D) printing is a cutting-edge technology that involves the joining of materials layer by layer to produce objects from 3D model data [1], [2]. 3D printing enables the direct creation of items with complex geometrical features in an efficient manner that does not require a mould tool and allows near-net-shape manufacture in a reasonably short time frame [3]. By minimizing the time needed for the trial production of new products, 3D printing not only reduces production costs and facilitates quick prototyping but also improves manufacturing speed and overall production efficiency. Additionally, it equips businesses with high responsiveness to market demands presenting valuable opportunities, in highly competitive markets [4].

Of the available 3D printing techniques, fused deposition modeling (FDM) is one of the most popular and extensively researched techniques in both academic and commercial settings. FDM offers a very cost-effective way to create 3D components with a respectable level of resolution that can reach up to 40 μm [5]. In this process, temperature control of the nozzle is achieved through computer control while a driver wheel pushes the material filament. After the material melts at the nozzle, it is deposited onto a panel or material that has already been cooled and solidified. The final product is created by stacking layers one by one under the control of a computer [4]. A number of printing parameters influence the properties of the parts produced through the FDM process. These factors include the height and width of the deposited fused lines, their orientation, the infill density, the temperature at which the material is extruded, and build orientation [6].

Polylactic acid (PLA) is one of the widely used polymers for 3D printing. PLA is a biodegradable and renewable polymer derived from renewable resources such as corn starch or sugarcane. Its popularity in

3D printing stems from its ease of processing, low toxicity, and good printability. However, PLA exhibits inherent limitations in terms of mechanical strength, toughness, and thermal stability, which can be addressed through the incorporation of fillers [7]. Various types of fillers and fibres have been explored to reinforce polymer matrices in 3D printing. For example, carbon-based fillers such as carbon fibres (CFs) and graphene nanoplatelets (GNPs) have gained interest because of their mechanical, electrical, and thermal characteristics. The incorporation of carbon-based fillers into PLA matrices can enhance the mechanical strength, electrical conductivity, and thermal conductivity of the resulting composites. Optimizing the filler loading is crucial in achieving the desired properties, as the concentration and uniform dispersion of the fillers can significantly affect the properties of the composites [8].

Past studies have extensively focused on investigating the effects of the carbon-based filler concentration and FDM parameters on the mechanical properties of 3D-printed parts. Daneshpayeh et al. [9] studied the strength of nanocomposites made from PLA, polyolefin elastomer, multiwall carbon nanotubes, and carbon black particles. Tensile test results showed that adding nanofillers to the binary matrix both separately and simultaneously led to improvements in strength, modulus, and elongation at break of up to 72%, 30%, and 22%, respectively. Caminero et al. [10] observed an enhancement in the tensile and flexural stresses and a decline in impact strength with the inclusion of GNPs into PLA. The build orientation during FDM printing was also found to have an impact, with the upright orientation exhibiting the best results. For CF-reinforced PLA, the alignment of carbon fibres in the printing direction increased the material anisotropy and improved the directional properties in terms of strength [11].

The FDM printing parameters also have a significant influence on 3D-printed carbon-based filler-reinforced PLA composites. Kumar et al. [12] achieved the maximum tensile strength with an infill density of 80%, a printing speed of 80 mm/s, and a layer height of 100 microns for CF-reinforced PLA. In another study, the best tensile strength was obtained with an infill density of 80%, a layer height of 0.2 mm, and the X-axis building direction using 5.5 wt.% CF-reinforced PLA [13]. Jiang and Smith [14] reported an increase in tensile strength and modulus of CF-reinforced polymer composites printed with a raster angle of [0°].

Liang et al. [15] proposed a combination of 0.5 wt.% graphene oxide and 9 wt.% CF as reinforcement to obtain 3D-printed composites with enhanced mechanical properties. Cao et al. [16] produced CF-reinforced PLA with a 30% volume fraction of CF using FDM. The incorporation of CF was found to reduce the tensile strength but significantly increased the Young's modulus and elongation at break. Hu et al. [17] explored the effect of CF loading (ranging from 2.5 wt.% to 15 wt.%) on the mechanical properties of CF-reinforced PLA composites produced through FDM. The highest tensile strength was observed with 7.5 wt.% CF, while the highest flexural strength and modulus were observed with 15 wt.% CF.

Although a lot of past studies have investigated PLA composites reinforced with carbon-based fillers they have not compared the performance of milled carbon fibres (mCFs) and GNPs as fillers. As they are different types of carbon fillers where mCFs are micro fillers while GNPs are nanofillers, a performance comparison between them would be of interest to material developers. Therefore, in this study, it is aimed to bridge this gap, by evaluating the mechanical properties of mCF/PLA and GNP/PLA composites with different filler fractions produced using FDM with different raster angles.

2. Methodology

2.1. Materials

For this study, PLA Luminy® LX175, developed by Total Corbion PLA, Netherlands was used as the matrix material. The 'Carbiso Mil 100 µm' milled carbon fibres (mCF) manufactured by Easy Composites, UK, and graphene nanoplatelets (GNP) (M15 grade) developed by Sigma-Aldrich, UK

were utilized as the filler materials. The carbon fibres had an average length of 100 µm, an average diameter of 7.5 µm, and a density of 400 kg/m^3. The particle size of the GNPs was 15 µm with a surface area of 120-150 m^2/g.

2.1. Methods

Before producing the composites, PLA, mCFs, and GNPs were pre-dried in a vacuum oven overnight at 60 ℃. Then, melt extrusion of PLA, GNP/PLA, and mCF/PLA was carried out in a Thermo Scientific HAAKE™ Rheomex PTW16 co-rotating twin-screw extruder. The matrix material (i.e., PLA) was fed using a volumetric feeder, while the filler materials (i.e., GNP and mCF) were fed using a gravimetric feeder. GNP/PLA and mCF/PLA with five different filler percentages (i.e., 3, 5, 8, 10, and 15 wt.%) were produced, and pure PLA was also extruded for comparison with the produced composite materials. The set temperature profile of the barrel heating zones of the twin-screw extruder was set as follows from the hopper to the die: 180–180–180–200–200–200–215–215–215–215 °C, while the screw rotational speed was set to 150 rpm. The extrudate was passed through a water bath and subsequently processed into pellets of 3 mm in length using a pelletizer.

The PLA, mCF/PLA, and GNP/PLA pellets produced through extrusion were then dried in an AIRID polymer dryer by 3devo. Next, the dried pellets were used to fabricate 3D printing filaments using a filament extruder by 3devo. The set temperature profile of the filament extruder heating zones was set from the hopper to the nozzle as follows: 185-195-195-190 °C. A screw rotational speed of 3.5 rpm was used, and the filament diameter was set to 1.75 mm, which is a standard filament diameter for 3D printing.

The SolidWorks software was used to design the 3D-printed test specimens required for mechanical testing. Figure 1 illustrates the designed standard specimens for tensile and flexural testing with dimensions of 185 × 16 × 4 mm and 80 × 10 × 4 mm, respectively. The specimens were then 3D-printed using a PRUSA 13 MK3S FDM printer. 3D printing was carried out in the flat building orientation with the printing parameters shown in Table 1.

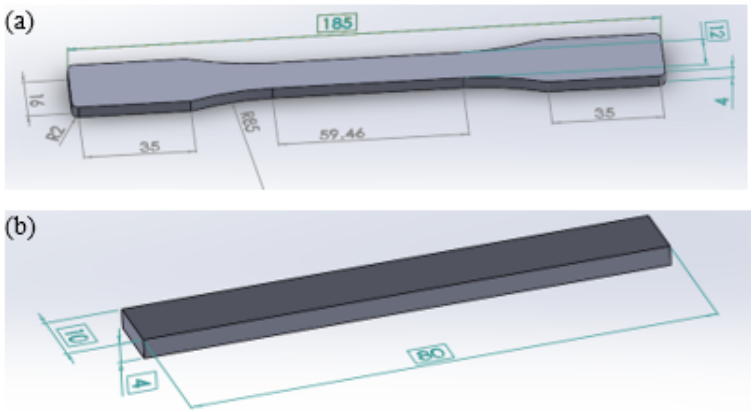

Figure 1. 3D designs of the (a) tensile and (b) bending test specimens.

The mechanical properties of the 3D-printed composites were evaluated via tensile and 3-point bend testing. For both tests, specimens were printed using three different infill patterns. The first two patterns utilized an aligned rectilinear infill, where the samples were printed with the same raster angles of [0º] and [45º], respectively, from top to bottom. The third pattern involved a rectilinear infill configuration, with alternating layers with raster angles of [0º, 90º]. The tensile specimens printed with different raster angles are illustrated in Figure 2. The tensile and flexural properties of the 3D-printed specimens were evaluated using an Instron 5967 universal tensile tester. The crosshead speed of the machine was set to

1 mm/min for the tensile test, according to the standard ASTM D638, and a 5-kN load cell was used. For the bending test, the crosshead speed of the machine was set to 3 mm/min according to the standard ASTM D790, and a load cell of 1 kN was used.

Table 1. 3D printing parameters for all samples.

Description	*Value*
First Layer Height	0.2 mm
Layer Height	0.15 mm
No. of Vertical Shells	2
Horizontal Shells	0
Infill Density	100%
Infill Speed	90 mm/s
Nozzle Temperature	215 °C
Bed Temperature	60 °C

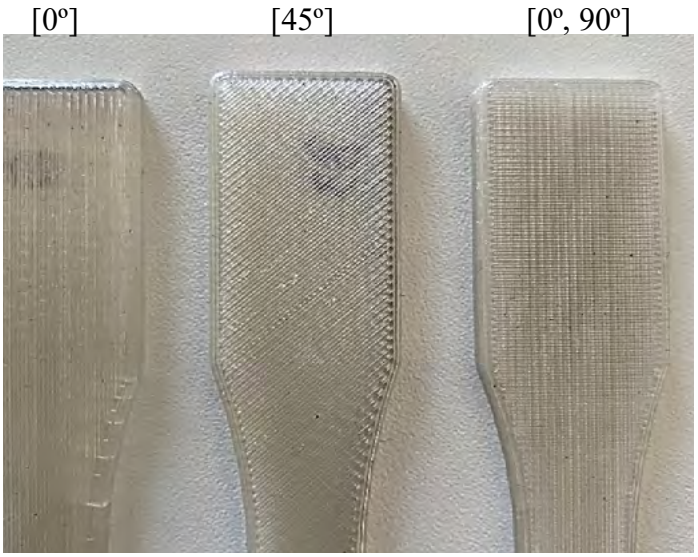

Figure 2. Pure PLA tensile specimens printed with different raster angles.

3. Results and Discussion

3.1. Tensile Properties

Figure 3 illustrates the tensile properties of the 3D-printed composites with different raster angles and filler percentages. It is clear from Figures 3(a) and 3(b) that the inclusion of both mCF and GNP resulted in an increase in the elastic modulus of the 3D-printed composites compared to that of pure PLA regardless of the raster angle. When assessing the effect on the ultimate tensile strength (UTS) and strain at break, Figures 3(c) and 3(e) show that there is no clear effect of incorporating mCF into the PLA matrix on the UTS and strain at break, while Figures 3(d) and 3(f) suggest that there is a reduction in the UTS and strain at break for GNP-reinforced PLA composites with a raster angle of [0º]. In contrast, the UTS and strain at break were found to have been enhanced by the addition of both mCF and GNP into the PLA matrix of 3D-printed specimens with raster angles of [45º] and [0º,90º]. Generally, GNP/PLA composites exhibited higher elastic modulus compared to mCF/PLA composites. This may be attributed to the excellent mechanical properties and high aspect ratio of GNP, which enables better

load transfer and reinforcement within the PLA matrix resulting in increased tensile modulus. However, the UTS of mCF/PLA composites was found to be higher than that of GNP/PLA composites for a majority of filler percentages. Similarly, the strain at break of mCF/PLA composites was found to be higher than that of GNP/PLA composites with raster angles of [0º] and [0º,90º].

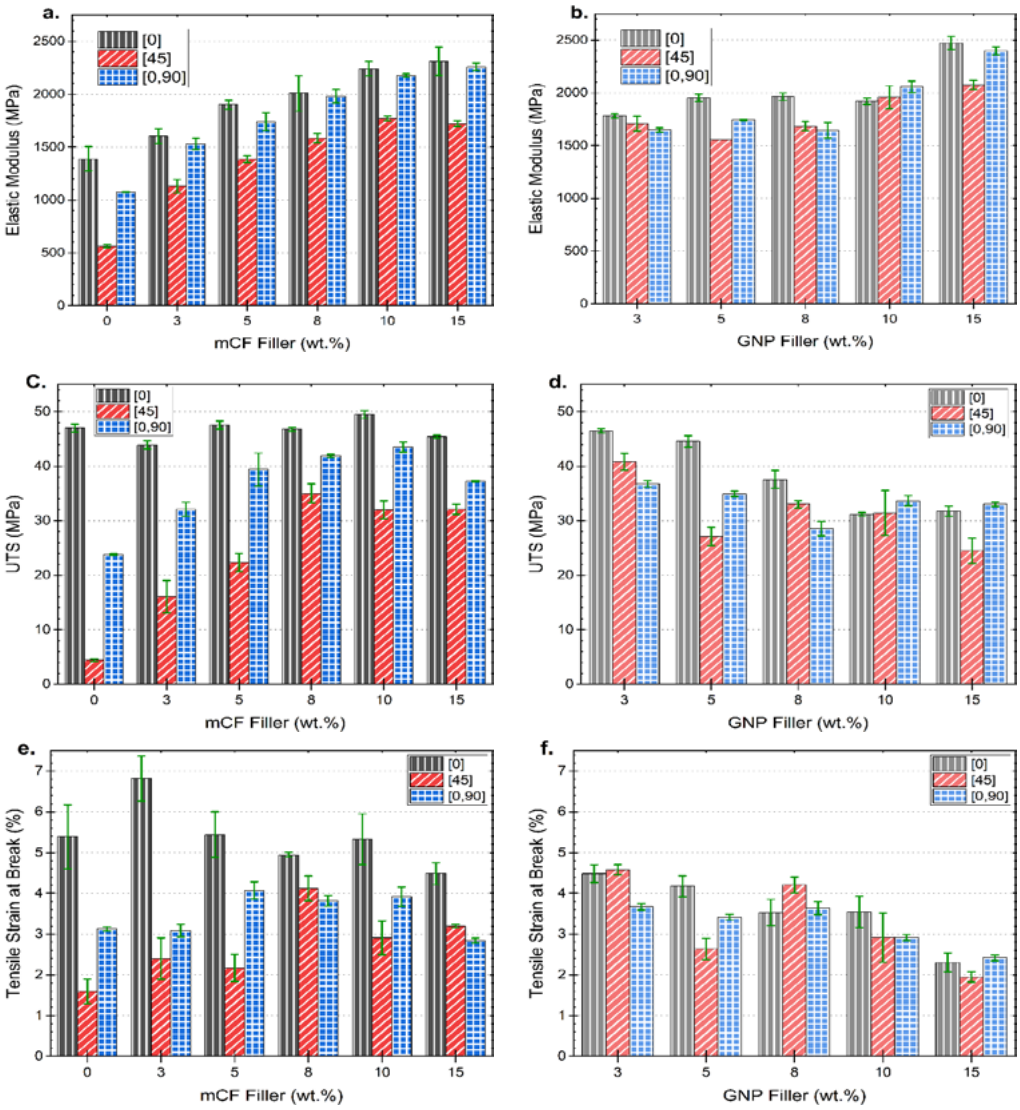

Figure 3. Tensile properties of 3D-printed mCF/PLA and GNP/PLA composites

In addition to the filler type, the filler content was also found to have a significant influence on the tensile properties. The elastic modulus showed a general increase with increasing mCF and GNP percentage regardless of the raster angle, with the highest elastic modulus of 2473.9 MPa being recorded by the 15 wt.% GNP/PLA specimen with a raster angle of [0º]. This was a 77% increase compared to the pure PLA specimen. The UTS and the strain at break did not exhibit a clear variation with increasing mCF content but showed a general reduction with increasing GNP content for samples produced with a raster angle of [0º]. This reduction in UTS with increasing GNP content may be due to the poor dispersion of the filler during melt blending causing the GNP particles to act as stress concentrators. The UTS of samples with raster angles of [45º] and [0º,90º] displayed a general increase with increasing mCF content but did not indicate a clear variation with increasing GNP content.

The strain at break of samples with raster angles of [45º] and [0º,90º] did not show a clear trend with increasing mCF or GNP content. The 10 wt.% mCF/PLA composite with a raster angle of [0º] reported the highest UTS value of 49.50 MPa, while the 3 wt.% mCF/PLA composite with a raster angle of [0º] showed the highest strain at break value of 6.82%.

For pure PLA and a majority of mCF/PLA composites, the highest tensile properties were reported for a raster angle of [0º], followed by [0º,90º], and [45º], respectively. A majority of the GNP/PLA composites also displayed the same behavior for the elastic modulus, but no clear trend was observed for the UTS and the strain at break.

3.2. Flexural Properties

A comparison of the flexural properties of 3D-printed composites with different raster angles and filler percentages is provided in Figure 4. Clearly, the inclusion of mCF and GNP fillers into the PLA matrix had a significant effect on the flexural properties. The filler type also had an impact, as the composites with mCF generally exhibited higher flexural modulus, ultimate flexural strength (UFS), and flexural strain at break compared to the composites with GNP as the filler.

When assessing the effect of filler content on the flexural properties, it can be observed from Figure 4(a), that the flexural modulus of mCF/PLA composites increased with increasing filler content regardless of the raster angle. The flexural modulus of GNP/PLA composites with raster angles of [0º] and [0º,90º] did not show a consistent variation with increasing filler content, but that of the composites with a raster angle of [45º] exhibited a general increase (see Figure 4(b)). The 15 wt.% mCF/PLA composite with a raster angle of [0º] reported the highest flexural modulus of 6132.63 MPa, which is a 107% increase compared to pure PLA. This is in agreement with the findings of the study by Hu et al. [17] where the highest flexural modulus was reported for 15 wt.% of CF. Unlike the flexural modulus, the UFS did not exhibit a clear variation with increasing filler content, and the effect depended on the raster angle as well (see Figures 4(c) and 4(d)). The UFS of mCF/PLA and GNP/PLA composites with raster angles of [45º] and [0º,90º] exhibited a general increase compared to their respective pure PLA samples, but the GNP/PLA composites with a raster angle of [0º] showed a significant decrease in the UFS with increasing GNP content. This decrease in UFS can be attributed to the poor dispersion and agglomeration of GNP particles at higher filler percentages, causing the GNP particles to act as stress concentrators and weaken the composite. The highest UFS was reported by the 10 wt.% mCF/PLA with a raster angle of [0º], which was found to be 94.57 MPa. However, this was not a significant improvement compared to the UFS value of 94.02 MPa of the pure PLA sample printed with the same raster angle. The flexural strain at break of both mCF/PLA and GNP/PLA showed a general reduction as the filler content increased for all raster angles, as shown in Figures 4(e) and 4(f). Despite this behavior, the flexural strain at break was found to be greater than that of pure PLA for most filler percentages, with 3 wt.% mCF/PLA with a raster angle of [0º] providing the highest strain at break value.

For pure PLA and mCF/PLA composites, the raster angle [0º] provided the highest flexural modulus followed by [0º,90º], and [45º], respectively. However, the flexural modulus of GNP/PLA composites did not display a clear trend with varying raster angles. The UFS of pure PLA and mCF/PLA composites reported a similar behavior to the flexural modulus. For a majority of the GNP/PLA composites, the raster angle [0º,90º] showed the lowest UFS. The lowest flexural strain at break was reported by the raster angle [0º,90º] for pure PLA, mCF/PLA, and GNP/PLA composites, while the maximum values were provided by raster angles of [45º] and [0º] for a majority of the mCF/PLA and GNP/PLA composites, respectively.

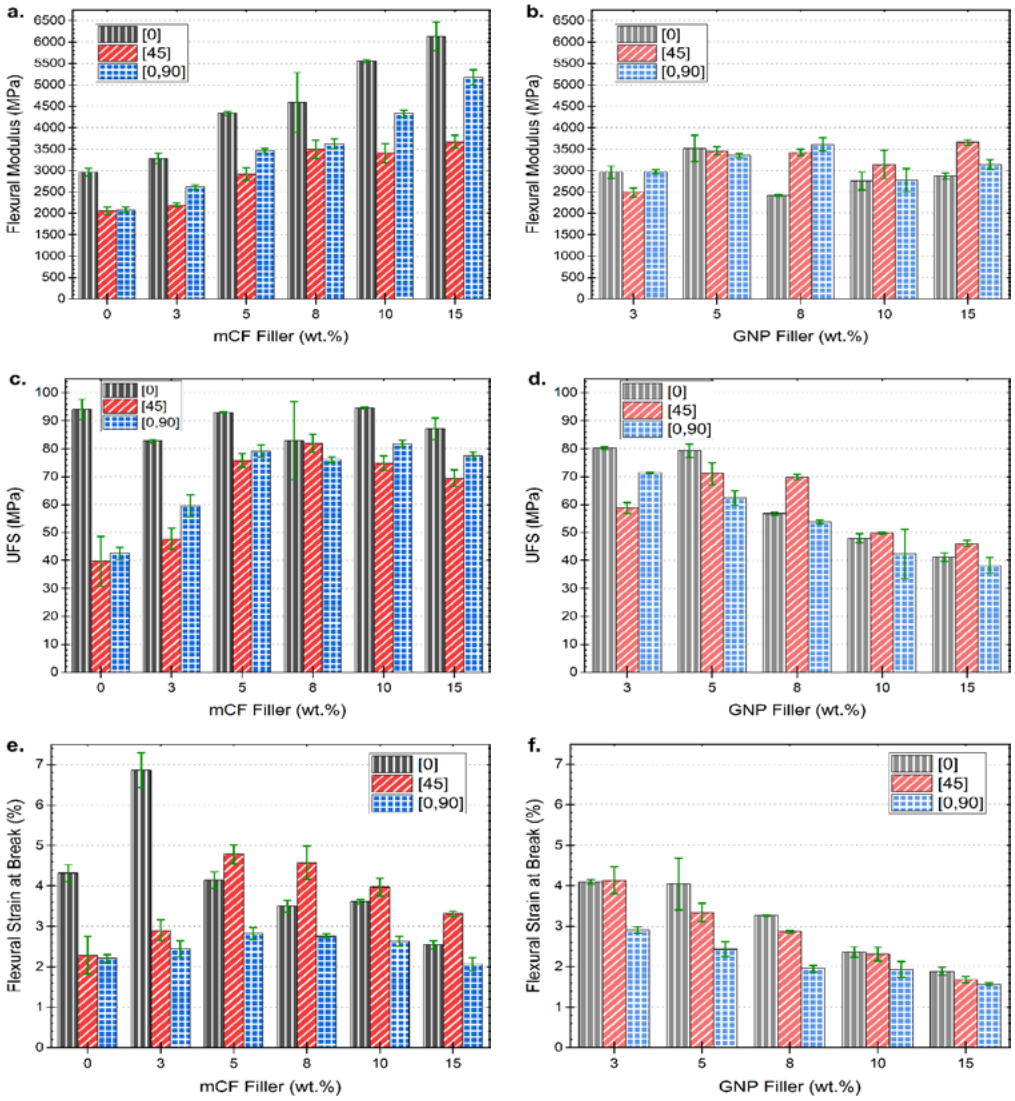

Figure 4. Flexural properties of 3D-printed mCF/PLA and GNP/PLA composites

4. Conclusions

In this study, the tensile and flexural properties of GNP-reinforced and mCF-reinforced PLA composites produced using the FDM 3D printing technique were studied. Test specimens were produced with five different filler fractions (i.e., 3, 5, 8, 10, and 15 wt.%) and three raster angles (i.e., [0°], [45°], and [0°, 90°]). The results indicated that the mechanical properties were affected by the filler type, filler percentage, as well as raster angle. The elastic modulus increased with increasing mCF and GNP content regardless of the raster angle. However, the UTS and the tensile strain at break showed a general reduction with increasing GNP content for samples produced with a raster angle of [0º]. The flexural modulus exhibited a general increase with increasing mCF and GNP content but also depended on the raster angle. The inclusion of mCF generally resulted in an improved UFS compared to pure PLA, but the GNP/PLA composites with a raster angle of [0º] showed a significant drop in the UFS with increasing GNP content. The flexural strain at break decreased with increasing filler content for both mCF/PLA and GNP/PLA. For a majority of the composites, the inclusion of mCF and GNP led to an increase in mechanical properties. However, mCF-reinforced PLA composites generally exhibited better performance than GNP-reinforced composites. A raster angle of [0º] exhibited the best mechanical performance in most cases followed by raster angles [0º,90º] and [45º], respectively.These findings aid

in selecting the best filler type, filler fraction, and printing parameters to obtain 3D-printed composites with a desired combination of mechanical characteristics for an intended application. Under future work, we aim to investigate the thermal, electrical, and morphological characteristics of mCF/PLA and GNP/PLA composites produced through FDM 3D printing.

References

[1] R. Shanthar, K. Chen, and C. Abeykoon. Powder-Based Additive Manufacturing: A Critical Review of Materials, Methods, Opportunities, and Challenges. *Adv. Eng. Mater.* 25(19), 2023.
[2] O. Exley, Y.S. Perera, and C. Abeykoon. Investigation of the effect of the degree of hollowness and internal cavity structure on the mechanical properties of 3D-printed parts. *Int. J. Lightweight Mater. Manuf.* 7:45-61, 2024.
[3] Y. Yuan, C. Abeykoon, W. Mirihanage, A. Fernando, Y.-C. Kao, and J.A.W. Harings. Prediction of temperature and crystal growth evolution during 3D printing of polymeric materials via extrusion. *Mater. Des.* 196, 2020.
[4] Y. Zheng, X. Huang, J. Chen, K. Wu, J. Wang, and X. Zhang. A Review of Conductive Carbon Materials for 3D Printing: Materials, Technologies, Properties, and Applications. *Materials*. 14(14), 2021.
[5] G. Postiglione, G. Natale, G. Griffini, M. Levi, and S. Turri. Conductive 3D Microstructures by Direct 3D Printing of Polymer/Carbon Nanotube Nanocomposites via Liquid Deposition Modeling. *Compos. Part Appl. Sci. Manuf.* 76: 110-114, 2015.
[6] C. Abeykoon, P. Sri-Amphorn, and A. Fernando. Optimization of fused deposition modeling parameters for improved PLA and ABS 3D printed structures. *Int. J. Lightweight Mater. Manuf.* 3: 284-297, 2020.
[7] L. McKeen. *The Effect of Sterilization on Plastics and Elastomers.* William Andrew Publishing, Boston, 2012.
[8] V. Dananjaya, S. Marimuthu, R. Yang, A.N. Grace, C. Abeykoon. Synthesis, properties, applications, 3D printing and machine learning of graphene quantum dots in polymer nanocomposites. *Prog. Mater. Sci.* 144, 2024.
[9] S. Daneshpayeh, F. Ashenai Ghasemi, V. Panahizadeh, and I. Ghasemi. Investigation and Optimization of the Tensile Properties of Nanocomposites Based on Polylactic Acid/Polyolefin Elastomer: Using Fuzzy Inference System and Particle Swarm Optimization Method. *Polym. Compos.* 43(9): 6521-6536, 2022.
[10] M. Á. Caminero, J. M. Chacón, E. García-Plaza, P. J. Núñez, J. M. Reverte, and J. P. Becar. Additive Manufacturing of PLA-Based Composites Using Fused Filament Fabrication: Effect of Graphene Nanoplatelet Reinforcement on Mechanical Properties, Dimensional Accuracy and Texture. *Polymers.* 11(5), 2019.
[11] Q. Ding, X. Li, D. Zhang, G. Zhao, and Z. Sun. Anisotropy of Poly(Lactic Acid)/Carbon Fiber Composites Prepared by Fused Deposition Modeling. *J. Appl. Polym. Sci.* 137(23), 2020.
[12] M. A. Kumar, M. S. Khan, and S.B. Mishra. Effect of Fused Deposition Machine Parameters on Tensile Strength of Printed Carbon Fiber Reinforced PLA Thermoplastics. *Mater. Today Proc.* 27: 1505-1510, 2020.
[13] M. Kamaal, M. Anas, H. Rastogi, N. Bhardwaj, and A. Rahaman. Effect of FDM Process Parameters on Mechanical Properties of 3D-Printed Carbon Fibre–PLA Composite. *Prog. Addit. Manuf.* 6(1): 63-69, 2021.
[14] D. Jiang, and D. E. Smith. Anisotropic Mechanical Properties of Oriented Carbon Fiber Filled Polymer Composites Produced with Fused Filament Fabrication. *Addit. Manuf.* 18: 84-94, 2017.
[15] L. Liang, T. Huang, S. Yu, W. Cao, and T. Xu. Study on 3D Printed Graphene/Carbon Fiber Multi-Scale Reinforced PLA Composites. *Mater. Lett.* 300, 2021.
[16] M. Cao, T. Cui, Y. Yue, C. Li, X. Guo, X. Jia, and B. Wang. Investigation of Carbon Fiber on the Tensile Property of FDM-Produced PLA Specimen. *Polymers.* 14(23), 2022.
[17] C. Hu, W. N. Hau, W. Chen, Q. -H. Qin. The Fabrication of Long Carbon Fiber Reinforced Polylactic Acid Composites via Fused Deposition Modelling: Experimental Analysis and Machine Learning. *J. Compos. Mater.* 55(11): 1459-1472, 2021.

BENDING BEHAVIOR OF FABRICS MADE OF FLAX/PA12 COMINGLED YARN

Théo Perrin[1], Gilles Arnold[1], Michel Tourlonias[1], Karine Gautier[1], Peng Wang[1]

1 : Laboratoire de Physique et Mécanique Textiles (LPMT, UR 4365)
Université de Haute-Alsace
11 rue Alfred Werner, 68093 Mulhouse, France, https://www.lpmt.uha.fr/
e-mail : theo.perrin@uha.fr, gilles.arnold@uha.fr, michel.tourlonias@uha.fr, karine.gautier@uha.fr
and peng.wang@uha.fr

Keywords: textile composites, natural fibres, thermoplastic, bending behavior, Kawabata Evaluation System

Abstract
Investigating various deformation modes is essential for accurately characterizing the behavior of the reinforcement. The interaction between these deformation modes requires further comprehensive analysis. This study focuses on the bending behavior of a plain fabric and a 2-2 twill made from flax yarns comingled and covered with PA12 multifilaments. The influence of the structure is studied by comparing the bending rigidity of the yarns and the fabrics. The results show that the fabric is more rigid than the yarns. In addition, the fabric bending rigidity gets closer the bending rigidity of the yarn with the increase of the length of the floated yarns. The influence of shear on flexural rigidity is also investigated. The bending rigidity of a fabric increases with the increase of the shear angle. This increase seems to level off at the same bending rigidity for the two fabrics.

1. Introduction

With current environmental conditions and with the importance of recycling to lower the need in raw materials, the composite industry is turning towards bio-sourced reinforcements and thermoplastic matrices. However, the manufacturing processes remain generally the same and stamping shaping techniques are widely used. During the forming process, the main deformation mode is in-plane shear. Nevertheless, bending behavior is critical to take into account the defects such as wrinkles and tow buckling during the simulation of the forming of non-developable shapes [1,2]. In this work, the influence of the fabric structure on the bending behavior is studied at different strain level of in-plane shear.

The bending property of fibrous reinforcement are not directly related to the tensile properties. It has to be measured and require specific tests as the fabrics present a very low bending stiffness. A first test that is commonly used is the cantilever test [3]. This method is easy to set up and still used as a standard test[4]. In this test, the sample is laid on a horizontal surface and pushed over an edge so that it bends under its own weight. The sample is pushed until the hanging tip reaches a plane inclined by 41,5°. This angle was chosen to simplify the bending rigidity calculation. The length of fabric pushed is measured and used to calculate the bending rigidity.

In order to determine the influence of the shear on the bending rigidity, the position of the yarns must be controlled. The bending tester of the Kawabata Evaluation System of Fabrics is better suited for this task[5]. It consists of two chucks. The back chuck is fixed and equipped with a torque sensor. The front chuck rotates so that the bending radius of the sample is uniform thus, applies pure bending on the sample. The gap between the chucks is 10mm wide. The fabric is bent through a range of curvatures between 2.5 and -2.5cm^{-1} at a rate of 0.5cm^{-1}/sec. The full bending cycle consists of a loading and an

unloading phase in the positive curvature direction (in blue in the Figure 1) followed by a loading and an unloading phase in the direction of the negative curvature (in orange in the Figure 1).

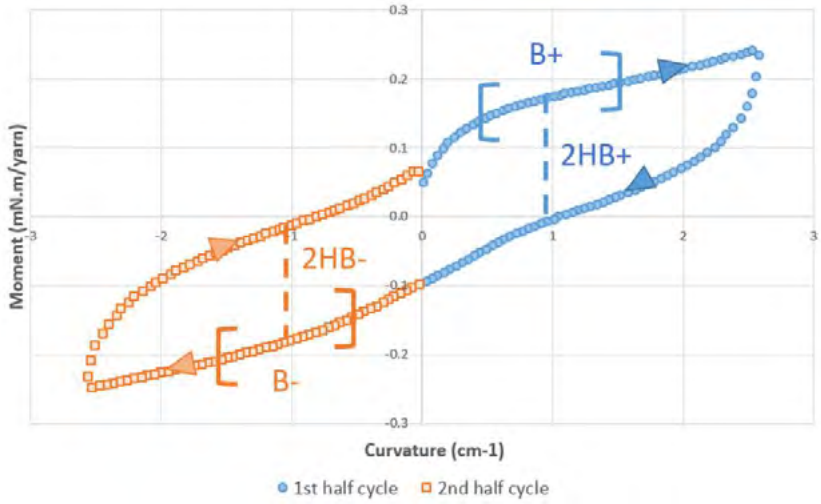

Figure 1. Raw bending data

2. Materials

Two fabrics of the same hybrid yarns are selected: a plain weave and a 2-2 twill. The yarns are made of flax comingled with polyamide 12 and covered with a polyamide 12 multifilament (Figure 1). The yarn density in the warp and the weft are identical. The mass fraction of the flax and of the PA12 are 64% and 36% respectively. Comingled yarns reinforcements are developed to behave like a dry fabric during the forming process thus, being easier to shape than prepregs. No injection step is required anymore in the process, the thermoplastic matrix being already inside the yarn. Moreover, it reduces the porosities of the final composite[6]. The covering increases the yarn's cohesion and reduces the hairiness, thus reducing the defects during the weaving process by lowering the friction.

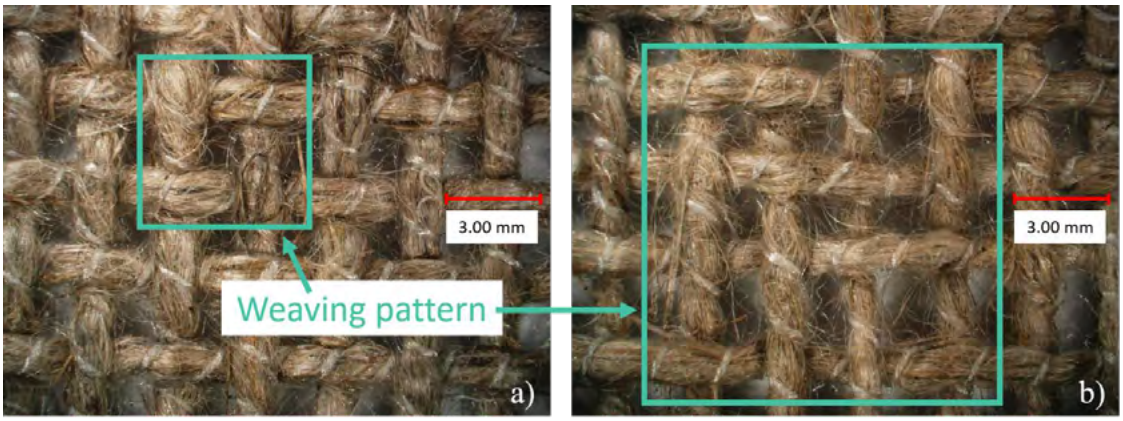

Figure 2. a) Plain fabric b) 2-2 twill

The two fabrics have the same yarn density in weft and warp (4 yarns/cm). The weaving pattern of the plain fabric is 5x5mm wide. The weaving pattern of the 2-2 twill is 10x10mm wide.

2.1. Samples preparation

All the samples are conditioned for at least 24 hours at 20°C and 65% of relative humidity[7]. To ensure a whole number of weaving patterns between the chucks, the samples of plain fabric and 2-2 twill are 8 yarns and 12 yarns wide. 4 yarns fit vertically between the chucks for each fabric.

In order to test yarns out of the fabric, a yarn-holder was designed to extract the yarn orthogonal to the tested direction (warp or weft), to ensure the orientation of the yarns and to control their tension and torsion (Figure 3). As the weave pattern is different, so is the crimp. The undulation of the extracted yarn needs to be eliminated. The yarns are straightened one by one with a fixed mass of 50g. The tension is maintained thanks to a paper frame glued to the yarns. This frame is cut after the sample is correctly set in the chucks. Each sample is made of 6 yarns.

Figure 3. Yarn tension set up

Similarly, in order to test the fabric in different configurations, a 3D printed guide is used to shear the samples to a given shear angle (Figure 4.a) prior to the bending test. The samples are then glued in a paper frame to keep the yarn orientation, before being set up in the chucks of the bending tester. The sample dimensions (8x8 yarns) were chosen to form a whole number of weaving patterns for both fabrics. With α being the angle between the warp and the weft, the sample is placed so that the warp and the weft form a $\frac{\alpha}{2}$ angle with the normal to the chucks (D in the Figure 4.b). The shearing angle is defined by the following equation (Eq. 2):

$$\gamma = \frac{\pi}{2} - \alpha \tag{2}$$

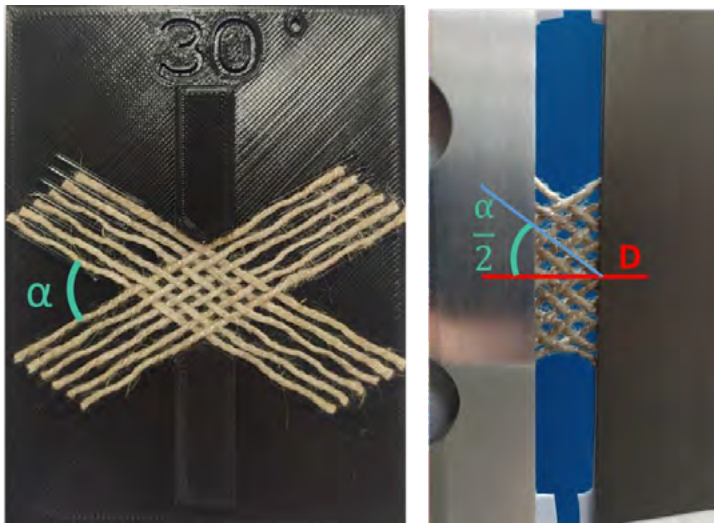

Figure 4. a) Shearing guide b) Sample set up in the chucks

A bias extension test has been conducted to define the locking angle, i.e. the angle at which the yarns of the warp and the weft get in contact and can't rotate around the interlacements. The locking angle for the plain weave is equal to 35° and the locking angle for the 2-2 twill is equal to 38.75°. Bth fabric samples are sheared at 0°, 10°, 20° and 30° and then tested in bending.

3. Methods

3.1. KES BENDING TESTS

Each sample goes through 5 cycles. The first cycle presents a different behavior than the following cycles (Figure 5). This trend is observed for the different weaves and for the yarns. The leading hypothesis is that the sizing applied on the yarn breaks during the first cycle thus, inducing a higher bending stiffness. The first cycle will be not used for the calculation of the parameters. The means are calculated on the cycles 2 through 5. In order to compare the different structures, the bending moment is divided by the number of yarns in the sample. The results are presented in the International System Units.

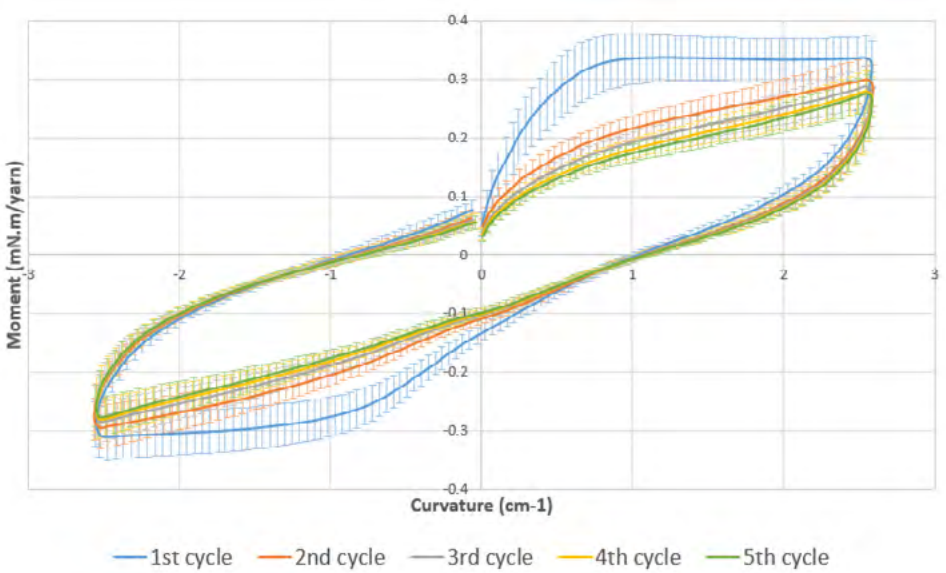

Figure 5. Bending behavior for the 2-2 twill in the warp direction during 5 cycles

3.2. GROSBEG MODEL

To describe the bending behavior, i.e. the bending moment M as a function of the curvature K, a linear model taking into account the hysteresis was developed by Grosberg[8]:

$$M(K) = B * K \pm 2HB \quad (1)$$

where B is the bending rigidity and 2HB is the bending hysteresis. Four parameters can be extracted from the raw data. The bending rigidity of the first direction B+ and second direction B- are determined respectively as the slope in a range of curvature between 0,5 and 1,5cm^{-1} and the slope between -0,5 and -1,5cm^{-1}. The bending hysteresis is obtained from the width between the loading and the unloading phase at 1cm^{-1} (2HB+) for the first direction and at -1cm^{-1} (2HB-) for the second direction. The mean of the bending rigidities and the mean of the bending hysteresis are used for the Grosberg model.

4. Results

4.1. Yarn and fabric comparison

The curves presented are the mean between weft and warp oriented samples. Both directions showed similar curve progression whether it be for the fabric or the yarn, the 2-2 twill or the plain fabric.

The figure 6 shows that the yarns extracted from both fabrics have similar behaviors. It illustrates that the chosen tension successfully eliminated the crimp coming from the different weaving patterns and that any difference in the fabrics bending rigidity is coming from the weaving pattern.

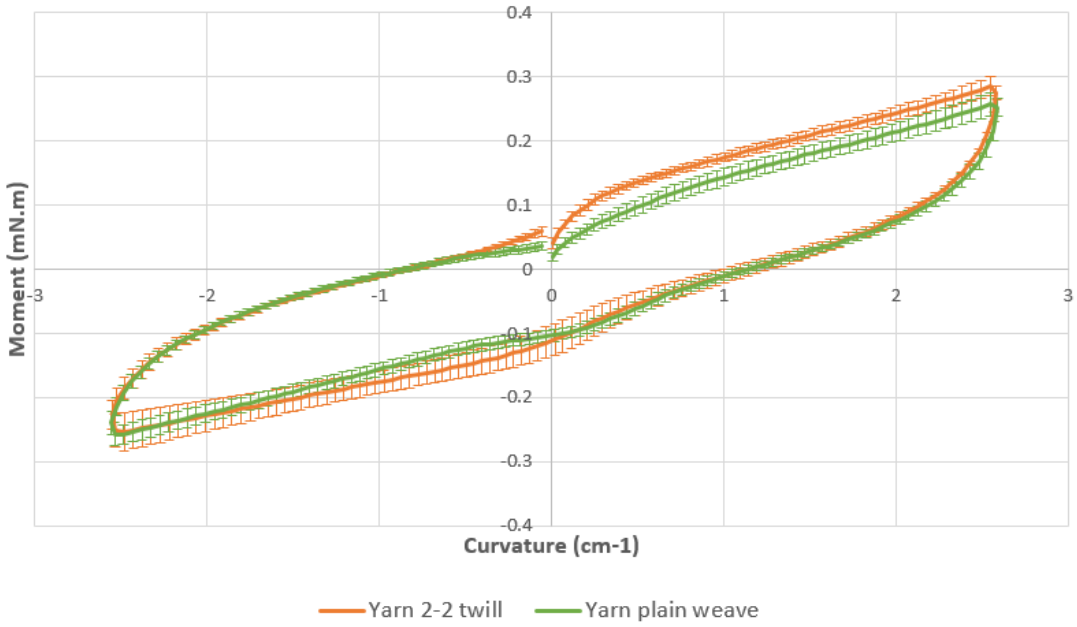

Figure 6: Comparison of the yarns bending behavior

The bending curves of the plain weave fabric and of the yarn extracted from it are shown in Figure 7. The fabric is more rigid than the yarn alone. It can be explained by the presence of yarns in the orthogonal direction. These yarns induce more friction and constrain the deformation of the yarns placed in the direction of the load.

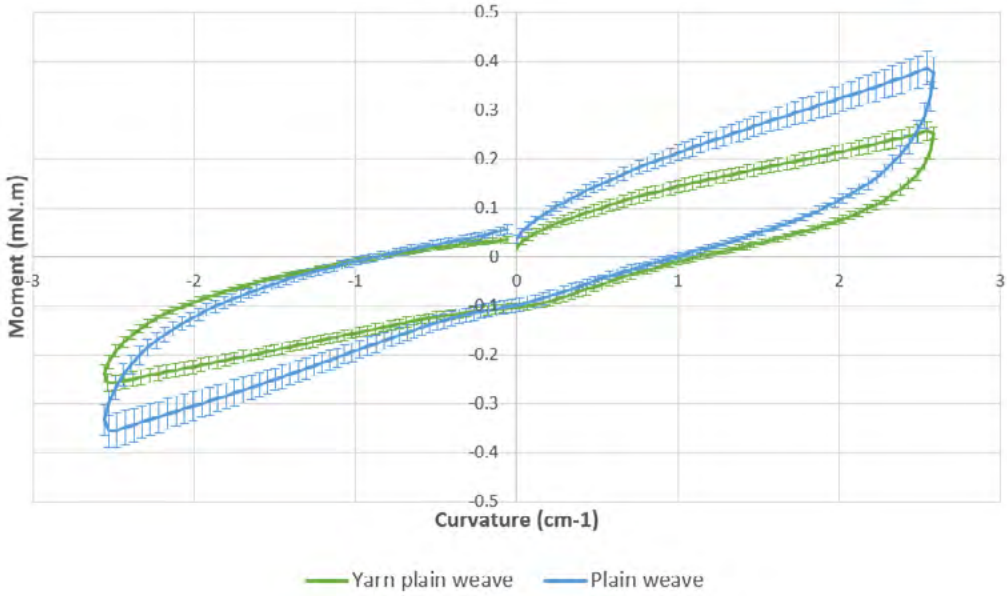

Figure 7. Bending curve of the plain weave and the yarn extracted from the same fabric

The difference in bending behavior between the fabric and the yarn for the 2-2 twill is not as clear. As the length of floated yarns is longer (Figure 1), the behavior of the fabric is closer to the behavior of the yarn alone. The fact that the 2-2 twill bending behavior is so close to the bending behavior of the yarn is surprising (Figure 8). It may be explained by the relatively short distance between the chucks. The

small yarn density of the fabric implies that the yarn in the direction of the bending load has only one or two interlacement, diminishing the structure influence contrary to the plain weave.

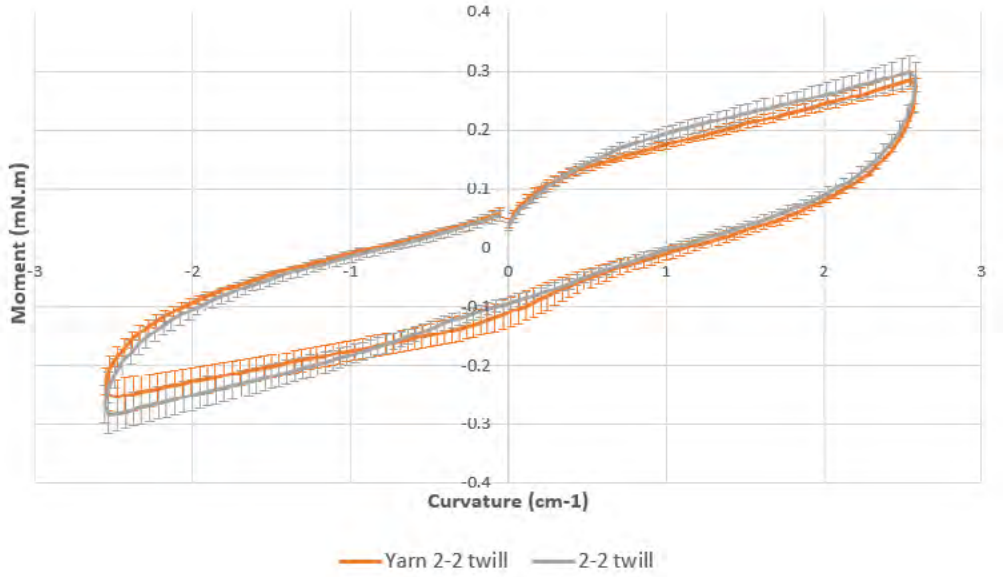

Figure 8. Bending curve of the 2-2 twill and the yarn extracted from the same fabric

Grosberg's bending rigidity is described in the figure 9. It confirms the conclusions drawn from the bending curves.

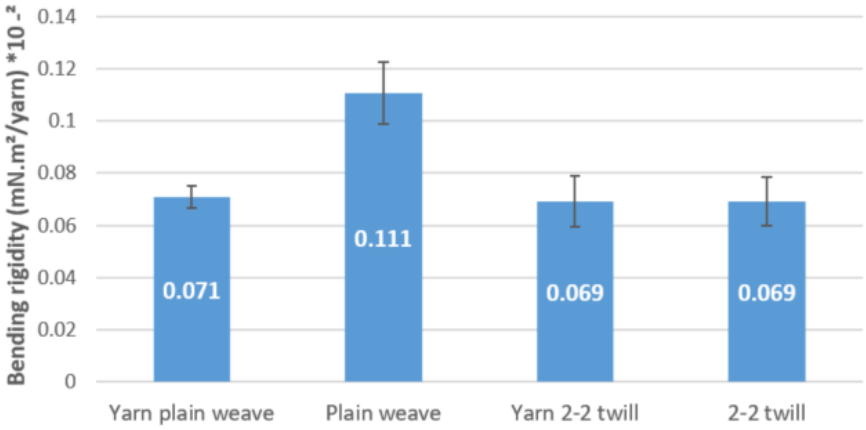

Figure 9. Bending rigidity parameter from the Grosberg model

4.2. Influence of the shear on the bending behavior

The bending curves for the 2-2 twill sheared at different angles are presented in the figure 10. The bending rigidity increases with the increase of the shearing angle. The increase seems to settle at 30°, close to the locking angle. The increase is explained by the orientation of the yarns and the increase of the contact surface between yarns that increases the friction[9].

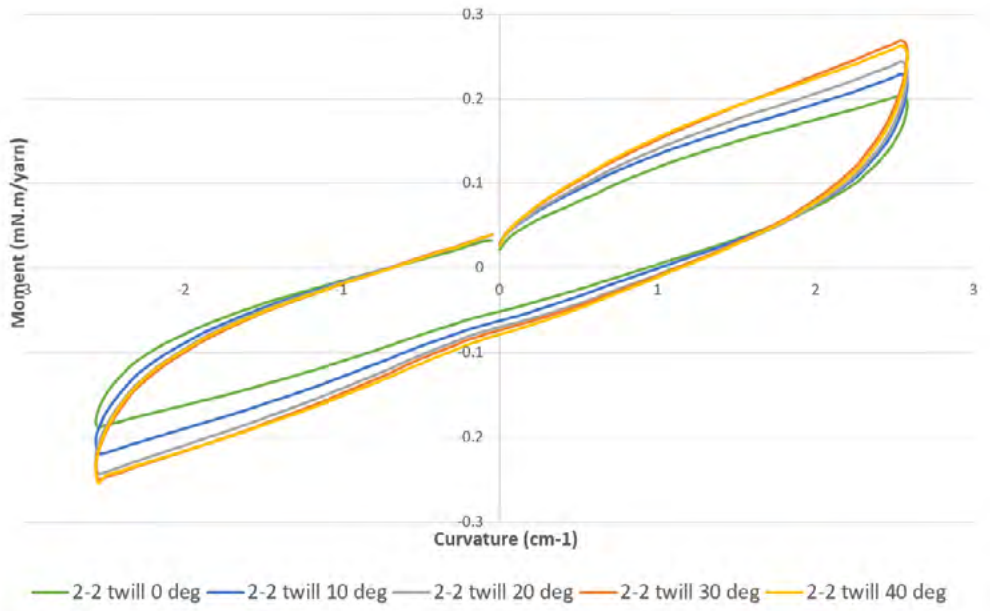

Figure 10. Bending curve of the 2-2 twill at different shearing angles

This trend can be observed with the bending rigidities. A similar behavior can be observed for the plain fabric (Figure 11). The two fabrics seem to reach a standstill at the same bending rigidity (derived from the Grosberg model). The fabrics may reach a critical packing density at which the bending behavior changes as the yarn are locked in the structure and can't slide. The plain fabric reaches the maximum bending rigidity faster than the 2-2 twill which weighs in the favor of this hypothesis.

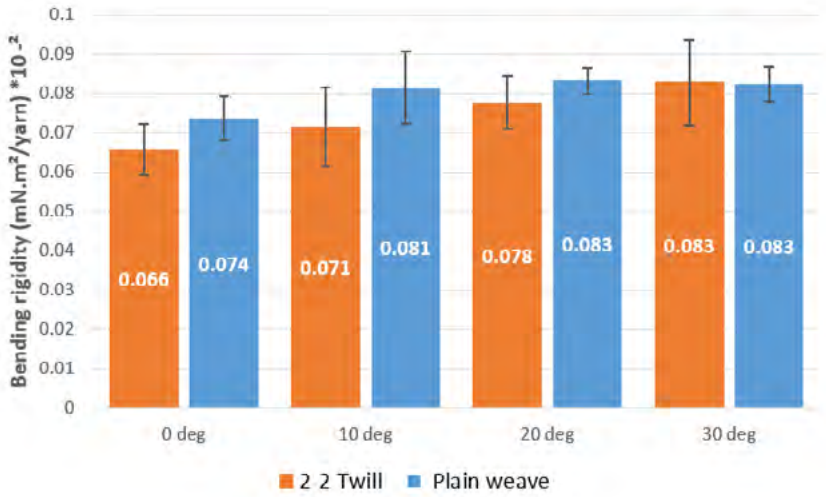

Figure 11. Bending rigidity parameter for the 2-2 twill and the plain fabric sheared at different angles

But the different sample configurations must be taken into account when measuring the bending moment. A first approach using the length of the yarns and the number of interlacement was tested but wasn't successful describing the sample's geometry and the loading of the yarns. A different model is being studied to better describe the bending rigidity at small curvatures. At small curvatures, the bending rigidity is mostly due to the friction between yarns and between fibers[8]. The Dahl model is a good candidate[10].

5. Conclusion

In this paper, the bending behavior of a single flax/PA12 yarn and two fabrics woven with this yarn were studied. This study showed that the woven structure has an impact on the bending behavior. The

more distance between the interlacement, the closer the bending behavior of the fabric is to the bending behavior of the yarn.
A preliminary investigation on the influence of the shear on the bending behavior has been conducted. The bending rigidity seems to increase with the shear up to a certain angle. The maximum value is the same for the plain fabric and the 2-2 twill. The sample disposition and loading characteristics should be further investigated.

Acknowledgments
This study is conducted within the framework of the CoqFib project, financed by the French National Research Agency.

References
[1] E. Capelle *et al.*, « Analysis of the tow buckling defect during the complex shape forming of a flax woven fabric », *ECCM 2012 - Compos. Venice Proc. 15th Eur. Conf. Compos. Mater.*, p. 11, 2012.
[2] P. Boisse, J. Huang, et E. Guzman-Maldonado, « Analysis and Modeling of Wrinkling in Composite Forming », *J. Compos. Sci.*, vol. 5, nº 3, p. 81, 2021.
[3] F. T. Peirce, « THE “HANDLE” OF CLOTH AS A MEASURABLE QUANTITY », *J. Text. Inst. Trans.*, vol. 21, nº 9, p. T377-T416, 1930.
[4] ASTM International, "ASTM D1388-96(2002): Standard test method for stiffness of fabrics," 2002. [Online].
[5] S. Kawabata, *The Standardization and Analysis of Hand Evaluation*. Textile Machinery Society of Japan, 1980.
[6] S. Pansart, « Prepreg processing of advanced fibre-reinforced polymer (FRP) composites », in *Advanced Fibre-Reinforced Polymer (FRP) Composites for Structural Applications*, Elsevier, p. 125-154, 2013.
[7] International Organization for Standardization, « Atmosphères normales de conditionnement et d’essai - (NF EN ISO 139:2005(F)) ». 2005.
[8] P. Grosberg, « The Mechanical Properties of Woven Fabrics Part II: The Bending of Woven Fabrics », *Text. Res. J.*, vol. 36, nº 3, p. 205-211, 1966.
[9] M. Tourlonias, M.-A. Bueno, G. Fassi, I. Aktas, et Y. Wielhorski, « Influence of friction angle between carbon single fibres and tows: Experimental analysis and analytical model », *Compos. Part Appl. Sci. Manuf.*, vol. 124, p. 105478, 2019.
[10] C. N. Ngoc, P. Bruniaux, et J. M. Castelain, « Modeling friction for yarn/fabric simulation Application to bending hysteresis ». 14TH EUROPEAN SIMULATION SYMPOSIUM AND EXHIBITION, Dresden, Volume: Simulation in Industry Modeling, Simulation and Optimization, 2002

©2024 | 2_PERRIN_Théo_996OZ.pdf:8

Enhancing the mechanical performance of locally sourced wood-based plywood through hybridization with natural fibre composites

C. Prunier[1,2], T. Jeannin[2], J. Rousseau[1], P. Butaud[2] and V. Placet[2]

[1] Laboratoire DRIVE Université de Bourgogne, Nevers, France
Email: clement.prunier@u-bourgogne.fr, jerome.rousseau@u-bourgogne.fr
[2] Université de Franche-Comté SUPMICROTECH-ENSMM, CNRS, Institut FEMTO-ST, F-25000 Besançon, France
Email: thomas.jeannin@univ-fcomte.fr, pauline.butaud@univ-fcomte.fr, vincent.placet@univ-fcomte.fr

Keywords: Plywood, hybrid materials, fatigue, natural fibres, bending

Abstract
This study investigates the fatigue behaviour of Douglas-fir plywood bonded with recycled polypropylene adhesive and reinforced with unidirectional flax fibres. Fatigue tests are realised under load-controlled repeated three-point bending at various stress levels. The results are compared to a benchmark plywood glued with a common polyvinyl-based adhesive. The results show that the recycled polypropylene-glued samples without reinforcement exhibit fatigue strength comparable to that of polyvinyl-glued plywood. Additionally, the inclusion of flax fibres significantly increases the fatigue strength and lifespan of the plywood. Specifically, the fatigue strength at 1 million cycles is approximately 60% of the quasi-static strength, compared to 40% for the reference polyvinyl-glued plywood.

1 Introduction

While wood continues to be extensively utilized in industries such as construction and furniture manufacturing, its significant variability in mechanical and physical properties necessitates the application of high safety factors. To mitigate this variability, manufacturers have turned to reconstituted wood like plywood. The layered structure of plywood, comprising multiple veneers, helps to reduce defects and minimize the impact of variability in each individual veneer. However, this reduction remains insufficient for industries such as the transport industry, where the drive to minimize mass has led to the adoption of synthetic materials that generally offer lower variability.

As a result, the literature on typical tests conducted in the transport industry, such as fatigue studies, is found to be lacking [1]. Most of the studies were performed before the advent of synthetic materials, as detailed by Tsai [2], and at the end of the last century for blades in wind energy applications. Ansell and Tsai [3] reported that the fatigue life of wood and wood products tested under bending ranges from 15% to 35% of the quasi-static strength, for a number of cycles ranging from 1 million to 50 million. They emphasized the diversity of the methods used and the high variability of the results obtained. Kommers et al. [4] realised fatigue tests on different wood species and plywoods and obtained a fatigue strength for Douglas fir samples of 35-40% of the quasi-static strength for 50 million cycles in repeated bending, and of 25-30% for the same amount of cycles in reversed bending. The tests revealed that there was no difference in behaviour between the solid planks and the plywood. The tests were pursued at a relatively high loading frequency (30 Hz) possibly causing heating in the samples. Also, they used a loading at a constant deflection, causing a possible variation of the peak stress in case of damages occurring in the sample.

©2024 | 2_PRUNIER_Clément_YBROG.pdf

One possible way to enhance the fatigue performance of plywood would be by combining it with composite materials in a hybrid structure. Wood hybridization with long fibre composite materials has been studied as a way to reduce wood variability and improve their mechanical properties, as presented in the review by Castanié et al.[1]. Synthetic fibre reinforcement was first studied, but natural fibres have shown promising results in more recent studies, permitting to reach a higher modulus of elasticity and strength of reinforced plywoods [5, 6]. The contribution of such reinforcement on the fatigue performance of plywood have never been studied to the author's knowledge. This is the main objective of the present study.
It focuses on the fatigue behaviour of plywood made with local low-quality Douglas fir veneers, glued with a recycled polypropylene thermoplastic grafted with maleic anhydride (rMAPP) chosen for its lower environmental impact and lower toxicity than the glues traditionally used in the wood panel industry. The main goal is to assess the effect of flax-rMAPP composites hybridization on the fatigue properties of the plywood.

2 Materials and methods

2.1 Materials

For this study, the plywoods are made with Douglas-fir sourced from the Centre-Val de Loire and Bourgogne-Franche-Comté regions of France. These veneers are qualified as low-quality as they contain cracks and knots. The veneers have a thickness of 3 mm, and a density of 500 kg/m^3. Veneers are dried after cutting and stored under non-controlled relative humidity and temperature.
The adhesive used to bond the veneers is a recycled polypropylene (rPP) obtained from agricultural wastes. It is mixed with a maleic anhydride grafted polypropylene (MAPP) Polybonds ® 3200, which contains 1% of pure maleic anhydride (MA). Maleic anhydride is a compatibilizer that enhances the adhesion with plant fibres at is allows for the creation of ester bonds between the PP molecules and the free OH groups of the wood and plant fibre surfaces. The melting flow index (MFI) of the rMAPP is of 6g/10 min (230 °C, 2.16 kg), and its ultimate tensile strain is 918% ± 45%. It is extruded in 70 µm films using a extruder calender.
Long flax fibres, in the shape of unidirectional tapes (FlaxTape ®), are used as reinforcements. They are supplied by Ecotechnilin, France. The tapes have an areal weight of 110 g/m². They are stored at 50% RH and 23 °C for a minimum of 48 h before the manufacturing.
Reference samples are produced with a common polyvinyl based glue (VG) called Paracol Wood D3 ®, serving as a benchmark for comparison.

2.2 Plywood stacking sequence

Plywoods are manufactured under thermocompression, with a temperature of 180 °C. A pressure of 1 MPa is applied during 53 minutes for non-reinforced plywoods, and 57 minutes for the reinforced ones. The applied pressure and pressure time were determined in the frame of a previous study [7]. Two stacking sequences are studied here, as presented on **Figure 1**. The first one, S1, is composed of 5 wood veneers, following a $[0_w/90_w/\overline{0_w}]$s stacking sequence, where "w" represents wood veneers. Two films of adhesive are placed between each veneer. The second lay-up, RS1, follows the same veneer stacking sequence but includes varying numbers of fibre flax fibre tapes between each layer, each separated by two films of adhesive. Its stacking sequence is $[0_w/0_{5F}/90_w/0_F/\overline{0_w}]$s, with "F" representing the flax fibre tape.

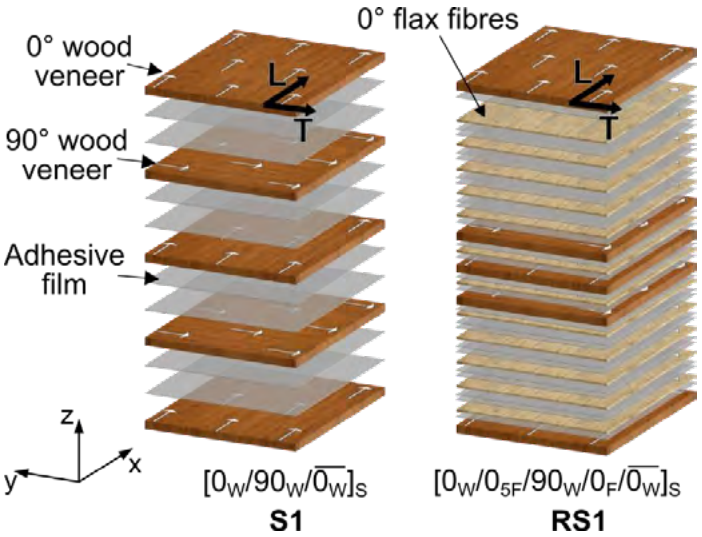

Figure 1. Schematic representation of the different stacking sequences studied: Without fibre reinforcement (S1) and with fibre reinforcement (RS1). "W" stands for wood and "F" for flax fibres.

2.3 Testing method

In the absence of a standard for fatigue testing on wood, a configuration similar to that recommended for quasi-static three-point bending tests (EN 310) was used. The sample shape and testing setup is presented in **Figure 2 (a)**. The sample width, b, is fixed at 50 mm. The supports span "l" must be equal to 20 times the thickness "e", as it limits the impact of shear plane stress. The tested samples had a thickness of 14.5 mm for the reference and S1 samples and 16 mm for the RS1 samples, resulting in a support span of 290 mm and 320 mm, respectively. The length of the sample is equal to l + 50 mm.
The fatigue testing is realised under repeated bending conditions, with a load ratio (R) of 0.1, as illustrated in **Figure 2 (b).** The loading signal has a sinusoidal shape, and its frequency is fixed at 5 Hz. The deflection is acquired with a laser sensor (10 mm range and 5 µm sensibility), and the load with a force cell of 10 kN full range. If the sample is not broken after 1 million cycles, the test is stopped automatically.

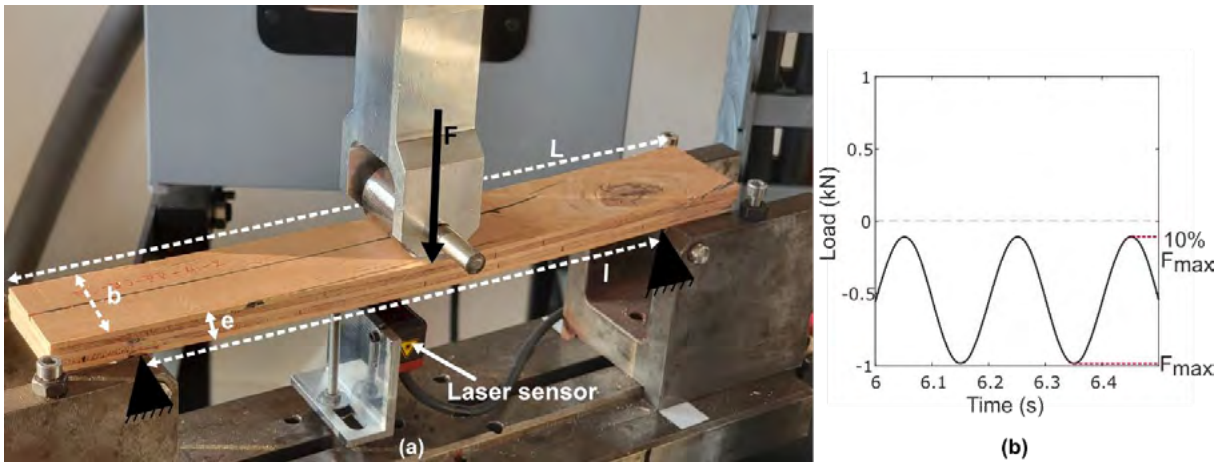

Figure 2. Illustration of fatigue testing parameters. (a) shows the testing setup for fatigue testing. b = width; e = thickness; L = length, l = supports span, F = load application point. (b) Illustrates the loading cycles for the repeated bending (R=0.1).

16 samples are tested for each stacking sequence (S1, RS1 and reference plywood glued with polyvinyl-based adhesive), divided into 4 different loading levels. These levels are defined as a percentage, ranging from 45% to 85% of the quasi-static (QS) strength measured in three point-point bending following the EN310 standard, with a deflection speed of 6 mm/min. Each sample comes from a different plate as a way to account for the variability among plates. The quasi-static strength (σ_{QS}) and load levels for each configuration are presented in **Table 1**.The load levels have been incrementally adjusted throughout the testing process based on the results obtained.

Table 1. Maximum stress and load levels for the different tested configurations

	σ_{QS} (MPa)	Load levels (%)
Reference (VG)	54.3	70;60;50;45
S1	63.3	70;65;60;50
RS1	79.4	70;75;80;85

3 RESULTS

The **Figure 3** displays the number of cycles reached by each tested sample, relatively to the percentage of their quasi-static strength (a) and to the maximum applied stress (b). Samples that did not break before 1 million cycles are marked by an arrow. The multiplicator next to the arrows indicate the number of samples that did not break before 1 million cycles for that stress level. The results of the preliminary quasi-statics test used to obtain the maximum stress value are marked by cross on the ordinate axis. The results of the reference samples are fitted with a power-law model, represented in red on the graphs.

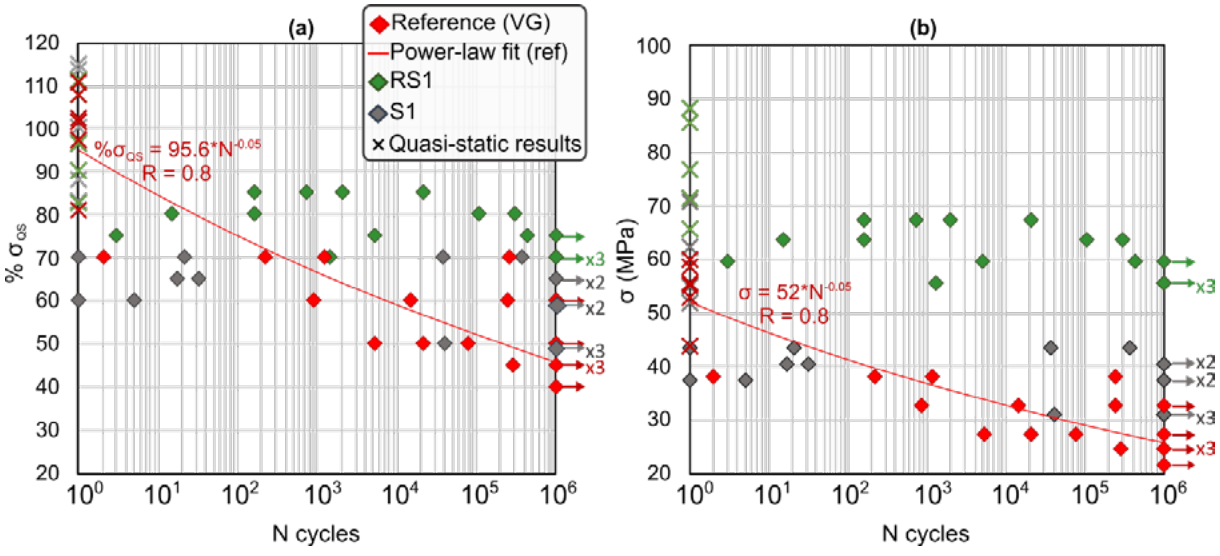

Figure 3. Fatigue curves showing the number of cycles at which rupture occurred, relatively to the percentage of the quasi-static strength (a) and to the applied stress (b). Dots marked by arrows indicate samples which did not break.

The fatigue results illustrate the significant variability among samples of the same material, which is also evident in the quasi-static tests.

The curve shows a fatigue strength around 45% for 1 million cycles. This results is in the range reported by Kommers et al. [4] on timber Douglas fir samples. The results for the S1 and RS1 stacking sequence display a significant variability that makes it difficult to represent them with a simple analytical model. The S1 stacking sequence, without reinforcements, show that samples breaking before 1 million cycles are all for stress levels above or equal to 50% σ_{QS}, with three samples out of four at this level reaching 1 million cycles. The results for the RS1 samples indicate a fatigue strength above 60%, as 3 samples out of 4 reached a million cycles for a load of 70% σ_{QS}. The superiority in fatigue strength of the RS1 samples is even more distinctive on the **Figure 3** (b), as the presence of fibre reinforcement already increased the average strength for the quasi-static samples. This improvement shows that the reinforcement of plywoods by unidirectional flax fibres does not only increase the quasi-static strength, but also enhances fatigue strength and lifespan. The results variability for sample reinforced with flax fibres composites might be influenced by the known rigidification of flax fibres occurring during fatigue solicitation [8].

4 Conclusion

The objective of this study was to evaluate to effect of unidirectional flax fibres hybridization of plywood made with low-quality Douglas fir veneers glued with a thermoplastic recycled polypropylene. Despite the significant scatter in the results, this study demonstrates that the plywood bonded with recycled polypropylene adhesive exhibited a fatigue strength comparable to that of plywood bonded with polyvinyl-based adhesive, thus validating recycled polypropylene as a viable alternative to traditional adhesives. Additionally, the incorporation of flax-rMAPP composite plies increases not only the bending quasi-static strength but also the fatigue strength.
The study demonstrates that incorporating flax-thermoplastic composites reinforcements in plywoods is a valid strategy for enhancing their performance in fatigue applications, potentially expanding their range of uses.

Acknowledgments

This work was supported by the "Investissements d'Avenir" program, ISITE-BFC project (ANR-15-IDEX-0003 contract) as part of the WooFHi project and by EIPHI Graduate School under (“ANR-17-EURE-0002”). We also sincerely wish to thank Louis Denaud, Guillaume Pot, Jean-Claude Butaud, Stéphane Girardon and Leyne Demoulin from the WMM (Wood Material and Machining) team at LaBoMaP research lab (Cluny, France) for providing the veneers and for the insightful discussions conducted within the framework of the WooFHi project on veneer peeling and the properties of wood veneers.

References

[1] Castanié, B.; Peignon, A.; Marc, C.; Eyma, F.; Cantarel, A.; Serra, J.; Curti, R.; Hadiji, H.; Denaud, L.; Girardon, S.; Marcon, B. (2024). Wood and plywood as eco-materials for sustainable mobility: A review, *Composite Structures*, Vol. 329, 117790. doi:10.1016/j.compstruct.2023.117790

[2] Tsai, K. T. (1987). *An Investigation into the Fatigue Behaviour of Wood Laminates for Wind Energy Converter Blade Design.*University of Bath

[3] Tsai, K. T.; Ansell, M. P. (1990). The fatigue properties of wood in flexure, *Journal of Materials Science*, Vol. 25, No. 2, 865–878. doi:10.1007/BF03372174

[4] Kommers, W. J. (1960). The fatigue behavior of wood and plywood subjected to repeated and reversed bending stresses

[5] Moezzipour, B.; Ahmadi, M.; Moezzipour, A. (2017). Physical and mechanical properties of reinforced ply wood with natural fibers, *Journal of the Indian Academy of Wood Science*, Vol. 14, No. 1, 70–73. doi:10.1007/s13196-017-0189-7

[6] Arya, S.; Kumar, R.; Chauhan, S.; Kelkar, B. U. (2023). Development of natural fiber reinforced thermoplastic bonded hybrid wood veneer composite, *Construction and Building Materials*, Vol. 368, No. 130459. doi:10.1016/j.conbuildmat.2023.130459

[7] Prunier, C.; Rousseau, J.; Butaud, P.; Jeannin, T.; Gabrion, X.; Placet, V. (2024). Investigating the influence of fabrication parameters, flax-fibre reinforcement and ageing on interlaminar shear strength in thermoplastic-bonded wood veneers, *Journal of Materials Science*, No. In press. doi:10.1007/s10853-024-09767-2

[8] Jeannin, T.; Gabrion, X.; Ramasso, E.; Placet, V. (2019). About the fatigue endurance of unidirectional flax-epoxy composite laminates, *Composites Part B: Engineering*, Vol. 165, 690–701. doi:10.1016/j.compositesb.2019.02.009

©2024 | 2_PRUNIER_Clément_YBROG.pdf:6

From the PEEK microstructure at welded interfaces to the mechanical properties of thermoplastic composites manufactured by a Laser-Assisted Tape Placement process

Noé Restif[1,2][a], Suzanne Laik[(1)b], Mael Péron[(2)c], Federica Daghia[(3)], Frédéric Jacquemin[(2)]

[(1)] CETIM, Technocampus Composites, Chemin du Chaffault, 44340 Bouguenais, France.
[(2)] Nantes Université, Ecole Centrale de Nantes, CNRS, GeM, UMR CNRS 6183, F-44600 Saint-Nazaire, France.
[(3)]Université Paris-Saclay, CentraleSupélec, ENS Paris-Saclay, CNRS, LMPS - Laboratoire de Mécanique Paris-Saclay, 91190, Gif-sur-Yvette, France.

[a]noe.restif@cetim.fr, [b]suzanne.laik@cetim.fr, [c]mael.peron@univ-nantes.fr (corresponding authors)

Keywords: Polymer-matrix composites (PMCs), PEEK, Carbon fibre, Laser Assisted Tape Placement, experimental characterization, interfaces, microstructure

Abstract
The Laser-Assisted Tape Placement (LATP) process of thermoplastic composites enables the rapid production of laminates. However, it generates cooling rates gradients between the surface and the bulk of the plies, probably causing a crystallinity gradient through the thickness of the laminates, although this has not been demonstrated. In this study, different characterizations techniques have been used to highlight this gradient in a carbon-black filled PEEK (CB/PEEK). It was shown that for a 600 µm-thickness ply, only a depth of 100 µm is affected by the laser, resulting in a microstructure less resistant to chemical etching, and low hardness and reduced Young's modulus related to low crack propagation speed. In the carbon-fibre reinforced PEEK (CF/PEEK) composite, the use of certain characterization techniques requires tough post-processing of the data because of the presence of carbon fibre. As this work is ongoing, this paper focuses on the link between the crystalline and G_{IC} mechanical properties related to the processing parameters. It has been shown that the crystallinity evolves inversely to G_{IC} and layup speed (LS) and in the same way to the tool temperature (TT). Also, for most of the manufacturing conditions studied, laminates have an intralaminar crack propagation.

1. Introduction

Thermoplastic matrix composites (TPC) are increasingly used in the aeronautic and automotive industries due to their many advantages over thermoset matrix composites (TSC). These advantages include their better impact resistance and toughness and their potential for being repaired or even recycled. Also, they offer the ability to produce laminates by « out of autoclave » (OOA) welding processes which are much less energy consuming and cost effective.
Among the OOA processes, the in-situ consolidation process by LATP was identified as being efficient and versatile to manufacture high performance and complex-shaped parts. This process involves several complex and interdependent phenomena within very short times: the consolidation phenomena (development of intimate contact, healing and crystallization for semi-crystalline TPC) that occurs at the interphase between the incoming tape and the previously consolidated laminate (substrate) and which is responsible of their bonding [1]; the deconsolidation mechanisms that occurs inside the tape and the substrate (into the bulk material), as for example the void growth which takes place during the heating phase by the laser [1], [2], [3].
As the mechanical properties of the manufactured laminates are impacted by the occurrence of all these phenomena, it is important to measure this impact. Until now, all the investigations in LATP process have just shown a correlation between the processing parameters and the overall laminates properties [4], without investigating the properties related to the consolidation and deconsolidation phenomena. In this study, the correlation between the phenomena occurring during the process and the final mechanical properties of the laminates is studied. Because these works are performed on a semi-crystalline PEEK matrix, a focus is made on the investigation of the properties related to the crystallization phenomena.

Several studies have suggested that laminates manufactured by LATP are subjected to a crystallinity gradient through their thickness due to a cooling-rate gradient, and particularly a variation between the welded interphases, more amorphous, and the bulk of the plies, more crystalline [5], [6].
In this paper, this crystallinity gradient and its effect on the micromechanical properties are demonstrated on a carbon-black filled (CB/PEEK) by using several characterization techniques as DSC (Differential Scanning Calorimetry), observations of cryofractured and chemically etched surfaces, and nanoindentation. On the carbon-fibre reinforced PEEK matrix composite (CF/PEEK), due to the presence of carbon fibre the use of these techniques in a conventional way is limited and, therefore requires the development of methods and tough post-processing of the data to properly interpret them. Hence, the results of the local characterization of CF/PEEK laminates are not presented in this paper. However, a correlation between the G_{IC} and the local and overall crystallinity of the laminates is established by a measurement of the degree of crystallinity on the failure surfaces of DCB (Double Cantilever Beam) specimens by X-Ray diffraction and on the entire laminate's thickness by DSC. Also, the observation of the fracture cross-sections allows to know the failure mode and therefore the local area assessed by XRD (intra-ply or inter-ply). Finally, the effect of the processing parameters on these mechanical and physical properties is analyzed, thanks to the investigation of eight different manufacturing conditions of the laminates.

2. Materials and methods

2.1. Materials

Two materials were used for this study: a carbon-black filled PEEK (with a content of CB < 1%), referred as CB/PEEK, and a unidirectional carbon-fibre reinforced PEEK, referred as CF/PEEK.
Both are in the shape of a tape coiled around a spool. The as-received tapes properties are mentioned in the following Table 1:

Table 1. As-received tapes properties of CB-PEEK and CF/PEEK

	Tg (°C)	Tm (°C)	Degree of crystallinity X (%) *	Void content (%) **
CB-PEEK	150	336	24.7	0
CF/PEEK	143	345	25.2	0.5 ± 0.4

*Measured by Differential Scanning Calorimetry (DSC)
**Measured on micrographs of embedded and micron-polished tape section

Due to confidentiality matters, further details about the materials cannot be disclosed.

2.2. Process

The production of laminates was performed at CETIM using SPIDE TP® process [7]. It consists in a LATP and filament winding process allowing for continuous deposition of the layers. The CB/PEEK was used to produce one cylindrical structure with a $[0]_{25}$ stack and the CF/PEEK was wounded around an oblong tool with two flat sides in order to manufacture eight laminates of $[0]_{30}$ stack. The processing parameters used for manufacturing the parts are presented in Table 2**.** Concerning the CF/PEEK laminates, the three processing parameters that were varied in this study were the Laser Setpoint Temperature (LST, fixed at 350, 450 and 500 °C) allowing for an automatic in-live control of the laser power and tilt angle, the Tool Temperature (TT, fixed at 25 and 250 °C) and the Layup Speed (LS, fixed at 5 and 10 m/min). Those laminates are identified through these parameters with the following reference code type "TT/LST/LS", as it is mentioned in Table 2. Also, the consolidation force was fixed at 250 N and was applied by a 60-shore silicon compaction roller.

Table 2. Manufacturing conditions of CB/PEEK and CF/PEEK laminates

	Reference	Tool Temperature (TT) [°C]	Laser Setpoint Temperature (LST) [°C]	Laser average power [W]*	Layup speed (LS) [m/min]
CB/PEEK		25	450	1373 ± 22	7
CF/PEEK	25/350/5	25	350	924 ± 32	5
	250/350/5	250	350	653 ± 53	5
	25/450/5	25	450	1271 ± 65	5
	250/450/5	250	450	1012 ± 43	5
	25/500/5	25	500	1376 ± 90	5
	250/500/5	250	500	1212 ± 21	5
	25/350/10	25	350	1341 ± 44	10
	25/450/10	25	450	1792 ± 97	10

*The laser power and tilt were continuously regulated through a feedback temperature loop set on the LST and based on the measurement of the illuminated area by an embedded infrared camera.

2.3. Characterization methods

2.3.1. Optical microscopy (OM)

All images of laminate cross-sections were produced with an optical microscope Keyence VH-Z100R. The polished samples were prepared by being embedded in a resin and polished using SiC sandpapers from P800 down to P2500 and a with diamond suspension from 3 to 1 µm grit size.

2.3.2 Scanning Electron Microscopy (SEM)

A ZEISS SUPRA 25 scanning Electron Microscope was used at an acceleration voltage of 15 kV to analyse the cryofractured and etched surfaces of the CB/PEEK. Specimens were metallized with Platinum prior to observation.

2.3.3 Differential Scanning Calorimetry (DSC)

DSC analyses were performed using a Mettler TOLEDO DSC 3. To obtain results over the entire thickness of the laminates, sampling consisted of cutting a thin cross-section using a microtome. Samples of approximately 10 mg were placed in 40 µl aluminum pans, with non-hermetically sealed lids. Two temperature ramp-ups and -downs were performed at heating rates of 10 °C/min between room temperature and 380 °C. Three samples were analyzed for each laminate in a nitrogen environment (to avoid any sample oxidation) at a flow rate of 50 ml/min. The degree of crystallinity of a sample was estimated by using Eq.1:

$$X = \frac{\Delta H_m - \Delta H_{cc}}{(1-\omega)\times\Delta H_{m\infty}} \quad (1)$$

where ΔH_m is the melting enthalpy, ΔH_{cc} is the cold crystallization enthalpy, ω is the weight fraction of matrix content, and $\Delta H_{m\infty}$ is the theoretical melting enthalpy of 100% crystalline PEEK which has been calculated to be 130 J/g by Blundell et al. [8].

2.3.4. Chemical etching

To further reveal the morphology of the crystalline phase, a chemical etching was performed on a polished cross-sectional surface of the CB/PEEK sample. It consisted in submerging the sample during 20 minutes in a permanganic and sulfuric acid solution allowing to preferentially dissolve the amorphous areas, therefore revealing the topography of the microstructure. This method is inspired by the works of Blundell et al. [9].

2.3.5. Cryofracture

Specimens of CB/PEEK laminates were sampled into the part and submitted to cryofracture. The samples were immerged in liquid nitrogen for 5 minutes and fractured using a hammer. A saw kerf was performed on the samples prior to LN_2 immersion to guide the fracture surface (see Figure 2). Such cryofracture treatment can reveal ductile and fragile zones linked to crystalline gradients within the specimens, which can be derived from the SEM observation of the cryofractured surfaces.

2.3.6 Nanoindentation

Nanoindentation tests were conducted on a polished cross-section of a CB/PEEK sample, using a Bruker TS77 with a diamond Berkovich tip. The analysis of approximately the third of the laminate thickness was done by performing 2 lines of 150 indents – one indent every 20 µm – starting from the last deposited ply. For each indent, the following parameters were applied : i) a ramp-up of 5 seconds to a maximum load of 2000 µN ii) a hold time of 2 seconds and iii) unloading during 5 sec (at 400 $\mu N.s^{-1}$) Through the load and penetration depth data recorded by the equipment, the hardness H (GPa) and reduced Young's modulus Er (GPa) were determined by the software according to the method of Oliver and Pharr [10].

2.3.7. Double cantilever Beam test (DCB)

In the CF/PEEK laminates, the Mode-I interlaminar fracture toughness G_{IC} was investigated by DCB tests, with a method inspired on ASTM D5528 and AITM 1-0053. The specimen dimensions are 250 mm x 25 mm x 6 mm and three DCB specimens for each manufacturing conditions were tested. The initial pre-crack on the edge of the specimens was generated by a metal foil covered with Kapton film of 50 mm-length placed at the middle of the laminate thickness during process. During testing, SCBF tools (refer to AITM 1-0053) were used to hold the specimens and apply the tensile load using an INSTRON 3369 universal testing machine. The specimens were mounted and subsequently loaded at a constant rate of 3 mm/min. A digital camera was used to record the crack propagation on a length of 50 mm and the pictures were then used to measure the evolution of the crack length during propagation. The G_{IC} propagation values were next calculated using the modified beam theory (cf. ASTM D5528).

2.3.8 X-ray diffraction (XRD)

XRD analyses were performed on a Bruker D8 Discover^{plus} to assess the crystallinity ratio close to the welded interphases. Measurements were carried out on 2 areas on the fracture surfaces of DCB specimens. One DCB specimen per condition has been analyzed. The X-ray wavelength is 1.5418 Å (Cu anode). Scans were performed with a 2Theta range between 5° and 100°. A peak deconvolution treatment of the XRD curve is necessary to obtain the degree of crystallinity of the PEEK matrix. Such post-treatment being complex due to the presence of the CF signal as well as the amorphous halo and crystalline peaks from the matrix, the intensity of the 110-peak of the PEEK, related to the degree of crystallinity [11], has been chosen as the crystallinity indicator and is presented in this paper.

3. Results

3.1. Investigation of the property gradients through the thickness of a CB/PEEK laminate

Firstly, the evolution of the degree of crystallinity through the thickness of the laminate was assessed by DSC, with a sampling method consisting of successively cutting thin longitudinal slices using a microtome. While different values were obtained according to the sampled slice (from 15 to 28 %), we were unfortunately faced with a low repeatability on the sampled slices thickness limiting the interpretation of the results. Hence, the results are not presented in this paper, but some key points have been identified to develop a new sampling method allowing to reduce the previously encountered issues and obtain reliable conclusions. Then, several chemical etching have been performed on the sample in order to reveal the crystalline microstructure. While the etching protocol is not enough mastered to clearly observe the spherulitic microstructures of the PEEK, the observation presented in Figure 1 (a and b) shows an alternation through the thickness of smooth areas and areas presenting three-pointed star microstructures. These areas have also been revealed by the observation with a binocular magnifier of the polished sample, as it is shown in Figure 1c.

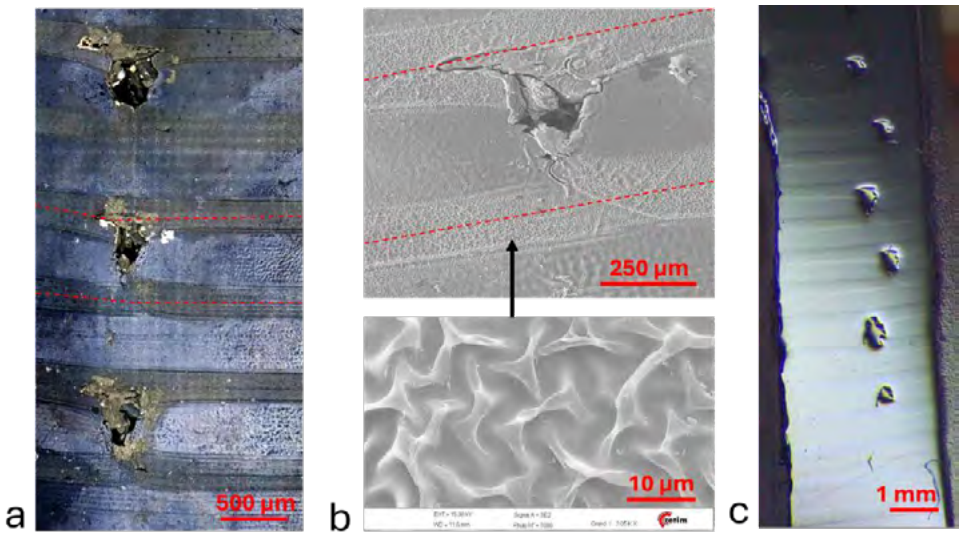

Figure 1. Images of cross-sectional surfaces of the CB/PEEK laminate: (a) etched surface observed by OM and (b) by SEM, with red dotted lines corresponding to the interfaces between two plies; (c) OM (binocular magnifier) images of the polished sample.

To assess the micro-mechanical performances gradients through the laminate's thickness, qualitative data have been obtained from the observation of cryofractured cross-sectional surfaces (Figure 2) and nanoindentation tests have allowed to determine quantitative results as the hardness and the reduced Young's modulus presented in Figure 3. Different behaviors through the thickness have been clearly visually and mechanically demonstrated.

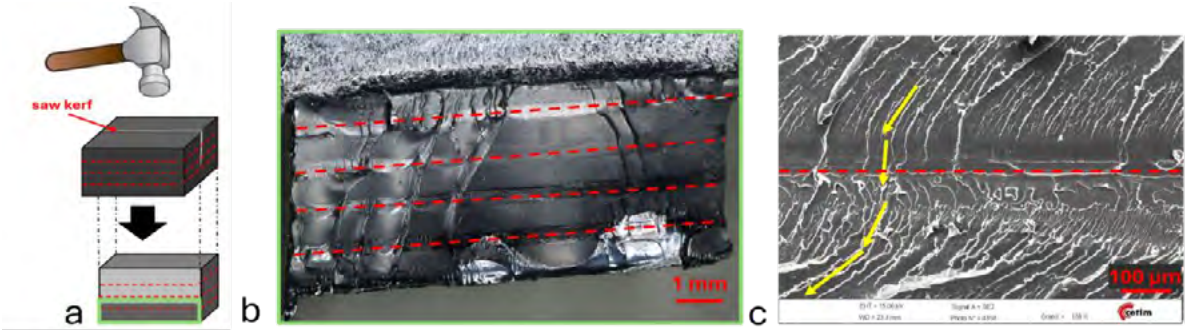

Figure 2. (a) Scheme of the cryofracture method; (b) Images of a cross-sectional cryofractured surface of the CB/PEEK laminate observed by OM and (c) by SEM; red dotted lines corresponding to the interface between two plies and yellow arrows indicating the crack propagation direction.

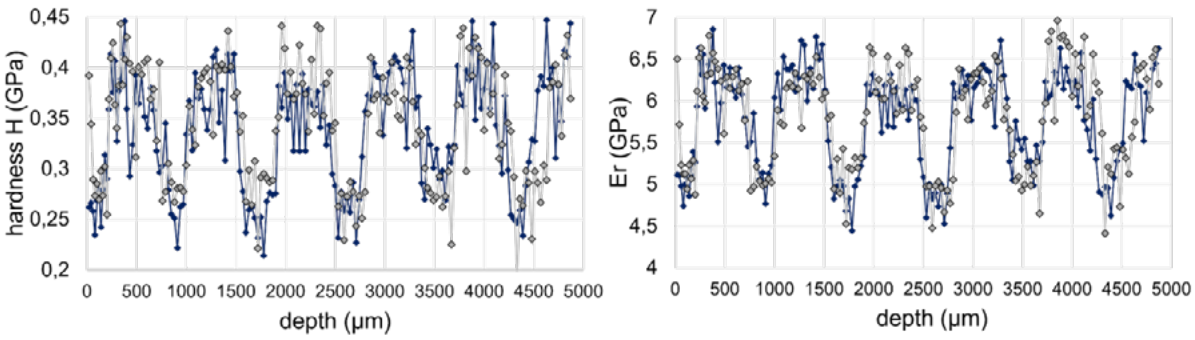

Figure 3. Graphs of hardness H and reduced Young's Modulus Er according to the thickness of the CB/PEEK laminate, with the zero-depth corresponding to the upper surface (last deposited ply).

3.2. Investigation of the physical and mechanical properties of CF/PEEK laminates

The correlation between G_{IC}, local and overall crystallinity, manufacturing conditions and failure mode are presented in Figure 4. Significant trends of the evolution of the G_{IC} against the crystallinity and the manufacturing conditions are observed in Figure 4a and Figure 4b. The failure modes must be taken into account when comparing mechanical test results, thus the cross-sections fractures of DCB specimens were observed and the ones corresponding to the 25/350/5 and 250/350/5 conditions are presented respectively in Figure 4c and Figure 4d.

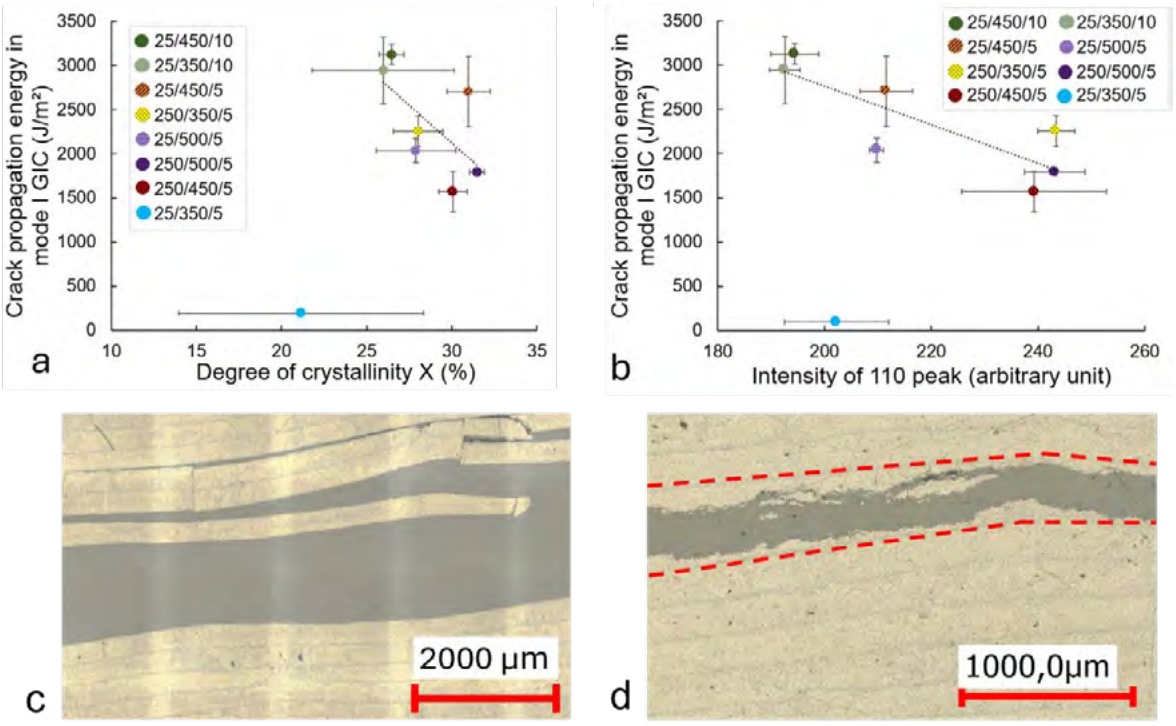

Figure 4. (a) GIC according to the degree of crystallinity of the entire thickness of the CF/PEEK laminates, measured by DSC; (b) G_{IC} according to the intensity of the 110-peak measured by XRD on the failures surfaces of DCB specimens. Error bars corresponding to the standard variation. (c) OM cross-section observations of the laminates referred as 25/350/5 and (d) 250/350/5.

4. Discussions

All the results of the investigations of the property gradients through the thickness of a CB/PEEK laminate are consistent and lead to the same conclusion: a 200 µm-thickness welded interphase between the plies (inter-plies) is generated by the process. This interphase is delimited by two edges located at 100 µm upper and lower to the initial surface of the tape or the substrate. It is differentiated by its more amorphous microstructure and its lower micro-mechanical stiffness and hardness properties compared to the bulk of the plies. Indeed, the observation of etched samples revealed weaker chemical resistance of the interphases, related to a lower crystallinity. Thanks to the presence of gaps between the edges of the tapes, the interfaces between two plies can be easily identified. These interfaces are marked by red dotted lines in Figure 1 (a and b) and correspond to the middle of the more-etched areas (presenting three-pointed star microstructures). Moreover, the welded interphases are revealed by the observation of polished sample with a binocular magnifier, which could be related to a difference of topology between the bulk of the plies and the interphases, due to a hardness difference. The realization of cryofracture tests and nanoindentation confirms this. As it is shown in Figure 2c, the orientation of the crack propagation lines (highlighted by yellow arrows) are different between the interphase and the rest of the ply. This reflects a locally slower crack propagation in the interphase, which emphasizes its more ductile behavior. The results of nanoindentation validate this observation by showing significantly lower hardness and reduced Young's modulus of the interphases (Figure 3).

Regarding the CF/PEEK, the studies of laminates manufactured under different manufacturing conditions allows to establish a correlation between the processing parameters, the degree of crystallinity, the G_{IC} and its corresponding failure mode. As we can see on Figure 4a and Figure 4b, the laminates can be easily classified into four categories.
The first category concerns the laminate manufactured with the condition 25/350/5, which does not follow the same trend than the other laminates, having the lowest G_{IC} despite a low crystallinity. This is explained by a different behavior of the corresponding DCB specimens presenting an interlaminar failure mode (Figure 4c), whereas all specimens from the other conditions demonstrate failure by an intralaminar failure mode (example of 250/350/5 presented in Figure 4d). The interlaminar failure mode is due to unfavorable processing parameters to the establishment of the intimate contact and healing phenomena, and indicates that the G_{IC} property of 25/350/5 laminate is influenced rather by the material health in the interlaminar regions than on the local crystallinity state through the laminate. A similar failure mode, indicating a lack of adhesion, was already observed on the ILSS specimens for the same manufacturing condition [2].
Then, the laminates manufactured under the other tested conditions can be divided into three other categories (Figure 4b): laminates having the lowest crystallinity were manufactured on an unheated tool and at the highest LS (10 m/min), while laminates having a medium crystallinity were manufactured on an unheated tool but with the lowest LS (5 m/min), and laminates manufactured on a tool heated at 250 °C present the highest crystallinity, whatever the layup speed or laser setpoint temperature.
To summarise, it was shown that the crystallinity evolves in the same way as the tool temperature and inversely to the layup speed. Moreover, the laminates manufactured under these conditions present the same trend: the G_{IC} seems inversely proportional to the degree of crystallinity, which confirms the observation of previous studies [12], [13]. Also, the deviation of the crack from the inter-ply areas (welded interphases) to intra-ply areas during propagation seems to confirm that the former consist in more ductile phases than the latter. This behavior could be due to a lower crystallinity of the welded interphases, as it was highlighted on CB/PEEK material, or it may reflect a preferential propagation into fibre-rich areas, because fibre-matrix interfaces are probably less tough than pure matrix. As the XRD measurements on the DCB failure surfaces do not provide the information of the crystallinity gradient through the specimen's thickness, further experimental investigations are in progress in order to confirm (or invalidate) the trend observed on the CB/PEEK.

5. Conclusion

During this study, experimental characterizations were performed to assess a crystallinity gradient through the thickness of a CB/PEEK laminate and to establish correlation between the processing parameters, the crystallinity and the G_{IC} mechanical property in CF/PEEK laminates manufactured under several conditions.
On the CB/PEEK, results show an alternance of two areas spaced apart from approximately 600 µm, related to the welded interphases and the bulk of the plies. The welded interphases are 200 µm thick and are straddling 2 plies, meaning that for the studied manufacturing conditions, a depth of 100 µm in the tape is sufficiently affected by the laser to decrease its crystallinity or other properties reflected this, as the local hardness and reduced Young's modulus.
Regarding the CF/PEEK, variation of properties between the bulk and the interphases are currently in progress. However, for most of the studied conditions, the observation of cross-sections of laminates fractured by DCB shows intralaminar failure, which demonstrates that the interphases are not the area with the weakest G_{IC} properties. For all manufacturing conditions, the crystallinity of the entire laminate's thickness and on the failure surfaces of the DCB specimens was assessed by DSC and XRD, respectively. It was shown that the G_{IC} decreases with an increase of the crystallinity. This trend is also related with processing parameters favorable to the development of crystallization phenomena, i.e. the lowest layup speed and the highest tool temperature that have been studied. Finally, in order to investigate the hypothesis according which the intralaminar failure mode is related to a lower local crystallinity at the welded interphases, as it was shown for unreinforced PEEK material, the investigation of micromechanical and crystalline properties of the welded interphases are in progress on CF/PEEK material.

Acknowledgments
The authors would like to thank Dr. Romaric Collet from Cetim for the technical investigation in nanoindentation tests, and Ms. Marie-José Moya from the GeM Institute for her XRD analysis technical support.

References

[1] R. Arquier, I. Iliopoulos, G. Régnier, and G. Miquelard-Garnier, "Consolidation of continuous-carbon-fiber-reinforced PAEK composites: a review," *Mater Today Commun*, vol. 32, pp. 104036, 2022. doi: 10.1016/j.mtcomm.2022.104036.

[2] N. Restif, S. Laik, M. Péron, F. Daghia, F. Jacquemin, "Multi-scale characterization of carbon-fibre reinforced PEEK composites manufactured by laser-assisted tape placement," pp. 613–622, May 2024. doi: 10.21741/9781644903131-68.

[3] M. A. Khan, P. Mitschang, and R. Schledjewski, "Parametric study on processing parameters and resulting part quality through thermoplastic tape placement process," *J Compos Mater*, vol. 47, no. 4, pp. 485–499, 2013. doi: 10.1177/0021998312441810.

[4] K. Yassin and M. Hojjati, "Processing of thermoplastic matrix composites through automated fiber placement and tape laying methods: A review," *Journal of Thermoplastic Composite Materials*, vol. 31, no. 12, pp. 1676–1725, 2018. doi: 10.1177/0892705717738305.

[5] M. J. Donough, Shafaq, N. A. St John, A. W. Philips, and B. Gangadhara Prusty, "Process modelling of In-situ consolidated thermoplastic composite by automated fibre placement – A review," *Composites Part A: Applied Science and Manufacturing*, vol. 163, pp. 107179, 2022. doi: 10.1016/j.compositesa.2022.107179.

[6] H. Pérez-Martín, P. Mackenzie, A. Baidak, C. M. Ó Brádaigh, and D. Ray, "Crystallinity studies of PEKK and carbon fibre/PEKK composites: A review," *Composites Part B: Engineering*, vol. 223, pp. 109127, 2021. doi: 10.1016/j.compositesb.2021.109127.

[7] A. M. El Bayssari, M. Péron, A. Barasinski, F. Jacquemin, F. Daghia, and D. Guillon, "A numerical and experimental identification of crystallinity gradients in carbon fiber reinforced thermoplastic composites obtained by laser assisted filament winding," *J Compos Mater*, vol. 58, no. 3, pp. 327–342, Jan. 2024. doi: 10.1177/00219983231223568.

[8] D. J. Blundell and B. N. Osborn, "The morphology of poly(aryl-ether-ether-ketone)," *Polymer*, vol.24, no. 8, pp. 953-958, 1983. doi: 10.1016/0032-3861(83)90144-1

[9] D. J. Blundell, R. A. Crick, B. Fife, J. Peacock, A. Keller, and A. Waddon, "Spherulitic morphology of the matrix of thermoplastic PEEK/carbon fibre aromatic polymer composites," *J Mater Sci*, vol. 24, pp. 2057-2064, 1989. doi: 10.1007/BF02385421

[10] W. C. Oliver and G. M. Pharr, "An improved technique for determining hardness and elastic modulus using load and displacement sensing indentation experiments," *J Mater Res*, vol. 7, no. 6, pp. 1564–1583, 1992. doi: 10.1557/JMR.1992.1564.

[11] F. Lagattu and M. C. Lafarie-Frenot, "Variation of PEEK matrix crystallinity in APC-2 composite subjected to large shearing deformations," Compos Sci and Techno, vol. 60, no. 4, pp. 605-612, 2000. doi: 10.1016/S0266-3538(99)00169-4

[12] D. Ray et al., "Fracture toughness of carbon fiber/polyether ether ketone composites manufactured by autoclave and laser-assisted automated tape placement," *J Appl Polym Sci*, vol. 132, no. 11, 2015. doi: 10.1002/app.41643.

[13] S.-L. Gao and J.-K. Kim, "Cooling rate influences in carbon fibre/PEEK composites. Part II: interlaminar fracture toughness," *Composites: Part A*, vol. 32, pp. 763-774, 2001. doi: 10.1016/S1359-835X(00)00188-3

ADVANCED LIGHTWEIGHT OF BATTERY TRAY FOR ELECTRIC VEHICLES (ALBATROSS PROJECT)

P. Rodríguez[1], S. Pintos[1], L. Mera[1] and L. Carral[1]

[1] AIMEN Technology center, Polígono Industrial de Cataboi SUR-PPI-2 (Sector) 2, Parcela 3
E36418 - O Porriño – Pontevedra-Spain
Email : paula.rodriguez@aimen.es Web Page : https://www.aimen.es/

Keywords: Electric vehicles, lightweight, thermosetting, thermoplastic, composites, joining.

Abstract
Electrification of vehicles is seen as key to achieving global legislative requirements for CO2 emissions reductions. Zero emissions within cities and higher quality and higher performance electrified vehicles are also making them more attractive. However, several issues currently limit further exploitation. Specifically, concerns of drivers regarding battery range, cost, the long-term reliability of batteries and excessive charging times.
The overarching aim of ALBATROSS is to create advanced battery pack designs and achieve a 20% weight reduction of the battery system. For this purpose, a completely redesign of top cover of BMW i3 has been done to manufacture this component in composite material.
A comparison between two composite materials has been done in order to compare performance of thermosetting and thermoplastic material. The thermoplastic material selected for top cover component was a comingled nonwoven fabric made with recycled carbon fibers with polyamide 6 (PA6) resin. Top cover component mechanical requirements are not too high, for that reason a short fibre composite can be use. In the other hand, thermosetting material selected for this comparison was an epoxy high strength carbon woven prepreg. In this work, redesign, process parametrization and joining of both composite materials have been collected and compared to analyze the differences in processability and properties.

1. Introduction

More than 14 million EVs were sold globally in 2023, 53% were battery electric vehicles (BEV) and 47% were plugin hybrid electric vehicles (PHEV) [1]. These values suppose a growing of 11% and 47% respect to the previous year for the same types of vehicles. However, several issues currently limit further sales. Specifically, concerns of drivers regard to battery range, cost, the long-term reliability of batteries and excessive charging times. Tesla has shown that better range is a key factor, having realized a 20-40% higher range that its competitors, leading to Tesla selling 1.8 million of vehicles in 2023 (20% more than the previous year) which corresponds with the 7% market share [2]. European manufacturers need to develop key technologies which address the buyer's main hesitation points. ALBATROSS [3] addresses the needs of European Electric and Hybrid-Electric passenger vehicle market by overcoming driver concerns developing an integrated approach based on smart batteries combined with lightweight designs. The light weighting solutions, based on modular multi- material systems for battery modules and trays, will be fabricated and joined using cutting edge, fast and cost-effective processes, with disassembly, recycling and reuse designed in as a part of an eco-design approach.
Lightweight of battery tray in ALBATROSS project is proposed to change certain components of the case from metal to composite material. Thus, reduction in weight will be achieve maintaining mechanical requirements. For this, a completely redesigning of each component will take place to maintain the properties of final components despite of the material change. The two components proposed in ALBATROSS project to be modified are the top cover, completely manufactured in composite material, and the reinforcement of metal side beams of the battery tray with composite patches. The main objective of this changes will be to achieve a reduction in weight of 40%.

2. Materials and Methods

In this paper, a comparison between thermosetting and thermoplastic composite material was carried out to evaluate the better option for top cover of battery tray for electric vehicles.
Thermoplastic material (TP) selected is a nonwoven fabric made from recycled carbon fibre and mixed with polyamide 6 fibers (G-TEX TM PA/60-SM45-200-1200) from Gen2carbon. These references of thermoplastic material are made with 60 wt% of thermoplastic fiber (PA/60), reinforced with standard modulus carbon fibre (strength between 4-5 GPa (SM45)) and 200 gsm of areal weight (200).
In the case of thermosetting material (TS), reference selected for this study is an Epoxy high strength carbon woven prepreg (Hexply® M77CS/35%/245T2/CHS-3K) from Hexcel. The resin (M77CS) content of this prepreg is 35% by weight reinforced with high strength carbon fibre (245T2/CHS-3K).
The manufacturing processes were different for each material attending their specific processability.,. In the case of thermoplastic material process by press machine was selected. Firstly, a parametrization for this manufacturing process with a design of experiment (DoE) was done to analyze the better results in terms of porosity. Nevertheless, for manufacturing of thermosetting material, vacuum bag process in oven has been done. In that case, the curing cycle of the TDS was applied.
The design of experiments (DoE) for thermoplastic materials was done by Doehlert design method (DM). This method is characterized by the definition of between 3 to 6 repetitions in the central point. The equation to calculate of the number of trials is the following (Eq.1).

$$\boldsymbol{N = 2k(k-1) + C_o} \quad (1)$$

Where $\boldsymbol{k}$ is the number of parameters analysed and $\boldsymbol{C_o}$ is the number of repetitions in the central point. In that case 3 factors were analyzed, Temperature, Pressure and Time with 3 repetitions in the central point. In Table 1the parameters used for DOE experiments are shown.

Table 1.Factors analyzed in DoE experiments.

Factor	*Temperature, ºC*	*Pressure, bar*	*Time, min*
1	290	40	30
0	270	30	25
-1	250	20	20

In Table 2 design of experiment by Doehlert method is shown. Also, a reference trial with supplier parameters has been done to compared with DoE trials in terms of porosity, thickness and percentage of fiber volume. According to the nature of the matrix, the temperature propose by the supplier is little lower than temperatures show by the authors in the literature (Tm recommended for PA 220ºC). For that reason, in DOE trials higher temperatures were studied.

Table 2. Process parameters for DOE trials.

# Trial	Design of experiments			Process parameters		
	Temperature, ºC	*Pressure, bar*	*Time, min*	Temperature, ºC	Pressure, bar	Time, min
Supplier parameters	-	-	-	230	43	60
#1	-1	-1	0	250	20	25
#2	-1	0	-1	250	30	20
#3	-1	0	1	250	30	30
#4	-1	1	0	250	40	25
#5	0	-1	-1	270	20	20
#6	0	-1	1	270	20	30

#7	0	1	-1	270	40	20
#8	0	1	1	270	40	30
#9	1	-1	0	290	20	25
#10	1	0	-1	290	30	20
#11	1	0	1	290	30	30
#12	1	1	0	290	40	25
#13	0	0	0	290	30	25
#14	0	0	0	290	30	25
#15	0	0	0	290	30	25

Thermosetting material, according to TDS, can be processed by both press machine or autoclave consolidation, maintaining during 3minutes at 140ºC or during 5 min at 130ºC, with a heating rate higher than 5ºC/min. Regarding pressure conditions, for a press consolidation 25 bar is needed, however for autoclave consolidation this pressure is lower, about 7 bar.
In this study, an adapted vacuum bag oven (VBO) curing cycle was defined to achieve the same properties than press machine and autoclave consolidation. In VBO process, pressure applied on the laminates is produced by the vacuum generated inside, about 1 bar, so probably the porosity inside the laminates will be very high. For that reason, a modification in the curing cycle must be done. The optimized curing cycle is made up of 2 stages; First stage at 80ºC for 15 minutes must be done, to eliminate the volatiles generated during the curing cycle. Volatiles can become trapped within the layers and cause an increase in the porosity of the material, which affects the mechanical properties. After this first step, a second step of 15 minutes at 125ºC was carried out to consolidate the laminates of composite. Each heating ramp was reducing respect the one presented in the TDS to guarantee the adequate elimination of volatiles, about 3ºC/min per each ramp. All process have been controlled by thermocouples inside the composite, to ensure the correct curing temperature and cycles time.
A completed redesign of top cover component has been done with mechanical properties of new thermoplastic and thermosetting composite materials. The optimal design after FEM simulations is the one presented in Figure 1. As can be seen, this component is composed of two flat parts and internal stiffeners which provide stiffness to the final structure.

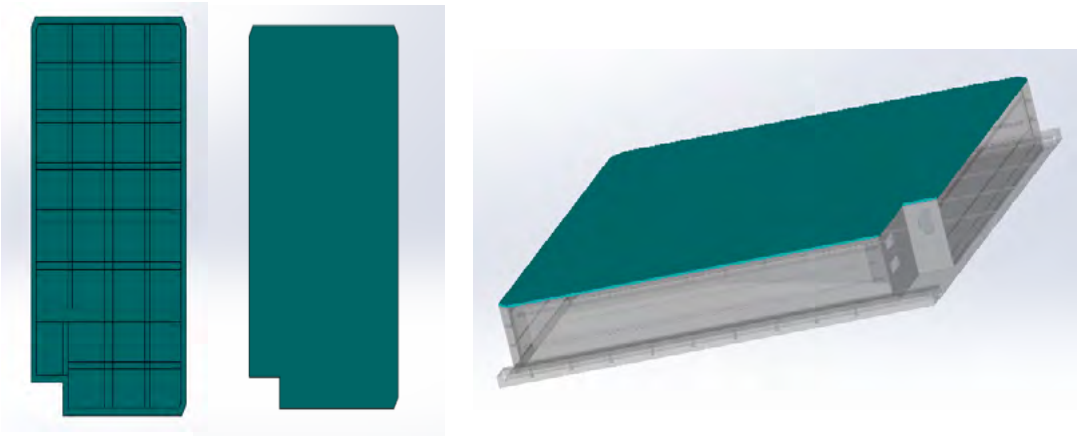

Figure 1. Design of top cover component and its assembly in the final battery tray.

Due to the manufacturing process, in both TP and TS materials, bonding of flat panels with stiffeners must be done. Both TP and TS single lap joint (SLJ) test was carried out by ASTM D5868:2001 standard to determine the best adhesive and conditions for manufacturing the joining. According to this standard, the specimens for this test were made up of two specimens of 100mm length, 25mm width and 2.5mm thickness (Figure 2). This standard establishes that the lap must be 25mm, nevertheless, a recalculation of the joint strength has be done at the end of the test with the final dimensions. Also, thickness of bondline must be controlled to guarantee the required thickness.

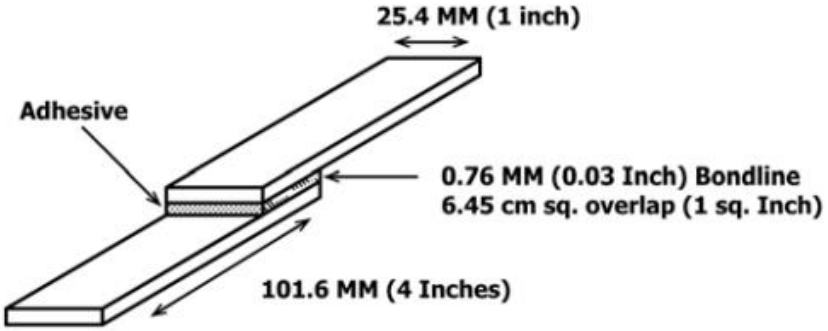

Figure 2. Single lap joint specimen dimensions according to ASTM D5868-01 Standard.

Then, adhesive bonding procedure of the panels were different according to the material and manufacturing processes. In case of TS material, one flat panel and the stiffeners can be manufactured together and the other flap panel which cover the stiffeners is manufactured separately. Then bonding of these two components is done by adhesive bonding. Tests with two different adhesives have been carried out: Acrylic adhesive paste (Crestabond M7-05 from Scott-Bader) and epoxy adhesive film (SA 75-90/S/250g/1270 pc11-8041 from Gurit). Manufacturing process for the bonding with this adhesive are the same as for curing the composite material, VBO. Single lap joint of these adhesives was done to evaluate mechanical performance of the joint. Also, it is important to comment that for SLJ specimens of TS material surface treatment is no needed due to the surface rugosity induced by peel-ply. Finally, due to the limitations in thickness for this component on the global dimension of the battery case, the grammage of the adhesive film was selected to not increase the total thickness above the thickness limit. Trials for bondline thickness control was done, after that it can be conclude that about 0.1mm will be the bondline thickness for 1 layer of adhesive film.
In case of TP material four adhesives were tested as follows: Crestabond M7-05 from Scott-Bader, Isobond 735 from Sicomin, SAF 30 from Bostik and DP8910NS Scotch-Weld from 3M. All of them are validated for bonding of aluminum and composite materials and resist temperatures between -40ºC to 90ºC. Curing cycles depend on the nature of each adhesive, in the following table (Table 3) curing cycle for each of them are shown. In this case, due to the smooth surface of the TP laminates after press manufactured process, it was needed a surface treatment with grit (80 grit) to enhance the energy surface of the material.

Table 3. Curing cycle of all adhesives propose for the bonding of top cover components.

Adhesive	*Curing cycle*
Crestabond M7-05	30 minutes at Room Temperature (RT)
Isobond 735	24h at RT + 8h at 60ºC
SAF30	24h at RT + 2h at 60ºC
DP8910NS	24h at RT

3. Results and discussion

The main objective of this study is to compare thermoplastic and thermosetting material defined in the previous paragraph, in terms of porosity, manufacturing benefits and joints performance. First, for thermoplastic material, after DOE parametrization the process parameters determined are 290ºC, 25 bar and 30 minutes of maintenance. In Figure 3 , an example of microscopy images is shown, after an image analyses, porosity of samples can be quantified. For this material and process parameters, porosity obtained for samples across the laminate is about 1.5-1%. The not optimized press machine processing cycles obtained a porosity between 22-8%.

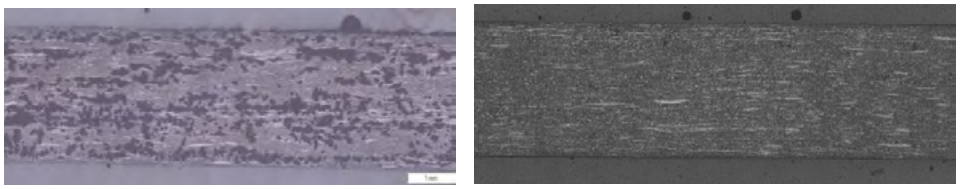

Figure 3. Microscopy images analysis of the porosity for TP material with not optimized cycle (left) and DOE optimized cycle (Right) on press machine.

Also, porosity of laminates manufactured with TE by VBO are analyzed by microscopy images to determine if the manufacturing process are adequate for this type of material. In Figure 4 microscopy images of laminates manufactured by VBO is shown, the porosity was analyzed concluding that the percentage of porosity across the laminates is between 2% and 1%. So, it can be concluded that this material is adequate for VBO process.

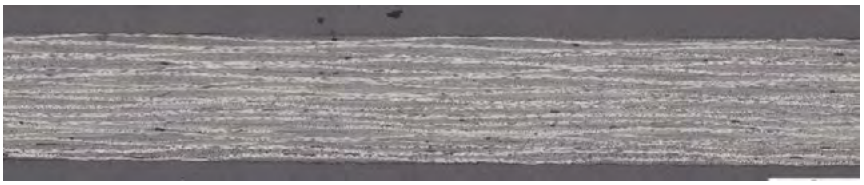

Figure 4. Microscopy images of M77 laminates manufactured by VBO process.

Then, mechanical characterization of both materials must be done to defined if the process parameters selected as adequate, in terms of porosity, are also appropriate in terms of mechanical behavior. In Table 4 mechanical properties for both materials are shown.
If results for TP and TS material are compared between then it is noted that, for all mechanical tests the values obtained for TS material are higher than for TP material. Values for tensile strength of TS material in 0º and 90º are higher than for TP material, 73.2 % and 69.9% respectively. Also, tensile modulus in both directions is 71.2% and 73.71% higher in TS material. For compression test results TS material compression strength increase 70.1% and 68.25% compares to TP material in both directions. Finally, for compression modulus results for TS material increase 74.54% and 87.7% respectively for each direction in comparison with TP material. This fact is mainly for the length of the fibre, TP materials are reinforced with short carbon fiber with random orientation while TS material is reinforced with bidirectional continuous carbon fiber. This difference in the orientation of reinforcement as well as dimensions and quality of fibers cause the differences in mechanical results between them, as expected.

Table 4. Mechanical properties of TP and TS material selected for this study.

	Standard	*G-TEX TM PA/60-SM45-200-1200*	Hexply® M77CS/35%/24 5T2/CHS-3K
Tensile strength Direction1 (0º), MPa	ASTM D3039	241.18	899.4
Young´s modulus Direction1 (0º), GPa	ASTM D3039	20.39	70.74
Tensile strength Direction2 (90º), MPa	ASTM D3039	218.12	923.95
Young´s modulus Direction2 (90º), GPa	ASTM D3039	17.81	67.74
Compression Strength Direction1 (0º), MPa	ASTM D6641	191.37	639.74
Compression Modulus Direction1 (0º), GPa	ASTM D6641	17.45	68.54
Compression Strength Direction2 (90º), MPa	ASTM D6641	170.02	535.46
Compression Modulus Direction2 (90º), GPa	ASTM D6641	7.93	64.46
Interlaminar shear strength, MPa	ASTM D2344	-	62.51
Interlaminar shear modulus, GPa	ASTM D2344	-	4.3
Shear Strength V-Notched Beam Method, MPa	ASTM D5379	204.75	-
Shear Modulus V-Notched Beam Method, GPa	ASTM D5379	19.74	-

Finally, SLJ tests for both materials were carried out to define the best configuration for the bonding of the final top cover component. For TP material, SLJ tests of four different adhesives was done to compare the mechanical results obtained for the bonding with adhesives of different nature. Also, failure mode was evaluated to identify the most adequate adhesive for this joint. In Figure 5 , a comparation of the single lap shear strength for each adhesive is shown. It is noted that the highest shear strength corresponds with adhesive DP8910, about 12MPa. It can be concluded that the bonding with DP8910 is, approximately, 20-25% higher than the bonding with the other three adhesives.

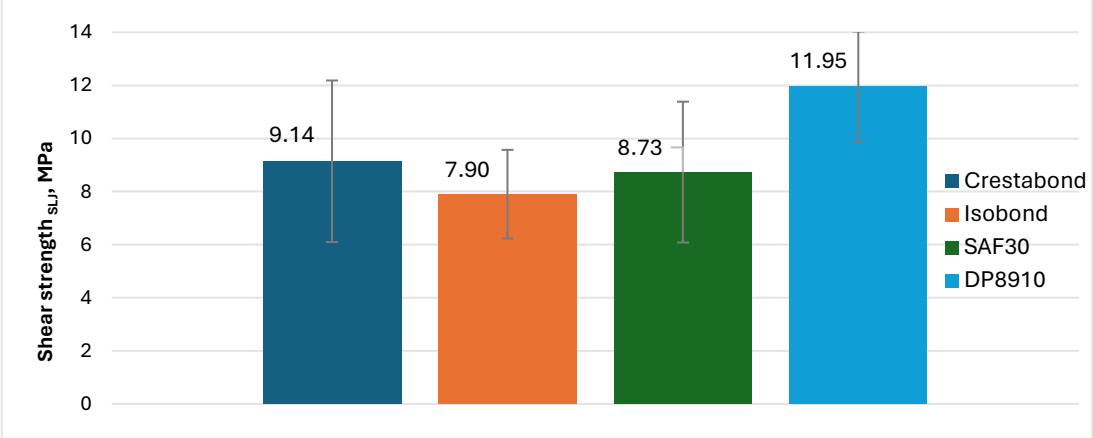

Figure 5. Comparative of the shear strength (MPa) for TP material with the different adhesives studied.

In Figure 6 and Figure 7 failure mode of specimens after test for the four adhesives selected for this study are shown. For ISOBOND 735, SAF30 and DP8910 adhesive failure of all specimens tested are presented and for CRESTABOND M7-05 a mixture of adhesive and cohesive failure (70% Adhesive + 30% cohesive) was obtained.

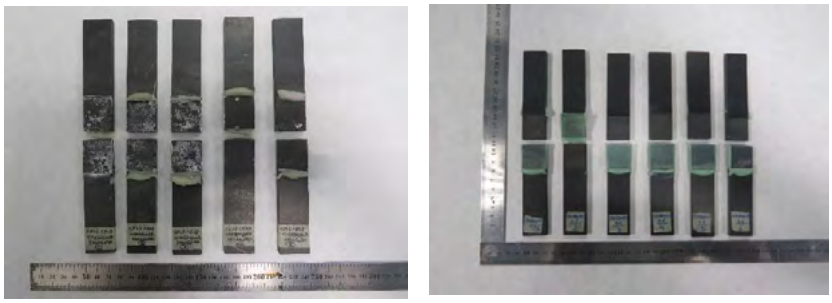

Figure 6. Failure mode of SLJ specimens after test for Crestabond M7-05 (Left) and ISOBOND 735 (Right).

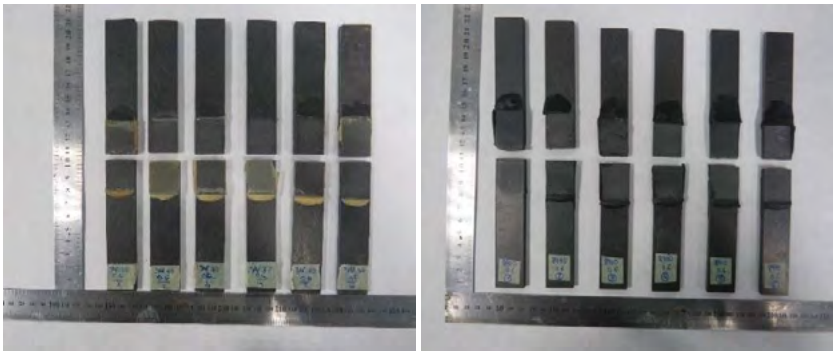

Figure 7. Failure mode of SLJ specimens after test for SAF30 (Left) and DP8910 (Right).

For TS material only two adhesives were studied due to the nature of the material. For this material in addition to compare an acrylic and an epoxy adhesive, two different types of adhesives will be compared too, paste versus film. In Figure 8 a comparative between both shear strength results for the adhesives are shown. Shear strength for SLJ specimens manufactured with the adhesive film SA70-95 are higher than the one manufactured with Crestabond M7-05, an increasing of 84%.

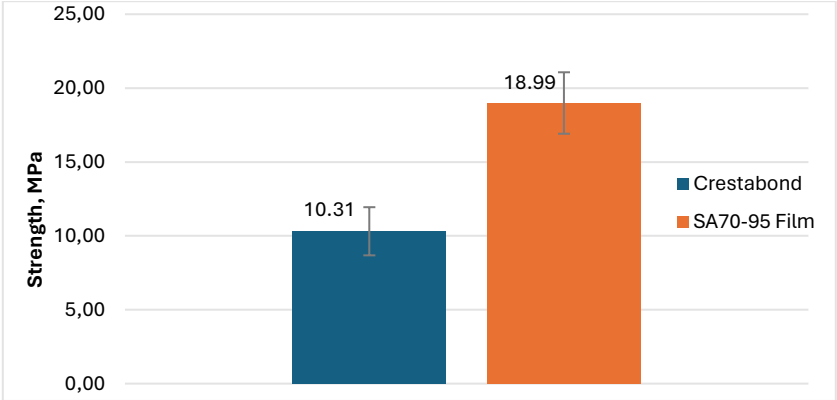

Figure 8. Comparative of shear strength for SLJ specimens made of TS material with the 2 adhesives study.

As in the previous case, failure mode after test was analyze. In Figure 9SLJ specimens after test are presented, it is noted that 100% adhesive failure mode was obtained for specimens manufactured with Crestabond M7-05 and a 100% cohesive failure mode was presented in lap area of specimens manufactured with film SA70-95.

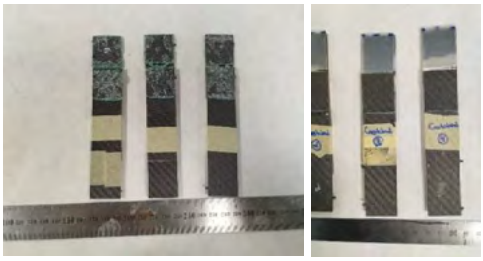

Figure 9. Failure mode of SLJ specimens after test for Crestabond M7-05 and SA70-95

If SLJ test results for TP and TS material are compared, an increasing in the shear strength of TS material with the adhesive film SA70-95 was achieved, about 37.1% higher than TP with DP8910 adhesive.

1. Conclusion

The main objective of this study was to compare TP and TS materials in terms of mechanical properties, porosity and adhesive bonding to the manufacturing of a composite top cover for a battery tray of an electric vehicle.

If the results for all mechanical tests are compared it can be concluded that TS material presented higher values due, principally, to the fabric carbon fibers format. As was explain in previous paragraphs, TP material was a nonwoven fabric made from recycled carbon fibre random orientated. Nevertheless, TS material is a carbon fiber woven prepreg (Bidirectional) which gives to the final piece highest mechanical properties.

For adhesive bonding with the difference configurations propose previously it can be concluded that highest shear strength is presented for the bonding of TS materials with the film adhesive SA70-95. Also, the failure mode for this adhesive is the most adequate according to the standard, 100% Cohesive.

For this reason, lightweight top cover for ALBATROSS battery tray was manufactured with TS

material (Hexply M77 from Hexcel) by VBO in oven process and bond both parts with adhesive film (SA 70-95 from Gürit). In Figure 10 ALBATROSS top cover for battery tray manufactured with TS material is shown.

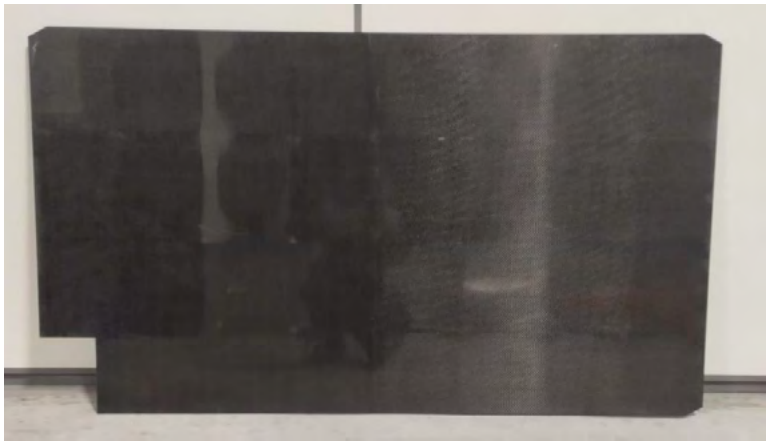

Figure 10. Lightweight top cover manufactured with Hexply M77 and join with adhesive film SA70-95.

2. Acknowledgements

This work has been supported by the European Union's H2020-LC-BAT-2019-2020 Building a low-Carbon, Climate Resilient future: Next Generation Batteries under grant agreement No 963580 – ALBATROSS.

3. Reference

[1] Global EV Sales Hit Record 1.5+ Million in December 2023 (9th of February 2024). INSIDEEVs Link: Global EV Sales Hit Record 1.5+ Million in December 2023 (insideevs.com)
[2] Tesla bate su récord de ventas a nivel mundial en 2023, pero ya tiene a BYD al acecho (3th of January 2024). Motor.es. Link: Tesla bate su récord de ventas a nivel mundial en 2023, pero ya tiene a BYD al acecho (motor.es)
[3] H2020 ALBATROSS Project. Link: Albatross (albatross-h2020.eu)

OPTIMIZING INTERFACIAL SHEAR STRENGTH IN BAMBOO FIBER COMPOSITES THROUGH POLYDOPAMINE SURFACE MODIFICATION

Carla N. Schnell[1], Gregory Mertz[2], Abdelghani Laachachi[3], David Ruch[4] and C.A. Fuentes [5]

[1]Department of Materials Research and Technology, Luxembourg Institute of Science and Technology (LIST), 5 rue Bommel, L-4940 Hautcharage, Luxembourg
Email: carla.schnell@list.lu Web Page: https://orcid.org/0000-0003-2498-8757
[2]Department of Materials Research and Technology, Luxembourg Institute of Science and Technology (LIST), 5 rue Bommel, L-4940 Hautcharage, Luxembourg
Email: gregory.mertz@list.lu Web Page : https ://orcid.org/0000-0003-1590-4216
[3]Department of Materials Research and Technology, Luxembourg Institute of Science and Technology (LIST), 5 rue Bommel, L-4940 Hautcharage, Luxembourg
Email: abdelghani.laachachi@list.lu Web Page: https://orcid.org/0000-0001-6579-5076
[4]Department of Materials Research and Technology, Luxembourg Institute of Science and Technology (LIST), 5 rue Bommel, L-4940 Hautcharage, Luxembourg
Email: david.ruch@list.lu Web Page : https ://orcid.org/0000-0001-8797-6820
[5]Department of Materials Research and Technology, Luxembourg Institute of Science and Technology (LIST), 5 rue Bommel, L-4940 Hautcharage, Luxembourg
Campus Brugge, Department of Materials Engineering, KU Leuven, Leuven, Belgium
Email: carlos.fuentes@list.lu Web Page: https://orcid.org/0000-0002-0766-9079

Keywords: Dopamine, Interfacial Shear Strength, Mechanical properties, Polyethyleneimine, Pull out test.

Abstract

This study explores enhancing the compatibility of bamboo fibers (BF) for composite through chemical modifications. A novel polydopamine (PDA) treatment was developed, using polyethyleneimine (PEI) to obtain a stable PDA solution and was compared to conventional in situ PDA polymerization. Untreated BF were subjected to PDA and polydopamine-polyethyleneimine (PDA-PEI) coating processes via in situ dopamine (DP) polymerization (4h and 24h) and a stable PDA-PEI solution (300s). BF surface characterization included scanning electron microscopy (SEM), X-ray photoelectron spectroscopy (XPS), Fourier-transform infrared spectroscopy (FTIR), and atomic force microscopy (AFM). Characterization revealed that DP polymerization with PEI controlled PDA grain size, resulting in smoother coating compared to PDA alone. The interfacial shear strength (IFSS) of BF with polypropylene (PP) and polylactic acid (PLA) indicates that a 4h treatment by in situ DP polymerization was insufficient, requiring a 24h treatment for significant improvements. Remarkably, the stable solution treatment led to substantial IFSS improvements of 21% for PP and 16% for PLA, drastically reducing the treatment time for industrial feasibility. Composites with PP and BF treated with the novel treatment exhibited an 8.0% increase in tensile strength and a 12% increase in Young's modulus, highlighting the potential of a polydopamine-based solution for improving fiber-matrix adhesion.

1. Introduction

The use of Fiber Reinforced Polymer (FRP) composites has become widespread, playing a key role in modern engineering. However, there has been a noticeable recent shift towards investigating natural fiber composites, motivated by the need for sustainable materials. Bamboo stands out as a very promising option in this field, as it grows rapidly in just 3-5 years, making it one of the fastest renewable resources around. Bamboo fiber (BF) is getting a lot of attention because it has some impressive

qualities, like being lightweight, having great mechanical properties comparable to glass fiber, and being biodegradable [1].

Despite the promising qualities of bamboo fiber, achieving robust interfacial bonding with conventional polymeric matrices, such as polypropylene (PP), remains a formidable challenge. This is primarily attributed to the inherently contrasting nature of natural fibers and typical polymeric matrices. Natural fibers like bamboo are hydrophilic due to their cellulose content, which readily absorbs moisture. In contrast, polymeric matrices such as PP are hydrophobic, leading to poor adhesion between the two materials. As composites inherently consist of two distinct phases, the interface formed between them assumes a pivotal role in facilitating stress transfer and optimizing load distribution efficiency within the composite structure. Indeed, the properties of the composite material are intricately linked to the quality of this interface. However, interfacial adhesion mechanisms, although critically influential, are often overlooked factors that profoundly impact the physical, mechanical, and thermal properties of plant-fiber-reinforced polymer composites [2].

Several treatments have been studied to enhance the interfacial bonding of bamboo fibers. These methods encompass alkali treatment [3], grafting of silane [4], fiber acetylation [5], and various other chemical treatments, which aim to reduce the polarity of the fibers through modification of the bamboo surface. However, these treatments often involve the use of solutions containing acidic, alkaline, or toxic organic compounds, posing potential environmental risks [6].

In this context, there is a notable potential to enhance interfaces through environmentally friendly surface modification techniques inspired by natural processes, such as those observed in mussels [4]. Dopamine (DA), a small catechol molecule containing terminal amino groups, has been used to oxidatively self-polymerize in mild alkaline pH, similar to the typical marine environment that leads to the formation of adhesive polydopamine (PDA) [7]. PDA functional coatings are some of the simplest and the most powerful alternatives available for surface modification[4]. Several authors have shown that PDA functional coatings significantly improve the adhesion of natural fibers with different polymer matrices [4, 6, 8, 9]. These coatings are among the simplest and most effective alternatives for surface modification, characterized by the self-assembly of a hierarchical roughened structure imparting hydrophobic behavior.

However, one limitation of PDA coating is its non-homogenous fiber covering [9], leaving the surface uneven with particles of varying sizes and with some regions lacking any coating at all. To address this point, polyelectrolytes have been proved to control the PDA grain size in the range of 10–100 nm [10]. Polyelectrolyte poly (ethylene imine) (PEI) inhibits the growing of PDA grains by adsorbing onto their surface, effectively reducing their size [6]. Additionally, the deposition process of PDA on fibers typically requires extended periods (over 20 hours). Utilizing homogenous and smaller particles with enhanced surface adhesion can help decrease deposition time. In this context, the addition of PEI serves a dual purpose: controlling the aggregation mechanism of PDA and accelerating its deposition onto the fiber.

In this study, bamboo fibers (BF) underwent chemical modification using dopamine (DA) through in situ oxidation, with treatments carried out in the presence of polyethyleneimine (PEI) to ensure a more uniform and fast deposition. The impact of both PDA and PDA-PEI deposition time (on the final chemical properties of the fibers and the Interfacial Shear Strength (IFSS) was investigated using two distinct polymer matrices (PP and PLA). Additionally, a stable PDA-PEI solution was prepared to minimize deposition time, and the fibers were rapidly dipped for deposition. Furthermore, a treatment using a stable dopamine and DPA solution was conducted, in which the fibers were dipped without in situ polymerization. Characterization techniques, including SEM, FTIR, AFM, TGA, and XPS, were employed to analyze the treated fibers. Composite materials were also prepared using melt mixing to evaluate the effects of the treatment.

2. Materials and methods

2.1 Fiber surface treatments

Bamboo fibers used in this study was provided by Bambooder Biobased Fibers B.V. (Netherlands), including both short (ranging from 1.1 to 3.7 mm in length) and long fibers (approximately 15 cm in length). The chemical composition of the fibers was analyzed using various methodologies. Water and ethanol extractives were quantified according to [11]. Subsequently, on the extracted-free fibers, the total lignin and ash content were determined following the method outlined by [12], and holocellulose content was assessed as per the protocol described by [13].

Untreated bamboo fibers, cleaned with distilled water and dried, served as the baseline for further experimentation. The deposition of polydopamine (PDA) and polydopamine-polyethyleneimine (PDA-PEI) coatings on the fibers was achieved through in situ polymerization. Untreated bamboo fibers were immersed in respective coating solutions under continuous stirring at room temperature (21 ± 2°C) for varying durations (4h and 24h) according to the following treatments: DPA 4H, DPA 24H. For the PDA coating, dopamine hydrochloride (Sigma Aldrich) was dissolved in a 0.5 mmol tris(hydroxymethyl) buffer solution, with the pH adjusted to a range of 8-9 using a 1 M hydrochloric acid solution (Carl Roth, Karlsruhe, Germany). Polymerization of dopamine was also investigated in the presence of poly(ethyleneimine) (PEI) at a concentration of 2 g/L and a molecular weight of 1,200 g/mol, and the treatments were designated as DPA-PEI 4H and DPA-PEI 24H. Additionally, bamboo fibers were immersed in stable solutions of PDA-PEI for 300 s. The preparation of stable PDA-PEI solutions involved a 20-hour dopamine polymerization process, with pH adjustment to 6.5 to halt polymerization. This treatment was denoted as PDA-PEI 300s. Following each treatment, the fibers were thoroughly rinsed with distilled water to remove any residual chemicals.

2.2 Fiber treatment characterization

The surface morphology of the bamboo fiber was observed by scanning electron microscopy (SEM) using an environmental machine Quanta FEG 200 (FEI, Eindhoven, The Netherlands). The samples were investigated without any conductive coating treatment and the images were recorded with the L300s detector at 15 kV and spot 5, and Elemental analysis was done by energy-dispersive X-ray spectroscopy (EDX) using an EDAX system (Mahwah, NJ, USA).

The surface elemental composition of BF was determined by X-ray photoelectron spectroscopy (XPS) using a Thermofisher Nexsa G2Kratos Axis Ultra DLD photoelectron spectrometer (Manchester, UK). The measurements were conducted with the monochromatic Al Kα radiation (1486.6 eV) and an Xray power of 150 W. The area of analysis was adjusted to 400 µm x 800 µm or 150 µm x 300 µm for each case, and all the analyses were done with a 0◦ take-off angle with respect to the surface normal.

FTIR measurements were performed to examine the chemical structure of the BF. ATR spectra were recorded on a Bruker Invenio spectroscope equipped with a diamond-attenuated total reflectance (ATR) accessory. Infrared absorbance spectra were collected in the range from 4000 to 400 cm−1using a resolution of 4 cm−1 and 32 co-added scans. The presented spectra were further baseline-corrected and normalized.

The topographical study of the BF was performed with an AFM MFP-3D (Oxford Instrument, UK) and images were acquired in air in AC mode at scan rates between 0.50 and 1.00 Hz. Semi-contact silicon 160AC-NA AFM tips (Olympus, Japan) with a cantilever spring constant of 26 N.m-1 and a resonance frequency of 300kHz were used. The surface topography of the tape's immobilized BF was acquired by maintaining the tip first resonance amplitude constant via the feedback loop of the AFM acting on the piezo Z direction. Data treatment was done with MountainSpip software (Digital Surf, France), cylinder form of the BF was removed prior to the roughness parameter (Sq) calculation.

The IFSS measurements were done by single fiber pull-out testing using a FAVIMAT + machine from Textechno (Germany), equipped with a load cell of 3200 cN (resolution of 1 µN). The FIMABOND

system from Textechno (Germany) was first used to embed the single fiber within two distinct polymer matrices, polypropylene (PP), and polylactic acid (PLA) **(Figure 1a).** The measure of the average fiber diameter was done by image analysis and the fiber embedding was done with a controlled embedding length (Le) of about 400 µm (the exact Le value was precisely measured for each case). At least 10 fibers with a diameter comprised between 100 and 50 µm were tested per case.

2.3 Composites preparation and characterization

BF reinforced Polyporpylene composites (PP-BF) using untreated, and PDA-PEI 300s treated BF were prepared by melt mixing in a Thermo Scientific™ HAAKE™ PolyLab™ QC Modular Torque Rheometer with roller blades. Melt mixing was carried out at 180°C, using a rotation speed of 60 rpm for 5 minutes. Dog-bone shaped specimens were prepared using a hydraulic press from Labtech **(Figure 1b).** The specimens were preheated for 6 minutes, heated for 5 minutes, and subjected to a pressure of 20 tons. The tensile strength and strain at break of the composites were tested in a Universal Testing Machine (3344 Instron, USA) with a load cell of 1000 N and an extension rate of 2.0 mm/min was used. For each treatment, at least ten samples were tested.

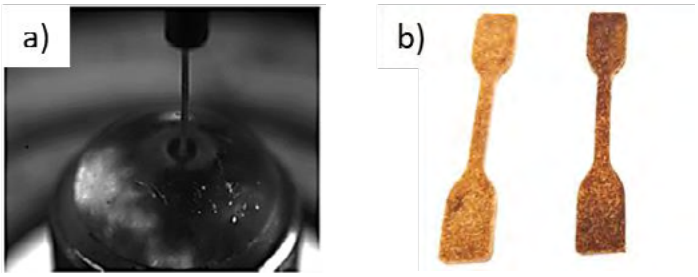

Figure 1. (a) Embedding of a single fiber on PP matrix. (b) PP-BF composites prepared with untreated and treated BF.

3. Results and discussions

3.1 Fiber chemical and surface analysis

The chemical composition analysis of the BF revealed the following percentages: 26.6% insoluble lignin, 5.7% soluble lignin, 69.8% holocellulose, 6.6% ethanol and water extractives, and 0.54% ash. These findings are consistent with those reported in the literature for other bamboo species [14], [15].

The FTIR spectra of untreated and treated bamboo fibers (BF) subjected to various treatments, including PDA 4H, PDA 24H, PDA-PEI 24H, and PDA-PEI 300s, are depicted in **Figure 2.** In the spectra of untreated BF, a characteristic band centered at 3340 cm^{-1} and a peak at 2898 cm^{-1}, attributed to the stretching vibration of hydroxyl groups (O–H) of cellulose and to the symmetric C–H stretching vibration of the alkyl and aliphatic groups [16]. The characteristic peaks located at 1735 cm^{-1} and 1245 cm^{-1} are assigned to the vibration band of carbonyl (C=O) in hemicellulose and the acyl-oxygen (CO–OR) stretching vibration in hemicellulose and lignin [8]. Upon treatment with PDA 24H and PDA-PEI 24H, a more pronounced absorption peak is evident, indicating the presence of new OH and NH groups (stretching vibrations of amino) corresponding to DPA and PEI. Furthermore, the FTIR spectra of BF treated with DPA 24H exhibit two additional peaks at 2915 cm^{-1} and 2858 cm^{-1}, corresponding to the -CH_3 and -CH_2 asymmetrical stretching vibrations and symmetric stretching from the PDA molecules [17]. Additionally, a new peak at 1648 cm^{-1} corresponding to the amide group formed as an intermediate during DPA polymerization, is observed in the spectra of all treated BF. These results confirm the successful deposition of dopamine on the fiber surface.

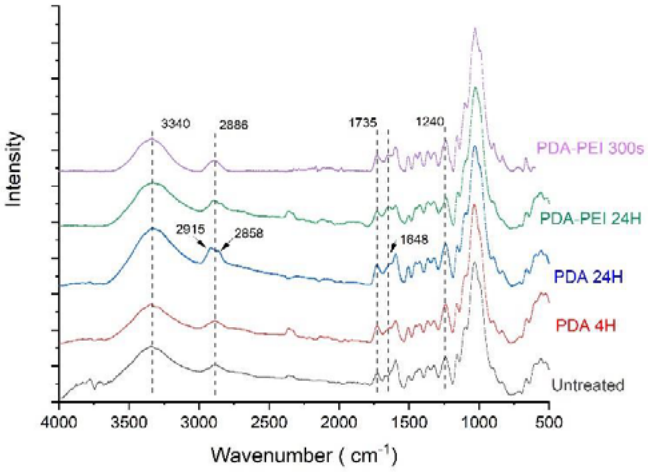

Figure 2: FTIR spectra of untreated BF and treated BF.

XPS measurements were conducted to assess the surface chemistry of both untreated and treated bamboo fibers (BF). The surface atomic composition and atomic ratios (O 1s / C 1s and N 1s / C 1s) of the different treated BF samples are summarized in **Table 1**. Treating the BF with PDA for 24 hours resulted in an increase in the nitrogen to carbon atomic ratio, suggesting a weak presence of PDA. Moreover, conducting dopamine polymerization in the presence of PEI (PDA-PEI 24H) led to a further increase in the nitrogen to carbon atomic ratio, attributed to the nitrogen content in the PEI chemical structure. This behavior aligns with previous studies [9], which observed similar trends when investigating flax fiber treatment using dopamine alone or dopamine polymerized in the presence of PEI. On other hand, comparing the PDA-PEI 300s treatment with the PDA-PEI 24H treatment revealed similar values, indicating a comparable surface chemistry of the BF with both treatments.

Table 1. Surface atomic composition of the BF determined by XPS analysis as a function of the treatment.

	Surface atomic composition			Surface atomic ratio	
Treatment	**C 1s %**	**O 1s %**	**N 1s %**	**O 1s/C 1s**	**N 1s/ C 1s**
Untreated	67.5	29.2	3.35	0.432 ± 0.030	0.050 ± 0.006
PDA-24H	71.6	21.8	6.65	0.305 ± 0.009	0.093 ± 0.006
PDA-PEI 24H	68.2	23.9	7.8	0.351 ± 0.043	0.114 ± 0.014
PDA-PEI 300s	69.0	23.3	7.7	0.338 ± 0.020	0.113 0.021

3.2 Fiber morphology and surface roughness

SEM images of untreated and treated BF surfaces are presented in **Figure 3**. The surface of the untreated BF shows the presence of some small particles, likely due to extractives or ash; nevertheless, EDX analysis revealed predominantly oxygen and nitrogen on the surface. Conversely, BF treated with PDA for 24 hours and PDA-PEI for 24 hours exhibited a weak nitrogen peak detected by EDX, suggesting the presence of the coating, with nitrogen potentially originating from the PDA and/or PEI chains. Previous studies have indicated that PDA coating is scarcely visible by SEM, hindering accurate quantification of fiber coverage by PDA [9]. Additionally, at the magnification level observed, large aggregates are not discernible. **Figure 4d,** nitrogen presence was not observed, but a homogeneous fiber surface is evident after treatment.

The AFM topography imaging of the untreated and treated BF (PDA 24H and PDA-PEI 300s) are represented in **Figure 4** with values of the extracted roughness measurements (Sq). The untreated images

show the morphology of the fiber and a roughness of 42.8 nm (**Figure 4a**). When BF present the deposition of PDA during 24h, aggregated grains is visible on the fiber surface (**Figure 4b**). The grains consisted of PDA spheres ranging from 1,5 microns to 100 nm in diameter. It is observed that the roughness increases to 98.1 nm with the PDA deposition. On other hand **Figure 4c** show the topography of the fiber surface treated with DPA-PEI 300s, where a more regular roughness slightly higher than the untreated one it is observed (42.5 nm). General surface morphology of the fiber is not well defined, showing that a layer is covering the fiber surface with some small particles.

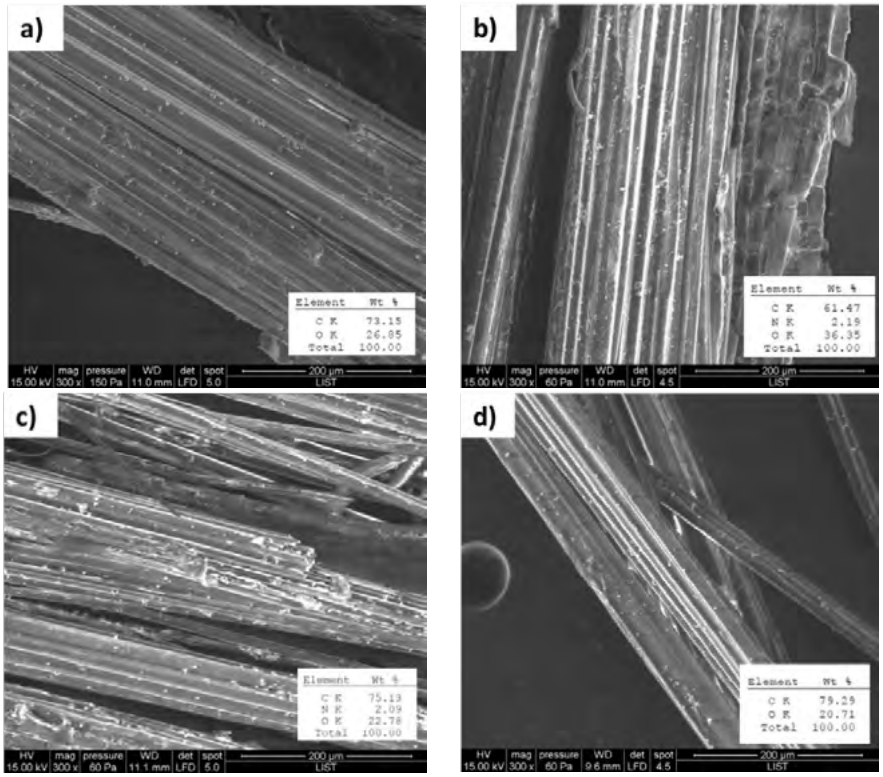

Figure 3: ESEM images of a) Untreated BF and treated BF with b) PDA 24h, c) PDA-PEI 24H, d) PDA-PEI 300s.

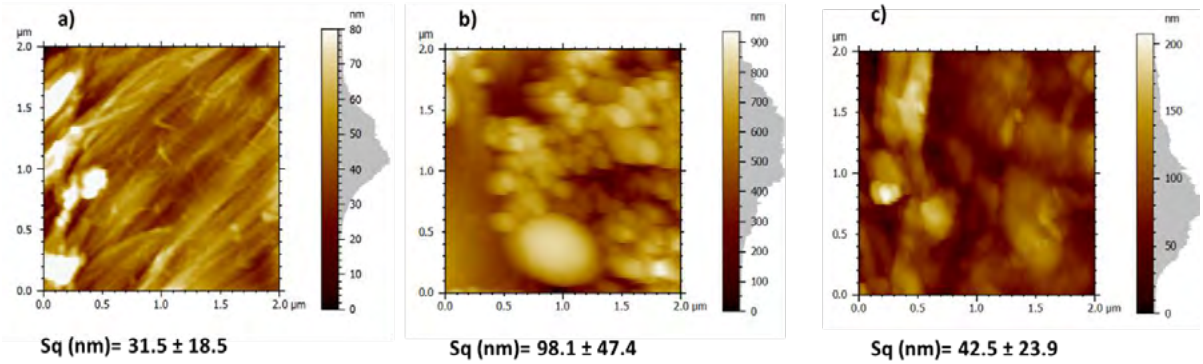

Figure 4. AFM topography images of the **a)** untreated BF and treated BF with **b)** PDA 24H, **c)** PDA-PEI 300s BF. The corresponding roughness data is also provided. The field of view for each image is 2.0 µm x 2.0 µm.

3.3 Pull out test and PP/BF composites mechanical properties

The interfacial adhesion between single bamboo fibers (BF) and PP and PLA matrices was assessed through single fiber pull-out testing. Results revealed **(Table 2)** a higher Interfacial Shear Strength (IFSS) for untreated fibers with PLA (12.1 MPa) compared to PP (7.78 MPa). However, the IFSS of fibers embedded in PP or PLA did not exhibit significant increases when subjected to a 4-hour polydopamine (PDA) deposition. In contrast, a 24-hour PDA treatment led to a remarkable enhancement in IFSS by 75% and 45% with PP and PLA, respectively, compared to untreated fibers. This improvement could be attributed to the reduction in fiber polarity resulting from dopamine deposition. Conversely, when fibers were treated with PEI-DPA for only 4 hours, a slight increase in IFSS was observed, indicating that the addition of PEI facilitated the deposition of PDA onto the fiber. Additionally, treatment with a stable solution (PDA-PEI 300s) resulted in increased IFSS for both matrices compared. to PDA-PEI 4H treatment. Specifically, the use of the stable solution led to a 21% and 16% increase in IFSS with PP and PLA compared to untreated, respectively, highlighting its efficacy in enhancing interfacial bonding.

The tensile strength and strain at break of PP/BF composites, prepared with untreated BF and PDA-PEI 300s treated BF, were investigated. The results revealed an improvement in tensile strength at break, increasing by 8.0% from 26.98 ± 2.4 MPa to 29.85 ± 2.0 MPa when using treated BF. Additionally, the Young's Modulus demonstrated a 12% enhancement compared to composites prepared with untreated BF, rising from 1170 ± 39 MPa to 1266 ± 95 MPa.

Table 2. Determination of the IFSS between untreated and treated BF based on single fiber pull-out testing and using PP and PLA as matrix.

Treatment	IFSS (MPa) with PP	IFSS (MPa) with PLA
Untreated	**7.78 ± 1.09**	**12.16 ± 1.32**
PDA 4H	**7.93 ± 0.91**	**11.16 ± 2.14**
PDA 24 H	**13.60 ± 1.31**	**17.68 ± 1.81**
PDA-PEI 4 H	**8.14 ± 1.40**	**13.21 ± 1.60**
PDA-PEI 300s	**9.44 ± 1.79**	**14.20 ± 1.32**

4. Conclusions

This study explores enhancing bamboo fiber (BF) compatibility for composite applications, addressing sustainability concerns. Despite BF's favorable properties, achieving robust interfacial bonding with conventional matrices remains challenging. Chemical treatments, including polydopamine (PDA) and polydopamine-polyethyleneimine (PDA-PEI), were investigated for surface modification. The deposition of PDA and PDA-PEI was examined, revealing enhanced interfacial shear strength (IFSS) with 24h and 4h durations, respectively. Particularly noteworthy was the utilization of a novel stable and versatile PDA-PEI solution, which yielded substantial IFSS improvements of 21% for polypropylene (PP) and 16% for polylactic acid (PLA), underscoring its potential for effective interfacial enhancement. Furthermore, composites with PP and BF treated with this innovative approach exhibited an 8.0% increase in tensile strength and a 12% increase in Young's modulus, thereby highlighting the potential of a polydopamine-based stable solution as a sustainable material for improving fiber-matrix adhesion.

Acknowledgments

The authors extend their gratitude to Bambooder Biobased Fibers B.V. and the Luxembourg National Research Fund (FNR), particularly for their invaluable financial support toward the BRIDGES call 2022-2 project N˚17771393.

References

1. Tran, L.Q.N., et al., *Tensile behavior of unidirectional bamboo/coir fiber hybrid composites.* Fibers, 2019. **7**(7): p. 62.
2. Lee, C.H., A. Khalina, and S.H. Lee, *Importance of interfacial adhesion condition on characterization of plant-fiber-reinforced polymer composites: A review.* Polymers, 2021. **13**(3): p. 438.
3. Wang, C. and S. Ying, *A novel strategy for the preparation of bamboo fiber reinforced polypropylene composites.* Fibers and Polymers, 2014. **15**: p. 117-125.
4. Hong, G., et al., *Mussel-inspired reinforcement of a biodegradable aliphatic polyester with bamboo fibers.* Journal of Cleaner Production, 2021. **296**: p. 126587.
5. Zaman, H.U. and R.A. Khan, *Acetylation used for natural fiber/polymer composites.* Journal of Thermoplastic Composite Materials, 2021. **34**(1): p. 3-23.
6. Hong GongHua, H.G., et al., *Mussel-inspired polydopamine modification of bamboo fiber and its effect on the properties of bamboo fiber/polybutylene succinate composites.* 2017.
7. Zhang, H., et al., *Mussel-inspired hyperbranched poly (amino ester) polymer as strong wet tissue adhesive.* Biomaterials, 2014. **35**(2): p. 711-719.
8. Lin, J., et al., *The effect of alkali treatment on properties of dopamine modification of bamboo fiber/polylactic acid composites.* Polymers, 2018. **10**(4): p. 403.
9. Montreuil, A., et al., *Flax fiber treatment by an alkali solution and poly (dopamine) coating: Effects on the fiber physico-chemistry and flax/Elium® composite interfacial properties.* Composites Part A: Applied Science and Manufacturing, 2024. **177**: p. 107963.
10. Mateescu, M., et al., *Polyelectrolytes to produce nanosized polydopamine.* Journal of colloid and interface science, 2016. **469**: p. 184-190.
11. Sluiter, A., et al., *Determination of extractives in biomass.* Laboratory analytical procedure (LAP), 2005. **1617**(4): p. 1-16.
12. Sluiter, A., et al., *Determination of structural carbohydrates and lignin in biomass.* Laboratory analytical procedure, 2008. **1617**(1): p. 1-16.
13. Wise, L.E., M. Murphy, and A.A. d'Addieco, *Chlorite holocellulose, its fractionnation and bearing on summative wood analysis and on studies on the hemicelluloses.* 1946.
14. Wahab, R., et al., *Chemical composition of four cultivated tropical bamboo in genus Gigantochloa.* Journal of Agricultural Science, 2013. **5**(8): p. 66.
15. Maulana, M., et al. *Chemical components content of seven Indonesian bamboo species*. in *IOP Conference Series: Materials Science and Engineering*. 2020. IOP Publishing.
16. Schnell, C.N., et al., *Use of micro/nano-and nanofibrillated cellulose to improve the mechanical properties and wet performance of xylan/chitosan films: a comparison.* ACS Applied Polymer Materials, 2023. **5**(10): p. 7867-7877.
17. Hong, G., et al., *Mussel-inspired polydopamine as a green, efficient, and stable platform to functionalize bamboo fiber with amino-terminated alkyl for high performance poly (butylene succinate) composites.* Polymers, 2018. **10**(4): p. 461.

MULTISCALE AND MULTIDIMENSIONAL CHARACTERISATION AND PATTERNING OF GRAPHENE-RELATED NANOMATERIALS AND NANOCOMPOSITES

Yuhan Li[1], Alexander Ford[2] and Milo S.P. Shaffer[1, 2 *]

[1]Department of Materials, Imperial College London, South Kensington Campus, London, SW7 2AZ, UK
[2]Department of Chemistry, Molecular Sciences Research Hub (MSRH), Imperial College London, 82 Wood Lane, London, W12 0BZ, UK

Keywords: Graphene, confocal microscopy, patterning, circuits, microelectronics

Abstract
Macroscale assemblies and composite structures, built upon graphene and graphene-related nanomaterials, are promising for a range of applications and devices. Consequently, there is growing demand for more comprehensive characterisation of graphene-based structures. Confocal laser scanning microscopy (CLSM) is developed, here, as a valuable tool for microstructural investigation of graphene nanomaterials and nanocomposites, exploiting the technique's distinctive features, including high-contrast and non-invasive imaging, as well as depth discrimination. Reflection-mode and fluorescence-mode CLSM have been demonstrated to be efficient tools for characterising flake distribution in graphene films. CLSM enables 3D imaging of graphene nanocomposites, providing valuable insights into the real dispersion status of nanofillers. CLSM volume imaging can also be correlated with high-resolution datasets obtained from scanning electron microscopy to fully represent nanocomposite structures. In addition to passive characterisation, CLSM can be used for simultaneous imaging and processing studies: GO films can be selectively reduced in-situ to produce electrically conductive functional patterns at a range of lengthscales from millimetre to sub-micron, using frame and line scan tools natively available in CLSM. The versatility is demonstrated by directly writing "RC" (parallel resistor-capacitor) circuits using the simple low power laser within the confocal microscope. This study demonstrates the potential of CLSM in the direct fabrication of microelectronic devices.

1. Introduction

Confocal laser scanning microscopy (CLSM) is a routine characterisation technique in biological and medical studies. CLSM uses monochromatic lasers as the incident light source and captures images of samples through point-by-point illumination and detection, providing enhanced contrast and resolution in fluorescence imaging of tissues and cells. With advances in instrumentation, modern confocal microscopes now enable precise raster scanning, enhanced optical sectioning, and super-resolution Airyscan methods.[1] These capabilities provide significant opportunities for investigating a broader range of systems, especially material structures and processes. CLSM has multiple imaging functions, including confocal reflection-mode (RL) and fluorescence-mode (FL) imaging, along with several extended topographical and spectral functions derived from confocal imaging techniques. These functions are valuable for understanding the morphology, topography, optical and photoluminescence properties of materials (Figure 1). The basic RL and FL imaging modes are useful for investigating material surface structures, capable of achieving higher resolution (~150 nm) and contrast than conventional optical microscopy, due to the short-wavelength UV laser available and the pointwise illumination optics. 3D non-destructive imaging through optical sectioning, is compelling for studying the internal structure of materials which are typically challenging to visualize on a large scale. One significant advantage of CLSM is quantitative topography analysis that can be performed concurrently with 3D reflection imaging, useful for investigating surface textures, roughness, film thickness, and

device architectures. More specialized total interference contrast (TIC) can provide thickness data down to single atom layers, as demonstrated for single layer graphene.[2] Both topographical CLSM and TIC imaging can be correlated with conventional transmission microscopy and calibrated to give real concentration and flake thickness information for graphene related materials (GRMs). In addition to static imaging, CLSM is also useful for studies of dynamic processes; such applications have been demonstrated through in-situ observation of the micelle formation in polymers and graphene oxide (GO) reduction.[3]

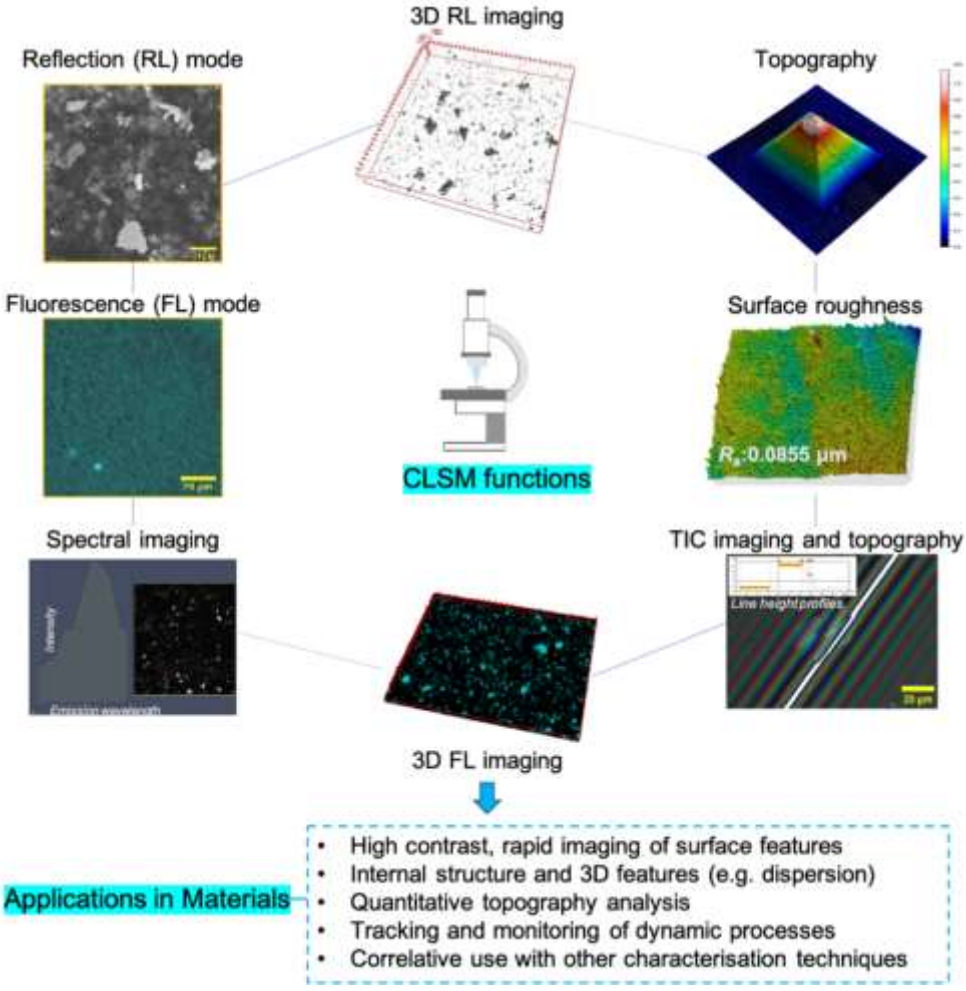

Figure 1. CLSM imaging modes and (potential) applications in material studies.

The non-invasive, high contrast, and rapid characterisation offered by confocal microscopy shows great potential for microstructural investigations of graphene and related structures. Reflection-mode confocal microscopy has been applied for the characterisation of exfoliated graphene and nanoribbons.[4] Large-scale evaluation of graphene coverage on copper substrates has proved valuable for monitoring and quality control during scalable synthesis.[5] Multi-modal confocal imaging, applying both RL and FL modalities, is useful for examining the large-scale film properties, including the flake distribution, film roughness, fluorescence features, and etc.[3b] CLSM imaging of graphene and various carbon nanocomposites is also attractive, useful for determining the alignment of graphene nanoplatelets in the matrix,[6] and the extent of carbon nanotube dispersion using 3D imaging.[7] Confocal stack imaging offers significant advantages in the structural analysis of nanocomposites by providing accurate microstructures, in contrast to the commonly used 2D projections obtained with conventional optical imaging. To enhance the general application of CLSM stack imaging, we have investigated and established experimental protocols and guidelines for utilising RL and FL confocal microscopy in the 3D microstructural reconstruction of graphene-based nanocomposites.

The most interesting CLSM capabilities move beyond just characterisation to include the conversion and patterning of materials to make devices in situ. In our previous study, confocal microscopy was applied to the innovative in-situ monitoring, laser reduction, and patterning of graphene oxide (GO) films.[3b] Multi-modal tracking allowed the conversion mechanism to be explored during the process, leading to enhanced control of the reduction and patterning process. Controlled ablations allowed 3D architectures to be written directly. This technique enables multiscale patterning of reduced GO, including both large-scale patterns (mm) and sub-micron scale conductive tracks, using a low power laser (<5 mW). One promising future application of this technique is the laser processing and development of microelectronic devices, through CLSM direct writing of functional electrical circuits. Using the tile function in confocal imaging, it is possible to fabricate pre-designed circuits efficiently. The approach is exemplified in this study to make model laser-reduced GO resistor-capacitor (RC) circuit elements. The RC circuits represent very simple and useful configurations commonly used for filtering and signal processing in electronic devices. Interestingly, the conventional circuit symbols for resistor and capacitor, when written in graphene-related films, demonstrate appropriate physical responses. In other words, the circuits are "WYSIWYG" (what you see is what you get). The in-situ laser patterning of circuit components using CLSM provides great efficiency over conventional multi-step lithographical methods,[8] which typically rely on the use of masks, and printing techniques, which require the development of appropriate graphene inks.[9]

2. Materials and methods

GO water solution (concentration: 0.4 wt%, flake size ~10 μm) was obtained from Graphenea Inc. Spray coating was used to prepare GO films. 1 ml of 0.4 mg ml^{-1} GO solution were continuously sprayed onto glass substrates by a handheld artist's airbrush with a nozzle diameter of 250 μm. The laser reduction and patterning of GO films were performed on a Zeiss LSM 800 confocal microscope. The laser processing and imaging set-up were detailed elsewhere.[3b] A 488 nm laser with 80% power was used for reduction. Impedance spectroscopy measurements were performed on a custom-made 2-point probe station. A pair of gold-plated spring-loaded pin electrodes were mounted parallel to each other within holes drilled into an epoxy block. An inter-contact distance of 5 mm was selected, with care taken to ensure equal extension of both pins perpendicular to the mounting block. The electrode assembly was mounted on the sliding rail of a syringe driver (KD Scientific Model 410), which was positioned vertically above a platform. The electrodes were wired to the terminals of a Gamry Instruments Interface 1000 potentiostat/galvanostat/ZRA, run with Gamry Instruments Framework™ Software. During experimentation, samples were positioned on the platform and the electrode pins were lowered vertically to touch the laser-patterned contacts by running the driver at a slow pace, avoiding scratching the delicate film that comprised the samples. Impedance spectroscopy experiments collected data at frequencies between 1 MHz and 1 Hz, with 10 samples being collected logarithmically per decade. Analysis and curve fitting was performed with EC-Lab® Version 11.42. SEM characterisation of GO and rGO was performed on a Zeiss Auriga field emission scanning electron microscopy (SEM) using an In-lens detector. Specifically, for SEM characterisation, GO films and rGO patterns were fabricated on conductively-doped silicon substrates (Agar Scientific Ltd). The samples were fixed onto aluminium stubs using carbon tapes and imaged without conductive coating.

3. Results

3.1 Fundamental patterning using frame scan and line scan

In a typical laser reduction and patterning process, applied to GO films, the localized reduction was realised using the 'frame scan' mode on the confocal microscope. Specifically, during the imaging process, the laser scans an area of the film line by line and generates an image frame. The frame size can be adjusted by variation of the objective and the digital zoom on CLSM, with a minimum focusing area of 3.2 μm * 3.2 μm (50X objective and 40X digital zoom). Fine control of reduction area has been

previously demonstrated through micro-fabrication of a dumbbell pattern on a single GO flake.[3b] Alternatively, the 'line scan' mode can be used to generate fine conductive lines (conductivity: ~ $7.1*10^3$ S m^{-1}).[3b] Similar to the frame scan mode, adjusting the objective can alter the resolution of the line produced (Figure 2), with the best resolution achieved using a 50X objective (Figure 2((a)) Laser power also significantly influences the width of laser reduced GO (LrGO) lines (Figure 2(b)), due to the photothermal reduction mechanism.[3b] For GO films with a thickness of around 40 nm, line thicknesses were measured to be approximately 2.9 µm, 2.2 µm, and 1.5 µm using laser power levels of 80%, 60%, and 40%, respectively (Figure 2(b)). Optimising the process parameters needed for any given GO film is straightforward, due to the availability of immediate feedback, and is efficient in comparison to time-consuming photolithography or etching methods. This flexibility in controlling the dimensions of the reduced regions by adjusting microscope and laser parameters makes the CLSM frame and line scan modes valuable, readily-accessible tools for patterning various circuit elements.

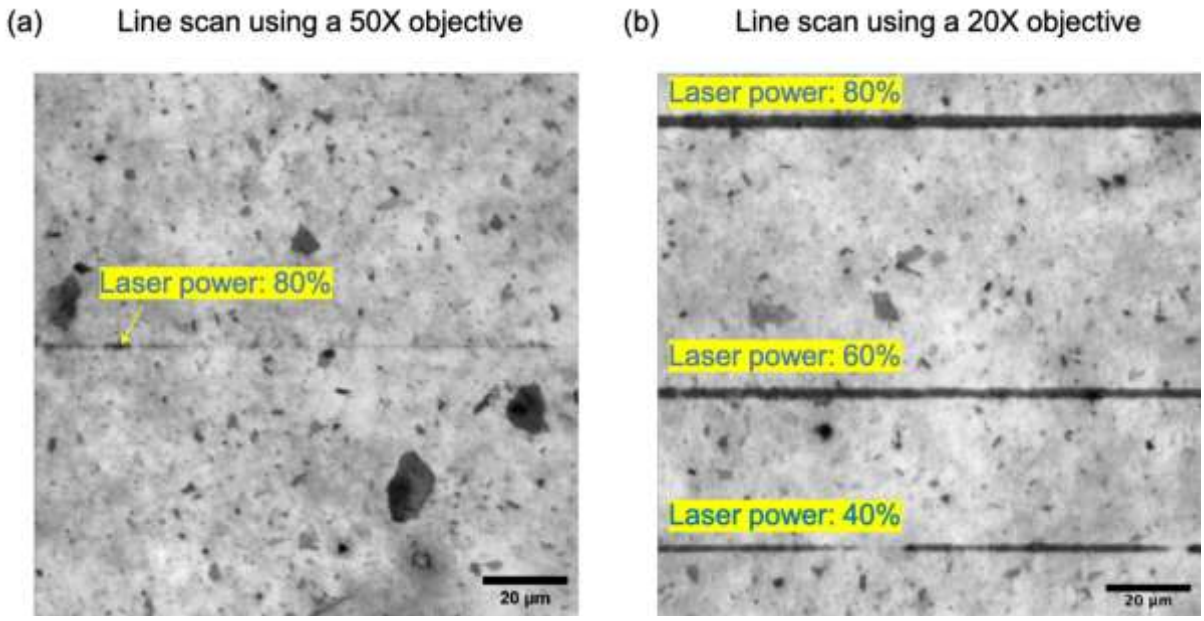

Figure 2. Transmission optical micrographs showing the rGO thin lines fabricated using line scan, applied to a sprayed GO flake film (approx. 40 nm thick) on a glass substrate. (a) Using a 50X objective, at 80% power. (b) Using a 20X objective, reduced at different laser powers.

The initial designs were fabricated on glass substrates to allow multimodal transmission optical imaging (Figure 2). Similar designs of LrGO patches and lines were also fabricated on conductively-doped silicon substrates to allow higher resolution SEM imaging. The GO and LrGO regions show significant differences in both optical and SEM imaging; the clear contrast is attributed to the different work functions and conductivities of the two materials. The LrGO patch, created through frame scanning, exhibited a distinct continuous reduced region with a well-defined boundary. The LrGO lines, reduced using both 20X and 50X objectives, confirmed the capability of the line scan mode to produce micron and sub-micron (~300 nm) scale conductive patterns.

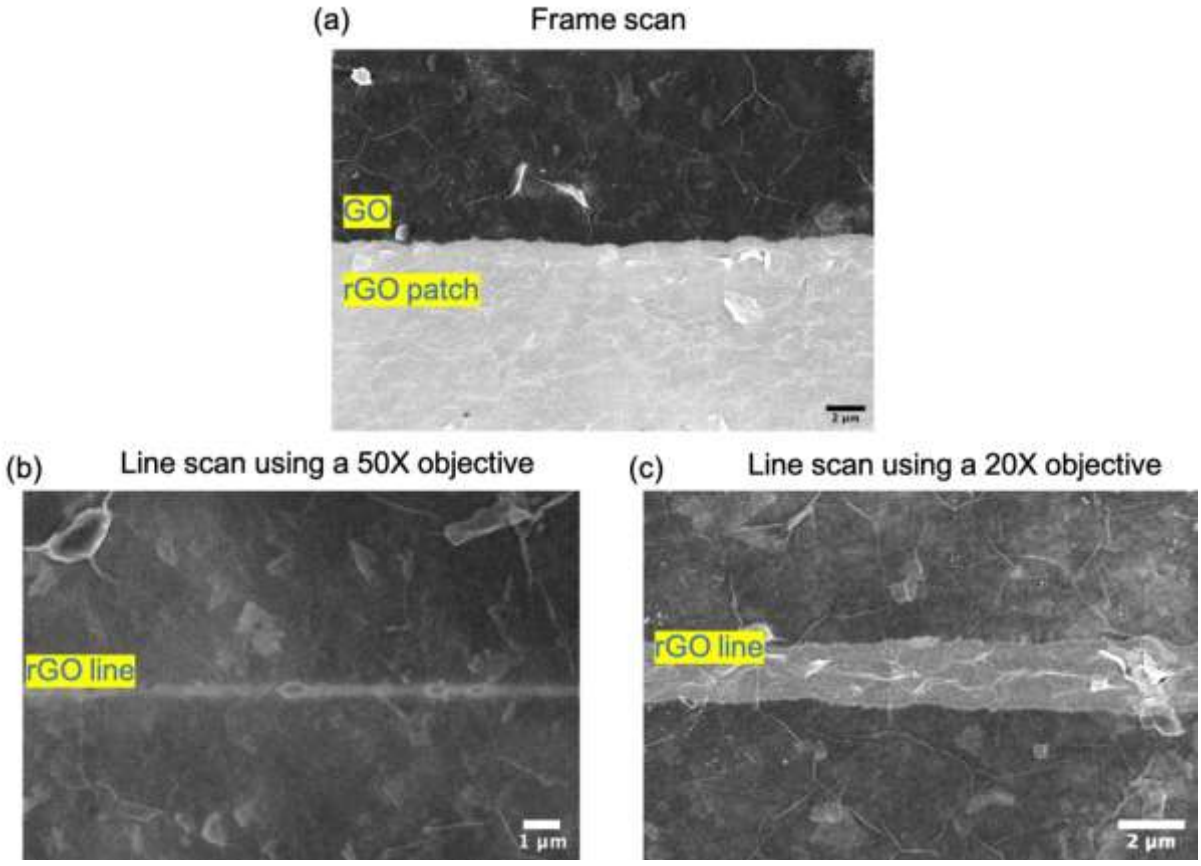

Figure 3. SEM images of LrGO patterns fabricated using frame scan and line scan, on conductive-silicon substrates, with two different objectives (x50 and x20), both at 80% laser power. The lighter region is the reduced graphitic material (rGO), and the darker background reflects the texture of the original GO materials. The finest line (b) is around 300nm wide.

3.2 Fabrication of circuit elements

To facilitate the creation of large-scale patterns, tile scanning proves a useful function in CLSM, enabling the imaging of extensive areas by stitching together partial images. Prior to patterning, the RC configuration was pre-drawn using the tile function in CLSM. The tile region was subdivided into patches of the actual frame size (Figure 4(a)). In the patterning process, laser scanning of the designated region was accomplished through automatic stage movement. The capacitor and the connection components of the circuit were patterned using frame scan. A 10% overlap was applied between neighboring patches to ensure good connectivity. Line scan was employed to fabricate the remaining resistor segments (Figure 4(b)). Patterning a micro-RC circuit using the tile scan function requires only a few minutes, demonstrating a good efficiency of the technique for flexible device processing with real time feedback.

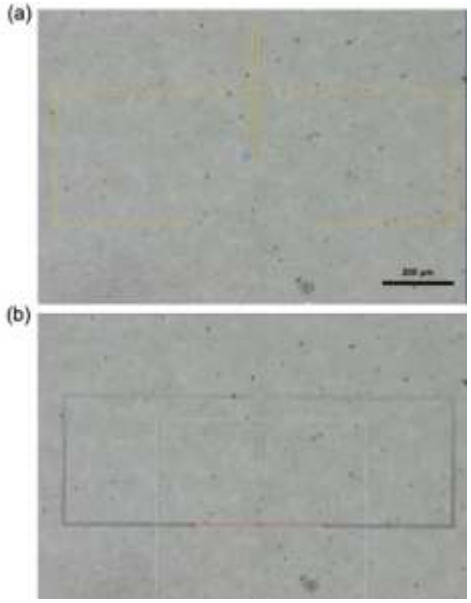

Figure 4. Transmission optical micrographs showing the patterning of a RC circuit using the tile function. (a) Frame division of the tile region of the circuits. (b) Area of line scan for the fabrication of the resistor. The red line shows the position of the line scan.

3.3 RC microcircuits

Three examples of parallel resistor-capacitor (R-C) circuits were written in GO films, with the equivalent circuit provided (see the inset of Figure 5(b)). The geometrical design was made based on the measured resistivity of rGO patches ($1.4 * 10^{-4}$ Ohm m) and lines ($6.9 * 10^{-4}$ Ohm m) to ensure that the circuits would produce measurable responses. In the designed configuration, the width of the connection lines (50 μm) was more than 10 times larger than that of the resistor (3 μm), to ensure that the resistor line segment forms the more dominant resistance of the circuit. The dimensions of the capacitor planes were approximately 500 μm * 50 μm, with a 5 μm spacing. Fine-control of reduction patterns was achieved (see high-resolution optical micrographs in Figure 6). The resistor length was easily adjusted by manipulating the digital zoom of the microscope. Other circuit parts were patterned with consistent dimensions, indicating a high level of repeatability. The impedance spectra show the effect of varying the resistor length (Figure 5(b)). All three circuits exhibit the classic "semicircular response" of an R-C element, indicating consistent patterning and a systematic response. The resistances were fitted at 124 kOhm, 251 kOhm, and 419 kOhm, respectively, for the 100, 400, 800 μm resistors, showing the expected qualitative trend, with values in the range predicted from the independent conductivity measurements. Specifically, the estimated resistance of the 100 μm line is 116 kOhm, based on measured line resistivity and dimensions. The values are not ideally proportional to length due to the contribution of the other circuit elements and the changing width of the track with length, due to the use of magnification control for writing. Interestingly the fitted capacitances for the three circuits were very consistent (1.403, 1.405, and 1.453 pF), showing excellent repeatability for the identical capacitor designs. However, the absolute value was larger than the estimated based on the capacitance of two ideally thin, flat, coplanar electrodes on a silica substrate ($2.6 * 10^{-14}$ F) (Zfit Software). The higher value likely reflects the much higher surface area of rGO flake material than the simple geometry implies. Combined with ionic mobility in GO, there is likely a electrochemical double layer contribution. Small deviations from the semicircular form may stem from film defects, contact issues between circuit elements, and ionic diffusion effects. Construction of a suitable equivalent circuit that accounts for such effects may be possible, but would require more detailed experiments for appropriate parameterization. Overall, the systematic response of the RC circuits demonstrated the capability of CLSM to print high-resolution microcircuits, showing great promise for applications in circuit fabrication.

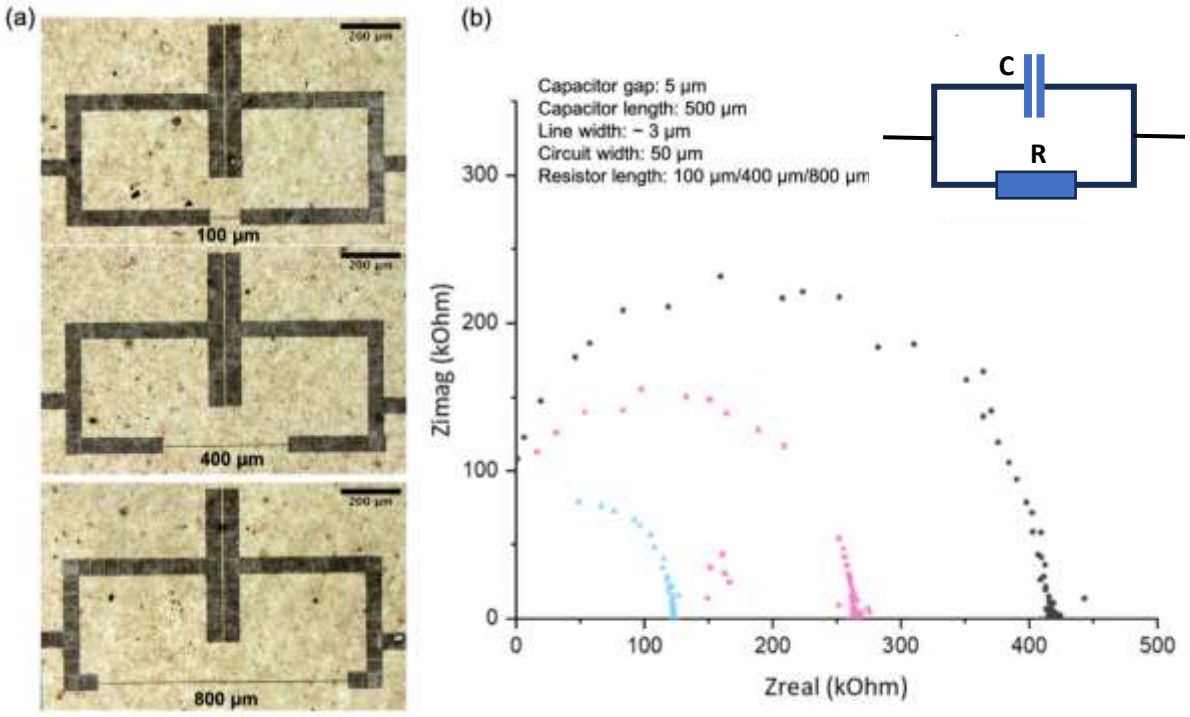

Figure 5. Three R-C circuits written directly in GO films, using CLSM (20X objective for both line and frame scan, at 80% laser power), visualised by transmission optical microscopy and measured electrically by impedance spectroscopy, showing the effect of changing the resistor length on the classic "semicircular response".

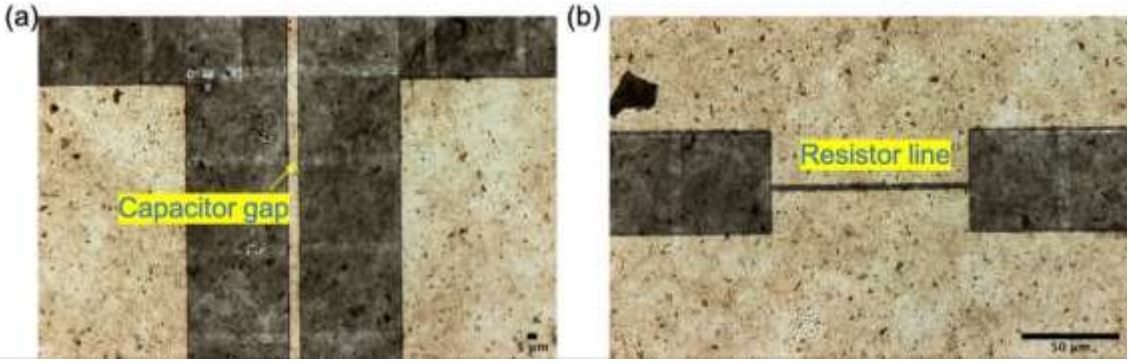

Figure 6. High-resolution transmission optical micrographs of the capacitor gap and resistor line elements. The capacitor gap and resistor line are accurately fabricated. The 10% overlap between the tiles is also visible.

4. Conclusions

This work demonstrates in-situ patterning of LrGO circuits using the integrated laser scanning and imaging functions of CLSM. Functioning high-resolution circuit elements can be conveniently fabricated on low-cost GO films using the native frame and line scan functions in CLSM. Compared to other techniques, one-step patterning using the built-in laser and the image tile function is efficient, and provides direct image feedback, demonstrating great efficiency and repeatability. Demonstration RC circuits have been designed and fabricated, exhibiting classical RC electrical responses. The approach may be readily extended to more complex circuit designs and prove useful for concept development, prototyping, or customized integrated devices. This study, alongside our previous research on CLSM, highlights the versatility of the technique for the characterisation, processing, and fabrication of graphene-based structures and devices.

Acknowledgements

The authors would like to acknowledge the support of Henry Royce Institute at Imperial College London for the use of confocal microscope. Yuhan Li would like to acknowledge the China Scholarship Council and Imperial College London for funding support.

References

[1] J. Huff, A. Bergter, J. Birkenbeil, I. Kleppe, R. Engelmann, U. Krzic, The new 2D superresolution mode for zeiss airyscan 2017.

[2] M. Vaupel, A. Dutschke, U. Wurstbauer, F. Hitzel, A. Pasupathy, Topography, complex refractive index, and conductivity of graphene layers measured by correlation of optical interference contrast, atomic force, and back scattered electron microscopy, *J. Appl. Phys.* **2013**, *114*, 183107.

[3] a) T. Kimura, M. Shintate, N. Miyamoto, In situ observation of the evaporation-induced self-assembling process of ps-b-peo diblock copolymers for the fabrication of titania films by confocal laser scanning microscopy, *Chemical Communications* **2014**, *51*, 1230; b) Y. Li, M. S. P. Shaffer, Confocal microscopy for in situ multi-modal characterization and patterning of laser-reduced graphene oxide, *Adv. Funct. Mater.* **2023**, *33*, 2300479.

[4] V. Panchal, Y. Yang, G. Cheng, J. Hu, M. Kruskopf, C.-I. Liu, A. F. Rigosi, C. Melios, A. R. Hight Walker, D. B. Newell, Confocal laser scanning microscopy for rapid optical characterization of graphene, *Communications physics* **2018**, *1*, 1.

[5] D. J. Kim, C.-W. Lee, Y. Suh, H. Jeong, I. Jo, J. Moon, M. Park, Y. S. Woo, B. H. Hong, Confocal laser scanning microscopy as a real-time quality-assessment tool for industrial graphene synthesis, *2D Materials* **2020**, *7*, 045014.

[6] F. Tarannum, R. Muthaiah, R. S. Annam, T. Gu, J. Garg, Effect of alignment on enhancement of thermal conductivity of polyethylene–graphene nanocomposites and comparison with effective medium theory, *Nanomaterials* **2020**, *10*, 1291.

[7] B. E. Smith, H. Yazdani, K. Hatami, Three-dimensional imaging and quantitative analysis of dispersion and mechanical failure in filled nanocomposites, *Composites Part A: Applied Science and Manufacturing* **2015**, *79*, 23.

[8] a) Y. Zhou, K. P. Loh, Making patterns on graphene 2010; b) N. H. Kim, B. J. Kim, Y. Ko, J. H. Cho, S. T. Chang, Surface energy engineered, high-resolution micropatterning of solution-processed reduced graphene oxide thin films, *Adv. Mater.* **2013**, *6*, 894.

[9] a) K. Y. Shin, J. Y. Hong, J. Jang, Micropatterning of graphene sheets by inkjet printing and its wideband dipole-antenna application, *Adv. Mater.* **2011**, *18*, 2113; b) F. Torrisi, T. Hasan, W. Wu, Z. Sun, A. Lombardo, T. S. Kulmala, G.-W. Hsieh, S. Jung, F. Bonaccorso, P. J. Paul, Inkjet-printed graphene electronics, *ACS Nano* **2012**, *6*, 2992.

©2024 | 2_SHAFFER_Milo S. P._HS8QT.pdf:8

OPTIMIZATION OF MICROSTRUCTURAL FACTORS OF HAP/COLLAGEN COMPOSITE FIBER BUNDLES AS ARTIFICIAL BONE UNIT

Mototsugu Tanaka[1] and Ken Komatani[2]

[1]Department of Mechanical Engineering, Kanazawa Institute of Technology, 7-1 Nonoichi, Ishikawa, Japan
Email: mototsugu@neptune.kanazawa-it.ac.jp
[2]Graduate Student, Department, Kanazawa Institute of Technology, 7-1 Nonoichi, Ishikawa, Japan
Email: mototsugu@neptune.kanazawa-it.ac.jp

Keywords: Artificial Bone, HAp/collagen Composite Fiber Bundles, Microstructural Optimization

Abstract
Recently, we have been trying to realize the novel hydroxyapatite (HAp)/collagen composite materials with the optimized microstructures by mimicking the real bone microstructures. However, the interaction between the microstructural factors in the HAp/collagen composite materials would be quite complicated. Therefore, this study aimed to optimize the microstructural factors of the HAp/collagen composite fiber bundles by the parametric study. Here, the collagen fibers were prepared by the bio-inspired method, and HAp crystals were deposited on their surface by the alternate immersion into the pseudo body fluid (biomimetic method). The osteonectin was introduced before and after the biomimetic precipitation, and the prepared HAp/collagen composite fibers were bundled by the electrophoresis. Their mechanical properties were evaluated by the micromechanical tests. The results indicated that their tensile strength was the highest when the alternating immersion duration, electrophoresis duration, electrophoresis current, crosslinking-agent density, and adhesive-protein density were 40[s], 30[min], 4[mA], 4[mmol/L], and 0.5[μg/μL], respectively. Their tensile strength tended to increase and then decrease as the value of the microstructural factors increased. This suggests that their tensile strength would be determined by the trade-off relationships, and could be maximized under the optimized conditions determined by the interaction of the microstructural factors.

1. Introduction

The materials mainly used to substitute the bone functions, such as the metals and the ceramics, have the higher stiffness compared to the natural bone tissues, resulting in the disturbance of the normal stress transfer to the healthy bone neighboring to the transplanted substitute materials and then the bone absorption owing to the lack of the mechanical stimuli. In addition, the periodic replacing operation would become necessary owing to the corrosion or deterioration of the metal or ceramic bone substitute materials. These problems would be solved if the bone tissues, which were originally existing at the bone defects, could be prepared artificially. It is well known that the bone tissues have the composite-like microstructures consisted of the collagen fiber bundles composed with the apatite crystals. Therefore, it is desired to develop the microstructural optimization method, which could maximize the mechanical properties of the hydroxyapatite (HAp)/collagen composite materials.

Our research group has investigated aiming to the microstructural optimization for the hierarchized HAp/collagen composite fiber bundles by the bottom-up approach, as illustrated in Figure 1. First, we had tried to optimize the density of the crosslinking agent for the collagen fibers prepared by the bio-inspired method, which is mimicking the in-vivo simultaneous reaction of the fibrosis and the crosslinking [1]. Then, we had tried to optimize the temperature and the duration of the HAp deposition

onto the surface of the collagen fibers by the biomimetic deposition method, where the collagen fibers are immersed into the calcium-ion-rich and phosphate-ion-rich solutions alternatively [2]. We also had tried to optimize the density of the osteonectin, which is an organic material as the adhesive protein for the collagen [3]. In addition, the hierarchized HAp/collagen composite fibers were bundled by the electrophoresis method and the optimization of the electrophoresis current was tried [4].

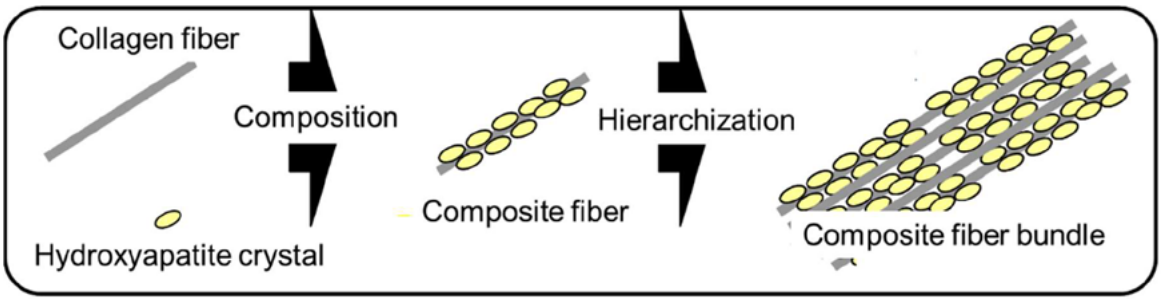

Figure 1. Schematic drawing for bottom-up approach of HAp/collagen composite fiber bundles.

These optimized microstructural factors in each hierarchy would be interacted with those in other hierarchies. In this case, the optimized microstructural factors in the smaller scale hierarchy would be not necessarily optimum in the larger scale hierarchy. This study aimed to optimize the microstructural factors of the hierarchized HAp/collagen composite fiber bundles by the parametric studies.

2. Experimental Procedures

2.1. Preparation of Collagen Fibers

In this study, the collagen peptides originated from the fishes were used to prepare the collagen fibers. In addition, the phosphate buffer phosphate buffer solution was used for pH control, the water-insoluble carbodiimide (1-ethyl-3-carbodiimide hydrochloride: EDC) was used as the crosslinking agent, and the sodium chloride was used to prevent the rapid fibrosis. First, the phosphate buffer phosphate buffer solution, EDC, and the sodium chloride of 1-2 [mol/L] were mixed into the collagen peptide solution of 0.1 [wt%]. Then, this mixed solution was warmed in the 25 [degree C] water for 7 days, followed by the storage in a refrigerator to delay the fibrosis. Here, this warming temperature is lower than the distortion temperature of the fish collagen.

2.2. Deposition of HAps

In this study, the alternate immersion was conducted using the calcium-ion rich and phosphate-ion rich solutions. The calcium-ion rich solution was prepared using the tris (hydroxymethyl) aminomethane hydrochloride, the tris-HCl buffer, and the calcium chloride. The phosphate-ion rich solution was prepared using the disodium hydrogenphosphate. The temperature of these solutions was maintained as 37 [degree C] using a constant temperature water bath. The collagen fibers were alternately immersed into these solutions, as illustrated in Figure 2.

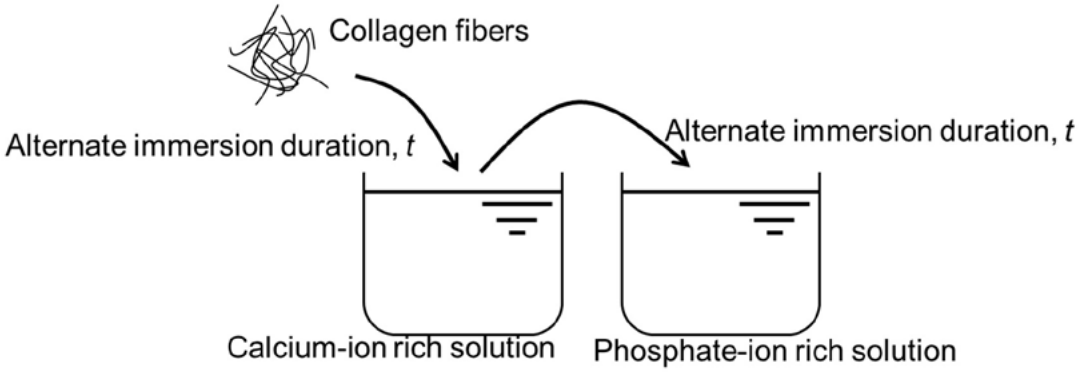

Figure 2. Schematic drawing for alternate immersion employed in this study.

2.3. Coating of Adhesive Protein

In this study, the recombinant osteonectin (SPARC/BM-40, originated from the human) was used as the adhesive protein for the coating of the HAp/collagen composite fibers. The amount of the osteonectin applied to the HAp/collagen composite fibers was 50 [μg]. This was mixed with the distilled water of 100 [μL]. First, the half amount of the osteonectin solution was applied to the collagen fibers before the deposition of the HAps using a microbullet. Then, the remained half amount of the osteonectin solution was applied to the collagen fibers after the deposition of the HAps. It was considered that the interface both between the collagen fibers and the HAps and between the HAp/collagen composite fibers was well bonded by conducting the osteonectin coating both before and after the HAp deposition, as illustrated in Figure 3.

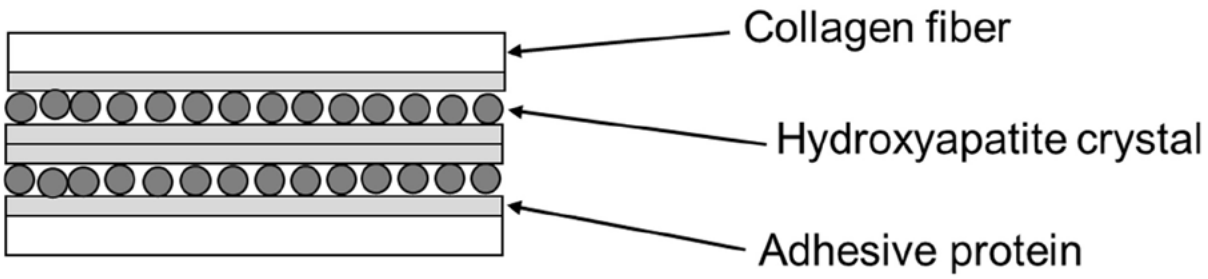

Figure 3. Schematic drawing for osteonectin coating employed in this study.

2.4. Bundling of HAp/collagen Composite Fibers

In this study, the electrophoresis was conducted to bundle the HAp/collagen composite fibers, as illustrated in Figure 4. The sodium chloride solution and the HAp/collagen composite fibers were poured into the bath of the electrophoresis device, and then the electric current was applied. Previously, the effect of the electrophoresis current on the tensile strength of the HAp/collagen composite fiber bundles without applying osteonectin was investigated [4]. The result indicated that the higher electrophoresis current would increase both the orientation and the damage of the HAp/collagen composite fibers, and the electrophoresis current of 4 [mA] maximized their tensile strength. Thus, it was suggested that this trade-off relation would determine the tensile strength of the HAp/collagen composite fiber bundles.

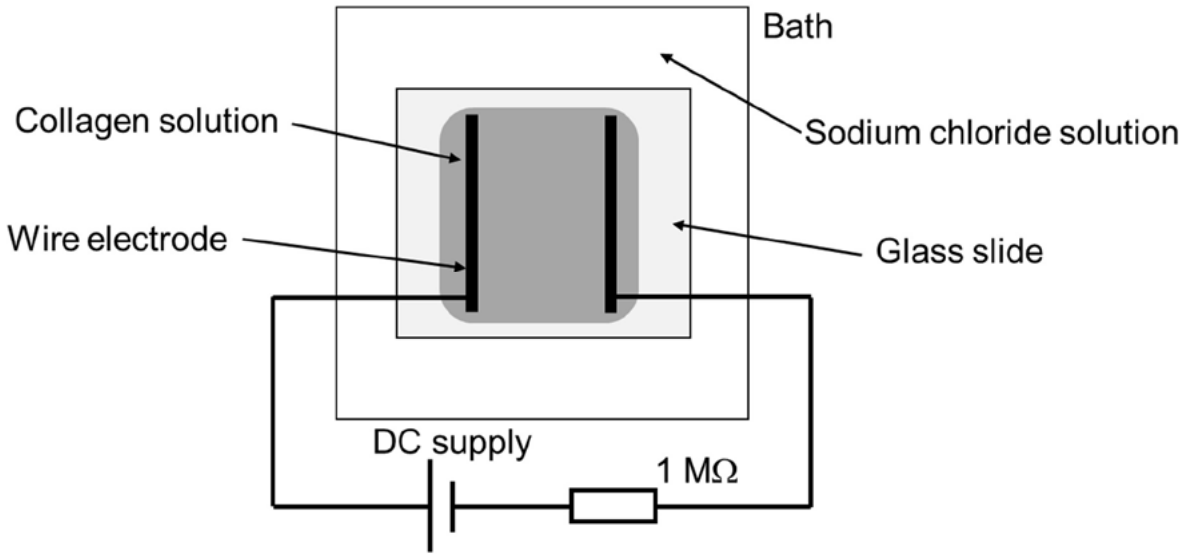

Figure 4. Schematic drawing for electrophoresis for HAp/collagen composite fibers.

2.5. Micro-tensile Test

In this study, the micro-tensile tests for the HAp/collagen composite fiber bundles were conducted using a device developed previously [1, 2, 3, 4], as illustrated in Figure 5. The extracted HAp/PLA composite

fiber bundles were adhered parallelly with a glass fiber (WFA230 100BS6, Nitto Boseki Co., Ltd.) and perpendicularly with a boron fiber (KPSI500, AVCO) in turn. The boron fiber was fixed parallelly with a spindle of a no-spin type micrometer. The glass fiber was fixed on the acrylic plate, which was coated with the release agent to decrease the friction force, perpendicularly to the boron fiber. The boron fiber was pulled by the micrometer, and the tensile deformation was applied to the HAp/collagen composite fiber bundles, and then the deflection of the glass fiber was generated. This deflection was observed using a digital microscope (VHX8000, KEYENCE) with a zoom lens (VHX-50L, KEYENCE). The magnification range of this zoom lens is 50 – 500 times. The tensile strength of the HAp/collagen composite fiber bundles was calculated using the deflection of the glass fiber based on the cantilever beam theory. Here, the cross-sectional shape was hypothesized as the circle, and the large deformation effect was ignored. During testing, the HAp/collagen composite fiber bundles was covered with water and the drying of them was prevented.

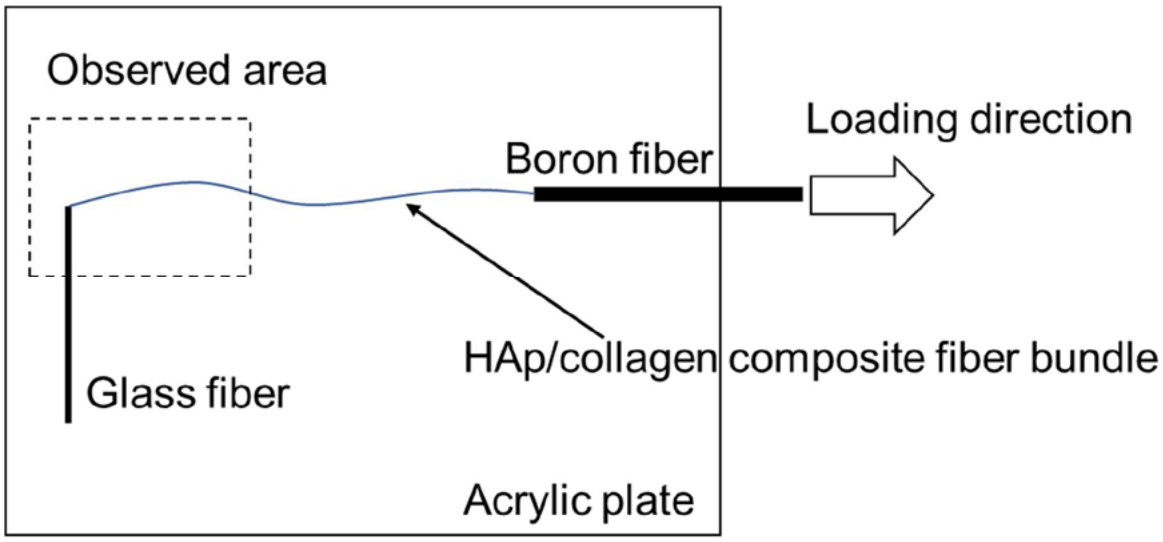

Figure 5. Schematic drawing for micro-tensile test.

3. Results and Discussion

3.1. Effect of Crosslinking-agent Density on Tensile Strength

The HAp/collagen composite fiber bundles were prepared under the alternate immersion duration of 50 [s], the electrophoresis current of 4 [mA], and the electrophoresis duration of 30 [min]. The density of the crosslinking agent was changed as 1, 3, 4, and 5 [mmol/L]. Here, the crosslinking-agent density of 5 [mmol] was the optimum condition for the HAp/collagen composite fiber bundles prepared without applying the osteonectin [4]. Figure 6 shows the effect of the crosslinking-agent density on the normalized tensile strength of the HAp/collagen composite fiber bundles. As a result, the tensile strength of the HAp/collagen composite fiber bundles was maximized when the density of the crosslinking agent was 4 [mmol/L]. This crosslinking-agent density is lower than the optimum condition for the HAp/collagen composite fiber bundles prepared without applying the osteonectin [4]. This suggests that the adhesive protein could act as the additional crosslinking agent. Thus, the tensile strength of the HAp/collagen composite fiber bundles would be maximized under the optimally balanced condition of the crosslinking agent and the adhesive protein.

3.2. Effect of Alternate Immersion Duration on Tensile Strength

The HAp/collagen composite fiber bundles were prepared under the crosslinking-agent density of 4 [mmol/L], the electrophoresis current of 4 [mA], and the electrophoresis duration of 30 [min]. Here, the alternate immersion duration was changed as 10, 30, 40, and 50 [s]. Figure 7 shows the effect of the alternate immersion duration on the normalized tensile strength of the HAp/collagen composite fiber bundles. As a result, the tensile strength of the HAp/collagen composite fiber bundles was maximized when the alternate immersion duration was 40 [s]. This suggests that the longer alternate immersion

duration would increase the amount of the deposited HAps, resulting in the increase of both the elastic modulus and the brittleness of the HAp/collagen composite fiber bundles. Thus, the tensile strength of the HAp/collagen composite fiber bundles would be determined also by this trade-off effect.

3.3. Effect of Electrophoresis Duration on Tensile Strength

The HAp/collagen composite fiber bundles were prepared under the crosslinking-agent density of 4 [mmol/L], the alternate immersion duration of 40 [s], and the electrophoresis current of 4 [mA]. Here, the electrophoresis duration was changed as 10, 20, 30, and 40 [min]. Figure 8 shows the effect of the electrophoresis duration on the normalized tensile strength of the HAp/collagen composite fiber bundles. As a result, the tensile strength of the HAp/collagen composite fiber bundles was maximized when the electrophoresis duration was 30 [min]. This suggests that the longer electrophoresis duration would increase the orientation and the adhesiveness of the HAp/collagen composite fibers. However, the excessive electrophoresis duration would increase the damage and the brittleness of the HAp/collagen composite fiber bundles. Thus, the tensile strength of the HAp/collagen composite fiber bundles would be determined also by this trade-off effect.

3.4. Effect of Adhesive-protein Density on Tensile Strength

The HAp/collagen composite fiber bundles were prepared under the crosslinking-agent density of 4 [mmol/L], the alternate immersion duration of 40 [s], the electrophoresis current of 4 [mA], and the electrophoresis duration of 30 [min]. Here, the density of the adhesive protein was changed as 0.1, 0.5, and 1.0 [μg/μL]. Figure 9 shows the effect of the adhesive-protein density on the normalized tensile strength of the HAp/collagen composite fiber bundles. As a result, the tensile strength of the HAp/collagen composite fiber bundles was maximized when the adhesive-protein density was 0.5 [μg/μL].

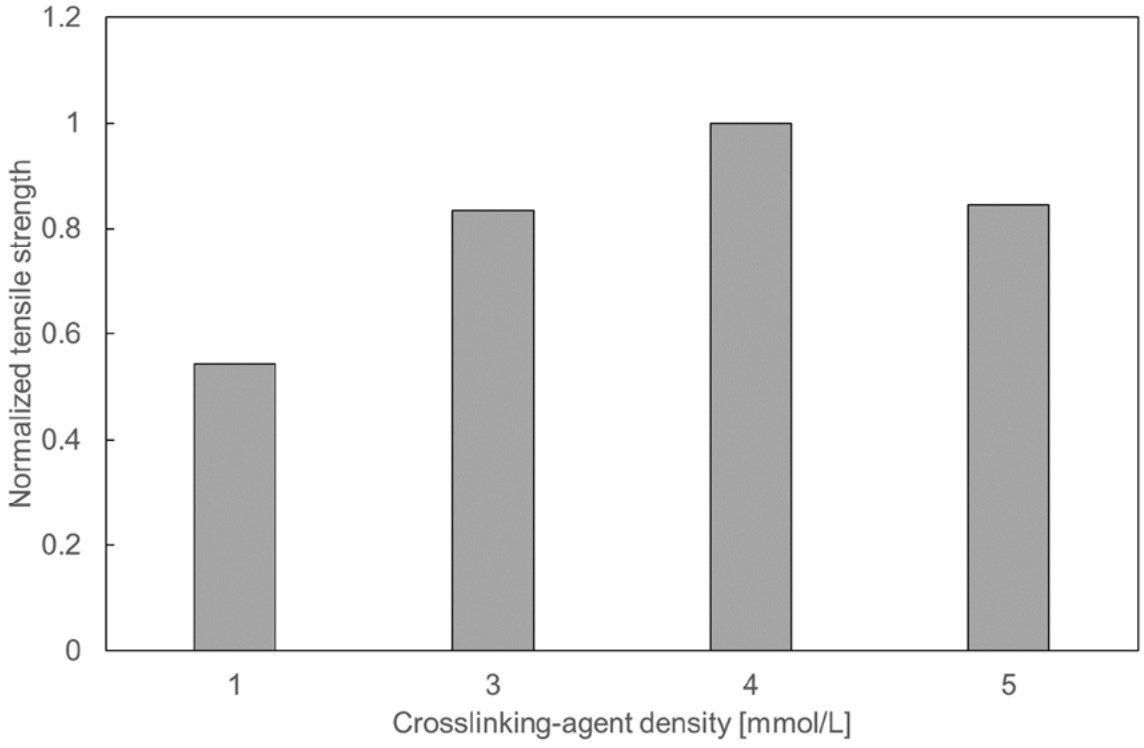

Figure 6. Effect of crosslinking-agent density on normalized tensile strength of HAp/collagen composite fiber bundles.

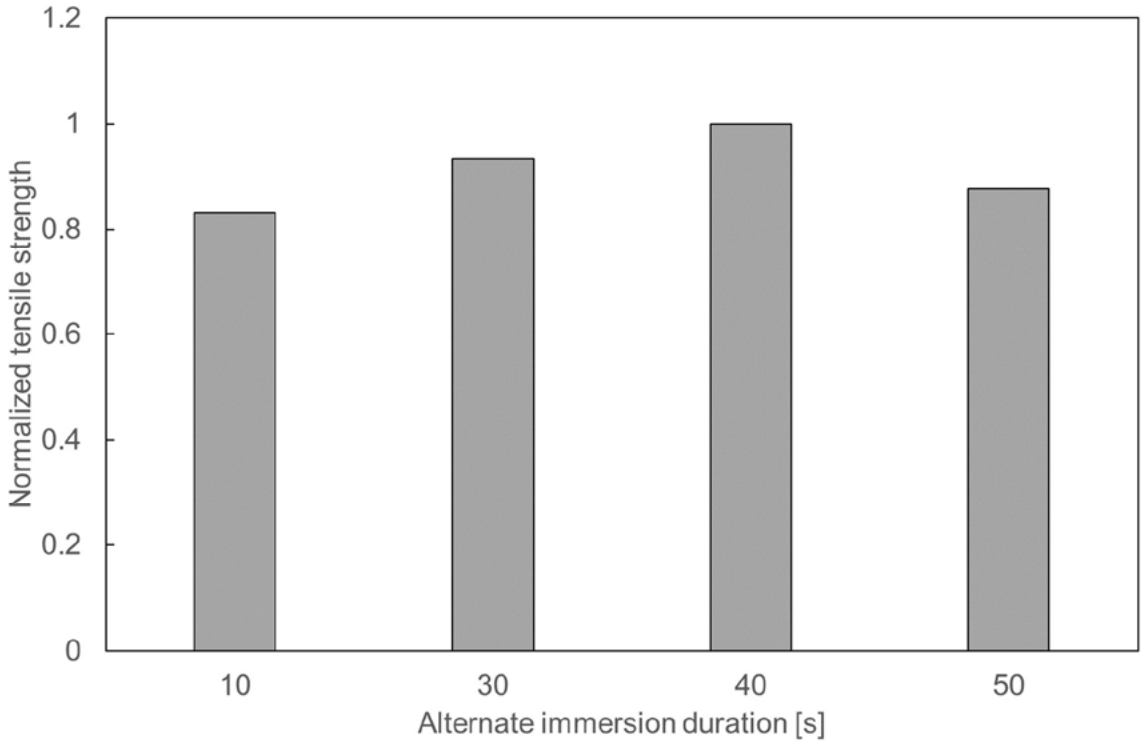

Figure 7. Effect of alternate immersion duration on normalized tensile strength of HAp/collagen composite fiber bundles.

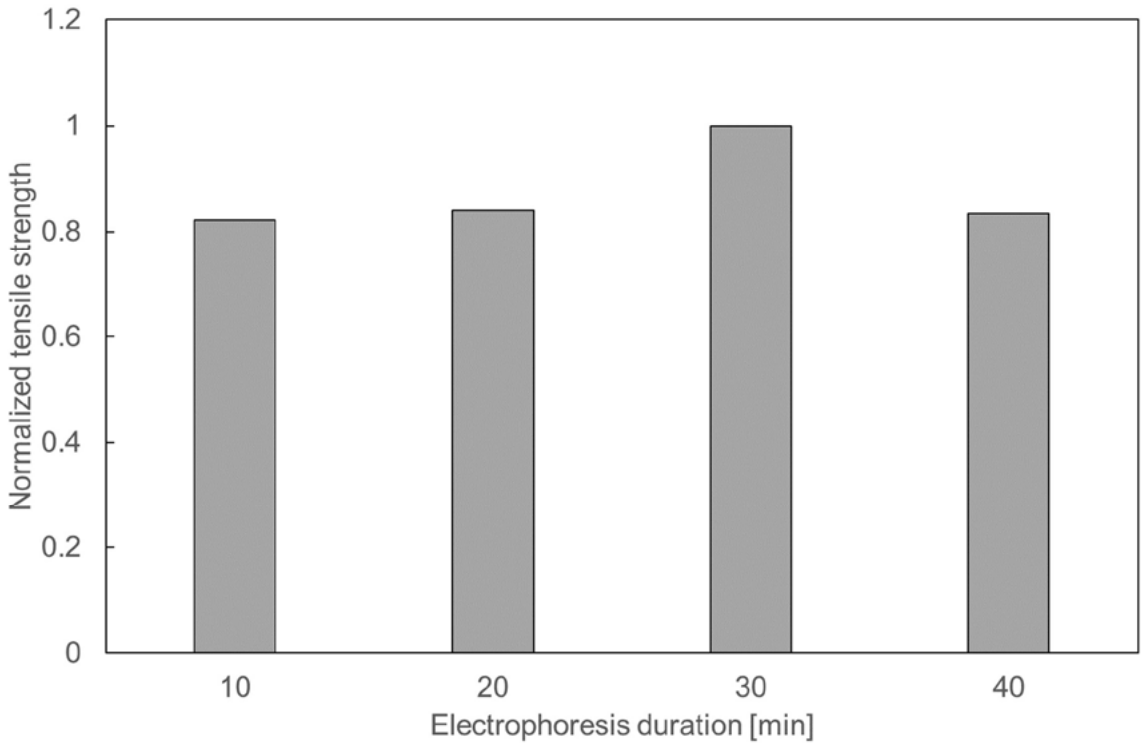

Figure 8. Effect of electrophoresis duration on normalized tensile strength of HAp/collagen composite fiber bundles.

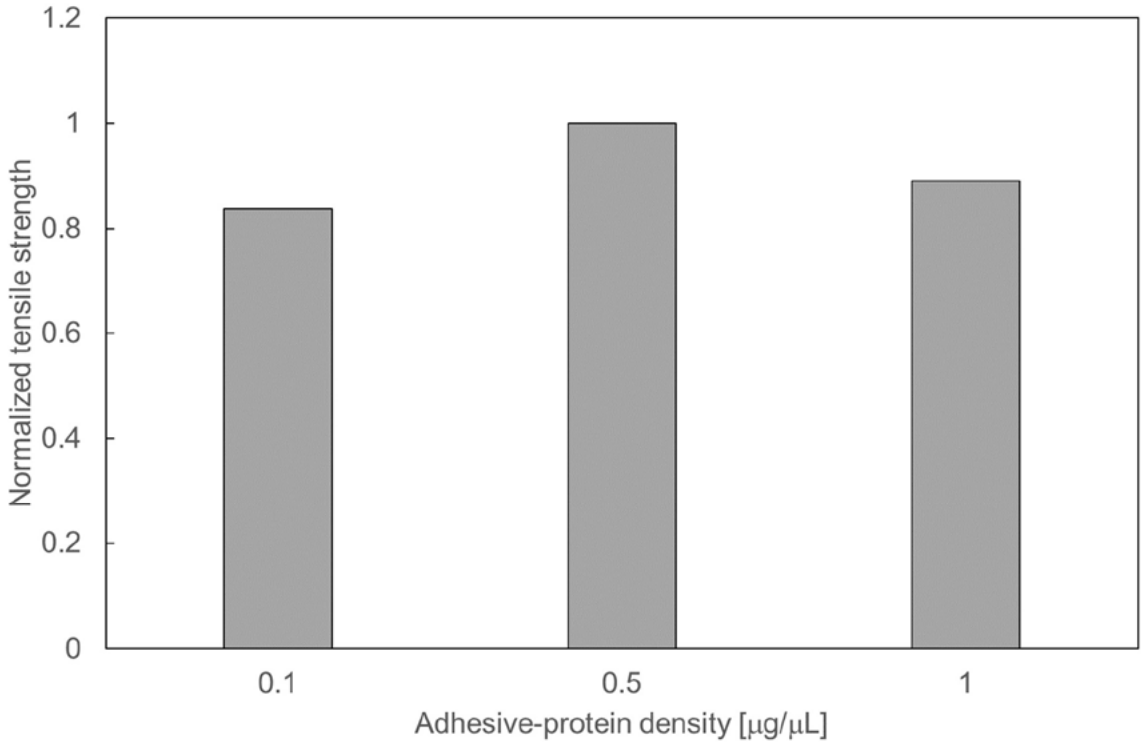

Figure 9. Effect of adhesive-protein density on normalized tensile strength of HAp/collagen composite fiber bundles.

3.5. Guideline to Maximize Tensile Strength

Finally, the tensile strength of the HAp/collagen composite fiber bundles was the highest when the alternating immersion duration, electrophoresis duration, electrophoresis current, crosslinking-agent density, and adhesive-protein density were 40[s], 30[min], 4[mA], 4[mmol/L], and 0.5[μg/μL], respectively, within the range of this study. The tensile strength of the HAp/collagen composite fiber bundles tended to increase and then decrease as the values of the microstructural factors increased. This suggests that their tensile strength would be determined by the trade-off relationships, and could be maximized under the optimized conditions determined by the interaction of the microstructural factors.

4. Conclusions

This study aimed to optimize the microstructural factors of the hierarchized HAp/collagen composite fiber bundles by the parametric studies. As a result, their tensile strength exhibited the tendency to increase and then decrease as the values of the microstructural factors increased. Therefore, the guideline for the optimum design of the microstructural factors to prepare the HAp/collagen composite fiber bundles could be determined.

Acknowledgments

This work was supported by JSPS KAKENHI Grant Number JP20K04167.

References

[1] M. Tanaka, M. Shimada, M. Nigorikawa and I. Kimpara. Investigation of Optimum Synthesis Condition of Collagen Fibers by Means of Micro-tensile Test. *Materials System*, 33:21-27, 2015, in Japanese.
[2] M. Tanaka, A. Kiyoshima, Y. Hasegawa and I. Kimpara. Influence of Alternate Dipping Condition on Tensile Strength of HAp/collagen Composite Fibers. *Materials System*, 36:25-29, 2019.
[3] M. Tanaka, Y. Hasegawa, A. Nakamura and I. Kimpara. Influence of Coating with Adhesive Protein on Tensile Strength of HAp/collagen Composite Fibers. *Materials System*, 37:37-41, 2020.

[4] M. Tanaka, K. Komatani, Y. Hasegawa and T. Ishii. Effect of Electric Current Value on the Tensile Strength of HAp/collagen Composite Fiber Bundles Prepared by Electrophoresis. *Journal of the Japan Society for Composite Materials*, 49:100-106, 2023, in Japanese.

DYNAMICS OF MOISTURE DIFFUSION IN EPOXY RESIN: EMPIRICAL AND MODELING INSIGHTS INTO ABSORPTION-DESORPTION BEHAVIOR

Hamza Tarin[1], Jamal Fajoui[1], Julie Cocaud[1], Yuan Wu[1], Pascal Casari[1], Frédéric Jacquemin[1], Amandine Célino[1], Sylvain Fréour[1], Abdellah Arhaliass[2], Ahmed Rhallabi[3], Azzam El Maasri[4]

[1] Nantes Université, Ecole Centrale Nantes, CNRS, GeM, UMR 6183, F-44600 Saint-Nazaire, France
[2] Nantes Université, CNRS, GEPEA, F-44600 Saint-Nazaire, France
[3] Nantes Université, Nantes Université, CNRS, Institut des Matériaux de Nantes Jean Rouxel, France
[4] 3CPN SARL, 81 rue des Bleuets, 44150 Vair Sur Loire, France
*hamza.tarin@univ-nantes.fr

Keywords: Epoxy resin, Fickian behavior, Dual Fickian behavior, Absorption-Desorption cycles, Finite Element Analysis (FEA), Durability

Abstract
Rapid advancements in the composite industry have led to an increase in the adoption of epoxy resins in high-pressure applications in industries such as water transport systems, due to their enhanced mechanical properties. Despite their advantages, studies have proven that water absorption in epoxy tubes can degrade their mechanical properties when subjected to extreme environmental conditions. Herein, this work characterizes the intricate dynamics of moisture diffusion kinetics in the epoxy resin subjected to severe environmental conditions, combining the experimental investigation and the numerical approach. The experimental investigation was conducted by subjecting the epoxy resin samples to cyclic hygrothermal conditions in a Temperature Humidity Test Chamber. Continuous gravimetric measurements were performed every 24 hours to track the diffusion kinetics in two moisture absorption-desorption cycles. It reveals the complex Dual-Fickian behavior in the initial absorption phase, which has transitioned to the Fickian behavior in subsequent cycles. Furthermore, the numerical analysis using ABAQUS has validated the experimental findings, highlighting the need for finer meshes to accurately predict the complex Dual-Fickian behavior in the epoxy resin.

1. Introduction

Epoxy resins have emerged as a popular material in the manufacturing process of composite pipes owing to their enhanced mechanical performances and resistance to severe environmental conditions, making them a preferred choice for high-pressure applications in oil and water transport systems [1]. They are favored over traditional materials such as steel or PVC, mainly due to their usability under high temperatures, cyclic loads, and resilience to corrosion. However, their application has been limited due to the sensitivity to moisture diffusion. Moisture absorption in the epoxy resin has been demonstrated to result in the degradation of the mechanical properties such as the decrease of its glass transition temperature and elastic modulus [1], thereby undermining the structural integrity of the pipe system.

Recent studies [1,2,3] have highlighted the complex moisture diffusion kinetics in the epoxy resin, differentiating between fickian and non-fickian behavior [2]. In real cases, the moisture diffusion process within polymers often exhibits two states, mobile and bound water [3]. Moisture diffusion in mobile state occurs when the water molecules in the environment start to migrate toward the voids, pores, or free volume of the polymer network until the saturation. While in the bound state, water molecules remain bonded to the polymer network through hydrogen bonding. This phenomenon of bound state is termed as Type I and Type II bonding. Type I bonding is a straightforward process

involving single hydrogen bonds, whereas Type II bonding is a much more complex process involving multiple hydrogen bonds. This complicated interaction between water molecules and the microscopic structures of the epoxy resin results in the higher activation energy being required to break the Type II hydrogen bonds, finally making the moisture diffusion process irreversible and leading to a more Non-Fickian behavior. The Dual-Fickian model [1,3] is often employed to characterize the Non-Fickian behavior of the epoxy resin and composites.

However, there remains a significant gap between the Non-Fickian theory and its application to numerical modeling in softwares such as ABAQUS and COMSOL. In order to accurately predict the moisture absorption-desorption behavior of the epoxy resin and resin-based composite structures, this study aims to investigate the moisture diffusion behavior of the epoxy resin subjected to cyclic hygrothermal aging conditions experimentally and numerically. The numerical model using Finite Element Analysis (FEA) will be developed to validate the experimental findings and give a deeper understanding of the Fickian and Dual-Fickian behavior of the epoxy resin.

2. Materials and experimental investigation

2.1. Cyclic moisture absorption-desorption tests

The epoxy resin (see Table 1), commonly used in composite structures in water transport applications, was studied in this work. Firstly, the samples were dried in a Binder climatic chamber (model KMF 720) at 70 °C and 7 % R.H., below the glass transition temperature (T_g) of the material, to avoid internal material damage and stabilize the mass distribution through the thickness. Subsequently, the samples were subjected to hygrothermal aging conditions until saturation in an environmental test chamber (EXCAL 5421) at 70 °C and 85 % R.H., followed by subsequent desorption and absorption cycles. Continuous gravimetric measurements were performed every 24 hours during the moisture absorption-desorption cycles, using a precision balance (model MC BA 10) to track the moisture diffusion kinetics. The moisture concentration (C(t)) at time t can be calculated as follows:

$$C(t)=\frac{m(t) - m_0}{m_0} \quad (1)$$

where m(t) is the mass of the sample measured at time t, and m_0 is the initial dried mass.

The moisture diffusion kinetics were monitored on three thin square epoxy resin samples (see Figure 1). The 2 mm thickness is much smaller than the 50 mm length and width of the sample, thus ensuring the main unidirectional diffusion along the thickness direction.

Table 1. Parameters of resin samples in cyclic moisture absorption-desorption tests.

Material	Composition	Dimensions (mm^3)
Epoxy resin	epoxy base + hardener	50×50×2.0-2.1

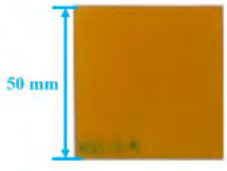

Figure 1. Epoxy resin sample (50×50 mm^2).

2.2. Experimental results and discussions

Figure 2 shows the results of cyclic moisture diffusion kinetics of a typical sample (A) among the three observed ones (A, B, C) since the three specimens exhibit a very similar moisture diffusion behavior which can be generalized. First of all, two complete moisture absorption-desorption cycles have been demonstrated, with only the first absorption phase exhibiting the Dual-Fickian behavior. The detailed discussion of each absorption and desorption phase is presented as follows:

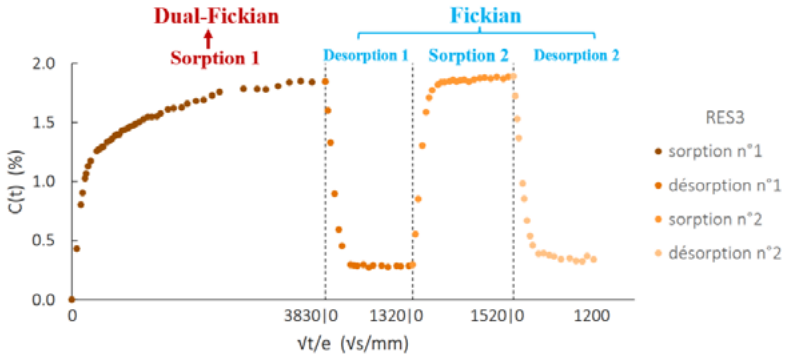

Figure 2. Two complete moisture absorption-desorption cycles of epoxy resin.

- **Sorption 1**

Firstly, the mass change obtained after a period of 23 months at 70 °C and 85 % R.H. is shown in the first absorption phase in Figure 2. It is interesting to find that the moisture diffusion kinetics of Sorption 1 exhibit the more complex Dual-Fickian behavior [3]. Generally, it is the superposition of two Fickian diffusion stages, in contrast to the typical Fickian behavior [1] with only one linear diffusion stage until the final saturation. It should be noted that the epoxy resin samples have reached their maximum absorption capacity after a period of 17 months ($\sqrt{t}/e \simeq 3200\ \sqrt{s}/mm$), ranging from 1.7 % to 2.0 %.

- **Desorption 1**

After the phase Sorption 1, the specimens were dried continuously at 70° C and 7 % R.H. for 2 months, as presented by the first desorption curve in Figure 2. The moisture content in the epoxy resin stabilizes to a non-zero value after only one week ($\sqrt{t}/e \simeq 400\ \sqrt{s}/mm$), which ranges from 0.3 % to 0.4 %. This is equal to 20 % of the saturated moisture content reached in Sorption 1. Fickian behavior is found to be the dominating behavior in Desorption 1 curve, compared to Dual-Fickian behavior in Sorption 1.

- **Sorption 2**

Subsequently, the second moisture absorption phase Sorption 2 was carried out over a shorter period of 3.5 months at 70° C and 85 % R.H. The initial moisture concentration at the start of Sorption 2 corresponds to the residual moisture content obtained at the end of the first desorption cycle. Interestingly, the moisture diffusion behavior of the epoxy resin in the second absorption phase corresponds to the Fickian model, contrary to the Dual-Fickian behavior in the first absorption phase. The saturation was reached more quickly within 10 days, compared to the longer 17 months in the first absorption phase. The saturated moisture content (between 1.8 % and 2.0 %) obtained at the end of the phase Sorption 2 was almost the same as that attained in Sorption 1. Furthermore, the saturation in Sorption 2 was reached at approximately $\sqrt{t}/e \simeq 400\ \sqrt{s}/mm$, which is similar to the phase Desorption 1. It indicates that Sorption 2 and Desorption 1 exhibit similar Fickian diffusion behavior, meaning that the moisture diffusion coefficients in these two phases may be almost the same.

- **Desorption 2**

Similarly, after the phase Sorption 2, the wet samples were dried at 70° C and 7 % R.H until saturation. Finally, the second desorption phase Desorption 2 which exhibits the Fickian behavior over a period of

2.5 months can be observed in Figure 2. The saturated moisture content was also close to that attained at the end of Desorption 1, i.e. between 0.3 % and 0.4 %.

In conclusion, the Dual-Fickian behavior in the first absorption cycle can be attributed to the superposition of two Fickian diffusion stages resulting from the complicated interactions of free and bound water with the polymer network [4]. Whereas, the first desorption phase, the second absorption phase, and the second desorption phase are dominated by the Fickian behavior mainly due to the presence of free water diffusion [5,6]. To better explain the observed moisture diffusion phenomena on the epoxy resin, the following numerical models will be developed to validate the different Non-Fickian and Fickian behavior in the two absorption-desorption cycles.

3. Numerical modeling of cyclic moisture diffusion process in epoxy resin

3.1. Dual-Fickian diffusion theory for epoxy resin

As introduced above, the Dual-Fickian behavior can be adopted to simulate the moisture diffusion process occurring within the resin and composite materials [1,3]. Generally, the Dual-Fickian model assumes that the total moisture concentration C(t) of a sample at time t can be calculated by the superposition of two Fickian stages, as shown by Eq. (2), where $C_1(t)$ represents the moisture concentration due to the first Fickian stage and $C_2(t)$ is the concentration in the second Fickian stage.

$$C(t)=C_1(t)+C_2(t) \tag{2}$$

Hence, it means that the two Fickian diffusion mechanisms work in parallel such that the mass uptake increases continuously until reaching the saturation. If the sample is a thin plate whose thickness is much smaller than the other dimensions, the moisture diffusion would mainly take place in the thickness direction. Thus, the moisture diffusion process in the epoxy resin can be simulated approximately by 1D modeling. The final Dual-Fickian model used can be written as Eq. (3) [7] :

$$C(t)=\sum_{i=\{1,2\}}\left[\left(1-\frac{8}{\pi^2}\sum_{n=0}^{\infty}\frac{1}{(2n+1)^2}\exp\left(-D_i\left(\frac{2n+1}{e}\right)^2\pi^2 t\right)\right)\times C_{Si}\right] \tag{3}$$

Where C(t) is the moisture concentration at time t; e is the thickness in the diffusion direction.

D_i and C_{Si} (i=1, 2) are the moisture diffusion coefficients and saturated concentration in two stages.

The above five parameters mainly determine the moisture diffusion rate and final saturation capacity.

3.2. Dual-Fickian model implemented in ABAQUS

In ABAQUS, the moisture diffusion kinetics within the epoxy resin can be simulated by analogy equating Fourier's law of heat with Fick's second law of diffusion. To implement the Dual-Fickian diffusion model in ABAQUS, the idea is to first perform two parallel Fickian models separately on the epoxy resin, each with its own parameter set : (D_1, C_{s1}) and (D_2, C_{s2}), as shown in Table 2. Then the final moisture concentration can be calculated by the sum of results exported from the two parallel Fickian models.

As displayed in Table 2, in the moisture/temperature diffusion analysis in ABAQUS, temperature T in the heat conduction analysis is analogous to moisture content C_i in the moisture diffusion model. To simulate each Fickian diffusion stage of the Dual-Fickian model, the thermal conductivity λ can be assumed as the moisture diffusion coefficient D_i, while the density ρ and heat capacity c_{th} in the heat conduction analysis can be set to 1 in the moisture diffusion model. The initial moisture conditions (C_{ini}) are set to zero to represent a dry state, while the boundary condition of each stage should be the same as the final saturated moisture content C_{si} obtained in the moisture absorption-desorption cycles.

Table 2. Dual-Fickian model implemented in ABAQUS using thermal-moisture analogy.

Properties		Field Variable	Parameters			Boundary condition
Thermal conduction		T	λ	ρ	c_{th}	T_{imp}
Dual-Fickian Diffusion	Stage 1	C_1	D_1	1	1	C_{s1}
	Stage 2	C_2	D_2	1	1	C_{s2}

Next, the key parameters of the Dual-Fickian model in the first absorption cycle can be obtained by fitting the experimental curves of three specimens, as shown in Table 3. Similarly, the key parameters of the Fickian model for the first desorption phase and the second absorption-desorption cycle can be calculated by fitting the experimental curves, as shown in Table 4.

Table 3. Key parameters of Dual-Fickian model in the first absorption cycle.

Parameters	D_1 (mm^2/s)	C_{s1} (%)	D_2 (mm^2/s)	C_{s2} (%)	C_s (%)
Value	$4{,}11\times10^{-6}$	1.16	$4{,}07\times10^{-8}$	0.64	1.8
Standard deviation	$\pm\ 0{,}14\times10^{-6}$	± 0.02	$\pm\ 0{,}30\times10^{-8}$	± 0.11	± 0.08

Table 4. Key parameters of Fickian model for the other cycles.

Cycles	Parameters	C_{ini} (%)	D (mm^2/s)	C_s (%)	C_{res} (%)
Desorption 1	Value	1.9	$3{,}53\times10^{-6}$	1.57	0.33
	Standard deviation	± 0.16	$\pm\ 0{,}18\times10^{-6}$	± 0.02	± 0.15
Sorption 2	Value	0.27	$3{,}70\times10^{-6}$	1.55	1.81
	Standard deviation	± 0.06	$\pm\ 0{,}15\times10^{-6}$	± 0.04	± 0.11
Desorption 2	Value	1.85	$3{,}42\times10^{-6}$	1.51	0.33
	Standard deviation	± 0.11	$\pm\ 0{,}16\times10^{-6}$	± 0.05	± 0.06

3.3. Numerical results and discussions

To validate the experimental results and improve the accuracy of predicting the complex moisture diffusion behavior of polymeric materials, the refinement of the computational modeling based on the Dual-Fickian model has been performed. Finite element models of epoxy resin samples were created by comparing two sizes of plates: 50 mm×50 mm and 25 mm×25 mm, each with a thickness of 2 mm. It aims to evaluate the influences of sample size and mesh refinement on computational efficiency and accuracy. The first idea was to employ a mesh size of 0.5 mm along the 2 mm thickness, followed by the subsequent modeling using finer meshes such as 0.4 mm and 0.25 mm (see Figure 3). It is clear that the finer mesh size exhibits a more accurate moisture concentration distribution, especially in the earlier moisture absorption/desorption stage.

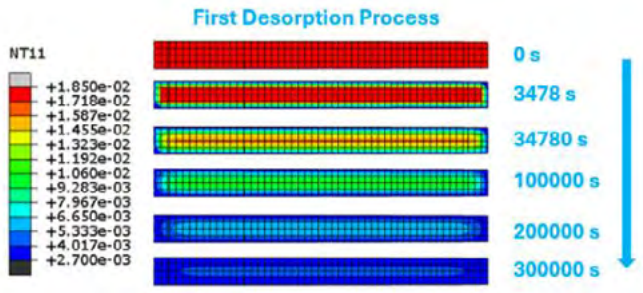

(a) Mesh size of 0.5 mm.

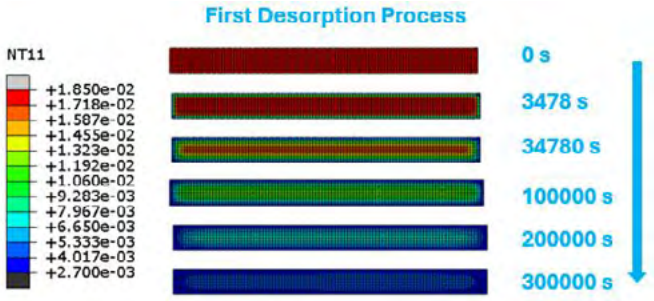

(b) Mesh size of 0.25 mm.

Figure 3. Moisture diffusion process in the phase Desorption 1.

Figure 4 plots the average moisture absorption-desorption curves obtained by the sum of two separate Fickian models in ABAQUS, with a mesh size of 0.5 mm, compared to the experimental results. Dots in the figure represent experimental results, while the smooth and dashed lines show the simulation results, with Sp and Dp signifying the phases of Sorption and Desorption, respectively. Two sizes of models with different lengths of 50 mm and 25 mm are also compared here. It is interesting to find that the moisture diffusion curves for both sample sizes show significant overlap, suggesting that the diffusion kinetics are independent of the plate size ranging from 50 mm to 25 mm. However, the computational time for the smaller 25 mm sample shows a significant decrease. To be emphasized, the numerical results in phase Sorption 1 deviate a little from the experimental curve during the earlier period, indicating a need for mesh refinement. However, good agreement with the experimental data can be found in subsequent cycles of Desorption 1, Sorption 2, and Desorption 2.

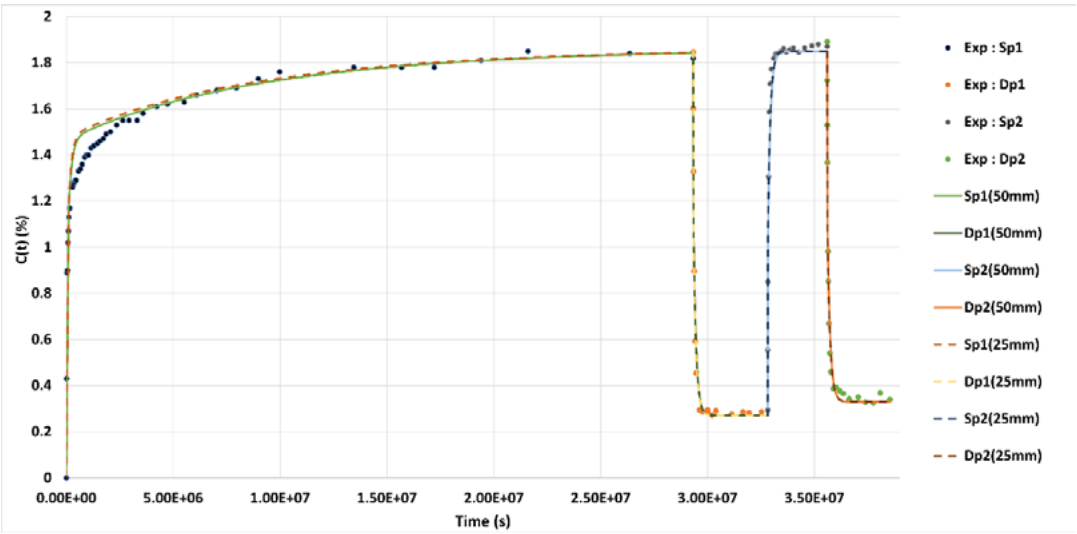

Figure 4. Modeling of moisture absorption-desorption cycles with a mesh size of 0.5 mm.

After refining the mesh size to 0.4 mm (see Figure 5), it can be observed that the curve in the first phase Sorption 1 is more consistent with the experimental results for both sample sizes. This improvement has proven that the finer mesh resolutions could lead to higher accuracy of the model, without altering the moisture diffusion behavior in the other latter cycles (Desorption 1, Sorption 2, and Desorption 2), which always remains consistent with the experimental results.

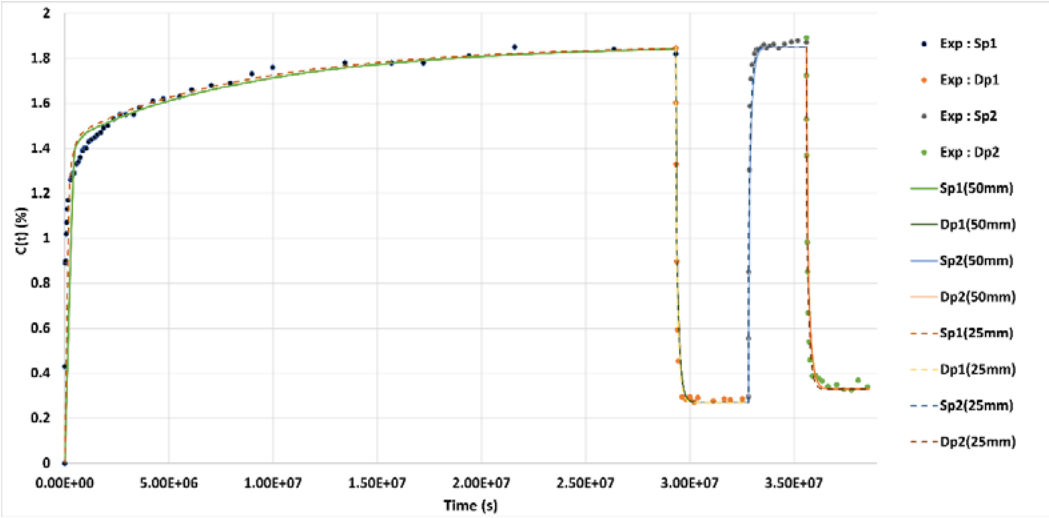

Figure 5. Modeling of moisture absorption-desorption cycles with a mesh size of 0.4 mm.

However, the simulation of the 50 mm sample could not be completed at a mesh resolution of 0.3 mm and 0.25 mm, due to the errors resulting from excessive computation time of over 4 hours. As a result, only the 25 mm model was analyzed (Figure 6), which shows that the moisture absorption curve in Sorption 1 can closely match the experimental data within a reasonable 30-minute computational time.

Thus, all results have demonstrated that reducing the sample size from 50 mm to 25 mm can effectively reduce the computational cost without compromising the accuracy. Furthermore, the finer meshes can significantly increase the fidelity of the first Dual-Fickian Sorption 1 cycle compared to the experimental data, but at the cost of increased computational time and memory.

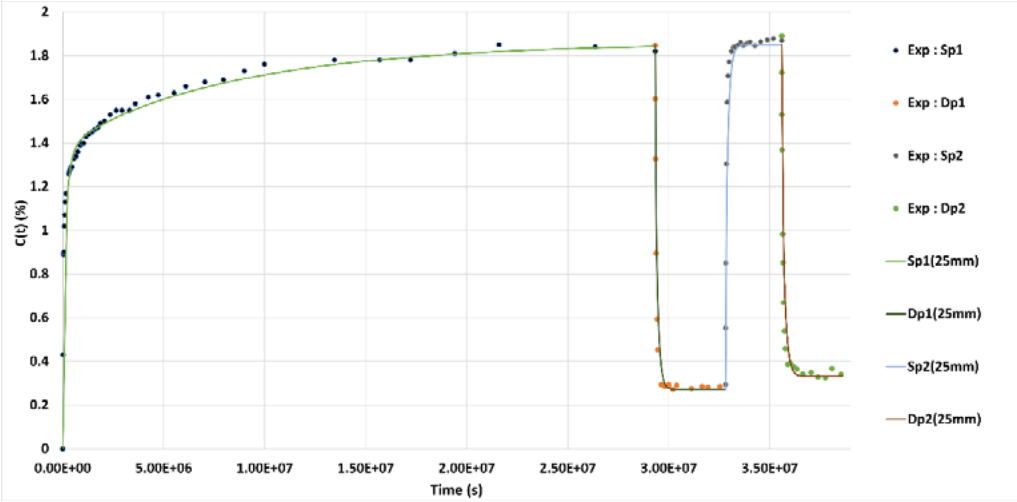

Figure 6. Modeling of moisture absorption-desorption cycles with a mesh size of 0.25 mm.

Eventually, the numerical analysis has proven that the curves (Desorption 1, Sorption 2, and Desorption 2) based on the Fickian model are independent of the mesh size. It highlights the predictable nature of moisture diffusion in the epoxy resin exhibiting the Fickian behavior. As the mesh is refined, the curve in the first phase Sorption 1 based on the Dual-Fickian model becomes increasingly in agreement with the experimental results. This improvement emphasizes the need for finer mesh analysis to accurately predict the more complex Dual-Fickian behavior in the epoxy resin.

4. Conclusions and Perspectives

In conclusion, all experimental and numerical results have given a comprehensive understanding of the intricate dynamics of the moisture diffusion process within the epoxy resin subjected to cyclic absorption-desorption aging conditions. The results of the first absorption phase Sorption 1 have verified the complexities of the Dual-Fickian behavior, whereas the subsequent cycles have exhibited the predictable and reproducible Fickian behavior. Particularly, the FEA simulations have validated the experimental results and highlighted the need for finer meshes to realize a more reliable prediction of the Dual-Fickian diffusion process. These findings can be used in the efficient material designs of pipes with the right resin formulations, resulting in an enhanced manufacturing process and a more durable and robust pipe.

However, future research should focus on integrating advanced experimental techniques such as microscopic observations to investigate the microstructural damages occurring within the material as a result of the complex nature of the Non-Fickian diffusion behavior. In addition, the role of the thickness on the moisture diffusion kinetics of the epoxy resin can be further validated using experimental and numerical methodologies.

References

[1] M. D. Placette, X. Fan, J. H. Zhao, D. Edwards. Dual stage modeling of moisture absorption and desorption in epoxy mold compounds. *Microelectron. Reliab.*, 52(7): 1401–1408, 2012.
[2] G. Bouvet, S. Cohendoz, X. Feaugas, S. Touzain, S. Mallarino. Microstructural reorganization in model epoxy network during cyclic hygrothermal ageing. *Polymer*, 122: 1–11, 2017.
[3] X. Fan and V. Nagaraj. Finite element modeling of anomalous moisture diffusion with dual stage model. In *2012 IEEE 62nd Electronic Components and Technology Conference*, San Diego, CA, USA: IEEE, 1190–1193, 2012.
[4] H. G. Carter and K. G. Kibler. Langmuir-Type Model for Anomalous Moisture Diffusion In Composite Resins. *J. Compos. Mater.*, 12(2): 118–131, 1978.
[5] K. I. Ivanova, R. A. Pethrick, S. Affrossman. Investigation of hydrothermal ageing of a filled rubber toughened epoxy resin using dynamic mechanical thermal analysis and dielectric spectroscopy. *Polymer*, 41(18): 6787–6796, 2000.
[6] F. R. Jones and J. P. Foreman. The response of aerospace composites to temperature and humidity. In *Polymer Composites in the Aerospace Industry*, P. E. Irving and C. Soutis, Eds., Woodhead Publishing, 335–369, 2015.
[7] J. Crank and J. Crank. *The Mathematics of Diffusion*, Second Edition. Oxford, New York: Oxford University Press, 1979.

SUSTAINABILITY OF HYBRID MATERIALS: APPROACHES TO MANUFACTURE AND CHARACTERIZE FIBER-METAL LAMINATES WITH ACTIVATABLE INTERFACES

Lukas Mayer[1], Joél Schukraft[1], Kay André Weidenmann[1], Anna Trauth[1]

[1] Institute for Material Resource Management (MRM), University of Augsburg, Am Technologiezentrum 8, 86159 Augsburg, Germany
Email: anna.trauth@uni-a.de

Keywords: fiber-metal laminates, interface design, interface strength, edge shear testing

Abstract
Fiber-metal laminates offer decisive advantages in use, especially considering fatigue properties, compared to monolithic materials. However, the recycling of these hybrid materials has been a challenge to date. A new approach aims to produce fiber-metal laminates with an interface that can be (re-) activated to separate the two components at the end of life. Since it is crucial to show that this inserted interlayer does not cause any significant weakening of the properties during use, this work aims to determine the interfacial properties of aluminum-carbon fiber-reinforced polymer laminates with thermoplastic-like thermoset and polystyrene interfaces by comparing them to the properties of the same fiber-metal laminate without an additional interlayer. Characterization was done by using the edge shear test to find the interlaminar shear strength of the different fiber-metal laminates. Further, it will be determined as to whether the variation of laser surface treatment parameters on the aluminum sheet influences the adhesion strength of the fiber-metal laminate.

1. Introduction

The perks of fiber-metal laminates (FMLs) are extensive, have long been discovered and utilized in various fields, particularly in the aerospace industry [1, 2]. The resistance to crack propagation, the enhanced fatigue life, and the high specific strength and stiffness, to name only a few, are all attributes that make FMLs a more than suitable candidate for primary and secondary aircraft structures. As Krishnakumar has thoroughly outlined, the list of advantages a fiber-metal laminate has over their monolithic components are extensive [3]. However, FMLs are not free of weaknesses and limitations. A prominent example is the risk of galvanic corrosion of aluminum- or titanium-based FMLs when paired with carbon fiber-reinforced polymers (CFRP) [4]. One way to overcome this drawback is the introduction of an additional (polymeric) layer, e.g. a glass fiber reinforced polymer, between the two constituents of the fiber-metal laminate [5]. As research suggests, another widely used option for this concept is the employment of an elastomer layer, creating a so called fiber-metal elastomer laminate (FMEL) [6]. In addition to counteracting corrosion, this modification to the FMLs brings further advantages. Several studies have shown that such an intermediate elastomer layer provides an improved damping and vibration behavior in an FML [7, 8]. In times of a growing environmental and sustainability awareness, the question arises as to whether the introduction of an interlayer material in an FML can be utilized to dehybridize the laminate after use to recycle the individual components at end of life. It is crucial that this inserted interface is activatable through clearly defined and controllable mechanisms and does not cause any significant weakening of the properties during use. In general, the determination of the interlaminar shear strength is a suitable method to characterize the interface and adhesion between the composite and metal [9]. Hence to investigate interface properties, the edge shear test is carried out within this study. In addition, this work aims to find out whether various parameters of the laser surface treatment of the aluminum have a significant influence on the interlaminar shear strength of the subsequent fiber-metal laminates, since influences of the surface morphology on resulting mechanical performance have already been demonstrated [10–12].

2. Experimentation

2.1. Materials

An AlMg3 aluminum alloy (EN AW-5754 H111; material no.: 3.3535) was chosen, as aluminum with a lower specific density than other metals supports the lightweight character of the CFRP and is also commonly used in FMLs for industrial applications [3, 13]. The 1 mm thick sheets were purchased from H.P. Kaysser GmbH + Co KG in the dimensions of 100 x 100 mm^2 [14]. As for the CFRP layer of the laminate the "UNIPREG® Kohlegelege 150 g/m²", a unidirectionally carbon fiber reinforced epoxy-based prepreg, was used. The use of a pre-impregnated semi-finished product (prepreg) makes sample preparation easier and more reproducible, as the semi-finished product is only cured under pressure, thus eliminating the need for time-consuming impregnation with resin [15]. Six layers of prepreg were arranged alternately in 0° and 90° to obtain a total thickness of approximately 1 mm, analogous to the thickness of the aluminum. For the first configuration of the FML a polystyrene (PS) film (Tecfilm® PS TC 00450 from Dr. Dietrich Müller GmbH), with a thickness of 0.5 mm, was inserted at the interface [16]. A second configuration considered was an interface made of a thermoplastic-like thermoset. The T-Link® (L-F610) film with a thickness of 127 µ from L&L Products Inc. was selected for this purpose. The T-Link® is a fully thermoplastic, epoxy-based adhesive film. The fact that the film develops adhesion under heat and pressure could indicate promising interfacial strength. [17] The T-Link® was stacked to form the activatable interface of a thickness of approximately 0.22 mm. In the end, three different configurations of FML were considered: Type 1: a polystyrene-fiber-metal laminate (psFML), type 2: a T-Link®-fiber-metal laminate (tFML), and type 3: a fiber-metal laminate without an additional material at the interface (FML). All laminate structures have the same configurations regarding the type of aluminum, the surface treatment of the aluminum, and the prepreg arrangement and were produced in an identical and reproducible process. Table 1 shows an overview of the structure of the three configurations.

Table 1: Laminate configuration of the three configurations: psFML, tFML, and FML.

Laminate	Thickness aluminum [mm]	Layers of CFK	Arrangement of Prepreg layers	Interlayer
psFML	1	6	$[0°/90°]_3$	Polystyrene
tFML	1	6	$[0°/90°]_3$	T-Link®
FML	1	6	$[0°/90°]_3$	-

2. Sample preparation

To ensure adhesion of the interface layer or CFRP layer to the aluminum, all aluminum sheets were surface treated with a laser before the joining process. The resulting rough surface of the aluminum enables mechanical interlocking between the polymer and the metal, which a smooth surface would not allow for [18]. The laser used for this was the "gieMARK 30+" fiber laser processing system from Gie-Tec GmbH, with a wavelength of 1064 nm. The laser power of the gieMark30+ is specified as a percentage. Here, 100% reflects the maximum possible power of the laser, 30W. [19] The frequency in kHz indicates how many laser pulses hit the surface per second. Together with the scan speed, which indicates how many mm of distance the laser covers in one second, it is therefore possible to influence how much the individual laser pulses overlap and how intensively the surface is treated. [20]

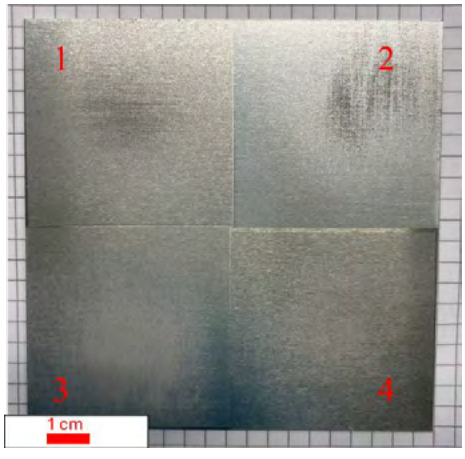

Figure 1: Surface treated aluminum sheet with the variants 1 (top left), 2 (top right), 3 (bottom left), and 4 (bottom right).

The jump speed (mm/s) provides information about the speed at which the laser jumps from one point to the next. The spot size in µm describes the beam diameter and the track spacing (also in µm) the distance between a series of laser pulses. [19, 20] To determine the influence of the line spacing of the laser treated aluminum surface, the line spacing must be greater than the spot size of the laser, otherwise the tracks overlap and thus ensure a completely melted surface. The line spacing was increased by 10 µm per variant, but should not exceed 100 µm, as too large a spacing can reduce the strength of joints, as was the case in [10]. Based on the results from [10] and [12], track spacings of 50 µm, 60 µm, 70 µm and 80 µm and a scanning speed of 1000 mm/s were selected. Table 2 provides an overview of the four sets of laser parameters (Variant 1 – Variant 4) considered for the surface treatment of the aluminum sheets. To ensure the best possible comparability and at the same time an efficient manufacturing process, these four parameter sets were realized on a sheet size of 10 x 10 mm^2 from which specimens for mechanical testing were extracted in a following step (Figure 1). This meant that all four parameter sets listed in Table 2 could be produced and cut out from one FML.

Table 2: Laser process parameters.

	Power [%]	Frequency [kHz]	Scan speed [mm/s]	Jump speed [mm/s]	Spot size [µm]	Line spacing [µm]
Variant 1	80	120	1000	1000	40	50
Variant 2	80	120	1000	1000	40	60
Variant 3	80	120	1000	1000	40	70
Variant 4	80	120	1000	1000	40	80

To join the surface treated aluminum sheets with the CFRP and the interface layer in between, a joining process was carried out with a heating press. First, the three different materials were arranged in a metal die coated with a PTFE glass fabric film: First the aluminum sheet, then the polystyrene film, or the T-Link® and then, the six alternating CFRP layers cut from a large prepreg roll. The PTFE film on the die serves as a non-stick layer and prevents the die from being contaminated due to the leakage of liquid polystyrene, T-Link® or epoxy resin. To ensure that the heating press also remains clean, the die was wrapped in aluminum foil after sealing. The joining process was carried out in a LaboPress P200S from VOGT Labormaschinen GmbH [21]. The process temperatures were derived from the processing temperatures of the T-Link® recommended by the manufacturer (140 -176 °C), which were also sufficiently hot for the polystyrene and prepreg [17]. Thus, the heating process was as follows: With the die already placed on the heating plates, the press was heated to 160 °C. Then a pressure of 8.5 bar was applied and held for 25 minutes. Afterwards the cooling of the press was switched on, while the pressure was still being applied. This was held for another 25 minutes. As the selected temperature in this joining process guaranteed successful melting of both the PS and the T-Link® layer, this procedure was kept the same for all FML configurations for better comparability. After removing the fiber-metal laminate optical investigation showed that the CFRP was fully cured and complete adhesion between all laminate components was achieved. Afterwards, a water jet cutter from WAZER, Inc. was used to cut specimens out of the laminates [22]. Based on the tests from [11], sample dimensions of 20 x 10 mm^2 were determined. However, as the samples had to be plane for the edge shear test and the water jet cutter cut with small tolerances, dimensions of 22 x 12 mm^2 were initially created, which were then ground to 20 x 10 mm^2 with a Stuers Tegramin 25 grinding machine [23].

2.3. Edge shear test

The edge shear test was used together with 3D Digital Image Correlation (DIC) to determine the interface properties of all FML configurations. The edge shear test is an apparatus, that enables the determination of the interlaminar shear strength of composite materials, such as fiber-metal laminates and was patented by Weidenmann et.al. [24]. The structure and mode of operation are as follows (cf. Figure 2): The specimen (9) is placed in a test area between the two clamping blocks (7). The blocks can be moved relative to the cutting edges (5) using the adjusting screws (4) to place the interface of the FML in the shear plane (between the blocks). Care must be taken to ensure that the blocks are neither pressed too hard nor too softly against the sample. Too much pressure can cause unwanted frictional

forces and mar the result, while too little pressure can cause the sample to tilt. The device is connected to the force transducer of the testing machine via the adapter (1). This allows the upper part (3) to be moved relative to the lower part (8) along the guide rods (2) by moving the testing machine crosshead up and down. If the upper part is lowered so that the cutting edges rest on the specimen, they exert a shear force on the specimen [24, 25]. The advantages of the edge shear test include the flexible adaptability to different specimen dimensions and the direct transfer of the shear load to the specimen, which causes a reliable shear failure and thus allows the interface properties to be identified [11, 24, 25]. The edge shear test was installed in the Z250 universal testing machine from ZwickRoell GmbH & Co. KG. The load cell of this machine enables a maximum force of 250 kN [26]. To achieve quasi-static test conditions, the test speed was set to 1 mm/min as in [11] and [27]. The test procedure was position-controlled, was initiated with a pre-force of 20 N and ended with a force cut-off threshold of 80% of the maximum force. For the DIC an Aramis 12M camera system from Carl Zeiss GOM Metrology GmbH with two cameras, together with the GOM Correlate Pro software from the same company were used to record and analyze the images [29]. The DIC system was connected to the testing machine via an I/O card, which transmitted the force and displacement signal in the form of a voltage signal, thus enabling the two systems to be synchronized in time. When the preload was reached, the voltage signal served as a trigger to start recording the measurement of both devices. Recordings were made with an acquisition rate of 10 Hz and an exposure time of 5 ms. The cameras were equipped with 50 mm lenses and placed approximately 30 cm in front of and at an angle of 25° to the sample.

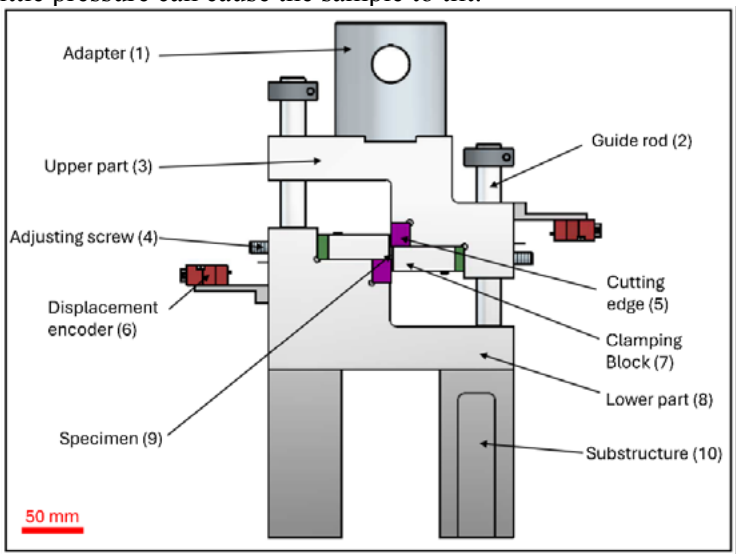

Figure 2: Labeled CAD-drawing of the edge shear test - test rig, adapted from [28].

3. Results and Discussion

The results of the edge shear test are displayed in Figure 3 by a force and displacement diagram of all three configurations of FML tested. These two parameters are the output of the Zwick test machine and offer an insight on the interfacial properties of all tested FMLs. The shear strain of the FMLs was measured by the 3D Digital Image Correlation, however, since the DIC was only introduced at a later stage of the research process and was not used with all parameter sets, the results of the Zwick test machine offer a broader overview of the findings. Therefore, only an individually selected depiction of the shear behavior (ϵ_{XY}) of the FMLs will be shown. During the evaluation of the results, several curves had to be slightly shifted for a meaningful comparison. As already mentioned in chapter 2.3, the recording of the results was initiated by a pre-force, however, at times, the test machine would start recording while remaining at this force, resulting in a flat slope and thus, distorting the actual outcome. A reason for this effect might be a further aligning of the sample within the fixture. This flat run up was eliminated by setting the new starting point of the force-displacement curve eliminating the delayed load application. Further, for the tFMLs the end of the experiment was defined by the first fracture within the laminate that corresponds to a significant load drop. After this point, the test machine was still recording deformation under a decreasing load. This was due to the fact, that with the T-Link® interlayer, the interface as well as the aluminum significantly deformed (cf. Figure 7) and no failure at the interface took place. This part of the force-displacement curves is not depicted in Figure 3. For alle three fiber-metal laminate configurations, the maximum load experienced by the sample was considered to evaluate the mechanical characteristics.

Figure 3 shows how the different interlayers influence the mechanical properties of the fiber-metal laminates, displaying all four laser parameter variants. While the T-Link® interlayer enhances the strength of the interface by reaching higher maximum loads, the deformation also significantly increases which indicates high deformation of the polymeric interface. The FML with the polystyrene interlayer shows slightly lower interface strengths, than the FML with no additional interlayer. This is in line with the assumption from chapter 2.1 that because the T-Link® develops adhesion during processing, it can improve the interfacial properties of the laminate.

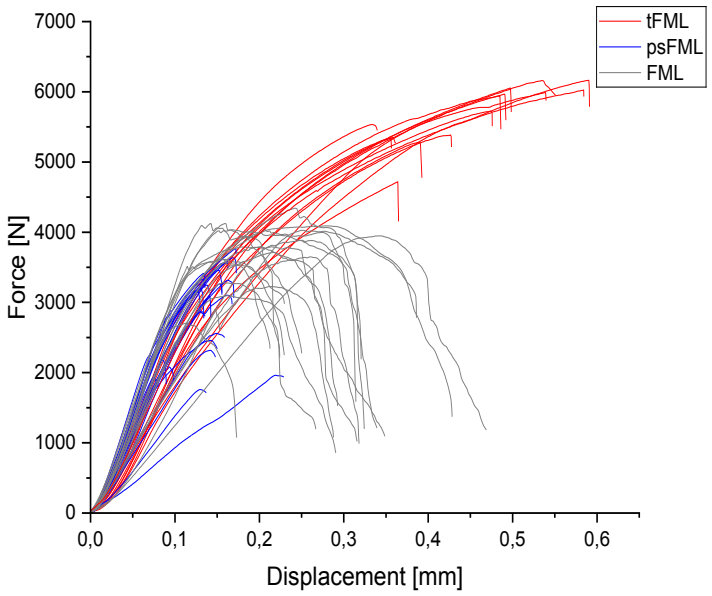

Figure 3: Force-Displacement curves of the three FMLs: tFML (red), psFML (blue), and FML (grey) including all four laser parameter variants.

Furthermore, the fracture behavior of the FML configurations can be deduced from Figure 3. The psFMLs and tFMLs fractured at the point of maximum load applied on the specimen, causing a sudden drop in force, while for the FMLs the interlaminar shear strength is not represented by a peak, but instead takes on a rounded curve. The failure of the interface occurs gradually during stress drop. For a more significant interpretation of the interfacial strength and evaluation of the influence of the laser treatment of the aluminum sheets, the interlaminar shear strength was calculated for all FML configurations using the maximum applied test load (F_{max}) related to the sheared area (given by length l and width b off the specimens):

$$\tau_{max} = \frac{F_{max}}{l \times b} \quad (1)$$

Figure 4 depicts the interlaminar shear strength (arithmetic mean value and standard deviation) for all variants of laser process parameters. It must be noted that the experiments were carried out as part of preliminary tests in which not all process steps had yet been optimized and therefore not all manufactured specimens were suitable for the edge shear test. Hence, the parameter sets tFML_1, tFML_2, tFML_3 and FML_1 feature a lower number of samples than the others and can therefore not be regarded as statistically validated. Thus, there is no standard deviation value for tFML_2, since only one sample was tested. Nevertheless, it can be said that there is no statistically significant difference between the laser treatment parameters. Within one FML configuration no parameter set results in a significant variation of interlaminar shear strength. Albeit, lying within the margin of error of other sets, the parameter set “3” offers the highest mean interlaminar shear strength for two out three FML configurations (tFML and FML). In addition, since standard deviation is lower for parameter set “2” for psFML and FML, this parameter set is also promising. To determine the shear strain of the FMLs the GOM Correlate Software of the DIC was used. With GOM Correlate, a three-dimensional rectangular surface component was generated over the length and width of the FML-interfaces to calculate the arithmetic mean of the shear strain in the XY-direction of the shear plane (ϵ_{XY}).

Figures 5 offers a detailed look of the failure behavior of the sample tFML_1e opposed to shear loading, that stands characteristic for the failure behavior of the fiber-metal laminates with a T-Link® interlayer. Point a) marks the starting point of a steep linear elastic slope, with very little strain on the sample. As can be seen at b) first signs of a shear strain (indicated by a yellow discoloration in the region of the interface) can be detected with the beginning of plastic deformation and it further increases while the curve starts to flatten (c).

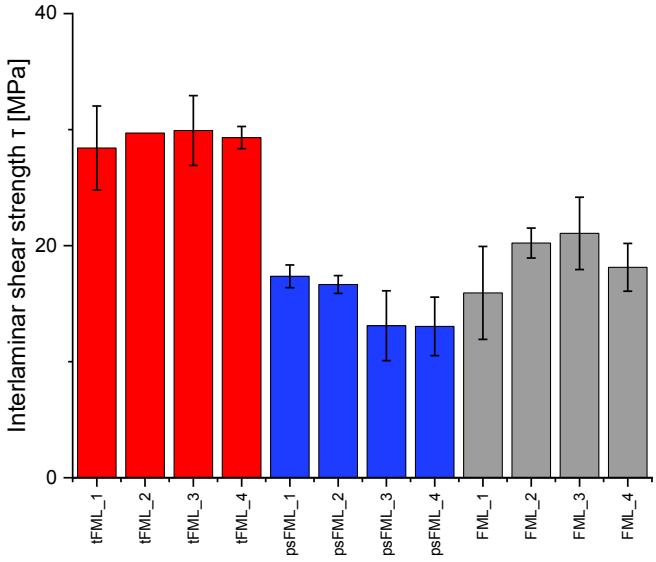

Figure 4: Interlaminar shear strength (arithmetic mean and standard deviation) of all FML configurations.

Point d) marks the maximum stress and therefore the interlaminar shear strength of the specimen. The drop in stress and the fractured and delaminated sample is shown at e). Looking at Figure 6, the delamination of the sample can be detected by the tear in the surface component generated by the GOM Correlate software, at the top of picture d) and e). These tears arise with an increasing deformation of the specimen, as the reference points on the sample move further apart and at the point of fracture are no longer detected as part of the initial surface component.

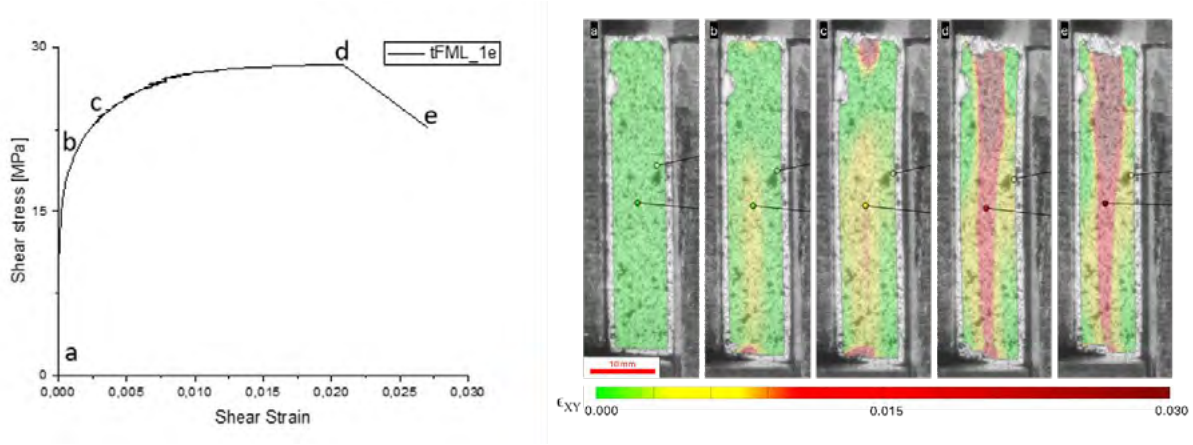

Figure 5:
Left: Exemplary shear stress and shear strain curve of the tFML_1e sample, labeled with characteristic areas (e indicates the sequential sample number of laminate type tFML with variant 1 of the laser parameter sets).
Right: Characteristic shear behavior (ϵ_{XY}) of tFML interfaces recorded by the DIC, shown by sample tFML_1e, with corresponding labels to Figure 5.

Further insights on the fracture behavior of the FMLs can be gathered from Figure 6, displaying samples of the psFML, tFML and FML configurations after they have been sheared in the edge shear test. While a) displays the plastic deformation of the aluminum after the edge shear test, b), c) and d) show the failure types of the laminates. The tFML (b) can be categorized as a cohesive failure, indicated by T-Link® marks on both components.

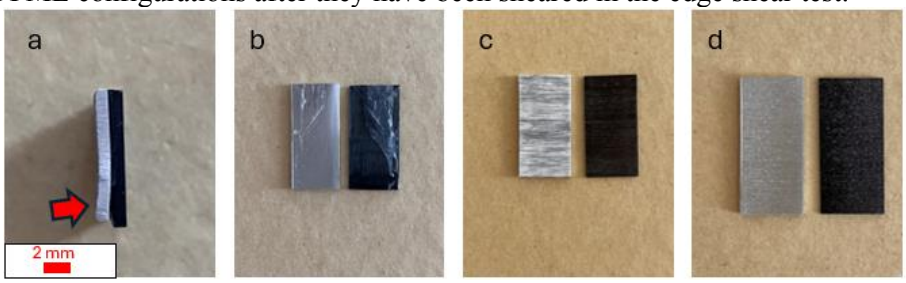

Figure 6: Side view of sheared tFML with deformed aluminum (a), top view of sheared tFML (b), sheared psFML (c), sheared FML (d).

For the psFML (c) and FML (d) adhesive failure occurred, with the psFML always delaminating between the polystyrene and CFRP layer. This may be due to the interlocking effect between the polystyrene and the laser treated aluminum surface, providing a better adhesion than between the PS and the CFRP. The fibers on the polystyrene layer (c) might stem from the hot press process and do most likely not indicate substrate failure of the CFRP.

4. Conclusions

In this work, the mechanical properties of fiber-metal laminates (FMLs) with T-Link® and polystyrene interlayers were investigated and characterized by determining the interlaminar shear strength of the laminates using the edge shear test. As part of this experiment, it was tested weather different laser surface treatment parameters influence the adhesion between aluminum and the adhering material. While no laser treatment parameter set lead to a significantly higher interlaminar shear strength of the FML variants than the other, parameter set “3” could be regarded as a suitable configuration for further research processes. In terms of mechanical properties and the interlaminar shear strength, the T-Link® interlayer provides a significant improvement over the FML without an additional material at the interface, while the psFML exhibits slightly lower interfacial properties. However, if the polystyrene can be utilized to successfully dehybridize the fiber-metal laminate it might still be a suitable candidate for certain applications with lower load forces, as the interlaminar shear strength comes close to the one of the FML.

Acknowledgments

The authors would like to thank the technicians of the Materials Resource Management Institute Augsburg for their time and help during the experimental procedures in the test laboratory.

References

[1] E. C. Botelho *et al.*, "A review on the development and properties of continuous fiber/epoxy/aluminum hybrid composites for aircraft structures," *Mat. Res.*, Jg. 9, Nr. 3, S. 247–256, 2006. doi: 10.1590/S1516-14392006000300002.
[2] R. C. Alderliesten and R. Benedictus, "Fiber/Metal Composite Technology for Future Primary Aircraft Structures," *Journal of Aircraft*, Jg. 45, Nr. 4, S. 1182–1189, 2008. doi: 10.2514/1.33946.
[3] S. Krishnakumar, "Fiber Metal Laminates — The Synthesis of Metals and Composites," *Materials and Manufacturing Processes*, Jg. 9, Nr. 2, S. 295–354, 1994, doi: 10.1080/10426919408934905.
[4] L. Hamill *et al.*, "Galvanic Corrosion and Mechanical Behavior of Fiber Metal Laminates of Metallic Glass and Carbon Fiber Composites." *Adv Eng Mater*, Jg. 20, Nr. 2, 2018, Art. Nr. 1700711. doi: 10.1002/adem.201700711.
[5] J. Bieniaś *et al.*, "Interlaminar Shear Strength and Failure Analysis of Aluminium-Carbon Laminates with a Glass Fiber Interlayer after Moisture Absorption," *Materials*, Early Access. doi: 10.3390/ma13132999.

[6] S. Roth *et al.*, "Material - and Process Characterization of Fibre-Metal-Elastomer Laminate Composites with high forming degrees, " in: *Technologies for economical and functional lightweight design: Conference proceedings,* K. Dröder und T. Vietor, Hg., Berlin, Heidelberg: Springer Vieweg, 2019, S. 147–154.
[7] V. Sessner *et al.*, "Damping Characterization of Hybrid Carbon Fiber Elastomer Metal Laminates using Experimental and Numerical Dynamic Mechanical Analysis," *J. Compos. Sci.*, Jg. 3, Nr. 1, S. 3, 2019. doi: 10.3390/jcs3010003.
[8] W. V. Liebig *et al.*, "Numerical and experimental investigations of the damping behaviour of hybrid CFRP-elastomer-metal laminates," *Composite Structures*, Jg. 202, S. 1109–1113, 2018. doi: 10.1016/j.compstruct.2018.05.051.
[9] C. Bellini *et al.* "Interlaminar shear strength study on CFRP/Al hybrid laminates with different properties," *Frattura ed Integrità Strutturale*, Jg. 14, Nr. 51, 2020, Art. Nr. 7. doi: 10.3221/IGF-ESIS.51.32.
[10] F. Moroni *et al.*, "Influence of laser treatment parameters on the mode I strain energy release rate of aluminum double cantilever beam joints," *International Journal of Adhesion and Adhesives*, Jg. 83, S. 31–40, 2018, doi: 10.1016/j.ijadhadh.2018.02.023.
[11] C. Zinn *et al.,* "Shear edge tests: a benchmark in investigating the influence of different surface pretreatment methods on the shear stress of intrinsically manufactured metal-CFRP hybrids," *IJAUTOC*, Jg. 2, 3/4, 2016, Art. Nr. 84321, doi: 10.1504/IJAUTOC.2016.084321.
[12] M. Alfano *et al.* "Study on the role of laser surface irradiation on damage and decohesion of Al/epoxy joints," *International Journal of Adhesion and Adhesives*, Jg. 39, S. 33–41, 2012. doi: 10.1016/j.ijadhadh.2012.03.002.
[13] C. Koblmiller, "Werkstoffe im Leichtbau: Aluminium," *Leichtbauwelt*, 25. Oktober 2022. https://www.leichtbauwelt.de/werkstoffe-im-leichtbau-aluminium/. Zugriff am: 17. April 2024.
[14] https://www.laserteile4you.de/materialien/aluminium/. Zugriff am: 17. April 2024.
[15] https://www.r-g.de/art/192150050-UUD-PP. Zugriff am: 17. April 2024.
[16] https://www.mueller-ahlhorn.com/produkte-materialien/material/technischen-folien/ps-polystyrol-folien/. Zugriff am 24. Mai 2024
[17] https://dhsutherland.com/wp-content/uploads/2019/02/L-F610-TDS.pdf. Zugriff am: 18. April 2024.
[18] W.-S. Kim *et al.*, "Evaluation of mechanical interlock effect on adhesion strength of polymer–metal interfaces using micro-patterned surface topography," *International Journal of Adhesion and Adhesives*, Jg. 30, Nr. 6, S. 408–417, 2010. doi: 10.1016/j.ijadhadh.2010.05.004.
[19] https://gie-tec.de/produkt/giemark30/. Zugriff am: 23. April 2024.
[20] A. Kurtovic, "Laserinduzierte Nanostrukturierung von Titanoberflächen für das strukturelle Kleben: Einfluss auf die Oberflächenmorphologie, Ermüdungs- und Adhäsionseigenschaften," Dissertation, Fakultät für Maschinenbau, Universität Paderborn, Paderborn, 2014.
[21] https://www.vogt-labormaschinen.de/laborpressen-laborpresse/labopress-model-p200s/. Zugriff am: 26. April 2024.
[22] https://wazer.com/product/tech-specs/. Zugriff am: 29. April 2024.
[23] https://www.struers.com/de-DE/Products/Grinding-and-Polishing/Grinding-and-polishing-equipment/Tegramin. Zugriff am: 30. April 2024.
[24] K. A. Weidenmann *et al.*, "Vorrichtung und ein Verfahren zur Bestimmung der Scherfestigkeit und des Schermoduls von Verbundwerkstoffen," EP3073244A1, 16401020.9, Sep 28, 2016.
[25] K. A. Weidenmann *et al.*, "The Edge Shear Test - An Alternative Testing Method for the Determination of the Interlaminar Shear Strength in Composite Materials," *Materials Science Forum*, Jg. 825-826, S. 806–813, 2015. doi: 10.4028/www.scientific.net/MSF.825-826.806.
[26] https://www.zwickroell.com/fileadmin/content/Files/SharePoint/user_upload/PI_DE/02_757 Material_Pruefmaschine_AllroundLine_Z250_PI_DE.pdf. Zugriff am: 30. April 2024.
[27] M. Stoll *et al*., "Optimization of corrosive properties of carbon fiber reinforced aluminum laminates due to integration of an elastomer interlayer," *21st Symposium on Composites, 2017; Bremen; Germany; Ed.: A. S. Herrmann*, S. 287–293, 2017. doi: 10.4028/www.scientific.net/KEM.742.287.
[28] Karlsruher Institut für Technologie (KIT) und Institut für Angewandte Materialien (IAM). "SSV Neubau."
[29] https://www.gom.com/de-de/produkte/3d-testing/aramis-adjustabl Zugriff am: 1. Mai 2024.

MXENES EMBEDDED PLA NANOCOMPOSITES FOR CHALLENGING VERSATILE APPLICATIONS

Vasileios Tzatzadakis[1], Alexandros Thomos[2], Franceska Gojda3, Fanourios Krasanakis[4], Athanasios Skouras[5], Athina Patelarou[6], Michail Zografakis-Sfakianakis[7], Konstantinos Giakoumidakis[8], Kiriaki Chrissopoulou[9], Spiros H. Anastasiadis[10], Evridiki Patelarou[11], Minas M. Stylianakis[12]

[1]Department of Nursing, School of Health Sciences, Hellenic Mediterranean University, Heraklion, Greece
Email: vtzatzadakis@hmu.gr, Web Page: https://nurs.hmu.gr/en/research-staff/
[2]Institute of Electronic Structure and Laser, Foundation for Research & Technology-Hellas, Heraklion, Greece
Email: alexandrosthomos@iesl.forth.gr, Web Page: https://www.iesl.forth.gr/en/people/thomos-alexandros
[3]Institute of Electronic Structure and Laser, Foundation for Research & Technology-Hellas, Heraklion, Greece,
Email: Fgkointa@iesl.forth.gr, Web Page: https://www.iesl.forth.gr/en/people/gkointa-frantzeska
[4]Institute of Electronic Structure and Laser, Foundation for Research & Technology-Hellas, Heraklion, Greece
Email: fanisk@iesl.forth.gr, Web Page: https://www.iesl.forth.gr/en/people/krasanakis-fanourios
[5]Department of Nursing, School of Health Sciences, Hellenic Mediterranean University, Heraklion, Greece
Email: askouras@hmu.gr, Web Page: https://www.researchgate.net/profile/Athanasios_Skouras
[6]Department of Nursing, School of Health Sciences, Hellenic Mediterranean University, Heraklion, Greece
Email: apatelarou@hmu.gr, Web Page: https://nurs.hmu.gr/en/patelarou-athina/
[7]Department of Nursing, School of Health Sciences, Hellenic Mediterranean University, Heraklion, Greece
Email: mzografakis@hmu.gr, Web Page: https://nurs.hmu.gr/zografakis-sfakianakis-michalis/
[8]Department of Nursing, School of Health Sciences, Hellenic Mediterranean University, Heraklion, Greece
Email: kongiakoumidakis@hmu.gr, Web Page: https://nurs.hmu.gr/giakoumidakis-konstantinos/
[9]Institute of Electronic Structure and Laser, Foundation for Research & Technology-Hellas, Heraklion, Greece
Email: kiki@iesl.forth.gr, Web Page: https://www.iesl.forth.gr/en/people/chrissopoulou-kiriaki
[10]Institute of Electronic Structure and Laser, Foundation for Research & Technology-Hellas, Heraklion, Greece
Email: spiros@iesl.forth.gr, Web Page: https://www.iesl.forth.gr/en/people/anastasiadis-spiros
[11]Department of Nursing, School of Health Sciences, Hellenic Mediterranean University, Heraklion, Greece
Email: epatelarou@hmu.gr, Web Page: https://nurs.hmu.gr/en/patelarou-evridiki/
[12]Department of Nursing, School of Health Sciences, Hellenic Mediterranean University, Heraklion, Greece
Email: stylianakis@hmu.gr, Web Page: https://nurs.hmu.gr/en/stylianakis-minas-2/

Keywords: PLA, MXenes, Nanocomposites, $Ti_3C_2T_x$, Biomedical applications

Abstract
The widespread utilization of polymers on a worldwide scale is undeniable and due to the ongoing expansion of plastics in everyday life, there is an increasing need for extending the service life of these products. In response to this requirement, we urge for a new approach towards the use of plastics, developed from a blend of polymers and nanomaterials. This practice will not only increase the lifetime of vital polymer equipment, but it will also integrate sustainable manufacturing processes into our modern working environment.
In order to achieve these goals, nanocomposites were developed with commercially accessible polylactic acid (PLA) in white color as the matrix and $Ti_3C_2T_x$ MXene as multi-purpose nanoparticles. PLA was chosen due to its intriguing combination of biocompatibility, intrinsic biodegradability and versatility, making it suitable for a wide range of applications. $Ti_3C_2T_x$ nanoflakes represent a new family of nanomaterials ranging from mechanical reinforcement to antimicrobial attributes [1]. The procedure to develop such nanocomposites includes the deliberate fabrication of separate dispersions containing the matrix and the nanomaterial respectively, which was accomplished in acetonitrile (ACN). ACN is an ideal solvent to disperse both PLA and the MXene nanoflakes [2], [3], [4]. An ultrasonic probe was used to facilitate the dispersion of $Ti_3C_2T_x$ nanoflakes. The supernatant was collected after a static period of 96h to ensure that the aggregated part of the dispersion has been already precipitated. Next, the resulting dispersions (PLA and MXenes) were thoroughly mixed and dried to get the desired material. In this study we used different concentrations to assess the properties of the nanocomposite. These concentrations, ranging from the baseline neat PLA to incremental adjustments, allowed for a detailed examination of the nanocomposite's properties. Tensile tests were conducted according to ASTM standards and the tensile properties of the nanocomposite were obtained for neat PLA and 3%v/v. In addition, differential scanning calorimetry (DSC) tests were conducted to study the thermal properties of the nanocomposites, while X-ray diffraction (XRD) measurements were performed to characterize the structural properties. Indicatively, using 600nm spectrophotometry the bacterial growth on the reference and MXene cultures were measured and cell density in both reference and composite cultures could be quantified and the anti-bacterial properties of the nanocomposite could be assessed. The observed improvements in mechanical strength, thermal stability and structure underscore the potential use of these nanocomposites for various applications requiring specific functional properties. In essence, the development of these nanocomposites addresses the need for prolonged service life in polymer-based products for versatile applications and signifies a transformative step towards a more sustainable and resilient future in materials science and manufacturing practices.

1. Introduction

Polylactic acid (PLA) is a biodegradable polymer derived mostly from renewable resources and has been in the center of attention during the last years due to its potential as an environmentally friendly alternative to conventional petroleum-based polymer plastics as well as its biocompatibility, thus providing the option to be utilized in various applications, including packaging, medical devices, and 3D printing for medical purposes. However, its inherent brittleness and relatively low mechanical properties remain a bottleneck and limit its broader application spectrum [1].
For that reason, the improvement of PLA performance has been in the center of attention, by incorporating various nanomaterials such as well-known carbon-based nanomaterials, like carbon nanotubes and graphene derivatives, which provably boost its mechanical and thermal properties [5]. In a similar frame, MXenes a newcomer class of 2D materials, consisting by transition metal carbides, nitrides and carbonitrides have emerged as promising candidates thanks to their exceptional electrical conductivity, mechanical strength, and thermal properties. Therefore, MXenes are highly attractive for various applications, including energy storage, electromagnetic shielding, biomedical applications, as well as ideal additives to develop polymer nanocomposites [6]. $Ti_3C_2T_x$ nanosheets have remarkable antibacterial properties due to their unique structure and surface chemistry. The sharp edges of MXene nanosheets can physically disrupt bacterial cell membranes, leading to cell disruption. Additionally, the material's high conductivity facilitates electron transfer, which can generate reactive oxygen species (ROS) that induce oxidative stress in bacteria. This dual mechanism effectively reduces bacterial growth and proliferation on the nano-modified polymer surfaces [7].

Motivated by the unique properties of MXenes, we incorporated $Ti_3C_2T_x$ nanoflakes within PLA, focusing on the manufacturing of PLA/$Ti_3C_2T_x$ nanocomposites. The goal is to evaluate the impact of the $Ti_3C_2T_x$ nanoflakes on the mechanical, thermal and antimicrobial properties of PLA. In this context, tensile tests were conducted to assess the mechanical strength, Young's modulus and the strain of the PLA nanocomposite, while differential scanning calorimetry (DSC) was utilized to analyze thermal transitions, crystallinity changes and stability of the nanocomposite material. In addition, X-ray diffraction (XRD) tests were performed to examine the crystalline phases and structural modifications induced by the addition of the $Ti_3C_2T_x$ nanoflakes and finally, preliminary antibacterial tests were done to access the potential applicability of the realized PLA/$Ti_3C_2T_x$ nanocomposites in biomedical applications. Upon analysis of the results, we adequately elucidated the synergistic effects of $Ti_3C_2T_x$ flakes on the properties of PLA proving that the development of such nanocomposites represents a significant step towards a sustainable future that meet the demanding requirements of modern technological applications, in terms of the automotive, aerospace and the field of biomedicine.

2. Experimental Procedure

2.1. Synthesis and incorporation of $Ti_3C_2T_X$ flakes within the PLA matrix

$Ti_3C_2T_x$ nanosheets were synthesized at the Institute of Electronic Structure and Laser, Foundation for Research & Technology-Hellas (IESL) in Heraklion, Greece. The MAX phase material, Ti_3AlC_2 (1g, Nanochemazone, Alberta, Canada) was chemically etched in order for the MXene few-layered material to be obtained. The etching process entails the removal of aluminum (Al) using hydrochloric acid and NaF salt. The reaction was performed at 80°C for 24h, using a heating mantle and an oil bath. After the completion of the reaction, the mixture was transferred to centrifuge tubes for neutralization. This involved centrifugation at 2000 rpm for 10 min, to discard the acidic supernatant and wash it with deionized water. The washing process was repeated until a neutral pH was achieved. After washing, the material was filtered in order to isolate the $Ti_3C_2T_x$ and hence the filtered material was dried in a vacuum oven at 80°C for 24h. To achieve delamination of the multilayered $Ti_3C_2T_x$ into the few-layered one, an ultrasonic probe was used, upon dispersion of the obtained powder in acetonitrile (ACN), a solvent that is both compatible to disperse $Ti_3C_2T_x$ and the PLA. Therefore, $Ti_3C_2T_x$ (10 mg) were dispersed in ACN (20 mL) and sonicated for 15 min into an ice bath to avoid any evaporation of the solvent. The dispersion was then left undisturbed for 96h to allow any agglomerates to settle down. The final concentration of the $Ti_3C_2T_x$ dispersion was determined to be 0.76 mg mL^{-1}.
In a similar concept, PLA was also dissolved in ACN. In particular, PLA was added in ACN in a beaker and stirred for 3 h. Subsequently, $Ti_3C_2T_x$/ACN was added to the dissolved PLA up to a concentration of 3% v/v ratio to the polymer. Upon removal of the solvent, the final nanocomposite was dried in a vacuum oven at 80°C for 48h to ensure the removal of any residual humidity or solvent traces.

2.2. Characterization of the Nanocomposites

Tension tests were performed according to the ASTM D638 standard, employing a IMADA tensile tester fitted with a 2.5kN load cell. For these tests, Type-V dog-bone specimens were selected. The tests were conducted at a constant loading rate of 10 mm min^{-1}, with a camera to capture deformation. Strains were calculated from the obtained images using Digital Image Correlation (DIC) analysis. The force values and strains were then synchronized using the timestamps to calculate the stress-strain curves. The X-ray diffraction (XRD) analysis was performed with a Bruker AXS X-ray diffractometer with CuKa radiation at a generator voltage of 40 kV and a generator current of 40 mA. Thermal properties of PLA and the formed nanocomposite were studied using a TA DSC_{250} calorimeter system. The polymer sample (PLA and PLA-based nanocomposite) were inserted in aluminum pans and the experiments were conducted in an inert N_2 atmosphere. The heating and cooling rates were at 10 °C min^{-1} and three consecutive runs were completed from 0 to 250 °C, while the first run was occurred in order to eliminate the thermal history of the sample. To investigate the antimicrobial properties, an E. coli strain was used to monitor the bacterial growths using optical density (OD) measurements at 600 nm (OD600). This method is a standard one to quantify the bacterial concentration in a liquid culture by measuring turbidity, which correlates with the number of the bacterial cells. Hence, sterilized PLA and PLA nanocomposite specimens were placed into separate wells of a 24-microplate and 2 mL of the bacterial culture was

added in each well containing the specimens. The microplate was then incubated at 37°C to promote the bacterial growth for 24h.

2.3. Results and Discussion

Figure 1 depicts the tension tests of PLA and the PLA-based nanocomposite specimens. It is mentioned that only three tension tests were done for neat PLA specimens while five tests were performed for the PLA nanocomposites. According to Figure 1b, the presence of $Ti_3C_2T_x$ nanosheets enhances the mechanical properties of PLA, altering its brittle nature into a more ductile one. As shown in Figure 2, the ultimate tensile strength (UTS) of PLA is 54.4 MPa, whereas the UTS of the nanocomposite is 58.9 MPa. Additionally, a noticeable increase in the Young's Modulus of the nanocomposite was observed since the Young's Modulus of PLA was 2.6 GPa, while the respective value for the nanocomposite was 3.2 GPa. This represents an increase by approximately 8.3% in UTS and by 23% in Young's Modulus. According to the significantly improved tensile properties of the nanocomposite compared to the neat polymer, it is assumed that highly uniform nanocomposites have been formed upon the incorporation of the $Ti_3C_2T_x$ nanosheets within the polymer matrix. Moreover, the functional groups located onto the surface of $Ti_3C_2T_x$ tend to strongly promote the formation of hydrogen bonds with the PLA chains, resulting in increased stress transfer and adhesion at the interface [8]. Moreover, the Young's modulus of $Ti_3C_2T_x$ may contribute to the PLA/MXene modulus of elasticity increase since the MXenes may serve as reinforcement to improve the material's resistance to deformation.

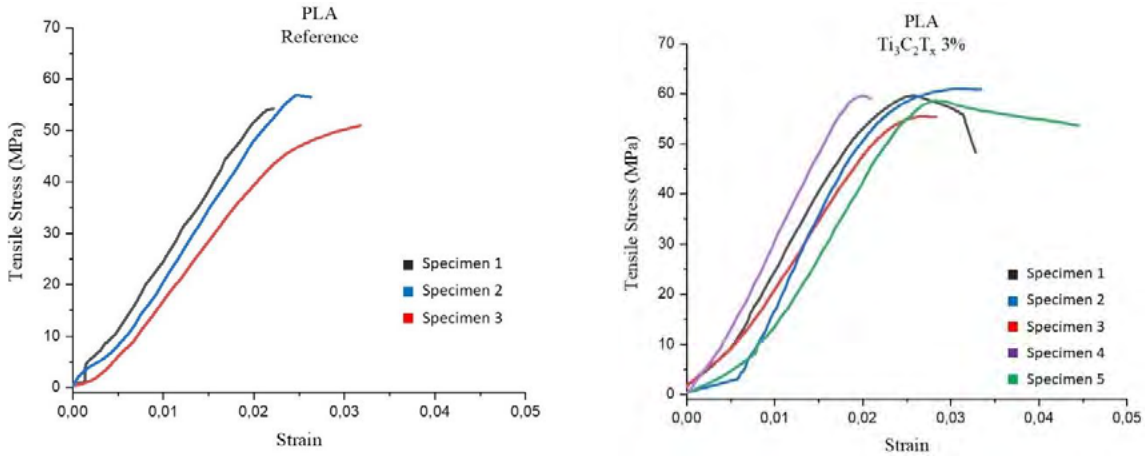

(a) (b)

Figure 1. Stress/Strain tensile tests on (a) PLA and (b) PLA/$Ti_3C_2T_x$ 3%v/v.

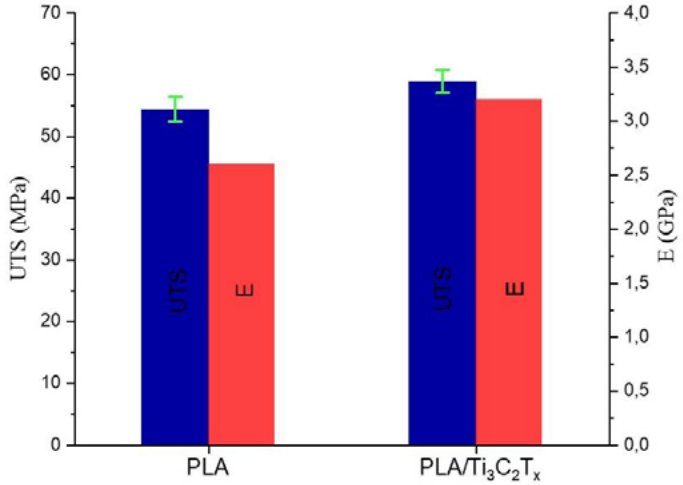

Figure 2. Ultimate tensile stress and Young's Modulus of PLA and PLA/$Ti_3C_2T_x$ 3%v/v.

Figure 3 depicts the DSC thermograph of the neat PLA and PLA/$Ti_3C_2T_x$ nanocomposite. The DSC results for the neat PLA showed a glass transition temperature (T_g) at 57.9°C, a melting temperature (T_m) at 150°C and an enthalpy of melting at 27.5 J/g. Accordingly T_g, T_m and enthalpy of melting were determined at 58°C, 149°C and 23 J/g respectively for the PLA/$Ti_3C_2T_x$ nanocomposite. It is obvious that the T_g and T_m remained almost unchanged suggesting that the incorporation of $Ti_3C_2T_x$ didn't affected the amorphous phase of PLA. However, a slight decrease of the enthalpy of melting was observed suggesting that the overall crystallinity of the PLA/$Ti_3C_2T_x$ nanocomposite decreased compared to the neat PLA. This decrease is possibly due to the presence of the $Ti_3C_2T_x$ flakes which interfere with the regular packing of PLA chains, thus affecting the polymer's crystallinity.

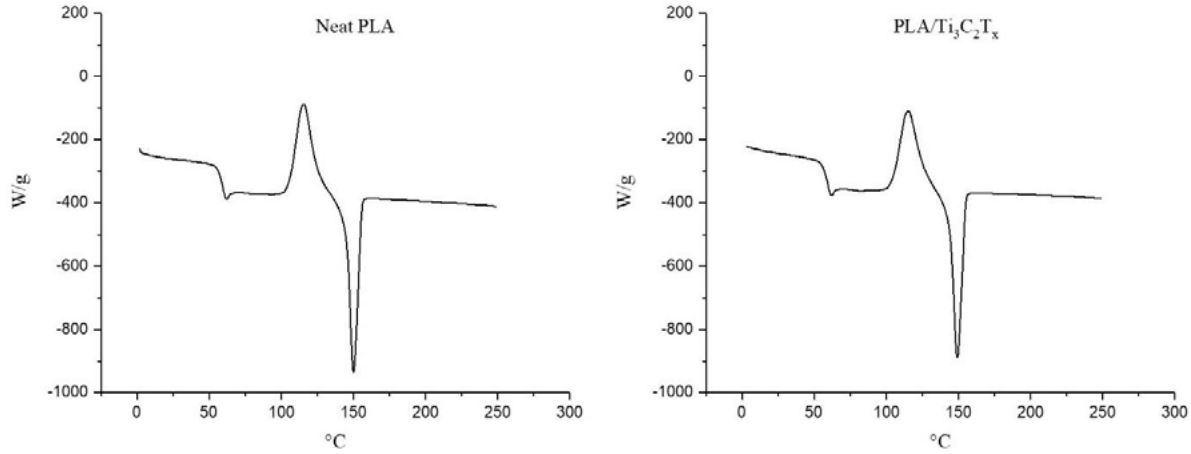

Figure 3. Differential scanning calorimetry of PLA and PLA/$Ti_3C_2T_x$ 3%v/v.

X-ray diffraction (XRD) can identify different materials based on their unique crystallographic structures. Initially, there are no peaks attributed to Ti_3AlC_2 implying the successful chemical etching of the MAX phase. Next, the characteristic peak at 2θ ~ 6.5° (002) corresponding to $Ti_3C_2T_x$ is slightly appeared (red frame), due to high exfoliation degree and interaction with the polymer matrix, as shown in Figure 4. In addition, the peaks at 2θ ~ 16° (004) and 2θ ~ 25° (006) also corresponding to $Ti_3C_2T_x$, have been superposed by the wide amorphous and semicrystalline regions of PLA at 2θ = 16.5° and 18.8° [9], [10].

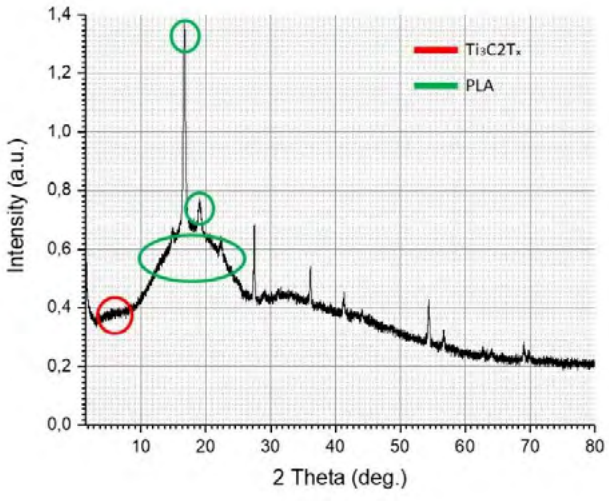

Figure 4. X-ray diffraction (XRD) patterns of PLA/$Ti_3C_2T_x$ 3%v/v.

To get an insight into the potential applicability of PLA/$Ti_3C_2T_x$ nanocomposites in biomedical applications, we also explored their antibacterial properties. The antimicrobial tests were measured using OD600, exhibiting a significant reduction by 36% in the optical density for the sample containing 3% v/v of $Ti_3C_2T_x$ compared to the neat PLA (Figure 5).

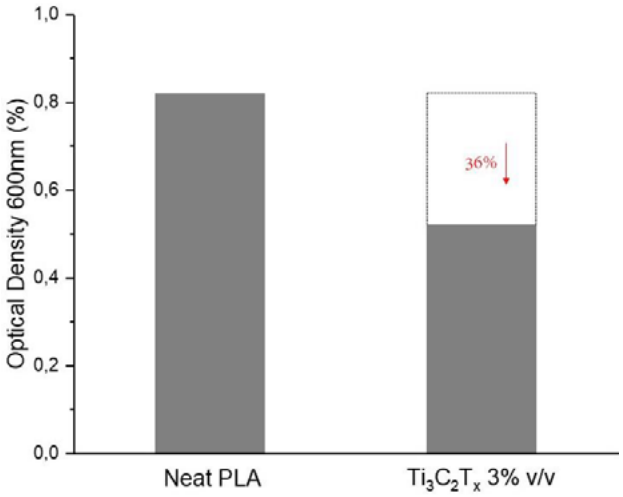

Figure 5. Antibacterial properties of PLA nanocomposite.

3. Conclusions

In conclusion, the embedding of $Ti_3C_2T_x$ nanosheets within the PLA matrix significantly affected its mechanical properties. The obtained results clearly presented an increased ultimate tensile strength and Young's modulus of the nanocomposite, while the fracture behavior of the neat PLA altered, since the nanocomposite was more ductile. The DSC and XRD analyses revealed modifications in the thermal behavior and structure, suggesting that the incorporation of $Ti_3C_2T_x$ did not significantly alter the amorphous phase of the polymer, although the overall crystallinity slightly decreased. These changes are due to the very homogenous PLA/$Ti_3C_2T_x$ nanocomposite formation which facilitated strong interfacial bonding and effective stress transfer. Finally, promising results concerning on the antimicrobial properties of the nanocomposite were obtained presenting a reduction of the E.coli bacterial growth by 36%. Consequently, the development of PLA/$Ti_3C_2T_x$ nanocomposites is a very promising concept towards their potential application in high-performance sectors such as biomedical engineering, where enhanced durability and functionality are critical. This study underscores the transformative potential of PLA embedding MXenes in fostering a more sustainable and resilient future in advanced manufacturing practices. Future research will focus on the investigation of more synergistic effects occurred due to incorporation of MXenes in polymer matrices, providing fresh air in the emerging fields of interest.

Acknowledgements

The authors would like to thank Prof. Nikolaos Papadakis and Mr. Fivos Simopoulos from the Department of Mechanical Engineering of the Hellenic Mediterranean University, for the mechanical tests and analysis, as well as Prof. Joseph Papamatheakis from the Institute of Molecular Biology and Biotechnology (IMBB) of FORTH for conducting the antimicrobial tests.

This research has been financed by the Hellenic Mediterranean University (HMU) Project titled "Conducting Educational and Postdoctoral Research at the Hellenic Mediterranean University", through the University's budget with resources of the Ministry of Education and Religious Affairs. The project has been approved by the HMU Senate decisions no. 2607/14-05-2022, no. 5994/13-09-2022 and no. 6514/03-10-2022.

References

[1] A. K. Trivedi, M. K. Gupta, and H. Singh, "PLA based biocomposites for sustainable products: A review," 2023, doi: 10.1016/j.aiepr.2023.02.002.

[2] G. L. Siparsky, K. J. Voorhees, and F. Miao3, "Hydrolysis of Polylactic Acid (PLA) and Polycaprolactone (PCL) in Aqueous Acetonitrile Solutions: Autocatalysis," 1998.

[3] K. Maleski, V. N. Mochalin, and Y. Gogotsi, "Dispersions of Two-Dimensional Titanium Carbide MXene in Organic Solvents," *Chemistry of Materials*, vol. 29, no. 4, pp. 1632–1640, Feb. 2017, doi: 10.1021/acs.chemmater.6b04830

[4] V. Harish *et al.*, "Review on Nanoparticles and Nanostructured Materials: Bioimaging, Biosensing, Drug Delivery, Tissue Engineering, Antimicrobial, and Agro-Food Applications," *Nanomaterials*, vol. 12, no. 3. MDPI, Feb. 01, 2022. doi: 10.3390/nano12030457.

[5] E. Ivanov *et al.*, "PLA/Graphene/MWCNT Composites with Improved Electrical and Thermal Properties Suitable for FDM 3D Printing Applications," *Applied Sciences 2019, Vol. 9, Page 1209*, vol. 9, no. 6, p. 1209, Mar. 2019, doi: 10.3390/APP9061209.

[6] B. M. Jun *et al.*, "Review of MXenes as new nanomaterials for energy storage/delivery and selected environmental applications," *Nano Research*, vol. 12, no. 3. Tsinghua University Press, pp. 471–487, Mar. 01, 2019. doi: 10.1007/s12274-018-2225-3.

[7] R. Nie *et al.*, "3D printing of MXene composite hydrogel scaffolds for photothermal antibacterial activity and bone regeneration in infected bone defect models," *Nanoscale*, vol. 14, no. 22, pp. 8112–8129, May 2022, doi: 10.1039/d2nr02176e.

[8] Y. Cheng *et al.*, "High-strength MXene sheets through interlayer hydrogen bonding for self-healing flexible pressure sensor," *Chemical Engineering Journal*, vol. 453, p. 139823, Feb. 2023, doi: 10.1016/J.CEJ.2022.139823.

[9] M. Naguib *et al.*, "Two-Dimensional Nanocrystals Produced by Exfoliation of Ti_3AlC_2," *Advanced Materials*, vol. 23, no. 37, pp. 4248–4253, Oct. 2011, doi: 10.1002/adma.201102306.

[10] I. S. Bayer, "Thermomechanical Properties of Polylactic Acid-Graphene Composites: A State-of-the-Art Review for Biomedical Applications," *Materials*, vol. 10, no. 7, Jul. 2017, doi: 10.3390/MA10070748.

BIO-DERIVED PHOSPHAZENE-TANNIC ACID MICROSPHERES AS FIRE RETARDANT ADDITIVES TO AN EPOXY TANNIC ACID NETWORK.

Rusheni Bhagya Senanayake[1], Houlei Gan[1], Russell J. Varley[1]*

[1]Carbon Nexus at the Institute for Frontier Materials, Deakin University, Waurn Ponds, Australia

*Corresponding author: russell.varley@deakin.edu.au

Keywords: Tannic acid, flame retardancy, epoxy resins

Abstract

The development of bio-inspired flame-retardant additives for epoxy resins with superior mechanical and thermal properties compared to their fossil derived counterparts is a necessary development for the composite materials industry to achieve sustainability. Nature has evolved materials for millions of years to achieved optimum performance which provides an opportunity to take advantage of these materials for everyday usage, and provide satisfactory alternatives to the use of fossil fuel derived chemicals. An example of this is the understanding of flame-retardant behaviour in nature and how this can be applied to the modern world. In this study, a bio-based flame-retardant colloidal additive has been synthesized, then added to an epoxy resin as a novel flame retardant and cured with the bio-dervied poly phenol tannic acid (TA). The colloids were synthesized through an efficient one step process reacting hexachlorocyclophosphazene (HCCP) and with tannic acid (TA) itself to create microspheres which are then used as flame retardant additives for the epoxy TA network. To investigate the thermal, mechanical, and flame-retardant properties, a series of sample specimens were made by adding the colloid at 5 wt.%, 10 wt.% and 15 wt.%. The cured epoxy thermosets displayed good T_g (170 ◦C,178 ◦C and 206 ◦C), improved char yields up to 39%, increased thermal stability and readily displayed self-extinguishing behaviour rated as V-0, according to the UL-94 test. This study highlights the potential to use TA, as both a bio-derived additive and effective hardener for an epoxy resin to create a highly bio-based highly fire-retardant high performance composite.

1. Introduction

Creating high performance lightweight structures that do not compromise the required properties for any given application, is a major challenge for materials development. This is particularly important in industries such as automotive, marine or aerospace where fuel savings are paramount as are lowering the cost of manufacture. One of these candidates for lightweight materials, fibre reinforced polymer composites, are now beginning to demonstrate their promise as affordable manufacturing processes become more widely available [1]. Historically, the most common matrices in polymer composites have been epoxy resins, which have been widely utilised in the electrical, automotive, and aerospace industries. This is primarily because of their excellent thermal and mechanical properties and ease of processability [2]. Despite the increased processing challenges of phenolic hardeners, they are often used when improved fire retardancy is required [3], providing an opportunity to explore alternative bio-based phenolics as both hardener and as an additive.

Tannic acid (TA), the focus of this study, is one such bio-derived phenolic that can be explored for this purpose. It can be sustainably sourced and has great potential to replace fossil fuel-derived resin systems. This polyphenolic compound, found in tree bark and other plants, features a structure with multiple galloyl (3,4,5-trihydroxyphenyl) units surrounding a glucose core. The reactivity of tannic acid is influenced by the acidity of its numerous hydroxyl groups, which is affected by electron delocalization around the aromatic ring [4]. Furthermore, it is highly aromatic, oligomeric, and has a highly functional nature. These properties suggest it may provide inherent fire retardancy while maintaining adequate reactivity when incorporated into a polymer network. Tannic acid has been used previously as a bio-derived phenolic hardener for epoxy resins, from fossil fuel or bioderived sources due to the reactive nature of the hydroxyl groups being able to attack the strained epoxide group[4-5]. However, given the number of available hydroxyl groups and the oligomeric structure of TA, it is unlikely they will all react with an epoxide group making it challenging to determine the ideal stoichiometry to achieve the optimum mechanical and thermal properties. Tannic acid has been as a char-forming agent, making it an ideal molecule for flame-retardant systems. The key mechanisms of fire retardancy include promoting char formation, which prevents or reduces the migration of volatiles from the condensed to the gaseous phase, radical scavenging to terminate combustible chain reactions, and diluting the gaseous phase with non-combustible gases or gases that undergo endothermic transitions at elevated temperatures [6].

Additionally, polymers that are highly aromatic tend to exhibit better fire retardancy due to their higher thermal stability and char formation. An effective fire-retardant system would utilize several of these mechanisms to achieve synergistic behaviour, a primary goal of much current fire retardancy research. Phosphorus and nitrogen-containing compounds display this synergy, as phosphorus can produce phosphoric acid to promote char formation and release PO and PO_2 radical scavengers into the gaseous phase, while nitrogen is responsible for the evolution of incombustible gases such as N_2 and NH_3, which dilute the gaseous phase. Derivatives of hexachlorocyclophosphazene (HCCP) and linear polyphosphazenes are examples of highly studied flame-retardant additives for epoxy resins that have proven to be highly effective at low concentrations, with minimal impact on thermal and mechanical properties[6-8].

This work uses tannic acid (TA), a sustainably sourced naturally occurring highly aromatic polyphenol as an alternative hardener to diglycidyl ether of bisphenol A (DGEBA) to improve the understanding of the structure property processing relationships of a partially bio-based epoxy network. Improvement in fire performance could be achieved by using the phosphorous nitrogen containing phosphazene motif with TA acting as both hardener and copolymer within the colloid. To do this, HCCP-TA colloids (TAPZ) were synthesised and added to a DGEBA-TA resin at concentrations from 5 wt% to 15 wt% and the effect on thermal properties as well as fire performance (UL-94, limiting oxygen index (LOI) and cone calorimetry) was investigated. Furthermore, the stoichiometry of the DGEBA-TA resin was also varied given the importance of stoichiometry and the additional OH groups available from the surface of the synthesised colloid (TAPZ). Ultimately the goal of this work was to determine if the addition of TAPZ to a DGEBA-TA epoxy resin could produce a highly fire-retardant, high-performance network based upon a very high concentration of bio-derived content.

©2024 | 2_VARLEY_Russell J._BS5GY .pdf:2

2.Experimentals

2.1 Materials

Hexachlorocyclophosphazene (HCCP), pyridine, acetonitrile, ethanol and tannic acid (MW 1702.20 g/mol), were purchased from Sigma-Aldrich (Australia). The epoxy resin, diglycidyl ether of bisphenol A (DGEBA, ZResin 30) was kindly supplied by GMS Composites, Australia. All chemicals were used without further purification, but the epoxy resin was degassed extensively at 65 °C for 24 h prior to use.

2.2 Sample preparation.

The synthesis of the phosphazene-TA (TAPZ) microspheres was conducted using a one-step nucleophilic reaction sequence between HCCP and tannic acid (TA) as shown in Figure 1 and is described as follows. To being, 0.2 g TA (0.12 mmol, 2.94 mmol OH groups) and 0.17 g HCCP (0.49 mmol; 2.94mmol Cl groups) were added to a round bottom flask and dissolved in acetonitrile (100 ml). The mixture was mechanically stirred under a nitrogen atmosphere at room temperature until the solution became clear. Pyridine was then added dropwise over the course of 1 hour, deprotonating the TA to promote nucleophilic attack and elimination of HCl, then continued to stir overnight at room temperature. The following day, the precipitate was isolated by centrifuge (4500 rpm, 20 min) and washed several times with acetonitrile and deionized water respectively. After freeze-drying a white color fine powder was obtained.

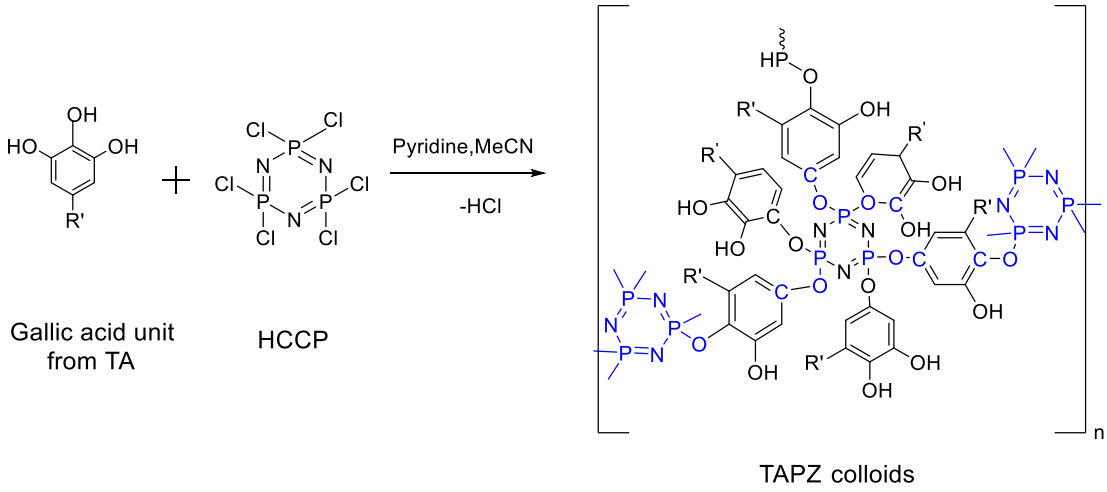

Figure 1: *Polycondensation between galloyl group from tannic acid and hexachlorocyclophosphazene in the presence of pyridine illustrating the crosslinking reaction leading to the formation of the spherical colloids.*

2.3 Epoxy thermoset preparation and composite fabrication.

The modified blends were prepared by adding TAPZ and DGEBA together in a round bottom flask and blended using a rotary evaporator at 60 °C until the colloids appeared to be evenly dispersed and no bubbles were present. The TA curative was then added, and mixing was continued until the complete disappearance of any bubbles at 60 °C under vacuum. The resin was then poured into preheated silicone moulds and cured in an air circulating oven at 150 °C for 5 h, followed by 177 °C for 5 h. The samples were cooled to room temperature overnight then removed from the moulds. The formulations prepared are shown in Table 1 and are based upon an assumption that TA has 15 reactive hydroxyl groups out of a potential 25. This formulation (TA-53) was used because previous work[4] suggested that this stoichiometry provided the best balance of mechanical and thermal properties.

Table 1: *Composition of resin systems produced, and their sample IDs used throughout.*

Sample ID	DGEBA (g)	TA (g)	TAPZ (g)
TA-53	40	12.8	-
TA-53-05	40	12.8	2.75 (5 wt%)
TA-53-10	40	12.8	5.86 (10 wt%)
TA-53-15	40	12.8	9.35 (15 wt%)

Carbon fibre composite samples were fabricated for cone calorimetry evaluation using a T_{300} grade carbon fibre, GSM 370g/m^2, 4 harness 6k satin weave. The TA-53, TA-53-15 resin solutions were prepared as described above, then dissolved in ethanol to allow convenient application to carbon fibre. The resin was carefully brushed onto woven carbon fabric in sufficient quantities to ensure that the final composite contained approximately 50 wt% resin content. The prepreg was allowed to dry at 70 °C for 2 h in a drying oven, prior to fabricating the composite via a hand lay-up method using 12 layers (300 mm × 200 mm) of carbon fibre. The preform was debulked, vacuum bagged, then cured in a hot-press at 180 °C for 5 h at a pressure of 0.5 MPa. The final composites were about 3 mm thick and were cut into 100 mm × 100 mm pieces.

3. Results and discussion

3.1 Characterization of TAPZ

The stoichiometry chosen for synthesizing TAPZ was guided by a study by Deniz et al.[6], which indicated that a 1:1 ratio of HCCP to TA provided the best fire retardancy. SEM images of the resulting microspheres, shown in Figure 2b) and c), clearly demonstrate their spherical shape and size. The FTIR spectra of the starting materials and TAPZ, displayed in Figure 2 a), reveal new characteristic peaks for the stretching vibrations of P-O-C at 940 cm^{-1} and P-N bonds at 1181 cm^{-1}, indicating a reaction between HCCP and TA. The near-complete disappearance of the peak at 615 cm^{-1}, which corresponds to the P-Cl bond, suggests that the phosphorus-bound chlorine has been almost entirely substituted.

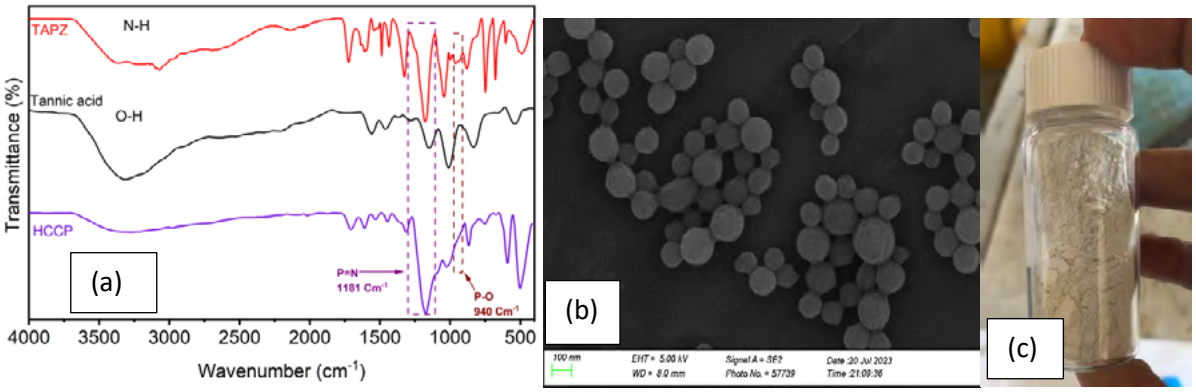

Figure 2: *(a) FT-IR spectra of TA, HCCP and TAPZ colloids, (b) SEM images of the TAPZ colloids illustrating their spherical nature and (c) an optical image of the prepared colloid.*

3.2 Thermal properties of the cured network.

One significant advantage of using TA as a bio-derived curative is its ability to form a high-performance network with a high glass transition temperature (T_g), thanks to its highly aromatic structure and numerous reactive functional groups. T_gs in the range of 150-170°C have been reported, though determining the optimal composition can be challenging due to the multiple OH groups distributed throughout the TA structure. Our previous research showed that TA-53 achieved a maximum T_g of 187.0 °C (tan δ max.) and produced a microstructurally homogeneous network, as confirmed by DMTA. This finding aligns with our current results shown in Table 2. However, increasing the concentration of TAPZ caused the tan δ peak to split into a more complex bimodal pattern. This indicates that enhanced interfacial reactions between the OH groups of TAPZ affect the dynamic mechanical properties, resulting in a second phase at a lower temperature.

The degradation behaviour and char formation of the cured epoxy networks were investigated using TGA, residual mass at 600 °C (R_{600}) are summarized in Table 2. The results indicate that the addition of TAPZ significantly decreases the $T_{5\%}$, likely due to the increased susceptibility of the P-O-C bonds in TAPZ to cleavage. Despite this reduction in thermal stability, the char level at 600 °C increases from approximately 23.9% to 39.4%, suggesting that these networks may exhibit enhanced fire-resistant properties.

Table 2: *Analysis of the DMTA spectra of the cured epoxy networks and decomposition properties of the networks as measured by TGA.*

Sample ID	T_g (°C) (tan δ max)	υ_e (mol/m^3)	$T_{5\%}$ (°C)	Char yield R_{600} (%)
TA-53	187.0	12055.8	362.4	23.9
TA-53-05	168.9	6880.3	318.4	34.5
TA-53-10	156.7	2762.9	312.4	42.4
TA-53-15	155.0	2859.4	282.4	39.8

3.3 Flammability performance of the network

To evaluate the impact of TA and TAPZ on the flammability of epoxy networks, their self-extinguishing behaviour was tested using the UL-94 vertical burn test. According to the results in Table 3, TA-53 achieved a rating (NR) as they failed to exhibit self-extinguishing behaviour, burning to the clamp and dripping during the first ignition. However, as TAPZ concentration increased, self-extinguishing behavior significantly improved. TA-53-5 self-extinguished within 3 seconds after the first flame and immediately after the second flame, earning a V-0 rating. Higher TAPZ concentrations in TA-53-10 and TA-53-15 led to instant self-extinguishing behaviour for both flame applications, also achieving V-0 ratings.

Limiting oxygen index (LOI) results in Table 3 revealed that increasing TAPZ concentration content consistently increased the LOI from 24% for TA-53 to 29% for TA-53-15. Overall, these results confirm that the addition of TAPZ microspheres significantly enhances fire performance, as evidenced by the LOI and UL-94 tests. It is noteworthy that typical epoxy resin systems have LOI values ranging from 19.8% for epoxy amine and anhydride systems to 22.3% for novolac epoxy resins[4].

Table 3: *UL 94, LOI analysis and ratings of the cured epoxy networks.*

Sample ID	After-flame time		Rating	Drip	LOI %
	t_1 (s)	t_2 (s)			
TA-53	BC	-	NR	YES	24.0 (±1.2)
TA-53-5	3	0	V-0	No	24.8 (±1.24)
TA-53-10	0	0	V-0	No	25.6 (±1.28)
TA-53-15	0	0	V-0	No	28.8 (±1.44)

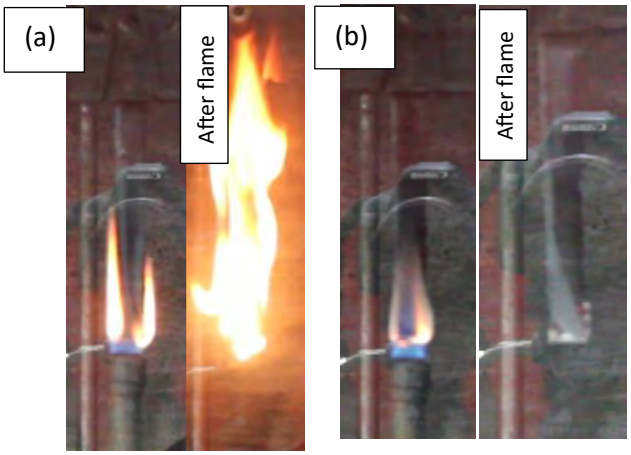

Figure 3: *Images of the UL-94 tests comparing the behaviour between the a) TA-53 sample which burnt to the clamp after the first flame b) TA-53-10 sample which highlights the self-extinguishing behaviour after the first and second flame applications. Each flame is applied for 10s then removed.*

Cone calorimetry was performed on the carbon fibre composites of the best performing modified resin sample only, TA-53-15 and compared to the TA-53. Representative plots of the heat release rates for each sample at heat fluxes of 35 kW/m² and 50 kW/m² are shown in Figure 4 a). As can be seen, the TA-53 displays the highest peak heat release rate then the TA-53-15. The ignition times however do consistently reduce for TA-53-15, reflecting the role of the TA and TAPZ in enhancing degradation. The PHHR measurements are plotted as a function of composition and TPAZ concentration in Figure 4b) which display reductions in PHHR of 61.9% and 51.7% for TA-53-15 compared to TA-53 at 35kW/m² and 50 kW/m² respectively. Clearly these results show that the combination of using TA as a curative, and TPAZ microspheres as an additive, a highly fire-retardant high-performance network was created in this work.

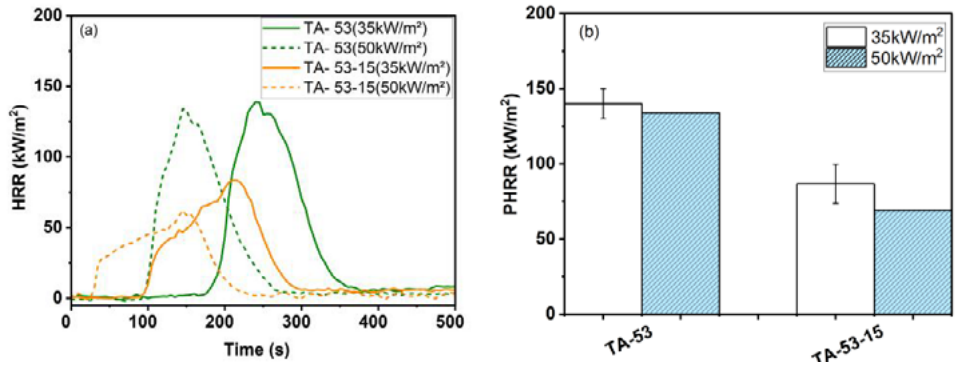

Figure 4:*Normalised a) HRR curves for the TA-53 and TA-53-15 exposed to 35 and 50kW/m², and the resultant b) PHRR.*

4. Conclusion

This study studied the effect of partially bio-derived fire-retardant microspheres (TAPZ) on the flame retardant behaviour of a partially bio-derived DGEBA-TA and showed that a highly bio-derived, highly fire-retardant and high-performance polymer network could be manufactured. The UL-94, LOI and cone calorimetry results displayed excellent property improvements over the unmodified system. A V-0 was easily achieved, LOI increased from 24 to 29% and the PHHR reduced 61.9% compared with the unmodified network. The CO and CO2 emissions were reduced greatly irrespective of heat flux. The microspheres did reduce Tg and mechanical properties and a significant increase in viscosity was observed. This work provided insights into the epoxide-hydroxyl reactions occurring at the TAPZ epoxy interface indicative of their availability

5. References.

[1] Shalin REe. Polymer matrix composites: Springer Science & Business Media; 2012.
[2] Ganteaume A, Jappiot M, Lampin C, Guijarro M, Hernando C. Flammability of some ornamental species in wildland–urban interfaces in southeastern France: laboratory assessment at particle level. Environmental Management. 2013;52:467-80.
[3] Xia Z, Kiratitanavit W, Facendola P, Thota S, Yu S, Kumar J, et al. Fire resistant polyphenols based on chemical modification of bio-derived tannic acid. Polymer Degradation and Stability. 2018;153:227-43.
[4] Senanayake RB, Gan H, Zhang J, Liu D, Varley RJ. Impact of Stoichiometry on the Network Structure, Properties, and Processing Relationships of an Epoxy Tannic Acid Resin System. ACS Applied Polymer Materials. 2024.
[5] Feng X, Fan J, Li A, Li G. Biobased Tannic Acid Cross-Linked Epoxy Thermosets with Hierarchical Molecular Structure and Tunable Properties: Damping, Shape Memory, and Recyclability. ACS Sustainable Chemistry & Engineering. 2020;8(2):874-83.
[6] Deniz A, Zaytoun N, Hetjens L, Pich A. Polyphosphazene–Tannic Acid Colloids as Building Blocks for Bio-Based Flame-Retardant Coatings. ACS Applied Polymer Materials. 2020;2(12):5345-51.
[7] Wu K, Wang X, Xu Y, Guo W. Flame retardant efficiency of modified para-aramid fiber synergizing with ammonium polyphosphate on PP/EPDM. Polymer Degradation and Stability. 2020;172:109065.
[8] Huo S, Song P, Yu B, Ran S, Chevali VS, Liu L, et al. Phosphorus-containing flame retardant epoxy thermosets: Recent advances and future perspectives. Progress in Polymer Science. 2021;114:101366.

ELECTROSPUN CNC-REINFORCED COMPOSITE FIBERS FOR ADVANCED 3D PRINTING APPLICATIONS

Shameek Vats[1(*)], Gregory Mertz[1], Clément Mugemana[1], C.A Fuentes[1,2]

[1] Department of Materials Research and Technology, Luxembourg Institute of Science and Technology (LIST), Luxembourg
[(*)]*Email:* shameek.vats@list.lu, Web Page: https://orcid.org/0000-0003-3724-7974
[1] Department of Materials Research and Technology, Luxembourg Institute of Science and Technology (LIST), Luxembourg
Email: gregory.mertz@list.lu, Web Page: https://orcid.org/0000-0003-1590-4216
[1] Department of Materials Research and Technology, Luxembourg Institute of Science and Technology (LIST), Luxembourg
Email: clement.mugemana@list.lu, Web Page: https://orcid.org/0000-0001-6003-5668
[1] Department of Materials Research and Technology, Luxembourg Institute of Science and Technology (LIST), Luxembourg
[2] Department of Materials Engineering, KU Leuven, Leuven, Belgium
Email: carlos.fuentes@list.lu, Web Page: https://orcid.org/0000-0002-0766-9079

Keywords: electrospinning, nanofibers, all cellulose fiber, 3D printing, fiber reinforced composite (FRC)

Abstract
In the realm of 3D printing, fiber-reinforced composites (FRC) offer immense potential for enhancing structural and mechanical properties. This study aims to investigate the enhancement of mechanical properties of electrospun fibers through two methods: regeneration by deacetylation and incorporation of cellulose nanocrystals (CNCs) derived from sustainable sources. Cellulose acetate (CA) was successfully electrospun and regenerated back to cellulose, and in the second method, CA nanofibers were produced from uniformly CNCs dispersion. The results show significant improvements in mechanical properties. The incorporation of CNCs enhances the mechanical strength of the fibers, while the regeneration process transforms the fibers into an all-cellulose structure. This study contributes to the advancement of sustainable and high-performance composite materials for additive manufacturing, promising applications across various industries.

1.Introduction

The development of high-performance composite materials for additive manufacturing has gained significant attention in recent years, driven by the need for versatile and sustainable solutions. Within this landscape, fiber-reinforced composites (FRC) have emerged as a particularly promising category of materials, offering enhanced mechanical properties and versatility. Electrospun fibers, known for their unique properties and structural characteristics, have garnered attention as a valuable component in composite materials. CNCs, derived from sustainable sources such as plant cell walls, have been shown to significantly enhance the mechanical properties of composite materials [1][2][3]. These CNCs have also been used as a reinforcing agent to improve the mechanical properties of electrospun fibers.

Electrospinning is a versatile and widely used technique for producing nanofibers with unique properties. The process involves the use of a high voltage to create a charged jet of polymer solution or melt, which is then collected on a grounded collector to form fibers [4][5]. The principles of electrospinning are based on the interaction between the electric field, surface tension, and viscosity of the solution, resulting in the formation of fibers with high surface-to-volume ratios and tunable properties [6][7]. This method offers several advantages, including the ability to control the morphology,

porosity, and composition of the nanofibers, resulting in high surface area structures. Electrospinning is known for its simplicity and versatility, allowing for the generation of ultrathin fibers with diameters ranging from a few micrometers to nanometers. The applications of electrospinning span across various fields, including biomedical devices, tissue engineering, filtration systems, energy storage, and composite materials, showcasing its broad utility and potential impact in diverse industries [8][9][10].

Cellulose acetate (CA) has emerged as a promising electrospinning polymer due to its unique advantages. One of the significant benefits of CA is its ability to be easily dissolved in solvents, making it a straightforward choice for electrospinning. Additionally, CA can be regenerated back to its natural form, cellulose, through a deacetylation process, which opens new possibilities for sustainable composite materials [11][12]. Furthermore, CA can be used to encapsulate cellulose nanocrystals (CNCs) within the electrospun fibers, allowing for the creation of reinforced composite materials. CNCs are biodegradable, non-toxic, and renewable, making them an attractive option for sustainable composite materials. The improved mechanical properties of CNC-reinforced electrospun fibers are attributed to the high aspect ratio and high surface area of CNCs, which provide a strong interface between the fiber matrix and the CNCs.

In this study, we investigate the fabrication and characterization of electrospun CA fibers both with and without incorporating cellulose nanocrystals (CNCs) derived from sustainable sources. Our study focuses on enhancing the mechanical properties of the fibers through two key approaches: regeneration via deacetylation and the incorporation of CNCs. The electrospinning of Cellulose Acetate (CA) is followed by a deacetylation process to transform the fibers into an all-cellulose structure. Subsequently, CA is then electrospun with uniformly dispersed CNCs. This study contributes to the advancement of sustainable and high-performance composite materials, with potential applications across various industries.

2. Materials & Methods

2.1. Polymer Solution

Cellulose acetate (CA) with a degree of substitution of 39.8% and a weight-average molecular weight (M_w) of 50,000 g/mol was obtained from Merck and used as received. Acetic acid (HOAc) and anhydrous acetone, both analytical grade reagents, were purchased from Merck and used as solvents for the electrospinning solutions. Ramie fibers were supplied by Stucken Melchers GmbH & Co. Chemical and used as the source material for the preparation of cellulose nanocrystals (CNCs). The CNCs were synthesized via acid hydrolysis following the protocols described by Goffin et al. (2011) and Habibi & Dufresne (2008) [13][14]. Two electrospinning solutions were prepared:

1. 10% (w/w) CA solution: CA was dissolved in a 1:1 (w/w) mixture of acetic acid and acetone under constant stirring left overnight at room temperature to obtain a homogeneous solution.
2. 10% (w/w) CA + 1% (w/w) CNC solution: CNCs were dispersed in the acetic acid/acetone mixture using ultrasonication for 30 minutes. CA was then added to the CNC dispersion and stirred until a uniform solution was achieved.

The equal volume ratio of acetic acid to acetone was crucial for ensuring stable electrospinning conditions.

2.2. Electrospinning

The electrospinning experiments were conducted using a Bioinicia LE-50 setup equipped with a Drying Heating Unit (DHU) to control the temperature and humidity within the spinning chamber. A 10 mL disposable syringe (Terumo) was used to load the polymer solution and deliver it to the spinneret through a PTFE tubing (Bola) with an outer diameter of 3.2 mm, inner diameter of 1.6 mm, and a thickness of 0.8 mm. An 18-gauge stainless steel blunt needle (B.Braun Medical) was used as the spinneret for fiber production.

2.3. Characterization

The morphology of the electrospun fibers was analyzed using an Environmental Scanning Electron Microscope (E-SEM), specifically the Quanta 200 FEG by FEI Company. Prior to observation, the electrospun samples were affixed to a metal microscope holder using conductive carbon tape to ensure proper conductivity and stability during imaging. The topography of the cellulose nanocrystals (CNCs) was analyzed using an MFP-3D Oxford Instruments Atomic Force Microscope (AFM). For Fourier-Transform Infrared (FTIR) characterization, a Netzsch TG 209 F1 Libra® instrument was utilized to analyze the chemical composition and functional groups present in the samples. The mechanical properties of the electrospun fibers were evaluated using a TexTechno Fiber Micro-Testing System_Fimatest (Germany). The tensile strength and strain at break of the samples were determined with a load cell of 3200 cN, at an extension rate of 0.5 mm/min and an initial grip distance of 20 mm.

3. Results & Discussions

3.1 Electrospinning

The electrospinning process plays a crucial role in determining the morphology and properties of the resulting fibers. In this study, electrospinning was employed to fabricate composite fibers with and without Cellulose Nanocrystals (CNCs) to investigate their impact on the structural characteristics. The electrospinning parameters, including solution concentration, flow rate, voltage, and distance between the needle tip and collector, were carefully optimized to ensure the production of uniform and well-defined fibers. By varying these parameters, we aimed to control the fiber diameter, alignment, and distribution of CNCs within the fibers. The following Table 1 presents a detailed overview of the electrospinning parameters used for the fabrication of both CA and CA+ CNC nanofibers, highlighting the differences in processing conditions and their potential influence on the final fiber properties.

Table 1. Electrospinning parameters for Cellulose Acetate Fibers with and without Cellulose Nanocrystals (CNCs)

Sample	Temperature (°C)	Relative Humidity (%)	Flow rate (mL/h)	Voltage (kV)	Distance (cm)
CA	20	38	12.5	14	12
CA+CNC	20	36	7.5	13.5	12

3.2 Regeneration by deacetylation

The electrospun cellulose acetate (CA) fibers were immersed in a solution of potassium hydroxide (0.5 M KOH) in ethanol to facilitate the deacetylation process which involves the removal of acetyl groups from the cellulose acetate molecule. The fibers were allowed to regenerate completely by soaking in the solution for 30 minutes. Subsequently, the fibers were transferred to an ethanol solution for 5 minutes to remove excess KOH and acetyl groups before being air-dried overnight at room temperature.

The successful regeneration of cellulose was confirmed by Fourier-Transform Infrared (FTIR) spectroscopy. The FTIR spectrum of the regenerated cellulose (Figure 1) exhibits characteristic peaks that are consistent with the literature. The broad band at around 3400 cm^{-1} corresponds to the stretching vibrations of the hydroxyl (-OH) groups in cellulose [15]. The peaks at 2900 cm^{-1} and 1430 cm^{-1} are attributed to the C-H stretching and bending vibrations, respectively. The strong absorption band at 1060 cm^{-1} is associated with the C-O-C stretching vibrations of the pyranose ring in cellulose [15]. The presence of these characteristic peaks in the FT-IR spectrum confirms the successful regeneration of cellulose from the CA precursor and the removal of acetyl groups during the deacetylation process. The regeneration of cellulose from CA is a crucial step in the production of all-cellulose materials with

controlled morphologies and properties. The deacetylation process allows for the removal of acetyl groups, which can affect the properties of the final material.

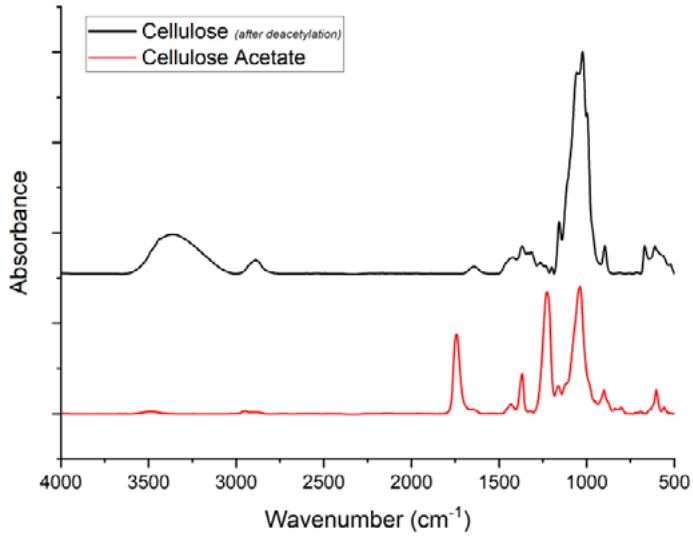

Figure 1. FTIR spectrum of regenerated cellulose (black line) obtained from deacetylation of electrospun cellulose acetate (red line) nanofibers.

3.3 Morphological Characterization

The morphology of the electrospun fibers was examined using Scanning Electron Microscopy (SEM), and the results are depicted in Figure 2. The initial cellulose acetate fibers (Figure 2a) displayed smooth and uniform surfaces, indicative of successful electrospinning using the selected solvent mixture. Upon deacetylation (Figure 2b), the resulting cellulose fibers retained their fibrous structure. This suggests that the deacetylation process effectively removed the acetyl groups without significantly compromising the integrity of the fibers. However, it was noted that the regeneration induced an aggregation of the fibers as observed in Figure 2b and was attributed to the immersion of the fibers in ethanol (0.5M KOH) and the drying processes, which favors the collapsing of the fibers.

Incorporation of cellulose nanocrystals (CNC) into the cellulose acetate fibers (Figure 2c) appeared to integrate well within the fiber matrix. The presence of CNCs did not disrupt the overall fibrous morphology, indicating that the electrospinning process was compatible with the addition of nanocrystals.

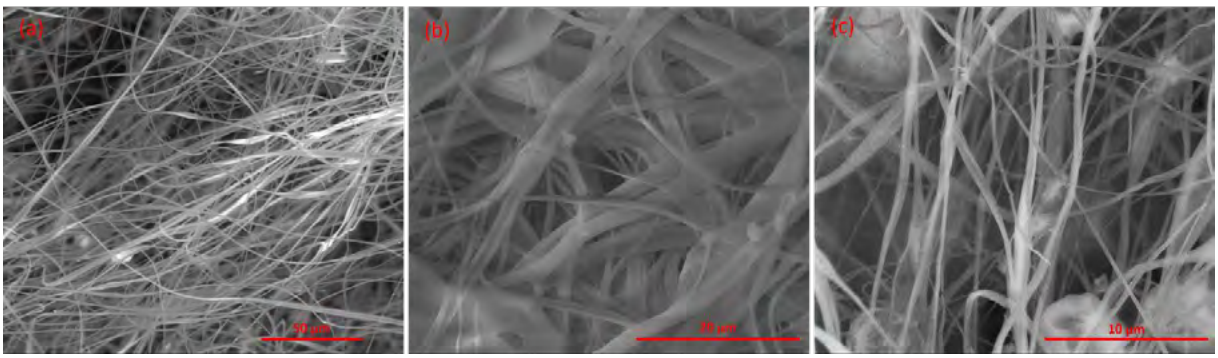

Figure 2. Scanning Electron Microscopy (SEM) images showcasing the morphology of electrospun fibers: (a) Cellulose acetate fibers [scale: 50 µm]; (b) Cellulose fibers after deacetylation [scale: 20 µm]; (c) Cellulose acetate fibers with cellulose nanocrystals (CNC) [Scale: 10 µm].

3.4 Topological Characterization

Atomic Force Microscopy (AFM) was employed to investigate the topography of the cellulose nanocrystals (CNCs). The AFM image (Figure 3) reveals the agglomeration of CNCs forming clusters or bundles, which is a common phenomenon due to their high surface energy and tendency to form hydrogen bonds [16]. Despite the agglomeration, the AFM characterization provided valuable insights into the dimensions of the CNCs. The average length of the agglomerated CNCs was observed to be 212.7 nm, while the average width was found to be 15.2 nm. These dimensions are consistent with the typical size range of CNCs found in literature [17], which are known to have lengths ranging from several hundred nanometers to a few micrometers and heights in the range of 5-20 nm [17]. The AFM characterization confirms the successful isolation of CNCs from the Ramie fibers and provides a basis for understanding their behavior in the electrospun fibers. The agglomeration of CNCs can affect their dispersion and distribution in the electrospun fibers, which can impact the final properties of the material. The AFM characterization can help to optimize the processing conditions to achieve a more uniform dispersion of CNCs in the electrospun fibers.

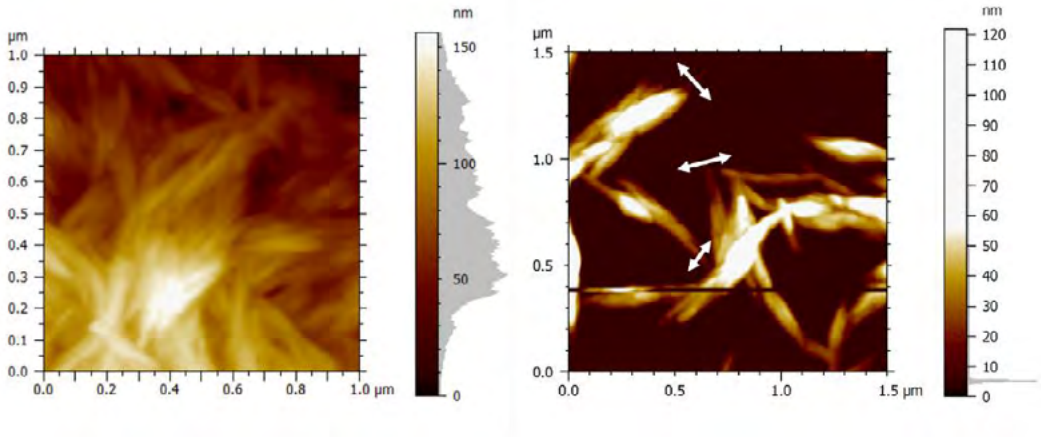

Figure 3. Atomic Force Microscopy (AFM images of dried agglomerated cellulose nanocrystals (CNCs) isolated from Ramie fibers

3.5 Mechanical Characterization

The mechanical properties of the electrospun fibers were evaluated using a tensile testing machine. The stress-strain curves of three different samples: cellulose acetate, regenerated cellulose acetate, and cellulose acetate containing CNCs was plotted. The results, shown in Figure 4, indicate significant improvements in mechanical properties with the regeneration of CA and with the addition of CNCs. The tensile strength of the electrospun cellulose acetate fibers was found to be 6.8 MPa. In comparison, the regenerated cellulose acetate fibers exhibited a tensile strength of 18.75 MPa, and the cellulose acetate + CNC fibers demonstrated a remarkable tensile strength of 37.3 MPa. Regenerating cellulose acetate increased the strength by approximately 175.7%. Furthermore, the incorporation of CNCs as a reinforcing agent led to a substantial increase in mechanical strength, with the CA containing CNCs fibers exhibiting a 448.5% improvement compared to the original cellulose acetate fibers. These values are higher than previously reported in literature [18][19].

The improvement in mechanical properties can be attributed to two key factors: the regeneration process and the incorporation of cellulose nanocrystals (CNCs). First, the deacetylation and subsequent regeneration of cellulose acetate back to cellulose significantly enhance the fiber's mechanical properties. The deacetylation process converts the CA into cellulose, facilitating the formation of stronger intermolecular hydrogen bonds between cellulose molecules which contributes to the enhanced

mechanical performance. Second, the addition of CNCs further increases the mechanical strength and stiffness of the fibers. CNCs act as reinforcement agents within the fiber matrix. The nanoscale dimensions of CNCs are localized within cellulose fibers by forming multiple hydrogen bonds between regenerated cellulose acetate and CNCs leading to strong polymer network and improved mechanical strength.

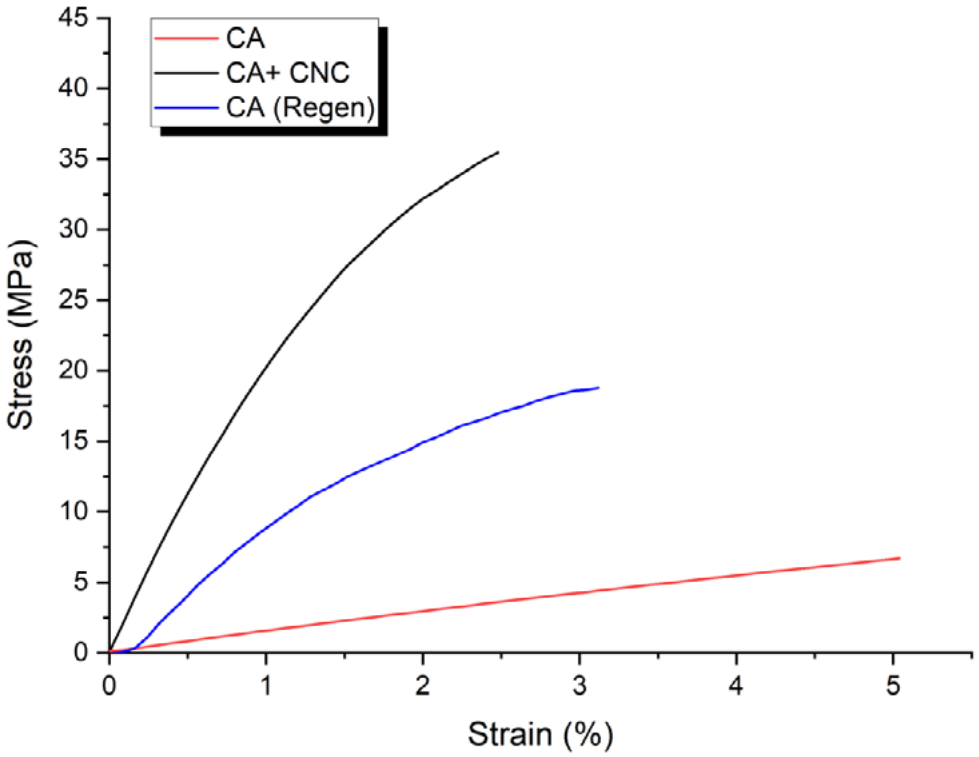

Figure 4. Tensile test analysis of the fiber mat from CA (red); after the regeneration (cellulose) (blue) and cellulose acetate reinforced with CNCs without regeneration (black).

Tensile test analysis of the samples revealed a notable increase in the strength of cellulose acetate fibers after following the regeneration highlighting the effect hydrogen bonds interactions on the mechanical strength of cellulose electrospun fibers. Furthermore, the incorporation of cellulose nanocrystals (CNCs) into the cellulose acetate fibers led to an additional significant improvement in mechanical strength. The CNCs provided reinforcement at the nanoscale, contributing to the overall robustness of the fibers. This systematic enhancement underscores the synergistic effect of combining deacetylation with nanocrystal reinforcement, thereby producing fibers with superior mechanical performance.

To demonstrate the application of the CNCs-reinforced cellulose fibers, for 3D printing filaments manufacturing, flax fibers were impregnated with Poly-Lactic Acid , by an innovative extrusion technique utilizing a custom-made nozzle, shown in Figure 5. The custom-designed nozzle allowed for precise control over the impregnation process, ensuring uniform dispersion of fibers within the PLA matrix. This technique enables the incorporation of fibers into the PLA filament for 3D printing applications.

In the future, the electrospun fibers composed of cellulose acetate and cellulose nanocrystals (CA+ CNC) will undergo regeneration to achieve mechanical properties that are comparable to or surpass those of pure PLA. These regenerated fibers will then be impregnated into PLA using the custom-made setup illustrated in Figure 5. While the figure currently depicts PLA impregnated with flax fibers, future

work will replace these with yarns of CNC-reinforced electrospun fibers. This approach is expected to enhance the mechanical properties and performance of the resulting 3D printing filaments, paving the way towards advanced material applications.

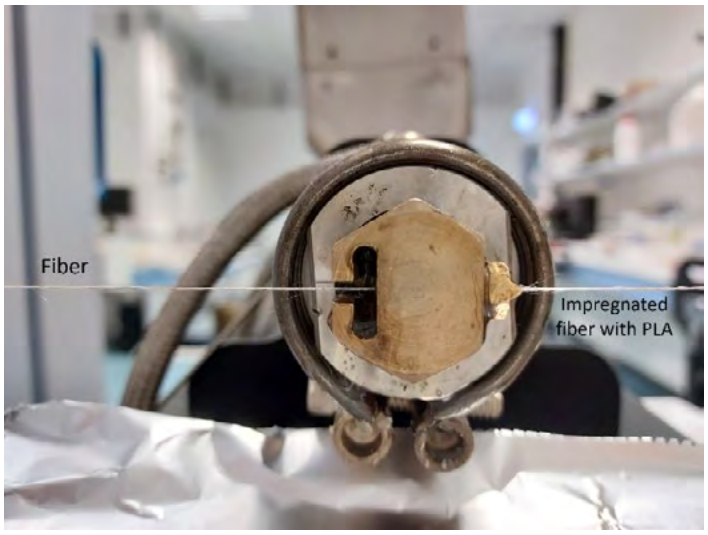

Figure 5. Impregnation of PLA with flax fiber forming a composite for 3D printing.

4. Conclusions

In conclusion, this study demonstrates two effective methods for enhancing the mechanical strength of electrospun cellulose acetate (CA) fibers. The successful regeneration of CA fibers to cellulose through a deacetylation process increased tensile strength from 6.8 MPa to 18.75 MPa, demonstrating the efficiency of the regeneration process. Moreover, the incorporation of cellulose nanocrystals (CNCs) into the electrospun CA fibers significantly enhanced their mechanical properties, raising the tensile strength to 37.3 MPa. These findings highlight the potential of CNCs-reinforced electrospun fibers for various applications, including composites, where high mechanical strength is crucial. The study emphasizes the importance of optimizing processing conditions to achieve the desired mechanical properties. Overall, this work not only confirms the successful regeneration of cellulose from cellulose acetate precursors but also showcases the enhanced mechanical properties achieved through CNC incorporation, offering promising possibilities for diverse applications in advanced material science and engineering.

Acknowledgments

The authors would like to gratefully acknowledge EU for the financial support under the MERA.NET project BioCel3D. Authors would also like to acknowledge Fonds National de la Recherche (FNR) for funding BioCel3D with project reference: INTER/MERA21/16531229/BioCel3D. The authors would also like to thank Dr. Carla Schnell for her assistance with mechanical characterization of the fibers.

References

[1] Rashid, Taslim Ur, Russell E. Gorga, and Wendy E. Krause. "Mechanical properties of electrospun fibers—a critical review." *Advanced Engineering Materials* 23.9 (2021): 2100153.
[2] Wanasekara, N. D., et al. "Orientation of cellulose nanocrystals in electrospun polymer fibres." *Journal of materials science* 51 (2016): 218-227.
[3] Redondo, Alexandre, et al. "Electrospinning of cellulose nanocrystal-reinforced polyurethane fibrous mats." *Polymers* 12.5 (2020): 1021.
[4] Doshi, Jayesh, and Darrell H. Reneker. "Electrospinning process and applications of electrospun fibers." *Journal of electrostatics* 35.2-3 (1995): 151-160.
[5] Reneker, Darrell H., and Iksoo Chun. "Nanometre diameter fibres of polymer, produced by electrospinning." *Nanotechnology* 7.3 (1996): 216.
[6] Li, Dan, and Younan Xia. "Electrospinning of nanofibers: reinventing the wheel?" *Advanced materials* 16.14 (2004): 1151-1170.
[7] Vats, Shameek. "Spinning Functional Fibers: An Interplay of Rheology, Miscibility & Crosslinking." Diss. University of Luxembourg, Luxembourg, 2021.
[8] van Der Heijden, Sam, et al. "Novel composite materials with tunable delamination resistance using functionalizable electrospun SBS fibers." *Composite Structures* 159 (2017): 12-20.
[9] Wang, L., and A. J. Ryan. "Introduction to electrospinning." *Electrospinning for tissue regeneration*. Woodhead Publishing, 2011. 3-33.
[10] Vats, Shameek, et al. "Combining responsiveness and durability in liquid crystal-functionalised electrospun fibres with crosslinked sheath." *Liquid Crystals* 49.5 (2022): 690-698.
[11] Frey, Margaret W. "Electrospinning cellulose and cellulose derivatives." *Polymer Reviews* 48.2 (2008): 378-391.
[12] Liu, H., & Hsieh, Y. L. (2002). Ultrafine fibrous cellulose membranes from electrospinning of cellulose acetate. *Journal of Polymer Science Part B: Polymer Physics*, *40*(18), 2119-2129.
[13] Goffin, Anne-Lise, et al. "From interfacial ring-opening polymerization to melt processing of cellulose nanowhisker-filled polylactide-based nanocomposites." *Biomacromolecules* 12.7 (2011): 2456-2465.
[14] Habibi, Youssef, and Alain Dufresne. "Highly filled bionanocomposites from functionalized polysaccharide nanocrystals." *Biomacromolecules* 9.7 (2008): 1974-1980.
[15] Chen, Mingjie, et al. "Solvent-free acetylation of cellulose by 1-ethyl-3-methylimidazolium acetate-catalyzed transesterification." *ACS sustainable chemistry & engineering* 7.20 (2019): 16971-16978.
[16] Vanderfleet, Oriana M., and Emily D. Cranston. "Production routes to tailor the performance of cellulose nanocrystals." *Nature Reviews Materials* 6.2 (2021): 124-144.
[17] George, Johnsy, and S. N. Sabapathi. "Cellulose nanocrystals: synthesis, functional properties, and applications." *Nanotechnology, science and applications* (2015): 45-54.
[18] Goetz, Lee A., et al. "All cellulose electrospun water purification membranes nanotextured using cellulose nanocrystals." *Cellulose* 25 (2018): 3011-3023.
[19] Del Río De Vicente, José Ignacio. "Cellulose nanocrystals functionalized cellulose acetate electrospun membranes for adsorption and separation of nanosized particles." (2021).

CHARACTERIZATION OF MECHANICALLY RECYCLED GLASS FIBER COMPOSITE REINTRODUCED INTO PETG THERMOPLASTIC FOR FUSED FILAMENT FABRICATION

Zijian Wang[1], Zhengshu Yan[1], Shirin R. Fakhr[1], and Larry Lessard[1]

[1]SCML, Mechanical Engineering, McGill University, Montreal H3A0G4, Canada
Email: larry.lessard@mcgill.ca, Web Page: https://www.mcgill.ca/composite/

Keywords: glass fiber composite, mechanical recycling, pelletization, fused filament fabrication

Abstract
Glass Fiber Reinforced Polymer Composites (GFRPCs) are frequently used for stiff, lightweight, and large structures. Due to the nature of the thermoset resins used, proper disposal at end-of-life has proven difficult. Wind turbine blades, decommissioned aircraft, automotive components, and large recreational water slides contribute to the increasing mass of waste GFRPC's annually. Landfilling of such structures poses a growing risk to the environment and limits access to the potentially reusable fiber reinforcements. One promising alternative is the mechanical grinding of GFRPC structures into recyclates which can then be re-introduced into Fused Filament Fabrication (FFF) to improve the strength and stiffness of printed parts. In this work, GFRPC recyclate made from recycled water slides and its pelletization with poly(ethylene terephthalate glycol) (PETG) was characterized at various stages of the mechanical recycling strategy up to and including pelletization. Recyclates produced from the grinding and milling process were sieved in a gyratory screener and the finest fraction of recyclate was pelletized with virgin PETG. Fiber length distributions were generated while TGA, DSC, and CT scanning were used for recyclate and pellet characterization. Improvements in sieve yield and pelletization quality control were found to be necessary while fiber length control saw some success.

1. Introduction

As the use for Glass Fibre Reinforced Polymer Composites (GFRPCs) has proliferated into major sectors including automotive, aerospace, marine, and recreation, the amount of non-biodegradable waste increases at the same time. With production estimated at 8 million tons and wastage estimated at 1.5 million tons annually, the need to develop effective recycling methods has been highlighted repeatedly in the literature [1-5]. However, due to the use of thermosetting resins and their highly stable molecular cross-linking, end-of-life processing is rendered very difficult, limiting the feasibility of commercialized recycling methods [2, 5, 6]. Lab-scale studies on alternatives to the current disposal routes of incineration and landfilling comprises mostly of thermal, chemical, or mechanical methods [2, 5, 7]. The latter approach has been highlighted as the simplest and most cost-effective, with only a few examples of commercialization [4, 7, 8]. Integration of mechanically recycled fiber reinforced composites, termed "recyclates", into thermoplastics for use in Fused Filament Fabrication (FFF) has gained recent attention and shown promising improvements in filament performance [7, 9-11]. Employing a multi-stage strategy comprised of mechanical size reduction, sieve processing, dehydration, pelletizing, and filament extrusion, recycling of GFRPCs for FFF has been limited to lab-scale tests [2, 7, 9]. Ensuring the compatibility between the recyclate and commonly used FFF thermoplastics such as poly(ethylene terephthalate glycol) (PETG) [12] is key to scaling this recycling solution. The large variance in fiber lengths and matrix residue sizes of the recyclate presents a challenge in doing so. Therefore, the ongoing research of the authors addresses various stages of the filament making process to evaluate and characterize the performance of recycled GFRPC when mixed with this

polyester. This report details the progress made to date in applying the aforementioned recycling strategy to incorporate recycled GFRPC from water slides into virgin PETG matrix up to and including the pelletization step.

2. Methodology

2.1. Material preparation and processing

Decommissioned water slide test panels measuring 30cm by 20cm made from glass fiber reinforced poly(ether-sulfone) (PES) matrix coated with polystyrene-based (PS) gel were provided by Proslide Technology, Canada. The panels were fed into a grinding machine (ECO-WOLF, USA) employing a hammer mill system fitted with 3mm hole size classifier to produce granulated material, referred to as 'as-ground'. A gyratory screening machine (110V 15.7" Stainless Steel Vibrating Screen, INTBUYING) fitted with an 840-150µm wire mesh sequence was used to sieve the ground recyclate to extract the fraction passing the 150µm mesh, henceforth referred to as 'fine' recyclate, for filament making. The top two output spouts were sealed to encourage the extraction of fine recyclate from the bottom, third layer. Sieve inputs of 250g, 500g, 750g, 1250g of recyclate were evaluated for sieving times and fine fraction yield. Fine fractions were combined once sieving was completed. Following this, neat PETG pellets supplied by Amco Polymers (USA) were dehydrated at 65°C for 6 hours, blended in a twin-screw extruder (Leistritz Extrusion Technology, Germany) with the sieved, fine recyclate at a 10 wt% recyclate ratio, and produced into composite pellets in a pelletizer (Bay Plastics Machinery, USA). Table 1 shows the parameter values used for this process.

Table 1. Process parameter values for pelletization of 10 wt% recyclate / PETG matrix

Process	Parameter	Units	Value
Extrusion	Feed roll speed	RPM	10
	Screw speed	RPM	150
	Subzone 1-2	°C	265
	Subzone 3	°C	260
	Subzone 4	°C	255
	Subzone 5	°C	250
	Subzone 6-8	°C	245
Pelletization	Feed roll speed	RPM	4
	Cutter speed	RPM	3.5

2.2. Characterization

During sieving, the fine recyclate was weighed at regular time intervals to determine the instantaneous percent yield and yield rates. Once the change in fine fraction weight achieved less than 1% of input quantity, the sieving process was stopped, and the final weight and time elapsed was recorded. Microscopy (Nikon, Japan) was performed to determine the fiber length distribution of as-ground and sieved recyclate. Individual fibers were manually measured through microscopy software and analyzed using 50µm bin widths. Distribution convergence was determined via calculation of the Standard Error of the Mean (SEM). A target of 3000 length measurements was set to achieve a convergent length distribution. Thermogravimetric Analysis (TGA) was performed on small samples of recyclate, heating from room temperature up to 600°C in a TGA machine (Q500, TA Instruments, USA) in a nitrogen oxide environment followed by the introduction of air to pyrolyze the remaining ashes. Glass fiber content was taken from weight readings following the pyrolysis of ashes at the 600°C mark. The weight fraction compositions of as-ground and sieved recyclate were also extracted from TGA results. Due to lower variability [13], the fiber diameter distribution of 300 fibers from the fine recyclate fraction was obtained following TGA as well to ensure smooth fiber contours were generated after pyrolysis of the matrix residue. Image analysis software (Avizo, Thermo Fisher Scientific, USA) was used to automatically measure the diameter of the fibers and 2.0µm bin widths were used to generate the

diameter distribution. Differential Scanning Calorimetry (DSC) was performed on samples of neat PETG in a DSC machine (Q100, TA Instruments, USA) to obtain the glass transition and melting temperatures. The internal morphology of composite pellets was also characterized by X-ray through Computed Tomography (CT) scanning (Xradia 630 Versa, ZEISS, Germany).

3. Results and discussion

3.1 Sieving

Figure 1 shows the time taken for each input sample size to achieve less than 1% change in fine recyclate yield for N ≤ 2 repeats. For each sample size, the total time required were 120, 210, 360, 540, and 825 seconds respectively for 250g, 500g, 750g, 1000g, and 1250g of input. It was found that the rate of material processing decreased non-linearly with linear increases in sieve input. Figure 2 shows the yield achieved for each input mass, averaging 18%.

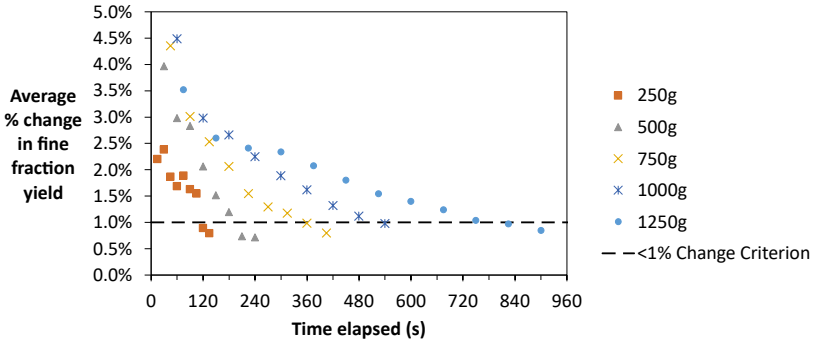

Figure 1. <1% change stopping criterion for input mass from 250g to 1250g in 250g intervals.

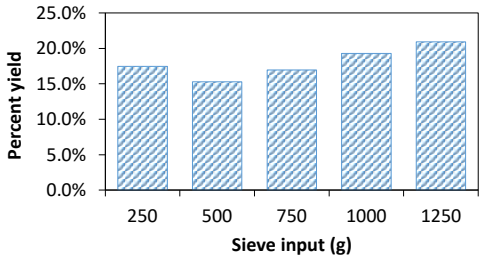

Figure 2. Total yield achieved per sieve input following sieve time according to <1% change criterion.

The resulting processing durations required indicated a possibility to optimize the input mass and the sieving time for increased processing speeds. The low yield of the fine fraction highlighted the prospective improvements on sieving to extract greater amounts of fine recyclates from the ground material. The sieve input, sieving time, and improvements to fine recyclate yield were evaluated in a different study, however.

3.2 Fiber length distributions

The distribution of fiber lengths was obtained following the procedure detailed in section 2.2. Figure 3 shows the resulting relative frequency distribution of as-ground and sieved recyclate with 1000 and 3000 fibers measured, respectively. The distributions revealed mean values of 288µm for as-ground and 177µm for sieved recyclate. The 50-200µm range corresponded to 48.7% of as-ground measurements while the same range corresponded to 59.2% for sieved measurements. A decrease in variance was therefore observed following the sieving step as shown by the narrower distribution. However, 46.0%

of fibers measured post-sieving still exhibited lengths above the finest mesh size of 150µm, indicating the passing of fibers vertically through the mesh. The vibrations caused by the gyratory sieve allowing for fiber reorientation while airborne could be a plausible explanation [14]. Considering the 0.6mm FFF printer nozzles to be used (Original Prusa i3 MK3S+, Prusa Research, Czech Republic), the cumulative frequency of fibers past this length was 10.1% greater in the as-ground material (11.7%) than in the sieved material (1.6%). Considering the fiber breakage that also occurs during FFF [15], the latter cumulative frequency will undoubtedly near 0% during printing. Therefore, sieving could avoid clogging during the 3D printing process. Figure 4 shows the SEM of the distribution for sieved recyclate, depicting a convergence of the distribution. Although the convergence of the as-ground recyclate distribution was not confirmed, the improvement in fiber length consistency can be seen.

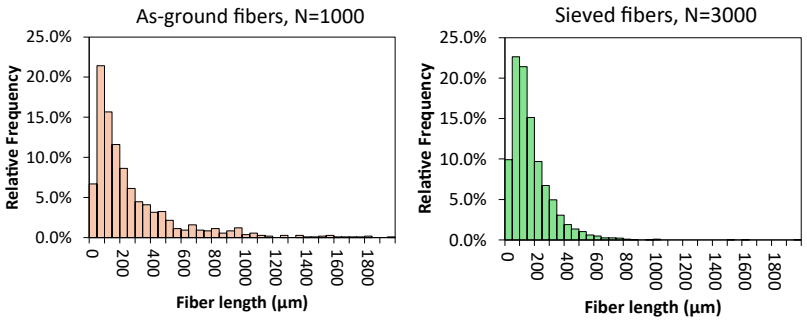

Figure 3. Fiber length distributions for **a)** as-ground fibers and **b)** sieved fine fibers

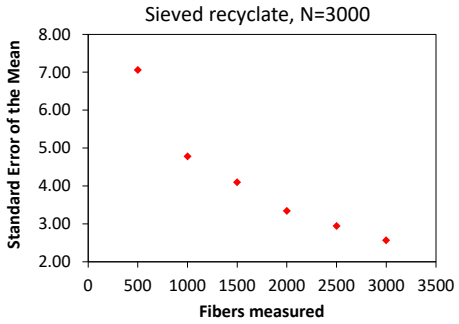

Figure 4. Standard Error of the Mean for sieved fine recyclate.

In summary, the reduction in number of fibers surpassing 0.6mm showed that sieving can provide a simple way to control the fiber length distribution for the given application. The passing of fibers vertically through meshes can be mitigated by addressing the intensity of vertical vibrations, allowing for better control of the distribution with the choice of mesh sizes. Lastly, increasing the number of length measurements into the thousands compared to previous work [7, 9] was shown to provide a better representation of the material sample. Future sieving work will address the convergence of as-ground recyclate measurements and the rejection of excessively short fibers or particulate residue prior to pelletization.

3.3 Fiber diameter distributions

Figure 5 shows the relative frequency distribution of fiber diameter for the fine recyclate fraction. For 300 fibers measured, the mean was found to be 18.3µm while the range spanned 13.6µm to 24.7µm. Importantly, these measurements aligned with commercial E-glass fiber diameters [13]. Although the effect of fiber diameter on printing performance was not investigated considering the comparatively large nozzle diameters used, validating the fiber diameter through measurement was valuable.

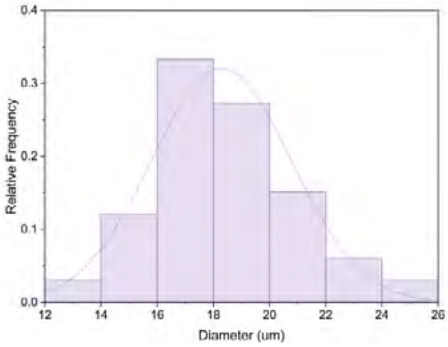

Figure 5. Fiber diameter distribution for N=300 fibers of sieved recyclate.

3.4 TGA

Figure 6 shows thermogravimetric analysis results for various stages of the recycling process. For as-ground recyclate depicted in Figure 6a, a 2.24% decrease in weight starting around the 100°C mark can be linked to moisture evaporation and to the carbonization of PS gel coating [16]. A sharp 47.1% weight reduction was observed around the 350°C mark, corresponding to the pyrolysis of PES matrix residue [17]. Therefore, it can be concluded that the as-ground recyclate comprised of 47.1 wt% PES matrix residue, 2.24 wt% gel coating, and 50.7 wt% glass fiber. The composition of sieved, fine recyclate similarly deduced from Figure 6b was 61.6 wt% fiber, 36.4 wt% residue, and 2.04 wt% gel coating. From Figure 6c, fibers represented 5.51-11.2 wt% of the pellet samples while 5.18% was attributed to the residue and the gel coating. Considering the literature values of decomposition temperature T_d for PETG of around 400°C [12], the remaining 86.6 wt% was attributed to the added PETG.

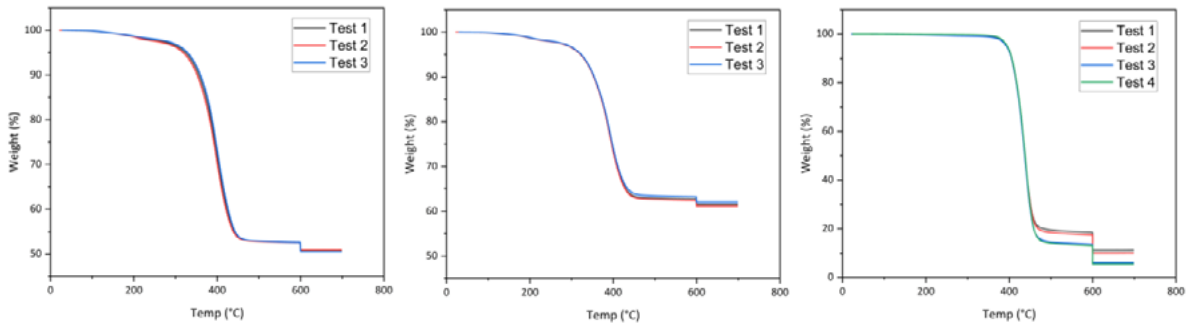

Figure 6. Thermogravimetric analysis results for **a)** as-ground recyclate, **b)** sieved recyclate, and **c)** 10 wt% sieved recyclate / PETG pellet

A few notable observations can be made from these results. Nearly half of the as-ground material is comprised of old matrix residue resulting from the mechanical size reduction steps. Importantly, a significant portion of residue remains post-sieving, explained by the bound residue particles on fibers shown in and also in the literature [4, 7]. Although a target of 10 wt% recyclate was set for pelletization, it can be seen here that the resulting proportion varies significantly between 10-16%, signifying blending inconsistencies during pelletization. TGA was also performed to confirm the decomposition temperature of pure PETG while following the same temperature profile used for the recyclates, as shown in . A T_d of around 400°C was again detected.

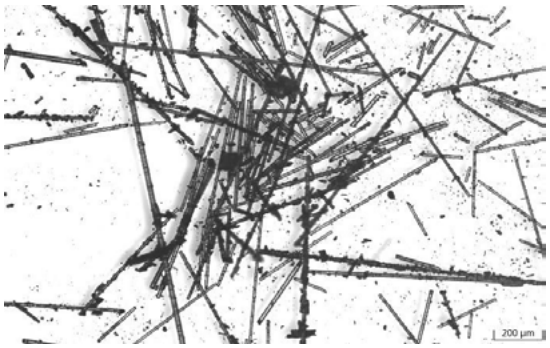

Figure 7. Microscopy image of sieved recyclate. Rough fiber surface caused by fiber-bound matrix residue.

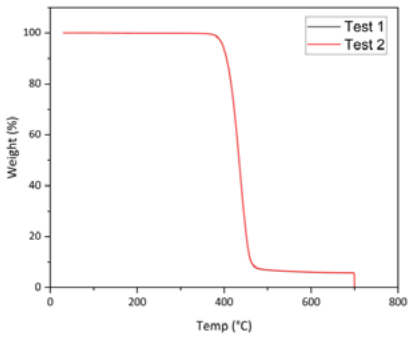

Figure 8. TGA performed on new, virgin PETG pellets.

To summarize, the results of TGA have been useful in depicting the reduction in residue content within the recyclate when undergoing sieving. The observed reduction represented positive signs in removing the highly stable and difficult-to-process thermoset residue from the recyclate. The deviation in recyclate content within the pellets as shown was also an important indication of the insufficient quality control during pelletization. TGA will be used again in subsequent studies following improvements on the sieving parameters to understand the changes in weight composition.

3.5 DSC

Differential scanning calorimetry was also performed on the virgin PETG pellets to confirm the glass transition temperature T_g and the melting temperature T_m. Glass transition was observed at 75°C in Figure 9a while the sample exhibited melting at 225°C shown in Figure 9b. These values were expected and were confirmed by tests found in the literature [12, 18].

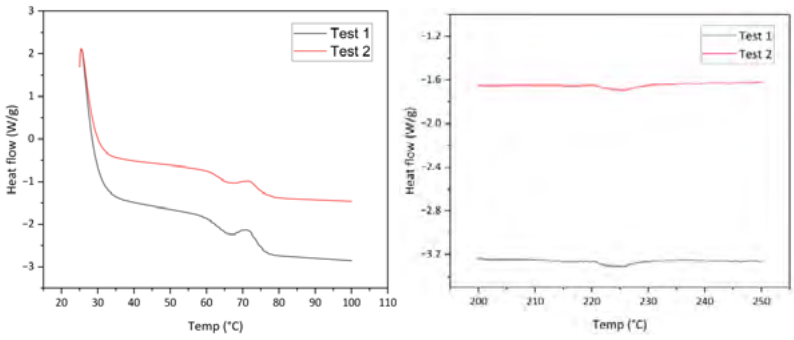

Figure 9. Differential scanning calorimetry curves of neat PETG pellet at **a)** the glass transition regime and at **b)** the melt regime.

The use of DSC in this study helped to confirm the material characteristics and also provided baseline measurements of T_g and T_m of PETG. These would allow for direct comparisons to the virgin matrix, supporting future rheological investigations in the pelletization, filament extrusion, and 3D printing of glass fiber recyclate/PETG composite.

3.6 X-ray scanning

Recyclate/PETG composite pellets 4mm in size were studied by X-ray and provided the internal morphology shown in . Small particles, presumably of recyclate, were seen to be scattered throughout the matrix, while the frequency and size of internal voids were observed to increase towards the center of the pellet. Insufficient dehydration prior to pelletization could lead to voids generated by water vapour while excessive cooling rates could have promoted cavitation [19].

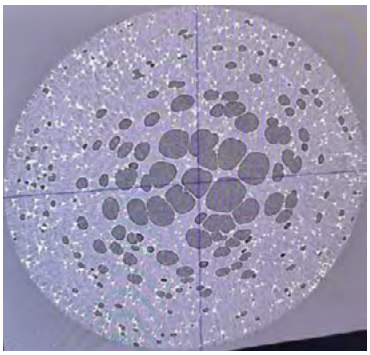

Figure 10. CT scan of 10 wt% recycled GFRPC / PETG composite pellet.

The scanning of pellets by computed tomography helped evaluate pellet quality by displaying the internal morphology. The significant presence of voids detected by CT scan provided additional justification in improving the control of the pellet quality during processing, notably during the dehydration and cooling stages.

4. Conclusions

The need to recycle glass fiber composite material has been repeatedly highlighted in the literature. Efforts in mechanically recycling this material were detailed in this report, covering the grinding, sieving, dehydration, and pelletization procedures. Nearly half of as-ground recyclate was found to be old PES residue while just over a third of sieved recyclate consisted of the same residue, indicating the positive effects of sieving in reducing residue content. Up to 18% sieve yield of fine recyclate was achieved, highlighting the need for sieving improvements. A convergent, narrow fiber length measurement distribution was acquired post-sieving, alluding to good fiber length control. The exact recyclate weight composition within pellets was found to deviate from the 10% target while excessive voids were detected post-pelletization, both of which suggesting the necessity in improving quality control during pelletization. Focus will be put on the latter as well as in filament extrusion, filament testing, and printed dog-bone tensile testing in subsequent work.

References

[1] S. J. Pickering, R. M. Kelly, J. R. Kennerley, C. D. Rudd, and N. J. Fenwick. A fluidised-bed process for the recovery of glass fibres from scrap thermoset composites. *Composites Science and Technology*, volume(60):509-523, 2000.

[2] O. Zabihi *et al*. A Sustainable Approach to the Low-Cost Recycling of Waste Glass Fibres Composites towards Circular Economy. *Sustainability*, volume(12):641, 2020.

[3] C. Branfoot, H. Folkvord, M. Keith, and G. A. Leeke. Recovery of chemical recyclates from fibre-reinforced composites: A review of progress. *Polymer Degradation and Stability*, volume(215):110447, 2023.
[4] J. Palmer, O. R. Ghita, L. Savage, and K. E. Evans. Successful closed-loop recycling of thermoset composites. *Composites Part A: Applied Science and Manufacturing*, volume(40):490-498, 2009.
[5] Q. Yang *et al*. Recycling waste fiber-reinforced polymer composites for low-carbon asphalt concrete: The effects of recycled glass fibers on the durability of bituminous composites. *Journal of Cleaner Production*, volume(423):138692, 2023.
[6] K. Garfias, M. Hakkarainen, and K. Odelius. Mechanical recycling of epoxy composites reinforced with short-cut aramid fibers: Surface functionalization – The missing piece of the puzzle. *Polymer*, volume(295):126747, 2024.
[7] A. Rahimizadeh, J. Kalman, K. Fayazbakhsh, and L. Lessard. Recycling of fiberglass wind turbine blades into reinforced filaments for use in Additive Manufacturing. *Composites Part B: Engineering*, volume(175):107101, 2019.
[8] J. Beauson, B. Madsen, C. Toncelli, P. Brøndsted, and J. Ilsted Bech. Recycling of shredded composites from wind turbine blades in new thermoset polymer composites. *Composites Part A: Applied Science and Manufacturing*, volume(90):390-399, 2016.
[9] A. Moslehi, A. Ajji, M.-C. Heuzey, A. Rahimizadeh, and L. Lessard. Polylactic acid/recycled wind turbine glass fiber composites with enhanced mechanical properties and toughness. *Journal of Applied Polymer Science*, volume(139):51934, 2022.
[10] N. Giani, L. Mazzocchetti, T. Benelli, F. Picchioni, and L. Giorgini. Towards sustainability in 3D printing of thermoplastic composites: Evaluation of recycled carbon fibers as reinforcing agent for FDM filament production and 3D printing. *Composites Part A: Applied Science and Manufacturing*, volume(159):107002, 2022.
[11] M. Morsidi, P. T. Mativenga, and M. Fahad. Fused Deposition Modelling Filament with Recyclate Fibre Reinforcement. *Procedia CIRP*, volume(85):353-358, 2019.
[12] P. Latko-Durałek, K. Dydek, and A. Boczkowska. Thermal, Rheological and Mechanical Properties of PETG/rPETG Blends. *Journal of Polymers and the Environment*, volume(27):2600-2606, 2019.
[13] C. Zweben. *Encyclopedia of Condensed Matter Physics.* Academic Press, Oxford, 2024.
[14] B. A. Wills and J. A. Finch. *Wills' Mineral Processing Technology*. Butterworth-Heinemann, Boston, 2016.
[15] Z. Yang, Z. Yang, H. Chen, and W. Yan. 3D printing of short fiber reinforced composites via material extrusion: Fiber breakage. *Additive Manufacturing*, volume(58):103067, 2022.
[16] F. Xu, X. Xia, J. Luo, D. Luo, and J. Xu. Maximized energy recovery by catalytic co-pyrolysis of dewatered sewage sludge and polystyrene to contribute in bio-circular economy: Synergistic compositional analysis of bio-oil and syngas through artificial neural networking. *Process Safety and Environmental Protection*, volume(186):1253-1262, 2024.
[17] K. M. Mukeba, K. E. Shelar, B. Faradizaji, E. B. Caldona, C. U. Pittman, and D. W. Smith. Semi-fluorinated Poly(aryl ether sulfone)s via step-growth polymerization of perfluorocyclohexene with bisphenols. *Polymer*, volume(253):124937, 2022.
[18] C. Yan *et al*. PETG: Applications in Modern Medicine. *Engineered Regeneration*, volume(5):45-55, 2024.
[19] C. Rauwendaal. *Understanding Extrusion*. Hanser, 2019.

WETTABILITY AND INTERFACIAL PROPERTIES OF BASALT FIBRES/BIOBASED EPOXY COMPOSITES WITH STAR-LIKE POLY(BUTYL METHACRYLATE)-POLY(GLYCIDYL METHACRYLATE) BLOCK COPOLYMER ADDITIVES

K. Zukiene[1], R. Pinto[2], G. Monastyreckis[2], M. Novakova[3], V. Spacek[3], T. Glaskova-Kuzmina[2], and D. Zeleniakiene[2]

[1]Department of Production Engineering, Kaunas University of Technology, Studentu 56, Kaunas 51424, Lithuania, Email:kristina.zukiene@ktu.lt, Web Page: https://ktu.edu/
[2]Department of Mechanical Engineering, Kaunas University of Technology, Studentu 56, Kaunas 51424, Lithuania, Email:rochele.pinto@ktu.edu, gediminas.monastyreckis@ktu.lt, tatjana.glaskova-kumina@ktu.lt, daiva.zeleniakiene@ktu.lt, Web Page: https://ktu.edu/
[3]Synpo a.s., S. K. Neumanna 1316, 530 02, Pardubice, Czech Republic, Email: marie.novakova@synpo.cz, vladimir.spacek@synpo.cz, Web Page: https://www.synpo.cz/en

Keywords: basalt fibres, biobased epoxy, wettability, star-like polymers, adhesion

Abstract
This study investigates the effect of the addition of star-like poly(butyl methacrylate)-poly(glycidyl methacrylate) (PBMA-PGMA) block copolymer to biobased epoxy resin on basalt fibre wettability and adhesion. Analysis of contact angle measurements of the modified epoxy resin on a surface of basalt fibre reveals improved wetting properties. Improvement in wettability is achieved despite an increase in resin viscosity, which is essential for enhancing composite quality. This finding is further confirmed by atomic force microscope analysis of the film morphology of the cured PBMA-PGMA-modified epoxy resin. The addition of 0.5 wt. % star-like copolymer remarkably increased the values of the epoxy film surface adhesion forces by 74.6%. The work of adhesion between the PBMA-PGMA-modified epoxy and basalt fibre was calculated to be 66.8 mJ/m^2, slightly lower than that of the unmodified epoxy. The change in adhesion at such low levels of the star-like copolymer can be attributed to the intermolecular interactions between PBMA-PGMA and epoxy.

1. Introduction

The interfacial adhesion between the fibres and the polymer matrix is crucial in determining the mechanical properties of fibre-reinforced composites. However, basalt fibres have difficulty interacting with the polymer matrix due to a lack of surface functional groups. This leads to a reduced load-carrying capacity of the composite. It is possible to improve the surface properties and surface interactions of basalt fibre/polymer resin composites by incorporating nanomaterials into the matrix or the surface treatment of the reinforced fibre [1,2]. These traditional surface modification methods have drawbacks, including the requirement of additional processing steps and challenges in dispersing nanomaterials evenly. An alternative surface modification method involves the surface segregation of a component with superior adhesive properties on the surface in blends of epoxy and thermoplastics [3]. Due to the significant differences in polarity and high interfacial tension, thermoplastics and thermosetting plastics form highly incompatible mixtures. Studies indicate that highly branched polymer additives, such as star-like acrylic polymers, can segregate effectively at the surface or fibre/polymer matrix interface and thus increase the adhesion at the phase boundary [4]. Adding star-like polymers derived from methyl methacrylate and butyl methacrylate, along with their derivatives containing hydroxy, carboxy, or epoxy functionalities, can enhance the mechanical properties of adhesives and composites [5].

The aim of the study was to evaluate the effect of the addition of a star-like poly(butyl methacrylate)-poly(glycidyl methacrylate) (PBMA-PGMA) block copolymer to biobased epoxy on the wettability and adhesion to basalt fibres.

2. Materials and methods

2.1. Materials

Commercial diglycidyl ether of bisphenol-A epoxy resin with the commercial name SR GreenPoxy 33 (SZ 8525), with ~31% biobased carbon content derived from plants (viscosity @ 25°C - 3240 mPa.s), was purchased from Sicomin (France). Cardanol-based phenalkamine hardener with the commercial name LITE 2401 was supplied by Cardolite Co (Belgium). A group transfer polymerisation with the arm-first strategy was used for the preparation of poly(butyl methacrylate)-poly(glycidyl methacrylate) (PBMA-PGMA) star-like block copolymer. The synthesis of the PBMA-PGMA copolymers was performed according to the reported procedure [6]. The polymer was supplied in the form of a 50% solution in tetrahydrofuran. Basalt fiber 220 g/m^2 in twill weave 2/2 was supplied by Basaltex NV (Netherlands).

2.2. Preparation of batches

The modified resin specimens were made by adding 0.5 wt.% of PBMA-PGMA star-like block copolymer into the required amount of SR Greenpoxy 33 resin and mixed using a magnetic hot plate stirrer at 40 °C for 24 h. To the modified epoxy mixtures, LITE 2401 hardener was added following the equivalent weight of the resulting resin formulation and films of about 0.12 mm thickness were fabricated.

2.3. Characterisation

Viscosity measurements were conducted using a Brookfield viscometer Model DV-II+Pro (Brookfield Instruments), equipped with an LV3 spindle at a) at room temperature.

The contact angle (CA) measurements were performed using the sessile drop method with a Pocket-Goniometer PG2 (Rycobel NV, Deerlijk, Belgium) at room temperature. Droplets of deionised water and diiodomethane were deposited onto the surface, and digital images of the droplet were captured. The surface tension of the basalt fibre/epoxy composite and the work of adhesion of the epoxy resin to the basalt fibres were determined according to the Owens and Wendt method and the Dupre equation, respectively. A previously published article provides further details on the methodology, equations, and force components of the surface energy of test liquids [7].

A NanoWizard III atomic force microscope (JPK Instruments, Bruker Nano GmbH, Berlin, Germany) was used to estimate the mean adhesion force (the attraction force between the probe and the surface averaged over the image measurement).

3. Results and discussion

Viscosity measurements showed that the viscosity of the bio-based epoxy is 2700 mPa s. Modification of the epoxy with a 0.5 wt. % PBMA-PGMA copolymer increased the viscosity to 4500 mPa s. Due to the increased viscosity of the modified epoxy, it was difficult to distribute the epoxy on the fibre surface to ensure adequate wetting. The intermolecular interactions between PBMA-PGMA and epoxy may explain the increase in the viscosity of epoxy as a result of the modification.

The investigation of the influence of PBMA-PGMA copolymer on the wettability properties of the epoxy resin showed that the contact angle of the PBMA-PGMA copolymer on the basalt surface was lower compared to neat epoxy because of the presence of an epoxy group capable of forming a strong interaction with the basalt fibre. Therefore, adding 0.5 wt. % PBMA-PGMA copolymer to the epoxy reduced its contact angle on the basalt surface from 55° to 43°. This indicates that despite the increase in viscosity, this modification increased the wettability of the epoxy resin, making it easier to spread on the basalt surface.

The mean adhesion force, i.e., the force of attraction between the scanning probe and the surface of modified and unmodified epoxy films averaged over the image, is presented in Fig. 1. It is evident that the surface of epoxy resin film and the epoxy film modified with 0.5 wt. % PBMA-PGMA copolymer exhibit quite different adhesion forces. The adhesion force of epoxy modified with a 0.5 wt. % PBMA-

PGMA copolymer film was significantly higher – 56.9 nN than that found for the epoxy film – 34.3 nN.

Table 1. Average contact angles (in degrees) of the epoxy, the epoxy modified with 0.5 wt. % PBMA-PGMA copolymer and PBMA-PGMA copolymer on basalt surface

Liquid	Contact angle (°)
epoxy	55
epoxy modified with 0.5 wt. % PBMA-PGMA copolymer	43
PBMA-PGMA copolymer	15

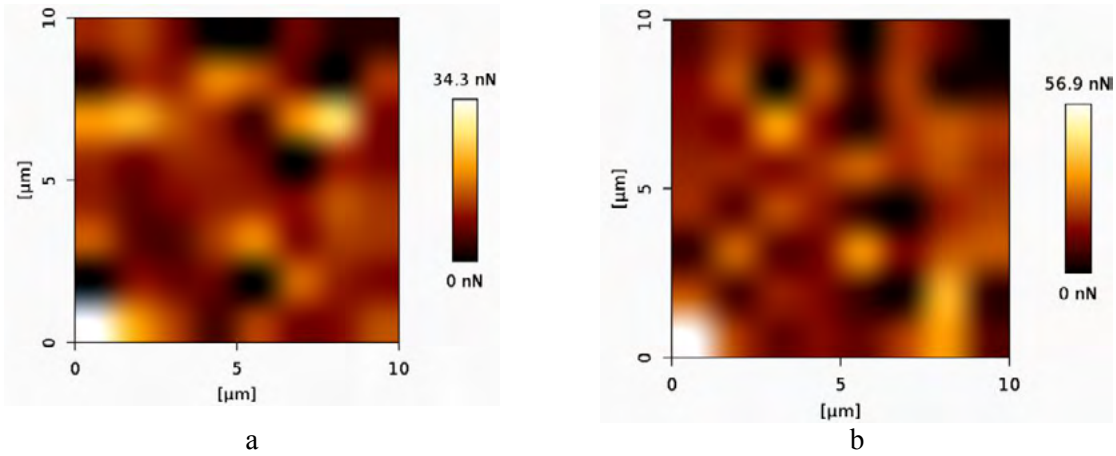

a b

Figure 1. Adhesion force images of epoxy resin (a) and 0.5 wt. % PBMA-PGMA modified epoxy resin (b) films.

The water and diiodomethane contact-angle measurements on the cured biobased epoxy and the biobased epoxy modified with 0.5 wt. % PBMA-PGMA copolymer films are shown in Table 2. The epoxy film exhibited a water contact angle of 69°, while the epoxy/PBMA-PGMA film − had a value of 74°. These results showed that the films exhibit hydrophilic characteristics. Therefore, the surface of unmodified resin films exhibits better wetting.

The surface energy of the epoxy resin film surface was estimated to be 49.1 mJ/m^2 (Table 3), which is typical for commercially available epoxy resins. The PBMA-PGMA copolymer decreased the surface energy of the epoxy resin to 48.9 mJ/m^2.

Table 2. Contact angles (in degrees) of polar and non-polar liquid on the surface of cured epoxy, PBMA-PGMA-modified epoxy films, and basalt fibre.

Specimen Type	Water	Diiodomethane
Epoxy	69	24
Epoxy/PBMA-PGMA	74	20
Basalt fibre [7]	45	51

For the calculation of the interfacial tension and the work of adhesion between the epoxy-basalt interface, the basalt surface energy values and its polar and dispersion components were taken from [8]. The interfacial energy γ_{12} between basalt and unmodified epoxy resin was calculated at 25 mJ/m^2. However, the addition of the PBMA-PGMA copolymer increased the value of the interfacial energy γ_{12} up to 30.5 mJ/m^2.

The interaction occurring at the phase boundary of the basalt fibre and epoxy was also evaluated by employing adhesion work using the Dupre equation. The work of adhesion values obtained for basalt fibre and epoxy resin were relatively low (72 mJ/m^2). These values are lower than those obtained for glass fibre and epoxy (89–95 mJ/m^2) [8]. In the case of copolymer PBMA-PGMA addition copolymer,

the work of adhesion of epoxy film surface is further reduced up to 66.8 mJ/m^2.

Table 3. Surface energy γ_s (mJ/m^2) dispersion γ_s^d and polar γ_s^p components determined by Owens-Wendt equation for epoxy and PBMA-PGMA-modified epoxy resin films.

Specimen Type	γ_s	γ_s^d	γ_s^p
Epoxy	49.1	41.9	7.2
Epoxy/PBMA-PGMA	48.9	44.3	4.6
Basalt fibre [7]	48.5	17.9	30.6

4. Conclusions

The star-like PBMA-PGMA block copolymer has been found to exhibit good wetting properties for basalt fibres, attributed to the presence of PGMA, which contains an epoxy group capable of forming strong interactions with the basalt fiber. PBMA-PGMA block copolymer has been demonstrated to enhance the wetting properties of the biobased epoxy resin despite an increase in the resin viscosity. The addition of the star-like copolymer reduced the epoxy resin's contact angle with the basalt fibre's surface by 22%, confirmed by AFM measurements. The enhancement is significant for basalt fibre-reinforced composites, as it helps to improve the adhesive properties, resulting in less porosity and air voids. However, calculations of the work of adhesion between the basalt fibre and PBMA-PGMA-modified epoxy resin estimated a lower value (66.8 mJ/m^2) than that known for glass fibre and epoxy.

Acknowledgments

This project has received funding from the Research Council of Lithuania (LMTLT), agreement No. S-MIP-23-134.

References

[1] A. Abdi, R. Eslami-Farsani, H. Khosravi. Evaluating the Mechanical Behavior of Basalt Fibers/Epoxy Composites Containing Surface-modified $CaCO_3$ Nanoparticles. *Fibers and Polymers,* 19:635-640, 2018.

[2] Y. Guo, M. Zhou, G.-Z Yin, E. Kalali, N. Wang, D.-Y. Wang. Basalt Fiber-Based Flame Retardant Epoxy Composites: Preparation, Thermal Properties, and Flame Retardancy. *Materials*, 14(4):902, 2021.

[3] X. Cheng and J.S. Wiggins, *Novel techniques for the preparation of different epoxy/thermoplastic blends*. In: Handbook of Epoxy Blends (eds. J. Parameswaranpillai, N. Hameed, J. Pionteck and E. Woo). Springer. 459-486, 2017.

[4] T. S. Laws, H. Mei, T. Terlier, R. Verduzco, G. E. Stein. Tailoring the Wettability and Substrate Adherence of Thin Polymer Films with Surface-Segregating Bottlebrush Copolymer Additives. *Langmuir*, 39 (20):7201-7211, 2023.

[5] R.Pinto, G. Monastyreckis, H. M. Aboelanin, V. Spacek, D. Zeleniakiene.. Mechanical properties of carbon fibre reinforced composites modified with star-shaped butyl methacrylate. *Journal of Composite Materials*, *56*(6): 951-959, 2022.

[6] H. M. Aboelanin, S. Podzimek, V. Spacek. Synthesis and molecular structure of highly compact star-like poly(methyl methacrylate) and poly(butyl methacrylate). *European Polymer Journal*, 194 112119:1-7, 2023.

[7] K. Zukiene, G. Monastyreckis, S. Kilikevicius, M. Procházka, M. Micusik, M. Omastová, A. Aniskevich, D. Zeleniakiene. Wettability of MXene and its interfacial adhesion with epoxy resin. *Materials Chemistry and Physics*, 257:123820, 2021.

[8] R. Ravel, M.F. Pucci, P.J. Liotier. Influence of the surface energy of a basalt fiber on capillary wicking and in-plane permeability. In the *23rd International Conference on Composites Materials (ICCM 23)*, 1-10, 2023.

[9] J.G. Swadenera, K.M. Liechti, A.L. Lozanne, The intrinsic toughness and adhesion mechanisms of a glass/epoxy interface. *Journal of the Mechanics and Physics of Solids*, 47(2):112-147, 1999.

DETERMINATION OF REINFORCING FIBERS FINENESS – COMPARISON OF MEASUREMENT METHODS, THEIR ACCURACY, ADVANTAGES AND LIMITATIONS

B. Tomkova[1]

[1]Technical University of Liberec, Dpt. of Material Engineering, Studentska 2, 461 17 Liberec, Czech Republic

Email: blanka.tomkova@tul.cz, Web Page: https://www.ft.tul.cz/en/departments/department-of-material-engineering-profiles/blanka-tomkova-ph-d

Keywords: fineness, linear density, multifilament, short fiber, fiber diameter, volume density

Abstract

Fiber fineness (linear density) is one of the basic characteristic of fiber material known to all textile engineers. However, its measurement is not simple and people outside the textile field, in an attempt to determine this parameter, often use the methods that are not entirely suitable for the type of the fibers they work with. This work offers current overview of the standardized measurement methods used to determine the fineness to show their suitability or unsuitability for a given type of fiber (both filaments and short ones), and to compare the accuracy of the obtained results.

1. Introduction

When we look at the literature, fineness is mostly defined as ”one of the most important properties of the fibers that are made into textile products. The fiber fineness has a number of effects on the properties of the yarn and hence the fabric that is made from it”[1]. But what does this description really mean? From a historical point of view, the small diameters of fibers have always presented particular challenges to the fiber industry, which have led to ways of defining fibers and their properties that are different from those used in traditional engineering materials [2].

The main goal of fiber engineers was to normalise characteristics, such as strength and stiffness, so that fibers can be compared. Most engineering materials are compared through normalising the applied force by dividing it with its cross-section to obtain the stress, and relating it to the strain, the ratio between level of the elongation and initial length of the material. The problem with fibers is, they are very fine, and often of irregular cross-section, so it cannot be easily measured [2]. This led to the creation of special system of textile units respecting the specific geometry of linear fiber systems.

The most useful and unambiguous measure of fiber fineness is the linear density, namely mass per unit length, sometimes called titre. The preferred unit is (tex) = (g/km). This has the advantage that it is applicable with appropriate prefixes to all the one-dimensional structures from polymer molecules to yarns, cords and ropes [3]. On the other hand its direct measurement in case of single fibers is somewhat tricky, specially in the case of short fibers. The accurate weighing of very small lengths requires considerable expertise and care, often beyond the limits of human capabilities in terms of sample preparation as well as the accuracy of laboratory scales. Nevertheless, this method is often mentioned, when composite researchers talk about how they analyzed the reinforcing fibers.

As there is no fundamental difference between textile fibers and reinforcing fibers in determination of their geometric properties, i.e. fineness, this overview is intended for non-textile engineers to deepen their understanding of fiber specifics often manifested by a large variability of the measured parameters. This variability can be significantly distorted by choosing an inappropriate measurement method, which can have a negative impact on further use of the fibers regardless they are used in standard yarns and textiles or as composite reinforcement.

In this work the glass and carbon multifilaments are used as typical reinforcing fibers, and polyamide and rayon as a representative of standard textile multifilaments. Glass wool, made from centrifugical spinning, wool and cotton fibers are used as a representatives of short (staple) fibers. Fineness of selected materials was measured by various microscopic methods, further were used the gravimetric and vibroscope methods, and finally the airflow method for fiber tufts. Fineness values obtained from different methods were evaluated by ANOVA statistics. Further the methods are compared in terms of their suitability for the given material, time-consuming and demanding equipment, and their advantages and limitations are discussed.

2. Materials and Testing Methods

To include the entire spectrum of textile fibers also used in textile composites, we tested glass and carbon multifilaments (reinforcing fibers), and polyamide and rayon (standard man-made multifilaments). Glass wool, wool and cotton fibers are representatives of short (staple) fibers, see Table 1.

Table 1. Type and geometry of tested fibers

Fiber Type	Nominal fineness T (dtex)	Nominal diameter d (μm)	Nominal length (f - number of fibers)
Carbon fiber Torayca T800 HB	0.37 ± 0.02	5.0 ± 0.2	multifilament f 6000
Glass fiber ECR 13-300D-608	3.25 ± 0.16	13.0 ± 0.6	multifilament f 923
Polyamide 6 Nexis 371	6.7 ± 0.3	27.4 ± 1.3	multifilament f 140
Rayon HT Glanzstoff Bohemia	1.82 ± 0.09	12.3 ± 0.6*	multifilament f 92
Glass wool Knauf Insulation	0.010 ± 0.003	2.0 ± 0.1	10 mm
Australian wool	3.17 ± 0.15	17.5 ± 0.8	65 ± 25 mm
Uganda cotton	2.2 ± 0,1	13.6 ± 0.6*	25 ± 5 mm

* the equivalent diameter, fibers have non-circular cross-section

Fineness of selected fibers was measured by microscopic methods using light, LCM and SEM microscopes, further we used the gravimetric and vibroscope methods, and finally the airflow method for fiber tufts. An overview of used devices and measuring standards is given in the Table 2.

Table 2. Testing methods for fineness measurement

Testing method	Measurement device	Measurement description
Microscopic	Optical microscope MEOPTA LEXT OLS5000 LCM microscope SEM microscope VEGA3 LMU	Fineness is derived from fiber diameter or cross-section measurements. The methods are described e.g. by Saville in [1]. The measurement is standardized only for wool and other animal fibers by ISO 137:2015 [4], and ASTM D2130-22 [5].
Gravimetric	Balance XSR 105 Metler Toledo Sartorius weighing scale	The method is based on single-fiber or fiber bundle weighing described in standard ASTM D1577-07 [6].

Vibroscope	Vibroscope Lenzing Technik	The method is based on analysis of natural fundamental frequency of vibration of a stretched fiber, described except ASTM [6] e.g. in ISO 1973:2021 [7].
Airflow	Micronaire SLD 019A Shirley developments LTD	The method is based on the measurement of fiber tuft plug resistance to air flow under two prescribed conditions, described in ISO 10306:2014 [8], and ASTM D1282-05 [9].

3. Measurement procedure

3.1 Gravimetric method – fiber bundle

This measurement is comparable with yarn linear density measurement, and it is very useful for analysis of multifilaments, that allow us to obtain a sufficient length *l*(km) of material. The bundle is directly weighed *m*(g), and its fineness is calculated from well known equation (Eq. 1):

$$T_{bundle}(tex) = {}^{m(g)}\!/_{l(km)} \tag{1}$$

Fineness of single fiber is than calculated, if we know nominal number *n* of the fibers in bundle (Eq. 2):

$$T_{fiber}(tex) = {}^{T_{bundle}(tex)}\!/_{n} \tag{2}$$

This method appears to be very simple, however, there is a number of limitations that we must take into account, if we want to obtain reliable results. The first assumption is that the multifil is homogeneous, all fibers are of the same material and have the same geometry. Furthermore, a reliable determination of the number of fibers is important. In practice, the nominal value stated by the manufacturer is usually used. Another option is manual counting, but its usability decreases significantly with increasing fiber count and decreasing diameter of the fibers. For fibers with a diameter of up to 10 microns (e.g. carbon), manual count is practically impossible. In this work, the method was used for all multifilaments, for each it was prepared and weighed 5 samples.

3.2 Gravimetric method – single-fiber

Although this method is mentioned by the ASTM standard [6], from a practical point of view it is only applicable for fibers with a fineness above 0,3 tex. The standard mentions this option is not recommended for fibers shorter than 30 mm. But, for example, a fine carbon fiber of this length weighs approx. 1,1 µg, which is below the edge of measurability even on very precise laboratory balances such as XSR 105 Metler Toledo. Moreover, it is practically impossible to separate one carbon fiber from the bundle and then control we are really working with one fiber only to acquire reliable results.

3.3 Microscopic method

This method is the most practical for determining the fineness of all types of fibers. Using micrographs the fineness is derived either from fiber diameter d(µm) ⇒ for circular fibers, or from fiber cross-section area ⇒ S(µm^2) - for non-circular fibers. For accurate tests it is recommended to measure not less than 150 fibers [1], in ISO standard for the wool [4] even 600 measurement are required. The fineness is calculated from following equations (Eq. 3), and volume density ρ(kg/m^{-3}) of the fibers under examination must be known for the calculation:

$$T_{fiber}(tex) = S(m^2) \cdot \rho(kg \cdot m^{-3}) \cdot 10^6; \qquad T_{fiber}(tex) = \frac{\pi \cdot d^2}{4}(m^2) \cdot \rho(kg \cdot m^{-3}) \cdot 10^6 \tag{3}$$

The easiest way to prepare the samples is, if the measurements can be made on the micrographs of the fibers in the longitudinal view, and we can use either optical or confocal microscopes, see Figure 1. This method is practical for most of more or less circular fibers with diameter higher than 10 microns.
In case of significantly non-circular fibers it is necessary to prepare cross-sectional samples (Figure 2, left), which requires rather demanding preparation and an experienced operator. Also the analysis of very fine micro/nano fibers, that requires the use of an electron microscope (Figure 2, right), is very time-consuming in samples preparation and demanding on operator skills. The choice of imaging device thus depends on tested material, and how quick and accurate results are required. In this work, all microscopic methods were used for all tested fibers.

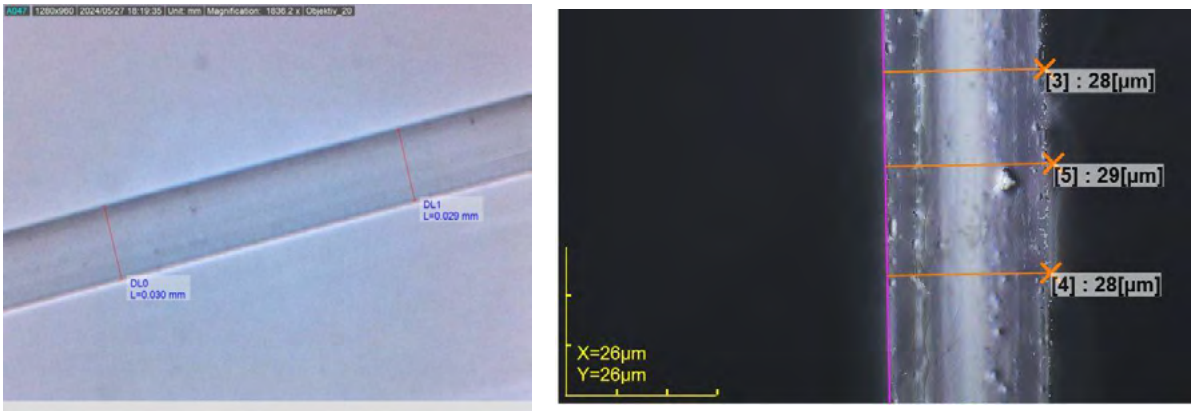

Figure 1. Fiber diameters measured on micrographs acquired from optical (left) and confocal (right) microscopes.

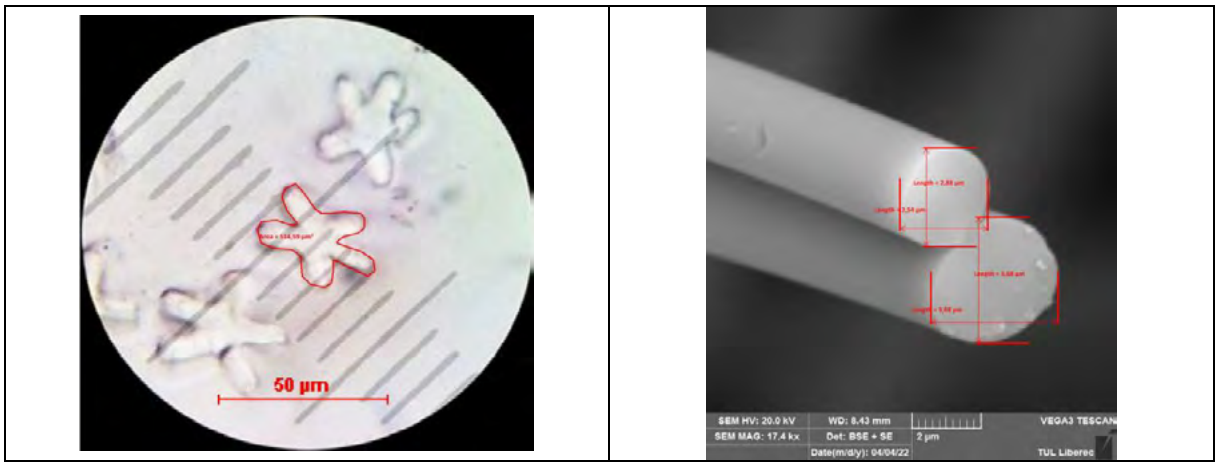

Figure 2. Fiber cross-section area (left) measured on micrographs acquired from optical microscope and fiber diameter acquired from SEM micrograph (right) using Feret's diameter method.

3.4 Vibroscope method

Main advantage of vibroscope method is that it is non-destructive test, which can be used in combination with a tensile test on the same specimen [3]. The method is based on measurement of natural fundamental frequency f(Hz) of vibration of a stretched fiber, which is related both to its linear density, expressed by length L(m) and mass M(kg) of the fiber, and to the tension P(N) used to keep the fiber tight, see Eq. 4. The fineness is automatically calculated and displayed on the device display.

$$f(Hz) = \frac{1}{2L(m)} \cdot \frac{P(N)}{M(kg)} \tag{4}$$

The method is suitable for fibers of minimum 40 mm length preferably in range 0.3-0.9 tex. It is useful mostly for man-made fibers. This method cannot be applied on electrically conductive fibers that spark in the device, and risk a short circuit (e.g. carbon). Here we measured ECR13 Glass, PA6, Rayon, wool and long enough cotton fibers.

3.5 Airflow method

This is an indirect method suitable for rapid measurement of fiber tufts. It is based on the fact that the air, which flows through a uniformly distributed mass of the fibers at a given pressure difference, is determined by the total surface area of the fibers [4]. The surface area of a fiber is proportional to its diameter but for a given weight of a sample the number of fibers increases with the drop of fiber fineness so that the specific surface area (area per unit weight) is inversely proportional to fiber diameter. Because the airflow varies with pressure difference, it is the ratio of airflow to differential pressure that is determined by the fiber diameter. Therefore the method can be used to measure either the airflow at constant pressure or the pressure drop at constant airflow [1]. The diameter d(m) of fibers is calculated from Eq. 5, and the fineness is than calculated from Eq. 3. Here we measured the fineness of glass wool, wool and cotton fibers.

$$d(m) = \sqrt{\frac{Q(m^3 \cdot s^{-1})}{K_g(-) \cdot \Delta P(Pa)} \cdot \frac{(1-\varepsilon)^2}{\varepsilon^3}} \qquad \begin{array}{l} Q(\mathrm{m^3.s^{-1}}) \Rightarrow \text{airflow} \\ \Delta P(\mathrm{Pa}) \Rightarrow \text{pressure drop} \\ K_g(-) \Rightarrow \text{geometric size factor} \\ \varepsilon(-) \Rightarrow \text{fiber tuft porosity} \end{array} \qquad (5)$$

4. Results and Discusion

The fineness values determined by individual measurement methods are presented in Tables 3, and 4. For each value, the time required for the measurement is also evaluated. The estimation includes the time needed for sample preparation, and total time for measurements. Finally the duration per one sample is derived from the total number of measurements.

Table 3. Fiber fineness T(dtex) determined from various measurement methods

Fiber Type	Multifilaments*			
	Carbon	Glass	PA6	Rayon
Optical microscope	0.43 ± 0.12 (F)	4.2 ± 1.2 (F)	7.5 ± 2.1 (F)	2.8 ± 0.7 (F)
Confocal microscope	0.31 ± 0.08 (F)	3.1 ± 0.8 (F)	7.1 ± 1.9 (F)	3.1 ± 0.8 (F)
SEM microscope	0.37 ± 0.11(M)	3.2 ± 0.8 (M)	7.8 ± 2.1 (M)	2.6 ± 0.7 (M)
Gravimetric multifilament	0.37 ± 0.09 (F)	3.4 ± 0.2 (F)	6.8 ± 0.4 (F)	2.2 ± 0.5 (F)
Gravimetric single fiber	NM	3.8 ± 1.7 (L)	7.0 ± 2.4 (M)	3.5 ± 2.1 (L)
Vibroscope	NM	2.97 ± 0.6 (M)	7.1 ± 1.1 (F)	2.6 ± 0.7 (M)
Airflow	NM	NM	NM	NM

*Duration ⇒ **F**(fast) – max. 15 min., **M**(mean) – 15-30 min., **L**(long) – over 30 min., **NM** – non-measurable

Table 4. Fiber fineness *T*(dtex) determined from various measurement methods

Fiber Type	Short fibers		
	Glass wool	Wool	Cotton
Optical microscope	0.15 ± 0.04 (F)	2.7 ± 0.7 (F)	2.9 ± 0.8 (F)
Confocal microscope	0.16 ± 0.04 (F)	2.3 ± 0.6 (F)	2.3 ± 0.6 (F)
SEM microscope	0.19 ± 0.05 (M)	2.1 ± 0.5 (M)	1.9 ± 0.5 (M)
Gravimetric multifilament	NM	NM	NM
Gravimetric single fiber	NM	2.7 ± 1.7 (M)	NM
Vibroscope	NM	2.47 ± 0.82 (F)	1.52 ± 0.63 (M)
Airflow	0.16 ± 0.08 (F)	3.36 ± 0.12 (F)	1.9 ± 0.2 (F)

*Duration ⇒ **F**(fast) – max. 15 min., **M**(mean) – 15-30 min., **L**(long) – over 30 min., **NM** – non-measurable

5. Conclusions

The acquired results show, for the multifilaments the gravimetric method is the fastest and least variable, but its accuracy depends on the accuracy of determining the number of fibers. The optical microscopy remains the most useful method in terms of fiber type, time requirements and demand equipment. However, the accuracy of the measurement decreases with the fiber diameter, so for fibers of submicron diameters, optical microscopy no longer works. For these materials, there is no choice but to use confocal and/or SEM microscopy. Both methods are demanding in terms of equipment, the advantage of confocal microscopy is the easy preparation of samples, on the other hand SEM allows greater magnification. These methods are also applied for new types of micro/nano fibers synthesized from natural sources. These materials are usually in the form of fiber tufts or fiber layers and their geometry is usually studied using SEM micrographs. Separation and testing of individual fibers from this type of material is practically impossible. In any case, the comparison of the obtained results shows that, except the multifilaments, the gravimetric method is not suitable for reliable determination of fiber fineness.

Acknowledgments

This work follows the results of the project supported from European Structural and Investment Funds in the frames of Operational Programme Research, Development and Education [project Hybrid Materials for Hierarchical Structures, Reg. No. CZ.02.1.01/0.0/0.0/16_019/0000843].

References

[1] B.P. Saville. *Physical testing of textiles*. Woodhead Publishing Ltd., Cambridge, 1999.
[2] A.R. Bunsell. *Handbook of tensile properties of textile and technical fibres*. Woodhead Publishing Ltd., Cambridge, 2009.
[3] W.E. Morton. *Physical properties of textile fibres*. Woodhead Publishing Ltd., Cambridge, 2008.
[4] ISO 137:2015. *Wool – Determination of fibre diameter – Projection microscope method*.
[5] ASTM D2130-22. *Standard Test Method for Diameter of Wool and Other Animal Fibers by Microprojection*. 2022.
[6] ASTM D1577-07. *Standard Test Method for Linear Density of Textile Fibers*. 2018.
[7] ISO 1973:2021. *Textile fibres — Determination of linear density — Gravimetric method and vibroscope method*.
[8] ISO 10306:1993. *Textiles — Cotton fibres — Evaluation of maturity by the air flow method*.
[9] ASTM D1282-18. *Standard Test Method for Resistance to Airflow as an Indication of Average Fiber Diameter of Wool Top, Card Sliver, and Scoured Wool*. 2018.

COMPRESSIBILTY OF CARBON FIBRE TOWS SUBJECTED TO COMBINED TENSION AND COMPRESSION, IN DRY OR LUBRICATED STATE

Alexandre Guilloux[1], Arnaud Gillet[2], Julien Valette [1,2], Jules Bailly [1,2]
[1] Company TENSYL, 48, rue Jacques de Vaucanson, Pôle Arts et Métiers, 17180 PERIGNY
Email: {alexandre.guilloux, julien.valette, jules.bailly }@tensyl.com
Web Page : www.tensyl.com
[2] Université Bordeaux, I2M, UMR 5295, CNRS, F-33400 Talence, France
Email: arnaud.gillet@u-bordeaux.fr

Keywords: Fibre tow, Transverse compression, Mechanical testing, Multiaxial loads

Abstract
Characterising the mechanical behaviour of carbon fibre tows is an essential part of any process simulation approach. During the manufacturing of composite parts using automated processes, carbon fibre tows are subjected to combined longitudinal tension and transverse compression stresses, in dry or lubricated states.
This paper presents an experimental set-up that highlights the influence of these conditions on the mechanical behaviour of carbon fibre tows. Tows width and thickness are measured in a variety of situations. The results of this experimental campaign have made it possible to identify certain characteristics that should be incorporated into a constitutive law, and to consider ways of improving the system.

1. Introduction

The Automatic Fibre Placement process has seen significant growth over the last few decades, particularly in the aerostructures sector, to reduce variability and increase productivity. This manufacturing process, belongs to the family of automated tow-based processes such as filament winding or pultrusion. These processes are defined by the automated deposition of reinforcement layers, consisting of tow or tape, and differ in the geometries of the parts addressed and the techniques for applying the mechanical stresses required to obtain the desired mechanical properties.

For parts with high mechanical requirements, the use of process simulation tools makes it possible to predict the effect of process parameters on the final charasteristics of the composite (fibre volume fraction, void volume fraction, residual stresses, microstructure). During processing, the reinforcement is subjected to mechanical stresses that contribute to its final state. It is therefore important to have a predictive model of the mechanical behaviour of a fibrous reinforcement, and to feed this model with data.

The identification of the mechanical behaviour of a tow is most often based on transverse compression tests [1,2], or on tests carried out on woven architectures with a posteriori recalibration using inverse methods [3]. It is common to include the presence or absence of the polymer in the liquid state, which will affect the mechanical behaviour [1,4]. On the other hand, there is little work devoted to identifying the response of a tow subjected to combined stresses [5,6].

In the case of automated processes, the tow is subjected to a combined state of longitudinal tension and transverse compression. In this study, a device for applying stresses representative of this family

of processes is presented. This allowed to characterise the mechanical response of high-strength carbon tows subjected to combined tensile and compressive stresses in different states of saturation.

2. Materials and methods

Carbon fibre tows (T700SC-12000-60E) with a linear density of 800 g/km were collected from a roll. They were tested either dry, or impregnated with silicon oil (Rhodorsil 47v350) or epoxy resin (SR1710+D8824).

An experimental set-up (fig. 1) has been devised to apply tensile-compression loading to the tows. It was mounted on an MTS tensile testing machine to apply compressive stress.

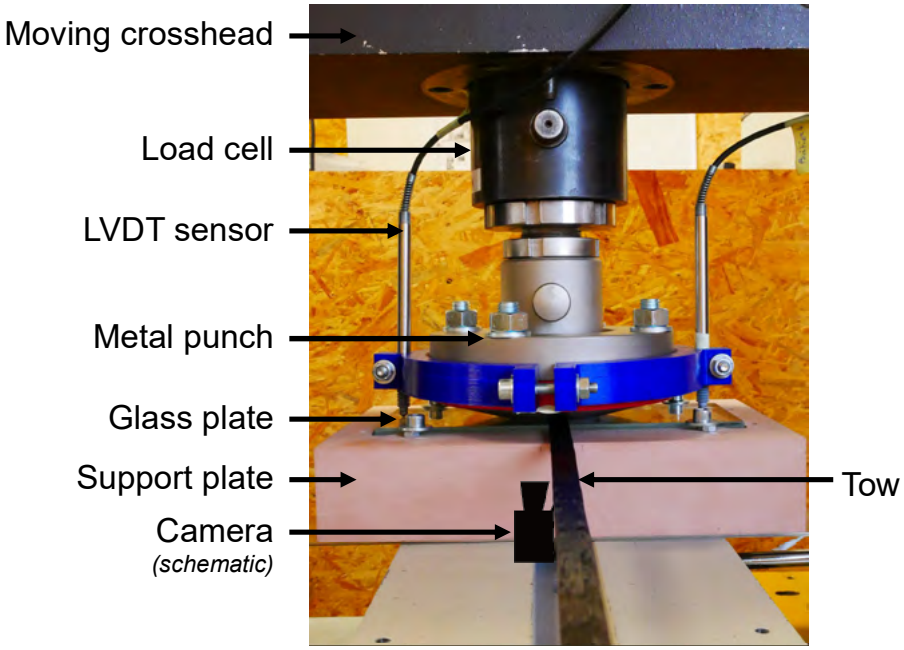

Figure 1. Experimental traction/compression set-up

Each tow was placed on a glass plate mounted on a support plate attached to the machine frame. An opening has been made in the support plate so that the tow can be observed during loading. For this purpose, a 2 megapixels camera was attached under the support plate, with its lens axis perpendicular to the compaction plane. The tow was tensioned using calibrated weights. A 56 mm diameter metal punch mounted on the machine with a 1 kN load cell allowed to apply pressure greater than 1 MPa. A spherical alignment unit was installed between the load cell and the punch to ensure the parallelism between the punch and the glass plate. Two LVDT sensors with a 5 μm precision are fixed at 180° to the punch to measure the glass plate/punch distance.

Two test protocols were set up. Tensile tests consisted of tensioning the tows without applying compression. The tension was maintained for 20 minutes to allow the tow width to stabilise. During this period, images were recorded using the camera at a frequency of 2 Hz. From each of these images, the tow boundaries were identified through an image segmentation algorithm in SCILAB. The width (w) of the tows were identified through a least square fit of the boundaries. This ensured that the width was stabilised.

Compression tests were also carried out on tows subjected to a controlled level of tension. Each sample tows were held under tension for 20 minutes to stabilise its dimensions. They were then compacted at a speed of 0.02 mm/min until the compaction force attains 500N. Before each test, mold release was applied on punch and glass plate. The average relative displacement of the punch, and hence the tow thickness (t), was measured at a frequency of 1 Hz using the two LVDT sensors.

Machine compliance was previously measured and eliminated in the result post-processing. The contact between the punch and the tow (corresponding to the initial thickness of the tow) is assumed to be established when the recorded force exceeds 0.8N, wich corresponds to the value of the noise of the load cell at no load. Throughout the compaction process, the camera captured the images of the sample bottom surface at 2 Hz. Tow widening was measured using the same procedure as for the tensile tests. The compaction pressure applied on the tow was calulated with the relation (Eq. 1):

$$P = \frac{F}{w L_p} \tag{1}$$

Were F is the compaction force, w the instantaneous width of the tow and L_p the diameter of the metal punch.

3. Results and discussion

The Table 1 summarizes the number of tests carried out for each tension/fluid combination. Since compression tests are systematically preceded by a 20-minute tension hold, the measured widths have been integrated into the tensile test measurements to ensure the repeatability of the measurements.

	Tensile force (N)	Number of tensile tests	Number of compression tests
Dry	7.7	12	12
	17.7	10	10
	42.7	6	6
Oil	7.7	6	3
	17.7	7	3
	42.7	4	3
Resin	7.7	7	4
	17.7	7	3
	42.7	7	3

Table 1. Test plan

3.1 Tensile tests

When a tow is subjected to a constant tension, there is an exponential decrease in width as a function of time. This value reaches an asymptote after approximately 15 minutes (Figure 1). The reduction in width during this period is less than 2%.

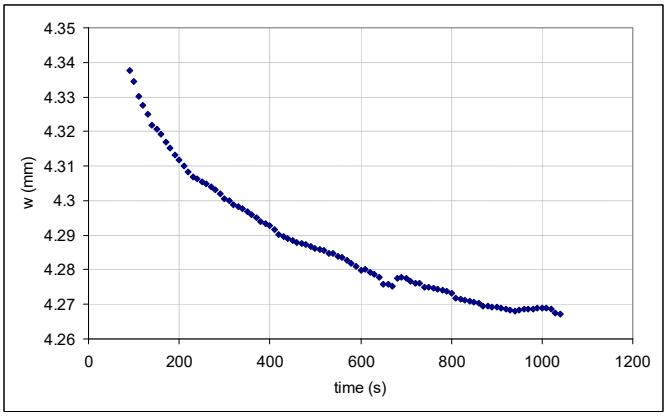

Figure 2. Evolution of the width of a tow with time (tow with resin), T=42.7N

Figure 3 shows the change in average width as a function of tensile force. The stabilised tow width decreases with the tension level for the three saturation states (dry, oil and resin), with a slope of around -0.03 mm/N. There is also a wide dispersion in width, with a standard deviation of up to 30% of the average width.

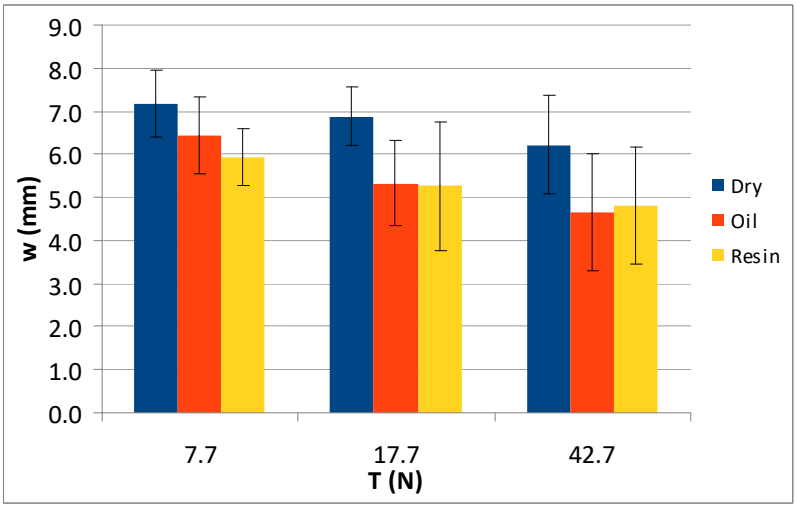

Figure 3. Mean width without compression with tensile force (mm)

It also seems that for the same level of tension, the presence of fluid induces a reduction in the width of the tows.

3.2 Compressive tests

Figure 4 shows the evolution of the thickness and width of a tow as a function of compaction pressure. It shows the typical behaviour of fibrous materials [2,7] with an exponential change in dimensions for moderate levels of compaction (up to around 0.3 MPa), followed by an asymptote (around 0.1 mm).

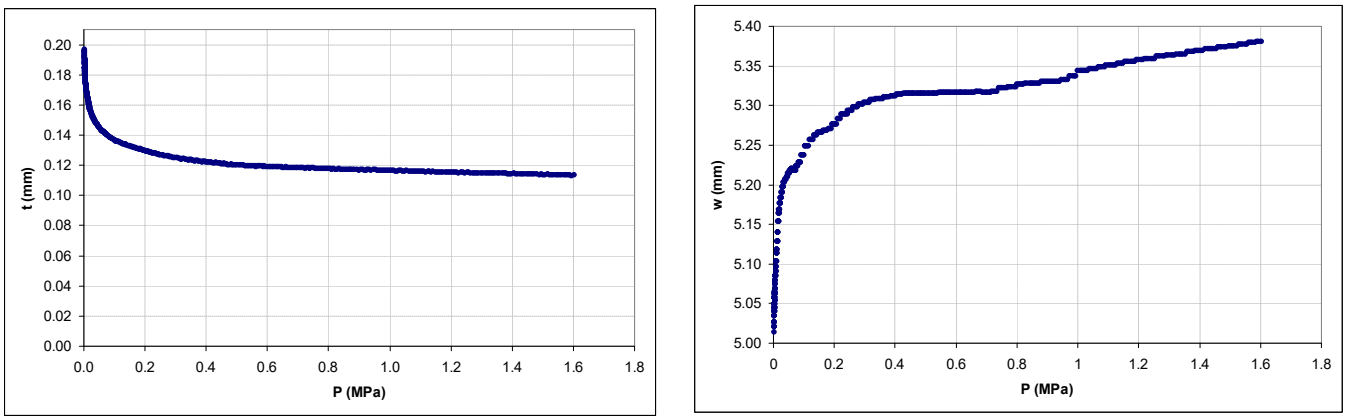

(a) (b)

Figure 4. Evolution of thickness (a) and width (b) with compaction pressure, tow impregnated with resin, tension = 7.7N

All the tows tested behaved in a similar way: the reduction in thickness for a compaction level of 1 MPa was around 40%, and the spread of the tow remained below 5%. In the case where the tow is not held in tension, [2] have observed greater spreading of the tow, up to -40% for the thickness and +17% for the width. Figure 5 shows the relative variations in thickness and width between pressures of 0.005

MPa and 1 MPa. Tow dimensions showed a high variability, already highlighted by several authors [6,8].

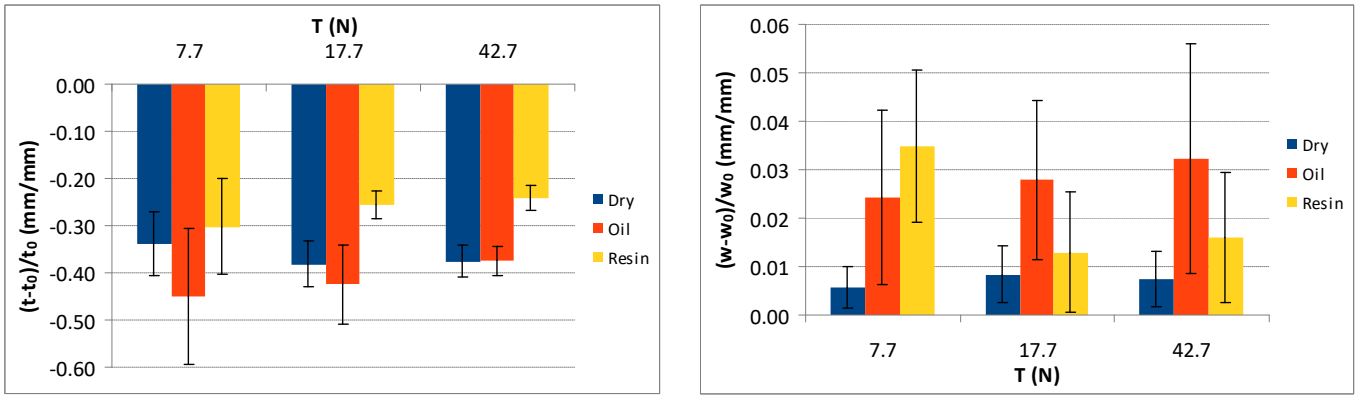

(a) (b)

Figure 5. Relative variation a) in thickness and b) in width between 0.005 MPa and 1 MPa

Tow compressibility seems to decrease slightly with the level of tension for saturated tows (-5% for 35N). On the other hand, it seems to increase for dry tows (+5% for 35N). The presence of fluid has no significant influence on compressibility.
Regarding width variation with pressure, the level of tensile force has no clear effect. The presence of fluid seems to have a moderate effect on width variation. There are several possible explanations, such as a reduction in tow/punch friction, lubrication of the intra-tow contacts or a drag effect due to the flow of fluid induced by compaction.

4. Conclusions

The measurements of compressibility of carbon fibre tows subjected to various levels of tensile force and saturation was presented. Tows width and thickness showed an important variability (standard variation around 20% of the mean). Both tensile force or presence of fluid had no or little influence on the compressive behaviour of the tows.
When subjected to compressive pressure, tows showed a moderate spread. The presence of fluid seems to have an effect on this behaviour.

These observations provide elements for the selection and parameters identification of a constitutive tow model, which will be used in numerical simulations of process involving continuous reinforcements subjected to combined tensile and compressive stresses.
Future developments of the experimental set-up are envisaged to carry out tests with different combinations of multiaxial loading (different range of parameters with automation of actuators, variation in the test matrix traction/compression on the same tow sample). Developments are also planned to understand the influence of the presence and type of fluid (effect of friction between the tool and the tow, as well as fluid/solid interaction).

References

[1] A. Sakkalatty Dharmalingam, J. Hemmer, A.-S. Lectez, C. Binetruy, S. Comas-Cardona. Evolution of single carbon and glass fibrous tow cross-sections in dry and lubricated states during compaction perpendicular to the fibers, Composites Part B 148 (2018) 235–242
[2] W. Wijaya, S. Bickerton, P.A. Kelly. Meso-scale compaction simulation of multi-layer 2D textile reinforcements: A Kirchhoff-based large-strain non-linear elastic constitutive tow model. Composites Part A 137 (2020) 106017
[3] P. Badel - Analyse mésoscopique du comportement mécanique des renforts tissés de composites utilisant la tomographie aux rayons X. Thèse LamCos 2008

[4] KIM, Young Roak, MCCARTHY, Stephen P., et FANUCCI, Jerome P. Compressibility and relaxation of fiber reinforcements during composite processing. Polymer composites, 1991, vol. 12, no 1, p. 13-19.
[5] S El-Ghezal Jeguirim, S Fontaine, Ch Wagner-Kocher, N Moustaghfir and D Durville
Transverse compression behavior of polyamide 6.6 rovings: Experimental study. Textile Research Journal 82(1) 77–87
[6] D. Kastanis, H. Steiner, E. Fauster & R. Schledjewski. Compaction behavior of continuous carbon fiber tows: an experimental analysis, Advanced Manufacturing: Polymer & Composites Science, 1:3, 169-174, (2015)
[7] Dmitry S. Ivanov, Stepan V. Lomov. Compaction behaviour of dense sheared woven preforms: Experimental observations and analytical predictions. Composites: Part A 64 (2014) 167–176
[8] Stepan V. Lomov, Larissa Gorbatikh, Matthieu Houlle, Zeljko Kotanjac, Vitaly Koissin,
Katleen Vallons, Ignaas Verpoest. Compression resistance and hysteresis of carbon fibre tows with grown carbon nanotubes/nanofibres. Composites Science and Technology 71 (2011) 1746–1753

CHANGE IN DYNAMIC-MECHANICAL PROPERTIES OF PLA FILM DUE TO UV RADIATION

Miroslava Pechočiaková[1], Jan Kabát[1]

[1]Faculty of textile Engineering, Department of Material Engineering, Technical University of Liberec, Studentská 1402/2, Liberec 46117, Czech Republic
Email: miroslava.pechociakova@tul.cz, Web Page: https://www.ft.tul.cz/en/departments

Keywords: polylactic acid, biopolymers, degradation of PLA, DMA, DSC

Abstract
This work points out the possibility of replacing single-use polymer materials from synthetic materials with materials that have sufficient recycling or spontaneous decomposition. On a global scale, the use of these materials could solve the issue of recycling single-use products made of synthetic polymers, which are a significant environmental threat.

1. Introduction

The amount of waste is still growing, it is necessary to take into account especially materials that have a short life cycle, such as packaging materials. These are specific for their single use and almost zero recycling. They are used as energy "recovery" in incinerators. The production of disposable packaging materials is represented by about 90 % in the global production of packaging materials, the issue of ecology and recycling is often overlooked. If the issues of recycling these materials are not addressed, this is an ecological threat that is very difficult to resolve. With the more widespread use of biodegradable plastics, we can significantly slow down the fact of uncontrolled pollution by non-degradable plastics. Biodegradable materials have the ability to decompose into water, biomass and carbon dioxide. Due to their structure, properties and primary raw material during production, they are suitable for accelerated degradation with the help of natural agents, which can lead to the solution of many ecological issues.

The practical part of this work deals with the production of composite films with a PLA matrix and natural hydrophilic fillers (ground flax and hemp particles as hydroscopic filler of PLA and ATBC plasticizer). Furthermore, the degradation of produced composites due to illumination, imitating sunlight and the change of thermic and thermodynamic properties at different times of illumination are addressed. The effect of filler (flax and hemp particles) and plasticizer (ATBC) on the change in phase temperatures of the monitored composites was monitored, as well as their effect on the crystalline fraction. The crystalline fraction was monitored for a more accurate description of the change in thermal and mechanical properties of PLA composite films submission.

2. Materials of experiment

2.1. PLA

The industrial-scale use of PLA (polylactic acid) is primarily in packaging materials. In the textile sector, it is used for fiber production due to its ease of spinnability and the similarity in morphology and properties to PET (polyethylene terephthalate) fibers. Fibers made from PLA are easily dyeable, have high strength, and products made from these fibers typically ensure good breathability. [1]

PLA products are frequently used in the medical field, especially as a biodegradable material that, if not coated, the human body can break down and decompose without toxic residues. [2] Among the first experimental PLA products were absorbable surgical sutures, followed by scaffolds, which are tissue carriers for cells. Surgical implants made from PLA can be in the form of clips, screws, plates, rods, or other shapes.

2.2. Composite fillers

Fillers in multiphase polymer systems based on cellulose are mainly used in the development of biodegradable materials. Primarily, they are added to increase liquid sorption into the system's structure. Secondarily, these fillers directly affect the final thermal and mechanical properties, mostly with the aim of improving them. [3]

Fillers can be cellulose-based, which is an organic substance found in plant cells, widely available and cheaper than most synthetically produced fillers. Examples include wood flour, cellulose fibers, lignin, nanocellulose, or crushed cellulose micro-particles. [4]

In this work, fillers from waste bast fibers were used, specifically flax and hemp fibers, which were crushed into micro-particles (see Figure 1).

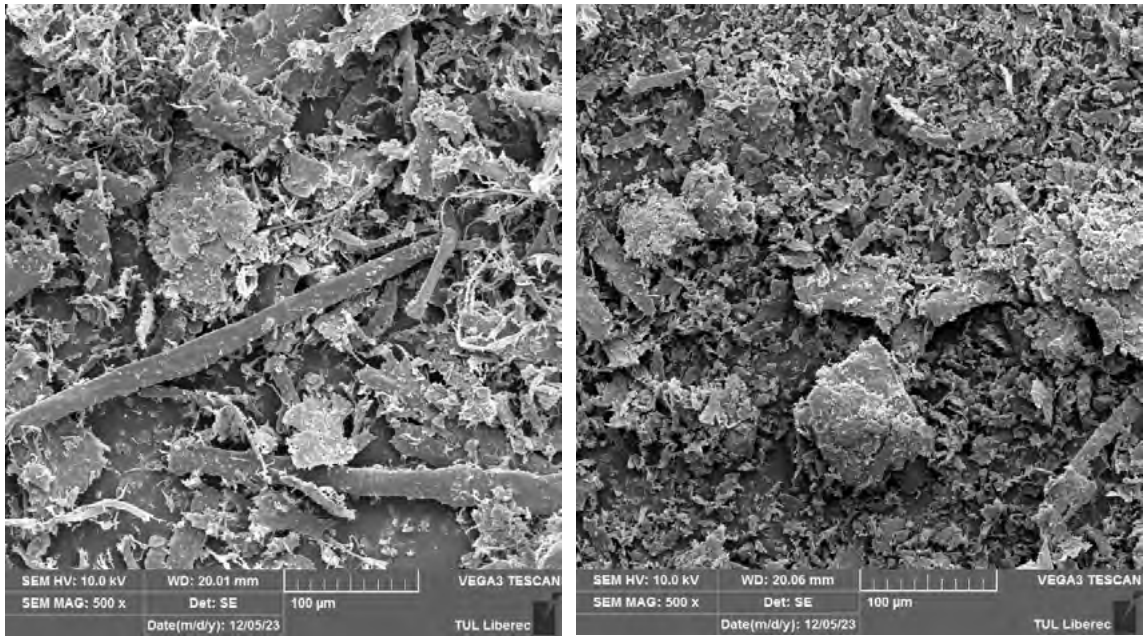

(a) (b)

Figure 1. Flax particles (a), hemp particles (b) at 500x magnification.

2.3. Description of Tested Samples

For the experimental part, single-phase, two-phase, and three-phase systems were used, their exact composition is described in this chapter, and extruded composite films were made from them. The matrix of these films consists of PLA, and non-spinnable waste fibers of hemp and flax were used as fillers. These fibers were subsequently crushed into microparticles (using a nanomill Fritsch, type Pulverisette 7) and introduced into the extruder at 5 weight percent for film production.

Additionally, the plasticizer ATBC, acetyl tributyl citrate, was used, which commonly ensures better flexibility of the material in biodegradable polymer films due to its composition, but it can also be used as an additive for better matrix/filler adhesion properties.

Designed systems and subsequently created films from them:

1) PLA
2) PLA + 5 wt% acetyl tributyl citrate (PLA/ATBC)
3) PLA + 5 wt% hemp (hereinafter PLA/h)
4) PLA + 5 wt% flax (hereinafter PLA/f)
5) PLA + 5 wt% acetyl tributyl citrate + 5 wt% hemp (hereinafter PLA/ATBC/h)
6) PLA + 5 wt% acetyl tributyl citrate + 5 wt% flax (hereinafter PLA/ATBC/f)

3. Method of measurement and discussion of results

3.1. UV degradation

The process of photodegradation is induced by sunlight, which exposes the irradiated material; it can reflect, transmit, scatter, or absorb sunlight. [5]

Photo-initiated conditions can significantly affect the biodegradation of the material. [6] Studies by Thomas Fernandez and his co-authors have shown that UV radiation affects the flexibility of the internal structure of certain polymers, thereby preventing microorganisms from accessing polymer chains. [7] Composite materials composed of PLA matrix and hydrophilic filler have an advantage as they can combine two-component degradation. Exposed material can be degraded by UV radiation using sunlight, while the hydrophilic filler absorbs liquid, which promotes the colonization of microorganisms and thus microbial degradation. [7]

Degradation using Xenotest is performed according to ISO 105-B02 standard, which establishes a specific methodology for determining UV resistance. In the case of this work, samples were exposed for 6, 12, 18, and 24 hours, where 6 hours of exposure corresponds to 907.2 [W/m^2]

3.2. Diferencial scaning calorimetr (DSC)

All manufactured samples underwent DSC analysis. Approximately 10 mg of each sample was weighed into aluminum pans, which were then sealed with aluminum lids. Prepared samples were presented to the instrument together with one reference pan, which contained no material. Tests were conducted on a Mettler Toledo DSC 3+ instrument, where the instrument measures the difference in heat flow during heating and cooling between the test and reference sample. The difference in heat flow between the test and reference sample is directly proportional to the instantaneous specific heat.

Measurement parameters: heating rate 10°C/min; temperature range 25 - 200 °C; nitrogen flow rate 50 ml/min, standard ČSN EN ISO 11357.

The DSC thermogram of the two-phase system of PLA material with the addition of flax filler, without light degradation, can be seen in Figure 2. The red curve represents the heating of the tested material, and the blue curve represents cooling.

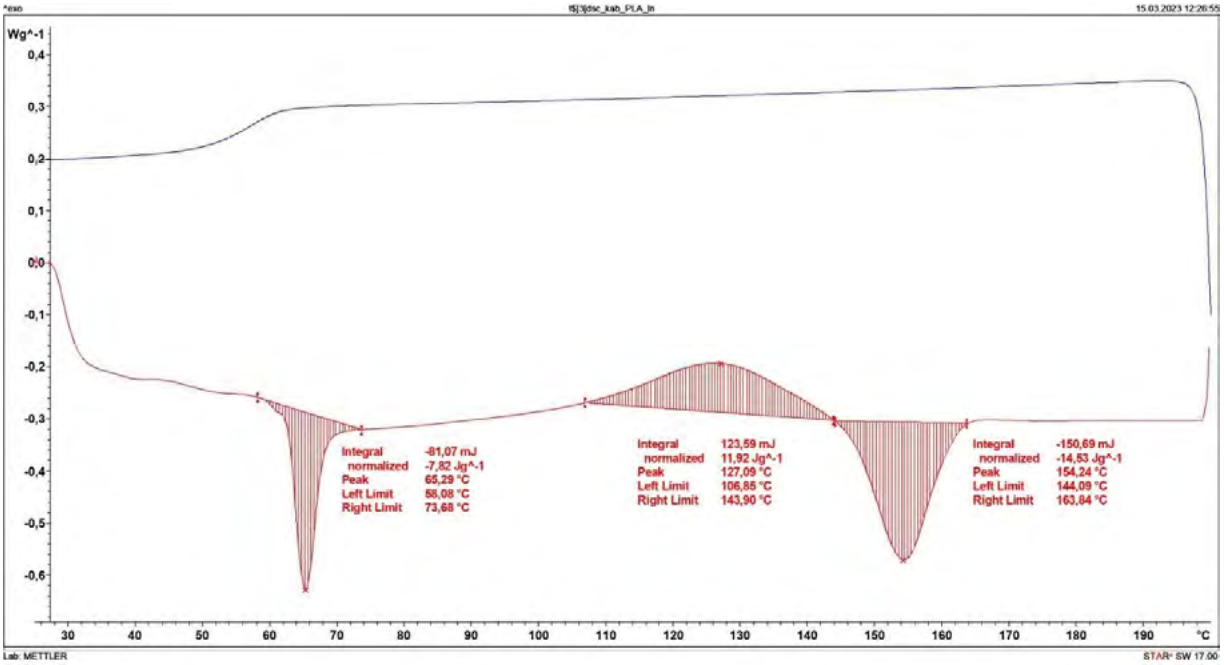

Figure 2. Thermogram of the two-phase system PLA.

From the measured thermograms (an example of which is shown in Figure 2); the values of T_g - glass transition [°C]; T_{cc} - cold crystallization [°C]; ΔH_m - enthalpy of melting [J.g^{-1}] and T_m - melting temperature [°C] were determined.

From the measured values, we can assume that irradiation does not affect T_g and T_m; the measured values are within the possible tolerance range. The only change occurs in T_{cc} due to the addition of the plasticizer ATBC. For the purposes of this work, the estimate of the crystalline content was calculated according to equation 1:[8]

$$x_c = \frac{\Delta H_m}{\Delta H_{m_{100}} 0{,}95} \cdot 100 \qquad (1)$$

The ΔH_m [J.g^{-1}] is the change in specific enthalpy of melting; ΔH_{m100}) [J.g^{-1}] is the change in specific enthalpy of melting of ideally crystalline PLA; 0.95 [-] is the proportion of PLA in the material.

The overall crystalline content was calculated from the measured enthalpy change of melting of the system. The crystalline content closely relates to the resulting properties of the system. The assumptions obtained from the thermograms of individual systems were confirmed, namely:

Systems with the addition of flax particles exhibit a similar crystalline content as the system made of pure PLA. A significant effect of irradiation on the crystalline content of these systems was not observed.

The addition of hemp to the system leads to a significant reduction in the crystalline content. This phenomenon may be caused by inadequate dispersion or poor cooperation of the filler with the matrix.

The plasticizer ATBC used as a softener in the systems behaved as a crystallization or nucleation agent in the range of 12 to 18 hours of irradiation. These substances positively affect the crystallization process, leading to the formation of a larger number of crystals or an increase in their sizes, for example, based on the added energy, in this case, the energy obtained from UV radiation.

The highest crystalline contents were recorded in the three-phase systems PLA / hemp / ATBC, where a change in enthalpy of -48.33 [J.g^{-1}] and a resulting crystalline content of 54.7% were measured at an irradiation length of 18 hours, compared to the system of pure PLA, which has a change in enthalpy of only -12.76 [J.g^{-1}] and a crystalline content of 14.4% at the same irradiation length. We can say that by adding hemp and ATBC, the crystalline content increases nearly four times the original value at an irradiation length of 18 hours.

3.3. Dynamical-mechanical analyses (DMA)

Dynamical Mechanical Analysis (DMA) is a methodology considered to be the most sensitive technique for characterizing the mechanical behavior of materials. Through DMA, a material is mechanically stressed and subjected to periodic stress in one of several different deformation modes, up to a certain degree of deformation. The sample can be stressed in compression, tension, shear, or flexure. The amplitudes of force and phase shift are analyzed as functions of temperature, time, and frequency. In this work, the samples were stressed in tension.

The viscoelastic response of the material is monitored, which is divided into two additional components. The idea of dividing the viscoelastic response into two components of the complex modulus perfectly describes two independent phenomena occurring within the material, which are influenced by the ratio of the crystalline and amorphous phases of the monitored material. [9]

E' - this component is called the real part of the viscoelastic modulus, representing the elastic modulus, describing the elastic (recoverable) part of the material. E'' - imaginary component, describing the viscous part of the material, i.e., the loss dissipative energy within the material. E^* - complex modulus, is the sum of the real and imaginary components, as shown in equation 2:

$$E^* = E' + E'' \tag{2}$$

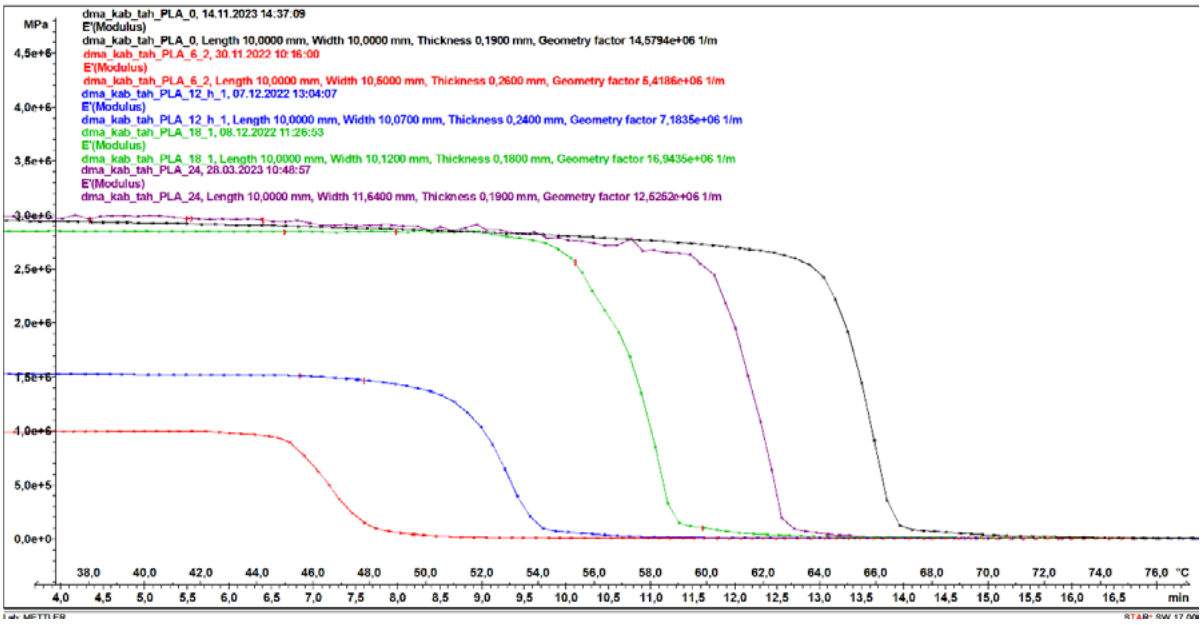

Figure 3. DMA measurement of PLA sample at various durations of UV radiation.

On Figure 3, you can see an example of the elastic modulus record of a pure PLA film, and other tested materials exhibited similar dependencies of the elastic modulus.

From the measured modulus dependencies on UV radiation, we can observe a trend of increasing modulus in the two and three-phase systems with the addition of plasticizer (ATBC). Although it is

a low-molecular-weight plasticizer, radiation, being a form of energy, can increase the crystalline content of the system. Higher moduli are exhibited by systems with exposure times of 12-18 hours; after exceeding this irradiation time, the mechanical properties return to their original state. At the same irradiation time, we also observe an increase in crystalline content. For example, PLA with 18 hours of irradiation showed a crystallinity of 14.4% compared to PLA/ATBC with 18 hours of irradiation, with nearly double the crystallinity at 28.4%. This could be due to the rearrangement of individual macromolecules influenced by radiation.

In the two-phase systems PLA/ATBC, there was a significant increase in modulus and improvement in thermal properties compared to pure PLA systems. The crystalline content in the ATBC system showed an almost double increase, but the modulus increased nearly threefold from its original value, from 2.8 MPa in PLA to almost 10 MPa in PLA/ATBC, at an irradiation length of 18 hours.

Systems with the addition of flax and hemp fillers exhibited lower resistance to stress, which may be due to inadequate homogeneity. With decreasing homogeneity and dispersion of individual particles in the structure, mechanical properties significantly decrease. This decrease is evident in systems with hemp, while systems with the addition of flax exhibited better mechanical and thermal properties, with the crystallinity being two or more times higher compared to systems with the addition of hemp.

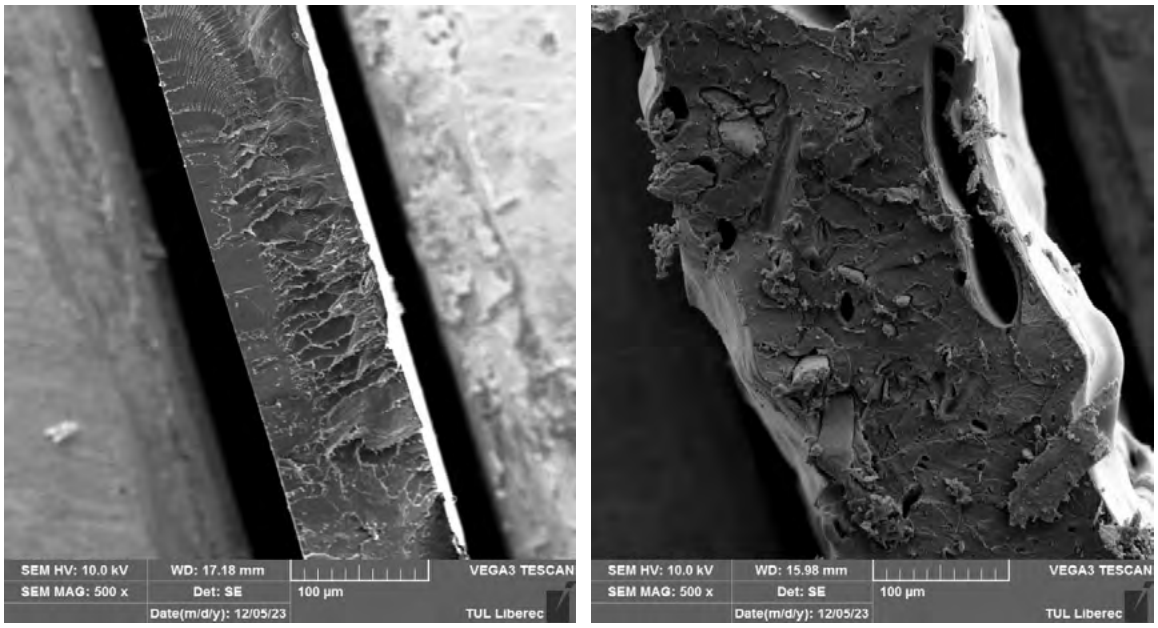

(a) (b)

Figure 4. The fracture surface of PLA (a), PLA/flax (b), magnified 500x.

4. Conclusions

The evaluation of the dependence of the viscoelastic modulus on the crystalline content was conducted based on measured values from DMA, and the crystalline content was calculated from the enthalpy change measured by DSC.

In the single-phase PLA system, there is a clear trend where the viscoelastic modulus E´ increases with the increasing crystalline content. Similar systems with the same trend can be expected to gradually increase both mechanical and thermal properties.

The two-phase PLA/ATBC system exhibits the highest measured values of the viscoelastic modulus as a function of the crystalline content, which increases with the modulus. These systems show an increase in the viscoelastic modulus by more than 2.5 times the value measured in the single-phase system of pure PLA.

Systems with the addition of flax, specifically the two-phase PLA/flax system and the three-phase PLA/ATBC/flax system, exhibited very similar characteristics. The increase in the viscoelastic modulus with the crystalline content was not significant, and upon exceeding a certain limit of crystalline content in the system, a decrease in the viscoelastic modulus is observed. Thus, the material exhibits an opposite behavior to what is expected, where increasing crystalline content corresponds to increased mechanical resistance. The assumption for this phenomenon is that upon exceeding a certain limit of crystalline content, the system tends to become brittle, thereby worsening its mechanical and thermal properties. The limit for the highest value of crystalline content, at which the system improves or at least maintains its properties, is approximately 17.8% for the two-phase PLA/flax system and approximately 21.8% for the three-phase PLA/ATBC/flax system.

Systems containing hemp in their structure exhibited different behavior. The two-phase PLA/hemp system achieved the lowest values across all tested systems, both in terms of viscoelastic modulus and crystalline content. However, a trend of increasing crystalline content along with the viscoelastic modulus can still be observed. The three-phase PLA/ATBC/hemp system achieved approximately five times the crystalline content compared to PLA/hemp. From the measured values, it can be concluded that the addition of plasticizer to systems with hemp can significantly increase the crystalline content and, consequently, the viscoelastic modulus.

In further research of materials from this work, it would be appropriate to subject the manufactured systems to higher relative humidities and then test these systems on DMA to observe changes in mechanical properties. A trial was conducted on the PLA/flax system, showing that higher relative humidity significantly reduces mechanical properties compared to the system exposed to lower relative humidity (Figure 5 and Figure 6), by more than two hundred times.

From the graphs (Figure 5 and 6), it is evident that humidity significantly affects the mechanical properties of the manufactured systems. Moisture is absorbed into the internal structures of the system through hydrophilic fillers, leading to a weakening of strength. This means that humidity plays a significant role in the entire degradation process, and it is necessary to always specify the environmental conditions under which the material is tested when addressing degradation questions.

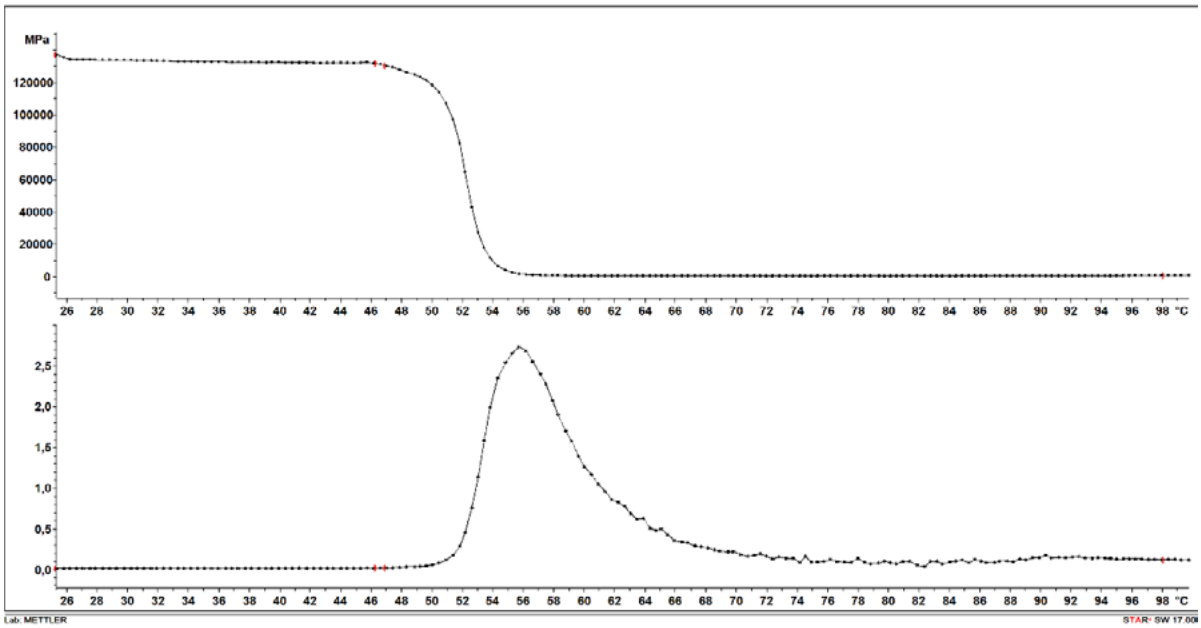

Figure 5. DMA of PLA/flax, measured at 40% relative humidity (RH).

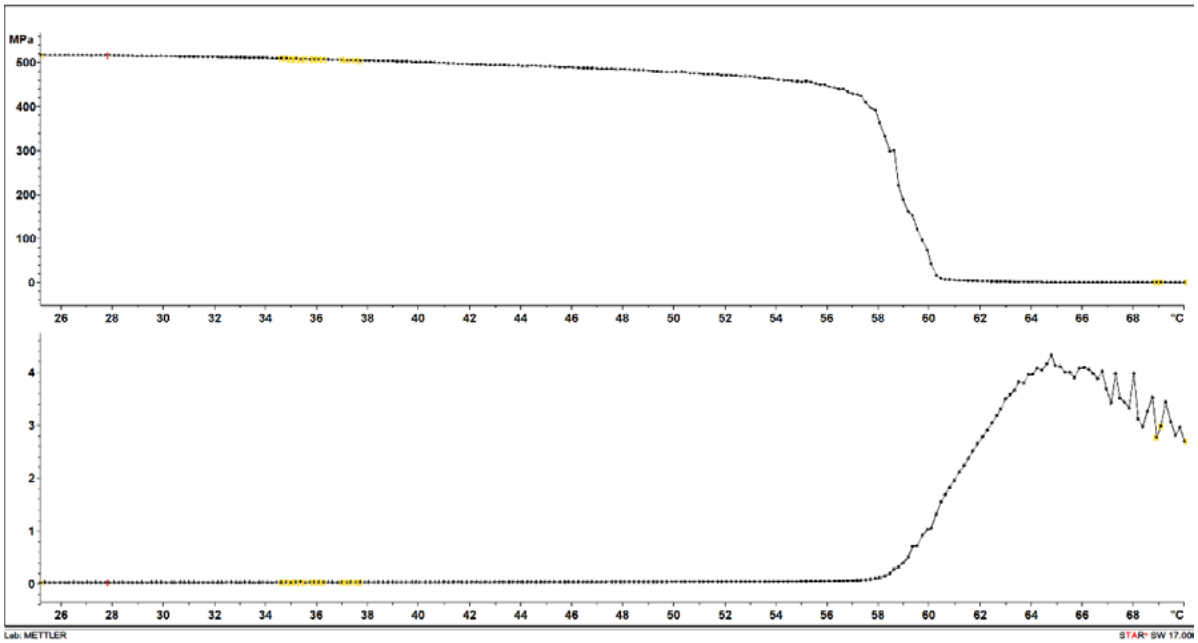

Figure 6. DMA of PLA/flax, measured at 70% relative humidity (RH).

References

[1] R. Narain. Polymer Science and Nanotechnology: Fundamentals and Applications. B.m.: *Elsevier*, 2020.

[2] D. Da Silva. Biocompatibility, biodegradation and excretion of polylactid acid (PLA) in medical implants and theranostic systems. *Chemical Engineering Journal*, 340, p. 8–15. 2018.

[3] T. Heinze. Cellulose: Structure and Properties. In: Orlando J. ROJAS, ed. Cellulose Chemistry and Properties: Fibers, Nanocelluloses and Advanced Materials [online]. Cham: Springer International Publishing, *Advances in Polymer Science*, p. 1–52. 2016.

[4] K. Pielichowski, J. Njuguna and T. M. Majka. Thermal Degradation of Polymeric Materials. B.m.: *Elsevier*, 2022.

[5] T.Lu, E. Solis-Ramos, Y. Yi and M. Kumosa. UV degradation model for polymers and polymer matrix composites. *Polymer Degradation and Stability* [online]., 154, 203–210. 2018

[6] A. Stloukal and B. Verney. Assessment of the interrelation between photooxidation and biodegradation of selected polyesters after artificial weathering. *Chemosphere*. 12., 2012.

[7] Z. Kijchavengkul and C. Auras. Assessment of aliphatic-aromatic copolyester biodegradable mulch films. Part II: Laboratory simulated conditions. *Chemosphere*. 71., 2008.

[8] L. Qin, C. Liu, J. Zhang, M. Xi, Sh. Pi, W. Guo, N. Li, Sh. Zhang and Zh. Wang. Sandwich-type phase-change composites with the dual-function of efficient heat management and temperature-regulated electromagnetic interference shielding performance. *Journal of Materials Chemistry C* [online], 11(4), 1381–1392, 2023.

[9] J. D. Menczel. and R. B. Prime. Thermal Analysis of Polymers: *Fundamentals and Applications*. B.m.: John Wiley & Sons, 2009.

CHARACTERIZATION AND PERFORMANCE EVALUATION OF LIGNIN-MODIFIED EPOXY RESIN FOR POTENTIAL USE IN NATURAL FIBER REINFORCED COMPOSITES

Zainab Al-Maqdasi[1], Maria Bohic[1,2], Daniela Rusanova-Naydenova[3], Roberts Joffe[1]

[1]Division of Materials Science, Department of Engineering Sciences and Mathematics, Luleå University of Technology, Universitetsområde Porsön, 97187, Luleå, Sweden
Email : zainab.al-maqdasi@ltu.se; roberts.joffe@ltu.se, Web Page: https://www.ltu.se/en/staff/z/zainab-al-maqdasi; https://www.ltu.se/en/staff/j/roberts-joffe
[2]Commissariat à l'Energie Atomique et aux Énergies Alternatives (CEA)-Grenoble, 17 Av. des Martyrs, 38000 Grenoble, France
Email: maria.bohic@cea.fr, Web Page: https://www.cea.fr
[3]SunCarbon AB, Industrigatan 1, 94138, Piteå, Sweden
Email: daniela@suncarbon.se, Web Page: https://www.suncarbon.se/
Keywords: sustainable composites, cellulosic fibers, lignin, fiber-matrix adhesion, moisture uptake

Abstract
This feasibility study encompasses the experimental findings of utilizing lignin as a potential multi-functional epoxy resin modifier for man-made cellulosic fiber composites. Two types of lignin at different concentrations are used (with no chemical alteration) to modify the epoxy resin. The modified resin's potential for use in natural fiber-reinforced composites is evaluated through the characterization of mechanical and thermal properties. The influence of moisture on the stability of the mechanical performance is also investigated through the characterization of conditioned samples (RH=100%, T=50 °C) against reference material. Preliminary results show that the addition of any type of lignin at low concentrations has a marginal effect on the overall system performance although the effect of the type of lignin remains hidden within the causes of self-agglomerations. The most notable difference concerning the lignin type used can be seen in the *Tg*-values for 5 wt% lignin addition.

1. Introduction

The use of natural fiber-reinforced composites has gained significant attention in various industries due to their potential to provide lightweight, eco-friendly, and sustainable alternatives to conventional materials. However, the properties of natural fibers are inconsistent and largely dependent on the growth/cultivation conditions. On the other hand, epoxy resins, have been widely used as matrix materials in these composites due to their excellent mechanical and thermal properties. However, the incorporation of natural fibers into epoxy matrices can be challenging, as it often requires the addition of modifiers to improve compatibility and adhesion between the fibers and resin [1]. Many byproducts of large industries, such as forestry, possess untapped potential which remains underutilized, despite their high value, due to their inconstant characteristics. Hence, there is immense value, from a sustainability standpoint, in developing materials with consistent properties that can compete with conventional counterparts but are derived from bio-based alternatives.

Regenerated Cellulose fibers (RCFs) are extracted from a wide range of natural resources, where cellulose is dissolved in chemicals to remove the non-cellulosic compounds and regenerated into more uniform and stable cellulose fibers. The production technologies of these materials are progressing and the new generations of RCFs are assessed to have a better environmental impact than, for instance,

cotton fibers. These fibers can have modulus as high as 40 GPa and elongations at break up to 12% [2] two traits widely desired by industries where high toughness is needed.

Lignin, a highly abundant renewable polymer, has shown promise as a potential modifier for epoxy resins. Its inherited high aromatic content, rigidity, and antioxidant properties have made it an attractive option for resin modification. Various technologies to extract lignin from lignocellulosic biomass exist. Among the traditional lignosulphonate, alkali lignin, organosolv, and hydrolysis lignin, the most common is the Kraft lignin, where the lignin is a by-product precipitated from Kraft black liquor via acidification to pH 2 [3]. Due to differences in isolation steps, each lignin possesses different functional groups and molecular weight arrangements which determine the final by-product properties. In recent years, alongside the usage of lignin as filler, researchers have focused on extracting lignin from different sources and evaluating its effectiveness as a modifier in natural fiber composites. Lignin exhibits a high cross-linking density that could be imparted to the resin resulting in increased stiffness [4]. It has been utilized as a low-profile filler in unsaturated polyester resins to produce modified resins with reduced impact on the environment [5]. When chemically modified, lignin resulted in improved properties of the composites compared to the unmodified fillers. Industrial interest in these materials as additives to the composites aims towards as little modification as possible and including as high concentrations as possible to reduce cost while increasing the bio-content efficiently. However, high concentrations of lignin in epoxy have been shown to result in a difficult-to-shape/process material due to the increased viscosity [6]. Recent research has explored the use of depolymerized lignin or modified lignin for the production of epoxy resins, but very little research has been done on the utilization of this material for natural fiber composites in their continuous form suitable for advanced composite applications [7]. Challenges related to the low dimensional stability of lignin [7] could be utilized in favor of increased compatibility. Mechanisms of improved compatibility could arise from mechanical interlocking between the constituents where the swollen particles could mechanically close the gaps at the interface and keep the efficient stress transfer within the structure [8].

The current study aims at using lignin without specific chemical alteration to modify epoxy resin for use in natural fiber composites. The influence of the increased concentration of the fillers on the mechanical, thermal, and moisture uptake characteristics is investigated. Moreover, a comparison is made between commercially available Kraft lignin extracted from the black liquor by the LignoBoost™ technology and an alternative lignin isolated from the Kraft black liquor at pH 6-7 using acidic bio-steam. The effect of the lignin type and concentration on the compatibility of the natural fiber and the epoxy matrix is also investigated and evaluated.

2. Experimental

2.1. Materials and Manufacturing

The resin used in the study is Araldite® LY1564 epoxy resin and XB3404-1 hardener (from Huntsman, Texas, US) mixed at a ratio of 100:36 wt/wt. The two types of lignin used are a commercial Kraft Lignin produced by the LignoBoost™ technology at Bäckhammar, Sweden (further referred to as CL) and a new alternative type of lignin extracted from the Kraft black liquor using SunCarbon proprietary process (further denoted as AL). Both lignin types were used as received without any further chemical modification. Moisture content ca. 5% and ash about 0.5% for both types of lignin. Both lignin powders were ground to refine the powder granules and then sieved through a 120 μm mesh and further dried in the oven at 50 °C for at least 24 hours prior to incorporation in the resin. The fibers used for this study are unsized, untwisted Cordenka 700 Super 3 RCFs (made by a modified viscose process) in the form of yarns (from Cordenka, Obernburg, Germany). The yarns consist of 1350 single filaments having a continuous length and semicircular cross-section with an equivalent diameter of ~12.5 μm.

For the manufacturing of lignin-modified epoxy, a predetermined amount of lignin was incorporated into the base epoxy using simultaneous tip-sonication and magnetic stirring. After 30 minutes, the tip was removed, and the hardener was added with continued mechanical stirring for an additional 3 minutes. To avoid the extensive local heating from the sonication, the mixing crucible was placed inside

an ice bath. Multiple concentrations of each type of lignin in the epoxy resin were produced. The resin was then cast into rectangular plates using a silicon mold and cured for 8 hours at 80 °C followed by 5 more hours for post-curing at 160 °C. These parameters were optimized based on the resin manufacturer's recommendations and internal experimental investigations. Neat Epoxy resin (further denoted as Neat EP) was used as a reference material and was cured following the abovementioned cycle. The samples are named following the style X%YL where X refers to the % of lignin (L) in the sample (based on the total weight of the composite), and Y denotes the type of lignin (either C for commercial or A for alternative).

Investigations on the effect of severe relative humidity (RH) included that pieces of the produced plates were conditioned at 50 °C in 100% RH for 531 hours (samples were not immersed in the water). For reference purposes, the plates were first dried in the oven for 2 weeks at 50 °C.

Samples for the pullout test were produced following the procedure described by Hajlane A. in [9] and shown in Figure 1 where three bundles were combined and threaded inside a mold, filled with resin, then cured and post-cured following the same cycles described above. Wooden tabs were attached at the free ends of the bundle to assist with gripping in the machine during the test. The resin slab was ground to achieve an even surface and to control the embedded length of the bundle.

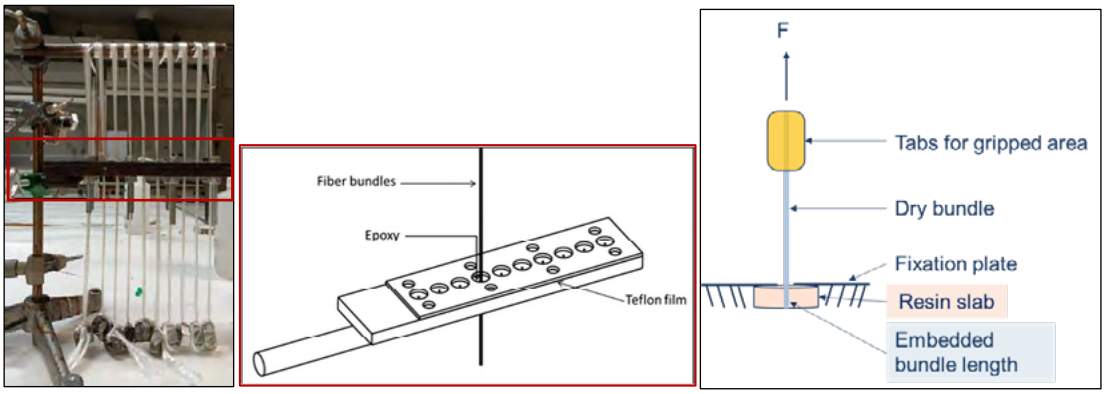

Figure 1. Setup for bundle pullout sample preparation. left) mold setup picture; middle) schematic of the mold details [9]; right) schematic of sample ready for test

2.2. Characterization

Mechanical properties: Instron 4411 universal testing machine equipped with 500 N loadcell and 3-point bending fixture was used for the characterization of flexural properties and fracture toughness following guidelines of ASTM D790, and ASTM D5045, respectively. A span-to-thickness ratio of 16:1 was used, and a loading rate was calculated accordingly. The flexural modulus was determined from the stress-strain curves at the initial linear region between strain values of 0.05% and 0.20%. Fracture surfaces were examined with a JEOL JCM-6000 table-top Scanning Electron Microscope. The hardness measurement was performed using an MXT-α micro-hardness tester equipped with a Vickers diamond and a camera communicating with Buehler software connected to a light optical microscope. A load of 10 grams was applied in 15 seconds and hardness measurement was obtained as an average of 10 indents at several locations of the sample.

Thermal properties: Mettler Toledo DSC 281 supported by STARe analysis software was used for thermal calorimetric analysis. Samples of ca. 5 mg were encapsulated into standard 40 µl aluminum crucibles sealed with pierced lids. The test was performed in an inert environment with nitrogen as a purge gas flowing at a rate of 80 ml/min. samples were heated twice from room temperature (25 °C) to

220 °C at a rate of 20 °C/min and the glass transition temperature (*Tg*) was determined from the second heating cycle.

Compatibility test: Adhesion between the fiber and the matrix was assessed by the pullout test using the universal testing machine. Samples were tabbed with wooden tabs with a gauge length of 100 mm and embedded length of ca. 2 mm. The polymer part was restricted to a plate while the tabbed end of the bundle was being loaded at a displacement rate of 2 mm/min. The interfacial shear strength (*IFSS*) was calculated from the maximum load at pullout according to the expression below:

$$IFSS = F/(d\,\pi\,l_e). \quad (1)$$

where F is the maximum force, d is the equivalent diameter of the bundle determined from the measured area of the bundle after the pullout and l_e is the embedded length of the bundle.

3. Results and Discussion

3.1. Mechanical Properties

Figure 2 (left) shows representative stress-strain curves of the tested materials in the flexural test. It could be seen that the addition of lignin resulted in an increased stiffness and marginal change in yield strength compared to the neat epoxy. Simultaneously, the samples showed reduced strain at break resulting from the embrittlement of the material by the addition of the fillers. Notably, 5% CL samples showed a great reduction in the flexural strength compared to the neat or the AL sample. This could be attributed to the lignin self-agglomerations occurring at the higher filler concentrations, and those particles act as stress concentrations and failure initiators. Numerical values for the flexural properties can be found in Table 1. Other research [10] reported a similar trend of stiffness increase at the addition of 3 wt% organosolv lignin to the epoxy resin and a negative impact of higher concentrations on the stress and strain at break. Similar trends are seen in the fracture toughness values presented in Figure 2 (right) where the addition of lignin at 3 wt% concentration resulted in a marginal increase in the K_{IC} values with a drop at 5wt%. It is also worth noting the large standard deviation due to the possible inhomogeneity of the samples. Moreover, due to the limited samples available for the test, all values of fracture toughness are reported even if some samples did not comply with all validity criteria. The inhomogeneities and agglomerations are evident in the SEM images and photographs presented in Figure 3 where, in general, the CL shows visible agglomerations (enclosed in the white circle) compared to the AL which looks much more homogeneous. However, it is possible that the presence of only a few defects of critical size has resulted in the noticed reduction in the fracture toughness values.

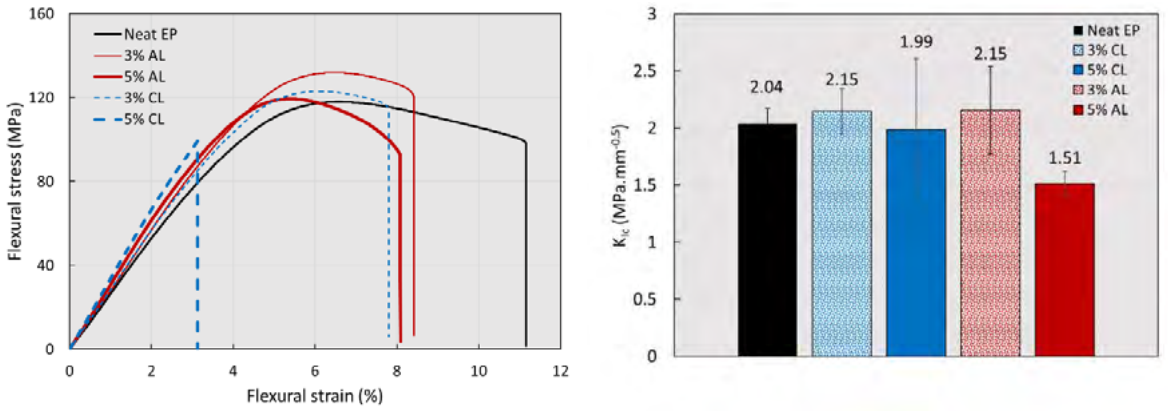

Figure 2. Mechanical properties of the tested materials. Left: flexural stress-strain curves; right: fracture toughness.

Table 1 shows the effect of the moisture content on the hardness values measured for the as-manufactured samples and the severely conditioned samples along with the relative % weight increase attributed to the moisture content at the end of the conditioning period. The hardness values have decreased significantly compared to unconditioned samples indicating the plasticization effect of the up-taken water on the materials. Overall, there is no significant effect of the low concentrations of lignin on the moisture uptake and only higher concentrations (5% AL) have resulted in higher moisture absorbance compared to neat epoxy samples. The reason could be attributed to the penetration of water molecules in between the gaps created by the agglomerations of lignin particles in addition to that absorbed by the lignin itself. Nonetheless, it seems that the presence of lignin might have restricted the plasticization effect of the water as suggested by the lower drop in the hardness for the lignin-modified samples compared to the neat epoxy.

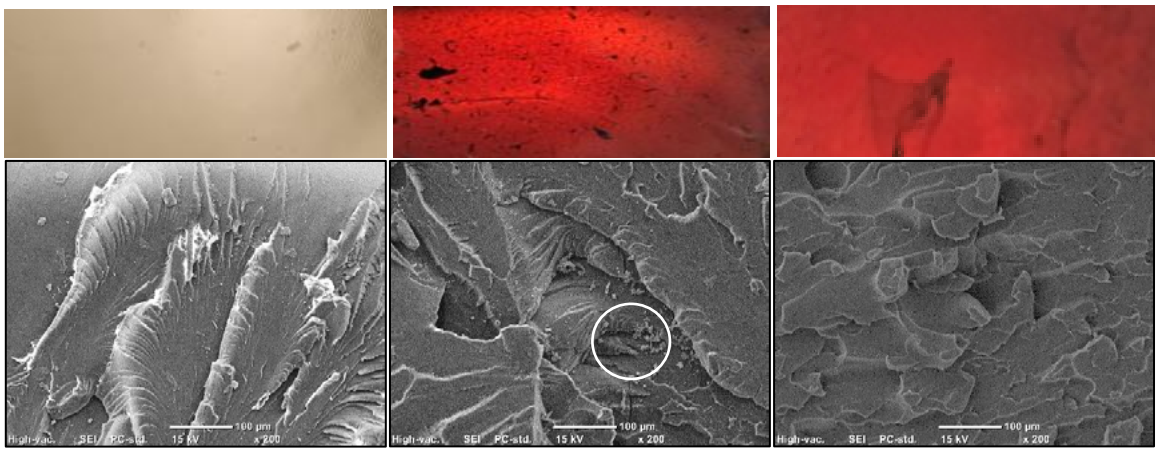

Figure 3. Photographs (top) and SEM images (bottom) of the Neat EP (left), 5%CL (middle), and 5%AL (right) samples. SEM images correspond to the fracture surfaces following the flexural test

Table 1. Numerical values of the mechanical properties of tested samples. Hardness values correspond to samples unconditioned and after conditioning for 531 hours at 50 ℃ and 100% RH

Sample	Flexural properties		Weight gain (%)	Hardness (HV)		
	E (GPa)	σ_{max} (MPa)		Unconditioned	Conditioned	Rel. diff. (%)
Neat EP	2.56 ± 0.1	117.5 ± 0.8	3.67	17.4 ± 1.3	13.4 ± 1.1	-22.6
1% AL	-	-	3.60	16.3 ± 0.6	14.3 ± 0.5	-16.0
3% AL	2.85 ± 0.1	115.4 ± 24.9	3.43	16.7 ± 1.0	14.8 ± 0.7	-10.4
5% AL	3.29 ± 0.2	106.3 ± 21.4	5.66	17.5 ± 0.8	13.2 ± 0.8	-23.5
1% CL	-	-	4.10	17.0 ± 0.8	13.6 ± 1.0	-16.8
3% CL	2.71 ± 0.2	121.0 ± 2.2	4.13	16.5 ± 0.8	13.9 ± 0.9	-16.7
5% CL	3.21 ± 0.1	91.0 ± 20.1	4.24	17.2 ± 0.8	12.5 ± 1.2	-28.6

3.2. Thermal Properties

Thermograms obtained from the second heating cycles of a DSC experiment are presented in Figure 4. It can be seen from the graph that except for 5% AL, the addition of lignin did not influence *Tg*. The large drop in *Tg* for the 5%AL (> 10 ℃) suggests a substantial interaction of the lignin with the epoxy structure at the molecular level that might cause earlier mobility of the molecules upon heating. The type of such interaction could further be investigated by FTIR.

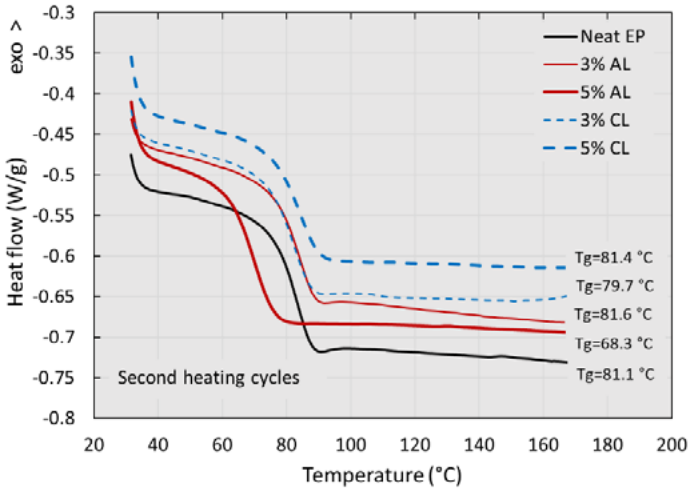

Figure 4. DSC data of selected formulations

3.3. Fiber/Matrix Adhesion

Representative load-displacement curves of the pullout test are shown in Figure 5 (left). The curves are typical for the RCFs as these fibers are known to exhibit bilinear deformation when extended [9]. The high elongations of the bundles cause dramatic failure with high energy being released shadowing the load due to friction typically associated with the sliding of the bundle out of the resin. However, the adhesion is characterized by the maximum load registered at the failure of the interphase, and the average values of the IFSS are presented in Figure 5 (right). At the tested concentrations of lignin-modified epoxy, results show no noticeable effect of the lignin on the adhesion between the fibers and the matrix. There is a slight decrease in values reported for the AL compared to the CL but considering the overlap of the error bars with the mean values, these results are not conclusive, as might be expected at this low concentration. Further tests are needed at higher concentrations to verify the impact of lignin on the compatibility between RCFs and epoxy resin.

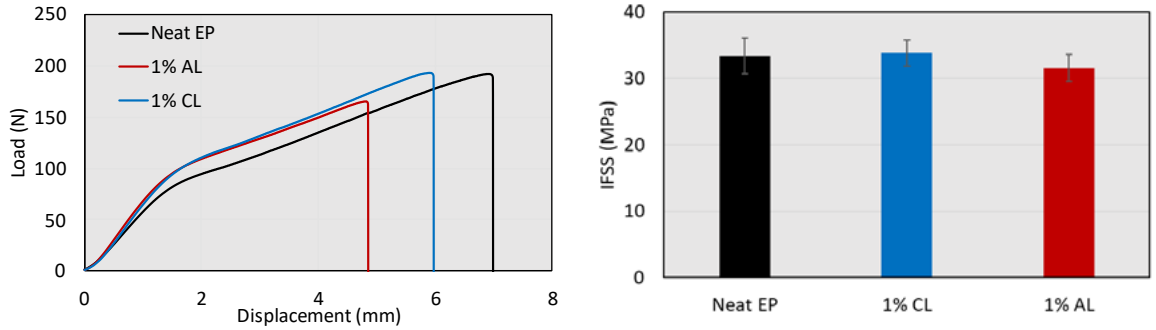

Figure 5. Pullout test results. Left) representative load-displacement curves; right) IFSS of Neat EP and 1% lignin modified composites

4. Conclusions

Partially bio-based epoxy resin was developed by the incorporation of lignin as a natural modifying filler. Two types of lignin powder extracted by different technologies are used in varying concentrations to modify commercial epoxy resin. Mechanical, thermal, and interphase properties were evaluated. Overall, test results did not show a clear advantage of one type of lignin over the other. The addition of

any type of lignin caused marginal changes in the mechanical properties of the resin at moderate concentrations (below 5 wt%). Above 5 wt%, negative influence was noticed in flexural strength, thermal stability (reduced *Tg*) and moisture uptake – all mostly attributed to possible agglomerations of lignin particles in the matrix. The role of lignin as a compatibilizer for cellulosic fibers in the epoxy matrix was not evident at the low concentrations tested within the current work. The most notable difference related to lignin origin could only be seen in the *Tg*-values for 5 wt% lignin addition. Complementary tests such as FTIR and more optimized processing parameters (longer sonication time, varying hardener concentration, etc.) could be performed to enable the establishment of more confident conclusions that would need to be correlated to lignin-type reactive groups and depolymerization degree (often seen in molecular weight distribution). Nevertheless, the results reported herewith suggest the potential to use lignin as a sustainable filler in the resin to increase its eco-friendliness by replacing part of the volume with bio-derived carbon content with no significant negative impact on the performance.

Acknowledgments
The authors would like to acknowledge Ms. Jessica Lindén (master's student within the course T7009T at LTU, Autumn 2023) for her contribution to the production of part of the experimental data. Marcus Elmer, CEO of SunCarbon AB is also acknowledged for his efforts in the work.

References

[1] V. Mittal, R. Saini, and S. Sinha, *Natural fiber-mediated epoxy composites - A review*, Composites part B Engineering, vol. 99, 2016, doi: 10.1016/j.compositesb.2016.06.051.
[2] H. Santamala, R. Livingston, H. Sixta, M. Hummel, M. Skrifvars, and O. Saarela, *Advantages of regenerated cellulose fibres as compared to flax fibres in the processability and mechanical performance of thermoset composites*, Composites Part A Applied Science and Manufacturing, vol. 84, pp. 377–385, 2016, doi: 10.1016/j.compositesa.2016.02.011.
[3] S. Mastrolitti *et al.*, *Sustainable lignin valorization: Technical lignin, processes and market development*, IEA Bioenergy Task 42, October, 2021.
[4] X. Lu and X. Gu, *A review on lignin-based epoxy resins: Lignin effects on their synthesis and properties,* International Journal of Biological Macromolecules, vol. 229. 2023. doi: 10.1016/j.ijbiomac.2022.12.322.
[5] J. S. Yeo, J. H. Lee, and S. H. Hwang, *Effects of lignin on the volume shrinkage and mechanical properties of a styrene/unsaturated polyester/lignin ternary composite system*, Composites part B Engineering, vol. 130, 2017, doi: 10.1016/j.compositesb.2017.07.084.
[6] F. Gortner, A. Schüffler, J. Fischer-Schuch, P. Mitschang, and P. Bachmann, *Influence of fungal decay on mechanical properties of bio-based sheet molding compounds (SMC),* Polymers and Polymer Composites, vol. 30, 2022, doi: 10.1177/09673911221145050.
[7] B. Kumar *et al.*, *Recent research progress on lignin-derived resins for natural fiber composite applications*," Polymers, vol. 13, no. 7. 2021. doi: 10.3390/polym13071162.
[8] S. Zeng, T. Zhang, M. Nie, G. Fei, and Q. Wang, *Effect of root-like mechanical-interlocking interface in polypropylene /aramid fiber composites from experimental to numerical study*, Composites part B Engineering, vol. 216, 2021, doi: 10.1016/j.compositesb.2021.108868.
[9] A. Hajlane, R. Joffe, and H. Kaddami, *Cellulose nanocrystal deposition onto regenerated cellulose fibres: effect on moisture absorption and fibre–matrix adhesion,* Cellulose, vol. 25, no. 3, 2018, doi: 10.1007/s10570-018-1680-z.
[10] C. P. Pappa, S. Torofias, and K. S. Triantafyllidis, *Sub-Micro Organosolv Lignin as Bio-Based Epoxy Polymer Component: A Sustainable Curing Agent and Additive*, ChemSusChem, vol. 16, no. 13, 2023, doi: 10.1002/cssc.202300076.

ECCM21

02-05 July 2024 | **Nantes - France**

Volume 2

Material science

ISBN: 978-2-912985-01-9
DOI: 10.60691/yj56-np80